CODEN: JASMAN 4966

THE JOURNAL of the Acoustical Society of America

Vol. 106, No. 1 July 1999

SOUNDINGS SECTION

GENERAL LINEAR ACOUSTICS [20]

NONLINEAR ACOUSTICS [25]

AEROACOUSTICS, ATMOSPHERIC SOUND [28]

(Continued)

CONTENTS—*Continued from preceding page*

UNDERWATER SOUND [30]

ULTRASONICS, QUANTUM ACOUSTICS, AND PHYSICAL EFFECTS OF SOUND [35]

STRUCTURAL ACOUSTICS AND VIBRATION [40]

NOISE: ITS EFFECTS AND CONTROL [50]

ARCHITECTURAL ACOUSTICS [55]

ACOUSTIC SIGNAL PROCESSING [60]

PHYSIOLOGICAL ACOUSTICS [64]

(Continued)

CONTENTS—*Continued from preceding page*

PSYCHOLOGICAL ACOUSTICS [66]

SPEECH PRODUCTION [70]

SPEECH PERCEPTION [71]

SPEECH PROCESSING AND COMMUNICATION SYSTEMS [72]

MUSIC AND MUSICAL INSTRUMENTS [75]

BIOACOUSTICS [80]

LETTERS TO THE EDITOR

(Continued)

CONTENTS—*Continued from preceding page*

ERRATA

ACOUSTICS RESEARCH LETTERS ONLINE

CUMULATIVE AUTHOR INDEX

NOTES CONCERNING ARTICLE ABSTRACTS

1. The number following the abstract copyright notice is a Publisher Item Identifier (PII) code that provides a unique and concise identification of each individual published document. This PII number should be included in all document delivery requests for copies of the article.
2. PACS numbers are for subject classification and indexing. See June and December issues for detailed listing of acoustical classes and subclasses.
3. The initials in brackets following the PACS numbers are the initials of the JASA Associate Editor who accepted the paper for publication.

Fault detection in engines through higher order spectral analysis of acoustic signatures

G. D. Meegan, H.R. Nelson, M. L. Barlett, and G. R. Wilson

Applied Research Laboratories, The University of Texas at Austin,
P.O. Box 8029, Austin, Texas 78713-8029, USA
meegan@arlut.utexas.edu barlett@arlut.utexas.edu wilson@arlut.utexas.edu

Abstract: This paper describes new engine fault detection methods that involve a higher order spectral analysis method known as the parametric spectral coherence (PSC). Measurements of radiated acoustic and vibrational signatures were conducted on a one-cylinder engine with a continuously worsening loss of cylinder compression. Compared to vibrational signatures, the radiated acoustic signatures provided the most dramatic indication of a loss of cylinder compression when PSC analysis was performed. It is demonstrated that the fault can be detected by simply monitoring the average spectral coherence or the peak spectral coherence of the acoustic signature, whereas the more traditional power spectral methods fail to detect the fault.

PACS numbers: 43.50.Yw, 43.60.Cg, 43.60.Lq

Introduction

The concept of machinery monitoring for the detection of faulty operation is not new. However, very little work has been done on monitoring and detecting faults in internal combustion engines. This deficiency seems to be due at least in part to the relative complexity of vibrational and acoustic signatures that are generated by internal combustion engines as compared with simpler rotating machinery. Nonetheless, if an effectivemethod of early fault detection in engines can be developed, engine maintenance costs can be reduced and reliability increased though the use of a predictive maintenance (PdM) or condition based maintenance (CBM) method. With CBM, a repair is performed only as needed—for example, when the engine starts to run poorly. With PdM, maintenance is performed only when a need for repair is *predicted*, according to some method of detecting a problem with the engine. Thereby, maintenance costs decrease and reliability increases.[1]

A typical application of machinery monitoring involves monitoring the vibration or acoustic power spectra of a machine for comparison with known spectra of normal and abnormal machinery. This method is widely used in detecting defects in rotating machinery such as turbines and electric motors. Some machinery monitoring devices are fully automated systems that continuously analyze power spectra. An alarm is triggered when an absolute spectral amplitude threshold is exceeded, indicating that a vibration at a specific frequency is unusually large.[2,3] This concept is illustrated in Fig. 1 where a power spectral acceptance envelope, as defined from historical data, is used to define the normal operation of a machine. In this case, we see that the spectral lines at $3f_0$ and $5f_0$ have exceeded the acceptance threshold—this indicates that there may be a problem.

Unfortunately, power spectral analysis methods of detecting faults in internal combustion engines are much less reliable than detecting faults in turbines and electric motors. The vibrational and acoustic signatures of internal combustion engines typically contain a complicated series of harmonics of the engine firing rate, which, itself, varies with throttle level or engine RPM.[4-6] In contrast, an electric motor typically operates at a fixed RPM and produces vibrations dominated by a single frequency equal to the rotation rate. The complicated spectral signatures of normally operating internal combustion engines make it

impossible to define a simple but effective spectral envelope for detecting faulty operation or imminent failure.

The application of higher order spectral analysis methods for the detection or classification of machinery faults has only recently been studied.[7,8] Unlike a power spectral analysis, a higher order spectral analysis provides a quantitative measure of spectral coherences that may exist in a vibrational or acoustic signature. These spectral coherences are independent of spectral power and indicate the existence of a nonrandom phase relationship between frequency pairs. Here we shall apply a higher order spectral analysis technique known as the parametric spectral coherence *C* defined by[7]

$$C(\omega_1,\omega_2) \quad = \quad \frac{\langle A(\omega_1)A(\omega_2)e^{j[\phi(\omega_1)-\frac{\omega_1}{\omega_2}\phi(\omega_2)]}\rangle}{\sqrt{\langle A^2(\omega_1)\rangle\langle A^2(\omega_2)\rangle}} \tag{1}$$

where < > denotes time averaging, and $A(\omega)$ and $\phi(\omega)$ are the magnitude and phase of the Fourier transform of a time series $x(t)$ defined according to

$$x(t) = \int_{-\infty}^{\infty} A(\omega)e^{j\phi(\omega)}e^{j\omega t}d\omega \tag{2}$$

From Eq. (1), it is apparent that *C* is a function of frequency pairs ω_1 and ω_2 and ranges from zero to one. *C* is nonzero when the following parametric phase relationship exists:[7]

$$\phi(\omega_1) \quad = \quad \frac{\omega_1}{\omega_2}\phi(\omega_2) + \text{constant} \tag{3}$$

Therefore, unlike more common higher order spectral analyses (i.e., the bispectrum), the parametric spectral coherence does not require frequency pairs to be harmonically related. For example, an engine or motor with reduction gearing will produce nonharmonically related frequencies that would go undetected with the bispectrum, whereas the parametric spectral coherence will detect all coherent tonals.

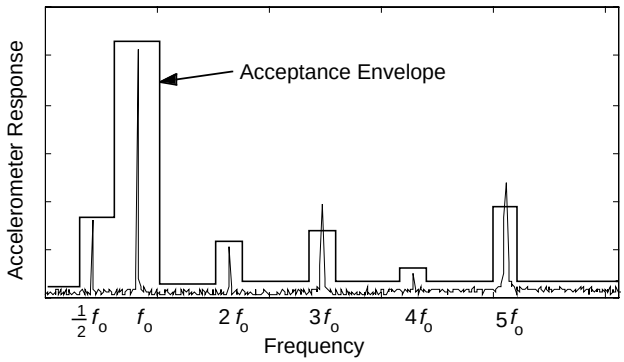

Fig. 1. Acceptance envelope method of power spectral fault detection.

Experiments

Figure 2 shows the experimental setup for the sound and vibration measurements on a single piston, two-stroke model airplane engine of 12.3 cm^3 displacement, known as the Super Tigre 75. The propeller was removed for the measurements reported here. Probe tube microphones were used for insertion into the exhaust manifold and at the tailpipe. The on-axis farfield acoustic signature was measured with a 1/4 inch B&K microphone with a foam wind screen. Engine vibrations were also measured with an accelerometer that was attached to the engine mount. The axis of the accelerometer was placed in line with the axis of piston motion (perpendicular to the page in Fig. 2).

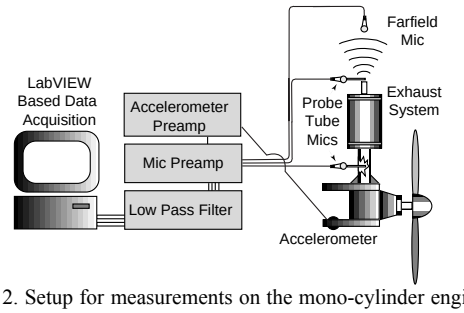

Fig. 2. Setup for measurements on the mono-cylinder engine.

An initial set of data on the mono-cylinder engine was collected under normal engine operation at constant throttle. Following these measurements, a fault was gradually induced in the engine by loosening the seal on the engine glow plug. This created a loss of compression in the cylinder by allowing some gas to escape from the glow plug tap on the cylinder head. On this particular engine, the glow plug could be loosened and tightened while collecting acoustic and vibrational data on the running engine. This allowed for measurement of progressive failure of the engine to the point that the engine stalls out.

Data analysis

In this section, data and analysis results are presented from the farfield acoustic measurements of a progressively worsening loss of cylinder compression in the one-cylinder engine. Results obtained from accelerometer and probe tube microphone sensors are qualitatively similar to those obtained from the farfield microphone. However, the farfield microphone sensor data yielded the most dramatic indication of faulty engine operation. This may be due to the particular type of fault we are studying here. Specifically, a loss of cylinder compression will have a direct effect on the pressure amplitude of the exhaust pulses generated with each combustion event. These exhaust pulses are the acoustic source that propagates through the exhaust system and to the farfield microphone. By comparison, one might expect that the engine block vibrations are only weakly coupled to the combustion events. Other types of faults, such as a main bearing failure, may be most strongly coupled to engine block vibrations and most easily detected through an analysis of vibrational signatures.

Power spectral plots of the farfield acoustic signature, averaged over consecutive time segments of the measurement, are shown in the left panel of Fig. 3. In general, the power spectrum is characterized by a complicated series of harmonics of the engine firing rate (120 Hz, in this case). Modeling results not reported here suggest that the underlying spectral noise floor is due largely to the acoustic response characteristics of the exhaust system. As the loss of compression worsens (towards the bottom of the figure), a suppression of distinct tonals is observed in the spectral data. Similar results were observed in the analysis of accelerometer and probe tube microphone data. Therefore, one may conclude that the fault is detectable through standard power spectral analysis methods. However, when an acceptance envelope is applied to the power spectral analysis results, fault detection is not successful. This failure is illustrated in the left panel of Fig. 3 where a possible acceptance envelope is overlaid on the power spectra—the faulty engine operation would go undetected by this method. Unlike much simpler rotating machinery, the series of harmonics that are present in normally functioning engines limit the usefulness of the power spectral acceptance envelope method. The effect of some faults in internal combustion engines is often a more subtle distortion of the power spectra that can be very difficult to detect by an automated vibration or noise monitoring system. For comparison, the results of a parametric spectral coherence analysis are shown in Fig. 4. The parametric spectral coherence is a function of frequency pairs ω_1 and ω_2 and is normalized to the power spectra according to Eq. (1). Notice that the diagonal (where $\omega_1 = \omega_2$) is identically 1, indicating that a tonal is always perfectly coherent

with itself. The loss of compression is found to be observable in the PSC analysis as a general loss of coherence. In the following section, methods for defining a simple coherence fault detector are presented that can be applied in much the same way as the acceptance envelope demonstrated in Fig. 1.

Coherence fault detector

The simplest type of coherence fault detector investigated here is a measure of the mean parametric spectral coherence. The mean parametric spectral coherence was calculated by simply averaging the coherence in Fig. 4, excluding the diagonal $\omega_1 = \omega_2$, over all frequency pairs to obtain a single measure of coherence in a given time interval. In this way, the analysis presented in Fig. 4 is reduced to the single point mean coherence measurements shown in Fig. 5. The mean coherence is well correlated to the progressive loss of cylinder compression as is detected by a loss of mean coherence. Therefore, mean coherence could be used as a simple metric for the development of automated methods of monitoring internal combustion engines for the detection of some types of faults. Two approaches are suggested: (1) A mean coherence threshold could be defined as shown in Fig. 5, based on machine history. A fault alarm would then be triggered when the mean coherence falls below the acceptable limit. (2) Trending methods could also be applied that may not require knowledge of machine history. For example, the rate of change in the mean coherence (the slope in Fig. 5) could be monitored so that a sudden change would indicate an engine fault.

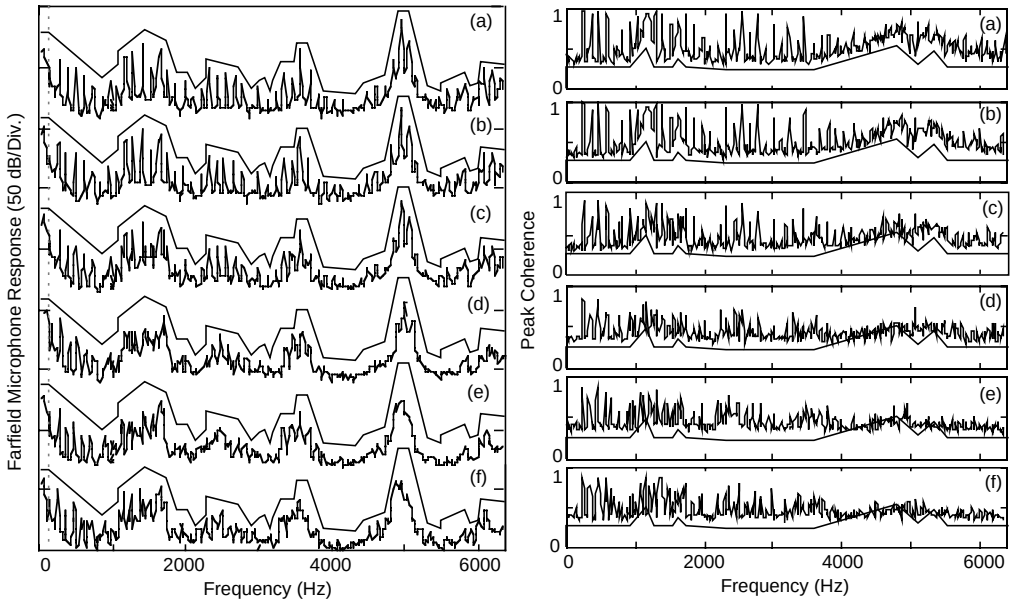

Fig. 3. Analysis of farfield acoustic signatures at time intervals (a) 0 to 4.8 seconds, (b) 4.8 to 9.6 seconds, (c) 9.6 to 14.4 seconds, (d) 14.4 to 19.2 seconds, (e) 19.2 to 24.0 seconds, and (f) 24.0 to 28.8 seconds. The loss of cylinder compression begins at 8 seconds and gradually increases. Left: Consecutive plots of the power spectral average as calculated from the farfield microphone measurement on the one-cylinder engine. The microphone was placed 57 cm from the tailpipe. A suppression of spectral lines is observed above 1 kHz when there is a loss of cylinder compression. The engine firing rate is 120 Hz and is indicated by the vertical dashed line. The power spectral acceptance envelope method fails to detect the fault. Right: The parametric spectral coherence was collapsed to a simpler plot of peak spectral coherence as a function of a single frequency. A $\Delta\omega = 200$ Hz main lobe mask was applied. The peak spectral coherence acceptance envelope method was successful in detecting the presence of a fault.

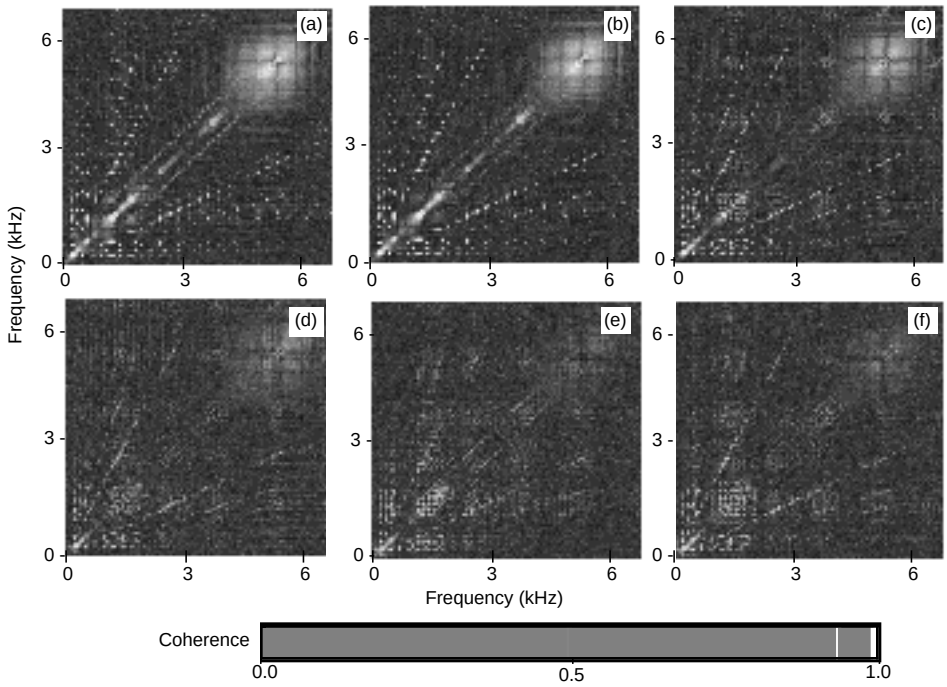

Fig. 4. The parametric spectral coherence was calculated for the farfield microphone measurements on the mono-cylinder engine at consecutive time intervals. A substantial loss of coherence occurs after the one-cylinder engine loss of compression at 8 seconds. The consecutive time intervals are: (a) 0 to 4.8 seconds, (b) 4.8 to 9.6 seconds, (c) 9.6 to 14.4 seconds, (d) 14.4 to 19.2 seconds, (e) 19.2 to 24.0 seconds, and (f) 24.0 to 28.8 seconds.

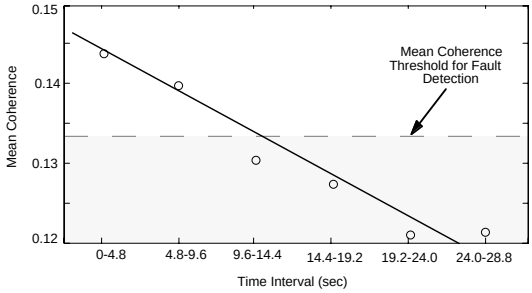

Fig. 5. The mean parametric spectral coherence was applied as a method of detecting the loss of compression. The dashed line specifies a coherence threshold alarm that is capable of detecting the fault.

The parametric spectral coherence can be plotted as a function of a single frequency to generate a waterfall plot, as is commonly used to track changes in the power spectra. The peak coherence C_p is defined here as a function of ω_1 according to

$$C_p(\omega_1) = C(\omega_1, \omega_2 = \omega_{max}), \qquad \omega_1 \neq \omega_{max} \tag{4}$$

where ω_{max} is the value of ω_2 that has the *maximum* coherence at coordinate $\omega_1 \neq \omega_2$. Collapsing Fig. 4 according to Eq. (4) results in the loss of distinct spectral peaks that are obvious in Fig. 4. This difficulty is because the peak coherence is dominated by the response

of the parametric spectral coherence near $\omega_1 = \omega_2$ (near the diagonal in Fig. 4). Although Eq. (4) requires $\omega_1 \neq \omega_2$, the $\omega_1 = \omega_2$ self-coherent tonals result in strong sidelobes in the two-dimensional space (ω_1, ω_2). Therefore, the sidelobes near $\omega_1 = \omega_2$ should be masked before calculating a peak coherence at a frequency ω_1. This calculation was accomplished by excluding the coherence for $|\omega_1 - \omega_2| < \Delta\omega$ so that we calculate the peak coherence as a function ω_1 according to

$$C_p(\omega_1) = C(\omega_1, \omega_2 = \omega_{max}), \qquad |\omega_1 - \omega_{max}| > \Delta\omega \tag{5}$$

where $\Delta\omega$ is the width of the $\omega_1 = \omega_2$ sidelobe to be nulled.

In the right panel of Fig. 3, we present the peak coherence as calculated from Eq. (5) with a sidelobe nulling of $\Delta\omega = 200$ Hz. We find that the resulting plots of peak coherence show clear tonal peaks corresponding to harmonics of the engine firing rate. As the loss of compression increases, we see clear evidence in the peak coherence analysis. In the right panel of Fig. 3, we also demonstrate how a lower limit acceptance envelope (minimum coherence criteria as a function of ω) successfully detects the fault when coherences drop below normal levels. Unlike the standard power spectral acceptance envelope method demonstrated on the left panel of Fig. 3, the peak coherence envelope provides effective fault detection.

Summary and conclusions

A series of acoustic measurements was conducted on properly functioning internal combustion engines and engines with progressively worsening faults. Results indicate that it is possible to detect faulty engine operation by monitoring either the power spectra or the parametric spectral coherence. However, standard approaches such as a power spectral acceptance envelope method fail to detect the fault. By comparison, PSC analysis was shown to provide new methods of fault detection that could easily be automated. The mean spectral coherence and peak spectral coherence analysis methods presented here could provide the basis for automated fault detection and classification systems for a wide range of machinery types.

Acknowledgments

This work was supported by the Office of Naval Research, contract number N00014-96-1-0298-7.

References

1 E. F. Pardue, K. R. Plety, and R. Moore, "Elements of reliability-based machinery maintenance," *Sound and Vib.,* 14-20, May (1992).

2 R. M. Jones, "A guide to the interpretation of machinery vibration measurements—Part I," *Sound and Vib.,* 24-35, May (1994).

3 R. M. Jones, "A guide to the interpretation of machinery vibration measurements—Part II," *Sound and Vib.,* 12-20, September (1994).

4 M. L. Munjal, *Acoustics of Ducts and Mufflers with Application to Exhaust and Ventilation System Design,* (Wiley, New York, 1987).

5 R. Hickling and M. M. Kamal, *Engine Noise: Excitation, Vibration, and Radiation,* (Plenum, New York, 1982).

6 D. E. Baxa, *Noise Control in Internal Combustion Engines,* (Wiley, New York, 1982).

7 K. W. Baugh, "Parametric phase coupling in the vibration spectra of rolling element bearings," *Mech. Systems and Signal Proc.,* 215-228, **8**, No. 2 (1994).

8 G. D. Meegan, H. R. Nelson, M. L. Barlett, and G. R. Wilson, "Analysis of engine noise for application in predictive maintenance," *J. Acoust. Soc. Am.,* **101**, No. 5, Pt. 2, 3029, (1997).

Turbulent acoustic streaming excited by resonant gas oscillation with periodic shock waves in a closed tube

Takeru Yano

Department of Mechanical Science, Hokkaido University, Sapporo, 060-8628, Japan
yano@mech-me.eng.hokudai.ac.jp

Abstract: Resonant gas oscillations with periodic shock waves in a closed tube are studied by executing large-scale computations of the compressible 2-D Navier–Stokes equations with a finite-difference method. In a quasi-steady state of oscillation, acoustic streaming (mean mass flow) of large Rs is excited, where Rs is the streaming Reynolds number based on a characteristic streaming velocity, the tube length, and the kinematic viscosity. When Rs $=$ 560, relatively strong vortices are localized near the tube wall. The resulting streaming pattern is almost stationary but quite different from that of the Rayleigh streaming. The streaming of Rs $= 6200$ involves unsteady vortices in a region near the center of the tube. Turbulent streaming appears in the result of Rs $= 56000$, where vortices of various scales are irregularly generated throughout the tube.

PACS numbers: 43.25.Cb, 43.25.Gf, 43.25.Nm

Introduction

We shall consider the streaming motions excited by fundamental resonant gas oscillation in a two-dimensional closed tube filled with an ideal gas. The tube, whose length is L and width is W, is closed at one end by a solid plug and the other by a piston (sound source) oscillating harmonically with an amplitude a and angular frequency ω (see Fig. 1). When the source frequency is in a narrow band around a resonant frequency, the resulting gas oscillation may not be a sinusoidal standing wave with fixed loops and nodes but a nonlinear oscillation of large amplitude including periodic shock waves traveling in the tube repeatedly reflected at the sound source and closed end.[1]

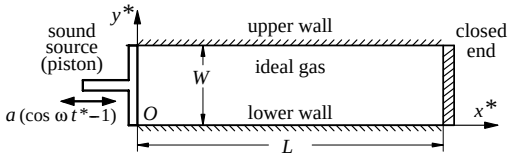

Fig. 1. Schematic of the model.

Such large-amplitude oscillations can induce streaming motions of large streaming Reynolds number Rs $= U_{\rm S}L_{\rm S}/\nu$, where $U_{\rm S}$ is a characteristic magnitude of streaming, $L_{\rm S}$ is a linear dimension of the system, and ν is the kinematic viscosity. It is known that the jet-like streaming of Rs $\gg 1$ usually becomes a turbulent flow.[2,3] However, the excitation of turbulent streaming in a resonant tube has remained unsolved. In the present study, we shall numerically demonstrate when and how the streaming motion in the tube becomes turbulent. Because very large-scale (extensive) computations are required, we restrict ourselves to the case in which the angular frequency at the sound source, ω, is equal to the fundamental resonance (angular) frequency $c_0\pi/L$, where c_0 is the speed of sound in an initially undisturbed gas.

In practical applications of high-intensity resonant oscillations in a closed tube,[4] the excitation of large Rs streaming may often be inevitable. The knowledge of classical streaming induced by the linear sinusoidal standing wave with fixed loops and nodes is useless because

there should be a steady creeping motion of Rs < 1.[5–7] An understanding of large Rs and turbulent streaming may be indispensable for the development of such applications.

Problem

We shall consider the fundamental resonance in a closed tube in a case of a wide tube and low frequency. That is, the tube length L satisfies the condition

$$L\omega/c_0 = \pi, \tag{1}$$

and the width W is sufficiently large compared with the typical dimension of the Stokes boundary layer on the wall,

$$W\omega/c_0 = A\pi \gg \epsilon = \sqrt{\nu\omega}/c_0, \tag{2}$$

where $A = W/L$ is an aspect ratio of the tube, and ϵ is a normalized typical linear dimension of the Stokes boundary layer on the wall.

The sound source is a piston located at $x = 0$ for $t < 0$, which begins oscillating harmonically with amplitude a and angular frequency ω at $t = 0$, where $x = x^*\omega/c_0$ and $t = \omega t^*$. The acoustic Mach number at the source, M, is supposed to be sufficiently small compared with unity,

$$M = a\omega/c_0 \ll 1. \tag{3}$$

In the present study, we assume that the order of M is comparable with that of ϵ, i.e.,

$$\alpha = \epsilon/M = O(1), \tag{4}$$

where α is a nondimensional constant. The acoustic Reynolds number at the sound source may then be given as

$$\mathrm{Re} = 2\pi/\epsilon\alpha, \tag{5}$$

which is sufficiently large compared with unity. In addition to condition Re $\gg 1$, if the dispersion and attenuation effects[8] due to the Stokes boundary layer are sufficiently small, a shock with a discontinuous wave front will be formed. The dispersion effect can be estimated by a nondimensional parameter $\epsilon/(A\sqrt{M})$, because, as shown below (see also Ref. 1), a nondimensional wave amplitude at a quasi-steady state (an almost steady state of gas oscillation) is of $O(\sqrt{M})$. Conditions (3) and (4) ensure that the wave amplitude increases to $O(\sqrt{M})$. By the second-order nonlinear effect, the streaming of $O(M)$ is induced, whose Reynolds number Rs is large so that streaming may exhibit a transition from laminar to turbulent.

Under conditions (1)–(4), we shall numerically solve the initial- and boundary-value problem of the two-dimensional Navier–Stokes equations for compressible flow. We assume that the temperature on the solid surface is constant. The gas in the tube is considered to be air (the ratio of specific heats is 1.4 and the Prandtl number is 0.7). Sutherland's formula is adopted for the temperature dependence of shear viscosity, and the bulk viscosity is neglected for simplicity. The flow field is supposed to be symmetric around $y = A\pi/2$, where $y = y^*\omega/c_0$.

Numerical method

We have to use a numerical method capable of resolving discontinuous shock waves. Therefore an upwind finite-difference TVD scheme[9] is employed, because the capability of the method has already been confirmed in the analysis of the near field of oscillating circular piston.[10] The 2-D Navier–Stokes equations are directly solved without introducing further assumptions. The turbulent streaming motion is not artificially excited but self-generated in the numerical solution for the case of sufficiently large Rs.

In many cases, the two-dimensional assumption is suitable for gas oscillation but, in reality, the excited turbulent motion may have a three-dimensional characteristic. Nevertheless, we can obtain valuable information from 2-D direct simulations. The execution of 3-D simulations would be extraordinarily expensive for the present problem.

The lower half of the tube, $M(\cos t - 1) \le x \le \pi$ and $0 \le y \le A\pi/2$, is subdivided into a 300×60 nonuniform mesh, where the minimum grid size is less than $\epsilon/4$. Mesh points

are clustered near the solid surface, and hence we can resolve the Stokes boundary layer and a secondary boundary layer of thickness of $O(1/\sqrt{\mathrm{Rs}})$.[2,3] The time step is $2\pi/120000$, and the CFL number is about 0.5. To clarify the transition process to turbulent streaming, very lengthy computations are required. For example, the cpu time for 250 cycles of piston oscillation exceeds 200 hours on the supercomputer at Hokkaido University.

As a preliminary test, we have calculated the case of $M = 0.0004$ and $\epsilon^2 = 0.0001$ ($\mathrm{Re} = 25$), where shock waves are not formed, and a steady creep flow of $\mathrm{Rs} = 0.5$ is induced. The streaming motion quantitatively agrees with those in Refs. 5–7. The results presented in the following have been validated by verifying the convergence that resulted from comparing the results obtained with different mesh sizes.

The important parameters that characterize the present problem are the source Mach number M, the normalized thickness of the Stokes layer, ϵ, and the aspect ratio A: $A = 0.1$ and ϵ is chosen as 4.5×10^{-4}. The latter corresponds to the source frequency $\omega/2\pi = 250$Hz in the air of the standard state. We have computed three cases of $M = 0.000036, 0.0004$, and 0.0036. The parameters and results are summarized in Table 1. Short animations of main results can be seen at URL: http://www.hucc.hokudai.ac.jp/~b11422.[11]

Table 1. Parameters and main results.

Mach number at Source	SPL* (Source)	SPL** (Max)	$\mathrm{Rs} = \frac{\pi}{\alpha\epsilon}$	$\frac{\epsilon}{A\sqrt{M}}$	Shock	Streaming
0.000036	104.9dB	147.5dB	560	0.75	finite thickness	stationary flow pattern
0.0004	125.8dB	161.9dB	6200	0.23	discontinuity	unsteady
0.0036	144.9dB	172.4dB	56000	0.08	discontinuity	turbulent

* SPL for the plane progressive sinusoidal wave radiated by the corresponding sound source.
** SPL based on the rms value of pressure perturbation at closed end in the quasi-steady state.

Resonant gas oscillation with periodic shock waves

First, we shall present the evolution of on-axis velocity amplitude from the initial state of uniform and at rest (Fig. 2). The amplitude initially grows in proportion to Mt. At a large t of $O(1/\sqrt{M})$, an almost steady state (quasi-steady state) is established, where the maximum amplitude of oscillation during one period is almost constant of $O(\sqrt{M})$. The quasi-steady state is supported mainly because of the balance of energy input at the source and energy dissipation at the shock front.

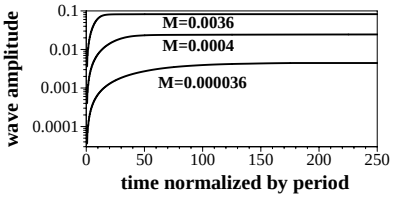

Fig. 2. Evolution of velocity amplitude on the symmetric axis, which is evaluated as the maximum of u minus the minimum of u at $t = n\pi/2$ ($n = 0, 1, 2, ...$), where $u = u^*/c_0$ is the axial component of nondimensionalized fluid velocity.

Figure 3 shows the wave profiles in the quasi-steady state. A wire-framed yellow disk in the figure is merely a virtual image of the sound source. Note that our computations are neither three-dimensional nor axisymmetric. Since $\epsilon/(A\sqrt{M})$ is not so small for $M = 0.000036$ (see Table 1), the dispersion effect due to boundary layer prevents the shock front from becoming steepened [Figs. 3(a) and 3(b)]. For the cases of $M = 0.0004$ and 0.0036, the shock front develops into a discontinuity. From Figs. 3(a), 3(c), and 3(e), one can readily see that the profile of axial fluid velocity has a small peak in the boundary layer (Richardson's annular effect).

Roughly speaking, the fluid motion outside the boundary layer can be regarded as the superposition of resonant oscillation and streaming motion. Accordingly, in the case in which

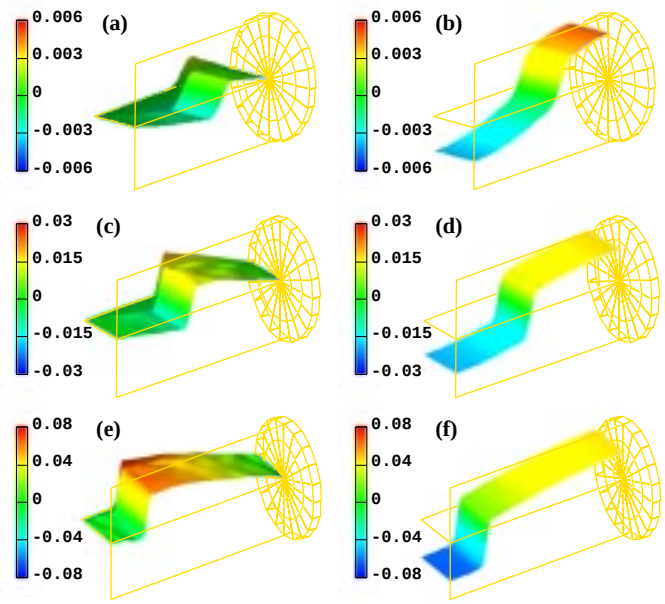

Fig. 3. Snapshots of wave profiles of the normalized axial velocity $u = u^*/c_0$ and sound pressure $p = (p^* - p_0)/\rho_0 c_0^2$. (a) u and (b) p for $M = 0.000036$ at $t = 879.5\pi$, (c) u and (d) p for $M = 0.0004$ at $t = 589.5\pi$, and (e) u and (f) p for $M = 0.0036$ at $t = 461.5\pi$. Each color bar indicates the value of u or p.

the streaming velocity is relatively large and irregular (see Figs. 4 and 5), the axial velocity outside the boundary layer is slightly uneven as shown in Figs. 3(c) and 3(e). Since entropy (and also vorticity) is convected by streaming, the profiles of density and temperature also possess the same unevenness. The pressure profile, on the other hand, is hardly affected by the boundary layer and streaming, and hence is almost independent of the distance from the lower wall.

Excitation of turbulent streaming

The normalized velocity of acoustic streaming (mean mass flow) is defined as

$$\boldsymbol{u}_{\mathrm{S}} = \begin{pmatrix} u_{\mathrm{S}} \\ v_{\mathrm{S}} \end{pmatrix} = \begin{pmatrix} \overline{\rho u} \\ \overline{\rho v} \end{pmatrix} = \frac{1}{2\pi} \int_{t-2\pi}^{t} \begin{pmatrix} \rho u \\ \rho v \end{pmatrix} dt, \tag{6}$$

where $\rho = \rho^*/\rho_0$ is a normalized density, $u = u^*/c_0$ and $v = v^*/c_0$ are x and y components of the normalized fluid velocity, and the bar denotes the time average. A typical streaming velocity in each case is of $O(M)$, i.e., the square of the maximum fluid velocity of $O(\sqrt{M})$. The nominal streaming Reynolds number Rs can therefore be estimated as $\pi/\alpha\epsilon$ (see Table 1). The actual maximum speeds of $\boldsymbol{u}_{\mathrm{S}}$ shown in Figs. 4(a)–4(c) are 1.3cm/s, 59cm/s, and 175cm/s, respectively.

We have confirmed numerically that, as in the linear standing wave problem, u_{S} and v_{S} are nearly equal to $\overline{u}$ and $\overline{v}$ because oscillation of ρ is out of phase with that of fluid velocity and hence the so-called velocity transform[7] is small compared with the magnitude of $\boldsymbol{u}_{\mathrm{S}}$. Because the magnitude of $\mathrm{div}\,\boldsymbol{u}_{\mathrm{S}}$ is sufficiently small almost everywhere compared with that of $\boldsymbol{u}_{\mathrm{S}}$, streaming behaves like a viscous incompressible fluid flow. The perturbation of time-averaged density $\overline{\rho} - 1$ is convected by the streaming motion (the time-averaged pressure is almost independent of it).

The color contours in Fig. 4 indicate the distribution of $\mathrm{curl}\,\boldsymbol{u}_{\mathrm{S}}$. In the case of $M = 0.000036$ (Rs $= 560$), the streaming pattern shown in Fig. 4(a) is almost invariant from $t = 440\pi$ to at least $t = 918\pi$. Because Rs is not small, vorticity in the Stokes layer is hardly diffused and, in addition, the streaming velocity is not large enough to propagate the vorticity in

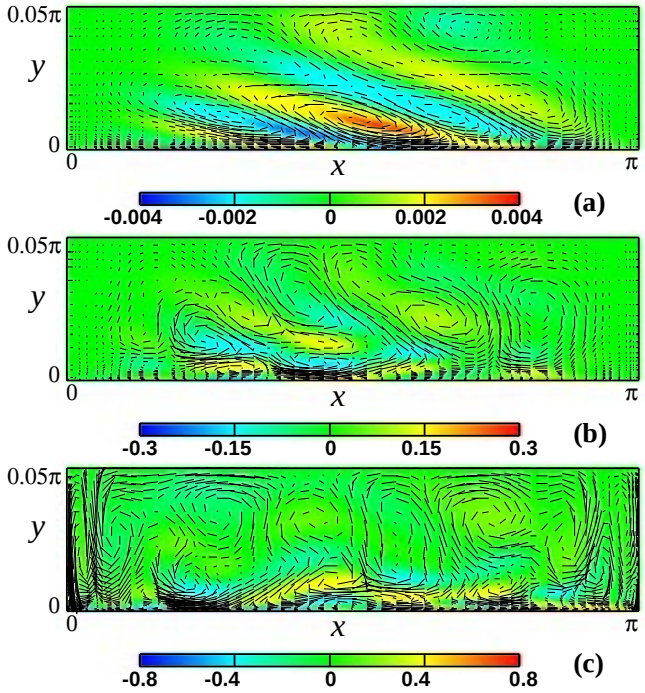

Fig. 4. Streaming patterns. Line segments represent the streaming velocity vector. The color bar denotes the strength of vorticity of streaming. (a): $M = 0.000036$ at $t = 918\pi$ (Rs $= 560$), (b): $M = 0.0004$ at $t = 628\pi$ (Rs $= 6200$), (c): $M = 0.0036$ at $t = 500\pi$ (Rs $= 56000$).

the vicinity of the wall to everywhere in the tube. As a result, some strong vortices are localized near the wall, and the flow pattern in Fig. 4(a) is quite different from that of the classical slow streaming of Rs < 1 excited by the linear standing wave.[5−7] Figure 4(b) shows the streaming pattern for $M = 0.0004$ (Rs $= 6200$), in which several unsteady vortices are produced. They are confined to a region near the center of the tube, at least up to $t = 628\pi$. Turbulent streaming appears in the case of $M = 0.0036$ (Rs $= 56000$), where irregular and unsteady vortices of various scales are produced throughout the tube [see Fig. 4(c) and Fig. 5(c)]. The turbulent motion causes the time-averaged density and temperature to fluctuate irregularly.

Figure 5 shows the temporal evolution of u_{S}/M. Compared with Fig. 2, one can see that u_{S} at $x \cong \pi/2$ grows abruptly when the oscillation attains the quasi-steady state. We here notice that u_{S} is small at $x \cong \pi/2$ in the classical streaming of Rs < 1.[5−7] The actual maximum speeds of u_{S} in Figs. 5(a)–5(c) are 1.2cm/s, 81cm/s and 200cm/s, respectively.

In the case of Rs $= 560$, although the streaming pattern shown in Fig. 4(a) is almost stationary, the local streaming velocity shown in Fig. 5(a) gradually varies for $t > 500\pi$. The axial streaming velocity for Rs $= 6200$ in Fig. 5(b) is unsteady after the oscillation has reached a quasi-steady state. However, we cannot examine whether the fluctuation of streaming is irregular because the numerical result for Rs $= 6200$ is limited to $t \leq 628\pi$; the required computation to answer the question is too large to be executed. In the case of Rs $= 56000$ [Fig. 5(c)], u_{S} fluctuates irregularly throughout the tube for $t > 60\pi$.

Conclusions

We have demonstrated numerically the excitation of turbulent acoustic streaming by resonant gas oscillation in a closed tube. When $M \ll 1$ and $\epsilon = O(M)$ (and hence Re $\gg 1$), shock waves are formed and the resonant gas oscillation attains a quasi-steady state at a large t of $O(1/\sqrt{M})$, where the normalized wave amplitude is of $O(\sqrt{M})$. The magnitude of the resulting acoustic streaming, which is induced by the second-order nonlinear effect of gas oscillation,

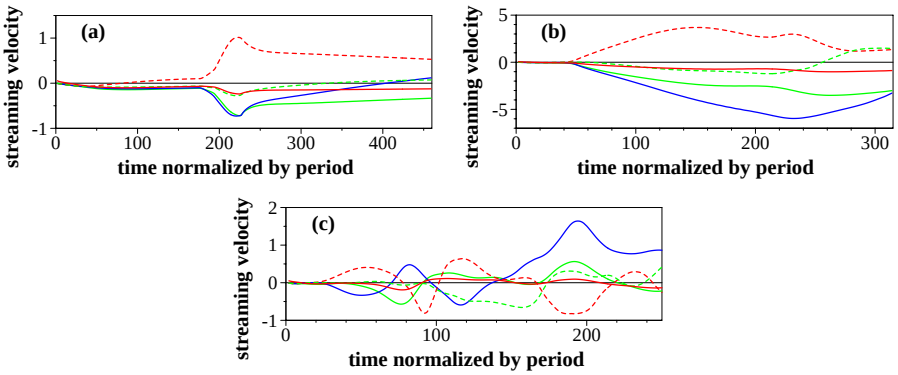

Fig. 5. Time evolution of u_S/M at $x = 1.4084$ and $y = 0.0012$ (red solid curve), $y = 0.0043$ (green solid curve), $y = 0.0130$ (blue solid curve), $y = 0.0348$ (red dashed curve), and $y = 0.0821$ (green dashed curve). (a): $M = 0.000036$ (Rs = 560), (b): $M = 0.0004$ (Rs = 6200), (c): $M = 0.0036$ (Rs = 56000).

is of $O(M)$, namely the streaming velocity is of the same order of magnitude as the piston velocity at the sound source. Accordingly, Rs is as large as Re. The instability of large Rs flow leads to the occurrence of turbulent acoustic streaming.

Finally, we conclude that, in the present computations, the Reynolds number based on the thickness of the Stokes layer is of $O(1)$, and streaming in the Stokes layer is disturbed but, as a whole, remains laminar. If the Reynolds number based on the Stokes layer thickness exceeds its transition Reynolds number, the oscillation in the Stokes layer itself will become turbulent, and the turbulence will occur in periodic bursts followed by a relaminarization in the same cycle of oscillation.[12]

Acknowledgments

The author would like to thank Professor Y. Inoue for his constant encouragement. This work was partially supported by The Sound Technology Promotion Foundation.

References and links

[1] W. Chester, "Resonant oscillations in closed tubes," J. Fluid Mech. **18,** 44–65 (1964).
[2] J. T. Stuart, "Double boundary layers in oscillatory viscous flow," J. Fluid Mech. **24,** 673–687 (1966).
[3] M. J. Lighthill, "Acoustic streaming," J. Sound Vib. **61,** 391–418 (1978).
[4] See, for example, G. W. Swift, "Thermoacoustic engines and refrigerators," Phys. Today **48,** 22–28 (July 1995). See, also, C. C. Lawrenson, B. Lipkens, T. S. Lucas, D. K. Perkins, and T. W. Van Doren, "Measurements of macrosonic standing waves in oscillating closed cavities," J. Acoust. Soc. Am. **104,** 623–636 (1998).
[5] Lord Rayleigh, *The Theory of Sound* (Dover, New York, 1945).
[6] W. L. Nyborg, "Acoustic streaming due to attenuated plane waves," J. Acoust. Soc. Am. **25,** 68–75 (1953).
[7] P. J. Westervelt, "The theory of steady rotational flow generated by a sound field," J. Acoust. Soc. Am. **25,** 60–67 (1953).
[8] M. F. Hamilton, Y. A. Il'inskii, and E. A. Zabolotskaya, "Dispersion," in *Nonlinear Acoustics,* edited by M. F. Hamilton and D. T. Blackstock (Academic Press, San Diego, 1998) pp. 151–175.
[9] S. R. Chakravarthy, "Development of upwind schemes for the Euler equations," *NASA Contractor Report* 4043 (1987).
[10] T. Yano and Y. Inoue, "Strongly nonlinear waves and streaming in the near field of a circular piston," J. Acoust. Soc. Am. **99,** 3353–3372 (1996).
[11] T. Yano, "Turbulent acoustic streaming," http://www.hucc.hokudai.ac.jp/~b11422.
[12] P. Merkli and H. Thomann, "Transition to turbulence in oscillating pipe flow," J. Fluid Mech. **68,** 567–575 (1975).

SOUNDINGS

Section Editor: Richard Stern

This front section of the *Journal* includes acoustical news, views, reviews, and general tutorial or selected research articles chosen for wide acoustical interest and written for broad acoustical readership.

ACOUSTICAL NEWS—USA

Elaine Moran
Acoustical Society of America, Suite 1 NO1, 2 Huntington Quadrangle, Melville, NY 11747-4502

Editor's Note: *Readers of this Journal are asked to submit news items on awards, appointments, and other activities about themselves or their colleagues. Deadline dates for news items and notices are 2 months prior to publication.*

138th Meeting of the Acoustical Society of America Meeting Announcement

The 138th meeting of the Acoustical Society of America (ASA) will be held Monday through Friday, 1–5 November 1999 at the Hyatt Regency Columbus in Columbus, Ohio. Registration will begin Monday, 1 November at 7:30 a.m.

Technical Program and Special Sessions

The technical program will consist of lecture and poster sessions. Technical sessions will be scheduled Monday through Friday, 1–5 November. The special sessions described below will be organized by the ASA Technical Committees/Groups.

Animal Bioacoustics (AB)

Detecting and identifying animals using acoustics
Noise that annoys animals
Signal processing techniques for animal bioacoustics

Architectural Acoustics (AA)

Archeological acoustics (Joint with Musical Acoustics)
Architectural renovation and restoration: Acoustic issues
Integration of synthesized musical instruments with acoustic environments (Joint with Musical Acoustics)
Tribute to Buzz Towne—Classroom acoustics

Biomedical Ultrasound/Bioresponse to Vibration (BB)

Modeling of nonlinear ultrasonic fields (Joint with Physical Acoustics)
Therapeutic applications of ultrasound

Education in Acoustics (ED)

Hands on demonstrations
Integrating acoustics into the curriculum of other academic disciplines
The use of multimedia in acoustics education
Undergraduate laboratory experiments

Engineering Acoustics (EA)

Acoustic nondestructive evaluation: New directions and techniques Part II (Joint with Physical Acoustics and Structural Acoustics and Vibration)
Acoustics of cellular telephones
Compatibility of hearing aids and cellular telephones: Standards progress
Transducer loss mechanisms

Musical Acoustics (MU)

African musical instruments and traditions
Daniel W. Martin tribute session (Joint with Architectural Acoustics)
Free reed instruments
Music, rhythm and development

Noise (NS)

Preservation of natural quiet
Product sound quality
Status of noise regulations

Psychological and Physiological Acoustics (PP)

Honoring the contributions of Robert C. Bilger (Joint with Speech Communication)

Signal Processing in Acoustics (SP)

Identification of structural systems for model validation and health monitoring (Joint with Structural Acoustics and Vibration)
Image signal processing in biomedical ultrasound (Joint with Biomedical Ultrasound/Bioresponse to Vibration)
Signal processing applications for low diffraction beams (Joint with Physical Acoustics)
Time-frequency applications in acoustics
Wavelets in acoustics

Speech Communication (SC)

Bionic ears: Influence on perception and production (Joint with Signal Processing in Acoustics)
From acoustics to words

Structural Acoustics and Vibration (SA)

Acoustic nondestructive evaluation: New directions and techniques Part I (Joint with Physical Acoustics and Engineering Acoustics)
Bridging FEA and SEA
The mid-frequency gap in structural acoustics

Underwater Acoustics (UW)

The effect of man-made sound on marine mammals
(Joint with Acoustical Oceanography and Animal Bioacoustics)
Multiple volumetric scattering
Robert J. Urick memorial session (Joint with Engineering Acoustics)

Tutorial Lecture, Distinguished Lecture, Hot Topics and Other Sessions

The Tutorials Committee has planned a Tutorial Lecture on ''The families of musical instruments: Physics and performance.'' A Distinguished Lecture on ''Smart Structures and Microelectromechanical Systems (MEMS) will be presented by B. T. Khuri-Yakub of Stanford University. A Distinguished Lecture titled ''Implementation of the acoustics reference set'' will be presented by Malcolm Crocker of Auburn University.

The Technical Committee on Architectural Acoustics will sponsor a Vern O. Knudsen Distinguished Lecture to be presented by Lawrence Kirkegaard.

The Committee on Archives and History will jointly sponsor two special lectures on the history of acoustics. The History of Musical Acoustics, jointly sponsored by the Technical Committee on Musical Acoustics, will be presented by Gabriel Weinreich of the University of Michigan. The History of Physical Acoustics, jointly sponsored by the Technical Committee on Physical Acoustics, will be presented by Robert T. Beyer of Brown University and David T. Blackstock of the Applied Research Laboratories, University of Texas at Austin.

 0001-4966/99/106(1)/1/4/$15.00

A ''Hot Topics'' session sponsored by the Tutorials Committee is also scheduled. A special performance session will feature the Ohio State University Marching Band, ''The Best Damn Band in the Land,'' in concert in the hotel ballroom on Thursday afternoon.

Gallery of Acoustics

The Interdisciplinary Technical Group on Signal Processing in Acoustics will sponsor its fourth Gallery of Acoustics at the Columbus meeting. The objective of the Gallery is to enhance ASA meetings by providing a compact and free-format setting for researchers to display their work to all meeting attendees in a forum emphasizing the diversity and interdisciplinary nature of acoustics. The Gallery of Acoustics provides a means by which we can all share and appreciate the natural beauty and aesthetic appeal of acoustical phenomena. The Columbus Gallery will be the first time that audio entries are included.

The Gallery will consist of posters, videos, and audio clips of images and/or sounds generated by acoustic processes or resulting from signal processing of acoustic data. images and videos can consist of actual visualizations of acoustic processes, or of aesthetically and technically interesting images resulting from various signal processing techniques. Audio clips and segments should also have both aesthetic and technical appeal.

Poster entries can be of whatever size and format the author feels best displays the images and information. Video entries must be VHS format, no longer than three minutes long, and should begin and end with a 20 second blank leader and trailer (not counted in the length of the entry). Audio entries can be submitted in digital form (*.wav or *.au files), or recorded on compact disc or standard audio cassette tape. All entries should be accompanied by all author's names and affiliations, and a brief description of the entry (similar in length to the technical session abstracts).

A panel of referees will judge entries on the basis of aesthetic/artistic appeal, ability to convey and exchange information, and originality. A cash prize of $350 will be awarded to the winning entry. The top three entries will, with the author's permission and cooperation, be posted on the Gallery web site.

The relevant deadlines are as follows:

1 Sept.—deadline for notice of intent to submit plus brief description of entry.
8 Oct.—deadline for receipt of all video entries and brief abstracts for all video and still entries
22 Oct.—deadline for receipt of still entries whose authors request that their entries be shipped to the meeting by the Gallery Committee Chair. Otherwise, contributors are responsible for shipping or carrying their still entries to the meeting.
1 Nov.—deadline for receipt in Columbus of entries whose authors have made their own arrangements for shipment to the meeting.

Entries, requests for information, and all other communications regarding the Gallery should be directed to one of the following contacts below:

Randall W. Smith
Northrup Grumman Corporation
Oceanic and Naval Systems
P.O. Box 1488, Mail Stop 9105
Annapolis, MD 21404
Tel: 410-260-5732; Fax: 410-260-5994
E-mail: randall_w_smith@mail.northgrum.com
Web: www.arlut.utexas.edu/asapweb/ (Click on Gallery)

Preston S. Wilson
Dept. of Aerospace and Mechanical Engineering
Boston University
100 Cummington Street, Room 101
Boston, MA 02215
Phone: 617-353-4854 (office) -4859 (lab)
Fax: 617-353-5866
E-mail: psw@bu.edu

Meeting Program

An advance meeting program summary will be published in the September issue of JASA and a complete meeting program will be mailed as Part 2 of the October issue. Abstracts will be available on the ASA Home Page (http://asa.aip.org) in September.

Tutorial Lecture

A Tutorial Lecture on The Families of Musical Instruments: Physics and Performance will be presented by Uwe J. Hansen, Department of Physics, Indiana State University, Terre Haute, IN and James M. Pyne, School of Music, Ohio State University, Columbus, OH, at 7:00 p.m. on Monday, 1 November.

Abstract

The Families of Musical Instruments: Physics and Performance. Uwe J. Hansen (Department of Physics, Indiana State University, Terre Haute, IN 47809) and James M. Pyne (School of Music, Ohio State University, Columbus, OH 43210)

Many researchers in the field of musical acoustics were persuaded to ''convert'' from other fields in order to pursue their ''true love.'' We hope to communicate some of the enjoyment associated with this endeavor by supporting the introduction of scientific concepts with musical examples. We will limit this presentation to discussions of representative examples of each instrument family. During each segment, the relevant instrument will be introduced, and at the conclusion of each section the piece of music performed will feature that instrument. All musical instruments require a power supply and an oscillating element for tone generation, all instruments also rely on resonance for pitch selection. Other structural elements are essential to enhance radiation efficiency to make the instrument audible. Finally, most instruments include mechanisms for pitch control to permit the possibility of melodic variation. The physics of these elements will be discussed for representative instruments along with measurement techniques to probe the secrets of various types of musical instruments. In addition each instrument will be highlighted by a performance of a representative piece of music. The finale will feature combinations of members of all instrument families in an ensemble performance.

Notes

Notes summarizing not only the scientific presentation but also commenting on the musical pieces performed will be available at the meeting. Those who register by 20 September are guaranteed receipt of a set of notes.

Registration

To partially defray the cost of the lecture a registration fee is charged. The fee is $15 for registration received by 20 September and $25 thereafter including on-site registration at the meeting. The fee for students with current ID cards is $7.00 for registration received by 20 September and $12.00 thereafter, including on-site registration at the meeting. Use the registration form in the printed meeting call for papers that was sent to all members in April or online at ⟨http://asa.aip.org/columbus/columbus.html) to register for the Tutorial Lecture.

Student Transportation Subsidies

A student transportation subsidies fund has been established to provide limited funds to students to partially defray transportation expenses to meetings. Students presenting papers who propose to travel in groups using economical ground transportation will be given first priority to receive subsidies, although these conditions are not mandatory. No reimbursement is intended for the cost of food or housing. The amount granted each student depends on the number of requests received. To apply for a subsidy, submit a proposal (E-mail preferred) to be received by 27 September: Elaine Moran, asa@aip.org, ASA, Suite 1NO1, 2 Huntington Quadrangle, Melville, NY 11747-4502, 516-576-2360, Fax: 516-576-2377. The proposal should indicate your status as a student, whether you have submitted an abstract, whether you are a member of ASA, method of travel, whether you will travel alone or with other students, names of those traveling with you, and approximate cost of transportation.

Young Investigator Travel Grant

The Committee on Women in Acoustics is sponsoring a Young Investigator Travel Grant to help with travel costs associated with presenting a paper at the Columbus ASA meeting. This award is designed for young professionals who have completed the doctorate in the past five years (not currently enrolled as a student), who plan to present a paper at the Columbus meeting. Up to $500 in support for travel and lodging costs is available. Applicants should submit a request for support, a copy of the abstract they have submitted for the meeting and a current resume/vita to Jan Weisen-

berger, Speech and Hearing Science, Ohio State University, 1070 Carmack Road, Columbus, OH 43210 (614-292-1281, jan+@osu.edu). Deadline for receipt of applications is 1 September 1999.

Students Meet Members for Lunch

The Education Committee has established a program for students to meet with members of the ASA over lunch. Students are strongly encouraged to contact Scott Sommerfeldt, N241 ESC, P.O. Box 24673, Brigham Young Univ., Provo, UT 84602-4673, USA; Tel: 801-378-2205; E-mail: s_sommerfeldt@byu.edu prior to the meeting. There will also be a sign up sheet available at the registration desk for those students who have not responded prior to the meeting. Members who wish to participate are also encouraged to contact Scott Sommerfeldt. Participants are responsible for the cost of their own meal.

Plenary Session, Awards Ceremony, Fellows' Luncheon and Social Events

Complimentary buffet socials with cash bar will be held early on Tuesday and Thursday evenings at the Hyatt Regency Columbus. The Plenary session will be held on Wednesday afternoon where Society awards will be presented and recognition of Fellows will be announced. A Fellows' Luncheon will be held on Thursday. The speaker will be Lonnie Thompson, Professor of Geological Sciences and Research Scientist at the Byrd Polar Research Center. ASA Fellows may purchase tickets using the registration form in the Call for Papers or online @ ⟨http://asa.aip.org/columbus/columbus.html

Technical Tours

Technical tours have already been arranged to Owens Corning Testing Systems Acoustics Laboratory and Owens Corning Acoustic Room System Demonstrations in Granville, Ohio; and the Center for Automotive Research and the Music Cognition Labs at the Ohio State University in Columbus. At least one tour will be scheduled each day, Monday through Thursday. Bus transportation will be provided at cost. A schedule of tours and sign-up sheets will be available at the meeting.

Exhibit

An equipment exhibition will be held on 2 and 3 November. The exhibition will include active noise control systems, computer-based instrumentation, sound level meters, sound intensity systems, signal processing systems, devices for noise control and acoustical materials, books and other exhibits on acoustics. Organizations interested in exhibiting should contact: Robert Finnegan, Advertising and Exhibits, American Institute of Physics, Suite 1NO1, 2 Huntington Quadrangle, Melville, NY 11747-4502, USA; Tel.: 516-576-2433; Fax: 516-576-2481; E-mail: rgf@aip.org. The contact for questions or information regarding local arrangements is Dick Godfrey, Tel.: 740-321-7085; E-mail: godfrey@owenscorning.com

Assistive Listening Devices

Anyone planning to attend the meeting who will require the use of an assistive listening device, is requested to advise the Society in advance of the meeting by writing to: Acoustical Society of America, Suite 1NO1, 2 Huntington Quadrangle, Melville, NY 11747-4502, asa@aip.org.

Accompanying Persons Program

Accompanying persons are welcome. The accompanying persons registration fees are $35 if paid by 20 September and $45 after 20 September. An accompanying persons hospitality room will be open from 8:00 a.m. to 11:00 a.m. daily, Monday through Friday. Information will be available on local activities including: Columbus City Center downtown shopping mall, Wexner Center for the Visual Arts, Columbus Museum of Art, and events sponsored by the Columbus Association for the Performing Arts. Tours to the Short North and German Village historic neighborhoods, Longaberger Basket Factory, Amish Country, Ohio Historical Center and Ohio Village, and Wright Patterson Air Force Museum are planned. One tour will be scheduled each day. Bus transportation will be provided at cost. A schedule of tours and sign-up sheets will be available at the meeting.

Registration Information

The registration desk at the meeting will open on Monday morning, 1 November, at 7:30 a.m. in the Clark Foyer at the Hyatt Regency Columbus Hotel. Use the registration form in the printed meeting call for papers that was sent to all members in April or online at ⟨http://asa.aip.org/columbus/columbus.html⟩ to register. Registration fees are as follows:

Category	Preregistration by 20 September	Registration after 20 September
Acoustical Society Members	$200	$250
Acoustical Society Members One-Day	$100	$125
Nonmembers	$245	$295
Nonmembers One-Day	$125	$150
Nonmember Invited Speakers (Note: The fee is waived for these speakers if they attend the meeting on the day of their presentation only)	$200	$250
Students (with current ID cards)	Fee waived	Fee waived
Emeritus members of ASA (Emeritus status pre-approved by ASA)	$35	$45
Accompanying Persons	$35	$45

Nonmembers who simultaneously apply for Associate Membership in the Acoustical Society of America will be given a $50 discount off their dues payment for the first year of membership. (Full price for dues: $100).

Invited speakers who are members of the Acoustical Society of America are expected to pay the registration fee, but nonmember invited speakers who participate in the meeting for one day only may register without charge. Nonmember invited speakers who wish to participate in the meeting for more than one day will be charged the member registration fee, which will include a one-year membership in the ASA upon completion of an application form at the meeting.

NOTE: A $25 PROCESSING FEE WILL BE CHARGED TO THOSE WHO WISH TO CANCEL THEIR REGISTRATION AFTER 15 OCTOBER.

Air Transportation

The Columbus International Airport is served by all major airlines and is a hub for America West. The airport designation is CMH.

Ground Transportation

The Hyatt Regency Columbus is located seven miles from Port Columbus International Airport. Transportation from the airport to the hotel may be by car, taxi, shuttle service, or public transportation. The one-way taxi fare is approximately $13 and the shuttle is $16 round trip. Shuttle service is provided by Executive Transportation and can be arranged upon arrival via a courtesy phone located in the baggage claim area at the airport. Public transportation is provided by the Central Ohio Transit Authority (COTA). Take Bus 92, which departs every half hour from the airport, to James & Main, then transfer to bus 2 and get off at Nationwide & High. The Hyatt is located on the northeast corner of this intersection. When boarding Bus 92, pay $1.20 fare and ask for a transfer slip. Services and attractions are located within walking distance from the conference hotel or easily accessible by public transportation.

Room Sharing

ASA will compile a list of those who wish to share a hotel room and its cost. To be listed, send your name, telephone number, E-mail address, gender, smoker or nonsmoker, by 20 September to the Acoustical Society of America, by E-mail: asa@aip.org or by postal mail to Attn: Room Sharing, Suite 1NO1, 2 Huntington Quadrangle, Melville, NY 11747-4502. The responsibility for completing any arrangements for room sharing rests solely with the participating individuals.

Weather

Columbus has a moderate climate and four distinct and colorful seasons. Early November temperatures will range from daytime highs of 50 to 60 degrees F, to nighttime lows of 35 to 45 degrees F. There is always a possibility of rain or even a few snow flurries.

Hotel Reservation Information

Guest rooms at discounted rates have been reserved for conference participants at the Hyatt Regency Columbus. To reserve a room, please contact the hotel directly. Early reservations are strongly recommended. Note that the conference rates are not guaranteed after 1 October. Please reference the Acoustical Society of America when making your reservation.

The Hyatt Regency Columbus is connected to the Greater Columbus Convention Center, in the heart of downtown Columbus, just seven miles from Port Columbus International Airport. Guests can enjoy an indoor swimming pool and exercise room, as well as complimentary shuttle service to downtown shopping and attractions.

Hyatt Business Plan accommodations include express continental breakfast, in-room fax machine, no access charges for ''800,'' local and credit card calls, personal computer hookup and 24-hour access to printers, copiers and office supplies, coffee maker and coffee, iron and ironing board, and USA Today, all for only $20 above the conference rate.

The Hyatt Regency Columbus regrets that it cannot hold your reservation after 6:00 p.m. on the day of arrival without guaranteeing the reservation with either a check or money order deposit covering the first night's room and tax, or a major credit card number with expiration date. Deposits will be refunded only if cancellation is received at least 24 hours prior to arrival. Any changes to departure after check-in will result in a $25.00 administration fee.

A limited number of rooms will be available at the government rate. To obtain this rate, a government ID must be presented at check-in and the room must be charged to a government credit card. Please make your reservations directly with the hotel:

Hyatt Regency Columbus
350 North High Street
Columbus, OH 43215
Tel.: 614-463-1234 or 800-233-1234
Fax: 614-280-3038

Room rates:
$120, plus 15.75% tax. Single or Double
$137, plus 15.75% tax. Triple (3 persons)
$147, plus 15.75% tax. Quad (4 persons)
Add'l $20/room plus tax Business Plan

Reservation cut-off date: 01 October 1999

Regional Chapter News

North Texas

Attendance at the North Texas Regional Science and Engineering Fair was up a modest 10%—about one thousand kids this year. We found thirty-eight acoustic (not acoustic-related, pure acoustic) projects, split equally between Junior and Senior High School Level projects. We reapportioned the $200 in prizes to fund one Senior First Place Award ($100) and two Junior First Place Awards ($50 each):

Junior Awards:

Megan Gallant/Carpenter Middle School: Leafing the Sound Barrier II. Last year Megan explored using landscape plantings as sound barriers. Starting with judges' suggestions from last year, she systematically studied effects of temperature, humidity, and ambient noise level (wind; time of day) on the absolute and relative intensity/loudness of a probe sound (recorded vacuum cleaner noise).

Chelsea Sandberg/Walter and Lois Curtis Middle School: Catch the Wave. Chelsea compared the computed and actual Doppler Shift generated by a moving source (a car horn) at three speeds.

The Senior Award:

Tommy McClure/Ector School: Xtreme Sounds. Tommy redesigned a subwoofer baffle to increase volume and clarity in automotive systems. In blind tests, 18 of 20 people picked his design over standard commercial enclosures. He calibrated against the work of installers who meet or exceed public lab certification. His cabinetwork is superb. What a treat.

The judges at this year's fair were Peter Assmann, Bob Lange, Debbie Rekart, and Mike Daly.

Masters degree program in architectural acoustics at Rensselaer Polytechnic Institute

Dean Alan Balfour of the School of Architecture at Rensselaer Polytechnic Institute in Troy, New York, has announced the University's first Master's Degree in Architectural Acoustics to be initiated and directed by Christopher Jaffe, Founder of Jaffe Holden Scarbrough Acoustics, Inc. of Norwalk, Connecticut.

The course is designed for those individuals interested in becoming professional acousticians and for architects whose interest lies in the degree of performing arts buildings and other public facilities. The program is focused on room acoustic research dedicated to improving predictability factors in architectural acoustic design.

This one year acoustic design and research masters program is accepting applications for the Fall '99. Call or visit RPI's website today for detailed information: 518-276-6478, www.rpi.edu.

USA Meetings Calendar

Listed below is a summary of meetings related to acoustics to be held in the U.S. in the near future. The month/year notation refers to the issue in which a complete meeting announcement appeared.

1999

30 Sept.–2 Oct.	Seventh Annual Conference on the Management of the Tinnitus Patient, Iowa City, IA [Rich Tyler, Dept. of Otolaryngology, Head and Neck Surgery, The University of Iowa, 200 Hawkins Dr., #E230 GH, Iowa City, IA 52242-1078, Tel.: 319-356-2471; Fax: 319-353-6739, E-mail: rich-tyler@uiowa.edu, WWW: http://www.medicine.uiowa.edu/otolaryngology/news/news.html].
7–10 Oct.	Symposium on Occupational Hearing Loss, Philadelphia, PA [American Institute for Voice and Ear Research, Attn: Barbara-Ruth Roberts, 1721 Pine St., Philadelphia, PA 19103, Tel.: 215-545-2068; Fax: 215-735-2725]. Deadline for submission of abstracts: 1 May.
1–5 Nov.	138th meeting of the Acoustical Society of America, Columbus, OH [Acoustical Society of America, Suite 1NO1, 2 Huntington Quadrangle, Melville, NY 11747, Tel.: 516-576-2360; Fax: 516-576-2377; E-mail: asa@aip.org; WWW: asa.aip.org].
2–4 Dec.	ACTIVE '99, Fort Lauderdale, FL [Institute of Noise Control Engineering, P.O. Box 3206 Arlington Branch, Poughkeepsie, NY 12603, Tel.: 914-462-4006; Fax: 914-463-0201; E-mail: INCEUSA@aol.com;/users.aol.com/inceusa/ince.html].
6–8 Dec.	INTER-NOISE 99, Fort Lauderdale, FL [Institute of Noise Control Engineering, P.O. Box 3206 Arlington Branch, Poughkeepsie, NY 12603, Tel.: 914-462-4006; Fax: 914-463-0201; E-mail: INCEUSA@aol.com;/users.aol.com/inceusa/ince.html].

BOOK REVIEWS

James F. Bartram
94 Kane Avenue, Middletown, Rhode Island 02842

These reviews of books and other forms of information express the opinions of the individual reviewers and are not necessarily endorsed by the Editorial Board of this Journal.

Editorial Policy: *If there is a negative review, the author of the book will be given a chance to respond to the review in this section of the Journal and the reviewer will be allowed to respond to the author's comments. [See "Book Reviews Editor's Note," J. Acoust. Soc. Am.* ***81****, 1651 (May 1987).]*

Sounds of our times, two hundred years of acoustics

Robert T. Beyer

Springer Verlag and AIP Press, New York, New York, 1999. xvi + 444 pp. Price $49.95.

Robert T. Beyer, the Hazard Professor of Physics Emeritus at Brown University, is too modest to say so, but he himself is a major protagonist in the realm of modern acoustic history that he surveys in *Sounds of Our Times, Two Hundred Years of Acoustics*. He is that rare breed of individual whose deep knowledge has to be regarded as also being extremely eclectic. A combination of scientist, philosopher, historian, raconteur, linguist, esthete, and whatever, Bob Beyer scintillates as a precious jewel within the fabric of the Acoustical Society of America.

Two principal books on the history of acoustics have been previously published. One is the rather folksy *Anecdotal History of the Science of Sound* by Dayton C. Miller (1866–1941), which was published by Macmillan in 1935. The second is the superb *Origins in Acoustics* by Frederick Vinton Hunt (1905–1972) that covered history up to the eighteenth century. Unfortunately, this book was cut off by Hunt's untimely death; the uncompleted manuscript, edited by Robert Apfel, was published in 1978 by Yale University Press and reissued in 1993 by ASA. In *Sounds of Our Times*, Bob Beyer picks up where Hunt left off. Citing his advanced age, Beyer stated in his Introduction that he was trying to steer a middle course between Miller's anecdotal style and the more scholarly, time-consuming style of F. V. Hunt. But the fact is that Beyer emerged with a work that is truly worthy of a professional historian (who would most likely lack his understanding of acoustics and the chronological perspective); it is scholarly yet it makes a fascinating read. Don't be fooled by the subtitle *Two Hundred Years of Acoustics*—there are many allusions to the past, including the Hellenic era, the Renaissance, etc.

The first chapter describes the state of acoustics in 1800, commencing with the emergence of Ernst E. F. Chladni (1756–1827) and Thomas Young (1773–1829). Chladni wrote *Die Akustik* (Breitkopf and Hartel, Leipzig; 1802), which constitutes a description of acoustical physics with hardly any mathematics thrown in. Thus Chladni essentially ignored the mathematics already developed by Euler, d'Alembert, and Lagrange. Young, a physician, a gifted mathematician, and also an accomplished linguist (he did some translation work on the Rosettta stone before Champollion), published a two-volume text *A Course of Lectures on Natural Philosophy and the Mechanical Arts* (Joseph Johnson, London, 1807) that contained three chapters summarizing the knowledge of acoustics existing then. Beyer describes the famous controversy stemming from Newton's erroneous estimate for sound velocity in air, the attempts to measure this parameter with the relatively crude instruments of the day, and the shameful fudging by some experimentalists to conform their results to Newton's estimate. But by 1800, careful measurements of sound propagation speed in air by Parisian academicians yielded values that were within 1% of the most accurate current measurements. The superior conductivity of sound in liquids was noted by a number of scientists, including Benjamin Franklin (1708–1790). Diffraction, reflection, and echoes were fairly well understood, and Chladni pointed out that the intensity of sound depended on the intensity of the vibration of the sound source. The advent of classical music in the invigorating era of Bach, Hadyn, and Mozart and the development and improvement of musical instruments led to an intensified interest in the physics of music. It also led to the understanding of the concept of frequency. Marin Mersenne (1588–1648) correlated the pitch of music with frequency but his investigative results were improved on by Joseph Sauveur (1653–1716) who systemized the musical scale in terms of fundamental frequencies. The first attempt at synthetic speech resulted in a voice machine designed by Christian Gottlieb Kratzenstein (1723–1795) and Wolfgang von Kempelen (1734–1804). Kratzenstein had constructed a set of resonators equipped with a vibrating reed. Understanding of the functional nature of the human ear was rather rudimentary at the time. Teaching of the deaf, which was pioneered in the eighteenth century, gave rise to two camps of educational philosophy, namely, one espousing sign training and the other using oral methods of instruction—opposing viewpoints which continued to coexist aside each other rather uneasily to this day.

Chapter 2 deals with the status of acoustics during 1800–1850. Because of the paucity of sound generators other than the voice and musical instruments and the lack of devices that could sense and measure sound in a reliable fashion, relatively little experimental progress could be made, pending the development of electrical apparatus toward the middle of the nineteenth century. However, some mathematical progress was achieved, beginning with Sophie Germaine's (1776–1831) magnificent development of fourth-order differential equations that govern the behavior of vibrating plates, a feat much admired by the great mathematician Karl Friedrich Gauss (1777–1855). It was eventually realized during this period that sound propagation is essentially an adiabatic process, not the isothermal one originally envisioned by Newton. The three-dimensional Navier–Stokes equation was also derived for describing the motion of viscous fluids. Christian Doppler (1803–1853) predicted light frequency shifts resulting from the motion of a star relative to an astronomical observer; and he astutely pointed out that the shift principle could also apply to sound waves. In his treatment of heat transfer, J. B. J. Fourier (1768–1830) developed his celebrated method of decomposing a finite and continuously periodic function into a series of simple harmonic functions, which was to have great implications for acoustics.

Chapter 3 is entirely devoted to describing the achievements of Hermann L. F. Helmholtz (1821–1894) and John Tyndall (1829–1893). Von Helmholtz is well known for his classic *On Sensations of Tone* (translated by Alexander J. Ellis, Dover, New York, 1954), a treatise on the physics, physiology, and psychology of music. Tyndall's contributions were small in comparison with those of the more famous von Helmholtz and Lord Rayleigh. Tyndall, however, was an exceptionally gifted teacher; and because of this, his book *Lectures On Sound* (Appleton, New York, 1867) did much to spread the gospel of acoustics among the English-speaking people; and it influenced teaching of acoustics in universities during and after his lifetime.

Lord Rayleigh (1842–1919), born John William Strutt, is the subject of Chapter 4. Rayleigh was a most remarkably talented person, who not only authored the two volumes of *The Theory of Sound* (reprint, Dover, New York, 1954) but also made many contributions in nearly all aspects of acoustics, including surface waves, nonlinear acoustics, aeroacoustics, musical acoustics, and even some psychoacoustics. His scientific versatility extended to optics, electricity, the nature of gases, and the discovery of argon (for which he won the 1904 Nobel Prize in physics).

Chapter 5 pays tribute to inventors, in particular, Joseph Henry (1799–1878); William F. Cooke (1806–1870), and Charles Wheatstone (1806–1870), both of whom partnered to lay down the foundations of telegraphy; Alexander Graham Bell (1847–1922), a teacher of the deaf before he invented the telephone; and (a partly-deaf and extremely math-phobic) Thomas Alva Edison (1847–1931) who developed the carbon microphone as well as the phonograph.

In Chapter 6, the last half of the nineteenth century witnessed the birth of seismology, development of devices for making sound visible, Ernst

 0001-4966/99/106(1)/15/2/$15.00

Mach's (1836–1916) study of shock waves, Marchese Alfonso Corti (1822–1876) and Ernst Reissner (1824–1873) shedding new light on the inner workings of the human ear, and the stirrings of architectural acoustics. The discovery of magnetostriction and piezoelectricity during this period set the stage for the advent of ultrasound.

The first quarter of the twentieth century is covered in Chapter 7. Electroacoustics evolved from the development of microphones, the loudspeaker, vacuum tubes which enable the construction of electronic amplifiers, oscillators applied to generating signals, and the oscilloscope. Wallace Clement Sabine (1868–1919) established the scientific foundation of architectural acoustics as the result of his efforts to deal with an overly reverberant classroom at Harvard University. Arthur Gordon Webster (1863–1923) introduced the concept of acoustic impedance at a meeting of the American Physical Society in 1914. Improved instrumentation allowed for better measurement of properties of ultrasonic propagation. Atmospheric acoustics also received renewed attention, entailing the studies of variability of sound signals from fog horns and sirens. The sinking of the *Titanic* in 1912 and the onset of World War I provided the impetus for the study of underwater sound. Much of the early work concentrated on submarine detection. The deleterious effects of cavitation on ship propellers were beginning to be understood. Bioacoustics was a rather dormant field until 1908 when Rolinat, Trouessart, and Hahn repeated the eighteenth-century investigations of bats' hearing conducted by Spallanzani and Jurine. But the ultrasonic nature of bat echolocation was not yet realized even in early twentieth century. It was also during this period that the term decibel was coined.

Chapters 8 and 9 cover the second and third quarters of this century. The Acoustical Society of America came into being, ultrasonic absorption and dispersion became hot topics of research, quantum mechanics provided the basis for understanding relaxation processes in ultrasound propagation and predicting sound absorption coefficients at cryogenic temperatures, ultrasound started to find use as diagnostic medical tools, Sir James Lighthill (1924–1998) expounded his aeroacoustic theories, the U.S. Navy developed sonar and conducted a great deal of research on underwater acoustics, Griffin, Pierce, and Galambos identified bat echolocation processes as being ultrasonic processes, and Georg von Békésy (1899–1972) conducted major research on the physiology of the human ear, which was to earn him the Nobel Prize in Medicine and Physiology. Harvey Fletcher (1884–1981), ASA's first president, led AT&T's Bell Laboratories in the quantification of psychoacoustics. The effect of noise on people became a matter of increasing concern, which culminated in the passage of the Noise Control Act of 1972 by the U.S. Congress.

The final chapter (Chapter 10) deals with the last quarter of the twentieth century. Current topics include new theories of scattering in linear acoustics, radiation pressure and levitation in nonlinear acoustics, introduction of solitons, the role of chaos theory in acoustics, sonoluminescence, internal waves in underwater acoustics, global scale acoustics, optoacoustics, structural acoustics, active sound and vibration acoustics, introduction of listener preference parameters into auditorium design in architectural acoustics, acoustic engines, ultrasonic refrigerators, new findings in physiological acoustics, otoacoustic emissions, cochlear implants, etc.

Each chapter is accompanied by an extremely comprehensive bibliography, infused with many illuminating, often witty, commentaries by the author. The tenth chapter is followed by reprints of two very interesting reviews of both volumes of Rayleigh's *Theory of Sound* written by none other than Herman von Helmholtz. These two reviews were originally published in separate issues of *Nature* in 1878.

Two sets of indices are provided: one is an index of names cited in the text and the other is the customary subject index.

Against the aforementioned books by Dayton Miller and Frederick Vinton Hunt, Beyer's text stands up very well indeed. In fact, *Sounds of Our Times* is far more informative than Miller's work; and it certainly can be characterized as a worthy continuation of Hunt's scholarly effort.

In summary, Beyer's *Sounds of Our Times* is destined to become a classic in its genre.

DANIEL R. RAICHEL

CUNY Graduate School
Mechanical and Aerospace Engineering Department and
School of Architecture and Environmental Studies
The City College of the City University of New York
New York, New York 10031

High-resolution finite-volume methods for acoustic waves in periodic and random media

Tiernan R. Fogarty
Department of Applied Mathematics, University of Washington, Seattle, Washington 98195-2420

Randall J. LeVeque
Department of Applied Mathematics and Department of Mathematics, University of Washington, Seattle, Washington 98195-2420

(Received 16 September 1998; revised 16 March 1999; accepted 24 March 1999)

High-resolution numerical methods originally developed for shock capturing in the context of nonlinear conservation laws are found to be very useful for solving acoustics problems in rapidly varying heterogeneous media. These methods are based on solving Riemann problems at the interface between grid cells, which resolve waves into transmitted and reflected components at each interface. The wave-propagation method developed in R. J. LeVeque [J. Comput. Phys. **131**, 327–353 (1997)] and implemented in the CLAWPACK software package is tested on several acoustics problems with periodic or random media in one and two space dimensions. A new limiter function is presented for solving problems in a periodic medium where numerical instabilities are observed with standard limiters. © *1999 Acoustical Society of America.* [S0001-4966(99)02807-6]

PACS numbers: 43.20.−f, 43.20.Bi, 43.20.Fn [AN]

INTRODUCTION

The wave-propagation algorithms developed by LeVeque[1] and implemented in CLAWPACK[2] have been found to perform very well on linear hyperbolic systems modeling wave propagation in rapidly varying heterogeneous media. In this paper we study acoustics in periodic and random media where the material parameters can vary by $O(1)$ on the scale of the grid cells, with drastic variation from cell to cell. Acoustics is one possible application. The same approach has been successfully applied to problems in elasticity and is also applicable to other hyperbolic systems with rapidly varying coefficients. Moreover the methods extend easily from linear to nonlinear problems.

Such methods can be used to solve problems which previously were not amenable to direct numerical simulation. While homogenized equations can give reasonable results if the wavelength of interest is long compared with the scale of the variations, direct simulation allows the modeling of a broader range of problems. It also allows solution of problems for which homogenization theories are not available or for which rapidly varying data from field measurements must be used directly. These methods could also be useful as a tool in developing and testing new homogenization theories, by providing a good reference solution for comparison.

The method studied uses a high-resolution finite-volume approach originally developed in the context of ''shock capturing'' for compressible gas dynamics. An essential feature is that a *Riemann problem* is solved at each interface between finite-volume cells to determine the set of waves emanating from the interface and affecting the solution vector in the neighboring grid cells. Propagating these waves alone results in the first order *Godunov method*, the first upwind method to be fully successful for highly nonlinear gas dynamics problems.[3] High-resolution methods are derived by adding second-order correction terms, based on ''limited'' versions of these waves. Special limiter functions are applied to reduce spurious oscillations near discontinuities and give sharp resolution of shocks along with nearly second-order accuracy of smooth solutions. Exposition of such methods and pointers to the rich literature can be found in many sources.[4–7]

For linear wave equations these methods have not been particularly popular, often with good reason since methods based on Riemann solvers and limiters are more expensive than standard finite-difference methods, and are often limited to second-order accuracy. For problems without shocks, where instead the accurate resolution of high-frequency smooth oscillations is often the primary concern, high-order finite difference or spectral methods can be much more efficient.

For problems with rapidly varying coefficients, however, high-resolution methods do seem to be worth serious consideration. Standard methods cannot give high accuracy near discontinuities in the material parameters and will often fail completely on problems where the parameters vary drastically on the grid scale. By contrast, solving the Riemann problem at each cell interface properly resolves the solution into waves, taking account of every discontinuity in parameters, and automatically handles the reflection and transmission of waves at each interface. This is crucial in developing the correct macroscopic behavior. As a result, Riemann-solver methods are quite natural for this application.

The use of a limiter function can also be advantageous for linear problems, even when the solution should remain smooth, since it greatly reduces numerical dispersion relative to linear second-order methods. Rapidly varying coefficients give rise to some potential difficulties in applying limiters which are discussed in Sec. I A. To overcome the difficulties presented by a medium with rapidly varying coefficients, a new method of limiting is introduced.

Another advantage of the Riemann-solver approach is that the same methods can be applied to nonlinear acoustics, since they were originally developed for nonlinear problems and work well even when shocks form. One need only de-

velop the necessary Riemann solver for the nonlinearity of interest. For example, CLAWPACK has been successfully applied to weakly nonlinear acoustics with rapidly varying coefficients by Kevorkian and Bosley[8] to test their homogenization theory results. It should be noted that in the linear case the Riemann problem is solved exactly by a matrix vector multiply and thus the computational cost of these methods remains low.

High-resolution methods were originally developed in the context of nonlinear hyperbolic systems of conservation laws of the form

$$q_t + f(q)_x = 0,$$

in one space dimension, where q is the vector of conserved quantities and $f(q)$ is the flux function. The wave-propagation method developed by LeVeque[1] (and the CLAWPACK software) applies more generally to hyperbolic systems, including variable-coefficient systems which are not in conservation form, e.g., the linear system

$$q_t + A(x)q_x = 0. \tag{1}$$

Acoustics in a heterogeneous medium was used as an example in Ref. 1 and results are shown there for several problems with a single interface in material properties, in both one and two dimensions. We assume that the reader is familiar with that paper and the notation used there, and will not repeat a full derivation of the method.

In this paper we study the application to acoustics problems in both one and two space dimensions, and in principle the methods should apply in three dimensions equally well. In one dimension, we study a situation where the ''exact'' solution is easily computed in order to perform grid-refinement studies and test the order of accuracy. The direct numerical simulation results are also compared with results of homogenization theory when possible. Both periodic and random media are tested. In two dimensions we test the methods on a medium which is piecewise constant with random fluctuations added, and on a correlated random medium.

All of the results presented here were obtained using the CLAWPACK software, with drivers and Riemann solvers that are available on the web, at http://www.amath.washington.edu/~rjl/clawpack/acoustics/ Animations of some of the results presented in this paper can also be found there. The CLAWPACK software is freely available in one, two, and three space dimensions, including Riemann solvers for both acoustics and elasticity. Automatic adaptive mesh refinement is also available in the AMRCLAW software package developed by Berger and LeVeque.[9,10] Follow links from the above-mentioned website.

I. ONE-DIMENSIONAL ACOUSTICS

The one-dimensional acoustics equations can be written as a first-order variable coefficient linear hyperbolic system

$$p_t + K(x)u_x = 0, \quad \rho(x)u_t + p_x = 0, \tag{2}$$

where the unknowns are the pressure perturbation $p(x,t)$ and the velocity $u(x,t)$. The variable coefficients are the density $\rho(x)$ and bulk modulus of compressibility $K(x)$. This system has the form of Eq. (1) with

$$q = \begin{bmatrix} p \\ u \end{bmatrix}, \quad A(x) = \begin{bmatrix} 0 & K(x) \\ 1/\rho(x) & 0 \end{bmatrix}.$$

The second equation of Eq. (2) expresses Newton's Law for the acceleration while the first equation corresponds to Hooke's Law, relating the change in pressure to the relative change in volume,

$$\Delta p = -K\frac{\Delta V}{V}.$$

This can alternatively be written as

$$\Delta V = -\frac{1}{K}V\Delta p, \tag{3}$$

where $1/K$ is the coefficient of compressibility.[11]

Here we study the case of heterogeneous media where $\rho(x)$ and $K(x)$ vary rapidly with x and $K(x)$ is scalar. We use a finite-volume method in which the ith grid cell is assumed to contain a homogeneous material with constant parameter values ρ_i and K_i. If ρ and K vary on the sub-grid scale, then we must choose appropriate average values to use in each grid cell. Since ρ is the density (mass per unit length, in one dimension), the average density of the ith cell is properly computed as

$$\rho_i = \frac{1}{\Delta x}\int_{x_{i-1/2}}^{x_{i+1/2}} \rho(x)dx. \tag{4}$$

To average the bulk modulus, Eq. (3) leads naturally to an expression for the total volume change of a heterogeneous cell resulting from a given change in pressure. A simple computation shows that the proper coefficient of compressibility for a mixed cell is obtained by averaging this,

$$\frac{1}{K_i} = \frac{1}{\Delta x}\int_{x_{i-1/2}}^{x_{i+1/2}} \frac{1}{K(x)}dx. \tag{5}$$

So K_i should be defined as the *harmonic average* of $K(x)$ over the ith cell, while ρ_i is defined as the *arithmetic average* of $\rho(x)$ by Eq. (4).

We are primarily concerned with the case where the functions $\rho(x)$ and $K(x)$ are piecewise constant with rapid variations, but using a grid which is sufficiently fine that ρ and K are in fact constant within each cell. Then use of this averaging is not necessary for the numerical method, but these same expressions are used in standard homogenization theories for periodic or randomly varying media which are discussed below.

We assume that the ith cell has material parameters ρ_i and K_i as described above and set

$$A_i = \begin{bmatrix} 0 & K_i \\ 1/\rho_i & 0 \end{bmatrix}.$$

The eigenvalues and eigenvectors of this matrix are given by

$$\lambda_i^1 = -c_i, \quad \lambda_i^2 = c_i, \quad r_i^1 = \begin{bmatrix} -\rho_i c_i \\ 1 \end{bmatrix}, \quad r_i^2 = \begin{bmatrix} \rho_i c_i \\ 1 \end{bmatrix}. \tag{6}$$

Here c_i is the sound speed in the ith cell, $c_i = \sqrt{K_i/\rho_i}$.

In the finite-volume method, we let Q_i^n represent the numerical approximation to the average value of $q(x,t)$ over

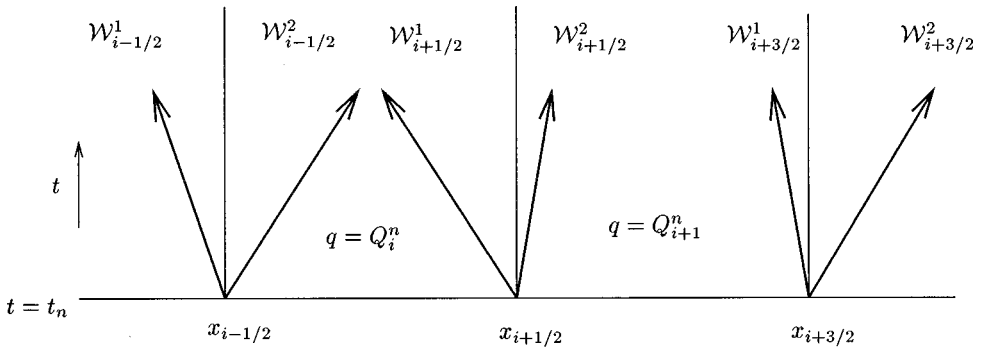

FIG. 1. Example of acoustic waves resulting from solving the Riemann problem and each cell interface. The waves $\mathcal{W}^2_{i-1/2}$ and $\mathcal{W}^1_{i+1/2}$ in cell i have speeds c_i and $-c_i$ respectively.

the ith cell at time t_n. The method updates these cell averages by determining the waves that enter this cell during the time step. If $\mathcal{W}$ represents the jump in q across some wave moving at speed λ, then the cell average is changed by $\Delta t \lambda \mathcal{W}/\Delta x$ over the course of a time step Δt.

The solution to the Riemann problem between states Q_{i-1} in cell $i-1$ and Q_i in cell i consists of two waves. The left-going wave moves into cell $i-1$ and hence must be an acoustic wave appropriate for the medium in this grid cell. So this wave has velocity $\lambda^1_{i-1/2} = -c_{i-1}$ and the jump across this wave must be a scalar multiple of the eigenvector r^1_{i-1} of the matrix A_{i-1},

$$\mathcal{W}^1_{i-1/2} = \alpha^1_{i-1/2} \begin{bmatrix} -\rho_{i-1} c_{i-1} \\ 1 \end{bmatrix} \equiv \alpha^1_{i-1/2} r^1_{i-1}. \tag{7}$$

Note that here we have changed notation slightly from Ref. 1 and use the subscript $i-1/2$ to index waves and speeds associated with the Riemann problem between cells $i-1$ and i, and reserve the index i to index quantities associated with the ith cell.

Similarly, the right-going wave moves into cell i with velocity $\lambda^2_{i-1/2} = c_i$ and the jump across this wave is a multiple of r^2_i,

$$\mathcal{W}^2_{i-1/2} = \alpha^2_{i-1/2} \begin{bmatrix} \rho_i c_i \\ 1 \end{bmatrix} \equiv \alpha^2_{i-1/2} r^2_i, \tag{8}$$

for some scalar $\alpha^2_{i-1/2}$ (see Fig. 1).

The pressure and velocity between the two waves must be continuous across the interface (the proper physical condition at the material interface) and so we must have

$$Q_{i-1} + \mathcal{W}^1_{i-1/2} = Q_i - \mathcal{W}^2_{i-1/2}. \tag{9}$$

From this condition we obtain a linear system which can be solved for the wave strengths $\alpha^1_{i-1/2}$ and $\alpha^2_{i-1/2}$,

$$\begin{bmatrix} -\rho_{i-1} c_{i-1} & \rho_i c_i \\ 1 & 1 \end{bmatrix} \begin{bmatrix} \alpha^1_{i-1/2} \\ \alpha^2_{i-1/2} \end{bmatrix} = \begin{bmatrix} p_i - p_{i-1} \\ u_i - u_{i-1} \end{bmatrix}. \tag{10}$$

Let $R_{i-1/2}$ be the matrix of right eigenvectors appearing in Eq. (10),

$$R_{i-1/2} = \begin{bmatrix} -Z_{i-1} & Z_i \\ 1 & 1 \end{bmatrix}, \tag{11}$$

where $Z \equiv \rho c$ is the *impedence* of each medium. Let $L_{i-1/2}$ be the inverse of $R_{i-1/2}$,

$$L_{i-1/2} = R^{-1}_{i-1/2} = \frac{1}{Z_{i-1} + Z_i} \begin{bmatrix} -1 & Z_i \\ 1 & Z_{i-1} \end{bmatrix} \equiv \begin{bmatrix} l^1_{i-1/2} \\ l^2_{i-1/2} \end{bmatrix}. \tag{12}$$

Then solving Eq. (10) gives

$$\begin{aligned} \alpha^1_{i-1/2} &= l^1_{i-1/2} \cdot (Q_i - Q_{i-1}), \\ \alpha^2_{i-1/2} &= l^2_{i-1/2} \cdot (Q_i - Q_{i-1}), \end{aligned} \tag{13}$$

where $l^p_{i-1/2}$ are the row vectors of $L_{i-1/2}$. These values determine the wave strengths in Eqs. (7) and (8). We see that an arbitrary jump in pressure and velocity across the interface can be resolved into left-going and right-going acoustic waves.

Note that there is a close connection between these coefficients and the standard *reflection and transmission coefficients* for the interface. Consider the special case where the jump in Q at the interface is consistent with a left-going wave in cell i, so that

$$Q_i - Q_{i-1} = \beta r^1_i = \beta \begin{bmatrix} -Z_i \\ 1 \end{bmatrix}$$

for some β. In this case we can view the Riemann problem at the interface as determining what happens at the instant when this left-going wave strikes the interface. Applying Eq. (13) in this special case gives

$$\alpha^1_{i-1/2} = \left(\frac{2Z_i}{Z_{i-1} + Z_i} \right) \beta, \quad \alpha^2_{i-1/2} = \left(\frac{Z_{i-1} - Z_i}{Z_{i-1} + Z_i} \right) \beta. \tag{14}$$

The resulting 1-wave (the left-going wave transmitted into cell $i-1$) has strength equal to β multiplied by the transmission coefficient, while in the right-going wave strength the reflection coefficient appears.

Similarly, if $Q_i - Q_{i-1}$ corresponds to a pure right-going wave from cell $i-1$, we would obtain the appropriate transmission and reflection coefficients for this case. An arbitrary jump $Q_i - Q_{i-1}$ can be viewed as a linear combination of these two special cases, and so in general the α^1 and α^2 each contain information about both a transmitted and a reflected wave. This viewpoint will be important in our development of the ''transmission-based limiter'' in Sec. I A.

Note that we have used a different normalization of the eigenvectors than in Ref. 1, multiplying the form used there by ρ. The form used here shows more clearly the fundamental significance of the impedence. If $Z_{i-1} = Z_i$ then the eigenvectors are the same in the two cells and a left-going wave in

cell i is also a left-going wave in cell $i-1$, and hence there is no reflection at the interface between these cells, merely a change of speed.

The first-order upwind method for the variable-coefficient problem can now be written as

$$Q_i^{n+1} = Q_i^n - \frac{\Delta t}{\Delta x}(\lambda_{i-1/2}^2 \mathcal{W}_{i-1/2}^2 + \lambda_{i+1/2}^1 \mathcal{W}_{i+1/2}^1). \quad (15)$$

This is derived using the idea of Godunov's method, that the cell average Q_i is modified by waves $\mathcal{W}^p$ moving into the cell with speed λ^p. See Ref. 1 for more details.

A second-order correction term can also be introduced, motivated by the Lax–Wendroff method for the constant coefficient case. This can be written as a correction to the first-order upwind method in terms of the ''correction fluxes''

$$\tilde{F}_{i-1/2} = \frac{1}{2}\sum_{p=1}^{2} |\lambda_{i-1/2}^p| \left(1 - \frac{\Delta t}{\Delta x}|\lambda_{i-1/2}^p|\right) \mathcal{W}_{i-1/2}^p.$$

The second-order method takes the form

$$Q_i^{n+1} = Q_i^n - \frac{\Delta t}{\Delta x}(\lambda_{i-1/2}^2 \mathcal{W}_{i-1/2}^2 + \lambda_{i+1/2}^1 \mathcal{W}_{i+1/2}^1) - \frac{\Delta t}{\Delta x}(\tilde{F}_{i+1/2} - \tilde{F}_{i-1/2}). \quad (16)$$

This reduces to the standard Lax–Wendroff method if $A_i = A$ is constant. In this case $\lambda^1 = -c$ and $\lambda^2 = c$ are constant and $\Sigma_p \lambda^p \mathcal{W}_{i-1/2}^p = A(Q_i - Q_{i-1})$ while $\Sigma_p (\lambda^p)^2 \mathcal{W}_{i-1/2}^p = A^2(Q_i - Q_{i-1})$. Then Eq. (16) reduces to

$$Q_i^{n+1} = Q_i^n - \frac{\Delta t}{2\Delta x} A(Q_{i+1}^n - Q_{i-1}^n) + \frac{1}{2}\left(\frac{\Delta t}{\Delta x}\right)^2 A^2((Q_{i+1}^n - Q_i^n) - (Q_i^n - Q_{i-1}^n)). \quad (17)$$

See Ref. 1 for more details of the relationship between these methods. Equation (16) is the form of the update formula used in the CLAWPACK software, using also flux limiters as described in the next section.

A. Flux limiters

The update formula Eq. (16) decomposes the update to Q into a first-order accurate upwind update and a second-order correction. The upwind method is excessively dissipative while the second-order Lax–Wendroff method is numerically dispersive, leading to the appearance of spurious oscillations in the solution. A high-resolution method is obtained by applying a nonlinear ''limiter'' to the second-order corrections to obtain a method with much better properties than either the upwind or Lax–Wendroff methods.[6] This is accomplished by replacing each wave $\mathcal{W}_{i-1/2}^p$ by a limited version

$$\tilde{\mathcal{W}}_{i-1/2}^p = \Phi_{i-1/2}^p \mathcal{W}_{i-1/2}^p,$$

for some scalar value $\Phi_{i-1/2}^p$ (for $p=1,2$). This limiter is determined by comparing each wave with the corresponding wave at the adjacent cell interface in the upwind direction. Hence we compare $\mathcal{W}_{i-1/2}^1$ with $\mathcal{W}_{i+1/2}^1$ and $\mathcal{W}_{i-1/2}^2$ with $\mathcal{W}_{i-3/2}^2$. In regions where the solution is smoothly varying these waves will differ by very little and we should use unmodified waves to achieve second-order accuracy. We want $\Phi_{i-1/2}^p \approx 1$ in this case. If the waves differ greatly then we must be near a discontinuity in the solution, or at least large values of q_{xx}. In this case the second-order corrections can lead to numerical dispersion and in these regions the waves should be limited by choosing $\Phi_{i-1/2}^p$ closer to zero. We take

$$\Phi_{i-1/2}^p = \phi(\theta_{i-1/2}^p),$$

where $\theta_{i-1/2}^p$ is some measure of the ratio of wave strengths. For example, we might take

$$\theta_{i-1/2}^1 = \frac{\|\mathcal{W}_{i+1/2}^1\|}{\|\mathcal{W}_{i-1/2}^1\|}, \quad \theta_{i-1/2}^2 = \frac{\|\mathcal{W}_{i-3/2}^2\|}{\|\mathcal{W}_{i-1/2}^2\|}, \quad (18)$$

where $\|\cdot\|$ is some norm such as the Euclidean norm. Many choices are possible for the limiter function ϕ. We have found that the ''minmod'' limiter works well:

$$\phi(\theta) = \max(0, \min(1, \theta)). \quad (19)$$

For variable-coefficient problems, the eigenvectors may change from cell to cell (and will change whenever the impedence differs), and hence the waves $\mathcal{W}_{i-1/2}^1$ and $\mathcal{W}_{i+1/2}^1$, for example, will not be co-linear in phase space. In this case simply comparing the magnitudes, as done in Eq. (18), may give an insufficient limiter. The two waves could be very different even if they have the same magnitude. In the CLAWPACK software the standard approach is to instead compare the projection of $\mathcal{W}_{i+1/2}^1$ onto $\mathcal{W}_{i-1/2}^1$ with the wave $\mathcal{W}_{i-1/2}^1$, defining

$$\theta_{i-1/2}^1 = \frac{\mathcal{W}_{i+1/2}^1 \cdot \mathcal{W}_{i-1/2}^1}{\mathcal{W}_{i-1/2}^1 \cdot \mathcal{W}_{i-1/2}^1}, \quad (20)$$

where $\cdot$ denotes the inner product, in place of Eq. (18) (and similarly for $\theta_{i-1/2}^2$). We have found that this works well for some problems with random or periodic media, but in certain cases this results in an unstable method when calculations are run to large times. (An example is shown in Fig. 7.) This appears to be the result of a nonlinear resonance phenomenon in the numerical solution introduced by the limiter, and may be related to physical resonances that have been investigated by Kevorkian and Bosley[8] in weakly nonlinear acoustics.

A more robust limiter is motivated by Fig. 2, which indicates that the wave $\mathcal{W}_{i+1/2}^1$, if allowed to strike the interface at $x_{i-1/2}$, would split into a transmitted wave $\mathcal{T}_{i-1/2}^1$ and a reflected wave $\mathcal{R}_{i-1/2}^1$. The figure suggests that only the transmitted wave $\mathcal{T}_{i-1/2}^1$ should be compared to $\mathcal{W}_{i-1/2}^1$. The transmission coefficient is $2Z_{i-1}/(Z_{i-1}+Z_i)$ and so we take

$$\theta_{i-1/2}^1 = \frac{\|\mathcal{T}_{i-1/2}^1\|}{\|\mathcal{W}_{i-1/2}^1\|} = \left(\frac{2Z_{i-1}}{Z_{i-1}+Z_i}\right)\left(\frac{\alpha_{i+1/2}^1}{\alpha_{i-1/2}^1}\right), \quad (21)$$

where $Z_i = \rho_i c_i$ is the impedence in the ith cell. Similarly, we take

$$\theta_{i-1/2}^2 = \frac{\|\mathcal{T}_{i-1/2}^2\|}{\|\mathcal{W}_{i-1/2}^2\|} = \left(\frac{2Z_i}{Z_{i-1}+Z_i}\right)\left(\frac{\alpha_{i-3/2}^2}{\alpha_{i-1/2}^2}\right), \quad (22)$$

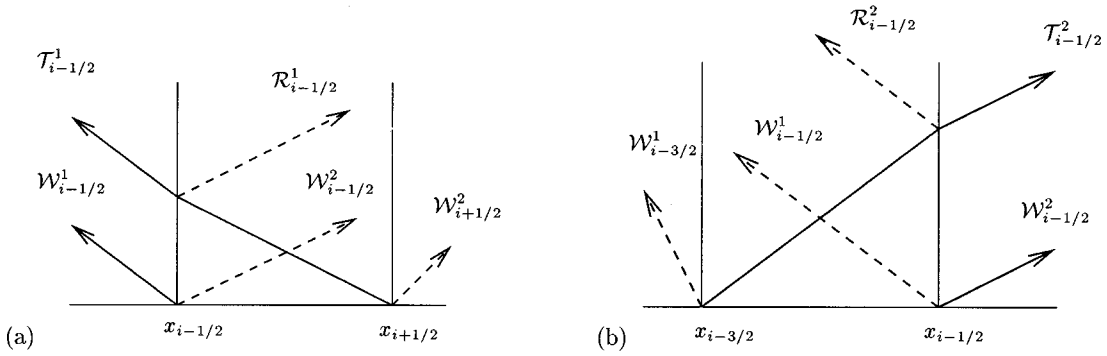

FIG. 2. Decomposition of waves into transmitted and reflected parts used in defining the transmission-based limiter in Eqs. (21) and (22).

as suggested by Fig. 2(b). We call this a *transmission-based limiter*. For more details see Fogarty.[12]

This idea is closely related to what is done in the positivity-preserving scheme of Liu and Lax.[13,14] If we recall Eq. (13), the naive limiter Eq. (18) corresponds to setting

$$\theta^1_{i-1/2}=\frac{\|l^1_{i+1/2}\cdot(Q_{i+1}-Q_i)r^1_{i+1/2}\|}{\|l^1_{i-1/2}\cdot(Q_i-Q_{i-1})r^1_{i-1/2}\|}, \tag{23}$$

for example, in this notation. The Lax–Liu limiter instead uses the same eigenvectors to split both jumps:

$$\theta^1_{i-1/2}=\frac{\|l^1_{i-1/2}\cdot(Q_{i+1}-Q_i)r^1_{i-1/2}\|}{\|l^1_{i-1/2}\cdot(Q_i-Q_{i-1})r^1_{i-1/2}\|}$$

$$=\frac{l^1_{i-1/2}\cdot(Q_{i+1}-Q_i}{l^1_{i-1/2}\cdot(Q_i-Q_{i-1})}. \tag{24}$$

Our transmission-based limiter is similar but applies $l^1_{i-1/2}$ only to the wave $\mathcal{W}^1_{i+1/2}$ which is approaching the interface, not to all of $Q_{i+1}-Q_i$:

$$\theta^1_{i-1/2}=\frac{l^1_{i-1/2}\cdot\mathcal{W}^1_{i+1/2}}{l^1_{i-1/2}\cdot(Q_i-Q_{i-1})}. \tag{25}$$

Similarly,

$$\theta^2_{i-1/2}=\frac{l^2_{i-1/2}\cdot\mathcal{W}^2_{i-3/2}}{l^2_{i-1/2}\cdot(Q_i-Q_{i-1})}. \tag{26}$$

II. THE COURANT NUMBER AND EXACT SOLUTIONS FOR SPECIAL MEDIA

If c_i is the sound speed in the ith cell, then

$$\nu=\max c_i\Delta t/\Delta x$$

is called the *Courant number*, and measures the largest fraction of a cell which any wave can pass through in one time step. The methods discussed here are stable for $\nu\leqslant 1$ when applied to a constant coefficient system, and are found to be stable on the general problem with the transmission-based limiter.

Now consider a special type of medium in which $K(x)=c\rho(x)$ everywhere for some constant value of c. Then by choosing the time step Δt so that $c\Delta t=\Delta x$ (so $\nu=1$) we insure that all waves propagate through exactly one grid cell in each time step. In this case the correction terms $\tilde{F}_{i-1/2}$ in Eq. (16) are all zero and the upwind method Eq. (15) reduces to the exact solution of the equations given by the method of characteristics. (At least the exact solution to the problem of a piecewise constant medium with piecewise constant initial data on the given grid.) This is an extremely useful way to generate problems for which the exact solution can be computed. Such media are sometimes used to check homogenization theories, as in the example of Santosa and Symes[15] used in the next section. In our case we use the exact solution obtained with $c\Delta t=\Delta x$ to check our numerical results obtained with smaller values of ν.

If c_i varies between cells then it will not be possible to choose a single time step for which $c\Delta t=\Delta x$ everywhere, at least not on a uniform grid with Δx constant. If one considers a Goupillaud medium, however, in which the width of layers of constant c vary in such a way that the travel time in each layer is the same, then the exact solution can again be constructed on an appropriate grid (one which is uniformly spaced in travel-time coordinates). This has been used, for example, by Burridge *et al.*,[16] to test homogenization theories. The wave-propagation approach we use would also give the exact solution in this case.

We stress, however, that our numerical method is more general and does not depend on any special properties of the medium or time step. Special media are used only to generate exact solutions for comparison purposes.

III. PERIODIC MEDIUM

As a first test of these methods for acoustic waves propagating in a heterogeneous material, we consider a one-dimensional periodic medium, as studied by Santosa and Symes.[15] The material parameters ρ and K are piecewise constant with

$$(\rho(x),K(x))=\begin{cases}(\rho_1,K_1) & \text{if } 0<x<\theta L\\ (\rho_2,K_2) & \text{if } \theta L<x<L,\end{cases} \tag{27}$$

and repeated periodically, where L is the period and θ the fractional volume of material 1. An acoustic wave with a wavelength large compared to L will obey an effective homogenized equation which has the dispersion relation

$$\omega(k)=\bar{c}k+\delta k^3+\cdots. \tag{28}$$

Long wavelengths (k small) propagate with the effective speed

$$\bar{c}=\sqrt{\bar{K}/\bar{\rho}},$$

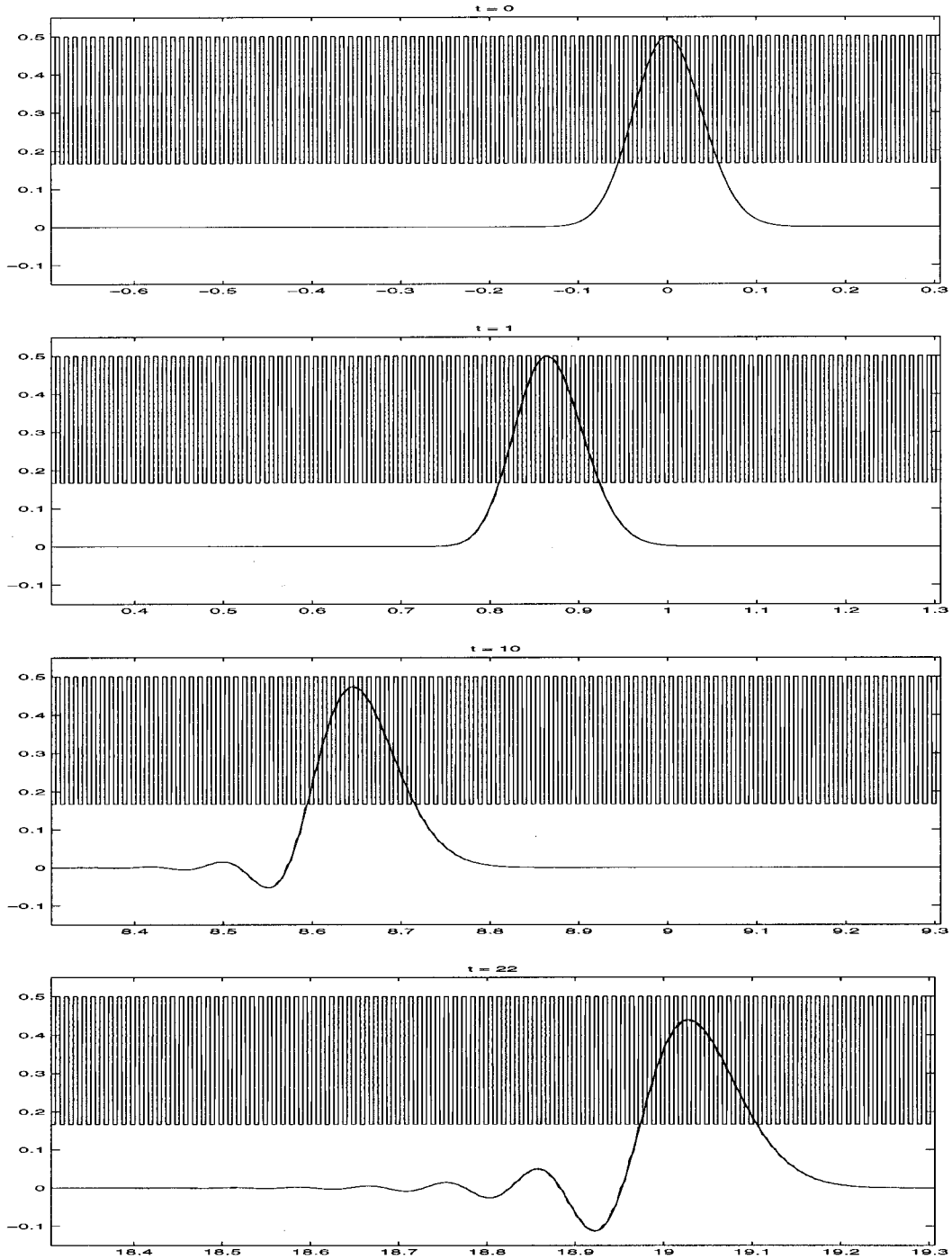

FIG. 3. Comparison of ''exact'' solution computed using $\Delta t = \Delta x$ and ''numerical'' solution with $\Delta t = 0.9\Delta x$, at four different times, on a fine grid with $\Delta x = 1/4000$. The structure of the periodic medium is also indicated by the step function. Note that periodic boundary conditions are used and the x-axis is relabeled at each time to indicate distance traveled since the initial time.

with $\hat{K}$ being the harmonic average of K and $\overline{\rho}$ the arithmetic average of ρ (see Sec. I) over each period:

$$\overline{\rho} = \theta\rho_1 + (1-\theta)\rho_2, \quad \hat{K} = (\theta/K_1 + (1-\theta)/K_2)^{-1}. \tag{29}$$

The expression for the small dispersion coefficient δ is given by Santosa and Symes.[15]

We consider the case studied numerically by Santosa and Symes,

$$\rho_1 = K_1 = 1, \quad \rho_2 = K_2 = 3, \quad \theta = 0.5, \quad L = 0.01,$$

in which case $\overline{c} \approx 0.866$ even though the wave speed $c \equiv 1$ everywhere.

Figure 3 shows a comparison of the exact solution obtained with Courant number 1 (as described in the previous section) and the numerical solution using $\Delta t = 0.9\Delta x$ (Courant number 0.9) on a very fine grid, for a propagating Gaussian pulse. The two solutions lie on top on one another to plotting accuracy. Note that the wave is observed to move at speed $\overline{c}$ (e.g., at time $t = 1$ it is at $x = 0.866$) and that for large t the dispersive nature of the effective equation is evident.

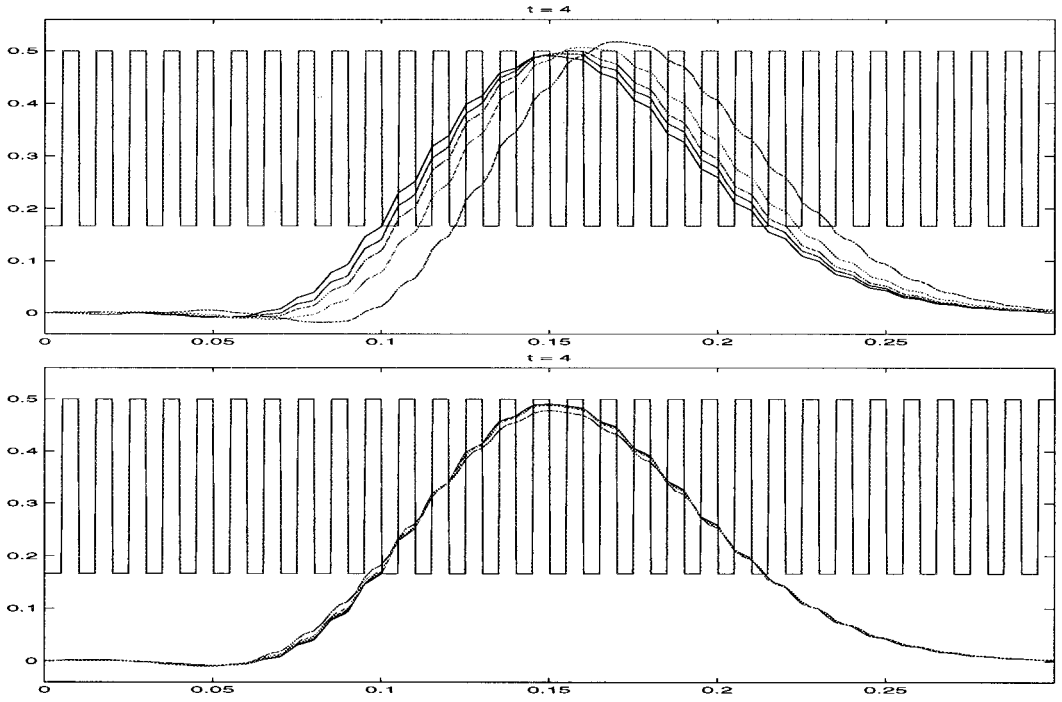

FIG. 4. Numerical solutions with the standard CLAWPACK limiter (upper figure) and the new transmission-based limiter (lower figure) obtained with $\Delta t = 0.9\Delta x$. In both figures the pulse is shown at five grid resolutions $N = 400$, 800, 1600, 3200, and 6400. In the upper figure the highest resolution is the pulse farthest to the left.

The problem is initialized by creating a Gaussian velocity pulse within the periodic medium on a large domain. The pulse splits with half of the perturbation energy traveling each direction. Once the two pulses have separated, the right-going pulse is used as initial data in the computational domain. Periodic boundary conditions are imposed and the x-axis is relabeled at each time to indicate distance traveled since initialization.

Figure 4 shows a comparison of numerical results obtained at $t = 4$ using $\Delta t = 0.9\Delta x$ on several coarser grids for both limiting methods, and Fig. 5 shows a log–log plot of the norm of the error versus Δx. This indicates that the method converges with an order of accuracy roughly 1.3 in the max-norm, when using the transmission-based limiter. Figure 5 also shows the errors obtained when the standard CLAWPACK limiter Eq. (20) is used, which are an order of magnitude larger. For larger t the method goes unstable with Eq. (20) and a result at $t = 17$ is shown in Fig. 6. The period of the oscillations matches that of the medium and this instability is thought to be due to resonances caused by the limiter.

The order of accuracy observed in Fig. 5 may seem low for this computation since the solution appears to be smooth. Note, however, that this smoothness is a result of the times at which we have chosen to display the results. Figure 7 shows the exact solution at a sequence of times between $t = 0$ and $t = 0.015$. The solution appears smooth at the beginning and end (and later at each multiple of 0.015), but in between these times it is not smooth. An animation of this transient behavior may be found on the website mentioned in the Introduction. The observed propagation at speed $\bar{c}$ arises only because of constant reflection and cancellation of waves moving within each material slice at the local speed $c = 1$. At most times the solution has a discontinuous first derivative at the material interfaces and so the loss of second-order accuracy is not surprising.

IV. RANDOM MEDIA

We now consider a random medium in one dimension where $\rho(x)$ and $K(x)$ are taken to be piecewise constant. We use a layered medium with 2000 layers in which values of ρ

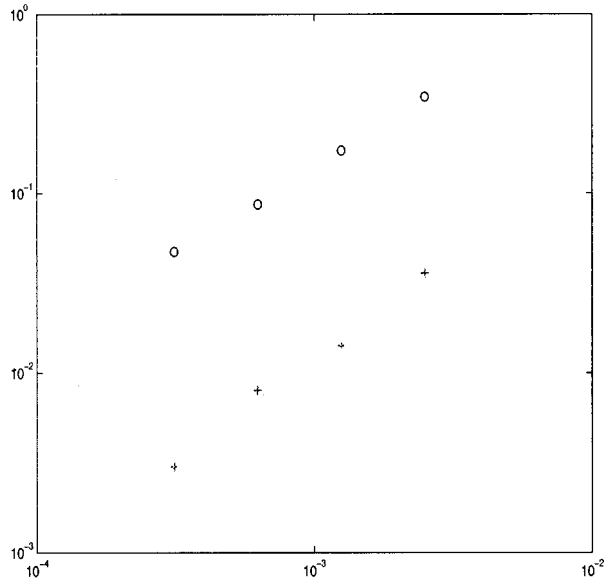

FIG. 5. Max-norm of error in the numerical solutions of Fig. 4. Numerical results for $N = 400,800,1600,3200$ are compared with numerical solution at $N = 6400$. A log–log plot of the error versus Δx is shown for both methods of limiting: Original CLAWPACK (○○○), and Transmission-based (+++). The observed order of accuracy is near 1.3 for the transmission-based limiter and 1.0 for the original limiter.

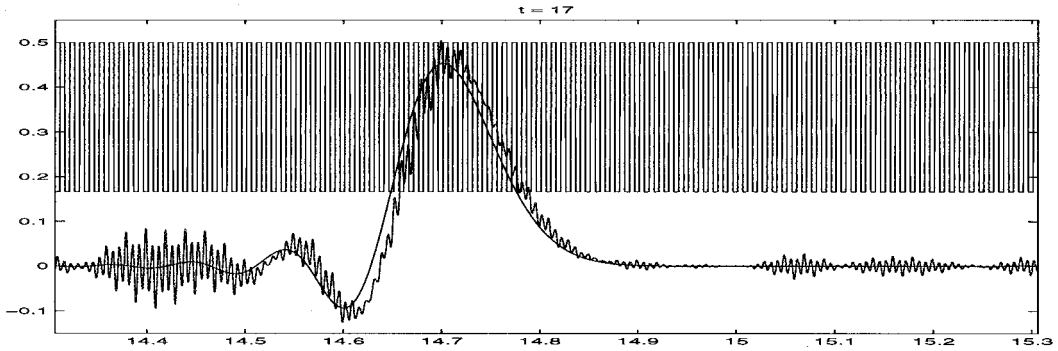

FIG. 6. Comparison of ''exact'' solution with $\Delta t=\Delta x$ and numerical solution with $\Delta t=0.9\Delta x$, with the original CLAWPACK limiter at time=17 with $N=4000$. This shows the numerical instability resulting with this limiter. Note that much better results are obtained with the transmission-based limiter; see Fig. 3.

and K are randomly chosen from uniform distributions between 0.2 and 1.8. The sound speed also varies randomly in each layer. The average sound speed is close to 1, while the effective sound speed is calculated to be $\bar{c}=\sqrt{\bar{K}/\bar{\rho}}\approx 0.85$. Figure 8 shows the density, bulk-modulus, and sound-speed profiles along with a pressure pulse which has propagated through this medium from the point $x=t=0$. The pressure perturbation was initialized as a Gaussian hump with amplitude 1 and zero velocity, centered at $x=t=0$. The initial pulse split into two pulses which propagate to the left and to the right with the predicted effective wave speed of $\bar{c}\approx 0.85$. In addition, some noise is generated by the randomness of the medium. Note that results are shown for 3 resolutions of a 2000 layer medium: $N=2000$, $N=4000$, and $N=8000$ and that the results agree very well, indicating that the noise observed is correct for this medium and not numerical. For this example, as with the periodic medium, we have used the modified limiting method to avoid an instability which develops with the standard CLAWPACK limiting methods.

As a second example in this same medium, we initialized the pressure perturbation to be a step function with value 0.5 for $-0.2\leqslant x\leqslant 0.2$ and 0 elsewhere. Again the initial velocity is zero. This perturbation splits up into two approximate ''square waves'' propagating in opposite directions. These discontinuous data generate much more noise due to the greater dispersion of the effective medium at high wave numbers. Figure 9 shows the computed results at time $t=0.1$, when the pulse is still splitting up, and at $t=0.8$. The same three grid resolutions are used as in the previous ex-

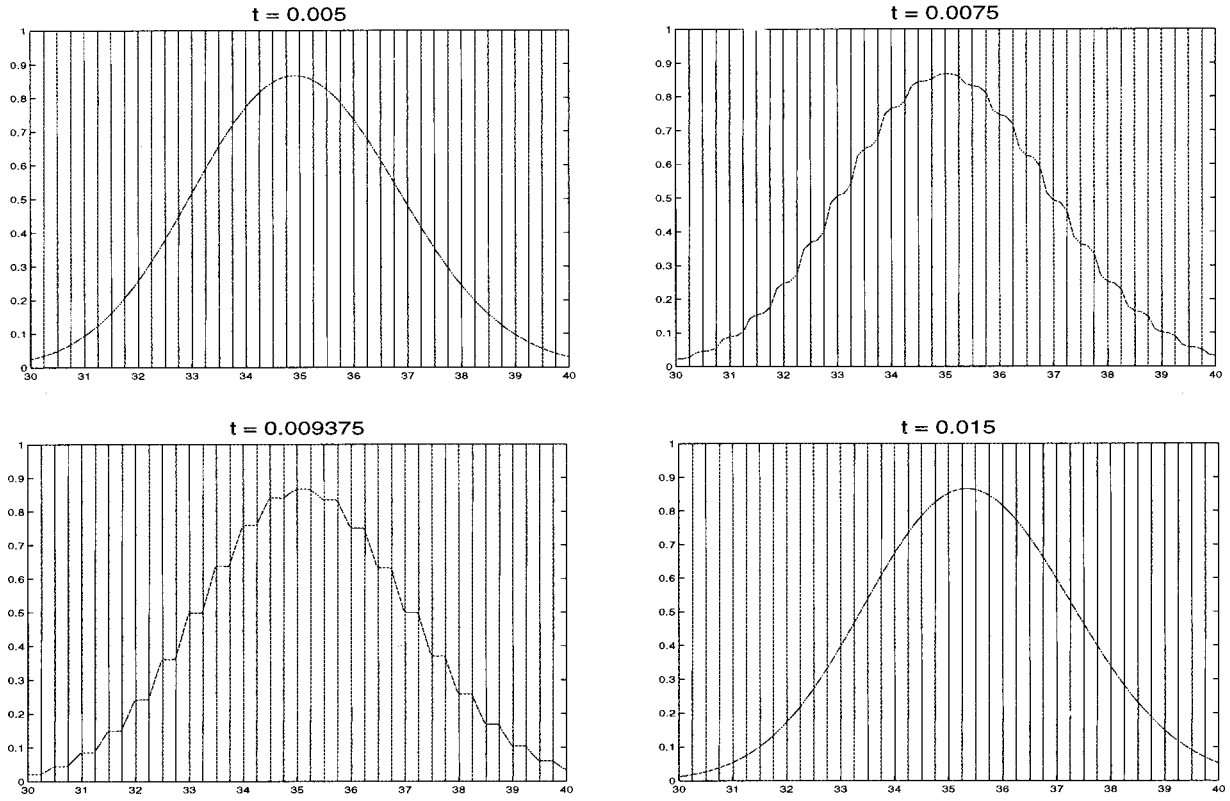

FIG. 7. Close up of right-moving pulse between $t=0.05$ and $t=0.015$ in the periodic medium with discontinuities indicated by the vertical lines.

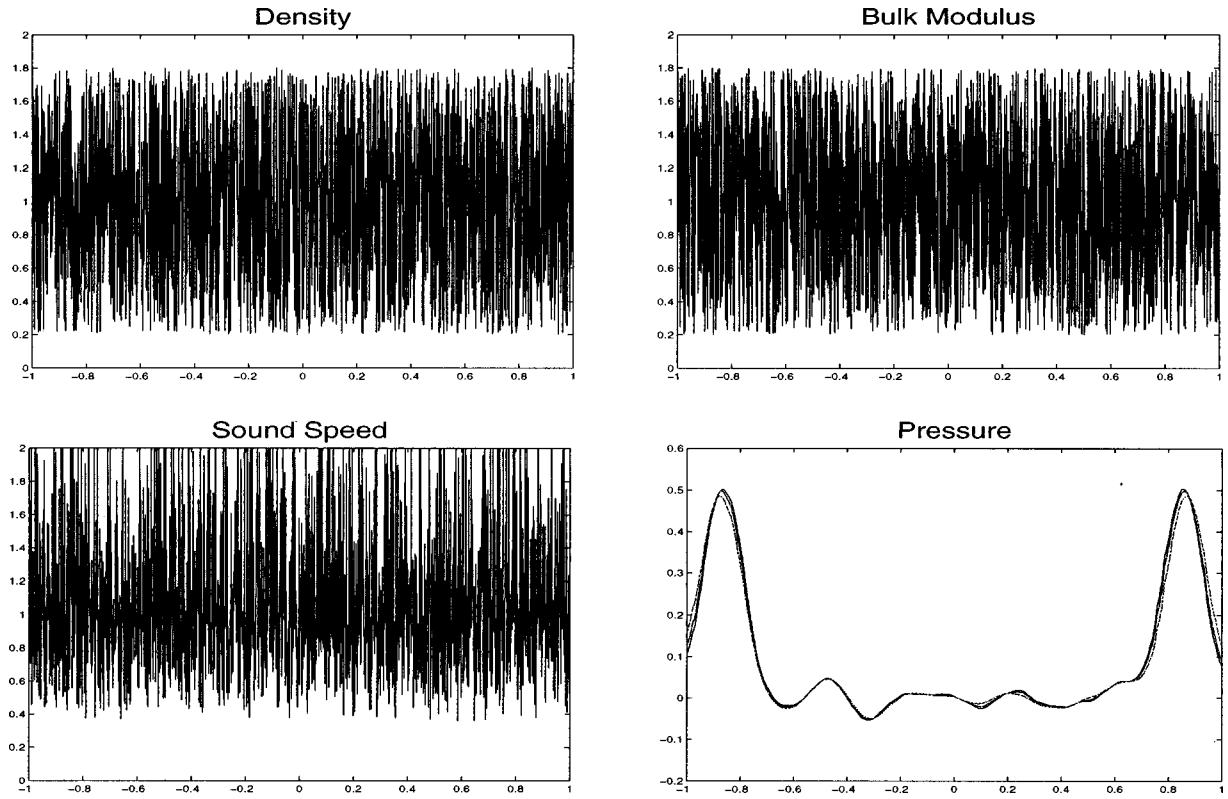

FIG. 8. One-dimensional random medium example of Sec. IV. Profiles of density (upper left), bulk modulus (upper right), sound speed (lower left). The lower right figure shows the computed pressure at $t=1.0$ on three grid resolutions: $N=2000$, $N=4000$, and $N=8000$.

ample. The calculation on the coarsest grid, in which there is only one grid cell in each layer, exhibits more numerical dissipation than in the previous test, but the basic form and effective propagation speed of the pulses is still captured well. This example illustrates that the method is capable of dealing with discontinuous data as well as discontinuous media.

V. TWO-DIMENSIONAL ACOUSTICS

LeVeque[1] extends the wave-propagation method to two space dimensions in a stable and accurate manner by using two sets of Riemann problems. A Riemann problem normal to each cell interface is first solved, which is simply a one-dimensional problem of the type solved above. Consider, for example, the interface between cells $(i-1,j)$ and (i,j). The material properties in these two cells are used to decompose the jumps in pressure and x-velocity between these cells into left-going and right-going acoustic waves. These waves are then each decomposed into up-going and down-going waves using a ''transverse Riemann solver.'' This solver takes into account the material properties in the grid cells above and below, giving the proper transmission and reflection of these waves. This is discussed in detail for variable-coefficient acoustics in Ref. 1.

A. Piecewise constant medium with random fluctuations

A numerical test is shown in Ref. 1 which consists of a plane wave hitting an interface between two materials at an

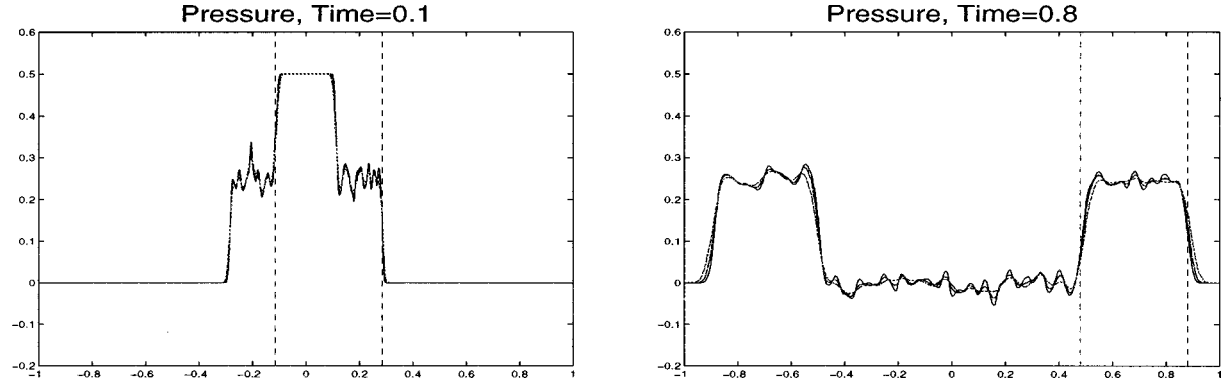

FIG. 9. One-dimensional random medium example of Sec. IV with square-wave initial data. The computed pressure is shown at two times, each with three grid resolutions: $N=2000$, $N=4000$, and $N=8000$. The dashed lines indicate the predicted location of the right-going pulse based on the effective sound speed $\bar{c}\approx 0.85$.

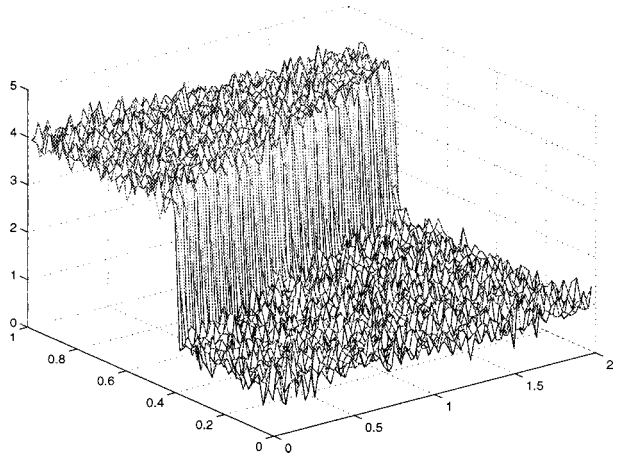

FIG. 10. Density profile for the two-dimensional example of Sec. V A.

oblique angle, giving rise to transmitted and reflected waves as shown in Fig. 11(a) (see also Zhang and LeVeque[17]). In this example, $K \equiv 1$ and ρ jumps from 1 to 4 at the interface.

To illustrate the ability of this algorithm to handle rapidly varying media in two dimensions, we modify this example by adding random fluctuations to the density ρ_{ij} in each grid cell, as shown in Fig. 10. Figure 11(b) shows the computed solution with the same plane wave as used in Fig. 11(a). The homogenized velocity in each medium is the same as in the piecewise constant case, and so we see essentially the same transmission and reflection of the plane wave as in Fig. 11(a), as expected. In addition small-amplitude noise is generated as the pulse propagates through the random medium, analogous to what is seen in Fig. 8 for the one-dimensional case.

B. Correlated random density distribution

As another multi-dimensional example we consider acoustic propagation through a medium with a correlated random density function, in which coherent density structures exist on the scale of the correlation length. We define the wave speed such that $c^{-1}(\mathbf{x}) = c_0^{-1} + \epsilon\beta(\mathbf{x})$ where $\beta(\mathbf{x})$ is a random function, which satisfies

$$\langle \beta(\mathbf{x}) \rangle = 0, \quad \langle \beta(\mathbf{x}_1)\beta(\mathbf{x}_2) \rangle = \langle \beta^2 \rangle N(|\mathbf{x}_1 - \mathbf{x}_2|),$$

and $N(s)$ is an isotropic statistically homogeneous two-point correlation function. We assume the $N(s)$ is very small for $s > l$, where l is the correlation length of the medium. If we let c_0 be the the wave speed in the unperturbed medium, then according to Boyse and Keller[18] the effective wave speed for the correlated medium should be given by

$$\overline{c} \sim c_0 + O(\epsilon^2).$$

Figure 12 shows a plane wave which has propagated to the right in a medium with a correlated random density. For this example we used the parameter values $c_0 = 1$, $\epsilon = 0.4$ and correlation length $l = 6$ in the domain $0 \leqslant x \leqslant 150$ and $0 \leqslant y \leqslant 50$. The velocity was initially zero and a Gaussian pressure pulse $p(x,y,0) = e^{-0.1(x-10)^2}$ where the full width at half maximum was nearly equal to the correlation length was used as initial data. The left-going signal has left the domain and only the right-going signal is visible in Fig. 12. As the

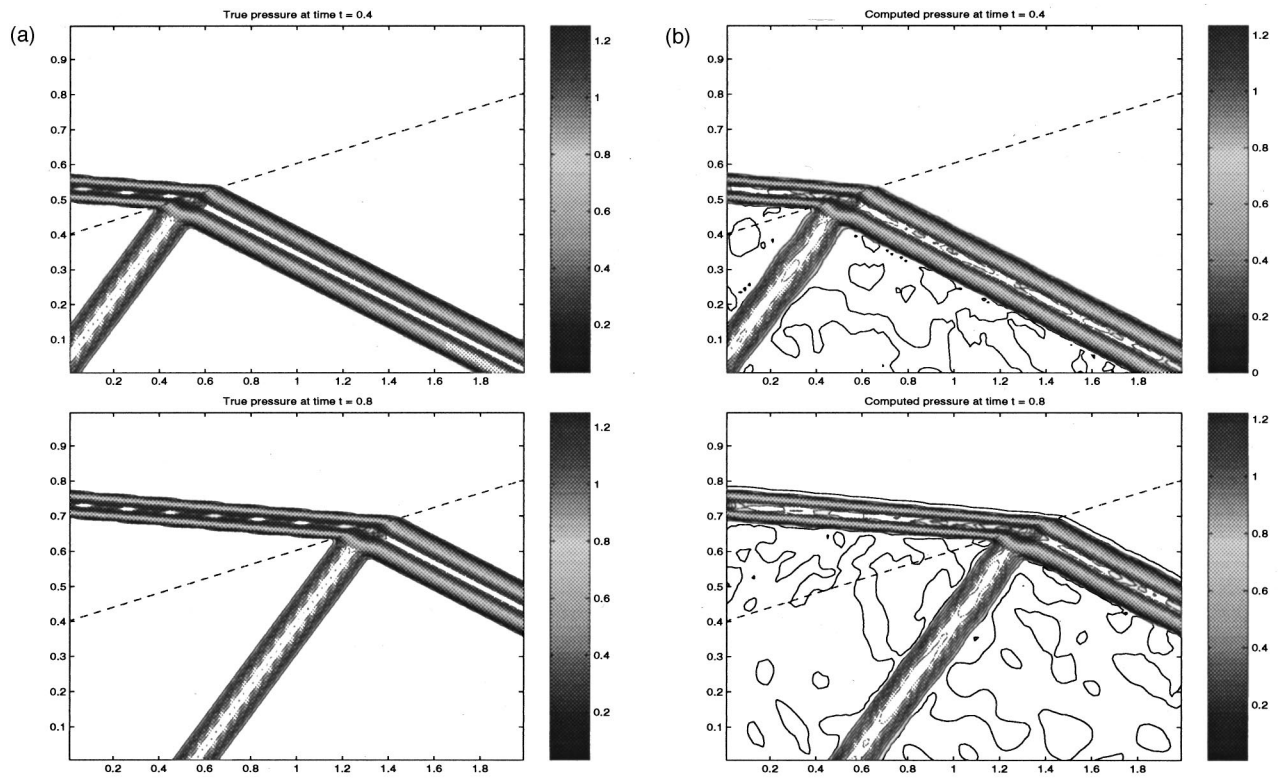

FIG. 11. Example of Sec. V A. Left: Plane wave hitting an interface in a piecewise constant medium. The exact solution is shown at two times, showing incident, transmitted and reflected waves. Right: Numerical solution for a medium with the same effective parameters but with random fluctuations added to the density as shown in Fig. 10. The grid size is 100×100.

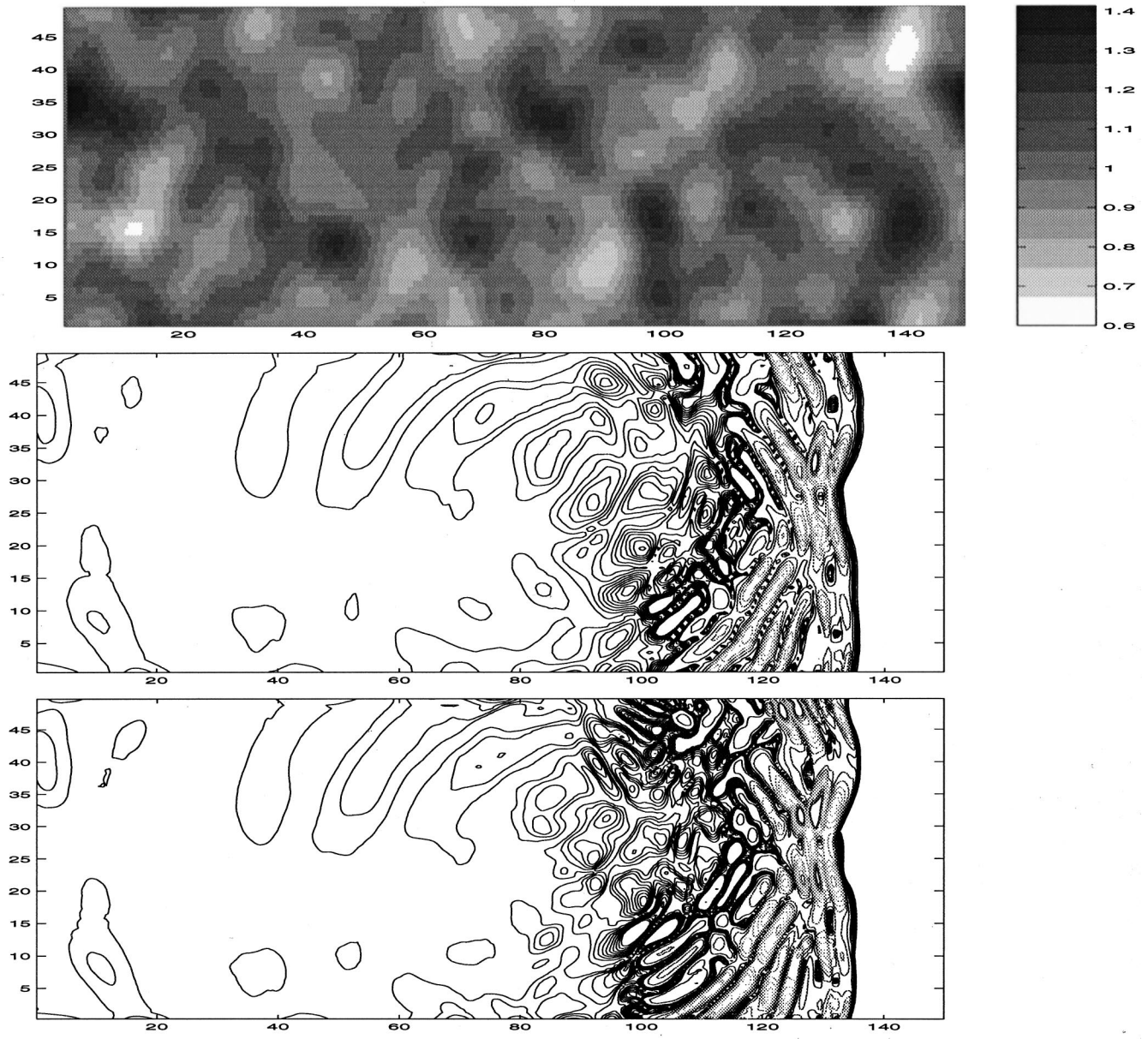

FIG. 12. Example of Sec. V B. Top: Density profile of medium. The other two figures show contour plots of a right-going pressure disturbance at two different resolutions: 50×300 (upper) and 100×600 (lower). The contour levels are not uniformly spaced, but chosen to better show small amplitude variations. The same levels are used for both resolutions.

pulse propagates there are very strong local interactions between the pulse and the density variations. The initial plane wave splits into a number of pulses with considerable two-dimensional structure. Figure 12 shows the result at $t=120$ computed with two different grid resolutions. Note that the primary structures are very similar. The evolution of this pulse is more clearly seen in the animation found via the website given in the Introduction.

VI. SUMMARY AND EXTENSIONS

A high-resolution finite-volume method has been introduced and tested on several examples of acoustics in rapidly varying media. For a one-dimensional periodic medium the numerical results agree well with both exact solutions and results of homogenization theory. For this type of medium the standard limiting method was shown to fail and a new limiting method was introduced. In a one-dimensional random medium the methods work well even when there is only one grid cell per layer. Examples in two dimensions were displayed, one with random fluctuations on a piecewise constant medium and the other in a correlated random medium. The examples illustrate that these high-resolution methods based on Riemann solvers, which split waves into transmitted and reflected parts at each cell interface, are capable of accurately modeling wave propagation in rapidly varying heterogeneous media.

These algorithms are easy to apply since they are already implemented in the CLAWPACK software (with extensions to three dimensions and adaptive refinement) as mentioned in the Introduction. Computationally they are more expensive than simple finite-difference methods such as Lax–Wendroff, but not prohibatively so. Rather than multi-

plying differnces in Q values by the coefficient matrix A as in Eq. (17), the factored form $R\Lambda R^{-1}$ is used, with an additional step of limiting the wave strengths $R^{-1}\Delta Q$. All of these steps follow a simple explicit procedure. Most importantly, use of this factored form, together with the limiter developed here, yields a method that gives good results on problems where the simpler finite-difference methods would fail.

The algorithms and software described here for acoustics can also be used for other wave-propagation problems in heterogeneous material. In particular, the full equations of linear elasticity (supporting shear waves as well as pressure waves) can be modeled by a first-order hyperbolic system. Preliminary experiments show good results for elastic wave propagation in rapidly varying media.

One can also model an arbitrary interface between a fluid (supporting only acoustic waves) and an elastic material by using the full elasticity equations everywhere but with the shear modulus parameter set to zero in the fluid region. This is currently being investigated in the context of specific applications including high-frequency therapeutic ultrasound and ocean acoustics models including the sea floor.

Extension from linear to nonlinear problems should be easy for many applications since these methods were originally developed for nonlinear problems. Some applications of CLAWPACK to nonlinear acoustics and elasticity can be found in Horne[19] and Kevorkian and Bosley.[8]

ACKNOWLEDGMENTS

This work was supported in part by NSF Grants Nos. DMS-9505021, DMS-96226645, and DOE Grant No. DE-FG03-96ER25292.

[1] R. J. LeVeque, ''Wave propagation algorithms for multi-dimensional hyperbolic systems,'' J. Comput. Phys. **131**, 327–353 (1997).
[2] R. J. LeVeque, ''CLAWPACK software,'' available from netlib.bell-labs.com in netlib/pdes/claw or from http://www.amath.washington.edu/~rjl/clawpack.html.
[3] S. K. Godunov, ''A difference method for numerical calculation of discontinuous solutions of the equations of hydrodynamics,'' Mat. Sb. **47**, 271–306 (1959).
[4] E. Godlewski and P.-A. Raviart, *Numerical Approximation of Hyperbolic Systems of Conservation Laws* (Springer-Verlag, New York, 1996).
[5] D. Kröner, *Numerical Schemes for Conservation Laws* (Wiley-Teubner series, 1997).
[6] R. J. LeVeque, *Numerical Methods for Conservation Laws* (Birkhäuser-Verlag, 1990).
[7] E. F. Toro, *Riemann Solvers and Numerical Methods for Fluid Dynamics* (Springer-Verlag, Berlin, 1997).
[8] J. Kevorkian and D. L. Bosley, ''Multiple-scale homogenization for weakly nonlinear conservation laws with rapid spatial fluctuations,'' Stud. Appl. Math. **101**, 127–183 (1998).
[9] M. J. Berger and R. J. LeVeque, ''AMRCLAW software,'' a test version is available at http://www.amath.washington.edu/~rjl/amrclaw/.
[10] M. J. Berger and R. J. LeVeque, ''Adaptive mesh refinement using wave-propagation algorithms for hyperbolic systems,'' SIAM (Soc. Ind. Appl. Math.) J. Numer. Anal. **35**, 2298–2316 (1998).
[11] L. D. Landau and E. M. Lifshitz, *Theory of Elasticity* (Pergamon, New York, 1975).
[12] T. Fogarty, ''Wave-propagation algorithms for acoustics in a rapidly varying heterogeneous medium,'' Masters' thesis, University of Washington, 1997 (ftp://amath.washington.edu/pub/rjl/students/fogarty:masters.ps.gz).
[13] P. D. Lax and X. D. Liu, ''Solution of two dimensional Riemann problem of gas dynamics by positive schemes,'' SIAM J. Sci. Comput. **19**, 319–340 (1998).
[14] X. D. Liu and P. D. Lax, ''Positive schemes for solving multi-dimensional hyperbolic systems of conservation laws,'' Computational Fluid Dynamics Journal **5**, 133–156 (1996).
[15] F. Santosa and W. Symes, ''A dispersive effective medium for wave propagation in periodic composites,'' SIAM J. Appl. Math. **51**, 984–1005 (1991).
[16] R. Burridge, G. S. Papanicolaou, and B. S. White, ''One-dimensional wave propagation in a highly discontinuous medium,'' Wave Motion **10**, 19–44 (1988).
[17] C. Zhang and R. J. LeVeque, ''Immersed interface methods for wave equations with discontinuous coefficients,'' Wave Motion **25**, 237–263 (1997).
[18] W. Boyse and J. B. Keller, ''Short acoustic, electromagnetic, and elastic waves in random media,'' J. Opt. Soc. Am. A **12**, 380,389 (1995).
[19] J. Horne, Ph.D. thesis, University of Washington, 1996.

Diffraction of an acoustic plane wave by a rectangular hole in an infinitely large rigid screen

Kohei Hongo[a)]
Department of Information Science, Toho University, 2-2-1 Miyama, Funabashi, 274-0072 Japan

Hirohide Serizawa[b)]
Department of Control and Computer Engineering, Numazu College of Technology, 3600 Ooka, Numazu, 410-8501 Japan

(Received 15 May 1998; revised 11 January 1999; accepted 17 March 1999)

The method of the Kobayashi potential (KP) is applied to evaluate an acoustic field diffracted by a rectangular hole in an infinite rigid screen. The screen thickness is assumed to be negligibly small. The KP method yields an eigenfunction expansion of the present geometry, and the expansion coefficients are obtained from the matrix equation. The intensity pattern of the far diffracted field, the velocity distribution on the hole, and the transmission coefficient are numerically evaluated. The intensity pattern results are compared with those obtained from the Kirchhoff's diffraction integral. The agreement between them is fairly good. Since no existing method has provided transmission coefficients for a rectangular hole in a rigid screen, these results are compared with the total scattering cross section of the soft disk, which is analogous to a circular hole in a rigid screen. Their frequency characteristics are found to show a similar variation. © *1999 Acoustical Society of America.* [S0001-4966(99)00507-X]

PACS numbers: 43.20.Fn [AN]

INTRODUCTION

The diffraction of an acoustic plane wave by a rigid rectangular plate with infinitesimal thickness was rigorously formulated by applying the method of the Kobayashi potential (KP).[1–3] The KP method uses the discontinuous properties of the Weber–Schafheitlin's (WS) type integrals to satisfy the required boundary conditions.[4,5] The WS integral is an infinite integral and its integrand consists of the product of two Bessel functions multiplied by the powered algebraic single term. This integral shows a discontinuous property when a particular relation holds among the power and orders of the Bessel functions. This method can be applied to potential and wave phenomena of the configuration associated with slit, strip, circular and rectangular holes or plates, as well as related geometries.[6–9] The potential functions used in this method may be regarded as eigenfunctions of a half-space with a hole or a plate. Hence, this method can be applied to more general configurations in a manner similar to mode matching techniques.

In this paper, the KP method is applied to evaluate the field diffracted by a rectangular hole in an infinitely large rigid screen, and then matrix equations of the expansion coefficients are derived. The expressions of the field distribution on the hole and radiation field are derived in a concise form. Therefore, these physical quantities are readily obtained once the expansion coefficients are determined.

The intensity patterns of the far diffracted fields are computed for both the normal and oblique incidences. The results are compared with those obtained using Kirchhoff's integrals. The agreement becomes better as the size of the hole becomes larger. The velocity distributions are computed for various sized holes. The velocity shows singularity at the edge, and the degree of the singularity becomes higher near the corner. The degree of singularity seems to be proportional to r^{-1} near the corner, which depends on the choice of the expansion functions.

The transmission coefficient is also an important physical quantity.[10] Since results by other methods for the rectangular hole in a rigid screen are not available, the computed results are compared with those of the total scattering cross section of the soft disk, whose Babinet problem is the circular hole in a rigid infinite screen. The variation of the frequency characteristics is very similar for circular and rectangular geometries, but the circular disk value is relatively lower than that of the rectangular hole with the same equivalent radius.

Questions arise as to how the choice of the expansion functions affects the convergence of the solution, as in the area of the moment method. We consider two kinds of wave functions, one that satisfies both the boundary and edge conditions (case 1), and the other that satisfies only the boundary condition on the screen except at the edge (case 2). We found that both cases converge to the solution, but the convergence rate is different. Furthermore, the field distribution computed from the functions of case 2 approaches that of case 1 even near the edge, in spite of the fact that the result of case 2 becomes zero at the edge.

I. MATHEMATICAL FORMULATION

A. Derivation of the field expressions

Consider an acoustic plane wave diffracted by a rectangular hole in an infinitely large rigid screen as shown in Fig. 1. The infinite screen's thickness is negligibly small and the hole size is $2a\times 2b$. The center of the hole is chosen as the origin of the Cartesian coordinates (x,y,z). The velocity po-

a)Electronic mail: hongo@is.sci.toho-u.ac.jp
b)Electronic mail: serizawa@cce.numazu-ct.ac.jp

 0001-4966/99/106(1)/29/7/$15.00

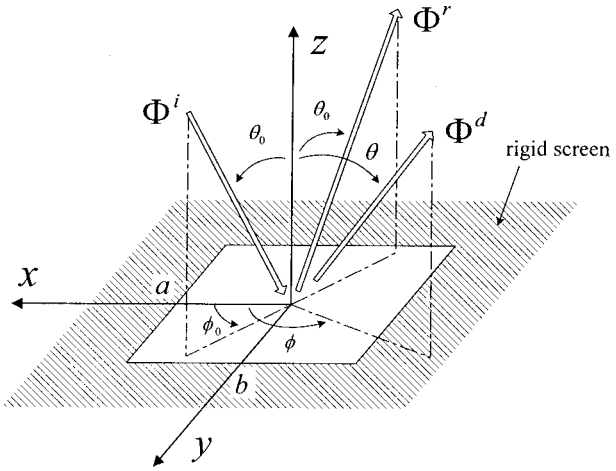

FIG. 1. Geometry of problem and coordinate system. A rectangular hole with a $2a\times 2b$ size in an infinite rigid screen located on plane $z=0$. (θ_0,ϕ_0) and (θ,ϕ) are angles of incidence and diffraction, respectively. Φ^r is reflected wave when plane $z=0$ is occupied by a whole rigid screen.

tentials of the incident and reflected waves for $z>0$, denoted by Φ^i and Φ^r, respectively, are given by

$$\Phi^i=\exp[jk(x\sin\theta_0\cos\phi_0+y\sin\theta_0\sin\phi_0)+jkz\cos\theta_0], \tag{1a}$$

$$\Phi^r=\exp[jk(x\sin\theta_0\cos\phi_0+y\sin\theta_0\sin\phi_0)-jkz\cos\theta_0], \tag{1b}$$

where harmonic time dependence $\exp(j\omega t)$ is assumed and omitted throughout. In the above equation, (θ_0,ϕ_0) are the incident angles. The velocity potential Φ^d of the diffracted wave is expressed by a 2-D Fourier transform of the Helmholtz equation and is determined so that the total potential functions satisfy the boundary conditions. The required boundary conditions for the potential functions are

$$\Phi^i+\Phi^r+\Phi^d_+=\Phi^d_-, \quad (x,y)\in D, \quad z=0, \tag{2a}$$

$$\frac{\partial}{\partial z}[\Phi^i+\Phi^r+\Phi^d_+]=\frac{\partial}{\partial z}\Phi^d_-, \quad (x,y)\in D, \quad z=0, \tag{2b}$$

$$\frac{\partial}{\partial z}[\Phi^i+\Phi^r+\Phi^d_+]=0, \quad (x,y)\in D^c, \quad z=+0, \tag{2c}$$

$$\frac{\partial}{\partial z}\Phi^d_-=0, \quad (x,y)\in D^c, \quad z=-0, \tag{2d}$$

$$\mathbf{R}^2\supset D=\{(x,y)|\ |x|<a,\ |y|<b\}.$$

Here D represents the domain of the hole and D^c is the complement of D. The subscripts $+$ and $-$ of Φ^d denote the regions $z>0$ and $z<0$, respectively. The conditions of Eqs. (2c) and (2d) can be satisfied using the WS integral properties, and the results, which also satisfy condition (2b), are given by

$$\Phi^d_\pm=\pm\sum_{m=0}^{\infty}\sum_{n=0}^{\infty}\int_0^\infty\int_0^\infty\{[A_{mn}J_{2n+\tau}(\beta)\cos\beta\eta+B_{mn}J_{2n+\tau+1}(\beta)\sin\beta\eta]J_{2m+\sigma}(\alpha)\cos\alpha\xi+[C_{mn}J_{2n+\tau}(\beta)\cos\beta\eta+D_{mn}J_{2n+\tau+1}(\beta)\sin\beta\eta]\times J_{2m+\sigma+1}(\alpha)\sin\alpha\xi\}\frac{\exp[\mp\zeta(\alpha,\beta)z_a]}{\alpha^\sigma\beta^\tau\zeta(\alpha,\beta)}d\alpha\,d\beta, \tag{3}$$

where $A_{mn}\sim D_{mn}$ are expansion coefficients. The symbols used in Eq. (3) are defined by

$$\zeta(\alpha,\beta)=\sqrt{\alpha^2+p^2\beta^2-\kappa^2}, \quad \xi=\frac{x}{a}, \quad \eta=\frac{y}{b},$$
$$z_a=\frac{z}{a}, \quad p=q^{-1}=\frac{a}{b}, \quad \kappa=ka. \tag{4}$$

The parameters σ and τ have some arbitrariness to choose provided that the resulting solution converges. This means that the equation (3) functions satisfy the conditions (2c) and (2d) irrespective of the parameters σ and τ. Hence, we can add the condition that the potential function satisfies the required edge condition.[11] In this condition, σ and τ are zero.

Enforcing the remaining condition (2a), we obtain the matrix equation by expanding the functions of ξ and η by a set of basis functions and by taking the moment with a set of weighting functions, where we use the Jacobi's polynomials as the expansion and weighting functions.[2] Thus, the matrix equation of the expansion coefficients $A_{mn}\sim D_{mn}$ becomes

$$\begin{aligned}
&[G(2m,2n,2s+1,2t+1)][A_{mn}]=[-\Lambda(\kappa_1,2s+1)\Lambda(\kappa_2,2t+1)],\\
&[G(2m,2n+1,2s+1,2t+2)][B_{mn}]=[-j\Lambda(\kappa_1,2s+1)\Lambda(\kappa_2,2t+2)],\\
&[G(2m+1,2n,2s+2,2t+1)][C_{mn}]=[-j\Lambda(\kappa_1,2s+2)\Lambda(\kappa_2,2t+1)],\\
&[G(2m+1,2n+1,2s+2,2t+2)][D_{mn}]=[\Lambda(\kappa_1,2s+2)\Lambda(\kappa_2,2t+2)],\\
&\quad s=0,1,2,\ldots, \quad t=0,1,2,\ldots,
\end{aligned} \tag{5}$$

where

$$G(m,n,s,t)=\int_0^\infty\int_0^\infty(\alpha^2+p^2\beta^2-\kappa^2)^{-1/2}\times\frac{J_m(\alpha)J_s(\alpha)}{\alpha}\frac{J_n(\beta)J_t(\beta)}{\beta}d\alpha\,d\beta, \tag{6a}$$

$$\Lambda(x,\nu)=\frac{J_\nu(x)}{x}, \quad \kappa_1=\kappa\sin\theta_0\cos\phi_0, \quad \kappa_2=q\kappa\sin\theta_0\sin\phi_0. \tag{6b}$$

Once the expansion coefficients are determined, the physical quantities such as intensity pattern, transmission coefficient, and velocity distribution on the hole can be computed. It is worthwhile to note that coefficients $A_{mn}\sim D_{mn}$ are determined separately. Only the A_{mn} coefficients are needed for a special case of the normal incidence.

B. Velocity distribution on the aperture

The distribution of the z component of the velocity on the hole is obtained from $v_z=-(\partial\Phi/\partial z)|_{z=0}$. The integration over the variables α and β can be performed analytically,[12] and the resulting expression becomes

$$v_z=\frac{1}{a\sqrt{1-\xi^2}\sqrt{1-\eta^2}}\sum_{m=0}^{\infty}\sum_{n=0}^{\infty}(-1)^{m+n}\{[A_{mn}T_{2n}(\eta)+B_{mn}T_{2n+1}(\eta)]T_{2m}(\xi)+[C_{mn}T_{2n}(\eta)+D_{mn}T_{2n+1}(\eta)]T_{2m+1}(\xi)\}. \tag{7}$$

Here $T_n(x)$ is the Chebyshev polynomial of the first kind. From the above equation, v_z behaves like $(1-\xi^2)^{-1/2}\times(1-\eta^2)^{-1/2}$ near the edge, as expected. This is consistent with the required edge condition for the component of the velocity tangent to the rigid screen near the edge.

C. Far field

The far-field expression may be evaluated from Eq. (3) with $\sigma=\tau=0$ by applying the stationary phase method of integration. By considering the even and odd properties of the integrands with respect to α and β and applying the standard procedure of the stationary phase method, we have

$$\Phi^d(r,\theta,\phi)=\frac{\pi q\kappa}{2}\frac{\exp(-jkr)}{kr}P(\theta,\phi), \tag{8a}$$

$$\begin{aligned}P(\theta,\phi)&=j\kappa\cos\theta f(\kappa\sin\theta\cos\phi,q\kappa\sin\theta\sin\phi)\\&=\sum_{m=0}^{\infty}\sum_{n=0}^{\infty}\{[A_{mn}J_{2m}(\kappa\sin\theta\cos\phi)+jC_{mn}J_{2m+1}(\kappa\sin\theta\cos\phi)]J_{2n}(q\kappa\sin\theta\sin\phi)\\&\quad+[jB_{mn}J_{2m}(\kappa\sin\theta\cos\phi)-D_{mn}J_{2m+1}(\kappa\sin\theta\cos\phi)]\\&\quad\times J_{2n+1}(q\kappa\sin\theta\sin\phi)\}.\end{aligned} \tag{8b}$$

D. Transmission coefficient

The radiated intensity of the diffracted wave is given by

$$\begin{aligned}W(\theta,\phi)&=\mathcal{R}\lim_{r\to\infty}r^2\frac{j\rho ck}{2}\Phi^{d*}\frac{\partial\Phi^d}{\partial r}\\&=2\left(\frac{\pi}{4}\right)^2\rho cq^2\kappa^2|P(\theta,\phi)|^2,\end{aligned} \tag{9}$$

where ρ is the density of the medium, c is the sound velocity, and $*$ denotes the complex conjugate. Transmission coefficient t is defined by the ratio of the total radiated power W_T into the $z<0$ dark space to the incident power $W_i=2\rho cq\kappa^2\cos\theta_0$:

$$t=\frac{W_T}{W_i}=\left(\frac{\pi}{4}\right)^2\frac{q}{\cos\theta_0}\int_0^{2\pi}d\phi\int_0^{\pi/2}|P(\theta,\phi)|^2\sin\theta\,d\theta. \tag{10}$$

Alternatively, we can use the simpler forward scattering theorem,[13] and the transmission coefficient becomes

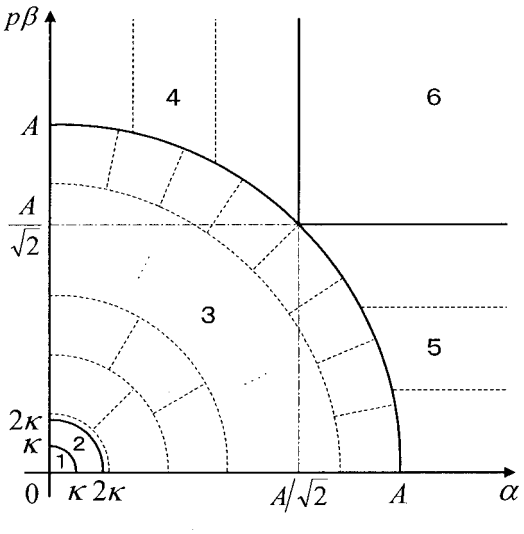

FIG. 2. Integration region is divided into six subregions. Gauss Legendre quadrature is used for regions 1–3, while asymptotic approximations of Bessel functions in the integrand are applied to regions 4–6.

$$\begin{aligned}t&=-\left(\frac{\pi}{2}\right)^2\frac{1}{\kappa\cos\theta_0}\mathcal{I}P(\pi-\theta_0,\phi_0+\pi)\\&=\left(\frac{\pi}{2}\right)^2\frac{1}{\kappa\cos\theta_0}\sum_{m=0}^{\infty}\sum_{n=0}^{\infty}\mathcal{R}\{[jA_{mn}J_{2n}(\kappa_2)+B_{mn}J_{2n+1}(\kappa_2)]J_{2m}(\kappa_1)+[C_{mn}J_{2n}(\kappa_2)-jD_{mn}J_{2n+1}(\kappa_2)]J_{2m+1}(\kappa_1)\},\end{aligned} \tag{11}$$

where κ_1 and κ_2 are defined in Eq. (6b).

II. COMPUTATION AND DISCUSSION

A. Computation of the expansion coefficients

To obtain the numerical results of the physical quantities, we must compute the matrix elements of Eq. (6a) given by double infinite integrals, which converge rather slowly. The method of computing these integrals is discussed elsewhere,[3] but we summarize the idea here for convenience. The full range of integration, which is equal to the first quadrant of the $(\alpha,p\beta)$ space, is divided into several subdomains consisting of annular sectors with different radii, as shown in Fig. 2. The symbol A denotes the maximum radius of the annular sectors, and the exterior of radius A is divided into three subregions, in which the integral variables include infinity. For the annular sectors, the integral is numerically carried out by applying the Gauss Legendre quadrature scheme, while the integral is analytically performed using the asymptotic approximations of the integrands for the region including infinity. The radius A has to be carefully chosen, since the validity of the asymptotic approximation of the Bessel functions is closely related to A. Thus, the double infinite integral is transformed into double finite integrals plus two types of integrals of a single variable and an analytical expression. In the present computation A is fixed to 400. The matrix equation size is truncated by $(nk)^2\times(nk)^2$, where $nk-1$ is the maximum value of indices

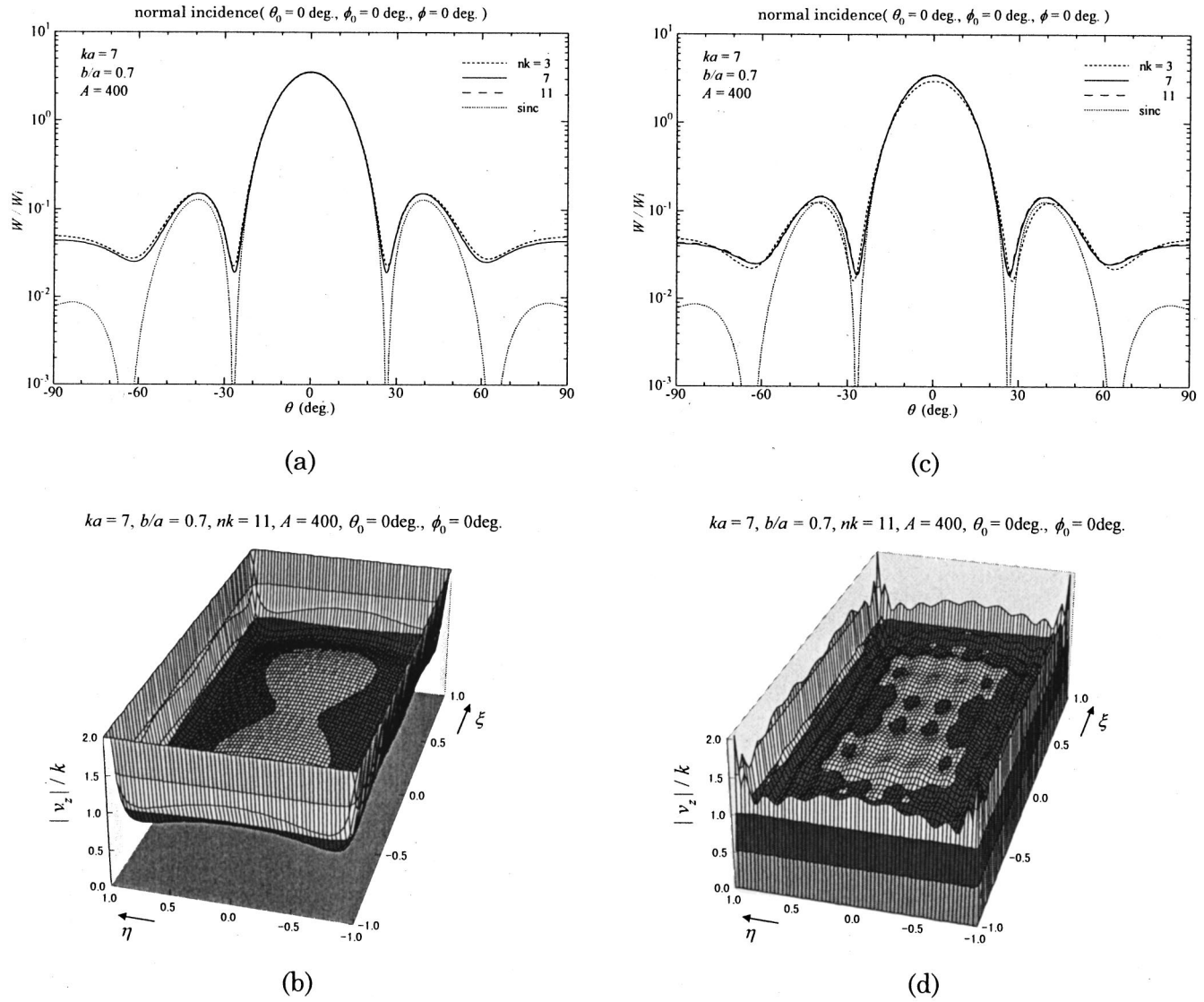

FIG. 3. Far intensity patterns and velocity distributions on hole computed using expansion functions given in Eq. (3). (a) and (b) are for 1 with $\sigma=\tau=0$ and (c) and (d) are for 2 with $\sigma=\tau=1$.

m, n, s, t in Eq. (5). By changing the value of nk, we can numerically verify the convergence of the solution.

When we use the KP method, how does the choice of the potential functions affect the convergence of the solution? We consider two kinds of functions, one satisfying the edge condition (case 1: $\sigma=\tau=0$) and the other not satisfying it (case 2: $\sigma=\tau=1$), and compute the expansion coefficients, the corresponding far intensity pattern, and the velocity distribution in each case. The case 2 expressions are given in the Appendix. The parameters are chosen as $\kappa=7$, $q=0.7$, and $nk=3,7,11$. As an example, magnitudes of the expansion coefficients A_{mn} for a normal incidence are computed when m and n are varied, although the plots of the results are omitted here. As m and n grow larger, the magnitudes of the coefficients A_{mn} decrease for case 1, but the coefficients of case 2 do not decrease. Figure 3(a) and (b) is the far intensity patterns and the amplitude of the velocity distribution on the hole, respectively. They are computed using the functions of case 1. Figure 3(c) and (d) is the corresponding results computed with the functions of case 2. The intensity patterns shown in Fig. 3(a) and (c) converge to the same values in spite of the nondecreasing coefficients of case 2. We think this is due to the fact that the far-field pattern has a stationary character, that is, it changes little for small changes in field distribution. Needless to say, the rate of convergence of case 1 is much faster than case 2. The curve denoted by ''sinc'' in each figure is the pattern computed from the Kirchhoff's integral (12). Figure 3(b) and (d) shows the magnitude of velocity distribution on the hole. Despite the fact that the velocity distribution of case 2 becomes zero at the edge [see Eq. (A1)], it becomes quite large near the edge as it does in case 1, which is close to an actual behavior near the edge. Both results have similar values except near the edge. We obtained results for other parameters and for oblique incidence, but we do not show them here to save space. We confirmed that the selection of the wave functions which satisfy the edge condition is very useful in actual computation. The subsequent computations are made by using the functions with $\sigma=\tau=0$.

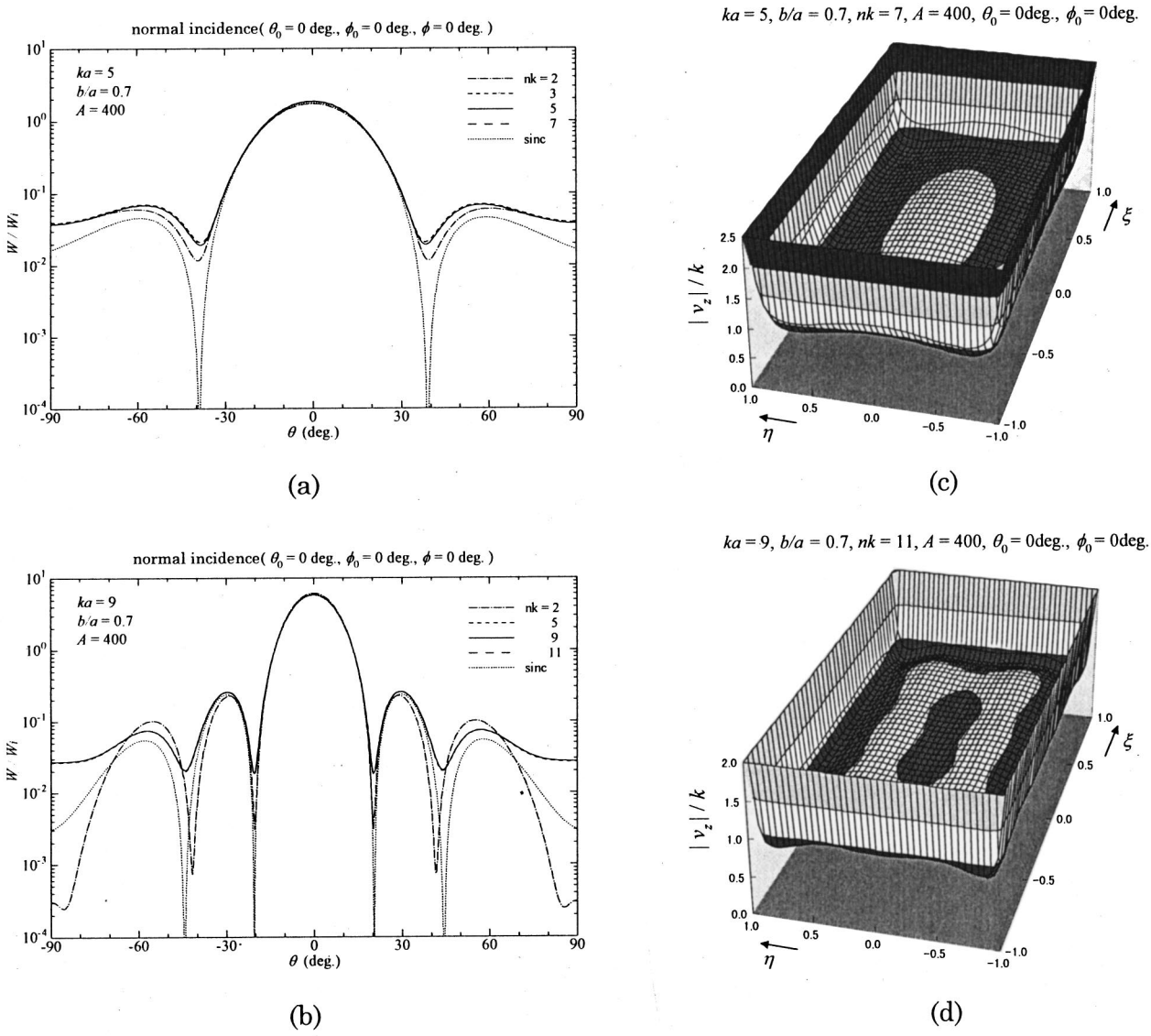

FIG. 4. Far intensity patterns and velocity distributions on hole for normal incidence ($\theta_0=0°$, $\phi_0=0°$). Hole size is $\kappa=ka=5$ and $\kappa=9$ with $q=b/a=0.7$ (curves denoted by ''sinc'' represent results by Kirchhoff's method).

B. Intensity patterns and velocity distributions on the hole

Figure 4 shows the power of the far diffracted fields and the velocity distributions on the hole for normal incidence. The hole size is selected as $\kappa=5$ and $\kappa=9$, and $q=b/a$ is fixed to 0.7. The observation point lies in the cut plane $\phi=0$. Figure 5 shows the corresponding results for oblique incidence ($\theta_0=30°$, $\phi_0=30°$). The observation point of the far field is in the cut plane $\phi=30°$. Roughly speaking, the results converge for $nk=\kappa$ or less. This criterion is similar to cases of eigenfunction expansions in circular cylindrical and spherical coordinate systems. The velocity v_z shows the singularity near the edge, which is proportional to $d^{-1/2}$, where d is the distance from the edge. In addition, the singularity becomes higher near the corner and is proportional to d^{-1}, which depends on the choice of the expansion functions. As is well known, the energy stored near the edge and corner must be finite. Both the amplitude and phase of the velocity v_z slowly vary except near the edge and corner. This means that the Kirchhoff's formula is a good approximation for predicting the diffracted field of acoustic waves. This seems to be due to an unpolarized character of the acoustic wave.

The result obtained by Kirchhoff's integral (denoted ''sinc'' in the legend) is also shown in each figure for comparison. Its expression is given by

$$\Phi_{PO}^{d}=-j\frac{q\kappa^2}{\pi}\frac{\exp(-jkr)}{kr}(\cos\theta+\cos\theta_0)\times\mathrm{sinc}[\kappa(\sin\theta\cos\phi+\sin\theta_0\cos\phi_0)]\times\mathrm{sinc}[q\kappa(\sin\theta\sin\phi+\sin\theta_0\sin\phi_0)], \tag{12}$$

where $\mathrm{sinc}(x)=\sin x/x$. The agreement between the two is very good, particularly for large values of κ.

C. Transmission coefficient

Figure 6(a) and (b) shows the frequency characteristics of the transmission coefficient t for normal and oblique inci-

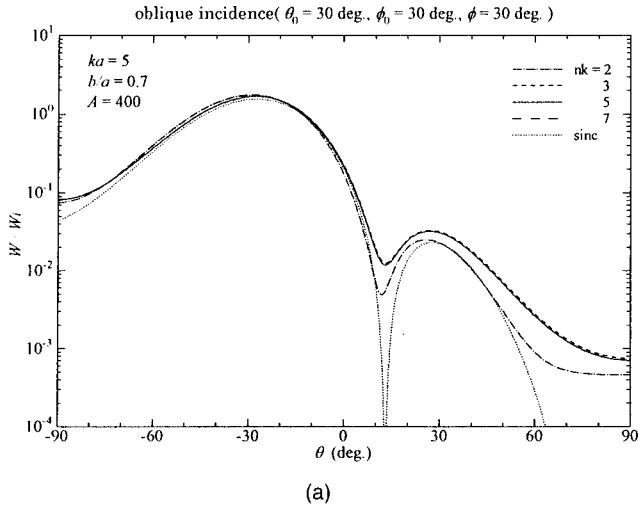

FIG. 5. Far intensity patterns for oblique incidence ($\theta_0=30°$, $\phi_0=30°$) corresponding to Fig. 4.

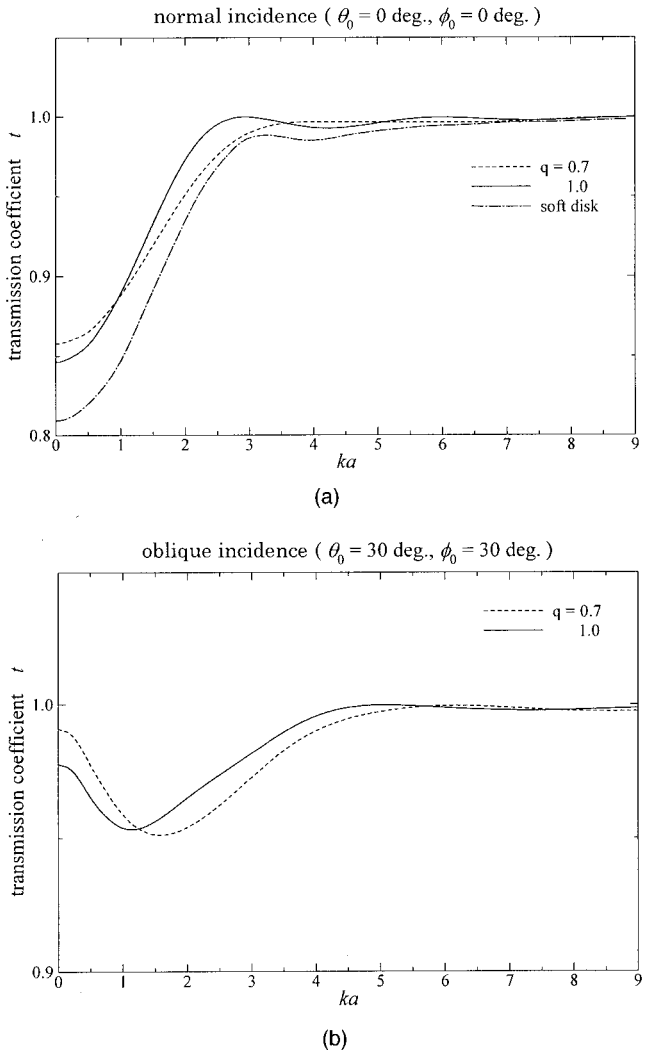

FIG. 6. Transmission coefficients t for (a) normal incidence ($\theta_0=0°$, $\phi_0=0°$) and (b) oblique incidence ($\theta_0=30°$, $\phi_0=30°$), when q is selected as $q=0.7$ and $q=1.0$. The result of square ($q=1$) hole for normal incidence is compared with Babinet's problem of a circular hole.

dences computed from Eq. (11), respectively. Two kinds of the parameters $q=b/a=1$ and $q=0.7$ are selected. The square hole result for the normal incidence is compared with that of the total scattering cross section of a circular soft disk with the same area as the square hole.[13] Both results show similar variation, but the level of the circular disk is lower, particularly for a small κ. The oblique incidence shows different variation from the normal incidence. The corresponding circular soft disk result for oblique incidence is not available. The transmission coefficients t approach finite values as κ decreases to zero for normal and oblique incidences. This situation is seen in the circular soft disk for the normal incidence.

III. SUMMARY AND CONCLUSIONS

An acoustic plane wave diffracted by a rectangular hole in an infinite rigid screen has been rigorously studied with the KP method. The screen thickness is assumed to be negligibly small. The velocity potential of the diffracted wave is expanded by a linear combination of the wave functions, which satisfy a part of the required boundary conditions and the edge condition. Some illustrations of the intensity pattern of the far field and the velocity distribution on the hole were obtained for both normal and oblique incidences. The frequency characteristics of the transmission coefficient were obtained and some of them were compared to the total scattering cross section of a circular soft disk with the same area as the square hole. Their agreement is rather good, considering the geometrical difference. By considering two kinds of expansion functions (one satisfies the edge condition while the other does not), we numerically studied how the choice of the expansion functions affects the convergence of the solution.

ACKNOWLEDGMENTS

We would like to thank the referees of the paper for helpful and valuable comments.

APPENDIX: EXPRESSIONS FOR $\sigma=\tau=1$

If we choose $\sigma=\tau=1$ in Eq. (3), the expressions for v_z on the hole and $P(\theta,\phi)$ are given as follows:

$$v_z=\frac{1}{a}\sqrt{1-\xi^2}\sqrt{1-\eta^2}\sum_{m=0}^{\infty}\sum_{n=0}^{\infty}(-1)^{m+n}$$
$$\times\left\{\left[A_{mn}\frac{U_{2n}(\eta)}{2n+1}+B_{mn}\frac{U_{2n+1}(\eta)}{2n+2}\right]\frac{U_{2m}(\xi)}{2m+1}\right.$$
$$\left.+\left[C_{mn}\frac{U_{2n}(\eta)}{2n+1}+D_{mn}\frac{U_{2n+1}(\eta)}{2n+2}\right]\frac{U_{2m+1}(\xi)}{2m+2}\right\}, \tag{A1}$$

$$P(\theta,\phi)=\sum_{m=0}^{\infty}\sum_{n=0}^{\infty}\left\{\left[A_{mn}\frac{J_{2m+1}(\kappa\sin\theta\cos\phi)}{\kappa\sin\theta\cos\phi}+jC_{mn}\right.\right.$$
$$\left.\times\frac{J_{2m+2}(\kappa\sin\theta\cos\phi)}{\kappa\sin\theta\cos\phi}\right]\frac{J_{2n+1}(q\kappa\sin\theta\sin\phi)}{q\kappa\sin\theta\sin\phi}$$
$$+\left[jB_{mn}\frac{J_{2m+1}(\kappa\sin\theta\cos\phi)}{\kappa\sin\theta\cos\phi}-D_{mn}\right.$$
$$\left.\left.\times\frac{J_{2m+2}(\kappa\sin\theta\cos\phi)}{\kappa\sin\theta\cos\phi}\right]\frac{J_{2n+2}(q\kappa\sin\theta\sin\phi)}{q\kappa\sin\theta\sin\phi}\right\}. \tag{A2}$$

Here $U_n(x)$ is the Chebyshev polynomial of the second kind. Equation (A1) shows deliberately incorrect edge condition for the normal velocity in the hole of the hard screen. The expansion coefficients $A_{mn}\sim D_{mn}$ are determined from the following matrix equation:

$$[G(2m+1,2n+1,2s+1,2t+1)][A_{mn}]$$
$$=[-\Lambda(\kappa_1,2s+1)\Lambda(\kappa_2,2t+1)],$$
$$[G(2m+1,2n+2,2s+1,2t+2)][B_{mn}]$$
$$=[-j\Lambda(\kappa_1,2s+1)\Lambda(\kappa_2,2t+2)],$$
$$[G(2m+2,2n+1,2s+2,2t+1)][C_{mn}]$$
$$=[-j\Lambda(\kappa_1,2s+2)\Lambda(\kappa_2,2t+1)],$$
$$[G(2m+2,2n+2,2s+2,2t+2)][D_{mn}]$$
$$=[\Lambda(\kappa_1,2s+2)\Lambda(\kappa_2,2t+2)], \tag{A3}$$

$$G(m,n,s,t)=\int_0^{\infty}\int_0^{\infty}(\alpha^2+p^2\beta^2-\kappa^2)^{-1/2}$$
$$\times\frac{J_m(\alpha)J_s(\alpha)}{\alpha^2}\,\frac{J_n(\beta)J_t(\beta)}{\beta^2}\,d\alpha\,d\beta. \tag{A4}$$

[1] T. Otsuki, ''Diffraction of an acoustic wave by a rigid rectangular plate,'' J. Phys. Soc. Jpn. **19**, 1733–1741 (1964).
[2] T. Otsuki, ''Diffraction of an acoustic wave obliquely incident upon a rigid rectangular plate,'' J. Phys. Soc. Jpn. **20**, 631–632 (1965).
[3] K. Hongo and H. Sugaya, ''Diffraction of an acoustic plane wave by a rectangular plate,'' J. Appl. Phys. **82**, 2719–2729 (1997).
[4] I. Kobayashi, ''Darstellung eines Potentials in zylindrischen Koordinaten, das sich auf einer Ebene innerhalb und ausserhalb einer gewissen Kreisbegrenzung verschiedener Grenzbedingung unterwirft,'' Sci. Rep. Tohoku Univ., Ser. 1 **20**, 197–212 (1931).
[5] I. N. Sneddon, *Mixed Boundary Value Problems in Potential Theory* (North-Holland, Amsterdam, 1966).
[6] Y. Nomura and S. Katsura, ''Diffraction of electromagnetic waves by ribbon and slit. I,'' J. Phys. Soc. Jpn. **12**, 190–200 (1957).
[7] K. Hongo and G. Ishii, ''Diffraction of an electromagnetic plane wave by a thick slit,'' IEEE Trans. Antennas Propag. **AP-26**, 494–499 (1978).
[8] K. Hongo, ''Diffraction by a flanged parallel-plate waveguide,'' Radio Sci. **7**, 955–963 (1972).
[9] K. Hongo, ''Diffraction of an electromagnetic plane wave by circular disk and circular hole,'' IEICE Trans. Electron. **E80-C**, 1360–1366 (1997).
[10] A. Sauter, Jr. and W. W. Soroka, ''Sound transmission through rectangular slots of finite depth between reverberant rooms,'' J. Acoust. Soc. Am. **47**, 5–11 (1970).
[11] R. E. Collin, *Field Theory of Guided Waves* (IEEE, New York, 1991), 2nd ed.
[12] I. S. Gradshteyn and I. M. Rhzhik, *Table of Integrals, Series and Products* (Academic, New York, 1980).
[13] J. J. Bowman, T. B. A. Senior, and P. L. E. Uslenghi, *Electromagnetic and Acoustic Scattering by Simple Shapes* (North-Holland, Amsterdam, 1969).

Three-dimensional transducer voltage in anisotropic materials characterization

Oleg I. Lobkis[a)]
Center For Nondestructive Evaluation, Iowa State University, Ames, Iowa 50011-2162

D. E. Chimenti[b)]
Center For Nondestructive Evaluation and Aerospace Engineering & Engineering Mechanics Department, Iowa State University, Ames, Iowa 50011-3040

(Received 21 July 1998; revised 17 February 1999; accepted 18 March 1999)

Air- and fluid-coupled ultrasound has been used to characterize experimentally the elastic behavior of composite materials by employing a 3-D voltage calculation to model transmission or reflection experiments. With sound propagation along material symmetry directions, integration over the incident-plane angle alone is generally sufficient to model the transducer voltage accurately, where a saddle-point calculation is used to evaluate the dependence of the diffraction integral on the out-of-incident-plane angle ϕ. In general material directions, however, this integration must be extended to account for ϕ-dependent variations in the reflection or transmission coefficient that give the scattering a strong, asymmetrical dependence on ϕ. This article presents theoretical and experimental results to illustrate this effect and explores the relationship between the 2-D and 3-D calculations. Experimental results demonstrating viscoelastic property reconstruction in composite plates in both air-coupled and liquid-coupled measurements are presented. It is shown that the influence of the ϕ-dependent integration on the voltage, embodied in the 3-D calculation, is particularly strong when the incident angles are small and the wave paths are large, as typically experienced in air-coupled measurements.
[S0001-4966(99)00707-9]

PACS numbers: 43.20.Gb, 43.20.Bi [AN]

INTRODUCTION

Ultrasonic materials characterization is widely used to assess both properties and defects of structural components. Recently, owing principally to the improvement in sources and receivers, the option of gas- or air-coupled ultrasonic testing has also become a realistic possibility. In this article, we extend the application of resonant sound transmission methods through ambient air (or reflection in liquid-coupled configurations) to anisotropic materials, where the incident sound wave vector projection is oriented in a general direction in the plane of an anisotropic laminate. The major results reported here are the establishment and demonstration of the importance of contributions to the received voltage from rays not contained in the incident plane, for sound propagation in a general, nonsymmetry direction. We show that the error made by ignoring these out-of-plane effects is especially large for engineered materials, such as composite laminates, at low angles of incidence.

We proceed by using a rigorous 3-D voltage calculation to isolate the effect of the geometry from the effect of material properties on the observed signals. In an asymptotic sense, contributions to the spectral integral representing the voltage arise from the poles of the transmission, or reflection, coefficient (containing the material properties) and the saddle point (dependent on extrinsic experimental parameters). Estimates of the C_{ij}, or its complex-valued counterpart C_{ij}^{*}, for a given sample are calculated iteratively using the measured data to test a maximum likelihood estimator, such as the sum of the squared errors. These methods have been demonstrated to yield very accurate estimates of viscoelastic properties in air-coupled measurements of Plexiglas, layered aluminum composite laminates, and uniaxial graphite-epoxy in either of the two symmetry directions.[1–3] In all the above cases, material symmetry normal to the plane of incidence strongly reduces the influence of out-of-plane rays on the received voltage. When this symmetry is absent, these contributions must be properly accounted for, as we shall see below.

Advances in transducer technology have improved signal-to-noise ratios in air-coupled (A/C) ultrasound. Highly efficient designs utilizing either much better impedance matching or ultra low-mass drivers have resulted in significantly higher pressure amplitudes in air. Foil transducers,[4] which are basically extensions of designs well-known in high-frequency audio tweeters, have been reported by several groups.[5–8] Piezocomposites have also been developed as high-efficiency sources and detectors of ultrasound in air[9–11] and have been applied to plate wave propagation and defect detection.[12] Elastic property measurements have been reported by Hosten *et al.*,[13] and others.[14] A more detailed review of recent literature in air-coupled ultrasonics can be found in Ref. 3.

Some of the experimental work reported here relates to air-coupled experiments and the remainder to fluid-coupled

[a)]On leave from Laboratory of Acoustic Microscopy, Institute of Biochemical Physics, Russian Academy of Science, 4 Kosygin St., 117334 Moscow, Russia.
[b)]Electronic mail: chimenti@iastate.edu

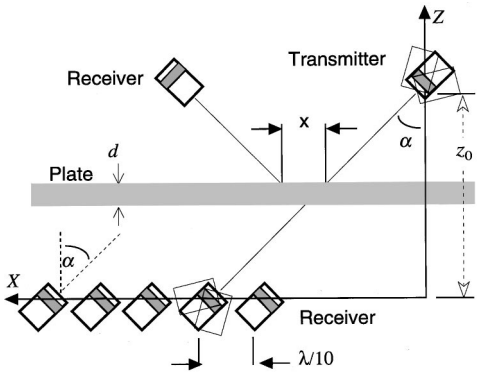

FIG. 1. Schematic diagram of the experimental geometry, showing transducer placement and position scanning operation in through-transmission and in reflection.

measurements, but the analysis is perfectly general and can apply to any coupling medium. After a review of the theoretical calculation leading to the 3-D voltage expression in a two-transducer measurement, we explain the importance of the out-of-incident plane integration for an anisotropic medium with the wave vector in a nonsymmetry direction. We also describe the experimental method and analysis; finally, we use these tools to characterize plates of composite laminates in air or water.

I. 3-D VOLTAGE CALCULATION

In the experimental bistatic transducer arrangement of Fig. 1, the received voltage will be a function of both the extrinsic experimental parameters and the intrinsic plate properties, through the plate-scattering (reflection or transmission) coefficient. We have shown that the extrinsic parameters can be isolated from the transmission characteristics[15] by modeling the 3-D field of the incident beam at the receiver and accounting for the receiver characteristics by appeal to reciprocity. In Fig. 1, a sound beam from the transmitter falls on the plate at an incident angle α, and the subsequent reflected or transmitted field induces a voltage in the receiving transducer. The effect of both transmitter and receiver can be accounted for through the Kino-Auld electromechanical reciprocity relations,[16,17] where the resulting spectral integrals are

$$V(x,f,\alpha)=i\kappa a^4\int_0^{2\pi}\int_0^{\pi/2-i\infty} S(\theta_i,\phi_i)D^T(\gamma)D^R(\gamma) \times \exp[i\kappa z_0\cos\theta_i+i\kappa(x_0+x) \times\sin\theta_i\cos\phi_i]\sin\theta_i\, d\theta_i\, d\phi_i, \quad (1)$$

where z_0 is the total vertical distance between the transducers, x is the transducer separation along the guided wave propagation direction from the symmetrical position x_0 ($=z_0\tan\alpha$), κ is the sound wave number in a fluid, a is the radius of the transducers, f is the frequency, and α is the incident angle (measured between the normal to the transducer face and the plate normal). These two rays, the plate normal and the transducer-face normal, define the incident plane. The scattering coefficient (reflection or transmission), $S(\theta_i,\phi_i,d,\{C_{ij}^*\})$, is a function of complex viscoelastic material properties, $D^T(\ )$ and $D^R(\ )$ are the beam directivity functions for the transmitting and receiving transducers,[15] d is the thickness of the plate, and γ is the angle between transmitter acoustical axis and each incident plane-wave direction of propagation (θ_i,ϕ_i) in three dimensions; that is, $\cos\gamma=\cos\theta_i\cos\alpha+\sin\theta_i\sin\alpha\cos\phi_i$.

In the air-coupled measurements, the narrow bandwidth of the transducers dictates an approach to data acquisition different from the one typically used in liquid-coupled experiments. To extract the maximum quantity of information in the air-coupled geometry, we have scanned the receiver position, as illustrated in Fig. 1, and these results can be combined[3] to yield an effective wave number voltage spectrum. This transformed spectrum can be constructed by a coherent summation of signals measured for a single wave number ξ, but at different values of x. The result of the coherent sum is in the form of Fourier transform, consisting operationally of summing the measured voltage signals, each weighted by the appropriate plane wave $\exp(-i\xi x)$, whose phase corresponds to the value of x where the measurement is made.[3]

The measured or calculated result can be converted from a wave number spectrum to an angular spectrum using Snell's law as $\xi=\kappa\sin\theta$, where θ is the phase-match angle. It is important to distinguish clearly here between the incident angle α and the phase-match angle θ. The incident angle measures the fixed geometrical orientation of the transducer with respect to the solid–fluid interface. The phase-match angle relates to the incidence of a particular component in the plane-wave spectrum comprising the incident beam. The angular voltage spectrum $W(\theta;\alpha)$ is given by

$$W(\theta;\alpha)=\int_{-\infty}^{\infty}V(x;\alpha)\exp[-i\kappa\sin\theta x]dx. \quad (2)$$

Then, to compensate for the narrowness of the transducer directivity functions, an aperture larger than the transducer operating at a single incident angle α is synthesized by making measurements at several incident angles and summing the resulting angular spectra. This last operation is performed incoherently for the sake of convenience, $W(\theta)=\Sigma_\alpha|W(\theta,\alpha)|$, effectively creating a transmission function amplitude with a square-window aperture. The aperture is determined by the range of values of α over which we choose to measure, in each case ensuring overlap of D^TD^R with measurements at neighboring values of α.

The function $W(\theta)$ represents the combination of Eqs. (1) and (2) and has a close relationship with the scattering coefficient amplitude of the plate. Calculating the integral over the x variable of the function $\exp[i\kappa x(\sin\theta_i\cos\phi_i-\sin\theta)]$ yields $2\pi\delta(\kappa\sin\theta_i\cos\phi_i-\kappa\sin\theta)$, where δ is the Dirac delta function. The result is

$$W(\theta)=2i\pi\kappa a^4\sum_{\alpha}\int_0^{\pi/2-i\infty}\exp(i\kappa z_0\cos\theta_i)\sin\theta_i\,d\theta_i$$
$$\times\int_0^{2\pi}S(\theta_i,\phi_i)D^T(\gamma)D^R(\gamma)$$
$$\times\exp(i\kappa x_0\sin\theta_i\cos\phi_i)$$
$$\times\delta(\kappa\sin\theta_i\cos\phi_i-\kappa\sin\theta)d\phi_i. \quad (3)$$

Now, we calculate the integral over ϕ_i. This task is simplified because of the presence of the δ-function, the only contributions to the integral arising from the roots of its argument, or $\sin\theta_i\cos\phi_i-\sin\theta=0$. Let us denote these roots as ϕ_0 and note that there are two of them, $\phi_0=\pm\arccos(\sin\theta/\sin\theta_i)$, one on either side of the x axis. In fact, all quantities in Eq. (3) are symmetrical in ϕ_i except $S(\theta_i,\phi)$ under limited conditions. If the transducer scan direction in an anisotropic solid is chosen not to be along a material symmetry axis, then $S(\theta_i,\phi_0)\neq S(\theta_i,-\phi_0)$. Under these conditions, serious disparities arise between the full 3-D voltage calculation and the diffraction-corrected 2-D result, as we shall demonstrate later both theoretically and experimentally. The result of performing the integral over ϕ_i is

$$W(\theta)=\sum_{\alpha}\int_0^{\pi/2-i\infty}[S(\theta_i,\phi_0)+S(\theta_i,-\phi_0)]$$
$$\times D^T(\gamma_0)D^R(\gamma_0)\exp[i\kappa z_0\cos\theta_i]$$
$$\times\frac{\sin\theta_i\,d\theta_i}{(\sin^2\theta_i-\sin^2\theta)^{1/2}}, \quad (4)$$

where γ_0 is the angle γ [introduced after Eq. (1)] evaluated at the points $\pm\phi_0$. From the expression for γ and the value of ϕ_0, we have $\cos\gamma_0=\cos\theta_i\cos\alpha+\sin\theta\sin\alpha$. We have also suppressed a multiplicative factor of $2i\pi a^4\times\exp(i\kappa x_0\sin\theta)$ in the above equation.

Finally, for convenience we introduce a new variable β defined by $\cos\beta=\cos\theta_i/\cos\theta$, and rewriting $W(\theta)$ the angular voltage spectrum is

$$W(\theta)=\sum_{\alpha}\int_0^{\pi/2-i\infty}[S(\theta_i,\phi_0)+S(\theta_i,-\phi_0)]$$
$$\times D^T(\gamma_0)D^R(\gamma_0)\exp[i\kappa z_0\cos\theta\cos\beta]d\beta. \quad (5)$$

The angles θ_i, ϕ_0, and γ_0 are related to the angles θ and β through

$$\cos\theta_i=\cos\theta\cos\beta,\quad \tan\phi_0=\sin\beta\cot\theta,$$
$$\cos\gamma_0=\cos\theta\cos\alpha\cos\beta+\sin\theta\sin\alpha. \quad (6)$$

The three integration angles above are referenced from the scan axis ($\beta=0$), which is contained in the incident plane.

There is an important point to note here. As shown in Ref. 15, the combined directivity functions $D^T(\gamma_0)D^R(\gamma_0)$ display no sidelobe behavior, contrary to what one would expect for either D^T or D^R individually. That is, the voltage represented by Eq. (3), where the scattering coefficient $S(\theta_i,\phi_i)$ is set to ±1 (perfect transmitter or reflector) will simply yield the phase and amplitude variations of the transducers only. When the field of a piston radiator is detected by a finite receiver, especially one identical to the transmitter, the phase averaging that occurs on the receiver results in an almost structureless directivity curve. Therefore, the combined piston transducer functions can be replaced by combined Gaussian directivity functions $D^T(\gamma_0)D^R(\gamma_0)\approx\exp(-b^2k^2a^2\sin^2\gamma_0)$, where $b\approx0.522$ is the parameter of correspondence between Bessel (piston) and Gaussian directivity functions.[15]

We can expand the angular dependence of the exponential argument near $\beta=0$ in the form

$$\sin^2\gamma_0\approx\sin^2(\theta-\alpha)+\cos\theta\cos\alpha\cos(\theta-\alpha)\sin^2\beta. \quad (7)$$

It is clear that for the summation on incident angle α, only rays in a relatively small angular interval $\Delta\theta\approx(\kappa a)^{-1}$ near $\theta=\alpha$ make a contribution to the signal. When $\theta=\alpha$, the first term in Eq. (7) above vanishes, and the remaining term of the expansion can be written as $\cos^2\theta\sin^2\beta$. This approximation allows us to separate the α and β variables of the Gaussian directivity function $\exp(-b^2k^2a^2\sin^2\gamma_0)\approx\exp(-b^2k^2a^2\sin^2(\theta-\alpha))\exp(-b^2k^2a^2\cos^2\theta\sin^2\beta)$. The sum over α of the term $\exp(-b^2k^2a^2\sin^2(\theta-\alpha))$ gives a θ-independent constant, which we suppress, and the resulting signal $W(\theta)$ can be written as

$$W(\theta)=\int_0^{\pi/2-i\infty}[S(\theta_i,\phi_0)+S(\theta_i,-\phi_0)]$$
$$\times\exp[i\kappa z_0\cos\theta\cos\beta$$
$$-b^2k^2a^2\cos^2\theta\sin^2\beta]d\beta. \quad (8)$$

The principal signal contribution to $W(\theta)$ in Eq. (8) will arise when β is within $|i\kappa z_0+b^2k^2a^2|^{-1/2}$ of the axis. Only for plane waves, when $\kappa z_0\to\infty$ and $\kappa a\to\infty$, does $W(\theta)$ become identical to the plane-wave scattering coefficient $S(\theta)$ for the xz incident plane. In experiments, the difference between $W(\theta)$ and $S(\theta)$ depends on the values of κz_0 and κa and the plate properties and orientation as well, because they are included in the integrand in Eq. (8). Therefore, for anisotropic media there is a substantial difference between the 3-D model result $W(\theta)$ and the approximate plane-wave signal $S(\theta)$. Ignoring this effect will cause any inversion procedure based on the simpler model to infer erroneous material property values, especially in the material damping, from experimental data. We demonstrate this effect below.

II. EXPERIMENTAL DETAILS

The major objective of this article is to present 2-D and 3-D calculations of transducer voltages under a variety of conditions, and to make comparisons of these calculations to actual experiments in order to illustrate graphically the applicability or limitations of the 2-D theory and some of the counterintuitive circumstances surrounding the need for a full 3-D calculation. Nonetheless, the experiments are also an important component of the work; the details of their performance are summarized in this short section. A full exposition of both types of experimental studies can be found elsewhere in the published literature. The air-coupled experiments have been described in detail in Refs. 2 and 3. Briefly,

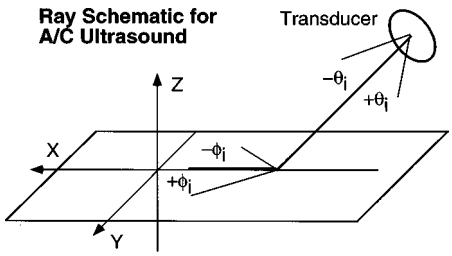

FIG. 2. Schematic representation of beam spread angles in, and out of, the incident xz plane.

identical foil capacitance transducers[4] have been used to generate and detect A/C ultrasound. While such devices can be operated in a wide bandwidth ($\sim$2 MHz) under favorable conditions, we have chosen to bandlimit the excitation of our transducers using a 3- or 5-cycle tone burst. The reason for this action is that all data reported here are acquired by (1) capturing the entire rf signal, (2) performing a time-frequency fast Fourier transform (FFT), and (3) isolating the frequency component of interest. This procedure insures accurate isolation of the single frequency for which the voltage versus angle is calculated. Following this strict protocol helps explain why there is such good agreement with the calculations.

This acquisition procedure is repeated for all scanning positions x, and the resulting signal has then been spatially Fourier transformed. The transform is only approximate because the experimental sum must be terminated at a finite value of x. During the measurements, however, signals are acquired until a signal-to-noise ratio of less than 1 is observed, preserving nearly all the available information content in the experimental signal.

The signal gains used in the measurements have been in the range of 40 to 60 dB, after the charge amplifier that follows the foil transducer. These numbers are, however, somewhat misleading because the excitation signal (from a RITEC RAM-10000) is also a function of frequency. Further, the rf excitation must be applied to the transmitter through an isolation-bias circuit, as described in Ref. 3. We estimate the signal-to-noise ratio of the raw tone burst signal arriving at the oscilloscope to be between 2 and 5, depending on angle, frequency, and other conditions. It is critical, however, to recall that only a single frequency is selected from the transform for further processing and summing according to the analysis presented in the previous section.

Measurements of the directivity function D^T or D^R for an air-coupled transducer agree well with calculated predictions[3] based on Eq. (1) for a 10-mm-diameter, piston-radiator, foil transducer operating at 700 kHz. We found that the foil transducers effectively transmit or receive waves in an angular region of about ± 3 deg. Figure 2 shows schematically the beam diffraction in the incident plane with angular spreading θ_i and spreading in the object plane of ϕ_i. It is well-known that the plate-scattering coefficients have a strong functional dependence on the in-plane angle θ_i, with the sharp maxima or minima occurring at angles corresponding to phase-matched guided wave-mode excitation conditions.

Because of the large acoustic impedance difference in air-coupled measurements between the plate solid material and the air, the range over which the scattering coefficients change (structure widths, for example) can be much less than the extrinsic beam spread θ_i, owing to diffraction. For liquid-coupled geometries, measurements are typically performed as a function of the excitation frequency, implying that beam spread changes over the measurement range. The liquid-coupled diffraction field is modeled as a piston radiator. It is important to recall, however, that the voltage of a piston-radiator field, measured by an *identical* piston radiator, smears the phase function of the transmitter field and yields the result[15] that the *combined* directivity functions $D^T D^R$ display almost no sidelobe behavior, as noted above. The piston function amplitudes can therefore be replaced by Gaussians. At the same time, no approximation to the signal phase has been performed. That is, our calculation here is *not* a far-field analysis, and therefore does not have the usual limitations associated with such phase approximations.

Returning to the 3-D aspects of the experiment, the plate transmission or reflection characteristics will select that part of the incident beam angular distribution (which may not be near the central ray at α in Fig. 1) to contribute to the output signal. Moreover, the beam diffraction normal to the incident plane can be asymmetrical for anisotropic materials because the effective material constants, in that case $C_{ij}(\psi)$, are themselves asymmetrical functions of the fiber angle ψ. For strongly anisotropic materials, such as fibrous composites, the material properties can change significantly and asymmetrically with small variations of the in-plane angle ϕ_i, meaning that the angular spread of the incident beam and the beam sensitivity of the receiver must be taken into account.

The water-coupled experiments are described in much fuller detail in Refs. 18–21. These earlier studies, too, consist of pitch–catch measurements with identical piston transducers. In this case, they have a center frequency of 7 MHz and a useable bandwidth of about 12 MHz. Data are acquired in a similar manner to the A/C measurements described above, except that a broadband chirp signal has been used for the excitation. Then, individual frequency components are selected for processing after FFT of the time-domain signal. The effects of transducer beam spread and water-path attenuation have been accounted for by careful construction of the measurement geometry. After signal component extraction from the time-frequency FFT, the signals are treated in a manner identical with the procedures in the A/C measurements.

III. AIR-COUPLED RESULTS

We first consider an isotropic plate, where the material properties do not depend on direction out of the incident plane. To be specific, we model the case of transmitted sound measured as a function of the incident-plane angle θ_i. The ordinate of this and subsequent curves in this section is labeled *voltage* to emphasize the experimental nature of the data. However, the voltage referred to here is the transducer voltage after being processed according to the procedure summarized in the previous section and described in detail in Refs. 3 and 15. This processing yields $W(\theta)$, a function closely related to the appropriate scattering coefficient, either

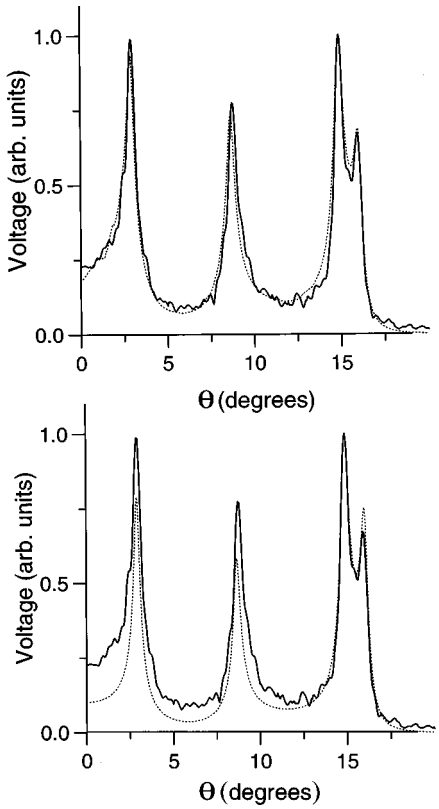

FIG. 3. Experimental (solid curve) and theoretical transmission function $W(\theta)$ (dotted upper), and plane-wave transmission coefficient $T(\theta)$ (dotted lower), as a function of angle from the normal. The material is a 2.3-mm Plexiglas plate measured at 700 kHz.

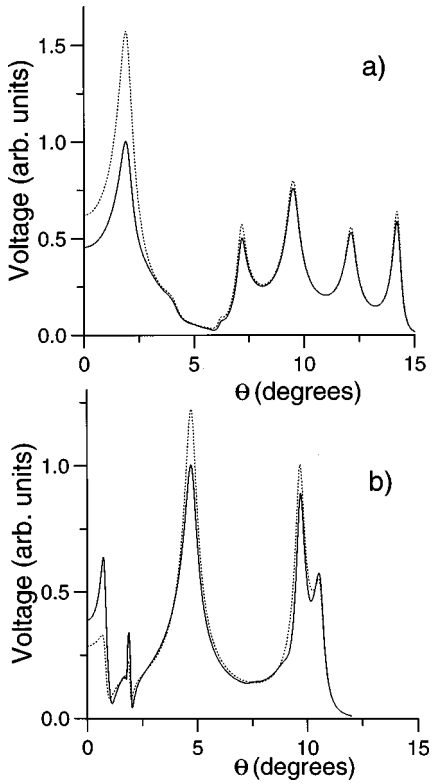

FIG. 4. Calculated transmission function $W(\theta)$ for a 3.6-mm uniaxial carbon–epoxy laminate plate with (solid curves) and without (dotted curves) ϕ_0-dependence of the transmission coefficient. The scanning direction is (a) perpendicular to the fibers in the upper graph, and (b) along them in the lower graph.

transmission or reflection. The transmission coefficient $T(\theta_i)$ [which replaces the generalized scattering coefficient $S(\theta_i)$] is a function of the in-plane angle. Only the beam spread in the incident xz plane contributes to the voltage integral in Eq. (8). Experimental and theoretical results at 700 kHz for a Plexiglas plate are presented in Fig. 3. The solid curve in both graphs is the measurement, the dotted curve in the upper frame is the calculated best-fit voltage function $W(\theta)$, and the dotted curve in the lower frame is the transmission coefficient $T(\theta)$ using the same material parameters as for the $W(\theta)$ calculation. The calculated peak positions, which correspond to the Lamb mode excitation angles, are identical in both curves $W(\theta)$ and $T(\theta)$. For this reason the plane-wave approximation can be reliably used for velocity estimation in isotropic plates, since the peak positions are determined by these values. At the same time, using this approximation to model material damping gives incorrect results unless the diffraction contribution is taken into account. This is because the widths of the peaks and their amplitudes, features critical to infer damping characteristics, are different for $W(\theta)$ and $T(\theta)$, as seen in the lower frame of Fig. 3.

For an anisotropic medium where sound propagates along a symmetry direction, such as in a uniaxial laminate along the fibers ($\psi=0$ deg) or perpendicular to them ($\psi=90$ deg), contributions from the two ϕ_0-ranges on either side of the incident plane $\pm\phi_0$ will be essentially identical. The reason is clearly because $T(\theta_i,+\phi_0)=T(\theta_i,-\phi_0)$ in Eq. (8). We present the calculated transducer voltage $W(\theta)$ for $\psi=90$ deg in Fig. 4(a) and for $\psi=0$ deg in Fig. 4(b), where the ϕ_0-dependence of the transmission coefficient $T(\theta_i,\phi_0)$ near each of the symmetry axes for a carbon–epoxy laminate *is* accounted for (solid curves) and *is not* accounted for (dotted curves). For either direction of scanning, along or normal to the fibers, the difference between the two curves is larger at small incident angles. At incident angles closer to normal incidence, the wave vector geometry implies that a larger angular range in ϕ_0 will contribute to the integral in Eq. (8). Near the longitudinal critical angle in particular, $W(\theta)$ is sensitive to changes in this velocity. The variation in C_{ij} with ϕ_0 causes changes in the output function $W(\theta)$ when compared with the case for which only the in-plane transmission coefficient $T(\theta_i,\phi_0=0)$ is used in the voltage calculation of Eq. (8).

An example of material property extraction from experimental data is presented in Fig. 5 for a scan direction perpendicular to the fibers $\psi=90$ deg. The sample is a 3.6-mm carbon–epoxy plate (AS/4-3501) measured at 600 kHz (upper plot) and 900 kHz (lower plot), and the data are compared to a best-fit calculated signal $W(\theta)$ from Eq. (8). The elastic property information is inferred from the data by noting that in some limited regions of the dispersion, behavior is dominated by one or two stiffnesses. For example, the peak (A_0 and S_0 modes) near 13 deg in the lower frame of Fig. 5 depends almost exclusively on C_{44} because 13 deg is greater than the shear critical angle. Fitting this peak alone yields an initial guess for the real part of C_{44}. The imaginary parts (of all peaks) are estimated from an examination of the effect on the peak widths of varying $\Im(C_{44})$. Other peaks in the spec-

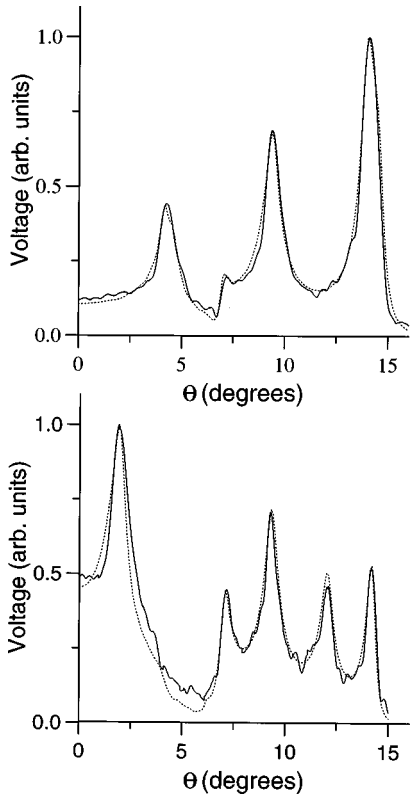

FIG. 5. Experimental (solid curves) and calculated (dashed curves) transmission function $W(\theta)$ when the incident plane is normal to the fibers ($\psi = 90$ deg) for a 3.6-mm carbon–epoxy laminated plate at frequencies of 600 kHz (upper frame) and 900 kHz (lower frame).

trum are estimated in a similar manner. The final adjustments and polishing are accomplished by the conjugate gradient method, as detailed in Ref. 3.

The inferred values of the viscoelastic constants are $C_{22}^{*}=C_{33}^{*}=15.3-0.3i$, $C_{23}^{*}=8.1-0.1i$, and $C_{44}^{*}=3.6-0.1i$. The signal dependence on other material constants is much weaker for this direction of scanning, and these constants cannot be reliably reconstructed. For the stiffnesses cited above, however, the sensitivity of this method is high enough to resolve shifts of only 1% or 2% in the constants.

Another example of elastic property inference from an experimental signal is presented in Fig. 6 for an in-plane angle $\psi_0=0$ deg. Since this is a symmetry direction, there is no significant contribution to the transmission function $W(\theta)$ from planes other than $\phi_0=0$ deg. The solid curve is the air-coupled measurement for a 3.6-mm uniaxial carbon–epoxy plate; the dotted curve shows the calculated transmission function $W(\theta)$ using best-fit values for the real and the imaginary parts of four of the five transversely isotropic material constants C_{ij}^{*} accessible in this measurement. The agreement is excellent, as it should be for fitted constants. Using these same constants, we have also modeled the data at $\psi=90$ deg shown above in Fig. 5. The calculated curve has some rapidly varying structure near 2 deg that is not completely observed in the data. These narrow resonances, characteristic of three modes S_1, S_2, and A_2 in close approach near the longitudinal critical angle, require finer spatial sampling to reconstruct their behavior. In this data, the A_3 mode near 1 deg, the A_1 mode at 5 deg, and the overlapping S_0 and A_0 modes at 10 deg are well modeled.

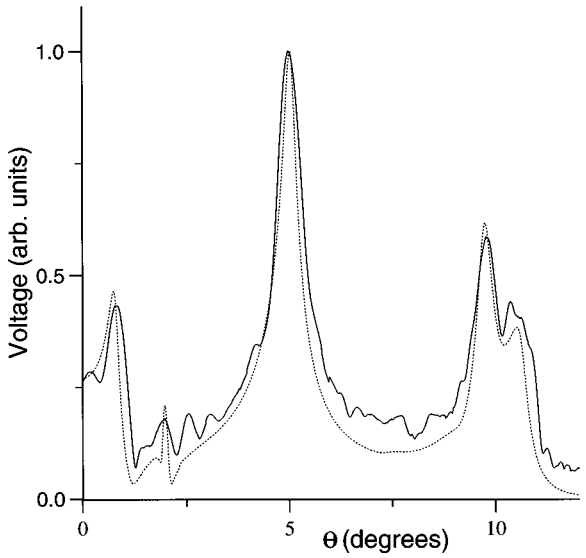

FIG. 6. Experimental (solid curve) and calculated (dashed curve) transmission function $W(\theta)$ and appropriate transmission coefficient $T(\theta)$ for a 3.6-mm uniaxial carbon–epoxy laminated plate in the $\psi=0$ deg direction at frequency of 900 kHz.

So long as the effective elastic stiffnesses in the $+\phi_0$ and $-\phi_0$ directions are identical, as they are for symmetry-axis propagation in composites, the phase of waves arriving from either $\pm\phi_0$ will be identical. The result is the detailed cancellation of their contributions in the receiver voltage of Eq. (8). As the incident angle α increases, the importance of this contribution from off-axis propagation diminishes for purely geometrical reasons. Conversely, at small values of α, rays in a wide range of ϕ_0 will contribute to the signal. In the limiting case of normal incidence, rays in any ϕ_0 direction can contribute equally to the signal.

For a general direction in the uniaxial plate (for example, $\psi=60$ deg), the ϕ_0-dependence of the transmission coefficient is critical for obtaining an accurate result, and the calculation must include this aspect. For a general in-plane angle, the plate properties are not symmetrical about a plane containing the direction of scanning and $T(\theta_i,+\phi_0)$ is not equal to $T(\theta_i,-\phi_0)$ in Eq. (8). For the uniaxial composite this effect is especially pronounced. A numerical demonstration of the importance of this underappreciated effect is shown in Fig. 7. Here, the voltage signal function $W(\theta)$ is calculated for the 3.6-mm uniaxial graphite–epoxy laminate at a frequency of 0.9 MHz. The solid curve includes the effect of the ϕ_0 dependence, while the dashed curve has been calculated while ignoring it. The distinction here is quite apparent. Both the positions *and* the heights of the transmission peaks are different in the two cases. Even the minima separating the resonances change between the two calculations. Virtually all features are different, except for the S_1 peak near 9 deg. These results illustrate graphically the significance of the voltage contribution from rays not contained in the incident plane.

Physically, the difference between the curves in Fig. 7 arises from the variation in the phase of the waves arriving from the $+\phi_0$ and $-\phi_0$ directions. Since the effective elas-

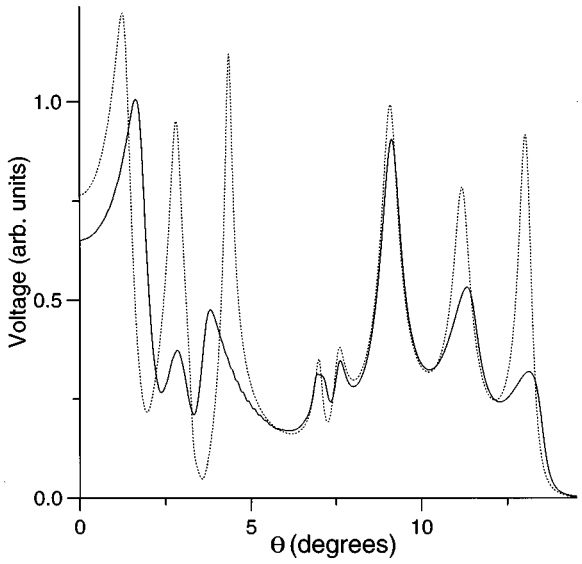

FIG. 7. Calculated transmission function $W(\theta)$ for a 3.6-mm uniaxial carbon–epoxy laminated plate in the $\psi=60$ deg direction at frequency of 900 kHz. Solid curve includes ϕ_0 contributions to voltage, and dashed curve is calculated without these terms.

tic stiffnesses in the complementary directions either side of $\phi_0=0$ deg (with $\psi=60$ deg) are quite different, waves propagating in the positive ϕ_0 direction have phase velocities different from those of waves for which ϕ_0 is negative. As a result, all these $+\phi_0$ and $-\phi_0$ waves have different values of phase at the receiver surface. Coherent summation of these waves changes the predicted signal from that of the incident-plane calculation and causes the peaks and their amplitudes to shift. This effect can easily lead to an incorrect estimate of C_{ij}^*, if the ϕ_i integration is ignored.

Air-coupled measurements with $\psi=45$ deg are shown in Fig. 8 for the same sample and experimental conditions as in Fig. 6. The solid curve is the experiment, and the dashed curve is the calculated function $W(\theta)$, using values for the C_{ij}^* determined in the experiments reported in Figs. 5 and 6 for the two symmetry directions. Only C_{11} was estimated from previous measurements on the same sample. The dotted curve is the plane-wave transmission coefficient $T(\theta)$, shown for comparison. Although the fit of Eq. (8) to the data is not exact, all the general features of the data are reproduced in the model. By contrast, the transmission coefficient, which is close to $W(\theta)$ without the ϕ_i integration, is clearly a poor fit to the voltage measurement. The fit is particularly bad at the smallest angles, where a broader spatial spectrum of rays emanating from each transducer is significant in determining the measured voltage. As the phase-match angle θ increases, the importance of the out-of-plane rays in the 3-D integration is greatly diminished, except when θ is close to the Rayleigh angle. This situation is largely the one that dominates in the liquid-coupled measurements discussed below.

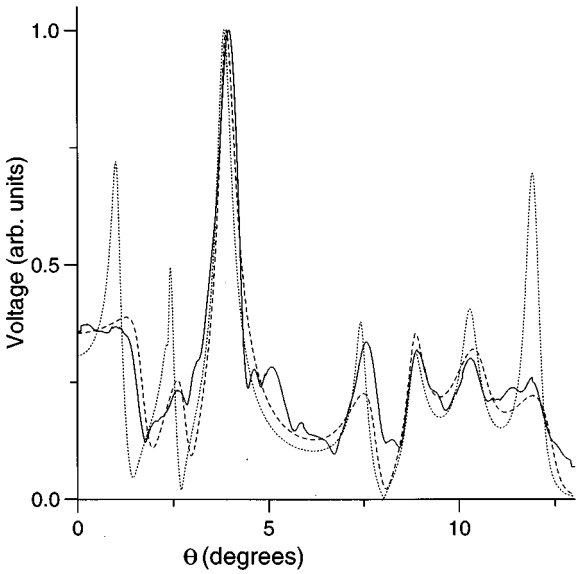

FIG. 8. Experimental (solid curve), calculated voltage function $W(\theta)$ (dashed curve), and plane-wave transmission coefficient $T(\theta)$ (dotted curve) for a 3.6-mm uniaxial carbon–epoxy laminated plate in the $\psi=45$ deg direction at frequency of 900 kHz.

IV. LIQUID-COUPLED RESULTS

To complete our investigation of the effects of ϕ_i integration, we consider the case of liquid-coupled reflection of sound beams from a 0.92-mm-thick uniaxial graphite–epoxy laminate (T300-CG914). The experimental geometry is illustrated in Fig. 1 for the reflection configuration, and the material is modeled as a homogeneous, transversely isotropic solid. Since PZT radiators designed for liquid-coupled operation often have a rather broad frequency bandwidth, materials property information is most conveniently and quickly gathered by stepping or sweeping frequency instead of scanning coordinate.

An analysis of the integrand in Eq. (1) shows that the main contribution to the ϕ_i integral is from waves propagating in a $\Delta\phi_i$ neighborhood about the direction containing the incident plane, $\phi_i=0$. The angular range $\Delta\phi_i$ is composed of two contributions, one from the phase term and one from the amplitude term. The value of $\Delta_p\phi_i$ for the phase term is proportional to $(\kappa(x+x_0)\sin\theta_i)^{-1/2}$; for the amplitude term $\Delta_a\phi_i$ depends on $(\kappa a\ \sin\theta_i \sin\alpha)^{-1}$. The intervals also depend on frequency and other experimental parameters. If the plane-wave reflection coefficient (RC) $R(\theta_i,\phi_i)$ [which replaces the generalized scattering coefficient $S(\theta_i,\phi_i)$] has variations that are negligibly small within the interval $\Delta\phi_i$, the saddle-point method can be used to estimate the out-of-plane integral over the ϕ_i variable in Eq. (1). We have

$$V(f,x,\alpha)=ia^4\sqrt{\frac{2\pi\kappa}{i(x+x_0)+2b^2\kappa a^2\ \sin\ \alpha}}\times\int_0^{\pi/2-i\infty}R(\theta_i,\phi_i=0)D^T(\theta_i-\alpha)D^R(\theta_i-\alpha)\times\exp[i\kappa z_0\cos\theta_i+i\kappa(x_0+x)\sin\theta_i]\sqrt{\sin\theta_i}\,d\theta_i, \tag{9}$$

where $b\approx0.522$ is the parameter that establishes equivalence between the Bessel and Gaussian directivity functions, as stated earlier.[15]

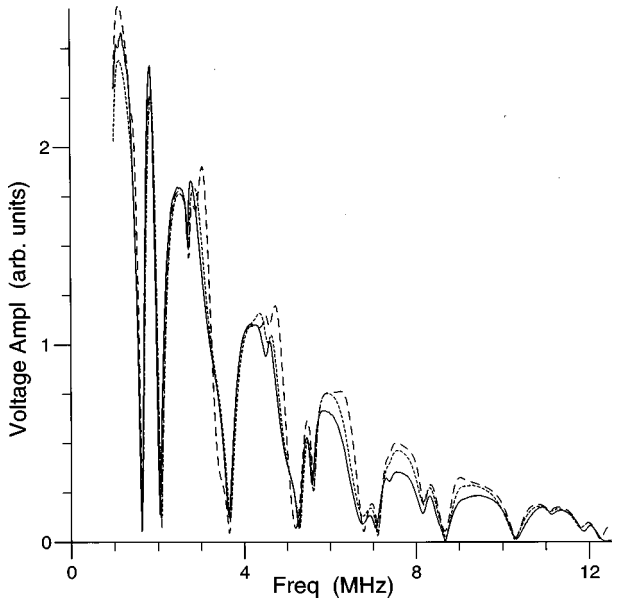

FIG. 9. Experimental (solid curve) and calculated voltage function $V(f)$ without ϕ_i integration (dashed curve) and with it (dotted curve) for a 0.92-mm uniaxial carbon–epoxy laminated plate in the $\psi=60$ deg direction for an incident angle of $\alpha=10$ deg and $x=5$ mm.

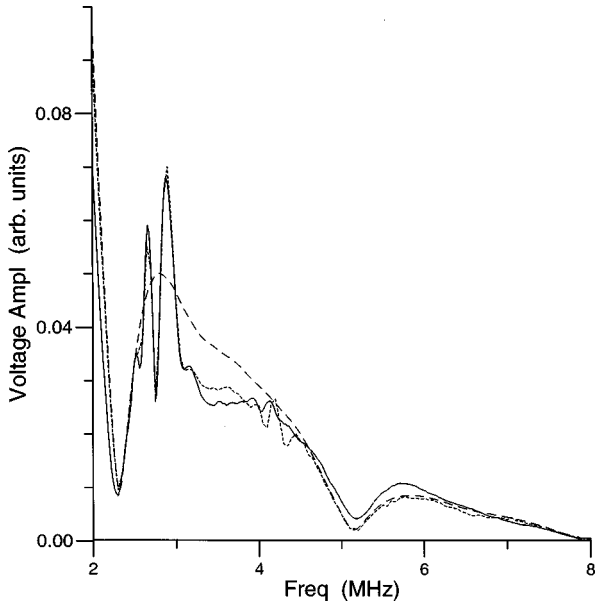

FIG. 10. Experimental (solid curve) and calculated voltage function $V(f)$ without ϕ_i integration (dashed curve) and with it (dotted curve) for a 0.92-mm uniaxial carbon-epoxy laminated plate in the $\psi=0$ deg direction for an incident angle of $\alpha=30$ deg and $x=20$ mm.

The 2-D, or modified 3-D, model in Eq. (9) above accounts explicitly for the angular dependence of the RC only in the incident plane and is approximately accurate only so long as the incident plane contains a material symmetry axis of the solid. This treatment ignores RC variations within the beam's lateral spread in the plane of the plate and is equivalent to including ϕ_i-coordinate beam diffraction, but ignoring ϕ_i-dependent material properties. It is a compromise that substantially simplifies computation and functions very well for isotropic plates,[15] where the RC is independent of the ϕ_i variable. Rapid evaluation of the voltage is especially important in iterative reconstruction of viscoelastic plate properties, and Eq. (9) is much more efficient than the full 3-D expression in Eq. (1). For anisotropic plates, Eq. (9) can still be effective, but its accuracy depends on the degree of anisotropy and on other experimental parameters, such as the transducer position, frequency, incident angle, and plate orientation.

The data and calculations show that when there is significant amplitude of the specularly reflected beam detected at the position of the receiver ($x \leqslant a \approx 5$ mm), i.e., when the wave path in the plate is short, the 3-D and 2-D voltage calculations of Eqs. (1) and (9) give almost identical results, even for arbitrary fiber orientation. To illustrate this fact, Fig. 9 shows experimental data (solid curve) and a fitted theoretical prediction for 2-D (dashed curve) and 3-D (dotted curve) models with an incident angle of $\alpha=10$ deg and a fiber orientation angle of $\psi=60$ deg, where the transducer axis separation is $x=5$ mm. The data and both predictions are nearly coincident, with only some slight differences.

For larger values of x, the influence of the RC variations within the beams' lateral spread can be more pronounced, and when the wave path is along a symmetry axis, the effect on the voltage has a form that is different from the case when it is not. The solid curve in Fig. 10 is the experimental data, and the dashed curve represents a 2-D calculation according to Eq. (9) for an incident angle of $\alpha=30$ deg and a transducer axis separation of $x=20$ mm ($x \gg a$). The fiber orientation angle here is $\psi=0$ deg. One can see that the 2-D model without the ϕ_i-dependent RC models the experimental voltage oscillations near 3 MHz not at all, and entirely misses the smaller oscillations near 4.25 MHz. The 3-D model calculation of Eq. (1) (dotted curve), however, shows a dependence nearly identical to that of the experimental data in the solid curve. The oscillations near 3 and 4.25 MHz arise from excitation of plate wave modes that contain significant horizontally polarized wave motion. These ''SH-like'' modes can be excited in fluid-coupled measurements only in anisotropic media, because of the intrinsic coupling between inplane and out-of-plane particle motion.[21] When an anisotropic plate is excited by a plane wave whose wave vector lies in the incident plane, this out-of-plane coupling disappears. This is nominally the situation of Fig. 10, since the fiber angle is $\psi=0$ deg. It is the three-dimensional nature of the experimental incident beam, however, that must be considered. The integration over ϕ_i in Eq. (1) (dotted curve) includes the effect of rays that have projections normal to the incident plane and can therefore couple to the SH-like modes.

In Fig. 10, near 3 MHz the SH_2-like plate wave is excited by the incident beam, and the SH_3-like shear horizontal plate wave accounts for the smaller peak near 4.25 MHz. For small out-of-plane angles, the vertical particle displacement of SH-like plate waves grows as ϕ_i^2. At the same time, the efficiency of their excitation and reception decreases because of the falloff in the directivity functions with increasing ϕ_i away from the incident plane. The competition between these two processes yields the results seen in Fig. 10. The much smaller SH_3 wave amplitude near 4.25 MHz, compared with that of the SH_2 wave near 3 MHz, illustrates the

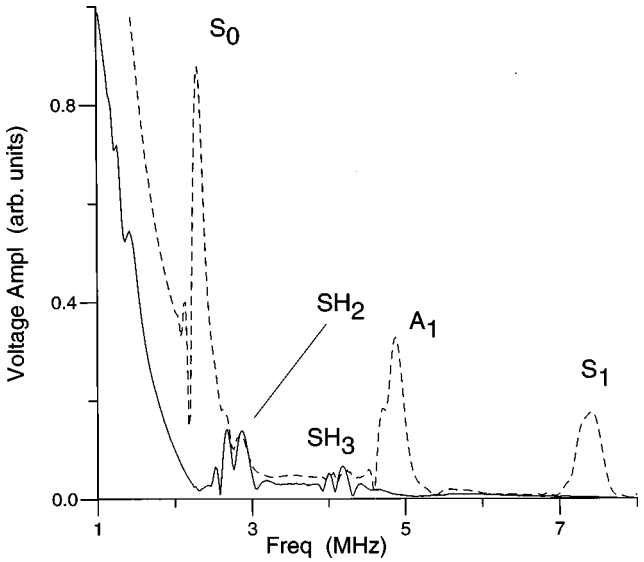

FIG. 11. Calculated voltage function $V(f)$ with ϕ_i integration for a 0.92-mm uniaxial carbon–epoxy laminated plate in the $\psi=0$ deg direction for an incident angle of $\alpha=30$ deg and $x=20$ mm. Solid curve is water-coupled result, and dashed curve is model case for a liquid density of $\rho_f=0.1$ g/cm^3. Plate mode peaks are labeled.

beam narrowing at the higher frequency. As frequency increases beyond 4 MHz, the amplitudes of other SH-like waves are too small to discern in the data.

The resulting experimental signal in Fig. 10 is the sum of a small specular component and two SH-like waves. The ordinary symmetrical and antisymmetric Lamb-like modes have almost no effect on the signal. The explanation lies in the similarity between the graphite-epoxy and water densities ($\rho_{GE}=1.6$ g/cm^3),[22] which leads to a rapid reradiation of wave energy in vertically polarized modes (such as the *A* and *S*-like modes). For example, the imaginary part of the guided wave number κ'' for the S_0 mode in the fiber direction with an incident angle of $\alpha=30$ deg and a frequency near 2 MHz is $\kappa''_{S_0}=1.4$ mm^{-1}. The amplitude of the leaky plate wave at any distance from the incident beam axis is proportional to[15] $\kappa''\exp(-\kappa''x)$. For a transducer axis separation distance of $x=20$ mm, the S_0 mode amplitude decreases much more rapidly than that of the specular component or that of the SH-like modes. It is clear that for the SH waves, $\kappa''=0$ in the symmetry direction $\psi=0$ deg, but outside the incident plane and still within the beams' lateral spread, the leakage rate is small but nonzero (e.g., $\kappa''_{SH_2}=0.013$ mm^{-1} for $\psi=4$ deg at a frequency of 3 MHz). This leaky wave radiation factor value is small, and for the specular region ($x\leqslant a$), when $\exp(-\kappa''x)\sim 1$, the SH wave amplitude is much smaller than the specular reflection or either of the two Lamb-like mode amplitudes.

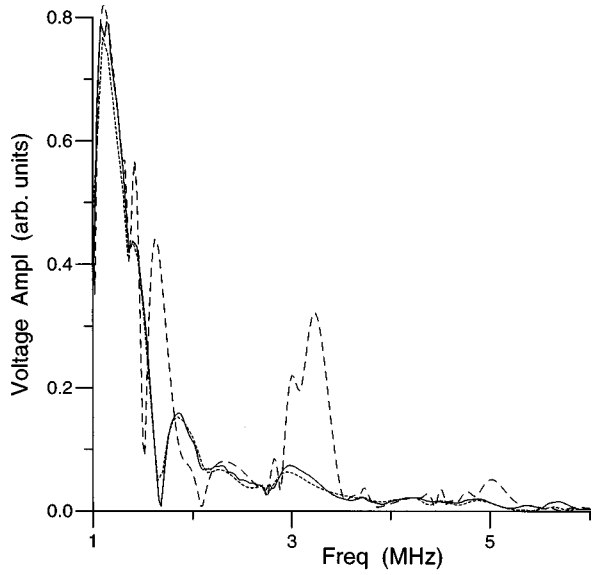

FIG. 12. Experimental (solid curve) and calculated voltage function $V(f)$ without ϕ_i integration (dashed curve) and with it (dotted curve) for a 0.92-mm uniaxial carbon–epoxy laminated plate in the $\psi=60$ deg direction for an incident angle of $\alpha=10$ deg and $x=20$ mm.

To demonstrate the influence of the liquid density on the output signal structure, Fig. 11 shows the 3-D calculated voltage for a water-coupled plate (solid curve) and for a model case where the liquid density is assumed to be $\rho_f=0.1$ g/cm^3 (dashed curve). The geometry parameters and the plate elastic properties are the same as in Fig. 10, but material damping is neglected and there is a change of scale. The structure of the receiver voltage is completely different for the lower-density liquid, and the amplitudes of the *A* and *S* modes are much higher than for the SH modes. The *A* and *S* modes also overlap one of the SH peaks near 3 MHz. The structure of the 3-D calculation is close to the 2-D result, in fact, because the *A* and *S* mode properties hardly change within the angular interval of the lateral beam spread. It should be noted that we have not observed the effect of the SH waves on the received voltage in symmetry directions in the air-coupled experiments discussed above and in Ref. 3 precisely because of the low air density.

The importance of the ϕ_i integration at arbitrary fiber angles is clear from the air-coupled results, and this conclusion extends, with some reservations, to the fluid-coupled case as well. Figure 12 presents the experimental data (solid curve) and calculations for the 2-D (dashed curve) and 3-D (dotted curve) for an incident angle of $\alpha=10$ deg and a fiber angle of $\psi=60$ deg. The transducer axis separation is $x=20$ mm. At this incident angle near the plate normal, the 3-D voltage curve decreases much faster with increasing frequency than the 2-D model, and it describes the experimental data much better. The reasons parallel the discussion for arbitrary direction scanning in the air-coupled case. Analogous results, but at an incident angle of $\alpha=30$ deg, show a much closer coincidence between 2-D and 3-D models, shown in Fig. 13 for the same fiber orientation angle $\psi=60$ deg and transducer shift $x=20$ mm as in Fig. 12. Here again, the measurement is the solid curve, the 2-D result is shown as dashed, and the 3-D calculation is dotted. There are two reasons for the closer agreement between 2-D and 3-D models. First, at the larger incident angle α the beams' effective lateral diffraction is narrower ($\Delta\phi_i\sim\alpha^{-1}$). Second, the anisotropy of the quasilongitudinal and quasishear partial waves is much stronger for lower incident angles.

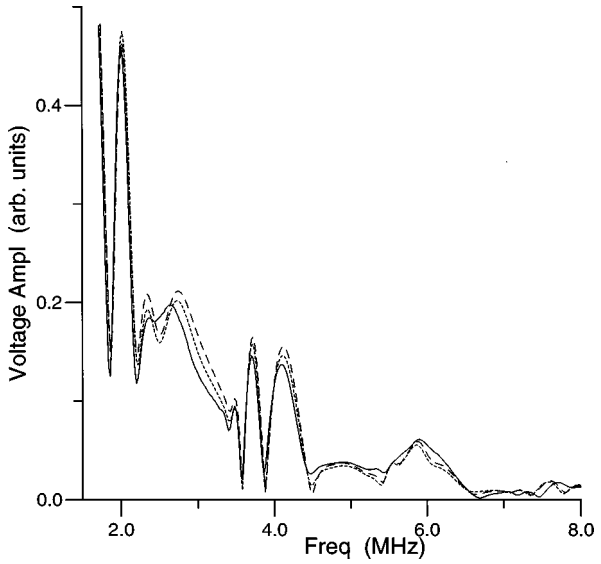

FIG. 13. Experimental (solid curve) and calculated voltage function $V(f)$ without ϕ_i integration (dashed curve) and with it (dotted curve) for a 0.92-mm uniaxial carbon–epoxy laminated plate in the $\psi=60$ deg direction for an incident angle of $\alpha=30$ deg and $x=20$ mm.

V. SUMMARY AND CONCLUSIONS

In conclusion, we have examined experimentally and theoretically the interaction of axially symmetric sound beams with anisotropic plate media. We find that the contribution of out-of-incident plane rays to the receiver voltage in a two-transducer measurement can be significant under several subtle, overlapping conditions. As we demonstrated, when the wave path is not coincident with a symmetry axis, when the wave path is larger than the transducer diameter, or when the incident angle is small, the 3-D calculation can be essential to achieve acceptable accuracy. A further effect arises because the group velocity is not coincident with the wave vector for general, nonsymmetry propagation directions. This effect also causes an additional asymmetry in the transmitted wave on the receiver surface and results in a smaller signal voltage than expected solely on the basis of incident-plane integration. When these conditions just cited obtain, measurements and calculations we presented above demonstrate conclusively that only a complete 3-D solution will suffice to model reflected or transmitted signals in a two-transducer geometry, whether in the limit of weakly perturbed guided wave propagation, such as air coupling, or in the case of strongly coupled elastic systems such as a reinforced plastic composite in water. Moreover, to extract accurate viscoelastic material property information from such measurements, the full 3-D calculation is nearly always an essential tool, because of the effect of diffraction on the apparent signal loss.

ACKNOWLEDGMENTS

This paper is based in part on work in the FAA Center for Aviation Systems Reliability at Iowa State University and supported by the FAA Technical Center, Atlantic City, New Jersey, under Grant No. 94G011. D. Schindel of Partec, Inc. provided the air-coupled foil transducers.

[1] D. E. Chimenti, A. Safaeinili, and O. I. Lobkis, ''Quantitative material characterization of elastic plates using air-coupled leaky Lamb waves,'' in *Review of Progress in Quantitative NDE*, Vol. 15, edited by D. O. Thompson and D. E. Chimenti (Plenum, New York, 1996), pp. 1067–75.
[2] A. Safaeinili, O. I. Lobkis, and D. E. Chimenti, ''Air-coupled ultrasound and leaky Lamb waves in composites,'' in *Review of Progress in Quantitative NDE*, Vol. 15, edited by D. O. Thompson and D. E. Chimenti (Plenum, New York, 1996), pp. 1059–66.
[3] A. Safaeinili, O. I. Lobkis, and D. E. Chimenti, ''Air-coupled ultrasonic estimation of viscoelastic stiffnesses in plates,'' IEEE Trans. Ultrason. Ferroelectr. Freq. Control **43**, 1171–80 (1996).
[4] Obtained from Parteq, Inc., Kingston, Canada.
[5] B. T. Khuri-Yakub, J. H. Kim, C.-H. Chou, P. Parent, and G. S. Kino, ''A new design for air transducers,'' in *IEEE Ultrasonics Symposium Proceedings*, edited by B. R. McAvoy (IEEE, New York, 1988), pp. 503–06.
[6] K. Suzuki, K. Huguchi, and H. Tanigawa, ''A silicon electrostatic ultrasonic transducer,'' IEEE Trans. Ultrason. Ferroelectr. Freq. Control **36**, 620–27 (1989).
[7] W. D. Wright, D. W. Schindel, and D. A. Hutchins, ''Studies of laser-generated ultrasound using a micromachined silicon electrostatic transducer in air,'' J. Acoust. Soc. Am. **95**, 2567–75 (1994).
[8] D. W. Schindel and D. A. Hutchins, ''The capacitance transducer as a standard ultrasonic source in solids,'' J. Acoust. Soc. Am. **97**, 1650–59 (1995).
[9] S. P. Kelly, R. Farlow, and G. Hayward, ''Applications of through-air ultrasound for rapid NDE scanning in the aerospace industry,'' IEEE Trans. Ultrason. Ferroelectr. Freq. Control **43**, 581–91 (1996).
[10] A. Gachagan, G. Hayward, S. P. Kelly, and W. Galbraith, ''Characterization of air-coupled transducers,'' IEEE Trans. Ultrason. Ferroelectr. Freq. Control **43**, 678–89 (1996).
[11] W. M. D. Wright, D. A. Hutchins, A. Gachagan, and G. Hayward, ''Polymer composite-material characterization using a laser/air-transducer system,'' Ultrasonics **34**, 825–33 (1996).
[12] M. Castaings and P. Cawley, ''The generation, propagation, and detection of Lamb waves in plates using air-coupled ultrasonic transducers,'' J. Acoust. Soc. Am. **100**, 3070–77 (1996).
[13] B. Hosten, D. W. Schindel, and D. A. Hutchins, ''Measurement of elastic constants in composite materials using air-coupled ultrasonic bulk waves,'' J. Acoust. Soc. Am. **99**, 2116–23 (1996).
[14] M. J. Anderson, J. A. Hill, C. M. Fortunko, N. S. Dogan, and R. D. Moore, ''Broadband electrostatic transducers: modeling and experiments,'' J. Acoust. Soc. Am. **97**, 262–72 (1995).
[15] O. I. Lobkis, A. Safaeinili, and D. E. Chimenti, ''Precision ultrasonic reflection studies in fluid-coupled plates,'' J. Acoust. Soc. Am. **99**, 2727–36 (1996).
[16] G. S. Kino, ''The application of reciprocity theory to scattering of acoustic waves by flaws,'' J. Appl. Phys. **49**, 3190–99 (1978).
[17] B. A. Auld, ''General electromechanical reciprocity relations applied the calculation of elastic wave scattering coefficients,'' Wave Motion **1**, 3–10 (1979).
[18] H. Zhang, D. E. Chimenti, and S. Zeroug, ''Transducer misalignment effects in beam reflection from elastic structures,'' J. Acoust. Soc. Am. **104**, 1982–91 (1998).
[19] P. J. Shull, D. E. Chimenti, and S. K. Datta, ''Elastic guided waves and the Floquet concept in periodically layered plates,'' J. Acoust. Soc. Am. **95**, 99–108 (1994).
[20] D. E. Chimenti and A. H. Nayfeh, ''Ultrasonic reflection and guided waves in fluid-coupled composite laminates,'' J. Nondestruct. Eval. **9**, 51–69 (1990).
[21] A. H. Nayfeh and D. E. Chimenti, ''Ultrasonic wave reflection from liquid-coupled orthotropic plates with application to fibrous composites,'' J. Appl. Mech. **55**, 863–70 (1988).
[22] D. E. Chimenti and S. I. Rokhlin, ''Relationship between leaky Lamb modes and reflection coefficient zeros for a fluid-coupled elastic layer,'' J. Acoust. Soc. Am. **88**, 1603–11 (1990).

Vortical and acoustical mode coupling inside a two-dimensional cavity with transpiring walls

Joseph Majdalani
Mechanical and Industrial Engineering Department, Marquette University, Milwaukee, Wisconsin 53233

(Received 26 May 1998; revised 12 March 1999; accepted 23 March 1999)

In a long, low aspect ratio, two-dimensional cavity, where gaseous motion is permitted along transpiring walls, a time-dependent field is established when low amplitude, sinusoidal pressure oscillations with nonzero mean are introduced. An accurate solution is extracted here for the time-dependent field by way of small parameter perturbations. Contingent upon small pressure-wave amplitudes, Navier–Stokes equations are linearized to the order of the mean flow Mach number to furnish interaction equations governing the unsteady field. The latter is decomposed into acoustic and solenoidal fields coupled through Dirichlet-type boundary conditions. Solving for the solenoidal field from the momentum equation employs separation of variables and multiple scale expansions based on a careful choice of an inner scale. In fact, the unique inner scale used in the two-variable derivative expansion method is original in the sense that it stems from an unconventional, nonlinear variable transformation. A uniformly valid solution is formulated subsequently for the temporal field. This explicit solution discloses the character of the acoustic boundary layer evolving from damped traveling waves. The rate of decay is found to depend on a viscosity parameter, revealing that deeper penetration of rotational waves is possible at low viscosity. Characterization of the boundary layer region is covered in addition to a standard error analysis. In closing, results are verified through comparisons to accurate numerical predictions. [S0001-4966(99)00907-8]

PACS numbers: 43.20.Hc, 43.20.Mv, 43.28.Py [LCS]

INTRODUCTION

When harmonic disturbances are introduced inside a rectangular cavity with transpiring walls, a rotational component of the time-dependent velocity is produced along with the plain, irrotational, acoustic field. The resulting time-dependent field can be difficult to analyze since it must include the influence of the steady flow component. The traditional approach to resolve the resulting coupled equations is paved with numerous mathematical obstructions that prevent exacting analytical solutions in finite form. Based on a technique used recently by the author,[1] an assault on the problem will be attempted here. The method relies heavily on regular and multiple scale perturbation tools, making use of naturally occurring similarity parameters that happen to be small quantities. By way of example, in linearizing the Navier–Stokes equations, the ratio of the acoustic-to-mean pressure amplitude will be used as a primary perturbation parameter. The Mach number at the transpiring wall will be found to be another instrumental perturbation parameter that is frequently encountered. Later, in resolving the solenoidal field, a small parameter reminiscent of the Stokes number will recur, providing a gauge to expand the solenoidal velocity in a series of progressively diminishing terms.

The originality of this work stems from the mathematical treatment of the interaction equations developed for the time-dependent field. This treatment involves a singular boundary value problem whose solution features a novel scaling transformation. In previous work, Majdalani and Van Moorhem[1] have tackled a similar problem involving unsteady axisymmetric motion inside a cylindrical tube and different boundary conditions. The former analysis employed the so-called ''composite-scale technique,'' a hybrid perturbation method that involved reducing three spatial length scales into one, nonunique, composite-scale function, before applying the derivative expansion method. The current methodology does not invoke composite-scale matching, but rather standard perturbation tools. In the process, one unique virtual scale will be identified as the outcome of a nonlinear variable transformation. To the author's knowledge, the nonlinear transformation that will be presented has not been addressed previously in multiple scale analysis. Contrary to the ad hoc approach employed previously by Majdalani and Van Moorhem,[1] a mathematically rigorous approach will be invested here in constructing the uniformly valid asymptotic formulation.

The practical motivation stems, in part, from the need to obtain an approximate solution for the time-dependent field that can be helpful in explaining and elucidating observations reported by Ma[2–4] and Barron[5] in two experimental investigations that involved a two-dimensional geometry. In both instances, sublimating carbon dioxide originating from the flat surface of heated blocks of dry ice was used to simulate the transpiring gas inside a long, segmented, rectangular chamber. In both cases, harmonic pressure waves were produced by means of a variable speed, reciprocating piston. In Barron's apparatus, a Scotch-yoke mechanism was used to drive the piston by imparting a purely sinusoidal motion at a well-prescribed frequency, a substantial improvement over Ma's slider-crank mechanism which could only approximate sinusoidal motions. In any event, both investigations suffered from a lack of applicable analytical models, a problem that is hoped to be remedied in the present development.

For the purpose of attaining a reliable solution, the paper starts in Sec. I with a brief description of the two-

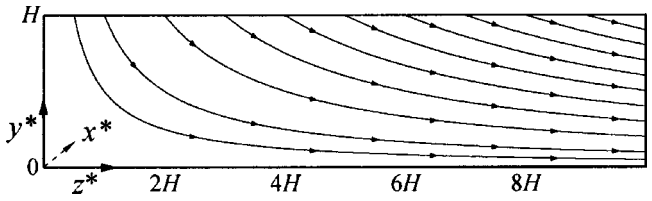

FIG. 1. Chamber half-space showing mean flow streamlines. In the orthogonal coordinate system indicated, the x^* axis is perpendicular to the plane of view, y^* is the normal distance measured from the rigid wall, and z^* is the axial distance measure from the head end.

dimensional geometry and bulk fluid motion, along with a statement of the fundamental criteria whose violation is inadmissible. This is followed in Sec. II by a formulation of the linearized Navier–Stokes equations which rests on decomposing variables into mean and small time-dependent fluctuations. In the process, interaction equations that incorporate the influence of the mean flow are derived for the time-dependent field to the order of the surface Mach number. In Sec. III, the classical mean flow velocity established inside a rectangular cavity is analyzed. The time-dependent field is decomposed in Sec. IV into acoustic, irrotational, pressure-driven, and rotational, solenoidal, vorticity-driven elements. Equations governing each set are produced along with pertinent boundary conditions. Unlike the acoustic set which can be readily resolved, the solenoidal set demands a special treatment and is conveniently deferred to a separate section. Hence, in Sec. V, separation of variables accompanies a careful scaling analysis in the development of a uniformly valid solution to the rotational field. Attempts to elucidate particular features of the new finding and to explain its impact on the overall time-dependent solution are undertaken in Sec. VI where the time-dependent boundary layer is characterized. The global error associated with the analytical formulation is evaluated and the order of the truncation error is established. Throughout this study, verifications are made at various stages by comparing analytical predictions to reliable computational data. By way of closing, several conclusions are reiterated in Sec. VII.

I. PROBLEM FORMULATION

We begin by describing the idealized geometry along with important criteria that must be met for the mathematical model to hold.

A. Geometry

The two-dimensional acoustic field is considered in the half-space of a long rectangular cavity of length L, width W, and height $H(W \gg H, L \gg H)$, with one acoustically compliant membrane (simulating a transpiring wall), through which mean transmission of a gas (of kinematic viscosity v_0) occurs at a steady blowing speed of V_b. Gas entering the chamber at $y^* = H$ is led to change course, swerve, and head downstream. As represented schematically in Fig. 1, the chamber is acoustically hard at the head end ($z^* = 0$). The sound field under investigation is choked at the downstream end due to a constriction in flow area (not shown). In addition, the lateral walls normal to the x^* axis are impenetrable (note that the x^* axis is perpendicular to the plane of view in Fig. 1). Since the chamber width is larger than its height, variations in the x^* direction are ignored. Under idealized conditions, the flow is perfectly symmetrical about the central plane $y^* = 0$. Taking advantage of symmetry, the domain investigation is limited to the half-space extending from the compliant wall to the central plane.

Superimposed on the mean fluid motion, a two-dimensional time-harmonic acoustic field of small amplitude (frequency ω_0 and pressure amplitude A_p) is admitted. This acoustic environment can be induced externally or triggered naturally from internally propagating pressure disturbances. In the forthcoming analysis, details of the acoustic source will not be addressed.

B. Principal criteria

In order to pursue a theoretical formulation of the time-dependent field, standard perturbation tools are implemented in conjunction with a fundamental assumption of a low mean flow Mach number of $O(10^{-3})$. In common nonreacting flows characterized by a typical speed of sound of 350 m/s, the low Mach number criterion casts a limit of 2 m/s on the mean flow speed. In reality, this upper threshold for the Mach number is not too restrictive since, in many applications, it corresponds to a condition of intense mean flow transmission known as ''hard blowing.'' Another basic assumption that must be tolerated to manage a solution constrains the acoustic pressure amplitude A_p to remain small by comparison to the mean pressure p_0 at the chamber head end. The latter must be uniform in order to maintain rigor and consistency in comparing terms of various orders of magnitude arising in the perturbation process which rests strongly on the pressure wave amplitude, A_p/p_0, a gauge to which other quantities are compared. This criterion is found to be contingent upon a geometrical restriction of $L/H < 100$. When these criteria are met, the forthcoming analysis will be seen to be applicable everywhere except near the choked end ($z^* = L$).

II. EQUATIONS OF MOTION

A standard normalization and small parameter linearization of the governing equations precedes the development of the interaction equations.

A. Conservation laws

Invoking Stokes' hypothesis of zero bulk viscosity, assuming constant viscosity, and disallowing body forces, conservation of mass and momentum can be cast in dimensionless form into

$$\frac{\partial \rho}{\partial t} + \nabla .(\rho \mathbf{u}) = 0, \tag{1}$$

$$\rho \frac{D\mathbf{u}}{Dt} = -\frac{\nabla p}{\gamma} + \frac{1}{\mathrm{Re}}\left[\frac{4}{3}\nabla(\nabla \cdot \mathbf{u}) - \nabla \times (\nabla \times \mathbf{u})\right], \tag{2}$$

where density ρ and pressure p are normalized by their mean values, ρ_0 and p_0, at the chamber head end, velocities are normalized by the chamber's intrinsic speed of sound a_0,

spatial coordinates (x, y, z) are the laboratory coordinates (x^*, y^*, z^*) normalized by H, and time $t(=a_0 t^*/H)$ is made dimensionless by referring t^* to the average time it takes for a pressure disturbance to travel from the compliant wall to the centerline, (H/a_0). The Reynolds number Re in Eq. (2) is $(a_0 H/\nu_0)$, γ is the ratio of specific heats, and $\mathbf{u}(y,z,t)$ is the total velocity, including both steady and unsteady components. Exacting the latter constitutes the main purpose of this article.

B. Approach

The procedure consists of decomposing the internal flow field into a steady and a time-dependent part. This is accomplished by writing each of the independent variables as a sum of their steady and time-dependent components. A small parameter perturbation scheme is suitable by virtue of the fundamental premise requiring the acoustic amplitude to be a small quantity relative to its mean counterpart.[6] In breaking the analysis into digestible pieces, we assume that the presence of time-dependent oscillations does not alter the general motion of the mean flow. This assumption can be later verified by realizing that terms that incorporate the time-dependent effects on the mean flow field are indeed secondary. Conversely, mean flow effects on the acoustic field are extraordinarily important and cannot be dismissed. Since superposition of the coupled elements is sought ultimately, equations that incorporate the coupling between steady and time-dependent components must be developed as well. Details are furnished below.

C. Variable decomposition

The local pressure can be expressed as the sum of its steady and acoustic components. Using, heretofore, asterisks to denote dimensional variables, and superscripts for perturbation orders, the dimensional pressure is split into

$$p^* = p^{*(0)}(y^*,z^*) + p^{*(1)}(y^*,z^*,t^*) = p^{*(0)} + A_p f(y^*,z^*)\cos(\omega_0 t^*), \tag{3}$$

where $p^{*(0)}$, subject to later verification, is taken to be a constant. In the time-dependent part of Eq. (3), A_p defines the acoustic pressure amplitude, and f is a normalized spatial function of $O(1)$. After normalizing by p_0, and substituting $p^{*(0)} \cong p_0$, Eq. (3) becomes

$$p = 1 + \epsilon_w f(y,z)\cos(\omega_0 t^*) = 1 + p^{(1)}(y,z,t), \tag{4}$$

where $\epsilon_w = A_p/p_0$ is the primary gauge parameter that provides a scale to which other terms can be compared. Density can be expanded in a similar way:

$$\rho(y,z,t) = \frac{\rho_0 + \rho^{*(1)}}{\rho_0} = 1 + \rho^{(1)}(y,z,t). \tag{5}$$

Velocity decomposition needs to be assessed carefully since its mean value is of the order of $V_b \mathbf{U}(y,z)$, where $\mathbf{U}(y,z)$ is a function of $O(1)$ to be described in Sec. III. Note that the term V_b defines the magnitude of the mean flow velocity crossing the plane $y=1$. Expanding the dimensional velocity into

$$\mathbf{u}^*(y,z,t) = V_b \mathbf{U}(y,z) + \mathbf{u}^{*(1)}(y,z,t), \tag{6}$$

we normalize by the chamber speed of sound a_0 and find that the nondimensional counterpart is of the order of the wall Mach number, M_b; the latter is a secondary perturbation parameter by virtue of $\epsilon_w < M_b \ll 1$. Note that ϵ_w remains very small, as defined in Eq. (4) and Sec. II B, being the amplitude of the small pressure disturbances normalized by the mean pressure. The dimensionless velocity becomes

$$\mathbf{u}(y,z,t) = M_b \mathbf{U}(y,z) + \mathbf{u}^{(1)}(y,z,t). \tag{7}$$

D. Interaction equations

Substituting Eqs. (4), (5), and (7) into Eqs. (1)–(2), one obtains, at the leading order expansion in the wave amplitude, a set for the steady flow motion:

$$\nabla . \mathbf{U} = 0, \tag{8}$$

$$\mathbf{U}.\nabla \mathbf{U} = \frac{1}{M_b \,\mathrm{Re}}\left[\frac{4}{3}\nabla(\nabla.\mathbf{U}) - \nabla\times(\nabla\times\mathbf{U})\right]. \tag{9}$$

Grouping terms that are comparable in magnitude to the first order in the wave amplitude, a linearized expansion of the interaction equations incorporating mean flow effects is attained:

$$\partial\rho^{(1)}/\partial t + \nabla.\mathbf{u}^{(1)} = -M_b \nabla.(\rho^{(1)}\mathbf{U}), \tag{10}$$

$$\frac{\partial \mathbf{u}^{(1)}}{\partial t} = M_b[\mathbf{u}^{(1)}\times(\nabla\times\mathbf{U}) + \mathbf{U}\times(\nabla\times\mathbf{u}^{(1)}) - \nabla(\mathbf{u}^{(1)}.\mathbf{U})] - \frac{\nabla p^{(1)}}{\gamma} + \frac{1}{\mathrm{Re}}\left[\frac{4}{3}\nabla(\nabla.\mathbf{u}^{(1)}) - \nabla\times(\nabla\times\mathbf{u}^{(1)})\right]. \tag{11}$$

Equations (10)–(11) reveal the intricate coupling between mean and time-dependent flow components which strongly affects the time-dependent solution character.

III. MEAN FLOW FIELD

When a classical mean flow stream function is assumed for the geometry at hand, both velocity and pressure distributions are determinable.

A. Velocity field

The velocity field $\mathbf{U}$ can be determined from the stream function $\mathbf{S}_f = \Psi \mathbf{e}_x$ obtained for a flow inside a rectangular cavity[7] where $\mathbf{U} = \nabla \times \mathbf{S}_f$. Using the classical stream function $\Psi(y,z) = -yz$, we have

$$\mathbf{U} = U_y \mathbf{e}_y + U_z \mathbf{e}_z = \frac{\partial \Psi}{\partial z}\mathbf{e}_y - \frac{\partial \Psi}{\partial y}\mathbf{e}_z = -y\mathbf{e}_y + z\mathbf{e}_z, \tag{12}$$

which does satisfy Eqs. (8)–(9).

B. Mean pressure correction

Having evaluated the velocity field from the stream function independently of mean pressure variations, one can use the steady momentum equation to deduce the pressure associated with the resulting field. Without incurring any loss

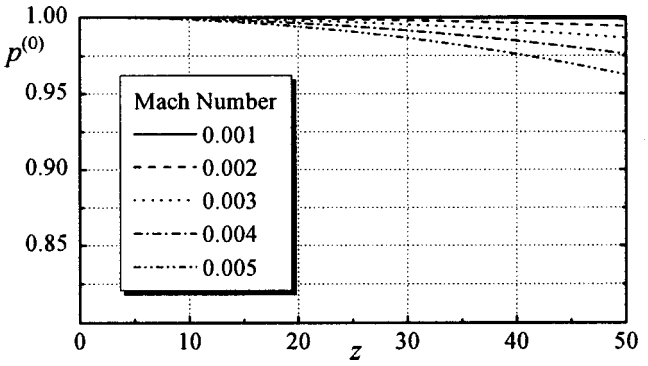

FIG. 2. Steady pressure distribution for practical mean flow Mach numbers.

in generality, one can set $p(y,z,t)=1+p_c(y,z)+p^{(1)}\times(y,z,t)$, where $p_c(y,z)$ is a spatial pressure correction term that we propose to determine. An auxiliary condition that must be met specifies that pressure at the chamber head end must be identical to the mean stagnation pressure where $p^{(0)}=1+p_c(0,0)=1$, or $p_c(0,0)=0$. The pertinent spatial correction can be obtained directly from Eq. (2) by direct substitution:

$$M_b\mathbf{U}.\nabla(M_b\mathbf{U})=-\frac{\nabla p_c}{\gamma}+\frac{1}{\mathrm{Re}}\times[\tfrac{4}{3}\nabla[\nabla.(M_b\mathbf{U})]-\nabla\times[\nabla(M_b\mathbf{U})]] \tag{13}$$

or

$$\nabla p_c/(\gamma M_b^2)=-\mathbf{U}.\nabla\mathbf{U}. \tag{14}$$

Equation (14) can be integrated to obtain, for $p_c(0,0)=0$, $p^{(0)}(y,z)=1-(\gamma/2)M_b^2(y^2+z^2)$; wherefrom

$$p^{(0)}(y,z)=1-(\gamma/2)M_b^2(y^2+z^2). \tag{15}$$

Note that in Eq. (15) the y-dependence can be safely ignored by comparison to the z-dependence, the former being smaller than unity, whereas z^2 varies from the order of unity to the order of 10^3. Additionally, since M_b is of $O(10^{-3})$, and z is less than 100, the error in assuming a constant steady pressure is insignificant, being of order $M_b^2z^2$. The corrected pressure distribution, shown in Fig. 2, indicates that axial pressure variations are indeed negligible except in very long chambers with large Mach numbers. Since the Mach number in the majority of cases does not exceed 0.005, the assumption of a uniform mean value needed to represent the steady pressure distribution is well justified. Having described the steady flow field character, its impact on the acoustic component is examined next.

IV. TIME-DEPENDENT FIELD

In order to resolve the effects of the steady field on the time-dependent field, the interaction equations are developed for small amplitude pressure and vorticity-driven disturbances inside the chamber. Proper boundary conditions are also examined.

A. Irrotational and solenoidal fields

The time-dependent velocity vector $\mathbf{u}^{(1)}$ is decomposed into two vectors of distinct characters, one that is irrotational and one that is solenoidal[8]

$$\mathbf{u}^{(1)}=\mathbf{u}_{\text{irrotational}}+\mathbf{u}_{\text{solenoidal}}=\hat{\mathbf{u}}+\tilde{\mathbf{u}} \tag{16}$$

contingent upon, $\nabla\times\hat{\mathbf{u}}=0$, and $\nabla\cdot\hat{\mathbf{u}}=0$. Similar decomposition of a small amplitude disturbance into two modes of fluctuations, a pressure mode and a vorticity mode, has been accomplished previously by numerous authors, including Chu and Kovásznay,[9] Carrier and Carlson,[10] and Flandro.[11]

Plugging Eq. (16) back into Eqs. (10)–(11), the interaction equations for small disturbances can be written for each of the modes. The total time-dependent velocity field can be constructed, thereafter, by superimposing the solution vectors linearly. Designating the irrotational mode variables by the circumflex ($\hat{}$), and the solenoidal variables by the tilde ($\tilde{}$), we express the time-dependent quantities as

$$\omega^{(1)}\equiv\nabla\times\mathbf{u}^{(1)}=\tilde{\omega}\equiv\nabla\times\tilde{\mathbf{u}}, \tag{17}$$

$$p^{(1)}=\hat{p}, \tag{18}$$

$$\rho^{(1)}=\hat{\rho}, \tag{19}$$

where vorticity is produced exclusively by the rotational mode and acoustic pressure is caused predominantly by the irrotational pressure mode. The pseudo-pressure generated by the vortical mode is ignored, being of second order in the wave amplitude.[9]

B. Time-dependent equations of motion

Substituting Eqs. (16)–(19) into the first order time-dependent set, given by Eqs. (10)–(11), yields the following two independent sets that are coupled through existing boundary conditions:

1. Acoustical model

$$\partial\hat{\rho}/\partial t+\nabla\cdot\hat{\mathbf{u}}=-M_b\nabla\cdot(\hat{\rho}\mathbf{U}), \tag{20}$$

$$\frac{\partial\hat{\mathbf{u}}}{\partial t}=-\frac{\nabla\hat{p}}{\gamma}-M_b\nabla(\hat{\mathbf{u}}\cdot\mathbf{U})+\frac{4\nabla(\nabla.\hat{\mathbf{u}})}{3\,\mathrm{Re}}. \tag{21}$$

2. Vortical model

$$\nabla\cdot\tilde{\mathbf{u}}=0, \tag{22}$$

$$\frac{\partial\tilde{\mathbf{u}}}{\partial t}=M_b[\mathbf{U}\times\tilde{\omega}-\nabla(\tilde{\mathbf{u}}\cdot\mathbf{U})]-\frac{\nabla\times\tilde{\omega}}{\mathrm{Re}}. \tag{23}$$

C. Auxiliary conditions

In order to determine the total time-dependent velocity $\mathbf{u}^{(1)}$, irrotational and vortical components have to be determined separately by solving Eqs. (20)–(21), and Eqs. (22)–(23). Resulting solutions must be superimposed in a manner to correctly satisfy two existing boundary conditions: (1) Velocity adherence at the wall demanding the axial time-dependent component of the velocity to vanish at $y=1$, thus yielding $\tilde{u}_z(1,z)=-\hat{u}_z(1,z)$, and (2) symmetry at $y=0$, giving $\partial u^{(1)}(0,z)/\partial y=0$.

D. Irrotational solution

Equations (20)–(21) can be cast into a second order hyperbolic partial differential equation (PDE), namely,

$$\frac{\partial^2 \hat{p}}{\partial t^2} - \nabla^2 \hat{p} = -M_b \left[\nabla . \left(\frac{\partial \hat{p}}{\partial t} \mathbf{U} \right) + \gamma \nabla^2 (\hat{\mathbf{u}} . \mathbf{U}) \right], \tag{24}$$

which can be solved to the first order in the Mach number by separation of variables. Following similar arguments to those presented in Ref. 1, the solution for the acoustic pressure $\hat{p}(z,t)$ can be expressed as

$$\hat{p}(z,t) = \epsilon_w \cos(k_m z) \exp(-ik_m t), \tag{25}$$

where the dimensionless wave number is given by $k_m = m\pi H/L$, $m = 1,2,3,...$, and m is the acoustic mode number. The acoustic velocity companion is determined directly from the momentum conservation Eq. (21) of order M_b. The result is

$$\hat{\mathbf{u}}(z,t) = i \frac{\epsilon_w}{\gamma} \sin(k_m z) \exp(-ik_m t) \mathbf{e}_z . \tag{26}$$

Note that both z and t are dimensionless quantities, as explained in Sec. II A.

E. Fundamental vortical equations

Using Euler's notation, we express rotational velocity and vorticity components in the following fashion:

$$\tilde{\mathbf{u}}(y,z,t) = \mathbf{V}(y,z) \exp(-ik_m t), \tag{27}$$

$$\tilde{\boldsymbol{\omega}}(y,z,t) = \overline{\boldsymbol{\omega}}(y,z) \exp(-ik_m t), \tag{28}$$

where

$$\mathbf{V}(y,z) = V_y \mathbf{e}_y + V_z \mathbf{e}_z , \tag{29}$$

$$\overline{\boldsymbol{\omega}} = \nabla \times \mathbf{V} = \overline{\omega} \mathbf{e}_x \tag{30}$$

are complex functions. It follows that the vortical mass and momentum conservation equations, given by Eqs. (22)–(23), become

$$\nabla . \mathbf{V} = 0, \tag{31}$$

$$i\mathbf{V} = \sigma [\nabla (\mathbf{V}.\mathbf{U}) - \mathbf{U} \times \overline{\boldsymbol{\omega}}] + \epsilon \nabla \times \overline{\boldsymbol{\omega}}, \tag{32}$$

where

$$\sigma = \frac{M_b}{k_m} = \frac{1}{Sr} = \frac{V_b}{\omega_0 H} < O(10^{-1}), \tag{33}$$

$$\epsilon = \frac{1}{k_m \, \mathrm{Re}} = \frac{1}{\mathrm{Re}_k} = \left(\frac{\sqrt{\nu_0 / \omega_0}}{H} \right)^2 < O(10^{-4}) \tag{34}$$

are naturally occurring dimensionless groupings representing the reciprocals of the Strouhal and kinetic Reynolds numbers, and satisfying

$$\epsilon/\sigma = \nu_0 / (V_b H) \ll 1. \tag{35}$$

Indubitably, $\mathrm{Re}_k = 2\lambda_S^2$ is another form of the Stokes number, λ_S, which is expected to play a nontrivial role in oscillatory flows. Equations (31)–(32) can be expanded in scalar form into

$$\frac{\partial V_y}{\partial y} + \frac{\partial V_z}{\partial z} = 0, \tag{36}$$

$$iV_y = \sigma \left[\frac{\partial}{\partial y} (V_y U_y) + U_z \frac{\partial V_y}{\partial z} + V_z \frac{\partial U_y}{\partial z} \right] - \epsilon \left(\frac{\partial^2 V_y}{\partial z^2} - \frac{\partial^2 V_z}{\partial y \partial z} \right), \tag{37}$$

$$iV_z = \sigma \left[\frac{\partial}{\partial z} (V_z U_z) + U_y \frac{\partial V_z}{\partial y} + V_y \frac{\partial U_z}{\partial y} \right] - \epsilon \left(\frac{\partial^2 V_z}{\partial y^2} - \frac{\partial^2 V_y}{\partial y \partial z} \right), \tag{38}$$

which reveal that direct analytical solutions to the coupled set are not tractable without exploitation of an important result that can be verified numerically, and proven theoretically, only *a posteriori*. Subject to later verification, the normal vortical velocity V_y is assumed to be of $O(M_b)$ by comparison to the axial component V_z. Being a smaller quantity, ignoring V_y at the first perturbation expansion level of V will not affect the solution which, let us recall, is only accurate to the first order in the Mach number. On that account, Eq. (38) becomes

$$iV_z = \sigma \left[\frac{\partial}{\partial z} (V_z U_z) + U_y \frac{\partial V_z}{\partial y} \right] - \epsilon \frac{\partial^2 V_z}{\partial y^2} + O(M_b). \tag{39}$$

V. VORTICAL SOLUTION

Using separation of variables, a careful scaling analysis, and two-variable multiple scale expansions, an explicit solution to the solenoidal velocity component is sought.

A. Separation of variables

Inserting Eq. (12) into Eq. (39), expanding and rearranging, one gets

$$z \frac{\partial V_z}{\partial z} = \left(\frac{i}{\sigma} - 1 \right) V_z + y \frac{\partial V_z}{\partial y} + \frac{\epsilon}{\sigma} \frac{\partial^2 V_z}{\partial y^2}, \tag{40}$$

which suggests using separation of variables in order to investigate a solution of the type

$$V_z(y,z) = Y(y) Z(z). \tag{41}$$

When inserted back into Eq. (40), Eq. (41) allows splitting the original PDE into two linear ordinary differential equations (ODEs), coupled through a separation constant λ_n:

$$\frac{z}{Z} \frac{dZ}{dz} = \left(\frac{i}{\sigma} - 1 \right) + \frac{y}{Y} \frac{dY}{dy} + \frac{\epsilon}{\sigma} \frac{d^2 Y}{dy^2} = \lambda_n , \tag{42}$$

where λ_n must be strictly positive for a nontrivial outcome. For every λ_n, a solution Z_n and Y_n are manageable. Integration of the axially dependent equation is straightforward. The exact result is $Z_n(z) = c_n z^{\lambda_n}$, where c_n is an integration constant associated with λ_n. Since the governing equation is linear, any linear combination of two or more solutions is also a solution, and one can write, in general, for all possible λ_n

$$V_z(y,z)=\sum_{\lambda_n} c_n z^{\lambda_n} Y_n(y), \tag{43}$$

where λ_n must be determined from the no-slip boundary condition at the wall giving rise to the strong coupling between pressure and vorticity modes. As a consequence, rotational and irrotational components of the axial velocity cancel out at $y=1$. This is achieved when $\tilde{\mathbf{u}}_z=-\hat{\mathbf{u}}_z$, or

$$V_z(1,z)=-(\epsilon_w/\gamma)i\sin(k_m z). \tag{44}$$

Inserting Eq. (44) into Eq. (43), writing out the MacLaurin series expansion for the Sine function, and equating summation terms lead to

$$\sum_{\lambda_n} c_n z^{\lambda_n} Y_n(1) \equiv -\frac{\epsilon_w}{\gamma} i \sum_{n=0}^{\infty} \frac{(-1)^n (k_m z)^{2n+1}}{(2n+1)!}, \tag{45}$$

which holds true when $\lambda_n=2n+1$, $n=0,1,...$, and

$$c_n=-\frac{\epsilon_w}{\gamma} i \frac{(-1)^n (k_m)^{2n+1}}{(2n+1)!}, \tag{46}$$

$$Y_n(1)=1, \tag{47}$$

turning Eq. (43) into

$$V_z(y,z)=-\frac{\epsilon_w}{\gamma} i \sum_{n=0}^{\infty} \frac{(-1)^n (k_m z)^{2n+1}}{(2n+1)!} Y_n(y). \tag{48}$$

In order to satisfy Eq. (42), the velocity eigenfunction $Y_n(y)$ remains to be determined from the two-point boundary value problem prescribed by

$$\epsilon \frac{d^2 Y_n}{dy^2} + \sigma y \frac{dY_n}{dy} + [i-(1+\lambda_n)\sigma] Y_n = 0, \tag{49}$$

a second order ODE that is constrained by two naturally occurring auxiliary conditions:

$$Y_n(1)=1 \quad \text{(no-slip)}, \tag{50}$$

$$\frac{dY_n(0)}{dy}=0 \quad \text{(axial symmetry)}. \tag{51}$$

Equation (49) exhibits a practical closed form solution following a careful application of the derivative expansion method. This approach is presented next.

B. Scaling analysis

The first step for the derivative expansion method to work is the judicious identification of the scale at which order balance is achieved between locally significant terms in the governing ODE. To that end, we make the conjecture that, near the regular singularity

$$y=\epsilon^{1/q} y_1^{-1/q}, \tag{52}$$

where y_1 is the relevant local scale and q is a stretching exponent that must be carefully determined. The derivatives become

$$\frac{dY_n}{dy}=-q\epsilon^{-1/q} y_1^{1+1/q} \frac{dY_n}{dy_1}, \tag{53}$$

$$\frac{d^2 Y_n}{dy^2}=q\epsilon^{-2/q} y_1^{1+2/q}\left[q y_1 \frac{d^2 Y_n}{dy_1^2} + (q+1)\frac{dY_n}{dy_1}\right]. \tag{54}$$

Substituting back into Eq. (49), we get

$$\epsilon^{1-2/q} q^2 y_1^{2+2/q} \frac{d^2 Y_n}{dy_1^2} + q y_1 [\epsilon^{1-2/q}(q+1) y_1^{2/q} - \sigma] \frac{dY_n}{dy_1} + [i-(1+\lambda_n)\sigma] Y_n = 0, \tag{55}$$

which clearly indicates that $q=2$ is a key stretching exponent that corresponds to a distinct limit for which balance between various terms in Eq. (55) will exist. The rescaled equation becomes

$$4 y_1^3 \frac{d^2 Y_n}{dy_1^2} + 2 y_1 (3 y_1 - \sigma) \frac{dY_n}{dy_1} + [i-(1+\lambda_n)\sigma] Y_n = 0, \tag{56}$$

where the modified scale is

$$y_1=\epsilon y^{-2}. \tag{57}$$

Thus when $y=O(\epsilon^{1/2})$, representing the characteristic thickness of the inner layer near $y=0$, the new variable y_1 will be of $O(1)$, which allows resolving accurately the rapid changes that can occur in such a small interval.

C. Two-variable multiple-scale expansions

Having determined the form of the inner scale, a standard multiple-scale procedure can be implemented to transform Eq. (49) into a PDE that is function of two virtual variables, $y_0=y$, and $y_1=\epsilon y^{-2}$. This requires expanding the derivatives in terms of the new variables

$$\frac{d}{dy}=\frac{\partial}{\partial y_0}\frac{dy_0}{dy}+\frac{\partial}{\partial y_1}\frac{dy_1}{dy}=\frac{\partial}{\partial y_0}-2\epsilon y_0^{-3}\frac{\partial}{\partial y_1}, \tag{58}$$

$$\frac{d^2}{dy^2}=\frac{\partial^2}{\partial y_0^2}+O(\epsilon). \tag{59}$$

Note that the current choice of an inner scale represents a minor departure from the conventional form of y/ϵ^{λ}, including $y_1=y/\sqrt{\epsilon}$, which would be ordinarily attempted by a skilled perturbation proponent. The latter form, recommended by most books on the subject, does not lead to a meaningful solution in the case at hand. Substituting Eqs. (58)–(59) back into Eq. (49), we obtain the following PDE:

$$\epsilon \frac{\partial^2 Y_n}{\partial y_0^2} + \sigma y_0 \left(\frac{\partial Y_n}{\partial y_0} - 2\epsilon y_0^{-3} \frac{\partial Y_n}{\partial y_1} \right) + [i-\sigma(1+\lambda_n)] Y_n + O(\epsilon^2) = 0. \tag{60}$$

Next, Y_n is expanded as a sum consisting of a leading order term and a series of consistently decreasing terms:

$$Y_n=Y_n^{(0)}+\epsilon Y_n^{(1)}+O(\epsilon^2), \tag{61}$$

where $Y_n^{(0)}$ is the leading order term that we propose to find. Inserting the two-term expansion of Y_n into Eq. (60), rearranging and collecting terms of $O(1)$ and $O(\epsilon)$, we get, respectively,

$$\epsilon^0: \quad \sigma y_0 \frac{\partial Y_n^{(0)}}{\partial y_0} + [i-(1+\lambda_n)\sigma] Y_n^{(0)} = 0, \tag{62}$$

$$\epsilon: \quad \sigma y_0 \frac{\partial Y_n^{(1)}}{\partial y_0} + [i-(1+\lambda_n)\sigma] Y_n^{(1)} = 2\sigma y_0^{-2} \frac{\partial Y_n^{(0)}}{\partial y_1} - \frac{\partial^2 Y_n^{(0)}}{\partial y_0^2}. \tag{63}$$

Partial integration of Eq. (62) gives $Y_n^{(0)}$:

$$Y_n^{(0)}(y_0, y_1) = C_1(y_1) \exp\{[(1+\lambda_n) - i/\sigma] \ln y_0\}, \tag{64}$$

where the constant of integration C_1 can, in general, be a function of y_1; following traditional multiple-scale arguments, C_1 must be determined in a manner to ensure that $Y_n^{(0)}$ remains uniformly valid, viz., $Y_n^{(0)} > \epsilon Y_n^{(1)}, \forall y$. This will occur when the first order term in Eq. (61) remains smaller that the leading order term in the series expansion for all y. This can only happen when the right hand side of Eq. (63) is zero. Differently stated, if the right hand side of Eq. (63) is not zero, the solution for $Y_n^{(1)}$ will include what is known in perturbation theory as ''secular'' terms. These are undesirable terms that make $Y_n^{(1)}$, in some regions of the solution domain, grow until $\epsilon Y_n^{(1)}$ exceeds $Y_n^{(0)}$. Evidently, this condition cannot be tolerated since it violates the original premise and, furthermore, invalidates the regular perturbation expansion of Y_n in a series of decreasing order terms. To suppress the source of secular terms, we set

$$2\sigma y_0^{-2} \frac{\partial Y_n^{(0)}}{\partial y_1} - \frac{\partial^2 Y_n^{(0)}}{\partial y_0^2} = 0, \tag{65}$$

where the derivatives are

$$\frac{\partial Y_n^{(0)}}{\partial y_1} = \frac{dC_1}{dy_1} \frac{Y_n^{(0)}}{C_1}, \tag{66}$$

$$\frac{\partial^2 Y_n^{(0)}}{\partial y_0^2} = (\lambda_n - i/\sigma)[(1+\lambda_n) - i/\sigma] \frac{Y_n^{(0)}}{y_0^2}, \tag{67}$$

which, when substituted back into Eq. (65), yield

$$\frac{dC_1}{dy_1} - \frac{(\lambda_n - i/\sigma)[(1+\lambda_n) - i/\sigma]}{2\sigma} C_1 = 0, \tag{68}$$

which can be easily solved for C_1:

$$C_1 = C_0 \exp\left\{ \frac{(\lambda_n - i/\sigma)[(1+\lambda_n) - i/\sigma]}{2\sigma} y_1 \right\}. \tag{69}$$

Recalling that $y_1 = \epsilon y^{-2}$, the general, uniformly valid solution for Y_n is

$$Y_n(y) = C_0 \exp\left\{ [(1+\lambda_n) - i/\sigma] \ln y + \frac{\epsilon(\lambda_n - i/\sigma)[(1+\lambda_n) - i/\sigma]}{2\sigma y^2} \right\} + O(\epsilon), \tag{70}$$

where C_0 can be determined readily from Eq. (50). Subsequently,

$$Y_n(y) = y^{(1+\lambda_n)} \exp\{-\xi[1-\sigma^2\lambda_n(1+\lambda_n)](y^{-2}-1)/2 - i[\ln y + \xi\sigma^2(1+2\lambda_n)(y^{-2}-1)/2]/\sigma\} + O(\epsilon), \tag{71}$$

where $\xi = \epsilon/\sigma^3$ is a nondimensional parameter that has a strong influence on the damping rate of Y_n.

D. Analytical solution in infinite series form

Employing Eq. (71) in Eq. (48), letting $\eta = (y^{-2}-1)/2$ for convenience, and summing up over all possible λ_n, renders

$$V_z(y,z) = -\frac{\epsilon_w}{\gamma} i \sum_{n=0}^{\infty} \frac{(-1)^n (k_m z)^{2n+1}}{(2n+1)!} y^{(2n+2)} \times \exp\{-[1-\sigma^2(2n+1)(2n+2)]\xi\eta - i[\ln y + \xi\sigma^2(4n+3)\eta]/\sigma\} + O(\epsilon). \tag{72}$$

From Eq. (27), $\tilde{u}_z$ can be written in an infinite series form that clearly displays the leading order quantities and smaller quantities of $O(\sigma^2)$:

$$\tilde{u}_z(y,z,t) = -\frac{\epsilon_w}{\gamma} iy \sum_{n=0}^{\infty} \frac{(-1)^n (k_m yz)^{2n+1}}{(2n+1)!} \times \exp\{-[1-\sigma^2(2n+1)(2n+2)]\xi\eta - i[\ln y + \xi\sigma^2(4n+3)\eta]/\sigma - ik_m t\} + O(\epsilon). \tag{73}$$

Fortunately, Eq. (73) is a rapidly converging series.

E. Accurate closed form equivalent

Equation (73) can be written in a closed form by disregarding small terms that do not affect the order of the error associated with the infinite series itself. The result is a practical, closed form equivalent

$$\tilde{u}_z(y,z,t) = -\frac{\epsilon_w}{\gamma} iy \sin(k_m yz) \exp[-(1-2\sigma^2)\xi\eta - i(\ln y + 3\xi\sigma^2\eta)/\sigma - ik_m t] + O(\epsilon). \tag{74}$$

F. Graphical verification

In order to verify that Eqs. (73) and (74) are concurrent, we first construct a solution for $\mathbf{u}^{(1)}$ by adding the irrotational component to $\tilde{u}_z$ in Eq. (59). This can be accomplished using either one of the two versions represented by Eqs. (73) and (74). In either case, the penetration depth δ of the resulting time-dependent velocity can be evaluated and compared to a reliable numerical solution to Eq. (39) achieved using a Runge–Kutta scheme of order seven.[12] In Fig. 3, a typical example is furnished that illustrates the excellent agreement between analytical predictions for $\tilde{u}_z$ and the numerical solution to Eq. (23). Since locating δ is sensitive to error accumulation, we overlay analytical predictions of δ vs σ in Fig. 4 for a wide range of physical parameters as obtained from Eqs. (73) and (74). Reassuringly, no discernible discrepancies are detected anywhere, indicating that Eq. (74) can be

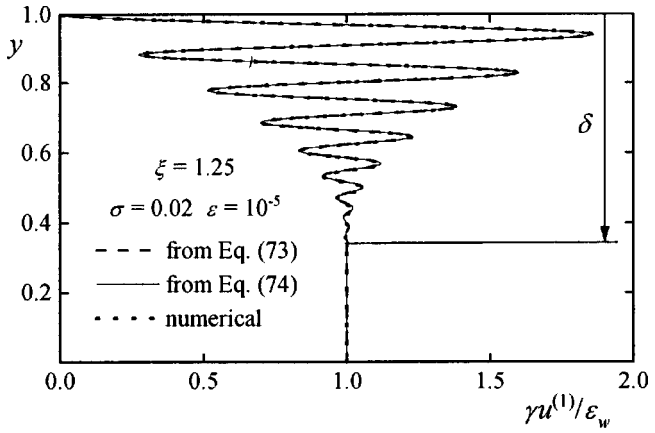

FIG. 3. Virtually indistinguishable results for the total time-dependent velocity at chamber midspan as predicted from numerical, infinite series, and closed form expressions corresponding to Eqs. (73) and (74).

exchanged for Eq. (73) without any appreciable loss in accuracy. This conclusion can be further confirmed by running a standard error calculation.

In addition to its simplicity and remarkable precision, Eq. (74) discloses the leading order terms which control the solution. These relate to the convection of unsteady vorticity by the mean flow in both axial and normal directions, time-dependent inertia, and viscous diffusion of time-dependent vorticity.

G. Normal velocity

The normal component $\tilde{u}_y$ can be determined in a manner to satisfy continuity. To that end, $\tilde{u}_z$ is used in Eq. (22) while a guessed function is proposed for $\tilde{u}_y$. From a conjectured form

$$\tilde{u}_y(y,z,t)=\frac{\epsilon_w}{\gamma}G(y)\cos(k_m yz)\exp[-(1-2\sigma^2)\xi\eta - i(\ln y+3\xi\sigma^2\eta)/\sigma - ik_m t]+O(\epsilon), \quad (75)$$

the unknown function $G(y)$ must be determined to satisfy continuity. Substituting Eq. (74) and Eq. (75) into Eq. (22), the spatial function $G(y)$ is extracted in a manner to ensure

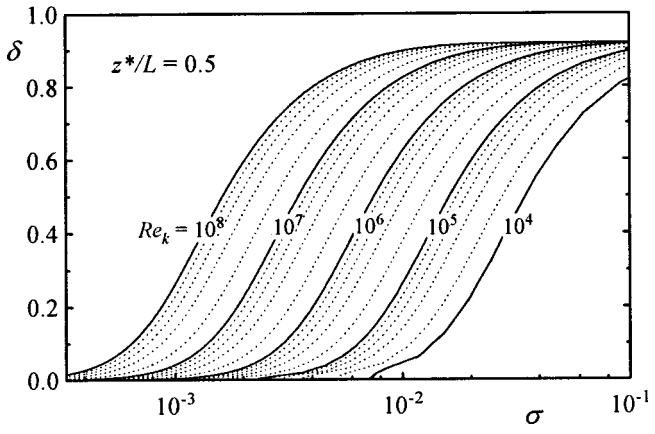

FIG. 4. Penetration depth predictions from infinite series and closed form expressions, viz., Eqs. (73) and (74). To the accuracy of the graph, differences between both formulations cannot be distinguished. Broken lines of constant Re_k are equally spaced.

that $\partial\tilde{u}_y/\partial y=-\partial\tilde{u}_z/\partial z$ is satisfied in the leading order terms. This occurs when

$$G(y)=-M_b y^3, \quad (76)$$

rendering

$$\tilde{u}_y(y,z,t)=-\frac{\epsilon_w}{\gamma}M_b y^3\cos(k_m yz)\exp[-(1-2\sigma^2)\xi\eta - i(\ln y+3\xi\sigma^2\eta)/\sigma - ik_m t]+O(\epsilon). \quad (77)$$

Clearly, the original assumption of $\tilde{u}_y/\tilde{u}_z=O(M_b)$—leading to Eq. (39)—is justifiable. Furthermore, numerical computations of $\tilde{u}_y$ indicate that Eq. (77) is indeed accurate. Such comparisons with numerical predictions of $\tilde{u}_y$ are excluded here for brevity.

VI. SOLUTION CHARACTER

The behavior and character of the time-dependent velocity can now be examined along with its accompanying boundary layer structure. The global error associated with the analytical outcome can also be evaluated to confirm theoretical predictions.

A. Total time-dependent velocity

Superimposing rotational and irrotational velocity fields in Eq. (16), $u_z^{(1)}$ can be formulated at $O(M_b)$:

$$u_z^{(1)}(y,z,t)=\frac{\epsilon_w}{\gamma}i\exp(-ik_m t)\{\sin(k_m z)-y\sin(k_m yz)\times\exp[-(1-2\sigma^2)\xi\eta - i(\ln y+3\xi\sigma^2\eta)/\sigma]\}, \quad (78)$$

whose real part is

$$u_z^{(1)}(y,z,t)=\frac{\epsilon_w}{\gamma}\Bigg[\overbrace{\sin(k_m z)\sin(k_m t)}^{\text{acoustic part}} \underbrace{\overbrace{-y\sin(k_m yz)\exp(-\zeta)}^{\text{solenoidal amplitude}}\ \overbrace{\sin(k_m t+\Phi)}^{\text{wave propagation}}}_{\text{solenoidal part}}\Bigg], \quad (79)$$

where

$$\zeta=\xi(1-2\sigma^2)(y^{-2}-1)/2, \quad (80)$$

$$\Phi=[\ln y+3\xi\sigma^2(y^{-2}-1)/2]/\sigma. \quad (81)$$

Evidently, $u^{(1)}$ is prescribed by $u_z^{(1)}$ which is a harmonic wave that proceeds from the wall ($y=0$) and travels in the direction of increasing y. It is characterized by a wave amplitude that diminishes exponentially with increasing distance from the wall. The decay constant associated with the exponential decrease can be extrapolated by inspecting Eqs. (79)–(80) to be the viscosity parameter ξ. The vortical wave amplitude is actually controlled by two terms: an exponentially decaying term, made possible by inclusion of viscous dissipation (i.e., ζ), that decreases with the distance from the

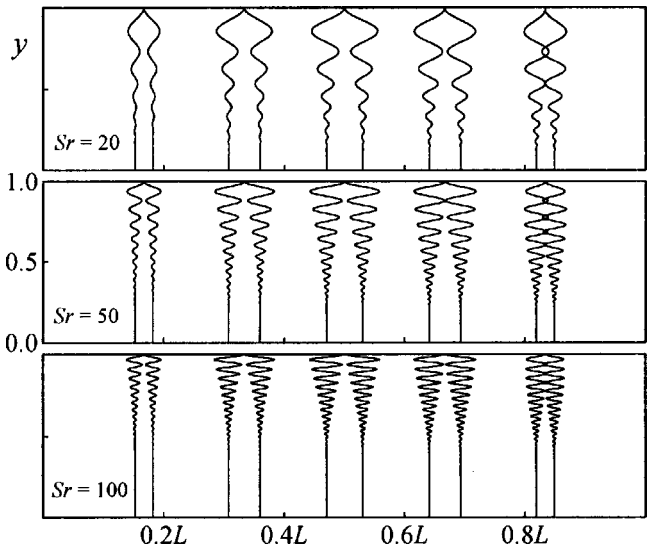

FIG. 5. Time-dependent velocity patterns shown at several axial stations for $\mathrm{Re}_k=10^6$ and typical values of the Strouhal number.

wall, and a sinusoidal term, made possible by inclusion of axial mean flow convection of unsteady vorticity, which varies harmonically with the distance from the head end, and also decreases with the distance from the wall. By inspection of the spatial damping function ζ in Eq. (74) and Eq. (79), increasing viscosity is found to cause the rotational wave to decay more rapidly, preventing a deeper inward penetration of vorticity. This effect is contrary to the boundary-layer ''thickening'' role played by viscosity in oscillatory flows between parallel rigid walls. Incorporation of blowing effects appears to alter the flow character quite dramatically. Results from Eq. (79) are congruent with numerical predictions which are achieved to a high order of accuracy (using a step size of 10^{-6} in conjunction with a nine-stage Runge–Kutta scheme that exhibits a global error of order seven).[12] This agreement, shown in Fig. 5, causes differences in graphical results to become visually indiscernible.

When, in Fig. 5, numerical and analytical velocity distributions are overlaid, no appreciable discrepancies can be perceived. Local velocity profiles shown correspond to instantaneous profiles separated by 180 degrees of a full oscillation cycle depicted at several axial locations for the fundamental pressure oscillation mode. Note that the solenoidal component of the velocity is more pronounced in the downstream portions of the cavity where time-dependent vorticity is intensified. The figure also indicates that the spatial wavelength of solenoidal waves diminishes at higher Strouhal numbers.

B. Acoustic boundary layer

We start by examining the rotational wave amplitude which controls the evolution of the time-dependent boundary-layer envelope:

$$\|\tilde{u}^{(1)}\|=\frac{\epsilon_w}{\gamma}y\,\sin(k_m yz)\exp[-(1-2\sigma^2)\xi\eta]. \tag{82}$$

Defining the boundary layer to extend from the compliant wall to the point where 99% of the rotational wave component has vanished, the corresponding boundary layer thickness will be the distance from the wall to the point where $\|\tilde{u}^{(1)}\|$ becomes $\alpha\equiv 1\%$ of its irrotational counterpart. The normalized penetration depth δ extending from the wall to the edge of the boundary layer can, therefore, be calculated from $y_p=1-\delta$, where

$$y_p\sin(k_m y_p z)\exp[-(1-2\sigma^2)\xi\eta]-\alpha|\sin(k_m z)|=0. \tag{83}$$

Plots of δ vs σ for a wide range of Re_k are shown in Fig. 6 at two axial stations that are 5% of the longitudinal length from each end: one near the head end ($z^*=0.05L$) and the other near the aft end ($z^*=0.05L$). The wide spread in the data makes it difficult to interpret the dependence of δ on actual physical parameters. This problem is alleviated by referring to Eq. (83) which clearly shows that the term involving exponential boundary layer decay is a strong function of a viscous damping parameter, ξ. This subtle realization motivates generating curves of δ vs ξ, for wide variations in Re_k. As shown in Fig. 7, entire families of curves, such as those shown in Fig. 4 (for $z^*=0.5L$) and Fig. 6 at discrete axial

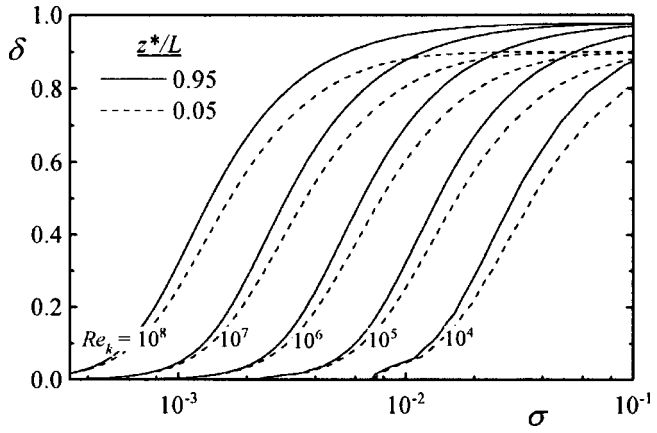

FIG. 6. Locus of the rotational boundary-layer thickness at two axial stations and $m=1$. Since δ grows from the head end, the upper family of curves (solid lines) corresponds to the downstream location.

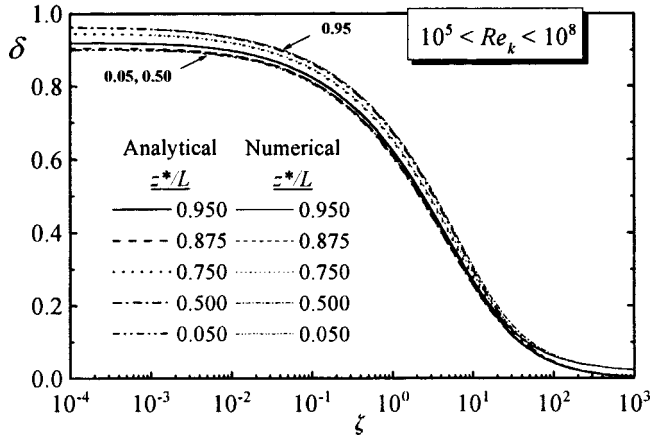

FIG. 7. The boundary-layer thickness determined numerically and analytically at five discrete locations. To the resolution of this graph, no changes in δ seem to occur in the cavity's forward half portion ($0.05\leqslant z^*/L\leqslant 0.5$). Except for large ξ, differences between numerical and analytical predictions are hardly noticeable.

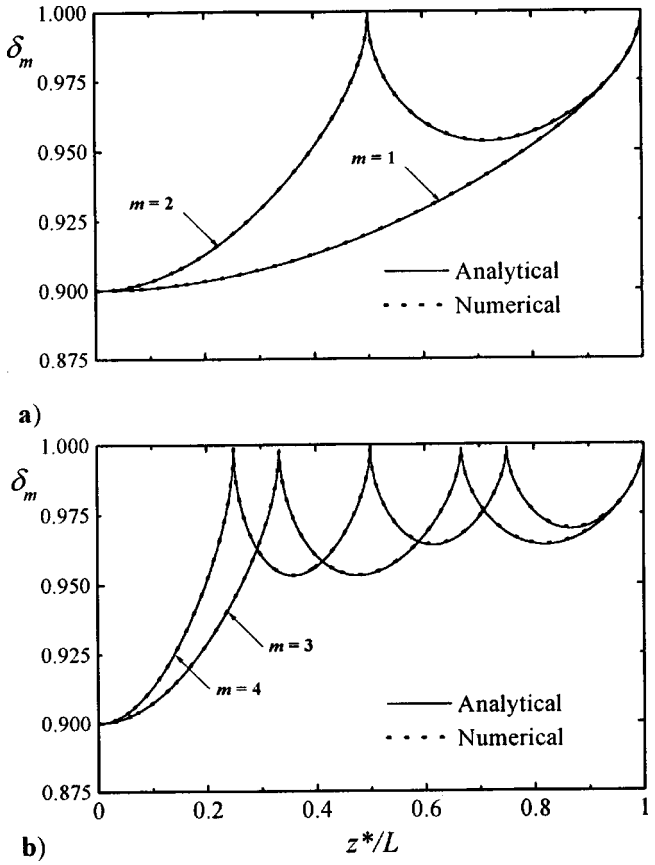

FIG. 8. Trace of the maximum boundary-layer thickness corresponding to ideal fluids and the first four acoustic modes: (a) $m=1,2$ and (b) $m=3,4$.

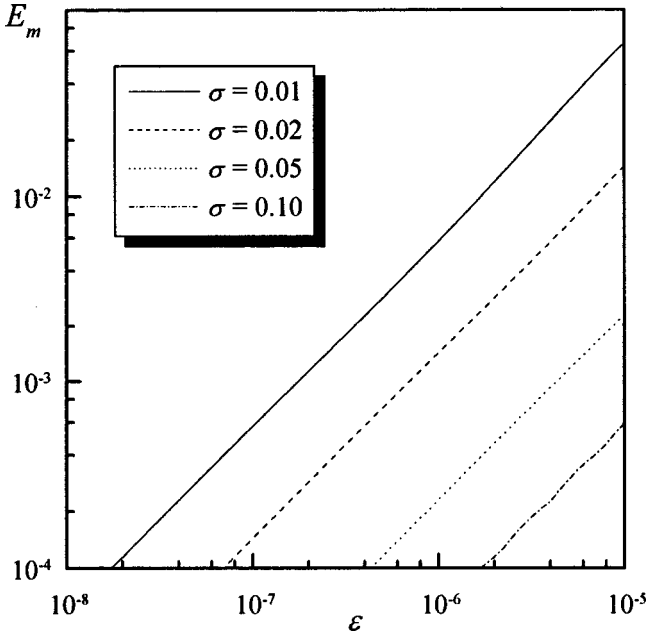

FIG. 9. Maximum absolute error.

stations, collapse splendidly into single curves per axial location. This significant result reveals that δ does not depend on Re_k and σ separately, but rather on $\xi=\omega_0^2 v_0 H V_b^{-3}$, a key similarity parameter that resembles, in importance, the Stokes number in oscillating flows over nontranspiring walls. However, unlike many similarity parameters, ξ cannot be disclosed by standard dimensional analysis.

Figures 7 and 8 bring into focus the character of the boundary-layer thickness over permeable walls that is defined in Fig. 3. For instance, it is clear from Eq. (83) that $\delta=f(\xi,m,z)$ must depend on ξ, the pressure mode number and, to a lesser degree, on the axial station within the chamber. For the fundamental pressure oscillation mode, $m=1$, Fig. 7 shows that, for large ξ, δ varies linearly with ξ, independently of z. Smaller ξ imply larger penetration depths due to a smaller argument in the exponentially decaying term. Furthermore, increasing the blowing speed, or decreasing viscosity, frequency, or chamber height seems to enhance the depth of penetration. Eventually, for sufficiently small ξ, δ tends asymptotically to a maximum fixed value per axial position. This maximum fixed value becomes independent of ξ and the corresponding depth becomes $\delta=f(m,z)$ as $\xi\rightarrow 0$.

In order to pinpoint this maximum possible penetration depth, δ_m, occurring per axial station and mode number, we realize that, for the same geometry and blowing speed, larger penetration occurs in fluids with smaller viscosity. In the ideal case of zero viscosity, rotational waves face minimum friction and, thereby, travel the furthest distance from the wall. The asymptotic limit on the thickness of the boundary layer can thus be determined from the inviscid formulation of the penetration depth—which only depends on the axial station z and pressure mode m. Setting $v_0=0$ or $\xi=0$ in Eq. (83), we get

$$(1-\delta_m)\sin[k_m(1-\delta_m)z]-\alpha|\sin(k_m z)|=0. \tag{84}$$

The resulting expansion formula is

$$\delta_m=1-\sqrt{\alpha|\sin(k_m z)|/(k_m z)}+O(1-\delta_m)^4, \tag{85}$$

which allows predicting the inviscid depth of penetration quite accurately. A maximum truncation error of $O(10^{-4})$ corresponds to the smallest value of δ_m, which is 0.9 for $z=0$. Having a smaller truncation error than $O(M_b)$, Eq. (85) can be exchanged for the numerical solution to Eq. (84). This is illustrated in Fig. 8 below for the first four acoustic modes where δ_m is shown to vary between 90% and 100% of the solution domain.

C. Global error analysis

In order to ensure that no mistakes were committed in the derivation process, and to verify the order of the error associated with the final expression for the time-dependent velocity field, viz., Eq. (79), we calculate the maximum absolute error E_m between the analytical prediction and the numerical outcome of Eq. (11) following Bosley's constructive recommendation.[13] Since the absolute error defined here represents the deviation from the numerical solution, the latter is determined very accurately by using a seventh order Runge–Kutta scheme and a subinterval of 10^{-6}. Assuming that the maximum absolute error exhibits the classical form

$$E_m=|u^{(1)}_{\text{numerical}}-u^{(1)}_{\text{analytical}}|_{\max}=K\epsilon^{\kappa}, \tag{86}$$

then the order of the error, κ, can be determined from the slope of the linear least-squares (LS) fit to the data set generated by plotting $\lg E_m$ vs $\lg \epsilon$ for different values of σ. As it can be inferred from Fig. 9, the order of the error κ is about unity. Linear slopes obtained from LS lines with high correlation coefficients confirm that, indeed, κ varies from 0.99 to 0.999 999 in decreasing ranges of ϵ. In fact, regardless of σ, we can write with confidence that

$$\kappa \xrightarrow[\epsilon \to 0]{} 1. \tag{87}$$

This reassuring observation leads us to conclude that the error associated with Eq. (79) is of $O(\epsilon)$.

VII. CONCLUSIONS

In this article, the oscillatory field that results from harmonic pressure disturbances superimposed on the mean flow inside a rectangular cavity is resolved using asymptotics. With regard to the time-dependent field, accurate expressions for the axial and normal velocity components are extracted. The normal velocity is found to be small, namely, of the order of the surface Mach number, by comparison to the axial counterpart. The latter dictates its character in the total solution which represents a traveling wave that decays with distance from the wall. The rate of decay is found to be a strong function of a nondimensional parameter, $\xi = \omega_0^2 \upsilon_0 H V_b^{-3}$, that has a profound impact on the solution. This so-called viscosity parameter combines both Strouhal and kinetic Reynolds numbers via $\xi = \mathrm{Sr}^3/\mathrm{Re}_k$. This dimensionless grouping appears in the analytical formulation to be the primary similarity parameter in control of the solution. At the outset, large viscosity leads to faster attenuation of the traveling wave envelope, and thereby, to smaller penetration depths of rotational waves. In addition to its strong dependence on ξ, the penetration depth of rotational waves is found to depend on the acoustic mode number m, and on the distance from the head end, z. An accurate expansion formula is extracted for the maximum penetration depth associated with ideal fluids with small viscosity. Finally, a standard analysis of the maximum error associated with the analytical derivation validates the rigor of the perturbation approach and confirms the order of the reported truncation error. Experimental verification remains to be addressed in a forthcoming article.

[1] J. Majdalani and W. K. Van Moorhem, ''Improved time-dependent flow field solution for solid rocket motors,'' AIAA J. **36**, 241–248 (1998).
[2] Y. Ma, ''A simulation of the flow near a burning propellant in a solid propellant rocket motor,'' Ph. D. dissertation, University of Utah (1990).
[3] Y. Ma, W. K. Van Moorhem, and R. W. Shorthill, ''Innovative method of investigating the role of turbulence in the velocity coupling phenomenon,'' Journal of Vibration & Acoustics-Transactions of the ASME **112**, 550–555 (1990).
[4] Y. Ma, W. K. Van Moorhem, and R. W. Shorthill, ''Experimental investigation of velocity coupling in combustion instability,'' J. Propul. Power **7**, 692–699 (1991).
[5] J. Barron, ''The onset of turbulence in a simulation of the oscillating flow over a burning propellant,'' Ph.D. dissertation, University of Utah (1997).
[6] M. Van Dyke, *Perturbation Methods in Fluid Mechanics* (The Parabolic Press, Stanford, CA, 1975).
[7] F. M. White, *Viscous Fluid Flow* (McGraw-Hill, New York, 1991), p. 153.
[8] A. Sommerfeld, *Mechanics of Deformable Bodies* (Academic, New York, 1950), p. 147.
[9] B. T. Chu and L. S. G. Kovásznay, ''Nonlinear interactions in a viscous heat-conducting compressible gas,'' J. Fluid Mech. **3**, 494–514 (1957).
[10] B. T. Carrier and F. D. Carlson, ''On the propagation of small disturbances in a moving compressible fluid,'' Q. Appl. Math. **4**, 1–12 (1946).
[11] G. A. Flandro, ''Solid propellant acoustic admittance corrections,'' J. Sound Vib. **36**, 297–312 (1974).
[12] J. C. Butcher, *The Numerical Analysis of Ordinary Differential Equations* (Wiley, Great Britain, 1987).
[13] D. L. Bosley, ''A technique for the numerical verification of asymptotic expansions,'' SIAM (Soc. Ind. Appl. Math.) Rev. **38**, 128–135 (1996).

Low-frequency shear wave propagation in periodic systems of alternating solid and viscous fluid layers

Boris Gurevich
The Geophysical Institute of Israel, P.O. Box 2286, Holon 58122, Israel

(Received 21 October 1998; accepted for publication 19 March 1999)

Waves in periodic layered systems at low frequencies can be studied using an asymptotic analysis of the Rytov's exact dispersion equations. Since the wavelength of the shear wave in the fluid (viscous skin depth) is much smaller than the wavelength of the shear wave in the solid, the presence of viscous fluid layers requires a consideration of higher terms in the asymptotic expansions. For a shear wave with the directions of propagation and of particle motion in the bedding plane, the attenuation (inverse Q) obtained by this procedure is $Q^{-1}=\omega\eta\phi/\mu_s(1-\phi)+\omega\phi\rho_f^2h_f^2/12\rho\eta+o(\omega)$, where ω is frequency, ρ is weighted average density of the solid/fluid system, h_f is the thickness of fluid layers, ϕ is fluid volume fraction, i.e., the ''porosity,'' μ_s is solid shear modulus, and ρ_f and η are the density and viscosity of the fluid, respectively. The term proportional to η is responsible for the viscous shear relaxation, while the term proportional to η^{-1} accounts for the visco-inertial (poroelastic) attenuation of Biot's type. This result shows that the characteristic frequencies of visco-elastic ω_{VE}, poroelastic ω_B, and scattering ω_R attenuation mechanisms obey the relation $\omega_{\mathrm{VE}}\omega_B=\omega_R^2$, which explains why the visco-elastic and poroelastic mechanisms are usually treated separately in the context of macroscopic theories that imply $\omega\ll\omega_R$. The poroelastic mechanism dominates over the visco-elastic one when the frequency-independent parameter $B=\omega_B/\omega_{\mathrm{VE}}=12\eta^2/\mu_s\rho_fh_f^2\ll1$, and vice versa.
[S0001-4966(99)00607-4]

PACS numbers: 43.20.Jr [AN]

INTRODUCTION

Waves in a medium consisting of periodically alternating fluid and solid layers have been studied extensively, partly as an exactly solvable example of a fluid-saturated porous medium.[1–4] However, most of the research has been focused on ideal and low-viscosity fluids and relatively high frequencies when the layered system exhibits behavior typical of fluid-saturated media as described by a high-frequency Biot theory of poroelasticity.[3,5–8] In this article, we focus on low frequencies and relatively high viscosity fluids and show that the behavior of a layered system under these conditions also exhibits some interesting features.

The properties of waves in periodic layered systems at low frequencies can be studied using a low-frequency asymptotic analysis of the known exact dispersion equations.[1,2,9] For the asymptotic analysis to be valid, the wavelengths of all the waves involved must be larger than the spatial period of the periodic system. Since the wavelength of the shear wave in the fluid (viscous skin depth) is much smaller than the wavelength of the shear wave in the solid or of the acoustic wave in the fluid, the presence of viscous fluid layers requires a consideration of higher terms in the asymptotic expansions. The procedure is exactly the same for shear waves with the directions of propagation and of particle motion in the bedding plane, and for extensional waves propagating parallel to layering. It will be illustrated here for shear waves only.

I. LOW-FREQUENCY DISPERSION EQUATION

Consider a system of periodically alternating solid and fluid layers of period d. The elastic solid is characterized by density ρ_s, bulk modulus K_s, and shear modulus μ_s. The viscous fluid is characterized by density ρ_f, bulk modulus (inverse compressibility) K_f, and dynamic viscosity η. The solid- and fluid-layer thicknesses are h_s and $h_f=d-h_s$, respectively.

We consider propagation of a shear wave in the direction x parallel to layering with the displacement in the direction y normal to x, but also parallel to the bedding (SH wave). For a given frequency ω, the solution of the mechanical problem can be looked for in the form

$$u_y=u_{y0}e^{i(ax-\omega t)}.$$

We want to obtain low-frequency asymptotic of the wave number a or the phase velocity $c=\omega/a$ as a function of ω. To employ the known results for solid layered systems, we can regard the fluid as another solid with a complex shear modulus $\mu_f=-i\omega\eta$. SH wave propagation in a periodic system of solid layers of two types s and f is governed by an exact dispersion equation[1,2,9]

$$p\left[\left(\tan\frac{\beta_sh_s}{2}\right)^2+\left(\tan\frac{\beta_fh_f}{2}\right)^2\right]+(1+p^2)\tan\frac{\beta_sh_s}{2}\tan\frac{\beta_fh_f}{2}=0. \tag{1}$$

Here, $\beta_s^2=\omega^2(1/c_s^2-1/c^2)$, $\beta_f^2=\omega^2(1/c_f^2-1/c^2)$, where $c_s=(\mu_s/\rho_s)^{1/2}$ and $c_f=(\mu_f/\rho_f)^{1/2}$ are shear velocities in the materials s and f, respectively, and p is given by

$$p=\frac{\mu_f\beta_f}{\mu_s\beta_s}.$$

For sufficiently long waves or low frequencies the arguments of the tangents are small. Thus, the tangents in Eq. (1)

can be replaced by their respective arguments. The so-simplified equation

$$p\left[\left(\frac{\beta_s h_s}{2}\right)^2+\left(\frac{\beta_f h_f}{2}\right)^2\right]+(1+p^2)\frac{\beta_s h_s}{2}\frac{\beta_f h_f}{2}=0, \tag{2}$$

can be solved analytically to give

$$c^2=\frac{h_s\mu_s+h_f\mu_f}{h_s\rho_s+h_f\rho_f}, \tag{3}$$

or

$$c^2=\frac{(1-\phi)\mu_s+\phi\mu_f}{\rho},$$

where $\phi=h_f/d$ is the volume fraction of the fluid layers (porosity), and $\rho=(1-\phi)\rho_s+\phi\rho_f$. For the fluid layers, the substitution

$$\mu_f=-i\omega\eta \tag{4}$$

yields the following expression for the velocity c^2:

$$c^2=\frac{(1-\phi)\mu_s-i\omega\eta\phi}{\rho}=\frac{(1-\phi)\mu_s}{\rho}\left(1-\frac{\phi}{1-\phi}\frac{i\omega\eta}{\mu_s}\right). \tag{5}$$

Due to the effect of viscosity the velocity is now complex, implying the presence of attenuation.

Equation (5) is the result given in textbooks as a low-frequency or long-wavelength approximation (see, e.g., Refs. 2, 8) with an obvious requirement that $\beta_s h_s$ and $\beta_f h_f$ must be small. However, one can observe that the wavelength of the viscous wave in the fluid is much smaller than that of the shear wave in the solid. Thus, the decrease of frequency ω also increases the relative magnitude of the terms containing β_f, so that higher terms in the power series expansion of $\tan(\beta_f h_f/2)$ may become significant. To analyze this phenomenon in greater detail, we must retain the second term in this expansion, i.e.,

$$\tan\frac{\beta_f h_f}{2}\simeq\frac{\beta_f h_f}{2}+\frac{1}{3}\left(\frac{\beta_f h_f}{2}\right)^3\simeq\frac{\beta_f h_f}{2}\left(1+\frac{1}{12}\frac{i\omega h_f^2\rho_f}{\eta}\right). \tag{6}$$

Substituting this approximation for $\tan(\beta_f h_f/2)$ while still replacing $\tan(\beta_s h_s/2)$ by its argument, we can rewrite Eq. (1) in the form

$$p\left[\left(\frac{\beta_s h_s}{2}\right)^2+\left(\frac{\beta_f h_f'}{2}\right)^2\right]+(1+p^2)\frac{\beta_s h_s}{2}\frac{\beta_f h_f'}{2}=0, \tag{7}$$

where

$$h_f'=h_f\left(1+\frac{1}{12}\frac{i\omega h_f^2\rho_f}{\eta}\right). \tag{8}$$

Equation (7) is identical to Eq. (2) with h_f' in place of h_f. Similarly to Eq. (3), the solution for c^2 is

$$c^2=\frac{h_s\mu_s+h_f'\mu_f}{h_s\rho_s+h_f'\rho_f}. \tag{9}$$

Substitution of (8) and (4) into (9) and retaining the terms up to the first power of ω finally gives the following expression for c^2:

$$c^2=\frac{(1-\phi)\mu_s}{\rho}\left(1-\frac{i\omega\eta}{\mu_s}\frac{\phi}{1-\phi}-\frac{1}{12}\frac{i\omega}{\eta}\frac{\phi\rho_f^2h_f^2}{\rho}\right). \tag{10}$$

The imaginary terms indicate the presence of dissipation. The corresponding dimensionless attenuation (inverse quality factor) can be written

$$Q^{-1}=\frac{\omega\eta}{\mu_s}\frac{\phi}{1-\phi}+\frac{1}{12}\frac{\omega}{\eta}\frac{\phi\rho_f^2h_f^2}{\rho}. \tag{11}$$

Equations (10) and (11) are the central results of this article. The most interesting feature of these equations is the presence of two dissipative terms with the same frequency dependency but different dependencies on fluid viscosity. In fact, both terms are familiar ones. The first term (proportional to η) is the same as in Eq. (5) and accounts for the contribution of the complex shear modulus of the fluid to the overall complex shear modulus of the layered system (viscous shear relaxation). The second term which scales with η^{-1} can be identified with the visco-inertial attenuation in a porous medium as described by Biot's theory of poroelasticity.[10–12] In Biot's theory, the shear wave attenuation in the low-frequency limit is given by

$$Q_B^{-1}=\frac{\omega}{\eta}\frac{\rho_f^2\kappa}{\rho}, \tag{12}$$

where κ denotes permeability. The permeability of a system of plain slits is[4,11]

$$\kappa=\frac{\phi h_f^2}{12}. \tag{13}$$

Substitution of Eq. (13) into Eq. (12) yields an expression identical to the second term in the right-hand side of Eq. (11).

One can see that both terms in Eq. (11) are related to the well-known mechanisms of wave attenuation in porous media: visco-elastic mechanism (viscous shear relaxation)[13,14] and visco-inertial Biot mechanism.[10–12] In our treatment, both terms have been derived, for an idealized porous medium, from the same standpoint.

II. DISCUSSION

To further analyze these results, we rewrite Eq. (11) in the form

$$Q^{-1}=\frac{\omega}{\omega_{\mathrm{VE}}}\frac{\phi}{1-\phi}+\frac{\omega}{\omega_B}\frac{\phi\rho_f}{\rho}. \tag{14}$$

Here, $\omega_{\mathrm{VE}}=\mu_s/\eta$ is the characteristic frequency of the visco-elastic mechanism. At this frequency the absolute value of the complex shear modulus of the viscous fluid equals the solid shear modulus. In turn, $\omega_B=\eta\phi/\kappa\rho_f$ is the Biot's characteristic frequency,[11,12] at which the wavelength of the shear wave (viscous skin depth in the fluid) equals the thickness of the fluid layers h_f. The expressions for the two characteristic frequencies may be multiplied to give

$$\omega_{\mathrm{VE}}\omega_B=\frac{\mu_s\phi}{\kappa\rho_f}=\frac{12\mu_s}{h_f^2\rho_f}=A\left(\frac{2\pi c_0}{d}\right)^2=A\omega_R^2, \tag{15}$$

where

$$c_0 = \lim_{\omega \to 0} c = \sqrt{\frac{(1-\phi)\mu_s}{\rho}}$$

is the static shear velocity in the system,

$$A = \frac{3\rho}{\pi^2 \phi^2 (1-\phi)\rho_f}$$

is a dimensionless parameter of order 1 depending only on the porosity and the ratio of solid-to-fluid densities, and ω_R is approximately the resonant frequency of the layered periodic system, at which the wavelength of the shear wave equals the period of the system. For a disordered (nonperiodic) system of layers, ω_R corresponds to the characteristic scattering frequency. Equation (15) partly explains why the visco-elastic and visco-inertial mechanisms of attenuation are usually treated separately. Indeed, from Eq. (15) it follows that either

$$\omega_{\mathrm{VE}} < \omega_R < \omega_B ,$$

or

$$\omega_B < \omega_R < \omega_{\mathrm{VE}} .$$

In other words, if one of the characteristic frequencies is smaller than the resonant (scattering) frequency ω_R, the other one is bound to be larger than ω_R. But, any theory that aims at describing the macroscopic effects can, by definition, describe only the behavior of the media on spatial scales much larger than the grain or pore size (or period for periodic media), i.e., for frequencies much smaller than ω_R. Thus, any macroscopic poroelastic theory can describe either the visco-elastic or the visco-inertial (Biot's) mechanism of attenuation in our idealized example of a porous medium. For a general three-dimensional periodic porous medium with a single characteristic pore size, this fact was proved mathematically by Boutin and Auriault[15] in the context of the theory of asymptotic homogenization of periodic structures, the theory that explicitly employs the ratio ω/ω_R as a small parameter. In our analysis, we have managed to obtain both terms together only because our approach is based not on any macroscopic theory, but on the dispersion Eq. (1) which is exact for all frequencies.

Furthermore, we can define a fundamental parameter of a layered system or a porous medium

$$B = \frac{\omega_B}{\omega_{\mathrm{VE}}} = \frac{\eta^2 \phi}{\mu_s \kappa \rho_f},$$

that shows which of the two viscosity-related dissipation mechanisms dominates at frequencies $\omega \ll \omega_R$ when the macroscopic description makes sense. We emphasize that the parameter B does not depend on the frequency, but only on the physical and geometrical properties of the layered system (or a porous rock). If $B<1$, the Biot's poroelastic mechanism is the primary mechanism, whereas for $B>1$ the visco-elastic mechanism dominates. For the permeability of 1 Darcy and viscosity of water, the parameter B is about 10^{-4}, but it may be larger for more viscous fluids (heavy oil, bitumen) and/or lower permeabilities. Also, observe that the closer the parameter B to 1, the closer both characteristic frequencies to each other and to the resonant (scattering) frequency ω_R, resulting in very small attenuation at frequencies $\omega \ll \omega_R$, where macroscopic description makes sense.

The three characteristic frequencies ω_{VE}, ω_R, and ω_B introduce three dimensionless frequencies: $V = \omega/\omega_{\mathrm{VE}} = \omega\eta/\mu_s$, $\Omega = \omega/\omega_R = \omega d/c_0$, and $l = \omega/\omega_B = \omega\kappa\rho_f/\eta\phi$. Equation (15) shows that $V/l = A^{-1}(\Omega/l)^2 = A(V/\Omega)^2 = B$, and $\Omega^2 = AVl$. The parameters $L = \sqrt{l}$ and Ω were introduced by Schoenberg and Sen.[5] Their work focused on the ''low frequency'' ($\Omega \ll 1$) but ''small viscous skin depth'' ($l \gg 1$) regime, i.e., on frequencies ω that are in the interval

$$\omega_B \ll \omega \ll \omega_R ,$$

which implies the medium with $B<1$. On the other hand, our asymptotic low frequency relations (10) and (11) are valid when $V \ll 1$, and $l \ll 1$ at the same time, i.e., when frequency is small compared with any of the characteristic frequencies

$$\omega \ll \omega_B , \quad \omega \ll \omega_{\mathrm{VE}} .$$

As mentioned above, the visco-elastic and visco-inertial mechanisms of attenuation in porous media are usually treated separately. In particular, the visco-elastic phenomenon is ignored in Biot theory by simply neglecting the shear stress in the fluid in the microscopic (pore-scale) constitutive equations. Pride *et al.*[16] analyzed the effect of this approximation and showed that it requires that the parameter $V = \omega\eta/\mu_s$ be small. Indeed, if V is very small, the visco-elastic attenuation is also very small, see Eq. (14). However, if at the same time the parameter l is even smaller than V, i.e., $l < V \ll 1$, the poroelastic effects would be even less pronounced than the visco-elastic ones. The condition for neglecting the visco-elastic effects *relative* to the poroelastic ones is $B = V/l \ll 1$. And, most importantly, this condition involves medium parameters only and is independent of frequency. Thus, if this condition holds for a particular medium, Biot theory would apply for all frequencies below the resonant frequency of individual pores. This is consistent with observations of Bedford,[4] who compared numerically the solutions of the exact dispersion equation for a layered solid/fluid system (with very small parameter B) with the prediction of Biot theory, and found an excellent agreement in a wide frequency range. This is not surprising in light of the results of Schoenberg and Sen[5] and Molotkov and Bakulin,[6,7] who showed analytically that in the case of low viscosity $B = V/l \ll 1$ the exact constitutive equations for a solid/fluid layered medium represent a partial case of the anisotropic Biot equations.

The procedure described above can also be applied to extensional waves propagating in the direction of layering. This will be done in a separate paper.

ACKNOWLEDGMENTS

I thank Jean-Louis Auriault and Michael Schoenberg for the in-depth discussions that inspired this work. The research was carried out with the support of the Israel Ministry of National Infrastructures.

[1] S. M. Rytov, ''Acoustical properties of a thinly laminated medium,'' Sov. Phys. Acoust. **2**, 68–80 (1956).
[2] L. M. Brekhovskikh, *Waves in Layered Media* (Academic, New York, 1981).
[3] M. Schoenberg, ''Wave propagation in alternating fluid/solid layers,'' Wave Motion **6**, 303–320 (1984).
[4] A. Bedford, ''Application of Biot's equations to a medium of alternating fluid and solid layers,'' J. Wave-Mat. Int. **1**, 34–53 (1986).
[5] M. Schoenberg and P. N. Sen, ''Wave propagation in alternating solid and viscous fluid layers: Size effects in attenuation and dispersion of fast and slow waves,'' Appl. Phys. Lett. **48**, 1249–1251 (1986).
[6] L. A. Molotkov and A. V. Bakulin, ''About the relation between the effective model of layered fluid–solid medium and transversely isotropic Biot model,'' European Association of Geoscientists and Engineers, Extended Abstracts, Paper C013, 1996.
[7] L. A. Molotkov and A. V. Bakulin, ''The effective model of a stratified solid–fluid medium as a special case of the Biot model,'' J. Math Sci. **91**, 2812–2827 (1998).
[8] L. A. Molotkov and A. E. Khilo, ''On the equations of the effective model for an elastic medium with fractures filled with a viscous fluid,'' *Problems in the Dynamic Theory of Seismic Wave Propagation* (Voprosy Dynamicheskoj Teorii Rasprostraneniya Seismicheskikh Voln in Russian) **30**, 88–95 (1990).
[9] R. M. Christensen, *Mechanics of Composite Materials* (Wiley-Interscience, New York, 1979).
[10] M. A. Biot, ''Theory of propagation of elastic waves in a fluid-saturated porous solid. I. Low-frequency range,'' J. Acoust. Soc. Am. **28**, 168–178 (1956).
[11] M. A. Biot, ''Theory of propagation of elastic waves in a fluid-saturated porous solid. II. Higher frequency range,'' J. Acoust. Soc. Am. **28**, 179–191 (1956).
[12] T. Bourbié, O. Coussy, and B. Zinszner, *Acoustics of Porous Media* (Technip, Paris, 1987).
[13] G. Mavko and A. Nur, ''Melt squirt in aesthenosphere,'' J. Geophys. Res. **80**, 1444–1448 (1975).
[14] R. J. O'Connell and B. Budiansky, ''Viscoelastic properties of fluid-saturated cracked solids,'' J. Geophys. Res. **82**, 5719–5740 (1977).
[15] C. Boutin and J.-L. Auriault, ''Dynamic behavior of porous media saturated by a viscoelastic fluid. Application to bituminous concretes,'' Int. J. Eng. Sci. **28**, 1157–1181 (1990).
[16] S. R. Pride, A. F. Gangi, and F. D. Morgan, ''Deriving the equations of motion for porous isotropic media,'' J. Acoust. Soc. Am. **92**, 3278–3290 (1992).

Low-frequency slow-wave dispersion computations by compound-matrix propagation

Sven Ivansson[a)]
Division of Systems and Underwater Technology, Defence Research Establishment, SE-172 90 Stockholm, Sweden

(Received 19 October 1998; revised 17 February 1999; accepted 19 March 1999)

Slow P-SV modes whose horizontal slowness tends to infinity while the horizontal wave number tends to zero, as the frequency tends to zero, exist in certain laterally homogeneous fluid-solid media. These modes can be characterized by an asymptotic analysis of the dispersion function. Only certain powers of frequency are possible for the asymptotic increase of the horizontal slowness as the frequency tends to zero: $-1/3$, $-1/2$, $-3/5$, and $-2/3$. In order to investigate the accuracy of the asymptotic predictions, dispersion-curve computations by propagator techniques are attempted for media composed of homogeneous fluid and solid layers. However, numerical precision is lost by cancellation effects for the elements of the solid-layer compound-matrix propagators that are involved. Guided by the asymptotic growth of these compound-matrix elements, cancellation-free expressions are derived for applications to the slow modes at very low frequencies. The harmful contributions causing loss of numerical precision are eliminated analytically. To demonstrate the success, a numerical case study is performed leading to conjectures about the next-to-leading terms in low-frequency asymptotic expansions of the slow-mode modal slownesses. [S0001-4966(99)00207-6]

PACS numbers: 43.20.Ks, 43.20.Mv, 43.40.Dx, 43.40.Ph [AN]

INTRODUCTION

We are concerned here with laterally homogeneous, also called range-independent, fluid-solid media that are linearly visco-elastic (absorption is allowed) and isotropic. The medium properties are assumed to vary with z only, where z is the depth coordinate. By ''fluid-solid'' we mean that there are a finite number of regions in depth, each of fluid or solid type. The medium can be terminated above and below by traction-free, rigid, or (for a solid region) mixed-condition boundaries, or by homogeneous fluid or solid half-spaces. The mixed-condition boundary is characterized by vanishing horizontal displacement and normal traction. A homogeneous half-space is itself considered as (part of) a fluid or solid region. All solid regions have nonvanishing thickness, but it is convenient to allow fluid regions to have vanishing thickness (except for a medium with one region only).

We only consider mono-frequency P-SV wave propagation, with harmonic time dependence $e^{-i\omega t}$ assumed throughout, where $\omega=2\pi f>0$ is the angular frequency and t is time. The complex horizontal slowness and the complex horizontal wave number are denoted by p and $k=\omega p$, respectively. $D(\omega,p)$ is the dispersion function, whose zeros determine the modal p. The symbol $\sim$ will be used to indicate asymptotic similarity of two quantities as ω and k become small while p becomes large. For matrices, it should be interpreted element wise.

Slow modes, such that the horizontal slowness tends to infinity with decreasing frequency, are well known to exist for certain simple fluid-solid media. The simplest case is a homogeneous solid plate with free boundaries for which the bending wave (flexural wave, antisymmetric Lamb wave) exhibits a dispersion curve $p(\omega)\sim q\omega^{-1/2}$, with a nonzero q, as the frequency tends to zero (e.g., Ref. 1). By submerging the plate in a fluid, the frequency dependence changes to $p(\omega)\sim q\omega^{-3/5}$, as predicted by Osborne and Hart.[2] Experimental evidence was recently provided by Desmet *et al.*[3] using optical techniques based on a laser-induced thermoelastic effect. In 1965, Lloyd and Redwood[4] predicted the existence of a low-frequency slow mode with $p(\omega)\sim q\omega^{-2/3}$ for solid-fluid-solid trilayers with a homogeneous fluid layer surrounded by two homogeneous solid layers having a free boundary. Experimental evidence was recently obtained by Hassan and Nagy[5] using an ultrasonic immersion transmitter and a laser interferometric receiver. Interest in such structures continues, e.g., Ref. 6, motivated, for example, by applications concerning antireflection coating and nondestructive ultrasonic tests. In connection with a study of the implications of fluid-filled cracks for long-period seismic radiation from events originating at volcanos, Ferrazzini and Aki[7] considered a simplified case with a homogeneous fluid layer surrounded by two homogeneous solid half-spaces. A new kind of low-frequency slow wave was shown to exist. The frequency dependence of the modal slowness is $-1/3$ according to $p(\omega)\sim q\omega^{-1/3}$.

A unified treatment of all P-SV low-frequency slow modes such that the horizontal wave number $k(\omega)$ tends to zero with ω was provided by Ivansson,[8] for our general laterally homogeneous fluid-solid media with an arbitrary number of fluid and solid regions and an arbitrary variation with depth of the medium parameters in each region. Utilizing the analyticity of the dispersion function $D(\omega,p)$, a complete characterization was given of the slow modes and the kinds of fluid-solid media in which they occur. The powers $-1/3$,

a)Electronic mail: sveni@sto.foa.se

$-1/2$, $-3/5$, $-2/3$ were shown to be the only possible ones for the asymptotic increase of the horizontal slowness $p(\omega)$ as ω tends to zero. Here, we have restricted ourselves to nonleaky modes, with a physically desirable exponential decrease or outward direction of oscillation in a terminating homogeneous half-space. (For leaky modes, the power $-1/5$ is possible as well.)

A basic technique in Ref. 8 was an asymptotic analysis of the dispersion function $D(\omega,p)$ as ω and $k=\omega p$ tend to zero. The particular representation of $D(\omega,p)$ was taken from compound-matrix theory, allowing a matrix factorization with a 2×2 matrix propagator from each fluid region and a 6×6 compound-matrix propagator from each solid region. Such a representation is also useful for numerical purposes. As is well known, e.g., Ref. 9, straightforward application of Thomson-Haskell 4×4 matrix propagators for solid layers suffers from loss of numerical precision at high frequencies in the evanescent regime of wave numbers, with rapid exponential variations in the vertical depth direction. The reason is that the linear independence of the columns of these 4×4 matrices is lost numerically owing to exponential growth. The loss of numerical precision would result from cancellation effects when large elements were added and subtracted at a subsequent computation of the determinant providing $D(\omega,p)$.

It is often of interest to consider fluid-solid media for which each region is composed of homogeneous layers. The 4×4 and 6×6 matrix propagators for a homogeneous solid layer can be given explicitly (e.g., Refs. 10 and 11). As applied for slow-mode computations with small ω and k but large p, however, these expressions suffer from another kind of problem with loss of numerical precision. There is no harmful exponential growth, since such growth will be small when $k=\omega p$ is small. Instead, the numerical problems appear by cancellation of large numbers already when the *individual* matrix elements are formed. Apparently, the corresponding contributions to the matrix elements should be eliminated analytically, and alternative, cancellation-free, expressions for the 4×4 and 6×6 propagator matrices for homogeneous solid layers should be derived.

In this paper, we derive such cancellation-free expressions guided by the asymptotic propagator-matrix results from Ref. 8. Potential applications include theoretical as well as experimental work for which accurate low-frequency slow-mode dispersion curves are needed. Inverse techniques for medium characterization using numerical modeling of Lamb-wave dispersion data are well known, e.g., Refs. 12–14, and extensions to lower frequencies might be possible and useful. As we will see, very accurate low-frequency dispersion computations can also be useful theoretically, for suggesting sharpened asymptotic estimates.

The plan of the paper is as follows. Our basic compound-matrix representation of the dispersion function is provided in Sec. I, along with asymptotic low-frequency expressions for the propagator matrices involved. The possible types of low-frequency slow modes are characterized in Sec. II and the Appendix, as a brief review and adaptation of results in Ref. 8. Cancellation-free low-frequency expressions for the elements of the 6×6 compound-matrix propagator for a homogeneous solid layer are derived in Sec. III. The ''simple'' 4×4 propagator matrix is treated in Sec. IV. Some examples of accurate dispersion-curve computations for low-frequency slow modes are presented in Sec. V, as made possible by the new cancellation-free expressions. Our conclusions are stated briefly in Sec. VI.

I. THE DISPERSION FUNCTION

The Lamé parameters for a fixed frequency are denoted $\lambda(z)$ and $\mu(z)$, whereas the density is denoted $\rho(z)$. The *P*- and *S*-velocities for a fixed frequency are denoted $\alpha(z)$ and $\beta(z)$, respectively. As in Ref. 8, we introduce the functions $\mathcal{H}(z)$, $\mathcal{L}(z)$, and $\varphi(z)$ by

$$\mathcal{H}(z)=\frac{1}{\lambda(z)+2\mu(z)},\quad \mathcal{L}(z)=\frac{\lambda(z)}{\lambda(z)+2\mu(z)}, \tag{1}$$

and

$$\begin{aligned}\varphi(z)&=\frac{4\mu(z)[\lambda(z)+\mu(z)]}{\lambda(z)+2\mu(z)}\\&=4\rho(z)\beta^2(z)[1-\beta^2(z)/\alpha^2(z)].\end{aligned} \tag{2}$$

To allow for a visco-elastic medium, the functions $\lambda(z)$ and $\mu(z)$ may depend on ω. It follows that $\alpha(z),\beta(z)$ and $\mathcal{H}(z),\mathcal{L}(z),\varphi(z)$ may depend on ω as well. The subscript $_0$ is used to indicate limits as ω tends to zero, and we write $\lambda_0(z)$ and $\mu_0(z)$, for example.

The subscripts $_F$ and $_S$ are used for fluid and solid regions, respectively. The subscripts $_L$ and $_U$ are occasionally used for parameters of a lower and an upper boundary condition (or homogeneous half-space), respectively. When the subscript $_0$ is needed in addition, we write $\varphi_{L,0}$, etc.

As in Ref. 10 Eqs. (7.25) and (7.27), we write the modal displacement-stress vector as $\mathbf{r}(z)=(r_1(z),r_2(z),r_3(z),r_4(z))^T$. The components of $\mathbf{r}$ concern horizontal displacement, vertical displacement, tangential stress on horizontal planes, and normal stress on horizontal planes, respectively. However, it is often more convenient to use the scaled vector

$$\begin{aligned}\mathbf{y}(z)&=(y_1(z),y_2(z),y_3(z),y_4(z))^T\\&=(\omega r_1(z),\omega r_2(z),r_3(z),r_4(z))^T.\end{aligned} \tag{3}$$

For depths z and ζ in the same fluid region, the field is determined by just two components

$$\mathbf{y}_F(z)=(y_2(z),y_4(z))^T=\mathbf{P}_F(z,\zeta)\cdot\mathbf{y}(\zeta), \tag{4}$$

where $\mathbf{P}_F(z,\zeta)$ is a 2×2 propagator matrix. For depths z and ζ in the same solid region,

$$\mathbf{y}_S(z)=\mathbf{y}(z)=\mathbf{P}_S(z,\zeta)\cdot\mathbf{y}(\zeta), \tag{5}$$

where $\mathbf{P}_S(z,\zeta)$ is a 4×4 propagator matrix. We will also need the compound matrix $\mathbf{P}_S(z,\zeta)^{\Delta_2}$, which is a 6×6 matrix with the 2×2 subdeterminants of $\mathbf{P}_S(z,\zeta)$ as its elements.[8]

According to Ref. 8 Theorem 2.1, the dispersion function can be expressed as

$$D(\omega,p)=(\mathbf{G}_L)^{\Delta}\cdot\cdots\cdots\begin{pmatrix}1&0\\0&0\\0&1\\0&0\\0&0\\0&0\end{pmatrix}\cdot\mathbf{P}_F(\{J_F\})$$
$$\cdot\begin{pmatrix}0&0&0&-1&0&0\\0&0&0&0&0&1\end{pmatrix}$$
$$\cdot[\mathbf{P}_S(\{J_S\})]^{\Delta_2}\cdot\cdots\cdots\{[(\mathbf{G}_U)^{\Delta}]_{\text{anti}}\}^T. \qquad (6)$$

The lower and upper boundary conditions enter by the row- and column-vectors $(\mathbf{G}_L)^{\Delta}$ and $\{[(\mathbf{G}_U)^{\Delta}]_{\text{anti}}\}^T$, respectively. For a lower or upper mixed-condition boundary of a solid region, for example, we have $(\mathbf{G}_L)^{\Delta}=(0,0,1,0,0,0)$ or $\{[(\mathbf{G}_U)^{\Delta}]_{\text{anti}}\}^T=(0,0,0,1,0,0)^T$, respectively. All intervals J_F (for a fluid region) and J_S (for a solid region) appear in an alternating fashion, from left to right in Eq. (6) and from deep to shallow on the z axis. $\mathbf{P}_F(\{J_F\})$ means $\mathbf{P}_F(z,\zeta)$ where $J_F=(\zeta,z)$, $\zeta<z$, and $\mathbf{P}_S(\{J_S\})$ is introduced in the analogous way.

The three Lemmas 3.1, 3.2, and 3.3 in Ref. 8 give information about the asymptotic behavior of the propagator matrices appearing in Eq. (6). The main part of Ref. 8 Lemma 3.3, which is the most important for our purposes here, states that as ω tends to zero and $p\sim q\omega^{-e}$, with $q\neq 0$ and $0<e<1$,

$$[\mathbf{P}_S(\{J\})]^{\Delta_2}$$
$$\sim\begin{pmatrix}
1 & \omega^2 p b_{12} & \omega\int\mathcal{H} & -\omega\int\mu^{-1} & -\omega^2 p b_{12} & \omega^2\left(\int\mathcal{H}\right)\left(\int\mu^{-1}\right)\\
B_{21} & 1 & \omega p\int\mathcal{L} & \omega p\int 1 & \omega^2 p^2\left(\int 1\right)\left(\int\mathcal{L}\right) & \omega^2 p b_{26}\\
B_{31} & -\omega p\int 1 & 1 & B_{34} & \omega p\int 1 & \omega\int\mu^{-1}\\
-\omega p^2\int\varphi & -\omega p\int\mathcal{L} & B_{43} & 1 & \omega p\int\mathcal{L} & -\omega\int\mathcal{H}\\
-B_{21} & \omega^2 p^2\left(\int 1\right)\left(\int\mathcal{L}\right) & -\omega p\int\mathcal{L} & -\omega p\int 1 & 1 & -\omega^2 p b_{26}\\
B_{61} & B_{62} & \omega p^2\int\varphi & B_{64} & -B_{62} & 1
\end{pmatrix} \qquad (7)$$

for a fixed solid-region interval $J=(\zeta,z)$ with $\zeta<z$. Here,

$$b_{12}=\left(\int\mu^{-1}\int\mathcal{L}\right)-\left(\int\mathcal{H}\int 1\right),$$
$$B_{21}=-\omega^2 p^3\left(\int 1\int\varphi\right),$$
$$b_{26}=\left(\int\mathcal{L}\int\mu^{-1}\right)-\left(\int 1\int\mathcal{H}\right),$$
$$B_{31}=\omega\left[\omega^2 p^4 J_b(\varphi)-\left(\int\rho\right)\right],$$
$$B_{34}=-\omega^2 p^2\left(\int 1\right)\left(\int 1\right),$$
$$B_{43}=-\omega^2 p^2\left(\int\varphi\right)b_{43},$$
$$b_{43}=\left(\int\mathcal{H}\right)+\left(\int\mathcal{L}\right)^2\Big/\left(\int\varphi\right),$$
$$B_{61}=\omega^2 p^2\left(\int\varphi\right)\left[\omega^2 p^4 J(\varphi)-\left(\int\rho\right)\right],$$
$$B_{62}=-\omega^2 p^3\left(\int\varphi\int 1\right),$$
$$B_{64}=-\omega\left[\omega^2 p^4 J_t(\varphi)-\left(\int\rho\right)\right].$$

We use here the shorthand notation $\int g$ for $\int_\zeta^z g(s)ds$, $\int g\int h$ for $\int_\zeta^z g(s)ds\int_\zeta^s h(t)dt$, and so forth for triple integrals, etc. $J_b(\varphi)$, $J(\varphi)$, and $J_t(\varphi)$ are certain moments of inertia of the function φ in the solid region. Specifically, $J_b(\varphi)=2(\int 1\int 1\int\varphi)=\int_\zeta^z(z-s)^2\varphi(s)ds$, $J(\varphi)=2(\int\varphi\int 1\int 1\int\varphi)/(\int\varphi)=\int_\zeta^z(s-z_c)^2\varphi(s)ds$, where $z_c\int_\zeta^z\varphi(s)ds=\int_\zeta^z s\varphi(s)ds$, and $J_t(\varphi)=2(\int\varphi\int 1\int 1)=\int_\zeta^z(s-\zeta)^2\varphi(s)ds$.

II. THE LOW-FREQUENCY SLOW MODES

By an asymptotic analysis for Eq. (6), using results such as (7), it is possible to determine all low-frequency slow P-SV modes such that $\lim_{\omega\to 0}p(\omega)=\infty$ and $\lim_{\omega\to 0}k(\omega)=0$. This has been detailed in Ref. 8. The nonleaky modes can only appear in the form

$$p(\omega)\sim q\omega^{-e}, \qquad (8)$$

in the sense that $\lim_{\omega\to 0}\omega^e p(\omega)=q$, with some $q\neq 0$ and $e=1/3$, 1/2, 3/5, or 2/3. It is the close numerical verification and investigation of those results that requires cancellation-free propagator-matrix expressions, to be derived in Secs. III and IV.

The modes with $e=1/3$, according to (8), can be regarded as asymptotically plane and horizontally propagating vertical-traction waves. They appear when each termination of the medium is a homogeneous solid half-space or a rigid boundary, with at least one termination of the former type, and there is at least one fluid region with nonvanishing thickness.

The remaining modes, with $e=1/2$, 3/5, or 2/3, are bending waves, characterized by a vertical displacement that is independent of depth asymptotically, within the whole medium or, for the modes with $e=2/3$, within some solid regions taken separately. The modes with $e=1/2$, for example, appear when the medium is terminated by free boundaries and there is at least one solid region in between. Certain mixed-condition boundary media are also allowed.

Some solid region must always be present in a medium for slow modes to exist. Further information on slow-mode existence conditions and characteristics is provided in the Appendix. It will be needed and referred to for some of our examples to follow.

III. NUMERICALLY STABLE SLOW-WAVE COMPOUND-MATRIX PROPAGATORS FOR HOMOGENEOUS SOLID LAYERS

To evaluate the dispersion function $D(\omega,p)$ according to Eq. (6), the 6×6 compound matrix $[\mathbf{P}_S(\{J_S\})]^{\Delta_2}$ must be computed for each solid region. For a solid region composed of homogeneous layers, it is well known how this can be done by multiplication of explicitly available expressions for the 6×6 compound matrices of the individual layers. Consider a particular homogeneous solid layer between ζ and z with thickness (with sign) $d=z-\zeta$, density ρ, and complex P- and S-velocities α and β, respectively, for the particular angular frequency ω. We also introduce the following additional notation:

$$\chi=(p^2-\alpha^{-2})^{1/2},\quad \nu=(p^2-\beta^{-2})^{1/2}, \tag{9}$$

$$CP=\cosh(\omega d\chi),\quad CQ=\cosh(\omega d\nu), \tag{10}$$

$$SDP=\chi^{-1}\sinh(\omega d\chi),\quad SDQ=\nu^{-1}\sinh(\omega d\nu), \tag{11}$$

$$STP=-\chi\sinh(\omega d\chi),\quad STQ=-\nu\sinh(\omega d\nu), \tag{12}$$

and $\gamma=2\beta^2p^2$. The elements of the 6×6 matrix $\mathbf{B}=[\mathbf{P}_S(z,\zeta)]^{\Delta_2}$, denoted B_{ij}, not to be confused with the same notation for the more general asymptotic estimates in (7), can be written

$$\begin{aligned}
B_{11}&=-2\gamma(\gamma-1)+(2\gamma^2-2\gamma+1)CP\,CQ\\
&\quad-2\beta^2\gamma STP\,STQ-(\gamma-1)^2p^2SDP\,SDQ,\\
B_{12}&=-\rho^{-1}p[(2\gamma-1)(1-CP\,CQ)+(\gamma-1)\\
&\quad\times p^2SDP\,SDQ+2\beta^2STP\,STQ],\\
B_{13}&=\rho^{-1}[p^2CP\,SDQ+CQ\,STP],\\
B_{14}&=-\rho^{-1}[p^2CQ\,SDP+CP\,STQ],\\
B_{16}&=\rho^{-2}[2p^2(1-CP\,CQ)+STP\,STQ\\
&\quad+p^4SDP\,SDQ],\\
B_{21}&=\rho p[2\beta^2(\gamma-1)(2\gamma-1)(1-CP\,CQ)\\
&\quad+(\gamma-1)^3SDP\,SDQ+4\beta^4\gamma STPSTQ],\\
B_{22}&=1+2\gamma(\gamma-1)(1-CP\,CQ)\\
&\quad+(\gamma-1)^2p^2SDP\,SDQ+2\beta^2\gamma STP\,STQ,\\
B_{23}&=-p[(\gamma-1)CP\,SDQ+2\beta^2CQ\,STP],\\
B_{24}&=p[(\gamma-1)CQ\,SDP+2\beta^2CP\,STQ],\\
B_{31}&=-\rho[(\gamma-1)^2CQ\,SDP+2\beta^2\gamma CP\,STQ],\\
B_{33}&=CP\,CQ,\\
B_{34}&=SDP\,STQ,\\
B_{41}&=\rho[(\gamma-1)^2CP\,SDQ+2\beta^2\gamma CQ\,STP],\\
B_{43}&=STP\,SDQ,\\
B_{61}&=\rho^2[4\beta^2\gamma(\gamma-1)^2(1-CP\,CQ)\\
&\quad+(\gamma-1)^4SDP\,SDQ+4\beta^4\gamma^2STP\,STQ].
\end{aligned} \tag{13}$$

The list is completed by the simple relations $B_{66}=B_{11}$, $-B_{15}=B_{26}=-B_{56}=B_{12}$, $B_{46}=-B_{13}$, $B_{36}=-B_{14}$, $-B_{51}=B_{62}=-B_{65}=B_{21}$, $B_{25}=B_{52}=1-B_{22}$, $B_{55}=B_{22}$, $-B_{53}=-B_{42}=B_{45}=B_{23}$, $-B_{32}=B_{35}=-B_{54}=B_{24}$, $B_{64}=-B_{31}$, $B_{44}=B_{33}$, and $B_{63}=-B_{41}$. All this follows from Ref. 11, Eqs. (15)–(18). The dependence on ω and d, through the frequency-thickness product ωd, has been isolated to the factors CP, CQ, SDP, SDQ, STP, STQ.

It is useful to note that

$$B_{16}=-4\underline{B_{13}}\,\underline{B_{14}}=-4\underline{B_{36}}\,\underline{B_{46}}, \tag{14}$$

$$B_{61}=-4\underline{B_{63}}\,\underline{B_{64}}=-4\underline{B_{31}}\,\underline{B_{41}}, \tag{15}$$

where an underlined quantity is to be evaluated with d replaced by $d/2$ in Eqs. (10)–(12). This is, of course, easy to verify directly, but it also follows from a consideration of general fluid-solid media with a vertical symmetry (Ref. 15 Appendix A).

Our goal is to accurately track low-frequency dispersion-function trajectories $p(\omega)$, such that $D(\omega,p(\omega))\equiv 0$, for the slow modes identified by asymptotic techniques in Sec. II and the Appendix. Hence, ω and even $k=\omega p$ will be small (tend to zero), while p will be large (tend to infinity like $q\omega^{-e}$ where q is a nonzero constant and $e=1/3$, 1/2, 3/5, or 2/3). Comparing the terms with largest magnitude for the different element expressions in Eqs. (13) to the element estimates in (7), it is apparent that numerical cancellation problems can be expected. For example, according to Eqs. (13), there are terms for B_{13},B_{14} and B_{31},B_{41} with magnitude $\mathcal{O}(\omega dp^2)$ and $\mathcal{O}(\omega dp^4)$, respectively. These terms must cancel, however, in order to produce the overall magnitudes $\mathcal{O}(\omega d)$ for B_{13},B_{14} and $\mathcal{O}(\max((\omega d)^3p^4,\omega d))$, $\mathcal{O}(\omega dp^2)$ for B_{31},B_{41}, respectively, as obtained from (7). Without using Eqs. (14) and (15), the cancellation effects for

B_{16} and B_{61} are still worse, since terms to be cancelled with magnitudes $\mathcal{O}(p^2)$ and $\mathcal{O}(p^6)$, respectively, are present according to Eqs. (13). As seen from (7), the magnitude of B_{16} is only $\mathcal{O}((\omega d)^2)$, whereas that of B_{61} is $\mathcal{O}(\max((\omega d)^4 p^6, (\omega d)^2 p^2))$.

A. Error magnification

The loss of numerical precision can be quantified in the following way. Let u be the machine-dependent round-off unit,[16] typically about 10^{-15} for double-precision computations. The dispersion function $D(\omega,p)$ will be viewed as a sum of a number of terms, where it is reasonable to assume that each term can be computed with relative accuracy of the order of u. It follows by a simple Taylor expansion of $D(\omega,p)$ that the obtainable relative accuracy for $p=p(\omega)$ is of the order of

$$\left|\frac{D_{\text{term,max}}(\omega,p)}{p\,\partial D(\omega,p)/\partial p}\right| u, \tag{16}$$

where $D_{\text{term,max}}(\omega,p)$ is the term with maximum magnitude among those from which $D(\omega,p)$ is computed. Of course, we would like to be able to compute $p(\omega)$ with relative accuracy of the order of u. This will indeed be possible for ideal representations of $D(\omega,p)$ with a crucial factor like $\omega^m p^n - q^n$, with e as the rational number m/n. The asymptotic techniques in the proofs in Ref. 8, Appendix C, provide approximate representations of this kind, cf. (7). It follows from the observations in the previous paragraph, however, that the direct application of the expressions in Eqs. (13) may suffer from serious error magnification according to (16).

To estimate the effects, consider the simple homogeneous solid plate with free boundaries and a bending wave with $e = 1/2$ (Appendix Sec. 2). From Eq. (A8) it follows that

$$\omega^2 p^4(\omega) \sim q^4 = \frac{3}{\beta^2 d^2 (1-\beta^2\alpha^{-2})}. \tag{17}$$

The dispersion equation is simply $D(\omega,p)=B_{61}=0$, and we expect from the asymptotic result (7), for B_{61}, that

$$\partial D(\omega,p)/\partial p \sim 16\rho^2\beta^2(1-\beta^2\alpha^{-2})(\omega dp)^2 p^{-1}. \tag{18}$$

Applying the expression for B_{61} from Eqs. (13) as it stands, the dominant term at small ω (large p) will be $4\rho^2\beta^2\gamma^3$. According to (16), the obtainable relative accuracy for $p(\omega)$ will be about $(2(\beta p)^8/3)u$, where we have made use of the estimate in (18). Assuming double-precision computations with $u=10^{-15}$, as an example, it will not be possible to trace $p(\omega)$ numerically beyond about $10\beta^{-1}$ with a relative accuracy limit of 10^{-7}.

There are two immediate ways to improve the accuracy somewhat, but none is adequate. First, we may compute the factor $(1-CP\,CQ)$, appearing in the expression for B_{61} according to Eqs. (13), as a unit with series expansion for small arguments. It follows that $(1-CP\,CQ)\sim -(\omega dp)^2$, B_{61} will be computed as a sum of three terms with the same order of magnitude, and $D_{\text{term,max}}(\omega,p)=4\rho^2\beta^2\gamma^3(\omega dp)^2$. Applying (16) again, the obtainable relative accuracy for $p(\omega)$ will be about $2(1-\beta^2\alpha^{-2})^{-1}(\beta p)^6 u$. With $u=10^{-15}$, the ability to follow $p(\omega)$ with a relative accuracy limit of 10^{-7} may extend to about $20\beta^{-1}$.

Second, we could apply Eq. (15) and expressions for $\underline{B_{31}}$ and $\underline{B_{41}}$ from Eqs. (13). We would get $D_{\text{term,max}}(\omega,p) = 4(\rho\gamma^2\omega d/2)(\rho\gamma^2\omega d/2) = 2\rho^2\beta^2\gamma^3(\omega dp)^2$, providing only a marginal further improvement, if any. Severe effects of error magnification according to (16) persist. They are obviously caused by the higher powers of p that result in the numerator of (16) as compared to the denominator.

B. The cure

We require cancellation-free low-frequency expressions for the matrix elements B_{ij} in Eqs. (13) to compute $p(\omega)$ with relative accuracy of the order of u down to extremely low frequencies for all slow-wave types in Sec. II and the Appendix. The delta-matrix factorization techniques in Refs. 11 and 17 are ineffective in this respect, since the terms to be cancelled persist regardless of the algebraic factorization used. The purpose of these factorizations was to enhance efficiency. However, efficiency gains are usually not critical for special studies of slow modes at low frequencies. Bearing this in mind, an alternative might be to abandon the exact analytical expressions and solve the ODE system [Ref. 8, Eq. (2.14)] for the compound-matrix elements numerically. When the solid region is composed of homogeneous layers, however, such a brute-force technique would imply unnecessary concerns about integration steps, local and global errors, etc., and it is not to be preferred.

We therefore assume that ωd and ωdp are small (tending to zero) while p is large (tending to infinity), and proceed to derive alternative expressions for Eqs. (13). On occasion, it may of course be sufficient to have cancellation-free expressions for a few particular elements only (like B_{61} for the free homogeneous solid plate), but we treat them all at once. The key to our desired expressions appears to be to decompose the hyperbolic-function quantities CP, CQ, SDP, SDQ, and STP, STQ with pair-wise common dominating terms, which will allow straightforward analytic elimination of the harmful contributions to the B_{ij}.

Choosing Riemann sheets in Eqs. (9) such that $\chi\sim p$ and $\nu\sim p$, we introduce σ_P, σ_Q and δ_P, δ_Q by

$$\sigma_P = \frac{p+\chi}{2}, \quad \sigma_Q = \frac{p+\nu}{2} \tag{19}$$

and

$$\delta_P = \frac{p-\chi}{2}, \quad \delta_Q = \frac{p-\nu}{2}. \tag{20}$$

It follows that

$$\delta_P = \frac{1}{4\alpha^2\sigma_P}, \quad \delta_Q = \frac{1}{4\beta^2\sigma_Q} \tag{21}$$

and that $\sigma_P\sim p$, $\sigma_Q\sim p$. Applying elementary relations for hyperbolic functions, we get

$$CP = \cosh(\omega dp) - cp, \quad CQ = \cosh(\omega dp) - cq, \tag{22}$$

$$SDP = p^{-1}\sinh(\omega dp) - sdp,$$
$$SDQ = p^{-1}\sinh(\omega dp) - sdq, \tag{23}$$

$$STP = -p\sinh(\omega dp) + \omega d\alpha^{-2} + stp,$$
$$STQ = -p\sinh(\omega dp) + \omega d\beta^{-2} + stq, \tag{24}$$

where the lower-case quantities are given by

$$cp = 2\sinh(\omega d\sigma_P)\sinh(\omega d\delta_P) \sim \frac{(\omega d)^2}{2\alpha^2}, \tag{25}$$

$$cq = 2\sinh(\omega d\sigma_Q)\sinh(\omega d\delta_Q) \sim \frac{(\omega d)^2}{2\beta^2}, \tag{26}$$

$$sdp = \frac{2\delta_P\{\omega dp[\cosh(\omega d\sigma_P)-1] - [\sinh(\omega dp) - \omega dp]\}}{p\chi} + \frac{2\cosh(\omega d\sigma_P)[\sinh(\omega d\delta_P) - \omega d\delta_P]}{\chi} \sim \frac{(\omega d)^3}{6\alpha^2}, \tag{27}$$

$$sdq = \frac{2\delta_Q\{\omega dp[\cosh(\omega d\sigma_Q)-1] - [\sinh(\omega dp) - \omega dp]\}}{p\nu} + \frac{2\cosh(\omega d\sigma_Q)[\sinh(\omega d\delta_Q) - \omega d\delta_Q]}{\nu} \sim \frac{(\omega d)^3}{6\beta^2}, \tag{28}$$

$$stp = 2\delta_P\{\omega d\chi[\cosh(\omega d\sigma_P)-1] + [\sinh(\omega dp) - \omega dp]\} + 2\chi\cosh(\omega d\sigma_P)[\sinh(\omega d\delta_P) - \omega d\delta_P] \sim \frac{(\omega d)^3 p^2}{3\alpha^2}, \tag{29}$$

$$stq = 2\delta_Q\{\omega d\nu[\cosh(\omega d\sigma_Q)-1] + [\sinh(\omega dp) - \omega dp]\} + 2\nu\cosh(\omega d\sigma_Q)[\sinh(\omega d\delta_Q) - \omega d\delta_Q] \sim \frac{(\omega d)^3 p^2}{3\beta^2}. \tag{30}$$

The expressions within brackets [. . .] here must be evaluated by series expansion for small arguments to preserve accuracy. It is best to compute the sinh function as $\sinh(x) = x + [\sinh(x) - x]$, since some computers apparently give poor accuracy for sinh.

From (7), we know which terms in Eqs. (13) need to be cancelled analytically. Some combinations of terms occur repeatedly. We introduce the following notation and, using Eqs. (22)–(24), cancellation-free expressions follow in terms of our lower-case quantities from Eqs. (25)–(30):

$$\begin{aligned} u_{12} &= CP\,CQ - 1 - p^2 SDP\,SDQ \\ &= -\cosh(\omega dp)[cp + cq] + p\sinh(\omega dp)[sdp + sdq] \\ &\quad + cp\,cq - p^2 sdp\,sdq, \end{aligned}$$

$$\begin{aligned} u_{22} &= p^4 SDP\,SDQ - STP\,STQ \\ &= p\sinh(\omega dp)[\omega d(\alpha^{-2} + \beta^{-2}) + stp + stq \\ &\quad - p^2(sdp + sdq)] - (\omega d\alpha^{-2} + stp)(\omega d\beta^{-2} + stq) \\ &\quad + p^4 sdp\,sdq, \end{aligned}$$

$$\begin{aligned} u_{13} &= p^2 CP\,SDQ + CQ\,STP - \omega d\alpha^{-2}\cosh(\omega dp) \\ &= \cosh(\omega dp)[stp - p^2 sdq] - (p^2 SDQ\,cp + STP\,cq), \end{aligned}$$

$$\begin{aligned} u_{14} &= p^2 CQ\,SDP + CP\,STQ - \omega d\beta^{-2}\cosh(\omega dp) \\ &= \cosh(\omega dp)[stq - p^2 sdp] - (p^2 SDP\,cq + STQ\,cp). \end{aligned} \tag{31}$$

Potentially harmful contributions have in this way been eliminated by grouping pair-wise common terms according to Eqs. (22)–(24). The contributions $\cosh^2(\omega dp) - 1 - p^2 p^{-2}\sinh^2(\omega dp)$ to u_{12} and $p^4 p^{-2}\sinh^2(\omega dp) - p^2\sinh^2(\omega dp)$ to u_{22} vanish identically, for example.

Cancellation-free expressions for some elements of $\mathbf{B} = [\mathbf{P}_S(z,\zeta)]^{\Delta_2}$ follow in much the same way:

$$\begin{aligned} B_{13} &= \rho^{-1}[\omega d\alpha^{-2}\cosh(\omega dp) + u_{13}], \\ B_{14} &= -\rho^{-1}[\omega d\beta^{-2}\cosh(\omega dp) + u_{14}], \\ B_{23} &= p[CP\,SDQ - 2\beta^2\rho B_{13}], \\ B_{24} &= -p[CQ\,SDP + 2\beta^2\rho B_{14}], \\ B_{31} &= \rho\left\{2\gamma\left[\cosh(\omega dp)\left(\frac{\sinh(\omega dp) - \omega dp}{p} - sdp\right) - \beta^2 u_{14} - SDP\,cq\right] - CQ\,SDP\right\}, \\ B_{41} &= \rho\{2\gamma[-\cosh(\omega dp)(SDQ - \omega d\beta^2\alpha^{-2}) + \beta^2 u_{13} \\ &\quad + SDQ\,cp] + CP\,SDQ\}. \end{aligned} \tag{32}$$

The expression $(\sinh(\omega dp) - \omega dp)/p$ needed for B_{31} must, of course, be computed by series expansion for small values of ωdp.

Cancellation-free expressions for B_{16} and B_{61} can be obtained in a convenient way by Eqs. (14) and (15). The elements B_{33}, B_{34}, and B_{43} need no additional treatment; see Eqs. (13). Introducing

$$u_{11} = 2\beta^2[(\gamma - 1)\rho^2 B_{16} - u_{22}] + p^2\,SDP\,SDQ, \tag{33}$$

we finally write

$$\begin{aligned} B_{11} &= CP\,CQ - u_{11}, \\ B_{22} &= 1 + u_{11}, \\ B_{12} &= -\rho^{-1}p[2\beta^2\rho^2 B_{16} + u_{12}], \\ B_{21} &= \rho p\{2\beta^2\gamma[2\beta^2\rho^2 B_{16} + 3u_{12}] \\ &\quad + (3\gamma - 1)SDP\,SDQ - 2\beta^2(p^2 SDP\,SDQ + u_{12})\}. \end{aligned} \tag{34}$$

A check with the estimates of (7) verifies that no risk of loss of precision by cancellation remains among our matrix elements.

IV. NUMERICALLY STABLE SLOW-WAVE "SIMPLE" PROPAGATORS

According to Eq. (6), the 2×2 propagator matrices $\mathbf{P}_F(z,\zeta)$ for the fluid layers are likewise needed for the evaluation of the dispersion function $D(\omega,p)$. For a homogeneous layer, such a matrix has the simple expression

$$\mathbf{P}_F(z,\zeta)=\begin{pmatrix} CP & \rho^{-1}STP \\ -\rho SDP & CP \end{pmatrix}, \tag{35}$$

where the notation from (9)–(12) has been used. There are no terms that need to be cancelled analytically; each element gets its predicted magnitude according to Ref. 8, Lemma 3.1, without particular numerical concern.

For a constant nonzero gradient θ of the squared medium slowness between ζ and z, it is well known that $\mathbf{P}_F(z,\zeta)$ can be expressed in terms of Airy functions (Ref. 18, Section 4.2.3). Putting

$$\begin{aligned} y(\zeta)&=(\omega^2/\theta^2)^{1/3}(p^2-\alpha^{-2}(\zeta)),\\ y(z)&=(\omega^2/\theta^2)^{1/3}(p^2-\alpha^{-2}(z)), \end{aligned} \tag{36}$$

the elements of $\mathbf{P}_F(z,\zeta)$ become

$$\begin{aligned} P_F(z,\zeta)_{11}&=\pi[\mathrm{Ai}(y(\zeta))\mathrm{Bi}'(y(z))-\mathrm{Bi}(y(\zeta))\mathrm{Ai}'(y(z))],\\ P_F(z,\zeta)_{12}&=\pi(\rho\omega)^{-1}\theta(\omega^2/\theta^2)^{1/3}[\mathrm{Bi}'(y(\zeta))\mathrm{Ai}'(y(z))\\ &\quad-\mathrm{Ai}'(y(\zeta))\mathrm{Bi}'(y(z))],\\ P_F(z,\zeta)_{21}&=-\pi\rho\omega\theta^{-1}(\omega^2/\theta^2)^{-1/3}[\mathrm{Bi}(y(\zeta))\mathrm{Ai}(y(z))\\ &\quad-\mathrm{Ai}(y(\zeta))\mathrm{Bi}(y(z))]\\ P_F(z,\zeta)_{22}&=\pi[\mathrm{Bi}'(y(\zeta))\mathrm{Ai}(y(z))-\mathrm{Ai}'(y(\zeta))\mathrm{Bi}(y(z))]. \end{aligned} \tag{37}$$

Considering computations for slow modes with $e>1/3$, the arguments $y(\zeta)$ and $y(z)$ to the Airy functions will obviously become large as ω becomes small. By choosing the cubic root $(\omega^2/\theta^2)^{1/3}$ appropriately, however, each of the elements of $\mathbf{P}_F(z,\zeta)$ according to (37) will be formed as a difference of two numbers, whose orders of magnitude do not exceed that of the norm of the matrix (Ref. 19, Section 10.4 and Ref. 8, Lemma 3.1). This appears to be sufficient for slow-mode computations, for which some solid region is always present (according to the existence conditions in the Appendix) and the dispersion function $D(\omega,p)$ involves a combination of several elements of $\mathbf{P}_F(z,\zeta)$. It should be observed, however, that Airy-function routines providing accurate values for large arguments are required.

The 4×4 propagator matrices $\mathbf{P}_S(z,\zeta)$ for homogeneous solid layers are not needed in the dispersion function $D(\omega,p)$, but they will be needed to compute mode forms as functions of depth.[20] Considering a particular homogeneous solid layer between ζ and z, with $d=z-\zeta$ as usual, the elements of $\mathbf{P}_S(z,\zeta)$ have been given in Ref. 11, Eqs. (4). Assuming that ωd and ωdp are small (tending to zero) while p is large (tending to infinity), cancellation-free expressions are easily obtained by using Eqs. (22)–(30) from Sec. III:

$$\begin{aligned} P_S(z,\zeta)_{11}&=CQ+\gamma(cq-cp),\\ P_S(z,\zeta)_{22}&=CP+\gamma(cp-cq),\\ P_S(z,\zeta)_{13}&=\rho^{-1}[\omega d\beta^{-2}+(stq-p^2sdp)],\\ P_S(z,\zeta)_{24}&=\rho^{-1}[\omega d\alpha^{-2}+(stp-p^2sdq)],\\ P_S(z,\zeta)_{12}&=p[2\omega d-SDP+2\beta^2(stq-p^2sdp)],\\ P_S(z,\zeta)_{21}&=p[2\omega d\beta^2\alpha^{-2}-SDQ+2\beta^2(stp-p^2sdq)],\\ P_S(z,\zeta)_{14}&=\rho^{-1}p(cq-cp),\\ P_S(z,\zeta)_{32}&=2\rho\beta^2p(\gamma-1)(cq-cp),\\ P_S(z,\zeta)_{31}&=-\rho[2\beta^2\gamma\rho P_S(z,\zeta)_{24}-(2\gamma-1)SDQ],\\ P_S(z,\zeta)_{42}&=-\rho\left\{2\gamma\left[\beta^2(stq-p^2sdp)\right.\right.\\ &\quad\left.\left.-\frac{\sinh(\omega dp)-\omega dp}{p}+sdp\right]+SDP\right\}. \end{aligned} \tag{38}$$

For the remaining elements, we have the simple relations $P_S(z,\zeta)_{23}=-P_S(z,\zeta)_{14}$, $P_S(z,\zeta)_{33}=P_S(z,\zeta)_{11}$, $P_S(z,\zeta)_{34}=-P_S(z,\zeta)_{21}$, $P_S(z,\zeta)_{41}=-P_S(z,\zeta)_{32}$, $P_S(z,\zeta)_{43}=-P_S(z,\zeta)_{12}$, and $P_S(z,\zeta)_{44}=P_S(z,\zeta)_{22}$. The expression $(\sinh(\omega dp)-\omega dp)/p$, now in $P_S(z,\zeta)_{42}$, should again be computed by series expansion for small arguments. A comparison to Ref. 8, Lemma 3.2, verifies that the potentially harmful terms have been eliminated.

V. EXAMPLES

The cancellation-free expressions are useful for investigating the accuracy of asymptotic slow-mode results numeri-

TABLE I. Dependence of $\beta p(\omega)-\beta q\omega^{-1/2}$ on $\omega d\beta^{-1}$ for a slow mode of type "$e=1/2$" for a free plate with $\alpha=2\beta$. The relative accuracy for the computed values of $p(\omega)$ is about 10^{-15}.

$\omega d\beta^{-1}$	$\beta p(\omega)$	$\beta q\omega^{-1/2}$	$\beta p(\omega)-\beta q\omega^{-1/2}$
10^{0}	1.663 988 169 705 32	1.414 213 562 372 63	0.249 774 607 332 69
10^{-1}	4.553 777 377 775 87	4.472 135 954 998 11	0.081 641 422 777 76
10^{-2}	14.168 051 684 346 0	14.142 135 623 726 3	0.025 916 060 619 7
10^{-3}	44.729 558 111 480 1	44.721 359 549 981 1	0.008 198 561 499 0
10^{-4}	141.423 948 950 918	141.421 356 237 263	0.002 592 713 655
10^{-5}	447.214 415 391 048	447.213 595 499 811	0.000 819 891 237
10^{-6}	1414.213 821 645 11	1414.213 562 372 63	0.000 259 272 48
10^{-7}	4472.136 036 987 27	4472.135 954 998 11	0.000 081 989 16
10^{-8}	14142.135 649 653 6	14142.135 623 726 3	0.000 025 927 3
10^{-9}	44721.359 558 180 0	44721.359 549 981 1	0.000 008 198 9
10^{-10}	141421.356 239 856	141421.356 237 263	0.000 002 593

TABLE II. Medium parameters for a solid-fluid-solid medium. Homogeneous layers without absorption are assumed. At the surface there is a free boundary, whereas the bottom below $z=600$ m is a homogeneous solid half-space.

	z (m)	P-veloc (km/s)	S-veloc (km/s)	ρ (kg/dm^3)
Solid	0–10	3.500	2.000	0.900
(''ice'')	10–25	4.000	2.200	0.950
	25–30	3.500	1.600	0.980
Fluid	30–40	1.450	⋯	1.000
(''water'')	40–60	1.400	⋯	1.000
	60–100	1.450	⋯	1.000
Solid	100–110	1.400	0.500	1.200
(''rock'')	110–150	3.500	2.000	2.000
	150–400	5.000	2.676	3.200
	400–600	5.000	2.676	8.200
	600–∞	8.000	4.000	2.000

cally. At first, we return to the homogeneous solid plate with free boundaries considered in Sec. III A, and its bending wave with $e = 1/2$. Applying the cancellation-free expression for the dispersion function B_{61} derived in Sec. III B, in conjunction with successive secant iterations for root finding [cf. Ref. 21, Eq. (4)], we traced $p(\omega)$ numerically down to extremely low frequencies with high relative accuracy. Using (16)–(18), the order of the relative accuracy for $p(\omega)$ with very accurately computed function values, etc., will certainly be about u (formally $u/4$), to be compared to what could be achieved with the defective dispersion-function expressions, as discussed in Sec. III A. In Table I, for instance, we show the dependence of $\beta p(\omega)-\beta q\omega^{-1/2}$ on $\omega d\beta^{-1}$ for a plate with $\alpha=2\beta$. It appears that the residual $p(\omega)-q\omega^{-1/2}$ is approximately proportional to $\omega^{1/2}$ as ω tends to zero, suggesting a sharpening of the statement $\lim_{\omega\to 0}\omega^{1/2}p(\omega)=q$, as $p(\omega)\sim q\omega^{-1/2}$ is to be interpreted. A theoretical proof that the second term in an asymptotic expansion of $p(\omega)$ is indeed proportional to $\omega^{1/2}$ is not difficult, with the dispersion function B_{61} treated as in Sec. III B. The relative accuracy for the computed values of $p(\omega)$, as shown in Table I, is about 10^{-15} all the way down to $\omega d\beta^{-1}=10^{-10}$, where $p(\omega)\approx 1.4\times 10^5\beta^{-1}$.

To illustrate a slow mode of the type $e=2/3$, as in Appendix Sec. 4, consider the solid-fluid-solid medium specified in Table II. It includes several homogeneous layers, with an ice-water-rock structure that may have some relevance to underwater acoustics. Absorption is not included, since it disappears as the frequency tends to zero [Ref. 22, Eq. (9.48)]. Following the terminology of Appendix Sec. 4, $m=1$, and the upper and lower terminations of the medium (a free surface of a solid region and a solid region including a homogeneous solid half-space) are designated to options (A) and (B), respectively. The expression for q for the predicted slow mode with $p(\omega)\sim q\omega^{-2/3}$ is derived from the relations $L_1=1$ and $A_1=-q^6[\int_{F_1}\rho^{-1}(z)dz]$, as obtained from the bottom [option (B)], combined with the relation $L_1=-\mathcal{J}A_1$, as obtained from the top. It follows that

$$q^6=\frac{1}{[\int_{F_1}\rho^{-1}(z)dz]\mathcal{J}}, \tag{39}$$

where $\mathcal{J}$ is the second-order moment of the function $\varphi_0(z)$ for the upper solid region. With medium parameters according to Table II, the value of q^6 becomes 661 348.054 646 320 s^2/km^6. We show in Table III the dependence of $p(\omega)-q\omega^{-2/3}$ on f, where $f=\omega/(2\pi)$ is the frequency. It appears that a constant limit, approximately 0.504 s/km, is approached as ω tends to zero. The relative accuracy for the shown values of $p(\omega)$ is about 10^{-9} all the way down to $f=10^{-9}$ Hz, where $p(\omega)\approx 2.7\times 10^6$ s/km. The cancellation-free expressions for the compound-matrix propagators (Sec. III B) make this high accuracy possible at these extremely low frequencies.

Further computations (not tabulated here) lead us to the conjecture that, as ω tends to zero, the residual $p(\omega)-q\omega^{-e}$ will be (approximately) proportional to $\omega^{1/3}$, $\omega^{1/2}$, and $\omega^{-1/5}$, for all slow modes with $e=1/3$ (Appendix Sec. 1), $e=1/2$ (Appendix Sec. 2), and $e=3/5$ (Appendix Sec. 3), respectively. For the slow modes with $e=2/3$ (Appendix Sec. 4), ω^0 or $\omega^{1/3}$ can appear, the latter for a homogeneous fluid half-space together with another homogeneous fluid half-space, a homogeneous solid half-space, or a rigid boundary. The theoretical verification of this conjecture would require an analysis of higher-order terms for asymptotic results like (7).

The shape of the modal depth functions for our $e=2/3$ example slow mode in the fluid and in the upper solid region is given by (A13) and (A14) of Appendix Sec. 4. This kind of bending wave, concentrated to the upper solid region, is transformed to the Scholte interface wave connected to the lower fluid-solid boundary at depth 100 m as the frequency is increased. Figure 1 shows a ''waterfall plot'' for the

TABLE III. Computed values of $p(\omega)$ for a slow mode of type ''$e=2/3$'' for the solid-fluid-solid medium of Table II, with relative accuracy about 10^{-9}.

$f=\omega/(2\pi)$ (Hz)	$p(\omega)$ (s/km)	$q\omega^{-2/3}$ (s/km)	$p(\omega)-q\omega^{-2/3}$ (s/km)
10^0	3.219 787 82	2.741 269 713 232 89	0.478 518 11
10^{-1}	13.225 472 0	12.723 846 890 862 7	0.501 625 1
10^{-2}	59.562 551 4	59.058 865 649 227 0	0.503 685 8
10^{-3}	274.630 760	274.126 971 323 289	0.503 788
10^{-4}	1272.888 45	1272.384 689 086 27	0.503 76
10^{-5}	5906.390 31	5905.886 564 922 70	0.503 74
10^{-6}	27 413.2009	27 412.697 132 328 9	0.5037
10^{-7}	127 238.973	127 238.468 908 627	0.504
10^{-8}	590 589.160	590 588.656 492 270	0.504
10^{-9}	2 741 270.22	2 741 269.713 232 89	0.50

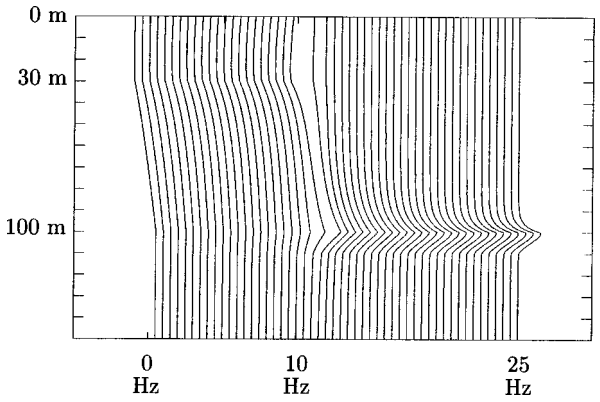

FIG. 1. ''Waterfall plot'' showing depth dependence of modal vertical displacement from 0.5 to 25 Hz. The medium is of type solid-fluid-solid, according to Table II, with fluid between 30 and 100 m. The vertical axis is for depth, from 0 m down to 150 m. It is clearly seen how the low-frequency bending wave, with depth dependence predicted by (A13) and (A14) and an almost negligible vertical displacement in the lower solid region, is transformed to a Scholte interface wave.

transformation process at frequencies between 0.5 and 25 Hz. Below about 11 Hz, the main characteristic of the mode is an almost constant nonzero vertical displacement within the upper solid (the upper 30 m). This is consistent with the bending-wave character of (A14). The Scholte interface-wave character of the mode dominates above 11 Hz. Interface modes at 100 Hz for a similar medium example were considered in Ref. 20, Section 5.3.

VI. CONCLUSIONS

Nonleaky low-frequency P-SV slow modes such that $\lim_{\omega\to 0} p(\omega)=\infty$ and $\lim_{\omega\to 0} k(\omega)=0$ appear for certain laterally homogeneous fluid-solid media. In each case, there is a real number e and a nonzero complex number q such that

$$\lim_{\omega\to 0} \omega^e p(\omega)=q. \tag{40}$$

Only four values of e are possible: 1/3, 1/2, 3/5, and 2/3.

The usual expressions for propagator matrices of homogeneous solid layers are numerically unstable for these slow modes at very low frequencies. This concerns the 6×6 compound matrix as well as the 4×4 ''simple'' matrix. Loss of numerical precision by cancellation effects appears for almost all of the individual matrix elements. The expressions for the elements of the 4×4 matrix involve terms with order of magnitude p^2 or $(\omega d)^{-2}$ times greater than the actual element magnitude, while the corresponding factor for most of the 6×6 matrix elements is p^4, $(\omega d)^{-2}p^2$, $(\omega d)^{-4}$, p^2, or $(\omega d)^{-2}$, where d is the layer thickness.

Guided by asymptotic results for the propagator matrices at small ω and k, we have derived cancellation-free expressions for the 6×6 and 4×4 propagator matrices of a homogeneous solid layer. They are not as efficient as the traditional expressions, for which matrix factorization techniques can be used to achieve very high efficiency,[11] but concerns about efficiency are not, in general, critical for special studies of low-frequency slow modes. An alternative to the new expressions could be to integrate the underlying ordinary differential equation (ODE) systems in the depth direction numerically.

Highly accurate slow-mode dispersion computations are now feasible for homogeneously layered fluid-solid media down to extremely low frequencies. In particular, the accuracy of the asymptotic results in Ref. 8 can be thoroughly investigated. From a numerical case study, we make the following conjecture for a sharpening of Eq. (40):

$$\lim_{\omega\to 0} \omega^{-\theta}[\omega^e p(\omega)-q]=r \tag{41}$$

or, equivalently, suggesting an asymptotic expansion of $p(\omega)$ as ω tends to zero,

$$p(\omega)\sim q\omega^{-e}+r\omega^{\theta-e}+\cdots. \tag{42}$$

Here, r is some nonvanishing number (different for different slow modes), and $\theta=2/3$, 1, or 2/5. The value 2/3 for θ seems to appear for all slow modes with $e=1/3$ and some with $e=2/3$ (those for which there is no, or just one, homogeneous fluid half-space in the medium, the other termination being a free or mixed-condition boundary in the latter case), and the value 1 for θ appears for all slow modes with $e=1/2$ and the remaining modes with $e=2/3$. The value 2/5 for θ seems to appear for all slow modes with $e=3/5$. It should be emphasized that we have not verified this conjecture theoretically, and that our numerical case study has not involved media with more than two solid regions.

In order to compute group slownesses and modal excitation factors, certain derivatives with respect to ω and p will also be needed.[20] The low-frequency cancellation-free expressions for these quantities turn out to be quite cumbersome. For some basic formulas, we refer to Ref. 15, Appendix B.

ACKNOWLEDGMENTS

I am grateful to Ilkka Karasalo for originally drawing my attention to the numerical problems involved with dispersion-function computations for bending waves at low frequencies. Thanks also to two anonymous reviewers for useful comments.

APPENDIX: FURTHER INFORMATION ON THE LOW-FREQUENCY SLOW MODES

We will here summarize, in adapted form, the results in Ref. 8 for the four slow-mode classes according to (8). We take the opportunity to be somewhat more specific than in Ref. 8 concerning proportionality constants, etc., but that reference should be consulted for the proofs. The cases with a mixed-condition boundary treated in Ref. 8, Section 7.2 are also incorporated.

1. Slow modes with $e=1/3$, i.e., $p(\omega)\sim q\omega^{-1/3}$

For such modes to appear, there must be at least one homogeneous solid half-space, and we assume that there is a lower homogeneous solid half-space. The modal depth functions in the corresponding solid region appear as [Ref. 8, Eq. (6.8)]

$$
\begin{aligned}
&y_1(\omega,z)\sim\omega^{1/3}\frac{A}{q},\\
&y_2(\omega,z)\sim\omega^{1/3}\frac{B}{q},\\
&y_3(\omega,z)\sim\omega^{2/3}q\left[C+A\int_\zeta^z\varphi_0(s)ds+\int_\zeta^z\mathcal{L}_0(s)ds\right],\\
&y_4(\omega,z)\sim 1,
\end{aligned}
\tag{A1}
$$

where ζ is the upper depth of the region, $A=[2\rho_L(\alpha_{L,0}^2-\beta_{L,0}^2)]^{-1}$, $B=\mp[2\rho_L\beta_{L,0}^4(\beta_{L,0}^{-2}-\alpha_{L,0}^{-2})]^{-1}=\mp 2/\varphi_{L,0}$, and $C=0$. In an overlying fluid region, of which there must be at least one with nonvanishing thickness, we get [Ref. 8, Eq. (6.9)]

$$
\begin{aligned}
&y_2(\omega,z)\sim\omega^{1/3}\frac{1}{q}\left[B-q^3\int_\zeta^z\rho(s)^{-1}ds\right],\\
&y_4(\omega,z)\sim 1,
\end{aligned}
\tag{A2}
$$

where ζ is again the upper depth of the region in question and B is obtained by the requirement of continuity of y_2 at the lower depth. For a subsequent solid region surrounded by fluid, the estimates (A1) apply again, with $A=-\int\mathcal{L}_0(s)ds/\int\varphi_0(s)ds$ where each of the two integrals is taken over the solid region in question. The constant C vanishes and B is of course obtained by continuity of y_2.

For the upper termination of the medium, there are three possibilities. It can be a fluid region with a rigid surface, for which (A2) applies with $B=0$. Continuity of y_2 throughout the medium immediately gives

$$
q^3=\pm\frac{2\varphi_{L,0}^{-1}}{\int_F\rho^{-1}(z)dz}. \tag{A3}
$$

The integral in the denominator of Eq. (A3) is taken over the fluid regions, hence the subscript F.

A second possibility is an upper solid region with a rigid surface. Again, (A1) applies, this time with $A=B=0$ and, with the integral taken over the solid region in question, $C=-\int\mathcal{L}_0(s)ds$. Using the last two columns of Ref. 8, Eq. (3.7), the relations for y_1 and y_2 can, in fact, be sharpened to

$$
\begin{aligned}
&y_1(\omega,z)\sim\omega^{5/3}q\left[a_{14,0}(z)+C\int_\zeta^z\mu_0^{-1}(s)ds\right],\\
&y_2(\omega,z)\sim\omega\int_\zeta^z\mathcal{H}_0(s)ds,
\end{aligned}
\tag{A4}
$$

where $a_{14,0}(z)$ is obtained from the quantity a_{14} of Ref. 8, Lemma 3.2, as defined for the part between ζ and z of our solid region. The expression for q^3 becomes as in Eq. (A3).

The third possibility, finally, is an upper homogeneous solid half-space. In this case, we take ζ as the lower boundary of the corresponding solid region, and (A1) applies with $A=[2\rho_U(\alpha_{U,0}^2-\beta_{U,0}^2)]^{-1}$, $B=\pm[2\rho_U\beta_{U,0}^4(\beta_{U,0}^{-2}-\alpha_{U,0}^{-2})]^{-1}=\pm 2/\varphi_{U,0}$, and $C=0$. The expression for q^3 becomes

$$
q^3=\pm\frac{2(\varphi_{L,0}^{-1}+\varphi_{U,0}^{-1})}{\int_F\rho^{-1}(z)dz}. \tag{A5}
$$

The $\pm$ in the formulas concern two Riemann sheets considered for homogeneous solid half-spaces: $+$ for $(p^2-\alpha^{-2})^{1/2}\sim(p^2-\beta^{-2})^{1/2}\sim p$ and $-$ for $(p^2-\alpha^{-2})^{1/2}\sim(p^2-\beta^{-2})^{1/2}\sim -p$, as defined for large p. Note that the region-dependent constants B change sign accordingly (except when they vanish). In other respects, however, the A, B, C values do not depend on the particular choice of q.

2. Slow modes with $e=1/2$, i.e., $p(\omega)\sim q\omega^{-1/2}$

For such modes to appear, there must be at least one solid region. Each of the boundaries must be either free or a mixed-condition boundary of a solid region. A single solid region terminated above and below by mixed-condition boundaries is to be excluded, however. The modal depth functions in a particular solid region with upper depth ζ appear as [Ref. 8, Eq. (6.10)]

$$
\begin{aligned}
&y_1(\omega,z)\sim\omega^{1/2}q\psi(z),\\
&y_2(\omega,z)\sim 1,\\
&y_3(\omega,z)\sim\omega^{1/2}q^3\Psi(z),\\
&y_4(\omega,z)\sim-\omega\left[A+\int_\zeta^z\rho(s)ds+q^4\int_\zeta^z\Psi(s)ds\right],
\end{aligned}
\tag{A6}
$$

where A is a region-dependent constant and $\psi(z),\Psi(z)$ are region-dependent functions. Specifically, $\psi(z)=z-z_c$ and $\Psi(z)=\int_Z^z\varphi_0(s)\psi(s)ds$. If the solid region has a mixed-condition boundary, z_c is the corresponding depth and Z is the opposite interface depth of the solid region, whereas $z_c=\int s\varphi_0(s)ds/\int\varphi_0(s)ds$ and $Z=\zeta$ otherwise. The integrals here are taken over the whole solid region, from top to bottom. In a fluid region with upper depth ζ we get

$$
\begin{aligned}
&y_2(\omega,z)\sim 1,\\
&y_4(\omega,z)\sim-\omega\left[A+\int_\zeta^z\rho(s)ds\right].
\end{aligned}
\tag{A7}
$$

Since y_4 is continuous and vanishes at both medium boundaries, the A value for the uppermost region must vanish and the relation

$$
q^4=\frac{\int\rho(z)dz}{J(\varphi_0)_{\text{sum}}} \tag{A8}
$$

drops out. Here, the integral is taken over the whole depth extent of the medium. $J(\varphi_0)_{\text{sum}}$ is the sum over the solid regions of the centered moments of inertia for the function $\varphi_0(z)$. However, for a solid region with a mixed-condition boundary, the contributing second-order moment of φ_0 should have its axis at the corresponding depth. In any case, this contribution equals $-\int\Psi(s)ds$, where the integral is taken over the solid region in question. Finally, we may note that the A values of the different regions will not be affected by the particular choice of q according to Eq. (A8).

3. Slow modes with $e=3/5$, i.e., $p(\omega)\sim q\omega^{-3/5}$

For such modes to appear, there must be at least one homogeneous fluid half-space, and we assume that there is a

lower homogeneous fluid half-space. The modal depth functions in the corresponding fluid region appear as [Ref. 8, Eq. (6.11)]

$$y_2(\omega,z)\sim 1,$$
$$y_4(\omega,z)\sim -\omega^{3/5}q^4A, \tag{A9}$$

where $A=\mp\rho_L/q^5$. In an overlying solid region, of which there must be at least one, we get

$$y_1(\omega,z)\sim\omega^{2/5}q\psi(z),$$
$$y_2(\omega,z)\sim 1,$$
$$y_3(\omega,z)\sim\omega^{1/5}q^3\Psi(z), \tag{A10}$$
$$y_4(\omega,z)\sim -\omega^{3/5}q^4\left[A+\int_\zeta^z\Psi(s)ds\right],$$

where ζ is the upper depth of the region, A is obtained by the requirement of continuity of y_4 at the lower depth, and $\psi(z),\Psi(z)$ are region-dependent functions defined as in Appendix Sec. 2. For a subsequent fluid region, the estimates (A9) apply again, with an appropriate value of A.

For the upper termination of the medium, there are three possibilities. It can be a fluid region with a free surface, for which (A9) applies with $A=0$. Continuity of y_4 throughout the medium immediately gives

$$q^5=\pm\frac{\rho_L}{J(\varphi_0)_{\text{sum}}}. \tag{A11}$$

A second possibility is an upper solid region with a free or mixed-condition surface, for which (A10) applies with $A=0$, and q^5 is again given by Eq. (A11). The functions $\psi(z),\Psi(z)$ and the contributing second-order moment of φ_0 will be changing for the mixed-condition option, as in Appendix Sec. 2.

The third possibility, finally, is an upper homogeneous fluid half-space, for which (A9) applies with $A=\pm\rho_U/q^5$, and

$$q^5=\pm\frac{\rho_L+\rho_U}{J(\varphi_0)_{\text{sum}}}. \tag{A12}$$

As in Appendix Sec. 1, the choice $\pm$ concerns two Riemann sheets considered for homogeneous half-spaces. Note that the region-dependent constants A do not depend on the particular choice of q according to Eq. (A11) or Eq. (A12).

4. Slow modes with $e=2/3$, i.e., $p(\omega)\sim q\omega^{-2/3}$

It is convenient here to introduce the concept of an aggregate solid region, by which we mean a maximal sequence of solid regions which may be separated by fluid regions with vanishing thickness. An aggregate solid region is said to be ''soft'' if it is above as well as below next to a fluid region (with nonvanishing thickness) or a free or mixed-condition boundary. For slow modes with $e=2/3$ to appear, there must be $m\geqslant 1$ fluid regions with nonvanishing thickness that do not include a free boundary or a homogeneous fluid half-space. We denote them by $F_1,F_2,\ldots,F_m$, as numbered from bottom to top. These fluid regions are obviously separated by soft aggregate solid regions. The modal depth functions in F_v, $v=1,\ldots,m$, appear as [Ref. 8, Eq. (6.13)]

$$y_2(\omega,z)\sim A_v+q^6L_v\left[\int_{\zeta_v}^z\rho^{-1}(s)ds\right],$$
$$y_4(\omega,z)\sim -\omega^{1/3}q^4L_v, \tag{A13}$$

where ζ_v is the upper depth of the region in question and L_v and A_v are constants. For the medium below F_1, there are two options:

(A) It can be a soft aggregate solid region terminated either by a free or mixed-condition boundary or by a fluid region that has a free boundary or includes a homogeneous fluid half-space. With this option, we can take $L_1=\mathcal{J}$ and $A_1=1-q^6\mathcal{J}[\int\rho^{-1}(s)ds]$, where the integral is taken over the fluid region F_1, and $\mathcal{J}$ is the sum of the centered second-order moments of φ_0 for the separate solid regions that make up the soft aggregate solid region. As usual, however, the axis of the moment for a solid region with a mixed-condition boundary should be changed to that boundary.

(B) It can simply be a rigid boundary to the fluid region or a nonsoft aggregate solid region (including its rigid boundary or homogeneous solid half-space). With this option, we can take $L_1=1$ and $A_1=-q^6[\int\rho^{-1}(s)ds]$, where the integral is taken over the fluid region F_1.

For the medium above F_m, there are two corresponding options. With the first option (A), we get $L_m=-\mathcal{J}A_m$ for some nonzero A_m. With the second option (B), we get $A_m=0$ for some nonzero L_m. Since the medium must contain at least one soft aggregate solid region, however, the second option is not allowed for both the upper and lower terminations unless $m>1$.

The modal depth functions in an individual solid region with upper depth ζ within one of the soft aggregate solid regions appear as [Ref. 8, Eq. (6.12)]

$$y_1(\omega,z)\sim\omega^{1/3}qL\psi(z),$$
$$y_2(\omega,z)\sim L,$$
$$y_3(\omega,z)\sim q^3L\Psi(z), \tag{A14}$$
$$y_4(\omega,z)\sim -\omega^{1/3}q^4L\left[A+\int_\zeta^z\Psi(s)ds\right],$$

where $\psi(z)$ and $\Psi(z)$ are defined as in Appendix Secs. 2 and 3. The constant A and the nonvanishing proportionality factor L are region dependent, but the value of L is common for all solid regions within the same soft aggregate solid region.

Continuity of y_2 and y_4 throughout the medium provides relations for recursively computing the constants L and A for the different regions. For L_v and A_v for our particular fluid regions $F_1,F_2,\ldots,F_m$, we obtain in this way, for $v=2,3,\ldots,m$,

$$L_v = L_{v-1} + \mathcal{J} A_{v-1},$$
$$A_v = A_{v-1} - q^6 L_v \left[\int_{F_v} \rho^{-1}(s)\, ds \right], \tag{A15}$$

where $\mathcal{J}$ is the usual second-order φ_0 moment sum for the soft aggregate solid region between F_{v-1} and F_v. The recursion for (L,A) according to Eqs. (A15) has the same form as that for (h_J, h_D) according to Ref. 8, Lemma 3.6. Incorporating the condition from the upper termination of the medium on L_m and A_m, we obtain a polynomial h of degree m [or $m-1$, for the case with the second option, (B), for both terminations of the medium] in q^6 for q. Except for the change of moment axis for a solid region with a mixed-condition boundary, h is not affected by the different cases within each of the two options, (A) and (B), for the lower and upper terminations of the medium, respectively. It is of course easy to give h explicitly for small values of m, the case $m=1$ is covered by Ref. 8, Eqs. (6.6) and (6.7).

[1] I. A. Viktorov, *Rayleigh and Lamb Waves* (Plenum, New York, 1967).

[2] M. F. M. Osborne and S. D. Hart, ''Transmission, reflection, and guiding of an exponential pulse by a steel plate in water (I. Theory),'' J. Acoust. Soc. Am. **17**, 1–18 (1945).

[3] C. Desmet, C. Glorieux, W. Lauriks, and J. Thoen, ''All-optical investigation of the lowest-order antisymmetrical acoustic modes in liquid-loaded membranes,'' J. Acoust. Soc. Am. **103**, 618–621 (1998).

[4] P. P. Lloyd and M. Redwood, ''Wave propagation in a layered plate composed of two solids with perfect contact, slip, or a fluid layer at their interface,'' Acustica **16**, 169–173 (1965).

[5] W. Hassan and P. Nagy, ''On the low-frequency oscillation of a fluid layer between two elastic plates,'' J. Acoust. Soc. Am. **102**, 3343–3348 (1997).

[6] F. Coulouvrat, M. Rousseau, O. Lenoir, and J.-L. Izbicki, ''Lamb-type waves in a symmetric solid-fluid-solid trilayer,'' Acustica **84**, 12–20 (1998).

[7] V. Ferrazzini and K. Aki, ''Slow waves trapped in a fluid-filled infinite crack: implication for volcanic tremor,'' J. Geophys. Res. B **92**, 9215–9223 (1987).

[8] S. Ivansson, ''A class of low-frequency modes in laterally homogeneous fluid-solid media,'' SIAM (Soc. Ind. Appl. Math.) J. Appl. Math. **58**, 1462–1508 (1998). *Note 1:* The confusion compared to Ref. 7 concerning the asymptotic behavior of a certain slow mode, e.g., p. 1487, is resolved by noting that ''wavelength'' in Ref. 7 apparently concerns the horizontal part $(=2\pi/\omega p)$. *Note 2:* It is stated towards the end of Section 7.2 how the region-dependent function $\psi(z)$ will be changed for a solid region with the mixed boundary conditions at one end. The definition of the function $\Psi(z)$ will also be changed, in this case, to $\int_Z^z \varphi_0(s)\psi(s)\,ds$ where Z is the opposite interface depth of the solid region.

[9] F. Schwab, K. Nakanishi, M. Cuscito, G. F. Panza, G. Liang, and J. Frez, ''Surface-wave computations and the synthesis of theoretical seismograms at high frequencies,'' Bull. Seismol. Soc. Am. **74**, 1555–1578 (1984).

[10] K. Aki and P. Richards, *Quantitative Seismology* (Freeman, San Francisco, 1980).

[11] S. Ivansson, ''Delta-matrix factorization for fast propagation through solid layers in a fluid-solid medium,'' J. Comput. Phys. **108**, 357–367 (1993).

[12] P.-C. Xu, A. K. Mal, and Y. Bar-Cohen, ''Inversion of leaky Lamb wave data to determine cohesive properties of bonds,'' Int. J. Eng. Sci. **28**, 331–346 (1990).

[13] M. R. Karim, A. K. Mal, and Y. Bar-Cohen, ''Inversion of leaky Lamb wave data by simplex algorithm,'' J. Acoust. Soc. Am. **88**, 482–491 (1990).

[14] O. Behrend, A. Kulik, and G. Gremaud, ''Characterization of thin films using numerical inversion of the generalized Lamb-wave dispersion relation,'' Appl. Phys. Lett. **62**, 2787–2789 (1993).

[15] S. Ivansson, ''Low-frequency slow-wave dispersion computations by compound-matrix propagation,'' FOA report R--98-00921, Defence Research Establishment, Stockholm (1998).

[16] G. Dahlquist, A. Bjorck, and N. Anderson, *Numerical Methods* (Prentice-Hall, NJ, 1974).

[17] S. Ivansson, ''Comment on 'Free-mode surface-wave computations' by P. Buchen and R. Ben-Hador,'' Geophys. J. Int. **132**, 725–727 (1998).

[18] F. Jensen, W. Kuperman, M. Porter, and H. Schmidt, *Computational Ocean Acoustics* (AIP, New York, 1994).

[19] M. Abramowitz and I. A. Stegun, *Handbook of Mathematical Functions* (U.S. National Bureau of Standards, 1964).

[20] S. Ivansson, ''The compound matrix method for multi-point boundary-value problems depending on a parameter,'' Z. Angew. Math. Mech. **78**, 231–242 (1998).

[21] S. Ivansson and I. Karasalo, ''Computation of modal wavenumbers using an adaptive winding-number integral method with error control,'' J. Sound Vib. **161**, 173–180 (1993).

[22] J. A. Hudson, *The Excitation and Propagation of Elastic Waves* (Cambridge U.P., Cambridge, 1980).

Greenspan acoustic viscometer: Numerical calculations of fields and duct-end effects

James B. Mehl
National Institute of Standards and Technology, Physical and Chemical Properties Division, Gaithersburg, Maryland 20899 and Department of Physics and Astronomy, University of Delaware, Newark, Delaware 19711-2570

(Received 20 October 1998; accepted for publication 14 April 1999)

Inertial and resistive end corrections for the Greenspan acoustic viscometer were computed using a boundary-integral-equation technique for determination of the acoustic field. Viscous effects were estimated using a boundary-layer approximation. The results apply to a circular duct coupling two concentric chambers and to ducts terminated by infinite plane baffles. The effects of rounding the sharp edge at the duct end were investigated and found to be described by simple scaling relations.
 [S0001-4966(99)05507-1]

PACS numbers: 43.20.Mv, 43.20.+g [DEC]

INTRODUCTION

The Greenspan acoustic viscometer (Fig. 1) consists of a cylindrical duct coupling two chambers whose volumes are large compared with the volume of the duct. Gillis *et al.*[1,2] have shown that the Greenspan viscometer is an accurate and convenient device for measuring the viscosity of gases. A full theory of the viscometer requires modeling the inertial and viscous effects of the convergent/divergent flow at the duct ends. These effects are investigated numerically in this paper. The present results are required if the uncertainty of viscosity measurements is to be reduced from approximately 1% to the order of 0.1%.

The theory of the Greenspan viscometer is based on the linear equations introduced by Kirchhoff to describe the coupled temperature, pressure, and velocity fields in gases.[3] In particular, the exact solutions of Kirchhoff are used to calculate the flow impedance of the viscometer duct. For infinitely long ducts and the range of parameters in typical applications, the calculations of the duct impedance can be regarded as exact. End corrections are, however, important for the ducts of convenient experimental designs.

In this work the acoustic field Φ and eigenvalue k are calculated for model shapes in the approximation of rigid boundaries and negligible dissipation. From these solutions, it is possible to determine the inertial end correction without further approximation, and to determine the first-order coefficient of viscous end effects.

A boundary-integral-equation (BIE) formalism was used in the calculations. For axisymmetric shapes like the Greenspan viscometer, the boundary value problem for the acoustic field can be expressed as a one-dimensional integral equation whose solution yields both the eigenvalue k and the eigenfunction, or velocity potential, Φ. This integral equation has been solved for Greenspan viscometers with a wide variety of dimensions. Analysis of the numerical results yielded values of the inertial and resistive end corrections. Among the advantages of the BIE technique is the exact representation of surfaces generated by rotating curves of arbitrary shape. Thus it has been possible to alter the resonator cross-section by replacing sharp corners with chamfered corners, and to evaluate the effects of chamfering on the inertial and resistive end corrections. Experimental determinations[2] of the inertial and resistive end effects are in good agreement with the calculations reported here.

The paper is organized as follows. The next section is a review of the acoustic model of the Greenspan viscometer, with emphasis on defining the parameters which need to be evaluated numerically. Some supporting material is in Appendix A. Duct-end effects are discussed in Sec II. Section III is a summary of the numerical approach, with further detail in Appendix B. The remainder of the paper is a presentation and discussion of the numerical results.

I. GREENSPAN VISCOMETERS

Martin Greenspan suggested the use of a double-Helmholtz resonator for measuring the viscosity of gases in 1953.[4] Recent experimental work[1,2] demonstrated that such resonators, now called Greenspan viscometers, are capable of measuring the viscosity of gases with an uncertainty less than 1%. Figure 1 shows the viscometer shape and defines some dimensions used throughout this paper. A cylindrical coordinate system concentric with the duct and chambers, with the origin at the center of the resonator, will also be assumed, unless noted otherwise.

The Greenspan viscometer has a low frequency mode in which the gas in the duct oscillates between the two chambers. For this mode, the contours in Fig. 2 show that the acoustic velocity within the duct is nearly constant. A zero-order approximation to the (circular) oscillation frequency can be obtained by assuming that gas in the duct has a constant velocity, and that the main effect of the chambers is a pure compliance. This leads to

$$\omega_0^2 = \frac{2c^2 A_d}{L_d V_c}, \tag{1}$$

where c is the speed of sound, A_d is the cross-sectional area of the duct, L_d is the length of the duct, and V_c is the volume of a single chamber. For practical viscometers, the product of the corresponding propagation parameter $k_0 = \omega_0/c$ and a typical resonator dimension is small compared with unity.

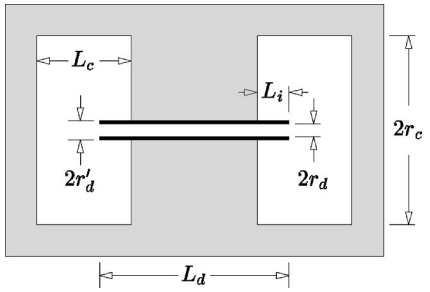

FIG. 1. Cross-section of Greenspan viscometer. The shaded portions are metal; the gas under test fills the open areas of the resonator. The transducers and fill duct are omitted.

Practical acoustic viscometers must be described by an acoustic model which includes viscous and thermal dissipation. The model is defined most succinctly by an equivalent circuit of acoustic elements.[1] The duct element is a *T*-equivalent circuit which represents the Kirchhoff equations.[3] The duct ends and the chambers are represented by series combinations of orifice impedances $\boldsymbol{Z}_{\text{end}}$ and chamber impedances $\boldsymbol{Z}_V$. Each of these lumped-circuit components is defined as the ratio of an acoustic pressure difference divided by a volume velocity. The chamber impedances can be modeled with accurate analytic approximations which include the effects of the thermal boundary layers at the chamber walls. The acoustic velocity field in the chambers is negligibly small except for the region within a few duct radii of the duct end. The inertial and dissipative effects of the velocity field within the chamber are thus localized and are most conveniently included in the orifice impedance.

The Kirchhoff equations provide an essentially exact description of the coupled pressure, temperature, and vorticity fields in ducts of infinite length. At the Helmholtz resonance of the viscometer, the flow in the duct is nearly uniform with a pressure node at $z=0$. This point is also a node for the acoustic temperature. The full theory shows that temperature oscillations in the duct are so weak that dissipation in the duct is almost entirely due to viscous effects. (The full model accounts for the small thermal losses in the chambers.[1])

Near the ends of the duct the Kirchhoff equations fail to represent the field accurately. The full solution in the duct could in principle be represented as the sum of the contributions from a single propagating mode and an infinite number of evanescent modes. The latter decay within a few duct radii of the ends. The viscous and inertial effects of the evanescent waves, and the viscous and inertial effects of localized fields in the chambers near the orifices, are included in the orifice impedance. An approximate theory of the end effects is developed in the next section.

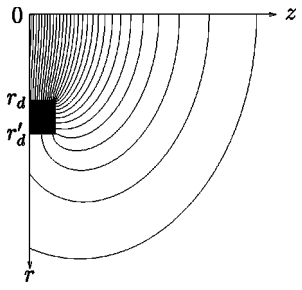

FIG. 2. The acoustic field near a duct end, for radial coordinate $r \geqslant 0$ and axial coordinate z along the axis of symmetry of the viscometer. The dark rectangle represents a half-cross-section of the end of a duct wall between radii r_d and r'_d. The field is shown as contours of uniformly spaced velocity potential (or pressure), as calculated in this work.

II. DUCT-END EFFECTS

The acoustic fields near acoustic orifices in thin plates and at the ends of ducts have been widely investigated.[5–25] The inertial effects are commonly expressed in terms of a lumped impedance $i\omega\rho\delta_I/A_d$. Here ρ is the gas density, $i\omega\rho/A_d$ is the inertance per unit length for nondissipative acoustic flow in a duct, and δ_I is the inertial end correction. Rayleigh[5] gives the exact value $\delta_I=\pi r_d/4$ for an orifice in an infinitesimally thin plate, and obtained an approximate value $\delta_I \approx 0.82 r_d$ for a duct end with an infinite plane baffle. The latter estimate was improved by Daniell,[6] and recently recalculated by Norris and Sheng,[24] who obtained $0.821\,59\,r_d$. Rayleigh's expression for the exact flow velocity in the infinitesimally thin orifice $u_z \propto 1/\sqrt{1-r^2/r_d^2}$ has a singularity of order $s^{-1/2}$ at the orifice edge, where s is the distance from the edge. The tangential velocity on the plate has a similar singularity.[10] The weaker singular behavior near the corner of an baffled end, $s^{-1/3}$, was built into the trial solutions used by Daniell. Unbaffled duct ends were investigated by Levine and Schwinger.[9] In the limit of an infinitesimally thin duct wall, the velocity near the end of the duct has a singularity of order $s^{-1/2}$, and the inertial end correction is approximately $0.61\,r_d$. As the thickness of the duct wall is increased from very small to large values, the inertial end correction varies uniformly between the limits for thin ducts and infinitely baffled ducts.[20,25]

Viscous forces associated with the divergences in the tangential flow near a duct end are the sources of additional contributions to the orifice impedance, which can be estimated (in the linear regime) using ideas that were apparently first applied to orifices by Nielsen.[10,16] The flow is represented by a superposition of acoustic and vorticity waves which together satisfy a nonslip boundary condition on solid boundaries. The vorticity waves are confined to a layer near the solid boundaries of approximate thickness $\delta_v = \sqrt{2\eta/\rho\omega}$, where η is the viscosity. When the viscous penetration length δ_v is small compared with other dimensions, and the surface curvature is large compared with δ_v, the transverse flow velocity near a boundary is approximately

$$u_t(\xi) \approx u_{a,t}[1-e^{-(1+i)\xi/\delta_v}], \tag{2}$$

where ξ is the distance from the duct wall, and $u_{a,t}$ is the transverse acoustic velocity near the wall. The corresponding force per unit area of boundary surface is

$$\eta \frac{\partial u_t}{\partial \xi}\bigg|_{\xi=0} = \frac{\eta}{\delta_v}(1+i)u_{a,t} = \frac{1}{2}\rho\omega\delta_v(1+i)u_{a,t}. \tag{3}$$

Nielsen estimated the orifice resistance by integrating the corresponding rate of dissipation per unit area, $\frac{1}{4}\rho\omega\delta_v u_{a,t}^2$. In his application to an orifice in a thin plate, the divergent integral had to be cut off at distance of order δ_v from the orifice edge. For duct ends, the weaker divergence in the

tangential flow velocity leads to a convergent integral, similar to the treatment of step-discontinuities in an infinite plane duct by Morse and Ingard.[26]

Panton and Miller[22] correlated the work of Thurston,[11] Ingard,[16] Thurston *et al.*,[17] and Ingard and Ising[19] on the impedance of orifices in thin plates. They found that the orifice inertance was constant below a mean orifice flow velocity of about $0.3\,\delta_v\omega$, and that the orifice resistance was constant below a mean orifice flow velocity of about $2\,\delta_v\omega$. These results support the existence of a low-velocity linear regime, where the Greenspan viscometer is intended to operate. The nonlinearity thresholds for thin plates and baffled duct ends may differ considerably, however, because the singular behavior of the tangential velocity in the limit of zero viscosity is different for the two cases.

The combined inertial and viscous contributions to the orifice impedance can be conveniently expressed

$$\boldsymbol{Z}_{\text{end}}=\frac{\rho\omega}{A_d}[i\,\delta_I+(i+1)\,\delta_R], \tag{4}$$

where the two components associated with the viscous boundary layer are represented by a the orifice resistance parameter δ_R. This parameter can be determined by calculating the additional dissipation near the duct end.[26]

The total, time-averaged, rate of energy loss due to the viscous boundary layer in an axisymmetric resonator is

$$P=\frac{\pi}{2}\rho\omega\delta_v\int u_{a,t}^2 r\,ds, \tag{5}$$

where ds is the element of arc length in the longitudinal cross-section of the viscometer. A portion P_0 of this loss will be included in the Kirchhoff equations representing the duct. The acoustic velocity in the duct, in the limit of small δ_v/r_d, is $u_z=u_{z0}\cos kz$, where $k=\omega/c$, so that

$$P_0=\frac{\pi}{2}\rho\omega\delta_v r_d u_{z0}^2\int_0^{L_d/2}\cos^2 kz\,dz. \tag{6}$$

The total power loss

$$P=P_0+\tfrac{1}{2}(\rho\omega\delta_R/A_d)U^2 \tag{7}$$

exceeds P_0 because of the localized additional losses near the duct end. Here $U=A_d u_{z0}\cos(kL_d/2)$ is the volume flow out of the duct. Equation (7) can be used to determine δ_R once the total power loss has been determined numerically.

The inertial length δ_I can be obtained most conveniently and with high accuracy by using the resonance condition

$$k\tan(kL_d/2)+k^2\delta_I-A_d/V_c=0, \tag{8}$$

derived from the equivalent-circuit model of the viscometer,[1] together with numerically determined values of the resonance parameter k. An alternative procedure, described later, is more directly related to the definition of inertance, but is less convenient because it requires calculation of the flow in the orifice at the duct end. The two methods yield equivalent results.

III. NUMERICAL APPROACH

In the limit of small dissipation, the acoustic pressure within the resonator is proportional to the velocity potential Φ, a solution of the boundary value problem

$$\begin{aligned}&(\nabla^2+k^2)\Phi(\boldsymbol{r})=0,\quad \boldsymbol{r}\in C,\\ &\frac{\partial\Phi}{\partial n}=0,\quad \boldsymbol{r}\in S,\end{aligned} \tag{9}$$

i.e., the Helmholtz equation in the resonator C subject to a Neumann boundary condition on the resonator surface S. An equivalent form of the same boundary value problem is the integral equation

$$\Phi(\boldsymbol{r}')\Omega(\boldsymbol{r}')=-\int_S\Phi(\boldsymbol{r})\boldsymbol{n}\cdot\boldsymbol{\nabla}G(\boldsymbol{r}',\boldsymbol{r})dS, \tag{10}$$

where $\boldsymbol{r}$ and $\boldsymbol{r}'$ are both on S, $\Omega(\boldsymbol{r}')$ is the internal solid angle subtended by S at $\boldsymbol{r}'$, and the fundamental solution, or Green's function, is

$$G(\boldsymbol{r}',\boldsymbol{r})=\frac{e^{ikR}}{R},\quad R=|\boldsymbol{r}-\boldsymbol{r}'|. \tag{11}$$

Solutions of this integral equation yield both the eigenfrequency $\omega=ck$ and the velocity potential Φ on the surface of the resonator. The numerical procedure described below enables the determination of smooth approximate values of the tangential velocity $u_{a,t}=\Phi'$ on the resonator boundary, as required for accurate calculations of δ_R.

The cross-sectional area of a Greenspan viscometer, which is both axisymmetric and has mirror symmetry with respect to the $z=0$, plane can be represented by parametric equations $r(t)$ and $z(t)$, both symmetric in t, with the midplane at $t=0$. The velocity potential on the surface can be written as a function of the parameter t. In Appendix B it is shown that $\Phi(t)$ is the solution of a one-dimensional integral equation

$$-\Omega(t')\Phi(t')=\int g_n(t',t)\Phi(t)h(t)r(t)dt, \tag{12}$$

where ds, the element of arc length in the cross-section, is equal to $h(t)dt$, and $g_n(t',t)$, is a kernel with a logarithmic singularity at $t=t'$.

An approximate solution of the integral equation (12) can be formulated as a series of Hermite cubic polynomials, each defined on a portion of the boundary. The solutions of interest have odd symmetry $\Phi(t)=-\Phi(-t)$. It suffices to define the geometry for $z\geqslant 0$ and to use this symmetry in formulating a solution. It is convenient to divide the resonator cross-section, or generator, for $z\geqslant 0$, into N elements, with the jth element corresponding to $j-1\leqslant t\leqslant j$. The elements could be chosen to have arbitrary shapes. However, shapes with sharp and rounded corners can be represented with only two types of elements: straight lines and circular arcs. The resonator shape is treated exactly within these constraints.

The velocity potential $\Phi(t)$ is approximated as a series of cubic Hermite polynomials so that, by construction, both $\Phi(t)$ and the tangential derivative $\Phi'=d\Phi/ds$ are continu-

ous at the nodes dividing the elements. (The latter condition cannot be applied at reentrant corners, as explained below.) The coefficients in the polynomial representation are the eigenfunction Φ_j and its tangential derivative Φ'_j at nodes $j=0,1,\ldots,N$. There are thus $2(N+1)$ unknown coefficients in the representation of the eigenfunction and its derivatives. By requiring that the approximate solution satisfy the integral equation (12) at each of the nodes, $N+1$ linear equations are obtained. Additional linear equations can be obtained by requiring that the second derivatives Φ'' be continuous at most of the internal nodes. This condition must be modified at corners, as described below. Two additional conditions are $\Phi(0)=0$ (at the plane of mirror symmetry) and $\Phi'=0$ for nodes on the axis (unless there is a cusp in the chamber cross-section). With appropriate conditions at each internal node, a total of $N+1$ additional linear equations is obtained. The solution to this set has the form

$$\Phi'_j=\sum_{l=0}^{N} D_{jl}\Phi_l. \tag{13}$$

The tangential derivatives can now be eliminated from the $N+1$ equations which approximate Eq. (12); this set can now be expressed

$$\sum_{j=0}^{N} A_{ij}(k)\Phi_j=0, \tag{14}$$

where the matrix elements $A_{ij}(k)$ are obtained by numerical integration over the elements of appropriate products of the basis functions and the kernel of the integral equation, and subsequent elimination the Φ'_j terms through Eq. (13).

Approximate values of the eigenvalue $k$are obtained by requiring the determinant of matrix $A_{ij}(k)$ to vanish. Once k is determined, Φ_j can be determined from Eq. (14), and Φ'_j from Eq. (13). Smoother value of Φ_j and Φ'_j can be obtained by solving Eq. (14) by inverse iteration.[27]

A. Corners

Near corners the eigenfunctions will have a two-dimensional character whose limiting behavior is restricted by the boundary conditions. Consider a (temporary) cylindrical coordinate system with polar coordinates (ζ,ρ,ϕ). Assume that the ζ axis corresponds to a corner and that the boundaries are at $\phi=0$ and ϕ_c, i.e., ϕ_c is the interior angle at the corner. Solutions of the Helmholtz equation expanded about the corner have the form

$$\Phi=\sum_{l} [a_l\cos(\mu_l\phi)+b_l\sin(\mu_l\phi)]J_{\mu_l}(k\rho). \tag{15}$$

The Neumann boundary condition, $\partial\Phi/\partial\phi=0$ at $\phi=0$ and $\phi=\phi_c$, requires that all $b_l=0$ and that $\mu_l\phi_c$ be a multiple of π. Accordingly, the lowest nonzero Bessel-function index is $\mu_1=\pi/\phi_c$. For a $\frac{1}{2}\pi$ internal corner this is $\mu_1=2$; for a $\frac{3}{2}\pi$ reentrant corner it is $\mu_1=\frac{2}{3}$. The leading term in the expansion of the Bessel function is $(k\rho)^{\mu_1}$. Accordingly, at $\frac{1}{2}\pi$ internal corners the eigenfunction Φ will have a vanishing tangential derivative as the corner is approached. This is the supplementary condition used instead of continuity of Φ'' at corner nodes with interior angle $\frac{1}{2}\pi$.

For a $\frac{3}{2}\pi$ reentrant corner at node l_c the eigenfunction will have a limiting behavior of the form, with $s-s_c$ the arc length from the corner and C a constant,

$$\Phi=\Phi_{l_c}\pm C|s-s_c|^{2/3}, \tag{16}$$

which has a singular tangential derivative. An improved approximation to $\Phi(t)$ was obtained by using, on the elements adjacent to $\frac{3}{2}\pi$ reentrant corners, suitably defined basis functions with this limiting behavior. Because the continuity condition on Φ' cannot be imposed at a reentrant corner, an alternative linear equation was required. This was obtained by use of Eq. (15) through order $|s-s_c|^2$ to relate values of Φ_j for $j=l_c$ and $l_c\pm1$ and values of Φ'_j for $j=l_c\pm1$. (The approximations to Φ on the singular elements adjacent to corner nodes do not involve the parameter Φ'_{l_c}, which was left undefined for singular elements.)

B. Shapes investigated

Numerical calculations were carried out for many variations of the geometry shown in Fig. 1. Five series of calculations were carried out for viscometers with the duct ends flush with the chamber walls ($L_i=0$). For each series the duct radius was varied from $0.02\,r_c$ to $0.5\,r_c$. The series differ in the ratio of the lengths r_c, L_c, and L_d. For series C these lengths were in the ratio 1:2:2. The effects of halving and doubling the duct length were checked with series B (1:2:1) and D (1:2:4). The effects of halving and doubling the chamber lengths were checked with series A (1:1:2) and E (1:4:2). The duct-end effects were found to depend most strongly on the ratio r_d/r_c and only weakly on the other dimensions. The effects of rounding the orifice edges were investigated mainly with the series C shapes, but checked with series A.

For the viscometers with $L_i\neq0$, as used in recent experiments, the duct extends into the chambers a distance L_i (the insertion length). The dependence of the orifice parameters on this length was investigated for a shape typical of the shapes used in recent experiments.[2] The effects of duct-wall thickness were also calculated.

C. Grid generation

Uniform spacing of the nodes does not yield optimum approximations of the eigenfunctions. Instead, the node spacings h_j were scaled to provide greater detail in regions where the eigenfunction was varying most rapidly, i.e., near reentrant corners. The numerical code was constructed so that a maximum node spacing $h_{\max}$ was used for surfaces where Φ is weakly varying. The spacing was uniformly graded down to a minimum node spacing $h_{\min}$ at reentrant corners, as shown in Fig. 3. The figure shows two singular elements of length $h_{\min}$ at the sharp corner, with neighboring normal elements of the same length, next-nearest neighboring elements graded up one step, etc. Various grading scales were tested. Typically the ratio of the lengths of adjacent elements was chosen to be between 1.05 and 1.1. The maximum and minimum node spacings were typically $h_{\max}=r_c/40$ and

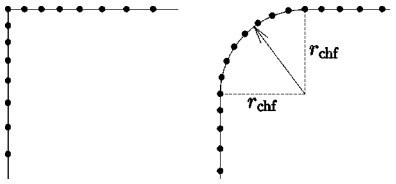

FIG. 3. Node positions near sharp and chamfered corners.

$h_{\min}=r_c/4000$ or $r_c/400$. The number of elements N varied from 216 to 404, depending on the series and on $h_{\min}$. The results reported in this paper have been calculated with many grid configurations and do not depend significantly on the details of the grids used.

The effects of chamfering reentrant corners was investigated by replacing the singular elements and adjacent straight elements by circular-arc elements; the node spacing on the circular-arc elements was always $h_{\min}$, with h_j graded upward in the straight elements adjacent to the circular-arc elements.

IV. NUMERICAL RESULTS

Figure 4 shows the cross-section of a viscometer and the numerically computed values of Φ_j and $|\Phi_j'|$. As expected, the eigenfunction is nearly constant within the chamber, and has a nearly linear dependence within the duct. The behavior near the duct orifice is more visible in the plot of $|\Phi'|$, which clearly shows the singular behavior. The singular behavior near the orifice edge is shown more clearly in Fig. 5. (The use of nonsingular basis functions in the elements adjacent to the reentrant corner yielded numerical values of Φ_j and Φ_j' nearly identical to those plotted here.)

Equation (10), with $\Omega(\boldsymbol{r}')=4\pi$ at internal points $\boldsymbol{r}'$, can be used to calculate internal values of the velocity potential from the boundary values. Figure 2 shows some typical results near an orifice of a duct extending into a chamber. The

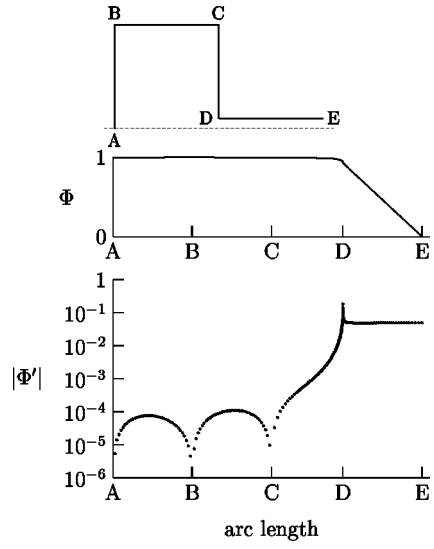

FIG. 4. Top: Outline of viscometer cross-section, with $L_c=r_c=L_d/2$ and $r_d=r_c/10$. Center and bottom: plots of Φ_j and $|\Phi_j'|$ at 321 nodes along the viscometer boundary, as a function of arc length along the boundary from reference point A to reference point E. The computed eigenvalue for this case is $k=0.002\,451\,50/r_d$.

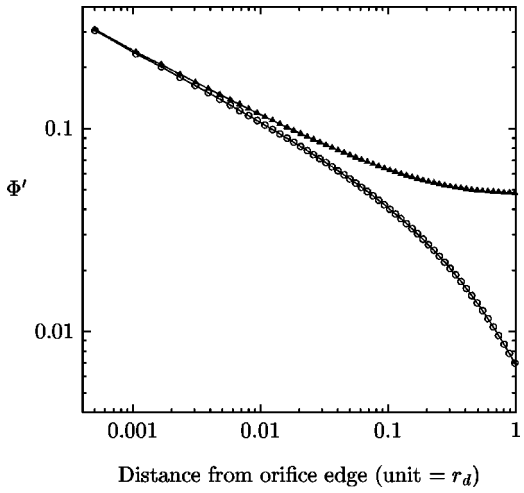

FIG. 5. The tangential derivative Φ' at nodes in the duct (triangles) and chamber (open circles) near the orifice, as functions of the distance from the orifice edge in units of the duct radius r_d, showing the expected divergent behavior. Viscometer dimensions are $r_c=L_c=L_d/2$, $r_d=r_c/10$.

flow pattern is typical; within the chamber the acoustic velocity drops rapidly over a distance of order r_d.

A. Eigenvalues and inertial end corrections

For each shape investigated, the eigenvalue k was calculated with at least two grid configurations. The results typically agreed to within a few parts in 10^8. A convenient method of summarizing the results is to use the numerical value of k and the viscometer dimensions, together with the equivalent-circuit model in the limit of no dissipation, and to calculate the inertial end correction δ_I. Somewhat greater consistency of the results can be obtained by the separation $\delta_I=\delta_I'+\delta_I''$, where most of the effects of chamber length are included in the term δ_I'.

In Appendix A it is shown that a cylindrical chamber with a concentric circular orifice in which the normal fluid velocity is $u_z(r)$ has an input impedance equal to the sum of

$$\boldsymbol{Z}_{\text{in}}'=\frac{\rho c^2}{i\omega V}\,\frac{kL_c}{\tan kL_c} \tag{17}$$

and

$$\boldsymbol{Z}_{\text{in}}''=\frac{4ik\rho c}{\pi r_d}\sum_{n=1}^{\infty}\frac{A_n J_1(z_{0n}r_d/r_c)}{[z_{0n}J_0(z_{0n})]^2}F_n(k). \tag{18}$$

Here z_{0n} is the nth root of $dJ_0(z)/dz=0$. The other quantities are

$$A_n=\int_0^{r_d}\tilde{u}_z(r)J_0(z_{0n}r/r_c)r\,dr, \tag{19}$$

where $\tilde{u}_z(r)$ is $u_z(r)$ divided by its value averaged over the orifice, and

$$F_n(k)=\frac{\coth[(z_{0n}L_c/r_c)\sqrt{1-(kr_c/z_{0n})^2}]}{\sqrt{1-(kr_c/z_{0n})^2}}\approx 1. \tag{20}$$

The first contribution, Eq. (17), is the zero-dissipation input impedance of the chamber modified for its finite length through the factor

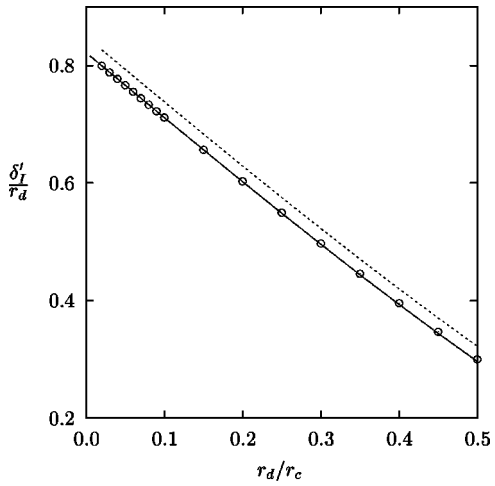

FIG. 6. Inertial end corrections δ_I' calculated from numerical eigenvalue k. The solid line was calculated for a model flow field in the orifice. The dotted line is Ingard's result for uniform flow in the orifice.

$$kL_c/\tan(kL_c)=1-\tfrac{1}{3}(kL_c)^2+O(kL_c)^4. \tag{21}$$

Equation (17) is thus approximately

$$\boldsymbol{Z}_{\text{in}}'\approx\frac{\rho c^2}{i\omega V}+\frac{i\omega\rho L_c}{3\pi r_c^2}. \tag{22}$$

The second term has the frequency/phase signature of an inertial term; the corresponding contribution to δ_I is

$$\delta_I''=\tfrac{1}{3}(r_d/r_c)^2L_c. \tag{23}$$

Similarly, the larger contribution to δ_I from Eq. (18) is

$$\delta_I'=4r_d\sum_{n=1}^{\infty}\frac{A_nJ_1(z_{0n}r_d/r_c)}{[z_{0n}J_0(z_{0n})]^2}F_n(k). \tag{24}$$

The inertial end corrections δ_I' were calculated for each resonator geometry using the numerical values of k and a modified form of Eq. (8), in which V_c was replaced by $V_c\tan(kL_c)/(kL_c)$, so that the effects of finite chamber size expressed in Eq. (17) are accounted for. Average results for the five series of viscometers are shown in Fig. 6. The results for the individual series differ from the average by a maximum of 0.001 at $r_d/r_c=0.5$, and by a much smaller amount in range of typical applications $r_d/r_c\leqslant 0.1$. Thus separation of the δ'' term accounts for nearly all dependence on viscometer dimensions other than the ratio r_d/r_c. A linear fit to the data in the range $r_d/r_c\leqslant 0.1$ yielded

$$\delta_I'/r_d=0.821\,59-1.1020r_d/r_c. \tag{25}$$

The correctness of this result is supported by the agreement, to five decimal places, of the constant term with the recent calculation of Norris and Sheng.[24]

The decrease with increasing duct radius is due to the change in coupling to the chamber modes in Eq. (24). Ingard[16] used a similar expression with a piston (constant) approximation to u_z in the orifice, for which

$$A_n=2J_1(z_{0n}r_d/r_c)/(z_{0n}r_d/r_c).$$

The dotted line in Fig. 6 was calculated using this expression. It clearly overestimates the end correction. A better result is obtained by using an approximation to the actual flow

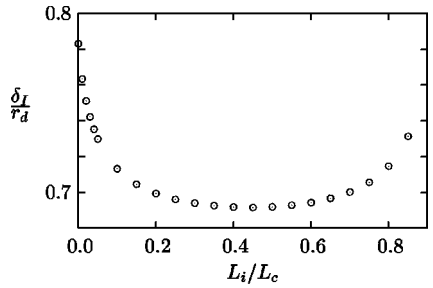

FIG. 7. Inertial end correction as a function of insertion length L_i, for a viscometer with $L_c=r_c=L_d/2$, $r_d/r_c=0.05$, and $r_d'/r_c=0.075$.

$$\tilde{u}_z=A+BX+CX^{-1/3}, \tag{26}$$

with $X=1-(r/r_d)^2$. The coefficients in this expression were obtained by calculating internal values of Φ for a series A viscometer with $r_d/r_c=0.05$. The results (similar to those in Fig. 2) were numerically differentiated to obtain u_z in the plane of the orifice. Equation (26) was fit to the results to obtain the coefficients $A=0.249\pm0.002$, $B=0.032\pm0.002$, and $C=0.490\pm0.001$. With these coefficients, the A_n were computed using Eqs. (19) and (26), and $\delta_I'/r_d=0.7666$ was obtained by summing Eq. (24), in excellent agreement with the value 0.7665 obtained from the numerical eigenvalue and the model. Under the assumption that Eq. (26) with these coefficients is a reasonable approximation to $\tilde{u}_z$ for the other values of r_d, Eq. (24) was then used to calculate δ_I'/r_d as a function of r_d/r_c. The results, shown as the solid line in Fig. 6, show that this approximation gives an excellent account of the orifice inertance.

The inertial end correction has also been calculated for viscometers with a finite insertion length $L_i>0$. Unfortunately the insertion of the duct end distorts the resonator shape so that the contribution δ_I'' can no longer be calculated in a simple way. Instead, the full inertial end correction must be calculated for each resonator geometry, using the numerical eigenvalues and an equivalent circuit with the input impedances of the chambers equal to $\rho c^2/i\omega V_c$. Results as a function of L_i/L_c are shown in Fig. 7 for a typical viscometer. The inertial end correction decreases initially as L_i increases from zero, reaches a minimum, and then increases again as the interaction with the back wall of the chamber increases. When the duct end is near the center of the resonator it most closely approximates an unbaffled end, with maximum distance to the chamber walls. The minimum value exceeds the value of Levine and Schwinger[9] for an unbaffled duct of zero thickness because the finite thickness of the duct acts as a partial baffle. The dependence on duct thickness is shown in Fig. 8. For each value of the fractional duct thickness $(r_d'-r_d)/r_d$, the end correction δ_I was found to be a linear function of r_d/r_c, and consistent with the trend in Fig. 6. The data were extrapolated to zero duct thickness to obtain the top curve in Fig. 8, which appears to smoothly approach the Levine–Schwinger value of 0.61 for zero fractional duct thickness.

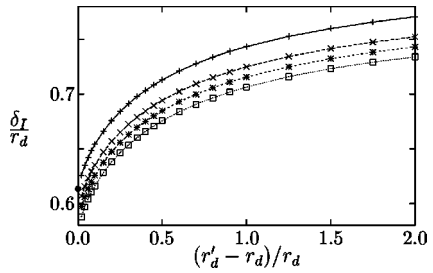

FIG. 8. Inertial end correction as a function of fractional duct thickness $(r'_d - r_d)/r_d$, for r_d/r_c equal to 0.1, □, 0.075, *, 0.05, ×, and extrapolated to zero, +. The single solid circle ● represents the result of Levine and Schwinger in the limit of zero duct thickness. The other resonator dimensions were $L_c = 2r_c$, $L_d = 5r_c/2$, and $L_i = r_c/2$.

B. Acoustic flow in the duct

The resonance frequencies of Greenspan viscometers are typically much lower than the cutoff frequencies for higher modes of a duct. Accordingly, near the center of the duct, the eigenvector is expected to be well approximated by a multiple of $\sin kz$, and the tangential derivative by a multiple of $\cos kz$. Insight into the divergent flow near the orifice can be gained by looking at the difference between Φ' in the duct and the best approximation $A \cos kz$. This difference $\Delta\Phi' = \Phi' - A \cos kz$ is plotted in Fig. 9. The constant A was determined by a fit to Φ' for $z < L_d/4$. The figure shows that the difference is smooth over five orders of magnitude. The divergent behavior of the tangential derivative near the orifice is evident. The complete solution in the duct can be expressed as the sum of the propagating mode and an infinite number of evanescent modes, the latter approximately proportional to $\exp(-z_{0n}\Delta z/r_d)$, where Δz is the distance from the orifice edge. The line in Fig. 9, which is proportional to the $n = 1$ evanescent wave, is clearly a good approximation to the plotted data in an intermediate range away from the orifice but above the digital noise farther into the duct. This agreement provides further support for the correctness of the numerical calculations.

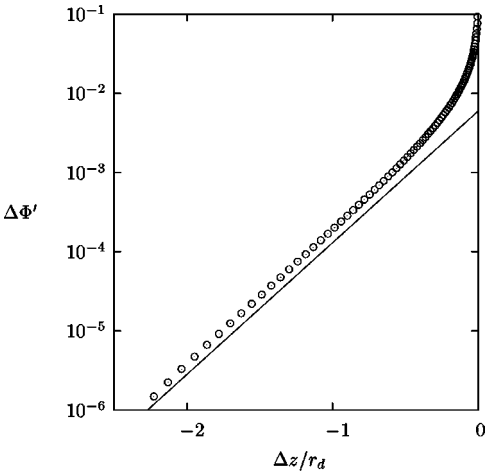

FIG. 9. Difference $\Delta\Phi' = \Phi' - A \cos kz$ between the tangential derivative of the velocity potential in the duct and $A \cos kz$, plotted as a function of the distance Δz from the orifice edge, for a viscometer with $L_c = r_c = L_d/2$ and $r_d/r_c = 0.1$. The constant A was determined by a fit to Φ' well within the duct. The differences near the orifice can be expressed in terms of an infinite sum of evanescent waves. The decay constant for the most-slowly decaying evanescent wave is shown as a solid line.

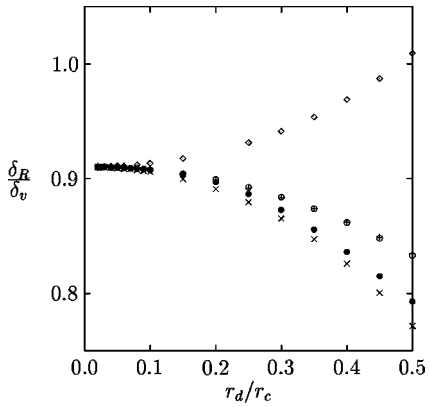

FIG. 10. Orifice resistance parameter as a function of duct radius, for five Greenspan viscometers with $L_1 = 0$; Series A, ×; B, ●; C, ○; D, +; E, ◇.

C. Orifice resistance

For each set of numerical calculations, the ratio δ_R/δ_v was calculated using Eqs. (5)–(7). The integral for P was calculated from the cubic representation of Φ' on each element and the numerically determined values of Φ_j and Φ'_j. The results are shown in Fig. 10 for the five series of resonators with duct ends flush with the chamber wall. For small duct radii, the orifice resistance parameter approaches 0.909 $\pm$ 0.001 for all series. The contribution from outside the duct approaches 0.499, and the contribution from inside the duct approaches 0.410.

The orifice resistance parameter was calculated as a function of insertion length for one case. The results are shown in Fig. 11. As the duct insertion increases from zero, the orifice resistance begins increasing rapidly, reaches a plateau, and then rises further as the duct end nears the back wall of the chamber. The initial increase is a trend toward an unbaffled duct end. When the duct is flush with the chamber wall the local field approximates that near an infinite baffle, where there is a single integrable singularity in the square of the tangential velocity. When the duct extends into the chamber there is a second singularity of the same order at the outer corner of the duct end. The numerical coefficient of the outer singularity increases as the duct wall thickness decreases. When the duct gets very thin, the combination of singularities approximates the stronger singularity of an in-

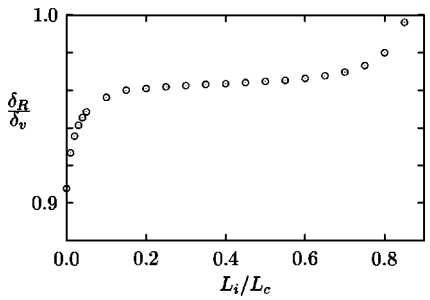

FIG. 11. Orifice resistance parameter as a function of insertion length L_i, for a viscometer with $L_c = r_c = L_d/2$, $r_d/r_c = 0.05$, and $r'_d/r_c = 0.075$.

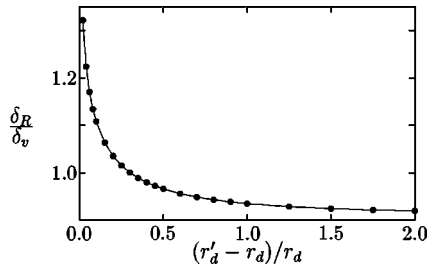

FIG. 12. Orifice resistance parameter as a function of relative duct thickness $(r_d'-r_d)/r_d$, for a resonator with $L_c=2r_c$, $L_d=5r_c/2$, and $L_i=r_c/2$. Calculations were made for r_d/r_c equal to 0.1, 0.075, and 0.05. The dependence of δ_R/δ_v on r_d/r_c was negligible.

finitesimally thin duct, so that the orifice resistance increases with decreasing duct thickness, as shown in Fig. 12.

D. Rounded corners

The effects of rounding sharp reentrant corners on the inertial and resistive end corrections have been investigated. The sharp orifice edge was replaced by a quarter-circular arc of radius $r_{\rm chf}$. Orifice inertance and resistance parameters were calculated as a function of $r_{\rm chf}$ for a large variety of conditions. The resistive end corrections were found to scale according to

$$\delta_R(r_{\rm chf})=\delta_R(0)[1-\tfrac{1}{3}(r_{\rm chf}/r_d)^{1/3}]. \tag{27}$$

The inertial end correction was only weakly dependent on chamfering, as expressed by the scaling law

$$\delta_I(r_{\rm chf})=\delta_I(0)[1-30.3(r_{\rm chf}/r_c)^{4/3}]. \tag{28}$$

The occurrence of the chamber radius in the latter suggests that the effect is associated with the slope in Fig. 6 rather than the intercept.

The decreases of both δ_R and δ_I by rounding of the sharp corners is qualitatively consistent with the trend observed in Thurston's measurements of the effects of severe beveling and rounding on the impedance of orifices in thin plates.[18] A more quantitative test was made during the development of the Greenspan viscometer.[2] The ends of a duct were chamfered slightly, so that $r_{\rm chf}/r_d\approx 0.07$. The corresponding decrease in δ_R predicted by Eq. (27) is 14%, which was confirmed experimentally within about 4%. The predicted and observed changes in δ_I were less than 1%.

V. CONCLUDING REMARKS

The boundary-integral-equation formalism described here has been shown to be a useful technique for calculating the acoustic field within Greenspan viscometers, including the singular effects near reentrant corners. The resulting acoustic solutions were used together with a boundary-layer approximation for the vorticity mode to determine the inertial and resistive components of the lumped acoustic impedances associated with the duct ends. Limiting cases of the results were shown to agree with known results for baffled and unbaffled duct ends. The reduction of the acoustic resistance at duct ends was found to follow a power law. In future applications, the results can be applied to the design of duct ends with rounded edges to minimize the maximum tangential velocity, a possible source of nonlinear effects.

ACKNOWLEDGMENTS

The author has had many helpful conversations with Michael Moldover and Keith Gillis. This work was supported in part by the Office of Naval Research.

APPENDIX A

An expression for the acoustic input impedance of a circular orifice in one end of a cylindrical chamber is derived in this section. The cylinder has rigid walls at $r=r_c$, $z=0$, and $z=L_c$. The orifice is at $z=0$, $r\leqslant r_d$. The normal component of the acoustic velocity in the plane of the orifice is $u_z(r)$. The acoustic pressure in the chamber can be expressed using Green's theorem

$$p(\mathbf{r}')=2\pi i\omega\rho\int_0^{r_d}u_z(r)G(\mathbf{r},\mathbf{r}')r\,dr. \tag{A1}$$

The Green's function is

$$G(\boldsymbol{r},\boldsymbol{r}')=\sum_{nl}\frac{\epsilon_l\Phi_{nl}(r,z)\Phi_{nl}(r',z')}{\pi r_c^2L_c[J_0(z_{0n})]^2(k_{nl}^2-k^2)}, \tag{A2}$$

where $\epsilon_l=2-\delta_{l0}$ is the Neumann symbol, the eigenfunctions are

$$\Phi_{nl}=J_0(z_{0n}r/r_c)\cos(l\pi z/L_c), \tag{A3}$$

the eigenvalues are

$$k_{nl}^2=(\zeta_{0n}/r_c)^2+(l\pi/L_c)^2, \tag{A4}$$

$J_m(\zeta)$ is a Bessel function, and ζ_{0n} the nth root of $J_0'(\zeta)=-J_1(\zeta)=0$. The specific acoustic input impedance of the orifice is the ratio of the mean pressure in the orifice $\langle p\rangle$ to the volume velocity $\langle u_z\rangle A_d$. The mean pressure can be obtained by averaging

$$p(r,z)=\frac{2i\omega\rho\langle u_z\rangle r_d^2}{r_c^2L_c}\sum_{nl}\frac{\epsilon_lA_n}{[J_0(\zeta_{0n})]^2}\times\frac{J_0(\zeta_{0n}r/r_c)}{(\zeta_{0n}/r_c)^2+(l\pi/L_c)-k^2}, \tag{A5}$$

where

$$A_n=\int_0^{r_d}\tilde{u}_z(r')J_0(\zeta_{0n}r'/r_c)r\,dr \tag{A6}$$

and $\tilde{u}_z$ is $u_z/\langle u_z\rangle$. Note that $A_0=\frac{1}{2}$, so that the $n=0$ sum can be split off. The input impedance of the chamber is

$$\boldsymbol{Z}_{\rm in}=\frac{\langle p\rangle}{\rho c\langle u_z\rangle}=\frac{i\omega\rho}{A_d}\frac{r_d^2L_c}{\pi^2r_c^2}\mathcal{S}(ikL_c/\pi)+\frac{i\omega\rho}{A_d}\frac{4ir_dL_c}{\pi^2r_c}\sum_{n=1}^{\infty}\frac{A_nJ_1(\zeta_{0n}r_d/r_c)}{\zeta_{0n}[J_0(\zeta_{0n})]^2}\mathcal{S}(\alpha_n), \tag{A7}$$

where

$$\mathcal{S}(\alpha)=\sum_{l=0}^{\infty}\frac{\epsilon_l}{l^2+\alpha^2}=(\pi/\alpha)\coth(\alpha\pi),$$

$$\alpha_n=\zeta_{0n}L_c\,\eta_n(\pi r_c)\,\eta_n,$$

$$\eta_n=\sqrt{1-(kr_c/\zeta_{0n})^2}\approx 1.$$

The input impedance is the sum of two terms equivalent to Eqs. (17) and (18).

APPENDIX B

Consider the integral equation (10) for axisymmetric problems with source points $\boldsymbol{r}(t)=(r,z,\phi)$ and field points $\boldsymbol{r}(t')=(r',z',0)$. The distance $R=|\boldsymbol{r}(t)-\boldsymbol{r}(t')|$ is

$$R(t',t,\phi)=\sqrt{r^2+r'^2-2rr'\cos\phi+(z-z')^2}. \tag{B1}$$

The area element is $dS=r\,d\phi\;h\,dt$, where

$$h(t)=ds/dt=\sqrt{(dr/dt)^2+(dz/dt)^2}.$$

For solutions independent of ϕ, Eq. (10) can be integrated over ϕ to obtain Eq. (12), where the kernel is

$$g_n(t',t)=\boldsymbol{n}(t)\cdot\int_0^{2\pi}\boldsymbol{\nabla}R\frac{d}{dR}\left(\frac{\exp(ikR)}{R}\right)d\phi. \tag{B2}$$

The basis set for approximate solutions of Eq. (12) can be defined as follows. The parameter t is scaled so that the jth element corresponded to $j-1\leqslant t\leqslant j$. The local coordinate on element j is $\tau_j=t-j+1$. The functions $H_m^j(\tau_j)$ are defined to vanish for $\tau_j<0$ and $\tau_j>1$, and to equal $H_m(\tau_j)$ on element j, where

$$\begin{aligned}&H_1(\tau)=1-3\tau^2+2\tau^3,\quad H_2(\tau)=\tau(1-\tau)^2,\\&H_3(\tau)=3\tau^2-2\tau^3,\quad H_4(\tau)=-\tau^2(1-\tau).\end{aligned} \tag{B3}$$

The linear combination

$$\begin{aligned}\Psi(t)=\sum_{j=1}^{N}&[\Phi_{j-1}H_1^j(\tau_j)+h_j\Phi'_{j-1}H_2^j(\tau_j)+\Phi_jH_3^j(\tau_j)\\&+h_j\Phi'_jH_4^j(\tau_j)]\end{aligned} \tag{B4}$$

interpolates Φ and its derivative Φ' with respect to arc length at all nodes. This form was used to approximate the solution $\Phi(t)$. For the linear and circular elements used in this work the derivative Ψ' is continuous at all nodes. As noted in the main text, a series expansion of Eq. (15) through order $|s-s_C|^2$ was used instead of Eq. (B4) on elements adjacent to a reentrant corner. The form of the expansion insured continuity of Ψ at the reentrant corners, but not of the derivatives. The form of the expansion was chosen to match Φ and Φ' at the adjacent nodes.

A numerical approximation to the integral equation (12) was obtained by using Eq. (B4) to approximate Φ, and requiring that the approximate form hold at the $N+1$ nodes t_i'. This yielded a set of $N+1$ linear equations of the form

$$-\Omega_i\Phi_i=\sum_{j=0}^{N}[B_{ij}\Phi_j+C_{ij}\Phi'_j], \tag{B5}$$

with suitably defined B_{ij} and C_{ij} determined by integrations of the kernel over the elements. Continuity of Ψ'' at all nonreentrant internal nodes requires

$$\begin{aligned}&6(\Phi_{j-1}-\Phi_j)/h_j^2+2(\Phi'_{j-1}+2\Phi'_j)/h_j\\&\quad=-6(\Phi_j-\Phi_{j+1})/h_{j+1}^2-2(2\Phi'_j+\Phi'_{j+1})/h_{j+1}.\end{aligned} \tag{B6}$$

An alternative condition for reentrant corners was obtained by using the values of Ψ'' from the series expansion of Ψ on the singular elements, and matching these to values on the adjacent nodes. As explained in the main text, these equations were supplemented by conditions on the first and last elements to permit a solution in the form of Eq. (13), which was then used to eliminate the derivatives from Eq. (B5) to obtain Eq. (14).

The matrix elements were calculated using the Quadpack adaptive numerical quadrature routine `qnda`.[28] Special care was taken with the weakly singular integrals which occurred when the range of integration included the collocation point t_j'. The singularities were of the logarithmic form, and were handled using identities similar to

$$\int_0^1 f(t)\log t\,dt=-f(0)+\int_0^1[f(t)-f(0)]\log t\,dt.$$

This procedure separated out the singular contribution and permitted the use of a non-singular quadrature routine for the remaining integration. The error limits for the adaptive quadrature were set as low as feasible for IEEE double precision computations. No effort was made to optimize the speed of calculation by relaxing the error limits. Sufficient checks were made to insure that the accuracy of the quadrature did not influence the accuracy of the results.

[1] K. A. Gillis, J. B. Mehl, and M. R. Moldover, ''Greenspan acoustic viscometer for gases,'' Rev. Sci. Instrum. **67**, 1850–1857 (1996).
[2] K. A. Gillis, J. B. Mehl, and M. R. Moldover, in preparation.
[3] G. Kirchhoff, ''Über den Einfluss der Wärmeleitung in einem Gase auf die Schallbewegung,'' Ann. Physik Chem. (Fifth Ser.) **134**, 177–193 (1868); English translation (''On the influence of heat conduction in a gas on sound propagation'') by R. B. Lindsay in *Benchmark Papers in Acoustics: Physical Acoustics*, edited by R. B. Lindsay (Dowden, Hutchinson, & Ross, Stroudsburg, PA, 1974), pp. 7–19.
[4] Martin Greenspan and Francis N. Wimenitz, ''An Acoustic Viscometer for Gases–I,'' NBS Report 2658 (1953).
[5] Lord Rayleigh, *The Theory of Sound*, 2nd ed. (Dover, New York, 1945), Vol. 2, Sec. 307, Appendix A.
[6] P. J. Daniell, ''The coefficient of end-correction,'' Philos. Mag. **30**, 137–146 (1915); 248–256 (1915).
[7] L. J. Sivian, ''Acoustic impedance of small orifices,'' J. Acoust. Soc. Am. **7**, 94–101 (1935).
[8] R. H. Bolt, S. Labate, and U. Ingard, ''The acoustic reactance of small circular orifices,'' J. Acoust. Soc. Am. **21**, 94–97 (1948).
[9] H. Levine and J. Schwinger, ''On the radiation of sound from an unflanged circular pipe,'' Phys. Rev. **73**, 383–406 (1948).
[10] A. K. Nielsen, ''Acoustic resonators of circular cross-section and with axial symmetry,'' Trans. Danish Acad. Tech. Sci. **10**, (1949).
[11] G. B. Thurston, ''Periodic fluid flow through circular tubes,'' J. Acoust. Soc. Am. **24**, 653–656 (1952).
[12] G. B. Thurston and C. E. Martin, ''Periodic flow through circular orifices,'' J. Acoust. Soc. Am. **25**, 26–31 (1953).
[13] A. W. Nolle, ''Small-signal impedance of short tubes,'' J. Acoust. Soc. Am. **25**, 32–39 (1953).
[14] A. F. Kuckes and U. Ingard, ''A note on acoustic boundary dissipation due to viscosity,'' J. Acoust. Soc. Am. **25**, 798–799 (1953).
[15] G. B. Thurston and J. K. Wood, ''End corrections for a concentric circular orifice in a circular tube,'' J. Acoust. Soc. Am. **25**, 861–863 (1953).

[16] K. Ingard, ''On the theory and design of acoustic resonators,'' J. Acoust. Soc. Am. **25**, 1037–1061 (1953).
[17] G. B. Thurston, L. E. Hargrove, and B. D. Cook, ''Nonlinear properties of circular orifices,'' J. Acoust. Soc. Am. **29**, 992–1001 (1957).
[18] G. B. Thurston, ''Nonlinear acoustic properties of orifices of varied shapes and edge conditions,'' J. Acoust. Soc. Am. **30**, 452–455 (1958).
[19] K. Ingard and H. Ising, ''Acoustic nonlinearity of an orifice,'' J. Acoust. Soc. Am. **42**, 6–17 (1967).
[20] Y. Ando, ''On the sound radiation from semi-infinite circular pipe of certain wall thickness,'' Acustica **19**, 219–225 (1969/70).
[21] D. K. Holger, T. A. Wilson, and G. S. Beavers, ''The inertance of a smooth-edged orifice,'' J. Acoust. Soc. Am. **51**, 1156–1163 (1972).
[22] R. L. Panton and A. L. Goldman, ''Correlation of nonlinear orifice impedance,'' J. Acoust. Soc. Am. **60**, 1390–1396 (1976).
[23] M. R. Stinson and E. A. G. Shaw, ''Acoustic impedance of small, circular orifices in thin plates,'' J. Acoust. Soc. Am. **77**, 2039–2042 (1985).
[24] A. N. Norris and I. C. Sheng, ''Acoustic radiation from a circular pipe with an infinite flange,'' J. Sound Vib. **135**, 85–93 (1989).
[25] M. Bernard and B. Denardo, ''Re-computation of Ando's approximation of the end correction for a radiating semi-infinite circular pipe,'' Acustica **82**, 670–671 (1996).
[26] P. M. Morse and K. U. Ingard, *Theoretical Acoustics* (McGraw-Hill, New York, 1968), pp. 480–490 and Chap. 9, Problem 12.
[27] Germund Dahlquist and Åke Björk, *Numerical Methods* (Prentice-Hall, Englewood Cliffs, NJ, 1974), Sec. 5.8.1.
[28] R. Piessens, E. de Doncker-Kapenga, C. Uberhuber, and D. Kahaner, *Quadpack: A Subroutine Package for Automatic Integration* (Springer, New York, 1983).

Wave motion in an isotropic elastic layer generated by a time-harmonic point load of arbitrary direction

J. D. Achenbach[a] and Y. Xu
Northwestern University, Center for Quality Engineering and Failure Prevention, 2137 Sheridan Road, Evanston, Illinois 60208

(Received 10 October 1998; accepted for publication 5 April 1999)

Wave motion in an infinite elastic layer due to the application of a time-harmonic point load of arbitrary direction, applied either internally or on one of the faces of the layer, is expressed as a sum of four expansions in Lamb-wave modes and horizontally polarized wave modes. The point load is decomposed into components normal and parallel to the plate faces. Each of these cases is decomposed into a symmetric and an antisymmetric loading case, relative to the mid-plane of the layer. The displacement solutions for the symmetric and antisymmetric cases are expressed as expansions of symmetric and antisymmetric modes, respectively. Appropriate orthogonality relations are derived from reciprocity considerations. Elastodynamic reciprocity is also used in conjunction with dummy wave modes to obtain the coefficients in the wave-mode expansion. © *1999 Acoustical Society of America.* [S0001-4966(99)02907-0]

PACS numbers: 43.20.Rz, 43.20.Bi, 43.20.Jr [DEC]

INTRODUCTION

The modes of wave propagation in an elastic layer are well known from Lamb's classical work,[1] and the Rayleigh–Lamb frequency equation, as well as the corresponding equation for horizontally polarized wave modes, have been analyzed in considerable detail.[2,3] It appears, however, that a direct way of expressing wave fields due to time-harmonic loading of a plate in terms of mode expansions has not been used, perhaps because an appropriate and usable orthogonality relation, and a suitable method to obtain the coefficients in the expansions, had so far not been recognized. Of course, wave modes have entered the solutions to problems of the forced wave motion of an elastic layer, at least for surface forces applied normally to the faces of the layer, but via the more cumbersome method of integral transform techniques and the subsequent evaluation of Fourier integrals by contour integration and residue calculus. For examples, see the work of Lyon[4] for the plane strain case, and Vasudevan and Mal[5] for axial symmetry.

In this paper the displacements excited by a time-harmonic point load of arbitrary direction, either applied internally or to one of the surfaces of the layer, are obtained directly as summations over symmetric and/or antisymmetric modes of wave propagation along the layer. This was possible by virtue of a novel application of the reciprocal identity of time-harmonic elastodynamic states. This integral identity relates two elastodynamic states of the same body. In the present paper the reciprocal identity has first been used to derive an orthogonality relation for modes of wave propagation in the layer. Next, it was used in a new manner to determine the coefficients of the expansion of the displacements by the use of a ''dummy solution.'' For the wave response to a point load the dummy solution must be carefully selected, as discussed in this paper.

[a]Electronic mail address of corresponding author: achenbach@nwu.edu

The general formulation used in the present analysis is based on a recent paper by Achenbach,[6] where the displacement fields are expressed in terms of thickness motion superposed on a carrier wave which defines the propagation along the layer; see also Weaver.[7] The carrier wave can be any solution of a reduced wave equation in the mid-plane of the layer. For the problem considered in this paper Hankel functions represent the appropriate carrier waves. The analysis of the thickness motions results in the usual Rayleigh–Lamb frequency equation.

Figure 1 shows the geometry. The displacement due to a load of arbitrary direction are expressed as the superposition of displacements due to the vertical component, P, and the horizontal component, Q. In turn, the displacements for these two loading cases are obtained as superpositions of the displacements for a symmetric and an antisymmetric problem. In this paper the displacement due to the horizontal load, Q, have been derived in detail. The displacements due to the vertical load, P, can be obtained similarly, and the expressions are given at the end of the paper.

Numerous treatments of point and line source excitation can be found in the technical literature. The review article on guided waves by Chimenti[8] has a section on this topic which lists a quite large number of papers that are based on the application of integral transforms and/or numerical techniques, particularly papers of a more recent origin and papers dealing with anisotropic plates. In addition to Refs. 4 and 5 we also mention the work of Miklowitz,[9] Weaver and Pao[10,11] and Santosa and Pao.[12] These four papers are for transient loads, and they use integral transforms, but the role of wave modes was discussed in some detail.

I. FORMULATION

Figure 1 shows a layer of homogeneous, isotropic, linearly elastic material of thickness $2h$, referred to a Cartesian coordinate system such that the x_1x_2-plane coincides with the mid-plane of the layer. The layer is subjected to a time-

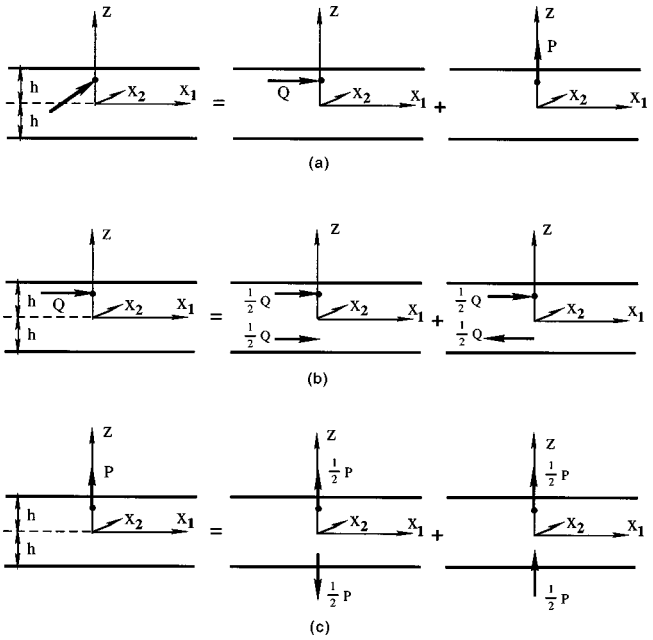

FIG. 1. Decomposition of point load problem.

harmonic point load in an arbitrary direction. Without loss of generality the coordinate system is chosen such that the load acts in the x_1z -plane. The dynamic response of the layer is sought as the superposition of the responses due to the vertical component, P, and the horizontal component, Q as indicated in Fig. 1(a). It is further convenient to split each of these two problems into two other problems whose solutions are symmetric and antisymmetric, respectively, relative to the mid-plane of the layer. These divisions are illustrated in Fig. 1(b) and (c). In this paper we will express the wave motion generated by the four loading configurations in terms of symmetric and antisymmetric modes of wave propagation in the layer.

It has been shown[6] that the Lamb-wave modes of wave propagation in the layer may be expressed in the general forms (Greek indices refer to the x_1 and x_2 axes)

$$u_\alpha^n=\frac{1}{k_n}V^n(z)\frac{\partial\varphi}{\partial x_\alpha}(x_1,x_2), \tag{1}$$

$$u_z^n=W^n(z)\varphi(x_1,x_2), \tag{2}$$

where we have omitted the time-harmonic term $\exp(i\omega t)$, k_n is a wave numberlike quantity, and $\varphi(x_1,x_2)$ is a solution of the reduced membrane wave equation in the x_1x_2-plane

$$\nabla^2\varphi+k_n^2\varphi=0. \tag{3}$$

Here $V^n(z)$ and $W^n(z)$ represent the dependence on the thickness coordinate. The modes may be separated into symmetric and antisymmetric modes relative to the mid-plane of the layer. For a given value of the circular frequency, ω, the wave number k_n is one of the many solutions of the relevant Rayleigh–Lamb frequency equation. For example for the symmetric modes we have

$$V_S^n(z)=s_1\cos(pz)+s_2\cos(qz), \tag{4}$$

$$W_S^n(z)=s_3\sin(pz)+s_4\sin(qz), \tag{5}$$

where

$$s_1=2\cos(qh), \tag{6a}$$

$$s_2=-[(k_n^2-q^2)/k_n^2]\cos(ph), \tag{6b}$$

$$s_3=-2(p/k_n)\cos(qh), \tag{6c}$$

$$s_4=-[(k_n^2-q^2)/qk_n]\cos(ph). \tag{6d}$$

Similarly for the antisymmetric modes

$$V_A^n(z)=a_1\sin(pz)+a_2\sin(qz), \tag{7}$$

$$W_A^n(z)=a_3\cos(pz)+a_4\cos(qz), \tag{8}$$

where

$$a_1=2\sin(qh), \tag{9a}$$

$$a_2=-[(k_n^2-q^2)/k_n^2]\sin(ph), \tag{9b}$$

$$a_3=2(p/k_n)\sin(qh), \tag{9c}$$

$$a_4=[(k_n^2-q^2)/qk_n]\sin(ph). \tag{9d}$$

In these expressions

$$p^2=\frac{\omega^2}{c_L^2}-k_n^2,\quad c_L^2=\frac{\lambda+2\mu}{\rho}, \tag{10a}$$

$$q^2=\frac{\omega^2}{c_T^2}-k_n^2,\quad c_T^2=\frac{\mu}{\rho}. \tag{10b}$$

In Eqs. (4)–(5) and (7)–(8), which follow from Eqs. (18)–(19) and (27)–(28) of Ref. 6, respectively, we have omitted arbitrary multiplying constants.

In addition to the Lamb-wave modes defined by Eqs. (1) and (2), we may also consider wave motions that are equivoluminal, with displacements that are parallel to the x_1x_2-plane. The corresponding wave modes are called horizontally polarized wave modes. They may be represented by

$$u_1^n=\frac{1}{l_n}U^n(z)\frac{\partial\psi}{\partial x_2}, \tag{11}$$

$$u_2^n=-\frac{1}{l_n}U^n(z)\frac{\partial\psi}{\partial x_1}, \tag{12}$$

and $u_z^n\equiv0$, where $\psi(x_1,x_2)$ is a solution of

$$\nabla^2\psi+l_n^2\psi=0. \tag{13}$$

Substitution into the displacement equation of motion shows that the displacements given by Eqs. (11) and (12) are elastodynamic displacement solutions provided that

$$\frac{d^2U^n}{dz^2}+q^2U^n=0, \tag{14}$$

where $q^2=(\omega/c_T)^2-l_n^2$. The solutions of Eq. (14), $U_S^n(z)=\cos(qz)$ and $U_A^n(z)=\sin(qz)$, represent symmetric and antisymmetric modes, respectively. The condition that the faces of the layer are free of surface tractions leads to the following relation between l_n and ω

$$q=\frac{n\pi}{2h}, \tag{15}$$

where $n=0,2,4$ for symmetric modes, and $n=1,3,5$ for antisymmetric modes. For a given value of ω, Eq. (15) provides the wave number of the nth mode, l_n.

By using Eqs. (11) and (12), the displacement components for the nth symmetric mode can be derived in polar coordinates as

$$u_r^n=\frac{1}{l_n}\cos\left(\frac{n\pi z}{2h}\right)\frac{1}{r}\frac{\partial\psi}{\partial\theta}, \tag{16}$$

$$u_\theta^n=-\frac{1}{l_n}\cos\left(\frac{n\pi z}{2h}\right)\frac{\partial\psi}{\partial r}. \tag{17}$$

II. WAVE MOTION GENERATED BY Q

Let us first consider the wave motion generated by the time-harmonic point load applied in the direction of the x_1 axis. In cylindrical coordinates ($x_1=r\cos\theta$, $x_2=r\sin\theta$,z), Eqs. (1)–(3) can be rewritten as

$$u_r=\frac{1}{k_n}V^n(z)\frac{\partial\varphi}{\partial r}(r,\theta), \tag{18}$$

$$u_\theta=\frac{1}{k}V^n(z)\frac{1}{r}\frac{\partial\varphi}{\partial\theta}(r,\theta), \tag{19}$$

$$u_z=W^n(z)\varphi(r,\theta), \tag{20}$$

$$\frac{\partial^2\varphi}{\partial r^2}+\frac{1}{r}\frac{\partial\varphi}{\partial r}+\frac{1}{r^2}\frac{\partial^2\varphi}{\partial\theta^2}+k_n^2\varphi=0. \tag{21}$$

The first point of consideration now is to select the right solution for $\varphi(r,\theta)$ of Eq. (21). For this we take guidance from the displacement solution for a time-harmonic point force, F, applied at the origin in the x_1-direction, in an unbounded solid. In a Cartesian coordinate system this solution can be written as

$$u_i=\frac{1}{k_T^2}\frac{F}{\mu}\frac{\partial}{\partial x_i}\frac{\partial}{\partial x_1}[-G(k_LR)+G(k_TR)]+\frac{F}{\mu}G(k_TR)\delta_{i1}, \tag{22}$$

where δ_{i1} is the Kronecker delta, and

$$G(k_\gamma R)=e^{-ik_\gamma R}/4\pi R, \tag{23}$$

where γ is L or T and

$$k_L^2=\omega^2/c_L^2, \tag{24a}$$

$$k_T^2=\omega^2/c_T^2, \tag{24b}$$

$$R^2=x_1^2+x_2^2+x_3^2. \tag{25}$$

The displacements in cylindrical coordinates follow from Eq. (22) as

$$u_r=\frac{F}{\mu}\left\{\frac{1}{k_T^2}\frac{\partial^2}{\partial r^2}[-G(k_LR)+G(k_TR)]+G(k_TR)\right\}\cos\theta, \tag{26}$$

$$u_\theta=\frac{F}{\mu}\left\{\frac{1}{k_T^2}\frac{1}{r}\frac{\partial}{\partial r}[G(k_LR)-G(k_TR)]-G(k_TR)\right\}\sin\theta, \tag{27}$$

$$u_z=\frac{F}{\mu}\frac{1}{k_T^2}\frac{\partial^2}{\partial z\,\partial r}[-G(k_LR)+G(k_TR)]\cos\theta, \tag{28}$$

where

$$R^2=r^2+z^2. \tag{29}$$

These solutions show a simple dependence on θ. It is to be expected that the presence of a traction-free plane parallel to the plane of r and θ does not change this dependence. This has been shown to be true by Chao[13] for a point load applied in a half-space, and it should also be true for a point load in a layer. By comparing Eqs. (18)–(20) with Eqs. (26)–(28) it then immediately follows that we should take

$$\varphi(r,\theta)=\Phi(r)\cos\theta, \tag{30}$$

where according to Eq. (21), $\Phi(r)$ must be the solution of

$$\frac{d^2\Phi}{dr^2}+\frac{1}{r}\frac{d\Phi}{dr}+\left(k_n^2-\frac{1}{r^2}\right)\Phi=0. \tag{31}$$

The solution to Eq. (31) for an outgoing wave compatible with the time factor $\exp(i\omega t)$ is

$$\Phi(k_nr)=H_1^{(2)}(k_nr). \tag{32}$$

We can equally well consider an incoming wave, i.e., a wave which converges on the origin:

$$\bar{\Phi}(k_nr)=H_1^{(1)}(k_nr). \tag{33}$$

For simplicity of notation we will use $\Phi(k_nr)$ in subsequent expressions rather than the Hankel functions. The notation of $\Phi'(k_nr)$ is used for the derivative with respect to the argument: $\Phi'(\xi)=d\Phi/d\xi$.

For the outgoing *symmetric* Lamb-wave modes, the corresponding displacements and stresses are

$$u_r^n=V_S^n(z)\Phi'(k_nr)\cos\theta, \tag{34}$$

$$u_z^n=W_s^n(z)\Phi(k_nr)\cos\theta, \tag{35}$$

$$u_\theta^n=V_S^n(z)\left(\frac{-1}{k_nr}\right)\Phi(k_nr)\sin\theta, \tag{36}$$

$$\sigma_{rz}^n=-\Sigma_{rz}^{Sn}(z)\Phi'(k_nr)\cos\theta, \tag{37}$$

$$\sigma_{zz}^n=\Sigma_{zz}^{Sn}(z)\Phi(k_nr)\cos\theta, \tag{38}$$

$$\sigma_{rr}^n=\Sigma_{rr}^{Sn}(z)\Phi(k_nr)\cos\theta-\bar{\Sigma}_{rr}^{Sn}(z)\times\left[\frac{1}{r}\Phi'(k_nr)-\frac{1}{k_nr^2}\Phi(k_nr)\right]\cos\theta, \tag{39}$$

$$\sigma_{\theta z}^n=\Sigma_{\theta z}^{Sn}(z)\left(\frac{-1}{k_nr}\right)\Phi(k_nr)\sin\theta, \tag{40}$$

$$\sigma_{r\theta}^n=\Sigma_{r\theta}^{Sn}(z)\left[-\frac{1}{r}\Phi'(k_nr)+\frac{1}{k_nr^2}\Phi(k_nr)\right]\sin\theta, \tag{41}$$

where $V_S^n(z)$ and $W_S^n(z)$ are defined by Eqs. (4) and (5), and

$$\Sigma_{rz}^{Sn}(z)=\mu[s_5\sin(pz)+s_6\sin(qz)], \tag{42}$$

$$\Sigma_{zz}^{Sn}(z)=\mu[s_7\cos(pz)+s_8\cos(qz)], \tag{43}$$

$$\Sigma_{rr}^{Sn}(r)=\mu[s_9\cos(pz)+s_{10}\cos(qz)], \tag{44}$$

$$\overline{\Sigma}^{Sn}_{rr}(z)=\mu[s_{11}\cos(pz)+s_{12}\cos(qz)], \tag{45}$$

$$\Sigma^{Sn}_{r\theta}(z)=\overline{\Sigma}^{Sn}_{rr}(z), \tag{46a}$$

$$\Sigma^{Sn}_{\theta z}(z)=-\Sigma^{Sn}_{rz}(z). \tag{46b}$$

In these expressions

$$s_5=4p\cos(qh), \tag{47a}$$

$$s_6=[(k_n^2-q^2)^2/qk_n^2]\cos(ph), \tag{47b}$$

$$s_7=[2(k_n^2-q^2)/k_n]\cos(qh), \tag{47c}$$

$$s_8=-[2(k_n^2-q^2)/k_n]\cos(ph), \tag{47d}$$

$$s_9=[2(2p^2-k_n^2-q^2)/k_n]\cos(qh), \tag{47e}$$

$$s_{10}=[2(k_n^2-q^2)/k_n]\cos(ph), \tag{47f}$$

$$s_{11}=4\cos(qh), \tag{47g}$$

$$s_{12}=-[2(k_n^2-q^2)/k_n^2]\cos(ph). \tag{47h}$$

Similarly for the *antisymmetric* Lamb-wave modes we have

$$u_r^n=V_A^n(z)\Phi'(k_nr)\cos\theta, \tag{48}$$

$$u_z^n=W_A^n(z)\Phi(k_nr)\cos\theta, \tag{49}$$

$$u_\theta^n=V_A^n(z)\left(\frac{-1}{k_nr}\right)\Phi(k_nr)\sin\theta, \tag{50}$$

$$\sigma_{rz}^n=-\Sigma_{rz}^{An}(z)\Phi'(k_nr)\cos\theta, \tag{51}$$

$$\sigma_{zz}^n=\Sigma_{zz}^{An}(z)\Phi(k_nr)\cos\theta, \tag{52}$$

$$\sigma_{rr}^n=\Sigma_{rr}^{An}(z)\Phi(k_nr)\cos\theta-\overline{\Sigma}^{An}_{rr}(z)\times\left[\frac{1}{r}\Phi'(k_nr)-\frac{1}{k_nr^2}\Phi(k_nr)\right]\cos\theta, \tag{53}$$

$$\sigma_{\theta z}^n=\Sigma_{\theta z}^{An}(z)\left(\frac{-1}{k_nr}\right)\Phi(k_nr)\sin\theta, \tag{54}$$

$$\sigma_{r\theta}^n=\Sigma_{r\theta}^{An}(z)\left[-\frac{1}{r}\Phi'(k_nr)+\frac{1}{k_nr^2}\Phi(k_nr)\right]\sin\theta, \tag{55}$$

where $V_A^n(z)$ and $W_A^n(z)$ are defined by Eqs. (7) and (8), and

$$\Sigma_{rz}^{An}(z)=\mu[a_5\cos(pz)+a_6\cos(qz)], \tag{56}$$

$$\Sigma_{zz}^{An}(z)=\mu[a_7\sin(pz)+a_8\sin(qz)], \tag{57}$$

$$\Sigma_{rr}^{An}(z)=\mu[a_9\sin(pz)+a_{10}\sin(qz)], \tag{58}$$

$$\overline{\Sigma}^{An}_{rr}(z)=\mu[a_{11}\sin(pz)+a_{12}\sin(qz)], \tag{59}$$

$$\Sigma_{r\theta}^{An}(z)=\overline{\Sigma}^{An}_{rr}(z), \tag{60a}$$

$$\Sigma_{\theta z}^{An}(z)=-\Sigma_{rz}^{An}(z). \tag{60b}$$

In these expressions,

$$a_5=-4p\sin(qh), \tag{61a}$$

$$a_6=-[(k_n^2-q^2)^2/qk_n^2]\sin(ph), \tag{61b}$$

$$a_7=[2(k_n^2-q^2)/k_n]\sin(qh), \tag{61c}$$

$$a_8=-[2(k_n^2-q^2)/k_n]\sin(ph), \tag{61d}$$

$$a_9=[2(2p^2-k_n^2-q^2)/k_n]\sin(qh), \tag{61e}$$

$$a_{10}=[2(k_n^2-q^2)/k_n]\sin(ph), \tag{61f}$$

$$a_{11}=4\sin(qh), \tag{61g}$$

$$a_{12}=-[2(k_n^2-q^2)/k_n^2]\sin(ph). \tag{61h}$$

It is of interest to check the conditions at $z=\pm h$. On the faces of the layer the surface tractions should vanish, which implies that

$$\sigma_{zz}^n(h)=\sigma_{zr}^n(h)=\sigma_{z\theta}^n(h)\equiv 0. \tag{62}$$

It may be checked that $\Sigma_{rz}^{Sn}(h)=0$ and $\Sigma_{z\theta}^{Sn}=0$ yield the Raleigh-Lamb frequency equation for symmetric modes,

$$\frac{\tan(qh)}{\tan(ph)}=-\frac{4pqk_n^2}{(k_n^2-q^2)^2}, \tag{63}$$

while $\Sigma_{zz}^{Sn}(h)=0$ is identically satisfied. Similarly $\Sigma_{zz}^{An}(h)=0$ is identically satisfied, while$\Sigma_{rz}^{An}=0$ and $\Sigma_{z\theta}^{An}(h)=0$ yield the Rayleigh–Lamb frequency equation for antisymmetric modes,

$$\frac{\tan(qh)}{\tan(ph)}=-\frac{(k_n^2-q^2)^2}{4pqk_n^2}. \tag{64}$$

For a specified value of the frequency ω, Eqs. (63) and (64) are equations for k_n. For each solution k_n, Eqs. (34)–(61) define a specific mode, i.e., a set of displacements and stresses defining symmetric or antisymmetric Lamb-wave motions of the layer.

For the horizontally polarized modes we write analogously to Eq. (30)

$$\psi(r,\theta)=\Psi(l_nr)\sin\theta, \tag{65}$$

where $\Psi(l_nr)$ follows from Eq. (13) as

$$\psi(l_nr)=H_1^{(2)}(l_nr). \tag{66}$$

For the outgoing symmetric wave modes, the corresponding displacements and stresses are

$$u_r^n=\cos\left(\frac{n\pi z}{2h}\right)\frac{1}{l_nr}\Psi(l_nr)\cos\theta, \tag{67}$$

$$u_\theta^n=-\cos\left(\frac{n\pi z}{2h}\right)\Psi'(l_nr)\sin\theta, \tag{68}$$

$$\sigma_{rr}^n=\mu\cos\left(\frac{n\pi z}{2h}\right)\left[\frac{2}{r}\Psi'(l_nr)-\frac{2}{k_nr^2}\Psi(l_nr)\right]\cos\theta, \tag{69}$$

$$\sigma_{r\theta}^n=\mu\cos\left(\frac{n\pi z}{2h}\right)\left[\Psi'(l_nr)+\left(l_n-\frac{2}{l_nr^2}\right)\Psi(l_nr)\right]\sin\theta. \tag{70}$$

The corresponding expressions for the antisymmetric modes follow by replacing $\cos(n\pi z/2h)$ by $\sin(n\pi z/2h)$.

Intuitively it is to be expected that, at least at some distance from the applied load, the wave motion generated by Q can be expressed as a summation over the symmetric and antisymmetric modes. Let us first consider the *symmetric*

problem, and write the displacement solutions as sums of symmetric Lamb-wave and horizontally polarized modes

$$u_r^{QS}=\sum_{m=0}^{\infty} A_m^S[s_1\cos(pz)+s_2\cos(qz)]\Phi'(k_m r)\cos\theta + \sum_{m=0}^{\infty} B_m^S\cos\left(\frac{m\pi z}{2h}\right)\frac{1}{l_m r}\Psi(l_m r)\cos\theta, \tag{71}$$

$$u_z^{QS}=\sum_{m=0}^{\infty} A_m^S[s_3\sin(pz)+s_4\sin(qz)]\Phi(k_m r)\cos\theta, \tag{72}$$

$$u_\theta^{QS}=\sum_{m=0}^{\infty} A_m^S[s_1\cos(pz)+s_2\cos(qz)]\left(\frac{-1}{k_m r}\right)\Phi(k_m r) \times\sin\theta-\sum_{m=0}^{\infty} B_m^S\cos\left(\frac{m\pi z}{2h}\right)\Psi'(l_m r)\sin\theta, \tag{73}$$

where s_1, s_2, s_3 and s_4 are defined by Eqs. (6a)–(6d). For a specified value of ω, k_m and l_m are the solutions of Eqs. (63) and (15), respectively. It is of importance to note that for the radial displacement the contribution due to horizontally polarized waves is $O(1/r)$ as compared to the Lamb-wave contribution. For the circumferential displacement the Lamb-wave contribution is $O(1/r)$ as compared to the horizontally polarized part. Only the Lamb-wave contributes to the displacement in the z-direction.

The expressions given by Eqs. (71)–(73) represent outgoing waves, but it remains to determine the constants A_m^S and B_m^S such that u_r^{QS}, u_z^{QS} and u_θ^{QS} correspond to the prescribed load. Next we propose a simple method to determine these constants.

III. USE OF ELASTODYNAMIC RECIPROCITY

The reciprocal identity relates two elastodynamic states of the same body. For two distinct time-harmonic states, labeled by superscripts A and B: f_i^A, u_i^A and f_i^B, u_i^B, where f_i^A and f_i^B are body forces, we have for a region V with boundary S (Ref. 14, p. 34)

$$\int_V (f_i^A u_i^B - f_i^B u_i^A)\,dV=\int_S (u_i^A\sigma_{ij}^B-u_i^B\sigma_{ij}^A)n_j\,dS, \tag{74}$$

where n_j are the components of the outward normal.

Let us consider the reciprocal identity in the annular domain $|z|\leqslant h$, $a\leqslant r\leqslant b$. For the two solutions we choose two symmetric Lamb-wave modes, mode m with wave number k_m and mode n with wave number k_n. Since the singularities of these modes are at $r=0$, the left-hand side of Eq. (74) vanishes, and we have

$$Q_{mn}(b)-Q_{mn}(a)=0, \tag{75}$$

where

$$Q_{mn}(b)=b\int_0^{2\pi}\int_{-h}^{h}\{[u_r^m\sigma_{rr}^n-u_r^n\sigma_{rr}^m]+[u_z^m\sigma_{rz}^n-u_z^n\sigma_{rz}^m] +[u_\theta^m\sigma_{r\theta}^n-u_\theta^n\sigma_{r\theta}^m]\}d\theta\,dz. \tag{76}$$

In Eq. (76) all field variables are evaluated at $r=b$. By substitution of the displacements and stresses for symmetric modes we obtain

$$Q_{mn}^S(b)=\pi b[I_{nm}^S\Phi'(k_m b)\Phi(k_n b) - I_{mn}^S\Phi'(k_n b)\Phi(k_m b)], \tag{77}$$

where we have used that

$$\overline{\Sigma}_{rr}^{Sn}=2\mu V_S^n \tag{78a}$$

and

$$\Sigma_{r\theta}^{Sn}=2\mu V_S^n, \tag{78b}$$

while I_{mn}^S is defined as

$$I_{mn}^S=\int_{-h}^{h}[\Sigma_{rr}^{Sm}(z)V_S^n(z)+\Sigma_{rz}^{Sn}(z)W_S^m(z)]dz. \tag{79}$$

Equation (75) then becomes

$$I_{nm}^S[\Phi'(k_m b)\Phi(k_n b)-\Phi'(k_m a)\Phi(k_n a)] - I_{mn}^S[\Phi'(k_n b)\Phi(k_m b)-\Phi'(k_n a)\Phi(k_m a)]=0. \tag{80}$$

This equation must be satisfied for arbitrary values of a and b. For $m\neq n$ this is possible only if $I_{mn}^S=I_{nm}^S\equiv 0$. However, I_{mn}^S and I_{nm}^S represent the same relation between two modes, and thus we conclude

$$I_{mn}^S\equiv 0 \quad \text{for} \quad m\neq n. \tag{81}$$

By using the displacements and stresses for the antisymmetric modes we obtain in the same manner

$$I_{mn}^A\equiv 0 \quad \text{for} \quad m\neq n, \tag{82}$$

where

$$I_{mn}^A=\int_{-h}^{h}[\Sigma_{rr}^{Am}(z)V_A^n(z)+\Sigma_{rz}^{An}(z)W_A^m(z)]dz. \tag{83}$$

Equations (81) and (82) are orthogonality conditions.

Next we consider Eq. (74) for two symmetric horizontally polarized modes. The result may again be written as Eqs. (75) and (76), where now

$$Q_{mn}^S(b)=\mu\pi b J_{mn}^S[-l_n\Psi'(l_m b)\Psi(l_n b) + l_m\Psi'(l_n b)\Psi(l_m b)], \tag{84}$$

where

$$J_{mn}^S=\int_{-h}^{h}\cos\left(\frac{m\pi z}{2h}\right)\cos\left(\frac{m\pi z}{2h}\right)dh=h\,\delta_{mn} \tag{85}$$

except for $m=n=0$ when

$$J_{00}^S=2h. \tag{86}$$

IV. DETERMINATION OF COEFFICIENTS

The coefficients A_m^S in Eqs. (71)–(73) can be determined by a second use of the reciprocal identity, Eq. (74). This time we consider the identity for the domain $0\leqslant r\leqslant b$, $-h\leqslant z\leqslant h$, $0\leqslant\theta\leqslant 2\pi$. For state A we choose the displacement and stress fields generated by the force Q, for simplicity first applied at $z_0=0$, $r=0$, $\theta=0$. The corresponding displace-

ments are represented by Eqs. (71)–(73). For state B we choose a dummy solution in the form of a single symmetric Lamb-wave mode consisting of the sum of an outgoing and a converging wave:

$$u_r^n = \tfrac{1}{2} V_s^n(z)[\Phi'(k_n r) + \overline{\Phi}'(k_n r)]\cos\theta, \tag{87}$$

$$u_z^n = \tfrac{1}{2} W_S^n(z)[\Phi(k_n r) + \overline{\Phi}(k_n r)]\cos\theta, \tag{88}$$

$$u_\theta^n = \frac{1}{2} V_S^n(z)\left(\frac{-1}{k_n r}\right)[\Phi(k_n r) + \overline{\Phi}(k_n r)]\sin\theta. \tag{89}$$

The displacements in Eqs. (87)–(89) are bounded at $r=0$. It can be verified that the left-hand side of Eqs. (76) becomes

$$Qu_r(0,0,0) = \tfrac{1}{2} Q V_s^n(0). \tag{90}$$

To evaluate the right-hand side at $r=b$, we recall the observation made under Eq. (73) that the corresponding field quantities for the Lamb-wave modes and the horizontally polarized modes are of different orders for large r. This implies that for sufficiently large b the product terms of the two kinds of modes can be neglected because they are $O(1/b)$. The consequence is that the dummy solutions Eqs. (87)–(89) only provide contributions in conjunction with the Lamb-wave terms in Eqs. (71)–(73). In that light the right-hand side of Eq. (74) can be evaluated by using the result for $r=b$, Eq. (77), for the first term in Eqs. (87)–(89). The second term yields similar expressions, and the complete result is

$$QV_S^n(0) = \sum_{m=0}^{\infty} A_m^S[Q_{mn}^S(b) + T_{mn}^S(b)], \tag{91}$$

where $Q_{mn}^S(b)$ follows from Eq. (77), and

$$T_{mn}^S(b) = \pi b[I_{nm}^S \Phi'(k_m b)\overline{\Phi}(k_n b) - I_{mn}^S \overline{\Phi}'(k_n b)\Phi(k_m b)]. \tag{92}$$

Inspection of Eqs. (77) shows that $Q_{mn}^s(b)$, vanishes for both $m \neq n$ and $m=n$. On the other hand, $T_{mn}^S(b)$ vanishes only for $m \neq n$. For $m=n$, Eq. (92) can be further simplified by using the following identity for Hankel functions (Ref. 15, p. 198):

$$\frac{d}{d\xi} H_v^{(1)}(\xi) H_v^{(2)}(\xi) - H_v^{(1)}(\xi) \frac{d}{d\xi} H_v^{(2)}(\xi) = \frac{4i}{\pi\xi}. \tag{93}$$

We obtain

$$T_{nn}^S = \frac{4i}{k_n} I_{nn}^S, \tag{94}$$

and Eq. (93) yields

$$A_n^S = \frac{k_n}{4i} \frac{QV_S^n(0)}{I_{nn}^S}, \tag{95}$$

where I_{nn}^S follows from Eq. (79) as

$$I_{nn}^S = \mu[c_1^s \cos^2(ph) + c_2^s \cos^2(qh)] \tag{96}$$

The constants c_1^S and c_2^S are

$$c_1^s = \frac{(k_n^2 - q^2)(k_n^2 + q^2)}{2q^3 k_n^3}[2qh(k_n^2 - q^2) - (k_n^2 + 7q^2)\sin(2qh)], \tag{97}$$

$$c_2^S = \frac{k_n^2 + q^2}{pk_n^3}[4k_n^2 ph + 2(k_n^2 - 2p^2)\sin(2ph)]. \tag{98}$$

Next we go through the same procedure, but now we choose for state B a dummy solution in the form of a single symmetric horizontally polarized mode consisting of the sum of an outgoing and a converging wave

$$u_r^n = \frac{1}{2}\cos\left(\frac{n\pi z}{2h}\right)\frac{1}{l_n r}[\Psi(l_n r) + \overline{\Psi}(l_n r)]\cos\theta, \tag{99}$$

$$u_\theta^n = -\frac{1}{2}\cos\left(\frac{n\pi z}{2h}\right)[\Psi'(l_n r) + \overline{\Psi}'(l_n r)]\sin\theta, \tag{100}$$

where $\Psi(l_n r)$ is defined by Eq. (66), and

$$\overline{\Psi}(l_n r) = H_1^{(1)}(l_n r). \tag{101}$$

Proceeding through the same steps as for the Lamb-wave modes we find

$$B_n^S = \frac{1}{4i}\frac{Q}{\mu J_{nn}}, \quad n = 0,2,4,\ldots. \tag{102}$$

The analogous result for the antisymmetric modes is

$$B_n^A = \frac{1}{4i}\frac{Q}{\mu J_{nn}}, \quad n = 1,3,5,\ldots. \tag{103}$$

V. HORIZONTAL LOAD AT ARBITRARY POSITION

Now we consider the case that the horizontal load is applied at a position $z=z_0$. It is then convenient to split the problem in two problems, a symmetric and an antisymmetric one, as illustrated in Fig. 1. For the symmetric problem the left-hand side of Eq. (74) must then be replaced by two contributions, each involving $\frac{1}{2}Q$ and, considering the Lamb-wave modes, either $V_S^n(z_0)$ or $V_S^n(-z_0)$. However, $V_s^n(z_0) = V_s^n(-z_0)$ and thus the two contributions are equal. It can then be verified that Eq. (95) becomes

$$A_n^S = \frac{k_n}{4i}\frac{QV_S^n(z_0)}{I_{nn}^S}. \tag{104}$$

For the antisymmetric problem the two forces of magnitude $\frac{1}{2}Q$ are in opposite directions, but the normal displacements are also, and it then easily follows that

$$A_n^A = \frac{k_n}{4i}\frac{QV_A^n(z_0)}{I_{nn}^A}, \tag{105}$$

$$I_{nn}^A = \mu[c_1^A \sin^2(ph) + c_2^A \sin^2(qh)], \tag{106}$$

where

$$c_1^A = \frac{(k_n^2 - q^2)(k_n^2 + q^2)}{2q^3 k_n^3}[2qh(k_n^2 - q^2) + (k_n^2 + 7q^2)\sin(2qh)], \tag{107}$$

$$c_2^A=\frac{k_n^2+q^2}{pk_n^3}[4k_n^2ph-2(k_n^2-2p^2)\sin(2ph)]. \tag{108}$$

The constants for the horizontally polarized modes can be modified analogously from Eqs. (102) and (103) as

$$B_n^S=\frac{1}{4i}\frac{\cos(n\pi z_0/2h)}{\mu J_{nn}}\ Q, \tag{109}$$

$$B_n^A=\frac{1}{4i}\frac{\sin(n\pi z_0/2h)}{\mu J_{nn}}\ Q. \tag{110}$$

VI. SUMMARY OF SOLUTIONS

As illustrated in Fig. 1, the displacement due to a load of arbitrary direction can be expressed as the superposition of displacements due to the vertical component, P, and the horizontal component, Q:

$$\mathbf{u}(r,\theta,z)=\mathbf{u}^P(r,\theta,z)+\mathbf{u}^Q(r,\theta,z). \tag{111}$$

Each of these solutions can be obtained as the superposition of a symmetric and an antisymmetric solution

$$\mathbf{u}^P=\mathbf{u}^{PS}+\mathbf{u}^{PA}, \tag{112a}$$

$$\mathbf{u}^Q=\mathbf{u}^{QS}+\mathbf{u}^{QA}. \tag{112b}$$

The displacement due to the horizontal load, Q, has been derived in some detail in the preceding sections. The displacements due to the vertical load can be obtained in a similar manner. Here we summarize all results.

horizontal load:

$$u_r^{QS}=\sum_{m=0}^{\infty}A_m^SV_S^m(z)\left[H_0^{(2)}(k_mr)-\frac{1}{k_mr}H_1^{(2)}(k_mr)\right]\cos\theta + \sum_{m=0}^{\infty}B_m^S\cos\left(\frac{m\pi z}{2h}\right)\frac{1}{l_mr}H_1^{(2)}(l_mr)\cos\theta, \tag{113}$$

$$u_z^{QS}=\sum_{m=0}^{\infty}A_m^SW_S^m(z)H_1^{(2)}(k_mr)\cos\theta, \tag{114}$$

$$u_\theta^{QS}=\sum_{m=0}^{\infty}A_m^SV_s^m(z)\left(\frac{-1}{k_mr}\right)H_1^{(2)}(k_mr)\sin\theta - \sum_{m=0}^{\infty}B_m^S\cos\left(\frac{m\pi z}{2h}\right)\times\left[H_0^{(2)}(l_mr)-\frac{1}{l_mr}H_1^{(2)}(l_mr)\right]\sin\theta, \tag{115}$$

where A_m^S follows from Eq. (104) and B_m^S from Eq. (109). Also

$$u_r^{QA}=\sum_{m=0}^{\infty}A_m^AV_A^m(z)\left[H_0^{(2)}(k_mr)-\frac{1}{k_mr}H_1^{(2)}(k_mr)\right]\cos\theta + \sum_{m=0}^{\infty}B_m^A\sin\left(\frac{m\pi z}{2h}\right)\frac{1}{l_mr}H_1^{(2)}(l_mr)\cos\theta, \tag{116}$$

$$u_z^{QA}=\sum_{m=0}^{\infty}A_m^AW_A^m(z)H_1^{(2)}(k_mr)\cos\theta, \tag{117}$$

$$u_\theta^{QA}=\sum_{m=0}^{\infty}A_m^AV_S^m(z)\left(\frac{-1}{k_mr}\right)H_1^{(2)}(k_mr)\sin\theta - \sum_{m=0}^{\infty}B_m^A\sin\left(\frac{m\pi z}{2h}\right)\times\left[H_0^{(2)}(l_mr)-\frac{1}{l_mr}H_1^{(2)}(l_mr)\right]\sin\theta, \tag{118}$$

where A_m^A follows from Eq. (105) and B_m^A from Eq. (110).

vertical load:

$$u_r^{PS}=-\sum_{m=0}^{\infty}C_m^SV_S^m(z)H_1^{(2)}(k_mr), \tag{119}$$

$$u_z^{PS}=\sum_{m=0}^{\infty}C_m^SW_S^m(z)H_0^{(2)}(k_mr), \tag{120}$$

where

$$C_m^S=\frac{k_m}{4i}\frac{PW_S^m(z_0)}{I_{mm}^S}, \tag{121}$$

$$u_r^{PA}=-\sum_{m=0}^{\infty}C_m^AV_A^m(z)H_1^{(2)}(k_mr), \tag{122}$$

$$u_z^{PA}=\sum_{m=0}^{\infty}C_m^AW_A^m(z)H_0^{(2)}(k_mr), \tag{123}$$

where

$$C_m^A=\frac{k_m}{4i}\frac{PW_A^m(z_0)}{I_{mm}^A}. \tag{124}$$

The terms I_{mm}^S and I_{mm}^A are given by Eqs. (96) and (106), respectively.

It is of interest to check the reciprocity of the solutions given by Eqs. (113)–(124). The simplest check of reciprocity for the case that P is applied at $r=0$, $z=0$, and Q is applied at $r=r$, $z=0$. In that case the displacement u_r at $r=r$, $z=0$, $\theta=0$ due to P should be just the same as the displacement u_z at $r=r$, $z=0$, $\theta=\pi$. It is easily verified that this equality is indeed satisfied.

VII. COMPARISON WITH PLANE STRESS SOLUTION

Equations (26)–(28) give the displacements in an unbounded solid for a point load applied at the origin of the coordinate system and pointing in the x_1-direction. Similarly to a derivation given by Achenbach *et al.*[14] (p. 28), it can be shown that the corresponding displacements due to a line load can be obtained from these expressions by replacing

$$G(k_\gamma R)\quad\text{by}\quad -\frac{i}{4}H_0^{(2)}(k_\gamma r). \tag{125}$$

This replacement results in displacement expressions for the case of plane strain. The other two-dimensional case, the case of plane stress, only differs in that different elastic constants must be used. For a comparison of the two-dimensional formulations for plane strain and plane stress, we refer to Achenbach,[6] p. 59. From the two sets of equa-

tions it can be seen that solutions for plane stress follow from the ones for plane strain by replacing

$$\lambda+2\mu \quad \text{by} \quad \frac{2\mu\lambda}{\lambda+2\mu} \tag{126}$$

or equivalently

$$c_L^2 \quad \text{by} \quad c_0^2, \quad \text{where} \quad c_0^2=4\frac{\kappa^2-1}{\kappa^2}c_T^2. \tag{127}$$

Here c_0 is the so-called plate velocity, and

$$\kappa=c_L/c_T. \tag{128}$$

The plane stress case is an approximation which is valid for a thin plate at low frequencies and small wave numbers. For simplicity we will take r sufficiently large so that terms of $O(1/r)$ can be ignored. For a thin plate with a uniform through-the thickness line load, the displacements in the r- and θ-directions then follow from Eqs. (26) and (28) as

$$u_r \cong -\frac{F}{\mu}\frac{c_T^2}{c_0^2}\frac{i}{4}H_0^{(2)}(k_0 r)\cos\theta, \tag{129}$$

$$u_\theta \cong \frac{F}{\mu}\frac{i}{4}H_0^{(2)}(k_T r)\sin\theta. \tag{130}$$

Here the plate velocity c_0 is defined by Eq. (127), and

$$k_0=\omega/c_0. \tag{131}$$

Now let us consider the lowest modes in the expansions (113) and (115) in the limit of $h\to 0$. For small wave numbers the frequency and wave number of the lowest symmetric mode are related by[6]

$$\omega \cong 2\left(\frac{\kappa^2-1}{\kappa^2}\right)^{1/2} c_T k_0. \tag{132}$$

After some manipulation we then find for small h

$$I_{00}^S \cong 128\mu\left(\frac{\kappa^2-1}{\kappa^2}\right)^3 k_0 h, \tag{133}$$

$$V_S^0 \cong 4\frac{\kappa^2-1}{\kappa^2}. \tag{134}$$

From Eq. (104) the constant A_0^S is then obtained as

$$A_0^S \cong \frac{1}{64i}\frac{1}{\mu}\left(\frac{\kappa^2}{\kappa^2-1}\right)^2\frac{Q}{2h}, \tag{135}$$

and thus from Eq. (113)

$$u_r \cong -\frac{Q}{2h}\frac{1}{\mu}\frac{\kappa^2}{\kappa^2-1}\frac{i}{16}H_0^{(2)}(k_0 r)\cos\theta. \tag{136}$$

Using $c_0=2[(\kappa^2-1)/\kappa^2]^{1/2}c_T$, Eq. (129) can be rewritten as

$$u_r \cong -\frac{Q}{2h}\frac{1}{\mu}\frac{c_T^2}{c_0^2}\frac{i}{4}H_0^{(2)}(k_0 r)\cos\theta. \tag{137}$$

Equations (129) and (137) show that the two radial displacements agree, since $Q/2h$ is equivalent to F.

For the circumferential displacement Eq. (115) yields for the lowest mode as $h\to 0$

$$u_\theta \cong \frac{Q}{2h}\frac{1}{\mu}\frac{i}{4}H_0^{(2)}(k_T r)\sin\theta. \tag{138}$$

Again Eq. (138) agrees with Eq. (130).

ACKNOWLEDGMENTS

This work was carried out in the course of research sponsored by the Office of Naval Research under Contract No. N00014-89-J-1362.

[1] H. Lamb, ''Waves in an elastic plate,'' Proc. R. Soc. London, Ser. A **93**, 114–128 (1917).
[2] R. D. Mindlin, ''Waves and vibrations in isotropic elastic plates,'' in *Structural Mechanics*, edited by J. N. Goodier and N. J. Hoff (Pergamon, New York, 1960), pp. 199–232.
[3] J. D. Achenbach, *Wave Propagation in Elastic Solids* (North Holland, Amsterdam, 1973).
[4] R. H. Lyon, ''Response of an elastic plate to localized driving force,'' J. Acoust. Soc. Am. **27**, 259–265 (1955).
[5] N. Vasudevan and A. K. Mal, ''Response of an elastic plate to localized transient sources,'' J. Appl. Mech. **52**, 356–362 (1985).
[6] J. D. Achenbach, ''Lamb waves as thickness vibrations superimposed on a membrane carrier wave,'' J. Acoust. Soc. Am. **103**, 2283–2286 (1998).
[7] R. L. Weaver, ''Diffuse waves in finite plates,'' J. Sound Vib. **94**, 319–335 (1984).
[8] D. E. Chimenti, ''Guided waves in plates and their use in materials characterization,'' Appl. Mech. Rev. **50**, 247–284 (1997).
[9] J. Miklowitz, ''Transient compressional waves in an infinite elastic plate or elastic layer overlying a rigid half-space,'' J. Appl. Mech. **29**, 53–60 (1962).
[10] R. L. Weaver and Y.-H. Pao, ''Axisymmetric elastic waves excited by a point source in a plate,'' J. Appl. Mech. **49**, 821–836 (1982).
[11] R. L. Weaver and Y.-H. Pao, ''Spectra of transient waves in elastic plates,'' J. Acoust. Soc. Am. **72**, 1933–1941 (1982).
[12] F. Santosa and Y.-H. Pao, ''Transient axially asymmetric response of an elastic plate,'' Wave Motion **11**, 271–296 (1989).
[13] C. C. Chao, ''Dynamical response of an elastic half-space to tangential surface loadings,'' J. Appl. Mech. **27**, 559–567 (1960).
[14] J. D. Achenbach, A. K. Gautesen, and H. McMaken, *Ray Methods for Waves in Elastic Solids* (Pitman Advanced, Boston, 1982).
[15] N. W. McLachlan, *Bessel Functions for Engineers* (Oxford University Press, London, 1961).

Finite-element analysis of the nonlinear propagation of high-intensity acoustic waves

C. Campos-Pozuelo
Instituto de Acústica, CSIC, Serrano, 144, 28006 Madrid, Spain

B. Dubus
Institut d'Electronique et de Microélectronique du Nord, département ISEN, UMR CNRS 9929, 41 boulevard Vauban, 59046 Lille Cedex, France

J. A. Gallego-Juárez
Instituto de Acústica, CSIC, Serrano, 144, 28006 Madrid, Spain

(Received 23 October 1997; accepted for publication 7 March 1999)

This paper deals with a three-dimensional numerical procedure based on the finite-element method for the modeling of finite-amplitude progressive acoustic waves. The method can predict the nonlinear propagation of acoustic fields produced by sources of arbitrary geometry. Based upon a perturbation method, a second-order analytical study is developed and the numerical procedure is formulated. Basic equations are derived and their ranges of validity established. The analytical validation of the numerical development is presented. An experimental validation is also carried out for the nonlinear acoustic field radiated by a stepped-plate transducer. © *1999 Acoustical Society of America.* [S0001-4966(99)00407-5]

PACS numbers: 43.25.Cb [MAB]

INTRODUCTION

High-intensity applications of sonic energy in industrial processing have increased during the last few years.[1] The applications of intense sound are based on nonlinear effects produced by finite-amplitude pressure variations. As is well-known, the propagation of acoustic waves can be described by linear laws only in the case of infinitesimal amplitudes. When the acoustical pressure is of finite amplitude, the equations of motion become nonlinear. This paper deals with the propagation of waves of finite, but moderate, amplitude in fluids.

The propagation of finite-amplitude waves through fluids involves, besides the nonlinear distortion of the waveform, which is the topic of this article, other associated second-order effects such as acoustic radiation pressure, acoustic streaming, and cavitation in liquids. These effects are not treated in this paper.

Classical works can be found in the literature about analytical approximations to describe the nonlinear behavior of progressive waves.[2] There are several reviews on the development of nonlinear acoustics,[3,4] and the main contributions in this field were compiled and commented upon by R. T. Beyer in 1984.[2] A recapitulation on this subject has been recently published by M. F. Hamilton.[5] Fubini,[6] in 1935, gave the first explicit solution referred to a plane wave. Analytical models referred to cylindrical and spherical waves can also been found in classical works.[7] More recently, M. F. Hamilton[5] and K. E. Froysa[8] have given analytical solutions for harmonic generation in weakly nonlinear Gaussian beams.

Approximate methods have been used by different authors for solving the nonlinear equations.[4] The perturbation method, which is used in this paper, is one of the most extended. It has proved to be an efficient tool in the evaluation of nonlinear equations. The description of this method can be widely found in the literature.[3–5,9–11]

The purpose of this work was to develop a numerical method to study the radiated field from high-intensity three-dimensional acoustical sources of arbitrary geometry.

Three-dimensional models have been developed referring to linear acoustic fields by using numerical methods. In particular, the finite-element method (FEM) has been widely used to model three-dimensional elastic or piezo-electric radiating structures.[12–14] Other numerical methods such as the boundary-element method (BEM),[15] alone or in combination with FEM (BEM–FEM), have also proved to be very powerful for linear radiation modeling.[16] The interest of extending these tools for realistic three-dimensional modeling of the nonlinear field is evident. This is the goal of the present work.

Nonlinear numerical models of parametric acoustic arrays, as well as piston transducers radiating in water, can be found in the literature.[17–19] In Refs. 17 and 18, the effects of nonlinearity, diffraction, and absorption are all considered of equal order of magnitude. In Ref. 19, a theoretical and experimental study of the near field of an axisymmetric array is presented. Three-dimensional nonlinear propagation models using the angular spectrum method have also been recently published.[20] In this method, predictions are based upon the measured pressure field at a parallel plane to the source, i.e., modeling needs of some previous experimental knowledge. In a recent review paper written by J. H. Ginsberg and M. F. Hamilton,[21] about computational methods in nonlinear acoustics, numerical models in the time and frequency domains are presented and discussed. The approximations detailed refer to one-dimensional plane, spherical, and cylindrical waves as well as numerical algorithms for directional three-dimensional waves. These algorithms are based on the

Khokhlov–Zabolotskaya–Kuznetsov and nonlinear progressive-wave equations, which are only valid for sources in which the characteristic dimension a verifies $ka \gg 1$ (k is the wave number).

In this article, a finite element three-dimensional model of the nonlinear propagation of acoustic waves is proposed. No restriction on the source geometry and/or vibration form is imposed. The model is implemented in the code ATILA initially developed by Decarpigny *et al.*[12–14] for studying linearly elastic and piezo-electric radiating structures. The procedure basically consists of applying a perturbation method to linearize the equations and then using the classical finite-element method. Second-order approximation is developed; this is the only restriction of the method. The numerical model is validated by comparing with analytical results obtained for several simple specific cases. In addition, experimental validation of the method is carried out by modeling and measuring the high-intensity acoustic field radiated by a stepped-plate transducer.

I. DEVELOPMENT OF THE NUMERICAL MODEL

In this section, the numerical method developed to model the three-dimensional propagation of finite, but moderate, amplitude acoustic waves is presented. Only wave propagation in unlimited media is considered. The theoretical basis and its limitations are presented first; the numerical method is detailed afterwards.

A. Theory: The fundamental equations of the problem. A method of successive approximations

The study considers finite-amplitude progressive, initially harmonic, waves in a homogeneous fluid. Only second-order terms in the parameter $(p_{ac}/\rho_0 c_0^2)$ (acoustic Mach number) are considered, p_{ac} being the acoustic pressure, ρ_0 the density at the instant at which the medium is at rest and undeformed, and c_0 the small-signal sound speed. Lagrangian coordinates are considered.

In order to obtain a three-dimensional second-order wave equation, the isentropic equation of state and equations expressing the conservation of mass (the continuity equation) and momentum are considered.[3,4] These equations can be respectively formulated as follows:

$$p = P\left(\frac{\rho}{\rho_0}\right)^{\gamma} - Q, \tag{1}$$

$$\frac{\rho_0 - \rho}{\rho} = \boldsymbol{\nabla}\cdot\mathbf{u}, \tag{2}$$

$$\rho_0 \frac{\partial^2 \mathbf{u}}{\partial t^2} = -\boldsymbol{\nabla} p, \tag{3}$$

where p is the pressure, ρ is the density of the fluid, $\mathbf{u}$ is the displacement, γ is the ratio of specific heats, $P=(\rho_0 c_0^2/\gamma)$ and Q is a constant depending on the considered fluid. Dissipation mechanisms are ignored because only free-field propagation and not very long distances are considered.[22]

Equation (1) can be approximated by expanding it in a Taylor series, retaining terms up to second order

$$\rho = \rho_0 + a_1(p-p_0) + \frac{a_2}{2}(p-p_0)^2, \tag{4}$$

where $a_1=(1/c_0^2)=(\rho_0/\gamma P)$, $a_2=-(P\gamma(\gamma-1)/\rho_0^2 c_0^6)$, and $(p-p_0)$ is the acoustic pressure.

From Eqs. (4), (2), and (3), we obtain the second-order wave equation

$$-\frac{1}{c_0^2}\frac{\partial^2 p}{\partial t^2} + \nabla^2 p = -\frac{\beta}{\rho_0 c_0^4}\frac{\partial^2 (p-p_0)^2}{\partial t^2}, \tag{5}$$

where $\beta=(\gamma+1)/2$ is the nonlinearity parameter of the fluid which determines the nonlinear characteristic of the propagation medium. For common fluids, the value of this parameter can be found in the literature (see Ref. 3, for example). The parabolic wave Eq. (5) is consistent with the expression proposed by Westervelt[23] and the one used by Garret *et al.*[19]

To solve the second-order Eq. (5), the successive approximations method was applied. This method assumes a solution for the acoustic pressure consisting of the addition of two terms in the form

$$p - p_0 = p_1 + p_2, \tag{6}$$

where p_1 represents the first-order approximation and p_2 the second-order correction, p_2 being much smaller than p_1 ($p_2 \ll p_1$). Neglecting the terms of third or higher orders, from Eq. (6), it can be written

$$\left(\frac{p-p_0}{\rho_0 c_0^2}\right)^2 \cong \left(\frac{p_1}{\rho_0 c_0^2}\right)^2.$$

Substituting Eq. (6) in Eq. (5), and taking into account that the linear solution p_1 verifies

$$-\frac{1}{c_0^2}\frac{\partial^2 p_1}{\partial t^2} + \nabla^2 p_1 = 0, \tag{7}$$

the following equation is obtained for the second-order correction, p_2:

$$-\frac{1}{c_0^2}\frac{\partial^2 p_2}{\partial t^2} + \nabla^2 p_2 = -\frac{\beta}{\rho_0 c_0^4}\frac{\partial^2 p_1^2}{\partial t^2}. \tag{8}$$

Considering the particular case of an initially generated harmonic wave,

$$p_1 = \cos(\omega t - \mathbf{kr}) f(\mathbf{r}), \tag{9}$$

and making use of Eq. (9), Eq. (8) becomes

$$\frac{4\omega^2}{c_0^2} P_2 + \nabla^2 P_2 = \frac{2\omega^2 \beta}{\rho_0 c_0^4} P_1^2, \tag{10}$$

where $p_1 = e^{j\omega t} P_1$ and $p_2 = e^{j2\omega t} P_2$. Equation (10) is a linear nonhomogeneous equation which can be solved by classical methods. For the simplest cases (plane, spherical, or cylindrical waves) it can be solved analytically. However, when acoustical fields of more complex geometry are considered, numerical evaluation becomes necessary. A numerical solution of this equation based on the finite-element method is proposed to be able to solve three-dimensional acoustical problems of arbitrary geometry.

First, the physical limitations of the theory are considered. The first and most important limitation derives from the

TABLE I. Values of the second- and third-order terms in water for different acoustic pressure levels. p_{ac} is the pressure level expressed in dB (Ref. $P_0 = 10^{-6}$ Pa), $p_{ac}/\rho_0 c_0^2$ is the ratio between the second order and the linear terms, and $(p_{ac}/\rho_0 c_0^2)^2$ is the ratio between the third order and the linear one.

	dB			
p_{ac}	180	220	250	300
$p_{ac}/\rho_0 c_0^2$	−127	−87	−56.5	−7
$(p_{ac}/\rho_0 c_0^2)^2$	−254	−174	−113	−14

second-order approximation, which prescribes the moderate perturbation condition and neglects all terms of third or higher order. In Table I, the values of the second- and third-order terms for different pressure levels in water are compared with the values of the linear term. Thus, for a given acoustical pressure, p_{ac}, the values of the second-order term divided by the linear one, $p_{ac}/\rho_0 c_0^2$, as well as the values of the third-order term divided by the linear one, $(p_{ac}/\rho_0 c_0^2)^2$, are reported. All quantities are expressed in dB (reference pressure 1 μPa).

From this table, the wide application range of the procedure in the case of the water can be noted. Even for very high pressure values (250 dB), the neglected term remains much smaller than the fundamental (113 dB smaller).

The same calculations carried out for air are displayed in Table II (reference pressure 20 μPa). For this case, the acoustic Mach number increases faster, so the perturbations are relatively significant even if the absolute values of the pressure are smaller. Thus, the range of application of the proposed method depends on the fluid considered. The value of the nonlinearity parameter, which has not been taken into account in this evaluation, is of the same order of magnitude for both fluids (3.5 for water and 1.3 for air).

A well-known feature of the propagation of a finite-amplitude wave is the increase of the wave distortion with distance.[6] Even for low-amplitude waves, the high-order components reach a certain intensity if the distance to the source is sufficiently long. This fact gives a spatial limitation for the application of the present approximation. In fact, it is only valid for distances much shorter than the discontinuity distance (distance for the formation of a shock wave). A more precise estimation could be given considering, specifically, the different types of waves. As an example of distances of applicability, the amplitude of the third-order component for a plane wave is calculated and compared with the linear and second-order component generated with a pressure amplitude of 150 dB (ref. 2×10^{-5} Pa) in air at 23 600 Hz. Results show that for this case, where the nonlinearities grow very quickly, at 12 cm from the source we have a third order 38 times smaller than the linear one, while the second-order one is only 6 times smaller.

TABLE II. Values of the second- and third-order terms in water for different acoustic pressure levels. p_{ac} is the pressure level expressed in dB (Ref. $P_0 = 2\times10^{-5}$ Pa), $p_{ac}/\rho_0 c_0^2$ is the ratio between the second order and the linear terms, and $(p_{ac}/\rho_0 c_0^2)^2$ is the ratio between the third order and the linear one.

	dB			
p_{ac}	160	170	180	190
$p_{ac}/\rho_0 c_0^2$	−37.5	−27	−17.5	−7.5
$(p_{ac}/\rho_0 c_0^2)^2$	−75	−54	−35	−15

However, this increase of the distortion is, of course, limited by the dissipation of acoustical energy, which affects the higher harmonics much more. The attenuation effect leads to the saturation of the acoustical waves.

B. Numerical method

The finite-element method is not detailed here because its general description can be found in many books (see, for example, Ref. 24). The finite-element formulation of the fluid structure problem leads to the following set of equations (see the Appendix):

$$\begin{bmatrix} [K_{uu}]-\omega^2[M_s] & -[L] \\ \rho^2 c^2 \omega^2 [L]^T & [H]-\omega^2[M] \end{bmatrix} \begin{bmatrix} \tilde{U} \\ \tilde{P} \end{bmatrix} = \begin{bmatrix} \tilde{f} \\ \rho c^2 \tilde{\Psi} \end{bmatrix}, \quad (11)$$

where $[K_{uu}]$ and $[M_s]$ are, respectively, the solid stiffness and consistent mass matrices, $\tilde{U}$ is the vector of the nodal values of the solid displacement field, $\tilde{f}$ is the vector of the nodal values of the applied forces, $\tilde{P}$ is the vector of the nodal values of the pressure field, $\tilde{\Psi}$ is the vector of the nodal values of the pressure-normal derivative on the fluid domain boundary, $[L]$ is the interface connectivity matrix, $[H]$ and $[M]$ are, respectively, the fluid stiffness and consistent mass matrices, and the superscript T means transposed.

The finite-element modeling of a radiating structure is performed by surrounding this structure with a limited fluid domain, upon the external boundary of which a nonreflection condition is prescribed for the acoustic field. This condition is implemented with the help of damping elements which are attached to the external boundary.

Second-order corrections in the radiated acoustic field, according to the theory developed in Sec. I A, imply modifications of the matricial Eq. (11). In Eq. (10), the nonlinear behavior of the fluid is represented by the right-hand side term $(2\omega^2\beta/\rho_0 c_0^4)P_1^2 = f_B$, which mathematically is equivalent to a mass source term in the fluid.[25]

The application of the weighted residual method to Eq. (10) leads to the following integral equation:[24]

$$\int\int\int_{\Omega_f} \left(\frac{\partial \nu}{\partial x_i}\frac{\partial p_2}{\partial x_i} - 4k^2 \nu p_2 - \frac{2\omega^2\beta\nu p_1^2}{\rho_0 c_f^4} \right) d\Omega_f - \int\int_{\Gamma_p \cup \Gamma_\psi \cup \Gamma_\infty} \nu \Psi_2 \, d\Gamma = 0, \quad (12)$$

where ν is an arbitrary scalar function. In the following, $\nu = p_2$ is chosen.

When discretization is applied, Eq. (12) is written

$$\sum_e \left\{ \frac{1}{\rho_0 c_f^2} \tilde{P}_2^{eT}([H^e]-\omega^2[M_l^e])\tilde{P}_2^e - \tilde{P}_2^{eT}\tilde{\Psi}_2^e - \tilde{P}_2^{eT}\tilde{R}_B^e \right\} = 0, \quad (13a)$$

with

$$\tilde{R}_B^e = -\frac{2\omega^2\beta}{\rho_0 c_f^4} \int\int\int_{\Omega_f^e} [N_p^e][N_p^e]\tilde{P}_1^e[N_p^e]\tilde{P}_1^e \, d\Omega_f^e. \quad (13b)$$

After assembling and applying the variational principle, the final expression is obtained

$$\{[H]-4\omega^2[M_l]\}\tilde{P}_2=\rho_0 c_f^2\tilde{\Psi}_2+\rho_0 c_f^2\tilde{R}_B. \tag{14}$$

In this equation, only the fluid terms of Eq. (11) are included because nonlinearities are considered only in the fluid medium, i.e., linear behavior is assumed for the acoustical source. $\tilde{P}_2$ is a vector that contains the nodal values of the second-order component of the pressure field. The $\tilde{P}_1$ vector is calculated using Eq. (11). After combining Eqs. (11) and (13b), we obtain the loading term $\tilde{R}_B$, which can be introduced into Eq. (14) to calculate $\tilde{P}_2$. The same boundary conditions for the linear modeling are considered, including the nonreflection condition upon the external boundary (see the Appendix).

The FEM solution is implemented in FORTRAN. On an HP workstation (9000/735, RISC 99 MHz), the runtimes for an axisymmetrical problem using parabolic elements (15 118 degrees of freedom) are 340 s for the calculation of the linear solution and 103 s for the calculation of the second-order correction.

II. ANALYTICAL VALIDATION OF THE NUMERICAL MODEL

In this section, an analytical validation of the model for the nonlinear propagation of some well-defined acoustic waves is presented. The results from the analytical study are compared with the numerical results in order to verify the validity of the new method proposed in this paper.

A. Analytical models for plane, spherical, and cylindrical waves

1. Plane waves

The simplest and best-studied case is the plane wave propagation. Various explicit solutions can be found in the literature (for example, an extensive and very complete theoretical treatment of plane progressive sound waves was made by Blackstock[26]). The successive approximations method used here can be found in Ref. 6.

For harmonic excitation of amplitude P_0, the acoustic pressure is assumed, according to Eq. (6), as an addition of two terms which have the form

$$p_1=P_0 e^{j(\omega t-kx)} \tag{15}$$

for the linear approximation, and

$$p_2=-\frac{\beta P_0^2}{4\rho_0 c_0^2}e^{j2(\omega t-kx)}(1+j2kx) \tag{16}$$

for the second-order correction.

The amplitude of the second harmonic increases linearly with increasing distance from the source. Consequently, the sinusoidal progressive wave is distorted because of the addition of the increasing second harmonic to the fundamental during propagation.

2. Spherical waves

A rigid sphere of radius r_0 whose surface undergoes constant amplitude harmonic oscillations is considered as a source of waves of pressure amplitude P_0. The well-known solution of the linear wave equation with these boundary conditions is:[22]

$$P_1=P_0 r_0\frac{e^{-jk(r-r_0)}}{r}. \tag{17}$$

Writing the wave Eq. (10) in spherical coordinates and inserting (17) in the nonhomogeneous term, the following wave equation for the second-order correction, P_2, is obtained:

$$\frac{4\omega^2}{c_0^2}P_2+\nabla^2 P_2=\frac{2\beta k^2 P_0^2 r_0^2}{\rho_0 c_0^2}\frac{e^{-j2k(r-r_0)}}{r^2}. \tag{18}$$

The following particular solution for Eq. (18) is proposed:

$$P_2=\left(A\frac{\log r/r_0}{r}+\sum_{n=2}^{\infty}\frac{C_n}{r^n}\right)e^{-j2k(r-r_0)}, \tag{19}$$

where A and C_n are indefinite constants. Substituting (19) into Eq. (18) leads to

$$A=j\frac{\beta P_0^2 r_0^2 k}{2\rho_0 c_0^2},\quad C_n=\frac{(-1)^n(n-2)!}{(j4k)^{n-1}}A. \tag{20}$$

For $r\geqslant 3\lambda$, all the terms in the series

$$\sum_{n=2}^{\infty}\frac{C_n}{r^n}$$

are much smaller than the principal term

$$A\frac{\log r/r_0}{r},$$

this series can then be neglected. The condition of rigid sphere

$$\left(\left[\frac{\partial P_2}{\partial r}\right]_{r=r_0}=0\right)$$

implies

$$P_2=A\left(\log\frac{r}{r_0}+B\right)\frac{e^{-j2k(r-r_0)}}{r}, \tag{21}$$

where $B=1/(1+j2kr_0)$.

According to Eq. (6), the second-order solution for a spherical wave is written as

$$p=P_1 e^{j\omega t}+P_2 e^{j2\omega t}. \tag{22}$$

From Eq. (21), we see that the second harmonic for spherical wave propagation decreases with the distance from the source. However, the ratio between second harmonic and fundamental increases with that distance.

3. Cylindrical waves

A rigid cylinder of infinite length and radius r_0 acting as a harmonic acoustic source of pressure amplitude P_0 is considered. The well-known linear solution is[22]

$$P_1 = A[J_0(kr) - jY_0(kr)], \tag{23}$$

where

$$A = \frac{P_0}{J_0(kr_0) - jY_0(kr_0)},$$

J_0 is the cylindrical Bessel function of the first kind, and Y_0 is the cylindrical Bessel function of the second kind. At distances from the cylinder larger than a wavelength, the Eq. (23) can be approximated by[22]

$$P_1 \cong A\sqrt{\frac{2}{k\pi r}}\, e^{-j(kr-\pi/4)}. \tag{24}$$

The second-order wave equation in cylindrical coordinates is written as

$$\frac{4\omega^2}{c_0^2} P_2 + \frac{1}{r}\frac{d}{dr} P_2 + \frac{d^2}{dr^2} P_2 = \frac{4\beta k A^2}{\pi \rho_0 c_0^2}\, \frac{e^{-j2(kr-\pi/4)}}{r}. \tag{25}$$

The following particular solution for Eq. (25) is proposed:

$$P_2 = f(r)\, \frac{e^{-j2kr}}{\sqrt{r}}. \tag{26}$$

Substituting Eq. (26) in Eq. (25) and neglecting all the terms of the order $1/(kr)^{5/2}$ leads to

$$P_2 = -C\, \frac{e^{-j2kr}}{j4k}\left(2 + \frac{1}{j4kr} - \frac{1}{2(j4kr)^2}\right) - C_2 \frac{e^{j2kr}}{j4k\sqrt{r}} + C_3 \frac{e^{-j2kr}}{\sqrt{r}}, \tag{27}$$

where

$$C = \frac{4\beta k A^2}{\pi \rho_0 c_0^2}\, e^{j(\pi/2)}$$

and C_2 and C_3 are two integration constants to be determined from the boundary conditions. Since only progressive waves are considered here, C_2 is set to zero. C_3 is calculated by prescribing boundary conditions (rigid cylinder). The total second-order solution is written as in Eq. (22).

For the cylindrical wave, we observe an intermediate behavior between plane and spherical waves: the second harmonic is almost constant while the fundamental decreases slower than for a spherical wave. The ratio between second harmonic and fundamental amplitude increases with the distance to the source.

B. Numerical–analytical comparison

By using the previous analytical model, the pressure distribution of the fundamental and second harmonic for plane, spherical, and cylindrical waves in water is calculated. These results are displayed in Fig. 1. As can be easily seen, the proportion of harmonics always increases with the distance to the source, and this increase is less important in the waves in which, for the same vibration amplitude of the source, the acoustic energy density is lower.

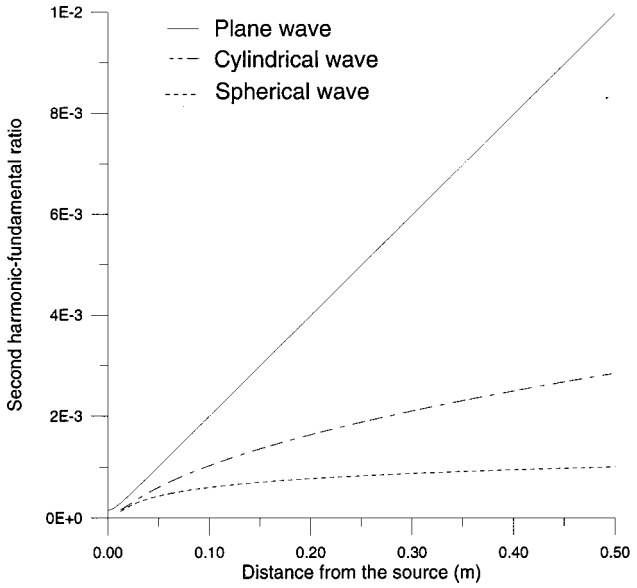

FIG. 1. Second harmonic-fundamental ratio versus distance from the source for progressive plane, spherical, and cylindrical waves in water ($\beta = 3.5$). Initial pressure $P_0 = 4 \times 10^5$ Pa, frequency $f = 15\,000$ Hz. (Reference pressure, 10^{-6} Pa.)

The new numerical model is applied for the calculation of the fundamental and second harmonic in plane, spherical, and cylindrical wave propagation. All calculations are made with the assumptions and limitations above mentioned.

Figure 2 shows a comparison between analytical and numerical results for the fundamental and second harmonic pressure amplitudes of a plane wave. It is apparent that excellent agreement is obtained.

The comparison between the analytical and numerical

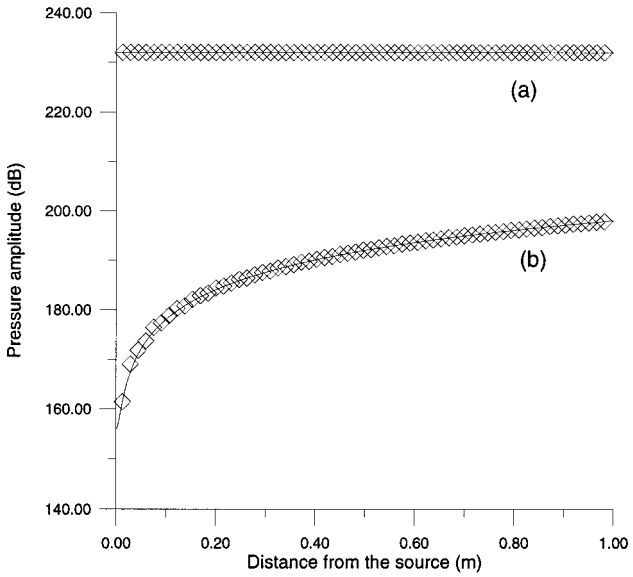

FIG. 2. Comparison between numerical ($\diamond$) and analytical (———) results for a plane wave in water ($\beta = 3.5$). (a) Fundamental. (b) Second harmonic. Initial pressure $P_0 = 4 \times 10^5$ Pa, frequency $f = 15\,000$ Hz. (Reference pressure, 10^{-6} Pa.)

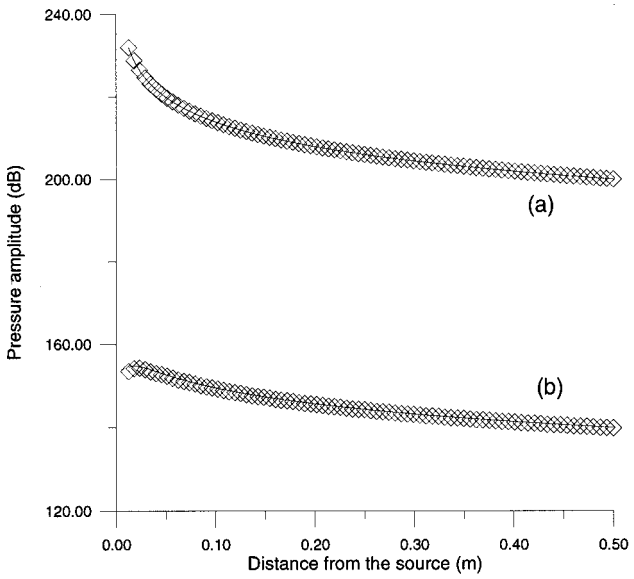

FIG. 3. Comparison between numerical (◇) and analytical (———) results for a spherical wave in water ($\beta=3.5$). (a) Fundamental. (b) Second harmonic. Initial pressure $P_0=4\times10^5$ Pa, frequency $f=15\,000$ Hz. (Reference pressure, 10^{-6} Pa.)

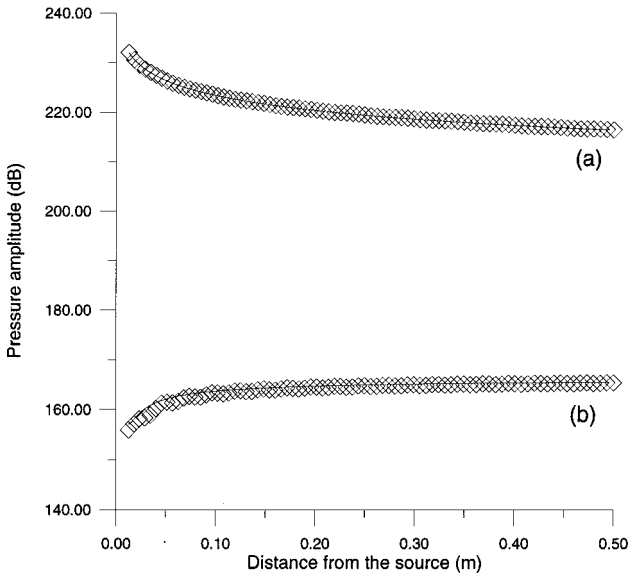

FIG. 4. Comparison between numerical (◇) and analytical (———) results for a cylindrical wave in water ($\beta=3.5$). (a) Fundamental. (b) Second harmonic. Initial pressure $P_0=4\times10^5$ Pa, frequency $f=15\,000$ Hz. (Reference pressure, 10^{-6} Pa.)

results for a spherical wave is shown in Fig. 3. Again, it is clear that a very good agreement is obtained.

The analytical–numerical comparison for a cylindrical wave is shown in Fig. 4. Once more, the agreement is very good.

III. EXPERIMENTAL VALIDATION

The nonlinear propagation of finite-amplitude waves in air is experimentally studied. A high-directional transducer is designed and constructed in order to have a high concentration of energy and thus, observable nonlinear effects.

A. Experimental study

The experimental setup for measuring frequency components of the acoustic pressure at different points is shown in Fig. 5. It mainly consists of a power transducer with an electronic driving system to generate the acoustical field and data acquisition equipment.

The electronic driving system implements a feedback device to automatically adjust the excitation frequency to the transducer resonance frequency.[27] The basic structure of the transducer is shown in Fig. 5. It consists essentially of a circular plate of stepped shape driven at its center by a piezoelectric vibrator. The vibrator itself consists of a piezoelectric element of transduction in a sandwich arrangement, and a solid horn which acts as a vibration amplifier. The longitudinal vibration, generated by the transducer element and amplified by the mechanical amplifier, drives the radiating plate, which vibrates flexurally in its first axisymmetrical mode. The radiating plate (6-cm diameter) is made of titanium alloy (Ti 6Al 4V) in order to have intense displacements without ultrasonic fatigue problems.[28] The elements of

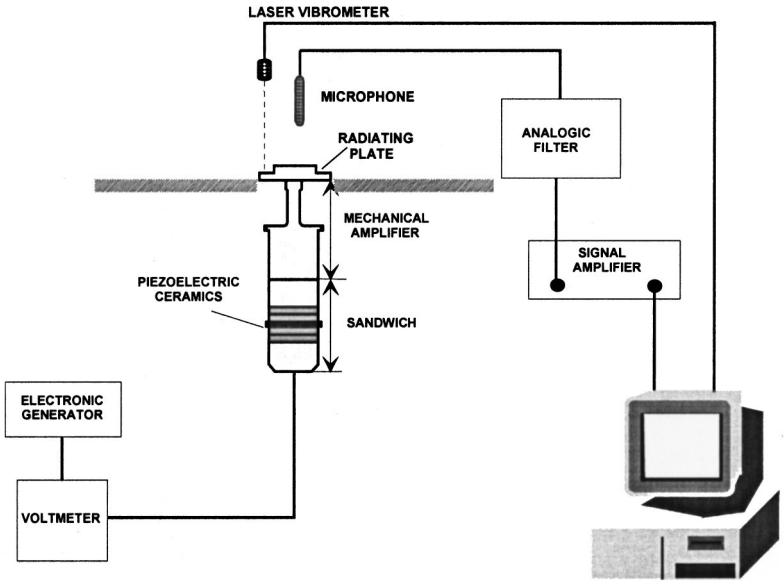

FIG. 5. Experimental setup.

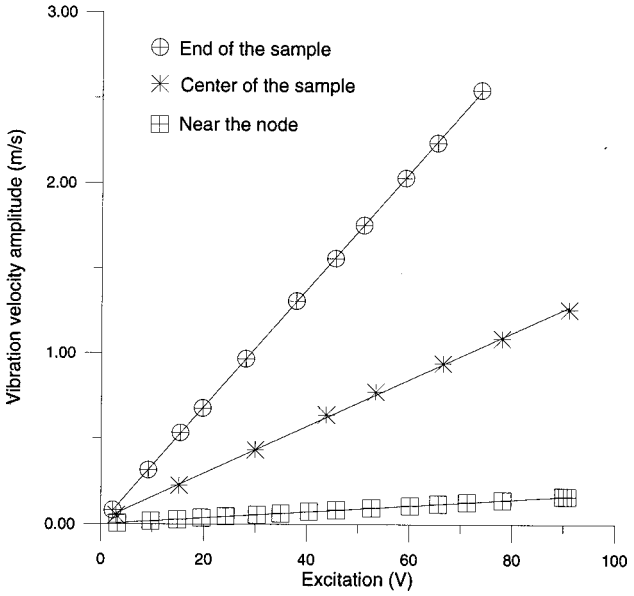

FIG. 6. Vibration velocity versus voltage excitation at different points on the radiator surface. Frequency $f=23\,600$ Hz.

the transducer are calculated to be resonant at the working frequency (23 600 Hz). The specific profile of the plate generates a directional piston-like radiation pattern which allows the production of high-intensity acoustic levels.[29]

The acoustic-pressure distribution and wave shapes are measured by using a Brüel & Kjaer condenser microphone type 4138 in an anechoic room. An automatic system is used to move the microphone. The signal is stored in a PC and Fourier analysis is performed in order to quantify the amplitudes of the harmonic components.

Measurements of the vibration displacement distribution and wave shape in the radiating plate of the transducer are also carried out by using a laser vibrometer, in order to calibrate it and verify the linearity of its behavior. All measurements are carried out in the linear range of the transducer. The obtained results are shown in Fig. 6, which displays the vibration amplitude at different points along a diameter of the plate versus electric excitation. A reasonably linear behavior is observed.

Figure 7 displays the measured acoustic field radiated by the transducer at the fundamental frequency (23 600 Hz). The directional piston-like radiation of the transducer is observed.

Figure 8 shows the measured acoustic-pressure distribution of the second harmonic in the space irradiated by the stepped-plate transducer. The second harmonic radiation pattern is even more directional that the fundamental one. The width of the main lobe is of 12 deg for the fundamental (measured at -3 dB from the maximum) and of 7 deg for the second harmonic. It should be noted that this value is not far from the square of the fundamental (7.9 deg) as obtained in Ref. 30.

Because of the piston-like radiation of the transducer, this experimental case is intermediate between plane and spherical waves.

Figures 9 and 10 show the experimental variation of the fundamental and second-harmonic amplitudes as a function of excitation at different points along the acoustic propagation axis (fundamental frequency, 23 600 Hz). All the measurements are carried out within the near field of the transducer. A linear variation of the fundamental is observed while the second harmonic shows a parabolic increase with excitation. The linear behavior of the fundamental confirms that, in the limits of pressures and distances in which measurements are conducted, the approximation assumed in Eq. (6) is valid. In the experimental working conditions, the discontinuity distance is approximately 50 cm for plane waves, and on the order of several kilometers for spherical waves (source radius $r_0=3\times10^{-2}$).[31]

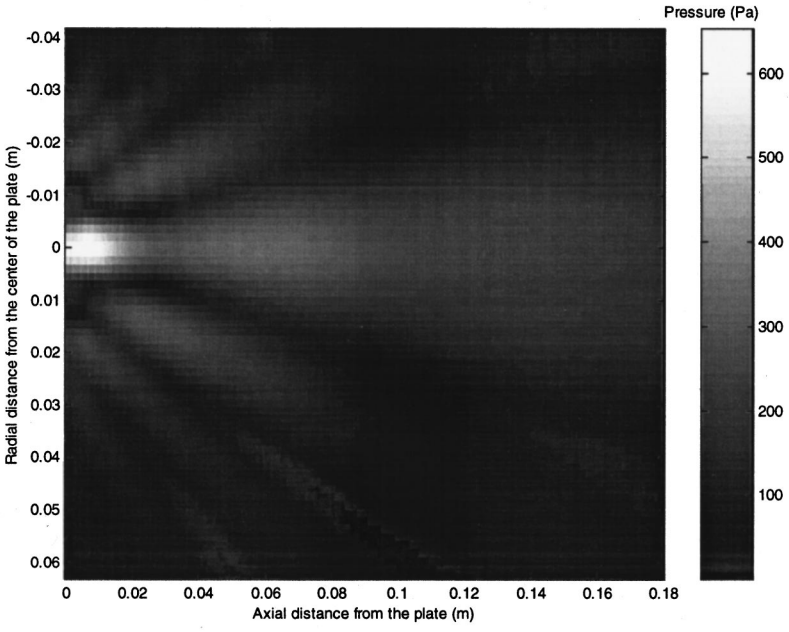

FIG. 7. Measured acoustic field of the transducer at the fundamental frequency (23 600 Hz). Excitation voltage, 50 V.

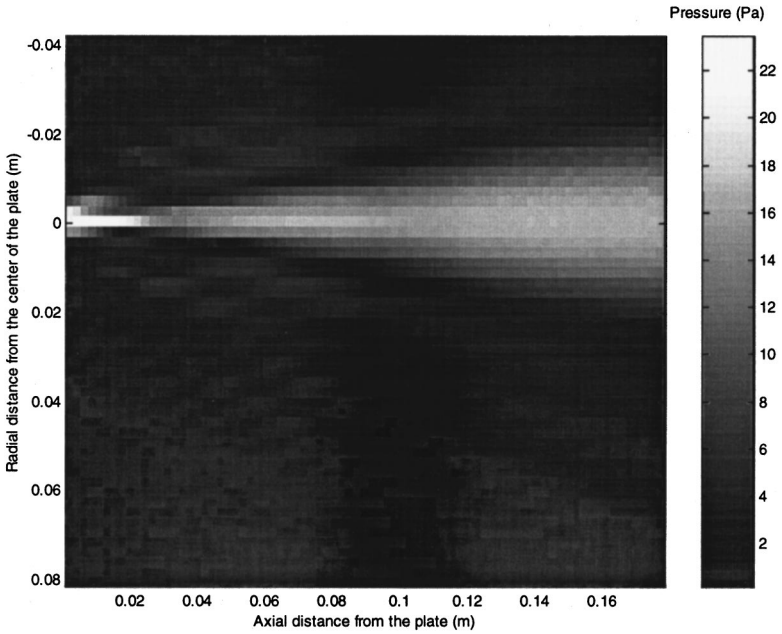

FIG. 8. Measured pressure distribution of the second harmonic (47 200 Hz) in the space irradiated by the transducer. Excitation voltage, 50 V.

B. Numerical–experimental comparison

To obtain numerical results, the finite-element procedure is applied to the study of the vibrational behavior and the nonlinear radiation of the previously described transducer. The transducer is represented by the radiating plate with a prescribed mechanical excitation at its center. Taking into account the symmetry of the problem, an axisymmetrical analysis is carried out. The finite-element mesh is shown in Fig. 11 where Γ represents the external surface. The actual mesh observes the $\lambda/4$ criterion in air, i.e., it is constituted of parabolic elements smaller than a quarter wavelength of the radiation in the propagation medium. The actual sides of all elements are equal or less than 1.8×10^{-3} m.

Figure 12 shows the comparison of the measured linear distribution of displacements in the radiating plate of the transducer with the numerical results. The good agreement obtained is a first experimental verification of the validity of the finite-element mesh used. Figure 13 shows the comparison of the numerical and experimental data for the sound-pressure distribution of the fundamental and second harmonic along the acoustic axis. The error bars indicate dispersion in the experimental data. The good agreement again obtained represents an experimental confirmation of the validity of the numerical nonlinear modeling method presented here.

IV. CONCLUSIONS

A numerical method for studying the nonlinear three-dimensional propagation of high-intensity acoustic waves

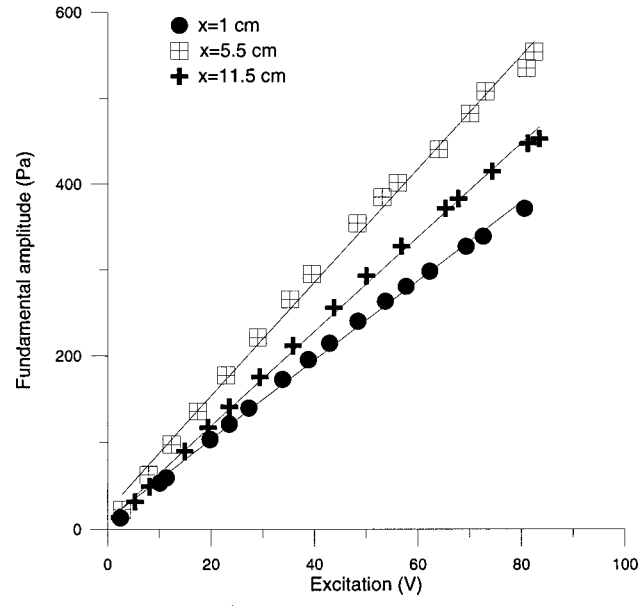

FIG. 9. Measured fundamental pressure amplitude versus excitation at different points along the acoustic axis.

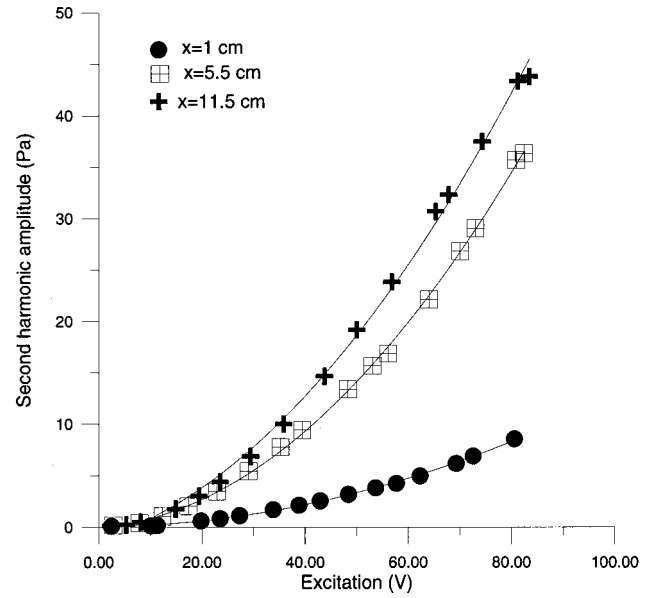

FIG. 10. Measured second-harmonic pressure amplitude versus excitation at different points along the acoustic axis.

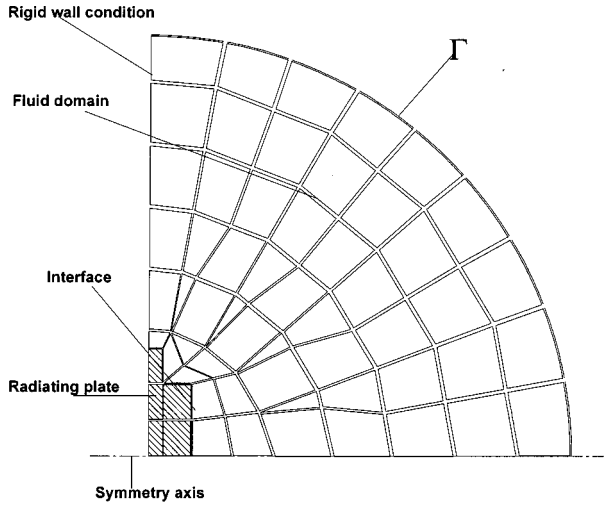

FIG. 11. Scheme of the finite-element mesh.

has been presented. It is based upon a combination of a second-order perturbation theory and the finite-element method. The new method has been applied to different cases, and the obtained results have been compared to analytical as well as experimental results. The good agreement obtained in all cases shows the validity of the numerical method, which allows one to model the nonlinear acoustic field radiated from any real source. The only restrictions are derived from the second-order approximation and computer limitations.

Modeling the nonlinear field of actual transducers opens up new possibilities in transducer design for industrial processing, where high-intensity effects are important and nonlinear behavior cannot be neglected. Thus, the method presented here can be an excellent tool to improve the design of high-power transducers and to analyze the influence of their geometry and elastic features on the nonlinear radiated field. Other applications such as modeling parametric arrays are also potentially interesting.

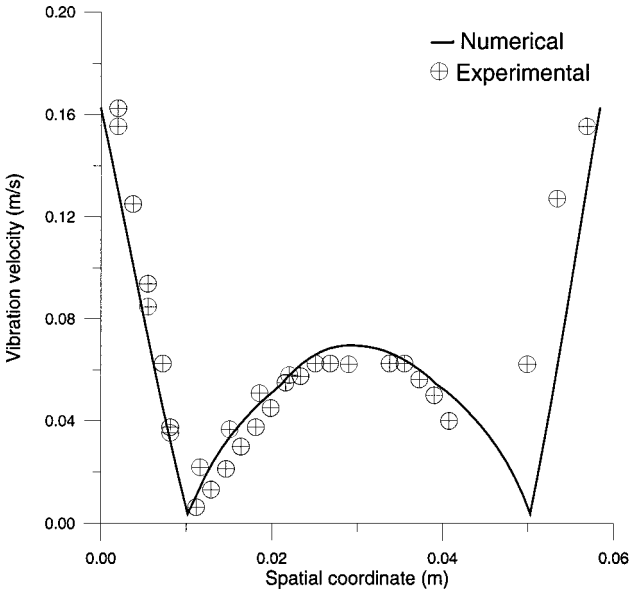

FIG. 12. Experimental–numerical comparison of the vibration velocity distribution along a diameter of the radiating plate.

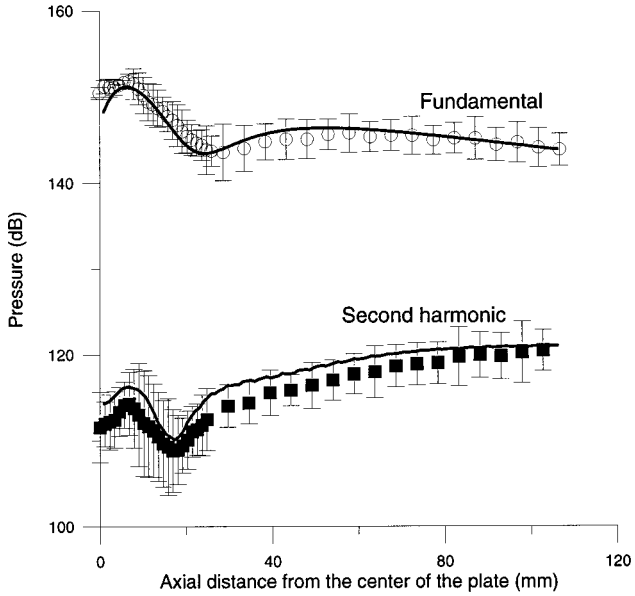

FIG. 13. Experimental numerical comparison of the fundamental and second-harmonic pressure amplitudes along the acoustic axis, expressed in dB (Reference pressure, 2×10^{-5} Pa). Fundamental frequency, 23 600 Hz.

ACKNOWLEDGMENTS

This research was supported by a postdoctoral fellowship of the DGICT (State Secretary of Universities and Research) Ref No.: EX94 70735053 and a post-doctoral contract of the CSIC (Higher Council for Scientific Research). The work was developed within the frame of the Projects CICYT-AMB96-A211-CO2 and BRITE/EURAM No. BRPR-CT96-0157. The authors would like to thank Dr. L. Elvira-Segura for his very valuable help in doing experiments.

APPENDIX: FINITE-ELEMENTS FORMULATION OF LINEAR ACOUSTIC WAVE PROPAGATION FOR AN OPEN FLUID

For a homogeneous, compressible, and infinite fluid Ω_f, (sound velocity c_f and density ρ_f), described in the frame of linear acoustics, the acoustic pressure p verifies in the frequency domain

$$\nabla^2 p + k^2 p = 0, \tag{A1}$$

where k is the wave number. Boundary conditions of Dirichlet type (prescribed pressure on the boundary domain Γ_p)

$$p = p^0, \tag{A2}$$

or of Neumann type (prescribed normal derivative of pressure on the boundary domain Γ_Ψ)

$$n_i \frac{\partial p}{\partial x_i} = \psi^0, \tag{A3}$$

are considered, $\vec{n}$ being the normal vector to Γ_Ψ. Γ_p and Γ_Ψ are oriented toward the fluid.

In the far field, Sommerfeld's radiation conditions prescribe that $\lim_{r\to\infty}(rp)$ is finite and

$$\lim_{r\to\infty}\left[r\left(jkp+\frac{\partial p}{\partial r}\right)\right]=0,$$

r being the distance to the acoustical center.

A. Variational formulation and discretization

When building a finite-element representation of the problem considered, the infinite extension of Ω_f is the main difficulty. The method consists of limiting Ω_f by a surface Γ pointing outwards, on which a reasonable boundary condition is prescribed. We consider a spherical surface Γ whose radius is large enough to verify Sommerfeld's conditions. Equations (A1), (A2), and (A3) are the Euler equation and the boundary conditions associated to the functional L_f, respectively,

$$L_f=\frac{1}{\rho_0\omega^2}\int\int\int_{\Omega_f}\frac{1}{2}\left[\left(\frac{\partial p}{\partial x_i}\right)^2-k^2p^2\right]d\Omega_f - \frac{1}{\rho_0\omega^2}\int\int_{\Gamma_\rho\cup\Gamma_\Psi\cup\Gamma\infty}p\psi\,d\Gamma. \tag{A4}$$

The solution of the problem is the minimum of L_f. The spatial discretization is performed by meshing the fluid domain in elements connected by nodes. The pressure p at a point in the element is related to the nodal values of the pressure $\tilde{P}^e$ by the interpolation functions

$$p=[N_p^e]\tilde{P}^e, \tag{A5}$$

where $[N_p^e]$ is a matrix constructed from the interpolation functions. From (A4) and (A5), L_f is written

$$L_f=\sum_e\left\{\frac{1}{2\rho_0^2c_f^2\omega^2}\tilde{P}^{eT}([H^e]-\omega^2[M^e])\tilde{P}^e - \frac{1}{\rho_0\omega^2}\tilde{P}^{eT}\tilde{\Psi}^e\right\}, \tag{A6}$$

where

$$[H^e]=\int\int\int_{\Omega_f^e}\rho_0c_f^2[B_p^e]^T[B_p^e]d\Omega_f^e,$$

$$[M^e]=\int\int\int_{\Omega_f^e}\rho_0[N_p^e]^T[N_p^e]d\Omega_f^e,$$

$$\tilde{\Psi}^e=\int\int_{\Gamma^e}[N_p^e]^T\psi$$

and $[B_p^e]$ is a matrix obtained from the derivatives of interpolation functions. After minimizing with respect to each nodal value and assembling, the linear system of equations is obtained,

$$\{[H]-\omega^2[M]\}\tilde{P}=\rho_0c_f^2\tilde{\Psi}. \tag{A7}$$

B. Damping elements

As Γ is located in the far field, the pressure and its normal derivative are related by the spherical wave relation

$$\frac{\partial p}{\partial r}=-\left(\frac{1}{r}+jk\right)p. \tag{A8}$$

This condition corresponds to the damping of the monopolar contribution of the outgoing wave. More elaborate conditions absorbing successive components of the pressure-field multipolar expansion are possible.[12]

After spatial discretization, Eq. (A8) is written on Γ

$$\tilde{\Psi}=\frac{1}{\rho_0c_f^2}[G]\tilde{P}. \tag{A9}$$

Combining (A7) and (A9) leads to the final set of equations

$$\{[H]-\omega^2[M]-[G]\}\tilde{P}=\rho_0c_f^2\tilde{\Psi}_{\text{int}}, \tag{A10}$$

where $\tilde{\Psi}_{\text{int}}$ denotes nodal values of $\tilde{\Psi}$ excluding the nodes located on Γ.

[1] J. A. Gallego-Juárez, ''Transducer needs for macrosonics,'' in *Power Transducers for Sonics and Ultrasonics*, edited by B. Hamonic and J. N. Decarpigny (Springer, Berlin), pp. 35–47 (1990).
[2] R. T. Beyer, ''Nonlinear acoustics in fluids,'' *Benchmark Papers in Acoustics Series* (Van Nostrand Reinhold, New York, 1984).
[3] L. Bjorno, ''Nonlinear acoustics,'' in *Acoustics and Vibration Progress*, Vol. 2, edited by R. W. B. Stephens and H. G. Leventhall (Chapman and Hall, London, 1976), pp. 101–198.
[4] R. T. Beyer, ''Nonlinear acoustics,'' in *Physical Acoustics*, edited by W. P. Mason (Academic, New York, 1965), Vol. II, Part B, pp. 231–332.
[5] M. F. Hamilton, ''Nonlinear effects in sound beams,'' in *Encyclopedia of Acoustics*, edited by Malcolm J. Crocker (Wiley, New York, 1997), Vol. I, pp. 249–256.
[6] E. Fubini-Ghiron, ''Anomalies in the propagation of an acoustic wave of larger amplitude,'' Alta Freq. **4**, 532–581 (1935). English version by R. T. Beyer in Ref. 2.
[7] D. T. Blackstock, ''On plane, spherical, and cylindrical sound waves of finite amplitude in lossless fluids,'' J. Acoust. Soc. Am. **36**, 217–219 (1964).
[8] K. E. Froysa, ''Weakly nonlinear propagation of a pulsed sound beam,'' J. Acoust. Soc. Am. **95**, 123–130 (1994).
[9] M. A. Breazeale and J. Philip, in *Physical Acoustics*, edited by W. P. Mason and R. N. Thurston (Academic, Orlando, 1984), Vol. XVII, pp. 1–60.
[10] C. Campos-Pozuelo and J. A. Gallego-Juárez, ''Finite amplitude standing waves in metallic rods,'' J. Acoust. Soc. Am. **97**, 875–881 (1995).
[11] C. Campos-Pozuelo and J. A. Gallego-Juárez, ''Finite amplitude flexural vibrations at ultrasonic frequencies in metallic bars,'' J. Acoust. Soc. Am. **98**, 1742–1750 (1995).
[12] R. Bossut and J-N. Decarpigny, ''Finite element modelling of radiating structures using dipolar damping elements,'' J. Acoust. Soc. Am. **86**, 1234–1244 (1989).
[13] B. Hamonic, ''Application of the finite element method to the design of power piezoelectric sonar transducers,'' in *Power Sonic and Ultrasonic Transducers Design*, edited by B. Hamonic and J. N. Decarpigny (Springer, Berlin, 1988), pp. 143–159.
[14] B. Hamonic, J. C. Debus, J. N. Decarpigny, D. Boucher, and B. Tocquet, ''Analysis of a radiating thin-shell sonar transducer using the finite-element method,'' J. Acoust. Soc. Am. **86**, 1245–1253 (1989).
[15] A. Lavie, ''Modelisation du rayonnement ou de la diffraction acoustique par une méthode mixte équation intégrales-champ nul,'' Ph.D. thesis, Lille University (1989).
[16] C. Campos-Pozuelo, A. Lavie, B. Dubus, G. Rodríguez-Corral, and J. A. Gallego-Juárez, ''Numerical and experimental study of radiated field of high-power ultrasonic transducers for industrial application in gases,'' Acoustical Society of America/Japan. Third Joint Meeting. J. Acoust. Soc. Am. **100**, 2774 (1996).
[17] J. N. Tjotta and S. Tjotta, ''Nonlinear equations of acoustics, with application to parametric acoustic arrays,'' J. Acoust. Soc. Am. **69**, 1742–1750 (1981).
[18] S. N. Nachef, D. Cathignol, J. N. Tjotta, A. M. Berg, and S. Tjotta,

''Investigation of a high intensity sound beam from a plane transducer. Experimental and theoretical results,'' J. Acoust. Soc. Am. **98**, 2303–2323 (1995).
[19] G. S. Garret, J. N. Tjotta, and S. Tjotta, ''Nearfield of a large acoustic transducer, part II: Parametric radiation,'' J. Acoust. Soc. Am. **74**, 1013–1020 (1983).
[20] C. J. Vecchio and P. A. Lewin, ''Finite amplitude acoustic propagation modeling using the extended angular spectrum method,'' J. Acoust. Soc. Am. **95**, 2399–2408 (1994).
[21] J. H. Ginsberg and M. F. Hamilton, ''Computational methods,'' in *Nonlinear Acoustics*, edited by M. F. Hamilton and D. T. Blackstock (Academic, New York, 1998).
[22] P. M. Morse, *Vibration and Sound* (Acoustical Society of America, New York, 1981).
[23] P. J. Westervelt, ''Parametric acoustic array,'' J. Acoust. Soc. Am. **35**, 535–537 (1963).
[24] O. C. Zienkiewicz, *The Finite Element Method*, 3rd ed. (McGraw-Hill, London, 1977).
[25] A. D. Pierce, *Acoustics* (Acoustical Society of America, New York, 1989).
[26] D. T. Blackstock, ''Propagation of plane sound waves of finite amplitude in nondissipative fluids,'' J. Acoust. Soc. Am. **34**, 9–30 (1962).
[27] J. A. Gallego-Juárez, G. Rodríguez-Corral, J. L. San Emeterio, and F. Montoya-Vitini, European Patent EP 450,030 (1991). US Patent 5,299,175 (1994).
[28] C. Campos-Pozuelo and J. A. Gallego-Juárez, ''Limiting strain of metals subjected to high-intensity ultrasound,'' Acust. Acta Acust. **82**, 823–828 (1996).
[29] J. A. Gallego-Juárez, ''High power ultrasonic transducers for use in gases and interphases,'' in *Power Sonic and Ultrasonic Transducers Design*, edited by B. Hamonic and J. N. Decarpigny (Springer, Berlin, 1988), pp. 175–184.
[30] J. C. Lockwood, T. G. Muir, and D. T. Blackstock, ''Directive harmonic generation in the radiation field of a circular piston,'' J. Acoust. Soc. Am. **53**, 1148–1153 (1973).
[31] J. A. Shooter, T. G. Muir, and D. T. Blackstock, ''Acoustic saturation of spherical waves in water,'' J. Acoust. Soc. Am. **55**, 54–62 (1974).

Modeling of an electrohydraulic lithotripter with the KZK equation

Michalakis A. Averkiou[a] and Robin O. Cleveland[b]
Applied Physics Laboratory, University of Washington, Seattle, Washington 98105

(Received 14 May 1998; accepted for publication 7 March 1999)

The acoustic pressure field of an electrohydraulic extracorporeal shock wave lithotripter is modeled with a nonlinear parabolic wave equation (the KZK equation). The model accounts for diffraction, nonlinearity, and thermoviscous absorption. A numerical algorithm for solving the KZK equation in the time domain is used to model sound propagation from the mouth of the ellipsoidal reflector of the lithotripter. Propagation within the reflector is modeled with geometrical acoustics. It is shown that nonlinear distortion within the ellipsoidal reflector can play an important role for certain parameters. Calculated waveforms are compared with waveforms measured in a clinical lithotripter and good agreement is found. It is shown that the spatial location of the maximum negative pressure occurs pre-focally which suggests that the strongest cavitation activity will also be in front of the focus. Propagation of shock waves from a lithotripter with a pressure release reflector is considered and because of nonlinear propagation the focal waveform is not the inverse of the rigid reflector. Results from propagation through tissue are presented; waveforms are similar to those predicted in water except that the higher absorption in the tissue decreases the peak amplitude and lengthens the rise time of the shock. [S0001-4966(99)04306-4]

PACS numbers: 43.25.Jh [MAB]

INTRODUCTION

Extracorporeal shock wave lithotripsy (ESWL) has been used successfully since 1980[1] to treat kidney and gall stones.[2] The noninvasive nature of this procedure has proven to be very attractive over its alternative method, surgical removal, even though the exact mechanism by which the shock wave fragments the stone is not clearly understood. In the case of kidney stones, ESWL is employed in about 85% of the encountered cases; for gall stones, it is used in about 20% of the cases, primarily in Europe. The first attempts to comminute human calculi with the use of acoustic energy are traced back to the early 1950s.[3] Since then, steady improvement in the application of this method has occurred,[4] and today ESWL is by far the method of choice.

ESWL involves the use of large amplitude acoustic shock waves that are generated extracorporeally and focused onto a stone within the body. Lithotripters typically have a high focusing gain so that pressures are high at the stone but substantially lower in the surrounding tissue. The positioning of the patient (alignment of stone with the lithotripter focus) is accomplished with fluoroscopy or ultrasonic imaging. Focusing is achieved geometrically, i.e., with ellipsoidal reflectors, concave focusing dishes, or acoustic lenses. The shock waves utilized have amplitudes of tens of Megapascals [a few hundred kilopascals] and durations of a few microseconds. Shock waves are typically fired at a 1-s pulse repetition rate.

The first mechanisms proposed for stone comminution were compressive failure[5] and spalling.[6] Compressive failure occurs when the large peak positive pressure of the shock wave enters the stone; if the applied stress exceeds the compressive strength of the material, failure will occur. Spalling is the process whereby the positive pressure enters the stone and reflects off the back surface of the stone. The acoustic wave is inverted upon reflection and the resulting tensile stress causes the material to fail (most solids are substantially weaker under tensile stress than compressive stress). A few years after lithotripsy was introduced, acoustic cavitation was suggested as an alternative mechanism for stone fragmentation.[7,8] Acoustic cavitation refers to the formation and subsequent implosive collapse of small cavities (bubbles) within a liquid. The collapse of cavitation bubbles can be violent enough to erode even the hardest metals used in ship propellers and turbine blades.[9] A fourth mechanism of stone failure that has recently been proposed is the process of dynamic fatigue.[10] In this scenario the incident shock wave need not exceed the static strength of the material, but simply cause the progressive development of microcracks in the material. Repetitive stress will fatigue the material (the cracks will grow) and eventually lead to catastrophic failure.

The side effects of ESWL were initially thought to be restricted to hematuria (blood in the urine).[1] However, there is now substantial evidence that ESWL leads to renal injury in a majority, if not all, treated kidneys.[11,12] The renal injury consists of primary damage to the vascular system seen as focal regions of hemorrhage at the focus and a fall in renal blood flow due to vasoconstriction with secondary effects resulting from ischemia.[13,14] The tissue equivalent of spalling occurs at air interfaces, such as in the lung and intestines, and has a damage threshold around 1 MPa;[15,16] however, in ESWL the shock wave is kept away from possible air pockets. Cavitation is also a possible mechanism for tissue damage. If cavitation bubbles have the ability to grow in tissue without significant restraint, then the subsequent bubble im-

[a]Present address: ATL Ultrasound, P.O. Box 3003, Bothell, WA 98041.
[b]Present address: Dept. of Aerospace and Mechanical Engineering, Boston University, Boston, MA 02215.

plosion would lead to tissue damage.[17] A third mechanism for tissue damage is shear, where small-scale inhomogeneities in the tissue distort the wavefront of the incoming shock wave, inducing a shear which can lead to destruction of the tissue.[18]

Before the issues of stone comminution and tissue damage are fully understood, it is necessary to know the acoustic field generated by a lithotripter. Measurements exist for lithotripsy shock waves in water. However, it is perhaps more important to know the acoustic field inside the body where it acts on both the tissue and the kidney stone. Numerical calculations have the potential for great utility in this situation because measurements are difficult to obtain in the body.

The electrohydraulic lithotripter accomplishes its focusing by means of a hemi-ellipsoidal reflector. A spark is discharged at the first focus, f_1, inside the reflector, which generates a shock wave that is reflected and focused at the second focus, f_2. Modeling of the acoustic field of an electrohydraulic lithotripter has been addressed before. Coleman *et al.*[19] used a 1-D version of the KZK equation (essentially the Burgers equation) to model focal waveforms. Diffractive effects were accounted for by assuming that the sound field behaved as a Gaussian beam. Christopher[20] solved the problem accounting for diffraction, absorption, and nonlinearity with the use of a nonlinear propagation model.[21] However, he found it necessary to artificially limit the peak negative pressure during calculations, justified by the fact that his predictions of peak negative pressure exceeded the expected tensile strength of water.

In this work we use the Khokhlov–Zabolotskaya–Kuznetsov (KZK) equation[22,23] to model the field of an electrohydraulic lithotripter outside the reflector. The equation accounts for diffraction (in the parabolic approximation), nonlinearity, and absorption. Results from the KZK equation have been compared with experimental measurements in the past, for continuous wave (CW) and pulsed propagation of focused and unfocused sound beams in water and glycerin, and was found to be in excellent agreement.[24–29]

A limiting factor on the KZK equation is the assumption of quasi-one-dimensional propagation, which manifests itself in the parabolic approximation of the diffraction. Indeed Tjøtta *et al.*[30] argue that the KZK equation is only appropriate for focused sound beams when the aperture radius a and focal length d are such that $a/d<0.5$, that is, the half-aperture is less than 16°. Physically it is argued that the discrepancy occurs because the parabolic approximation does not properly capture the edge wave behavior. The error increases in magnitude with the aperture angle. In the studies mentioned above focusing gains were moderate (less than 20). Hart and Hamilton[31] introduced a coordinate transformation in the frequency domain code that enabled them to consider gains as high as 70. In a previous work by one of the authors[32] the linear field of focused pistons of gains up to 120 and aperture angles up to 90° was considered. It was found that the KZK equation was consistent with O'Neil's exact solution[33] in the focal region for aperture angles up to 30°. In the results presented here the focusing gain was 24.5 and $a/d=0.62$ (a half-aperture angle of 32°). Although this would appear to be slightly outside the parameter space where the KZK equation is valid, the limitations given above were for a uniform focused piston source. As discussed below the ellipsoidal reflector is equivalent to a focused source with an amplitude shading that is approximately Gaussian. This means that the amplitude of the edge wave for an electrohydraulic lithotripter is significantly smaller than would occur with a uniformly focused piston source. Indeed focused Gaussian fields may be matched to focused uniform fields with a transformation that scales the Gaussian gains by a factor of 0.5 or $1/\sqrt{12}$[34,35] depending on the assumptions. Our gain of 24.5 is thus effectively an effective uniform piston gain of $12\cdot 25$ or less. The edge wave error induced by the parabolic equation is therefore much less than would otherwise be expected.

In Sec. I we present the theoretical model and its numerical solution. The method by which we model propagation within the reflector and initialize the code is described. In Sec. II we describe the experimental setup and the measurements performed. In Sec. III we present our results. The numerical results for linear propagation are compared with the exact on-axis solution by Hamilton.[36] We demonstrate that the parabolic approximation is indeed valid for the large aperture considered here. We then consider the effect of nonlinear propagation within the bowl. Comparisons with experimental data from a clinical lithotripter are shown. In our numerical results we show propagation curves for both the peak positive and peak negative pressures as well as time waveforms both on-axis and off-axis. We calculate the field for a lithotripter with a pressure release reflector. We also calculate the field for the case of propagation through tissue.

I. THEORETICAL MODEL

In this section we present a description of the theoretical model used (the KZK equation) and its numerical solution. The KZK equation is a quasi-one-dimensional model and is not appropriate for modeling propagation within the reflector where waves travel in both directions. Instead ray theory is used to model propagation within the bowl. The results from ray theory are used as initial conditions for the KZK equation for subsequent propagation outside the bowl.

A. KZK equation

Our model equation is an axisymmetric form of the KZK equation. We write it here in an integro-differential form in terms of the acoustic pressure p,

$$\frac{\partial p}{\partial z}=\frac{c_0}{2}\int_{-\infty}^{t'}\left(\frac{\partial^2 p}{\partial r^2}+\frac{1}{r}\frac{\partial p}{\partial r}\right)dt''+\frac{\delta}{2c_0^3}\frac{\partial^2 p}{\partial t'^2}+\frac{\beta}{2\rho_0 c_0^3}\frac{\partial p^2}{\partial t'}. \tag{1}$$

The variables are z the coordinate along the axis of the sound beam, r the radial distance from the beam axis, $t'=t-z/c_0$ a retarded time (based on the small-signal sound speed, c_0), δ the sound diffusivity,[37] β the coefficient of nonlinearity,[38] and ρ_0 the ambient density of the fluid. The three terms on the right hand side of Eq. (1) account for diffraction, absorp-

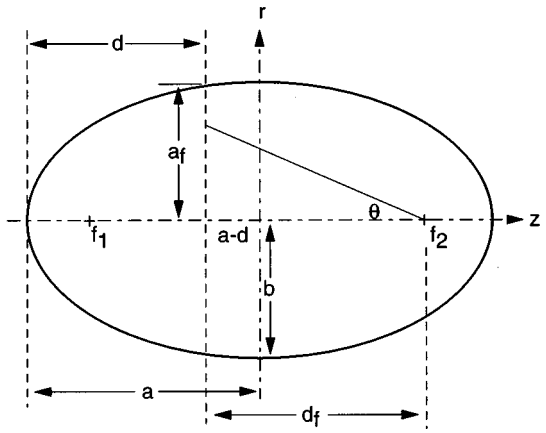

FIG. 1. Geometry of ellipsoidal reflector.

tion, and nonlinearity, respectively. As discussed by Cleveland *et al.*,[39] absorption and dispersion due to multiple relaxation phenomena can be augmented to the KZK equation.

The KZK equation is solved in the numerical code in dimensionless form. We introduce four normalized variables, $P=p/p_0$, $\sigma=z/d_f$, $\rho=r/a_f$, and $\tau=\omega_0 t'$, where, p_0 is the source pressure, d_f the focal length, a_f the aperture, and ω_0 a characteristic angular frequency. The KZK equation becomes:[40]

$$\frac{\partial P}{\partial \sigma}=\frac{1}{4G}\int_{-\infty}^{\tau}\left(\frac{\partial^2 P}{\partial \rho^2}+\frac{1}{\rho}\frac{\partial P}{\partial \rho}\right)d\tau'+A\frac{\partial^2 P}{\partial \tau^2}+N\frac{\partial P^2}{\partial \tau}. \quad (2)$$

The three dimensionless parameters that describe the relative importance of diffraction, absorption, and nonlinearity are:

$$G=z_0/d_f, \quad A=\alpha_0 d_f, \quad N=d_f/\overline{z}, \quad (3)$$

respectively. The first parameter, G, is the small-signal focusing gain, where $z_0=\omega_0 a_f^2/2c_0$ is the Rayleigh distance. The absorption parameter contains the thermo-viscous attenuation coefficient $\alpha_0=\delta\omega_0^2/2c_0^3$. In the nonlinearity parameter the term $\overline{z}=\rho_0 c_0^3/\beta\omega_0 p_0$ is the plane wave shock formation distance. The source condition appropriate for a uniform focused source is

$$P=f(\tau+G\rho^2)H(1-\rho) \quad \text{at } \sigma=0. \quad (4)$$

Equation (2) was solved numerically in the time domain using finite-difference operators to approximate the derivatives. The algorithm used was similar to that given by Lee and Hamilton[40] for unfocused, diverging sound beams except that a rectangular grid was used to accommodate the geometry of focused beams.[41]

B. Source condition for an electrohydraulic lithotripter

The KZK equation can only be applied to acoustic propagation from the aperture of the lithotripter's reflector (also referred to as the bowl). The evolution of the waves inside the bowl is considered here. A schematic of the ellipsoidal reflector is shown in Fig. 1. The foci of the ellipse are f_1 and f_2, and d is the distance from the edge to the point where the ellipse is truncated (the reflector is typically not a complete hemi-ellipsoid). The distance d_f and a_f are the effective focal length and source radius to be used with the KZK equation.

The ellipsoidal reflector has similar characteristics to a focused piston source and the pressure field at the mouth of the bowl is adapted from Eq. (4),

$$P=D(\rho)f(\tau+G\rho^2)H(1-\rho), \quad (5)$$

where $D(\rho)$ is the amplitude shading across the ellipse, $f(t)$ is the source waveform, and $G\rho^2$ is a phase term that effects the focusing of the bowl.

The shading function can be determined from the geometry of the ellipsoid. The surface of an ellipsoidal reflector is defined by

$$\frac{z^2}{a^2}+\frac{r^2}{b^2}=1, \quad (6)$$

where a and b are the major and minor axes of the ellipse. We define the eccentricity to be $\epsilon=\sqrt{1-(b/a)^2}$. The distance d measured from the tip of the ellipse to the exit plane. From geometry we find that the effective radius is

$$a_f=b\sqrt{1-(d/a-1)^2}, \quad (7)$$

and the effective focal length is

$$d_f=a(\epsilon+1-d/a). \quad (8)$$

Equations (7) and (8) are used as the equivalent focused piston parameters in Eq. (3). In these simulations the geometrical parameters were chosen to be: $a=13.80$ cm, $b=7.75$ cm, $\epsilon=0.8274$, $d=12.41$, $a_f=7.71$ cm, and $d_f=12.82$ cm. These values match those of the Dornier HM3 lithotripter which was the clinical machine on which we took measurements.

The directivity function at the mouth of the ellipse $D(\rho)$ can be derived from geometrical acoustics,[36]

$$D(\rho)=\cos(\theta)\Big/\left[1+\frac{4\epsilon\sin^2(\theta/2)}{(1-\epsilon)^2}\right], \quad (9)$$

where

$$\theta=\arctan\sqrt{\left[(1-\epsilon^2)\rho^2\frac{1-(d/a-1)^2}{(1+\epsilon-d/a)^2}\right]}. \quad (10)$$

For the ellipsoidal bowls used in lithotripters the eccentricity is typically $\epsilon\approx 0.8$. When $\epsilon=0$ (spherical bowl) then $D(\rho)=1$ and Eq. (5) reduces to Eq. (4), i.e., a uniform focused piston source. As ϵ increases, the directivity function is no longer unity and is effectively an amplitude shading function (source apodization). Thus we model the ellipsoidal reflector as a focused source with radius a_f, focal length d_f, and with amplitude source shading defined by $D(\rho)$. For $\epsilon\approx 0.8$ the amplitude at the edge of the aperture is approximately 10% of the amplitude on-axis. The significantly reduced amplitude of the edge wave is what allows us to use the KZK equation beyond its ordinary limit.

Hamilton[36] gives an analytic solution for the linear on-axis field of a spherical wave reflected by an ellipsoidal reflector that accurately models diffraction. We use his expression to verify our axial numerical results for a linear case.

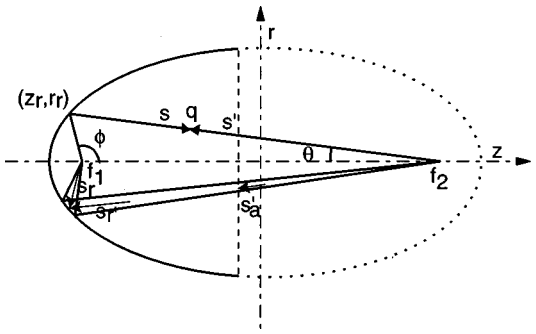

FIG. 2. Geometry of rays within the ellipsoidal reflector.

C. Ray theory within the bowl

The equations shown above for the acoustic field at the mouth of the reflector, although compact, are not easily adapted to account for finite-amplitude effects within the bowl. It is therefore necessary to develop the expressions for ray theory within the bowl. First, we consider the case of small-signal propagation. We assume that propagation is governed by geometrical acoustics, that is, diffraction is negligible within the bowl.

The spark source is assumed to produce a spherically spreading wave. The ellipsoidal reflector is such that spherically spreading waves generated at f_1 reflect off the ellipsoidal bowl, and spherically converge on f_2. Figure 2 shows one set of rays for the ellipsoidal reflector. A ray departs f_1 at an angle ϕ with respect to the z-axis. It intersects with the reflector at location (z_r, r_r) and converges on f_2 along a line at an acute angle of θ to the z-axis. At a given point q on the ray we define s to be the path length from f_1 to q, and s' to be the distance from f_2 to q. By the geometry of the ellipse $s+s'=2a$. The intersection of the outgoing rays and the ellipse occurs at $r_r=a(1-\epsilon^2)\sin\phi/(1-\epsilon\cos\phi)$, $z_r=-a(\epsilon-\cos\phi)/(1-\epsilon\cos\phi)$. The angle θ for the reflected ray is given by $\theta=\tan^{-1}[r_r/(\epsilon a-z_r)]$ [see also Eq. (10)]. The distance from f_2 to the reflector is given by $s_r'=a(1-\epsilon^2)/(1-\epsilon\cos\theta)^2$, and the distance from f_1 to the reflector is $s_r=2a-s_r'$.

The shading can now be calculated. Consider a ray that starts a distance s_0 from f_1, the ray tube area along the path to the reflector is $A_1(s)=A_0(s/s_0)^2$, where A_0 is the initial ray tube area. The ray tube area along the reflected ray is $A_2(s)=k(s'/s_r')^2$, recall that $s'=2a-s$. The constant k can be determined by equating the ray tube areas A_1 and A_2 at the reflector and $k=A_0(s_r/s_0)^2$. The general expression for the ray tube area within the bowl is therefore

$$A(s)=\begin{cases} A_0\left(\dfrac{s}{s_0}\right)^2 & s\leqslant s_r \\ A_0\left(\dfrac{s_r}{s_0}\right)^2\left(\dfrac{2a-s}{s_r'}\right)^2 & s>s_r. \end{cases} \tag{11}$$

The ray tube area at the aperture $s=s_a$ is therefore

$$A(s_a)=\frac{s_1(2a-s_a')}{s_2 s_0}A_0,$$

where $s_a'=((1+\epsilon)a-d)/\cos\theta$ is the distance from f_2 to the aperture.

Therefore for the case of linear propagation the waveform at the aperture is a scaled version of the waveform at s_0, where the scaling factor is $\sqrt{A_0/A(s_a)}$. This expression agrees with the directivity function given in Eq. (9). For the case of a nonrigid reflector, with pressure reflection coefficient R, the expression becomes $R\sqrt{A_0/A(s_a)}$.

The analysis can now be extended to include nonlinear effects. To achieve this it is necessary to further assume that the is no self-interaction between rays, that is, nonlinear effects are restricted to distortion along ray tubes given by linear theory. It is also assumed that nonlinear distortion within the bowl can be accounted for by weak shock theory.[42]

We assume that the spark generates a triangle wave of peak amplitude $\hat{p}_0$ and duration T_{h0}. A triangle wave is a good approximation to the waveform generated by an explosive source[43] such as in an electrohydraulic lithotripter. Although we use a triangular waveform it is possible to generalize the approach to the evolution of shock waves followed by an arbitrary waveform.[44] For a plane triangular wave, weak shock theory predicts that the peak amplitude and duration of the pulse will vary as

$$\hat{p}=\frac{\hat{p}_0}{\sqrt{1+ax}}, \tag{12}$$

$$T_h=T_{h0}\sqrt{1+ax}, \tag{13}$$

where x is the propagation distance and $a=\beta\hat{p}_0/\rho_0 c_0^3 T_{h0}$.

For the shocks inside the bowl the waves initially spread spherically outward, reflect off the ellipsoidal bowl, and then spherically converge. For finite-amplitude waves in a slowly varying ray tube modified versions of Eqs. (12) and (13) can be used to describe the triangle waves where the real distance x is replaced by the ''distortion distance'' $\tilde{x}$.[45] The distortion distance for an arbitrary ray tube in a homogeneous medium is

$$\tilde{x}=\int_{s_0}^{s}\sqrt{\frac{A(s_0)}{A(s')}}\,ds', \tag{14}$$

where s is a distance along the ray, s_0 is the initial location along the ray, and A is the ray tube area.

When the expression for the ray tube area is substituted into Eq. (14), the effective nonlinearity distance within the bowl is

$$\tilde{x}(s)=\begin{cases} s_0\ln\left(\dfrac{s}{s_0}\right) & s\leqslant s_r \\ s_0\ln\left(\dfrac{s_r}{s_0}\right)-s_r'\dfrac{s_0}{s_r}\ln\left(\dfrac{2a-s}{s_r'}\right) & s>s_r. \end{cases} \tag{15}$$

The effective nonlinearity distance at the aperture is

$$\tilde{x}_a=s_0\ln(s_r/s_0)-s_r'(s_0/s_r)\ln[(2a-s_a')/s_r'].$$

The inclusion of the reflection coefficient simply modifies the second term of the nonlinear distortion distance and one obtains

$$\tilde{x}_a = s_0 \ln(s_r/s_0) - R s_r'(s_0/s_r)\ln[(2a - s_a')/(s_r')]. \quad (16)$$

The expressions describing the peak pressure and duration of the triangle wave at the aperture are therefore

$$\hat{p}_a = R \frac{s_r(2a - s_a')}{s_r' s_0} \frac{\hat{p}_0}{\sqrt{1 + a\tilde{x}_a}}, \quad (17)$$

$$T_{ha} = T_{h0}\sqrt{1 + a\tilde{x}_a}. \quad (18)$$

These expressions can be used to consider the effects of nonlinear distortion within the ellipsoidal reflector. Coleman reported that the waveform measured on-axis at the aperture of a Dornier HM3 was a triangle wave with amplitude 8 MPa.[46] Coleman later reported the aperture waveform to be triangular with a peak amplitude of approximately 5 MPa and a duration of 3.75 μs.[19] For our calculations we assumed that the waveform at the aperture was a triangle wave of peak pressure 6.54 MPa (between the reported values) and duration 4 μs. The selection of 6.54 MPa was chosen because it was approximately the average of the values reported by Coleman and it gave a nonlinearity parameter [Eq. (3)] of exactly 1.4. Using linear theory to backpropagate to 1 cm away from the spark, the initial condition becomes a triangle waveform of amplitude 7.91 MPa and 4-μs duration. Figure 3 shows the amplitude shading and the aperture waveforms on the axis and the edge of the ellipsoidal reflector compared to linear theory. Nonlinear distortion within the bowl leads to a loss in amplitude for the weak shock theory case which is strongest on axis (6.06 MPa vs 6.54 MPa). Nonlinear effects also lead to an elongation of the waveform; again this is most marked on-axis (4.32 μs vs 4 μs). The latter distortion will produce a change in the curvature of the leading wavefront which should produce a defocusing effect at f_2. However, for this case the effects of nonlinear distortion in the bowl are very small.

Christopher also used a triangle wave as an initial waveform. In his calculations he assumed that 1 cm from f_1 the waveform was a triangle wave of amplitude 40 MPa and duration 2 μs. Figure 4 compares the predicted waveforms at the mouth of the reflector for linear and weak shock theory for this initial condition. On-axis, weak shock theory predicts an amplitude of 20.2 MPa compared to 30.7 MPa for linear theory. The duration on-axis is 3.27 μs for weak shock theory and 2 μs for linear theory. For this source condition nonlinear distortion significantly affects the propagation problem, producing a large decrease in amplitude and defocusing of the wavefront. Christopher assumed linear propagation within the bowl, but his model also accounted for diffraction within the bowl. However, as discussed below, the acoustic field predicted at the mouth of the ellipsoid by geometrical acoustics agrees well with predictions with the exact on-axis linear solution which includes diffraction.

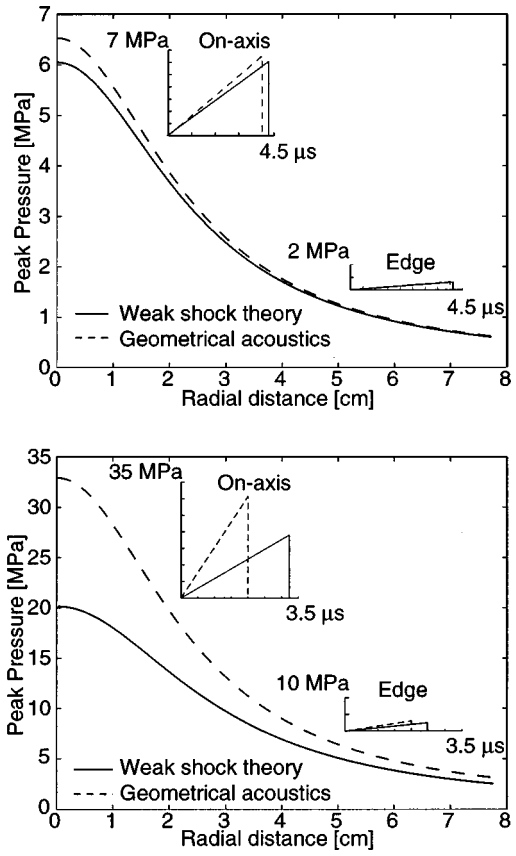

FIG. 3. Amplitude shading across the bowl mouth and waveforms both on-axis and at the edge of the bowl. (a) Comparison of linear geometrical acoustics and weak shock theory for propagation in the bowl for amplitudes used in this paper. When nonlinear effects are accounted for there is a small reduction in amplitude and pulse elongation; the effect is largest on-axis but is not significant for these pressures. (b) Comparison of linear geometrical acoustics and weak shock theory for the initial conditions used by Christopher. Nonlinear distortion significantly reduces the amplitude of the pulse and elongates it, with the greatest effect being on-axis.

II. EXPERIMENTAL SETUP

Pressure measurements were taken in an unmodified Dornier HM3 lithotripter at Methodist Hospital, Indianapolis, IN. A replaceable PVDF membrane hydrophone (no. 702-031, Sonic Industries, Hatsboro, PA) was used to capture the shock waves generated by the lithotripter. Individual membranes were supplied with a calibration value which is reported to be within ± 1.5 dB over the frequency range 1–20 MHz. We confirmed the calibration over the range of 2–20 MHz by comparilson with a Marconi PVDF hydrophone (type Y-33-7611, GEC-Marconi, Chelmsford, UK) calibrated at the National Physical Laboratory (Teddington, UK). We were not able to obtain a calibration below 1 MHz but, assuming that the response remains moderately flat, we estimate the error in the measured pressure to be $\pm 20\%$. Waveforms were recorded on a digital oscilloscope (Tektronix, Beaverton, OR) and downloaded to a computer using LabVIEW (National Instruments, Austin, Texas).

The lithotripter was placed in patient-ready condition—its water bath filled with standard Dornier degased, softened water at 37 °C. We used refurbished electrodes (Service Trends, Kennesaw, GA) between shot 50 and 2000 with a voltage setting of 18 kV. The Dornier water has high conductivity (700 μS/cm) that adversely affects the response of the PVDF membrane; the hydrophone requires a conductivity of less than 5 μS/cm. We placed the shock wave hydrophone inside a small plastic tank (dimensions $22\times32\times30$ cm) of deionized water inside the HM3 water bath. The bottom surface of the tank, where the shock wave enters, was

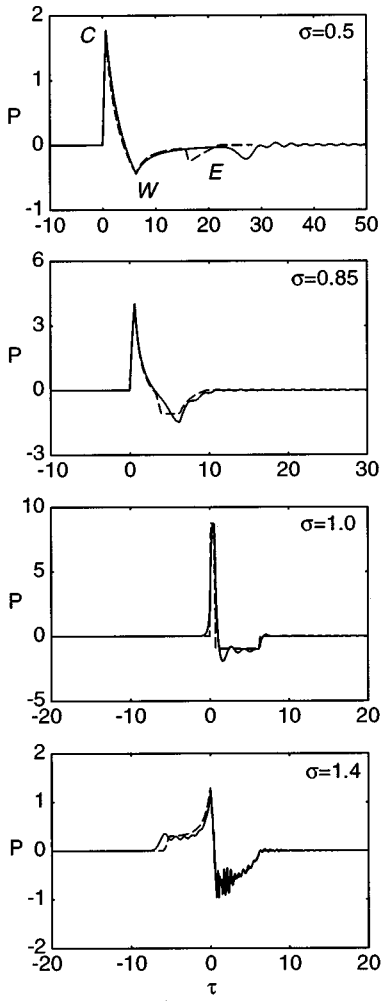

FIG. 4. Comparison between numerical results from the KZK equation (solid line) and Hamilton's exact linear analytical solution (dashed line) for time waveforms along the axis of an ellipsoidal reflector. In the pre-focal region the edge wave of the numerical solution is delayed.

fitted with a thin sheet of low density polyethylene. The polyethylene sheet had a negligible effect on the shock wave.

The hydrophone was located at the focus of the lithotripter by placing a small radio-opaque marker on the active portion of the membrane so that it could be visualized using the fluorography system associated with the HM3. The membrane was moved using the hydraulic gantry system of the HM3 until the marker was at the focal point as determined by the crosshairs on the fluoroscope screens. The marker was removed for shock wave measurements.

The hydrophone was moved to other locations by the hydraulic gantry system. Location was determined by means of two masks placed on the fluoroscopic screens. The masks had calibrated grids drawn on them that were aligned with the blast path of the lithotripter. At least ten measurements were taken at each location and the PVDF membrane and polyethylene sheet were cleared of bubbles after every shot.

III. RESULTS

Our numerical and experimental results are shown in this section. We compared results with linear theory for an ellipsoidal reflector to demonstrate that the application of the initial conditions for the KZK code was correct. Next we compared computed lithotripsy waveforms in water with experimentally measured shock waves. Finally, the code was used to predict the acoustic field for two cases: (1) a lithotripter with a pressure release reflector and (2) a standard lithotripter but with the shock waves propagating in tissue.

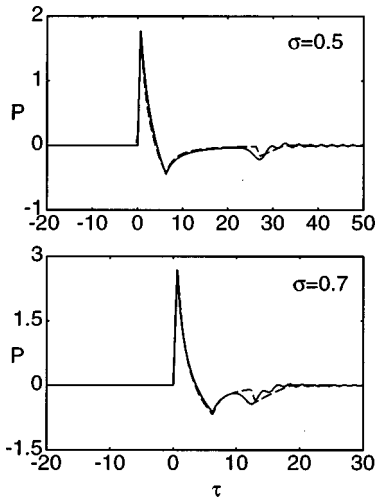

FIG. 5. Comparison between the numerical simulation (solid line) and the modified (according to the paraxial approximation) exact linear analytical solution by Hamilton (dashed line) for time waveforms along the axis of an ellipsoidal reflector. The arrival times of the edge waves agree.

A. Comparison with linear theory

Figure 4 shows a comparison between numerical results for linear propagation along the axis of the ellipsoidal reflector and the exact analytical solution of Hamilton.[36] The source condition was the triangular pulse discussed above with a rise time of 400 ns and duration of 4 μs. In the figures that follow we used the normalized axial distance $\sigma = z/d_f$ with $\sigma = 1$ being the ellipsoidal reflector focus, f_2. Recall that the effective ellipsoid radius and focal distance used by the Dornier HM3 are $a_f = 7.7$ cm and $d_f = 12.8$ cm, respectively. In Fig. 4 at $\sigma = 0.5$ we indicate the three main parts of the waveform: the center wave (or direct wave) denoted as *C*, the edge wave (or diffracted wave) denoted as *E*, and the wake denoted as *W*. A discussion of these three wave components may be found in Ref. 36. In the near field, note that the edge wave in the KZK solution lags behind that of the exact solution. This is an inherent limitation of the parabolic approximation in the diffraction term.

We illustrate the effect of the parabolic approximation on the solution by applying the parabolic approximation to the exact analytical solution. This was done by replacing the distance to the edge of the aperture $R_e = \sqrt{z^2 + a^2}$ by the first two terms of its binomial expansion $R_e \approx z(1 + 0.5(a/z)^2)$. This is effectively what happens when the parabolic approximation is applied to the wave equation. Figure 5 shows that the comparison between the numerical results and the ''parabolic'' analytical solution is better. This suggests that the main difference between our model and the exact solution is in terms of the edge wave prediction due to the parabolic approximation. In the rest of the axial ranges we have good agreement between the numerical and the analytical solution.

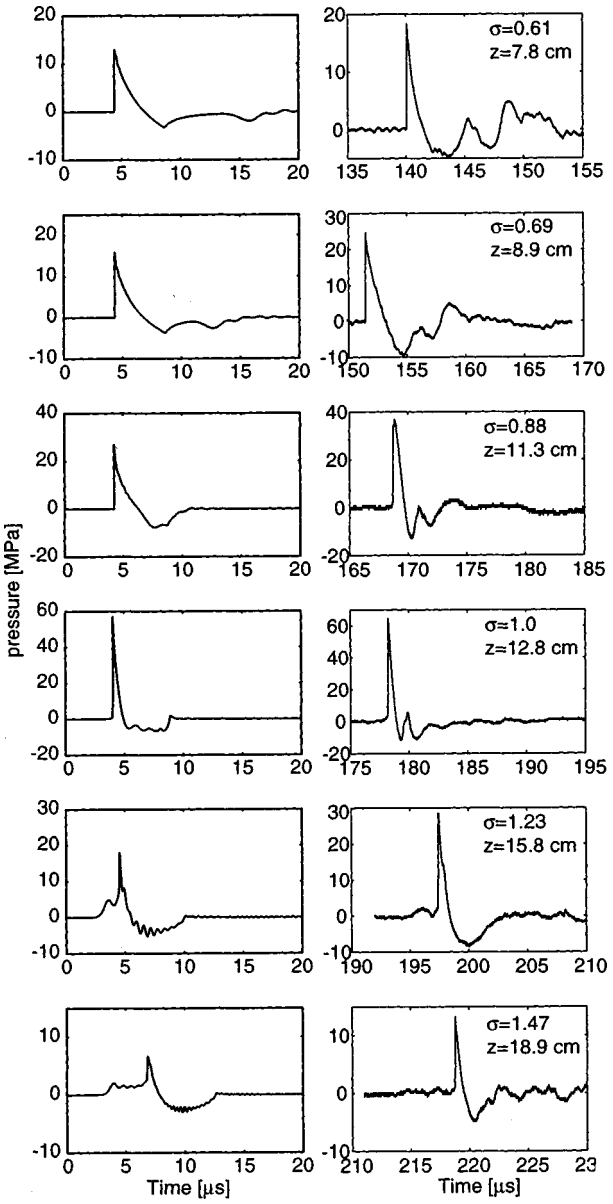

FIG. 6. Comparison between measured lithotripter shock waves (right column) and the numerical simulation (left column) for $A=2.6\times10^{-3}$, $N=1.4$, and $G=24.5$, along the axis of the electrohydraulic lithotripter.

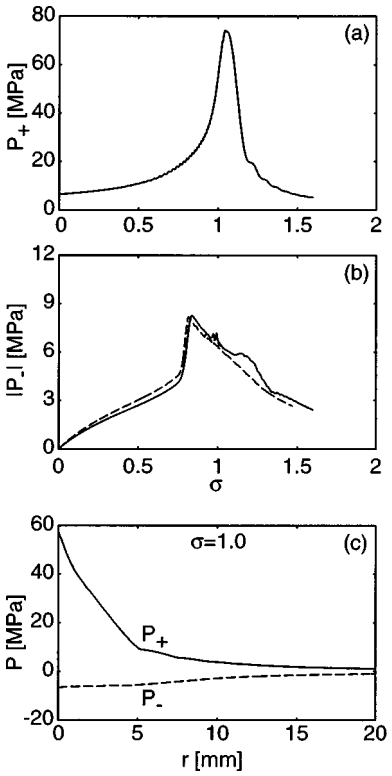

FIG. 7. Propagation curves for P_+ (a), $|P_-|$ (b), and beam patterns at $\sigma=1$ (c), for the numerical results shown in Fig. 6. The maximum of P_+ occurs just after the focus where as $|P_-|$ reaches a maximum pre-focally. Dashed lines in (b) show numerical results calculated with 5000 points per cycle.

The ripples at $\sigma=1.4$ are a Gibb's-type phenomenon, and they can be removed by finer discretization at the expense of longer run times.

B. Comparison with experiment

Results of calculations for the HM3 lithotripter were compared with data measured in the Dornier HM3 lithotripter at Methodist Hospital, in Fig. 6. The water parameters used for the numerical solution were α_0 ($f=0.25$ MHz) $=0.0016$Np/m, $\beta=3.5$, $\rho_0=1000\,\mathrm{kg/m^3}$, and $c_0=1485\,\mathrm{m/s}$. The source condition used was the same triangular pulse used in Sec. III A and the exit plane pressure amplitude was $p_0=6.54\,\mathrm{MPa}$. The absorption and nonlinearity parameters [as defined in Eq. (3)] were $A=2.6\times10^{-3}$ and $N=1.4$, and the focusing gain was $G=24.5$. For the diffraction calculation the step in the radial direction was such that the source radius was broken into 300 points. The triangular time waveform at the exit plane was sampled at 316 points per cycle (the duration of the triangular waveform being one cycle). Distance was measured from the ellipse exit plane and the distance to the focus was $d_f=12.82\,\mathrm{cm}$. The comparisons started at $z=7.8\,\mathrm{cm}$ (5-cm pre-focal) and extended out to $z=15.8\,\mathrm{cm}$ (3-cm post-focal).

At close range ($\sigma=0.61$) the numerical prediction for the edge wave was not very accurate; as discussed in the previous section, the calculated edge wave arrives delayed. Closer to the focus ($\sigma=0.88$) there was much better agreement for the arrival of the edge wave. At the focus ($\sigma=1$) the waveforms were in good agreement and the peak positive pressure was about 60 MPa in both the prediction and the measurement. However, the code predicted a significantly longer negative tail than was measured. The discrepancy may be due to an inherent limitation of the PVDF hydrophone to measure large negative pressures in water. Wurster *et al.*[47] claim that PVDF membranes do not properly capture the peak negative pressure of lithotripsy waveforms and underestimate the duration of the negative tail by a factor of 2. In the post-focal region ($\sigma>1$) the edge wave arrived before the center wave and it is seen as a small precursor to the shock wave in both the predicted and measured waveforms. Considering the great variability of waveforms measured in spark-discharge-type lithotripters, the agreement between the measured and predicted waveforms is good.

In Fig. 7(a) and (b) predictions for the axial peak-positive pressure (P_+) and the magnitude of the peak-negative pressure ($|P_-|$) are shown. The highest positive pressure was about 80 MPa and occurred close to the geo-

metric focus. However, the largest negative pressure was much lower (about 10 MPa) and occurred at $\sigma=0.84$ (2.0 cm in front of the focus). This result was in agreement with other measurements of the HM3.[48] If cavitation is shown to be a major mechanism in stone comminution then the positioning of patients may need to be adjusted to place the stone in a pre-focal region where cavitation activity would be strongest. The dashed line in Fig. 7(b) was calculated with 5000 points per cycle to demonstrate that the ripples in the solid line (316 points per cycle) were an artifact. In Fig. 7(c) P_+ (solid line) and P_- (dashed line) in the transverse direction at $\sigma=1$ are shown which indicate the radial extent of the lithotripsy field. The 6-dB beam width for P_+ was only 2.6 mm and for P_- was 9 mm. The magnitude of the negative pressure was above 1 MPa for a radial distance of 2 cm.

C. Pressure release bowl

Commercial electrohydraulic lithotripters use an ellipsoid made of brass or aluminum; both materials are acoustically hard compared to water, and may be modeled as rigid reflectors. Here we consider an ellipsoid that is made of an acoustically soft material, that is, it appears to be a pressure release reflector. In the numerical model the pressure release reflector was implemented by inverting the waveforms at the mouth of the ellipse. This was valid for our simulations because, as discussed above, the effect of nonlinear distortion within the bowl for our aperture conditions was almost negligible. If shock wave propagation in water was a linear process, then the waveforms from a lithotripter with a pressure release reflector would be the inverse of the results shown in Fig. 6. However, the high amplitudes utilized result in nonlinear effects and the calculated waveforms, shown in Fig. 8, were quite different from the waveforms calculated for a rigid reflector. At a range $\sigma=0.7$ the waveform resembled an inverted replica of the waveform obtained with a rigid reflector, but the center wave was steepening in the reverse direction and thus it had a slower decay time. The rest of the calculated waveforms did not resemble those of the rigid reflector. The maximum peak-positive pressure at the focus ($\sigma=1$) was about 30 MPa, considerably lower than that of the rigid reflector. The magnitude of the peak-negative pressure was about 25 MPa, considerably higher than the rigid reflector.

In Fig. 9 the variation of P_+ and $|P_-|$ along the ellipsoid axis is shown. Both P_+ and $|P_-|$ were maximized close to the geometric focus. The magnitude of the negative pressure was considerably greater than the positive pressure from the source all the way to the focus. Recently, Bailey[49,50] performed experiments with pressure release reflectors. His measured waveforms appear to be close to those calculated except that the magnitude of the negative pressures never exceeded 15 MPa. Two possible reasons for the discrepancy are that the hydrophone was not capable of measuring the large negative pressure (as discussed above), and that the reflector used in the experiments had a reflection coefficient $R=-0.88$ and our model assumed a perfect pressure release reflector $R=-1$.

We note that, despite the large negative pressures generated by the pressure release reflector, Bailey found that

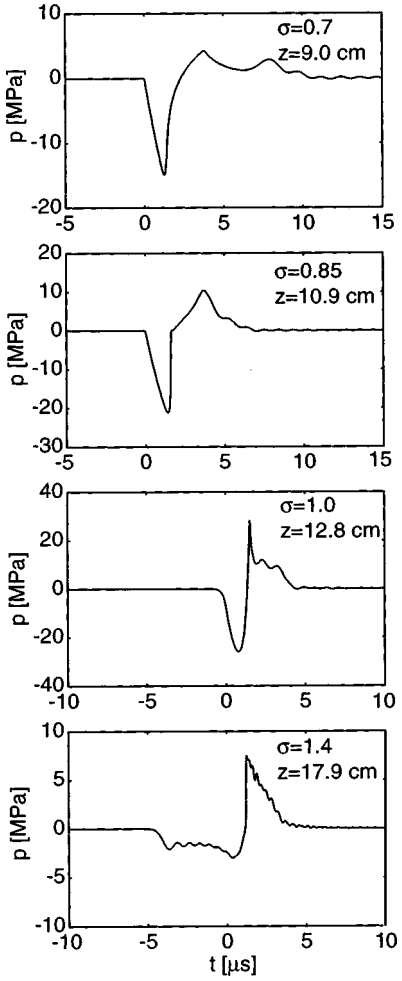

FIG. 8. Theoretical predictions for shock waves along the axis of a lithotripter with a pressure release reflector for $A=2.6\times10^{-3}$, $N=1.4$, and $G=24.5$. The waveforms are not simply inverted replicas of the waveforms shown in Fig. 6.

cavitation damage (as measured by pitting of metal foils) was significantly less than the cavitation damage of the rigid reflector. It was observed that the small pitting from the pressure release reflector was spread over a wider area than that

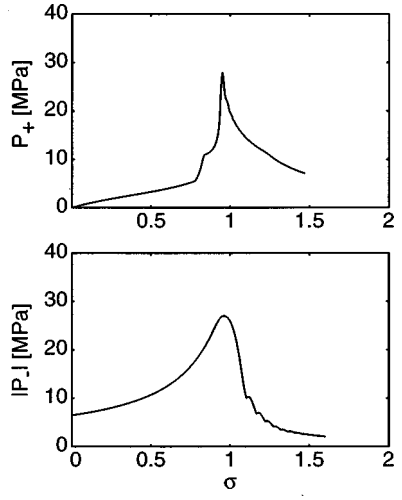

FIG. 9. Propagation curves for P_+ and $|P_-|$ for the pressure release reflector. Both curves have a maximum at the focus.

from the rigid reflector; but the conclusion was that the pressure release waveform produced minimal cavitation damage.[51] It appeared that the trailing positive spike in the pressure release waveform prematurely squashed cavitation bubbles and prevented the violent collapse that occurs for bubbles excited by the waveform of the rigid reflector.

D. Propagation in tissue

The results presented above are relevant for validating the numerical predictions with measurements in water. A powerful application of the code is the ability to predict the propagation of lithotripsy shock waves through tissue. The approach taken here was simplistic but the model has the potential to be used in a much more complicated way. Tissue was modeled as a homogeneous thermoviscous fluid where values for the absorption, the sound speed, the density, and the coefficient of nonlinearity were chosen to be representative of tissue in general. In addition, we assumed that all propagation took place in this approximate tissue model (no water path). It is possible to extend the numerical model to account for both propagation through layers of tissue with different parameters, and more realistic absorption using multiple relaxation processes.[39]

The parameters used for a model tissue were α_0 ($f=0.25\,\mathrm{MHz}$)$=1.52\,\mathrm{Np/m}$ (deduced from a nominal value of 7 Np/m/MHz and adjusted with a $f^{1.1}$ frequency dependence to $f=0.25\,\mathrm{MHz}$), $\rho=1000\ \mathrm{kg/m^3}$, $c=1520\,\mathrm{m/s}$, and $\beta=5.5$. The normalized absorption and nonlinearity parameters used in the numerical code were $A=0.195$ and $N=2.05$. The exit plane pressure amplitude remained the same as for the run in water, i.e., $p_0=6.54\,\mathrm{MPa}$. The calculated waveforms are shown in Fig. 10; the effect of the increased absorption acted as a low-pass filter and smoothed the waveforms. The higher absorption lead to peak amplitudes that were considerably lower than those for the waveforms in water (Fig. 6). At the focus, $\sigma=1$, the peak-positive pressure was 38% and the peak-negative pressure was 86% of the values in water. The peak-positive pressure P_+ was reduced more than $|P_-|$ because the amplitude of the peak-positive pressure is more sensitive to the presence of high frequency components than the peak-negative pressure. The Gibb's-type oscillations in the post-focal region were removed as a result of the absorption low-pass filtering. The shock wave rise time at the focus was 242 ns (calculated as the time to go from 10% to 90% of peak amplitude) and at $\sigma=1.1$ was 331 ns. For comparison, in water at $\sigma=1$ the estimated rise time was less than 1 ns but this estimation was somewhat limited by the discretization of the code. In the right hand side column off-axis waveforms are shown at the axial range $\sigma=1.0$. The pressure amplitude was greatly reduced off-axis and the shock wave rise time increased. At a distance of $\rho=0.15$ (12 mm) the waveform looked like a sinusoid and the amplitude was less than 3 MPa.

Figure 11 shows axial propagation curves for P_+ and $|P_-|$ in tissue. The major features here are that P_+ is maximized just after the focus and $|P_-|$ is maximized pre-focally, both traits were also seen in water simulations in Fig. 7. In Fig. 11(c), the transverse variation of P_+ and P_- is shown at a range $\sigma=1.0$. Both P_+ and $|P_-|$ retain relatively high

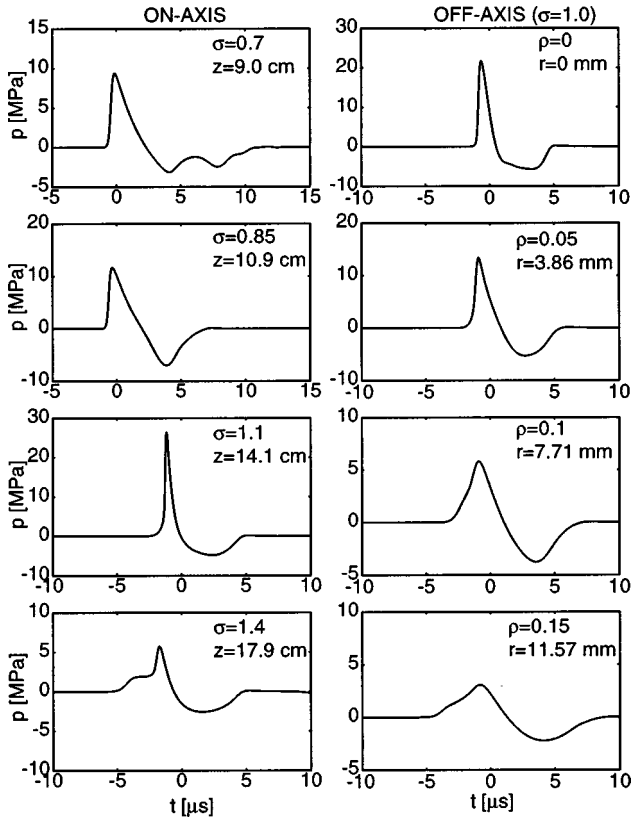

FIG. 10. Theoretical predictions for lithotripter shock waves in tissue with $A=2.6\times10^{-3}$, $N=1.4$, and $G=24.5$. The left-hand column shows axial waveforms and the right hand column shows radial waveforms (at the focus). The extra absorption in tissue smooths the waveforms, reducing the peak pressures and increasing the rise time.

amplitudes up to a range of 5 mm and cavitation activity should be monitored in that area. Cavitation activity may also be present up to (but not limited to) a range of 20 mm where $P_+=1.2\,\mathrm{MPa}$ and $P_-=-1.0\,\mathrm{MPa}$. The width of the focal spot (as defined by the 6-dB points) is broader by 70% in tissue than in water. The extra absorption in the tissue removes high frequency components and prevents tight focusing and results in a broader beam.

The predicted *in vivo* pressure field is in good agreement with measurements made in pigs of shock waves generated by an HM3.[52] The *in vivo* measurements indicated a 30% reduction in the peak-positive pressure at the focus. The calculations presented here predicted a 62% reduction in peak pressure but this was for propagation through 12.8 cm of tissue in pig measurements, the tissue propagation path was on the order of 6 cm. It is reasonable to expect the calculation to underestimate the peak pressure because more absorption was included. The *in vivo* rise time was measured to be on the order of 100 ns, which was longer than measured in water. The predicted rise time in tissue was 240 ns, also longer than predicted in water. The presence of the extra absorption would also account for the predicted rise time being longer than the measured rise time. The width of the focal spot *in vivo* was measured to be 20 mm, compared to 12 mm in water; a broadening of 67% very close to that predicted with this model.

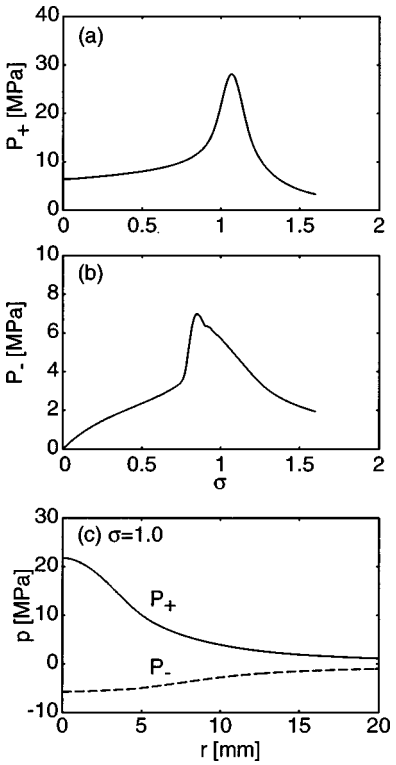

FIG. 11. Propagation curves and beam profiles for P_+ and $|P_-|$ for lithotripsy shock wave propagation in tissue. In this case, P_+ peaks post-focally indicating self-defocusing.

IV. CONCLUSION

The KZK equation was successfully used to model the acoustic field of an electrohydraulic lithotripter from the reflector exit plane to f_2 and beyond. The use of linear geometrical acoustics within the bowl was found to be adequate for exit plane pressures of about 7 MPa which result in focal pressures of about 60 MPa. For higher exit plane pressures, weak shock theory within the bowl is necessary. Comparisons of axial waveforms captured with a hydrophone in water with simulations from the KZK model showed good agreement. Possible reasons for the amount of discrepancy between experiment and simulation are that the model neglected the effects of masking of the aperture wave by the spark plug or the gas bubble at f_1. Also the model neglected the effect of spark variability at f_1. From both the model and the measurements it was found that the magnitude of the peak-negative pressure of the lithotripter shock wave was maximized prefocally. The model was also used to propagate an inverted shock wave that would be formed by a pressure release reflector. Our simulation results compared favorably with recent experimental results. According to our simulation, this type of reflector may result in negative pressures of up to 25 MPa. However, the structure of the focal waveform suggests that the resulting cavitation field is weaker than that of rigid reflectors.

Finally, modeling of propagation through tissue demonstrated the effects of increased absorption. The absorption acted as a low-pass filter; it increased the shock rise time and reduced the peak-positive pressure. In addition, the loss of the high frequency energy to absorption meant that the shock did not focus quite as tightly in tissue as it did in water. The code neglected the effects of refraction between layers of tissue and small-scale tissue inhomogeneities which could further broaden the size of the focal spot. The magnitude of the negative pressures in the tissue remained above 1 MPa for a transverse distance up to 20 mm from the axis (40 mm in diameter), as wide as a kidney. This suggests the extent of the area around the stone that may be subject to cavitation-type adverse bioeffect.

Further investigation is needed to correlate cavitation bioeffects with predicted and measured lithotripsy pressures. The present code appears to be an excellent tool for understanding the acoustic field generated by an electrohydraulic lithotripter both in water and in tissue.

ACKNOWLEDGMENTS

This work was funded by the National Institutes of Health through Grant No. DK43881. The help of Dr. M. F. Hamilton with theoretical aspects of this work is gratefully acknowledged. We also thank Drs. A. P. Evan and J. A. McAteer for providing access to the HM3 lithotripter at Methodist Hospital and for technical assistance. Cleveland acknowledges support of the Acoustical Society of America through the 1995/96 F.V. Hunt Fellowship.

[1] C. Chaussy, W. Brendel, and E. Schmiedt, ''Extracorporeally induced destruction of kidney stones by shock waves,'' Lancet **II**, 1265–1268 (1980).
[2] T. Sauerbruch, M. Delius, G. Paumgartner, J. Holl, O. Wess, W. Weber, and W. Brendel, ''Fragmentation of gallstones by extracorporeal shock waves,'' N. Engl. J. Med. **314**, 812–822 (1986).
[3] H. Lamport, H. F. Newman, and R. D. Eichhorn, ''Fragmentation of biliary calculi by ultrasound,'' Fed. Proc. **9**, 73–74 (1950).
[4] M. Delius and W. Brendel, ''Historical roots of lithotripsy,'' J. Lith. and Stone Disease **2**, 161–163 (1990).
[5] C. Chaussy, *Extracorporeally Shock Wave Lithotripsy: New Aspects in the Treatment of Kidney Stone Disease* (S. Karager, Basel, 1982).
[6] M. Delius, W. Brendel, and G. Heine, ''A mechanism of gallstone destruction by extracorporeal shock waves,'' Naturwissenschaften **75**, 200–201 (1988).
[7] A. J. Coleman, J. E. Saunders, L. A. Crum, and M. Dyson, ''Acoustic cavitation generated by an extracorporeal shockwave lithotripter,'' Ultrasound Med. Biol. **13**, 69–76 (1987).
[8] L. A. Crum, ''Cavitation microjets as a contributory mechanism for renal calculi disintegration in ESWI,'' J. Urol. (Baltimore) **140**, 1587–1590 (1988).
[9] L. A. Crum, ''Acoustic cavitation,'' 1982 Ultrasonics Symposium Proceedings (IEEE), Vol. 1, pp. 1–11.
[10] B. Sturtevant, ''Shock wave physics of lithotripters,'' in *Smith's Textbook of Endourology*, edited by A. D. Smith, G. H. Badlani, R. V. Clayman, G. H. Jordan, L. R. Kevoussi, J. E. Lingeman, G. M. Preminger, and J. W. Segura (Quality Medical Publishing, St Louis, MO, 1996), pp. 529–552.
[11] J. V. Kaude, C. M. Williams, M. R. Millner, K. N. Scott, and B. Finlayson, ''Renal morphology and function immediately after extracorporeal shock-wave lithotripsy,'' Am. J. Roentgenol. **145**, 305–313 (1985).
[12] A. P. Evan and J. A. McAteer, ''*Q*-Effects of shock-wave lithotripsy,'' in *Kidney Stones: Medical and Surgical Management*, edited by F. Coe, C. Pak, and G. M. Preminger (Raven, New York, 1996), pp. 549–570.
[13] A. P. Evan, L. R. Willis, B. Connors, G. Reed, J. A. McAteer, and J. E. Lingeman, ''Shock wave lithotripsy induced renal injury,'' Am. J. Kidney Disease **17**, 445–450 (1991).
[14] L. R. Willis, A. P. Evan, B. Connors, and J. E. Lingeman, ''Relationship between kidney size and acute impairment of renal hemodynamics by shock wave lithoripsy in pigs,'' Proc. VIII Int'l Symp. Urolithiasis (1996).
[15] D. Dalecki, C. H. Raeman, S. Z. Child, and E. L. Carstensen, ''A test for cavitation as a mechanism for intestinal hemorrhage in mice exposed to a piezoelectric lithotripter,'' Ultrasound Med. Biol. **22**, 493–496 (1996).

[16] C. Hartman, S. Z. Child, R. Mayer, E. Schenk, and E. L. Carstensen, ''Lung damage from exposure to the fields of an electrohydraulic lithotripter,'' Ultrasound Med. Biol. **16**, 675–679 (1990).
[17] A. J. Coleman and J. E. Saunders, ''A review of the physical properties and biological effects of the high amplitude acoustic fields used in extracorporeal lithotripsy,'' Ultrasonics **31**, 75–89 (1993).
[18] D. D. Howard and B. Sturtevant, ''*In vitro* studies of the mechanical effects of shock wave lithotripsy,'' Ultrasound Med. Biol. **23**, 1107–1122 (1997).
[19] A. J. Coleman, M. J. Choi, and J. E. Saunders, ''Theoretical predictions of the acoustic pressure generated by a shock wave lithotripter,'' Ultrasound Med. Biol. **17**, 245–255 (1991).
[20] P. T. Christopher, ''Modeling the Dornier HM3 lithotripter,'' J. Acoust. Soc. Am. **96**, 3088–3095 (1994).
[21] P. T. Christopher and K. J. Parker, ''New approaches to nonlinear diffractive field propagation,'' J. Acoust. Soc. Am. **90**, 488–499 (1991).
[22] E. A. Zabolotskaya and R. V. Khokhlov, ''Quasi-plane waves in the nonlinear acoustics of confined beams,'' Sov. Phys. Acoust. **15**, 35–40 (1969).
[23] V. P. Kuznetsov, ''Equation of nonlinear acoustics,'' Sov. Phys. Acoust. **16**, 467–470 (1970).
[24] A. C. Baker and V. F. Humphrey, ''Distortion and high-frequency generation due to nonlinear propagation of short ultrasonic pulses from a plane circular piston,'' J. Acoust. Soc. Am. **92**, 1699–1705 (1992).
[25] J. A. TenCate, ''An experimental investigation of the nonlinear pressure field produced by a plane circular piston,'' J. Acoust. Soc. Am. **94**, 1084–1089 (1993).
[26] S. Nachef, D. Cathignol, J. Naze Tjøtta, A. M. Berg, and S. Tjøtta, ''Investigation of a high intensity sound beam from a plane transducer: Experimental and theoretical results,'' J. Acoust. Soc. Am. **98**, 2303–2323 (1995).
[27] M. A. Averkiou and M. F. Hamilton, ''Measurements of harmonic generation in a focused finite-amplitude sound beam,'' J. Acoust. Soc. Am. **98**, 3439–3442 (1995).
[28] M. A. Averkiou and M. F. Hamilton, ''Nonlinear distortion of short pulses radiated by plane and focused circular pistons,'' J. Acoust. Soc. Am. **102**, 2539–2548 (1997).
[29] M. A. Averkiou, Y.-S. Lee, and M. F. Hamilton, ''Self-demodulation of amplitude- and frequency-modulated pulses in a thermoviscous fluid,'' J. Acoust. Soc. Am. **94**, 2876–2883 (1993).
[30] E. H. Vefring, J. Naze Tjøtta, and S. Tjøtta, ''Effects of focusing on the nonlinear interaction between two collinear finite amplitude sound beams,'' J. Acoust. Soc. Am. **89**, 1017–1027 (1991).
[31] T. S. Hart and M. F. Hamilton, ''Nonlinear effects in focused sound beams,'' J. Acoust. Soc. Am. **84**, 1488–1496 (1988).
[32] M. A. Averkiou, ''Reflection of focused sound from curved rigid surfaces,'' M.S. thesis, The University of Texas at Austin (1989).
[33] H. T. O'Neil, ''Theory of focusing radiators,'' J. Acoust. Soc. Am. **21**, 516–526 (1949).
[34] M. A. Averkiou, ''Experimental investigation of propagation and reflection phenomena in finite amplitude beams,'' Ph.D. dissertation, The University of Texas at Austin (1994).
[35] F. H. Fenlon and F. S. McKendree, ''Axisymmetric parametric radiation—A weak interaction model,'' J. Acoust. Soc. Am. **66**, 534–547 (1979).
[36] M. F. Hamilton, ''Transient axial solution for the reflection of a spherical wave from a concave ellipsoidal mirror,'' J. Acoust. Soc. Am. **93**, 1256–1266 (1993).
[37] J. Lighthill, *Waves in Fluids* (Cambridge University Press, Cambridge, 1980), pp. 78–83.
[38] D. T. Blackstock, ''Nonlinear acoustics (theoretical),'' in *American Institute of Physics Handbook*, 3rd ed. (McGraw-Hill, New York, 1972), Chap. 3n.
[39] R. O. Cleveland, M. F. Hamilton, and D. T. Blackstock, ''Time-domain modeling of finite-amplitude sound in relaxing fluids,'' J. Acoust. Soc. Am. **99**, 3312–3318 (1996).
[40] Y. S. Lee and M. F. Hamilton, ''Time-domain modeling of pulsed finite-amplitude sound beams,'' J. Acoust. Soc. Am. **97**, 906–917 (1995).
[41] Y.-S. Lee, ''Numerical solution of the KZK equation for pulsed finite amplitude sound beams in thermoviscous fluids,'' Ph. D. dissertation, The University of Texas at Austin (1993).
[42] D. T. Blackstock, ''Connection between the Fay and Fubini solutions for plane sound waves of finite amplitude,'' J. Acoust. Soc. Am. **39**, 1019–1026 (1966).
[43] R. H. Cole, *Underwater Explosions* (Princeton University Press, Princeton, NJ, 1948).
[44] D. T. Blackstock, ''Propagation of a weak shock followed by a tail or arbitrary waveform,'' in *Proceedings of the Eleventh International Congress on Acoustics*, Paris, France, Vol. 1, pp. 305–308 (1983).
[45] C. L. Morfey and F. D. Cotaras, ''Propagation in inhomogeneous medium,'' in *Nonlinear Acoustics*, edited by M. F. Hamilton and D. T. Blackstock (Academic, New York, 1997), Chap. 12.
[46] A. J. Coleman, J. E. Saunders, and M. J. Choi, ''An experimental shock wave generator for lithotripsy studies,'' Phys. Med. Biol. **34**, 1733–1742 (1989).
[47] C. Wurster, J. Staudenraus, and W. Eisenmenger, ''The fibre optic probe hydrophone,'' Proc. 1994 IEEE Ultrson. Symp. Vol. 2, pp. 941–944 (1994).
[48] A. J. Coleman and J. E. Saunders, ''An survey of the acoustic output of commercial extracorporeal shock wave lithotripters,'' Ultrasound Med. Biol. **15**, 213–227 (1989).
[49] M. R. Bailey, ''Control of acoustic cavitation with application to lithotripsy,'' Technical Report ARL-TR-97-1, Applied Research Laboratories, The University of Texas at Austin (1997).
[50] M. R. Bailey, D. T. Blackstock, R. O. Cleveland, and L. A. Crum, ''Comparison of electrohydraulic lithotripters with rigid and pressure-release ellipsoidal reflectors: I. Acoustic field,'' J. Acoust. Soc. Am. **104**, 2517–2524 (1998).
[51] M. R. Bailey, D. T. Blackstock, R. O. Cleveland, and L. A. Crum, ''Comparison of electrohydraulic lithotripters with rigid and pressure-release ellipsoidal reflectors: II. Cavitation fields,'' J. Acoust. Soc. Am. (submitted).
[52] R. O. Cleveland, D. A. Lifshitz, B. A. Connors, A. P. Evan, L. R. Willis, and L. A. Crum, ''*In vivo* pressure measurement of lithotripsy shock waves,'' Ultrasound Med. Biol. **24**, 293–306 (1998).

Sound propagation over a large wedge: A comparison between the geometrical theory of diffraction and the parabolic equation

J. S. Robertson
Department of Mathematics and Computer Science, Georgia College & State University, Milledgeville, Georgia 31061-0490

(Received 13 January 1999; accepted for publication 23 March 1999)

Low-frequency propagation over wedges, hills, and barriers is an important problem with many applications. Two different propagation models (the geometrical theory of diffraction and the parabolic equation) are used to compare the sound field generated by a steady single-frequency source in front of, over, and behind a large, rigid, V-shaped wedge. Predictions along the boundary made with both models at several frequencies are compared and found to be in excellent agreement. The results provide additional evidence that the parabolic equation is able to account accurately for propagation effects caused by terrain irregularities. © *1999 Acoustical Society of America.* [S0001-4966(99)01007-3]

PACS numbers: 43.28.Fp, 43.20.Bi, 43.20.Fn [LCS]

INTRODUCTION

Sound propagation over obstacles such as ridges and barriers remains an important problem with many practical applications. Reference 1 presented a very thorough study of this question, comparing predictions made with the geometrical theory of diffraction (GTD) to experimental results involving a variety of barrier shapes. This work extended theoretical work in GTD done by others, namely Refs. 2 and 3, as well as experimental work reported in Ref. 4.

More recent work has examined propagation of high-level impulses over barriers,[5] scattering from barriers with a bump or trough in the shape of a Gaussian curve,[6] and scale-model experiments aimed at further verifying GTD.[7] Reference 8 examined ways to compute efficiently the three-dimensional sound pressure field around a barrier using full wave methods. Related problems have been considered in the context of underwater acoustics, e.g., Ref. 9.

The parabolic equation (PE) has been used extensively in studies of low-frequency atmospheric sound propagation in a variety of contexts.[10–15] There has been only one theoretical study[17] of propagation over a ridge, but that paper did not contain any comparisons to predictions by other models. More recently, Ref. 16 used the parabolic equation to estimate the insertion loss of screens while the atmosphere was under the influence of wind.

In this paper we consider propagation over a symmetric wedge as predicted by both the GTD and PE, and compare the results of the two models. The excellent agreement that will be demonstrated will provide further verification that the PE is a robust and accurate predictor of acoustic propagation, and can be a useful tool when studying propagation effects caused by irregular terrain.

I. PROBLEM GEOMETRY

The wedge geometry is depicted in Fig. 1. As shown in this figure, a cw source is at point $\mathcal{S}$, located a distance h_S above a flat, perfectly reflecting surface. A symmetrical wedge made of perfectly reflecting surfaces is located above the plane with height h_w and width d_w. The center of the wedge is at distance d_c from the source. A receiver $\mathcal{R}$ is located on the surface at distance r from the source. Note that r is always measured parallel to the horizontal plane.

The propagation domain is divided into four distinct regions, numbered I through IV as shown in the figure. In the subsections which follow, we will determine the outward-propagating sound field in each of these regions using ray theory and GTD.

A. Region I

In Region I, there are two rays as suggested in Fig. 2: a direct ray from the source $\mathcal{S}$ and an image ray from the image source $\mathcal{S}'$. The image appears to be located at a distance h_S below the ground plane. If r_0 is the distance from $\mathcal{S}$ to the receiver and r_1 the distance from $\mathcal{S}'$ to the receiver $\mathcal{R}_{\mathrm{I}}$, then the sound field in Region I is described by

$$\phi_{\mathrm{I}}=\frac{e^{ikr_0}}{r_0}+\frac{e^{ikr_1}}{r_1}, \tag{1}$$

where $k=2\pi f/c_0$, with f the source frequency and c_0 the sound speed.

B. Region II

In Region II, the sound field is more complex. The source and its image give rise to direct rays like those in Region I as suggested in Fig. 3(a). But owing to the upslope, the sound field contribution from each ray at $\mathcal{R}_{\mathrm{II}}$ is doubled. Letting r_0 and r_1 retain the same meanings as they had in Region I, the direct sound field is

$$\phi_{\mathrm{direct,II}}=2\frac{e^{ikr_0}}{r_0}+2\frac{e^{ikr_1}}{r_1}. \tag{2}$$

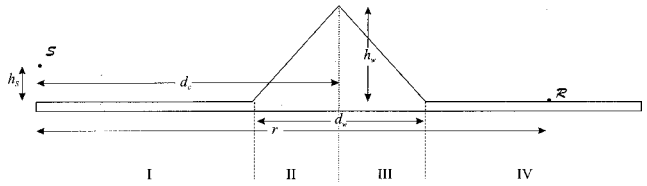

FIG. 1. The geometry of the wedge. Note the division into four separate computational regions.

The factor of 2 in each term on the right-hand side of Eq. (2) accounts for the image sources in the upslope plane of the wedge.

In addition, there is a ray which is diffracted from the leading edge of the wedge. The geometry for this ray is shown in Fig. 3(b). Following the results in Ref. 1, the diffracted sound field is given by

$$\phi_{\mathrm{diff,II}}=\frac{e^{ikR_1}}{R_1}\left[V\left(\frac{r_0r_1}{R_1},1,\theta_1-\theta_0\right)+V\left(\frac{r_0r_1}{R_1},1,\theta_1+\theta_0\right)\right]. \quad (3)$$

In this equation, r_0 is the distance from the source $\mathcal{S}$ to the leading edge of the wedge and r_1 is the distance from the leading edge to the receiver $\mathcal{R}_{\mathrm{II}}$. Moreover, $R_1=r_0+r_1$, while θ_0 and θ_1 are the angles made between r_0 and r_1 with the horizontal ground as measured from the leading edge. T_1 represents the interior angle made by the horizontal ground and the upslope.

The function V is defined as follows:

$$V(A,B,\theta)=V^+(A,B,\theta)+V^-(A,B,\theta), \quad (4)$$

where A and B are dummy arguments,

$$V^{\pm}(A,B,\theta)=-\frac{e^{i\pi/4}}{\sqrt{2\pi kAB}}\frac{1}{2\nu}\cot\left(\frac{\pi\pm\theta}{2\nu}\right)F'[BX^{\pm}(\theta)], \quad (5)$$

and

$$X^{\pm}=2kA\cos^2\left(\frac{2N^{\pm}\nu\pi-\theta}{2}\right), \quad (6)$$

where $\nu=2-T_1/\pi$. In addition,[19]

$$F'(x)=-2i\sqrt{x}e^{-ix}\int_{\sqrt{x}}^{\infty}e^{i\tau^2}\,d\tau=-2i\sqrt{x}e^{ix}F(\sqrt{x}), \quad (7)$$

where

$$F(x)=\int_x^{\infty}e^{i\tau^2}\,d\tau. \quad (8)$$

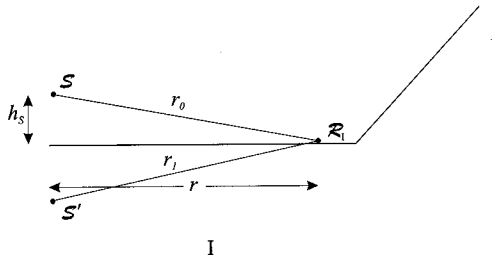

FIG. 2. Ray geometry in Region I.

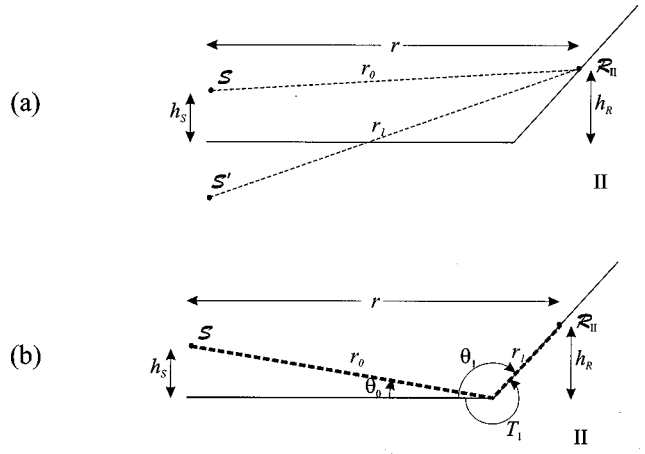

FIG. 3. Ray geometry in Region II: (a) Direct rays; (b) singly diffracted ray.

It is worth noting that the function $F(x)$ defined in Eq. (8), which Ref. 1 calls a Fresnel integral, is not in a standard form. It is more common to see Fresnel integrals given in the following forms:[18]

$$C(x)=\int_0^x\cos(\tau^2\pi/2)\,d\tau, \quad (9)$$

and

$$S(x)=\int_0^x\sin(\tau^2\pi/2)\,d\tau. \quad (10)$$

Using the more common notation represented in Eqs. (9) and (10), Eq. (8) can be rewritten as

$$F(x)=\sqrt{\pi/2}[1/2-C(\sqrt{2/\pi}x)]+i\sqrt{\pi/2}[1/2-S(\sqrt{2/\pi}x)]. \quad (11)$$

This substantially simplifies the use of existing numerical routines to compute $F(x)$.

Finally,

$$N^+=\begin{cases}0 & \text{for } \theta\leqslant\pi-T_1,\\ 1 & \text{for } \theta>\pi-T_1,\end{cases} \quad (12)$$

and

$$N^-=\begin{cases}-1 & \text{for } \theta<T_1-\pi,\\ 0 & \text{for } T_1-\pi\leqslant\theta\leqslant3\pi-T_1,\\ 1 & \text{for } \theta>3\pi-T_1.\end{cases} \quad (13)$$

The total sound field in Region II is obtained by summing the results of Eqs. (2) and (3):

$$\phi_{\mathrm{II}}=\phi_{\mathrm{direct,II}}+\phi_{\mathrm{diff,II}}. \quad (14)$$

C. Region III

In Region III, all rays are diffracted rays as shown in Fig. 4. The source and image both generate a singly diffracted ray over the crest of the wedge as shown in Fig. 4(a). The distance from the source and its image to the crest is r_0

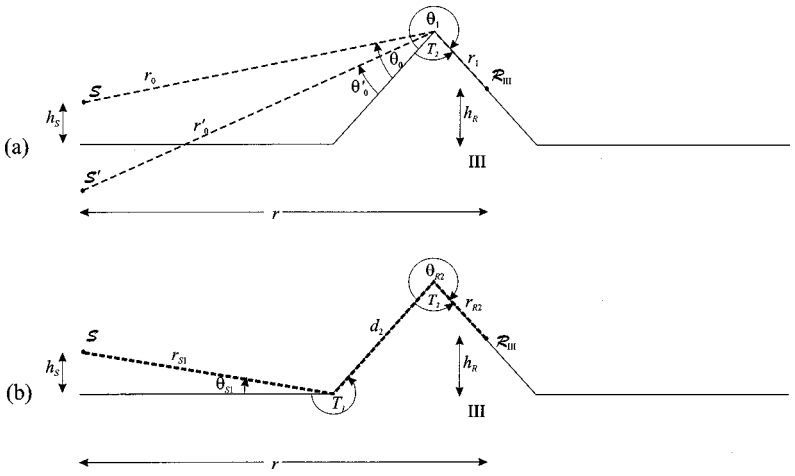

FIG. 4. Ray geometry in Region III: (a) Singly diffracted rays; (b) doubly diffracted ray.

and r_0', respectively. The ray angles are θ_0 and θ_0' as indicated. The diffracted ray path on the far side of the wedge is identical for both rays. The length of the diffracted ray is r_1 and this ray segment lies at angle θ_1 as shown in the figure. The sound field in Region III due to this pair of singly diffracted rays is

$$\phi_{\text{diff,III}}=\frac{e^{ikR_1}}{R_1}\left[V\left(\frac{r_0r_1}{R_1},1,\theta_1-\theta_0\right)+V\left(\frac{r_0r_1}{R_1},1,\theta_1+\theta_0\right)\right]+\frac{e^{ikR_1'}}{R_1'}\left[V\left(\frac{r_0'r_1}{R_1'},1,\theta_1-\theta_0'\right)+V\left(\frac{r_0'r_1}{R_1'},1,\theta_1+\theta_0'\right)\right], \tag{15}$$

where V, $V^{\pm}$, F, ν, and $N^{\pm}$ are as defined in Eqs. (4)–(13). Note that the interior angle used in the diffraction calculation is now T_2 as shown in Fig. 4(a).

The double diffracted ray is shown in Fig. 4(b). The first leg has length r_{S1} and makes angle θ_{S1} with the ground plane. The angle of the leading edge is T_1. The second leg of the ray lies along the upslope and has length d_2. The third leg lies along the backslope, with length r_{R2} and angle θ_{R2}. The angle of the crest of the wedge is T_2.

The field of the doubly diffracted ray is given by[1]

$$\phi_{\text{doub-diff,III}}=2\frac{e^{ik(r_{S1}+d_2+r_{R2})}}{r_{S1}+d_2+r_{R2}}\times V_1\left(\frac{r_{S1}(d_2+r_{R2})}{r_{S1}+d_2+r_{R2}},B,\nu_1\pi-\theta_{S1}\right)\times V_2\left(\frac{(r_{S1}+d_2)r_{R2}}{r_{S1}+d_2+r_{R2}},1,\theta_{R2}\right), \tag{16}$$

for $X_1^-(\nu_1\pi-\theta_{S1})\leqslant X_2^-(\theta_{R2})$. [Recall that $X^{\pm}$ was defined in Eq. (6).] Otherwise,

$$\phi_{\text{doub-diff,III}}=2\frac{e^{ik(R_{S1}+d_2+R_{R2})}}{R_{S1}+d_2+R_{R2}}\times V_1\left(\frac{R_{S1}(d_2+R_{R2})}{R_{S1}+d_2+R_{R2}},1,\nu_1\pi-\theta_{S1}\right)\times V_2\left(\frac{(R_{S1}+d_2)R_{R2}}{R_{S1}+d_2+R_{R2}},B,\theta_{R2}\right), \tag{17}$$

for $X_1^-(\nu_1\pi-\theta_{S1})\leqslant X_2^-(\theta_{R2})$. Note that ν_1 is computed using T_1 as the interior angle. In addition, the quantity B is now defined as

$$B=d_2(d_2+R_{S1}+R_{R2})/[(d_2+R_{S1})(d_2+R_{R2})]. \tag{18}$$

The total sound field in Region III is obtained by summing the results of Eq. (15) and Eqs. (16) and (17) (as appropriate):

$$\phi_{\text{III}}=\phi_{\text{diff,III}}+\phi_{\text{doub-diff,III}}. \tag{19}$$

D. Region IV

In Region IV, there are five rays as shown in Fig. 5. The source and image each contribute a singly diffracted ray as suggested in Fig. 5(a). In this case the strength of the sound field is doubled owing to the presence of the rigid boundary beneath $\mathcal{R}_{\text{IV}}$. Thus

$$\phi_{\text{diff,IV}}=2\frac{e^{ikR_1}}{R_1}\left[V\left(\frac{r_0r_1}{R_1},1,\theta_1-\theta_0\right)+V\left(\frac{r_0r_1}{R_1},1,\theta_1+\theta_0\right)\right]+2\frac{e^{ikR_1}}{R_1}\left[V\left(\frac{r_0'r_1}{R_1'},1,\theta_1-\theta_0'\right)+V\left(\frac{r_0'r_1}{R_1'},1,\theta_1+\theta_0'\right)\right], \tag{20}$$

where all parameters are determined as in the calculation done for Eq. (15).

There is a doubly diffracted ray which diffracts from both the leading edge and the crest of the wedge as shown in Fig. 5(b). This ray also experiences reinforcement at the receiver owing to the presence of the rigid surface beneath it. The expression for this portion of the field is found using the

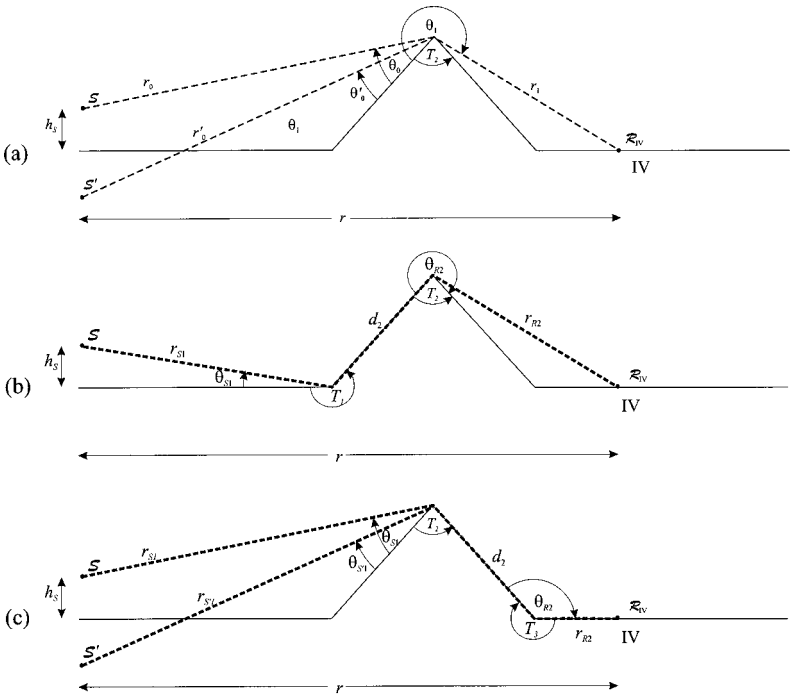

FIG. 5. Ray geometry in Region IV: (a) Singly diffracted rays; (b) first doubly diffracted ray; (c) pair of doubly diffracted rays.

formulas given in Eqs. (16) and (17). We will omit giving that expression here in the interest of saving space, but will denote this portion of the field in Region IV as $\phi_{\text{doub-diff,IV}(b)}$.

There are two more doubly diffracted rays—one from the source and one from its image—which diffract from the crest and the trailing edge as depicted in Fig. 5(c). The calculation of this field is done as for the other doubly diffracted fields, but using the parameters shown in the figure. We denote this part of the field in Region IV as $\phi_{\text{doub-diff,IV}(c)}$.

Thus the total sound field in Region IV is given as:

$$\phi_{\text{IV}} = \phi_{\text{diff,IV}} + \phi_{\text{doub-diff,IV}(b)} + \phi_{\text{doub-diff,IV}(c)}. \tag{21}$$

E. Ray theory results

We now use these results to determine the relative sound pressure level in four cases. The leading edge of the wedge is 4500 m from the source. The wedge is symmetrical with a height of 100 m centered at 5000 m from the source. The source height is fixed at 40 m. The sound speed is 340 ms^{-1}. In all instances the receiver is on the surface.

We determine the relative sound pressure level L_r from the following expression:

$$L_r = 20 \lg |\phi(r)|. \tag{22}$$

The results for all four regions (I through IV) and for four different frequencies are shown in Fig. 6.

In Region I, note that the relative sound pressure levels are identical. This is an expected result in this region. As the sound propagates past the leading edge and up the slope, there is an increase in level[20] of about 5 dB. In the 10 Hz case (represented by the solid curve), the increase is the greatest at the top of the wedge. In the other three cases, the maximum level occurs before the crest. In the 40 Hz and 80 Hz cases, the fluctuation in relative sound pressure level suggests interference between the individual rays arriving at the upslope.

In Region III, there are no more direct rays. The relative sound pressure level experiences a marked decrease of about 12 dB in the 10 Hz case and changing to more than 20 dB in the 80 Hz case. In all cases the receiver is moving deeper into a shadow zone behind the wedge and such drop-offs are expected.

As the receiver moves into Region IV, the relative sound pressure level begins to increase. This increase is similar in cause to the one seen in Region II, as the horizontal surface acts to reinforce the singly diffracted rays arriving from the crest of the wedge. After increasing quickly, the levels begin a slow decrease as range increases. This is essential geomet-

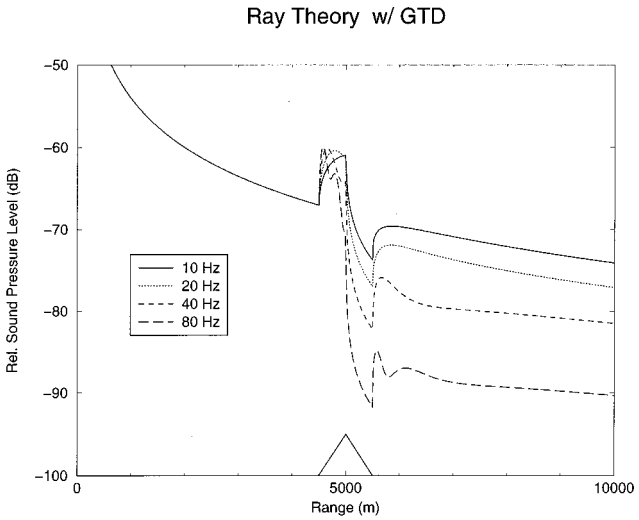

FIG. 6. Relative sound pressure versus range for four different frequencies. The ray model was used in this calculation. The relative position of the wedge is shown at the bottom of the graph.

ric spreading loss. In some sense, the levels in Region IV indicate the strength of the acoustic shadow cast by the wedge. When the frequency is 10 Hz, the shadow is very weak, but its strength increases as the frequency increases.

Having calculated the sound field with ray theory, we now seek to do the same with the parabolic equation.

II. THE PARABOLIC EQUATION

Let $p(r,z)$ be the acoustic pressure caused by the presence of a cw point source in a homogeneous atmosphere, where r and z denote the range and height in cylindrical coordinates. The time-independent wave field, denoted as $\wp$, is obtained by assuming that the source is harmonic with frequency f, so that $p=\wp\exp(-2\pi ift)$. In the source-receiver plane, it can be shown that $\wp$ satisfies the reduced wave equation

$$\nabla^2\wp+k^2n^2\wp+=0, \tag{23}$$

where c_0 is a reference sound speed, $c(r,z)$ is the sound speed, $n(r,z)=c_0/c(r,z)$ is the index of refraction.

It can be shown that away from the source, the quantity $\wp$ takes on the asymptotic form

$$\wp=\psi\frac{e^{ikr}}{\sqrt{kr}}. \tag{24}$$

Equation (24) is an essential feature of the parabolic equation when the quantity ψ is related to the slow-scale (i.e., many wavelengths) variation in the acoustic pressure. Furthermore, through careful scaling and asymptotic arguments, it can also be shown that ψ satisfies

$$2ik\psi_r+\psi_{zz}+k^2(n^2-1)\psi=0. \tag{25}$$

Our numerical implementation of Eq. (25) is based upon the implicit finite-difference model described in Ref. 21 and the enhancements described in Refs. 14 and 13. In this implementation, the numerical solution to Eq. (25) is represented as ψ_n^m, where

$$\psi_n^m=\psi(r_m,z_n),\quad m=1,\ldots,M,\quad n=1,\ldots,N. \tag{26}$$

In Eq. (26), (r_m,z_n) corresponds to a point on the range-depth mesh, and M and N are integers indicating the maximum number of range and depth points on the mesh. As the bottom boundary changes shape, N may be increased or decreased as necessary. A fast tridiagonal system solver is used in conjunction with the Crank–Nicolson scheme to march the solution forward in range.[21] This kind of approach is well-suited for many propagation situations, for example, those involving piecewise linear boundaries.

The usual PE starting field requires some modification when used over a perfectly reflecting ground surface. As discussed in Ref. 14, we add an image source which is located beneath the perfectly reflecting ground surface and require that the sum of the images sources satisfy the boundary condition. The point source is modeled here by the function

$$G(z,z_s)=\sqrt{\frac{k}{2}}\exp\{-[k(z-z_s)/2]^2\}, \tag{27}$$

where z_s is the source height above the ground surface. The image source is modeled by replacing z_s by $-z_s$ in Eq. (27). Let $g(z)=G(z,z_s)+G(z,-z_s)$ represent the linear superposition of the source and its image. The expression $g(z)$ is then used to model the starting field.[14]

Proper handling of the upper boundary condition is critical if long-range propagation predictions are to be made with the PE model. A systematic approach that has been met with success is to use a so-called nonreflecting boundary condition, sometimes called a generalized impedance boundary condition (GIBC), at the upper surface. The details of this boundary condition for the parabolic equation were presented in Ref. 15, and both its accuracy and suitability for atmospheric acoustic propagation calculations were demonstrated in Ref. 14.

A. Surface boundary conditions

We will assume that the ground surface is a perfectly reflecting boundary, i.e., one for which the pressure gradient normal to the ground surface is zero. Such a boundary, when horizontal, is modeled by the following condition:

$$\psi_z=0. \tag{28}$$

Here, the subscript refers to partial differentiation with respect to the indicated variable.

When the surface boundary is not flat, we will assume it to be piecewise linear. As shown in Fig. 1, this begins at $r=d_c-d_w/2$, changes at $r=d_c$, and ends at $r=d_c+d_w/2$. We will follow the method presented in Ref. 21 for this boundary treatment.

Because the normal derivative of $\wp$ must vanish, we have that

$$\wp_{\mathbf{n}}=0 \tag{29}$$

along the boundary. For a piecewise-linear surface,

$$(\cos\alpha)\wp_z-(\sin\alpha)\wp_r=0, \tag{30}$$

where α represents the angle between the horizontal and the sloping boundary surface. Using Eq. (24) and the fact Eq. (25) can be placed into the form $\psi_r=a\psi+b\psi_{zz}$, where $a=ik(n^2-1)/2$ and $b=i/2k$, it can be shown that ψ satisfies a second-order ordinary differential equation (treating r and other quantities as constants):

$$\psi_{zz}+q_1\psi_z+q_2\psi=0, \tag{31}$$

where

$$q_1=-(\cot\alpha)/b, \tag{32}$$

and

$$q_2=(ik-1/2r+a)/b. \tag{33}$$

Equation (31) can be considered an initial value problem with appropriate initial conditions specified at the bottom point. The boundary condition used in the difference scheme is a discretized version of the solution to Eq. (31). The details are discussed at length in Ref. 21.

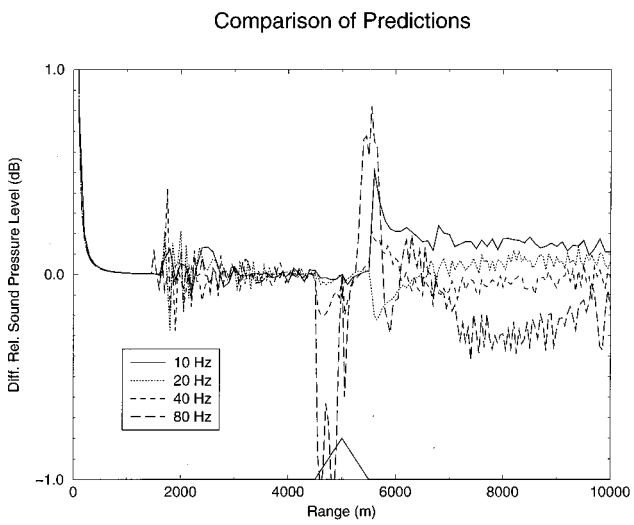

FIG. 7. Relative sound pressure versus range for four different frequencies. The parabolic equation was used in this calculation. The relative position of the wedge is shown at the bottom of the graph.

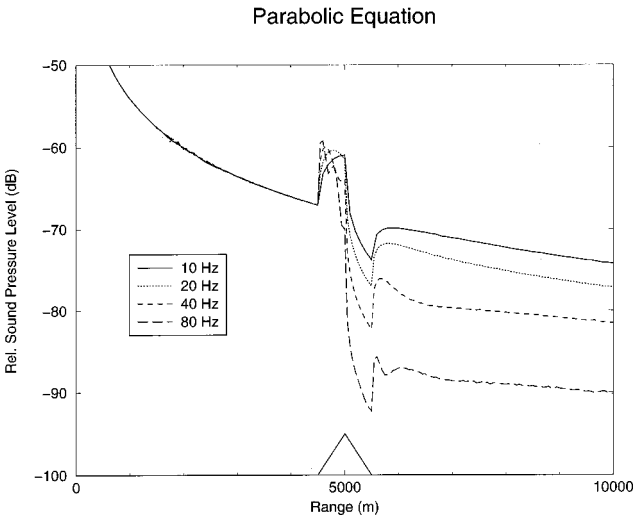

FIG. 8. Difference in relative sound pressures between the ray model and the parabolic equation versus range for four different frequencies. The relative position of the wedge is shown at the bottom of the graph.

B. Parabolic approximation results

Figure 7 displays the results of running the parabolic equation for four different frequencies. The source height was 40 m and the upper boundary was placed at 1000 m above the ground plane. The reference sound speed is $340\,\mathrm{ms}^{-1}$ and the sound speed is taken as constant throughout and equal in magnitude to the reference speed. The ground surface was taken to be rigid throughout the computational domain. The ground begins to slope up at a range of 4500 m to a height of 100 m at range 5000 m. After this, it slopes back down to the ground plane until range 5500 m, and then remains horizontal for the rest of the computation.

The step sizes used are summarized in Table I. Note that the ratio $\Delta r/\Delta z = 5$. This ensures that points added or deleted from the grid always coincide with the wedge boundary on either the upslope or downslope. The relative sound pressure level L_r is determined from

$$L_r = 20 \lg \left| \frac{\psi(r,z)}{\sqrt{kr}} \right|, \tag{34}$$

as it was in the ray case, but using ψ instead of ϕ.

Note the strong similarity between the respective curves in Figs. 7 and 6. There is evidence of some discretization errors, especially at a range of 2000 m, and beyond about 5500 m, but those errors turn out to be small.

TABLE I. Step sizes used in the parabolic equation. In this table, Δr is fixed at 0.147 wavelengths (approximately) and Δz is fixed at 0.029 wavelengths (approximately).

f (Hz)	Δr (m)	Δz (m)
10	5.0	1.0
20	2.5	0.5
40	1.25	0.25
80	0.625	0.125

III. COMPARISON OF RESULTS

A more detailed comparison of the predictions made by either model is shown in Fig. 8. This figure depicts the difference in relative sound pressure levels between the GTD prediction and the PE prediction plotted as a function of range.

Over most of the range, the differences are smaller than 0.5 dB. For small values of r, the differences are larger than this owing to the use of the Gaussian starting field in the PE (which is known to be inaccurate for very short ranges). Beyond about 500 m the two models are in almost perfect agreement. Shortly before range 2000 m, some fluctuation in all four cases begins to occur. These fluctuations are related to the discretization error at that range mentioned in the discussion of Fig. 7. A lobe from the Gaussian starting field has reflected from the upper boundary and propagated back to the ground surface. The scale used in Fig. 8 simply magnifies the apparent strength of the reflection.

There are fluctuations of about 1 dB at the leading edge, the crest, and the trailing edge of the wedge. These are discretization errors that are expected in the vicinity of sharp boundary changes. Beyond the trailing edge, the differences are small but sustained. This may be due in part to the neglect of a triply diffracted ray (leading edge-crest-trailing edge) which was not included in the computation of the ray result. (A formulation for triply diffracted rays is contained in Ref. 3.) Note that the fluctuations seen can be reduced by using smaller step sizes in range and height, but with an increased cost in computation time.

In any case, the curves in Fig. 8 clearly show that the PE and GTD produce nearly identical predictions. This provides further evidence of the predictive power of the PE and follows from the extensive validation of GTD against experimental data discussed in Ref. 1 and other sources. Similar work remains to be done with nonrigid boundaries, however, and this is an active area of current research.

IV. SUMMARY

We have considered the propagation of a steady cw sound signal over a rigid surface composed of a horizontal boundary and a symmetrical wedge. The geometrical theory of diffraction is used to determine the sound field on both sides of the wedge. Then, the parabolic equation is made to do the same calculation in the same domain.

Our comparison of the prediction results made with both models demonstrates that the relative sound pressure levels over a wedge predicted by both the geometrical theory of diffraction and an implicit finite-difference implementation of the parabolic equation are in very good agreement. Because diffraction theory has been well validated by experimental data, this comparison also serves to extend confidence in calculations made with the parabolic equation.

ACKNOWLEDGMENTS

The author appreciates the many useful suggestions made by the editor and the two reviewers. Many beneficial discussions were held with P. Coppola, J. Zimmermann, and P. G. Angel. Finally, a special note of thanks is owed to W. L. Siegmann.

[1] K. B. Rasmussen, ''On the effect of terrain profile on sound propagation outdoors,'' J. Sound Vib. **98**, 35–41 (1985).
[2] R. G. Kouyoumjian and P. H. Pathak, ''A uniform geometrical theory of diffraction for an edge in a perfectly conducting surface,'' Proc. IEEE **62**, 1448–1461 (1974).
[3] T. Kawai, ''Sound diffraction by a many-sided barrier or pillar,'' J. Sound Vib. **79**, 229–242 (1981).
[4] B. A. De Jong, A. Moerkerken, and J. D. van der Toorn, ''Propagation of sound over a grassland and over an earth barrier,'' J. Sound Vib. **86**, 23–46 (1983).
[5] D. J. Saunders and R. D. Ford, ''A study of the reduction of explosive impulses by finite sized barriers,'' J. Acoust. Soc. Am. **94**, 2859–2867 (1993).
[6] Y. L. Li, S. J. Franke, and C. H. Liu, ''Wave scattering from a ground with a Gaussian bump or trough in an inhomogeneous medium,'' J. Acoust. Soc. Am. **93**, 1067–1075 (1993).
[7] K. B. Rasmussen, ''Model experiments related to outdoor propagation over an earth berm,'' J. Acoust. Soc. Am. **96**, 3617–3620 (1994).
[8] D. Duhamel, ''Efficient calculation of a three-dimensional sound pressure field around a noise barrier,'' J. Sound Vib. **197**, 547–571 (1996).
[9] L. F. Bondar', V. A. Bulanov, N. N. Dyul'dina, B. A. Kosyrev, and Yu. N. Morgunov, ''Influence of a seamount on the propagation of acoustic signals in the ocean,'' Sov. Phys. Acoust. **34**, 201–202 (1988).
[10] K. Gilbert and M. White, ''Application of the parabolic equation to sound propagation in a refracting atmosphere,'' J. Acoust. Soc. Am. **85**, 630–637 (1989).
[11] M. West, K. Gilbert, and R. A. Sack, ''A tutorial on the parabolic equation (PE) model used for long range sound propagation in the atmosphere,'' Appl. Acoust. **37**, 31–49 (1992).
[12] M. White and K. Gilbert, ''Application of the parabolic equation to the outdoor propagation of sound,'' Appl. Acoust. **27**, 227–238 (1989).
[13] J. S. Robertson, W. L. Siegmann, and M. J. Jacobson, ''Low-frequency sound propagation modeling over a locally-reacting boundary using the parabolic approximation,'' J. Acoust. Soc. Am. **98**, 1130–1137 (1995).
[14] J. S. Robertson, P. J. Schlatter, and W. L. Siegmann, ''Sound propagation over impedance discontinuities with the parabolic approximation,'' J. Acoust. Soc. Am. **99**, 761–767 (1996).
[15] R. J. Jardine, W. L. Siegmann, and J. S. Robertson, ''Alternative nonreflecting boundary conditions for PE modeling of atmospheric acoustic propagation,'' in *Theoretical and Computational Acoustics—Volume 2*, edited by D. Lee and M. H. Schultz (World Scientific, Singapore, 1994).
[16] K. B. Rasmussen and M. G. Arranz, ''The insertion loss of screens under the influence of wind,'' J. Acoust. Soc. Am. (submitted).
[17] J. S. Robertson, M. J. Jacobson, W. L. Siegmann, and D. P. Santandrea, ''Acoustical effects of a large ridge on low-frequency sound propagation in stationary and moving atmospheres,'' Appl. Acoust. **31**, 265–280 (1990).
[18] The FORTRAN source code which implements Fresnel functions uses the definitions of $S(x)$ and $C(x)$ given here. It can be obtained via the world-wide web from http://net-lib.utk.edu/.
[19] There is a minor typo in the expression given for $F'(x)$ given in Eq. (5) of Ref. 1. It has been corrected here.
[20] Such reinforcement is well known. For example, see O. L. Angevine, ''The prediction of transformer noise,'' Sound Vib. 16–18 (October 1994).
[21] D. Lee and S. T. McDaniel, ''Ocean acoustic propagation by finite difference methods,'' Comput. Math. Appl. **14**, 305–423 (1987).

Seabed sediment attenuation profiles from a movable sub-bottom acoustic vertical array

L. Neil Frazer and Shung-Sheng Fu
Department of Geology and Geophysics, School of Ocean and Earth Science and Technology, University of Hawaii at Manoa, Honolulu, Hawaii 96822

Roy H. Wilkens
Hawaii Institute of Geophysics and Planetology, School of Ocean and Earth Science and Technology, University of Hawaii at Manoa, Honolulu, Hawaii 96822

(Received 2 March 1997; revised 2 February 1999; accepted 11 March 1999)

The acoustic lance [S. S. Fu, M.Sc. Thesis, University of Hawaii at Manoa (1994); Fu *et al.*, J. Acoust Soc. Am. **99**, 234–241 (1996)] consists of a linear array of acoustic receivers below an acoustic source, all mounted on the outside of a core barrel or independent probe which is embedded in the seafloor. In earlier studies lance travel time data were processed to give *in situ* compressional wave sound speed as a function of depth. In this study lance waveforms are processed to extract compressional wave attenuation $A=Q^{-1}$ as a function of depth. The processing technique is unusual because the L_1 norm is used instead of the usual L_2 norm, the model space of attenuation profiles is exhaustively searched within the limits of discretization, and the marginal posterior probability density function of attenuation is computed explicitly at each depth. The technique is described in terms of Bayesian inverse theory using the notation of Tarantola. © *1999 Acoustical Society of America.* [S0001-4966(99)05306-0]

PACS numbers: 43.30.Ma, 43.60.Pt [SAC-B]

INTRODUCTION

In this study we use a new processing technique to generate *in situ* compressional wave attenuation profiles in three different types of surficial marine sediment. The measurements are in the band 5–20 kHz, and the profiles are in the interval 0–4 mbsf (meters below sea floor). The profiles show that attenuation can vary rapidly with depth, with sediment type, and with location in the same sedimentary environment.

The acoustic lance (Fu, 1994; Fu *et al.*, 1996a) is an instrument developed to obtain *in situ* compressional sound speed and attenuation profiles for the upper few meters of seabed sediment. As shown in Fig. 1, the lance consists of a linear array of receivers mounted on a core barrel or probe. A broadband source and a solid state recording system are mounted on the weight-stand of the probe, above the receivers. In use, lance is lowered by cable from a surface vessel; when the tip of the probe touches bottom, a trigger turns on the electronics. The lance signal spectrum is in the range of 5 kHz to 20 kHz, as shown in Fig. 2. A typical set of recorded waveforms is shown in Fig. 3.

Earlier studies using lance waveforms have concentrated on the extraction of sound speed profiles, whereas this study is concerned mainly with the extraction of attenuation profiles. Methods of extracting attenuation from seismic data have been reviewed by Jannsen *et al.* (1985) and Bromirski *et al.* (1992, 1995). Attenuation is much more difficult to extract than sound speed, as whole waveforms must be used, and if multiple receivers are used then corrections must be made to the data so that the spectrum of the source–receiver wavelet is effectively the same at each receiver. For this reason many attenuation studies use data containing multiple seismic phases recorded on the same instrument. Our method of extracting attenuation from the waveforms is an application of geophysical inverse theory to the well known spectral ratio method.

In seismic studies, attenuation results are often presented in terms of attenuation $A=Q^{-1}$ where Q is a dimensionless quantity called the acoustic quality factor. A review of the mathematics of Q, including a rigorous definition suitable for both low and high frequencies, was given by O'Connell and Budiansky (1978). For the high frequency waves of this study a good physical interpretation of A is provided by regarding A as $1/\pi$ times the fractional loss in amplitude per cycle. The plane wave $\exp[i2\pi fx/c]$, where f is temporal frequency, x is distance and c is sound speed, decays like $\exp(-\alpha x)$, where α is given by $\alpha=\pi fA/c$. It follows that A is twice the ratio of the imaginary and real parts of $1/c$. Attenuation is used in some papers as a synonym for α, but here the word attenuation is always used to mean A. Note that when A is constant, α is proportional to the first power of frequency. The attenuation measured from lance data is *effective* attenuation, as it contains the effects of both *intrinsic* attenuation and *scattering* attenuation. The well known relation between these three quantities is

$$A_{\text{eff}}=A_{\text{intr}}+A_{\text{sc}}. \tag{1}$$

Although the dependence of A on frequency is much debated (e.g., Stoll, 1985; Kibblewhite, 1989), here we accept the important assumption that A is independent of frequency. This assumption is not essential for our method, but it is

 0001-4966/99/106(1)/120/11/$15.00

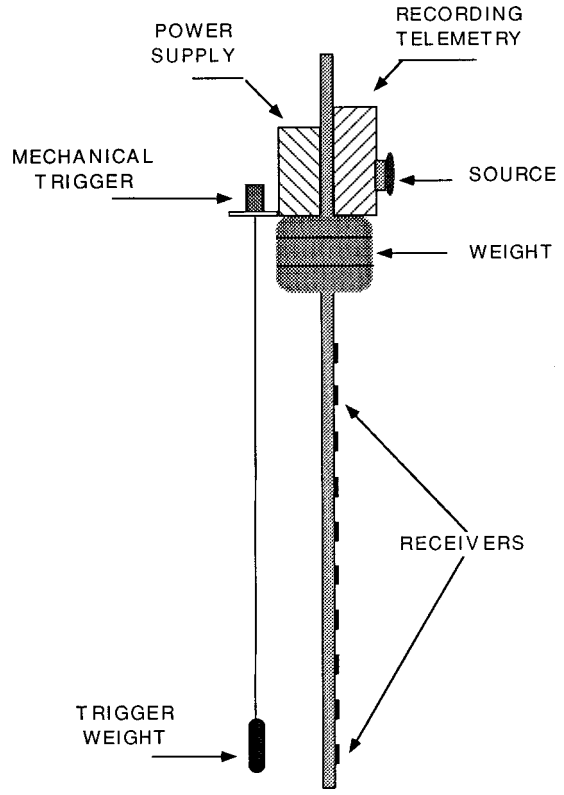

FIG. 1. Configuration of the acoustic lance.

appropriate for our data set which spans less than 3 octaves in frequency.

Attenuation profiles from four lance data sets will be obtained below. Two of the data sets are from deployments at sites 624 and 627, located in Kiel Bay, Baltic Sea (Fu *et al.*, 1996b; Wilkens and Richardson, 1996). The seabed of Kiel Bay is composed of high-porosity clays that contain gas bubbles in some areas, and show evidence of significant biological activity (Richardson, 1994; Orsi *et al.*, 1996). However, sediment velocities do not suggest the presence of gas bubbles at sites 624 and 627 (Fu *et al.*, 1996b).

The third lance data set we analyze is site A2 in the Halekulani sand channel off the island of Oahu, Hawaii. The sediments there are carbonate sands. As the gravity corer was unable to penetrate this hard bottom, a jet probe was used to penetrate the sand approximately 2 m in depth. The lance was left in the sand for two months prior to taking the acoustic measurements.

The fourth lance data set analyzed is from site S90 on

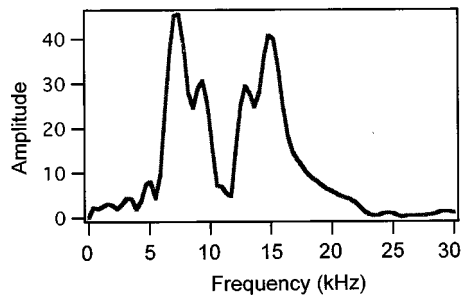

FIG. 2. The amplitude spectrum of the lance signal recorded in seawater.

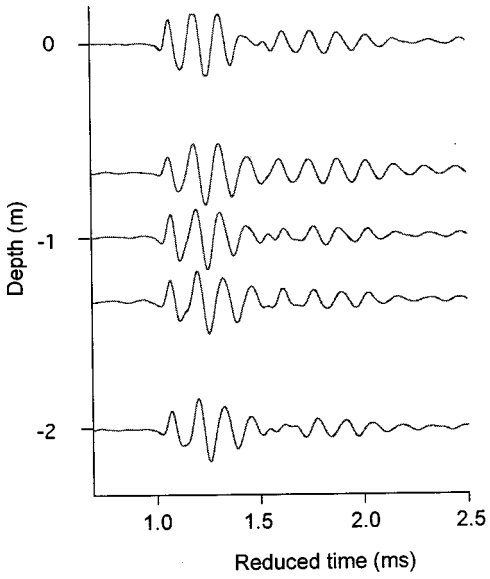

FIG. 3. Lance signals recorded at Site 624, Keil Bay, Baltic Sea. Each waveform has been advanced by $D/1634$ ms where D is the distance from the uppermost receiver in meters, and 1634 m/s is the average sediment sound speed. Waveforms were individually normalized.

the Eel River delta in northern California. The silty sediments of this area are strongly influenced by biological reworking and periodic flood deposition from the Eel and Mad rivers (Nittrouer and Kravitz, 1995).

SPECTRAL RATIOS

In processing the lance data for attenuation we assume that a lance signal at depth z below the receiver has a spectrum of the form

$$S(\omega,z)=H(\omega)\frac{1}{z}\exp\left[i\omega\int_0^z\frac{dz}{c(z)}\right]. \tag{2}$$

In this equation $\omega=2\pi f$ is radian frequency; H is the spectral transfer function of the system consisting of acoustic source, receiver and recording system; $1/z$ is the geometrical spreading factor for spherical spreading; and $c(z)$ is the sound speed profile. Sound speed is taken to have the simple form

$$\frac{1}{c}=\frac{1}{c_R}\left(1+\frac{iA}{2}\right), \tag{3}$$

in which $1/c_R$ is the real part of $1/c$. Parametrizations of sound speed that include the frequency dependence of c_R and A were extensively tested, but they gave no improvement in results over the frequency-independent formula just given. From the expression for S it follows that the ratio of signal spectra S_1 and S_2, from receivers at respective depths z_1 and z_2, is given by

$$\frac{S_2}{S_1}=\frac{H_2}{H_1}\frac{z_1}{z_2}\exp\left(i\omega T_{12}-\frac{\omega}{2}T_{12}A_{12}\right), \tag{4}$$

in which the traveltime from receiver 1 to receiver 2 is

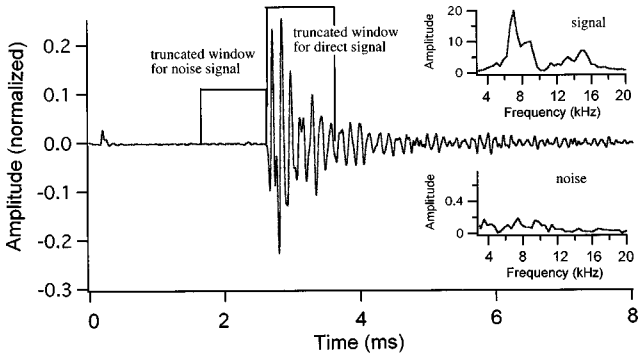

FIG. 4. Time windows for spectral estimation of noise and signal.

$$T_{12}=\int_{z_1}^{z_2} dz\,\frac{1}{c_R(z)}, \tag{5}$$

and the attenuation of the interval between the two receivers is

$$A_{12}=\frac{1}{T_{12}}\int_{z_1}^{z_2} dz\,\frac{A(z)}{c_R(z)}. \tag{6}$$

To remove the effect of the unknown source receiver transfer functions H_1 and H_2, we also conduct the same experiment in seawater, which, relative to sediment, has an insignificant attenuation. The spectral ratio for the seawater experiment is

$$\frac{W_2}{W_1}=\frac{H_2}{H_1}\frac{z_1}{z_2}\exp(i\omega T_w), \tag{7}$$

in which W_1 and W_2 are the spectra of the signals recorded in the water at receivers 1 and 2, respectively, and T_w is the arrival time difference in seawater. Dividing the sediment ratio by the seawater ratio, and taking the modulus, gives the *corrected* spectral ratio,

$$\left|\frac{S_2/S_1}{W_2/W_1}\right|=\exp\left(-\frac{\omega}{2}T_{12}A_{12}\right). \tag{8}$$

Taking the logarithm of each side, and defining the data quantity $\phi_{12}(f)$ by

$$\phi_{12}=\ln\left|\frac{S_2/S_1}{W_2/W_1}\right|, \tag{9}$$

gives the spectral ratio formula

$$\phi_{12}(f)=-\pi f T_{12}A_{12}. \tag{10}$$

It follows that on a plot of $\phi(f)$ vs f the plotted points should cluster about the straight line through the origin with slope $-\pi T_{12}A_{12}$; this is the basis of the spectral ratio method.

As will be seen below, in our data set the line $\phi(f)$ does not go through the origin. We attribute this to a change in receiver transfer function H from sediment to water. Examination of the derivation above shows that if going from sediment to water changes the gain on each receiver by a slightly different factor then the equation for $\phi(f)$ will have a nonzero intercept. To allow for this, we use the following more general spectral ratio formula:

$$\phi_{12}(f)=B-\pi f T_{12}A_{12}, \tag{11}$$

in which B is unknown, but independent of f. Other types of error are also present; for example, some energy travels through the probe itself. The effects of these other types of errors are neglected in the theory, but they are accounted for to some extent in our error analysis.

We wish to give more weight to values of ϕ at frequencies where the signal-to-noise ratio is high. From the definition of ϕ_{12} as a spectral ratio of the data we estimate the L_1 standard error in ϕ_{12} by

$$|d\phi_{12}|=\frac{|dS_1|}{|S_1|}+\frac{|dS_2|}{|S_2|}+\frac{|dW_1|}{|W_1|}+\frac{|dW_2|}{|W_2|}, \tag{12}$$

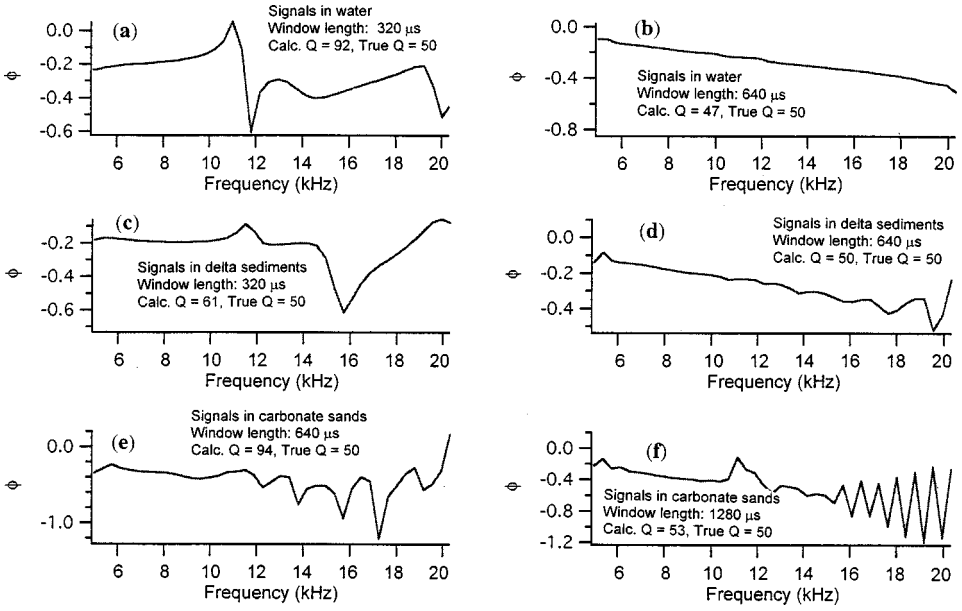

FIG. 5. Tests of window length by synthetic propagation. Each panel shows $\phi(f)$ calculated from an actual lance signal that has been synthetically propagated a distance of 1 m using a dispersive propagation operator. The same window length was used for spectral estimation of the signal before and after propagation. Note the oscillations of ϕ outside of the band of the source, indicating a need for an inversion procedure that incorporates signal to noise ratios.

at each frequency. To estimate the error $|dS_1|$ we Fourier analyze the noisy time series in a time window immediately preceding arrival of the signal S_1, assigning the amplitude spectrum value of the noise to $|dS_1|$, and similarly for the other signals in water and sediment. The windows used for Fourier analysis of signals and noise are shown in Fig. 4.

As spectral estimation is an important component of our procedure, we tested windows of different length and shape. Following Bromirski *et al.* (1995), tests were conducted by taking an actual recorded lance signal, and propagating it synthetically to the next receiver (1 m distant) using a dispersive propagation operator with given attenuation. The original seismogram and the dispersively propagated seismogram were then analyzed (by the inverse theory procedure given later in the paper) using various time windows for spectral estimation. Equation (11) of Bromirski *et al.* (1995) gives the propagation operator as

$$\varphi(f)=\exp\left\{ i2\pi T\left|\frac{f_r}{f}\right|^{\gamma}\left[1+i\tan\left(\frac{\pi\gamma}{2}\right)\right]\right\}, \tag{13}$$

in which T is the traveltime difference between the receivers, f_r is a reference frequency, and $\gamma=\pi^{-1}\tan^{-1}A$. This propagation operator is based on the Kjartansson (1979) constant-Q formula for dispersion.

Figure 5 shows plots of $\phi(f)$ for various window lengths, using various actual signals. The value of A used for propagation and the value of A obtained from $\phi(f)$ are also shown on each panel. Panels (a) and (b) of Fig. 5 show that a 640 μs window is satisfactory for analysis of the water signals, and that when too short a window is used ϕ is badly behaved. Panels (c) and (d) show that a 640 μs window is also adequate for analysis of the Eel River delta signals. Based on these results we used a 640 μs window for analysis of the Eel River data. For the Kiel Bay analyses a 640 μs window was also used. Although the signals in the carbonate sand were not longer than those from Eel River, panels (e)–(f) show that a 1280 μs window works well for the carbonate sand. A 2560 μs window (not shown) works almost as well, however, it was not used on the data analysis because a window that long would include surface reflections.

INVERSE THEORY

Consider the forward equation

$$\boldsymbol{d_o}=\boldsymbol{G}(\boldsymbol{m})+\boldsymbol{e}, \tag{14}$$

in which $\boldsymbol{d_o}$ is a vector of measured data values, $\boldsymbol{m}$ is a vector of parameters whose values are sought, $\boldsymbol{G}$ is a model of the physical process, and $\boldsymbol{e}$ is a vector of data errors. Notice that we distinguish between the measured data $\boldsymbol{d_o}$ and the true data $\boldsymbol{d}$ whose value is unknown. For example, the pressure values recorded by our hydrophones are not the true pressure values because the hydrophone is imperfect. This is an example of instrument error. Errors caused by noise processes in the apparatus used to record the data are also called instrument errors. On the other hand some types of error are due the inadequacy of our physical model, and these types of errors are referred to as theory errors. In our case an example

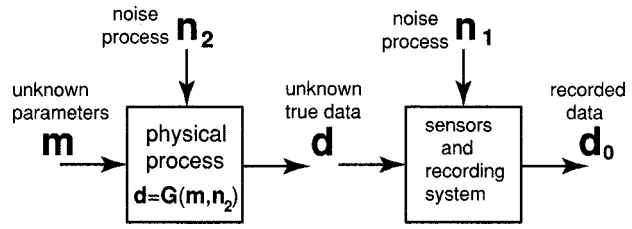

FIG. 6. A two-stage model for geophysical inversion. Noise process $\boldsymbol{n}_2$ includes geophysical parameters whose values we are not attempting to obtain from the experiment, but which may affect the data; the statistics of $\boldsymbol{n}_2$ are assumed to be known. Noise process $\boldsymbol{n}_1$ affects the sensors and recording system; its statistics are also assumed known. In general, the dependence of $\boldsymbol{d}$ on $\boldsymbol{n}_2$ is nonlinear, and the dependence of $\boldsymbol{d_o}$ on $\boldsymbol{n}_1$ is nonlinear.

of theory error is energy in the seismogram due to scattering off of the probe itself, as a better model of the propagation would include the probe.

One goal of inverse theory is to find the most likely value of $\boldsymbol{m}$ that is consistent with the observed data $\boldsymbol{d_o}$. This value of $\boldsymbol{m}$ is called the maximum *a posteriori* model, or MAP. If the computational power available is substantial, and the physical process $\boldsymbol{G}$ is not too complicated, then one can also afford to pursue the real goal of inverse theory, which is to generate $\sigma_M(\boldsymbol{m})$, the posterior probability density function of $\boldsymbol{m}$. The function σ_M contains all the information available about $\boldsymbol{m}$: for example, the value of $\boldsymbol{m}$ at which σ takes its maximum is the MAP value of $\boldsymbol{m}$. This approach to inversion is set forth in detail in the book by Tarantola (1987). Tarantola's fundamental relation is

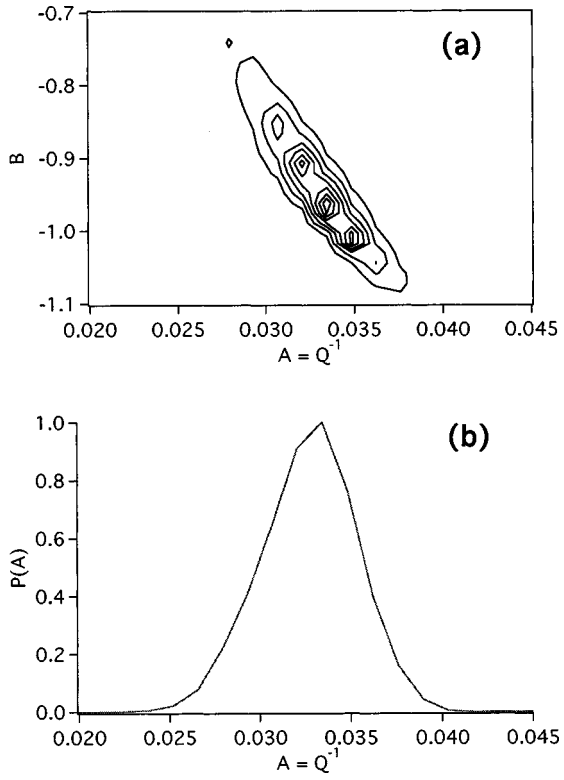

FIG. 7. Inversion for the interval between receiver 2 and receiver 4 at site 624. (a) The posterior distribution $\sigma(A,B)$. (b) The marginal posterior distribution of A obtained from $\sigma(A,B)$ by integration over B.

$$\sigma(\boldsymbol{m},\boldsymbol{d}) \propto \nu(\boldsymbol{d_o}|\boldsymbol{d})\,\theta(\boldsymbol{d}|\boldsymbol{m})\rho(\boldsymbol{m}), \tag{15}$$

where σ is the joint posterior distribution of model and data, ν is the instrument distribution, θ is the theory distribution and ρ is the prior distribution of $\boldsymbol{m}$. [This equation becomes very familiar as soon as one inserts typical forms of the distributions on the right hand side; for example: $\nu = \exp(-\|\boldsymbol{d}-\boldsymbol{d_o}\|_\nu^2)$, $\theta = \exp(-\|\boldsymbol{d}-\boldsymbol{G}(\boldsymbol{m})\|_\theta^2)$, and $\rho = \exp(-\|\boldsymbol{m}-\boldsymbol{m}_0\|_m^2)$, where $\|\cdot\|_\nu$ and $\|\cdot\|_\theta$ are norms in the data space, and $\|\cdot\|_m$ is a norm in the model space.]

Duijndam (1988) has noted that relation Eq. (15) can be derived using the concept of conditional probability and its consequence, Bayes rule. As usual we define $p(a|b)$, the conditional probability of event a given event b, by the relation $p(a|b)=p(a,b)/p(b)$ where $p(a,b)$ is the joint probability of a and b, and $p(b)$ is the probability of b. Accepting the notion of conditional probability, one sees that $p(a,b)$ can be written as $p(a|b)p(b)$ or as $p(b|a)p(a)$, and equating these two expressions gives Bayes rule in the form $p(a|b)=p(b|a)p(a)/p(b)$. Here we will extend Duijndam's remarks by using Bayes rule to derive Eq. (15) in a way that reveals how θ and ν are related to the noise processes. As shown in Fig. 6, suppose that the instrument is subject to a noise process with unknown parameters $\boldsymbol{n}_1$ and that the propagation (i.e., the theory) is contaminated by a different noise process with unknown parameters $\boldsymbol{n}_2$. Beginning with Bayes rule we write

$$p(\boldsymbol{m},\boldsymbol{d},\boldsymbol{n}_1,\boldsymbol{n}_2|\boldsymbol{d_o}) = \frac{p(\boldsymbol{d_o}|\boldsymbol{m},\boldsymbol{d},\boldsymbol{n}_1,\boldsymbol{n}_2)\,p(\boldsymbol{m},\boldsymbol{d},\boldsymbol{n}_1,\boldsymbol{n}_2)}{p(\boldsymbol{d_o})}. \tag{16}$$

Notice that $p(\boldsymbol{d_o})$ must be nonzero because it is a value of $\boldsymbol{d}$ that has actually been observed. Henceforth we omit the denominator, and use the proportional sign ''$\propto$'' in place of the equal sign. Next notice that $\boldsymbol{d_o}$ depends only on $\boldsymbol{d}$ and on the instrument noise process $\boldsymbol{n}_1$, hence $p(\boldsymbol{d_o}|\boldsymbol{m},\boldsymbol{d},\boldsymbol{n}_1,\boldsymbol{n}_2)$ may be written $p(\boldsymbol{d_o}|\boldsymbol{d},\boldsymbol{n}_1)$. Our relation has now simplified to

$$p(\boldsymbol{m},\boldsymbol{d},\boldsymbol{n}_1,\boldsymbol{n}_2|\boldsymbol{d_o}) \propto p(\boldsymbol{d_o}|\boldsymbol{d},\boldsymbol{n}_1)\,p(\boldsymbol{m},\boldsymbol{d},\boldsymbol{n}_1,\boldsymbol{n}_2). \tag{17}$$

Using conditional probabilities we substitute the product $p(\boldsymbol{d}|\boldsymbol{m},\boldsymbol{n}_1,\boldsymbol{n}_2)p(\boldsymbol{m},\boldsymbol{n}_1,\boldsymbol{n}_2)$ for $p(\boldsymbol{m},\boldsymbol{d},\boldsymbol{n}_1,\boldsymbol{n}_2)$, giving

$$p(\boldsymbol{m},\boldsymbol{d},\boldsymbol{n}_1,\boldsymbol{n}_2|\boldsymbol{d_o}) \propto p(\boldsymbol{d_o}|\boldsymbol{d},\boldsymbol{n}_1)\,p(\boldsymbol{d}|\boldsymbol{m},\boldsymbol{n}_1,\boldsymbol{n}_2)\,p(\boldsymbol{m},\boldsymbol{n}_1,\boldsymbol{n}_2). \tag{18}$$

As the true data $\boldsymbol{d}$ do not depend on the instrument noise, $p(\boldsymbol{d}|\boldsymbol{m},\boldsymbol{n}_1,\boldsymbol{n}_2)$ simplifies to $p(\boldsymbol{d}|\boldsymbol{m},\boldsymbol{n}_2)$. Also, as $\boldsymbol{m}$, $\boldsymbol{n}_1$, and $\boldsymbol{n}_2$ are independent variables, the joint distribution $p(\boldsymbol{m},\boldsymbol{n}_1,\boldsymbol{n}_2)$ reduces to the product $p(\boldsymbol{m})p(\boldsymbol{n}_1)p(\boldsymbol{n}_2)$. Our relation becomes

$$p(\boldsymbol{m},\boldsymbol{d},\boldsymbol{n}_1,\boldsymbol{n}_2|\boldsymbol{d_o}) \propto p(\boldsymbol{d_o}|\boldsymbol{d},\boldsymbol{n}_1)\,p(\boldsymbol{d}|\boldsymbol{m},\boldsymbol{n}_2)\,p(\boldsymbol{m})\,p(\boldsymbol{n}_1)\,p(\boldsymbol{n}_2). \tag{19}$$

Finally, integration over the unknown noise parameters $\boldsymbol{n}_1$ and $\boldsymbol{n}_2$ yields

$$\int d\boldsymbol{n}_1 \int d\boldsymbol{n}_2 p(\boldsymbol{m},\boldsymbol{d},\boldsymbol{n}_1,\boldsymbol{n}_2|\boldsymbol{d_o}) \propto \left\{ \int d\boldsymbol{n}_1 p(\boldsymbol{d_o}|\boldsymbol{d},\boldsymbol{n}_1)p(\boldsymbol{n}_1) \right\} \times \left[\int d\boldsymbol{n}_2 p(\boldsymbol{d}|\boldsymbol{m},\boldsymbol{n}_2)p(\boldsymbol{n}_2) \right] p(\boldsymbol{m}). \tag{20}$$

Comparing this relation with Tarantola's relation we see that the left hand side is $\sigma(\boldsymbol{m},\boldsymbol{d})$, the term $\{\cdots\}$ is the instrument distribution $\nu(\boldsymbol{d_o}|\boldsymbol{d})$, the term $[\cdots]$ is the theory distribution $\theta(\boldsymbol{d}|\boldsymbol{m})$, and $p(\boldsymbol{m})$ is just the prior distribution of the data, $\rho(\boldsymbol{m})$.

The derivation just given shows that Tarantola's equation can be quickly derived by Bayes rule; it also shows that knowledge of the *way* in which errors arise in particular cases can be used to infer the forms of ν and θ. For example, if one takes $\nu \propto \exp[-\|\boldsymbol{d}-\boldsymbol{d_o}\|_\nu^2]$ then the noise process with parameters $\boldsymbol{n}_1$ can be used to obtain the (covariance) matrix in the norm $\|\cdot\|_\nu$. This fact will not be of much help here, as our noise is poorly understood, but it is helpful in other problems. A reader who has trouble with the derivation just given should try repeating it without $\boldsymbol{n}_1$ and $\boldsymbol{n}_2$. The Tarantola relation Eq. (15) is then obtained in two quick steps but without insight into ν and θ.

We now take the usual next step with Tarantola's equation, eliminating the true data $\boldsymbol{d}$ from the left hand side by integrating over the data space, thereby obtaining the posterior distribution of the model itself,

$$\sigma_M(\boldsymbol{m}) \propto \rho(\boldsymbol{m}) \int d\boldsymbol{d}\,\nu(\boldsymbol{d_o}|\boldsymbol{d})\,\theta(\boldsymbol{d}|\boldsymbol{m}). \tag{21}$$

When the model space has dimension two then one can display σ_M by a contour plot or perspective view, but when the model space has dimension greater than two it is often helpful to display the marginal posterior distributions of the components of $\boldsymbol{m}$ (e.g., Basu and Frazer, 1990). The marginal posterior distribution (MPD) of the kth component of $\boldsymbol{m}$ is obtained by integrating over all the N_M-1 other components:

$$\sigma_k(m_k) \propto \int dm_1 \cdots \int dm_{k-1} \int dm_{k+1} \cdots \int dm_{N_M} \sigma_M(\boldsymbol{m}). \tag{22}$$

This last relation is used below to display the attenuation profiles.

DATA ANALYSIS

It is possible to invert for the attenuation profile in a single step. However, as a form of quality control, we choose a two-step inversion procedure. In the first step we invert separately for the interval attenuations A_{ij} for each pair of receivers $i<j$. (Notice that this includes nonadjacent receivers; thus many intervals overlap.) The interval attenuations found in this way are not necessarily consistent with each other. In the second step we use the interval attenuations as

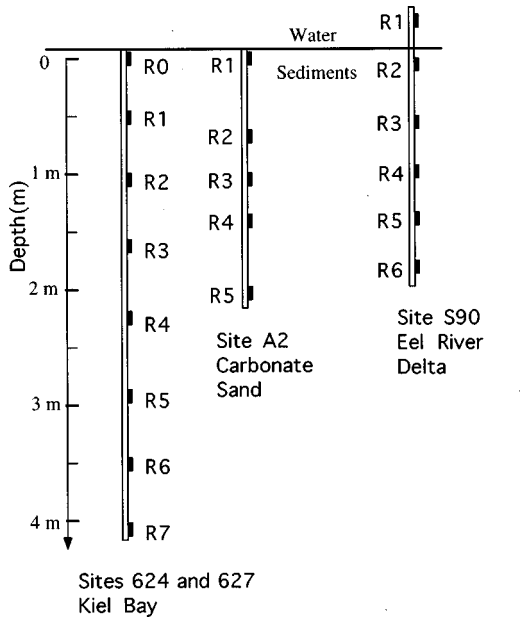

FIG. 8. Lance receiver positions at four experimental sites, showing numbered receivers.

data to invert for the attenuation profile. The second step can be regarded as a means of forcing the attenuations of overlapping intervals to be mutually consistent.

In the first inversion step we seek the attenuation of a single interval between two receivers. The data vector $\boldsymbol{d_o}$ is the vector $[\phi(f_1),\phi(f_2),\cdots,\phi(f_{N_f})]$ where N_f is the number of frequencies, and the model vector $\boldsymbol{m}$ is $[A,B]$. The instrument error due to the noise in the hydrophone and recording system is thought to be negligible compared to the theory error, so we chose an instrument function $\nu(\boldsymbol{d_o}|\boldsymbol{d}) \propto \delta(\boldsymbol{d_o}-\boldsymbol{d})$. Our theory errors are significant, as indicated by the need to include a nonzero intercept B, but they are poorly understood and we cannot relate them to any specific aspect of the propagation. Thus we take

$$\theta(\boldsymbol{d}|\boldsymbol{m}) \propto \exp\left(-\sum_f \frac{|\phi(f)-B+\pi f T A|}{|d\phi(f)|} \right), \tag{23}$$

where $|d\phi|$ is obtained from the noise and signal amplitude spectra by formula Eq. (12). The prior distribution $\rho(\boldsymbol{m})$ is imposed in the form of a search window, and as the manifold of $\boldsymbol{m}$ is roughly Cartesian, so we take $\rho(\boldsymbol{m})$ to be constant within the search window and zero outside of it. Notice that the manifold of $\boldsymbol{m}$ would not be Cartesian if the model vector were $[Q,B]$ instead of $[A,B]$. In consequence of the delta function for ν, the integration in going from $\sigma(\boldsymbol{m},\boldsymbol{d})$ to $\sigma_M(\boldsymbol{m})=\sigma(A,B)$ is trivial, and $\sigma_M(\boldsymbol{m})$ is given by the right hand side of the last equation with $\boldsymbol{d_o}$ substituted for $\boldsymbol{d}$.

Figure 7 shows the results of a first step inversion for the interval between receivers 2 and 4 at site 624. Figure 7(a) shows the contours of the posterior distribution $\sigma(A,B)$. The contour plot was generated by explicitly computing σ over the portion of model space indicated by the axes of the figures. Figure 7(b) shows the marginal posterior distribution (MPD) of the attenuation, $\sigma_A(A) \propto \int dB\sigma(A,B)$. In this example the peak of $\sigma(A,B)$, i.e., the MAP model, has the same attenuation value as the peak of the MPD. This is not always the case, and the theory indicates that the value of A from the MAP model is preferable to the value of A at which the MPD $\sigma_A(A)$ takes its peak.

For the second inversion step we need a theoretical relation between the attenuation of a large interval and the

TABLE I. Single interval attenuations at sites 624, 627, SA1 and S90.

	Individual $A=Q^{-1}$ value & error							
	Site 624 Kiel Bay		Site 627 Kiel Bay		Site A2 Carb. sand		Site S90 Eel River	
Receiver pair	A_{ij}	dA_{ij}	A_{ij}	dA_{ij}	A_{ij}	dA_{ij}	A_{ij}	dA_{ij}
A_{12}	0.11	±0.009	0.0068	+0.008	0.0348	±0.011	0.0627	±0.41
A_{13}	0.0333	±0.003	0.0217	±0.005	0.0535	±0.010	0.0637	±0.036
A_{14}	0.0127	±0.002	0	+0.002	0.0441	±0.008	0.0505	±0.013
A_{15}	0.0286	±0.004	0.0036	±0.004	0.0441	±0.005	0.0208	±0.007
A_{16}	0.0213	±0.007	0.0042	±0.002	nd	nd	0.0049	+0.007
A_{17}	0.0244	±0.002	0.0088	±0.003	nd	nd	nd	nd
A_{23}	0	+0.001	0.034	±0.005	0.1403	±0.025	0.0648	±0.04
A_{24}	0	+0.001	0	+0.001	0.0743	±0.013	0.0389	±0.019
A_{25}	0.0164	±0.002	0	+0.001	0.0512	±0.006	0.0356	±0.028
A_{26}	0.0019	±0.002	0.0036	±0.003	nd	nd	0.0014	+0.017
A_{27}	0.0172	±0.002	0.0036	±0.003	nd	nd	nd	nd
A_{34}	0	+0.002	0	+0.001	0.0125	±0.032	0.0565	±0.032
A_{35}	0.0257	±0.004	0	+0.001	0.0268	±0.001	0	+0.024
A_{36}	0.0132	±0.003	0.0011	+.0004	nd	nd	0	+0.008
A_{37}	0.0151	±0.002	0.0025	+0.003	nd	nd	nd	nd
A_{45}	0.0526	±0.005	0.0196	±0.009	0.0187	±0.026	0.0108	+0.07
A_{46}	0.0263	±0.004	0.0026	+0.003	nd	nd	0	+0.011
A_{47}	0.0244	±0.006	0.0069	+0.003	nd	nd	nd	nd
A_{56}	0	+0.001	0	+0.002	nd	nd	0	+0.026
A_{57}	0.0133	±0.005	0	+0.002	nd	nd	nd	nd
A_{67}	0.0435	±0.005	0.014	+0.013	nd	nd	nd	nd

attenuations of its subintervals. Recalling Eq. (6) it can be seen that for the interval between receiver 1 and receiver 4 the relation is

$$A_{14}=\frac{1}{T_{14}}(T_{12}A_{12}+T_{23}A_{23}+T_{34}A_{34}), \tag{24}$$

in which T_{ij} is the traveltime difference between receivers i and j. For a set of four receivers the data vector is given by $\boldsymbol{d}=[A_{12},A_{13},A_{14},A_{23},A_{24},A_{34}]$ and the model vector is $\boldsymbol{m}=[A_{12},A_{23},A_{34}]$. This notation is not confusing if it is remembered that the appearance of a single interval attenuation, A_{12}, for example, in $\boldsymbol{d}$ represents an observation, while its appearance in $\boldsymbol{m}$ represents a quantity to be determined. (Note that an inversion constrained to preserve single interval attenuations would be trivial.) For an experiment with only four receivers the theory is the linear matrix equation,

$$\begin{bmatrix} A_{12} \\ A_{13} \\ A_{14} \\ A_{23} \\ A_{24} \\ A_{34} \end{bmatrix} = \begin{bmatrix} 1 & 0 & 0 \\ T_{12}/T_{13} & T_{23}/T_{13} & 0 \\ T_{12}/T_{14} & T_{23}/T_{14} & T_{34}/T_{14} \\ 0 & 1 & 0 \\ 0 & T_{23}/T_{24} & T_{34}/T_{24} \\ 0 & 0 & 1 \end{bmatrix} \cdot \begin{bmatrix} A_{12} \\ A_{23} \\ A_{34} \end{bmatrix} + \begin{bmatrix} e_{12} \\ e_{13} \\ e_{14} \\ e_{23} \\ e_{24} \\ e_{34} \end{bmatrix}, \tag{25}$$

in which e_{ij} is the error in A_{ij}. In the general case of N receivers the number of rows in the data vector and system matrix is $N(N-1)/2$ where N is the number of receivers. If a particular receiver is omitted then the rows and columns corresponding to that receiver are suppressed. This affects the condition of the matrix, an important item in a conventional L_2 inversion for the MAP model. Here we generate σ_M explicitly, so the condition of the matrix does not affect the computation.

In the second step of inversion, our data consist of the interval attenuations obtained in step 1. The errors in the theory are negligible compared to the errors in the data, so we take the theory distribution to be $\nu(\boldsymbol{m}|\boldsymbol{d})=\delta(\boldsymbol{d}-\boldsymbol{G}\cdot\boldsymbol{m})$. In the four-receiver example of Eq. (25) $\boldsymbol{G}$ is the 3×4 matrix on the right hand side. Each data error $|dA_{ij}|$ is estimated as the half-width of the peak of the marginal distribution $\sigma_{A_{ij}}(A_{ij})$. For the instrument distribution we therefore choose

$$\nu(\boldsymbol{d_o}|\boldsymbol{d})\propto\exp\left[-\sum_{i<j}\frac{|A_{ij}-A_{ij}^o|}{|dA_{ij}|}\right] \tag{26}$$

in which the A_{ij}^o are the interval attenuations obtained in step 1. The delta nature of θ makes the integration in Eq. (20) trivial and the posterior distribution for the model becomes

$$\sigma_M(\boldsymbol{m})\propto\exp\left[-\sum_{i<j}\frac{|(\boldsymbol{G}\cdot\boldsymbol{m})_{ij}-A_{ij}^o|}{|dA_{ij}|}\right], \tag{27}$$

in which $(\boldsymbol{G}\cdot\boldsymbol{m})_{ij}$ is the row of $\boldsymbol{G}\cdot\boldsymbol{m}$ corresponding to interval ij. The distribution $\sigma_M(\boldsymbol{m})$ is explicitly generated by exploration of the model space, but for display purposes we generate the marginal distributions. An example of a marginal distribution with five receivers is

$$\sigma_{23}(A_{23})\propto\int dA_{12}\int dA_{34}\int dA_{45}\sigma_M(\boldsymbol{m}). \tag{28}$$

ATTENUATION RESULTS

As shown in Fig. 8, in the lance deployments at Kiel Bay, eight receivers penetrated the sediments at both sites. The signals from the first receiver (R0) were clipped and were therefore not used for the attenuation calculations, thus the shallowest interval at which attenuation can be measured is approximately 0.5–1.0 mbsf. The remaining 7 receivers (6 intervals) give 21 different receiver pairs, and thus 21 different depth intervals. For each pair of receivers we construct the posterior distribution $\sigma(A,B)$ as shown in Fig. 7(a) and the MPD $\sigma_A(A)$, shown in Fig. 7(b). Not all contour plots were as definitive as this one. As shown in Table I, 16 intervals were analyzed at site 624, and 13 intervals were analyzed at site 627.

At the Halekulani sand channel only five receivers penetrated this relatively hard sediment. At the Eel River site, five receivers penetrated the deltaic sediments, with one receiver remaining above the sediment water interface. Lance signals from Eel River were noisy in the band 15–20 kHz, because source placement on the core head resulted in significant energy traveling down the body of the corer. (This placement was for protection of the source in case the corer overturned.) Almost every spectral ratio from Eel River had

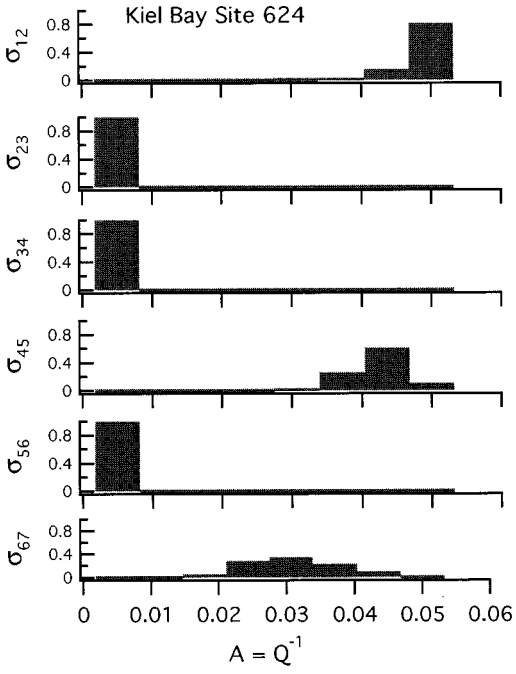

FIG. 9. The marginal posterior distribution (MPD) of attenuation at each depth, site 624 (silty clay), Kiel Bay. Row 1 shows $\sigma_{12}(A_{12})$, row 2 shows $\sigma_{23}(A_{23})$, and so forth.

outliers in the 15–20 kHz band, so this band was automatically suppressed in the attenuation calculation by the signal-to-noise weighting in Eq. (23).

As an example of the second stage inversion, we use site 624; the matrix equation analogous to Eq. (24) for Kiel Bay, site 624 is

$$
\begin{bmatrix}
(A_{12}^{(o)})0.11 \\
(A_{13}^{(o)})0.0333 \\
(A_{14}^{(o)})0.0127 \\
(A_{15}^{(o)})0.0286 \\
(A_{16}^{(o)})0.0213 \\
(A_{17}^{(o)})0.0244 \\
(A_{25}^{(o)})0.0164 \\
(A_{27}^{(o)})0.0172 \\
(A_{35}^{(o)})0.0127 \\
(A_{36}^{(o)})0.0132 \\
(A_{37}^{(o)})0.0323 \\
(A_{45}^{(o)})0.0526 \\
(A_{46}^{(o)})0.0263 \\
(A_{47}^{(o)})0.0244 \\
(A_{57}^{(o)})0.0133 \\
(A_{67}^{(o)})0.0435
\end{bmatrix}
=
\begin{bmatrix}
1 & 0 & 0 & 0 & 0 & 0 \\
0.502 & 0.498 & 0 & 0 & 0 & 0 \\
0.33 & 0.328 & 0.342 & 0 & 0 & 0 \\
0.247 & 0.246 & 0.256 & 0.25 & 0 & 0 \\
0.198 & 0.197 & 0.205 & 0.201 & 0.198 & 0 \\
0.166 & 0.165 & 0.171 & 0.167 & 0.166 & 0.166 \\
0 & 0.327 & 0.341 & 0.333 & 0 & 0 \\
0 & 0.197 & 0.205 & 0.201 & 0.198 & 0.198 \\
0 & 0 & 0.506 & 0.494 & 0 & 0 \\
0 & 0 & 0.342 & 0.334 & 0.33 & 0 \\
0 & 0 & 0.256 & 0.25 & 0.247 & 0.247 \\
0 & 0 & 0 & 1 & 0 & 0 \\
0 & 0 & 0 & 0.503 & 0.497 & 0 \\
0 & 0 & 0 & 0.336 & 0.332 & 0.332 \\
0 & 0 & 0 & 0 & 0.5 & 0.5 \\
0 & 0 & 0 & 0 & 0 & 1
\end{bmatrix}
\begin{bmatrix}
A_{12} \\ A_{23} \\ A_{34} \\ A_{45} \\ A_{56} \\ A_{67}
\end{bmatrix}, \tag{29}
$$

in which the column vector of errors on the right hand side is understood. To generate the posterior distribution $\sigma_M(\boldsymbol{m})$ for this equation we use Eq. (27) with eight possible values of A at each depth. This gave $6^8 \approx 262\,000$ different attenuation profiles. The MPDs $\sigma_{ij}(A_{ij})$, generated by Eq. (28) with the integration replaced by a sum, are shown in Fig. 9. Figures 10–12 show the MPDs for the other sites. The second stage inversion was carried out twice for the Eel River data (Fig. 13) because at that site the first receiver was slightly above the water bottom. Similar results are obtained whether the first receiver is included or excluded, although when the first receiver is excluded the MPDs are broader.

Results for all four sites are summarized as attenuation profiles in Fig. 13, where dashed lines show the MAP pro-

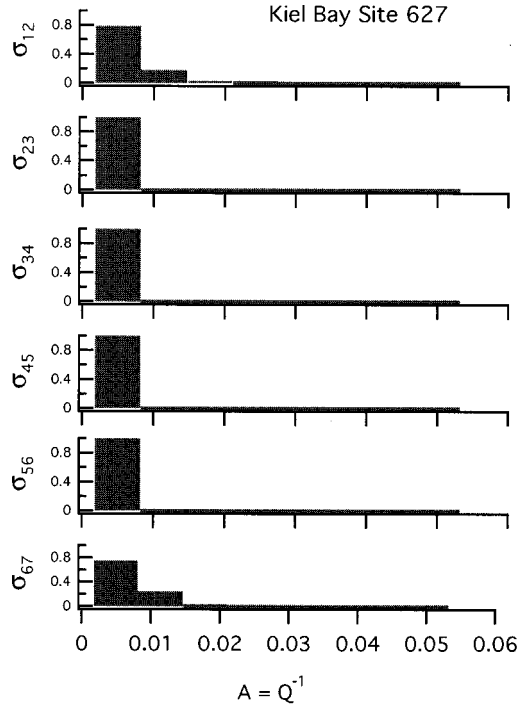

FIG. 10. MPD of attenuation at each depth, site 627 (silty clay), Kiel Bay.

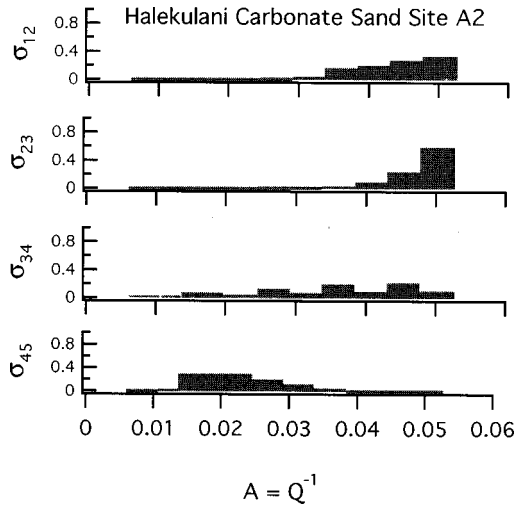

FIG. 11. MPD of attenuation with depth, site A2, Halekulani sand channel (carbonate sand), Oahu, Hawaii.

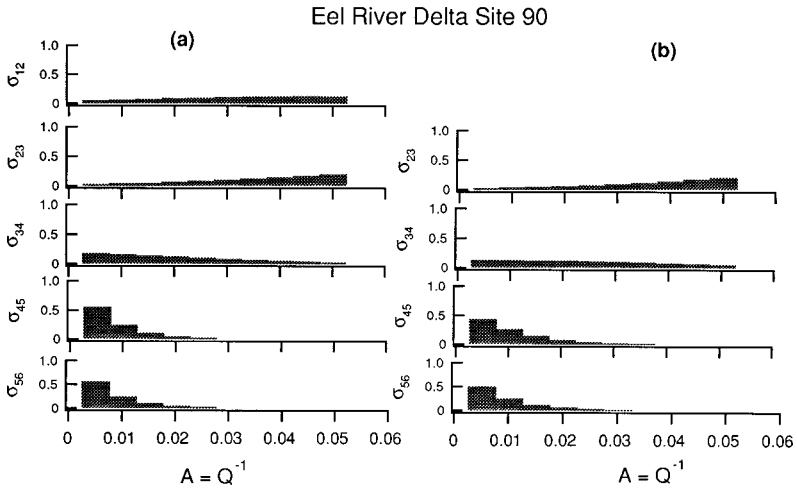

FIG. 12. MPD of attenuation with depth, site S90, Eel River (silty mud), northern California. (a) Using receivers 1–6. (b) Using receivers 2–6.

files and solid lines show the profiles generated by picking the peak of $\sigma_A(A)$ at each depth, i.e., picking the peaks in Figs. 9–12. Table II includes the compressional sound speed distribution in depth in the interval 0–4.1 mbsf. At sites 624 and 627, it can be seen that sound speed is fairly constant at both sites, varying between 1430 m/s and 1460 m/s (Fu *et al.*, 1996b). Thus the differences in attenuation at the two sites do not correlate with sound speed. The attenuation profile at Kiel Bay, site 624, shows high attenuation zones at 0.5–1.1 mbsf and 2.3–2.9 mbsf, and moderate attenuation in the interval 2.9–3.5 mbsf. These higher attenuation zones are thought to result from the presence of very small amounts of gas bubbles, although the sound speed and signal character do not suggest gas bubbles at this site (Fu *et al.*, 1996b). Site 627, also from Kiel Bay, shows uniformly low attenuation with low variability, suggesting that gas bubbles are not present there even in small amounts. In contrast with the soft silty clays of Kiel Bay, the results from the Halekulani sand channel show a high attenuation, decreasing slowly with with depth, possibly due to compaction. The data from the Eel River delta show the highest attenuation values, decreasing relatively rapidly with depth. The high attenuations at shallow depths in the Eel River delta and the Halekulani sand may both be due to biological reworking; however, the high attenuation in the Eel river sediments may also be the result of periodic flood deposition, as microbedding in sediments is known to increase attenuation (e.g., Frazer, 1994).

DISCUSSION

The sediments at sites 624 and 627 in Kiel Bay are soft silty clays with high water content. Waves and bottom currents induced by storms can impact the seafloor to all water depths in this area (Orsi *et al.*, 1996). The attenuation profile at Kiel Bay, site 624, shows high attenuation zones at 0.5–1.1 mbsf and 2.3–2.9 mbsf, and moderate attenuation in the interval 2.9–3.5 mbsf. Although acoustic turbidity is common in the sediments of Kiel Bay, resulting from the methane gas bubbles beginning about 1 m below the seafloor (Richardson and Briggs, 1996; Orsi *et al.*, 1996), sound speed and signal character do not suggest gas bubbles at these two sites (Fu *et al.*, 1996b). Sound speed does not vary much with depth here, being confined to the interval 1428–1460 m/s (Table II). The zones of higher attenuation may be sand layers formed by storm impact or layers of laminated coarser silt. Sand size particles are known to increase attenuation (Hamilton, 1972) as is micro-bedding (e.g., Frazer, 1994). Site 627, also from Kiel Bay, shows uniformly low attenuation with low variability, suggesting much more homogeneous fine grained sediments.

In contrast with the soft silty clays of Kiel Bay, the results from the Halekulani sand channel, off Oahu island, show a high attenuation decreasing slowly with depth. The sediments covering Halekulani sand channel are carbonate sands. Sand deposits in the Hawaiian Islands are varied in response to microclimates mainly created by island topogra-

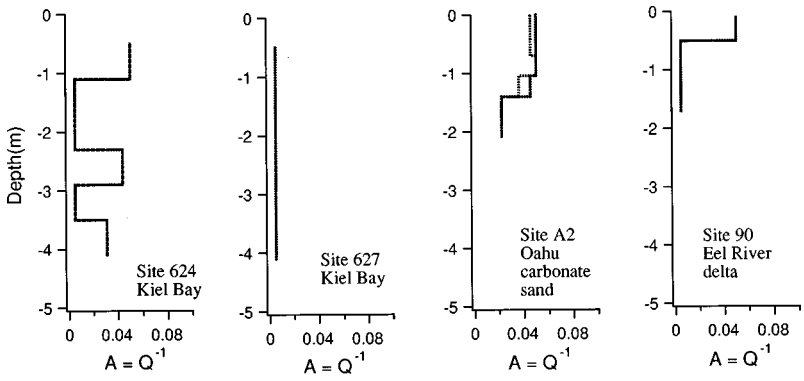

FIG. 13. Summary attenuation profiles. Dashed lines are MAP profiles and the solid lines are peaks from the MPD at each depth. (a) Site 624 (Kiel Bay, silty clay). (b) Site 627 (Kiel Bay, silty clay). (c) Site A2 (Oahu, Hawaii, carbonate sand). (d) Site S90 (Eel River, silty mud).

TABLE II. Compressional sound speeds and attenuations at sites 624, 627, SA1 and S90.

High-porosity clay, Site 624, Kiel Bay			High-porosity clay, Site 627, Kiel Bay		
Depth (mbsf)	Soundspeed (m/s)	Attenuation $A=Q^{-1}(Q)$	Depth (mbsf)	Soundspeed (m/s)	Attenuation $A=Q^{-1}(Q)$
0–0	1480[a]	nd	0–0	1480	nd
0–0.5	1430	nd	0–0.5	1430	nd
0.5–1.1	1439	0.05 (20)	0.5–1.1	1447	$\leqslant$0.005 ($\geqslant$200)
1.1–1.7	1428	$\leqslant$0.005 ($\geqslant$200)	1.1–1.7	1428	$\leqslant$0.005 ($\geqslant$200)
1.7–2.3	1446	$\leqslant$0.005 ($\geqslant$200)	1.7–2.3	1446	$\leqslant$0.005 ($\geqslant$200)
2.3–2.9	1429	0.043 (23)	2.3–2.9	1447	$\leqslant$0.005 ($\geqslant$200)
2.9–3.5	1444	$\leqslant$0.005 ($\geqslant$200)	2.9–3.5	1453	$\leqslant$0.005 ($\geqslant$200)
3.5–4.1	1442	0.033 (30)	3.5–4.1	1460	$\leqslant$0.005 ($\geqslant$200)
Halekulani Carb. sand, Site A2			Eel River Delta, Site S90		
Depth (mbsf)	Soundspeed (m/s)	Attenuation $A=Q^{-1}(Q)$	Depth (mbsf)	Soundspeed (m/s)	Attenuation $A+Q^{-1}(Q)$
0–0	1548	nd	0–0	1477	nd
0–0.69	1617	$\geqslant$0.05 ($\leqslant$20)	0.1–0.5	1480	$\geqslant$0.05 ($\leqslant$20)
0.69–1.03	1653	$\geqslant$0.05 ($\leqslant$20)	0.5–0.9	1493	$\leqslant$0.005 ($\geqslant$200)
1.03–1.37	1660	0.045 (22)	0.9–1.3	1492	$\leqslant$0.005 ($\geqslant$200)
1.37–2.07	1626	0.022 (45)	1.3–1.7	1524	$\leqslant$0.005 ($\geqslant$200)

[a]Sound speeds at 0 m bsf are averaged bottom water sound speed.

phy, waves, tidal currents, stream discharge and catastrophic events (Coulbourn *et al.*, 1988); however, there is no apparent relation between grain size and the spatial location of a sample or the vertical location of a sample within the deposit in the Halekulani sand channel (Ericson *et al.*, 1995). Although decreasing attenuation with depth in sands may result from reduced porosity by compaction (Hamilton, 1972), our experiment was in a carbonate sand layer of only 2 m thickness, and compaction should not contribute significantly to the attenuation decrease with depth. More likely, sediment reworking by bottom water currents or waves reduces the strength of grain contacts, resulting in increased attenuation as well as lowered rigidity.

The data from the Eel River delta, northern California, show high attenuation values at shallow depths of 0.1–0.5 mbsf, decreasing relatively rapidly with depth. Site S90 is located on the downslope of the delta in water of depth 90 m. The sediments at the site are a mixture of silts and clays, and the study area is strongly influenced by both biological reworking and periodic flood deposition from the Eel and Mad rivers (Nittrouer and Kravitz, 1996). Initial laboratory measurements on core data collected at 1 cm intervals show higher variability in sound speed (from 1450–1520 m/s at 400 kHz) within the interval of 0.1–0.5 mbsf, than outside this interval, which suggests that microbeds due to periodic floods may be present in this shallow depth zone. Gorgas *et al.* (1996) also saw a strong correlation between attenuation and sound speed in the core data. They suggest that the faster layers may have a higher sand content, and thus a higher attenuation.

ACKNOWLEDGMENTS

Fu and Wilkens were supported in this work by the Office of Naval Research. Frazer thanks the National Science Foundation for support under EAR95-26786. Operational support was also provided by the Coastal Benthic Boundary Layer Program and the Naval Research Laboratory. SOEST contribution 4793.

Basu, A., and Frazer, L. N. (**1990**). ''Rapid determination of critical temperature in simulated annealing inversion,'' Science **249**, 1409–1412.

Bromirski, P. D., Frazer, L. N., and Duennebier, F. K. (**1992**). ''Sediment shear Q from airgun OBS data,'' Geophys. J. Int. **110**, 465–485.

Bromirski, P. D., Frazer, L. N., and Duennebier, F. K. (**1995**). ''The Q-gram Method: Q from instantaneous phase,'' Geophys. J. Int. **120**, 73–86.

Coulbourn, W. T., Campbell, J. F., Anderson, P. N., Daugherty, P. M., Greenberg, V. A., Izuka, S. K., Lauritzen, R. A., Tsutsui, B. O., and Yan, C. (**1988**). ''Sand deposits offshore Oahu, Hawaii,'' Pacific Science **42**, 267–299.

Duijndam, A. J. W. (**1988**). ''Bayesian estimation in seismic inversion, Part I: Principles,'' Geophys. Prosp. **36**, 878–898.

Ericson, M., Wilkens, R. H., Fu, S. S., and Prasad, M. (**1995**). Development of a Broadband FM subbottom profiler for seafloor imaging and sediment classification (unpublished report), Sea Engineering Inc., Waimanalo, HI 96795.

Frazer, L. N. (**1994**). ''A pulse in a binary sediment,'' Geophys. J. Int. **118**, 75–93.

Fu, S. S. (**1994**). ''*In situ* acoustic profiles of the sediment-seawater interface,'' M.Sc. Thesis, Department of Geology and Geophysics, University of Hawaii at Manoa.

Fu, S. S., Wilkens, R. H., and Frazer, L. N. (**1996a**). ''Acoustic lance: New *in situ* seafloor velocity profiles,'' J. Acoust. Soc. Am. **99**, 234–241.

Fu, S. S., Wilkens, R. H., and Frazer, L. N. (**1996b**). ''*In situ* velocity profiles in gassy sediments: Kiel Bay,'' Geo-Marine Lett. **16**, 249–253.

Gorgas, T., Wilkens, R. H., Fu, S. S., and Richardson, M. D. (**1996**). ''Acoustic data from the Eel River shelf, northern California,'' EOS Trans. Am. Geophys. Union **77**, F332–F333.

Hamilton, E. L. (**1972**). ''Compressional-wave attenuation in marine sediments,'' Geophysics **37**, 620–646.

Jannsen, D., Voss, J., and Theilen, F. (**1985**). ''Comparison of methods to determine Q in shallow marine sediments from vertical reflection seismograms,'' Geophys. Prosp. **33**, 479–497.

Kibblewhite, A. C. (**1989**). ''Attenuation of sound in marine sediments: A review with emphasis on new low-frequency data,'' J. Acoust. Soc. Am. **86**, 716–738.

Kjartansson, E. (**1979**). ''Constant Q-wave propagation and attenuation,'' J. Geophys. Res. **84**, 4737–4748.
Nittrouer, C. A., and Kravitz, J. H. (**1995**). ''Integrated continental margin research to benefit ocean and earth sciences,'' EOS Trans. Am. Geophys. Union **76**, 121, 124 and 126.
Nittrouer, C. A., and Kravitz, J. H. (**1996**). ''STRATAFORM: A program to study the creation and interpretation of sedimentary strata on continental margins,'' Oceanography **9**, 146–152.
O'Connell, R. J., and Budiansky, B. (**1978**). ''Measures of dissipation in viscoelastic media,'' Geophys. Res. Lett. **12**, 721–724.
Orsi, T. H., Werner, F., Milkert, D., Anderson, A. L., and Bryant, W. R. (**1996**). ''Environmental overview of Eckernfoerde Bay, Northern Germany,'' Geo-marine Lett. **16**, 140–147.
Richardson, M. D. (**1994**). ''Investigating the Coastal Benthic boundary layer,'' EOS Trans. Am. Geophys. Union **75**, 201, 205–206.
Richardson, M. D., and Briggs, K. B. (**1996**). ''*In situ* and laboratory measurements in soft mud and hard-packed sand sediments: Implications for high-frequency acoustic propagation and scattering,'' Geo-Marine Lett. **16**, 196–203.
Stoll, R. D. (**1985**). ''Marine sediment acoustics,'' J. Acoust. Soc. Am. **77**, 1789–1799.
Tartantola, A., and Valette, B. (**1982**). ''Inverse problem=quest for information,'' J. Geophys. **50**, 159–170.
Tarantola, A. (**1987**) *Inverse Problem Theory* (Elsevier Science, The Netherlands).
Wilkens, R. H., and Richardson, M. D. (**1996**). ''The influence of gas bubbles on sediment acoustic properties: *In situ*, laboratory, and theoretical results from Eckernforde Bay, Baltic Sea, Germany,'' submitted to Continental Shelf Research.

Target strength of an oily deep-water fish, orange roughy (*Hoplostethus atlanticus*) I. Experiments

Sam McClatchie,[a] Gavin Macaulay, Roger F. Coombs, Paul Grimes, and Alan Hart
National Institute of Water and Atmospheric Research Ltd (NIWA), PO Box 14-901, Kilbirnie, Wellington, New Zealand

(Received 3 September 1997; revised 20 February 1998; accepted 13 April 1999)

Target strengths (TS) of orange roughy (*Hoplostethus atlanticus*) are difficult to measure *in situ* because this species lives at 800–1200 m, has low TS at 38 kHz, shows strong avoidance behavior, and sometimes co-occurs with species having much higher TS. Orange roughy have wax-invested swimbladders and fish are ~20% wax esters by weight. Estimates of orange roughy near-dorsal aspect tilt-averaged target strength ($\langle TS \rangle$) are controversial, varying from [−39, −35] dB to [−52, −48] dB for a 35-cm fish in different studies. $\langle TS \rangle$ is estimated using experiments on both live and dead fish, and new swimming orientation data. Target strength of previously frozen and thawed fish decline rapidly, stabilizing after ~12 h as air and oil diffuse out of tissues during rehydration. A $\langle TS \rangle$ of −46.3 dB is predicted for a 35-cm live orange roughy (bootstrapped 95% confidence intervals = −48.0 to −45.5 dB). This value is 3.7 dB higher than Australian estimates of ≈−50 dB for $\langle TS \rangle$ of a 35-cm live orange roughy. It is shown that the magnitude of the difference between *in situ* estimates of $\langle TS \rangle$ and experimental measurements of $\langle TS \rangle$ on live fish can be explained by the effect of strong avoidance reactions to a towed transducer on the tilt angle of the fish. Previously much higher estimates of dead orange roughy $\langle TS \rangle$ were an artifact of air pockets caused by freezing. Comparison of orange roughy TS_{max} measured in our experiments with a large dataset for nonswimbladder and swimbladder fish shows that orange roughy have an unusually low target strength at 38 kHz. [S0001-4966(99)05007-9]

PACS numbers: 43.30.Sf, 43.30.Ft [SAC-B]

INTRODUCTION

[1]Estimation of the absolute biomass of orange roughy (*Hoplostethus atlanticus*, Collett) using underwater acoustic techniques depends upon accurate estimates of target strength. An acoustic survey of orange roughy is conducted with vertically oriented downward-looking transducers. Near-dorsal aspect target strength, or TS, is often used loosely in the literature to refer to several different measurements. Here we distinguish between $\langle TS \rangle$, TS_{max}, and TS_θ. The calculation methods for target strength are given in the methods. Tilt-averaged TS, or $\langle TS \rangle$, is the target strength averaged with respect to fish orientation for a given size of fish. TS_{max} is the maximal TS measured from a fish that is generally in near-dorsal aspect (i.e., fish normal to the axis of the acoustic beam) but is often measured at an orientation angle that is offset from true dorsal aspect in both swimbladder and nonswimbladder fish. TS_θ is the TS measured at a given angle (θ) of orientation, where $TS_{\theta=0}$ is the dorsal aspect. The usual convention is for positive angles to represent head-up orientation in the pitch plane: $TS = 10 \log_{10} \sigma_{bs}$ where σ_{bs}, the backscattering cross-section $= \sigma/4\pi$; $\sigma_{bs} = L_f^2$, where L_f is the scattering length.

Ideally, the best way to measure $\langle TS \rangle$ is by taking a large sample of echoes from individual fish in monospecific aggregations exhibiting natural, undisturbed behavior. Many factors (such as interaction between fish directivity and swimming movements) cause even such direct *in situ* estimates on a single species to be variable.[1,2] There are three principal barriers to making accurate *in situ* $\langle TS \rangle$ estimates on orange roughy. First, orange roughy live at 800–1200 m depth,[3] and the acoustic transducer must be lowered close enough to resolve echoes from individual fish in an aggregation. Orange roughy exhibit strong avoidance reactions to both towed and falling objects.[4] When a transducer is near enough to orange roughy to estimate *in situ* $\langle TS \rangle$, the tilt angle distribution of the fish is likely to be skewed due to their avoidance reactions so that *in situ* estimates of $\langle TS \rangle$ are likely to be biased (toward lower values). Second, the orange roughy swimbladder is filled with wax esters[5–7] resulting in a low $\langle TS \rangle$ at 38 kHz, which exacerbates signal-to-noise problems. Third, the occurrence of orange roughy with other species with much higher $\langle TS \rangle$ is a source of important uncertainties in current *in situ* estimates of target strength of orange roughy off Tasmania.[8] Knowledge of species mix is based on research and commercial trawl catches and differs between Australia and New Zealand, and with region in New Zealand. The most abundant species are black oreo (*Allocyttus niger*) and smooth oreo (*Pseudocyttus maculatus*) on Puysegur Bank,[9] and smooth oreos, deep water dogfish (*Squalidae*), slickheads (*Alepocephalidae*), rattails (*Macrouridae*), and basketwork eels (*Diastobranchus capensis*) on the Chatham Rise.[10]

An alternative to *in situ* measurements is to bring live orange roughy to the surface for direct measurements of TS_θ in an experimental tank. Again, there are several problems: Fish have successfully been captured only by trawling, which inevitably damages them, and although we found that

[a]Electronic mail: s.mcclatchie@niwa.cri.nz

TABLE I. Summary of published and current target strength measurements for orange roughy. Fish size is the standard length of orange roughy measured from the anterior tip of the snout to the base of the caudal peduncle, *n* is the number independent target strength measurements. Also shown is whether there are any confidence intervals for the estimated target strengths, and whether there is any associated data on fish orientation. ID=identification, CI=confidence interval, TS_{max}=maximum (generally~dorsal aspect target strength), $\langle TS \rangle$=tilt-averaged target strength, $\langle TS \rangle_{35\ cm}$=tilt-averaged target strength for a 35-cm fish ±95% confidence intervals (where available). Studies are arranged chronologically. ''Change in acoustic backscatter compared to commercial catches'' refers to a fishing down experiment conducted on an Australian seamount. Acoustic backscatter was measured before and after commercial fishing and the estimate of fish caught by the trawlers over the same period on the seamount was used to estimate $\langle TS \rangle$ indirectly from integrated backscattering, the biomass caught in commercial trawls and the size distribution of the fish.

n	Method	Target ID	Fish size cm	$\langle TS \rangle$ dB	$\langle TS \rangle_{35}$ cm dB [95% CI]	TS_{dorsal} dB	TS-length regression with CI	Orientation data	Source
16 fish	Live fish experiments	-	27.9–36.7	−49.7 to −42.9	−46.3 [−48 to −45.5]	-	$\langle TS \rangle = 16.374 \log_{10} SL - 71.621$	camera & expt	This study
16 fish	Thawed dead fish experiments	-	26–42	−42.2 to −34.2	−35.9	-	yes	no	see Ref. 11
50 targets at 100–150 m range	Split beam *in situ*	mixed orange roughy and myctophiids	mean =36	−52 to −48	≈−50	-	no	no	see Refs. 8, 14
5 fish	Thawed dead fish at 6 m	-	21–48	-	-	−52 to −44.4	no	no	see Ref. 8
1 fish	Freshly dead fish, lowered to 750 m	-	35	-	-	−53.5 to 50.1	no	no	see Ref. 8
1 fish	Ellipsoid model	-	35			−53 to −47.2	no	no	see Ref. 8
-	Change in acoustic backscatter compared to commercial catches	nearly pure orange roughy	[35.4 to 35.9] ±[6.5 to 7.4][a]	−53.6 to −49.7	-	-	no	no	see Ref. 13
-	Change in acoustic backscatter compared to commercial catches	75%–95% orange roughy	mode =36, range ~25–44	−42 to −41	-	-	no	no	see Ref. 12

[a]Range of mean fish lengths and standard deviations given for the Australian orange roughy fishery (Ref. 13).

orange roughy can be kept alive in chilled seawater, they tend to be moribund. There are also pressure and temperature differences between *in situ* conditions and the experimental tanks available to us. Despite these limitations, we felt it was useful to measure $\langle TS \rangle$ on both live and dead orange roughy by experiment because of uncertainties in the current *in situ* estimates of $\langle TS \rangle$. Our study is only the second to make detailed experimental measurements on dead orange roughy[11] and is the first to make experimental measurements on the live fish.

The published $\langle TS \rangle$ and TS_θ for orange roughy (see Table I) are controversial in terms of both their magnitudes and the validity of different measurement methods used. TS_θ has been measured directly on dead fish in a tank[11] and then used to calculate $\langle TS \rangle$. Average target strength has been estimated indirectly by relating echo integration data to accumulated commercial catch.[12,13] This method used a ''fishing down'' experiment conducted on a spawning aggregation of orange roughy over an Australian seamount. Acoustic backscatter was measured before and after commercial fishing and $\langle TS \rangle$ was estimated indirectly from integrated backscattering, the biomass of orange roughy caught in the com-

mercial trawls as the population was fished down and the size distribution of the fish. ⟨TS⟩ has also been estimated directly by relating modal sizes of fish in demersal and pelagic trawl catches to modes in target strength distributions recorded with a Simrad EK500 split-beam echosounder.[8,14] Kloser *et al.* estimated $TS_{\theta=0}$ for five dead fish tethered beneath the modified EK500 near the surface and for one dead fish lowered from 200 to 750 m.[8,14] They also presented a very approximate estimate of $TS_{\theta=0}$ derived from a simple model.[8,14]

The magnitude of target strengths estimated by these different methods varies enormously (summarized in Table I).[8,14] We need both a more accurate estimate of ⟨TS⟩ and a length to ⟨TS⟩ regression to improve absolute biomass estimates from both new and existing echo integration survey data. Table I indicates that present estimates of minimum and maximum ⟨TS⟩ range from what are now suspected to be erroneously high values of [−42, −34] dB[11] through [−42, −41] dB[12] down to [−52, −48] dB,[14] [−54, −50] dB,[13] and ~−50 dB.[8] The size range of the orange roughy that these measurements are based on was 25–44 cm standard length (Table I). Estimates of ⟨TS⟩ have been progressively reduced over the last ten years as different methods for estimating target strength have been applied.

In this paper we aim to narrow the range of the estimates of ⟨TS⟩ for orange roughy. We estimate ⟨TS⟩ for a range of sizes of both live and dead orange roughy. To achieve this we made tank measurements of TS_θ at various fish orientations and combined them with new field data on swimming angles to calculate ⟨TS⟩. We also compare the TS_{max} of orange roughy to a large dataset on the TS_{max} of fish both with and without swimbladders. We explain why Do and Coombs' estimates of ⟨TS⟩ for orange roughy were too high, present what we believe to be the best current estimates, and show that orange roughy have unusual acoustic properties. We follow our experimental analyses with a companion paper developing a model for acoustic scattering by orange roughy. The model incorporates the pressure and temperature dependence of sound speed in orange roughy oils.

I. METHODS

A. Orange roughy sample collection

Frozen samples of orange roughy, covering a representative range of sizes, were collected during research trawl surveys on the Chatham Rise, New Zealand, using the National Institute of Water and Atmospheric Research research vessel *T*ANGAROA during April 1994. Live orange roughy were collected with the same vessel in September 1996, off the Wairarapa and Kaikoura coasts of New Zealand using 5–10 min (bottom time) tows of an orange roughy bottom trawl with a modified, knotless, codend. The last 2.7 m of the codend was supported with metal hoops containing a canvas bag, so that the meshes would not collapse on the fish when retrieved aboard the vessel, and the fish would be retained in the bag of water. Once on board the liveliest orange roughy with the least scale damage were removed from the codend in plastic bags filled with water and slowly cooled to near their normal ambient temperature (~6 °C). Fish were transferred to ~1000 litre holding tanks in *T*ANGAROA's fish hold. The orange roughy were kept at 4–6 °C for 1–5 days on the ship before returning to port. The holding tanks were moved to the aquarium at Greta Point, Wellington where the fish were maintained in aerated and chilled static seawater. Water quality was difficult to maintain as the orange roughy regurgitated their stomach contents over several days. Whenever this occurred, the seawater was changed. The fish were kept in darkness or dim light as much as possible. Fish often tended to be quiescent in the tanks but were periodically quite active, especially at night. Experiments on live orange roughy were conducted immediately after the voyage in September 1996, whereas the experiments on dead, previously frozen, orange roughy were performed December 1995–January 1996, 20 months after the fish were originally collected.

B. Orientation dependence of target strength

Measurements of TS_θ were made on 16 dead orange roughy. Fish were removed from the freezer to begin thawing at room temperature while soaking in a 1:320 solution of photographic wetting agent in seawater. The fish were allowed to soak for between 5 and 7 h to allow them to thaw out before measurements were made. Each fish was kept under water when transferring from the wetting agent to the experimental tank, and the gills and mouth were carefully flushed to remove any air pockets.

Measurements of TS_θ were also made on 16 live fish. Most of the fish were moribund in the aquarium and their survival was limited to a maximum of about five days. They did not survive long in the test tank and measurements had to be carried out as quickly as possible, and as a consequence were only made in the pitch plane which we judged to be more important than the roll plane for the reasons given later. The live fish were immersed in the wetting agent for 5–15 min prior to being placed in the experimental tank. Eight of the live fish were subsequently frozen and their TS_θ remeasured after thawing to determine the effect of freezing on target strength. Fish that were too lively immediately prior to the experiments were sedated with Aqui-S® (17 ppm).

Each fish was suspended on nylon lines strung beneath a motor-driven rotating frame. The design[15] permits the fish to be rotated in either pitch, roll, or yaw planes. To match the scattering lengths with orientation data, the transmit number from the sounder was recorded concurrently with the angle of rotation read from a graduated scale mounted on the rotation frame shaft. For orientation experiments data from 2 to 3 full 360° rotations were recorded. Only the data from ±90° about dorsal aspect are reported here. One 360° rotation took about 8 min. All rotation experiments were conducted in the same manner to reduce nonsystematic biases and live fish rotations were done immediately after attaching the fish to the rotation device. Some of the variability in our measurements may be due to the effect of the fish moving slightly on the nylon lines suspending the target in the beam. Slight changes in the position of the fish in the beam may have occurred as the support lines stretched. Although we measured the position of the fish at the start and end of each experiment, we cannot state absolutely that there were no

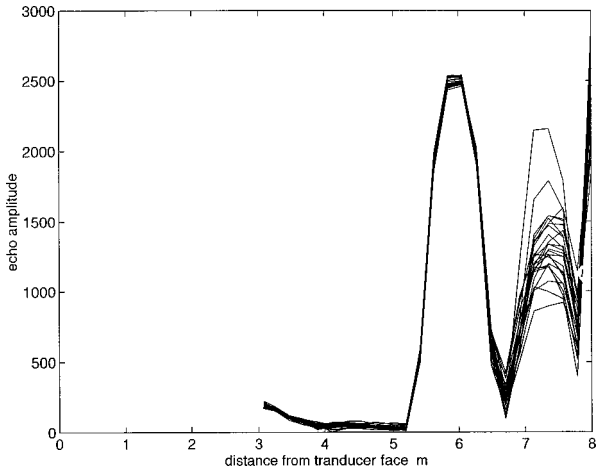

FIG. 1. 250 transmits from the echosounder showing the separation of the target sphere, fish, and the tank wall echoes. The software clips the back wall echo. Fish were rotated while these data were recorded, producing variable echo amplitude.

small shifts off the beam axis during our measurements. To estimate the magnitude of this problem we simulated the effect of moving the target off the beam axis by as much as 30 cm.

After the initial rotations, $TS_{\theta=0}$ was monitored for up to a day on four previously frozen, dead fish and rotations carried out at hourly interval for up to 8 h for a fifth. The latter was done to determine whether $TS_{\theta=0}$ and $\langle TS \rangle$ showed the same trends. Only the initial rotations were carried out on the live orange roughy.

C. Acoustic data collection

All published orange roughy acoustic survey work carried out to date, as well as our survey equipment, used 38 kHz, this frequency providing a good compromise between range and signal-to-noise ratio considerations. All the measurements described here have been made at 38 kHz.

Data were collected using CREST (Computerised Research EchoSounder Technology).[16] The CREST system was connected to a purpose built 38-kHz transducer from Edo Corporation (Edo model 6978), and was mounted in the side of a flat-nosed torpedo-shaped towed body. The transducer beam is circular and has a 3-dB beam width of approximately 7°. During the experiments, the towed body containing the transducer was suspended vertically at one end of a 3.9-m-deep concrete tank measuring 8 m in length and 4 m wide.

The 38.1-mm-diameter tungsten carbide target sphere was carefully centered on the beam axis and left in place during all the experiments. A single fish was suspended in line with, and at the same depth as, the target sphere. The fish was separated from the sphere by about 1 m to allow resolution of the separate echoes (pulse duration was 1 ms, giving a pulse length of 1.5 m) (Fig. 1). Examination of echo amplitudes as a function of range showed that the sphere had no effect on the echo at the range of the fish. TS_θ was measured by direct comparison of the backscattering from a fish with that from the target sphere. For a given orientation of the fish TS_θ was calculated from the tilt-dependent scattering length, $L_f(\theta)$:

$$L_f(\theta) = L_t \frac{v_f}{v_t} \left(\frac{R_f}{R_t} \right)^2 10^{\alpha \Delta R/10},$$
$$TS_\theta = 20 \log_{10} L_f(\theta), \tag{1}$$

where f denotes fish, t denotes the target sphere, L is the scattering length in m, v is the voltage, and R is the range in m from the transducer face, and $\Delta R = R_f - R_t$. The fish orientation with dorsal surface normal to the axis of the acoustic beam is represented by $\theta = 0$. The absorption coefficient, α, is insignificant over the ranges of ΔR involved and a nominal value of 0.008 dB m^{-1} was used. Note that 4π only enters the equation when backscattering cross-section terminology is used to describe the calculation of TS.

D. Acoustic noise

There are two main sources of acoustic noise in our test tank (wind and solar heating) both arising because it is outside. The wind noise was minimized by covering the tank with a windbreak of 5 by 2 mm mesh agricultural netting. Solar heating caused temperature stratification on warm days that proved to be a more important source of variability in the data. The noise associated with solar heating is presumably due to diffraction arising from temperature gradients in the tank.[17] We could not control this and we discarded those experiments where the signal returned from the calibration sphere was (subjectively) judged to be too noisy from a ping-by-ping display of the echo. Water temperature at the depth of the fish ranged from 17 to 20 °C in the dead fish experiments and 13–14 °C in the live fish experiments.

E. Tilt angle measurements

Orientation data for orange roughy in the ocean were obtained using a still, stereo camera system (A. MacDiarmid, NIWA, Greta Point, unpublished data). The system also included a video camera and floodlights. The stereo photographs were taken using a strobe flash both with and without the floodlights operating. The tilt angles of individual fish in the pitch plane were measured from stereo pairs of photographs. Tilt angle in the roll plane was not measured. The camera disturbs the fish, but over a series of frames there were enough pictures of orange roughy to get an orientation distribution. The existing tilt distribution data are less than perfect, but they look reasonable in terms of mean angle and standard deviation of the distribution when compared with other tilt distributions from the literature.[18]

F. Target strength averaging

To calculate $\langle TS \rangle$ we followed Foote.[19] The distribution of backscattering cross-sections as a function of angle (θ) in the pitch plane, $L_f(\theta)^2$, was weighted by the probability density function (pdf) of the swimming angles in the pitch plane, $g(\theta)$. Swimming angles in the pitch plane closely approximated a normal distribution, with a mean of $-7°$ (head down) and a standard deviation of 19° (Fig. 2). In our tank experiment weighting by the beam pattern was not nec-

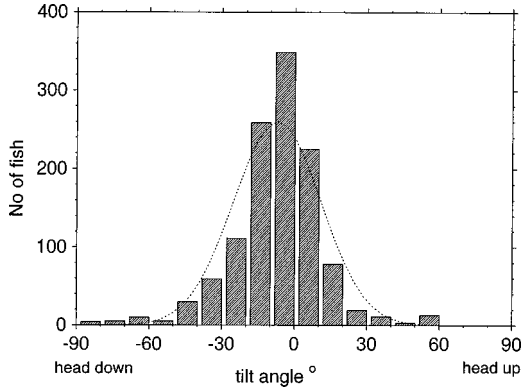

FIG. 2. Frequency distributions of orange roughy swimming orientations in the pitch plane estimated from underwater camera data. 0° would be dorsal aspect to a down-looking acoustic beam. Positive angles are head up orientation. The dotted line is a normal distribution fitted to the pooled data collected with lights both on and off [mean $=-7°$ and standard deviation $=19°$] used to estimate $\langle TS\rangle$ [see Eq. (2)].

essary because measurements of target strength were made on the beam axis. Tilt-averaged target strength, $\langle TS\rangle$, is given by

$$\langle TS\rangle = 10\log_{10}\left(\int L_f(\theta)^2 g(\theta)\, d\theta\right). \quad (2)$$

$\langle TS\rangle$ was estimated for 16 dead orange roughy ranging from 16 to 40 cm and for 16 live orange roughy ranging from 28 to 37 cm standard length (SL, measured from tip of mouth to base of the caudal peduncle).

II. RESULTS

A. TS_θ of dead fish

Most of the rotations were carried out in the pitch plane and an example of the change in TS_θ with orientation is shown in Fig. 3. The patterns are characterized by strong nulls, indicating that rotation by only a few degrees has a large effect on target strength. An example of the response in the roll plane is also shown in Fig. 3. The roll plane response is smoother than the pitch plane response. There was a substantial amount of variability between individual fish in the relation between target strength and orientation.

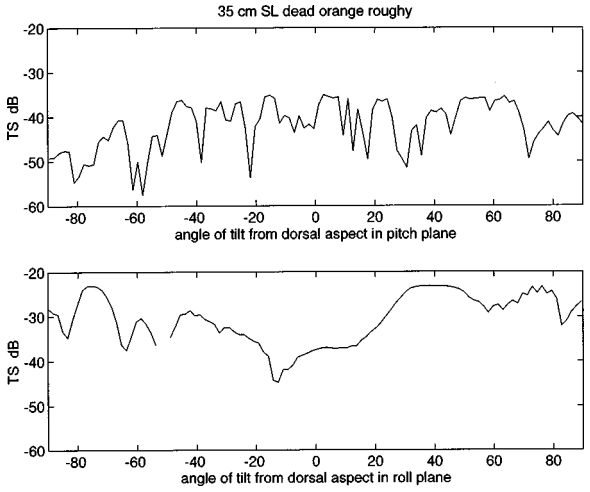

FIG. 3. Dependence of TS_θ on orientation in both the pitch plane and the roll plane for a 35-cm standard length dead orange roughy. Dorsal aspect corresponds to 0° angle of tilt. Positive angles are head toward the transducer (head up swimming angle) in the pitch plane. Several pings were lost from the data record during this particular roll plane experiment.

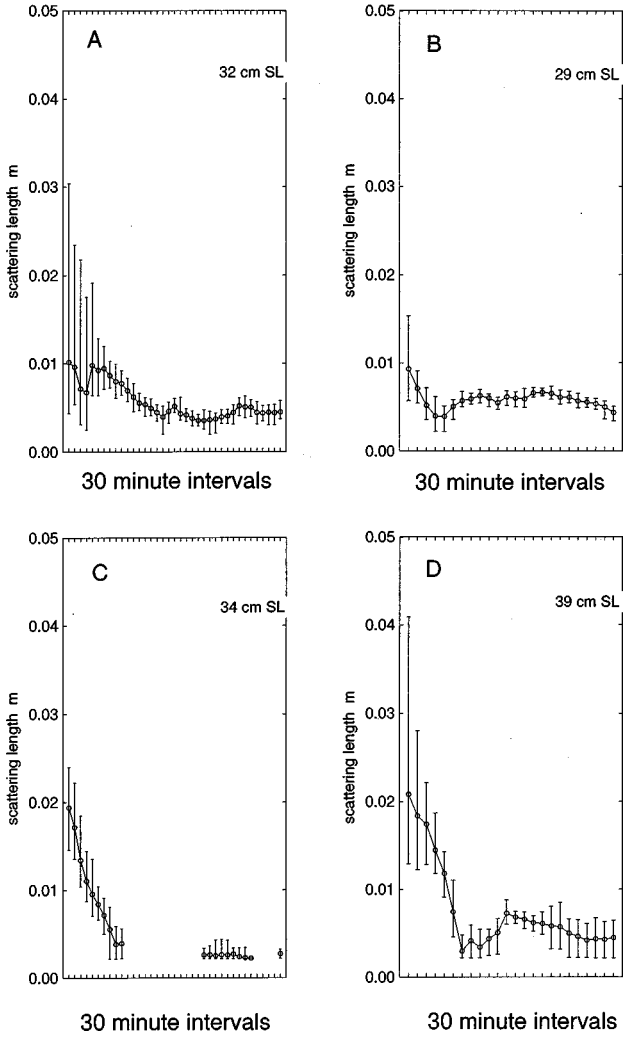

FIG. 4. Change in scattering lengths ($L_f(\theta=0)$, m) for four dead orange roughy in dorsal aspect recorded over 13–23 h. Circles are means over 30-min periods and vertical bars are the ranges. SL=standard length, cm. Note that horizontal scales differ between graphs. (A) First datum at 6.75 h from leaving the freezer, and every 30 min thereafter; (B), first datum at 5.7 h; (C), first datum at 5.1 h; (D), first datum at 5.3 h. The delay before logging data was to give the fish time to thaw.

There were also large changes in the measured scattering length of individual dead fish with time. Scattering lengths become relatively stable after 10–15 h (Fig. 4). The ''stabilized'' $TS_{\theta=0}$ of the thawed orange roughy was in the range -51 to -44 dB, which is comparable with the target strength of live orange roughy. The variability in our measurements, as illustrated by the ranges for scattering lengths measured in 30-min periods (Fig. 4), also generally decreased with time. There was considerable variability in the patterns between different fish. Scattering lengths of larger fish (39 and 34 cm) declined more rapidly than that of smaller fish (32 and 29 cm) (Fig. 4). The problem of estimating target strength from these dead orange roughy data led us to make the measurements on live fish.

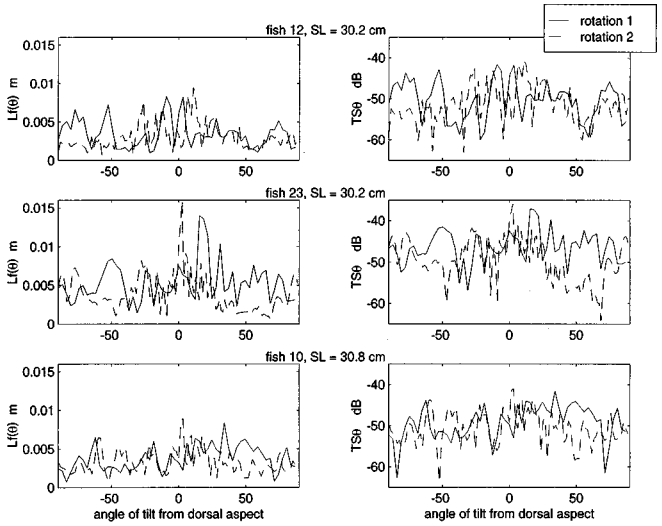

FIG. 5. Tilt dependence of scattering lengths, $L_f(\theta)$, and target strength, TS_θ, for three live orange roughy of ~30-cm standard length (fish sizes are given on the graph). Two replicate rotations of the fish are shown. Positive angles of tilt are the equivalent of the fish having head-up orientation in the pitch plane for a downward looking transducer geometry. Dorsal aspect ($\theta = 0$) represents the dorsal surface of the fish aligned normal to the axis of the acoustic beam.

B. TS_θ of live fish

Orange roughy are highly directional scatterers, which is expected for nonresonant targets of this size.[17] The tilt-dependence of TS_θ for live fish was characterized by strong peaks and nulls at different fish orientations, as was the case for dead fish. The patterns of the tilt dependence for an individual fish differed between successive replicate rotations. Visual inspection shows that there is a considerable degree of coherence between peaks and nulls but that the position of peaks may be offset by as much as 5–10° in successive replicates (Figs. 5 and 6). The effect of the difference in TS_θ between replicate rotations on our estimates of ⟨TS⟩ is quite small. For the three fish in Fig. 5, ⟨TS⟩ estimated from both replicates was the same (see fish sized 30.2, 30.2, and 30.8 cm in Fig. 12). For the three fish in Fig. 6, the replicate runs produced estimates of ⟨TS⟩ within 1.5 dB (see fish sized 32.3, 32.4, and 32.7 cm in Fig. 12). The data presented in the ⟨TS⟩ length regression (Fig. 11) are all from rotation 2 of the experiment (see Fig. 12). This choice was made because we assumed that the rotation speed of the fish was more constant in the second rotation.

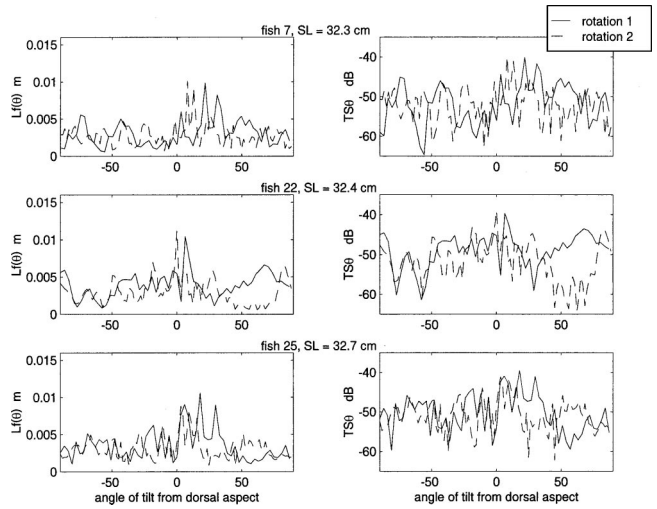

FIG. 6. Tilt dependence of scattering lengths, $L_f(\theta)$, and target strength, TS_θ, for three live orange roughy of ~32-cm standard length (fish sizes are given on the graph). Two replicate rotations of the fish are shown. Geometry as in Fig. 5.

The highly directional nature of scattering from orange roughy indicates that fish tilt orientation will have a very strong effect on ⟨TS⟩. The direction of maximal backscattering was offset from true dorsal aspect by 5–10 degrees in five of the six fish examined (Figs. 5 and 6). The tilt dependence of $L_f(\theta)$ and TS_θ is often referred to as the fish beam pattern. The beam patterns for fish of the same size differ because although some fish have the same size, morphology and tissue composition they are not identical.

C. Tilt angle distribution

Tilt angle distribution with the video camera lights on differed slightly from the distribution with the lights off, there being a slight skew toward the fish being tilted more head down for the former and head up for the latter. However, the differences were not great and the data were combined for this work (Fig. 2). Although tilt angles in the roll plane were not measured, the extent of this was assessed subjectively from the photographs and video. While the pitch plane variation was very evident, there was little obvious variability in the roll plane, the fish maintaining an upright position.

D. Tilt-averaged target strength, ⟨TS⟩

Practical difficulties of working with the live fish, as outlined earlier, limited the range of measurements we made and tilt averaging was only carried out in the pitch plane. The ⟨TS⟩ of live orange roughy was consistently lower than the ⟨TS⟩ of the same individual frozen and then thawed ($n = 8$). The difference between live and dead fish ranged from 1.9 to 9.8 dB (Table II) with most values for dead fish being about 6–7 dB higher than for the same fish when alive. The difference was highly statistically significant (Fig. 7). There also appeared to be some effect from the duration of freezing and the difference in the means for 20-month frozen and fresh-frozen fish was just significant at the 5% level (Fig. 7). The results are plotted as a function of fish size in Fig. 8. The difference between dead fish frozen for a longer or shorter period was considerably less than the difference between live and dead fish (Figs. 7 and 8).

Dead fish increased in weight by up to 2% over 8 h in the experiments, which we attribute to water uptake as fish re-hydrate during thawing (Fig. 9). It was also evident that the fish lost oil because a small oil slick appeared on the surface above the fish. A CAT-scan of a recently thawed, previously frozen orange roughy revealed the presence of air-filled lacunae in the body cavity (Fig. 10). We think that these lacunae filled with water as the fish re-hydrate during thawing and take up water into their tissue. However, we infer from the much higher ⟨TS⟩ measured on dead, previ-

TABLE II. Comparison of tilt-averaged target strengths, ⟨TS⟩, of eight live orange roughy that were frozen immediately after the live measurements and then re-measured after thawing. ⟨TS⟩ of dead orange roughy frozen for 20 months are shown for comparison.

SL, cm dead orange roughy	⟨TS⟩ frozen, thawed orange roughy, dB	SL, cm live orange roughy	⟨TS⟩ live orange roughy, dB	⟨TS⟩ live, frozen, thawed orange roughy, dB
16.0	−42.28	-	-	-
18.0	−42.60	-	-	-
27.0	−39.60	-	-	-
27.0	−41.80	-	-	-
-	-	27.9	−48.08	−42.14
-	-	28.1	−47.26	−39.94
29.0	−39.13	-	-	-
-	-	29.4	−46.71	−41.94
30.0	−39.20	30.0	−48.32	-
-	-	30.2	−46.74	-
-	-	30.2	−44.22	−42.46
-	-	30.8	−47.32	-
-	-	-	-	-
31.0	−38.65	-	-	-
-	-	31.8	−48.51	−41.31
32.0	−39.47	-	-	-
32.0	−37.21	32.0	−48.95	-
-	-	-	-	-
-	-	32.4	−47.10	-
-	-	32.7	−47.43	-
-	-	33.4	−49.64	−39.73
34.0	−36.88	-	-	-
34.0	−38.69	-	-	-
34.0	−39.13	-	-	-
		34.3	−46.75	−38.75
35.0	−38.70	-	-	-
-	-	35.4	−46.79	-
36.0	−35.84	-	-	-
-	-	36.3	−45.33	-
-	-	36.7	−42.85	−37.76
37.0	−37.11	-	-	-
39.0	−35.08	-	-	-
40.0	−35.47	-	-	-

ously frozen fish that some residual air remains in the body of the thawed fish. This residual air is likely to be the cause of higher ⟨TS⟩ for dead fish.

A representative size distribution for orange roughy in New Zealand waters is shown in Fig. 11. The modal size is 36 cm and most fish fall between 30 and 40 cm. Application of ⟨TS⟩ in acoustic survey to estimate biomass requires a regression relationship with confidence limits to predict ⟨TS⟩ for fish in the size range of ~30–40 cm. We used bootstrapping to obtain 95 percentile confidence limits for the regression based on our live fish data (Fig. 11). The regression

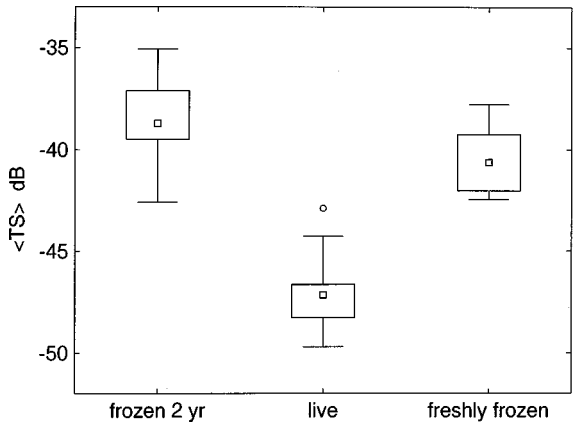

FIG. 7. Comparison of tilt-averaged target strengths, ⟨TS⟩, of eight live orange roughy that were frozen immediately after the live measurements and then re-measured after thawing. ⟨TS⟩ of dead orange roughy frozen for 20 months are shown for comparison. Box plots show median, 25th, and 75th percentiles, and ranges. The open circle marks an outlier defined as having a value>(mean+75th percentile)+1.5×(75th percentile−25th percentile).

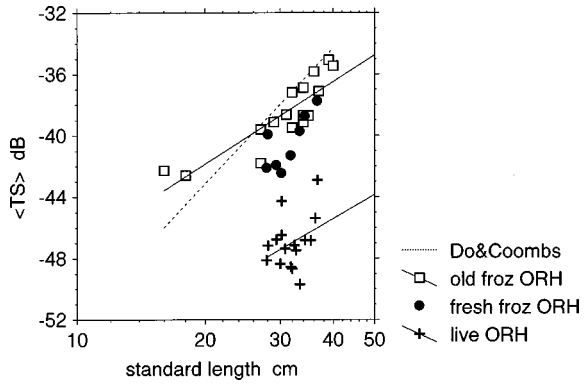

FIG. 8. Relationship between ⟨TS⟩ and orange roughy size. Data for 20-month frozen fish (old froz ORH) and live fish that were killed, frozen and re-measured (fresh froz ORH) gave much higher ⟨TS⟩ than for live fish (live ORH). The regression fitted to data published by Do and Coombs (Ref. 11) gives ⟨TS⟩ of the same order as our measurements on thawed dead fish.

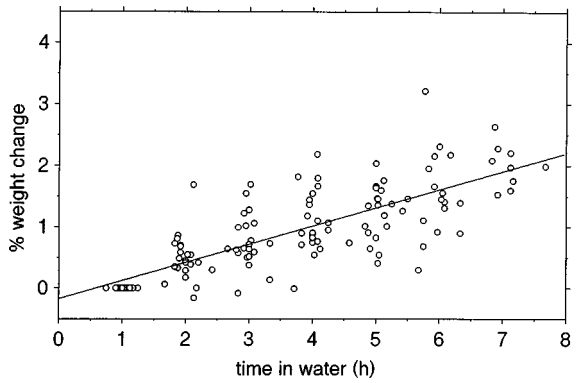

FIG. 9. Percent change from initial weight for individual dead orange roughy ($N=25$ fish) measured hourly over 8 h. The weight change appears to be due to water uptake as frozen fish thaw during immersion in seawater. Dead fish used for experiments were weighed only when frozen and at the end of the experiment to avoid removing the fish from water. Hourly data are from other fish than those used to measure TS_θ.

predicts ⟨TS⟩ of −46.3 dB for a 35-cm live orange roughy (bootstrapped 95% confidence intervals = −48.0 to −45.5 dB).

Variation in the estimates of ⟨TS⟩ for fish of the same size is quite large. For example, the ⟨TS⟩ of three fish ~30-cm long differed by ~4.5 dB (see Fig. 11). We tested whether the observed variability was due to measurement error (i.e., a precision problem) or whether it was due to individual variability between fish. We estimated ⟨TS⟩ for

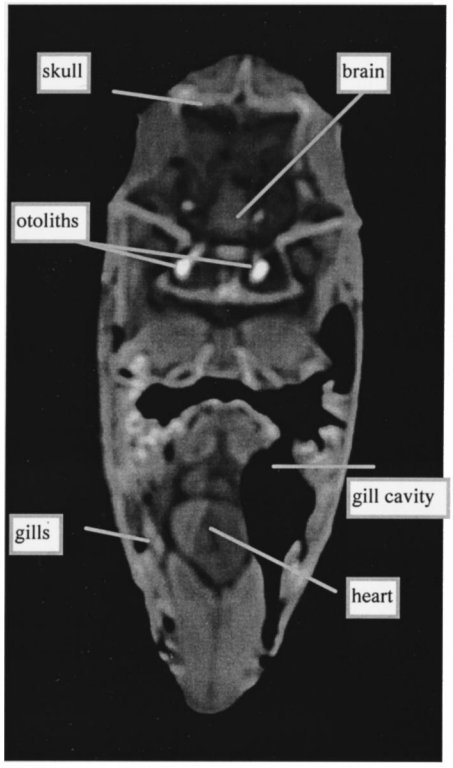

FIG. 10. CAT scan of the head section of a freshly thawed, previously frozen orange roughy. Density of the fish tissues is shown by the gray scale, with darker gray representing less density. The fish had been lying on its side during freezing and the organs in the fish had settled to that side. The black spaces in the fish body are air filled lacunae. A scan from fish that had never been out of water had water in this area.

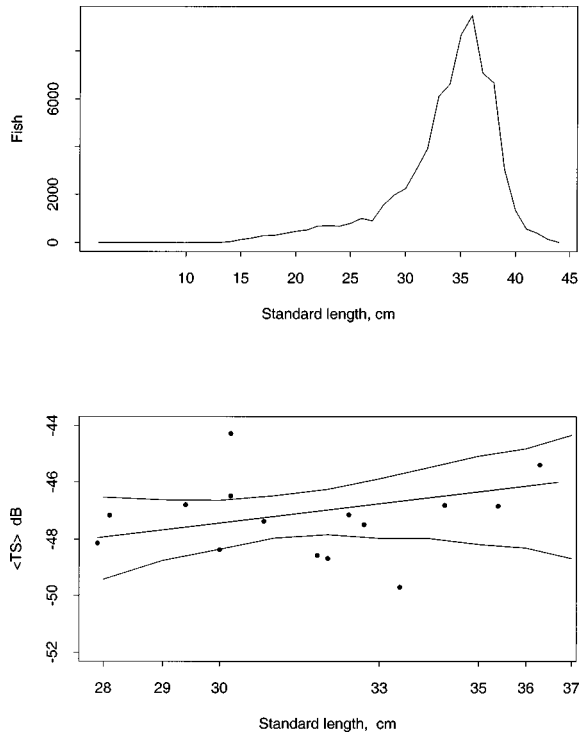

FIG. 11. (A) representative size distribution of orange roughy from the June 1995 survey of the main north Chatham Rise spawning plumes. Modal size = 36 cm. (B) Length-target strength regression for live orange roughy ($n=16$). The regression equation is: $\langle TS\rangle = 16.374 \log_{10}$ Standard Length $- 71.621$ where ⟨TS⟩ is in dB and Standard Length is in cm. 95 percentile confidence limits were estimated by bootstrapping.

each of the two replicated rotations of each live fish and plotted the result with the mean of both rotations (Fig. 12). For the same three fish ~30 cm long we were able to demonstrate excellent precision in our measurements (Fig. 12). While the precision of our measurements is not quite so good for all 16 fish, it is within ~1 dB for 12 of the 16 live fish (Fig. 12). This clearly demonstrates that the variability in the

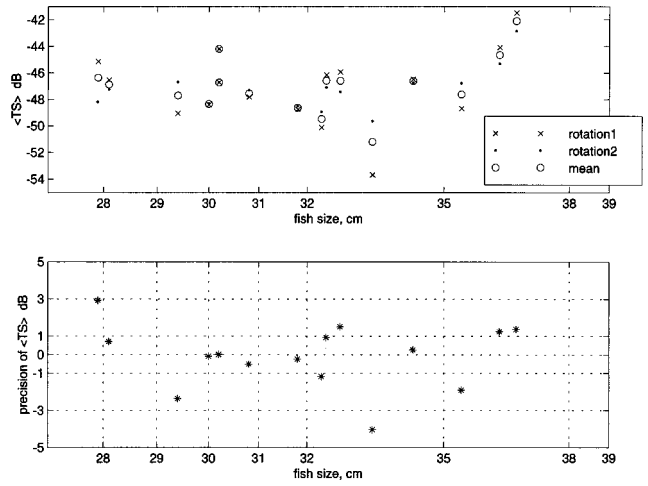

FIG. 12. Estimated precision of ⟨TS⟩ measurements on live orange roughy. The upper panel shows ⟨TS⟩ estimated from two replicated rotations of each fish ($n=16$), and the mean of both rotations. The lower panel shows the difference between ⟨TS⟩ estimated from rotation 1 and rotation 2. The difference in ⟨TS⟩ between rotations is an estimate of precision for the experimental measurements.

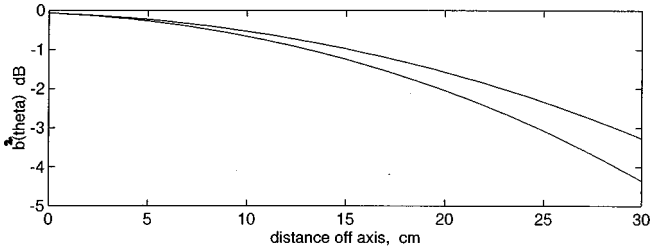

FIG. 13. The effect of movement off the axis of the beam for a target at 6.2-m range (lower curve) and 7.2-m range (upper curve) was estimated by calculating the beam pattern $b^2(\theta)$ in dB for deviations as large as 30 cm normal to the axis.

⟨TS⟩ length regression is due to individual variability between fish.

III. DISCUSSION

At the range of the fish (6.2 m) we calculated the two way beam pattern, $b^2(\theta)$, for different angles of deviation from the beam axis to assess the effect of the fish moving slightly off-axis due to stretching of the support lines. Even for the unlikely case of the fish being off-axis by 10 cm, the reduction in target strength was less than 1 dB (Fig. 13). This shows that small shifts in the position of the fish off the beam axis could not have caused the considerable time-series changes in target strength that we measured in the dead fish.

A weakness in our measurements is that a complete set is available only for rotation in the pitch plane while there is as much, and more consistent, variation in target strength in the roll plane (see Fig. 3 and also Ref. 11). Do and Coombs[11] used both pitch and roll plane tilt distributions when calculating ⟨TS⟩. They averaged over ±30° in the roll plane but the camera data do not support such a large range since the fish essentially stay upright. We believe that the main effect in the roll plane during acoustic surveys will be due to the positions of individual fish in the transducer beam. For our survey work we tow the same transducer used to make the tank measurements so the nominal effect of the beam moving across individual fish will be only ±3.5°. Over this range of roll tilt angles the variation in target strength due to roll is negligible (Fig. 3) so we do not consider neglecting it to cause a large error.

There is a surprising paucity of studies where experiments have been done using the same method on both live and dead fish of the same species. As far as we are aware, there are none for nonswimbladder fishes. For swimbladder fish, Nakken and Olsen[21] (Fig. 48) presented a time series of target strength for one live, tethered cod at 38 kHz showing oscillations in TS_{max} of 3–5 dB. The data suggest that the magnitude of the oscillations (due to swimming) is a function of orientation, and can be much greater at some orientations (15–20 dB) than at the angle of maximum target strength.

We were able to compare target strength for dead and live Atlantic mackerel (*Scomber scombrus*) from published data. Foote[20] described tethered dead fish experiments by Nakken and Olsen[21] and MacLennan[22] summarized a caged live fish experiment carried out by Edwards and

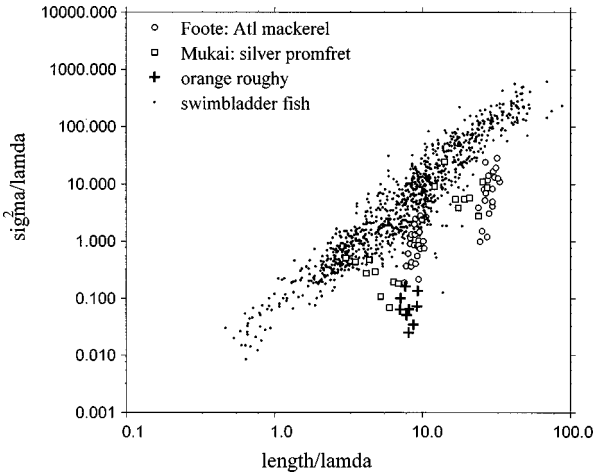

FIG. 14. Relation between maximum target strength expressed as wavelength-normalized acoustic cross-section and fish size for nonswimbladder, marine fishes. Data are from experimental studies where target strength of individual fish can be matched to fish size (Ref. 18). Lambda=acoustic wavelength, *m*. Sigma=acoustic cross-section, m^2. The small dots represent data from fish with swimbladders shown for comparison with nonswimbladder fish.

Armstrong.[23] Bearing in mind the different limitations of each of these types of studies, the data suggest that target strength of live mackerel at 38 kHz may be as much as 8–10 dB lower than that of dead mackerel. This result accords with ours where we found that live orange roughy had ⟨TS⟩ 2–10 dB lower than dead orange roughy at 38 kHz. However, we note that the ''stabilized'' $TS_{\theta=0}$ of the thawed orange roughy was in the range −51 to −44 dB, which is comparable with the target strength of live orange roughy.

It is useful to compare our estimates of orange roughy target strength to other fish species to determine whether this fish is in any way unusual. Since orange roughy have a wax-invested swimbladder it is more sensible to compare them to nonswimbladdered fish. We compared orange roughy TS_{max} to a dataset for nonswimbladder fish presented in the context of a much larger dataset for fish with swimbladders.[18] It is apparent from Fig. 14 that at 38-kHz orange roughy have considerably lower TS_{max} than Atlantic mackerel of the same size.[20] Orange roughy TS_{max} is closer to, but still generally lower than, existing estimates for silver pomfret target strength.[24] This suggests to us that these oily deep water fish have unusual acoustic properties. We elaborate on the effect of wax esters in a paper presenting a model of orange roughy target strength.[25]

Our experimental results show that orange roughy are highly directional scatterers and we expect fish orientation to have a correspondingly large effect on estimates of ⟨TS⟩. Orange roughy show a characteristic avoidance response to falling objects such as a steel bar, or to a camera frame lowered on a hydro wire.[4] In a recent survey we documented an avoidance response when our acoustic towbody was flown within 100 m of orange roughy aggregating over a seamount (Fig. 15). An acoustic transect was made across a seamount rising to 750 m depth using two CREST echosounders. The first sounder was connected to the hull mounted transducer. The second sounder was connected to the acoustic towbody deployed at 650 m depth, so that the

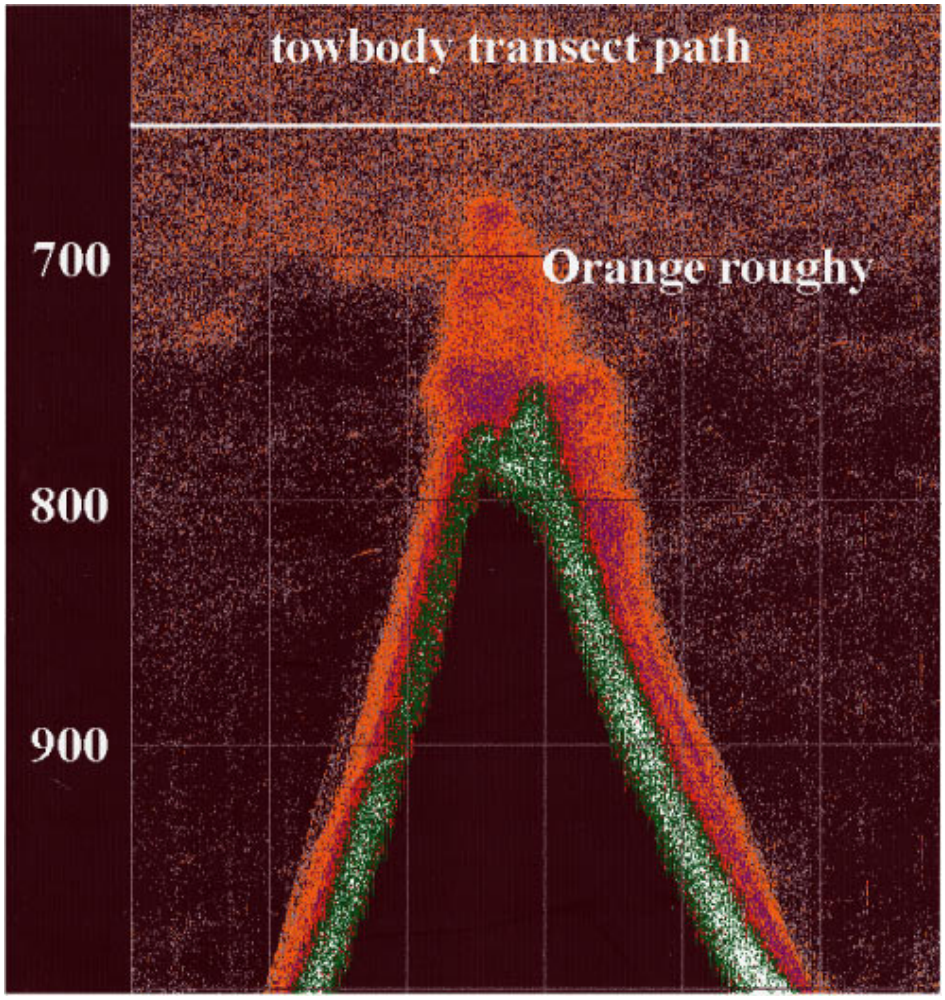

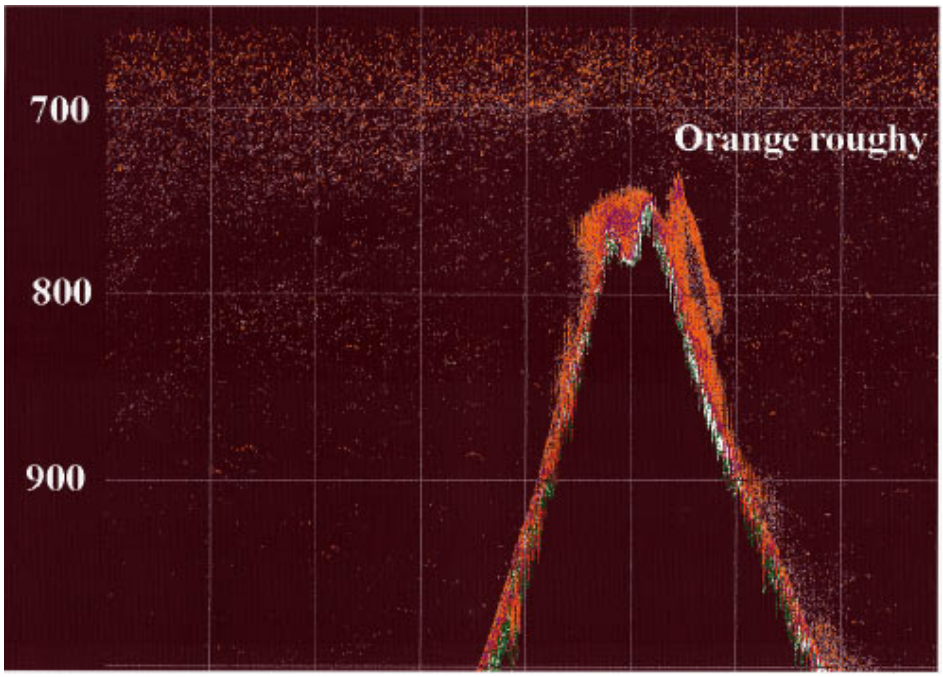

FIG. 15. Echograms documenting the avoidance response of orange roughy to a deep towed acoustic transducer. (A) shows a transect across the Graveyard seamount rising to 750 m using the ships hull-mounted transducer. An aggregation of orange roughy was present on the summit of the seamount. (B) shows the same transect run concurrently using a second CREST echosounder connected to the towbody transducer deployed at 650 m depth (shown by the line in the top echogram). The towbody was about 800 m behind the ship so the echograms were about 17 min apart as the ship passed over the seamount at 1.5 kn. The orange roughy appeared to detect the towbody and avoided it by moving away down the slope of the seamount, to the right on the echogram. Echograms were produced from two 38-kHz CREST echosounders.

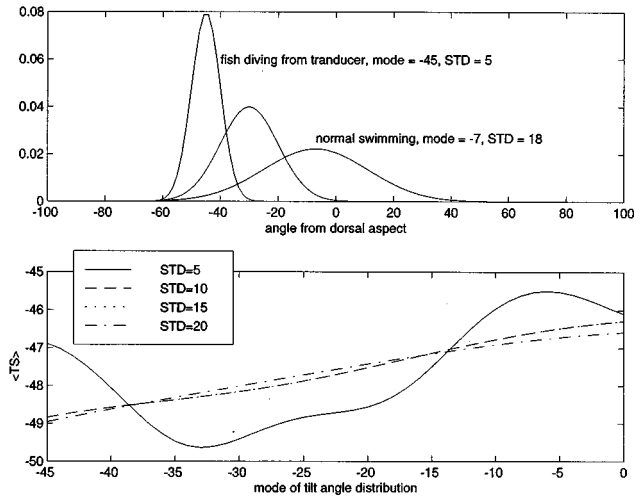

FIG. 16. Simulated effect of avoidance behavior on the ⟨TS⟩ of orange roughy. PDFs of tilt angle distributions were created from normal distributions with modes of 0 to −45° and standard deviations (STD) of 5°–25° to simulate the effect of orange roughy diving away from a towed transducer (only three distributions shown). ⟨TS⟩ was calculated for each tilt distribution using experimental measurements of TS_θ from a live orange roughy of 34.3 cm and the simulated tilt angle distributions. The potential magnitude of the avoidance effect on ⟨TS⟩ is 2.5 dB due to orange roughy diving away from a towed transducer. Narrower tilt angle distributions (STD=5°) cause variable ⟨TS⟩ due to strong peaks and nulls in the distribution of TS_θ.

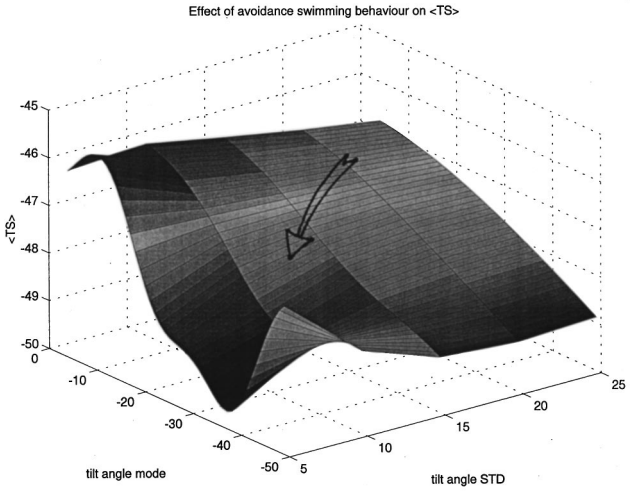

FIG. 17. Combined effect of a change in the mode and the standard deviation of the tilt angle distribution of orange roughy on ⟨TS⟩. Tilt angle modes range from 0 to −45° where the minus sign indicates head down orientation in the pitch plane. Standard deviations range from 25° to 10°. Narrower tilt angle distributions cause variable ⟨TS⟩ (see Fig. 16) due to strong peaks and nulls in the distribution of TS_θ. The arrow represents the trajectory of ⟨TS⟩ when avoidance behavior simultaneously shifts both the mode and the standard deviation toward lower values.

towbody over flew the summit by 100 m, just above the top of a distinct orange roughy aggregation. The result was that the orange roughy avoided the transducer and moved away down the slope of the seamount (Fig. 15).

Such an avoidance response would change the orientation distribution—the tilt angle—of the orange roughy. In order to estimate *in situ* ⟨TS⟩ it is necessary to be within ~100 m of the fish in order to resolve the individual fish echoes, since orange roughy schools tend to be densely aggregated. We argue that collecting *in situ* ⟨TS⟩ at this range is not possible without affecting the behavior, and specifically the tilt angle, of the fish because of their strong avoidance response. Current estimates of *in situ* ⟨TS⟩ were collected within 100–150 m of mixed orange roughy and myctophiid targets (see Table I).[8,14] We simulated the effect of avoidance on ⟨TS⟩ using tilt angle distributions representing orange roughy diving to avoid a towbody. To do this we recalculated ⟨TS⟩ from the TS_θ measured in our experiments on a 34.3-cm live orange roughy, chosen because this size was representative of the length-frequency mode (see Fig. 11). The avoidance behavior is likely to involve a shift in the tilt angle distribution mode to more negative values as the fish dive (head down in the pitch plane) and a narrowing of the tilt angle distribution (smaller standard deviation).

We estimated ⟨TS⟩ for tilt angle modes ranging from 0° to −45° and standard deviations ranging from 5° to 25° (Fig. 16). The simulated effect of avoidance on ⟨TS⟩ is marked. For fish diving away from the transducer (head down, tilt angle mode=−45°, standard deviation=10°), the ⟨TS⟩ is reduced by 2.5 dB (Fig. 16). Narrower tilt angle distributions (standard deviation=5°) cause variable ⟨TS⟩ due to strong peaks and nulls in the distribution of TS_θ. The trajectory of ⟨TS⟩ due to avoidance behavior lies along the diagonal of the surface in Fig. 17. Although this result does not prove that the ~3-dB difference between current *in situ* estimates of ⟨TS⟩ and our experimental measurements on live fish is due to avoidance of the acoustic towbody, it shows that avoidance is a feasible explanation. We suggest that a new approach is necessary to estimate the ⟨TS⟩ of orange roughy *in situ* and that current estimates of *in situ* ⟨TS⟩ be regarded as preliminary.

IV. CONCLUSIONS

(1) The scattering lengths of dead orange roughy decline significantly for 12–16 h after frozen fish are placed in seawater. We attribute this to changes in body composition mainly due to rehydration after freezing. Rehydration increases the volume of organs in the body and fills air spaces that develop during freezing. Tilt-averaged target strength of thawed dead orange roughy was 2–10 dB higher than for live fish. However, after the dead fish ''stabilized'' their $TS_{\theta=0}$ was comparable to that of live fish, falling in the range −51 to −44 dB.

(2) We estimate a tilt-averaged target strength (⟨TS⟩) of −46.3 dB for a 35-cm live orange roughy. Bootstrapped 95% confidence intervals for this estimate are −48.0 to −45.5 dB. The range of our ⟨TS⟩ [−49.7, −42.9 dB] are somewhat higher than the range of previous estimates [−53.6, −47.2 dB] for the similar sized fish.[8,14] Most of our estimates of ⟨TS⟩ fell in the range −49 to −45 dB.

(3) TS_{max} for orange roughy falls below that for comparable sized nonswimbladdered fish, showing that this species has an unusually low target strength at 38 kHz.

(4) The ≈3-dB difference between mean *in situ* estimates of ⟨TS⟩ and experimental measurements of ⟨TS⟩ on live 35-cm fish can be explained by the effect of strong avoidance reactions to a towed transducer on the tilt angle of the orange roughy.

ACKNOWLEDGMENTS

We thank Kate Medlicott and Garbriel Sertzou for their diligent work during the experiments. We are grateful to Alistair MacDiarmid for permitting us to use his unpublished data on orange roughy orientation distributions. We appreciate the support of Wilbert Knol and Malcolm Hopkins as well the NIWA Workshop staff, and thank Karen Field and Malcolm Clark for fish samples. We thank Rudy Kloser, Zhen Ye, Patrick Cordue, and Ian Doonan for enthusiastic and valuable interactions. Chris Francis's comments on a draft manuscript and the detailed and careful journal reviewer's comments both improved our manuscript and stimulated new analyses. We thank the Department of Radiology at Wakefield hospital for the CAT scan of orange roughy. Funding for this project was provided by the Ministry of Fisheries through Contract No. DEOR702.

[1] J. J. Dawson and W. A. Karp, ''*In situ* measures of target-strength variability of individual fish,'' Rapp. P.-V. Reun.-Cons. Int. Explor. Mer. **189**, 264–273 (1990).
[2] E. Ona, ''Physiological factors causing natural variations in acoustic target strength of fish,'' J. Mar. Biol. Assoc. U.K. **70**, 107–127 (1990).
[3] M. R. Clark and D. M. Tracey, ''Changes in a population of orange roughy, *Hoplostethus atlanticus*, with commercial exploitation on the Challenger Plateau, New Zealand,'' Fish. Bull. **92**, 236–253 (1993).
[4] A. J. Koslow, R. Kloser, and C. A. Stanley, ''Avoidance of a camera system by a deepwater fish, the orange roughy (*Hoplostethus atlanticus*),'' Deep-Sea Res. **42**, 233–244 (1995).
[5] J. R. Sargent, R. R. Gatten, and N. R. Merrett, ''Lipids of *Hoplostethus atlanticus* and *H. mediterraneus* (Beryciformes: Trachichthyidae) from deep water to the west of Britain,'' Marine Biology **74**, 281–286 (1983).
[6] C. F. Phleger and M. R. Grigor, ''Role of wax esters in determining buoyancy in *Hoplostethus atlanticus* (Beryciformes: Trachichthyidae),'' Marine Biology **105**, 229–233 (1990).
[7] M. R. Grigor, W. H. Sutherland, and C. F. Phleger, ''Wax-ester metabolism in the orange roughy *Hoplostethus atlanticus* (Beryciformes: Trachichthyidae),'' Marine Biology **105**, 223–227 (1990).
[8] R. J. Kloser, A. Williams, and J. A. Koslow, ''Problems with acoustic target strength measurements of a deepwater fish, orange roughy (*Hoplostethus atlanticus*, Collett),'' ICES J. Mar. Sci. **54**, 60–71 (1997).
[9] M. R. Clarke and D. M. Tracey, ''Orange roughy off the southeast coast of the South Island and Puysegur Bank: exploratory and research fishing, June–August 1992,'' MAF Fisheries, Wellington, New Zealand Fisheries Technical Report 35 (1993).
[10] O. Anderson and J. Fenaughty, ''Trawl surveys of orange roughy on the Chatham Rise, 1984 to 1992,'' NIWA, Wellington, New Zealand Fisheries Data Report 81 (1996).
[11] M. A. Do and R. F. Coombs, ''Acoustic measurements of the population of orange roughy (*Hoplostethus atlanticus*) on the north Chatham Rise, New Zealand,'' New Zealand Journal of Marine and Freshwater Research, **23**, 225–237 (1989).
[12] N. G. Elliott and R. J. Kloser, ''Use of acoustics to assess a small aggregation of orange roughy, *Hoplostethus atlanticus* (Collett), off the eastern coast of Tasmania,'' Australian Journal of Marine and Freshwater Research, **44**, 473–482 (1993).
[13] R. J. Kloser, J. A. Koslow, and A. Williams, ''Acoustic assessment of the biomass of a spawning aggregation of orange roughy (*Hoplostethus atlanticus*, Collett) off South-eastern Australia, 1990–93,'' Marine and Freshwater Research, **47**, 1015–1024 (1996).
[14] R. J. Kloser, A. Williams, and J. A. Koslow, ''The acoustic target strength of a deepwater fish, orange roughy (*Hoplostethus atlanticus*), based on modelling and *in situ* measurements on schools and tethered fish,'' CSIRO Marine Laboratories, Final report to Fisheries Research and Development Corporation Grant number 90/25.
[15] R. W. G. Haslett, ''Automatic plotting of polar diagrams of target strength of fish in roll, pitch and yaw,'' Rapp. P.-V. Reun.-Cons. Int. Explor. Mer **170**, 74–81 (1977).
[16] R. F. Coombs, ''An adaptable acoustic data acquisition system for fish stock assessment,'' In International Conference on Underwater Acoustics, 5–7 December 1994, Australian Acoustical Society, University of New South Wales, Sydney, pp. 18–22 (1994).
[17] C. S. Clay and H. Medwin, *Acoustical Oceanography: Principles and Applications* (Wiley, New York, 1977), p. 544.
[18] S. McClatchie, J. Alsop, and R. F. Coombs, ''A re-evaluation of relationships between fish size, acoustic frequency, and target strength,'' ICES J. Mar. Sci. **53**, 780–791 (1996).
[19] K. G. Foote, ''Averaging of fish target strength functions,'' J. Acoust. Soc. Am. **67**, 504–515 (1980).
[20] K. G. Foote, ''Importance of the swimbladder in acoustic scattering by fish: A comparison of gadoid and mackerel target strengths,'' J. Acoust. Soc. Am. **67**, 2084–2089 (1980).
[21] O. Nakken and K. Olsen, ''Target strength measurements of fish,'' Rapp. P.-V. Reun.-Cons. Int. Explor. Mer **170**, 52–69 (1977).
[22] D. N. MacLennan and E. J. Simmonds, *Fisheries Acoustics* (Chapman & Hall, London, 1992), p. 325.
[23] J. I. Edwards and F. Armstrong, ''Target strength measurements on herring, sprat and mackerel,'' ICES CM. 1983/B:23: 22 p. (mimeo) (1983).
[24] T. Mukai, N. Sano, K. Iida, and S. Sasaki, ''Relation between dorsal aspect target strength of fish caught in the East China Sea and their swimbladder,'' Nippon Suisan Gakkaishi, **60**, 215–222 (1994).
[25] S. McClatchie and Z. Ye, ''Target strength of the deep-water fish, orange roughy (*Hoplostethus atlanticus*). Part II: Modeling'' (unpublished).

Nonlocal boundary conditions for finite-difference parabolic equation solvers[a)]

David Yevick[b)]
Department of Electrical Engineering, Queen's University, Kingston, Ontario K7L 3N6, Canada

David J. Thomson[c)]
Defence Research Establishment Atlantic, P.O. Box 1012, Dartmouth, Nova Scotia B2Y 3Z7, Canada

(Received 10 June 1998; revised 6 April 1999; accepted 12 April 1999)

Theoretical/numerical models of underwater sound propagation usually incorporate a downgoing radiation condition on the transverse component of the acoustic field. Most one-way or parabolic equation (PE) solvers approximate this radiation condition by appending an absorbing layer to the computational mesh and setting the field to zero at the base of this layer. Papadakis *et al.* [J. Acoust. Soc. Am. **92**, 2030–2038 (1992)] replaced such approximate treatments with a nonlocal boundary condition (NLBC) that *exactly* transforms the semi-infinite PE problem to an equivalent one in a bounded domain. Papadakis' approach requires the evaluation of a spectral (wave number) integral whose integrand is inversely proportional to the impedance of the subbottom medium. In this paper, an alternate procedure is analyzed for obtaining NLBCs directly from the z-space Crank–Nicolson solvers for both the Tappert and Claerbout PEs. Formulas for the field ψ at range $r+\Delta r$ are derived in terms of the known field at the previously calculated range values from 0 to r by expanding the appropriate ''vertical wave number'' operator for the downgoing field in powers of the translation operator $\mathcal{R}=\exp(-\Delta r\partial_r)$. The effectiveness of these NLBCs is examined for several numerical examples relevant to one-way underwater sound propagation. [S0001-4966(99)05207-8]

PACS numbers: 43.30.Bp [SAC-B]

INTRODUCTION

For many applications involving underwater sound propagation, the underlying physics is accurately represented in terms of one-way wave fields that satisfy a parabolic equation (PE). This is convenient, since PEs are amenable to efficient numerical solution by marching algorithms for range-varying as well as range-invariant waveguides (see Ref. 1 and the references therein). Because the ocean subbottom is penetrable to sound waves (particularly at low frequencies), a downgoing radiation condition must be imposed on the transmitted component of the field. In numerical implementations of one-way wave propagation, this condition is usually approximated by appending an *ad hoc* absorbing layer[1–5] to the computational mesh and then applying a local pressure-release boundary condition at the base of the layer. Alternatively, this approximate boundary treatment can be replaced with a nonlocal boundary condition (NLBC) that *exactly* converts the PE problem with a transverse radiation condition at infinity into an equivalent PE problem in a bounded domain.

A nonlocal boundary condition for the standard parabolic equation of underwater acoustics[1,6,7] was first formulated and implemented in a finite-difference PE code by Papadakis.[8] The derivation of Papadakis' result involves transforming the one-way wave equation from coordinate space to the horizontal wave number domain where each spectral component of the PE field ψ satisfies a local impedance boundary condition across the interface $z=z_b$. The transformation back to coordinate space yields a nonlocal boundary condition for ψ, which, for the standard PE, can be cast as a Neumann-to-Dirichlet (NtD) map of the form

$$\psi(r,z_b)=B\int_0^r \psi_z(t,z_b)\,\frac{\exp[ib(r-t)]}{\sqrt{r-t}}\,dt. \tag{1}$$

The constants B and b depend on the material properties of the region in the vicinity of $z=z_b$, across which the medium may undergo a jump discontinuity. Equation (1) has been implemented in several applications to underwater acoustics, e.g., Refs. 9–11. This spectral method for obtaining an NLBC was extended by Papadakis[12] to treat the third-order, wide-angle PE of Claerbout,[1,13] which is capable of accommodating wider-angle propagation. Other NLBC forms for use with both standard and/or wide-angle PEs have been derived and implemented for applications in underwater acoustics,[9,14–16] optics,[17,18] radar,[19–21] and atmospheric acoustics.[22,23]

In this paper, we consider an alternative formalism for deriving nonlocal boundary conditions suitable for use with single-term approximations to the PE propagators of one-way waves.[24,25] This method is developed entirely in coordinate space and is specific to finite-difference PE solvers. It is based on the series expansion of a ''vertical wave number'' operator that arises in identifying the downgoing component of the factored Helmholtz equation in the (uniform) region $z>z_b$. The coefficients that relate the field at range r to the

[a)]Some of the material in this paper was presented at the 133rd meeting of the Acoustical Society of America, 16–20 June 1997, State College, PA.
[b)]Electronic mail: yevick@ibm.net
[c)]Electronic mail: thomson@drea.dnd.ca

previously computed values of the field along the boundary are readily obtained by a convolution procedure.

The rest of the paper is organized in the following way. First, we establish the relevant single-term PE approximations for underwater acoustics. Then, we formulate a finite-difference solution procedure which allows us to identify the pseudodifferential equation satisfied by the downgoing wave in $z>z_b$. A nonlocal boundary condition along $z=z_b$ suitable for implementation is obtained by direct expansion of the vertical wave number operator associated with this wave field. We finally demonstrate the effectiveness of such NLBCs for single-term PE propagators by applying them to several test cases relevant to underwater sound propagation.

I. THEORY

A. One-way wave equation

We first construct the one-way propagation equation for a medium with varying density $\rho(z)$ in a region $0<z<z_b$ between the surface ($z=0$) and bottom ($z=z_b$) of a stratified ocean with sound speed and absorption designated by $c(z)$ and $\alpha(z)$, respectively. Since range-varying waveguides are usually modeled as a sequence of range-independent sections, there is no loss of generality in restricting ρ, c, and α in this way. For some reference wave number $k_0=\omega/c_0$, the field ψ can be related to the complex pressure p according to

$$p(r,z)=\frac{\psi(r,z)\exp(ik_0r)}{\sqrt{k_0r}}. \tag{2}$$

Introducing the pseudodifferential operator $\sqrt{1+X}$, where

$$X=N^2-1+k_0^{-2}\rho\frac{\partial}{\partial z}\left(\rho^{-1}\frac{\partial}{\partial z}\right), \tag{3}$$

with $N(z)=n(z)[1+i\alpha(z)]$ and $n(z)=c_0/c(z)$, outgoing propagating waves in the far field ($k_0r\gg1$) can then be described by the formal ''one-way'' evolution equation[6]

$$\frac{\partial\psi}{\partial r}=ik_0\{-1+\sqrt{1+X}\}\psi. \tag{4}$$

B. Standard PE

To develop a compact form of the nonlocal finite-difference boundary condition that incorporates *a priori* the discrete nature of the propagation problem, we choose to first analyze the standard PE (SPE) of ocean acoustics, which is obtained by approximating the square-root operator in Eq. (3) by

$$-1+\sqrt{1+X}\approx\frac{1}{2}X=\frac{1}{2}(N^2-1)+\frac{1}{2}k_0^{-2}\rho\frac{\partial}{\partial z}\left(\rho^{-1}\frac{\partial}{\partial z}\right). \tag{5}$$

Substituting Eq. (5) into Eq. (4) yields the SPE

$$2ik_0\frac{\partial\psi}{\partial r}+\rho\frac{\partial}{\partial z}\left(\rho^{-1}\frac{\partial\psi}{\partial z}\right)+k_0^2(N^2-1)\psi=0. \tag{6}$$

To generate an NLBC for Eq. (6), we follow Papadakis and simplify the problem further by assuming that the region $z>z_b$ is homogeneous, i.e., one where ρ_b and N_b are constant. Then, for $z>z_b$, Eq. (6) reduces to

$$2ik_0\frac{\partial\psi}{\partial r}+\frac{\partial^2\psi}{\partial z^2}+k_0^2(N_b^2-1)\psi=0. \tag{7}$$

Using the centered finite-difference approximations over the interval from r to $r+\Delta r$

$$\frac{\partial\psi}{\partial r}\approx\frac{\psi(r+\Delta r,z)-\psi(r,z)}{\Delta r}, \tag{8}$$

$$\psi\approx\frac{\psi(r+\Delta r,z)+\psi(r,z)}{2}, \tag{9}$$

results in the implicit Crank–Nicolson formulation of Eq. (7), which we write in the form

$$\left\{k_0^2\nu^2+k_0^2(N_b^2-1)+\frac{\partial^2}{\partial z^2}\right\}\psi(r+\Delta r,z)$$
$$=\left\{k_0^2\nu^2-k_0^2(N_b^2-1)-\frac{\partial^2}{\partial z^2}\right\}\psi(r,z), \tag{10}$$

where $\nu^2=4i/(k_0\Delta r)$. The goal now is to express the unknown field $\psi(r+\Delta r,z)$ in terms of the known history of field values from $0\rightarrow r$ along the boundary $z=z_b$.

To this end, we introduce the r-space translation operator

$$\mathcal{R}=\exp(-\Delta r\partial_r), \tag{11}$$

and observe that

$$\mathcal{R}^j\psi(r,z)=\psi(r-j\Delta r,z). \tag{12}$$

In terms of $\mathcal{R}$, the Crank–Nicolson representation in Eq. (10) can be cast in the equivalent form as

$$\left\{\frac{\partial^2}{\partial z^2}+\Gamma_0^2\right\}\psi(r+\Delta r,z)=0, \tag{13}$$

where Γ_0 is a z-space vertical wave number operator defined by

$$\Gamma_0^2=k_0^2\left(N_b^2-1+\nu^2\frac{1-\mathcal{R}}{1+\mathcal{R}}\right). \tag{14}$$

Equation (13) can be formally factored into components that govern upgoing and downgoing wave fields. Heuristically, we identify the one-way radiation condition satisfied by the downgoing field at $z=z_b$ as

$$\left\{\frac{\partial}{\partial z}-i\Gamma_0\right\}\psi(r+\Delta r,z_b)=0. \tag{15}$$

A rigorous justification of this step is given elsewhere.[25] When $N_b=1$ in Eq. (14) so that the region $z>z_b$ is lossless and c_0 is chosen equal to c_b, this nonlocal boundary condition reduces to an absorbing boundary condition that is transparent to downgoing waves. Otherwise, it includes those waves that are reflected by the discontinuity in N across the plane $z=z_b$. On the other hand, we can relate Eq. (15) to the exact boundary condition that applies just *inside* the computational region $0<z<z_b$ by making use of the continuity of

pressure and vertical particle velocity across the ocean-bottom interface. Across the plane of discontinuity at $z=z_b$, we immediately find from Eq. (15) that

$$\left.\frac{\partial\psi/\partial z}{\rho_w\psi}\right|_{z_b-0}=\left.\frac{\partial\psi/\partial z}{\rho_b\psi}\right|_{z_b+0}\equiv\frac{i\Gamma_0}{\rho_b}, \tag{16}$$

from which we obtain the required impedance boundary condition

$$\left\{\frac{\partial}{\partial z}-i(\rho_w/\rho_b)\Gamma_0\right\}\psi(r+\Delta r,z_b)=0. \tag{17}$$

Equation (17) accounts for the total impedance jump (sound speed, attenuation, and density) encountered by waves that cross the lower boundary of the waveguide. A numerically tractable, *nonlocal* representation of Eq. (17) results by expanding Γ_0 in a power series in $\mathcal{R}$. This is readily accomplished, for example, by obtaining the Taylor series for the numerator and denominator separately and then convolving the coefficients. Dividing the interval $0\rightarrow r+\Delta r$ into $J+1$ intervals of width Δr and applying the definition of $\mathcal{R}$ from Eq. (12) yields

$$\left\{\frac{\partial}{\partial z}-i\mathcal{B}\right\}\psi[(J+1)\Delta r,z_b]=i\mathcal{B}\sum_{j=1}^{J+1}g_{0,j}\psi[(J+1-j)\Delta r,z_b], \tag{18}$$

where $\mathcal{B}=(\rho_w/\rho_b)k_0\sqrt{N_b^2-1+\nu^2}$. The right-hand side of Eq. (18) is seen to depend solely on the *known* values of the field along the boundary $z=z_b$. This equation allows the boundary value of the acoustic field at the advanced point of a given range-propagation step to be determined in terms of the history of boundary-field values for all previous range steps. The simple analytic nature of this operational procedure, which does not require the evaluation of the inverse Fourier transform of the reciprocal of the impedance spectral function, as in Papadakis' method, allows it to be applied to higher-order PEs in a straightforward way.

C. Wide-angle PE

To extend the above operator formalism to a wider-angle PE, we substitute the [1,1]-Padé approximation for $\sqrt{1+X}$,

$$-1+\sqrt{1+X}\approx\frac{\frac{1}{2}X}{1+\frac{1}{4}X}=\frac{\frac{1}{2}(N_b^2-1)+\frac{1}{2}k_0^{-2}\partial_z^2}{1+\frac{1}{4}(N_b^2-1)+\frac{1}{4}k_0^{-2}\partial_z^2}, \tag{19}$$

into Eq. (4) to obtain Claerbout's rational-linear PE (for $z>z_b$),

$$2ik_0\left\{1+\frac{1}{4}(N_b^2-1)+\frac{1}{4}k_0^{-2}\frac{\partial^2}{\partial z^2}\right\}\frac{\partial\psi}{\partial r}+\frac{\partial^2\psi}{\partial z^2}+k_0^2(N_b^2-1)\psi=0. \tag{20}$$

Applying the same steps leading to Eq. (17) now yields

$$\left\{\frac{\partial}{\partial z}-i(\rho_w/\rho_b)\Gamma_1\right\}\psi(r+\Delta r,z_b)=0, \tag{21}$$

TABLE I. Geoacoustic profile for the Bucker case.

Depth (m)	Sound speed ($m\,s^{-1}$)	Density ($g\,cm^{-3}$)	Attenuation dB λ^{-1}
0	1500	1.0	0.0
120	1498	1.0	0.0
240	1500	1.0	0.0
>240	1505	2.1	0.0

where Γ_1 is a wider-angle vertical wave number operator defined by

$$\Gamma_1^2=k_0^2\left(N_b^2-1+\nu^2\frac{1-\mathcal{R}}{1+\mathcal{R}}\left[1+\frac{1}{4}\nu^2\frac{1-\mathcal{R}}{1+\mathcal{R}}\right]^{-1}\right). \tag{22}$$

After a Taylor series expansion is performed in $\mathcal{R}$, we obtain a nonlocal impedance boundary condition similar to the one given in Eq. (18) but with a new set of coefficients $g_{1,j}$ replacing the $g_{0,j}$ on the right-hand side.

Although it seems reasonable to suppose that the above operator technique can be extended to handle higher-order parabolic equations, such an extension does not appear to be straightforward. In particular, the procedure requires that the downgoing component of the acoustic field be identified in order to construct an appropriate one-way equation similar to Eqs. (17) or (21). Unfortunately, for wide-angle PEs constructed from higher-order Padé approximants, the resulting expression contains nested roots, and the selection of the appropriate root and its subsequent Taylor series evaluation is difficult to determine and implement. Alternatively, multiterm PEs based on Padé and split-step Padé approaches[26,27] can be employed to cast a higher-order PE propagator as a sum of [1,1]-Padé propagators. In this case, the above procedure can in principle be employed to relate the boundary condition after the *m*th partial step to the previous values of the field at multiple units of the step-length Δr. The main difficulty with this approach is the issue of correctly apportioning the NLBC for the *total* acoustic field into the partial sums.

II. NUMERICAL RESULTS

In this section, we consider three shallow-water propagation examples to demonstrate our numerical implementation of the one-way, nonlocal boundary conditions derived earlier. For each example, the PE+NLBC calculations are based on the Claerbout approximation in Eqs. (20) and (22). Two of the examples involve range-independent waveguides, and for these cases we compare our PE+NLBC results against solutions generated using the wave number integration code SAFARI.[28] For the range-dependent example, we compare our results to solutions produced by the coupled-mode model COUPLE.[29]

The geoacoustic profile for the first example is given in Table I. This range-independent environment exhibits jump discontinuities in both sound speed and density along $z=240$ m. As a result of the small variation in sound speed, only a few normal modes possess real propagation wave numbers. However, the large density jump yields a significant number of virtual modes close to the real wave number

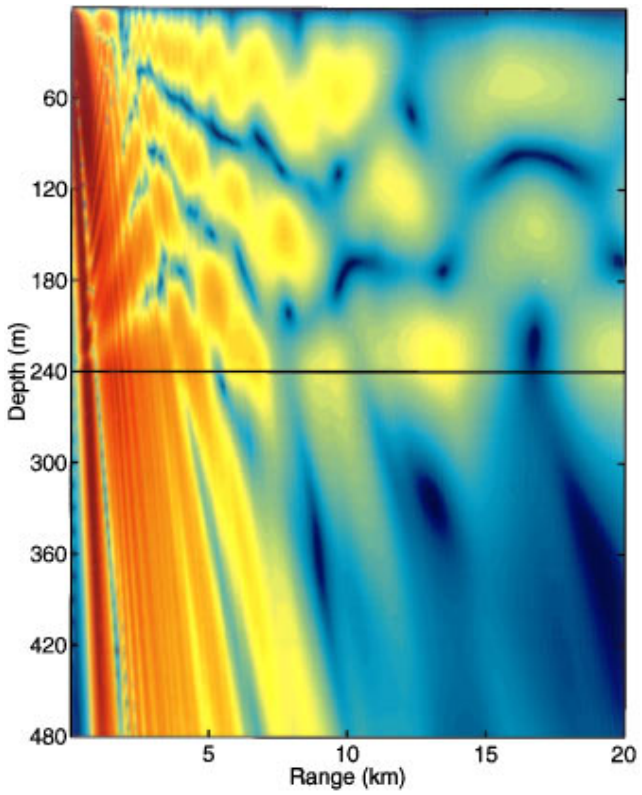

FIG. 1. PE transmission losses for the bilinear profile. The NLBC is applied along $z=480$ m.

axis (Ref. 1, pp. 249–251). This example has been used previously to examine the capability of PE codes for handling density contrasts.[10,30,31] Our focus here, however, is to show that the NLBCs can not only absorb energy that is transmitted into the sea bottom but also account for the reflection/transmission process along the sea-bottom interface. A 100-Hz acoustic source is located at $z=30$ m. For the full-field results shown in Fig. 1, the PE computational grid spanned the domain $0<z<480$ m and the PE solver employed a range step size of $\Delta r=5$ m, a depth step size of $\Delta z=1$ m, and a reference sound speed of $c_0=1500\,\mathrm{m\,s^{-1}}$. The transmission loss levels ($-10\log_{10}|p|^2$) vary from 50 dB (red) to 100 dB (blue). For ranges $r<5$ km, the energy

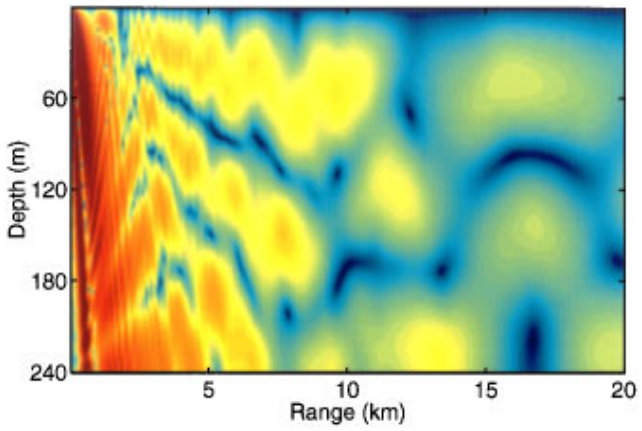

FIG. 2. PE transmission losses for the bilinear profile. The NLBC is applied along $z=240$ m.

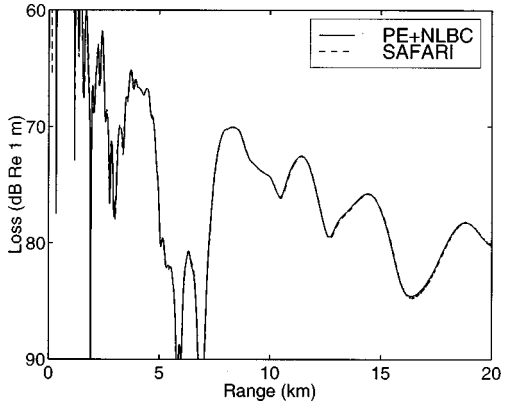

FIG. 3. Transmission loss versus range comparison for the bilinear profile. The receiver depth is $z=90$ m.

clearly undergoes bottom reflection along $z=240$ m, while the slow bottom sound speed allows considerable transmission into the region $z>240$ m. There is no evidence of reflection along $z=480$ m where the NLBC was applied. This indicates that the NLBC successfully annihilates the downgoing energy and behaves as a transparent boundary. Figure 2 shows the results of a calculation in which the computational grid is further reduced to the region $0<z<240$ m. The agreement of the field structure in this figure with the corresponding field of Fig. 1 indicates that the NLBC applied along $z=240$ m correctly handles the reflection and transmission of sound at the sea-bottom interface. When a traditional absorbing layer is used for this example, the computational grid needs to be extended to a depth of $z=2000$ m to adequately suppress reflections. A more detailed depiction of the transmission losses in Fig. 2 is shown in Figs. 3 and 4 for receivers at depths $z=90$ and 240 m, respectively. Also shown in these figures are the reference curves generated using SAFARI. The agreement is observed to be excellent. For this example, the PE calculations obtained with the absorbing bottom required a depth grid 8.3 times larger and executed 1.6 times slower that the PE+NLBC calculations.

Table II lists the geoacoustic profile for the second example, a shallow-water environment that is representative of the southern Mediterranean Sea. The sea bottom is further characterized as an elastic solid with shear speed $c_s=600$ $\mathrm{m\,s^{-1}}$ and shear attenuation $\alpha_s=1.5$ dB λ^{-1}. This configu-

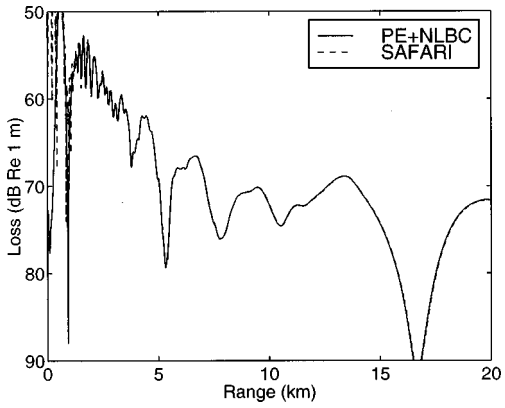

FIG. 4. Transmission loss versus range comparison for the bilinear profile. The receiver depth is $z=240$ m.

TABLE II. Geoacoustic profile for the southern Mediterranean case.

Depth (m)	Sound speed ($m\,s^{-1}$)	Density ($g\,cm^{-3}$)	Attenuation dB λ^{-1}
0.0	1532.8	1.0	0.0
21.1	1531.3	1.0	0.0
22.8	1530.1	1.0	0.0
27.1	1520.1	1.0	0.0
30.1	1518.8	1.0	0.0
46.2	1512.9	1.0	0.0
80.0	1509.0	1.0	0.0
>80.0	1750.0	2.0	0.6

ration was used previously by Bucker[32] to illustrate the effect of a rigid sea bottom on sound propagation. In addition, Bucker showed how the elastic bottom could be approximated with an equivalent fluid which accounts for the extra transmission losses due to shear wave conversion. Bucker's method involves replacing the solid bottom with a stack of sub-bottom acoustic layers having the same density as water but with depth-dependent sound-speed and attenuation profiles. The layer profiles are chosen so that the reflection coefficient R' of the equivalent fluid matches the reflection coefficient R of the true solid near grazing angles that give rise to trapped modes. Recently, Zhang and Tindle[33] introduced an alternative prescription for modeling a solid half space with an equivalent fluid. By a similar matching of reflection coefficients, their method uses the shear parameters of the bottom to transform the true bottom density ρ_b into a complex-valued density ρ_b'. As a result, their method can readily be incorporated into the NLBC formalism introduced in the present paper. This is an alternative to the formally exact spectral approach of combining an acoustic PE with nonlocal boundary conditions to accommodate an elastic bottom.[9,16]

Following Zhang and Tindle, the southern Mediterranean elastic bottom in this paper is modeled with an equivalent fluid having the same compressional sound speed and attenuation as given in Table II but with a complex density given by

$$\rho_b' = \rho_b[(1-2/N_s^2)^2 + 4i\gamma_s\gamma_b/(k_0^2 N_s^4)], \tag{23}$$

where $N_s = (c_0/c_s)(1+i\alpha_s)$. The quantities $\gamma_s = k_0\sqrt{N_s^2-1}$ and $\gamma_b = ik_0\sqrt{1-N_b^2}$ are the vertical wave numbers of the shear and compressional waves in $z > z_b$, respectively. The reference sound speed c_0 can be adjusted within limits to give the best match between R and R' in the vicinity of the propagating modes. The complex density in Eq. (23) is easily incorporated into the NLBCs described earlier via the constant $\mathcal{B}$ in Eq. (18).

Our calculations for this example were carried out at a frequency of 100 Hz for a source and receiver at a depth of 50 m. The NLBC was evaluated along the sea bottom at $z_b = 80$ m. The PE computational grid used $\Delta r = 10$ m and $\Delta z = 0.5$ m. The reflection coefficient of the equivalent fluid was matched to the reflection coefficient of the elastic bottom at a grazing angle of 12 deg, which corresponds to a phase speed of $c_0 = 1512\,m\,s^{-1}$. Using these parameters, the density of the solid half space is changed from $\rho_b = 2\,g\,cm^{-3}$ to $\rho_b' = 0.965 + 0.277i\,g\,cm^{-3}$. To highlight the effect of shear on sound propagation, transmission loss versus range results are shown in Fig. 5 for both the acoustic ($c_s = 0$, upper curve) and elastic (lower curve) bottom types. Clearly, the excitation of shear waves in the bottom is a dominant loss mechanism for this particular environment. For comparison to the PE+NLBC results, the corresponding reference values computed using SAFARI are shown in Fig. 6. The PE results are observed to agree well with the SAFARI results for both acoustic and elastic bottom types. The validity of the equivalent fluid approximation is evident in this example. The PE calculations involving an absorbing bottom require that the depth grid be extended to $z = 160$ m to achieve stability. In this case, the execution time for the PE +NLBC calculations increased by a factor of 1.4, indicating that the overhead in computing the NLBC convolutions can be significant. Since the number of terms in Eq. (18) increases with increasing range, the marching procedure further slows as the range increases. If the sea bottom is lossy, however, the sums can often be truncated without significant loss of information, but this aspect of the numerical implementation is not pursued in the present paper.

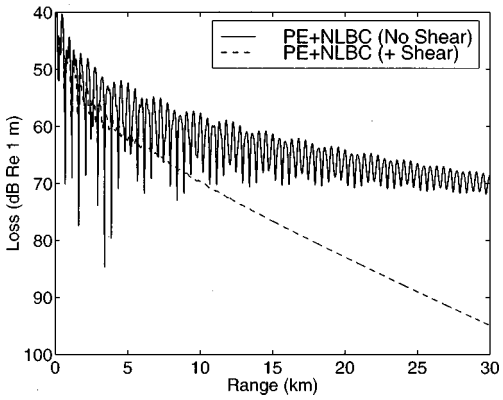

FIG. 5. PE+NLBC transmission loss versus range comparison for the southern Mediterranean profile. The receiver depth is $z = 50$ m.

The geoacoustic description for the third example is given in Table III, and corresponds to the deep-end section ($r = 0$) of the lossy wedge-test case introduced as one of the Acoustical Society of America (ASA) range-dependent benchmark problems.[26,34,35] Jump discontinuities in sound

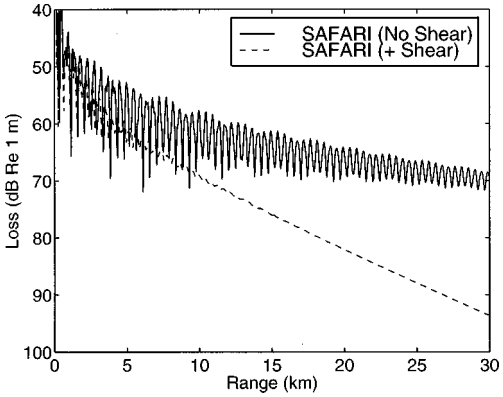

FIG. 6. SAFARI transmission loss versus range comparison for the southern Mediterranean profile. The receiver depth is $z = 50$ m.

TABLE III. Deep-end geoacoustic profile for ASA wedge case.

Depth (m)	Sound speed ($m\,s^{-1}$)	Density ($g\,cm^{-3}$)	Attenuation dB λ^{-1}
0	1500	1.0	0.0
200	1500	1.0	0.0
>200	1700	1.5	0.5

speed, density, and absorption occur along the sloping bottom of the wedge, i.e., the line $z=200-r/20$ m. The apex of the wedge is located at $r=4000$ m. A 25-Hz acoustic point source is located at $r=0, z=100$ m.

The standard practice of approximating a range-dependent waveguide by a sequence of range-independent sections and then marching the outgoing field according to a simple range-updating procedure is known to violate energy conservation principles at the vertical interfaces between sections.[36] Several approximate techniques have been developed for ameliorating this difficulty.[37–41] Since our main purpose here is to validate the NLBCs for this range-dependent example, however, we will use a standard staircase approximation and compare our results with those obtained using a false-absorbing bottom. All PE calculations for this example were computed using $\Delta r=5$ m, $\Delta z=0.5$ m, and $c_0=1500\,m\,s^{-1}$.

For the full-field results shown in Fig. 7, the PE computational grid spanned the domain $0<z<250$ m and the NLBC was applied along $z=250$ m. The transmission-loss levels vary from 40 dB (red) to 90 dB (blue). There is no evidence of any sound reflecting from the edge of the computational domain. If the NLBC is replaced with an absorbing layer, the computational grid needs to be extended to a depth of $z=1000$ m to adequately suppress reflections. Transmission losses versus range are compared in Fig. 8 for a receiver at a depth of 30 m. Except at short ranges, the PE+NLBC solution is observed to agree well with the other PE solution which incorporates an absorbing layer in the region $500<z<1000$ m. Corresponding results for a receiver at a depth of 150 m are shown in Fig. 9. Except for the slight differences near the field null at $r\approx3$ km, the curves are in excellent agreement. For this case, the PE+NLBC calculations required only one-quarter of the depth grid of the PE with the absorbing bottom for an equivalent level of accuracy, while the execution time was faster by a factor of 3.9.

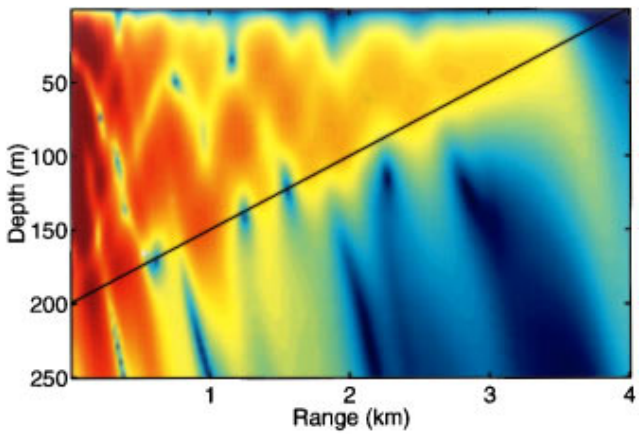

FIG. 7. PE transmission losses for the ASA wedge profile. The NLBC is applied along $z=250$ m.

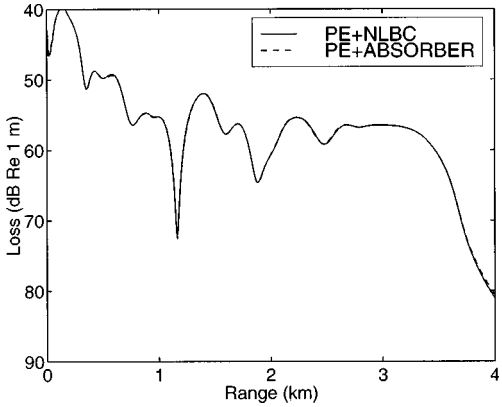

FIG. 8. Transmission loss versus range comparison for the ASA wedge profile. The receiver depth is $z=30$ m.

For this example, the NLBC can also be combined with Collins' rotated PE[37] to yield ''two-way'' accuracy for the outgoing component of the field by aligning the computational grid with the sloping bottom of the wedge. In rotated coordinates, continuity of pressure and vertical-particle velocity are satisfied naturally along the sea-bottom interface, just as in a range-independent problem. Although the sea surface must now be represented by a staircase boundary, the vanishing of the field on the horizontal steps, in the limit of small vertical steps, is sufficient to approximate the pressure-release boundary condition everywhere. As has been shown elsewhere,[42] by appending a low-impedance air-layer backing to the surface of the wedge, the calculations for the rotated PE may be made to proceed in exactly the same way as for the unrotated PE. In this way, reflection from an external pressure-release boundary is replaced with reflection from an internal fluid/fluid boundary across which the usual boundary conditions apply. The underwater reflection coefficient associated with the water/air boundary should be close to -1.

If we rotate and translate the (r',z') coordinate system about the source position $r=0, z=z_s$, it is convenient to regard r' and z as the independent variables, so that r and z' are determined by

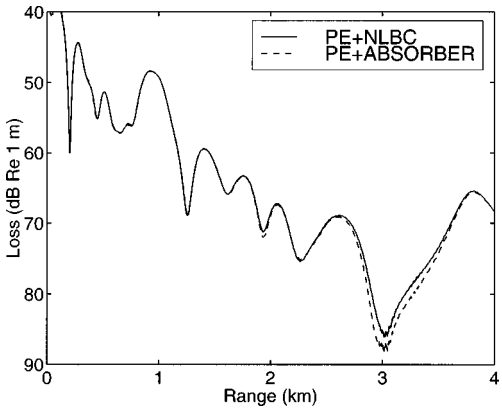

FIG. 9. Transmission loss versus range comparison for the ASA wedge profile. The receiver depth is $z=150$ m.

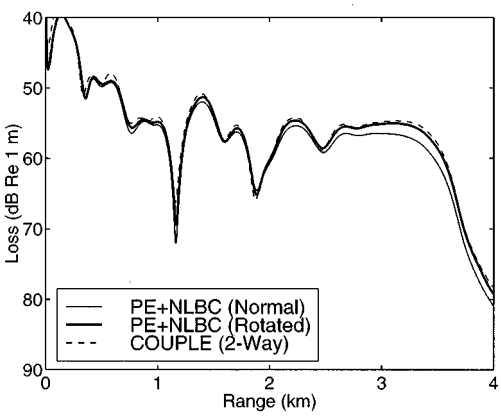

FIG. 10. Transmission loss versus range comparisons for the ASA wedge profile. The receiver depth is $z=30$ m.

$$r+r_0=\frac{r'+z\sin\theta}{\cos\theta},$$
$$z'=(r+r_0)\sin\theta+z\cos\theta. \tag{24}$$

Here, $\theta=\arctan(0.05)\approx 2.86$ deg is the wedge angle and $r_0=z_s\tan\theta=5$ m is the offset along the r-axis. The (r,z')-pairs corresponding to a receiver along $z=30$ m are determined from Eq. (24). The transmission loss versus range curves for the rotated PE with a nonlocal boundary condition (obtained using an air layer with density $\rho_a=0.0012\,\mathrm{g\,cm^{-3}}$, sound speed $c_a=300\,\mathrm{m\,s^{-1}}$, and absorption $\alpha_a=0.5$ dB/λ) and the unrotated (normal) PE with a nonlocal boundary condition are compared in Fig. 10 to reference values generated by COUPLE.[29] It is evident that the rotated PE+NLBC solution does not exhibit the cumulative loss of energy that is evident in the normal PE calculation.

III. CONCLUSIONS

In this paper, we have analyzed an approach to deriving nonlocal boundary conditions (NLBCs) that transforms the semi-infinite PE problem with a radiation condition at infinity into an equivalent PE problem in a bounded domain. In contrast to spectral-based NLBC methods, which require the evaluation of an integral transform from wave number space to physical space, the present algorithm is carried out entirely in the physical domain. It is, however, specific to finite-difference PE solvers as it depends on the series expansion of a vertical wave number operator for the downgoing radiation field in $z>z_b$. By invoking an impedance-continuity condition, we extended this NLBC to a boundary layer at $z=z_b-0$ that separates a uniform half space from the waveguide in $0<z<z_b$ to account for the reflection/transmission process along this (possibly discontinuous) interface. In addition to the standard PE, we similarly derived the NLBC that is appropriate for the Claerbout approximation. Several numerical examples were presented to demonstrate the effectiveness of the NLBC in reducing the computational domain and dispensing with the need for an *ad hoc* absorbing layer. In addition, the equivalent fluid approximation of Zhang and Tindle[33] was shown to be easily incorporated into the NLBC formulation. We conclude that this new nonlocal boundary condition method is an accurate and useful procedure for analyzing paraxial or near-paraxial acoustic-field propagation problems that can be described in the context of single-term approximations to the exact PE propagator.

ACKNOWLEDGMENTS

Financial support for one of us (D.Y.) was provided through the research and development Contract No. W7708–6–0327 with the Esquimalt Defence Research Detachment, a Division of the Defence Research Establishment Atlantic. The same author would like to acknowledge the continued funding provided by the National Research Council of Canada, the Ontario Center for Materials Research, BNR, and Corning Glass.

[1] F. B. Jensen, W. A. Kuperman, M. B. Porter, and H. Schmidt, *Computational Ocean Acoustics* (AIP, New York, 1994), Chap. 6, pp. 343–412.
[2] V. Shevshenko, ''The expansion of the fields of open waveguides in proper and improper modes,'' Radiophys. Quantum Electron. **14**, 972–977 (1974).
[3] J. Bérenger, ''A perfectly matched layer for the absorption of electromagnetic waves,'' J. Comput. Phys. **114**, 185–200 (1994).
[4] D. Yevick, J. Yu, and Y. Yayon, ''Optimal absorbing boundary conditions,'' J. Opt. Soc. Am. A **12**, 107–110 (1995).
[5] D. Yevick, J. Yu, and F. Schmidt, ''Analytic studies of absorbing and impedance-matched boundary layers,'' IEEE Photonics Technol. Lett. **9**, 73–75 (1997).
[6] F. D. Tappert, ''The parabolic approximation method,'' in *Wave Propagation and Underwater Acoustics*, edited by J. B. Keller and J. S. Papadakis (Springer, New York, 1977), Chap. 5, pp. 224–287.
[7] J. A. Davis, D. White, and R. C. Cavanagh, ''NORDA Parabolic Equation Workshop, 31 March–3 April 1981,'' Tech. Note 143, Naval Ocean Research and Development Activity, NSTL Station, MS, 1982; available from NTIS, No. AD-121 932.
[8] J. S. Papadakis, ''Impedance formulation of the bottom boundary condition for the parabolic equation model in underwater acoustics,'' in J. A. Davis, D. White, and R. C. Cavanagh, ''NORDA Parabolic Equation Workshop, 31 March–3 April 1981,'' Tech. Note 143, Naval Ocean Research and Development Activity, NSTL Station, MS, 1982; available from NTIS, No. AD-121 932, p. 83.
[9] J. S. Papadakis, M. I. Taroudakis, P. J. Papadakis, and B. Mayfield, ''A New method for a realistic treatment of the sea bottom in the parabolic approximation,'' J. Acoust. Soc. Am. **92**, 2030–2038 (1992).
[10] D. J. Thomson and M. E. Mayfield, ''An exact radiation condition for use with the *a posteriori* PE method,'' J. Comput. Acoust. **2**, 113–132 (1994).
[11] V. A. Dougalis and N. A. Kampanis, ''Finite element methods for the parabolic equation with interfaces,'' J. Comput. Acoust. **4**, 55–88 (1996).
[12] J. S. Papadakis, ''Exact, nonreflecting boundary conditions for parabolic-type approximations in underwater acoustics,'' J. Comput. Acoust. **2**, 83–98 (1994).
[13] J. F. Claerbout, ''Coarse grid calculations of waves in inhomogeneous media with application to delineation of complicated seismic structure,'' Geophysics **35**, 407–418 (1970).
[14] S. W. Marcus, ''A generalized impedance method for application of the parabolic approximation to underwater acoustics,'' J. Acoust. Soc. Am. **90**, 391–398 (1991).
[15] T. W. Dawson, D. J. Thomson, and G. H. Brooke, ''Non-local boundary conditions for acoustic PE predictions involving inhomogeneous layers,'' in *3rd European Conference on Underwater Acoustics, Vol. 1*, edited by J. S. Papadakis (Crete University Press, Heraklion, 1996), pp. 183–188.
[16] M. E. Mayfield and D. J. Thomson, ''An FFT-based non-local boundary condition for the parabolic equation,'' in *3rd European Conference on Underwater Acoustics, Vol. 1*, edited by J. S. Papadakis (Crete University Press, Heraklion, 1996), pp. 237–242.
[17] V. A. Baskakov and A. V. Popov, ''Implementation of transparent boundaries for numerical solution of the Schrodinger equation,'' Wave Motion **14**, 121–128 (1991).
[18] A. V. Popov, ''Accurate modeling of transparent boundaries in quasi-optics,'' Radio Sci. **31**, 1781–1790 (1996).
[19] S. W. Marcus, ''A hybrid (finite-difference–surface Green's function)

method for computing transmission losses in an inhomogeneous atmosphere over irregular terrain,'' IEEE Trans. Antennas Propag. **40**, 1451–1458 (1992).
[20] M. F. Levy, ''Horizontal parabolic equation solution of radiowave propagation problems on large domains,'' IEEE Trans. Antennas Propag. **43**, 137–144 (1995).
[21] M. F. Levy, ''Transparent boundary conditions for parabolic equation solutions of radiowave propagation problems,'' IEEE Trans. Antennas Propag. **45**, 66–72 (1997).
[22] M. E. Mayfield and D. J. Thomson, ''A non-reflecting boundary condition for use in PE calculations of sound propagation in air,'' J. Acoust. Soc. Am. **92**, 2406 (1992).
[23] R. J. Jardine, W. L. Siegmann, and J. S. Robertson, ''Alternative nonreflecting boundary conditions for PE modeling of atmospheric acoustic propagation,'' in *Environmental Acoustics, Vol. 2*, edited by D. Lee and M. H. Schultz (World Scientific, Singapore, 1994), pp. 849–868.
[24] F. Schmidt and P. Deuflhard, ''Discrete transparent boundary condition for the numerical solution of Fresnel's equation,'' Comput. Math. Appl. **29**, 53–76 (1995).
[25] F. Schmidt and D. Yevick, ''Analysis of boundary conditions for the Fresnel equation,'' J. Comput. Phys. **134**, 96–107 (1997).
[26] M. D. Collins, ''Benchmark calculations for higher-order parabolic equations,'' J. Acoust. Soc. Am. **87**, 1535–1538 (1990).
[27] M. D. Collins, ''A split-step Padé solution for the parabolic equation method,'' J. Acoust. Soc. Am. **93**, 1736–1742 (1993).
[28] H. Schmidt, ''SAFARI Seismo-Acoustic Fast field Algorithm for Range-Independent environments,'' SACLANT Undersea Research Centre, San Bartolomeo, Italy, Rep. SR-113, 1988.
[29] R. B. Evans, ''A coupled mode solution for acoustic propagation in a waveguide with a stepwise depth variations of a penetrable bottom,'' J. Acoust. Soc. Am. **74**, 188–195 (1983).
[30] D. Lee and S. T. McDaniel, ''Ocean acoustic propagation by finite-difference methods,'' Comput. Math. Appl. **14**, 305–423 (1987).
[31] D. Yevick and D. J. Thomson, ''A hybrid split-step/finite-difference PE algorithm for variable-density media,'' J. Acoust. Soc. Am. **101**, 1328–1335 (1997).
[32] H. P. Bucker, ''An equivalent bottom for use with the split-step algorithm,'' J. Acoust. Soc. Am. **73**, 486–491 (1983).
[33] Z. Y. Zhang and C. T. Tindle, ''Improved equivalent fluid approximations for a low shear speed ocean bottom,'' J. Acoust. Soc. Am. **98**, 3391–3396 (1995).
[34] F. B. Jensen and C. M. Ferla, ''Numerical solutions of range-dependent benchmark problems in ocean acoustics,'' J. Acoust. Soc. Am. **87**, 1499–1510 (1990).
[35] D. J. Thomson, ''Wide-angle parabolic equation solutions to two range-dependent benchmark problems,'' J. Acoust. Soc. Am. **87**, 1514–1520 (1990).
[36] M. B. Porter, F. B. Jensen, and C. M. Ferla, ''The problem of energy conservation in one-way models,'' J. Acoust. Soc. Am. **89**, 1058–1067 (1991).
[37] M. D. Collins, ''The rotated parabolic equation and sloping ocean bottoms,'' J. Acoust. Soc. Am. **87**, 1035–1037 (1990).
[38] M. D. Collins and E. K. Westwood, ''A higher-order energy-conserving parabolic equation for range-dependent ocean depth, sound speed, and density,'' J. Acoust. Soc. Am. **89**, 1068–1075 (1991).
[39] M. D. Collins and R. B. Evans, ''A two-way parabolic equation for acoustic backscattering in the ocean,'' J. Acoust. Soc. Am. **91**, 1357–1368 (1992).
[40] D. Lee and W. L. Siegmann, ''Finite difference treatment of irregular interfaces: an error analysis,'' J. Comput. Acoust. **3**, 1–14 (1995).
[41] G. H. Brooke, D. J. Thomson, and P. M. Wort, ''A sloping-boundary condition for efficient PE calculations in range-dependent acoustic media,'' J. Comput. Acoust. **4**, 11–27 (1996).
[42] D. J. Thomson, G. H. Brooke, and E. S. Holmes, ''PE approximations for scattering from a rough surface,'' Defence Research Establishment Pacific, Victoria, B.C., Technical Memorandum 95–21, 1995.

Parameter uncertainty analysis on acoustic response in fluid filled poroelastic media

Yongke Mu and Mohsen Badiey
Ocean Acoustics Laboratory, Graduate College of Marine Studies, University of Delaware, Newark, Delaware 19716

Alexander H.-D. Cheng
Department of Civil and Environmental Engineering, University of Delaware, Newark, Delaware 19716

(Received 3 August 1998; revised 31 March 1999; accepted 12 April 1999)

This paper examines the effect of input parameter uncertainty in the prediction of acoustic response in ocean sediment. Due to the relatively large number of physical parameters in the model, and the difficulty of their direct measurement in the ocean environment, uncertainty in the predicted acoustic response is expected. Utilizing a second order Taylor series expansion, this paper demonstrates a methodology for estimating the output uncertainty in terms of statistical moments from the input uncertainty. The methodology is then tied to a practical procedure that uses engineering measurements and empirical relations to determine parameters such as shear modulus, bulk modulus, and permeability, from porosity. A related issue of pore size distribution and its effect on acoustic response is also investigated.
[S0001-4966(99)04207-1]

PACS numbers: 43.30.Bp [SAC-B]

INTRODUCTION

The problem of acoustic waves propagating in the ocean over a porous seabed is of interest in many ocean related applications. While the acoustic model for the ocean is simple, that for the sediment can be complex. Depending on the need of accuracy, the sediment has been modeled as a fluid, an elastic solid, or a viscoelastic solid. More properly, however, sediment should be modeled as fluid infiltrated porous medium as it is composed of granular solids forming a porous skeleton that is submerged under water.

Modeling the seabed as a poroelastic material using Biot's theory[1,2] was pioneered by Stoll.[3] Although the poroelasticity theory provides a more correct account of acoustic wave propagation in sediments, its application requires the knowledge of additional physical parameters—a minimum of 13 physical parameters are needed. In the ocean environment it is difficult to conduct comprehensive testing to obtain all the needed parameters. To overcome the difficulty, we have presented a practical procedure that needed the measurement of only a few engineering properties,[4] such as those obtained by the standard geotechnical method of pile penetration tests and density logging. Assisted with empirical relations, the complete set of Biot model parameters can be inferred.

Due to practical constraints, the input parameters needed in the Biot model, as well as any other models, cannot be accurately determined. There exists a number of sources for the uncertainty:

- The laboratory and field techniques of direct measurement have limited accuracy.
- Porous sediment is a random material. A homogenized constant material property is only an approximation, hence the predicted response is an approximation that contains uncertainty.
- Due to the cost of offshore and shipboard operation, generally few samples of sea bottom can be taken in a large region.
- The empirical relations employed to determine one parameter from the other are usually obtained from fitting data that have considerable scattering.
- The Biot model contains certain conceptual parts that require microscopic geometric factors that cannot be easily identified.

Based on the above considerations, it is likely that the predicted acoustic responses will contain uncertainties that are too large to be overlooked. Proper guidelines must be given concerning the confidence level of the predicted output.

The purpose of this paper is to develop the stochastic techniques that can quantify the output uncertainty, given the input uncertainty from various sources. To provide compact information, statistical moments are typically used. Provided with the mean, variance, and covariance of the input parameters, the output is predicted in the same statistical moments.

The methodology employed is the second order perturbation which is relatively easy to use and provides good accuracy. The inclusion of the second order terms demonstrates that the mean of the output response depends not only on the mean of the input parameters, but also on their standard deviations. In other words, the common deterministic practice of using only mean parameters as input does not yield the correct mean output response.

This stochastic analysis tool is applied to investigate the uncertainty involved in determining the three complex wave velocities, V_{P1}, V_{P2}, and V_S, of the Biot's poroelastic wave model. First, a single-parameter analysis based on the uncertainty of shear modulus is performed. Next, a practical engineering procedure that utilizes empirical relations to determine parameters such as shear modulus, bulk modulus, and

permeability, from porosity, is examined. As an extension, a related issue of pore size distribution and its effect on acoustic response is also investigated.

I. BIOT'S POROELASTIC ACOUSTIC WAVE SPEEDS

The derivation of Biot–Stoll sound speed can be found in a number of places.[1,2,5,6] Here only the final result is presented for later reference. The fast (V_{P1}) and slow (V_{P2}) compressional wave velocities, and the shear wave velocity (V_S) are expressed in the following forms:[7]

$$\begin{pmatrix} V_{P1} \\ V_{P2} \end{pmatrix} = \left[\frac{2(HM-C^2)}{B \mp A^{1/2}} \right]^{1/2}, \tag{1}$$

$$V_S = \left(\frac{Gm'}{\rho m' - \rho_f^2} \right)^{1/2}, \tag{2}$$

where

$$\rho = (1-\phi)\rho_s + \phi\rho_f \tag{3}$$

is the bulk density, with ρ_f the fluid density, ρ_s the solid grain density, and ϕ the porosity. The material coefficients are:

$$A = (m'H - \rho M)^2 + 4(\rho_f H - \rho C)(\rho_f M - m'C), \tag{4}$$

$$B = \rho M + m'H - 2\rho_f C, \tag{5}$$

$$H = \frac{(K_s - K)^2}{D-K} + K + \frac{4}{3}G, \tag{6}$$

$$M = \frac{K_s^2}{D-K}, \tag{7}$$

$$C = \frac{K_s(K_s-K)}{D-K}, \tag{8}$$

$$D = K_s\left[1 + \phi\left(\frac{K_s}{K_f} - 1 \right) \right]. \tag{9}$$

We note that K is the bulk modulus of the porous frame, G is the shear modulus of the frame, K_f is the bulk modulus of the pore water, and K_s is the bulk modulus of the solid grains.

The intergranular Coulomb friction is modeled by introducing the complex moduli G and K as:

$$G = G_0(1 + i\delta'), \tag{10}$$

$$K = K_0(1 + i\delta''), \tag{11}$$

where $i = \sqrt{-1}$, G_0, and K_0 are, respectively, shear and bulk moduli of the frame, and δ' and δ'' are, respectively, specific losses associated with shear and volumetric deformation of the frame. In Eqs. (1), (2), (4), and (5), m' is given by

$$m' = (1+c)\frac{\rho_f}{\phi} - i\frac{\mu_f F(\kappa)}{k\omega}, \tag{12}$$

in which c is the added mass coefficient, μ_f is fluid dynamic viscosity, k is the intrinsic permeability (with dimension of length square), and ω is the angular frequency. We also note that $F(\kappa)$ is a viscosity correction factor. It is related to the ease of fluid passing through the porous medium. For circular tubes model, it takes the form[2]

$$F(\kappa) = \kappa T/4\left[1 + 2i\frac{T}{\kappa} \right], \tag{13}$$

in which

$$T = \frac{\mathrm{ber}'(\kappa) + i\,\mathrm{bei}'(\kappa)}{\mathrm{ber}(\kappa) + i\,\mathrm{bei}(\kappa)}, \tag{14}$$

where ber and bei are, respectively, the real and imaginary part of the Kelvin function of the first kind of order zero, and ber′ and bei′ are their derivatives.[8] The argument κ is defined as

$$\kappa = a\sqrt{\frac{\omega\rho_f}{\mu_f}}, \tag{15}$$

where a is a pore size factor and

$$a = \eta\sqrt{\frac{k}{\phi}} \tag{16}$$

with $\eta = 3.2$, based on a combination of hydraulic radius theory and laboratory observation.[4] In a random medium, the viscosity correction factor can be modified according to the grain or pore size distributions.[9,10]

II. STATISTICAL MOMENT ANALYSIS

In this section we first review and then extend a powerful statistical moment analysis that uses an approximation based on Taylor's series expansion. This technique has been successfully applied in several occasions.[11–13]

Let $f(\boldsymbol{\zeta})$ be a random response function whose randomness is a consequence of a number of random variables expressed in a vector form $\boldsymbol{\zeta} = (\zeta_1, \zeta_2, \ldots, \zeta_n)$. The mean value (expectation) of the random vector $\boldsymbol{\zeta}$ is $\overline{\boldsymbol{\zeta}} = (\overline{\zeta_1}, \overline{\zeta_2}, \ldots, \overline{\zeta})$, and the perturbation from the mean is $\boldsymbol{\zeta}' = \boldsymbol{\zeta} - \overline{\boldsymbol{\zeta}}$. The random function $f(\boldsymbol{\zeta})$ can be expanded around $\overline{\boldsymbol{\zeta}}$ based on Taylor's series

$$f(\boldsymbol{\zeta}) = f(\overline{\boldsymbol{\zeta}}) + \sum_{i=1}^{n} \frac{\partial f(\overline{\boldsymbol{\zeta}})}{\partial \overline{\zeta_i}} \zeta_i' + \frac{1}{2}\sum_{i=1}^{n}\sum_{j=1}^{n} \frac{\partial^2 f(\overline{\boldsymbol{\zeta}})}{\partial \overline{\zeta_i}\partial \overline{\zeta_j}} \zeta_i' \zeta_j' + O(\zeta')^3. \tag{17}$$

In a typical perturbation analysis, the series is truncated at the second order terms $O(\zeta')^2$. Here the second order terms are retained and the third order terms $O(\zeta')^3$ are truncated. The accuracy of the truncated series is dependent on the smallness of the perturbation quantities. However, past experiences[13–15] based on Monte Carlo and other analysis have shown that relatively large deviations from the mean can be tolerated.

Taking the mean from the above equation, we have

$$\overline{f(\boldsymbol{\zeta})} \approx f(\overline{\boldsymbol{\zeta}}) + \frac{1}{2}\sum_{i=1}^{n}\sum_{j=1}^{n} \frac{\partial^2 f(\overline{\boldsymbol{\zeta}})}{\partial \overline{\zeta_i}\partial \overline{\zeta_j}} \sigma_{\zeta_i\zeta_j}, \tag{18}$$

where $\sigma_{\zeta_i\zeta_j}$ is the covariance between the variables ζ_i and ζ_j. The covariance becomes the variance $\sigma_{\zeta_i}^2$ when $i = j$.

Equations (18) shows that the mean values of a function is not equal to the function evaluated at the mean parameter values [i.e., $\overline{f(\boldsymbol{\zeta})} \neq f(\overline{\boldsymbol{\zeta}})$], unless the functional relation of f with respect to $\boldsymbol{\zeta}$ is linear. This is a consequence of the second order terms in Eq. (17).

From Eqs. (17) and (18), the perturbation of function $f(\boldsymbol{\zeta})$ can be expressed as

$$f'(\boldsymbol{\zeta}) = f(\boldsymbol{\zeta}) - \overline{f(\boldsymbol{\zeta})} \approx \sum_{i=1}^{n} \frac{\partial f(\overline{\boldsymbol{\zeta}})}{\partial \overline{\zeta_i}} \zeta_i' \,. \tag{19}$$

The variance of the function is then obtained by taking the mean of the self-product of Eq. (19)

$$\sigma_f^2 \approx \sum_{i=1}^{n} \sum_{j=1}^{n} \frac{\partial f(\overline{\boldsymbol{\zeta}})}{\partial \overline{\zeta_i}} \frac{\partial f(\overline{\boldsymbol{\zeta}})}{\partial \overline{\zeta_j}} \sigma_{\zeta_i \zeta_j}. \tag{20}$$

Similarly, for any two functions $f(\boldsymbol{\zeta})$ and $g(\boldsymbol{\xi})$, their covariance may be written as

$$\sigma_{fg} \approx \sum_{i=1}^{n} \sum_{j=1}^{n} \frac{\partial f(\overline{\boldsymbol{\zeta}})}{\partial \overline{\zeta_i}} \frac{\partial g(\overline{\boldsymbol{\xi}})}{\partial \overline{\xi_j}} \sigma_{\zeta_i \xi_j}. \tag{21}$$

Equations (18), (20), and (21) are the basic formulas that allow us to approximate the first and the second moment of the response function in terms of the first two moments of the random variables.

The above concept can be illustrated by a simple example. Consider an elastic seabed with its shear wave velocity given by

$$V_S = \sqrt{\frac{G}{\rho}}. \tag{22}$$

Here G and ρ are assumed to be random variables. In a deterministic analysis, the mean parameter values are used in Eq. (22) to calculate the shear wave velocity as

$$\tilde{V}_S = \sqrt{\frac{\overline{G}}{\overline{\rho}}}. \tag{23}$$

The stochastic analysis based on Eqs. (18) and (20), however, produces the following results:

$$\overline{V}_S \approx \tilde{V}_S \left(1 - \frac{1}{8} \frac{\sigma_G^2}{\overline{G}^2} + \frac{3}{8} \frac{\rho_\rho^2}{\overline{\rho}^2} - \frac{1}{8} \frac{\rho_{\rho G}}{\overline{\rho}\,\overline{G}} \right), \tag{24}$$

$$\sigma_{V_S}^2 \approx \frac{1}{4} \tilde{V}_S^2 \left(\frac{\sigma_G^2}{\overline{G}^2} + \frac{\sigma_\rho^2}{\overline{\rho}^2} - 2 \frac{\sigma_{\rho G}}{\overline{\rho}\,\overline{G}} \right). \tag{25}$$

Equation (24) shows that the mean shear wave velocity contains some correction terms as compared with the deterministic formula Eq. (23). Equation (25) reveals that the normalized variance $\sigma_{V_S}^2 / \tilde{V}_S^2$ is one-quarter of the sum of the normalized variances of shear modulus and density, less than twice the normalized covariance. Hence, the existence of correlation between the density and the shear modulus reduces the uncertainty in predicting the shear wave velocity.

Assume that the shear modulus is measured using a laboratory or a field technique, and is estimated to have a mean of $\overline{G} = 5 \times 10^7$ Pa and a standard deviation of $\sigma_G = 5 \times 10^6$ Pa (10% of $\overline{G}$). The density is measured to be $\overline{\rho} = 1900\,\mathrm{kg/m^3}$ with a standard deviation $\sigma_\rho = 95\,\mathrm{kg/m^3}$ (5% of $\overline{\rho}$). Since it is difficult to estimate the covariance $\sigma_{\rho G}$; it is assumed to be zero. The mean and standard deviation can be calculated from Eqs. (24) and (25) as $\overline{V}_S = 162$ m/s and $\sigma_{V_S} = 9.1$ m/s. We can then predict within a 95% confidence level that the shear wave velocity is in the range $V_S = 162 \pm 18.1$ m/s (plus/minus two standard deviations). It is noted that in this case the discrepancy between $\overline{V}_S$ and $\tilde{V}_S$ is negligibly small.

In a different scenario, we consider the case that only a density log is available and the shear modulus is to be determined from an empirical relation. We assume that the water density $\rho_f = 1025\,\mathrm{kg/m^3}$ and the solid grain density $\rho_s = 2650\,\mathrm{kg/m^3}$ have been precisely determined. The porosity can be evaluated from Eq. (3) as

$$\phi = \frac{\rho_s - \rho}{\rho_s - \rho_f}. \tag{26}$$

The statistics of ϕ can be found from Eqs. (18), (20), and (26):

$$\overline{\phi} = \frac{\rho_s - \overline{\rho}}{\rho_s - \rho_f}, \tag{27}$$

$$\sigma_\phi^2 = \overline{\phi}^2 \left(\frac{\overline{\rho}}{\rho_s - \overline{\rho}} \right)^2 \frac{\sigma_\rho^2}{\overline{\rho}^2}. \tag{28}$$

Sediment shear modulus is related to many factors, such as porosity, confining pressure, stress history, etc. Under certain conditions, the following simple relation is found from curve fitting of field data (see Sec. III B below for more discussion):

$$G = \beta z^{1/2} \frac{(1-\phi)^{\alpha_2 + 0.5}}{\phi^{\alpha_2}}. \tag{29}$$

In the above, z is the depth of the sediment sample in meter, G is shear modulus in Pa, and α_2 and β are empirical constants. A least square fit of filed data[4] gives $\overline{\alpha}_2 = 1.6$ and $\overline{\beta} = 2.5 \times 10^7$. There exist a considerable scattering of data and a coefficient of variation of 30%, i.e., $\sigma_\beta / \overline{\beta} = 0.3$, is assessed for β. Using Eq. (29) in Eqs. (18) and (20) we can find

$$\overline{G} \approx \tilde{G} \left\{ 1 + \left[\overline{\alpha}_2 (\overline{\alpha}_2 + 1) + 2 \overline{\alpha}_2 \left(\overline{\alpha}_2 + \frac{1}{2} \right) \frac{\overline{\phi}}{1 - \overline{\phi}} + \left(\overline{\alpha}_2^2 - \frac{1}{4} \right) \left(\frac{\overline{\phi}}{1 - \overline{\phi}} \right)^2 \right] \frac{\sigma_\phi^2}{\overline{\phi}^2} \right\}, \tag{30}$$

$$\sigma_G^2 \approx \tilde{G}^2 \left[\frac{\sigma_\beta^2}{\overline{\beta}^2} + \left(\overline{\alpha}_2 + \left(\overline{\alpha}_2 + \frac{1}{2} \right) \frac{\overline{\phi}}{1 - \overline{\phi}} \right)^2 \frac{\sigma_\phi^2}{\overline{\phi}^2} \right]. \tag{31}$$

In the above we used the notation

$$\tilde{G} = \overline{\beta} z^{1/2} \frac{(1 - \overline{\phi})^{\overline{\alpha}_2 + 0.5}}{\overline{\phi}^{\overline{\alpha}_2}} \tag{32}$$

and assumed $\sigma_{\phi\beta}=0$.

For the last terms in Eqs. (24) and (25), we need the following covariances that can be obtained from Eq. (21),

$$\sigma_{\rho G}\approx -\overline{\rho}\widetilde{G}\left[\overline{\alpha}_2+(\overline{\alpha}_2+0.5)\frac{\overline{\phi}}{1-\overline{\phi}}\right]\frac{\sigma_{\rho\phi}}{\overline{\rho}\,\overline{\phi}}, \tag{33}$$

$$\sigma_{\rho\phi}=\overline{\rho}\,\overline{\phi}\frac{\overline{\rho}}{\rho_s-\rho}\frac{\sigma_\rho^2}{\overline{\rho}^2}. \tag{34}$$

With the substitution of Eqs. (30)–(34) into Eqs. (24) and (25), we find that $\overline{V}_S$ and $\sigma_{V_S}^2$ are functions of the given statistical moments $\overline{\rho}$, $\overline{\alpha}_2$, $\overline{\beta}$, σ_ρ^2, and σ_β^2 only.

Using the same solid and fluid density as the previous case, and the sediment density $\overline{\rho}=1900$ kg/m, with $\sigma_\rho/\overline{\rho}=0.05$, and the aforementioned $\overline{\alpha}_2$, $\overline{\beta}$, and σ_β^2 values, we obtain $\overline{\phi}=0.462$ and $\sigma_\phi/\overline{\phi}=0.127$. Assuming a sediment depth of 5 m, we evaluate $\overline{G}=5.79\times10^7$ Pa (cf. $\widetilde{G}=5.28\times10^7$ Pa), $\sigma_G/\overline{G}=0.48$, and $\sigma_{\rho G}/\overline{\rho}\,\overline{G}=0.02$. Finally, we find $\overline{V}_S=167$ m/s (cf. $\widetilde{V}_S=174$ m/s), and $\sigma_{V_S}=38.2$ m/s. Using a range $V_S=167\pm38.2$ m/s (plus/minus one standard deviation), the shear wave velocity has only a 68% confidence level to fall within that range.

III. POROELASTIC UNCERTAINTY ANALYSES

In this section, the statistical moment technique developed in the preceding section is applied to the poroelastic sediment model.

A. Shear modulus effect

First, the statistical structure of a data set taken from the Atlantic Generating Station (AGS) site is analyzed. The AGS site is located on the New Jersey Continental Shelf. As a possible nuclear power plant site, it was extensively surveyed in the early 1970s.[16,17] Its geological data set is perhaps one of the most detailed on the Inner Atlantic Shelf. We have processed 24 core data which provided an excellent insight into the random layering nature of the shallow water sediment.[18,19]

Figure 1 shows the shear modulus profile versus sediment depth for the 24 cores (left diagram), with shear modulus plotted in logarithmic scale. Past experience has shown that the shear modulus is log-normally distributed.[9,19] We hence define a new variable $g=\log_{10}G$ and express the statistical moments by the ensemble average at fixed depths

$$\overline{g(z)}=\overline{\log_{10}G(z)}=\frac{1}{n}\sum_{i=1}^{n}\log_{10}G_i(z), \tag{35}$$

$$\sigma_g^2=\frac{1}{n-1}\sum_{i=1}^{n}[\log_{10}G_i(z)-\overline{\log_{10}G(z)}]^2, \tag{36}$$

where the subscript i refers to the core number and n is the total number of core data at the given depth. The mean shear modulus profile and the $\pm\sigma_g$ envelopes are presented as the right diagram in Fig. 1. We observe that both the mean and the standard deviation are nonstationary, i.e., depth dependent. Hence the statistical analysis performed below is referred to at a given depth.

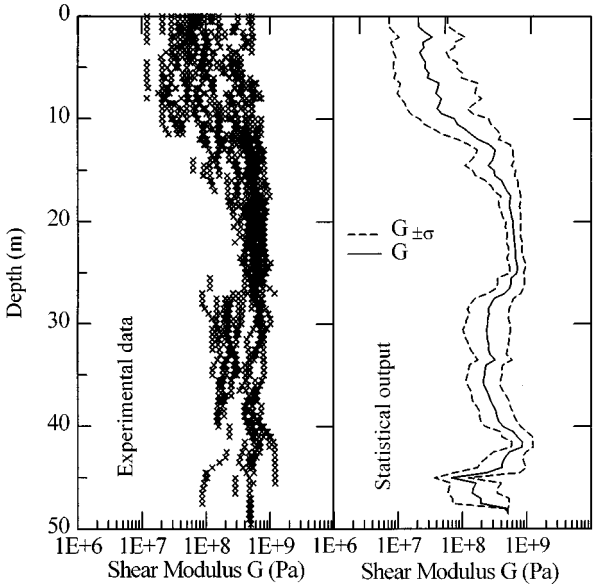

FIG. 1. Shear modulus versus depth of 24 AGS cores (left diagram), and mean shear modulus ± one standard deviation (right diagram).

As a first step of the analysis, we assume that only the shear modulus is a random variable, and hold all other variables deterministic. Using the statistical moments of $g=\log_{10}G$ instead of G in the analysis, the statistical moments of the compressional and shear velocities are found as follows:

$$\overline{V}_{P1,P2}\approx V_{P1,P2}(\overline{H})+\frac{1}{2}\frac{\partial^2V_{P1,P2}(\overline{H})}{\partial\overline{H}^2}\sigma_H^2, \tag{37}$$

$$\overline{V}_S\approx V_S(\overline{G})+\frac{1}{2}\frac{\partial^2V_S(\overline{G})}{\partial\overline{G}^2}\sigma_G^2, \tag{38}$$

$$\sigma_{V_{P1,P2}}^2\approx\left(\frac{\partial V_{P1,P2}(\overline{H})}{\partial\overline{H}}\right)^2\sigma_H^2, \tag{39}$$

$$\sigma_{V_S}^2\approx\left(\frac{\partial V_S(\overline{G})}{\partial\overline{G}}\right)^2\sigma_G^2, \tag{40}$$

where

$$\frac{\partial V_{P1,P2}}{\partial H}=\frac{1}{V_{P1,P2}}\left[\frac{M}{B\mp A}-\frac{(HM-C^2)(m'A\mp Y)}{(B\mp A)^2A}\right], \tag{41}$$

$$\frac{\partial^2V_{P1,P2}}{\partial H^2}=-\frac{1}{V_{P1,P2}}\frac{\partial V_{P1,P2}}{\partial\overline{H}}\left[\frac{M}{B\mp A}-\frac{(HM-C^2)(m'A\mp Y)}{(B\mp A)^2A}\right]+\frac{(HM-C^2)}{V_{P1,P2}}\times[-2m'^2A^3\pm4m'A^2Y\mp m'A^2-2AY^2\pm(B\mp A)Y^2], \tag{42}$$

TABLE I. Physical properties of a hard sediment (Ref. 5).

Parameter	Symbol	Unit	Value
Grain density	ρ_s	kg/m^3	2650
Fluid density	ρ_f	kg/m^3	1000
Grain bulk modulus	K_s	Pa	3.6×10^{10}
Fluid bulk modulus	K_f	Pa	2.25×10^{9}
Frame bulk modulus	K_o	Pa	4.36×10^{7}
Frame shear modulus	G_o	Pa	2.61×10^{7}
Fluid viscosity	μ_f	kg/m·s	1.0×10^{-3}
Permeability	k	m^2	1.0×10^{-10}
Porosity	ϕ	—	0.47
Degree of saturation	S	—	1.0
Shear specific loss	δ'	—	0.01
Volumetric specific loss	δ''	—	0.0075
Added mass coefficient	c	—	0.25

$$\frac{\partial V_S}{\partial G}=\frac{1}{2}\left[\frac{m'}{G(\rho m'-\rho_f^2)}\right]^{1/2}, \tag{43}$$

$$\frac{\partial^2 V_S}{\partial G^2}=-\frac{1}{4}\left[\frac{m'}{G^3(\rho m'-\rho_f^2)}\right]^{1/2}, \tag{44}$$

and

$$Y=(m'H-\rho M)m'+2\rho_f(\rho_f M-m'C). \tag{45}$$

We note that all statistical moments must be expressed in terms of $\overline{g}$ and σ_g^2, hence we introduce

$$\overline{H}=H(\overline{G}), \tag{46}$$

$$\sigma_H^2\approx\tfrac{16}{9}\sigma_G^2, \tag{47}$$

$$\overline{G}\approx10^{\overline{g}}[1+(\ln 10)^2\sigma_g^2], \tag{48}$$

$$\sigma_G^2\approx[10^{\overline{g}}\ln 10]^2\sigma_g^2. \tag{49}$$

To obtain quantitative result, we shall use a data set referred to as the hard sediment case,[5] as shown in Table I. To fix ideas, we first plot the real and imaginary parts of wave velocities assuming that all data are deterministic as Fig. 2 for comparison purpose.

In the stochastic analysis, we assume that all parameters are exact except for shear modulus, which has a mean of $\overline{g}=\log_{10}(2.61\times10^7)=7.42$ and a standard deviation of $\sigma_g=0.25$. Equations (37)–(49) are used to calculate the statistical moments of the poroelastic wave velocities. First we examine the mean velocities. Figures 3 and 4 show the real and imaginary parts of the mean shear velocity $\overline{V}_S$ as functions of frequency. We plot the deterministic case ($\sigma_g=0$) in dashed lines and the stochastic case with $\sigma_g=0.25$ in solid lines. These results (Figs. 3 and 4) clearly show that the uncertainty in the input shear modulus has an effect on the output prediction of mean shear velocity. On the other hand, for the mean compressional wave velocities, $\overline{V}_{P1}$ and $\overline{V}_{P2}$, the effect has been shown to be negligible,[9] hence it is not presented here.

Given $\sigma_g=0.25$, we present in Fig. 5 the real and imaginary parts of standard deviations $\sigma_{V_{P1}}$, $\sigma_{V_{P2}}$, and σ_{V_S}, as functions of frequency. Comparing with Fig. 2, we observe that most of the curves have the same shape as their mean velocity counterparts. In Fig. 6 we present the coefficients of

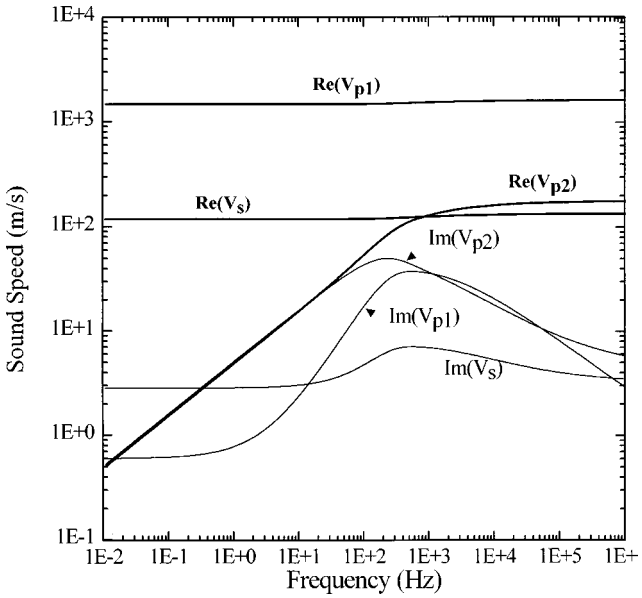

FIG. 2. Real and imaginary parts of deterministic compressional (V_{P1}, V_{P2}) and shear (V_S) velocities versus frequency for the hard sediment case.

variation, namely the standard deviation σ_V normalized by its mean $\overline{V}$. We notice that the standard deviations of the shear (σ_{V_S}) and the second compressional wave ($\sigma_{V_{P2}}$) are a significant portions of their mean (approximately 29% and 13%). The magnitude is the same for the real and the imaginary parts. Furthermore, they are independent of the frequency. For the first compressional wave, however, the behavior is different. The real part of standard deviation is of negligible magnitude when compared to its mean, whereas the imaginary part is of significant relative magnitude with a strong frequency dependency. The shear modulus uncertainty has a larger effect on the first compressional wave attenuation at lower frequencies than at higher frequencies. This is because that below the relaxation frequency the first compressional wave attenuation is dominated by the Cou-

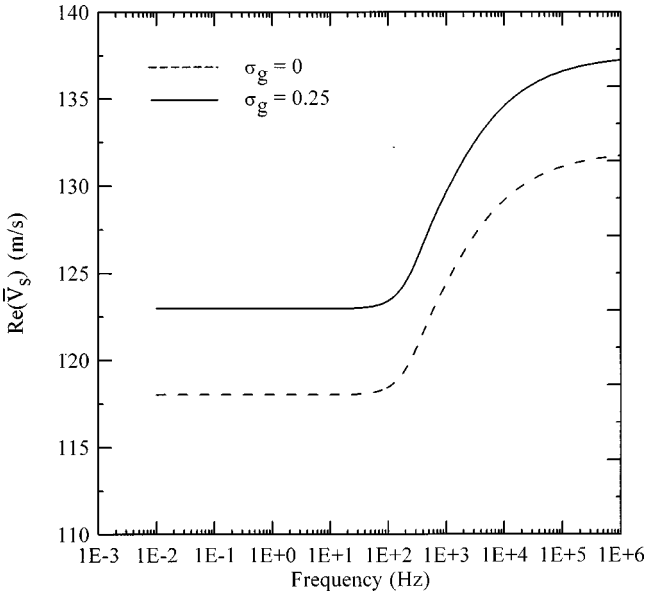

FIG. 3. Real part of mean shear velocity versus frequency.

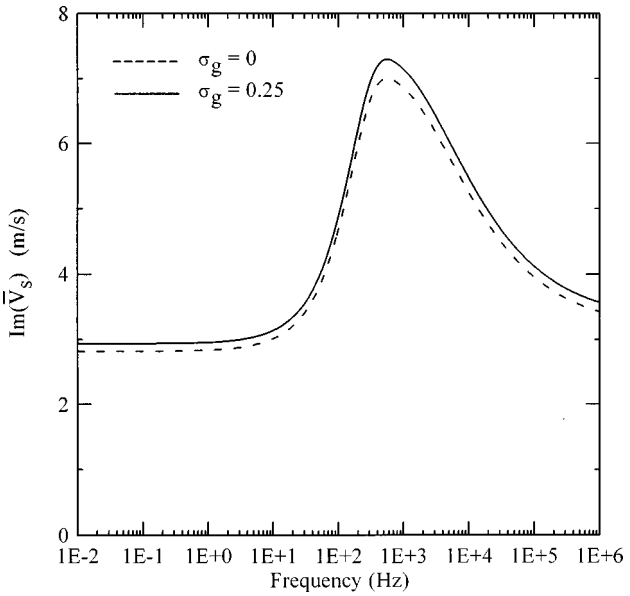

FIG. 4. Imaginary part of mean shear velocity versus frequency.

lomb friction as shown in Eqs. (10) and (11), of which the shear modulus plays an important part. At frequencies higher than relaxation frequency, the attenuation is mostly attributed to the fluid viscous dissipation.

B. Porosity effect

Parametric studies[4,19] have shown that poroelastic waves are sensitive to porosity variation. Porosity not only appears explicitly in the macroscopic theory, Eqs. (1)–(16), but also plays an important role in the micromechanical relations among the parameters. Physical parameters such as the permeability k, shear modulus G, and frame bulk modulus K are known to be related to porosity. If these physical quantities are not directly measured, there exists an opportunity to inferr them from empirical relations using measured porosity. The effect of porosity is hence further enhanced.

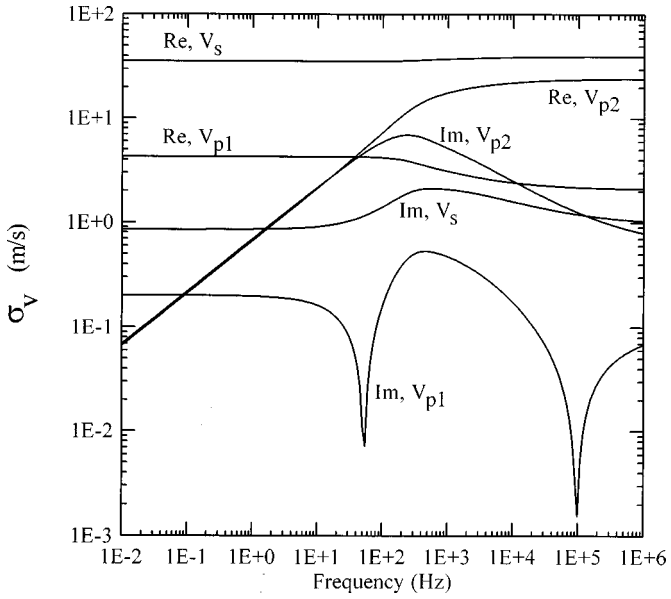

FIG. 5. Real and imaginary part of standard deviation of wave velocity.

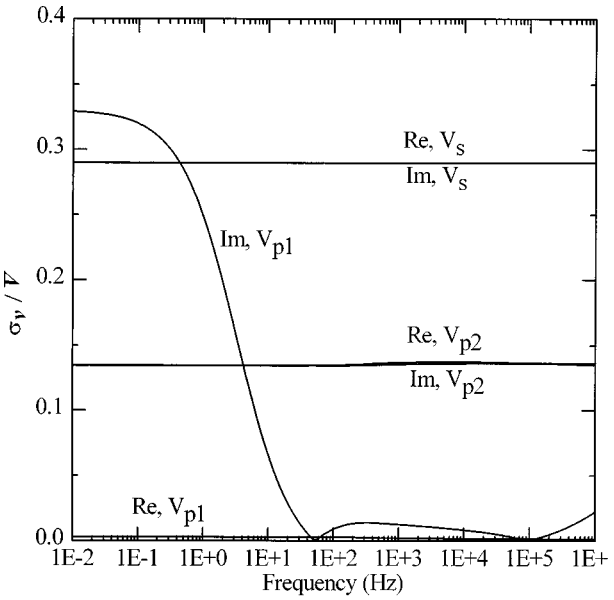

FIG. 6. Real and imaginary part of coefficient of variation of wave velocity.

The statistical relationship between porosity and other physical parameters have been studied by a number of researchers.[4,20–22] These relationships allow a practical procedure to be established that evaluate sediment wave velocities using only a few directly measured parameters.[4,22] Due to the difficulty of collecting the full set of data in ocean environment, this practical aspect and its consequence to the uncertainty of the predicted acoustic output must be assessed.

Studies of experimental data have established many empirical formulas that are widely in use.[21,22] Under the assumptions of fully saturated sediment and small strain, the shear modulus can be found from the porosity ϕ as:[18,22]

$$G=\alpha_1\left[\frac{1-\phi}{\phi}\right]^{\alpha_2}\sigma^{1/2}, \tag{50}$$

where

$$\sigma=\frac{1}{3}g(1+2\mathcal{K}_0)(\rho_s-\rho_f)\int_0^z[1-\phi(z)]dz \tag{51}$$

is the average effective confining pressure of sediment, g is the gravitational acceleration, $\mathcal{K}_0$ is the coefficient of earth pressure at rest which takes the value of 0.5 for most marine sediments, and α_1 and α_2 are empirical constants. Assuming that porosity is relatively a constant in the upper, unconsolidated part of sediment, Eq. (51) can be integrated and used in Eq. (50) to yield Eq. (29), which is repeated here:

$$G=\beta z^{1/2}\frac{(1-\phi)^{\alpha_2+0.5}}{\phi^{\alpha_2}}, \tag{52}$$

where α_2 and β are empirical constants. Compilation of field data taken at the AGS site suggest that:[4] $(\alpha_2,\beta)=(1.1, 6.8\times10^7)$ for sand dominated sediment; $(\alpha_2,\beta)=(1.2, 2.1\times10^7)$ for clay dominated sediment; and $(\alpha_2,\beta)=(1.6, 2.5\times10^7)$ for unidentified sediment.

Permeability is strongly related to the porosity. For the deep sea sediments, Bryant *et al.*[23] analyzed field data and demonstrated that the permeability is a function of porosity only, with a linear relation between log-permeability and the porosity. For shallow sea sediments, the well-known Kozeny–Carman equation is good for most of cases and is generally accepted.[24] The Kozeny–Carman equation can be expressed as:[20]

$$k=\gamma d_{\text{mean}}^2\frac{\phi^3}{(1-\phi)^2}, \tag{53}$$

where d_{mean} is the mean grain size and $\gamma=5.5\times10^{-3}$ is an empirical constant.

Hamilton[25] investigated the statistical relationship between bulk modulus and porosity from experimental data. For sediment with less than 1 m of overburden pressure, he proposed the following empirical relation:

$$K=a_1\exp(-a_2\phi)\ \ (\text{Pa}), \tag{54}$$

where the empirical constants a_1 and a_2 are

$a_1=5.1\times10^{10}$, $a_2=9.8$ For natural marine sands,

$a_1=5.4\times10^{10}$, $a_2=9.8$ For natural silty clay.

Assuming $G=G(\phi)$, $K=K(\phi)$, and $k=k(\phi)$, and given a mean porosity $\bar{\phi}$ with its variance σ_ϕ^2, we can derive the approximate formulas of statistical moments for wave velocities following Eqs. (18), (20), and (21). The presentation is lengthy hence is summarized in the Appendix. Only the analysis is given below.

As a demonstration, we adopt the parameters of the hard sediment case (Table I), except for G, K, k, and ϕ. We assume that the porosity has a mean of $\bar{\phi}=0.47$ and a standard deviation of $\sigma_\phi=0.07$, which is about 15% of the mean. We consider a sandy sediment and accordingly the choice of empirical constants. We also assume a sediment depth of 1 m and choose a grain size of 164 μm based on a table compiled in Badiey *et al.*[4] The shear modulus, bulk modulus, and permeability are determined from Eqs. (52) to (54), together with the statistical moment formulas Eqs. (A13), (A14), (A16), and (A41)–(A43). We find $G=6.6\times10^7\pm2.1\times10^7$ Pa, $K=5.1\times10^8\pm2.4\times10^8$ Pa, $k=8.1\times10^{-11}\pm3.9\times10^{-11}$ m^2, where they are shown as the mean plus/minus one standard deviation. We can introduce further standard deviations to these parameters given the uncertainty of the empirical equations. However, to isolate the effect of porosity, no further uncertainty is added.

The statistical prediction of the sediment waves is given in Figs. 7–10. Figure 7 gives the mean propagation velocities (the real parts). The dashed lines represents the deterministic prediction, i.e., without an input parameter uncertainty, $\sigma_\phi=0$. The solid lines are the statistical prediction of the mean with a $\sigma_\phi=0.07$. The differences are appreciable although they appear diminished by the logarithmic plotting scale.

Figure 8 shows the mean attenuations of the sediment waves in dB/λ unit. Here the attenuation is defined as

$$\alpha=8.686\pi\frac{2|V_i|}{|V_r|}(\text{dB}/\lambda), \tag{55}$$

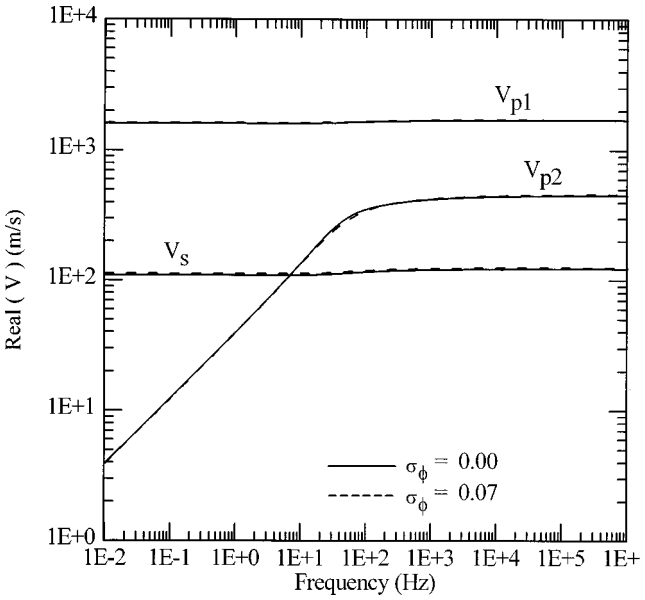

FIG. 7. Porosity uncertainty effect on the mean propagation velocities.

where V_i and V_r are the imaginary and real parts of the complex velocity. We again observe an appreciable difference in the predicted mean attenuations.

Figures 9 and 10 show the standard deviations of the velocities and the attenuation due to a standard deviation $\sigma_\phi=0.07$. They are shown here as the coefficient of variation, i.e., standard deviation normalized by mean. First we observe the relatively large standard deviations compared to their mean values. For the propagation velocities, Fig. 9 shows that the coefficients of variation of $P1$ and S waves are weakly dependent on the frequency, whereas that for the $P2$ wave is more strongly dependent on frequency. Figure 10 shows that the attenuations are all very sensitive to the porosity variation. They also exhibit interesting frequency-dependent pattern that is caused by the interplay of effects of porosity, shear modulus, bulk modulus, and permeability.

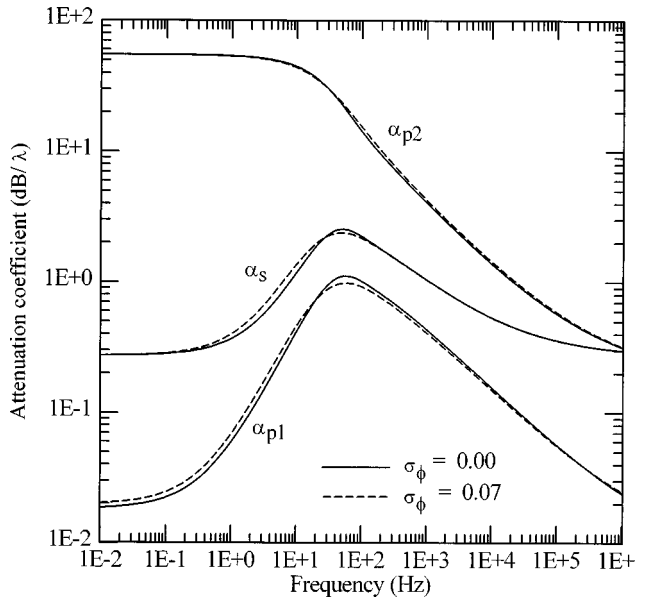

FIG. 8. Porosity uncertainty effect on the mean attenuation.

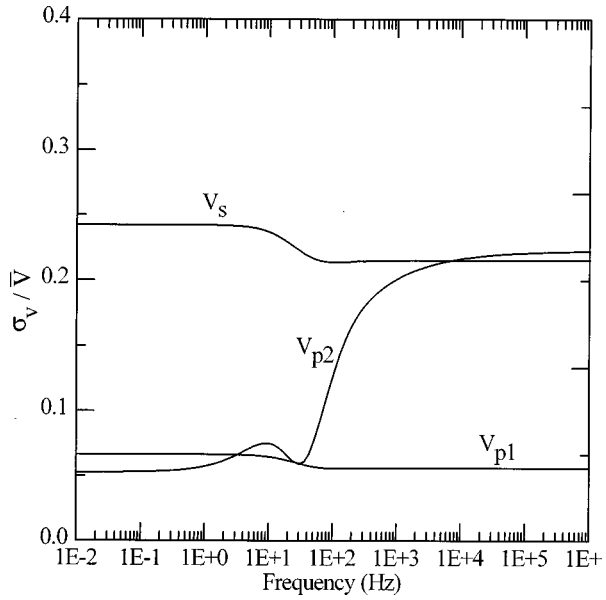

FIG. 9. Coefficients of variation of the propagation velocities due to porosity uncertainty.

Particularly we can identify a peak around the relaxation frequency for the $P2$ wave. For the $P1$ and S waves, the peaks are located at lower frequencies.

IV. PORE SIZE DISTRIBUTION

In this section we address a different stochastic issue, namely the effect of pore size distribution on the deterministic prediction of acoustic wave propagation in sediments. In Biot's theory the seepage flow in the pores and its associated viscous dissipation are considered through a conceptual model of flow in parallel circular tubes or slits. In the original theory[1,2] the flow channels are considered to be single-sized. In reality, the pore size has a probability distribution. In porous media flow the effect of pore size distribution on

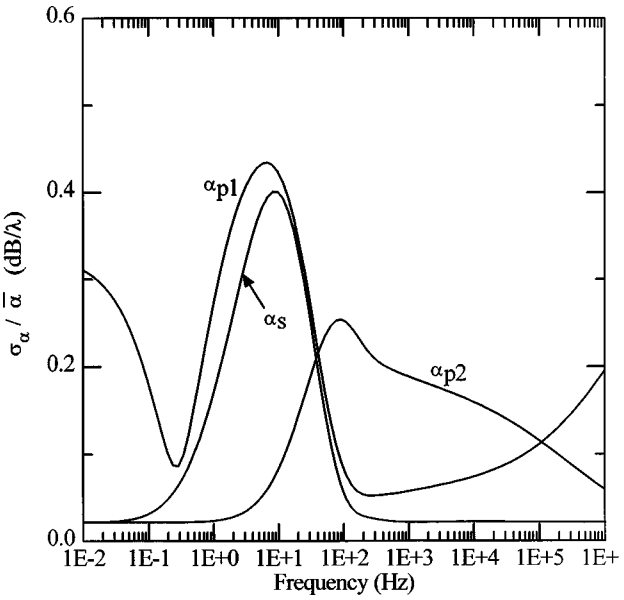

FIG. 10. Coefficients of variation of the attenuation due to porosity uncertainty.

permeability has received considerable attention.[26–28] For poroelasticity theory, the pore size effect has also been studied.[10,29] The analysis below follows an earlier work,[10] but contains a modification of the application of probability theory.

Consider that the pore size is log-normally distributed,[10] we denote r as the pore radius, and $\theta = -\ln r$, such that θ is normally distributed. The probability density function $e(r)$ can be written as:

$$e(r) = \frac{1}{\sqrt{2\pi}\sigma_\theta} \exp\left[-\frac{(\theta - \bar{\theta})^2}{2\sigma_\theta^2} \right]. \tag{56}$$

The pore size distribution effect appears in two parameters, the permeability k, and the viscosity correction factor $F(\kappa)$.

For the viscosity correction factor, the pore size effect is introduced through the definition of κ, see Eq. (15),

$$\kappa = r \sqrt{\frac{\omega \rho_f}{\mu_f}}, \tag{57}$$

where r replaces the pore size factor a. Carefully tracing through the derivation of $F(\kappa)$ and integrating over the probability distribution at the proper place[9] we obtain

$$F(\omega) = \int_0^\infty \frac{\kappa T(\kappa)}{4\left[1 + \frac{2i}{\kappa} T(\kappa) \right]} e(r) dr. \tag{58}$$

We note that the dimensionless parameter κ no longer exists and $F(\omega)$ is a function of ρ_f and μ_f (assumed to be constant for water), $\bar{r}$ and σ_r (or $\bar{\theta}$ and σ_θ), and the frequency ω. If the viscosity friction force and the average seepage velocity, which are involved in the definition of $F(\kappa)$, are separately averaged, they yield a different formula from the above,[10]

$$F(\omega) = \frac{\int_0^\infty \kappa T(\kappa) e(r) dr}{\int_0^\infty 4\left[1 + \frac{2i}{\kappa} T(\kappa) \right] e(r) dr}. \tag{59}$$

Chotiros,[29] on the other hand, averaged only the pore size factor a and used it in Eq. (15). These treatments would lead to the same result if the dependency of the viscosity correction factor on the pore size is a linear function. However, for a real sediment this appears not to be the case. In fact, the results are somewhat different, as we shall demonstrate.

To investigate the effect of pore size distribution, we select the sediment 'A' in Ref. 10, which gives a mean pore radius at $\bar{\theta} = 2.43$ ($r = 0.0877$ mm) and a standard deviation $\sigma_\theta = 0.68$. Figures 11 and 12, respectively, plot the real and the imaginary parts of F as a function of frequency. We show in the figures the comparison of the present solution with those of Refs. 10 and 29. Also shown is the result of $\sigma_\theta = 0$ which corresponds to the case of ignoring the pore size distribution effect. We observe that not only the pore size distribution effect is significant as compared to the case without its consideration, but also different results can be produced if different assumptions are used. Hence it is important that a more careful consideration is given.

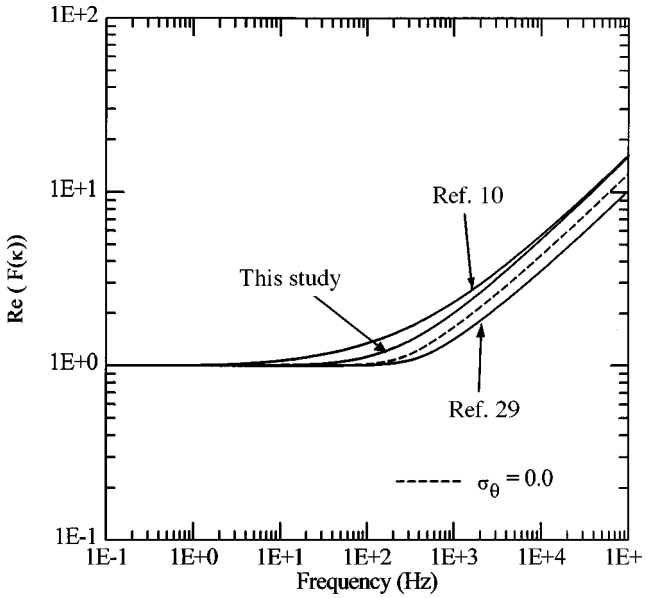

FIG. 11. Pore size distribution effect on the real part of viscosity correction factor.

The pore size effect on permeability has been extensively investigated in porous media literature. For example, we can adopt the series-parallel duct model of Childs and Collis-George:[26]

$$k=\frac{\phi^2}{4}\left[\overline{r^2}-\int_0^\infty\int_{r''}^\infty e(r'')e(r')r'^2\,dr'\,dr''\right], \tag{60}$$

where $\overline{r^2}$ is the mean value of r^2.

The above theory is used to investigate the pore size distribution effect on acoustic wave velocities and attenuations. Consider the data set of a hard sediment (Table I) with the exception of permeability, which is determined from Eq. (60), and the viscosity correction factor, which is numerically evaluated from Eq. (58). The mean pore radius 0.164 mm, and the standard deviations $\sigma_\theta=0.72$ (approximately 40% error on θ) are used.

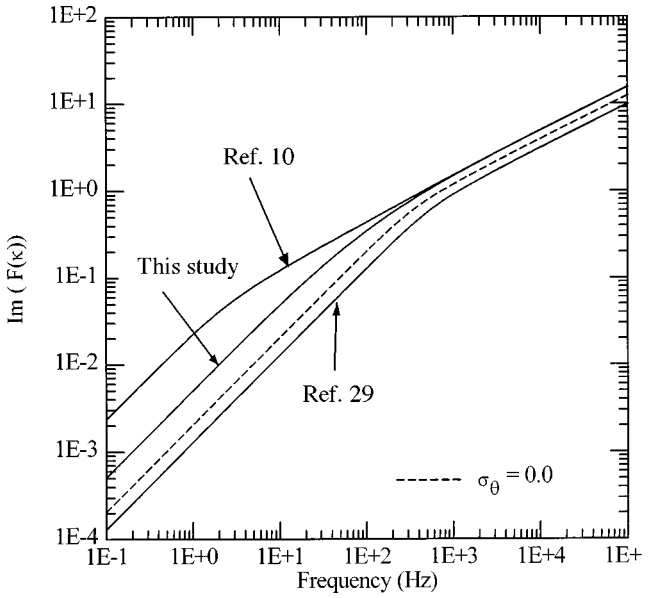

FIG. 12. Pore size distribution effect on the imaginary part of viscosity correction factor.

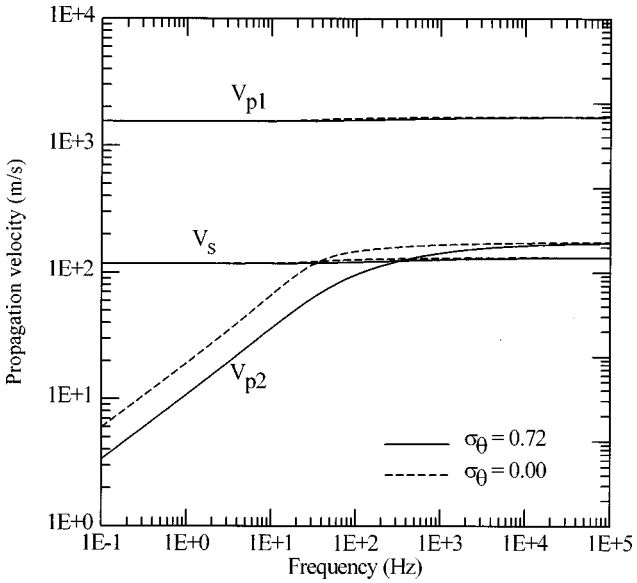

FIG. 13. Pore size distribution effect on the propagation velocities.

Figures 13 and 14, respectively, show the propagation velocities and the attenuations versus frequency. The solid lines correspond to the case of the given σ_θ, while the dashed lines represent the case of ignoring the pore size distribution effect ($\sigma_\theta=0$). We find that both the velocities and the attenuations shift right when pore size distribution is considered. This also means a shift in the relaxation frequency.

Next, the reflection and transmission coefficients at the ocean-sediment interface are examined. The sensitivity of reflection coefficient to various sediment parameters has been investigated.[7,19] It was found that the reflection coefficient is particularly sensitive to the porosity variation. It is expected that the pore size distribution play a similar role.

Consider a plane wave in the ocean incident on a semi-

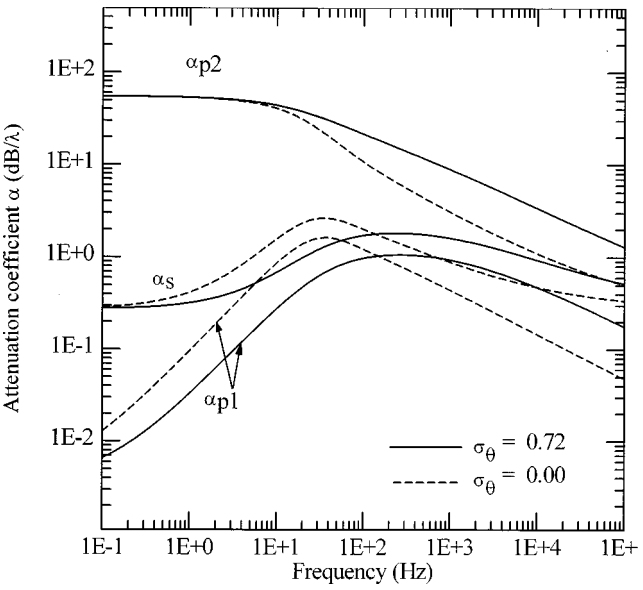

FIG. 14. Pore size distribution effect on the attenuation coefficients.

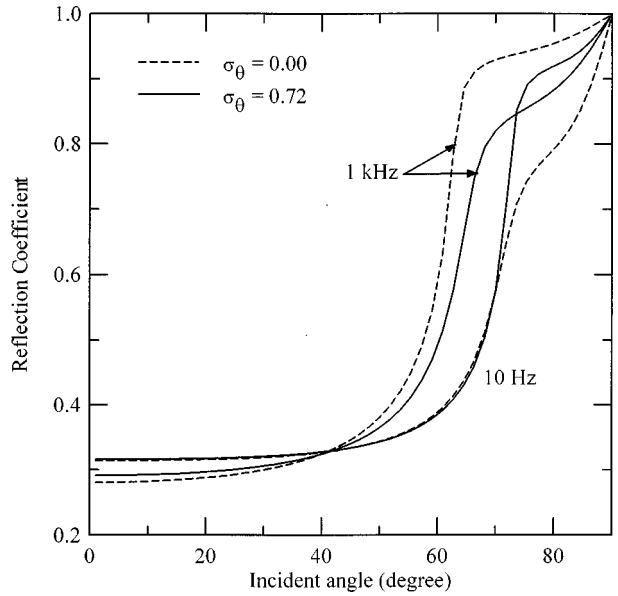

FIG. 15. Pore size distribution effect on the reflection coefficient.

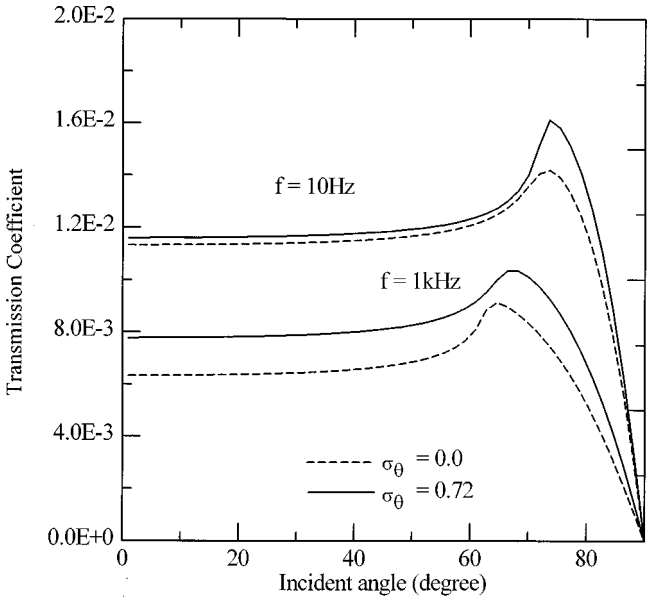

FIG. 17. Pore size distribution effect on the transmission coefficient of the second compressional wave.

infinite homogeneous sediment bed at a certain incident angle.[7] The sediment properties are those of the hard sediment (Table I) with the pore size distribution statistics: $\overline{\theta} = 1.81$ (at $r = 0.164$ mm), and $\sigma_\theta = 0.72$. The reflection coefficient in the water and the three transmission coefficients in the sediment are examined in Figs. 15–18 at two frequencies, 10 Hz and 1 kHz. We found that the pore size distribution has a large effect on the reflection and transmission coefficients which is dependent on the frequency and incident angle. For the reflection coefficient, larger effect happens at incident angles greater than the critical incident angle. For the transmission coefficients, pore size distribution is important in all ranges of incident angles.

V. SUMMARY AND CONCLUSION

The Biot's poroelastic wave theory is analyzed for its sensitivity to the input parameter uncertainty. First, the methodology of evaluating statistical moments is established using a second order Taylor series expansion. The basic issue of uncertainty analysis is illustrated from an elastic wave theory. Poroelastic analysis is then conducted with a single parameter uncertainty involving the shear modulus. The mean and standard deviation of the propagation velocities and attenuations of the three waves are shown. Next, the common procedure of using empirical formula to infer one physical parameter from the other is examined. Based on the current practice, it is assumed that the shear modulus, bulk modulus, and permeability are determined from the porosity. A stochastic analysis that considers these empirical relations is conducted. The porosity uncertainty is shown to have a significant impact on the prediction of the wave propagation velocities and attenuations. In most of the responses, a dependence on frequency is observed. The work is then extended to a slightly different issue: the effect of pore size distribution on the deterministic prediction of the acoustic responses. A formula different from an earlier work is proposed. It is demonstrated that the viscosity correction factor evaluated from this formula is significantly different from the earlier formulas. The effects of pore size distribution on the wave propagation velocities, attenuations, and on the reflection and transmission coefficients of plane wave incident on semi-infinite seabed are then demonstrated.

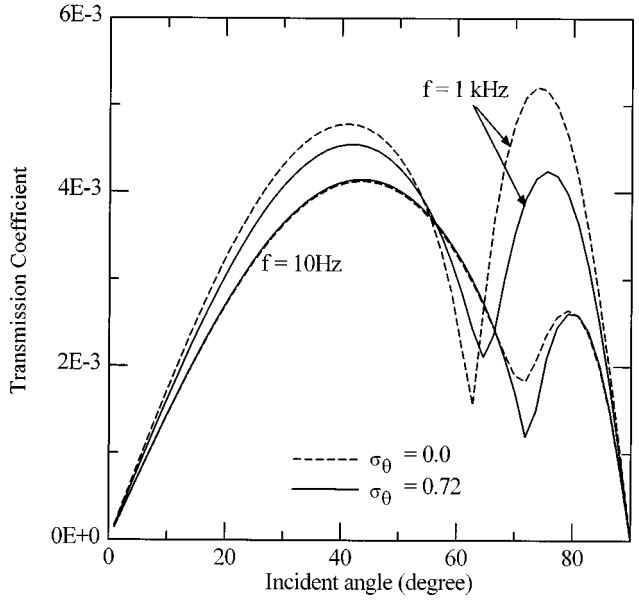

FIG. 16. Pore size distribution effect on the transmission coefficient of the first compressional wave.

Based on the above analyses we conclude that physical parameter uncertainty in shallow water environment is an important issue that must be openly addressed. This is particularly true if certain ''engineering tests'' are conducted to infer one parameter from the other utilizing empirical relations. The current methodology offers a practical way of translating the input parameter uncertainty into a reliability estimate of the output response prediction.

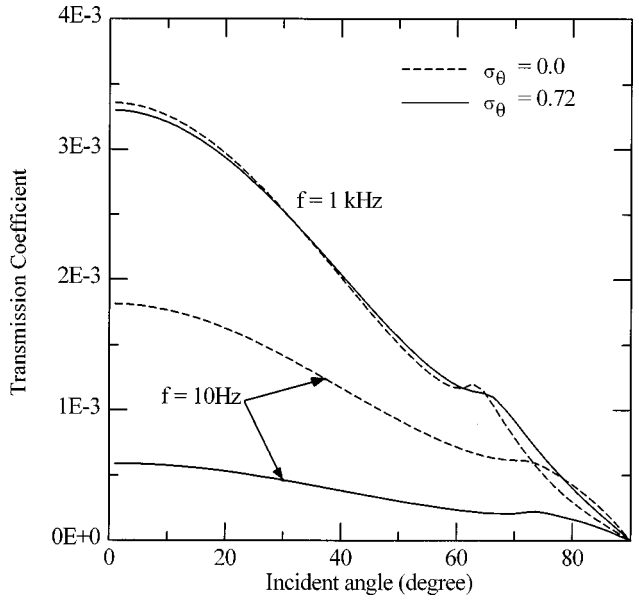

FIG. 18. Pore size distribution effect on the transmission coefficient of the shear wave.

APPENDIX: DERIVATION OF STATISTICAL MOMENTS OF WAVE VELOCITIES DUE TO POROSITY VARIATION

For simplicity, let $A_1=HM-C^2$, $A_2=B$, and $A_3=\rho m'-\rho_f^2$. Equations (1) and (2) can be abbreviated as

$$\begin{pmatrix} V_{P1} \\ V_{P2} \end{pmatrix} = \left[\frac{2A_1}{A_2 \mp (A_2^2 - A_1 A_3)^{1/2}} \right]^{1/2}, \tag{A1}$$

$$V_S = \left(\frac{Gm'}{A_3} \right)^{1/2}, \tag{A2}$$

such that we have

$$\overline{V}_{P1,P2} \approx V_{P1,P2}(\overline{A}_1, \overline{A}_2, \overline{A}_3) + \frac{1}{2} \sum_{i,j=1}^{3} \frac{\partial^2 V_{P1,P2}}{\partial A_i \partial A_j} \sigma_{A_i A_j}, \tag{A3}$$

$$\overline{V}_S \approx V_S(\overline{G}, \overline{m'}, \overline{A}_3) + \frac{1}{2} \left(\frac{\partial^2 V_S}{\partial G^2} \sigma_G^2 + \frac{\partial^2 V_S}{\partial m'^2} \sigma_{m'}^2 + \frac{\partial^2 V_S}{\partial A_3^2} \sigma_{A_3}^2 + \frac{\partial^2 V_S}{\partial G \partial m'} \sigma_{Gm'} + \frac{\partial^2 V_S}{\partial G \partial A_3} \sigma_{GA_3} + \frac{\partial^2 V_S}{\partial m' \partial A_3} \sigma_{m'A_3} \right), \tag{A4}$$

$$\sigma^2_{V_{P1,P2}} \approx \sum_{i,j=1}^{3} \frac{\partial V_{P1,P2}}{\partial A_i} \frac{\partial V_{P1,P2}}{\partial A_j} \sigma_{A_i A_j}, \tag{A5}$$

$$\sigma^2_{V_S} \approx \left(\frac{\partial V_S}{\partial G} \right)^2 \sigma_G^2 + \left(\frac{\partial V_S}{\partial m'} \right)^2 \sigma_{m'}^2 + \left(\frac{\partial V_S}{\partial A_3} \right)^2 \sigma_{A_3}^2 + \frac{\partial V_S}{\partial G} \frac{\partial V_S}{\partial m'} \sigma_{Gm'} + \frac{\partial V_S}{\partial G} \frac{\partial V_S}{\partial A_3} \sigma_{GA_3} + \frac{\partial V_S}{\partial A_3} \frac{\partial V_S}{\partial m'} \sigma_{m'A_3}, \tag{A6}$$

in which the derivatives can be easily obtained from Eqs. (A1) and (A2) and will not be listed here. All the derivatives are evaluated at $(A_1,A_2,A_3)=(\overline{A}_1,\overline{A}_2,\overline{A}_3)$ with $\overline{A}_1=A_1(\overline{H},\overline{M},\overline{C})$, $\overline{A}_2=A_2(\overline{H},\overline{M},\overline{C},\overline{\rho},\overline{m'})$, and $\overline{A}_3=A_3(\overline{\rho},\overline{m'})$.

The mean values of the Biot moduli $(\overline{H},\overline{M},\overline{C})$ may be expressed as

$$\overline{H}=H(\overline{B}_1,\overline{K},\overline{G}) - \frac{2\overline{K}^2}{\overline{B}_1} \frac{\sigma_K^2}{\overline{K}^2} + \frac{2(K_s-\overline{K})^2}{\overline{B}_1} \frac{\sigma_{B_1}^2}{\overline{B}_1^2} - \frac{2\overline{K}(K_s-\overline{K})}{\overline{B}_1} \frac{\sigma_{B_1K}}{\overline{B}_1 \overline{K}}, \tag{A7}$$

$$\overline{M}=M(\overline{B}_1) + 2 \frac{K_s^2}{\overline{B}_1} \frac{\sigma_{B_1}^2}{\overline{B}_1^2}, \tag{A8}$$

$$\overline{C}=C(\overline{B}_1,\overline{K}) + \frac{2K_s(K_s-\overline{K})}{\overline{B}_1} \frac{\sigma_{B_1}^2}{\overline{B}_1^2} - \frac{K_s \overline{K}}{\overline{B}_1} \frac{\sigma_{B_1K}}{\overline{B}_1 \overline{K}}, \tag{A9}$$

where $B_1=D-K$. We further find the mean of these direct and indirect quantities:

$$\overline{B}_1=B_1(\overline{K},\overline{\phi}), \tag{A10}$$

$$\overline{\rho}=\rho(\overline{\phi}), \tag{A11}$$

$$\overline{m'}=m'(\overline{\phi},\overline{k},\overline{\kappa}) + \frac{1}{2} \left[\frac{2(1+c)\rho_f}{\overline{\phi}^3} \sigma_\phi^2 - i \frac{\mu_f}{\overline{k}\omega} \frac{\partial^2 F}{\partial \kappa^2} \sigma_\kappa^2 - i \frac{2\mu_f F}{\overline{k}^3 \omega} \sigma_k^2 + i \frac{2\mu_f}{\overline{k}^2 \omega} \frac{\partial F}{\partial \kappa} \sigma_{k\kappa} \right], \tag{A12}$$

$$\overline{K}=K(\overline{\phi}) + a_1 a_2^2 \exp(-a_2 \overline{\phi}) \sigma_\phi^2, \tag{A13}$$

$$\overline{G}=G(\overline{\phi}) + \beta z^{1/2} \left\{ (\alpha_2+0.5) \left[\frac{(\alpha_2+0.5)(1-\overline{\phi})^{\alpha_2-1.5}}{\overline{\phi}^{\alpha_2}} + \frac{2\alpha_2(1-\overline{\phi})^{\alpha_2-0.5}}{\overline{\phi}^{\alpha_2+1}} \right] + \frac{\alpha_2(\alpha_2+1)(1-\overline{\phi})^{\alpha_2+0.5}}{\overline{\phi}^{\alpha_2+2}} \right\} \sigma_\phi^2, \tag{A14}$$

$$\overline{\kappa}=\kappa(\overline{k},\overline{\phi}) + \frac{\eta}{4} \sqrt{\frac{\overline{k}\omega\rho_f}{\overline{\phi}\mu_f}} \left(3 \frac{\sigma_\phi^2}{\overline{\phi}^2} - \frac{\sigma_k^2}{\overline{k}^2} - \frac{\sigma_{k\phi}}{k\phi} \right), \tag{A15}$$

$$\overline{k}=k(\overline{\phi}) + \gamma d_{\text{mean}}^2 \frac{6\overline{\phi}}{(1-\overline{\phi})^4} \sigma_\phi^2. \tag{A16}$$

The variances and covariances as needed in Eqs. (A3)–(A6) are:

$$\sigma_{A_1}^2 = F_1^2 \sigma_{B_1}^2 + \overline{M}^2 \sigma_K^2 + \tfrac{16}{9} \overline{M}^2 \sigma_G^2 + 2\overline{M} F_1 \sigma_{B_1K} + \tfrac{8}{3} \overline{M} F_1 \sigma_{B_1G} + \tfrac{8}{3} \overline{M}^2 \sigma_{KG}, \tag{A17}$$

$$\sigma_{A_2}^2=\overline{M}^2\sigma_\rho^2+F_2^2\sigma_{B_1}^2+\overline{H}^2\sigma_{m'}^2+F_3^2\sigma_K^2+\tfrac{16}{9}\overline{m'^2}\sigma_G^2$$
$$+2\overline{M}F_2\sigma_{\rho B_1}-2\overline{M}\overline{H}\sigma_{\rho m'}+2\overline{M}F_3\sigma_{\rho K}-\tfrac{8}{3}\overline{M}\overline{m'\sigma}_{\rho G}$$
$$-2\overline{H}F_2\sigma_{B_1m'}+2F_2F_3\sigma_{B_1K}-\tfrac{8}{3}\overline{m'F}_2\sigma_{B_1G}$$
$$-2\overline{H}F_3\sigma_{m'K}+\tfrac{8}{3}\overline{H}\overline{m'\sigma}_{m'G}-\tfrac{8}{3}\overline{m'F}_3\sigma_{KG}, \tag{A18}$$

$$\sigma_{A_3}^2=\overline{m'^2}\sigma_\rho^2+\overline{\rho}^2\sigma_{m'}^2+2\overline{m'\rho}\sigma_{\rho m'}, \tag{A19}$$

$$\sigma_{A_1A_2}=F_1F_2\sigma_{B_1}^2+\overline{M}F_3\sigma_K^2-\tfrac{16}{9}\overline{m'\overline{M}}\sigma_G^2$$
$$+\tfrac{4}{3}(\overline{M}F_2-\overline{m'F}_1)\sigma_{GB_1}+\tfrac{4}{3}(\overline{M}F_3-\overline{m'\overline{M}})\sigma_{GK}$$
$$+(F_1F_3+\overline{M}F_2)\sigma_{B_1K}+\overline{M}F_1\sigma_{B_{1\rho}}-\overline{H}F_1\sigma_{B_1m'}$$
$$+\overline{M}^2\sigma_{K\rho}-\overline{M}\overline{H}\sigma_{Km'}+\tfrac{4}{3}\overline{M}^2\sigma_{G\rho}-\tfrac{4}{3}\overline{M}\overline{H}\sigma_{Gm'}, \tag{A20}$$

$$\sigma_{A_1A_3}=\overline{m'F}_1\sigma_{\rho B_1}+\overline{m'\overline{M}}\sigma_{\rho K}+\tfrac{4}{3}\overline{m'\overline{M}}\sigma_{\rho G}+\overline{\rho F}_1\sigma_{m'B_1}$$
$$+\overline{\rho}\overline{M}\sigma_{m'K}+\tfrac{4}{3}\overline{\rho}\overline{M}\sigma_{m'G}, \tag{A21}$$

$$\sigma_{A_2A_3}=\overline{m'\overline{M}}\sigma_\rho^2-\overline{\rho}\overline{H}\sigma_{m'}^2+(\overline{\rho}\overline{M}-\overline{m'\overline{H}})\sigma_{m'\rho}+\overline{m'F}_2\sigma_{\rho B_1}$$
$$+\overline{m'F}_3\sigma_{\rho K}-\tfrac{4}{3}\overline{m'^2}\sigma_{\rho G}+\overline{\rho F}_2\sigma_{m'B_1}$$
$$+\overline{\rho}F_3\sigma_{m'K}-\tfrac{4}{3}\overline{\rho}\overline{m'\sigma}_{m'G}, \tag{A22}$$

$$\sigma_{GA_3}=(\rho_f-\rho_s)\sigma_{G\phi}+\rho\sigma_{Gm'}, \tag{A23}$$

$$\sigma_{m'A_3}=\rho\sigma_{m'}^2+m'\sigma_{\rho m'}, \tag{A24}$$

in which the coefficients F_i are derivatives of A_i:

$$F_1=(M\alpha_B^2-H)\frac{M}{B_1}, \tag{A25}$$

$$F_2=(m'\alpha_B^2-\rho+2\rho_f\alpha_B)\frac{K_s^2}{B_1^2}, \tag{A26}$$

$$F_3=(m'\alpha_B+\rho_f)\frac{2K_s}{B_1}-m', \tag{A27}$$

where $\alpha_B=K/K_s$ is the Biot's effective stress coefficient, and $\alpha_B\approx1$ for ocean sediments. The variances and covariances are further broken down into the basic parameters:

$$\sigma_{B_1}^2=\left(\frac{K_s^2}{K_f}\right)^2\sigma_\phi^2+\sigma_K^2-\frac{K_s^2}{K_f}\sigma_{K\phi}, \tag{A28}$$

$$\sigma_{m'}^2=\left(\frac{1+c}{\overline{\phi}^2}\rho_f\right)^2\sigma_\phi^2-\left(\frac{\mu_f}{\overline{k\omega}}\frac{\partial F}{\partial\overline{\kappa}}\right)^2\sigma_\kappa^2-\left(\frac{\mu_fF(\overline{\kappa})}{\overline{k}^2\omega}\right)^2\sigma_k^2$$
$$+i\frac{(1+c)\mu_f\rho_fF(\overline{\kappa})}{\overline{\phi}^2\overline{k}^2\omega}\sigma_{k\phi}+\frac{(1+c)\mu_f\rho_f}{\overline{\phi}^2\overline{k\omega}}\frac{\partial F}{\partial\overline{\kappa}}\sigma_{\kappa\phi}$$
$$-\frac{\mu_f^2F(\overline{\kappa})}{\overline{k}^3\omega^2}\frac{\partial F}{\partial\overline{\kappa}}\sigma_{\kappa k}, \tag{A29}$$

$$\sigma_\rho^2=(\rho_s-\rho_f)^2\sigma_\phi^2, \tag{A30}$$

$$\sigma_\kappa^2=\frac{\eta^2\overline{k\omega}\rho_f}{4\overline{\phi}\mu_f}\left(\frac{\sigma_\phi^2}{\overline{\phi}^2}+\frac{\sigma_k^2}{\overline{k}^2}-2\frac{\sigma_{k\phi}}{\overline{k\phi}}\right), \tag{A31}$$

$$\sigma_{B_1K}=\frac{K_s^2}{K_f}\sigma_{K\phi}-\sigma_K^2, \tag{A32}$$

$$\sigma_{B_1m'}=-\frac{(1+c)\rho_f}{\overline{\phi}^2}\frac{K_s^2}{K_f}\sigma_\phi^2-i\frac{\mu_f}{\overline{k\omega}}\frac{\partial F}{\partial\overline{\kappa}}\frac{K_s^2}{K_f}\sigma_{\kappa\phi}$$
$$+i\frac{\mu_fK(\overline{\kappa})}{\overline{k}^2\omega}\frac{K_s^2}{K_f}\sigma_{k\phi}+\frac{(1+c)\rho_f}{\overline{\phi}^2}\sigma_{K\phi}$$
$$-i\frac{\mu_fF(\overline{\kappa})}{\overline{k}^2\omega}\sigma_{Kk}+i\frac{\mu_f}{\overline{k\omega}}\frac{\partial F}{\partial\overline{\kappa}}\sigma_{K\kappa}, \tag{A33}$$

$$\sigma_{B_1\rho}=(\rho_f-\rho_s)\frac{K_s(K_s-K_f)}{K_f}\sigma_\phi^2-(\rho_f-\rho_s)\sigma_{K\phi}, \tag{A34}$$

$$\sigma_{\rho m'}=\rho_f(\rho_s-\rho_f)\frac{1+c}{\overline{\phi}^2}\sigma_\phi^2+i\frac{\mu_f(\rho_s-\rho_f)}{\overline{k\omega}}\frac{\partial F}{\partial\kappa}\sigma_{\kappa\phi}$$
$$-i\frac{\mu_f(\rho_s-\rho_f)F(\overline{\kappa})}{\overline{k}^2\omega}\sigma_{k\phi}, \tag{A35}$$

$$\sigma_{K\kappa}=\frac{\eta a_1a_2}{2}\left(\frac{\overline{k\omega}\rho_f}{\overline{\phi}\mu_f}\right)^{1/2}\exp(-a_2\overline{\phi})\left(\frac{\sigma_\phi^2}{\overline{\phi}}-\frac{\sigma_{k\phi}}{\overline{k}}\right), \tag{A36}$$

$$\sigma_{G\kappa}=\frac{\beta z^{1/2}\eta}{2}\left(\frac{\overline{k\omega}\rho_f}{\overline{\phi}\mu_f}\right)^{1/2}\left[\frac{(\alpha_2+\frac{1}{2})(1-\overline{\phi})^{\alpha_2-1/2}}{\overline{\phi}^{\alpha_2}}\right.$$
$$\left.+\frac{\alpha_2(1-\overline{\phi})^{\alpha_2+1/2}}{\overline{\phi}^{\alpha_2+1}}\right]\left(\frac{\sigma_\phi^2}{\overline{\phi}}-\frac{\sigma_{k\phi}}{\overline{k}}\right), \tag{A37}$$

$$\sigma_{k\kappa}=\frac{\gamma d_{\text{mean}}^2\eta\overline{\phi}^2(3-\overline{\phi})}{2(1-\overline{\phi})^3}\left(\frac{\overline{k\omega}\rho_f}{\overline{\phi}\mu_f}\right)^{1/2}\left(\frac{\sigma_{k\phi}}{\overline{k}}-\frac{\sigma_\phi^2}{\overline{\phi}}\right), \tag{A38}$$

$$\sigma_{\kappa\phi}=\frac{\eta}{2}\left(\frac{\overline{k\omega}\rho_f}{\overline{\phi}\mu_f}\right)^{1/2}\left(\frac{\sigma_{k\phi}}{\overline{k}}-\frac{\sigma_\phi^2}{\overline{\phi}}\right), \tag{A39}$$

$$\sigma_{Gm'}=\rho_f(1+c)\frac{\sigma_{G\phi}}{\overline{\phi}^2}+i\frac{\mu_fF(\overline{\kappa})}{\overline{k}^2\omega}\sigma_{Gk}$$
$$-i\frac{\mu_f}{\overline{k\omega}}\frac{\partial F(\overline{\kappa})}{\partial\kappa}\sigma_{G\kappa}. \tag{A40}$$

Finally, all quantities must be related to the variance of porosity through the following relations:

$$\sigma_K^2=a_1^2a_2^2\exp(-2a_2\overline{\phi})\sigma_\phi^2, \tag{A41}$$

$$\sigma_G^2=\beta^2 z\left[\frac{(\alpha_2+0.5)(1-\overline{\phi})^{\alpha_2-0.5}}{\overline{\phi}^{\alpha_2}}+\frac{\alpha_2(1-\overline{\phi})^{\alpha_2+0.5}}{\overline{\phi}^{\alpha_2+1}}\right]^2\sigma_\phi^2, \tag{A42}$$

$$\sigma_k^2=\left[\gamma d_{\text{mean}}^2\frac{\overline{\phi}^2(3-\overline{\phi})}{(1-\overline{\phi})^3}\right]^2\sigma_\phi^2, \tag{A43}$$

$$\sigma_{KG}=\beta z^{1/2}a_1a_2\exp(-a_2\overline{\phi})\left[\frac{(\alpha_2+0.5)(1-\overline{\phi})^{a_2-0.5}}{\overline{\phi}^{\alpha_2}}+\frac{\alpha_2(1-\overline{\phi})^{\alpha_2+0.5}}{\overline{\phi}^{\alpha_2+1}}\right]\sigma_\phi^2, \tag{A44}$$

$$\sigma_{Kk}=-\gamma d_{\text{mean}}^2\frac{\overline{\phi}^2(3-\overline{\phi})a_1a_2}{(1-\overline{\phi})^3}\exp(-a_2\overline{\phi})\sigma_\phi^2, \tag{A45}$$

$$\sigma_{Gk}=\gamma d_{\text{mean}}^2\frac{\beta z^{1/2}\overline{\phi}^2(3-\overline{\phi})}{(1-\overline{\phi})^3}\left[\frac{(\alpha_2+0.5)(1-\overline{\phi})^{\alpha_2-0.5}}{\overline{\phi}^{\alpha_2}}+\frac{\alpha_2(1-\overline{\phi})^{\alpha_2+0.5}}{\overline{\phi}^{\alpha_2+1}}\right]\sigma_\phi^2, \tag{A46}$$

$$\sigma_{K\phi}=a_1a_2\exp(-a_2\overline{\phi})\sigma_\phi^2, \tag{A47}$$

$$\sigma_{k\phi}=\frac{\gamma d_{\text{mean}}^2\overline{\phi}^2(3-\overline{\phi})}{(1-\overline{\phi})^3}\sigma_\phi^2, \tag{A48}$$

$$\sigma_{G\phi}=\beta z^{1/2}\left[\frac{(\alpha_2+0.5)(1-\overline{\phi})^{\alpha_2-0.5}}{\overline{\phi}^{\alpha_2}}+\frac{\alpha_2(1-\overline{\phi})^{\alpha_2+0.5}}{\overline{\phi}^{\alpha_2+1}}\right]\sigma_\phi^2. \tag{A49}$$

The above results assume that the parameters K, k, and G are determined through porosity using empirical relations. If these parameters are independently measured, all variance and covariances that involve these parameter drop out in the above equations.

[1] M. A. Biot, ''Theory of propagation of elastic waves in a fluid-saturated porous solid, Part I: Low frequency range,'' J. Acoust. Soc. Am. **28**, 168–178 (1956).

[2] M. A. Biot, ''Theory of propagation of elastic waves in a fluid-saturated porous solid, Part II: Higher frequency range,'' J. Acoust. Soc. Am. **28**, 179–191 (1956).

[3] R. D. Stoll, *Sediment Acoustics* (Springer-Verlag, New York, 1989).

[4] M. Badiey, A. H.-D. Cheng, and Y. Mu, ''From geology to geoacoustics—Evaluation of Biot–Stoll sound speed and attenuation for shallow water acoustics,'' J. Acoust. Soc. Am. **103**, 309–320 (1998).

[5] R. D. Stoll and T. K. Kan, ''Reflection of acoustic waves at a water-sediment interface,'' J. Acoust. Soc. Am. **70**, 149–156 (1981).

[6] T. Yamamoto, ''Propagator matrix for continuously layered porous seabeds,'' Bull. Seismol. Soc. Am. **73**, 1599–1620 (1983).

[7] M. Badiey, A. H.-D. Cheng, and I. Jaya, ''Propagator matrix for plane wave reflection from inhomogeneous anisotropic poroelastic seafloor,'' J. Comput. Acoust. **2**, 11–27 (1994).

[8] M. Abramowitz and I. A. Stegun, *Handbook of Mathematical Functions* (Dover, New York, 1972).

[9] Y. Mu, ''Response of poroelastic seabed to acoustic and water waves,'' Doctoral dissertation, University of Delaware (1998).

[10] T. Yamamoto and A. Turgut, ''Acoustic propagation through porous media with arbitrary pore size distribution,'' J. Acoust. Soc. Am. **83**, 1744–1751 (1988).

[11] A. H.-D. Cheng and D. Ouazar, ''Theis solution under aquifer parameter uncertainty,'' Ground Water **33**, 11–15 (1995).

[12] P. Indelman, G. Dagan, A. H.-D. Cheng, and D. Ouazar, ''Sensitivity analysis of flow in multiple leaky aquifer system,'' J. Hyd. Eng., ASCE **122**, 41–45 (1996).

[13] A. Naji, A. H.-D. Cheng, and D. Ouazar, ''Analytical stochastic solutions of saltwater/freshwater interface in coastal aquifers,'' Stochastic Hydrology & Hydraulics (submitted).

[14] A. L. Gutjahr and L. W. Gelhar, ''Stochastic models of subsurface flow: Infinite versus finite domains and stationarity,'' Water Resour. Res. **17**, 337–350 (1981).

[15] G. Dagan, ''A note on higher-order corrections of the head covariances in steady aquifer flow,'' Water Resour. Res. **21**, 573–578 (1985).

[16] Dames and Moore, ''Supplementary subsurface investigation: Vibrocore program, Atlantic Generating Station, for the Public Service Electric and Gas Company, Newark, NJ'' (1974).

[17] H. J. Miller and C. Dill, ''Final Report, Geophysical investigation of Atlantic Generating Station site and offshore region, for the Public Service Electric and Gas Company, Newark, NJ'' (1974).

[18] M. Badiey, I. Jaya, and A. H.-D. Cheng, ''Shallow water acoustic/geoacoustic experiments at the New Jersey Atlantic Generating Station site,'' J. Acoust. Soc. Am. **96**, 3593–3604 (1994).

[19] M. Badiey, A. H.-D. Cheng, and I. Jaya, ''Deterministic and stochastic analyses of acoustic plane wave reflection from inhomogeneous porous seafloor,'' J. Acoust. Soc. Am. **99**, 903–913 (1996).

[20] P. C. Carman, *Flow of Gases Through Porous Media* (Academic, New York, 1956).

[21] B. O. Hardin and F. E. Richart, Jr., ''Elastic velocities in granular soils,'' J. Soil Mech. Funda. Div., ASCE **89**, 33–65 (1963).

[22] T. Yamamoto, M. V. Trevorrow, M. Badiey, and A. Turgut, ''Determination of the seabed porosity and shear modulus profiles using a gravity wave inversion,'' Geophys. J. Int. **98**, 173–182 (1989).

[23] W. R. Bryant, W. Hottman, and P. Trabant, ''Permeability of unconsolidated and consolidated marine sediments, Gulf of Mexico,'' Mar. Geotech. **1**, 1–14 (1975).

[24] A. Turgut and T. Yamamoto, ''Synthetic seismograms for marine sediments and determination of porosity and permeability,'' Geophysics **53**, 1056–1067 (1988).

[25] E. L. Hamilton, ''Elastic properties of marine sediments,'' J. Geophys. Res. **76**, 579–604 (1971).

[26] E. C. Childs and N. Collis-George, ''The permeability of porous materials,'' Proc. R. Soc. London, Ser. A **201**, 392–405 (1950).

[27] W. Brutsaert, ''Probability laws for pore-size distributions,'' Soil Sci. **101**, 85–92 (1966).

[28] W. Brutsaert, ''The permeability of a porous medium determined from certain probability laws for pore size distributions,'' Water Resour. Res. **4**, 425–434 (1968).

[29] N. P. Chotiros, ''Biot model of sound propagation in water-saturated sand,'' J. Acoust. Soc. Am. **97**, 199–214 (1995).

Modeling acousto-elastic waveguide/object scattering with the Rayleigh hypothesis

J. A. Fawcett[a)]
Saclant Undersea Research Centre, Viale San Bartolomeo 400, 19138 San Bartolomeo, La Spezia, Italy

(Received 20 May 1998; revised 29 March 1999; accepted 12 April 1999)

In this paper the plane-wave scattering matrices for a range-dependent seabed and upper free surface are computed using the Rayleigh hypothesis at the surfaces. These matrices can then be used to compute the pressure field within a waveguide bounded by these surfaces; they can also be easily combined with the scattering matrix characterizing an object. Computational examples are given for range-dependent acousto-elastic waveguides and the fields compared with those computed by other methods. An example with a steel cylinder in the waveguide is also shown. © *1999 Acoustical Society of America.* [S0001-4966(99)04407-0]

PACS numbers: 43.30.Dr, 43.30.Gv, 43.30.Hw [SAC-B]

INTRODUCTION

In an earlier paper[1] we described how scattering in a range-dependent waveguide could be computed by using a plane-wave decomposition method. However, it was not specified how to compute the scattering matrices for the range-dependent surfaces, although for the case of a sloping interface, a simple shifting matrix yielded accurate results.[1] In Ref. 2 perturbation theory was used to compute the transmission matrix for a rough seabed. In this paper we use the Rayleigh hypothesis, that is, we make assumptions about the scattered field consisting solely of up- or down-going waves, to solve efficiently the scattering problem at rough interfaces. The Rayleigh hypothesis has been used previously and studied numerically and theoretically[3,4] in the context of scattering from rough surfaces. In computational work, using a methodology almost identical to that of this paper, Koketsu *et al.*[5] used the Rayleigh hypothesis in conjunction with invariant embedding to consider scattering and transmission through range-dependent layers for some geophysical problems. In this paper, we consider propagation geometries and frequencies more related to underwater acoustics waveguides to investigate the potential of this method.

The method of this paper uses expansions in terms of plane waves to solve propagation/scattering problems. There are other possible expansion sets. In Ref. 6, Murphy *et al.* used expansions of wave fields in terms of point sources (line sources in two-dimensions) with unknown complex coefficients and, as in this paper, invoked continuity conditions at points along the seabed interface in order to determine these coefficients (and hence the total wave field in the waveguide).

The Rayleigh hypothesis makes assumptions about the vertical plane-wave components of the scattered wave field, but there is no division with respect to right- and left-going energy. Thus backscattered energy is automatically included in the numerical solution. Using the Rayleigh hypothesis to solve waveguide propagation/scattering problems is certainly not the only, nor, perhaps, the most efficient method for our computational examples, but it does handle three difficult problems in underwater acoustics modeling in an unified fashion: (1) range dependence; (2) elasticity; (3) backscatter. When combined with the invariant embedding method[1,5] it can handle any number of rough interfaces and also the problem of a scattering object in the waveguide.

In this paper we consider the water column to be isovelocity. In fact, this is probably not necessary. If the refractive index squared is linear near the interfaces, then one could use Airy functions rather than plane waves to describe the vertical propagation of the energy; or, perhaps, simply taking the profile to be isovelocity near the scattering interface or object would be sufficiently accurate. The propagation of the wave field between a set of interfaces, when the intervening sound speed profile varies vertically, could be described by a propagator matrix and the theory described below could be easily modified to handle these cases.

I. THEORY

We first consider a single range-dependent interface between water and an underlying sediment. In the water the incident compressional potential is taken to have the form of a plane wave,

$$\phi_p^{\mathrm{inc}} = \exp(i(k_x x + \gamma z)) \tag{1}$$

and we will write for the scattered field in the water column,

$$\phi^w = \sum_{n=-N}^{N} a_n \exp(i(k_n x + \gamma_{n,w} z)). \tag{2}$$

In the sediment, the compressional and shear potentials have the form

$$\phi^{\mathrm{sed}} = \sum_{n=-N}^{N} b_n \exp(i(k_n x - \gamma_{n,p} z)), \tag{3}$$

and

$$\psi^{\mathrm{sed}} = \sum_{n=-N}^{N} c_n \exp(i(k_n x - \gamma_{n,s} z)), \tag{4}$$

a)Now at: Defense Research Establishment Atlantic, P.O. Box 1012, Dartmouth, Nova Scotia B2Y 3Z7, Canada, Ph. (902)-426-3100 ext. 324, Fax: (902)-426-9654.

where

$$\gamma_{n,w} \equiv \sqrt{\omega^2/c_w^2 - k_n^2},$$
$$\gamma_{n,p} \equiv \sqrt{\omega^2/c_p^2 - k_n^2}, \quad \gamma_{n,s} \equiv \sqrt{\omega^2/c_s^2 - k_n^2}. \tag{5}$$

Here c_w and c_p denote the compressional sound speeds of the water and sediment, respectively; c_s denotes the sediment shear speed. The approximation we have made is that we have **assumed** that the scattered wave field consists only of an up-going spectrum in the water and only a down-going spectrum in the sediment.

In order to determine the unknown coefficients we will invoke the conditions of continuity of normal displacement and the normal component of traction at the interface, as well as the vanishing of the tangential component of traction. We impose this continuity at $K=2N+1$ discrete points $[x_k, z(x_k)]$ along the interface [i.e., the number of plane waves used in the expansions of Eqs. (2)–(4)]; the spacing is set at $\Delta x = \pi/\Delta k$, where Δk is determined from the relationship

$$\Delta k = \frac{k_{\max}}{N} \tag{6}$$

and $k_{\max}$ is the largest horizontal wave number considered computationally (chosen to be larger than ω/c_w). It is important to note that, although the continuity conditions are imposed at discrete points along the interface, the values of the interface derivatives used in the continuity equations are the values obtained from the analytic description of the interface; there are no stairstep approximations used.

From the continuity conditions and the vanishing of the tangetial component of traction at the seabed interface there is a system of $3K$ equations in $3K$ unknowns, which when solved yield the scattering coefficients. If this same system is solved for various incident wave numbers k_n then a generalized reflection matrix R^{du}, and transmission matrices for the compressional and shear potentials can be computed. Computationally, this means performing the LU decomposition of the system matrix once and solving for multiple right-hand sides. For the upper pressure release surface of the waveguide, there is only one set of unknown coefficients corresponding to down-going plane waves for the compressional potential in the water; these coefficients are determined by the condition that the scattered plus incident pressure should be equal to zero along this surface. For some computations, we will take this surface to be flat, in which case the upper reflection matrix is diagonal with the value of -1.

In order to understand the method used by Refs. 1 and 5 to compute the composite scattering matrix from individual scattering matrices, consider a down-going field, characterized by a vector of plane-wave coefficients $\mathbf{p}^{\text{inc}}$, incident upon the lower interface. This field undergoes a generalized reflection yielding an up-going wave field (we assume it is all up-going) which can be expressed in the form,

$$\mathbf{p}_1^u = R^B \mathbf{p}^{\text{inc}}, \tag{7}$$

where R^B denotes the scattering matrix for the lower interface. This up-going field is then reflected by the upper surface, becoming a down-going field incident upon the lower interface yielding the first multiple scattering component,

$$\mathbf{p}_2^u = R^B R^U R^B \mathbf{p}^{\text{inc}}, \tag{8}$$

where in Eq. (8) the generalized reflection from the upper surface is described by the matrix R^U, which also contains the appropriate two-way vertical phase difference from the reference level of the lower surface to the upper surface. In general there is an infinite number of multiple interactions between the lower and upper interfaces, so that the total vector of up-going plane-wave components is given by

$$\mathbf{p}^u = \left(I + \sum_{k=1}^{\infty} (R^B R^U)^k \right) R^B \mathbf{p}^{\text{inc}}. \tag{9}$$

Formally summing up this series we obtain

$$\mathbf{p}^u = (I - R^B R^U)^{-1} R^B \mathbf{p}^{\text{inc}}. \tag{10}$$

For a receiver below the source, the incident down-going components consist of the down-going components from the source $\mathbf{p}_d^{\text{inc}}$ and the initial up-going components $\mathbf{p}_u^{\text{inc}}$ after reflection from the top surface. Hence, Eq. (10) can be written

$$\mathbf{p}_u = (I - R^B R^U)^{-1} R^B (\mathbf{p}_d^{\text{inc}} + R^U \mathbf{p}_u^{\text{inc}}). \tag{11}$$

The vector of down-going components in the waveguide can then be expressed in terms of the up-going components and the incident field,

$$\mathbf{p}_d = \mathbf{p}_d^{\text{inc}} + R^U \mathbf{p}_u^{\text{inc}} + R^U \mathbf{p}^u. \tag{12}$$

There are similar expressions for a receiver above the source.

In the formulation discussed above, the Rayleigh hypothesis was invoked for the scattered field at the interface. In fact, we can include down-going plane waves in the expansion of Eq. (2) by using the condition at the upper interface to relate the up-going and down-going coefficients. For example, if the upper pressure release surface is flat then we can include up-going and down-going waves in our expansion with the condition that the coefficient a_n' for the down-going component is related to the up-going coefficient a_n by

$$a_n' = -\exp(2i\gamma_{n,w} L) a_n, \tag{13}$$

where L is the depth of the waveguide, so that the expansion in the water column can still be written entirely in terms of a_n. In terms of the reflection matrix computed in this manner $\tilde{R}^B$

$$\mathbf{p}_u = \tilde{R}^B (\mathbf{p}_d^{\text{inc}} + R^U \mathbf{p}_u^{\text{inc}}), \quad \mathbf{p}_d = R^U \mathbf{p}_u + (\mathbf{p}_d^{\text{inc}} + R^U \mathbf{p}_u^{\text{inc}}), \tag{14}$$

where R^U is diagonal with entries $-\exp(2i\gamma_w L)$.

It is also possible to include a scattering object in the waveguide by specifying its plane-wave scattering matrix and combining this matrix with the waveguide matrices.[1] In Ref. 1 it was shown how to analytically compute the scattering matrix for a cylinder.

II. NUMERICAL IMPLEMENTATION AND EXAMPLES

The numerical implementation is straightforward. We take a complex-valued contour of wave numbers of the form

$$k(t) = t - i\epsilon \sin(t\pi/\alpha) \tag{15}$$

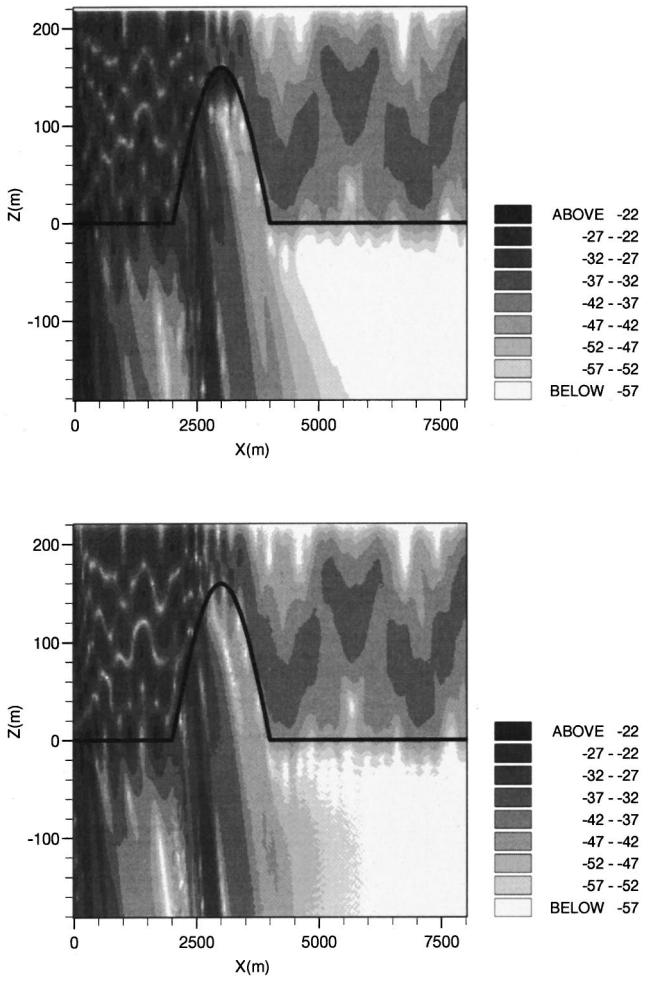

FIG. 1. A comparison of the two-dimensional fields computed by the Rayleigh hypothesis and FEPE.

for $-k_{\max} \leqslant t \leqslant k_{\max}$. The parameter ϵ is a small number (e.g., $\epsilon = f/20\,000$ seems to work well) and α is a number slightly bigger than $k_{\max}$. This contour is then sampled at $2N$ discrete points. These same wave numbers are used in the Rayleigh expansions at the interfaces. The reflection and transmission matrices for the interfaces are computed and the wave field in the waveguide constructed using Eqs. (11) and (12) or possibly Eq. (14). The relationship between the wave number discretization (or equivalently, the number of wave numbers) and the spatial extent of the computation approximately obeys the Nyquist sampling restriction.

A. Low-frequency propagation

In this first example we consider a waveguide 220 m deep with a ridge modeled by

$$z(x) = 160 \cos(x\pi/2000); \quad -1000 < x < 1000. \tag{16}$$

A 25-Hz source is located 10 m below the sea surface. The sediment in this example was taken to be fluid with $V_p = 2000$ m/s and $\rho = 1.5$ g/cm^3. In Fig. 1 we show the two-dimensional field computed by the Rayleigh-method and FEPE.[7]

For this example, we used the formulation which includes down-going plane waves in the expansion of the reflected wave field in the water column; however, there is very little difference between the results of this and the up-going only formulation. As can be seen, the agreement between the two methods is excellent. However, a slight problem with the Rayleigh expansion can be seen for the transmitted field at the peak of the bathymetry where the field values are too high. This problem may be due to the fact that only down-going waves are assumed in the sediment, whereas in terms of rays, a near horizontal ray in the water column could be sufficiently bent upward by transmission into the bathymetry to be up-going in direction.

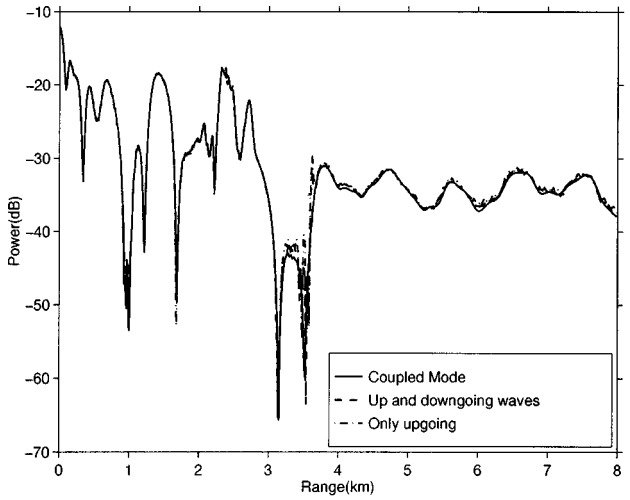

FIG. 2. A comparison of the transmission loss as computed by the Rayleigh method and COUPLE.

In Fig. 2 we show a comparison between the transmission loss for a receiver located at 135 m depth as computed by COUPLE[8] using the fully coupled solution and by the Rayleigh method with both of the formulations. There is excellent agreement between all three curves.

B. Elastic computations

We now consider an elastic sediment case. As a straightforward benchmark case, we first consider the bottom to be

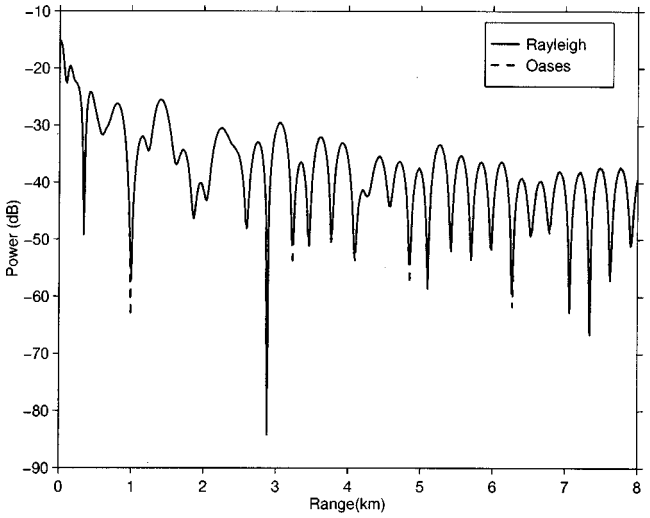

FIG. 3. A comparison of the transmission loss for an elastic bottom as computed by the Rayleigh method and OASES.

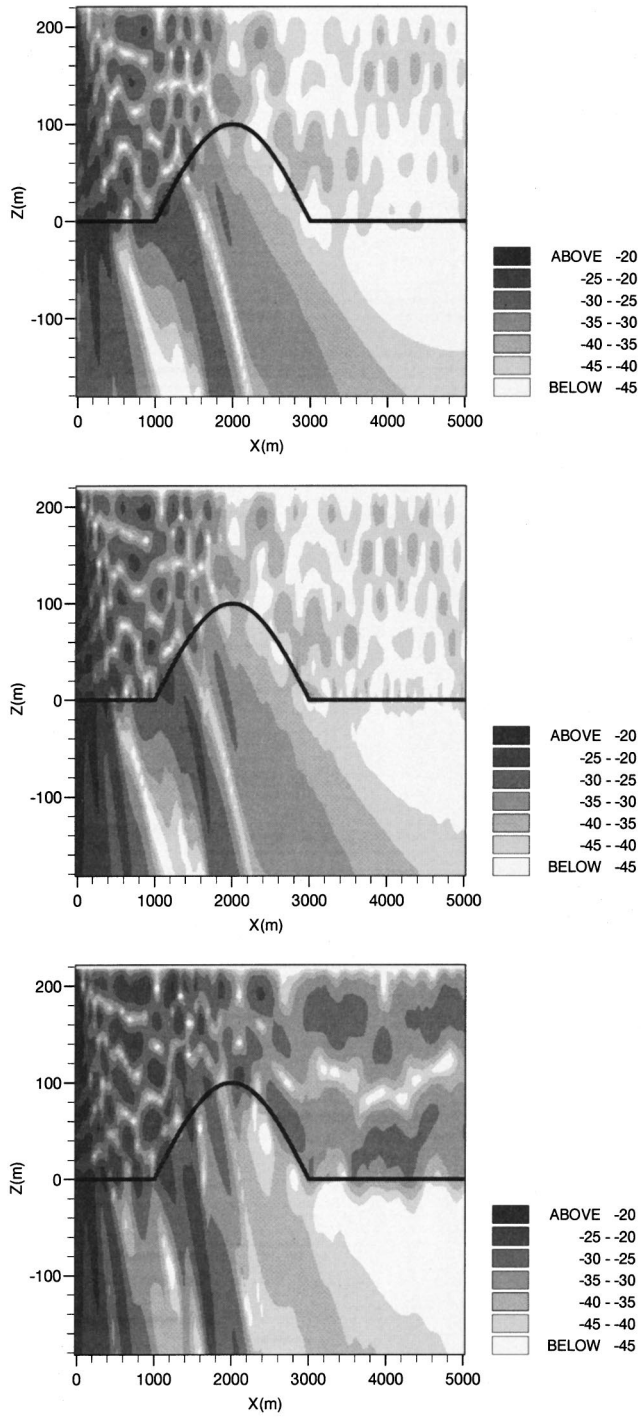

FIG. 4. A comparison of the two-dimensional fields computed by FEPES and the Rayleigh method for the elastic sediment and for $V_s = 10$ m/s.

flat; the bottom compressional speed is $V_p = 2000$ m/s, $V_s = 800$ m/s, and $\rho = 1.5$ g/cm^3. In Fig. 3 a comparison of the field as computed by OASES[9] and the Rayleigh method are presented. As can be seen the transmission loss curves are essentially identical. This example is not a test of the Rayleigh hypothesis, since the interface is flat, but does show that our matching conditions at the discrete spatial points yield accurate reflection coefficients.

In Fig. 4 a ridge 100 m high with a horizontal extent of 2000 m is introduced with the elastic properties as above. The first two plots show the compressional potential (scaled by the density) as computed by FEPES[10] and the Rayleigh results, respectively. The last plot shows the same bathymetry but for a shear speed of 10 m/s; the amount of energy making it past the ridge is significantly higher in this case.

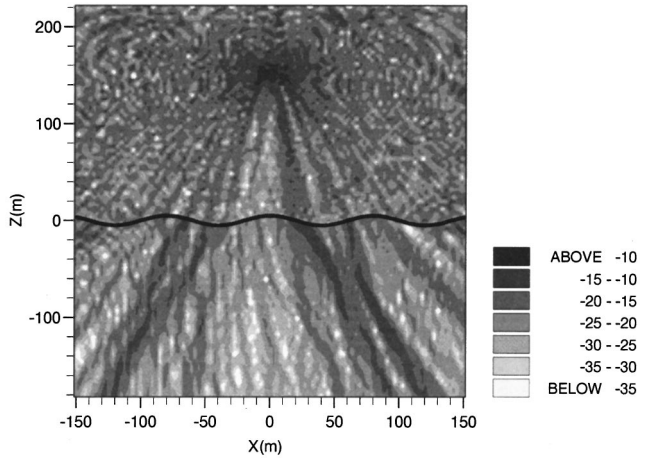

FIG. 5. Two-dimensional propagation loss for a rough elastic bottom and rough free surface for a 500-Hz point source.

C. Rough seabed and rough free surface

In this example the free surface has the form:

$$z_{\text{top}}(x) = 0.5 \sin(\pi x/40) \tag{17}$$

and the bottom surface has the form

$$z_{\text{bot}}(x) = 5.0 \cos(\pi x/40). \tag{18}$$

The sediment has the elastic parameters $v_p = 2400$ m/s, $v_s = 800$ m/s, and $\rho = 2.0$ g/cm^3. The compressional potential is shown in Fig. 5, for a 500-Hz point source located at 70 m depth. As can be seen the top and bottom have caused significant scattering within the waveguide, although the ''mean'' features of the wave field have remained intact.

D. Rough seabed, rough free surface, and scattering object

We now include a 3 m radius, solid steel cylinder in the waveguide. The full elasticity of the cylinder is accounted for by solving the fluid/elastic cylinder problem in free-space for the coefficients of the scattered Hankel functions; these coefficients are then used in the definition of the cylinder's plane-wave scattering matrix.[1,2] The point source is located 20 m to the left and above the cylinder. The source is located 60 m below the upper surface. In the first panel of Fig. 6 we show a 50×50 m section of the field scattered by the cylinder in free-space. Note that the spectral representation of the field along the horizontal axis passing through the center of the cylinder has poor convergence.

The shadow zone behind the cylinder is evident and the interference pattern between the incident and reflected fields can be seen on the front side of the cylinder. In the second panel the rough upper free surface has been added. This significantly changes the appearance of the field and the shadow zone behind the cylinder has more energy entering into it, although a shadow zone region can still be discerned. Fi-

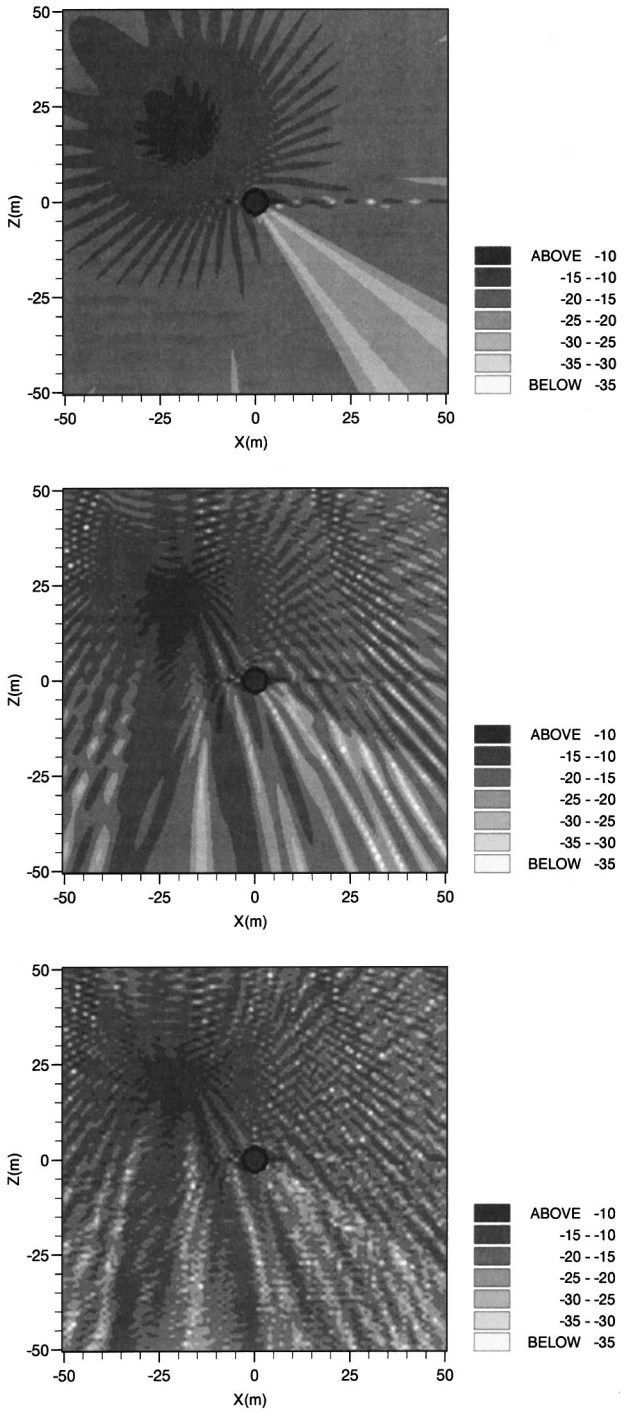

FIG. 6. Scattering from a 3 m radius steel cylinder for (a) free-space, (b) rough surface above (no bottom), (c) rough surface above and below for 500 Hz.

nally, in the last panel the bottom surface has been added in. This has the effect of distorting the wave field, but the mean characteristics of the field are the same as those of panel 2.

III. SUMMARY

We have shown that using the Rayleigh hypothesis allows one to accurately model acousto-elastic waveguides with significant range dependence. Also a scattering object can be easily included in the waveguide. There are situations of very strong range dependence where the method has some problems. Whether it is possible to improve the method in these cases by applying various constraints on the solution[4] or by using different expansion sets (such as that used by Ref. 6) would be an interesting area of research. Computationally, the method is efficient, particularly for the 500-Hz examples, where the solution for these smaller regions (but with significant variation of the top and bottom surfaces) took only about 262 s on an ALPHA Station 500.

The examples we consider all had an isovelocity water column; this restriction could be relaxed by using, for example, Airy function expansions in the vertical coordinate and accounting for a vertical profile in between the lower and upper surfaces of the water column.

[1] J. A. Fawcett, ''A plane-wave decomposition method for modeling scattering from objects and bathymetry in a waveguide,'' J. Acoust. Soc. Am. **100**, 183–192 (1996).
[2] J. A. Fawcett, ''Scattering from an elastic cylinder buried beneath a rough water/sediment interface,'' in *High Frequency Acoustics in Shallow Water*, Proceedings of a conference held in Lerici, Italy, 30 June–4 July 1997, edited by N. G. Pace, E. Pouliquen, O. Bergem and A. P. Lyons, SACLANTCEN Conference Proceedings CP-45, pp. 147–154, 1997.
[3] A. Purcell, ''The Rayleigh equations for a multi-sinusoidal periodic surface,'' J. Acoust. Soc. Am. **103**, 683–694 (1998).
[4] D. Berman and J. Perkins, ''Rayleigh method for scattering from random and deterministic surfaces,'' J. Acoust. Soc. Am. **88**, 1032–1044 (1990).
[5] K. Koketsu, B. L. N. Kennett, and H. Takenaka, ''2-D reflectivity method and synthetic seismograms for irregularly layered structures—II,'' Geophys. J. Int. **105**, 119–130 (1991).
[6] J. E. Murphy, G. Li, S. Chin-Bing, and D. King, ''Multifilament source model for short-range underwater acoustic problems involving penetrable ocean bottoms,'' J. Acoust. Soc. Am. **99**, 845–850 (1996).
[7] M. D. Collins, ''FEPE user's guide,'' NORDA TN-365, Naval Ocean Research and Development Activity, Stennis Space Center, MS (1988).
[8] R. B. Evans, ''A coupled mode solution for acoustic propagation in a waveguide with stepwise depth variation of a penetrable bottom,'' J. Acoust. Soc. Am. **74**, 188–195 (1983).
[9] H. Schmidt, ''OASES, Version 1.8—Application and Update Notes,'' 1996.
[10] M. D. Collins, ''Higher order Padé approximations for accurate and stable elastic parabolic equations with applications to interface wave propagation,'' J. Acoust. Soc. Am. **89**, 1050–1057 (1991).

Acoustic tomography of a coastal front in Haro Strait, British Columbia

P. Elisseeff and H. Schmidt
Department of Ocean Engineering, Massachusetts Institute of Technology, Cambridge, Massachusetts 02139

M. Johnson and D. Herold
Applied Ocean Physics and Engineering Department, Woods Hole Oceanographic Institution, Woods Hole, Massachusetts 02543

N. R. Chapman and M. M. McDonald
Centre for Earth and Ocean Research, University of Victoria, Victoria, British Columbia V8W 2Y2, Canada

(Received 24 March 1997; revised 11 February 1999; accepted 6 March 1999)

An experiment validating the concept of acoustically focused oceanographic sampling (AFOS) was recently implemented in Haro Strait, British Columbia (Canada). Four 16-element vertical receiver arrays were moored around the location of a coastal front driven by estuarine and tidal forcing. Various signals were transmitted from array to array and from a moving source to the arrays over a period of five weeks. Tomographic signals were transmitted over a wide frequency band (150 Hz to 15 kHz). The novelty of the Haro Strait data set resides in its unusual tomographic features: ranges are short (less than 3 km), sound speed perturbations are small (2 to 3 m/s), and currents are relatively strong (3.5 kts). Light-bulb-generated wideband acoustic signals are used in this paper in conjunction with local nonacoustic measurements in order to image the three-dimensional sound speed and current fields within the water mass enclosed by the moored arrays. The combined use of integral and local data leads to a significant decrease of the field estimate uncertainty while maintaining a coverage of the area not achievable by nonacoustic means. [S0001-4966(99)00307-0]

PACS numbers: 43.30.Pc, 43.60.Rw [SAC-B]

INTRODUCTION

Ocean acoustic tomography was suggested two decades ago as a means of performing large-scale measurement of oceanographic quantities such as temperature and current in deep ocean.[1] Its feasibility has since been repeatedly demonstrated.[2–7] A number of studies have been made in order to adapt deep ocean methods to coastal environments, in which shallow water propagation and high environmental variability make the inversion significantly more difficult.[8–11] While coastal tomography remains a topic of active research, recent developments in wireless communication technology combined with significant increases in computing power have opened the way to acoustically focused oceanographic sampling (AFOS).[12] The AFOS consists of a network of acoustic arrays connected to a fleet of autonomous underwater vehicles (AUV) and to a shore station using wireless local area network technology. Nonacoustic moorings may be integrated in the network as additional nodes when available. A real-time field estimate of temperature or current in the region of interest is computed by combining the various integral and local data sets available. Integral, synoptic data is provided by the acoustic tomographic inversion while nonacoustic sensors yield local point measurements. The real-time field estimate and its associated error field are then used to adaptively direct AUVs towards regions where high resolution is required due to large gradients or large uncertainties. The AFOS provides *rapid environmental assessment*, which is important for coastal oceanography and operation of naval systems.

In this context a feasibility experiment was recently performed in Haro Strait, British Columbia.[13] Its first objective was to test the available technology when integrated into a single network. Its second objective was to demonstrate the scientific relevance of AFOS by investigating mixing mechanisms in the highly active Haro Strait region. Four 16-element vertical receiver arrays were moored south of Stuart Island around the location of a coastal front driven by estuarine and tidal forcing (see Fig. 1). Four nonacoustic moorings were located around the acoustic network, measuring local current, temperature, and salinity. An extensive and varied acoustic data set was generated in the course of five weeks (June–July 1996). Tomographic signals were transmitted over a wide frequency band (150 Hz to 15 kHz). The novelty of the Haro Strait data set resides in its unusual tomographic features: ranges are short (less than 3 km), sound speed perturbations are small (2–3 m/s), and currents are relatively strong (up to 5 kts). Operational constraints place stringent demands on the oceanic field estimate provided by AFOS. Its computational load must be light enough, namely of the order of a few minutes at most. The inversion must be able to withstand large environmental uncertainties as well as accommodate a wide variety of data sets. In order to satisfy the robustness constraint, classical deep ocean travel time tomography and oceanographic data assimilation tech-

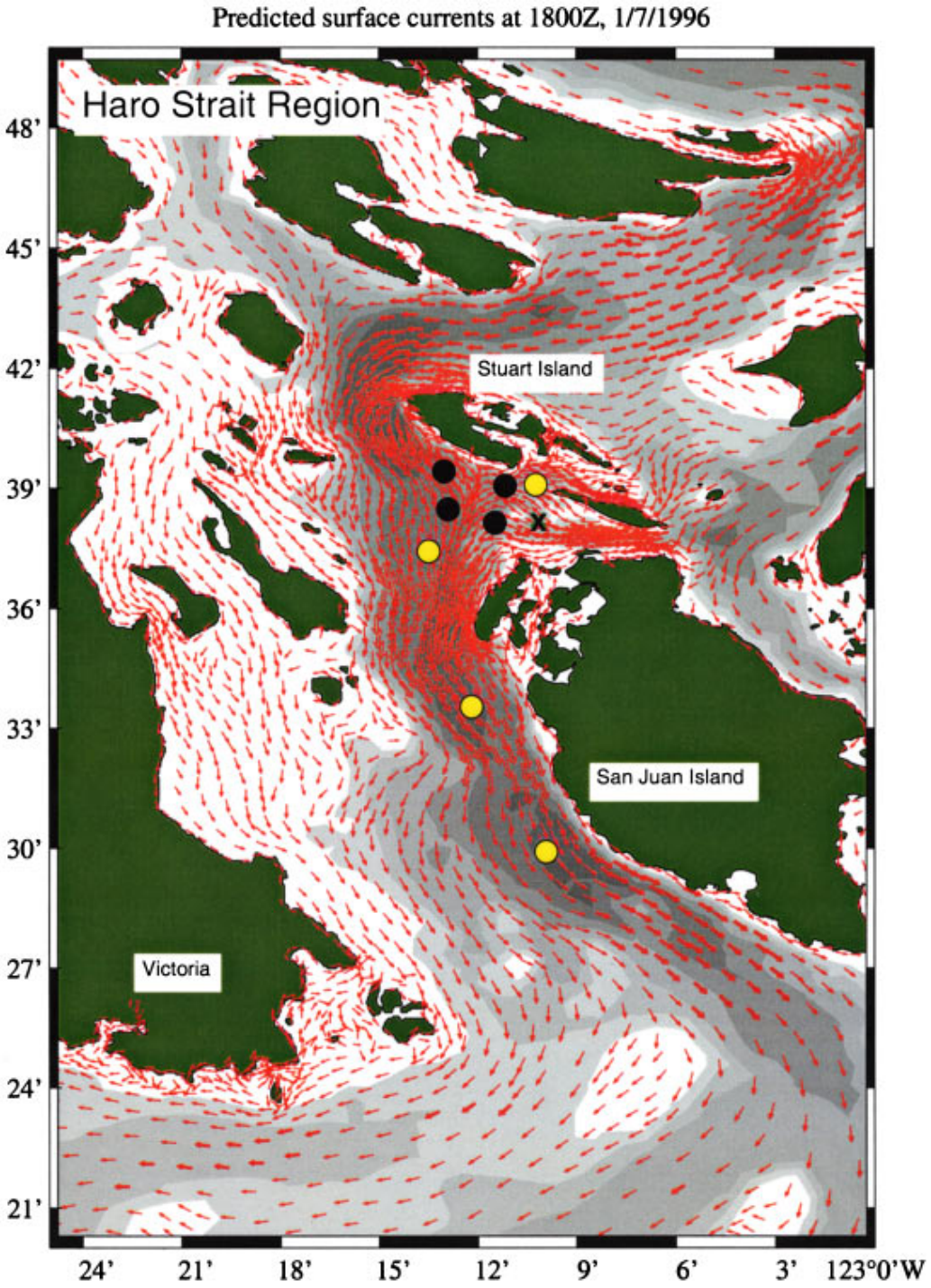

FIG. 1. Topographic map of the Haro Strait region with predicted ebb tide currents during the experiment. Tomographic arrays (black circles) were deployed to investigate the front south of Stuart island. Current meter moorings (yellow circles) and a meteorological surface buoy (black cross) will help clarify the larger-scale circulation (courtesy of R. Pawlowicz, IOS).

niques are combined in this paper and adapted to the Haro Strait environment. While these techniques are not new in themselves, the combined use of interdisciplinary models and data sets in the context of coastal ocean imaging raises several issues as of yet unresolved. Resolution and parameter sensitivity of the various models, for instance, have been shown to be critical factors in successfully coupling oceanographic and acoustic models.[14] The possible gains from jointly extracting environmental information from integral and local data sets, while heuristically and qualitatively clear, are still hardly quantified. Furthermore, the integration of synoptic acoustic estimates with nonacoustic data sets and models in coastal environments remains a topic of active research.[15,16]

Far from exhaustively answering the above issues, this paper proposes to explore the analytical and quantitative aspects involved in the combination of multiple data sets, both integral and local, in the operational setting of the Haro Strait experiment. The experimental configuration is described in the next section. The combined inversion formalism is devel-

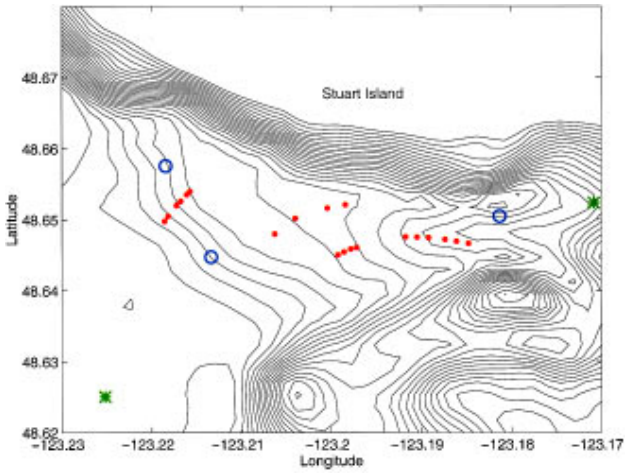

FIG. 2. Bathymetric map of the experimental site. Contours are 10 m apart. Blue circles: WHOI receiver arrays. Green starts: IOS moorings. Red dots: source locations.

oped in the following section. Numerical results, including synthetic data as well as Haro Strait data, are presented in Sec. III.

I. BACKGROUND

A. Experimental configuration

Four vertical acoustic line arrays (hereafter called WHOI moorings) were initially deployed south of Stuart island (see Figs. 1 and 2). The southeastern mooring, located near Danger Shoal, was lost at an early stage of the experiment because of unexpectedly strong tidal currents. Each mooring consisted of 16 receivers, a 1.5-kHz tomographic source, and a 15-kHz communication source (see Fig. 3). A chain of thermistors was added to moorings NW and NE. The acoustic data acquired on each receiver array were sent back to shore via a surface radio link at a rate of 35 kbauds.

Four nonacoustic moorings (hereafter referred to as IOS moorings) were deployed along the Haro Strait channel (see Fig. 1). Local temperature, salinity, current magnitude, and current direction were recorded by these moorings at discrete depths. Only the two IOS moorings closest to the network of

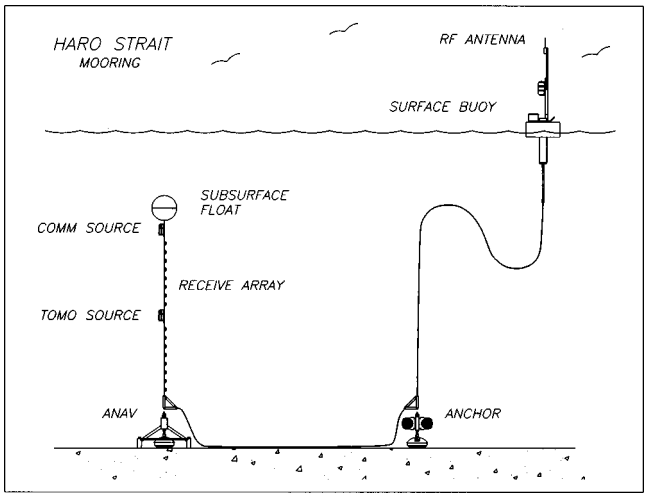

FIG. 3. Haro Strait mooring design.

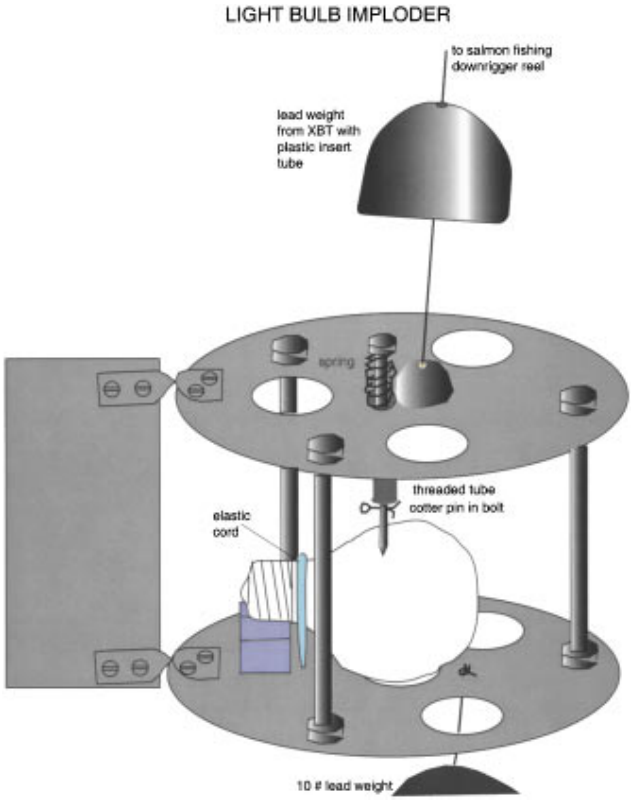

FIG. 4. Source design.

acoustic arrays are used in this analysis. The IOS mooring sensors were located at a depth of 25, 70 (SW only), and 120 m. During the 2-h time period studied in this paper, current magnitudes of up to 3.5 kts and temperatures variations of up to 1.5 °C were observed.

The moving source used in this paper consisted of ship-deployed light bulbs. Source locations were obtained using differential Global Positioning System (GPS) data, and the locations corresponding to the shots used in this paper are shown in Fig. 2. These shots were recorded on all three moorings, and were all deployed within a time period of approximately 90 mins. Source depths ranged from 30 to 70 m. Source levels were approximately 160 to 170 dB//1 μPa. The light bulbs were lowered to a specified depth in the casing apparatus shown in Fig. 4. The shot was then triggered by breaking the bulb at depth using an operator-released lead mass that dropped along the cable from the ship to the casing. Light bulbs generate a short reproducible bubble pulse waveform whose spectral peak is typically about 500 Hz at a depth of 50 m, with a 3-dB bandwidth of approximately 300 Hz. Although there is significant spectral content to several kHz, the band was limited in this experiment by the relatively low sampling frequency of 1750 Hz. An example of the raw acoustic signal from one of the light bulbs is shown in Fig. 5.

B. Data conditioning

Individual acoustic time series were match filtered using a single arrival as a substitute for the actual source signal. Absolute timing was provided by the acoustic acquisition system.[17] The magnitude of the matched filter output was

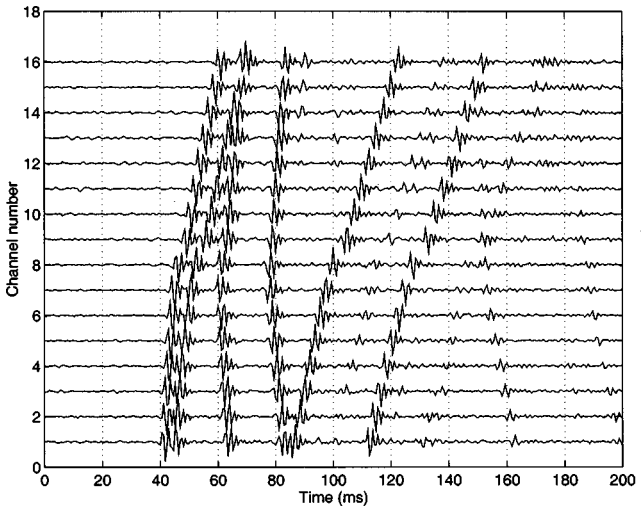

FIG. 5. Raw time series: shot 32, 20 June 1996 02:43 GMT, SW WHOI mooring.

then low-pass filtered using a zero-phase third-order Butterworth filter with a cutoff frequency of 500 Hz. Direct and surface ray arrival times were subsequently measured by identification of the corresponding local maxima of the filtered time series (see Fig. 6). Acoustic sensor localization was carried out by minimizing the mean square difference between the measured arrival times and the arrival times predicted using the sensor model described in Sec. II A.

Raw temperature, salinity, and current time series were measured by the IOS moorings at a frequency of 12 samples per hour. Temperature and salinity were converted to sound speed using Mackenzie's formula.[18] Individual samples were grouped by 50-min bins and averaged. Standard deviations were found to be between 6 and 13 cm/s for the current field, and 1 and 25 cm/s for the sound speed field.

II. ANALYSIS

In order to combine heterogeneous data sets, a variety of observation models is required. Acoustic sensor displacements are accounted for by a sensor model. This model relates acoustic sensor displacements to array design parameters and local current magnitude at the array. The current model provides predictions of the tidal current field at any point in the observed region. The acoustic model relates sound speed to acoustic travel times. Statistical field estimates provide *a priori* information on the actual field estimates. *A posteriori* current information is provided by local current measurements and acoustic sensor displacements. *A posteriori* sound speed information is provided by local sound speed measurements and acoustic tomographic data. In a first stage an estimate of the current field is computed by objective analysis of the available current data.[19] The current estimate is then externally melded with the tidal current model prediction following a standard data assimilation procedure. The sound speed field is then objectively analyzed using range-averaged acoustic tomographic estimates and local nonacoustic data.

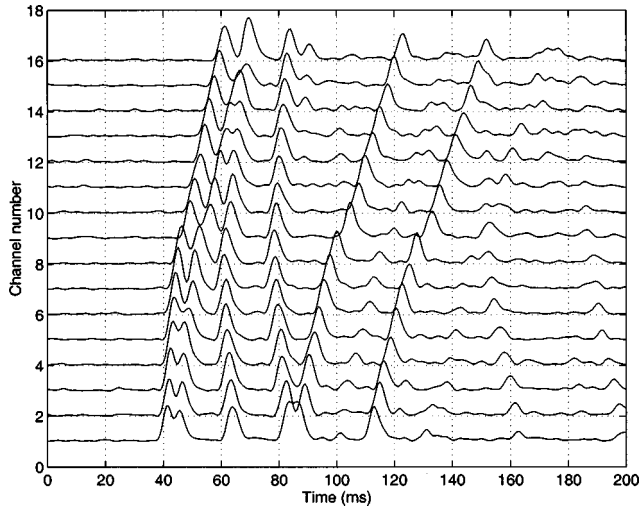

FIG. 6. Filtered time series: shot 32, 20 June 1996 02:43 GMT, SW WHOI mooring.

A. Observation models

1. Sensor model

The horizontal displacements of a moored line array placed in a uniform flow can be expressed as[20]

$$\boldsymbol{\delta r} = a\left[z - b\,\ln\left(1 - \frac{z}{c}\right)\right]\boldsymbol{\nu} = a f(z)\,\boldsymbol{\nu} \tag{1}$$

where $\boldsymbol{\nu}$ is a unit vector in the direction of the flow,

$$a = \frac{d}{w}, \tag{2}$$

$$b = \frac{D}{d} - \frac{W}{w}, \tag{3}$$

$$c = \frac{W}{w} + L, \tag{4}$$

d is the cable drag per unit length, w is the cable weight per unit length, D is the drag of the subsurface buoy, W is the buoyancy of the subsurface buoy, and L is the total length of the cable. The coefficients b and c are true constants which depend on the design of a given array. The coefficient a depends quadratically on current magnitude and may be more conveniently expressed as $a = \alpha U^2$, where U is the current magnitude at the location of the array. An acoustic transmission in the horizontal direction $\mathbf{p}$ will then be affected by the projection δR of the array displacements in that direction:

$$\delta R = a f(z)(\boldsymbol{\nu}^T \mathbf{p}). \tag{5}$$

Let us now assume the uniform current $\mathbf{U}$ at the array can be decomposed into a reference state $U_o \boldsymbol{\nu}$ and a perturbation $\mathbf{u}'$. Let us further assume the term $\boldsymbol{\nu}^T \mathbf{p}$ is included in a. The coefficient a can then be expressed as

$$a = a_o + a' = a_o + 2\alpha U_o (\boldsymbol{\nu}^T \mathbf{p}) \boldsymbol{\nu}^T \mathbf{u}', \tag{6}$$

where the subscript o refers to the reference state and second-order terms have been neglected. In the case of short-range transmissions, an acoustic estimate $\tilde{a}$ of a' can be easily computed by minimizing the mean square error between measured ray arrival times at the array and their the-

oretical value using an adequate sound speed profile (uniform or historical average) and a reference current vector $U_o\boldsymbol{\nu}$. The measured array shape perturbation can be written as

$$\tilde{a}=2\alpha(\boldsymbol{\nu}^T\mathbf{p})\boldsymbol{\nu}^T\mathbf{u}'+n_a, \tag{7}$$

where the noise term n_a is assumed to be Gaussian. Equation (7) establishes a direct linear relationship between the measured value $\tilde{a}$ and the current perturbation $\mathbf{u}'$ at the array.

2. Current model

An accurate three-dimensional, baroclinic (depth-dependent) finite-element model of tidal currents in the Haro Strait region was recently developed by Foreman *et al.*[21] In order to decrease the computational load involved in predicting local currents, a two-dimensional, barotropic (depth-independent) version of Foreman's model is used in this paper. The latter model is able to properly account for 90% of the tidal flow variance at the SW IOS mooring and 72% at the NE IOS mooring in Haro Strait. For the purpose of this analysis, Foreman's model can be summarized as

$$\mathbf{U_o}=g(\mathbf{r},t), \tag{8}$$

where $\mathbf{U_o}$ is the predicted tidal current at the location $\mathbf{r}$ at the time t. The predicted field is used throughout the analysis as the background field. The current perturbation $\tilde{\mathbf{u}}$ measured by the IOS current meters can be related to the true value $\mathbf{u}'$ as

$$\tilde{\mathbf{u}}=\mathbf{u}'+\mathbf{n}_{u,cm}, \tag{9}$$

where the measurement noise vector $\mathbf{n}_{u,cm}$ is assumed to be Gaussian.

3. Acoustic model

For a given source–receiver geometry acoustic travel times perturbations $\boldsymbol{\tau}$ can be related to sound speed perturbations by the following linear expression:[7]

$$\boldsymbol{\tau}=\mathbf{E}\mathbf{c}'+\mathbf{n}_{u,a}, \tag{10}$$

where the noise vector $\mathbf{n}_{u,a}$ is assumed to be Gaussian of covariance matrix $\mathbf{R}_{nn}^{(a)}$. In order to reduce the number of degrees of freedom of the original inverse problem the range-independent sound speed perturbation $\delta c(z)$ is decomposed using an arbitrary set of orthogonal functions:

$$\delta c(z)=\phi(z)^T\mathbf{c}'. \tag{11}$$

In the present paper the functions $\phi_j(z)$ are assumed to be ''gate'' functions, set to zero everywhere except within a specified depth interval $[z_j,z_{j+1}]$ where it is set to unity. These depth intervals are nonoverlapping and cover the entire water column (from 0 to 200 m). The matrix $\mathbf{E}$ can then be expressed as

$$[\mathbf{E}]_{ij}=-\int_{\text{ray}\#i}\frac{\phi_j(z_i)}{c_o^2(r_i,z_i)}\,ds_i, \tag{12}$$

where c_o is the background sound speed profile. The range r_i and depth z_i along the ith ray are an implicit function of the ray curvilinear abscissa s_i.

B. Inversion formalism

1. Current inversion

Three types of information can be combined in the estimation of the current field: point measurements of current at the two IOS moorings, array shape acoustic estimates at the three WHOI moorings, and *a priori* predictions by Foreman's model. The available point measurements of current can be consolidated through Eq. (9) as

$$\begin{bmatrix}\tilde{\mathbf{u}}_{x,cm}\\ \tilde{\mathbf{u}}_{y,cm}\end{bmatrix}=\begin{bmatrix}\mathbf{I} & \mathbf{O}\\ \mathbf{O} & \mathbf{I}\end{bmatrix}\begin{bmatrix}\mathbf{u}'_{x,cm}\\ \mathbf{u}'_{y,cm}\end{bmatrix}+\begin{bmatrix}\mathbf{n}_{x,cm}\\ \mathbf{n}_{y,cm}\end{bmatrix}, \tag{13}$$

where the x subscript refers to the east/west direction and the y subscript refers to the north/south direction. Similarly, the array shape data can be consolidated using Eq. (7) as

$$\tilde{\mathbf{a}}=[\mathbf{H}_1\quad\mathbf{H}_2]\begin{bmatrix}\mathbf{u}'_{x,a}\\ \mathbf{u}'_{y,a}\end{bmatrix}+\mathbf{n}_a. \tag{14}$$

The matrices $\mathbf{H}_1$ and $\mathbf{H}_2$ are both diagonal and

$$[\mathbf{H}_1]_{jj}=2\alpha_j(\boldsymbol{\nu}_j^T\mathbf{p}_j)\nu_{j,x}, \tag{15}$$

$$[\mathbf{H}_2]_{jj}=2\alpha_j(\boldsymbol{\nu}_j^T\mathbf{p}_j)\nu_{j,y}. \tag{16}$$

The term α_j corresponds to the shape factor α of the acoustic array involved in the jth transmission. Combining (13) and (14) leads to the global observation model of the current field:

$$\begin{bmatrix}\tilde{\mathbf{u}}_{x,cm}\\ \tilde{\mathbf{u}}_{y,cm}\\ \tilde{\mathbf{a}}\end{bmatrix}=\begin{bmatrix}\mathbf{I} & \mathbf{O} & \mathbf{O} & \mathbf{O} & \mathbf{O} & \mathbf{O}\\ \mathbf{O} & \mathbf{O} & \mathbf{O} & \mathbf{I} & \mathbf{O} & \mathbf{O}\\ \mathbf{O} & \mathbf{H}_1 & \mathbf{O} & \mathbf{O} & \mathbf{H}_2 & \mathbf{O}\end{bmatrix}\begin{bmatrix}\mathbf{u}'_{x,cm}\\ \mathbf{u}'_{x,a}\\ \mathbf{u}'_{x,i}\\ \mathbf{u}'_{y,cm}\\ \mathbf{u}'_{y,a}\\ \mathbf{u}'_{y,i}\end{bmatrix}+\begin{bmatrix}\mathbf{n}_{x,cm}\\ \mathbf{n}_{y,cm}\\ \mathbf{n}_a\end{bmatrix}, \tag{17}$$

where $\mathbf{u}'_{x,i}$ and $\mathbf{u}'_{y,i}$ represent the current field perturbation interpolated at the nodes of a specified grid. Equation (17) can be recast in a more compact format as

$$\tilde{\mathbf{u}}=\mathbf{H}\mathbf{u}'+\mathbf{n}_u. \tag{18}$$

The covariances matrices $\mathbf{R}_{uu}$ of $\tilde{\mathbf{u}}$ and $\mathbf{R}_{nn}$ of $\mathbf{n}_u$ can be computed using the space–time correlation function of the current field (see the Appendix). The empirical estimation of this correlation function is discussed in the next section. Equation (18) can then be inverted as[22,7]

$$\hat{\mathbf{u}}'=\mathbf{K}_u\tilde{\mathbf{u}}, \tag{19}$$

where the gain matrix $\mathbf{K}_u$ is given by

$$\mathbf{K}_u=\mathbf{R}_{uu}\mathbf{H}^T(\mathbf{H}\mathbf{R}_{uu}\mathbf{H}^T+\mathbf{R}_{nn})^{-1}. \tag{20}$$

The associated error covariance matrix of the current perturbation estimate is[7]

$$\mathbf{P}_u=(\mathbf{I}-\mathbf{K}_u\mathbf{H})\mathbf{R}_{uu}. \tag{21}$$

This concludes the first stage (objective analysis) of the current data assimilation procedure.

The current perturbation estimate $\mathbf{u}'$ can then be merged with the model prediction using the following melding

scheme. The final field estimate at a given node $\mathbf{r}$ for a given component is assumed to be a linear combination of the predicted field and the measured field:[16]

$$\hat{U}(\mathbf{r}) = (1-\lambda(\mathbf{r}))U_o(\mathbf{r}) + \lambda(\mathbf{r})(U_o(\mathbf{r}) + \hat{u}'(\mathbf{r})). \tag{22}$$

The north/south and east/west components are melded independently of each other. Based on the statistical properties of the model and measurement errors a minimum variance estimate of λ can be derived:[16]

$$\lambda_{\mathrm{MV}}(\mathbf{r}) = \frac{\sigma_m^2(\mathbf{r}) - \rho(\mathbf{r})\sigma_m(\mathbf{r})\sigma_d(\mathbf{r})}{\sigma_m^2(\mathbf{r}) + \sigma_d^2(\mathbf{r}) - 2\rho(\mathbf{r})\sigma_m(\mathbf{r})\sigma_d(\mathbf{r})}, \tag{23}$$

where $\sigma_m(\mathbf{r})$ is the estimated error of the model prediction $U_o(\mathbf{r})$, $\sigma_d(\mathbf{r})$ is the error of the data-based perturbation estimate $\hat{u}'(\mathbf{r})$, and $\rho(\mathbf{r})$ is the correlation between the two. The measurement error $\sigma_d(\mathbf{r})$ is given by the relevant diagonal term of $\mathbf{P}_u$ in Eq. (21). In the absence of an accurate error model of the current prediction made by Foreman's model, the optimal interpolation scheme used by the Harvard Ocean Prediction System is adopted:[23]

$$\lambda_{\mathrm{OI}}(\mathbf{r}) = \frac{\sigma_{\max} - \sigma_d(\mathbf{r})}{\sigma_{\max} - \sigma_{\min}}, \tag{24}$$

where $\sigma_{\min}$ and $\sigma_{\max}$ are the minimum and maximum values of $\sigma_d(\mathbf{r})$. The melded estimate is therefore equal to the model prediction at points where the measurement error is maximal, and is set equal to the measured estimate at point where the measurement error is minimal. The robustness of this melding scheme was demonstrated in several oceanographic data assimilation experiments.[23]

2. Sound speed inversion

Two types of information can be combined in the estimation of the sound speed field: point measurements of sound speed at the two IOS moorings and acoustic travel times measured at the three WHOI moorings. This is done in two stages: first the acoustic travel times are used to estimate range-averaged sound speed profiles and their error covariance along the available transmission tracks. These sound speed profiles are then merged with the point measurements and interpolated in order to yield an estimate of the sound speed field.

The covariance matrix $\mathbf{R}_{cc}^{(a)}$ of the sound speed perturbation in Eq. (10) can be estimated using the space–time correlation function of the sound speed field (see the Appendix). The empirical estimation of this correlation function is discussed in the next section. Equation (10) can then be inverted as[7]

$$\hat{\mathbf{c}}' = \mathbf{K}_c^{(a)}\boldsymbol{\tau}, \tag{25}$$

where the gain matrix $\mathbf{K}_c^{(a)}$ is given by

$$\mathbf{K}_c^{(a)} = \mathbf{R}_{cc}^{(a)}\mathbf{E}^T(\mathbf{E}\mathbf{R}_{cc}^{(a)}\mathbf{E}^T + \mathbf{R}_{nn}^{(a)})^{-1}. \tag{26}$$

The associated error covariance matrix of the range-averaged sound speed estimate is[7]

$$\mathbf{P}_c^{(a)} = (\mathbf{I} - \mathbf{K}_c^{(a)}\mathbf{E})\mathbf{R}_{cc}^{(a)}. \tag{27}$$

The range-averaged sound speed estimate at a given depth z_o can be expressed as

$$\hat{c}'(z_o) = \int_0^1 \beta(\mathbf{r}_{\mathrm{src}}, \mathbf{r}_{\mathrm{rcv}}, z_o, \eta) c'(\mathbf{r}_{\mathrm{src}} + \eta(\mathbf{r}_{\mathrm{rcv}} - \mathbf{r}_{\mathrm{src}}))\, d\eta, \tag{28}$$

where $\mathbf{r}_{\mathrm{src}}$ and $\mathbf{r}_{\mathrm{rcv}}$ are the source and receiver locations and c' is the true sound speed perturbation. The weighting or ray sampling function β is given by

$$\beta(\mathbf{r}_{\mathrm{src}}, \mathbf{r}_{\mathrm{rcv}}, z_o, \eta) = \beta_o \sum_i \frac{\phi_j(z_i)}{\cos\theta_i}, \tag{29}$$

where β_o is a normalization factor such that $\beta(\eta)$ integrates to one between 0 and 1. The term ϕ_j is the orthogonal function of Eq. (12) corresponding to the depth bin z_o. The sum is performed over all rays joining the source and the array of receivers. The local ray depth z_i and the local ray grazing angle θ_i are implicit functions of η. The weighting function β is equal to 1 for a source and a receiver located at the same depth in the absence of boundary interaction. The acoustic profile estimates of several transmissions can be consolidated for a given depth as

$$\tilde{\mathbf{c}}_a = \mathbf{F}\mathbf{c}_i' + \mathbf{n}_{c,a}, \tag{30}$$

where $\mathbf{c}_i'$ is the interpolated sound speed field on a specified grid and $\mathbf{n}_{c,a}$ represents additive Gaussian noise. The matrix $\mathbf{F}$ is given by

$$[\mathbf{F}]_{kj} = \beta(\mathbf{r}_{\mathrm{src}}^{(k)}, \mathbf{r}_{\mathrm{rcv}}^{(k)}, z_o, \eta_j^{(k)})\Delta\eta_j^{(k)}, \tag{31}$$

where $\mathbf{r}_{\mathrm{src}}^{(k)}$ and $\mathbf{r}_{\mathrm{rcv}}^{(k)}$ are the end points of the kth transmission, $\eta_j^{(k)}$ is the local nondimensional range corresponding to the jth node of the global interpolated grid $\mathbf{c}_i$, and $\Delta\eta_j^{(k)}$ is the nondimensional length of the jth cell intercepted by the ray considered.

Similarly to what was done for the current data, the sound speed perturbation $\tilde{\mathbf{c}}$ measured by the IOS moorings at various times can be related to the true perturbation $\mathbf{c}'$ as

$$\tilde{\mathbf{c}}_{cm} = \mathbf{c}_{cm}' + \mathbf{n}_{c,cm}, \tag{32}$$

where the measurement noise vector $\mathbf{n}_{c,cm}$ is assumed to be Gaussian. Equations (30) and (32) can combined to yield

$$\begin{bmatrix} \tilde{\mathbf{c}}_{cm} \\ \tilde{\mathbf{c}}_a \end{bmatrix} = \begin{bmatrix} \mathbf{I} & \mathbf{O} \\ \mathbf{O} & \mathbf{F} \end{bmatrix} \begin{bmatrix} \mathbf{c}_{cm}' \\ \mathbf{c}_i' \end{bmatrix} + \begin{bmatrix} \mathbf{n}_{c,cm} \\ \mathbf{n}_{c,a} \end{bmatrix}, \tag{33}$$

which can, in turn, be recast in the more compact form

$$\tilde{\mathbf{c}} = \mathbf{G}\mathbf{c}' + \mathbf{n}_c. \tag{34}$$

Equation (34) can be inverted using the method outlined for Eq. (18). Particular attention must be paid to the covariance matrix of $\tilde{\mathbf{c}}$. As pointed out by Cornuelle and Worcester, the covariance matrix of acoustic sound speed estimates is often nondiagonal and significant errors can be induced by neglecting covariance terms.[24] The present method allows these covariance terms to be taken into account by simply inserting the relevant terms of $\mathbf{P}_c^{(a)}$ [Eq. (27)] into the covariance matrix of $\tilde{\mathbf{c}}$ (see the Appendix). In the case of the Haro Strait data set, the absence of a known source transmission time made it necessary to include a global acoustic sound speed

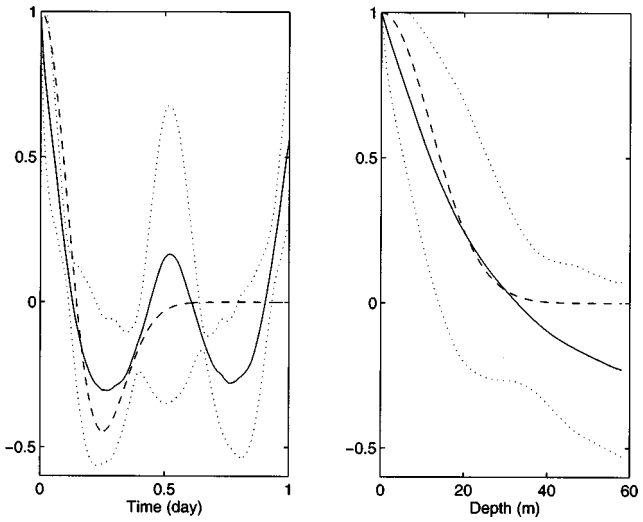

FIG. 7. Sound speed correlation function. Left panel: temporal correlation (IOS mooring data). Right panel: correlation in depth (CTD data). Solid line: average measured correlation. Dotted line: 95% confidence interval. Dashed line: modeled correlation ($T_c = 3.5$ h, $L_z = 12$ m).

offset (single scalar variable) in the model vector $\mathbf{c}'$ in Eq. (34), as only sound speed differences across depths and tracks could be acoustically resolved.

C. Correlation functions

The sound speed and current field perturbations were assumed to be stationary in time and space. The temporal correlations were estimated using the current and sound speed time series measured at the IOS moorings (see Figs. 7 and 8). Figure 8 shows two types of correlations: the correlation measured in the main direction of the flow, i.e., north/south at the IOS SW mooring and east/west at the IOS NE mooring, is smooth and has a relatively broad peak. The correlation measured across the flow has a narrow peak and denotes the presence of turbulence. Inasmuch as this turbulence is not properly accounted for in the tidal model and cannot be spatially resolved by the array of moorings, it will be ignored in the present analysis. The current correlation function in time is therefore fitted using the measurements made in the North/South direction in the middle of the channel, which accounts for most of the flow energy. In the absence of detailed experimental data regarding the spatial variability of the tidal flow, the current spatial correlation was estimated using the field predicted by Foreman's model (see Fig. 9). The correlation function of both flow components was assumed to be of the form[19]

$$\Gamma_u(\Delta x, \Delta y, \Delta t) = e^{-(1/2)R_u^2}, \tag{35}$$

where

$$R_u^2 = \left(\frac{\Delta x}{L_x}\right)^2 + \left(\frac{\Delta y}{L_y}\right)^2 + \left(\frac{\Delta t}{T_u}\right)^2.$$

The correlation lengths L_x and L_y were both set equal to 1000 m for the east/west component and 1500 m for the north/south component. The correlation time T_u was estimated to be approximately 2 h.

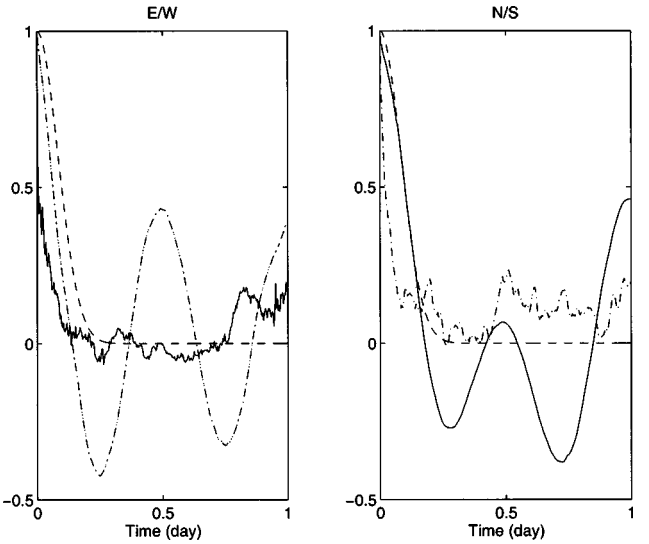

FIG. 8. Current temporal correlation function. Left panel: east/west component. Right panel: north/south component. Solid line: IOS SW mooring. Dash–dotted line: IOS NE mooring. Dashed line: modeled correlation ($T_u = 2$ h).

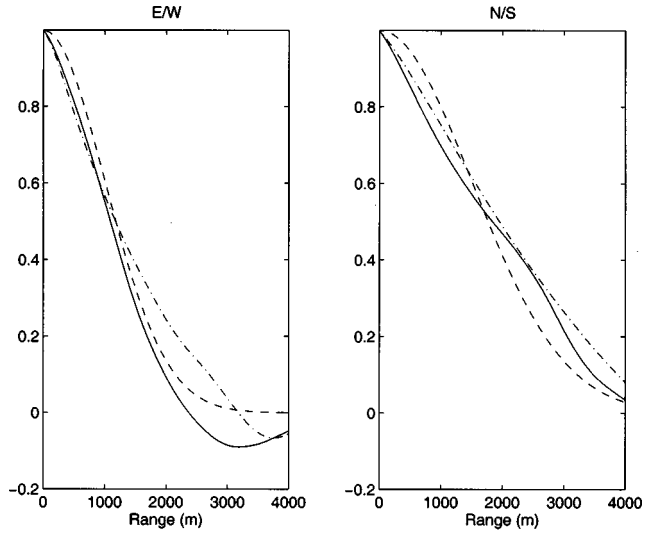

FIG. 9. Current spatial correlation function. Left panel: east/west component. Right panel: north/south component. Solid line: correlation along the east/west axis. Dash–dotted line: correlation along the north/south axis. Dashed line: modeled correlation ($L_u = 1000$ m, $L_v = 1500$ m).

The sound speed correlation in depth was estimated using a set of conductivity-temperature-salinity (CTD) casts taken over the month of June 1996. Detailed experimental data of the sound speed spatial variability being scarce as well, the horizontal spatial correlation function of the sound speed field was assumed to be identical to that of the north/south component of the tidal flow. The temporal correlation function of the sound speed field was fitted using a modified Gaussian as suggested by Carter and Robinson.[19] The complete correlation function of the sound speed field was assumed to be as follows:

$$\Gamma_c(\Delta x, \Delta y, \Delta z, \Delta t) = \left[1 - \left(\frac{\Delta t}{T_c}\right)^2\right] e^{-(1/2)R_c^2}, \tag{36}$$

where

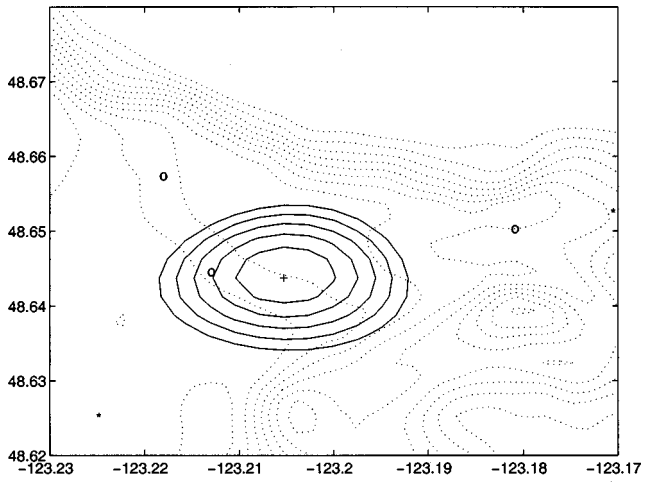

FIG. 10. Resolution kernel of the sound speed inversion. Solid lines: isokernel lines (0.5 to 1.0). Dotted lines: isobaths. Stars: IOS moorings. Circles: WHOI moorings.

$$R_c^2=\left(\frac{\Delta x}{L_x}\right)^2+\left(\frac{\Delta y}{L_y}\right)^2+\left(\frac{\Delta z}{L_z}\right)^2+\left(\frac{\Delta t}{T_c}\right)^2.$$

The correlation lengths L_x and L_y were set equal to 1500 m. The correlation depth T_z was estimated at 12 m. The correlation time T_c was estimated at 3.5 h. The difference in correlation times between the current and the sound speed correlation functions is due to variations in the functional form used to fit to the data. The width of both main lobes is approximately the same.

Due to the periodic character of tidal forcing, the data show a relatively high degree of temporal correlation over the course of several days. However, the actual correlation level past the first 12 h is highly dependent on location and, for current, orientation of the measurement. The model correlation functions Γ_c and Γ_u were consequently constrained to vanish for lags extending beyond approximately half a day, so that a single functional form could fit a wide variety of data. Data gathered more than a few correlation lengths or times away from the estimation time were therefore not taken into account.

D. Resolution

The resolution matrix **T** relates the field perturbation estimate $\hat{x}$ to its true value x'.[7] It is conveniently expressed in dimensionless form and can be be thought of as the prism through which the observer perceives reality. In the ideal case **T** is the identity matrix and the estimated quantity is equal to its true value. In practice it is rarely so. The kth column of **T** represents the field estimate generated in response to a true field which is zero everywhere except at the kth node where it has a unit value. This response is sometimes called the resolution kernel; an example is shown in Fig. 10. The width of the resolution kernel, i.e., the resolution length, is a measure of the spatial distance over which

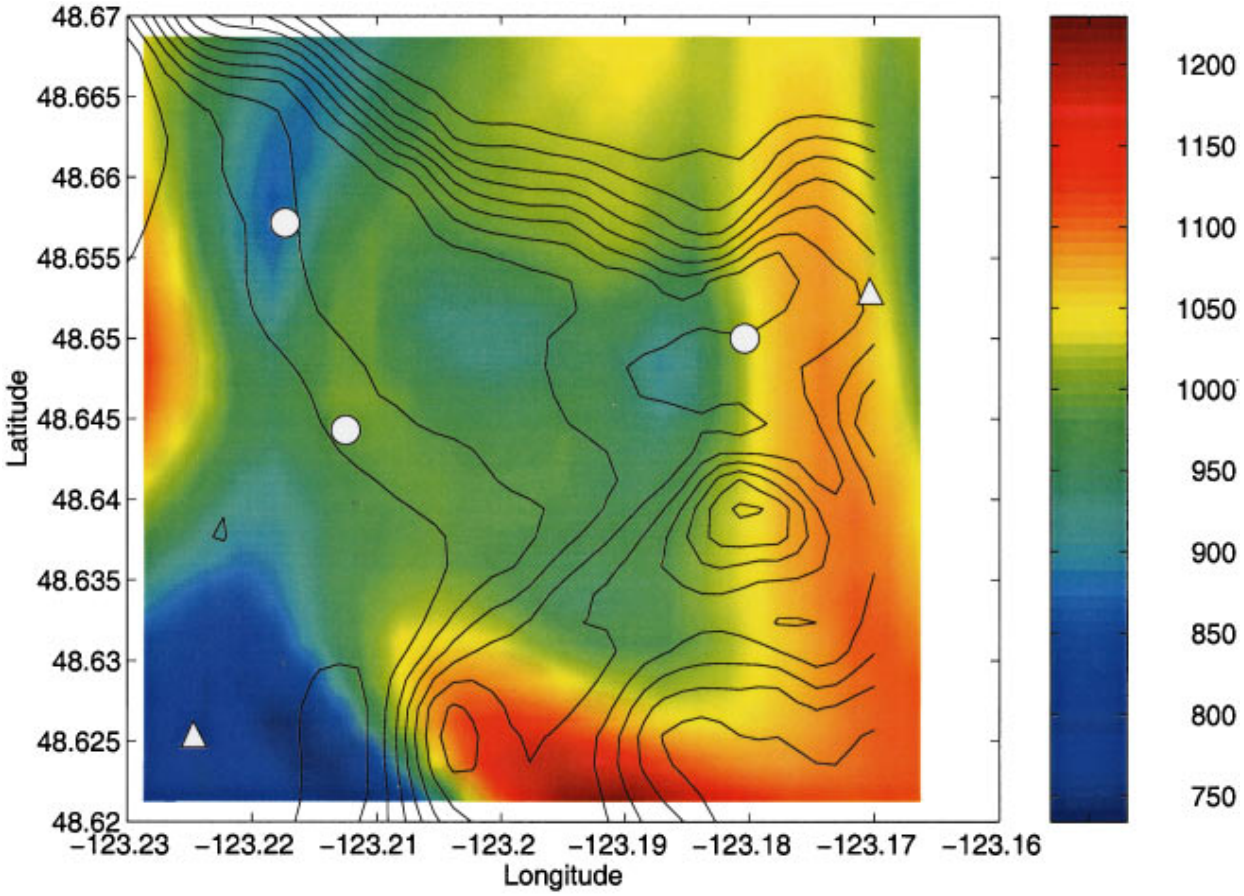

FIG. 11. East/west resolution length of the sound speed inversion. Solid lines: isobaths. Triangles: IOS moorings. Circles: WHOI moorings.

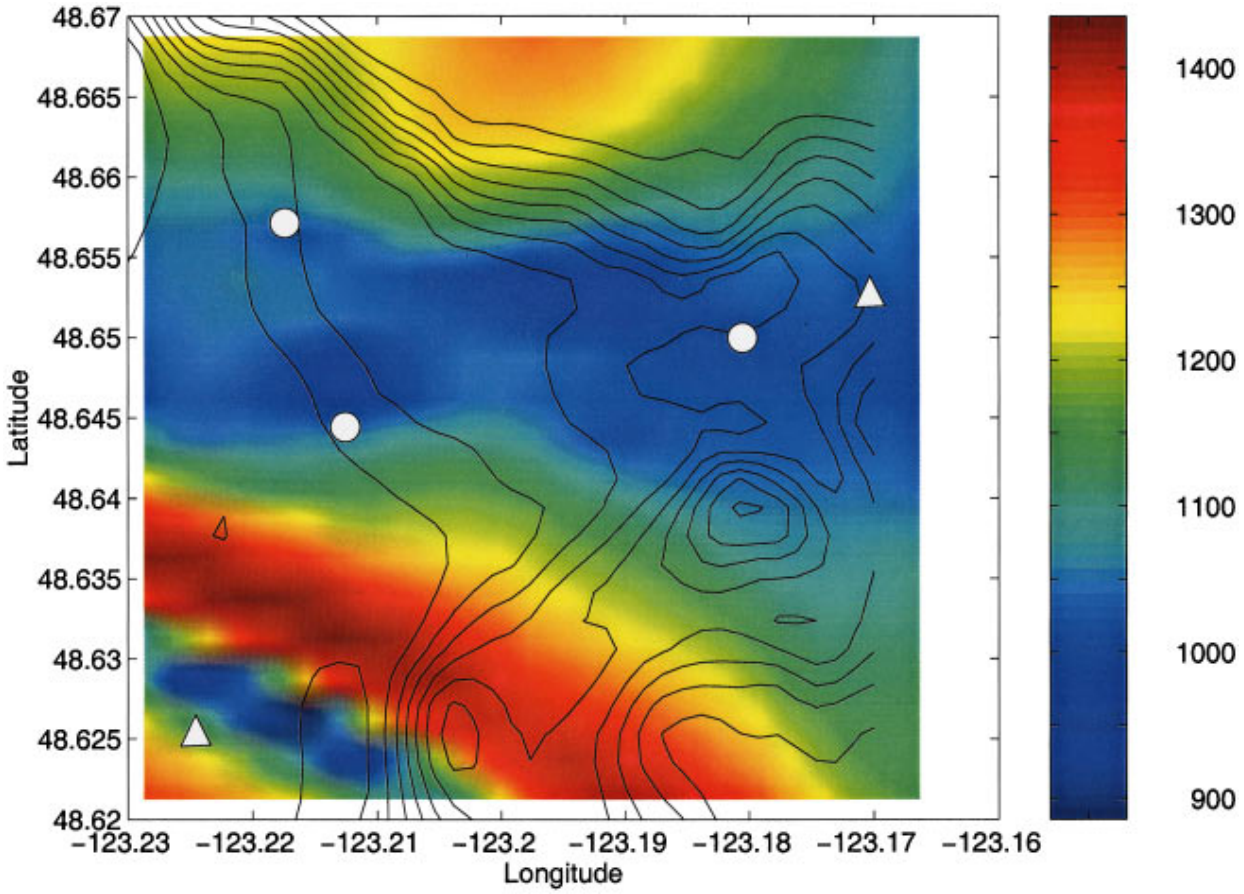

FIG. 12. North/south resolution length of the sound speed inversion. Solid lines: isobaths. Triangles: IOS moorings. Circles: WHOI moorings.

the estimate is averaged, and as such gives an indication of the level of detail the inversion procedure might be able to resolve. Various metrics can be chosen in order to compute the resolution length. Chiu suggested computing the width of the region which contains half the total energy spread by the kernel around the original true value.[25] However, this becomes a problem when sampling is very sparse and irregular as the resolution kernel is no longer necessarily well behaved and energy might be unevenly spread. By interpreting the resolution kernel (or its absolute value) as a two-dimensional probability density function, one can easily compute its second moment, which will provide a measure of resolution length. In addition, an equivalent bias of the inversion can be estimated by comparing the first moment to the true location.

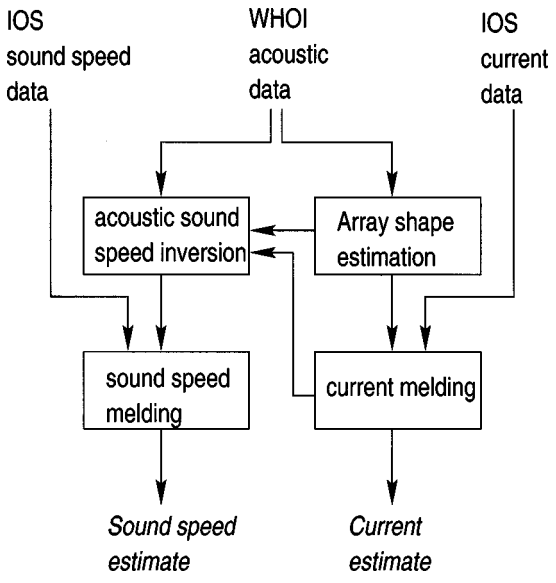

FIG. 13. Flow chart of the current and temperature field estimation scheme.

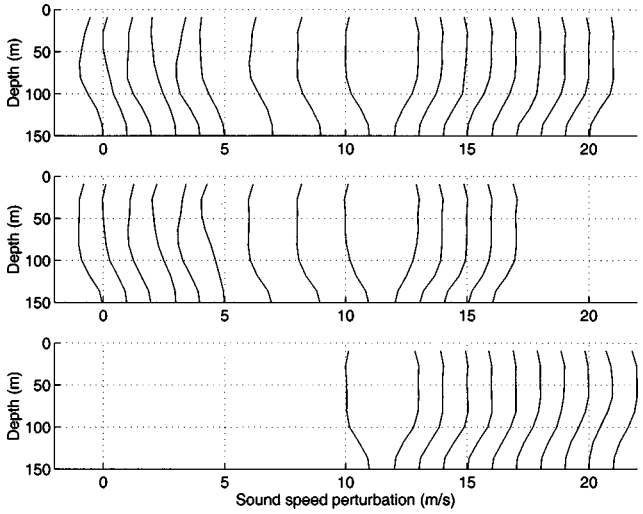

FIG. 14. Inverted acoustic sound speed profiles (synthetic data). Shots 20 to 42. Shots which were not properly captured by the acquisition system, or for which surface and direct arrivals were indistinguishable, are missing. Top panel: SW WHOI mooring. Middle panel: NW WHOI mooring. Bottom panel: NE WHOI mooring.

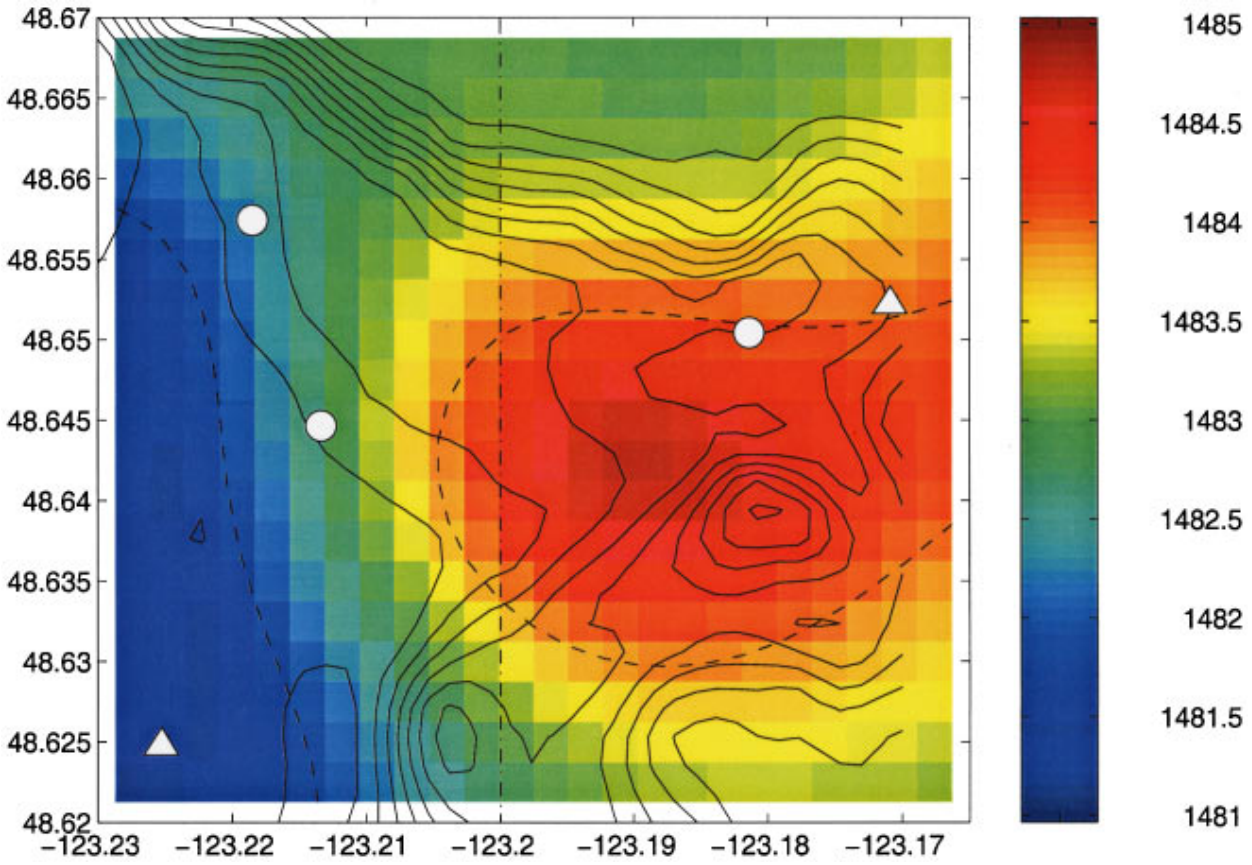

FIG. 15. Inverted sound speed field perturbation (synthetic data). Solid lines: isobaths. Dash–dotted line: actual front location. Dotted lines: isovelocity lines (1482 and 1484 m/s) Triangles: IOS moorings. Circles: WHOI moorings.

This bias is, in general, close to zero within the sampling network and starts becoming non-negligible outside the network envelope.

East/west and north/south resolution length maps are shown in Figs. 11 and 12. The east/west and north/south resolution lengths are respectively about 950 and 1000 m at the center of the network of arrays. The east/west resolution length estimate is biased near the eastern and western boundaries of the computational domains as the kernel cannot extend beyond the boundary and becomes distorted. The same effect is seen along the northern and southern boundaries for the north/south resolution length estimate. In particular, the low length region in the south-western corner is an artifact due to the proximity of the boundary combined with the experimental geometry.

E. Computational issues

A flow chart of the complete current and temperature field estimation scheme is given in Fig. 13. The acoustic sound speed profiles were first computed along each propagation track and then melded with the nonacoustic data instead of being included directly in the three-dimensional inversion for several reasons. Due to the particular experimental configuration of Haro Strait, the acoustic inversion has virtually no resolution in range for a given shot. The acoustic data provides good resolution in depth and across shot tracks. This information can be efficiently extracted by processing shots individually before the global inversion. In addition the computational load associated with a global three-dimensional inversion is of order $O(N^6)$ for a grid of dimension N^3. On the other hand, the segmented three-dimensional inversion is of order $O(N^5)$ if carried out depth by depth, or even $O(N^4)$ if a single depth or a few selected depths are of interest. This decrease of the computational load by one to two orders of magnitude is critical in enabling this inversion to be performed in a few minutes (on a DEC-Alpha 3000) and then fed back to the sampling network, in particular to the moving sources and AUVs. Segmenting the sound speed in this manner also facilitates inversion quality control by enabling the operator to verify the validity of the acoustically derived sound speed profiles prior to melding with other data sets. The computational load of the inversion is further decreased by clipping the data sets. Data points within three correlation depths of the desired depth and acquired during a period of three correlation times before the time of inversion are taken into account. Other data points are discarded. The current field estimation was made first. It was then used as background field in the sound speed estimation.

III. RESULTS

A. Synthetic data

In order to evaluate the accuracy of the inversion procedure a synthetic data set was generated. The simulated environment was identical to that of Haro Strait. The sound speed

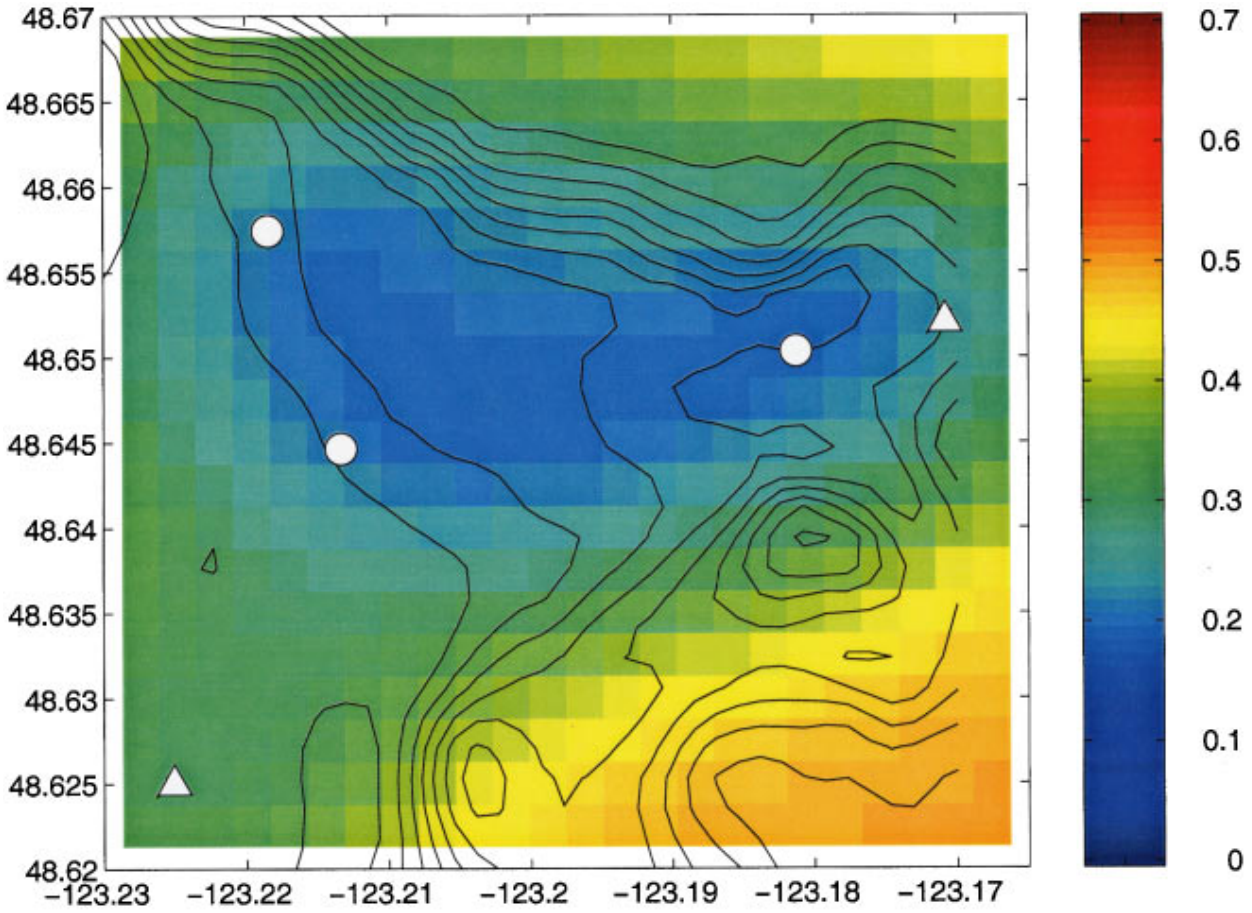

FIG. 16. Estimated error of the inverted sound speed field perturbation (synthetic data). Solid lines: isobaths. Triangles: IOS moorings. Circles: WHOI moorings.

field was assumed to be split in two isovelocity regions: the water sound speed was equal to 1484 m/s on the eastern side of the −123.20 meridian, and 1482 m/s on the western side. The transition at the meridian was set be discontinuous, which is not physical but allows a better understanding of the resolution limits of the inversion. The environment was assumed to be steady. In the absence of cyclical tidal variations, the sound speed correlation function was assumed to be a pure Gaussian.

The sound speed profiles computed using Eq. (25) are shown in Fig. 14. Actual profiles are isovelocity. The lower half of the water column is not insonified by the direct and surface rays and is therefore not resolved by the inversion. The surface layer is weakly resolved by the first few shots, which were fired at short range between the SW and NW WHOI moorings. Some inaccuracies are consequently observed in the corresponding sound speed profiles.

The estimated sound speed field is shown in Fig. 15. The associated error field is shown in Fig. 16. Two separate effects can be observed in Fig. 15. First the sound speed field is smeared in space due to the assumed correlation. The front is no longer a sharp discontinuity but a smooth transition zone with a width of about 1200 m, or a little less than a correlation length (1500 m). Then the front is shifted by about half a correlation length to the west of the actual front line at the latitude of maximum discrepancy. This is related to the confidence level in the acoustic data gathered between the two westernmost WHOI moorings. Due to the short ranges of the shots fired between these two moorings, the estimated error of the acoustic sound speed profiles is high relative to those measured along longer tracks east of the SW

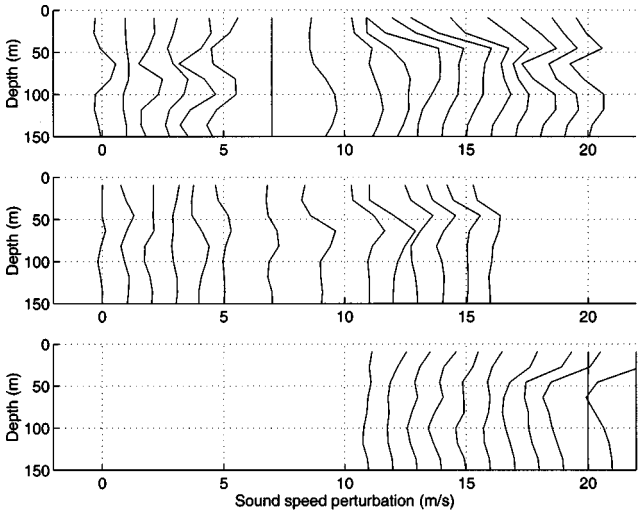

FIG. 17. Inverted acoustic sound speed profiles (Haro Strait data). Shots 20 to 42. Shots which were not properly captured by the acquisition system, or for which direct and surface arrivals were indistinguishable, are missing. Top panel: SW WHOI mooring. Middle panel: NW WHOI mooring. Bottom panel: NE WHOI mooring.

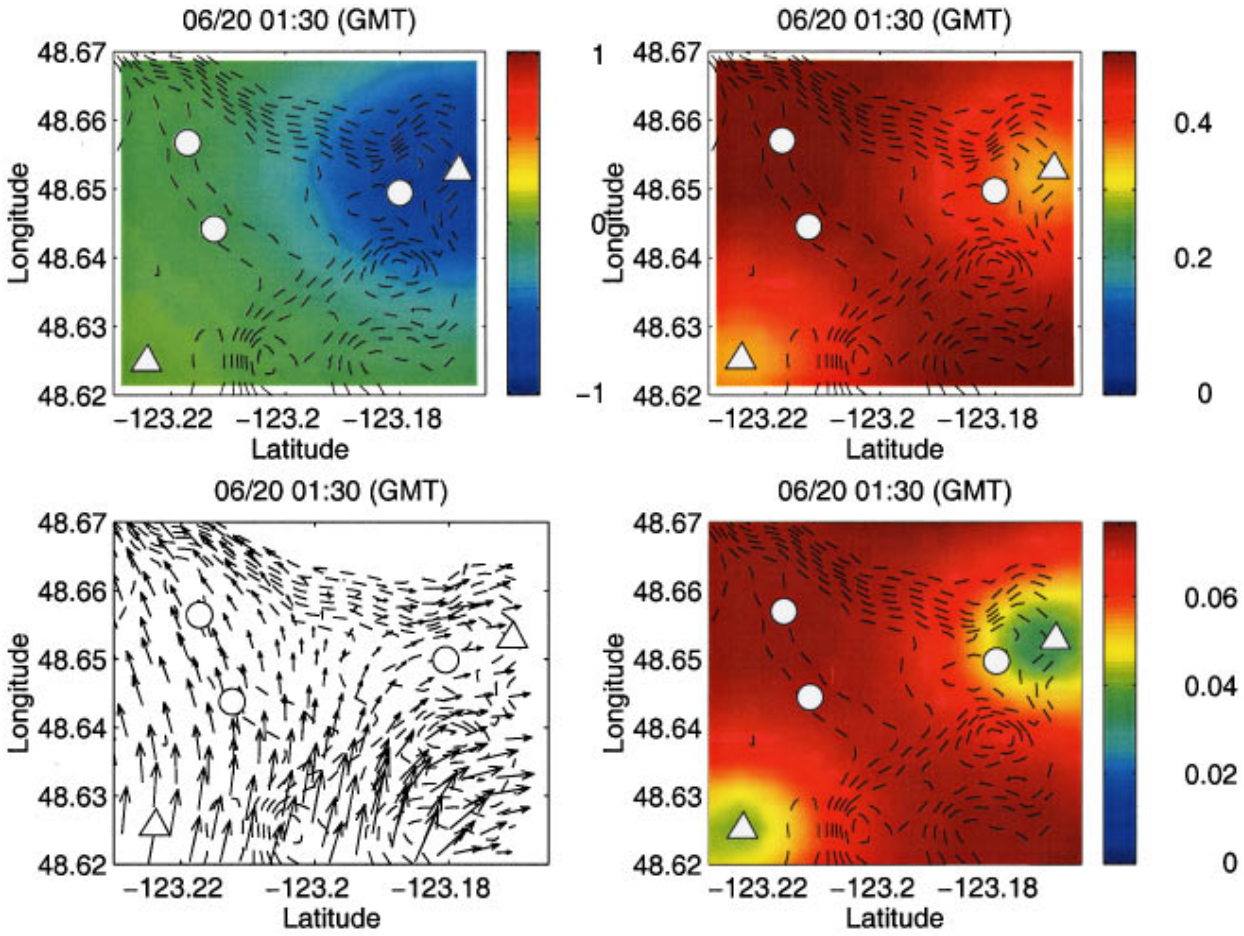

FIG. 18. Top view of the Haro Strait site at 01:30 GMT at a depth of 25 m. Upper left panel: sound speed (m/s); upper right panel: sound speed error (m/s); lower left panel: current field (m/s); lower right panel: current perturbation error prior to melding (m/s). Dashed lines: isobaths. Triangles: IOS moorings. Circles: WHOI acoustic moorings.

WHOI mooring. When the various acoustic profiles are merged with the local IOS measurements, the inverse estimate is constrained to be 1484 m/s on the east side of the −123.20 meridian with a relatively low error and 1482 m/s on the west side with a somewhat higher error level. The smoothness constraint imposed by the correlation function then shifts the estimated front position towards the region of higher uncertainty.

Tidal currents were included in the sound speed reference state. Current effects on the estimated sound speed field are most pronounced between the SW and NW WHOI moorings where the flow is strongest and parallel to the acoustic propagation track. Neglecting the current field in the inversion leads to an antisymmetric shift of the sound speed field between the SW and NW WHOI moorings, resulting in an east/west inflection of the 1483 m/s isovelocity line at this location.

B. Haro Strait data

The acoustic sound speed profiles estimated using the actual Haro Strait data set are shown in Fig. 17. The final field estimate merging integral acoustic data with local nonacoustic data is shown for three different times in Figs. 18, 19, and 20. The 01:30 GMT estimate does not yet incorporate acoustic data. The error field is consequently relatively high except near the IOS mooring locations. The 02:30 GMT estimate includes acoustic data from the first seven shots. Those shots were fired mostly between the SW and NW WHOI moorings and a significant decrease can be observed on the sound speed error map (upper right) near the location of the shots. A local decrease can be observed on the current error map (lower right) at the location of the SW and NW WHOI moorings. This is due to the fact that acoustically derived array shape data are now assimilated in the current estimate. The 03:30 GMT estimate includes all acoustic data. The sound speed error level has been significantly lowered over the entire region surrounded by the WHOI moorings. The combination of acoustically derived array shape data at the NE WHOI mooring with data from the nearby IOS mooring leads to a sharp decrease of the current error level. Interestingly enough, this decrease is not observed at other locations where the current estimate relies on a single type of data only.

C. Discussion

The scarcity of relevant oceanographic data, particularly in coastal environments such as Haro Strait, makes it difficult to compare the field estimates described above with an independent data set. Aside from the synthetic data test discussed in Sec. III A, the actual estimates can be compared to

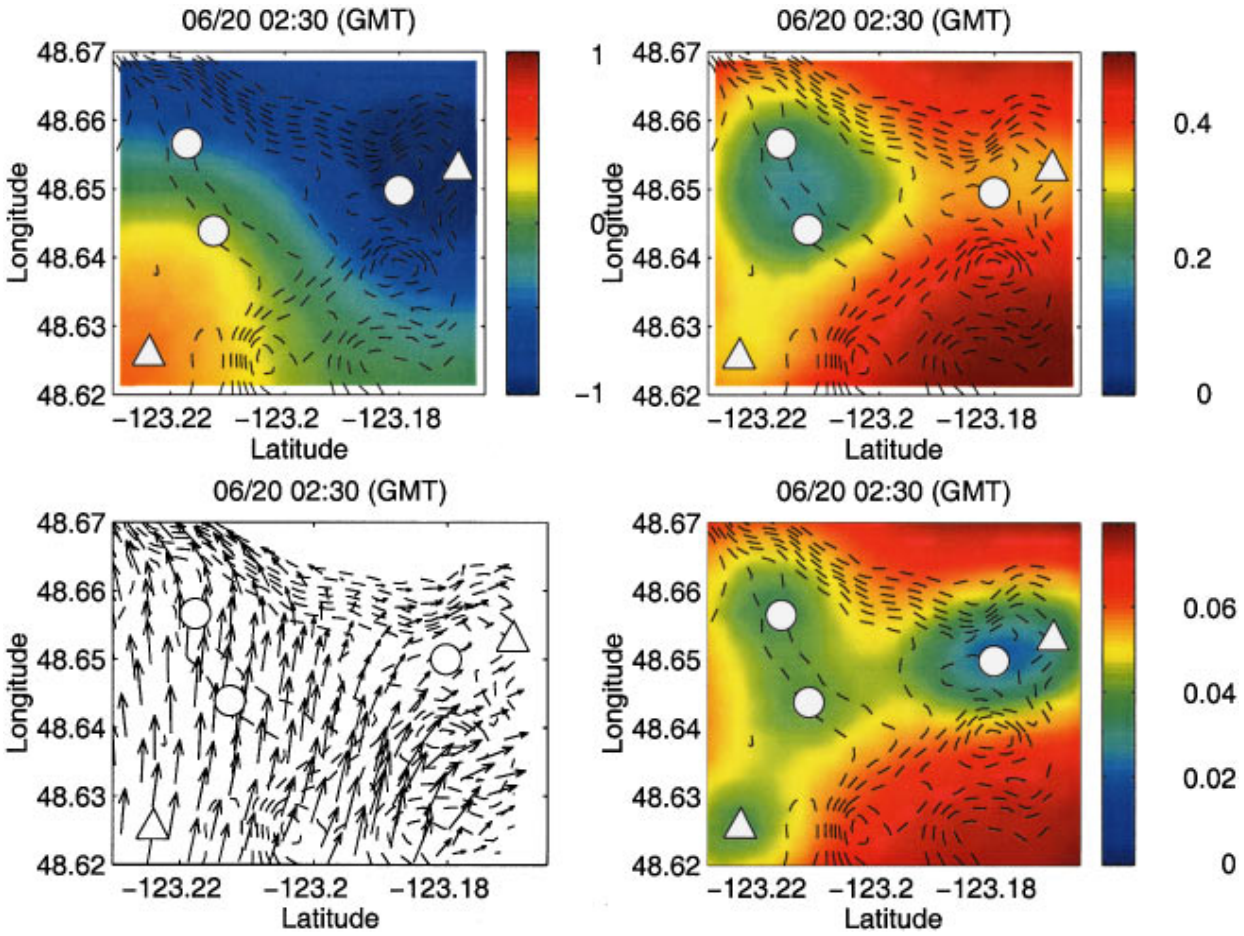

FIG. 19. Top view of the Haro Strait site at 02:30 GMT at a depth of 25 m. Upper left panel: sound speed (m/s); upper right panel: sound speed error (m/s); lower left panel: current field (m/s); lower right panel: current perturbation error prior to melding (m/s). Dashed lines: isobaths. Triangles: IOS moorings. Circles: WHOI acoustic moorings.

independent temperature records taken at the NW and NE WHOI moorings. Although no concomitant salinity measurements were performed, these temperature records can be converted into an equivalent sound speed by taking into account the strong correlation between temperature and salinity. A linear regression on a set of CTD casts taken a week after this experiment yields the following result:

$$c = 1.3043T + 1470.6, \tag{37}$$

where c is the sound speed in m/s and T is the temperature in °C. The regression correlation (R^2) is 0.94. The 95% confidence intervals for the gradient and constant terms are ± 0.0233 and ± 0.22, respectively. The resulting comparison is shown in Fig. 21. Acoustic data are assimilated from 02:00 on. The temperature being around 10 °C, the error induced by the regression is approximately 0.43 m/s, which accounts for some of the 0.8 m/s bias observed in Fig. 21. The remainder is attributable to the inversion itself and possible calibration offsets between the WHOI thermistors and the IOS temperature sensors.

The combination of multiple data sets enables the inversion procedure to overcome the individual limitations these might have. The acoustic data set, for instance, is limited in its ability to measure an absolute sound speed by the fact that the source transmission time is not known accurately and must be estimated when localizing array elements. Thanks to clock synchronization across the acoustic network, sound speed differences can still be measured across different depths and different tracks. On the other hand, the IOS mooring time series provide us with an absolute sound speed reference, but are obviously limited in coverage as shown in Fig. 18, which shows the field estimates before any acoustic data is taken into account. The acoustic array shapes by themselves are a local indication of the current magnitude, but contain almost no information regarding its direction. However, they yield a relatively low-error current estimate in magnitude and direction when combined with the IOS time series and assimilated into Foreman's tidal model. By furthermore coupling the sound speed inversion with the current inversion, the current/sound speed ambiguity inherent to any acoustic inversion can be, to some extent, resolved without resorting to reciprocal transmissions. This is made possible by extracting the information contained in different data sets through the combined inversion described in Sec. II.

Combining oceanographic with acoustic data and models traditionally brings up several issues, both theoretical and computational. The resolution of an oceanic field estimate, for instance, must match that of the acoustic model if an accurate acoustic prediction is to be made based on this field estimate and at an acceptable computational cost.[26] If the

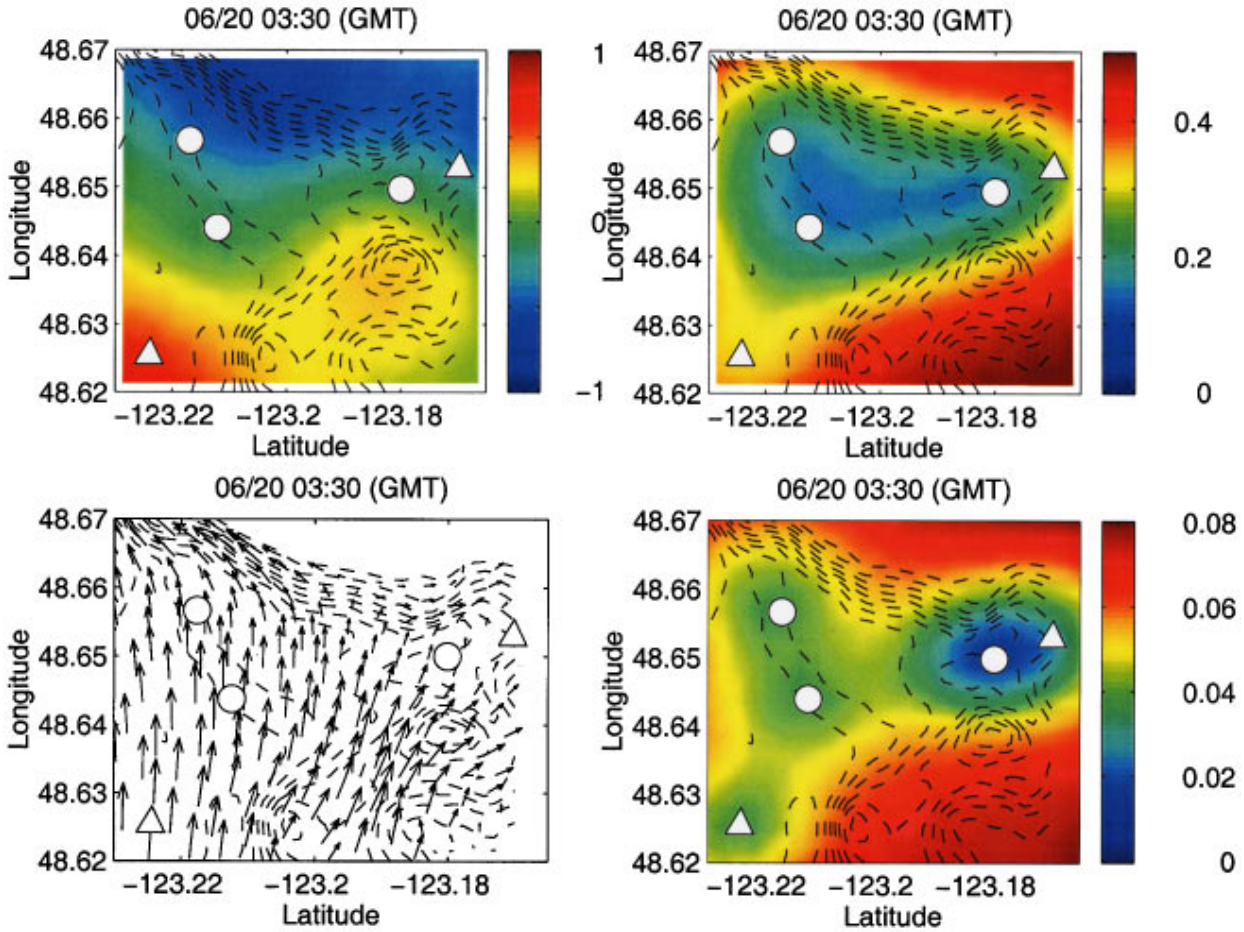

FIG. 20. Top view of the Haro Strait site at 03:30 GMT at a depth of 25 m. Upper left panel: sound speed (m/s); upper right panel: sound speed error (m/s); lower left panel: current field (m/s); lower right panel: current perturbation error prior to melding (m/s). Dashed lines: isobaths. Triangles: IOS moorings. Circles: WHOI acoustic moorings.

field estimate is itself inaccurate, the acoustic prediction might diverge widely from reality due to the nonlinear dependence of the wave equation on environmental fields. In the present analysis the current field used as input to the acoustic model is produced by a barotropic tidal model. No vertical stratification is therefore added to the reference acoustic sound speed profile. Furthermore, given the short ranges involved in the Haro Strait experiment, an individual acoustic transmission has no resolution in range and rays are sensitive primarily to the range-averaged sound-speed profile. The effect of using the tidal current field estimate as input to the ray tracer is then linear for all practical purposes. The effective sound speed profile is offset by some small constant quantity, which yields an approximately constant shift in travel times at the receiver array. The vertical variability of the current field is modeled as additional noise.

The robustness of the current melding scheme [see Eq. (22)] is ensured by the fact that data and model are melded *externally*, i.e., linearly. Of the four basic operations described in Fig. 13, three are therefore linear. The only nonlinear operation is the array shape estimation, based on mean square travel time difference minimization. Due to the short ranges involved in this paper, this operation can be carried out before the actual sound speed inversion by assuming some constant sound speed profile. Were longer ranges to be involved, the shape estimation would need to be either based on independent short-range acoustic transmissions or included in the sound speed inversion. The robustness of the overall inversion scheme derives then from its linearity, i.e., its simplicity, and the combination of different data sets with different resolutions and coverages.

Finally, it is worth noticing that, due to the particular experimental configuration adopted in Haro Strait, the final field estimate might be somewhat biased (see Sec. III A). In addition, the error estimate of the sound speed field does not formally propagate the error of the current estimate it used as its input. Error modeling, in particular in the case of oceanographic and acoustic model coupling, is still an active area of research and an accurate error model for the final field estimate lies beyond the scope of this paper. However, the error fields analyzed with the Haro Strait experiment do show the potential impact of melding different types of data and models on the resulting estimate uncertainty. The combination of various data streams and models is able to exploit the advantages of each data set, e.g., resolution or coverage, and compensate to some extent their limitations.

IV. CONCLUSION

The low-frequency acoustic data set gathered in Haro Strait in June 1996 was used in conjunction with nonacoustic

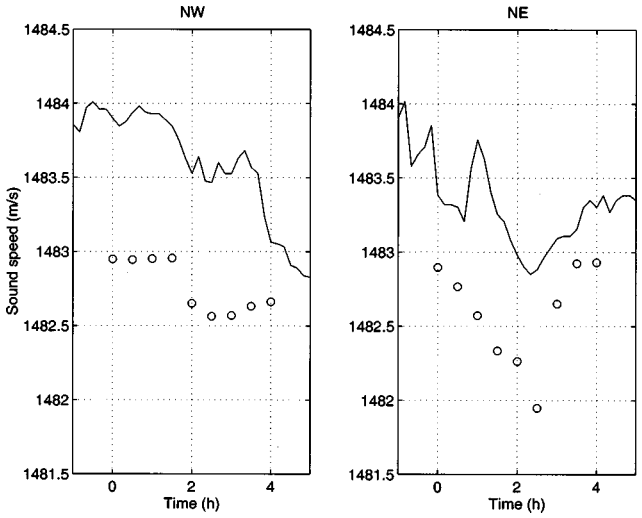

FIG. 21. Comparison with thermistor data. Left panel: NW WHOI mooring. Right panel: NE WHOI mooring. Solid line: top thermistor (approximate depth: 25 m). Dashed line: second thermistor (approximate depth: 35 m). Circles: sound speed estimate at the relevant mooring location at a depth of 25 m.

measurements in order to image a water mass of approximately 3 km by 3 km by 200 m. A fast and robust inversion algorithm combining linear techniques previously used in deep ocean tomography and oceanographic data assimilation was developed, yielding the real-time oceanic field estimates required in the context of acoustically driven rapid environmental assessment. The use of data melding and data assimilation techniques allowed us to resolve to some extent the current/sound speed ambiguity inherent to any nonreciprocal acoustic transmission. In addition, the combined use of integral and local data lead to a significant decrease of the field estimate uncertainty while maintaining a coverage of the area not achievable by nonacoustic means.

ACKNOWLEDGMENTS

The authors wish to thank the crew of the R. B. Young and the Woods Hole technicians for their invaluable help in carrying the Haro Strait experiment. Current and temperature time series were kindly provided by Kevin Bartlett (Institute of Ocean Sciences). Foreman's tidal model was run with the much appreciated help and assistance of Rich Pawlowicz (Institute of Ocean Sciences). Discussions with Carlos Lozano (Harvard University) on data assimilation helped shape the analysis presented in this paper. Finally, the authors gratefully acknowledge the reviewers' numerous comments, which contributed to making this paper significantly better than the original manuscript. Funding was provided by the Office of Naval Research through Grant No. N00014-95-1-0495.

APPENDIX: MODEL AND NOISE COVARIANCE MATRICES

1. Sound speed field

The acoustic model covariance matrix $\mathbf{R}_{cc}^{(a)}$ used in (26) was computed as

$$\mathbf{R}_{cc}^{(a)}=\sigma_c^2\Gamma_c(\mathbf{r}_i,\mathbf{r}_j,t_i,t_j),$$

where $\mathbf{r}_i$ refers to the location (depth) of the ith node of a given acoustic inversion (single shot, range independent). The times t_i and t_j were set equal to each other. The standard deviation σ_c was estimated to be 72 cm/s using CTD data. The acoustic noise covariance matrix $\mathbf{R}_{nn}^{(a)}$ was computed as

$$\mathbf{R}_{nn}^{(a)}=\left(\sigma_t^2+\left(\frac{\sigma_u}{c_o}\frac{R}{c_o}\right)^2\right)\mathbf{I},$$

where R is the source range. The first term accounts for local travel time errors. The standard deviation σ_t was set to 0.6 ms by inspection of the shots with the shortest ranges. The reference sound speed was set equal to 1500 m/s. The second term accounts for the presence of current variations in depth along the acoustic track. The current standard deviation in depth σ_u was estimated to be 38 cm/s using the current time series measured at three different depths.

The model covariance matrix $\mathbf{R}_{cc}^{(c)}$ used in the inversion of Eq. (34) was defined as

$$[\mathbf{R}_{cc}^{(c)}]_{ij}=\sigma_c^2\Gamma_c(\mathbf{r}_i,\mathbf{r}_j,t_i,t_j),$$

where $\mathbf{r}_i$ and t_i refer to the location in space and time of the ith node of the corresponding grid. The noise covariance matrix $\mathbf{R}_{nn}^{(u)}$ used in the inversion of (34) was computed as

$$[\mathbf{R}_{nn}^{(c)}]=\begin{bmatrix}\tilde{\sigma}_c^2\mathbf{I} & \mathbf{O}\\ \mathbf{O} & \tilde{\mathbf{P}}_c(a)\end{bmatrix}.$$

The sound speed time series standard deviation $\tilde{\sigma}_c$ was estimated at 13 cm/s. The relevant acoustic sound speed estimate error matrices $\mathbf{P}_c^{(a)}$ given by (27) were aggregated in $\tilde{\mathbf{P}}_c^{(a)}$. Error correlations among different sound speed estimates of the same profile were therefore taken into account.

2. Current field

The model covariance matrix in (20) is defined by

$$\mathbf{R}_{uu}=E[\mathbf{u}'\mathbf{u}'^T],$$

where the first half of $\mathbf{u}'$ includes east/west components and the second half includes north/south components. Due to the complexity and the variability of the cross correlation between the east/west and north/south components, each component was assumed to be uncorrelated with its counterpart. The model covariance matrix was therefore written as

$$\mathbf{R}_{uu}=\begin{bmatrix}\mathbf{R}_{u,x} & \mathbf{O}\\ \mathbf{O} & \mathbf{R}_{u,y}\end{bmatrix}$$

and

$$[\mathbf{R}_{u,x/y}]_{ij}=\sigma_{u,x/y}^2\Gamma_u(\mathbf{r}_i,\mathbf{r}_j,t_i,t_j),$$

where $\mathbf{r}_i$ and t_i refer to the location in space and time of the ith node. After comparison of the IOS current-meter data with Foreman's tidal model, the east/west standard deviation $\sigma_{u,x}$ was estimated to vary between 18 and 24 cm/s; the north/south standard deviation $\sigma_{u,y}$ was estimated to vary between 16 and 22 cm/s. Both were set to 22 cm/s in the current inversion.

Similarly, the noise covariance matrix $\mathbf{R}_{nn}^{(u)}$ was given by

$$\mathbf{R}_{nn}^{(u)} = \begin{bmatrix} \tilde{\mathbf{R}}_{u,x} & \mathbf{O} & \mathbf{R}_{au,x}^T \\ \mathbf{O} & \tilde{\mathbf{R}}_{u,y} & \mathbf{R}_{au,y}^T \\ \mathbf{R}_{au,x} & \mathbf{R}_{au,y} & \mathbf{R}_{aa} \end{bmatrix},$$

where the matrices $\tilde{\mathbf{R}}_{u,x/y}$ were computed using the definition of $\mathbf{R}_{u,x/y}$ with the actual measurement locations. The covariance of the array shape factors $\tilde{a}$ with the current components $u_{x/y}$ was computed as

$$\mathbf{R}_{au,x} = \mathbf{H}_1 E[\mathbf{u}_{x,a}\mathbf{u}_x^T], \quad \mathbf{R}_{au,y} = \mathbf{H}_2 E[\mathbf{u}_{y,a}\mathbf{u}_y^T],$$

where $\mathbf{H}_1$ and $\mathbf{H}_2$ are given by (15) and (16) and the expectations by $\sigma_u^2 \Gamma_u$. For simplicity's sake the covariance of array shape factors was assumed to be

$$\mathbf{R}_{aa} = \sigma_a^2 \mathbf{I},$$

where the standard deviation σ_a was estimated at 0.02 by comparison of the array shape data with the predictions based on Foreman's model.

[1] W. Munk and C. Wunsch, ''Ocean acoustic tomography: a scheme for large scale monitoring,'' Deep Sea Res. **26A**, 123–161 (1979).

[2] D. Behringer, T. Birdsall, M. Brown, B. Cornuelle, R. Heinmiller, R. Knoz, K. Metzger, W. Munk, J. Spiesberger, R. Spindel, D. Webb, P. Worcester, and C. Wunsch, ''A demonstration of ocean acoustic tomography,'' Nature (London) **299**, 121–125 (1982).

[3] B. M. Howe, ''Multiple receivers in single vertical slice ocean acoustic tomography experiments,'' J. Geophys. Res. **92**(C9), 9479–9486 (1987).

[4] B. Cornuelle, W. Munk, and P. Worcester, ''Ocean acoustic tomography from ships,'' J. Geophys. Res. **94**, 6232–6250 (1989).

[5] B. D. Dushaw, P. F. Worcester, B. D. Cornuelle, and B. M. Howe, ''Barotropic currents and vorticity in the central north Pacific Ocean during summer 1987 determined from long-range reciprocal acoustic transmission,'' J. Geophys. Res. **99**, 3263–3272 (1994).

[6] R. H. Headrick, J. L. Spiesberger, and P. J. Bushong, ''Tidal signals in basin-scale acoustic transmissions,'' J. Acoust. Soc. Am. **93**, 790–802 (1993).

[7] W. Munk, P. Worcester, and C. Wunsch, *Ocean Acoustic Tomography* (Cambridge U.P., Cambridge, 1995).

[8] H. A. DeFerrari and H. B. Nguyen, ''Acoustic reciprocal transmission experiments, Florida Straits,'' J. Acoust. Soc. Am. **79**, 299–315 (1986).

[9] C. S. Chiu, J. H. Miller, and J. F. Lynch, ''Inverse techniques for coastal acoustic tomography,'' in *Theoretical and Computational Acoustics—Volume 2*, edited by D. Lee and M. H. Schultz (World Scientific, Singapore, 1994), pp. 917–931.

[10] C. S. Chiu, J. H. Miller, W. W. Denner, and J. F. Lynch, ''Forward modeling of the Barents sea tomography vertical line array data and inversion highlights,'' in *Full Field Inversion Methods in Ocean and Seismo-acoustics*, edited by O. Diaschok, A. Caiti, P. Gerstoft, and H. Schmidt (Kluwer Academic, Dordrecht, 1995), pp. 237–242.

[11] J. F. Lynch, G. Jin, R. Pawlowicz, D. Ray, Plueddemann, C. S. Chiu, J. H. Miller, R. H. Bourke, A. R. Parsons, and R. Muench, ''Acoustic travel-time perturbations due to shallow-water internal waves and internal tides in the Barents sea polar front: Theory and experiment,'' J. Acoust. Soc. Am. **99**, 803–821 (1996).

[12] H. Schmidt, J. G. Bellingham, and P. Elisseeff, ''Acoustically Focused Oceanographic Sampling in coastal environments,'' in *Rapid Environmental Assessment*, edited by E. Pouliquen, A. D. Kirwan, and R. T. Pearson, Conference Proceedings Series CP-44, SACLANTCEN, 1997, pp. 145–157.

[13] J. G. Bellingham, H. Schmidt, and M. Deffenbaugh, ''Acoustically focused oceanographic sampling in the Haro Strait experiment,'' J. Acoust. Soc. Am. **100**, 2612 (1996).

[14] D. Lee, ''Three-dimensional effects: interface between the Harvard Open Ocean Model and a three-dimensional acoustic model,'' in *Oceanography and Acoustics: Prediction and Propagation Models*, edited by A. R. Robinson and D. Lee (AIP, New York, 1994).

[15] A. R. Robinson, J. C. Carman, and S. M. Glenn, ''A dynamical system for acoustic applications,'' in *Oceanography and Acoustics: Prediction and Propagation Models*, edited by A. R. Robinson and D. Lee (AIP, New York, 1994), pp. 80–117.

[16] C. J. Lozano, A. R. Robinson, H. G. Arango, A. Gangopadhyay, Q. Sloan, P. J. Haley, L. Anderson, and W. Leslie, ''An interdisciplinary ocean prediction system: assimilation strategies and structured data models,'' in *Modern Approaches to Data Assimilation in Ocean Modeling*, edited by P. Malanotte-Rizzoli (Elsevier, Amsterdam, 1996), pp. 413–452.

[17] M. Grund, M. Johnson, and D. Herold, ''Haro Strait tidal front mapping experiment,'' Technical report, Woods Hole Oceanographic Institution, February 1997.

[18] K. V. Mackenzie, ''Nine-term equation for sound speed in the oceans,'' J. Acoust. Soc. Am. **70**, 807–812 (1981).

[19] E. F. Carter and A. R. Robinson, ''Analysis models for the estimation of oceanic fields,'' J. Atmos. Ocean. Technol. **4**, 49–74 (1987).

[20] T. K. Kapoor, ''Three-dimensional acoustic scattering from arctic ice protuberances,'' Ph.D. thesis, Massachusetts Institute of Technology, June 1995.

[21] M. G. G. Foreman, R. A. Walters, R. F. Henry, C. P. Keller, and A. G. Dolling, ''A tidal model for eastern Juan de Fuca Strait and the southern Strait of Georgia,'' J. Geophys. Res. **100**(C1), 721–740 (1995).

[22] A. Tarantola, *Inverse Problem Theory—Methods for Data Fitting and Model Parameter Estimation* (Elsevier, Amsterdam, 1987).

[23] P. Malanotte-Rizzoli, editor, *Modern Approaches to Data Assimilation in Ocean Modeling* (Elsevier, Amsterdam, 1996).

[24] B. D. Cornuelle and P. F. Worcester, ''Ocean acoustic tomography: integral data and ocean models,'' in *Modern Approaches to Data Assimilation in Ocean Modeling*, edited by P. Malanotte-Rizzoli (Elsevier, Amsterdam, 1996), pp. 97–115.

[25] C. S. Chiu, J. F. Lynch, and O. M. Johanessen, ''Tomographic resolution of mesoscale eddies in the Marginal Ice Zone: a preliminary study,'' J. Geophys. Res. **92**(C7), 6886–6902 (1987).

[26] W. L. Siegmann, D. Lee, G. Botseas, A. R. Robinson, and S. M. Glenn, ''Sensitivity issues for interfacing mesoscale ocean prediction and parabolic acoustic propagation models,'' in *Oceanography and Acoustics: Prediction and Propagation Models*, edited by A. R. Robinson and D. Lee (AIP, New York, 1994), pp. 133–160.

An iterative approach for approximating bubble distributions from attenuation measurements

J. W. Caruthers[a] and P. A. Elmore
Naval Research Laboratory, Stennis Space Center, Mississippi 39529

J. C. Novarini
Planning Systems, Inc., 21294 Johnson Street, Long Beach, Mississippi 39560

R. R. Goodman[b]
Applied Research Laboratory, Pennsylvania State University, State College, Pennsylvania 16804

(Received 18 February 1998; accepted for publication 9 April 1999)

A precise theory exists, based on an integral equation, by which acoustic signal attenuation versus frequency, due to a known bubble-density distribution versus bubble radius, may be calculated. Lacking a simple inversion scheme for the integral equation, an approximation which accounts only for attenuation due to resonant bubbles is available (and often applied) to calculate a bubble distribution. An iterative approach for improving on that resonant bubble approximation is presented here. That new approach is based on alternating calculations and corrections between attenuation data and the bubble distribution presumed to have produced it. This iterative technique is tested, first, on two simulated data sets of bubble distributions. It is then applied to attenuation data measured as a function of frequency from 39 to 244 kHz during the Scripps Pier Experiment [Caruthers *et al.*, Proc. 16th Int. Cong. on Acoust., pp. 697–698 (1998)]. The results of the simulations demonstrate the validity of the method by faithfully reproducing the initial distributions for the simulated attenuation data. When applied to the real data, the method leads to a bubble distribution whose use in a direct solution of the integral equation reproduces the measured data with greater accuracy than does the resonant bubble approximation alone. © *1999 Acoustical Society of America.* [S0001-4966(99)04307-6]

PACS numbers: 43.30.Es, 43.30.Pc, 43.35.Bf [SAC-B]

INTRODUCTION

Calculating bubble distributions from *in situ* data of acoustic transmission loss is problematic. Given a bubble-size distribution, the attenuation coefficient in nepers per meter, $\beta(\omega)$, is calculated from[1–4]

$$\beta(\omega)=\frac{2\pi c_0}{\omega}\int_0^\infty \frac{a\,\delta\,n(a)da}{(\omega_R^2(a)/\omega^2-1)^2+\delta^2}. \tag{1}$$

In Eq. (1), c_0 is the speed of sound in bubble-free sea water, ω is the angular frequency of the insonifying field, a is the bubble radius, $n(a)da$ is the number of bubbles per unit volume with radii between a and $a+da$, $\omega_R(a)$ is the resonance frequency of a bubble with radius a, and δ is the damping parameter. Equation (1) is a Fredholm integral equation of the first kind. We refer to it as the formal theory, and later treat it as an operator (FT) acting on the bubble population to produce attenuation. An attempt to invert Eq. (1) to find the bubble-density distribution, $n(a)$, from measurements of $\beta(\omega)$ over a range of frequencies leads to an ill-conditioned system of integral equations, making direct calculations of $n(a)$ impractical. That is, a simple inverse operator (FT^{-1}) of FT, which would act on attenuation to produce a bubble distribution, is not available.

As reviewed by Medwin[5] and Commander and Moritz,[6] simplifying assumptions presented in Ref. 1 make it possible to perform the integration in Eq. (1). These assumptions are (a) δ is a constant, (b) only those bubbles at resonance with the insonifying field contribute significantly to attenuation, (c) the bubble distribution changes slowly about the resonance radius, and (d) surface tension is negligible. When these simplifications are applied, Eq. (1) reduces to an expression that can be inverted, yielding

$$n(a)\approx 4.6\times 10^{-6} f^3\beta(f). \tag{2}$$

In Eq. (2), $\beta(f)$ is in dB/m and $f(=\omega/2\pi)$ is the frequency at which bubbles of radius a resonate. For convenience, we call this theory the resonant bubble approximation (RBA). [When depth (z) is included there is an additional factor of $(1+0.1z)^{-1}$ in Eq. (2).]

The RBA may be applied to bubble distributions that are power laws, i.e., a^{-s}.[5,6] Experiments at sea indicate that real bubble distributions are in the form of power laws,[7–12] so the RBA may be applied meaningfully to measurements, as done, for example, in Ref. 13. Some of the shortcomings of the RBA are discussed by Refs. 5 and 6. Medwin[5] mentions that approximating the damping factor to be constant leads to an underestimation of the attenuation calculated by RBA when s is 4. Commander and Moritz[6] discuss overestimations made in the bubble distributions due to the neglect of off-resonance scattering effects in the RBA theory. To obtain better estimations of the bubble distribution based on attenu-

[a]Electronic mail: jerald.caruthers@nrlssc.navy.mil
[b]Currently at the Naval Research Laboratory, Stennis Space Center under an Intergovernmental Personnel Agreement.

ation measurements, Commander and McDonald[14] present a rather involved finite-element method for calculating bubble distributions from attenuation measurements by solving a system of integral equations.

We also have observed inadequacies with the RBA. Specifically, applying the precise theory to an estimate of the bubble distribution derived from the RBA produces significant differences between the resulting attenuation and the original data for certain distributions and in certain size ranges. Rather than use the approach given in Ref. 14 to get better estimates of $n(a)$ from $\beta(f)$, we have developed a simpler mathematical method to improve bubble-distribution estimation using a two-step iterative procedure.

The new iterative technique is based on the solution of the Fredholm integral equation by the method of successive approximations and is presented symbolically in Sec. I. Improvement is judged based on a successful recovery of the measured attenuation when using the formal theory operating on the improved bubble distribution. We test the approach in Sec. II A using simulated-bubble distributions which, in turn, produce simulated-attenuation data based on Eq. (1). Through the iterative process, we show that small corrections to the estimates of bubble distribution can produce noticeable effects on the resulting attenuation, and these distribution corrections allow a significantly closer match to the simulated attenuation data. In Sec. II B, we apply this approach to real attenuation data which we believe has sufficient accuracy to warrant the first-order corrections produced by the iterative technique. Conclusions are presented in Sec. III.

I. ITERATIVE APPROACH

Let us assume that sound-attenuation measurements were made in a bubbly liquid at N frequencies, i.e., $[\beta(f_i), i=1,...,N,\ f_1<f_i<f_N]$. The measurements are assumed to have produced true, unbiased values. For the present, we assume attenuation to be a continuous function over a full range of frequencies beyond the limits of our data. Let that function be β_t. (We suppress the arguments of attenuation and bubble distribution in the following development and use the subscript t to denote ''true.'')

Theoretically, the ''true'' attenuation, β_t, would be the result of the application of the formal theory given by Eq. (1) to the true bubble distribution, n_t, if that distribution were known. Symbolically, we represent Eq. (1) by

$$\beta_t = FT[n_t]. \tag{3}$$

Let us apply the RBA to the true attenuation. Treating the resonant bubble approximation as an operator, *RBA* (italicized now to represent that operator), is an approximation to FT^{-1}. Symbolically, we represent Eq. (2) by

$$n_0 = RBA[\beta_t] \approx FT^{-1}[\beta_t] = n_t, \tag{4}$$

which defines a distribution n_0. The quantity n_0 is an estimate of the true distribution, n_t.

The estimated distribution is different from the true value by an error, i.e., an anomalous distribution, defined by

$$n_\epsilon = n_t - n_0. \tag{5}$$

Both the true and anomalous distributions are unknown; however, we are given β_t and we can calculate n_0. If we could estimate the error, we could produce a better estimate of n_t. To accomplish this, let us apply the formal theory to n_0 with the results being defined as β_0, i.e.,

$$\beta_0 = FT[n_0]. \tag{6}$$

Rearranging Eq. (5) and substituting it into Eq. (6), then noting that FT is a linear operator and substituting from Eq. (3) yields

$$\beta_0 = FT[n_t - n_\epsilon] = \beta_t - FT[n_\epsilon]. \tag{7}$$

Applying *RBA* to β_0 and defining the results to be n_0', then substituting from Eq. (7), we obtain

$$\begin{aligned} n_0' &= RBA[\beta_0] = RBA[\beta_t - FT[n_\epsilon]] \\ &= n_0 - RBA[FT[n_\epsilon]]. \end{aligned} \tag{8}$$

We define the new error, n_ϵ', made in estimating n_0 with n_0', to be the last term on the right of Eq. (9), i.e.,

$$n_\epsilon' = RBA[FT[n_\epsilon]]. \tag{9}$$

So far, we have not required n_ϵ or n_ϵ' to be small. If, however, we now assume that the anomalous distributions, n_ϵ and n_ϵ', are first order only, then $RBA[FT[n_\epsilon]]$ differs from n_ϵ to second order only. Hence, to first order, we can approximate n_ϵ by n_ϵ', and n_ϵ' can be calculated from Eqs. (8) and (9). That is, $n_\epsilon \approx n_\epsilon' = n_0 - n_0'$. Finally, n_ϵ can be used in Eq. (5) to correct n_0 to produce the desired improved approximation for n_t. Finally, we can write

$$n_t = n_0 + n_\epsilon \approx n_0 + n_\epsilon' = n_0 + (n_0 - n_0') = 2n_0 - n_0'. \tag{10}$$

For our purposes here, a correction to first order is sufficient. If, however, one desired higher-order improvements, one might continue by recognizing in Eq. (7) a relationship for the first-order anomalies, $\beta_\epsilon = FT[n_\epsilon]$, that is analogous to Eq. (3) which would then lead to the next order solution, and so forth. That is, we can continue the process of successive approximations for the solution of integral equations.

II. APPLICATION OF THE ITERATIVE APPROACH

In this section, we investigate the properties of the iterative approach using simulated bubble distributions and actual measured data. At the beginning of the previous section we suggested that, to account for off-resonance effects, we needed a continuous (actually a quasicontinuous) function of attenuation versus frequency extending beyond the frequency limits of the data. The validity of the extension beyond the end points can be judged based on the ability of the process to match the end points. For the following simulation subsection, we generate the data in the form we need it. In the experimental-data subsection, we must extrapolate and interpolate the data $[\beta(f_i),\ i=1,...,N,\ f_1<f_i<f_N]$, to achieve the desired results. In both sections, we use the depth correction to Eq. (2) with depth set at 4 meters, the depth at which the experiment was conducted.

TABLE I. Details of simulated bubble distributions.

Case I. Total void fraction $=5.00\times10^{-7}$	
$n(a)=5.39\times10^{-8}\,a^{-4}$	$128\ \mu\text{m}\geqslant a\geqslant 14\ \mu\text{m}$
$=0$	otherwise
Case II. Total void fraction $=6.00\times10^{-7}$	
$n(a)=1.03\times10^{-7}\,a^{-4}$	$128\ \mu\text{m}\geqslant a> 40\ \mu\text{m}$
$=4.00\times10^{10}\,a^{0}$	$40\ \mu\text{m}\geqslant a> 20\ \mu\text{m}$
$=1.57\times10^{48}\,a^{8}$	$20\ \mu\text{m}\geqslant a\geqslant 14\ \mu\text{m}$
$=0$	otherwise

A. Simulated attenuation data

The effectiveness of the iterative approach is first tested with two cases of simulated data: case I, a single power law with $s=4$; and case II, three segments of power laws with $s=4$, 0, -8. Outside the limits of radii, $[a_{\min},a_{\max}]$, there are no bubbles. The details of the properties of these bubble distributions are listed in Table I. Power laws are chosen to describe the distributions in order to be somewhat descriptive of the experimental findings in Refs. 7–13. The true distributions, n_t, for cases I and II are plotted with the solid lines in Figs. 1(a) and 2(a), respectively. The corresponding true attenuations, β_t, produced by these distributions, are plotted with the solid curves in Figs. 1(b) and 2(b), respectively. They are calculated by applying the formal theory, Eq. (1), to the bubble distribution using numerical integration.[15]

The dotted curves, n_0, in each of the two distribution diagrams [Figs. 1(a) and 2(a)] are the results of applications of the RBA to the true attenuation. The formal theory applied to n_0 produces the dotted curves, β_0, in the attenuation diagrams [Figs. 1(b) and 2(b)]. The distributions, n_0', resulting from the application of the RBA to β_0 are not shown. The errors are calculated from $n_\epsilon\approx n_0-n_0'$ and the first-order estimates, n_t', of n_t [from Eq. (10)] are shown as the dashed curves in the distribution diagrams. Application of the formal theory to n_t' produces β_t', which is shown as the dashed curves in the attenuation diagrams. Clearly, n_t' and β_t' are better approximations to n_t and β_t, respectively, than are n_0 and β_0.

For case I, $n=a^{-4}$, applying the RBA to the true attenuation curve leads to an underestimation of the bubble distribution at the ends of the distributions. Although the difference appears to be small, the resultant attenuation curve is noticeably less than the true attenuation. After using the iterative approach, the resulting bubble distribution is in better agreement with the true distribution. Using the formal theory on this bubble distribution gives an attenuation curve that more closely matches the true attenuation. The disagreement between the two attenuation curves at the peak is caused by the decline in the bubble distribution calculated from the iterative approach at the minimum bubble-radius cutoff.

For case II, multiple power laws, applying the RBA to the true attenuation curve leads to an underestimation of the bubble distribution for the portion of the curve that is proportional to a^{-4}. The RBA then overestimates the bubble distribution for portions that are proportional to a^0 and a^8. The attenuation curve calculated from the RBA bubble distribution is lower than the true attenuation curve for low frequencies and higher for the high frequencies. The iterative approach produces a bubble distribution that better approximates the true attenuation for all bubble sizes. A sharp increase is seen in the iterative-approach distribution for small bubble sizes; however, we note that there is an order-of-magnitude error in the first step of the procedure, which probably invalidates its accuracy for those smaller bubble sizes. A possible source of increasing error between the formal theory and the RBA for the smaller bubble radii is the neglect of surface tension in developing the RBA. A second-order correction might improve the accuracy. Nevertheless, the iterative results are still better than the RBA, and the resultant attenuation curve better approximates the true attenuation curve.

A possible generalization of these results is that error occurs in the RBA primarily when there is a significant change in the power law. This is evident at the minimum and maximum radii of each power-law segment.

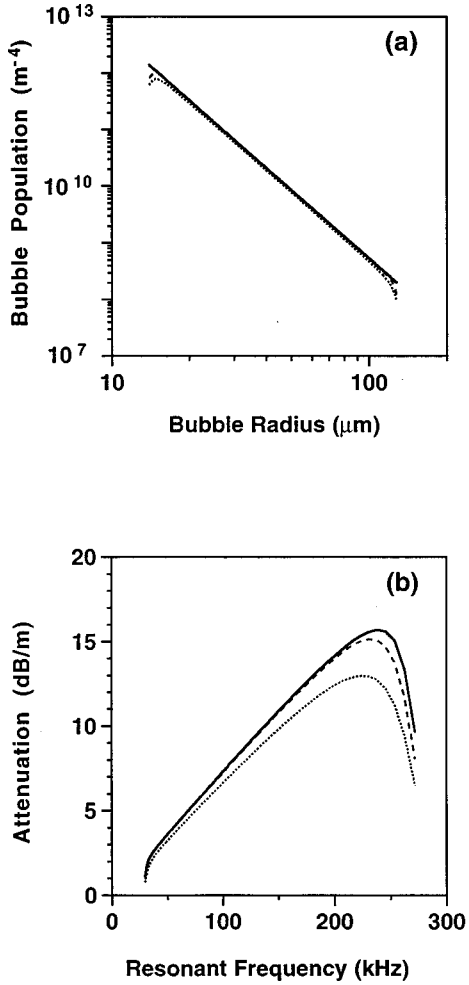

FIG. 1. Simulation case I: (a) bubble distribution, (b) attenuation. The *a priori* bubble distribution, n_t, and the true attenuation, β_t, it produces are plotted with the solid lines in (a) and (b), respectively. The bubble distribution calculated from RBA, n_0, and its resultant attenuation, β_0, are plotted with dotted lines. The corrected bubble distribution calculated from the iterative approach, n_t' and resulting estimate of the true attenuation, β_t' are plotted with dashed lines.

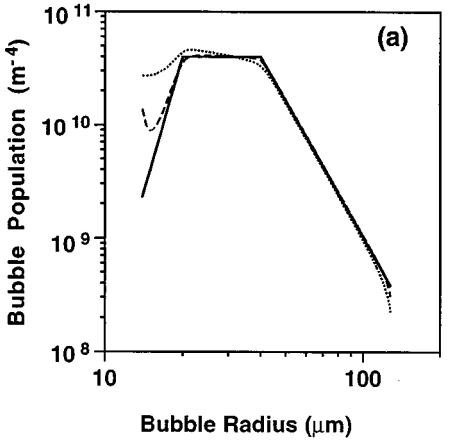

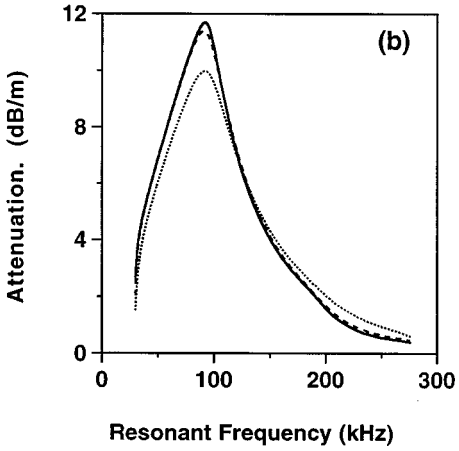

FIG. 2. Simulation case II: (a) density distribution, (b) bubble distribution. Details same as for Fig. 1.

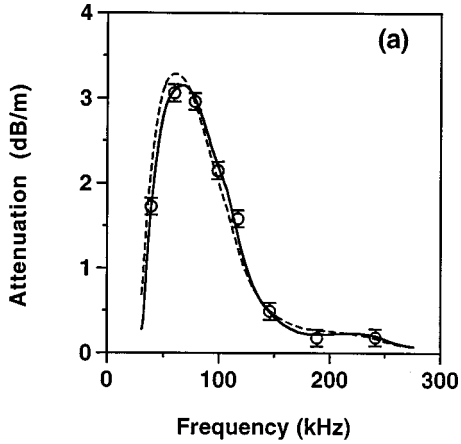

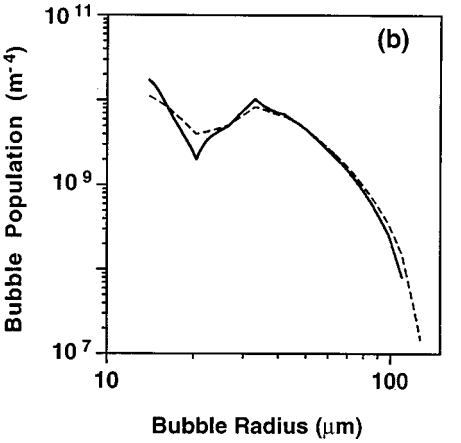

FIG. 3. Application of the iterative approach to experimental data. A sample of attenuation measurements obtained at the Scripps Pier Bubble Experiment are given in (a) by the open circles with expected error bars. The bubble distribution as calculated by the RBA, n_0, and the resultant attenuation, β_0, are plotted with the dashed lines in (b) and (a), respectively. The bubble distribution as calculated by the iterative approach, n_t', and the resulting corrected attenuation, β_t', are plotted with solid lines.

B. Experimental attenuation data

Applying the iterative approach to experimentally measured attenuation versus frequency data requires two additional steps: extrapolation and interpolation. We are given data taken at N discrete points $[\beta(f_i),\ i=1,...,N,\ f_1<f_i<f_N]$. Because of off-resonance effects, bubble radii outside the range $[a_{\min},a_{\max}]$ corresponding to the frequency range $[f_1,f_N]$ also contribute in the formal theory to the attenuation near the ends of the frequency range [i.e., around $\beta(f_1)$ and $\beta(f_N)$]. Therefore, extrapolating the attenuation data out to higher and lower frequencies is required if we wish to include the end data points in the resulting fit. Furthermore, if N is not sufficiently large to perform the integration with adequate accuracy, interpolation is required as a second step. Scalloping in the bubble-distribution domain, with cusps at the resonant-bubble radii for the frequency of the data points, can occur due to inappropriate (i.e., nonphysical) interpolation. We have chosen linear interpolation of the points in the plot of the attenuation data as a function of the log(frequency) for our examples to minimize this effect, as was determined by trial and error. (A more elaborate interpolation scheme could be found, but we believe that this is probably unwarranted in our first-order approximation.) The resulting quasicontinuous data are labeled β_t, once again to imply true attenuation.

For our measured-data test, we have chosen attenuation data taken during the Scripps Pier Bubble Experiment.[16] The data we use here involves the average of ten measurements over 10 s and a path length of 2 m. Attenuation is measured at eight frequencies from 39 to 244 kHz. The discrete measurements, $\beta(f_i)$, and their frequencies are shown in Fig. 3(a). Indications are that the accuracy of the measurements is near ± 0.1 dB/m, so a fairly close fit to these data is prescribed. The data were extrapolated to 30 kHz at the lower end and 276 kHz at the upper end, in order to fit our end measurements, and they are interpolated as discussed above. These data are then the true attenuation, β_t, discussed in the previous section [not shown in Fig. 3(a)].

The iteration process alternates between the attenuation diagram [Fig. 3(a)] and the bubble-distribution diagram [Fig. 3(b)], as was done for the simulated data. However, the figure sequence (a), (b) of this figure is reversed from the simu-

lation sets (Figs. 1 and 2), because, in this case, we begin with attenuation data rather than bubble-distribution data as in the previous cases. That is, now the true distribution, n_t is not known *a priori* in the case of real data.

Given β_t, the sequence of calculations (described in the previous section) is then

$$n_0 = RBA(\beta_t) \Rightarrow \beta_0 = FT[n_0] \Rightarrow$$

$$n_0' = RBA[\beta_0] \Rightarrow n_t' = 2n_0 - n_0',$$

and the test of the results is the ability of $\beta_t' = FT[n_t']$ to match the data $\beta(f_i)$. In Fig. 3(a) we see that the RBA produces a bias of the results by up to 0.2 dB/m. In correcting the bias, we produce a match to the data within the specified accuracy of the data (± 0.1 dB/m).

Note that there is a sharp rise in the distribution for bubble radii smaller than about 25 μm. This rise is quite sensitive to the attenuation data point at 244 kHz [Fig. 3(a)]; note that it appears to be somewhat high. On the other hand, that point could be real and caused by a residual population of very small bubbles.

III. SUMMARY AND CONCLUSIONS

We have presented an iterative approach to inverting Eq. (1) for application to cases where accurate attenuation-versus-frequency data are known, and, correspondingly, accurate bubble-density distributions are sought. Simulated bubble distributions were used to produce a quasicontinuous set of true attenuation data by the forward evaluation of Eq. (1). The iterative approach was shown to produce a bubble distribution that matched the known bubble distribution better than the application of the RBA alone. As a second test of the validity of the resulting bubble distribution, the application of Eq. (1) to this distribution produced attenuations that were a closer match to the true attenuations than a distribution calculated by the RBA.

For the case of real, measured attenuation data, the true bubble distribution is not known. Therefore, only the second test can be applied. The iterative approach was applied to data taken during the Scripps Pier Bubble Experiment, and, in accordance with the second test, a bubble distribution was determined that was an improvement over the resonant bubble approximation.

The accuracy of the data taken during the Scripps Pier Bubble Experiment justified the improvement provided by the iterative approach. It should be noted, however, that results of the approach will be to produce a distribution that will attempt to follow the data, accurate or not. The approach is suggested, therefore, only for attenuation data with sufficient accuracy to warrant its use.

ACKNOWLEDGMENTS

This work is supported by the Acoustic Program of the Office of Naval Research (ONR). P. A. Elmore was funded by the ONR and the Naval Research Laboratory through the postdoctoral program of the American Society of Engineering Education.

[1] *Physics of Sound in the Sea* (Peninsula, Los Altos, CA, 1989), pp. 460–477.
[2] H. Medwin, ''Acoustic fluctuations due to microbubbles in the near-surface ocean,'' J. Acoust. Soc. Am. **56**, 1100–1104 (1974).
[3] K. W. Commander and A. Prosperetti, ''Linear pressure waves in bubbly liquids: Comparison between theory and experiments,'' J. Acoust. Soc. Am. **85**, 732–746 (1989).
[4] L. M. Brekhovskikh and Y. P. Lysanov, *Fundamentals of Ocean Acoustics* (Springer, Berlin, 1991), p. 259.
[5] H. Medwin, ''Acoustical determinations of bubble-size spectra,'' J. Acoust. Soc. Am. **62**, 1041–1044 (1977).
[6] K. Commander and E. Moritz, ''Off-resonance contributions to acoustical bubble spectra,'' J. Acoust. Soc. Am. **85**, 2665–2669 (1989).
[7] H. Medwin, ''*In situ* acoustic measurements of bubble populations in coastal ocean waters,'' J. Geophys. Res. **75**, 599–611 (1970).
[8] P. A. Kolovayev, ''Investigation of the concentration and statistical size distribution of wind-produced bubbles in the near surface ocean layer,'' Oceanology (English Translation) **15**, 659–661 (1976).
[9] B. D. Johnson and R. C. Cooke, ''Bubble populations and spectra in coastal waters: a photographic method,'' J. Geophys. Res. **84**, 3761–3766 (1979).
[10] A. L. Walsh and P. J. Mulhearn, ''Photographic measurements of bubble populations from breaking waves at sea,'' J. Geophys. Res. **92**, 14553–14565 (1987).
[11] H. Medwin and N. D. Breitz, ''Ambient and transient bubble spectral densities in quiescent seas and under spilling breakers,'' J. Geophys. Res. **94**, 12751–12759 (1989).
[12] S. Vagle and D. M. Farmer, ''The measurements of bubble-size distributions by acoustical backscatter,'' J. Atmos. Oceanic Tech. **9**, 630–644 (1992).
[13] H. Medwin, ''*In situ* acoustic measurements of microbubbles at sea,'' J. Geophys. Res. **82** No. 6, 971–976 (1977).
[14] K. W. Commander and R. J. McDonald, ''Finite-element solution to the inverse problem in bubble swarm acoustics,'' J. Acoust. Soc. Am. **89**, 592–597 (1991).
[15] W. H. Press *et al.*, *Numerical Recipes in C: The Art of Scientific Computing, Second Edition* (Cambridge University Press, New York, 1992), p. 134.
[16] J. W. Caruthers, P. A. Elmore, S. J. Stanic, and R. R. Goodman, ''The Scripps Pier Bubble Experiment of 1997,'' Proceedings of the 16th International Congress on Acoustics and the 135th meeting of the Acoust. Soc. of Am. (1998), pp. 697–698.

Pressure-induced interaction between bubbles in a cavitation field

K. Heinrich Kuttruff[a)]
Institute of Technical Acoustics, Rheinisch-Westfälische Technische Hochschule Aachen, Templergraben 55, D-52056 Aachen, Germany

(Received 6 October 1997; revised 9 March 1999; accepted 6 April 1999)

This paper describes the interaction between cavities in transient multibubble cavitation which is due to the pressure waves emitted by collapsing bubbles. These waves sum up to a time-dependent ''secondary pressure'' which accelerates the collapse of contracting bubbles. Since, in each cycle of the exciting sound field the smallest bubbles are the first to implode, this interaction results in an energy transfer from smaller bubbles to larger ones, which undergo particularly violent collapses. This effect is demonstrated by a few examples. © *1999 Acoustical Society of America.* [S0001-4966(99)03507-9]

PACS numbers: 43.35.Ei [HEB]

INTRODUCTION

The dynamic behavior of single cavitation bubbles in liquids has been the subject of numerous investigations. Of particular interest are situations in which a cavity collapses or implodes more or less violently (''hard'' cavitation). In this instance, the bubble emits a strong and short pressure impulse into the surrounding liquid; at the same time, rather extreme conditions may occur in the interior of the cavity which are responsible for sonoluminescence, for sonically induced chemical reactions, or for the erosion of material at nearby solid surfaces. Comprehensive descriptions of these effects may be found in several standard texts.[1–3] Recently developed methods to generate single cavitation bubbles and to excite them to perfectly stable although nonlinear pulsations[4] have opened the possibility to compare theoretical predictions with the real behavior of collapsing bubbles, at least partially.

In the regular case, however, cavitation occurs in form of a more-or-less extended cloud containing numerous bubbles. This holds, for instance, for flow-induced cavitation, for the wake of shock waves as generated in lithotriptors, for ultrasonic cleaning tanks, and other technical devices. It is obvious that these bubbles will not pulsate or collapse independently of each other, but that their motions are mutually coupled by some sort of interaction. In the following, we shall refer to such a bubble cloud as a ''cavitation field.''

One particular kind of bubble interaction is that due to secondary ''Bjerknes forces'' which are proportional to the pressure gradient in the above-mentioned pressure impulses.[3,5] These forces are attractive or repulsive, causing a displacement of a bubble as a whole.

In this paper, we shall consider the effect of the pressure impulses themselves (and not of their gradients). In their totality, they constitute a kind of time-dependent ''secondary pressure'' which has to be added to the exterior liquid pressure. This secondary pressure accelerates (or decelerates) the pulsation of all bubbles present in the cavitation field. Here, it will be calculated by modeling the pressure impulses on the basis of the Rayleigh–Plesset equation and by combining them using simple statistical methods. Although several possible effects such as nonspherical bubbles or energy loss due to radiation are neglected, the results will demonstrate the type of interaction, namely to transfer energy from smaller bubbles to larger ones during the implosion phase.

I. THE DYNAMICS OF SINGLE BUBBLES

Before discussing the interaction between bubbles, a brief recapitulation of single spherical bubble motion will be given. To describe it, several nonlinear differential equations have been formulated.[6–8] For the present purpose the simplest of them is sufficient, namely the Rayleigh–Plesset equation[6] valid for incompressible liquids

$$\rho\left(R\ddot{R}+\frac{3}{2}\dot{R}^2\right)+P(t)+P_s-P_i+\frac{2\sigma}{R}+\frac{4\mu\dot{R}}{R}=0. \qquad (1)$$

Here, R denotes the bubble radius as a function of time t; as usual, overdots indicate partial differentiations with respect to time; ρ is the density, σ is the surface tension, and η is the viscosity of the liquid. $P(t)$ stands for the exterior pressure acting on the bubble wall; it contains the hydrostatic pressure P_0 and possibly a time-varying pressure due to an external sound field. P_i denotes the gas pressure inside the cavity, assuming adiabatic changes of state

$$P_i=P_{i0}\left(\frac{R_0}{R}\right)^{3\kappa}. \qquad (1a)$$

(R_0=reference bubble radius, P_{i0}=corresponding gas pressure, κ=adiabatic exponent of the gas.) P_s is the secondary pressure in the liquid, caused by the motion of all other bubbles of the cavitation field. Since we are dealing with just one isolated cavity, we set $P_s=0$ in this section.

Once Eq. (1) is solved, the pressure wave emitted by a collapsing bubble can be calculated, at least approximately. For a rigorous treatment of this problem, we ought to consider the nonlinearity of wave propagation, at least in the

a)Electronic mail: kuttruff@akustik.rwth-aachen.de

next vicinity of the bubble. However, the results of numerical calculations carried out by several authors[9,10] show that from a certain distance r on, the peak pressure diminishes according to the $1/r$-law and that its value is close to that obtained with the acoustical approximation. Therefore, the following discussion will be based on linear wave propagation.

Accordingly, we consider the bubble as a spherical sound source characterized either by the variation of its radius $R(t)$ or by the pressure P_i on its surface. In the first case, the pressure in the radiated wave would be given by

$$p_s(r,t)=\rho\frac{R}{r}(R\ddot{R}+2\dot{R}^2), \tag{2a}$$

while the case of prescribed surface pressure leads to

$$p_s(r,t)=P_i\cdot\frac{R}{r}=\rho\frac{R}{r}\left(R\ddot{R}+\frac{3}{2}\dot{R}^2\right). \tag{2b}$$

[The second expression follows from Eq. (1) with $\mu=\sigma=0$ and holds for the vicinity of maximum contraction.] In both equations, the time variable on the right side is $t-r/c$ because of the finite traveling time of an impulse, which means that we have to give up the simplification of an incompressible liquid at this point.

The difference between Eqs. (2a) and (2b) indicates that none of them is quite correct as long as $\dot{R}^2$ is not vanishingly small. From their similarity, however, we may conclude that each of them is at least a useful approximation. We decide to employ the latter because it is simpler.

Under certain circumstances, we can even obtain a closed expression for the pressure wave. This is true if the parameters of the motion are chosen in such a way that the bubble will undergo a rapid collapse once in a while and will rebound afterwards. Then, we can approximate the unknown function $R(t)$ by its Taylor series truncated after the second nonzero term

$$R(t)\approx R_m[1+\alpha^2(t-t_c)^2]. \tag{3}$$

(R_m denotes the minimum radius reached for $t=t_c$.) The constant $\alpha^2=\ddot{R}_{t=t_c}/2R_m$ is easily obtained from the above differential equation with $\dot{R}=0$, since the internal gas pressure $P_{\max}=P_{i0}(R_0/R_m)^{3\kappa}$ predominates all other terms at time t_c (except, of course, $\rho R\ddot{R}$)

$$\alpha^2=\frac{P_{\max}}{2\rho R_m^2}. \tag{4}$$

Inserting Eq. (3) into Eq. (1a) yields the gas pressure in the bubble as a function of time

$$P_i(t)=P_{\max}[1+\alpha^2(t-t_c)^2]^{-3\kappa}. \tag{5}$$

This expression is a fairly good approximation to the real gas pressure since—due to the high power in Eq. (1a)—P_i has dropped to nearly zero before the errors of the approximation in Eq. (2) become significant.

II. THE BUBBLE FIELD

Now, consider an infinite field of cavitation bubbles randomly distributed in space with constant mean density n.

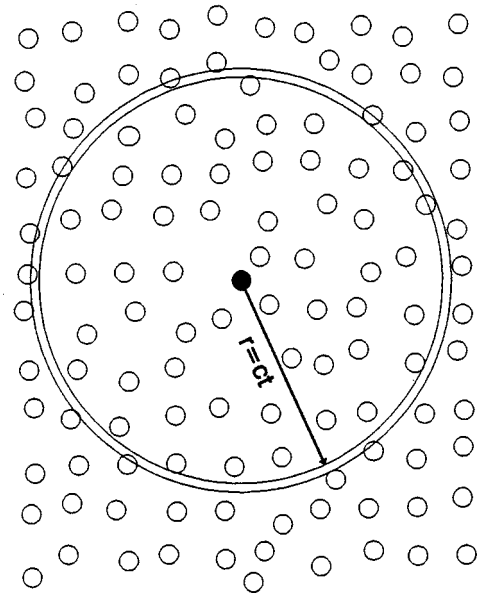

FIG. 1. Schematic cavitation field consisting of equal bubbles.

Each collapse of a bubble will produce a pressure wave and thus contribute to the secondary pressure P_s in Eq. (1). An exact treatment of this multibubble problem would require the simultaneous solution of infinite differential equations of the type presented above, namely one for each cavity. However, if we content ourselves with the simple approximations for R and P_i expressed in Eqs. (3) and (5), we can arrive at simple expressions for the secondary pressure.

For this purpose, we assume for the moment that all bubbles have equal size (see Fig. 1), and that they all are exposed to the same external conditions. Hence, each of them will implode at the same time t_c and emit the same pressure wave p_s, given by Eq. (2b). The total secondary pressure $P_{s,\mathrm{eq}}$ acting on a given bubble (here in the center of the figure) is the superposition of all these waves, taking into account their finite traveling times. The contribution of all bubbles within an infinitely thin spherical shell with radius r is $nP_i(t-t_c-r/c)R_m dV/r$, with $dV=4\pi r^2\,dr$; hence, the integration of p_s over the whole volume yields

$$P_{s,\mathrm{eq}}(t)=nR_m\int\int\int P_i\left(t-t_c-\frac{r}{c}\right)\frac{dV}{r}$$

$$=4\pi nc^2R_m\int_{-\infty}^{t-t_c}P_i(\tau)\cdot(t-t_c-\tau)\,d\tau, \tag{6}$$

with the substitution $t-t_c-r/c=\tau$. Since $P_i(\tau)$ is a rapidly varying function having noticeable values only in the next vicinity of $\tau=0$, the second bracket in the second integral of Eq. (6) may be replaced with $t-t_c$, which leaves

$$P_{s,\mathrm{eq}}(t)=4\pi nc^2R_m(t-t_c)\int_{-\infty}^{t-t_c}P_i(\tau)\,d\tau$$

$$=4\pi nc^2BR_m^2\sqrt{2\rho P_{\max}}(t-t_c)\quad\text{for } t>t_c; \tag{7}$$

for $t<t_c$, the secondary pressure is zero. The numerical constant is $B=\Gamma(1/2)\Gamma(3\kappa-1/2)/\Gamma(3\kappa)$; for an adiabatic exponent of $\kappa=1{,}4$ (air) its value is 0.953. This equation holds also for acoustically driven cavitation bubbles, provided the

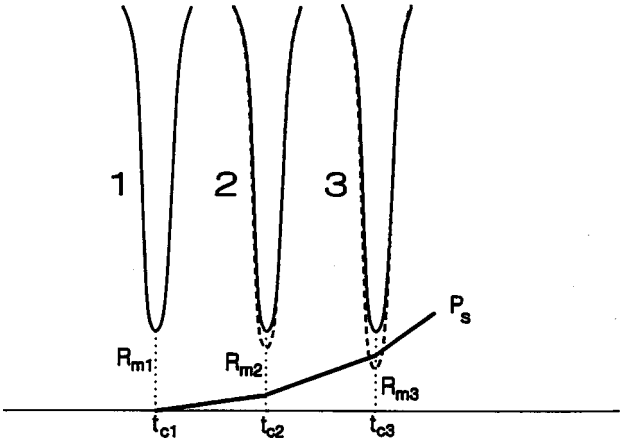

FIG. 2. Calculation of the secondary pressure in cavitation fields.

acoustic wavelength in the liquid is large compared with the range of interaction, which is usually the case.

Now, we drop the assumption of equally sized bubbles. Accordingly, the total bubble density n must be replaced with the distribution density $n(R_0)$. To obtain a formal expression for the secondary pressure at a given time t, Eq. (7) is integrated with respect to R_0, taking into account only those contributions for which $t_c<t$. Hence, the range of integration has to be extended to the R_0 of those bubbles which have already collapsed at time t

$$P_s(t)=4\pi c^2 B\int_0^{R_0(t_c=t)} n(R_0)R_m{}^2\sqrt{2\rho P_{\max}}\cdot(t-t_c)\cdot dR_0. \tag{8}$$

This integral tells us that a bubble with a given initial radius R_0 and collapse time t_c remains uninfluenced by the motion of larger cavities, but that its collapse is accelerated by the implosions of all smaller bubbles. On the other hand, this particular bubble influences the motion of all larger bubbles, but not those of the smaller ones. Thus, the interaction between the cavities is not mutual but is directed from smaller towards larger bubbles.

III. NUMERICAL EXAMPLES

For the numerical demonstration of bubble interaction, the variable R_0 is subdivided into classes with finite class width ΔR_0. Accordingly, n_k $(k=1,2,...)$ denotes the density of bubbles with reference radius $(R_0)_k$; the associated minimum radii and times where they occur are $(R_m)_k$ and t_k, respectively. Then, Eq. (8) is replaced with a sum over all bubble classes for which $t_k<t$

$$P_s(t)=4\pi Bc^2\Delta R_0\sum_k n_k\sqrt{2\rho(P_{\max})_k}\cdot(R_m)_k^2(t-t_k). \tag{9}$$

The evaluation Eq. (9) is illustrated by Fig. 2: Numerical solution of Eq. (1) with $P_s=0$ yields $(P_{\max})_1$, $(t_k)_1$, and $(R_m)_1$ for the bubbles belonging to the class with smallest reference radii (class no. 1). With these values, the first term of Eq. (9) and hence the first section of P_s can be formed. By inserting this into Eq. (1), a further solution of this differential equation leads us to the values $(P_{\max})_2$, $(t_k)_2$, and $(R_m)_2$ (class no. 2). In this way, we proceed until all bubble classes have been worked off.

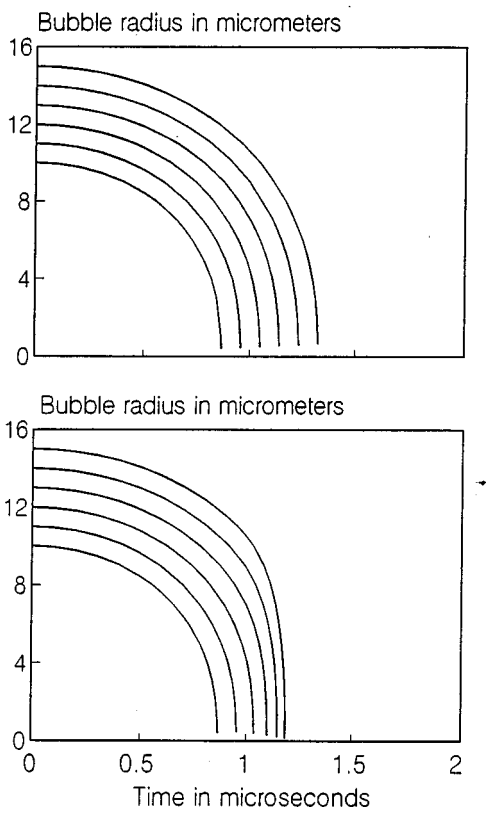

FIG. 3. Radius-time curves for Rayleigh collapse of air bubbles in water. The initial radii R_0 are uniformly distributed between 10 and 15 μm. Above: Independent bubbles. Below: Interacting bubbles, 3500 bubbles per mm^3.

As a first example, we consider the collapse of bubbles in water under the influence of constant external pressure $P=P_0$ with all bubbles at rest at the beginning of the process, i.e., the so-called Rayleigh collapse. R_0 denotes the initial radius of the bubbles which are at rest. If the initial gas pressure P_{i0} in the cavities is small compared with the ambient pressure, the bubble will contract with ever-increasing speed. In the final state of its collapse, the bubble is abruptly decelerated by the highly compressed gas, which acts like a cushion; afterwards it will rebound.

In the present case, the reference radii of the bubbles are their initial radii R_0, which are assumed to be uniformly distributed in a range from 10 to 15 μm with a total bubble density of 3500 per mm^3. For the class width in Eq. (9), $\Delta R_0=0.25\,\mu$m was chosen. Further assumptions are that the static water pressure is $P_0=1$ bar, and $P_{i0}/P_0=0.1$. The radius-time curves of different bubble sizes are calculated until their first collapse.

The result is plotted in Fig. 3. Each diagram shows six selected radius-time curves. The upper ones have been calculated assuming independent bubbles $(P_s=0)$, while the lower curves include the interaction between the bubbles. Obviously, the latter curves are increasingly steeper in their final portions, and hence all bubbles implode within a shorter time interval. At the same time, the ends of the radius-time curves become deeper with increasing bubble size, resulting in increasing maximum pressures inside the bubbles. This

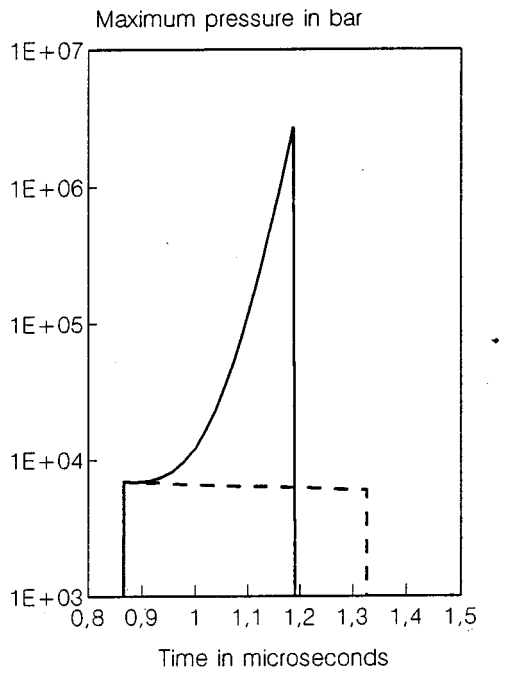

FIG. 4. Maximum gas pressure in the imploding bubbles of Fig. 3, as a function of collapse time t_c (dashed line: without interaction).

pressure is plotted in Fig. 4 as a function of the collapse time t_c. Without any interaction, the final gas pressure would be the same for all bubbles, as indicated by the dashed line.

These effects are still more pronounced for a somewhat more realistic process, namely the growth and collapse of bubbles in a sinusoid pressure field. In the present example, the assumed excitation signal had a frequency of 20 kHz; the pressure amplitude was 1.05 bar. The distribution of initial bubble radii and the class width were the same as before; however, the total bubble density was only 500 per mm^3. The radius-time curves obtained for this situation are plotted in Fig. 5, again for independent (upper part) and for interacting (lower part) bubbles. In the latter case, the final portions of the curves are pressed together as in the first example. Again, it is obvious that the collapses of larger bubbles are strongly accelerated by those of the smaller cavities. Figure 6 plots the maximum gas pressure in the bubble as a function of collapse time for 0, 200, 500, and 1000 bubbles per mm^3. It is evident that the latest collapses are associated with very high internal pressures and that all implosions occur within a reduced time interval.

If the constant distribution of bubble sizes is replaced with a more realistic distribution, for instance a gamma distribution, the results are qualitatively similar, showing an even more pronounced concentration of energy towards the largest bubbles.

IV. CONCLUSIONS

In any kind of hard cavitation, energy delivered by an external pressure field is concentrated towards very small regions, due to the rapid contractions of the cavities. Likewise, a considerable temporal energy concentration takes place, since the final collapse of a cavitation bubble occurs

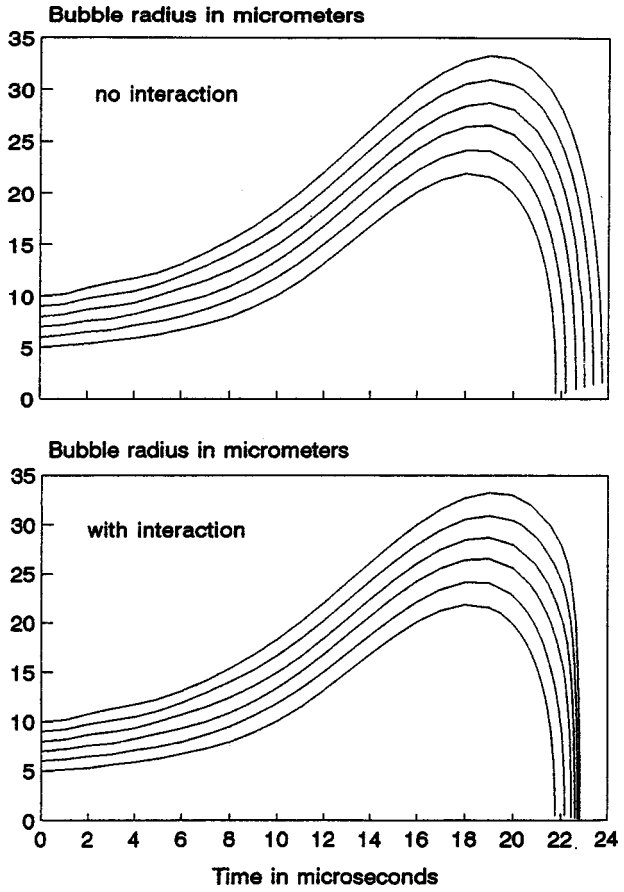

FIG. 5. Radius-time curves of cavities in a sound field with a frequency of 20 kHz and a pressure amplitude of 1.05 bar. The initial radii R_0 are uniformly distributed between 5 and 10 μm Above: Independent bubbles. Below: Interacting bubbles, 500 bubbles per mm^3.

within very short times. This concentration is the reason for the typical effects accompanied with strong cavitation, which have been addressed in the Introduction.

The results presented in this paper show that in extended cavitation fields an additional concentration of energy takes place. Due to the interaction of cavitation bubbles, energy is conveyed from smaller bubbles to larger ones. This means that small bubbles remain uninfluenced by the collapses of other bubbles. Larger bubbles, however, which implode later than the smaller ones, have the chance to collect energy from the latter and will therefore undergo more violent collapses. The most violent implosions are those which occur latest in a sound cycle. This agrees with experimental observations: If the sonoluminescence originating from an acoustically excited cavitation field is recorded with a photo-multiplier, only a few luminescence pulses are observed in each sound cycle, although the number of bubbles imploding in the same cycle is larger by orders of magnitude. These light pulses appear within a certain fraction of the sound cycle and are more or less randomly distributed in it.[11] If the excitation amplitude is not too high, their intensities show a marked increase towards the end of this time span.[12] A similar observation holds for the pressure waves emitted by the collapsing bubbles: in each period, only of few of them are really strong enough to be detected by schlieren optics, for instance, although each collapsing bubble. And these particu-

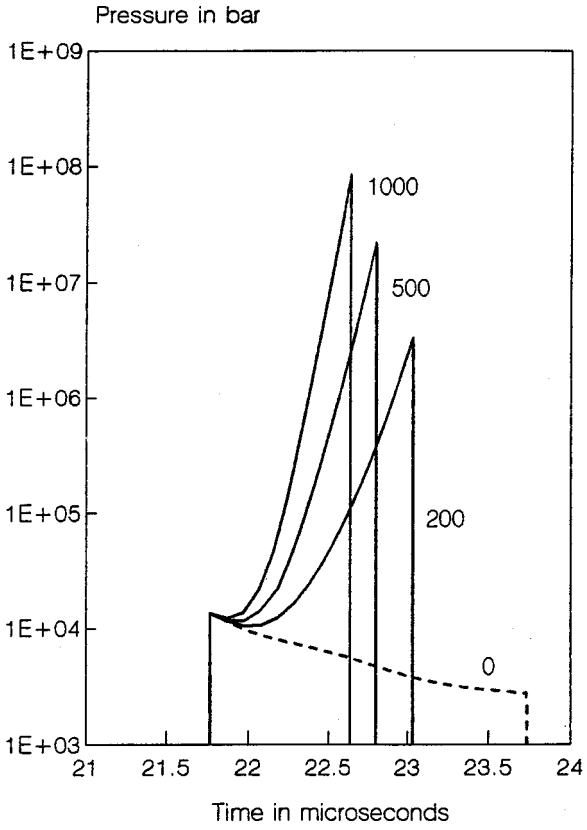

FIG. 6. Maximum gas pressure in the imploding bubbles of Fig. 5, as a function of collapse time t_c (dashed line: without interaction). Parameter is the total bubble density in mm^3.

larly strong waves appear mainly in that phase, in which the last bubbles vanish by implosion.[13]

It should be noted that the analysis of the described interaction could be refined by replacing Eq. (1) with a more exact differential equation, for instance with the Keller–Miksis equation,[7] or by using the van der Walls (''hard core'') equation[14] instead of Eq. (1a). Furthermore, the energy losses of a vibrating bubble due to radiation have not been taken into account. These refinements would certainly modify the numerical results. Nevertheless, the above calculations demonstrate the tendency of the interaction, namely to convey energy from early imploding bubbles towards those cavities which collapse last, and further, that the effect of this interaction is by no means negligible.

ACKNOWLEDGMENTS

The author is indebted to the reviewers of this paper, to which he owes many valuable suggestions. He is also grateful to T. Niederdränk for critically reading the manuscript.

[1] H. G. Flynn, ''Physics of Acoustic Cavitation in Liquids,'' in *Physical Acoustics*, edited by W. P. Mason (Academic, London, 1964), Vol. I, Part B, pp. 57–172.
[2] F. R. Young, *Cavitation* (McGraw-Hill, London, 1989).
[3] T. G. Leighton, *The Acoustic Bubble* (Academic, London, 1994).
[4] D. F. Gaitan, L. A. Crum, R. A. Roy, and C. C. Church, J. Acoust. Soc. Am. **91**, 3166–3183 (1992).
[5] R. Mettin, I. Akhatov, U. Parlitz, C. D. Ohl, and W. Lauterborn, Phys. Rev. E **56**, 2924 (1997).
[6] B. E. Noltingk and E. A. Neppiras, Proc. Phys. Soc. London, Sect. B **63**, 674–685 (1950).
[7] J. B. Keller and M. Miksis, J. Acoust. Soc. Am. **68**, 628–633 (1980).
[8] F. R. Gilmore, Hydrodyn. Lab. Report 26-4, Calif. Inst. Tech., 1952.
[9] R. Hickling and M. S. Plesset, Phys. Fluids **7**, 7–14 (1964).
[10] S. Fujikawa and T. Akamatsu, J. Fluid Mech. **97**, 481–512 (1980).
[11] T. J. Matula, R. A. Roy, and P. D. Mourad, J. Acoust. Soc. Am. **101**, 1994–2002 (1997).
[12] H. Kuttruff, Acustica **12**, 230–254 (1962).
[13] T. Niederdränk, Ph.D. thesis, Aachen, 1998.
[14] R. Löfstedt, B. P. Barber, and S. J. Putterman, Phys. Fluids A **5**, 2911–2928 (1993).

Acoustic wave generation in viscoelastic rods by time-gated microwaves

Christophe Bacon and Bernard Hosten
Laboratoire de Mécanique Physique, Université Bordeaux 1, UPRES A 5469 CNRS 351, cours de la Libération, 33405 Talence Cedex, France

Pierre-Alain Bernard
Laboratoire de Modélisation Avancée des Systèmes Thermiques et des Ecoulements Réels, Ecole Nationale Supérieure de Chimie et de Physique de Bordeaux, Avenue Pey-Berland, BP108, 33402 Talence, Cedex, France

(Received 10 June 1998; accepted for publication 9 April 1999)

A one-dimensional model is developed to predict the acoustic waves generated in viscoelastic rods by electromagnetic microwave pulses. The wave generation is due to the rapid thermal expansion caused by microwave absorption. The distribution of the temperature rise along the rod is taken to be either uniform or linear. The effects of this distribution and of the microwave pulsewidth are investigated numerically. Some tests are carried out on PVC rods instrumented with accelerometers. The presence of the accelerometer mass at the end of the rod is taken into account in the model. The comparison between the experimental and the theoretical accelerations leads to the evaluation of the maximum temperature rise during one pulse. Although this temperature rise is found to be extremely low, it produces acoustic waves easily detectable with the accelerometer. The inverse problem to estimate the viscoelastic properties of the rod and the temperature rise is approached by means of a numerical minimization technique. [S0001-4966(99)04507-5]

PACS numbers: 43.35.Mr [HEB]

INTRODUCTION

Polymers are widely used in mechanical structures for their damping properties. These materials exhibit viscoelastic properties, particularly under dynamic loadings such as impact. So, there is a great need for the identification of their viscoelastic characteristics in order to use them in numerical simulations of impacts for instance.

The problem is that the mechanical characteristics of this kind of materials depend very markedly on the frequency. Thus, quasistatic measurements at low frequencies or ultrasonic measurements at high frequencies are not sufficient for the complete knowledge of the material at intermediate frequencies, i.e., in a frequency range between some Hertz and 10 or 20 kHz corresponding to impact loadings. However, an appropriate material model can be used provided that it has been experimentally validated. To do this, it is important to carry out measurements at some intermediate frequencies. A comprehensive review of the experimental techniques is out of the scope of this paper. The reader is referred to the reviews of Nolle,[1] McSkimin,[2] Ferry,[3] and Nowick and Berry.[4] Particularly, such frequencies can be reached by measuring waves generated by harmonic or impact excitations on a slender rod. A great number of papers have been devoted to the determination of viscoelastic characteristics by means of a dynamically loaded slender rod. We can distinguish the methods where the rod specimen is loaded harmonically[5–11] and the methods where the specimen is impacted.[12–15] In the latter case, the viscoelastic properties are evaluated by studying the change in shape of a stress pulse as it travels back and forth along a viscoelastic polymer rod. In both cases, the wave generation requires the contact of a shaker or a projectile.

The present paper deals with the identification of polymer mechanical properties by means of a viscoelastic rod irradiated with short rectangular pulses of electromagnetic microwave energy. The method does not require a mechanical contact for the wave generation. Owing to the rapid thermal expansion caused by microwave absorption, acoustic waves are generated in such a rod. The measurement of the signals due to these waves should permit the identification of the mechanical properties of viscoelastic materials.

The production of acoustic waves resulting from thermal expansion due to a sudden heating has been investigated intensely in the case of laser radiation on elastic materials.[16–22] Hutchins presented an extensive review of both experimental and theoretical works on the subject.[17] In the case of a laser impact, the heating happens very close to the impacted surface since the electromagnetic absorption is strong. On the contrary, in the case of microwave irradiation, the absorption is very much lower and the depth of wave generation is more important. Consequently, any interface in the specimen may contribute to the wave generation even if it is far from the irradiated surface. For instance, it will be shown in the present paper that the wave generation happens at both ends of an irradiated polymeric specimen rod. In the classical methods of nondestructive control, the waves generally interfere with a defect present in the volume of the specimen but they are not generated by this defect. For microwave generation, since the electromagnetic absorption is low, the acoustic waves may be generated at the surface of the defect. This phenomenon, which will not be discussed in this paper,

could be interesting for the detection of volume defects. Moreover, in the methods of laser impact, the impacted surface is very small. Consequently, a two-dimensional or three-dimensional analysis is required. In the case of microwave generation, the irradiated surface is much more important and a unidimensional analysis is generally sufficient.

For elastic materials irradiated with microwave energy, the theoretical background has been presented by White[16] and by Borth and Cain.[23] However, the production of elastic waves from microwave energy was essentially noticed for their physiological effects: Human subjects hear a distinct ''click'' when the head is irradiated with a high-energy microwave pulse.[23,24] This effect arises from sound waves generated in the tissues of the head by rapid thermal expansion. The ability to use the ultrasonic wave generation by electromagnetic microwaves for the nondestructive evaluation of materials has been investigated recently.[25]

The studies quoted above deal with microwave generation in elastic materials. The purpose of the present paper is to predict the waves generated in viscoelastic rods by microwave pulses. It will be considered that the electromagnetic absorption in the polymeric material being tested is weak. As a consequence, the temperature rise caused by the energy absorption can be assumed to be almost uniform over all the specimen. A linear distribution of the temperature will also be taken into account. An accelerometer located at one end of the rod will be used for the measurements. Afterward, some experimental results on PVC rods will be presented in order to validate the model.

I. THEORY

Let us consider a rod which is straight, cylindrical, slender and made of linearly viscoelastic material. Its cross-sectional area and its density are A and ρ. Its length is L. If the lateral dimensions of the rod is much shorter than the wavelength, the radial inertia can be neglected. Then, the normal stress $\sigma(x,t)$ is related to the axial displacement $u(x,t)$ at axial coordinate x and at time t by:

$$\frac{\partial \sigma(x,t)}{\partial x} = \rho \frac{\partial^2 u(x,t)}{\partial t^2}. \tag{1}$$

It is more convenient to write the above equation in the Fourier domain:

$$\frac{\partial}{\partial x}\tilde{\sigma}(x,\omega) = -\rho\omega^2 \tilde{u}(x,\omega), \tag{2}$$

where $\tilde{\sigma}(x,\omega)$ and $\tilde{u}(x,\omega)$ denote the Fourier transforms of the stress and the displacement, respectively. The angular frequency ω is related to the frequency v by $\omega = 2\pi v$.

In the frequency domain, the linear viscoelastic behavior of the material can be expressed as:

$$\tilde{\sigma}(x,\omega) = E^*\tilde{\epsilon}(x,\omega) - E^*\beta\tilde{\theta}(x,\omega), \tag{3}$$

where $E^*(\omega)$ is the complex modulus of the material, β is its coefficient of linear thermal expansion and $\tilde{\epsilon}(x,\omega)$ and $\tilde{\theta}(x,\omega)$ are the Fourier transforms of the longitudinal strain and the temperature rise above the initial temperature, respectively. To facilitate the analysis, it will be assumed that the temperature increase is so small that it does not affect the mechanical behavior of the material. The complex modulus is related to the loss factor, the storage and loss moduli, $\delta(\omega)$, $E'(\omega)$ and $E''(\omega)$, respectively, by $E^* = |E^*|e^{i\delta}$ or $E^* = E' + iE''$.

From Eqs. (2) and (3), it can be demonstrated that the Fourier transforms of the axial displacement, the axial particle velocity $\tilde{v}(x,\omega)$ and the axial acceleration $\tilde{a}(x,\omega)$ can be calculated if the longitudinal strain and the temperature rise are known, i.e.:

$$\begin{aligned}
\tilde{u}(x,\omega) &= \frac{1}{(\omega S^*)^2}\left[\beta\frac{\partial\tilde{\theta}(x,\omega)}{\partial x} - \frac{\partial\tilde{\epsilon}(x,\omega)}{\partial x}\right],\\
\tilde{v}(x,\omega) &= i\omega\tilde{u}(x,\omega),\\
\tilde{a}(x,\omega) &= -\omega^2\tilde{u}(x,\omega),
\end{aligned} \tag{4}$$

where the complex slowness S^* is given by $S^{*2} = \rho/E^*$ and is related to the attenuation (or damping coefficient) $\alpha(\omega)$ and the phase velocity $c(\omega)$ by:

$$S^* = S' - iS'' = \frac{1}{c(\omega)} - i\frac{\alpha(\omega)}{\omega}. \tag{5}$$

In the hypothesis of small strains, the longitudinal strain is related to the axial displacement by $\epsilon(x,t) = \partial u(x,t)/\partial x$. Consequently, Eq. (2) becomes:

$$\frac{\partial^2\tilde{\epsilon}(x,\omega)}{\partial x^2} + \omega^2 S^{*2}\tilde{\epsilon}(x,\omega) - \beta\frac{\partial^2\tilde{\theta}(x,\omega)}{\partial x^2} = 0. \tag{6}$$

In the case where the last term is zero (uniform or linear temperature along the x-axis), the general solution of Eq. (6) can easily be found:

$$\tilde{\epsilon}(x,\omega) = \tilde{P}(\omega)e^{-i\omega S^* x} + \tilde{N}(\omega)e^{i\omega S^* x}, \tag{7}$$

where the functions $\tilde{P}(\omega)$ and $\tilde{N}(\omega)$ define the Fourier transforms of the strains at $x=0$ due to the waves traveling in the directions of increasing and decreasing x, respectively.

Then, when these functions are known, it is easy to find the Fourier transforms of the axial particle velocity $\tilde{v}(x,\omega)$, the acceleration $\tilde{a}(x,\omega)$ and the normal force $\tilde{F}(x,\omega)$ at the cross-section of axial coordinate x by using Eqs. (3), (4), and (7).

The determination of functions $\tilde{P}(\omega)$ and $\tilde{N}(\omega)$ involves the knowledge of the boundary conditions at both ends of the rod. The rod end at $x=0$ is free. Consequently, the normal stress at $x=0$ must be zero, i.e., $\tilde{\sigma}(0,\omega)=0$. From Eqs. (3) and (7), this condition gives a relation between $\tilde{P}(\omega)$ and $\tilde{N}(\omega)$:

$$\tilde{N}(\omega) = \beta\tilde{\theta}(0,\omega) - \tilde{P}(\omega). \tag{8}$$

A second boundary condition is necessary in order to obtain $\tilde{P}(\omega)$ and $\tilde{N}(\omega)$ independently. The rod is instrumented with an accelerometer having a mass m at the end $x=L$. Thus, the normal force at this end is related to the axial velocity by:

$$\tilde{F}(L,\omega) = -Z_a\tilde{v}(L,\omega), \tag{9}$$

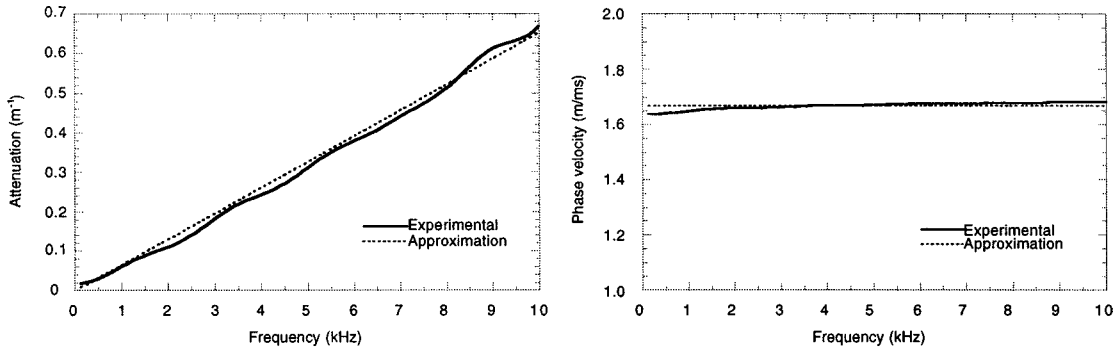

FIG. 1. Experimental attenuation and phase velocity of a PVC rod obtained by an impact test.

where Z_a is the mechanical impedance of the accelerometer. At low frequencies, the accelerometer can be assumed to be a rigid mass. Then, its mechanical impedance is given by $Z_a = im\omega$.

Consequently, if the temperature distribution along the rod is linear or uniform (whatever the time t), the Fourier transforms of the longitudinal strain at $x=0$ due to the waves propagating in the direction of increasing x is:

$$\tilde{P}(\omega) = \frac{\beta\tilde{\theta}(L,\omega) - \beta\tilde{\theta}(0,\omega)e^{i\omega S^* L} - (Z_a S^*/\rho A)[\beta\tilde{\theta}(0,\omega)e^{i\omega S^* L} - (\beta/i\omega S^*)(\partial\tilde{\theta}/\partial x)]}{2i\,\sin(-\omega S^* L) - 2(Z_a S^*/\rho A)\cos(\omega S^* L)}. \tag{10}$$

By using successively Eqs. (10), (8), (7), and (4), the acceleration of any cross-section x can be obtained easily if the temperature rises, $\theta(0,t)$ and $\theta(L,t)$, at both the rod ends are known.

In the case of deeply penetrating microwave radiations in a weakly absorbing material, the temperature distribution can be supposed to be uniform along the viscoelastic rod. Under this hypothesis, the temperature rise does not depend on the axial coordinate x, i.e., $\theta(x,t)=\theta(t)$ and $\tilde{\theta}(x,\omega) = \tilde{\theta}(\omega)$.

For short rectangular microwave pulses (time-gated microwaves) where heat conduction can be ignored, if the test duration is very short, it can be assumed with sufficient accuracy that the temperature rise $\theta(t)$ increases linearly during the pulsewidth $(0<t<\tau)$ and remains almost constant afterward.[23] Then, the function $\theta(t)$ has the form:

$$\theta(t) \approx \begin{cases} \theta_{\max}\dfrac{t}{\tau}, & 0<t<\tau \\ \theta_{\max}, & \text{elsewhere} \end{cases}, \tag{11}$$

where $\theta_{\max}$ is the maximum temperature rise. This maximum temperature depends particularly on the power density of the microwave radiations and on the pulsewidth.

II. NUMERICAL SIMULATIONS

As an illustration, numerical simulations have been carried out for a PVC rod irradiated with microwave energy and instrumented by an accelerometer. To perform these computations, the mechanical characteristics of the material are measured by an impact method.

A. Preliminary impact tests

The viscoelastic mechanical properties of the PVC have been measured by performing preliminary impact tests on a long rod (1.38 m) having a 15.5 mm diameter. Its mass density is 1440 kg/m^3. The method used is based on the method of Lundberg and Blanc.[13] The specimen rod was instrumented with a single bridge of strain gauges (located in the middle of the rod) and the nonimpacted end was left free during the test. The waves were generated by the impact of a small spherical projectile on the first end. The measurements of the longitudinal strains due to the generated incident wave and its reflection at the nonimpacted free end allow us to evaluate the phase velocity $c(\omega)$ and the attenuation coefficient $\alpha(\omega)$. The results are presented in Fig. 1.

The Kramers–Kronig[26] relationship implies a frequency dependence of the phase velocity in the presence of damping. However, since the damping is relatively low, it is shown in Fig. 1 that the phase velocity is almost constant in the measurement frequency range. Consequently, for the numerical simulations, a reasonable approximation is to consider that the attenuation is a linear function of the frequency and the phase velocity is almost constant. As a consequence, the real and the imaginary parts of the material complex slowness do not depend on the frequency and these two values are sufficient to represent the mechanical behavior of the specimen.

B. Numerical simulations

Next, numerical simulations have been carried out for a rod made with the same material as in Section A and having a length L of 20 cm. The accelerometer mass m is 0.65 g.

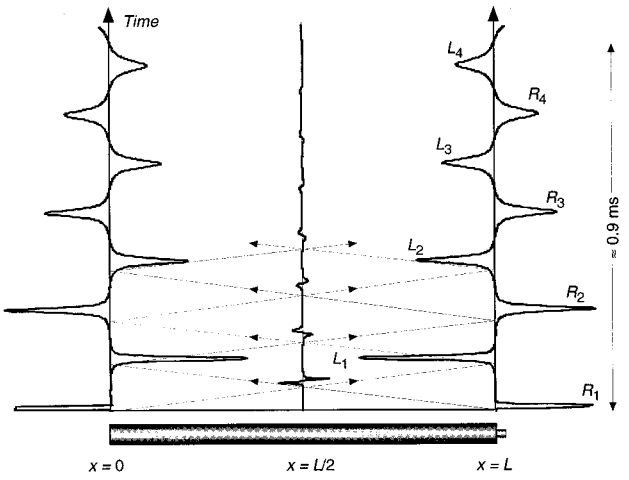

FIG. 2. Numerical prediction of the accelerations at $x=0$, $x=L/2$ and $x=L$ (PVC, $L=20$ cm, $\tau=10$ μs).

The pulsewidth τ is chosen to be 10 μs. The calculations of the accelerations have been performed at three different cross-sections $x=0$, $x=L/2$, and $x=L$. The results are plotted in Fig. 2. The filter representative of the accelerometer charge amplifier is not introduced at this stage of the computation.

It can be observed that two waves are generated simultaneously at both the ends of the rod (Right and Left ends). At the location of the accelerometer $(x=L)$, these two waves produce a first acceleration pulse R_1 and a second pulse L_1. Afterward, the successive pulses $(R_2,L_2,R_3,L_3,\ldots)$ of the simulated accelerations are induced by the multiple echoes of these two initial perturbations. The amplitudes of these pulses decrease since the propagation in the viscoelastic rod attenuates the waves. However, it can be noticed that the amplitude of the pulse R_2 at $x=L$ is slightly larger than the amplitude of the pulse R_1. Indeed, the pulse R_1 is caused by a single wave while the pulse R_2 is caused by the addition of the wave propagating in the positive direction and its own reflection. As a consequence, if the wave attenuation and the accelerometer mass were negligible, the amplitude of the pulse R_2 would be twice the amplitude of the pulse R_1.

The accelerations simulated at both ends are almost symmetric but a very small difference is observable between the two signals. This difference is due to the presence of the accelerometer. This is the reason why the acceleration at $x=L/2$ is not zero.

When the temperature distribution is not uniform, waves are generated not only at both ends of the rod but also everywhere along the rod since the continuity of the normal stress must be maintained. If the temperature distribution is linear, numerical simulations can be performed with the help of the equations determined in Sec. II.

The effect of the microwave pulsewidth and of the time shape of $\theta(t)$ has also been investigated numerically (see Fig. 3). The acceleration signals at $x=L$ have been simulated in four different cases by keeping the value of $\theta_{\max}$ constant. Three pulsewidths ($\tau=1$ μs, 5 μs, and 10 μs) have been chosen with the linear variation of the temperature rise given

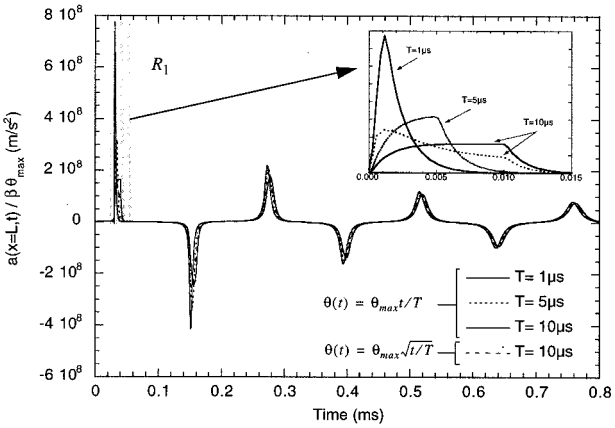

FIG. 3. Effect of the pulsewidth and of the time shape of the temperature rise on the acceleration signal (PVC, $L=20$ cm).

by Eq. (11). Furthermore, for the case with a pulsewidth of 10 μs, a square root variation has also been used for comparison with the linear variation (this function has been used by White[16] in the case of a transient surface heating).

The comparison of the simulated acceleration signals shows that the influence is important only for the first pulse R_1. The differences between the four signals become smaller and smaller when the time increases. In the frequency range of interest of the accelerometer (0–20 kHz), it has been noticed that the simulated acceleration spectra of the above four cases are very close. Consequently, if the signals are filtered by the accelerometer electronic device, the difference between these four cases would be almost invisible. However, the modification of the pulsewidth leads to a change of the maximum temperature rise $\theta_{\max}$ and the amplitude of the acceleration signals is proportional to this maximum temperature. Thus, if it can be assumed that the time variation of the temperature is linear during the pulsewidth, the acceleration amplitude would be proportional to the pulsewidth.

III. EXPERIMENTAL VERIFICATION

In order to validate the model which has been developed, some tests have been performed with PVC rods having several lengths and one diameter of 15.5 mm.

A. Experimental setup

The time-gated electromagnetic microwaves are produced by a magnetron at 9.5 GHz (see Fig. 4). The power is

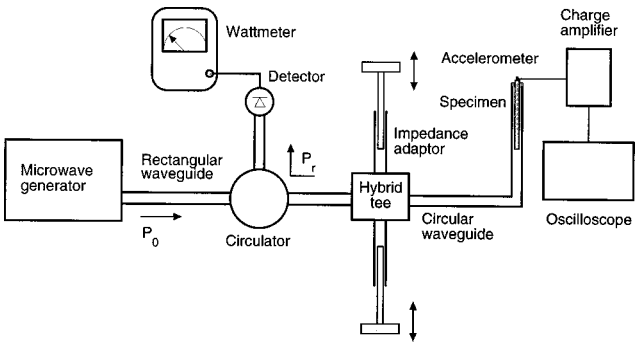

FIG. 4. Setup to generate and acquire acoustic waves.

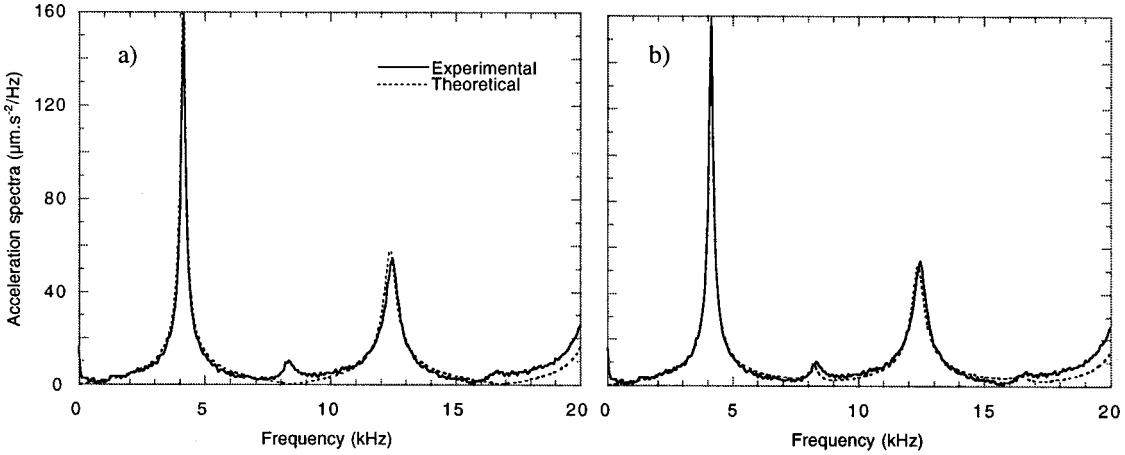

FIG. 5. Acceleration spectra (PVC, $L=20$ cm): (a) uniform temperature rise; (b) linear distribution of the temperature rise.

in the order of 1 kW. The pulsewidth can be 0.8 μs or 1.6 μs. The repetition rate is chosen sufficiently low in order to avoid the overlap between two consecutive records. The electromagnetic waves propagate in a rectangular waveguide. The incident power, P_0, which arrives in the circulator, is sent toward the specimen. To obtain the maximum power, an impedance adaptor is adjusted in order to get the minimum reflected power measured with a wattmeter. It is made up of a hybrid tee associated to two sliding short circuits.[27]

The specimen rod, with a diameter of 15.5 mm, is held vertically inside the vertical circular waveguide (having a diameter of 24 mm) by means of a piece of foam put on the end of this waveguide where the microwaves propagate in the TE_{11} fundamental mode.

A piezoelectric miniature accelerometer (Brüel & Kjaer 4374) is attached to the end of the rod by means of a very thin layer of ultrasonic couplant. Its mass m is 0.65 g and its charge sensitivity is 0.129 pC/ms^{-2}. Its dynamic frequency range is between 1 Hz and 20 kHz approximately. In order to investigate the influence of the accelerometer mass, a heavy accelerometer (Brüel & Kjaer 4371) is also used. Its mass is about 11 g. Its charge sensitivity is 1.021 pC/ms^{-2}.

The signal from the accelerometer is amplified by a charge amplifier (Brüel & Kjaer 2525). The amplified acceleration signals are recorded by a digital oscilloscope (LeCroy 9310). The signals are averaged on 100 sweeps in order to eliminate the electronic noise. Then, the signals are transferred to a computer for processing.

B. Identification of the complex slowness and the maximum temperature rises

The maximum temperature rise can be evaluated by comparing the theoretical and the experimental results if the coefficient of linear thermal expansion is known ($\beta \approx 80.10^{-6}$/°C for the PVC). In order to do this, the difference between the moduli of the Fourier transforms of the experimental and the theoretical accelerations in the accelerometer frequency range must be minimized by a numerical procedure. The calculations can be carried out with four parameters (the maximum temperature rises at both ends and the real and imaginary parts of the complex slowness) or two parameters (the maximum temperature rises at both ends) if it is considered that the mechanical behavior of the material is known (determined by the preliminary impact tests). The

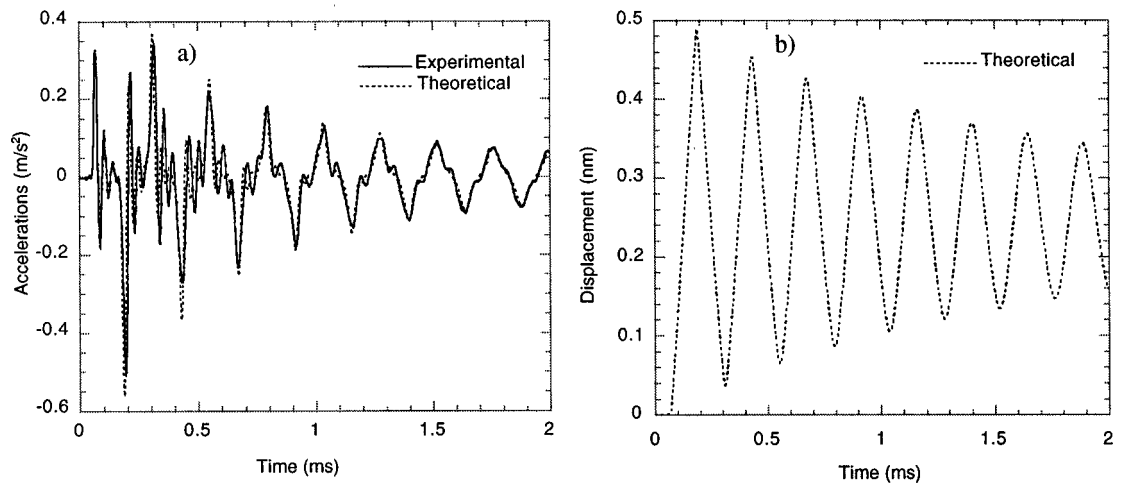

FIG. 6. (a) Experimental and theoretical acceleration signals (PVC, $L=20$ cm); (b) theoretical displacement.

TABLE I. Viscoelastic properties obtained by preliminary impact tests (see Sec. II A) and microwave tests.

	S' (10^{-3} ms/m)	S'' (10^{-3} ms/m)	E' (GPa)	$\tan\delta$ (10^{-2})
Impact tests	599	10.4	4.01	3.5
Microwave tests	598±2	10.1±0.8	4.02±0.03	3.4±0.3

minimization allows one to find the optimal set of parameters **p** that fits the experimental and the theoretical acceleration spectra at best. Thus, the function to minimize is given by:

$$J(\mathbf{p})=\sum_{v=10\ \mathrm{Hz}}^{20\ \mathrm{kHz}} ||\tilde{a}_{\exp}(v)|-|\tilde{a}(v,\mathbf{p})||, \tag{12}$$

where $|\tilde{a}_{\exp}(v)|$and $|\tilde{a}(v,\mathbf{p})|$are the moduli of the Fourier transforms of the experimental and the theoretical accelerations, respectively. The set of parameters is:

$$\mathbf{p}=(S',S'',\theta_{\max}(x=0),\theta_{\max}(x=L))$$

or (13)

$$\mathbf{p}=(\theta_{\max}(x=0),\theta_{\max}(x=L)),$$

where the complex slowness $S'-iS''$ is assumed to be constant in this frequency range.

C. Results

The tests have been performed on PVC rods having lengths from 8 cm to 30 cm (with a mass density of 1440 kg/m^3). Only the results obtained with the rod having a 20 cm length will be presented and compared to the theoretical accelerations given by the model described above. The maximum temperature rise will be estimated by using the numerical minimization procedure described above. Several effects will be investigated, i.e.: the spatial distribution of the temperature rise along the rod, the effect of the pulsewidth on the maximum temperature rise and the effect of the accelerometer mass.

The miniature accelerometer having a mass of 0.65 g has been used in the first tests. The results are given in Fig. 5.

Two different cases have been investigated: either the distribution of the temperature rise is uniform, or the temperature rise varies linearly along the rod. In the first case, the experimental and the theoretical spectra are quite close but the second small peak observed in the experimental spectrum (at about 8 kHz) is not predicted by the model [see Fig. 5(a)]. On the contrary, this small peak is present [see Fig. 5(b)] if a linear decrease of the maximum temperature rise of 20% between the ends $x=0$ and $x=L$ is considered. This result shows that the microwave energy is weakly absorbed by the material. The maximum temperature rise found by the minimization procedure at the first end is about 3.5×10^{-5} °C for a pulsewidth of 1.6 μs. This result was expected as the imaginary part of the relative complex permittivity $\epsilon_r'-i\epsilon_r''$ is very low ($\epsilon_r'=2$, $\epsilon_r''=0.05$ at 10 GHz). This temperature is extremely low but it is sufficient to generate acoustic waves which are measurable with the accelerometer. From the results obtained by the minimization procedure, the theoretical acceleration signal has been calculated and compared to the experimental signal [see Fig. 6(a)]. For the comparison, the theoretical acceleration signal is filtered with the help of a transfer function. The first pulse R_1 generated at the accelerometer location is due to a wave which did not propagate. Consequently, the transfer function corresponding to the electronic accelerometer device is calculated by comparing the experimental and the theoretical first pulses R_1on a long rod ($L=25$ cm) where the first two pulses are well separated.

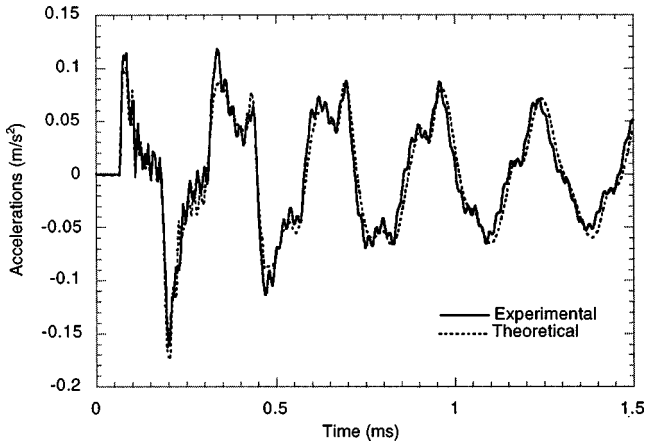

FIG. 7. Experimental and theoretical acceleration signals (PVC, $L=20$ cm), acceleration measured with a heavy accelerometer ($m=11$ g).

Additionally, it is interesting to show the displacement of the specimen end [see Fig. 6(b)] calculated with the model. With regard to the low temperature rise, this displacement is also very low (less than 0.5 nm in this case) and it would be very difficult to measure.

It can be seen that the minimization method involving four parameters allows one to find the viscoelastic mechanical characteristics given by the preliminary impact tests with a good accuracy. Table I shows the mean values given from tests on rods having lengths from 8 cm to 25 cm. As a consequence, the apparatus could be used in the nondestructive evaluation of viscoelastic materials.

The tests have been performed with two different pulsewidths (0.8 μs and 1.6 μs). It has been observed that the ratio between the maximum temperature rises measured with both these pulsewidths is close to 2 (between 1.7 and 1.9). This fact is consistent with the assumption of a linear increase of the temperature during the pulsewidth.

In the tests shown so far, the influence of the miniature accelerometer mass was quite low. For the purposes of comparison, a test has been carried out with a heavy accelerometer having a mass of 11 g (see Fig. 7).

The signal obtained with the help of the model described in Sec. I is compared to the measured acceleration. It can be seen that the predicted signal is quite close to the experimental one.

IV. CONCLUSIONS

A one-dimensional model has been developed in order to predict the acoustic waves generated in viscoelastic rods by electromagnetic microwave pulses. The wave generation

is due to the rapid thermal expansion caused by microwave absorption. In this model, it is assumed that the electromagnetic absorption in the polymeric material is weak. Consequently, the distribution of the temperature rise along the rod is either uniform or linear. The presence of the accelerometer mass at the end of the rod is taken into account.

The effects of the microwave pulsewidth and of the time shape of the temperature rise have been investigated numerically. It has been concluded that, in the frequency range of the accelerometer, these parameters have a significant effect on the amplitude of the acceleration signal but not much effect on its time shape.

In order to validate the model experimentally, some tests have been carried out on PVC rods instrumented with two different accelerometers. The maximum temperature rise during one pulse has been estimated by comparing the experimental and theoretical accelerations by means of a numerical minimization procedure. The main conclusion is that this temperature is extremely low (about 3.5×10^{-5} °C with a pulsewidth of 1.6 μs) but sufficient to generate acoustic waves. With the electromagnetic power of 1 kW, it would be difficult to measure these waves with a displacement transducer since the maximum displacement is less than one nanometer.

By performing a test with a heavy accelerometer, it has been shown that the model can predict the acceleration signal by taking into account the accelerometer mass.

The accurate determination of the mechanical characteristics of the viscoelastic material by means of the minimization procedure shows that the acoustic wave generation by electromagnetic microwaves could be used as a new method of nondestructive evaluation of materials. Compared with the impact methods, the advantage of the presented method is that the wave generation does not require contact with the specimen. Consequently, the shape of the wave generated is very reproducible and the measurement accuracy can be increased by performing signal averaging. Moreover, the pulse duration can be very short while it is experimentally very difficult to get short pulses by means of a mechanical impact on a viscoelastic rod. Thus the frequency range of the signal can be increased. The inverse problem to measure the properties of materials and its sensitivity will be presented in a future paper.

[1] A. W. Nolle, ''Methods for measuring the dynamic mechanical properties of rubberlike materials,'' J. Appl. Phys. **19**, 753–774 (1948).

[2] H. J. McSkimin, ''Ultrasonic methods for measuring the mechanical properties of liquids and solids,'' in Physical Acoustics, Vol. 1A, 271–334, edited by W. P. Muson (Academic Press, New York, 1964).

[3] J. D. Ferry, *Viscoelastic Properties of Polymers* (Wiley, New York, 1970).

[4] A. S. Nowick and B. S. Berry, *Anelastic Relaxation in Crystalline Solids* (Academic, New York, 1972).

[5] K. W. Hillier and H. Kolsky, ''An investigation of the dynamic mechanical properties of some high polymers,'' Proc. Phys. Soc. London, Sect. B **62**, 111–121 (1949).

[6] K. W. Hillier, ''A method of measuring some dynamic elastic constants and its application to the study of high polymers,'' Proc. Phys. Soc. London, Sect. B **62**, 701–713 (1949).

[7] H. Kolsky, ''The propagation of stress pulses in viscoelastic solids,'' Philos. Mag. **1**, 693–711 (1957).

[8] D. M. Norris and W. C. Young, ''Complex modulus measurement by longitudinal vibration testing,'' Exp. Mech. **10**, 93–96 (1970).

[9] W. M. Madigosky and G. F. Lee, ''Improved resonance technique for materials characterization,'' J. Acoust. Soc. Am. **73**, 1374–1377 (1983).

[10] T. Pritz, ''Transfer function method for investigating the complex modulus acoustical materials: rodlike specimen,'' J. Sound Vib. **81**, 359–376 (1982).

[11] J. L. Buchanan, ''Numerical solution for the dynamic moduli of a viscoelastic bar,'' J. Acoust. Soc. Am. **81**, 1775–1786 (1987).

[12] R. H. Blanc, ''Détermination de l'équation de comportement des corps viscoélastiques linéaires par une méthode d'impulsion,'' Doctoral thesis, Université d'Aix-Marseille (1971).

[13] B. Lundberg and R. H. Blanc, ''Determination of mechanical material properties from the two-point response of an impacted linearly viscoelastic rod specimen,'' J. Sound Vib. **126**, 97–108 (1988).

[14] I. N. Trendafilova, S. Ödeen, and B. Lundberg, ''Identification of viscoelastic materials from electro-optical displacement measurements at two sections of an impacted rod specimen,'' Eur. J. Mech. A/Solids **13**, 793–802 (1994).

[15] S. Ödeen and B. Lundberg, ''Determination of complex modulus from measured endpoint accelerations of an impacted rod specimen,'' J. Sound Vib. **165**, 1–8 (1993).

[16] R. M. White, ''Generation of elastic waves by transient surface heating,'' J. Appl. Phys. **34**, 3559–3567 (1963).

[17] D. A. Hutchins, ''Ultrasonic generation by pulsed power,'' in *Physical Acoustics*, Vol. XVIII, edited by W. P. Mason and R. N. Thurston (Academic Press, New York, 1988).

[18] H. Lin, H. J. Maris, L. B. Freund, K. Y. Lee, H. Luhn, and D. P. Kern, ''Study of vibrational modes of gold nanostructures by picosecond ultrasonics,'' J. Appl. Phys. **73**, 37–45 (1993).

[19] M. Dubois, F. Enguehard, and L. Bertrand, ''Analytical one-dimensional model to study the ultrasonic precursor generated by a laser,'' Phys. Rev. E **50**, 1548–1551 (1994).

[20] A. Hénault, A. Cournoyer, F. Enguehard, and L. Bertrand, ''A study of dynamic thermal expansion using a laser-generated ultrasound 1D model,'' Prog. Nat. Sci. **6**, S370–S373 (1996).

[21] F. Enguehard and L. Bertrand, ''Effects of optical penetration and laser pulse duration on laser generated longitudinal acoustic waves,'' J. Appl. Phys. **82**, 1532–1538 (1997).

[22] F. Enguehard and L. Bertrand, ''Temporal deconvolution of laser-generated longitudinal acoustic waves for optical characterization and precise longitudinal acoustic velocity evaluation,'' J. Acoust. Soc. Am. **103**, 771–784 (1998).

[23] D. E. Borth and C. A. Cain, ''Theoretical analysis of acoustic signal generation in materials irradiated with microwave energy,'' IEEE Trans. Microwave Theory Tech. **MTT-25**, 944–953 (1977).

[24] J. C. Lin, ''Further studies on the microwave auditory effect,'' IEEE Trans. Microwave Theory Tech. **MTT-25**, 938–943 (1977).

[25] B. Hosten and P. A. Bernard, ''Ultrasonic wave generation by time-gated microwaves,'' J. Acoust. Soc. Am. **104**, 860–866 (1998).

[26] M. O'Donnell, E. T. Jaynes, and J. G. Miller, ''Kramers-Kronig relationship between ultrasonic attenuation and phase velocity,'' J. Acoust. Soc. Am. **63**, 696–701 (1981).

[27] P. A. Bernard, C. Marzat, and J. Miane, ''Automatic matching of microwave energy transfer and simultaneous measurements of permittivity,'' J. Microwave Power Electromagn. Energy **23**, 218–224 (1988).

Forced response of sandwich ring with viscoelastic core subjected to traveling loads

Yuh-Chung Hu and Shyh-Chin Huang
Department of Mechanical Engineering, National Taiwan University of Science and Technology, 43 Keelung Road, Section 4, Taipei, Taiwan, Republic of China

(Received 4 September 1998; accepted for publication 31 March 1999)

The forced vibrations of a three-layer sandwich ring with viscoelastic material (VEM) core subjected to traveling loads are investigated. The VEM layer is added to provide damping, and subsequently to reduce vibration. The derived differential equations contain three displacements, which are one transverse displacement and two tangential displacements of the two face layers. The modal expansion technique then yields the forced solution being characterized of six generalized coordinates for each circumferential wave number *n*. The closed form solutions to the harmonic traveling point loads are solved and discussed. Examples for various cases are illustrated as well and the influences of the viscoelastic core and the face layers on dynamic response and damping effects are particularly discussed. The results show that a very thin VEM can suppress the vibration very effectively. © *1999 Acoustical Society of America.* [S0001-4966(99)02307-3]

PACS numbers: 43.40.At, 43.40.Ey, 43.40.Tm [PJR]

LIST OF SYMBOLS

a_j	radius of curvature of each layer, $j=1-3$
D_j	bending stiffness of face layers, $j=1,3$
E_j	Young's modulus of face layers, $j=1,3$
F_θ; F_r	load amplitudes in tangential and in radial
f_θ; f_r	loads in tangential and in radial
$G(\omega)$	frequency dependent complex modulus of VEM
h_j	thickness of each layer, $j=1-3$
$\mathbf{K}_a$; $\mathbf{K}_b$	stiffness matrices of the discretized EOMs
K	kinetic energy of the whole system
K_j	membrane stiffness of face layers, $j=1,3$
$\mathbf{M}$	mass matrix of the discretized EOMs
m_{jj}	elements of mass matrix $\mathbf{M}$, $j=1-3$
n	circumferential wave number
$\mathbf{Q}_a$; $\mathbf{Q}_b$	generalized force vectors
q_j	generalized force, $j=1-4$
r	coordinate in radial direction
t	time
U	strain energy of the whole system
V_j	tangential displacement of each layer, $j=1-3$
v_j	tangential displacement of the mid-plane for each layer, $j=1-3$
W	transverse displacement
W_{in}	total external work
w	transverse displacement
$\mathbf{X}_a$, $\mathbf{X}_b$	generalized coordinate vectors

Greek symbols

α_n, ϕ_n, η_n, ξ_n, ζ_n, ψ_n	generalized coordinates
β_j	rotational angle of each layer, $j=1-3$
Δ	characteristic function
δ	Dirac delta function
$\epsilon_{\theta\theta}$, ϵ_θ	strains
κ_{ij}	elements of stiffness matrix, $i,j=1-3$
π	pi
θ	coordinate in tangential direction
ρ_j	density of each layer, $j=1-3$
Ω	load rotating speed
ω	driving frequency

INTRODUCTION

Ring elements are commonly seen in mechanical systems, e.g., bearings and tires. The dynamic response of rings, hence, has been investigated for over a century. Many researchers have steadily and systematically improved our knowledge of the behavior of rings by investigating the effects of rotary inertia and shear (Bickford and Reddy, 1985), fundation stiffness (Bert and Chen, 1978; Reddy and Bickford, 1985), prestress (Padovon, 1973), or rotation (Srinivasan and Lauterbach, 1971; DiTaranto and Lessen, 1964). Endo *et al.* (1984) verified part of the developed theory by experiments. All the mentioned papers yet dealt with just the free vibration. Huang and Soedel (1987a,b) made use of a modal expansion technique and developed a general solution process for the forced vibration of rotating rings; the solution was decomposed of four generalized coordinates associated with each circumferential wave number (n).

To reduce the vibration of structure elements, either active or passive suppression technique can work out. Constrained layer damping (CLD) treatment has proven an effective, passive way of suppressing the vibration and noise of structures. Theoretical works about CLD on beams can be traced to DiTaranto (1965), and Mead and Markus (1969) for the axial and bending vibration of beams. After them, many

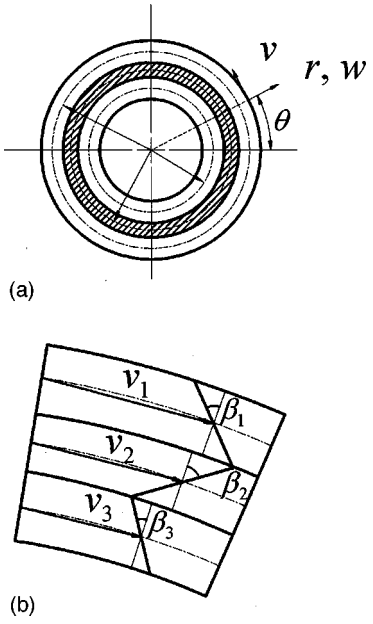

FIG. 1. (a) Coordinates system of the sandwich ring. (b) Displacements distribution.

authors presented many improved formulations and techniques in this field. Some adopted their model to study the damping mechanism of the viscoelastic layer (Douglas and Yang, 1978), and some modified or extended the model for different applications (Mead and Yaman, 1991; Rao and He, 1993; Roy and Ganesan, 1993; Yan and Dowell, 1972). Johnson (1995) summarized a brief review of techniques for designed-in passive damping for vibration control. Lately, Huang *et al.* (1995) employed an energy principle for the equations of a beam with partial active/passive constrained layer damping treatments. Lu *et al.* (1977, 1991) investigated a circular cylindrical shell with beam-type constrained damping treatment, in which the viscoelastic layer was treated as viscoelastic spring. Ramesh and Ganesan (1994) developed a finite element model for the vibration and damping analysis of a cylindrical shell with a viscoelastic core. Theoretical works on CLD were mostly applied on beam or plate structures.

In the present paper, the damping effects due to a thin VEM (viscoelastic material) core is of interest practically; it is a possible way to reduce the vibration level of a bearing ring. Therefore, the response and damping of a sandwich ring subjected to traveling loads are investigated. Based on the previous theory developed by Hu and Huang (1996), three displacements are contained in the differential equations, which are one radial displacement and two tangential displacements of the face layers. The closed form solutions to a stationary harmonic point load, to a constant traveling point load, and to a harmonic traveling point load are demonstrated and interpreted. The influence of the VEM layers on dynamic response and damping effects is discussed.

I. BASIC ASSUMPTIONS

Consider a three-layer sandwich ring of unit width with viscoelastic core, as shown in Fig. 1(a). The face layers are assumed isotropic and elastic. The core is of linear viscoelastic material with a frequency dependent shear modulus $G(\omega)$. The Love's assumption applies and thus the displacements for the three layers are

$$\begin{aligned} V_1(r,\theta,t) &= v_1(\theta,t)+\left(r-\frac{h_1+h_2}{2}\right)\beta_1(\theta,t),\\ V_2(r,\theta,t) &= v_2(\theta,t)+r\beta_2(\theta,t),\\ V_3(r,\theta,t) &= v_3(\theta,t)+\left(r+\frac{h_2+h_3}{2}\right)\beta_3(\theta,t),\\ W(r,\theta,t) &= w(\theta,t), \end{aligned} \tag{1}$$

as illustrated in Fig. 1(b). To comply with no-slip constraints between layers, the mid-plane tangential displacement and the rotational angle of the core yield as

$$\begin{aligned} v_2 &= \frac{1}{2}\left[\left(v_1-\frac{h_1}{2}\beta_1\right)+\left(v_3+\frac{h_3}{2}\beta_3\right)\right],\\ \beta_2 &= \frac{1}{h_2}\left[\left(v_1-\frac{h_1}{2}\beta_1\right)-\left(v_3+\frac{h_3}{2}\beta_3\right)\right]. \end{aligned} \tag{2}$$

It is assumed that the shear strains in face layers are negligible, and that the core undergoes pure shear. Therefore, the strain-displacement relationships are derived as

$$\begin{aligned} \epsilon_{\theta\theta 1} &= \frac{1}{a_2+r}\left[\frac{\partial v_1}{\partial\theta}+\left(r-\frac{h_1+h_2}{2}\right)\frac{\partial\beta_1}{\partial\theta}+w\right],\\ \epsilon_{\theta r1} &= \frac{1}{a_2+r}\left(a_1\beta_1-v_1+\frac{\partial w}{\partial\theta}\right), \end{aligned} \tag{3}$$

$$\begin{aligned} \epsilon_{\theta\theta 3} &= \frac{1}{a_2+r}\left[\frac{\partial v_3}{\partial\theta}+\left(r+\frac{h_2+h_3}{2}\right)\frac{\partial\beta_3}{\partial\theta}+w\right],\\ \epsilon_{\theta r3} &= \frac{1}{a_2+r}\left(a_3\beta_3-v_3+\frac{\partial w}{\partial\theta}\right), \end{aligned} \tag{4}$$

$$\begin{aligned} \epsilon_{\theta r2} = \frac{1}{a_2+r}\Bigg\{&\frac{a_2}{h_2}\left[\left(v_1-\frac{h_1}{2}\beta_1\right)-\left(v_3+\frac{h_3}{2}\beta_3\right)\right],\\ &-\frac{1}{2}\left[\left(v_1-\frac{h_1}{2}\beta_1\right)+\left(v_3+\frac{h_3}{2}\beta_3\right)\right]+\frac{\partial w}{\partial\theta}\Bigg\}. \end{aligned} \tag{5}$$

The omission of shear strains of face layers implies that $\epsilon_{\theta r1}=0$, $\epsilon_{\theta r2}=0$, and subsequently,

$$\beta_1=\frac{v_1}{a_1}-\frac{1}{a_1}\frac{\partial w}{\partial\theta},\quad \beta_3=\frac{v_3}{a_3}-\frac{1}{a_3}\frac{\partial w}{\partial\theta}. \tag{6}$$

II. EQUATIONS OF MOTION

The governing equations of a sandwich ring with a VEM core are then derived via the Hamilton's principle. As the transverse vibration is generally of greatest significance, the inertia of the VEM core in the tangential direction is neglected. The governing equations

$$\rho_1 h_1 a_1 \ddot{v}_1 - \frac{K_1}{a_1}\left(\frac{\partial^2 v_1}{\partial\theta^2}+\frac{\partial w}{\partial\theta}\right) - \frac{D_1}{a_1^3}\left(\frac{\partial^2 v_1}{\partial\theta^2}-\frac{\partial^3 w}{\partial\theta^3}\right) + \frac{a_2}{h_2}\frac{2a_1-h_1}{2a_1}\frac{2a_2-h_2}{2a_2}G(\omega)\left(\frac{2a_1-h_1}{2a_1}\frac{2a_2-h_2}{2a_2}v_1 - \frac{2a_3+h_3}{2a_3}\frac{2a_2+h_2}{2a_2}v_3\right) + \frac{a_2}{h_2}\frac{2a_1-h_1}{2a_1}\frac{2a_2-h_2}{2a_2}G(\omega)\left(\frac{2a_3+h_3}{2a_3}\frac{2a_2+h_2}{2a_2}-\frac{2a_1-h_1}{2a_1}\frac{2a_2-h_2}{2a_2}\right)\frac{\partial w}{\partial\theta}=0, \tag{7}$$

$$\rho_3 h_3 a_3 \ddot{v}_3 - \frac{K_3}{a_3}\left(\frac{\partial^2 v_3}{\partial\theta^2}+\frac{\partial w}{\partial\theta}\right) - \frac{D_3}{a_3^3}\left(\frac{\partial^2 v_3}{\partial\theta^2}-\frac{\partial^3 w}{\partial\theta^3}\right) - \frac{a_2}{h_2}\frac{2a_3+h_3}{2a_3}\frac{2a_2+h_2}{2a_2}G(\omega)\left(\frac{2a_1-h_1}{2a_1}\frac{2a_2-h_2}{2a_2}v_1 - \frac{2a_3+h_3}{2a_3}\frac{2a_2+h_2}{2a_2}v_3\right) - \frac{a_2}{h_2}\frac{2a_3+h_3}{2a_3}\frac{2a_2+h_2}{2a_2}G(\omega)\left(\frac{2a_3+h_3}{2a_3}\frac{2a_2+h_2}{2a_2}-\frac{2a_1-h_1}{2a_1}\frac{2a_2-h_2}{2a_2}\right)\frac{\partial w}{\partial\theta}=a_3 f_\theta, \tag{8}$$

$$(\rho_1 h_1 a_1+\rho_2 h_2 a_2+\rho_3 h_3 a_3)\ddot{w} + \frac{K_3}{a_3}\left(\frac{\partial v_3}{\partial\theta}+w\right) - \frac{D_3}{a_3^3}\left(\frac{\partial^3 v_3}{\partial\theta^3}-\frac{\partial^4 w}{\partial\theta^4}\right) + \frac{K_1}{a_1}\left(\frac{\partial v_1}{\partial\theta}+w\right) - \frac{D_1}{a_1^3}\left(\frac{\partial^3 v_1}{\partial\theta^3}-\frac{\partial^4 w}{\partial\theta^4}\right) - \frac{a_2}{h_2}\left(\frac{2a_3+h_3}{2a_1}\frac{2a_2+h_2}{2a_2}-\frac{2a_1-h_1}{2a_1}\frac{2a_2-h_2}{2a_2}\right)\frac{2a_1-h_1}{2a_1}\frac{2a_2-h_2}{2a_2}G(\omega)\frac{\partial v_1}{\partial\theta} + \frac{a_2}{h_2}\left(\frac{2a_3+h_3}{2a_1}\frac{2a_2+h_2}{2a_2} - \frac{2a_1-h_1}{2a_1}\frac{2a_2-h_2}{2a_2}\right)\frac{2a_3+h_3}{2a_1}\frac{2a_2+h_2}{2a_2}G(\omega)\frac{\partial v_3}{\partial\theta} - \frac{a_2}{h_2}\left(\frac{2a_3+h_3}{2a_1}\frac{2a_2+h_2}{2a_2}-\frac{2a_1-h_1}{2a_1}\frac{2a_2-h_2}{2a_2}\right)^2 G(\omega)\frac{\partial^2 w}{\partial\theta^2}=a_3 f_r, \tag{9}$$

where the membrane stiffness K_j and the bending stiffness D_j are

$$K_j=E_j h_j, \quad D_j=\frac{E_j h_j^3}{12}, \quad j=1,3. \tag{10}$$

III. ANALYTIC SOLUTIONS TO FORCED VIBRATION

The forced response, with the employment of modal expansion, can be characterized by six generalized coordinates, $\psi_n(t)$, $\phi_n(t)$, $\alpha_n(t)$, $\zeta_n(t)$, $\xi_n(t)$, and $\eta_n(t)$, as

$$\begin{aligned} v_1(\theta,t)&=\sum_{n=1}^{\infty}[\psi_n(t)\cos(n\theta)+\phi_n(t)\sin(n\theta)],\\ v_3(\theta,t)&=\sum_{n=1}^{\infty}[\alpha_n(t)\cos(n\theta)+\zeta_n(t)\sin(n\theta)],\\ w(\theta,t)&=\sum_{n=1}^{\infty}[\xi_n(t)\cos(n\theta)+\eta_n(t)\sin(n\theta)]. \end{aligned} \tag{11}$$

To solve for the six generalized coordinates associated with each n number, Eq. (11) is substituted into the equations of motion, Eqs. (7)–(9), and by the use of the orthogonality of trigonometric functions, the following sets of linear second order differential equations, in terms of matrix notation are obtained:

$$\mathbf{M}\ddot{\mathbf{X}}_a+\mathbf{K}_a\mathbf{X}_a=\mathbf{Q}_a, \quad \mathbf{M}\ddot{\mathbf{X}}_b+\mathbf{K}_b\mathbf{X}_b=\mathbf{Q}_b, \tag{12}$$

where the matrices $\mathbf{M}$, $\mathbf{K}_a$, and $\mathbf{K}_b$, the generalized coordinates vectors $\mathbf{X}_a$ and $\mathbf{X}_b$, and the generalized force vectors $\mathbf{Q}_a$ and $\mathbf{Q}_b$ are of the forms:

$$\mathbf{M}=\begin{bmatrix} m_{11} & 0 & 0\\ 0 & m_{22} & 0\\ 0 & 0 & m_{33}\end{bmatrix}, \tag{13}$$

$$\mathbf{K}_a=\begin{bmatrix} \kappa_{11}(\omega) & \kappa_{12}(\omega) & -\kappa_{13}(\omega)\\ & \kappa_{22}(\omega) & -\kappa_{23}(\omega)\\ & & \kappa_{33}(\omega)\end{bmatrix},$$

$$\mathbf{K}_b=\begin{bmatrix} \kappa_{11}(\omega) & \kappa_{12}(\omega) & \kappa_{13}(\omega)\\ & \kappa_{22}(\omega) & \kappa_{23}(\omega)\\ & & \kappa_{33}(\omega)\end{bmatrix}, \tag{14}$$

$$\mathbf{X}_a=\{\phi_n(t) \quad \zeta_n(t) \quad \xi_n(t)\}^T,$$

$$\mathbf{X}_b=\{\psi_n(t) \quad \alpha_n(t) \quad \eta_n(t)\}^T, \tag{15}$$

$$\mathbf{Q}_a=\{0 \quad q_1(t) \quad q_2(t)\}^T,$$

$$\mathbf{Q}_b=\{0 \quad q_3(t) \quad q_4(t)\}^T. \tag{16}$$

The expressions of m_{ii}, κ_{ij}, and q_j are given in the Appendix, Eqs. (A1)–(A3). Equation (12) characterizes the forced response of a continuous system in terms of six generalized coordinates for each n number and therefore provides a feasible way to solve analytically for the forced vibration for various loading cases.

Harmonic steady-state response is usually of the most engineering importance, and for such a case the VEM property is commonly given in terms of a frequency-dependent, complex modulus $G(\omega)$. It subsequently inspires a frequency-dependent complex stiffness matrix. In the present paper, the VEM property is adopted directly from the paper of Douglas and Yang (1978),

$$G(\omega)=0.142\left(\frac{\omega}{2\pi}\right)^{0.494}(1+1.46i) \ \text{MPa}, \quad \text{where } i=\sqrt{-1}. \tag{17}$$

The real and imaginary parts of the modulus are commonly called the storage and the loss modulus, respectively. The storage modulus is a measure of the VEM elastic stiffness

and the loss modulus determines how much energy is dissipated.

For harmonic forces, the generalized force vectors can be written as

$$\mathbf{Q}_a=\overline{\mathbf{Q}}_a e^{i\omega t},\quad \mathbf{Q}_b=\overline{\mathbf{Q}}_b e^{i\omega t}. \tag{18}$$

The generalized coordinates can be found analytically as

$$\begin{aligned}\mathbf{X}_a&=(\mathbf{K}_a-\omega^2\mathbf{M})^{-1}\overline{\mathbf{Q}}_a e^{i\omega t}=\mathbf{\Gamma}_a\overline{\mathbf{Q}}_a e^{i\omega t},\\ \mathbf{X}_b&=(\mathbf{K}_b-\omega^2\mathbf{M})^{-1}\overline{\mathbf{Q}}_b e^{i\omega t}=\mathbf{\Gamma}_b\overline{\mathbf{Q}}_b e^{i\omega t},\end{aligned} \tag{19}$$

where the matrices, $\mathbf{\Gamma}_a$ and $\mathbf{\Gamma}_b$, are of the forms,

$$\begin{aligned}\mathbf{\Gamma}_a&=\begin{bmatrix}\Gamma_{11}(\omega) & \Gamma_{12}(\omega) & -\Gamma_{13}(\omega)\\ & \Gamma_{22}(\omega) & -\Gamma_{23}(\omega)\\ & & \Gamma_{33}(\omega)\end{bmatrix},\\ \mathbf{\Gamma}_b&=\begin{bmatrix}\Gamma_{11}(\omega) & \Gamma_{12}(\omega) & \Gamma_{13}(\omega)\\ & \Gamma_{22}(\omega) & \Gamma_{23}(\omega)\\ & & \Gamma_{33}(\omega)\end{bmatrix},\end{aligned} \tag{20}$$

and the expressions of $\Gamma_{ij}(\omega)$ are given in the Appendix, Eqs. (A4) and (A5).

IV. STATIONARY HARMONIC POINT LOADS

A sandwich ring subjected to stationary harmonic point loads in both radial and tangential directions acting on the inner face layer is shown in Fig. 2(a). The harmonic point loads in both transverse and tangential directions are expressed as

$$\begin{aligned}f_0(\theta,t)&=F_\theta\delta(\theta-\theta_0)e^{i\omega t},\\ f_r(\theta,t)&=F_r\delta(\theta-\theta_0)e^{i\omega t},\end{aligned} \tag{21}$$

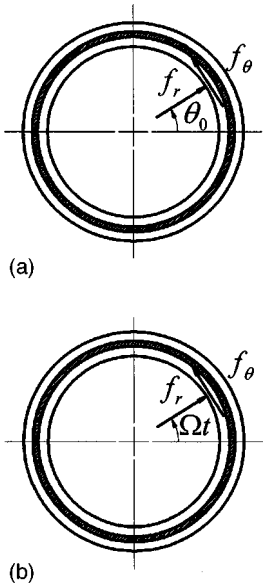

FIG. 2. (a) A sandwich ring subjected to stationary point loads. (b) A sandwich ring subjected to traveling point loads.

in which the Dirac delta function represents the point loads. The generalized force vectors are then obtained as

$$\begin{aligned}\mathbf{Q}_a&=\begin{Bmatrix}0\\ a_3F_\theta\sin(n\theta_0)/\pi\\ a_3F_r\cos(n\theta_0)/\pi\end{Bmatrix}e^{i\omega t},\\ \mathbf{Q}_b&=\begin{Bmatrix}0\\ a_3F_\theta\cos(n\theta_0)/\pi\\ a_3F_r\sin(n\theta_0)/\pi\end{Bmatrix}e^{i\omega t}.\end{aligned} \tag{22}$$

The steady-state solutions of the generalized coordinates are now solved for

$$\begin{Bmatrix}\phi_n(t)\\ \zeta_n(t)\\ \xi_n(t)\end{Bmatrix}=\begin{Bmatrix}\Gamma_{12}(\omega)\dfrac{a_3F_\theta}{\pi}\sin(n\theta_0)-\Gamma_{13}(\omega)\dfrac{a_3F_r}{\pi}\cos(n\theta_0)\\ \Gamma_{22}(\omega)\dfrac{a_3F_\theta}{\pi}\sin(n\theta_0)-\Gamma_{23}(\omega)\dfrac{a_3F_r}{\pi}\cos(n\theta_0)\\ -\Gamma_{23}(\omega)\dfrac{a_3F_\theta}{\pi}\sin(n\theta_0)+\Gamma_{33}(\omega)\dfrac{a_3F_r}{\pi}\cos(n\theta_0)\end{Bmatrix}e^{i\omega t}, \tag{23}$$

$$\begin{Bmatrix}\psi_n(t)\\ \alpha_n(t)\\ \eta_n(t)\end{Bmatrix}=\begin{Bmatrix}\Gamma_{12}(\omega)\dfrac{a_3F_\theta}{\pi}\cos(n\theta_0)+\Gamma_{13}(\omega)\dfrac{a_3F_r}{\pi}\sin(n\theta_0)\\ \Gamma_{22}(\omega)\dfrac{a_3F_\theta}{\pi}\cos(n\theta_0)+\Gamma_{23}(\omega)\dfrac{a_3F_r}{\pi}\sin(n\theta_0)\\ \Gamma_{23}(\omega)\dfrac{a_3F_\theta}{\pi}\cos(n\theta_0)+\Gamma_{33}(\omega)\dfrac{a_3F_r}{\pi}\sin(n\theta_0)\end{Bmatrix}e^{i\omega t}. \tag{24}$$

Subsequently, the forced response in terms of the ring's displacement functions are obtained as

$$\begin{Bmatrix}v_1(\theta,t)\\ v_3(\theta,t)\\ w(\theta,t)\end{Bmatrix}=\sum_{n=1}^{\infty}\begin{Bmatrix}\Gamma_{12}(\omega)\dfrac{a_3F_\theta}{\pi}\cos n(\theta-\theta_0)-\Gamma_{13}(\omega)\dfrac{a_3F_r}{\pi}\sin n(\theta-\theta_0)\\ \Gamma_{22}(\omega)\dfrac{a_3F_\theta}{\pi}\cos n(\theta-\theta_0)-\Gamma_{23}(\omega)\dfrac{a_3F_r}{\pi}\sin n(\theta-\theta_0)\\ \Gamma_{23}(\omega)\dfrac{a_3F_\theta}{\pi}\sin n(\theta-\theta_0)+\Gamma_{33}(\omega)\dfrac{a_3F_r}{\pi}\cos n(\theta-\theta_0)\end{Bmatrix}e^{i\omega t}. \tag{25}$$

V. TRAVELING HARMONIC POINT LOADS

The response to traveling loads is another case of interest because there exists a practical need, for example in bearing mechanics, to understand some design considerations on damping technology to this special topic. Consider the harmonic traveling point loads with a circular speed Ω in both the transverse and tangential directions acting on the inner face layer, as shown in Fig. 2(b). The traveling point loads, in practice, may come from the ball contact in a ball bearing. The load location θ_0 at any instant can be represented as $\theta_0=\Omega t$. Then, the forces in both transverse and tangential directions are expressed as

$$f_\theta(\theta,t)=F_\theta\delta(\theta-\Omega t)e^{i\omega t},$$
$$f_r(\theta,t)=F_r\delta(\theta-\Omega t)e^{i\omega t}. \tag{26}$$

The generalized force vectors are then evaluated as

$$\mathbf{Q}_a=\begin{Bmatrix} 0 \\ \dfrac{a_3F_\theta}{2\pi i}e^{i\omega_+ t}-\dfrac{a_3F_\theta}{2\pi i}e^{i\omega_- t} \\ \dfrac{a_3F_r}{2\pi}e^{i\omega_+ t}+\dfrac{a_3F_r}{2\pi}e^{i\omega_- t} \end{Bmatrix},$$

$$\mathbf{Q}_b=\begin{Bmatrix} 0 \\ \dfrac{a_3F_\theta}{2\pi}e^{i\omega_+ t}+\dfrac{a_3F_\theta}{2\pi i}e^{i\omega_- t} \\ \dfrac{a_3F_r}{2\pi i}e^{i\omega_+ t}-\dfrac{a_3F_r}{2\pi i}e^{i\omega_- t} \end{Bmatrix}, \tag{27}$$

where

$$\omega_+=\omega+n\Omega, \quad \omega_-=\omega-n\Omega. \tag{28}$$

Note that the excitation frequencies are the combinations of harmonic frequency and the traveling speed. The steady-state solutions of the generalized coordinates can now be solved for

$$\begin{Bmatrix} \phi_n(t) \\ \zeta_n(t) \\ \xi_n(t) \end{Bmatrix}=\begin{Bmatrix} \Gamma_{12}(\omega_+)\dfrac{a_3F_\theta}{2\pi i}+\Gamma_{13}(\omega_+)\dfrac{a_3F_r}{2\pi} \\ \Gamma_{22}(\omega_+)\dfrac{a_3F_\theta}{2\pi i}+\Gamma_{23}(\omega_+)\dfrac{a_3F_r}{2\pi} \\ \Gamma_{23}(\omega_+)\dfrac{a_3F_\theta}{2\pi i}+\Gamma_{33}(\omega_+)\dfrac{a_3F_r}{2\pi} \end{Bmatrix}e^{i\omega_+ t}$$
$$+\begin{Bmatrix} -\Gamma_{12}(\omega_-)\dfrac{a_3F_\theta}{2\pi i}-\Gamma_{13}(\omega_-)\dfrac{a_3F_r}{2\pi} \\ -\Gamma_{22}(\omega_-)\dfrac{a_3F_\theta}{2\pi i}-\Gamma_{23}(\omega_-)\dfrac{a_3F_r}{2\pi} \\ +\Gamma_{23}(\omega_-)\dfrac{a_3F_\theta}{2\pi i}+\Gamma_{33}(\omega_-)\dfrac{a_3F_r}{2\pi} \end{Bmatrix}e^{i\omega_- t}, \tag{29}$$

$$\begin{Bmatrix} \psi_n(t) \\ \alpha_n(t) \\ \eta_n(t) \end{Bmatrix}=\begin{Bmatrix} \Gamma_{12}(\omega_+)\dfrac{a_3F_\theta}{2\pi}+\Gamma_{13}(\omega_+)\dfrac{a_3F_r}{2\pi i} \\ \Gamma_{22}(\omega_+)\dfrac{a_3F_\theta}{2\pi}+\Gamma_{23}(\omega_+)\dfrac{a_3F_r}{2\pi i} \\ \Gamma_{23}(\omega_+)\dfrac{a_3F_\theta}{2\pi}+\Gamma_{33}(\omega_+)\dfrac{a_3F_r}{2\pi i} \end{Bmatrix}e^{i\omega_+ t}$$
$$+\begin{Bmatrix} \Gamma_{12}(\omega_-)\dfrac{a_3F_\theta}{2\pi}-\Gamma_{13}(\omega_-)\dfrac{a_3F_r}{2\pi} \\ \Gamma_{22}(\omega_-)\dfrac{a_3F_\theta}{2\pi}-\Gamma_{23}(\omega_-)\dfrac{a_3F_r}{2\pi} \\ \Gamma_{23}(\omega_-)\dfrac{a_3F_\theta}{2\pi}-\Gamma_{33}(\omega_-)\dfrac{a_3F_r}{2\pi} \end{Bmatrix}e^{i\omega_- t}. \tag{30}$$

Eventually the forced response are solved to be

$$\begin{Bmatrix} v_1(\theta,t) \\ v_3(\theta,t) \\ w(\theta,t) \end{Bmatrix}$$
$$=\sum_{n=1}^{\infty}\begin{Bmatrix} \Gamma_{12}(\omega_+)\dfrac{a_3F_\theta}{2\pi}+\Gamma_{13}(\omega_+)\dfrac{a_3F_r}{2\pi i} \\ \Gamma_{22}(\omega_+)\dfrac{a_3F_\theta}{2\pi}+\Gamma_{23}(\omega_+)\dfrac{a_3F_r}{2\pi i} \\ -\Gamma_{23}(\omega_+)\dfrac{a_3F_\theta}{2\pi i}+\Gamma_{33}(\omega_+)\dfrac{a_3F_r}{2\pi} \end{Bmatrix}e^{i(\omega_+ t-n\theta)}$$
$$+\begin{Bmatrix} \Gamma_{12}(\omega_-)\dfrac{a_3F_\theta}{2\pi}-\Gamma_{13}(\omega_-)\dfrac{a_3F_r}{2\pi i} \\ \Gamma_{22}(\omega_-)\dfrac{a_3F_\theta}{2\pi}-\Gamma_{23}(\omega_-)\dfrac{a_3F_r}{2\pi i} \\ \Gamma_{23}(\omega_-)\dfrac{a_3F_\theta}{2\pi i}+\Gamma_{33}(\omega_-)\dfrac{a_3F_r}{2\pi} \end{Bmatrix}e^{i(\omega_- t+n\theta)}. \tag{31}$$

For the special case of the traveling constant ($\omega=0$) point loads with circular speed Ω, the response can be deduced directly from Eq. (31) to

$$\begin{Bmatrix} v_1(\theta,t) \\ v_3(\theta,t) \\ w(\theta,t) \end{Bmatrix}$$
$$=\sum_{n=1}^{\infty}\begin{Bmatrix} \Gamma_{12}(n\Omega)\dfrac{a_3F_\theta}{2\pi}+\Gamma_{13}(n\Omega)\dfrac{a_3F_r}{2\pi i} \\ \Gamma_{22}(n\Omega)\dfrac{a_3F_\theta}{2\pi}+\Gamma_{23}(n\Omega)\dfrac{a_3F_r}{2\pi i} \\ -\Gamma_{23}(n\Omega)\dfrac{a_3F_\theta}{2\pi i}+\Gamma_{33}(n\Omega)\dfrac{a_3F_r}{2\pi} \end{Bmatrix}e^{in(\Omega t-\theta)}$$
$$+\begin{Bmatrix} \Gamma_{12}(-n\Omega)\dfrac{a_3F_\theta}{2\pi}-\Gamma_{13}(-n\Omega)\dfrac{a_3F_r}{2\pi i} \\ \Gamma_{22}(-n\Omega)\dfrac{a_3F_\theta}{2\pi}-\Gamma_{23}(-n\Omega)\dfrac{a_3F_r}{2\pi i} \\ \Gamma_{23}(-n\Omega)\dfrac{a_3F_\theta}{2\pi i}+\Gamma_{33}(-n\Omega)\dfrac{a_3F_r}{2\pi} \end{Bmatrix}e^{-in(\Omega t-\theta)}. \tag{32}$$

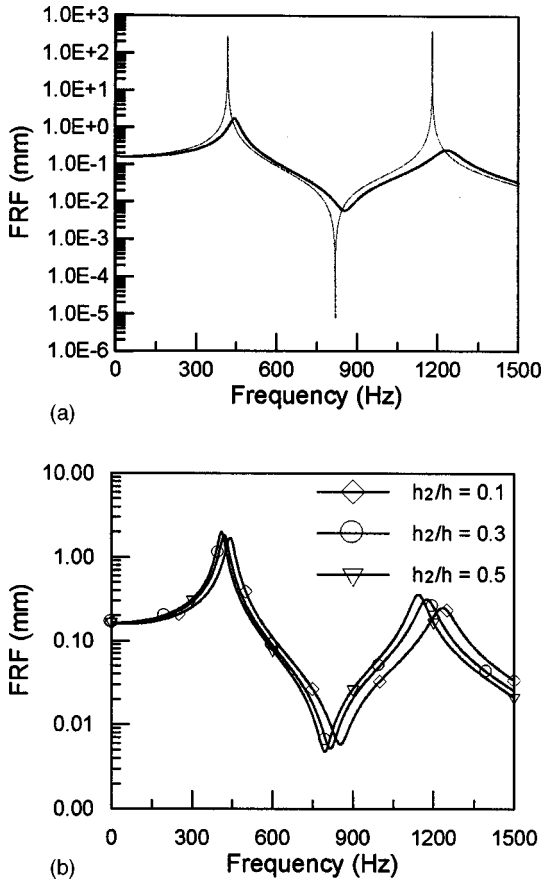

FIG. 3. (a) Frequency response to a stationary harmonic point load. (b) Frequency response for different thickness ratio (h_2/h).

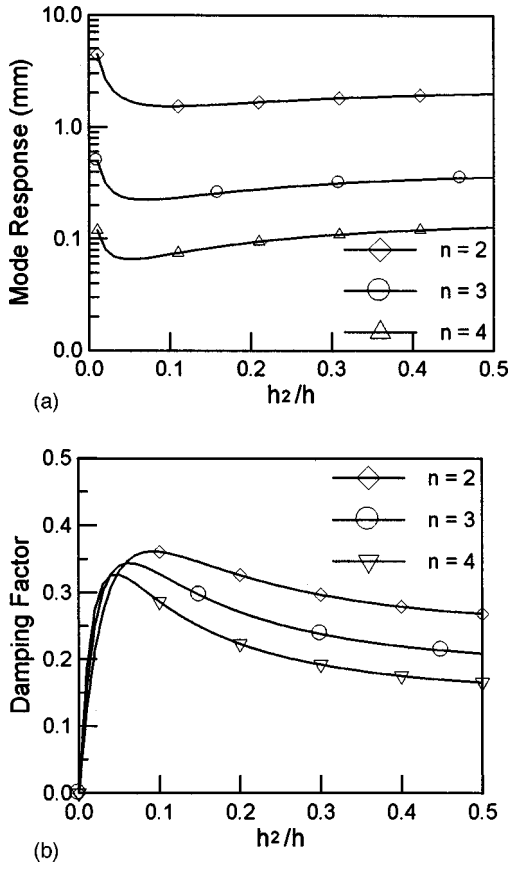

FIG. 4. (a) The varying of response amplitude to VEM thickness. (b) The varying of damping factor to VEM thickness.

Note that from Eq. (32) that it is seen that the response is composed of multi-frequency which is made up of integer multiples of traveling speed. This is a peculiar feature of the traveling load. The speeds that cause resonance are usually referred to as the critical speeds. The number of critical speeds is usually more than that of the ring's natural frequency.

VI. NUMERICAL RESULTS AND DISSCUSSION

The validity of the present model was first verified with the classical ring theory numerically for the case of no VEM layer. The results (not shown) agreed very well with each other and hence added credibility to the present model. In the following, the damping effects due to the VEM layer are particularly discussed. Effects of parameters, such as the thickness of face layers and of the VEM core, are studied as well. The geometric and material properties for the numerical examples are, unless specified otherwise, given as follows: face layers (aluminum): $E_1=E_3=70\,\text{GPa}$, $\rho_1=\rho_3=2710\,\text{Kg/m}^3$, $h_1=h_3=h=2\,\text{mm}$, $a_3=100\,\text{mm}$; VEM core: $\rho_2=1104\,\text{Kg/m}^3$, $h_2=0.2\,\text{mm}$. In order to concentrate on the parameter effects on damping ability, the tangential force, without loss of generality, is set to zero for simplicity.

The responses to a stationary harmonic point load are calculated directly from Eq. (25) by using the first ten terms. Figure 3(a) shows the frequency response function up to the first two modes, in which the dashed curve represents the case of no VEM core, i.e., $h_2=0$, which is exactly the case of a single-layer ring of thickness $2h$. The solid curve represents the case of $h_2=0.2\,\text{mm}$ and significant damping effects are observed. Figure 3(b) shows the frequency responses for three different thickness ratios. Note that, in the shown cases, the thicker VEM layer does not ensure better vibration suppression. Figure 4(a) furthermore shows VEM thickness effects on individual modal responses for the first three flexible modes. As shown the response amplitudes decrease rapidly while a thin VEM is added. The amplitude soon reaches a minimum and after that further increase of VEM thickness, on the contrary, increases the response amplitude. The VEM thickness seems to impose the similar effects on modes. Figure 4(b) shows the damping factors of the three modes. The damping factor soon reaches a maximum value and then decreases with the increase of VEM thickness. The results mean that a thin VEM layer can add damping into the structure very effectively. However, for the cases shown, once the thickness ratio (h_2/h) exceeded the best value, thicker VEM contradictorily reduced damping ability.

This trend agrees with most of passive constrained layer damping (PCLD) applications. It is known that the shear strains of the VEM core pre-dominate the absorption of energy in constrained layer. The face layers must provide enough constraint to the VEM core to produce large shear strains in it. When VEM exceeds a best value, further increase of VEM subsequently reduces the shear constraint al-

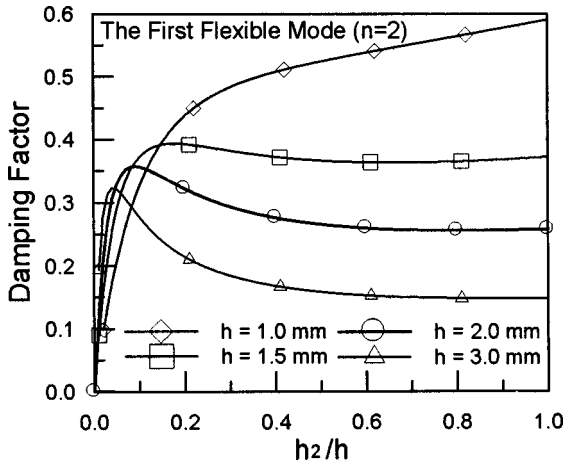

FIG. 5. The varying of damping factor to thickness ratio for various ring thickness.

though thicker VEM increases the capacity of absorbing energy. Furthermore, the loss modulus of VEM is frequency dependent, but a thicker VEM causes a drop-off on the resonant frequency of the system and results in the decrease of damping effects. According to the shown results, there exists a best design on the thickness of the VEM core to have the maximum damping effects. Figure 5 intends to show how the damping varies with the ring's thickness. The results showthat the best thickness ratio h_2/h decreases with the ring's thickness.

Now, consider a traveling constant point load with magnitude 40 N/mm acting on the inner face layer in radial direction. The frequency response is calculated directly from Eq. (32) and illustrated in Fig. 6 for the first five critical speeds. The dashed curve represents the case without the VEM core, i.e., $h_v=0$. Significant damping effects are observed on each critical speed and that at higher critical speeds there exhibits better damping effects. Comparing Fig. 3 and Fig. 6, one sees that there is more resonance in the case of a traveling constant load than in the case of a stationary harmonic load. This is due to the traveling speed introducing multi-excitation frequencies.

At last, the case of traveling harmonic loads is demonstrated. Consider a traveling harmonic point load with driving frequency ω and traveling speed Ω acting on the inner face layer in the radial direction. The response amplitudes for

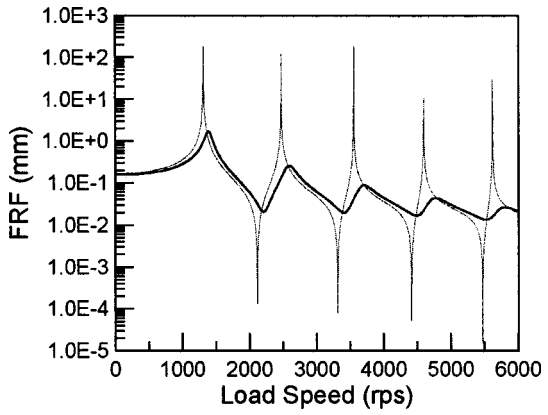

FIG. 6. Frequency response of a traveling constant point load.

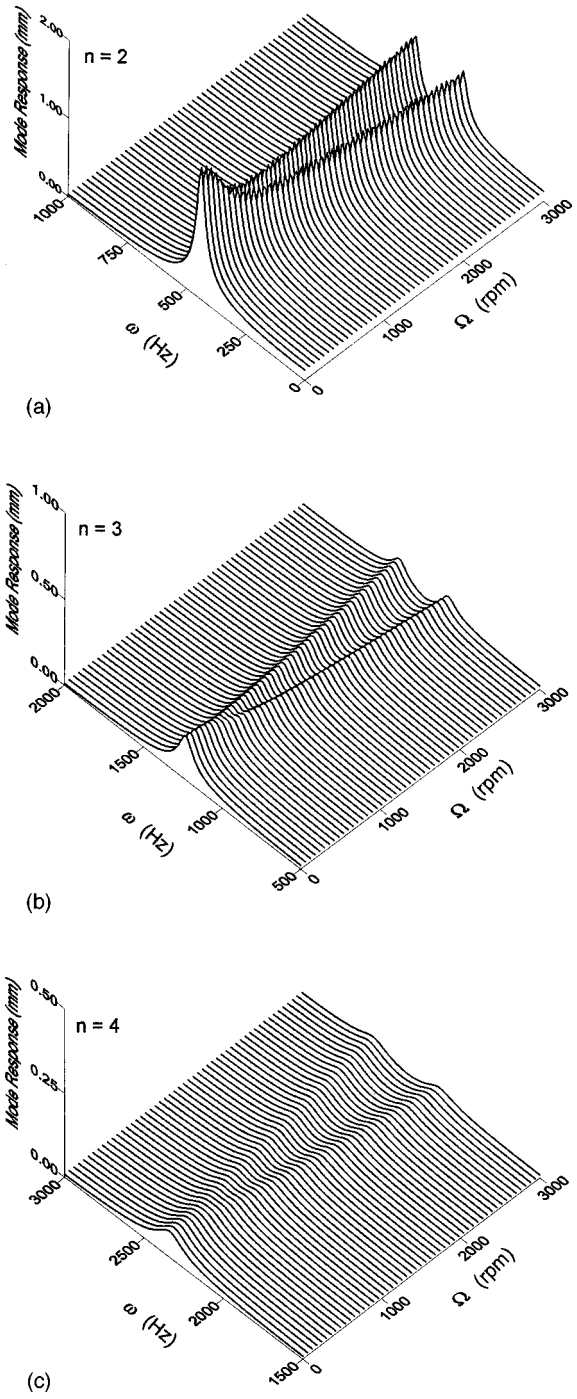

FIG. 7. (a) The displacement response of the first $(n=2)$ flexible mode. (b) The displacement response of the second $(n=3)$ flexible mode. (c) The displacement response of the third $(n=4)$ flexible mode.

the first three flexible modes, $n=2$, 3, and 4, are solved and illustrated in Fig. 7. These 3-D figures are intended to show the interaction between Ω and ω. It is seen that the appearance of the traveling load splits the resonant frequency for each n number into two. It is known that one offset refers to the forward wave and the other one refers to the backward wave. Figure 8 illustrates the interplay between the VEM thickness h_2, the driving frequency ω, and the traveling speed Ω for the first three flexible modes. This figure reveals that thin VEM slightly lifts the resonant frequencies, but thicker VEM eventually drops the resonant frequencies. The

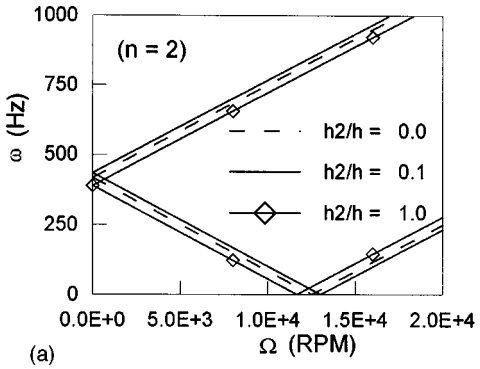

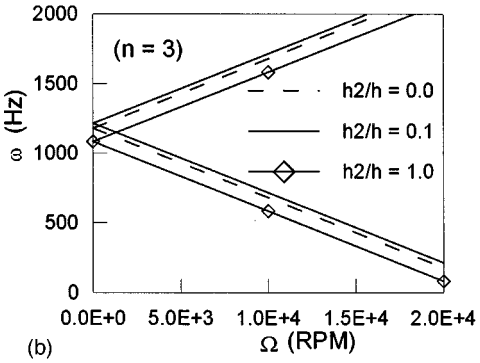

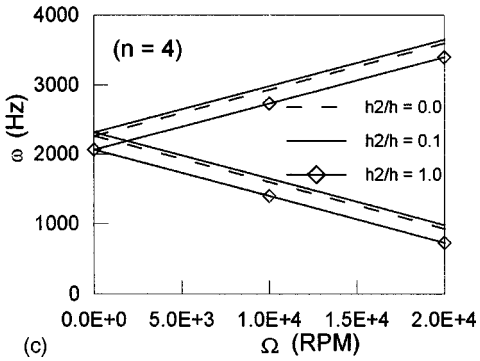

FIG. 8. (a) The resonant frequency for the first ($n=2$) flexible mode. (b) The resonant frequency for the second ($n=3$) flexible mode. (c) The resonant frequency for the third ($n=4$) flexible mode.

total response summed up to the first ten terms is shown in Fig. 9 for two cases of different VEM thickness.

VII. CONCLUSIONS

This paper presents a mathematical model for the forced response of three-layer sandwich rings with viscoelastic core. The differential equations contain three displacements, which are one transverse displacement and two tangential displacements of the face layers. The closed form solutions to various loading cases such as a stationary harmonic point load, a traveling constant point load, and a traveling harmonic point load were obtained via the use of modal expansion technique. Numerical examples illustrated the damping effects of the VEM core and from the analysis some design considerations on damping mechanism using the VEM core were drawn.

It is know that the shear strains of the VEM core dominate the absorption of energy. The face layers therefore must provide enough constraint to the VEM core. Thicker VEM

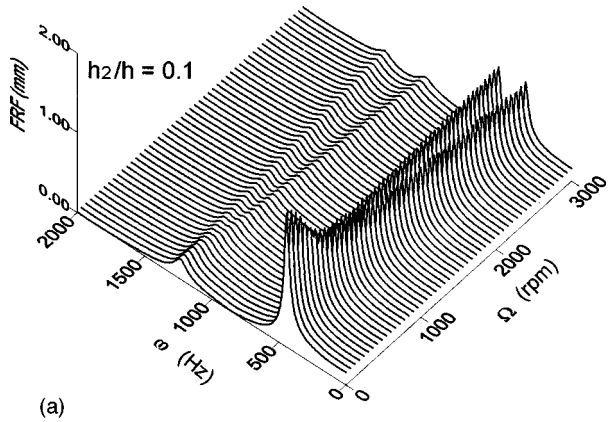

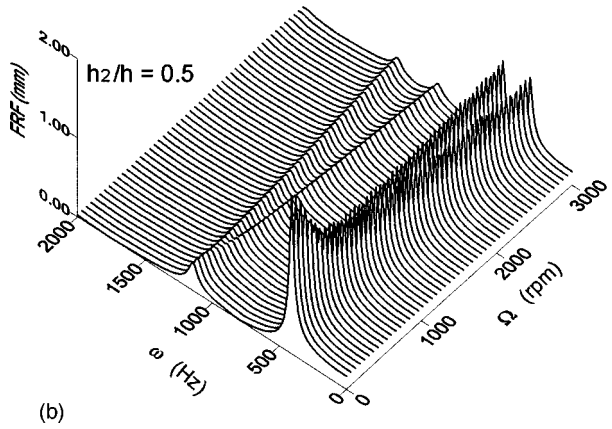

FIG. 9. (a) The maximum displacement in radial dir. to traveling harmonic point load, $h_2/h=0.1$. (b) The maximum displacement in radial dir. to traveling harmonic point load, $h_2/h=0.5$.

increases the capacity of energy absorption but simultaneously reduces the constraining ability of CL. Responses to traveling loads were investigated as well. A load speed invoked the bifurcation of resonant frequencies. One offset refers to the so-called forward traveling wave and the other one refers to the backward traveling wave. The damping effects at higher critical speeds are more significant than the lower ones. Through the foregoing studies, a thin VEM core could provide effective damping and this technique could be applied to bearing elements to reduce vibration level.

APPENDIX

$$m_{11}=\rho_1 h_1 a_1, \tag{A1a}$$

$$m_{22}=\rho_2 h_2 a_2, \tag{A1b}$$

$$m_{33}=\rho_1 h_1 a_1+\rho_2 h_2 a_2+\rho_3 h_3 a_3, \tag{A1c}$$

$$\kappa_{11}(\omega)=\left(\frac{K_1}{a_1}+\frac{D_1}{a_1^3}\right)n^2+\frac{a_2}{h_2}G(\omega)\left(\frac{2a_1-h_1}{2a_1}\,\frac{2a_2-h_2}{2a_2}\right)^2, \tag{A2a}$$

$$\kappa_{12}(\omega)=-\frac{a_2}{h_2}G(\omega)\left(\frac{2a_1-h_1}{2a_1}\,\frac{2a_2-h_2}{2a_2}\right)\times\left(\frac{2a_3+h_3}{2a_3}\,\frac{2a_2+h_2}{2a_2}\right), \tag{A2b}$$

$$\kappa_{13}(\omega)=-\left(\frac{K_1}{a_1}n+\frac{D_1}{a_1^3}n^3\right)+\frac{a_2}{h_2}G(\omega)\left(\frac{2a_1-h_1}{2a_1}\,\frac{2a_2-h_2}{2a_2}\right)\times\left(\frac{2a_3+h_3}{2a_3}\,\frac{2a_2+h_2}{2a_2}-\frac{2a_1-h_1}{2a_1}\,\frac{2a_2-h_2}{2a_2}\right)n, \tag{A2c}$$

$$\kappa_{22}(\omega)=\left(\frac{K_3}{a_3}+\frac{D_3}{a_3^3}\right)n^2+\frac{a_2}{h_2}G(\omega)\left(\frac{2a_3+h_3}{2a_3}\,\frac{2a_2+h_2}{2a_2}\right)^2, \tag{A2d}$$

$$\kappa_{23}(\omega)=-\left(\frac{K_3}{a_3}n+\frac{D_3}{a_3^3}n^3\right)-\frac{a_2}{h_2}G(\omega)\left(\frac{2a_3+h_3}{2a_3}\,\frac{2a_2+h_2}{2a_2}\right)\times\left(\frac{2a_3+h_3}{2a_3}\,\frac{2a_2+h_2}{2a_2}-\frac{2a_1-h_1}{2a_1}\,\frac{2a_2-h_2}{2a_2}\right)n, \tag{A2e}$$

$$\kappa_{33}(\omega)=\left(\frac{K_1}{a_1}+\frac{K_3}{a_3}\right)+\left(\frac{D_1}{a_1^3}+\frac{D_3}{a_3^3}\right)n^4+\frac{a_2}{h_2}G(\omega)\times\left(\frac{2a_3+h_3}{2a_3}\,\frac{2a_2+h_2}{2a_2}-\frac{2a_1-h_1}{2a_1}\,\frac{2a_2-h_2}{2a_2}\right)^2 n^2, \tag{A2f}$$

$$q_1(t)=\frac{\int_0^{2\pi}a_3 f_\theta(\theta,t)\sin(n\theta)\,d\theta}{\int_0^{2\pi}\sin^2(n\theta)\,d\theta},$$

$$q_2(t)=\frac{\int_0^{2\pi}a_3 f_r(\theta,t)\cos(n\theta)\,d\theta}{\int_0^{2\pi}\cos^2(n\theta)\,d\theta}, \tag{A3a}$$

$$q_3(t)=\frac{\int_0^{2\pi}a_3 f_\theta(\theta,t)\cos(n\theta)\,d\theta}{\int_0^{2\pi}\cos^2(n\theta)\,d\theta},$$

$$q_4(t)=\frac{\int_0^{2\pi}a_3 f_r(\theta,t)\sin(n\theta)\,d\theta}{\int_0^{2\pi}\sin^2(n\theta)\,d\theta}, \tag{A3b}$$

$$\Gamma_{11}(\omega)=\{[\kappa_{22}(\omega)-m_{22}\omega^2][\kappa_{33}(\omega)-m_{33}\omega^2]-[\kappa_{23}(\omega)]^2\}/\Delta(\omega), \tag{A4a}$$

$$\Gamma_{22}(\omega)=\{[\kappa_{11}(\omega)-m_{11}\omega^2][\kappa_{33}(\omega)-m_{33}\omega^2]-[\kappa_{13}(\omega)]^2\}/\Delta(\omega), \tag{A4b}$$

$$\Gamma_{33}(\omega)=\{[\kappa_{11}(\omega)-m_{11}\omega^2][\kappa_{22}(\omega)-m_{22}\omega^2]-[\kappa_{12}(\omega)]^2\}/\Delta(\omega), \tag{A4c}$$

$$\Gamma_{12}(\omega)=\{\kappa_{13}(\omega)\kappa_{23}(\omega)-\kappa_{12}(\omega)[\kappa_{33}-m_{33}\omega^2]\}/\Delta(\omega), \tag{A4d}$$

$$\Gamma_{13}(\omega)=\{\kappa_{12}(\omega)\kappa_{23}(\omega)-\kappa_{13}(\omega)[\kappa_{22}-m_{22}\omega^2]\}/\Delta(\omega), \tag{A4e}$$

$$\Gamma_{23}(\omega)=\{\kappa_{12}(\omega)\kappa_{13}(\omega)-\kappa_{23}(\omega)[\kappa_{11}-m_{11}\omega^2]\}/\Delta(\omega), \tag{A4f}$$

$$\Delta(\omega)=[\kappa_{11}(\omega)-m_{11}\omega^2][\kappa_{22}(\omega)-m_{22}\omega^2][\kappa_{33}(\omega)-m_{33}\omega^2]-\kappa_{12}^2(\omega)[\kappa_{33}(\omega)-m_{33}\omega^2]-\kappa_{23}^2(\omega)\times[\kappa_{11}(\omega)-m_{11}\omega^2]-\kappa_{13}^2(\omega)[\kappa_{22}(\omega)-m_{22}\omega^2]+2\kappa_{12}(\omega)\kappa_{23}(\omega)\kappa_{13}(\omega). \tag{A5}$$

Bert, C. W., and Chen, T. L. C. (**1978**). ''On vibration of a thick flexible ring rotating at high speed,'' J. Sound Vib. **61**, 517–530.

Bickford, W. B., and Reddy, E. S. (**1985**). ''On the vibration of rotating rings,'' J. Sound Vib. **101**, 13–22.

DiTaranto, R. A. (**1965**). ''Theory of vibratory bending for elastic and viscoelastic layered finite-length beams,'' ASME, Journal of Applied Mechanics **32**, 881–886.

DiTaranto, R. A., and Lessen, M. (**1964**). ''Coriolis acceleration effect on the vibration of rotating thin-walled circular cylinder,'' J. Appl. Mech. **31**, 700–701.

Douglas, B. E., and Yang, J. C. S. (**1978**). ''Transverse compressional damping in the vibratory response of elastic-viscoelastic beams,'' AIAA J. **16**, 925–930.

Endo, M., Hatamura, K., Sakata, M., and Taniguchi, O. (**1984**). ''Flexural vibration of a thin rotating ring,'' J. Sound Vib. **92**, 261–272.

Hu, Yuh Chung, and Huang, Shyh Chin (**1996**). ''A linear theory of three-layer damped sandwich shell vibrations,'' ASME International Mechanical Engineering Congress and Exposition, Active Control of Vibration and Noise **DE-93**, 229–238.

Huang, S. C., and Soedel, W. (**1987a**). ''Effects of coriolis acceleration on the free and forced in-plane vibrations of rotating rings on elastic foundation,'' J. Sound Vib. **115**, 253–274.

Huang, S. C., and Soedel, W. (**1987b**). ''Response of rotating rings to harmonic and periodic loading and comparison with the inverted problem,'' J. Sound Vib. **118**, 253–270.

Huang, S. C., Inman, D. J., and Austin, E. M. (**1995**). ''Some design considerations for active and passive constrained layer damping treatments,'' J. Smart Material and Structure **5**, 301–313.

Johnson, C. D. (**1995**). ''Design of passive damping systems,'' ASME, Special 50th Anniversary Design Issue **117**, 171–176.

Lu, Y. P. (**1977**). ''Forced vibrations of damped cylindrical shells filled with pressurized liquid,'' AIAA J. **15**, 1242–1249.

Lu, Y. P., Roscoe, A. J., and Douglas, B. E. (**1991**). ''Analysis of the response of damped cylindrical shells carrying discontinuously constrained beam elements,'' J. Sound Vib. **150**, 395–403.

Mead, D. J., and Markus, S. (**1969**). ''The forced vibration of a three-layer, damped sandwich beam with arbitrary boundary conditions,'' AIAA J. **10**, 163–175.

Mead, D. J., and Yaman, Y. (**1991**). ''The harmonic response of rectangular sandwich plates with multiple stiffening: A flexural wave analysis,'' J. Sound Vib. **145**, 409–428.

Padovan, J. (**1973**). ''Natural frequencies of rotating prestressed cylinders,'' J. Sound Vib. **31**, 469–482.

Ramesh, T. C., and Ganesan, N. (**1994**). ''Orthotropic cylindrical shells with a viscoelastic core: A vibration and damping analysis,'' J. Sound Vib. **175**, 535–555.

Rao, Mohan D., and He, Shulin (**1993**). ''Dynamic analysis and design of laminated composite beams with multiple damping layers,'' AIAA J. **31**, 736–745.

Reddy, E. S., and Bickford, W. B. (**1985**). ''On the in-plane vibrations of a rotating ring with equi-spaced spokes,'' J. Sound Vib. **103**, 533–544.

Roy, P. K., and Ganesan, N. (**1993**). ''A vibration and damping analysis of circular plates with constrained damping layer treatment,'' Comput. Struct. **49**, 269–274.

Srinivasan, A. V., and Lauterbach, G. F. (**1971**). ''Traveling waves in rotating cylindrical shells,'' Journal of Engineering for Industry **93**, 1229–1232.

Yan, M. J., and Dowell, E. H. (**1972**). ''Governing equations of vibrating constrained-layer damping sandwich plates and beams,'' ASME, Journal of Applied Mechanics **39**, 1041–1046.

Active control of multiple tones in an enclosure

A. Sampath and B. Balachandran
Smart Materials and Structures Research Center, Department of Mechanical Engineering, University of Maryland, College Park, Maryland 20742

(Received 16 February 1998; revised 22 January 1999; accepted 3 April 1999)

In this paper, analytical and experimental investigations into active control of multiple tones in a three-dimensional enclosure are presented. The frequency range of the disturbance is chosen to encompass one or more structural and/or enclosure resonances. Distributed piezoceramic actuators and distributed polyvinylidene fluoride (PVDF) sensors are mounted on one of the enclosure boundaries. Acoustic sensors are used inside and outside the enclosure. An analytical formulation based on a state-space model is developed for local vibration control on an enclosure boundary and/or local noise control inside the enclosure for bandlimited disturbances. The error sensor signals are minimized by using digital feedforward control schemes based on filtered-U gradient descent algorithms. Analytical predictions from the current work are found to compare well with the results obtained in our previous experimental investigations. The current efforts are relevant to sound fields such as those enclosed in rotorcraft cabins. © *1999 Acoustical Society of America.*
[S0001-4966(99)03207-5]

PACS numbers: 43.50.−x, 43.50.Ki [MRS]

INTRODUCTION

In recent years, the trend in the designs of modern passenger cars, fixed-wing aircraft, helicopters, and other vehicles has been toward systems with light bodies and small engines, which have high fuel-efficiency. However, in light structures, structural vibration and interior noise become important problems. To understand these problems, it is necessary to examine noise transmission into enclosures with flexible boundaries. In a typical noise spectrum in the interior of a rotorcraft, many dominant peaks occur in the range of 50 Hz–5000 Hz.[1] Hence, in related noise reduction (NR) efforts, one is required to attenuate sound fields with many dominant tones. In previous efforts, digital interior noise control has been used primarily for control of harmonic disturbances (e.g., Refs. 2–5). The focus of studies considering narrow-band and broadband disturbances has been on attenuation of acoustic radiation into free space (e.g., Refs. 6–8).

Recently, active control of bandlimited disturbances in enclosures has been receiving considerable attention.[9–12] Here, the words ''bandlimited disturbances'' are used to imply that the energy associated with the signal is concentrated in a finite bandwidth in the frequency domain. With this notion, one can account for both deterministic disturbances comprising one or more tones and random disturbances. Doppenberg and Koers[9] conducted a numerical study of digital control of quasiperiodic noise in an enclosure. Cabell *et al.*[10] reported experimental results on noise control of bandlimited disturbances in the interior of a McDonnell Douglas DO-9 aircraft fuselage. Recently, the authors[11,12] carried out experimental investigations into active control of bandlimited disturbances in a three-dimensional enclosure. They realized spatial local control of enclosed sound fields with multiple tones by using distributed piezoelectric actuators and a combination of acoustic and/or vibration error sensors.

The efforts presented in Refs. 13–16 are also closely related to the current efforts. Koshigoe *et al.*[13] conducted numerical investigations into feedforward control of sound transmission into an enclosure due to an acoustic pulse excitation. Banks and Smith[14] examined control of tonal disturbances in two-dimensional enclosures by using piezoelectric materials on the enclosure boundaries. They used Linear Quadratic Regulator (LQR) optimal control analysis. Wu *et al.*[15] conducted numerical investigations into active absorption of acoustic waves by using Linear Quadratic Gaussian (LQG) analysis, and they demonstrated broadband echo reduction in a one-dimensional duct. Baumann *et al.*[16] presented a control scheme, which is based on LQG theory, to accomplish active structural acoustic control of broadband disturbances.

In this study, numerical and experimental investigations into feedforward control of multiple tones transmitted into a three-dimensional enclosure are presented. Distributed piezoelectric actuators and acoustic error sensors are used in the control scheme. A finite dimensional state-space model for a panel-enclosure system has been developed to accommodate structural-acoustic interactions. This model allows one to study transient responses and interactions that may occur among different frequency components of the response. Feedforward filtered-U least mean square (LMS) control algorithms[17] are implemented in both the numerical simulations and in the experiments for controlling bandlimited disturbances with frequency components close to multiple panel and/or enclosure resonances. This work, which is a direct extension of the recent studies conducted by the authors,[11,12] is believed to be one of the first studies to report analytical and experimental results on active control of multiple tones in enclosed spaces. For clarity, it needs to be noted that selected experimental results on control of multiple tones were reported in Refs. 11, 12. Here, in addition to some of these results results obtained in other experiments have also been included. In terms of analytical development,

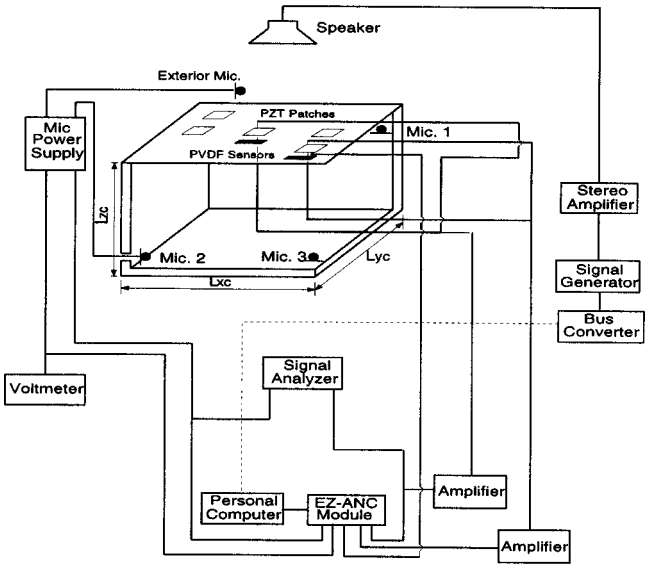

FIG. 1. Experimental setup.

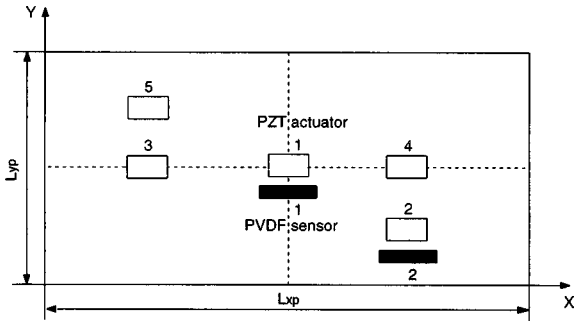

FIG. 2. Actuator and sensor locations on the panel.

in our earlier work,[3] equations governing the plate-piezo system and the panel-enclosure system were presented along with frequency domain analysis for control of tonal disturbances. Here, the equations used for the plate-piezo system and the panel-enclosure system are the same as that used in Ref. 3, except for the modification used to account for multiple actuator pairs used in the current work. The development that follows these equations is unique to the current work. The development of a state-space model for the panel-enclosure system and the time-domain simulations conducted by using this model to examine the effectiveness of the LMS controller in handling disturbances with multiple tones is a primary contribution of the current work. It is to be noted that unlike the nonmodel based approaches that are commonly used to examine the effectiveness of feedforward control schemes, here, a model based approach has been used to examine transient behavior. In addition, the model developed here is also currently being used to investigate feedback control schemes.

The rest of this article is organized as follows. In the next section, the experimental arrangement is described. In Sec. II, the time-dependent state-space model is described, and in Sec. III, numerical implementation of the analytical model is presented. In Sec. IV, numerical and experimental results are presented and discussed. Finally, concluding remarks are provided.

I. EXPERIMENTAL ARRANGEMENT

In this section, the experimental setup and the implementation of the control scheme are detailed. The setup is identical to that used by Balachandran *et al.*[3]

A. Panel-enclosure system

In Fig. 1, the experimental arrangement is illustrated. The rectangular enclosure has five rigid walls made from 2.54 cm thick acrylic sheets and a flexible wall made from 0.0625 cm thick aluminum material. This aluminum panel, which is clamped along all four edges, has the dimensions $L_{xp}=66.04$ cm and $L_{yp}=50.80$ cm. The inner dimensions of the enclosure are 60.96 cm×45.72 cm×50.80 cm. To generate the external noise disturbance, a commercially available three-way 38.10 cm speaker is mounted at a distance of approximately 76.20 cm from the top of the enclosure. The speaker is driven by using one of the channels of a commercially available stereo amplifier. It is to be noted that the sound field generated by the speaker exhibits some amount of spatial asymmetry over the panel due to the specific arrangement of the speaker cones. Piezoceramic (PZT-5H) patches are symmetrically mounted on the top and bottom surfaces of the panel. The locations of the PZT patches are shown in Fig. 2. In the pairs numbered 1 and 2, each actuator has the dimensions of 5.08 cm×2.54 cm and a thickness of 0.031 75 cm, and in the pairs numbered 3, 4, and 5, each actuator has the dimensions of 5.08 cm×2.286 cm and a thickness of 0.0254 cm. In each pair, the actuators are wired out of phase to cause extension in one and contraction in the other. This results in a ''localized'' bending moment at the edges of a pair. (This ''localized'' bending moment represents the control input here.) PVDF piezo film sensors (DT2-052 K/L)[18] are bonded to the top surface of the plate, and they are indicated by the shaded areas in Figs. 1 and 2. The centers of the actuator pairs 1–5 are located at $(\frac{1}{2}L_{xp},\frac{1}{2}L_{yp})$, $(\frac{3}{4}L_{xp},\frac{1}{4}L_{yp})$, $(\frac{1}{4}L_{xp},\frac{1}{2}L_{yp})$, $(\frac{3}{4}L_{xp},\frac{1}{2}L_{yp})$, and $(\frac{1}{4}L_{xp},\frac{3}{4}L_{yp})$, respectively. The centers of the PVDF sensors numbered 1 and 2 are located, respectively, at (33.02 cm, 21.59 cm) and (49.53 cm, 9.40 cm) on the surface of the plate.

Half-inch (1.27 cm) and one-inch (2.54 cm) condenser microphones are used as sensors to measure pressure levels inside and outside the enclosure. The external microphone, which is of free-field type, is an half-inch condenser microphone. This microphone is placed approximately 2.54 cm above the panel-enclosure system and this sensor provides the reference signal to the control system. The internal microphones, which are numbered 1–3, are of pressure and random type, and they are located inside the enclosure at the coordinates (58.42 cm, 43.18 cm, 48.26 cm), (2.54 cm, 15.24 cm, 2.54 cm), and (58.42 cm, 2.54 cm, 2.54 cm), respectively. These coordinates are chosen to ensure that all of the enclosure modes are sensed. For the experimental results reported in this study, the PZT pairs 1 and 2 are used as actuators and Mic. 1 and/or PVDF sensor 1 are used as error sensors. (The actuator pairs 3, 4, and 5 are being used in other ongoing experiments.)

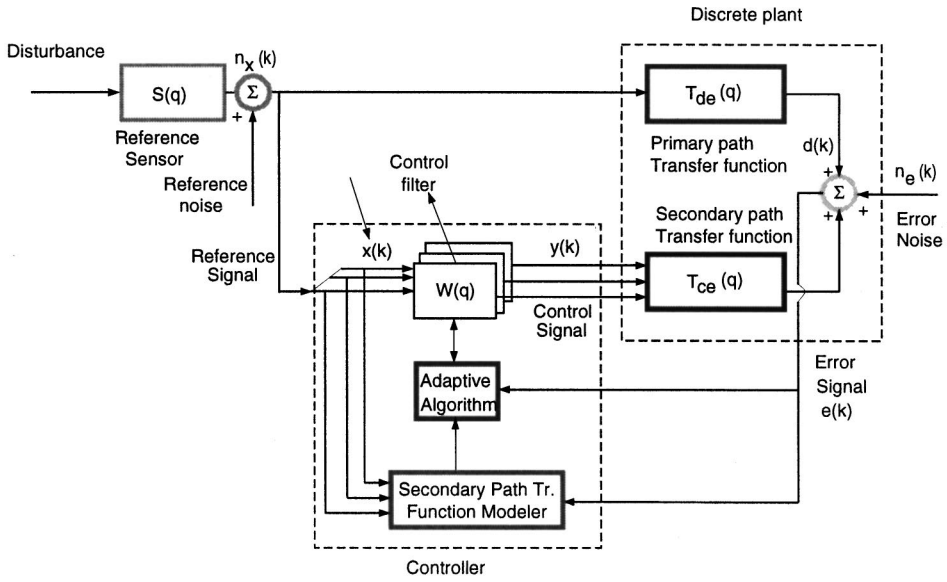

FIG. 3. Arrangement for adaptive feedforward control.

B. Digital feedforward control

Here, local digital noise control is carried by using least mean square (LMS) adaptive feedforward algorithm.[19,20] The control scheme is implemented by using digital signal processing (DSP) hardware and EZ-ANC software. The hardware consists of an ADSP-2101 DSP unit, three AD1847 codes (each with two A/D converters), a serial communication port for personal computer access, and a host of connectors.[21] A schematic of the implementation is shown in Fig. 3.

The path between the primary disturbance measured at the reference sensor and an output in the discrete plant measured at an error sensor represents a primary path; the corresponding operator in the discrete-time domain is represented by $T_{de}(q)$. The path between the control signal into a piezoceramic actuator pair and an output measured at an error sensor in the discrete plant represents a secondary path; the corresponding operator in the discrete-time domain is represented by $T_{ce}(q)$. The discrete signals $n_x(k)$ and $n_e(k)$ are representative of the measurement noise in the reference and error signals, respectively. The operator $S(q)$ is representative of the reference sensor. It is assumed that the reference sensor signal is coherent with the primary disturbance signal that is input into the controller. The principal components of the controller shown in Fig. 3 are the control filters, the adaptive algorithm, and the secondary path transfer function modeler. The reference sensor signal is filtered by a control filter whose weights are adjusted adaptively by using the adaptive algorithm. The output of the controller represents a set of control signals that is input into the actuators. The three-dimensional panel-enclosure setup shown in Fig. 1 can be considered as a multi-input multi-output (MIMO) linear system consisting of M actuators and L sensors. The response of the l_ath acoustic error sensor and l_vth vibration error sensor can be written as[22]

$$e_{l_a}(k)=d_{l_a}(k)+\sum_{m=1}^{M} T_{l_a m}(q)W_m(q)x(k),$$

$$e_{l_v}(k)=d_{l_v}(k)+\sum_{m=1}^{M} T_{l_v m}(q)W_m(q)x(k), \tag{1}$$

where d_{l_a} and d_{l_v} are, respectively, the responses of the l_ath acoustic error sensor and l_vth vibration error sensor due to the primary disturbance alone. In Eq. (1), $T_{l_a m}(q)$ is the discrete-time operator associated between the l_ath acoustic error sensor and the mth actuator. In Eq. (2), $T_{l_v m}(q)$ is the discrete-time operator associated between the l_vth vibration error sensor and the mth actuator. In both equations, $W_m=\Sigma_{i=0}^{I} w_{mi}q^{-i}$ is the representation of the Ith order adaptive filter with coefficients w_{mi}, and this filter's output is the control input to the mth actuator. Furthermore, $x(k)$ is the sampled reference signal, q^{-1} represents a unit delay, and $q^{-i}x(k)=x(k-i)$. As illustrated in Fig. 3, the control signal $y(k)$ is obtained by digitally filtering the reference input signal. An IIR filter is used for this purpose in the experiments reported here. Other details about the controller can be found in Ref. 21.

The performance function for minimization J is chosen as the average of the sum of the squares of the error signals at the error sensors and can be written at the kth instant of time as

$$J(k)=\frac{c_1}{L_m}\sum_{l_a=1}^{L_m} e_{l_a}^2(k)+\frac{c_2}{L_v}\sum_{l_v=1}^{L_v} e_{l_v}^2(k), \tag{2}$$

where c_1 and c_2 are the weighting factors for the error sensors, e_{l_a} and e_{l_v} are, respectively, the values of the acoustic and vibration error signals, and L_m and L_v are, respectively, the total number of acoustic error sensors and the total number of vibration error sensors. The performance function is minimized by using a gradient based adaptive feedforward filtered-U algorithm. A simplified version of the recursive least mean square (RLMS) algorithm that does not include the derivatives of the past outputs is implemented. The adaptive algorithm involves modifying the weights of the digital filter in order to produce the required control input so that the quadratic function J is minimized. In LMS control imple-

mentations, assuming that the filter weights w_{mi} vary on a slow time scale so as to be considered invariant on the time scale of the system response, the filter weights are updated according to the equation

$$w_{mi}(k+1)=w_{mi}(k)-\mu\Delta w_{mi}(k). \tag{3}$$

However, in the experiments conducted in this study, the weight update equation is modified to be

$$w_{mi}(k+1)=w_{mi}(k)(1-\mu\alpha)-\mu\Delta w_{mi}(k), \tag{4}$$

where μ is a positive number referred to as the convergence coefficient, $w_{mi}(k)$ is the filter weight at the kth instant of time, α is a ''small'' positive number referred to as the filter weight leakage coefficient, and the filter weight increment $\Delta w_{mi}(k)$ at the kth instant of time is given by

$$\Delta w_{mi}(k)=\frac{2c_1}{L_m}\sum_{i=1}^{L_m} e_{l_a}(k)u_{la}(k-i) + \frac{2c_2}{L_v}\sum_{i=1}^{L_v} e_{l_v}(k)u_{lv}(k-i), \tag{5}$$

where $u_{la}(k-i)$ and $u_{lv}(k-i)$ are the filtered signals that would be respectively obtained at the l_ath acoustic sensor and l_vth vibration sensor if the system were excited with the mth actuator by feeding in the reference signal delayed by i samples through the IIR filter.

In the experiments, the number of forward and backward filter coefficients in the IIR filter, the actuator gains, and the convergence coefficient of the gradient descent algorithm are initially adjusted by trial and error to ensure a downward trend in the sound pressure level (SPL) at the chosen error microphone and/or the vibration level at the chosen vibration error sensor. As the magnitudes of the values at the error sensors start to decrease, the convergence coefficient is gradually decreased from an initial value of about 400 to a final value of about 50 in order to prevent large fluctuations in the values at the error sensors and to attain steady state values at the chosen error sensors.

For the different experiments conducted, the sampling frequency for the controller is set at 5.21 kHz. Here, a value of one is assigned to each of the weighting factors c_1 and c_2 associated with the error sensors to provide equal weighting to both acoustic and vibration sensors. Based on the results of our earlier work,[5] it is known that use of acoustic sensors alone can result in increased panel vibration levels while the SPL inside the enclosure is reduced. In particular, when one is trying to control sound fields dominated by enclosure modes, it can be beneficial to include a ''large'' value for c_2 compared to c_1 to prevent the panel vibration levels from becoming larger in the controlled case. On a related note, if one wishes to use an energy density based performance function, the quantities c_1 and c_2 can be appropriately chosen based on the work presented in Ref. 5. In the present work, the typical range of values of different parameters of the control system are the following: IIR filter weights; forward: 60 and backward: 60, convergence coefficient μ: 50–400, and filter weight leakage coefficient α: 8. The typical range of values of different parameters for the secondary path identification system are as follows: FIR filter weights: 60, convergence coefficient μ: 300–500, and filter weight leakage coefficient α: 8. The values of the convergence coefficient presented here need to be multiplied by appropriate calibration and other parameters associated with the converters on the digital signal processing boards used in the experiments before they can be compared to the values of the convergence coefficient used in the simulations of Sec. III.

II. ANALYTICAL DEVELOPMENT

In this section, the development of the motion of the panel-enclosure system is described. In Secs. II A and II B, the governing equations are provided for the sound pressure field in the enclosure and the plate-piezo system, respectively. The material provided in Secs. II A and II B, which follows from our earlier work,[3] is included here for completeness. In Sec. II C, the state-space model is presented.

The physical model considered for this study is depicted in Fig. 1. The dimensions of the aluminum plate are L_{xp} and L_{yp} in the X and Y directions, respectively. The inner dimensions of the enclosure are L_{xc}, L_{yc}, and L_{zc} in the X, Y, and Z directions, respectively. The external sound disturbance is assumed to be a spatially symmetric plane wave, normally incident on the surface of the panel. Piezoceramic patches are bonded symmetrically to the top and bottom surfaces of the panel and they are used to provide the secondary inputs to the panel-enclosure system. Condenser microphones located outside and inside the enclosure are used as acoustic sensors.

A. Panel-enclosure system

The sound pressure $p(x,y,z,t)$ in the cavity is described by the wave equation

$$\nabla^2 p-\frac{1}{c_0^2}\frac{\partial^2 p}{\partial t^2}-\gamma_a\frac{\partial p}{\partial t}=0, \tag{6}$$

where γ_a is the damping coefficient of air in the enclosure and c_0 is the speed of sound in air. The air particle velocity u in the cavity is related to the sound pressure p by

$$\nabla p=-\rho_0\frac{\partial u}{\partial t}, \tag{7}$$

where ρ_0 is the air density. On the five rigid boundaries of the three-dimensional enclosure, the condition that the normal velocity is zero leads to $\partial p/\partial n=0$ where n indicates the direction normal to the surface of the boundary (positive outward). At the flexible panel/cavity interface, continuity of the normal air particle velocity and the normal panel surface velocity leads to

$$\left(\frac{\partial p}{\partial z}\right)_{z=L_{zc}}=-\rho_0\left(\frac{\partial^2 w}{\partial t^2}\right), \tag{8}$$

where $w(x,y,t)$ is the normal displacement of the thin isotropic panel whose governing system is provided in the next section.

Expanding the pressure inside the enclosure in terms of the normalized *in vacuo* mode shapes of the enclosure $\Phi(x,y,z)$, one arrives at

$$p=\sum_{i=1}^{N}\Phi_i(x,y,z)q_i(t)=\sum_{i=1}^{N}\psi_i(x)\phi_i(y)\Gamma_i(z)q_i(t), \quad (9)$$

where N is the total number of enclosure modes considered in the analysis, $q_i(t)$ is the modal amplitude of pressure, and $\psi(x)$, $\phi(y)$, and $\Gamma(z)$ are the enclosure eigenfunctions in the X, Y, and Z directions, respectively (e.g., Refs. 23, 24).

B. Plate-piezo system

In the derivation of the equation of flexural vibrations for a thin, isotropic panel bearing piezoceramic patches with applied voltage inputs, the thickness of each patch is assumed to be negligible compared with that of the plate. Also, the size of the actuators is assumed to be small compared with the wavelengths considered, so that the coupling terms due to the presence of PZTs can be ignored. The equation of motion can be shown to be[3,25,26]

$$D\nabla^4 w+\rho_p h_p\ddot{w}+\gamma_p\dot{w} =p_{\text{in}}(x,y,t)-p_{\text{out}}(x,y,t) -\sum_{i=1}^{K}\frac{(h_p+h_{\text{pzt}})E_{\text{pzt}}d_{31}}{(1-\nu)}\nabla^2\chi(x_i,y_i)V_i(t), \quad (10)$$

where the subscripts p and pzt, respectively, stand for panel and PZT patch, the pressure loading on the plate is represented by $p_{\text{in}}-p_{\text{out}}$, K is the number of PZT pairs bonded to the surface of the plate, and γ_p is the damping coefficient of the plate. The term p_{in} is the pressure inside the enclosure just below the plate surface and the term p_{out} is the pressure above the plate surface. The quantities ρ_p, E_p, h_p, and ν represent the density, Young's modulus, the thickness of the panel, and the Poisson's ratio for the panel material, respectively. The Poisson's ratio and the density for the PZT material are assumed to be the same as the corresponding quantities of the panel, and D is the stiffness constant of the panel defined as $E_p h_p^3/12(1-\nu^2)$. The function $\chi(x_i,y_i)$ is unity where the ith PZT pair is present and zero elsewhere, and the quantity V_i is the externally applied voltage into the ith PZT pair.

The panel displacement is expanded in terms of the normalized panel modeshapes as

$$w(x,y,t)=\sum_{k=1}^{M}\Psi_k(x,y)\,\eta_k(t)=\sum_{k=1}^{M}\alpha_k(x)\beta_k(y)\,\eta_k(t), \quad (11)$$

where M is the total number of panel modes considered in the analysis and $\eta_k(t)$ is the modal amplitude of panel displacement. In Eq. (11), the eigenfunctions $\Psi_k(x,y)$ are written in terms of the eigenfunctions of clamped–clamped beams in x and y directions as $\Psi_k(x,y)=\alpha_k(x)\beta_k(y)$.[27]

C. State-space model

After substituting Eq. (9) into Eq. (6), taking into account the boundary condition at the panel/cavity interface at the top of the enclosure [Eq. (8)] and making use of the orthonormality properties of the panel and enclosure modeshapes, one can obtain the following coupled equation of motion for the pressure field inside the enclosure[26]

$$[C_{ap}]\{\ddot{\eta}\}+[C_{aa}]\{q\}+\frac{1}{c_0^2}\{\ddot{q}\}+\frac{1}{c_0^2}\text{diag}[2\zeta_a\omega_a]\{\dot{q}\}=\{0\}, \quad (12)$$

where $[C_{aa}]$ is the coupling matrix between different enclosure modes, $[C_{ap}]$ is the coupling matrix between the panel and enclosure modes, ω_a and ζ_a are, respectively, the natural frequency and the damping factor of an enclosure mode,

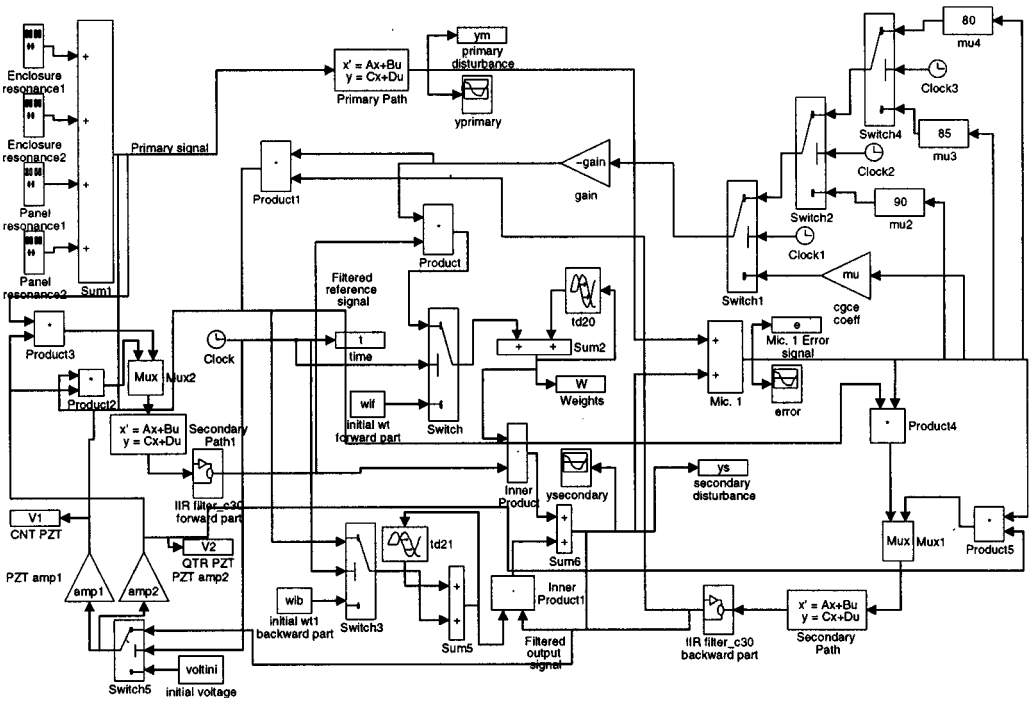

FIG. 4. Arrangement for numerical implementation of adaptive feedforward control.

$\{\eta\}=[\eta_1\eta_2\cdots\eta_M]^T$, and $\{q\}=[q_1q_2\cdots q_N]^T$. The sizes of $[C_{ap}]$, $[C_{aa}]$, $\{\eta\}$, and $\{q\}$ are $N\times M$, $N\times N$, $M\times 1$, and $N\times 1$, respectively.

After multiplying the governing equation of motion for the plate-piezo system [Eq. (10)] throughout by the panel modeshapes, integrating over the panel area, and making use of the orthonormality properties of the panel modeshapes, one can obtain the following coupled equation of motion for the plate-piezo system

$$[C_{pp1}]\{\dot{\eta}\}+[C_{pp2}]\{\eta\}+\rho_p h_p\{\ddot{\eta}\}+\rho_p h_p\,\mathrm{diag}[2\zeta_p\omega_p]\{\dot{\eta}\}$$
$$=[C_{pa}]\{q\}-\{P_{\mathrm{out}}\}-\{P_{\mathrm{pzt}}\}, \tag{13}$$

where $[C_{pp1}]$ and $[C_{pp2}]$ are the coupling matrices between different panel modes, $[C_{pa}]$ is the coupling matrix between the panel and enclosure modes, ω_p and ζ_p are, respectively, the natural frequency and the damping factor of a panel mode, P_{out} is the primary pressure term due to the external disturbance, and P_{pzt} is the secondary pressure term due to the PZT patches. The sizes of $[C_{pp1}]$, $[C_{pp2}]$, $[C_{pa}]$, $\{P_{\mathrm{out}}\}$, and $\{P_{\mathrm{pzt}}\}$ are, respectively, $M\times M$, $M\times M$, $M\times N$, $M\times 1$, and $M\times 1$. The pressure terms $\{P_{\mathrm{out}}(x,y,t)\}$ and $\{P_{\mathrm{pzt}}(x,y,t)\}$ can be written as $\{P_{\mathrm{out}}(x,y,t)\}_{M\times 1}=\{P^r_{\mathrm{out}}(x,y)\}_{M\times 1}P^t_{\mathrm{out}}(t)$ and $\{P_{\mathrm{pzt}}(x,y,t)\}_{M\times 1}=[P^r_{\mathrm{pzt}}(x,y)]_{M\times K}\{V(t)\}_{K\times 1}$. Here $P^t_{\mathrm{out}}(t)$ is the time-dependent scalar amplitude of the incident pressure wave and $\{V(t)\}$ is the time-dependent vector of voltage inputs into the K actuator pairs.

Let a state vector be defined as $\{X\}=[\eta\,\dot{\eta}\,q\,\dot{q}]^T$ and an input vector be defined as $\{U\}=[P^t_{\mathrm{out}}(t)V(t)]^T$. Then, Eqs. (12) and (13) can be written together as

$$\begin{pmatrix}\dot{\eta}\\ \ddot{\eta}\\ \dot{q}\\ \ddot{q}\end{pmatrix}=\begin{pmatrix}[O]_{M\times M} & [I]_{M\times M} & [O]_{N\times N} & [O]_{N\times N}\\ -\dfrac{1}{\rho_p h_p}[C_{pptot}] & -\mathrm{diag}[2\zeta_p\omega_p] & \dfrac{1}{\rho_p h_p}[C_{pa}] & [O]_{M\times N}\\ [O]_{M\times M} & [O]_{M\times M} & [O]_{N\times N} & [I]_{N\times N}\\ \dfrac{c_0^2}{\rho_p h_p}[C_{ap}][C_{pptot}] & c_0^2[C_{ap}]\mathrm{diag}[2\zeta_p\omega_p] & -\dfrac{c_0^2}{\rho_p h_p}[C_{ap}][C_{pa}]-c_0^2[C_{aa}] & -\mathrm{diag}[2\zeta_a\omega_a]\end{pmatrix}\begin{pmatrix}\eta\\ \dot{\eta}\\ q\\ \dot{q}\end{pmatrix}$$
$$+\frac{1}{\rho_p h_p}\begin{pmatrix}[0]_{M\times 1} & [0]_{M\times K}\\ -[P^r_{\mathrm{out}}(x,y)] & -[P^r_{\mathrm{pzt}}(x,y)]\\ [0]_{N\times 1} & [0]_{N\times K}\\ c_0^2[C_{ap}][P^r_{\mathrm{out}}(x,y)] & c_0^2[C_{ap}][P^r_{\mathrm{pzt}}(x,y)]\end{pmatrix}\begin{pmatrix}P^t_{\mathrm{out}}(t)\\ V(t)\end{pmatrix}, \tag{14}$$

where $[C_{pptot}]=[C_{pp1}]+[C_{pp2}]$. Equation (14) is in the standard state-space form

$$\{\dot{X}\}=[A]\{X\}+[B]\{U\}, \tag{15}$$

where the definitions of matrices $[A]$ and $[B]$ are evident from Eq. (14). The output of the system can be written in the form

$$\{Y\}=[C]\{X\}+[D]\{U\}. \tag{16}$$

The definition of $[C]$ matrix is dependent on both the types and locations of sensors used. The definition of $[D]$ matrix is dependent on the types of sensors and their locations and on the PZT actuator locations. For example, when a single acoustic sensor at the location (x_m,y_m,z_m) is used for pressure measurement, the $[C]$ and $[D]$ matrices, respectively, take the form

$$[C]=[\{0\}_{1\times M}\{0\}_{1\times M}\Phi_1(x_m,y_m,z_m)\cdots$$
$$\Phi_N(x_m,y_m,z_m)\{0\}_{1\times N}]_{1\times 2(M+N)}, \tag{17}$$

$$[D]=[00\cdots 0]_{1\times(K+1)}. \tag{18}$$

The performance function and filter equations are similar in structure to Eqs. (2) and (3). It is to be noted that the quantities ω_p and ω_a used in the elements of matrix $[A]$ are the *uncoupled* natural frequencies of the panel and the enclosure, respectively; that is, ω_p are the natural frequencies of a plate clamped along all edges and ω_a are the natural frequencies of a rigid enclosure. Furthermore, the modeling issues for PVDF sensors are not addressed here although PVDF sensors are used as vibration sensors to monitor the vibration levels of the panel in the different experiments.

III. NUMERICAL IMPLEMENTATION

The state-space model is numerically implemented by using SIMULINK,[28] and the arrangement used here is shown in Fig. 4. The model consists of primary and secondary paths, which are both represented by appropriate state-space models. The primary disturbance is assumed to be of form $f(t)=\Sigma_i a_i\sin(\omega_i t+\phi_i)$ where a_i, ω_i, and ϕ_i are, respectively, the amplitude, frequency of excitation, and phase angle associated with the ith tone. The amplitude of the primary disturbance is assumed to be 2.0 V, and the sensitivity of the exterior reference microphone and the interior error microphone (Mic. 1) (see Fig. 1) is assumed to be 1 V/Pa so that a constant amplitude of 100 dB is input into the panel-enclosure system. For simplicity, ϕ_i is taken to be zero. The primary disturbance comprising multiple frequencies is generated, first by generating the individual disturbances at the different tones and next by combining them using a summation block (see Fig. 4). This primary signal is filtered by

using an IIR filter with the number of filter coefficients ranging from 20 to 40. PZT pairs 1 and 2 are used as actuators and Mic. 1 is used as the error sensor (see Figs. 1 and 2). (The sensitivity of Mic. 1 used in the experiments is 50.1 mV/Pa.) Here, the number of cavity modes N and the number of panel modes M are each taken to be equal to forty. The viscous damping loss factors ζ_p and ζ_a are, respectively, taken to be 0.004 and 0.013 based on experimental modal analysis. The material properties used to generate the numerical results are as follows: (a) Young's modulus of aluminum panel and PZT are, respectively, $E_p = 6.9 \times 10^{10}\,\mathrm{N/m^2}$ and $E_{\mathrm{pzt}} = 7.24 \times 10^{10}\,\mathrm{N/m^2}$; (b) density of air and aluminum panel are, respectively, $\rho_0 = 1.21\,\mathrm{Kg/m^3}$ and $\rho_p = 2700\,\mathrm{Kg/m^3}$; (c) speed of sound in air $c_0 = 333\,\mathrm{m/s}$; (d) dielectric constant of PZT $d_{31} = 274 \times 10^{-12}\,\mathrm{m/V}$; and (e) ν for the aluminum panel is taken to be 0.3.

In the numerical implementation, the filter weights for the feedforward part and the feedback part of the IIR filter are updated separately. The initial conditions for all of the filter weights are assumed to be zero. Other details about the numerical implementation are provided in Ref. 26. The sampling frequency for each simulation is set at 2 kHz and each simulation is run for 4.0 s.

Before, the different numerical and experimental results are presented, the following similarities and differences between the experimental and numerical implementations need to be noted.

(a) Each control filter is an IIR filter both in the simulations and experiments, and the filter weights are updated by using a simplified version of the recursive least mean square (RLMS) algorithm in the simulations.

(b) Both in simulations and experiments, the convergence coefficient had to be changed dynamically so as to prevent large fluctuations in the voltage inputs into the actuator pairs. It is to be noted that a time-domain simulation enables one to examine this issue.

(c) It was observed while conducting the experiments that the magnitudes of the voltage inputs into actuator pair 2 were significantly higher than those input into actuator pair 1 (refer to Fig. 2 for actuator locations on the plate). A similar trend was also observed in the numerical simulations. One needs to note that actuator pair 2 has more authority than actuator pair 1 in controlling disturbances that correspond to spatial modes with nodal lines through the center of the panel.

(d) The digital controller used in the experiments is capable of doing on-line system identification of the secondary path transfer functions. This feature is absent in the numerical simulations and a mechanics based model is used to define the primary and secondary paths in the simulations.

(e) The speaker dynamics and the reference sensor dynamics are not accounted for in the numerical simulations.

(f) The feedforward adaptive algorithm used in the experiments [Eq. (4)] is based on a modified version of the gradient descent algorithm and includes leakage coefficients in the filter weight update equations. The adaptive algorithm used in the numerical implementation is based on Eq. (3) and does not include leakage coefficients in the filter weight update equations.

TABLE I. First few system resonances and associated damping factors.

Mode No.	Mode type	Frequency (Hz) Theory	Expt. panel on stand	Expt. panel on enclosure	Damping factor η %
(1,1)	panel	43.3	42.8	48.5	0.8
(2,1)	panel	74.0	74.3	72.5	0.4
(1,2)	panel	100.8	97.3	98.0	0.9
(3,1)	panel	124.2	120.5	123.5	0.8
(2,2)	panel	129.2	128.8	130.0	2.1
(1,0,0)	enclosure	273.1		271.3	1.3
(0,0,1)	enclosure	327.8		324.3	0.2
(0,1,0)	enclosure	364.2		367.0	1.1
(1,0,1)	enclosure	426.6		424.8	0.9
(1,1,0)	enclosure	455.2		448.3	2.1

IV. RESULTS AND DISCUSSION

A. Experimental results

The experimentally determined system resonance frequencies and damping factors are shown in Table I. In both the numerical simulations and experiments, four types of disturbances are considered: (a) disturbance with a frequency component close to the resonance frequency of the (2,1) panel mode, (b) disturbance with a frequency component close to the resonance frequency of the (0,0,1) enclosure mode, and (c) disturbance with frequency components close to the resonance frequencies associated with the (2,1) and (1,2) panel modes, and (d) disturbance with frequency components close to the resonance frequencies associated with the (2,1) and (1,2) panel modes and (0,0,1) and (1,0,1) enclosure modes. Noting that the chosen disturbance frequencies are not exactly equal to the resonance frequencies of the system, in the experiments, the speaker was effective in realizing disturbances with tones close to the resonance frequencies of (2,1) and (1,2) modes in the enclosure. Results complimenting those shown in this section can be found in our previous efforts.[11,12,26]

1. Tonal disturbances

a. Case I: Excitation frequency close to a panel resonance. The results presented in Fig. 5 correspond to a disturbance whose frequency is close to the (2,1) panel resonance frequency. [For the results shown in Fig. 5, the spectra of the steady-state responses are measured by using a spectrum analyzer, the root-mean-square (rms) values of the prominent Fourier components are determined, and these values are used in determining the corresponding SPL values. This is also true for Figs. 8, 9, 10, and 12.] At the frequency component of 70 Hz, the sound pressure levels (SPL) values at Mic. 1 sensor in the uncontrolled and controlled cases are 74.5 dB and 46.9 dB, respectively. There is a noise reduction of about 27.6 dB. Harmonics of the disturbance frequency are also noticeable in the microphone response, due to nonlinear behavior of the actuators. A set of experimental results

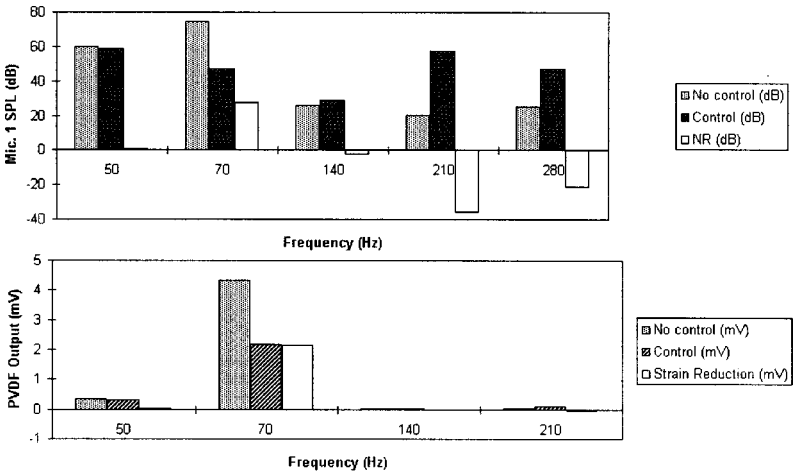

FIG. 5. Responses observed at tonal disturbance of 70 Hz: actuator pairs 1 and 2 and error sensor Mic. 1 are used.

is provided in Figs. 6 and 7 to qualitatively illustrate the nonlinear behavior. In each plot, an accelerometer output at a panel location close to actuator pair 1 is shown when a harmonic voltage input is provided into this actuator pair. As the input magnitude is increased in each case, the second and third harmonics become prominent in the panel response. Based on several experiments conducted and analysis in progress, it has been noted that the magnitudes of the harmonics depend on the actuator location on the panel and the proximity of the excitation frequency component to a system resonance frequency. Although the influence of the actuator nonlinearities has not been completely addressed, the present experiments do point to the importance of considering actuator nonlinearities. Returning to Fig. 5, it is noted that there is an increase in the SPL associated with the higher harmonics. Since the higher frequency components are absent in the reference microphone signal, the controller is unable to attenuate the higher harmonics. In addition, it needs to be noted that the controller has not been designed for a nonlinear system. A frequency component around 50 Hz, which is close to the (1,1) panel resonance frequency, is also present in the microphone response. Since this component is present in the uncontrolled case, it is believed that this component is due to the system dynamics and not due to the actuators. Again, as this component is absent in the reference microphone signal, the controller is unable to attenuate this frequency component. On examining the PVDF sensor reading shown in Fig. 5, it is clear that there is a substantial reduction (about 50%) in the panel vibration level at the sensor location. This shows that for this panel controlled mode, reduction in panel vibration amplitude leads to significant noise reduction inside the enclosure at the considered microphone location.

b. Case II: Excitation frequency close to an enclosure resonance. The results presented in Figs. 8 and 9 correspond to a disturbance whose frequency is close to the (0,0,1) enclosure resonance frequency. The error sensors Mic. 1, Mic. 2, and Mic. 3 are used here. A peak close to 50 Hz, which is close to the (1,1) panel resonance frequency, is again noticeable from the figures although this mode is not excited directly. As in the earlier case, no noise reduction is achieved at this frequency. At the disturbance frequency of 339 Hz, noise reductions of about 26.1 dB, 3.3 dB, and 17 dB are

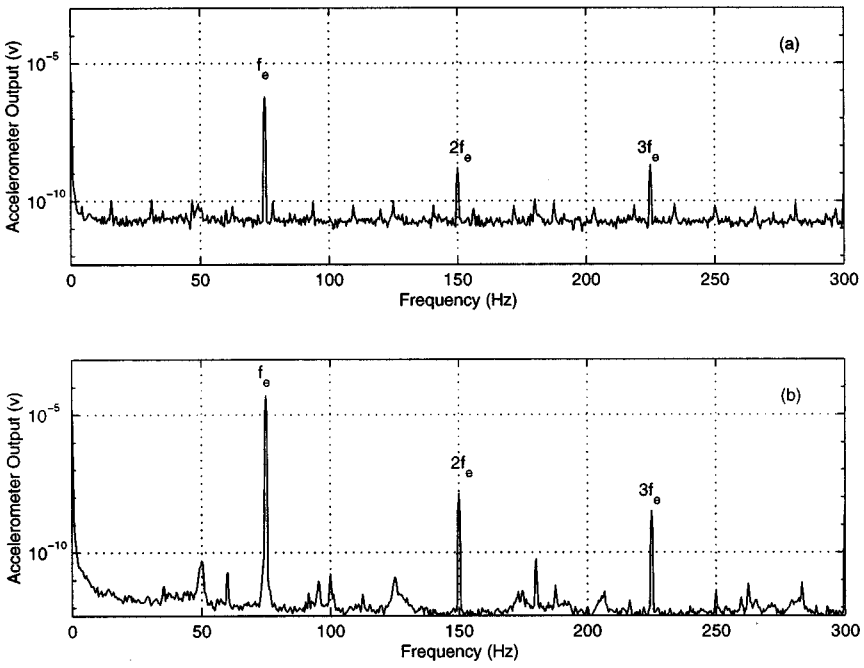

FIG. 6. Panel response to harmonic excitation into actuator pair 1 at 75 Hz: (a) excitation amplitude of 16 V rms and (b) excitation amplitude of 90 V rms.

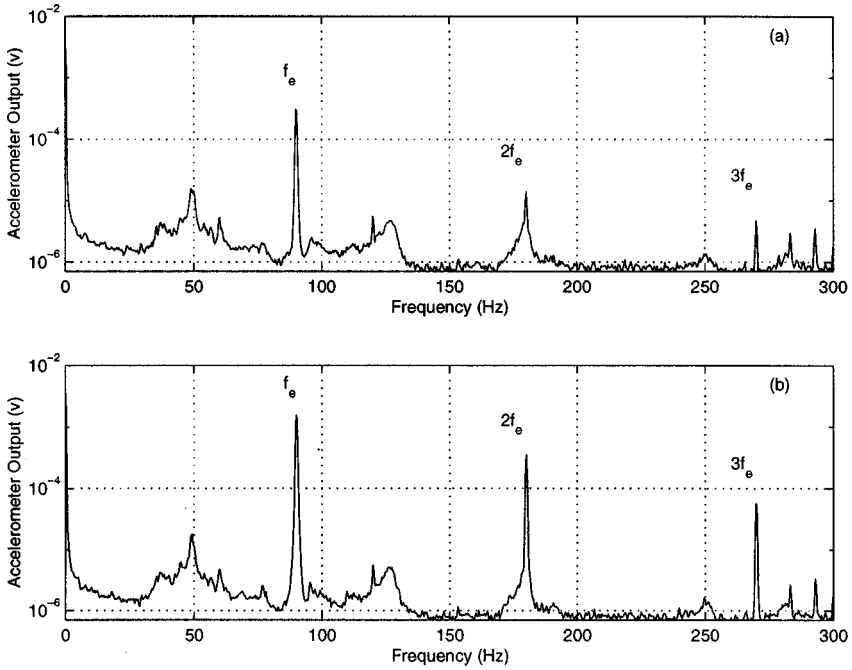

FIG. 7. Panel response to harmonic excitation into actuator pair 1 at 90 Hz: (a) excitation amplitude of 16 V rms and (b) excitation amplitude of 90 V rms.

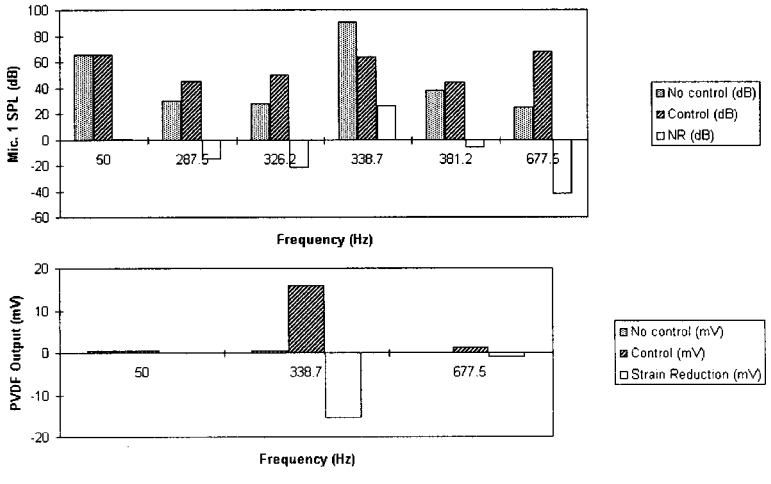

FIG. 8. Responses observed at tonal disturbance of 339 Hz: actuator pairs 1 and 2 and error sensors Mics. 1–3 are used.

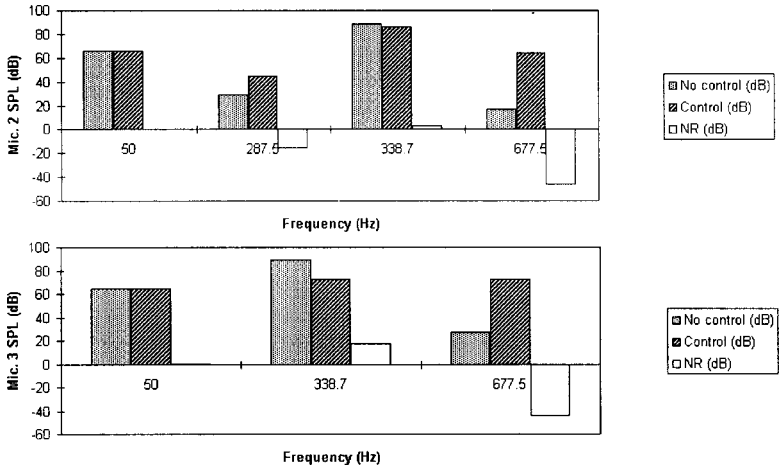

FIG. 9. Responses observed at tonal disturbance of 339 Hz: actuator pairs 1 and 2 and error sensors Mics. 1–3 are used.

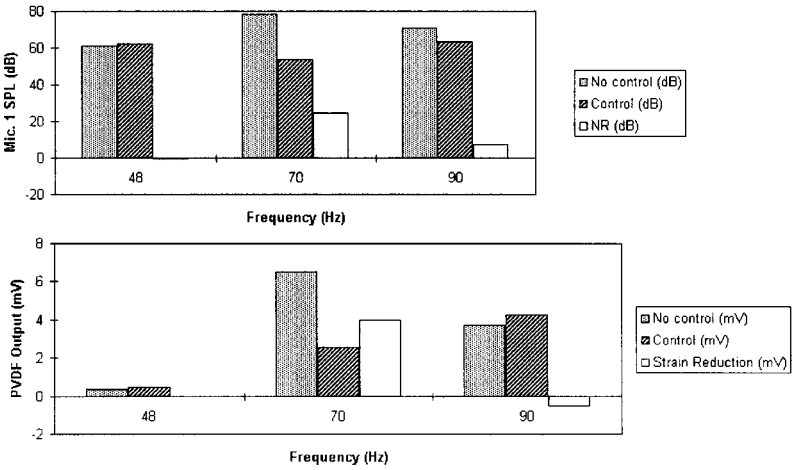

FIG. 10. Responses observed for disturbance with components at 70 Hz and 90 Hz: actuator pairs 1 and 2 and error sensor Mic. 1 are used.

achieved at Mics. 1, 2, and 3, respectively. However, the vibration levels of the panel are significantly increased after control, as seen from the PVDF response in Fig. 8, indicating that for this cavity controlled mode, noise reduction may be accompanied by an increase in panel vibration level. Again, the frequency components that are not present in the reference microphone signal are not attenuated in the controlled case. Some of these frequency components can be attributed to the nonlinear behavior of the actuators. Again, there is a significant increase in the second harmonic of the disturbance frequency at all three interior microphone locations; this frequency component is not present in the reference microphone signal.

2. Disturbances with multiple tones

a. Case I: Disturbance with components close to (2,1) and (1,2) panel resonance frequencies. The responses in the uncontrolled and controlled cases are presented in Fig. 10. It is evident from the figure that there is noise attenuation at the disturbance frequency components of 70 Hz and 90 Hz. The noise reduction is more pronounced at the dominant 70 Hz frequency component. The PVDF strain sensor response indicates that the local vibration level is attenuated at 70 Hz whereas the local vibration level at 90 Hz is increased. The local noise reduction is about 24.6 dB at the 70 Hz component and 7.5 dB at the 90 Hz component. The spectra of the voltage inputs into actuator pairs 1 and 2 are displayed in Fig. 11. The magnitude of input into actuator pair 1 at the different frequency components is higher than those for actuator pair 2. This can be explained in terms of the locations of actuator pairs 1 and 2 (refer to Fig. 2). Actuator pair 2, which is located away from the center of the panel, has more authority than actuator pair 1 in controlling disturbances that can excite spatial modes with nodal lines through the center of the panel. Many spectral peaks are discernible in the voltage input into actuator pair 1. These peaks are located at the values of 20 Hz [difference between the (2,1) and (1,2) resonance frequencies], 140 Hz (harmonic of 70 Hz), and 160 Hz [sum of the (2,1) and (1,2) resonance frequencies]. These peaks can be due to nonlinear behavior of the actuators. Although these harmonics are not prominent in the spectrum associated with actuator pair 2, recent experiments have indicated that voltage inputs with large magnitudes do produce these harmonics due to the nonlinear behavior of the actuators.

b. Case II: Disturbance with components close to (2,1) and (1,2) panel resonance frequencies and (0,0,1) and (1,0,1) enclosure resonance frequencies. The responses in the uncontrolled and controlled cases are shown in Fig. 12. It is clear that the (0,0,1) depth mode at 339 Hz is dominant in the system response. Local noise reductions of about 22.7 dB and 15.6 dB are achieved for the frequency components at 339 Hz and 425 Hz, respectively, implying that the dominant mode at 339 Hz is reduced significantly. However, the noise reductions at the frequency components of 70 Hz and 90 Hz are not significant. Furthermore, the local noise reduction at 339 Hz is accompanied by an increase in the local vibration level as is discernible from the PVDF strain sensor response. This trend is again similar to that presented in Fig. 8. Other results corresponding to control of multiple tones in enclosed spaces are discussed by Sampath.[26] All of these different results indicate that for the chosen experimental setup as well as other enclosed spaces, one can realize substantial local noise attenuation in the presence of multiple tones in the disturbance. However, when enclosure modes are present, a

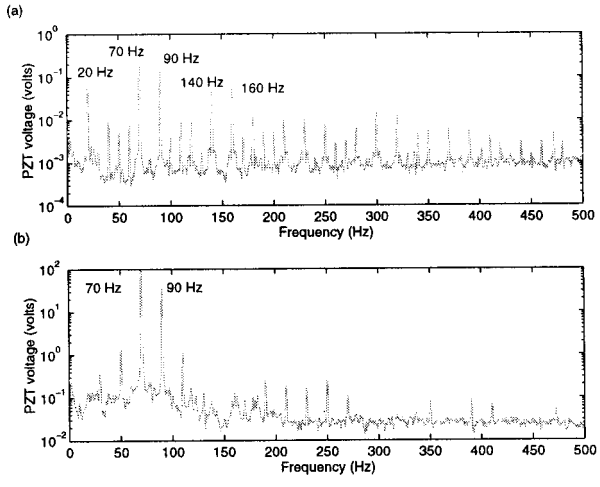

FIG. 11. Spectra of voltage inputs into the actuator pairs: (a) actuator pair 1 and (b) actuator pair 2.

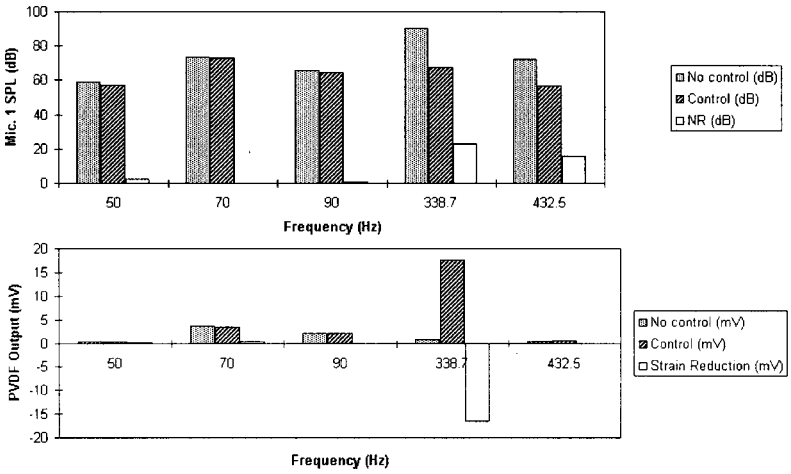

FIG. 12. Responses observed for disturbance with components at 70 Hz, 90 Hz, 339 Hz, and 425 Hz: actuator pairs 1 and 2 and error sensor Mic. 1 are used.

local noise reduction is not necessarily accompanied by a local vibration reduction. In the next section, results of simulations carried out to confirm the experimental findings are provided.

B. Simulation results

In this section, numerical simulations for the plate-enclosure system using the state-space model are presented for tonal and bandlimited disturbances when actuator pairs 1 and 2 and acoustic error sensor (Mic. 1) are used. The number of enclosure modes N and the number of panel modes M are each taken to be equal to 40. The material properties of the aluminum panel and the piezoceramic patches and the structural damping loss factors have been presented in Sec. III. The initial conditions for the filter weights of the feedforward part and feedback part of the IIR filter are taken to be zero. The controller is assumed to be switched on after about 0.1 s. The convergence coefficient μ is adjusted after a certain amount of time to prevent large fluctuations in the voltage inputs into the actuator pairs; this is done to ensure convergence. The value of the convergence coefficient that is used to begin the simulation is $\mu=100\times10^{-6}$; at about 1.0 s, this value is reduced to $\mu_2=90\times10^{-6}$, and at about 2.0 s and 3.0 s, this value is further reduced to $\mu_3=85\times10^{-6}$ and $\mu_4=80\times10^{-6}$, respectively. The power spectra shown in the different figures have been obtained based on the last few seconds of time histories in the respective cases.

1. Tonal disturbances

a. Case I: Excitation frequency close to a panel resonance. The time histories and power spectra of the uncontrolled and controlled SPLs at Mic. 1 are presented in Fig. 13 for a tonal disturbance with a frequency close to the (2,1) panel resonance frequency. (The gains for PZT amplifiers 1 and 2 are set at 20 and 40, respectively.) It can be seen from the controlled response that multiple peaks (in addition to the peak at 70 Hz) occur at higher frequencies indicating energy spillover into high frequency components. The different peaks occur at the frequencies of 70 Hz, 129 Hz, 268 Hz, 330 Hz, 369 Hz, 430 Hz, 468 Hz, 570 Hz, and 633 Hz in the response. The SPL values at the frequency of 70 Hz in the uncontrolled and controlled cases are, respectively, 101.34 dB and 80.95 dB indicating that a 20.39 dB noise reduction is achieved. The voltage inputs into actuators 1 and 2 are

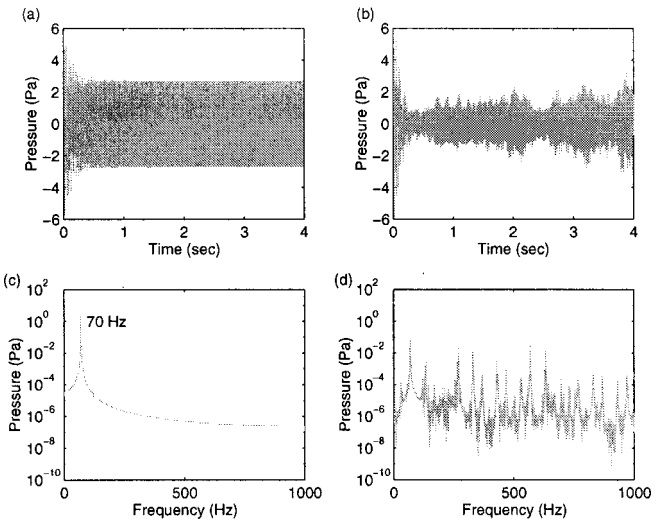

FIG. 13. Mic. 1 SPL at 70 Hz tonal disturbance: (a) time history in uncontrolled case, (b) time history in controlled case, (c) power spectrum in uncontrolled case, and (d) power spectrum in controlled case.

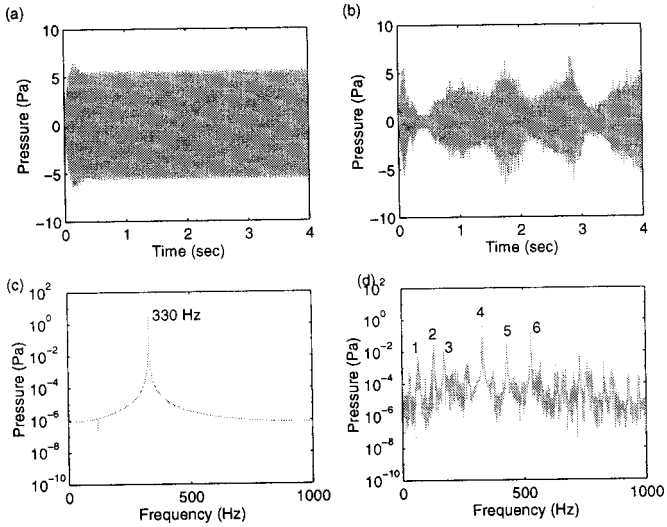

FIG. 14. Mic. 1 SPL at 330 Hz tonal disturbance: (a) time history in uncontrolled case, (b) time history in controlled case, (c) power spectrum in uncontrolled case, and (d) power spectrum in controlled case.

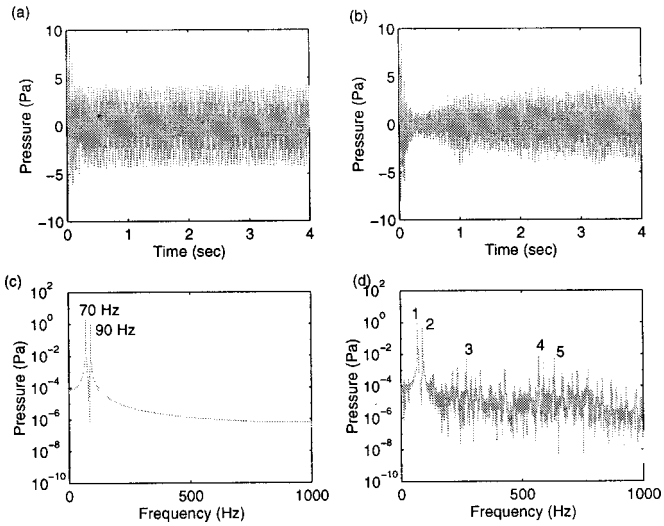

FIG. 15. Mic. 1 SPL when 20 filter weights are used in each control filter: (a) time history in uncontrolled case, (b) time history in controlled case, (c) spectrum in uncontrolled case, and (d) spectrum in controlled case.

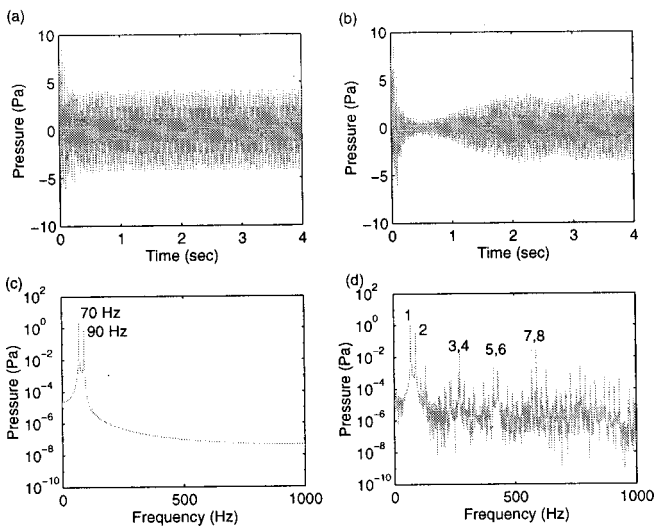

FIG. 17. Mic. 1 SPL when 40 filter weights are used in each control filter: (a) time history in uncontrolled case, (b) time history in controlled case, (c) spectrum in uncontrolled case, and (d) spectrum in controlled case.

about 45 V and 89 V, respectively. On comparing the numerical results presented in Fig. 13 with the experimental results presented in Fig. 5, it is noted that a noise reduction of about 27.6 dB is achieved in the experiments compared to the noise reduction of about 20.39 dB realized in the simulations. Furthermore, the voltage input into actuator pair 2 is about 61 V in the experiments compared to about 89 V in the numerical simulations.

b. Case II: Excitation frequency close to an enclosure resonance. The time histories and power spectra of the uncontrolled and controlled responses are presented in Fig. 14 for a tonal disturbance with a frequency close to the (0,0,1) enclosure resonance frequency. (The gains for PZT amplifiers 1 and 2 are set at 10 and 20, respectively.) It can be seen from the controlled response that multiple peaks occur below and above the excitation frequency of 330 Hz. The peaks numbered 1 to 3 occur below 330 Hz at the frequencies of about 65 Hz, 129 Hz, and 173 Hz, respectively. The peaks numbered 5 and 6 occur above 330 Hz at about 434 Hz and 531 Hz, respectively. The SPL values at the frequency of 330 Hz in the uncontrolled and controlled cases are 109.13 dB and 85.68 dB, respectively, indicating that a local noise reduction of about 23.45 dB is achieved. In the experiments, when Mics. 1–3 are used as error sensors, a noise reduction of about 26 dB at Mic. 1 sensor is achieved (refer to Figs. 8 and 9).

2. Disturbances with multiple tones

a. Case I: Disturbance with components close to (2,1) and (1,2) panel resonance frequencies. The numerical results are presented in Figs. 15–17 for different numbers of filter coefficients in each IIR filter. The results presented in these figures are summarized in Table II. The experimental results,

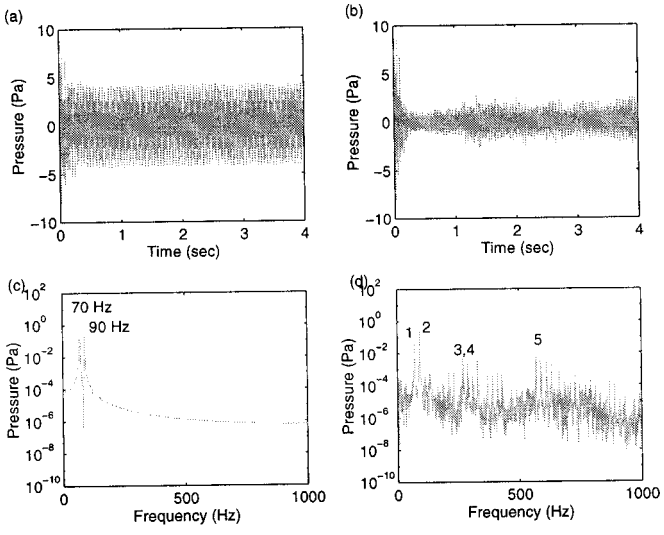

FIG. 16. Mic. 1 SPL when 30 filter weights are used in each control filter: (a) time history in uncontrolled case, (b) time history in controlled case, (c) spectrum in uncontrolled case, and (d) spectrum uncontrolled case.

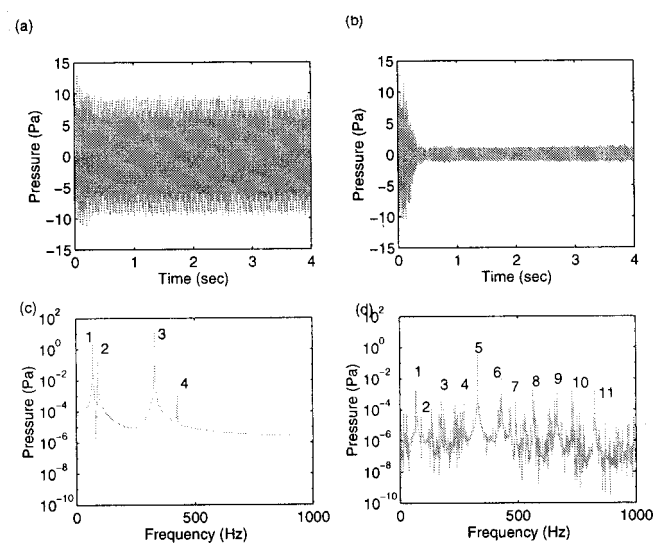

FIG. 18. Mic. 1 SPL when 30 filter weights are used in each control filter: (a) time history in uncontrolled case, (b) time history in controlled case, (c) spectrum in uncontrolled case, and (d) spectrum in controlled case.

TABLE II. Numerical results: Mic. 1 SPL.

		IIR, 20 wts.		IIR, 30 wts.		IIR, 40 wts.	
Freq. (Hz)	No control dB	Control dB	NR dB	Control dB	NR dB	Control dB	NR dB
70	106.43	102.6	3.83	76.29	30.14	100.8	5.63
90	97.46	92.08	5.38	86.21	11.25	90.7	6.76

TABLE IV. Numerical results: Voltage inputs into actuator pairs.

	IIR, 20 wts.		IIR, 30 wts.		IIR, 40 wts.	
Frequency (Hz)	Pair 1 volts	Pair 2 volts	Pair 1 volts	Pair 2 volts	Pair 1 volts	Pair 2 volts
70	12.7	25.5	72.4	145.0	43.0	86.0
90	9.8	19.5	8.4	16.8	24.6	49.3

which were obtained for a case with 60 filter weights in each control IIR filter, are presented in Fig. 10 and are summarized in Table III.

In the numerical simulations, the amplitudes of the 70 Hz and the 90 Hz components in the primary disturbance are each assumed to correspond to 100 dB. The gains for PZT amplifiers 1 and 2 are set at 20 and 40, respectively. It is seen from the figures that the 70 Hz frequency component is dominant compared to the one at 90 Hz frequency. The noise reduction values at 70 Hz are about 3.83 dB, 30.14 dB, and 5.63 dB, respectively, when 20, 30, and 40 filter weights are used in each IIR control filter. The corresponding values at 90 Hz are 5.38 dB, 11.25 dB, and 6.76 dB. The observations indicate that beyond a certain threshold, an increase in the number of filter coefficients in the IIR filter may not necessarily result in more noise reduction in the enclosure. This trend is again similar to that observed while conducting the experiments and is probably due to overparameterization of the transfer function by using higher number of filter coefficients (e.g., Ref. 29). Furthermore, it is seen from Table IV that lower voltage inputs into the actuator pairs are observed when either 20 or 40 filter weights are used indicating that a secondary signal of sufficient amplitude is not produced to cancel the primary disturbance resulting in lower noise reduction values. From the experimental observations presented in Table III, it is noted that about a 24.6 dB reduction in the dominant mode of 70 Hz is obtained (with 60 filter weights) compared to about 30.1 dB in the numerical simulations with 30 filter weights. Furthermore, in the experiments, the local noise reduction for the component corresponding to 90 Hz is about 7.5 dB compared to about 11.25 dB seen in the simulations. Also, the voltage inputs into actuator pair 2 in the simulations with 30 filter weights and in the experiments with 60 filter weights are of comparable magnitudes (about 145 V in the simulations and about 96 V in the experiments).

b. Case II: Disturbance with components close to (2,1) and (1,2) panel resonance frequencies and (0,0,1) and (1,0,1) enclosure resonance frequencies. The numerical results in the uncontrolled and controlled cases are presented in Fig. 18 and summarized in Table V. In this case, the disturbance has frequency components close to the resonance frequencies of the (2,1) panel mode, (1,2) panel mode, (0,0,1) enclosure mode, and (1,0,1) enclosure mode. The corresponding experimental observations (with 60 filter weights in each IIR filter) are presented in Fig. 12 and summarized in Table VI. In the simulations, the amplitudes of different frequency components in the primary disturbance are each assumed to be 2.0 V. The gains for PZT amplifiers 1 and 2 are set at 5 and 10, respectively. In the numerical simulations, the local noise reduction values at 70 Hz, 90 Hz, 330 Hz, and 425 Hz are, respectively, 49.4 dB, 86.6 dB, 32.8 dB, and 18.8 dB indicating that all the disturbance components are reduced by significant levels and that the frequency components close to the panel mode resonances are controlled better than those close to the enclosure mode resonances. It is noted from the experimental observations (Table VI) that the (0,0,1) enclosure mode component is the dominant one among all of the components considered and hence more noise reduction is achieved for this component. Noise reduction is also achieved for the other components. However, the noise reduction values for the (2,1) and (1,2) panel mode components and (1,0,1) enclosure mode components are, respectively, 0.15 dB, 0.66 dB, and 15.57 dB indicating that enclosure mode components are controlled better than the panel mode components, in contrast to the simulation results. The qualitative trends in the voltage inputs in both the simulations and the experiments are found to be comparable, although higher magnitudes of voltage inputs are observed in the simulations.

TABLE III. Experimental results: Mic. 1 SPL and actuator voltage inputs.

		IIR, 60 wts.		Actuator voltage	
Frequency (Hz)	No control dB	Control dB	NR dB	Pair 1 volts	Pair 2 volts
50	61.19	62.25	−1.06		
70	78.56	53.96	24.6	0.23	95.52
90	71.03	63.49	7.54	0.14	35.6

V. CONCLUDING REMARKS

Analytical and experimental investigations into interior acoustics control of multiple tones are conducted with a control scheme based on using multiple piezoelectric actuators and different combinations of acoustic and/or vibration error sensors. The multiple tones in the disturbance have been chosen to correspond to panel and/or enclosure resonances. In the experiments conducted thus far, it is observed that local noise reductions up to 28 dB are obtained when acoustic sensors are used. To understand the observed trends in the

TABLE V. Numerical results: Mic. 1 SPL and actuator voltage inputs.

		IIR, 30 wts.		Actuator voltage	
Frequency (Hz)	No control dB	Control dB	NR dB	Pair 1 volts	Pair 2 volts
70	98.01	48.64	49.37	10.5	21.1
90	89.03	2.45	86.58	3.8	7.6
330	113.84	81.02	32.82	47.8	96.0
425	44.89	26.14	18.75	0.01	0.02

TABLE VI. Experimental results: Mic. 1 SPL and actuator voltage inputs.

		IIR, 60 wts.		Actuator voltage	
Frequency (Hz)	No control dB	Control dB	NR dB	Pair 1 volts	Pair 2 volts
50	59.27	57.02	2.25		
70	73.2	73.05	0.15	0.073	10.91
90	65.36	64.7	0.66	0.045	3.82
339	90.06	67.35	22.71	0.90	29.2
432	72.48	56.92	15.57	0.14	0.95

experimental results for different actuator and sensor combinations, an analytical formulation based on a state-space model is developed. This model, which accommodates structural-acoustic coupling, is utilized for local vibration control on an enclosure boundary and/or local noise control inside the enclosure. A numerical tool is also presented for the implementation of the analytical model for deterministic bandlimited disturbances comprising multiple panel and/or enclosure resonance frequencies. It is noted from both numerical simulations and experimental observations that the convergence coefficient in the chosen adaptive filter scheme had to be decreased over time in order to avoid large fluctuations in the voltage inputs into the actuator pairs and ensure convergence of the performance function value. Furthermore, it is also noted that there is an optimal range of filter coefficients beyond which higher noise reduction may not be achieved when higher number of filter coefficients are used in the considered control filters. Good comparisons between the numerical and experimental results indicate that the analytical formulation presented can be useful for examining transient and steady-state system dynamics during active control of multiple tones inside an enclosure. For example, the state-space formulation and the accompanying numerical simulations can in particular be useful for examining how the convergence coefficient in an adaptive scheme needs to be changed for a given structural-acoustic system. However, the present model needs to be refined and extended further. For active control of multiple tones in an enclosure, some issues that will need further consideration include the following: (a) overparametrization in control filters, (b) energy spillover into lower and higher frequencies, (c) actuator and sensor locations, (d) stability of chosen digital filter scheme, and (e) nonlinear behavior of actuators. It is believed that the current work can serve as a good starting point to address these issues.

ACKNOWLEDGMENTS

The authors are grateful for the support received from the U.S. Army Research Office (ARO) under Contract Nos. DAAL 0392G0121 and DAAH 049610334, and from Scientific Systems, Inc. (SSCI), Woburn, MA. Dr. Gary Anderson and Dr. Tom Doligalski are the technical monitors for the ARO contracts. Dr. Raman Mehra is the technical monitor for the SSCI contract. The reviewers are thanked for providing many constructive suggestions.

[1] B. Balachandran and A. Sampath, ''Active interior noise control studies,'' Presented at the American Helicopter Society National Technical Specialists' Meeting on Rotorcraft Structures, Williamsburg, VA, Oct. 31–Nov. 2, 1995.

[2] H. C. Lester and R. J. Silcox, ''Active control of interior noise in a large scale cylinder using piezoelectric actuators,'' NASA/SAE/DLR 4th Aircraft Interior Noise Workshop, Germany, May 1992.

[3] B. Balachandran, A. Sampath, and J. Park, ''Active control of noise in a three-dimensional enclosure,'' Smart Mater. Struct. **5**, 89–97 (1996).

[4] R. J. Silcox, C. R. Fuller, and R. A. Burdisso, ''Concepts on an integrated design approach to the active control of structurally radiated noise,'' Trans. ASME, J. Vib. Acoust. **117**, 261–270 (1995).

[5] A. Sampath and B. Balachandran, ''Studies on performance functions for interior noise control,'' Smart Mater. Struct. **6**, 315–332 (1997).

[6] C. R. Fuller, C. H. Hansen, and S. D. Snyder, ''Experiments on active control of sound radiation from a panel using a piezoceramic actuator,'' J. Sound Vib. **150**, 179–190 (1991).

[7] R. L. Clark and C. R. Fuller, ''Experiments on active control of structurally radiated sound using multiple piezoceramic actuators,'' J. Acoust. Soc. Am. **91**, 3313–3320 (1992).

[8] Y. Gu and C. R. Fuller, ''Active control of sound radiation from a fluid-loaded rectangular uniform plate,'' J. Acoust. Soc. Am. **93**, 337–345 (1993).

[9] E. J. J. Doppenberg and P. H. J. Koers, ''Active noise control of quasi-periodic noise in an enclosure using on-line identification,'' Proceedings of the ASME Winter Annual Meeting, Anaheim, California, DSC, Vol. 38, pp. 1–5, Nov. 8–13, 1992.

[10] R. H. Cabell, H. C. Lester, G. P. Mathur, and B. N. Tran, ''Optimization of actuator arrays for aircraft interior noise control,'' 15th AIAA Aeroacoustics Conference, Long Beach, CA, Paper No. 93-4447, October 25–27, 1993.

[11] A. Sampath and B. Balachandran, ''Active structural acoustic control of bandlimited disturbances,'' Proceedings of the SPIE 1996 North American Conference on Smart Structures and Materials, San Diego, CA, Feb. 26–29, Vol. 2717, pp. 422–433, 1996.

[12] A. Sampath and B. Balachandran, ''Active control of transmission of bandlimited disturbances into a three-dimensional enclosure,'' presented at the Proceedings of the ASME International Congress and Exposition, Atlanta, GA, Nov. 17–22, 1996.

[13] S. Koshigoe, A. Teagle, and A. Gordon, ''A time domain study of active control of sound transmission due to acoustic pulse excitation,'' J. Acoust. Soc. Am. **97**, 313–323 (1995).

[14] H. T. Banks and R. C. Smith, ''Active control of acoustic pressure fields using smart material technologies,'' NASA ICASE Report No. 93-31, 1993.

[15] Z. Wu, V. K. Varadan, and V. V. Varadan, ''Active absorption of acoustic waves using state-space model and optimal control theory,'' J. Acoust. Soc. Am. **97**, 1078–1087 (1995).

[16] W. T. Baumann, F.-S. Ho, and H. H. Robertshaw, ''Active structural acoustic control of broadband disturbances,'' J. Acoust. Soc. Am. **92**, 1998–2005 (1992).

[17] L. J. Eriksson, ''Development of the filtered-U algorithm for active noise control,'' J. Acoust. Soc. Am. **89**, 257–265 (1991).

[18] AMP, Incorporated, 1995, *Piezo Film Sensors and Product Guide*, Valley Forge, PA.

[19] B. J. Widrow and S. D. Stearns, *Adaptive Signal Processing* (Prentice-Hall, Englewood Cliffs, NJ, 1985).

[20] P. A. Nelson and S. J. Elliott, *Active Control of Sound* (Academic, New York, 1994).

[21] S. D. Snyder and G. Vokalek, *EZ-ANC User's Guide, Active Noise Control Development System*, Causal Systems, Adelaide, Australia, 1994.

[22] S. J. Elliott, I. A. Stothers, and P. A. Nelson, ''A Multiple error LMS algorithm and its application to the active control of sound and vibration,'' IEEE Trans. Acoust., Speech, Signal Process. **ASSP-35**, 1423–1434 (1987).

[23] P. M. Morse and K. U. Ingard, *Theoretical Acoustics* (McGraw-Hill, New York, 1968).

[24] A. D. Pierce, *Acoustics, An Introduction to its Physical Principles and Applications* (McGraw-Hill, New York, 1981).

[25] S. Koshigoe and J. W. Murdock, ''A unified analysis of both active and passive damping for a plate with piezoelectric transducers,'' J. Acoust. Soc. Am. **93**, 346–355 (1993).

[26] A. Sampath, ''Schemes for noise control in three-dimensional enclosures,'' Ph.D. Dissertation, Mechanical Engineering, University of Maryland, College Park, 1997.
[27] R. D. Blevins, *Formulas for Natural Frequency and Modeshape* (Van Nostrand Reinhold, New York, 1979).
[28] *Simulink, User's Guide* (The Math Works, Inc., MA, 1996).
[29] S. Sastry and M. Bodson, *Adaptive Control: Stability, Convergence, and Robustness* (Prentice–Hall, New Jersey, 1989).

Low frequency passive noise control of a piston structure with a weak radiating cell

Bradley W. Ross and Ricardo A. Burdisso
Vibration and Acoustic Laboratories, Department of Mechanical Engineering, Virginia Polytechnic Institute and State University, Blacksburg, Virginia 24061-0238

(Received 15 April 1998; accepted for publication 31 March 1999)

The concept of a weak sound radiating cell is proposed to reduce the low-frequency radiated noise from structures. The cell consists of two mechanically coupled surfaces such that, when placed on a vibrating structure, the response of the two surfaces are nearly out-of-phase and nearly of the same strength over a wide frequency range. This structure response leads the cell to behave as an acoustic dipole and thus a poor sound-radiating source. The control of low-frequency structurally radiated noise is then achieved by covering the structure with an array of these weak radiating cells, i.e., surface treatment. Thus the surface treatment essentially transforms the response of the structure to that of a distributed array of dipoles yielding a low sound radiating structure. A theoretical model of a single weak radiating cell applied to a simple piston structure was developed and experimental verification was performed. Overall sound power level reductions of over 6 dB were experimentally achieved between 400 and 1600 Hz with maximum reductions of over 30 dB at discrete frequencies.
 [S0001-4966(99)02007-X]

PACS numbers: 43.50.Sr, 43.55.Fw [PJR]

INTRODUCTION

The cancellation of sound has become a major point of interest as a result of stiffened federal regulations and increased consumers' desires for a quieter product. In the past this has led to extensive research to gain a better understanding of the acoustic behavior of structures such as helicopters,[1] airplanes,[2] and power transformers.[3] The attenuation of structurally radiated noise, in particular at low frequencies, from these and other systems has been intensively pursued. Traditional methods of noise control include applying passive treatments to the radiating structures such as structural damping and sound absorptive materials. However, absorptive materials in particular are not a practical means of attenuation at low frequencies because of the thickness requirement to absorb the large acoustic wavelengths. In light of this, researchers have investigated alternate passive control techniques designed to reduce the low-frequency sound radiation from structures. Attempts have been made to increase the transmission loss of panels by embedding arrays of acoustic resonators.[4,5] The placement of optimally sized masses on a structure for modal restructuring has also been investigated.[6] For almost a century now, passive tuned vibration absorbers (TVAs) have been investigated to impede tonal and broadband motion of a structure.[7]

Recently, active control has emerged as a viable technology to solve the problem of low-frequency noise radiated from structures.[8] This has allowed for the traditional tuned vibration absorber technology to be extended to hybrid absorbers, e.g., combination of passive and active methods.[9,10] The use of active control has also resulted in the concept of hybrid and active skins for radiating structures.[11,12]

More relevant to the research in this paper, recent work on active control has revealed that partitioning a structure or panel into individually actuated subpanels that cancel the local volume velocity is an effective approach for low-frequency sound reduction.[13–17] The active volume velocity control approach uses actuators to reduce either the vibration of the subpanel or its radiation efficiency, e.g., modifying the response of the subpanel from a monopole to a dipole acoustic source. For example, in work performed by St. Pierre *et al.*, a loudspeaker is embedded into a vibrating panel and used to control the sound radiated by minimizing the volume velocity.[13] The panel and loudspeaker make up the components of the actively created dipole source. Unfortunately, the complexity, power requirement, additional weight, unreliability, and high cost of active control systems have significantly limited their practical application to realistic systems.

Here the concept of a weak radiating cell as a new low-frequency *passive* noise control device is presented. The cell consists of two mechanically coupled surfaces such that, when placed on a vibrating structure, the responses of the two surfaces are nearly out-of-phase and nearly of the same strength over a wide frequency range; i.e., acoustic dipole. The uniqueness of the proposed concept lies in the fact that the cell converts the motion of the vibrating structure into an inefficient radiating acoustic dipole source without the adverse effects introduced by active control. The control of low-frequency structurally radiated noise is then achieved by covering the structure with an array of these weak radiating cells, i.e., surface treatment. Thus the surface treatment essentially transforms the response of the structure to that of a distributed array of dipoles yielding a low sound radiating structure. A theoretical model of a single weak radiating cell applied to a simple piston-type structure is developed and verified analytically and experimentally.

I. THEORY OF A WEAK RADIATING CELL

At frequencies for which the acoustic wavelength exceeds the dimensions of a source, the volume velocity of the source essentially determines the radiated power. If the vol-

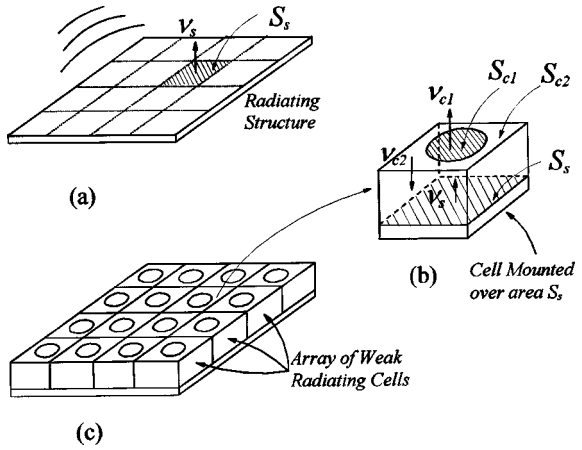

FIG. 1. Attenuation of structurally radiated sound using weak radiating cell concept: (a) untreated plate, (b) single cell, and (c) plate with array of cells.

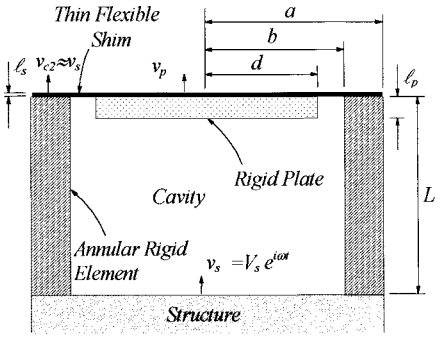

FIG. 2. Weak radiating cell implementation.

ume velocity of the source is nearly zero, such as in a dipole, the radiated power is consequently minimized.[18] Thus an efficient method to reduce the sound radiation from a structure would be to partition the surface of the structure into small sectors, each of which would independently respond as a dipole with zero volume velocity. To this end, the concept of a weak sound radiating cell is introduced to reduce the low-frequency radiated noise from structures.

The weak radiating cell consists of two mechanically coupled surfaces such that, when placed on a vibrating structure, the responses of the two surfaces are nearly out-of-phase and of nearly the same strength over a wide frequency range. This leads the two surfaces to behave as an acoustic dipole and thus as a poor sound radiating source. Figure 1 illustrates the concept. A structure radiates sound into the surrounding fluid as shown in Fig. 1(a). The sound power radiated by a small area, S_s, with dimensions smaller than the acoustic wavelength, is determined by its volume velocity $Q_s = v_s S_s$, where v_s is the average velocity over the small area. At low frequencies, the velocity of the area is nearly uniform and the area behaves as a monopole. Note that the total radiated power from the plate is due to the contribution of all the areas of the structure including their far-field coupling. Figure 1(b) illustrates a weak radiating cell covering the surface S_s. The concept of the weak radiating cell is to convert the motion of the small area from that of a monopole into a dipole source. To this end, the motion of the nearly uniform velocity v_s of the surface S_s is transformed into the motion of the two surfaces S_{c1} and S_{c2} with velocities v_{c1} and v_{c2}, respectively. The cell is then designed such that the motion of these two surfaces are out-of-phase and of relative magnitude that leads to $v_{c1}S_{c1} + v_{c2}S_{c2} \cong 0$. Conceptually, by covering the structural surface with an array of cells as shown in Fig. 1(c), the response of the structure is converted to that of an array of dipoles, thus leading to an essentially zero volume velocity structural source and minimum sound radiation. It is important to reiterate that researchers have proposed active control methods to minimize the volume velocity of small panels.[13–17] This purely active approach can have significant drawbacks that could limit its applicability in real systems. A more efficient method would be to first obtain volume velocity cancellation passively, as proposed in this work, and then implement active control to further enhance the performance of the system if so desired. The hybrid approach is a matter of current research and will be reported in the near future.

An implementation of the weak radiating cell concept is illustrated in Fig. 2. Without loss of generality and for the sake of clarity in the presentation, the small area S_s of the radiating structure is assumed to be a circular piston with uniform velocity, v_s. Hence for geometric consistency, the cell will also adhere to a circular configuration. Thus Fig. 2 shows a diametrical cross-section of the cell. The cell consists of a rigid annular element of area, S_{c2}, which is mounted to the radiating structure surface. Because this element is assumed to be very stiff, the velocity of the surface S_{c2} is assumed to be same as the velocity of the structure, $v_{c2} \cong v_s$. The second radiating surface of the cell, S_{c1}, is obtained by attaching a rigid plate to the rigid element through a thin flexible shim which in turn creates a sealed cavity. The shim allows for stiffness in the radial direction with compliance in the axial direction. The mechanical behavior of the cell can be depicted as a single degree of freedom lumped parameter system v_p, i.e., motion of the rigid plate, with a base input v_s. Assuming harmonic input $v_s = V_s e^{i\omega t}$, the response of the system $v_p = V_p e^{i\omega t}$ is given as[19]

$$\left[c_m + i\left(\omega m_p - \frac{k}{\omega}\right)\right] V_p = \left(c_m - i\frac{k}{\omega}\right) V_s, \tag{1}$$

where m_p is the system mass which includes both the mass of the rigid plate and the equivalent mass of the shim, c_m is the shim damping, k is the total stiffness of the system $k_m + k_f = k$ with k_m being the shim's mechanical stiffness and k_f the stiffness due to the compressibility of the fluid in the cavity, and V_p and V_s are the complex velocity of the rigid plate and piston, respectively.

The complex source strengths for the original piston structure and the weak radiating cell can be obtained by integrating the surface velocity. The complex source strength of the original piston structure is simply $Q_s = S_s V_s$. The source strength of the cell is computed by integrating[18]

$$Q_c = \int_0^a V(r) 2\pi r \, dr, \tag{2}$$

where the radial complex velocity distribution $V(r)$ of the cell is defined as

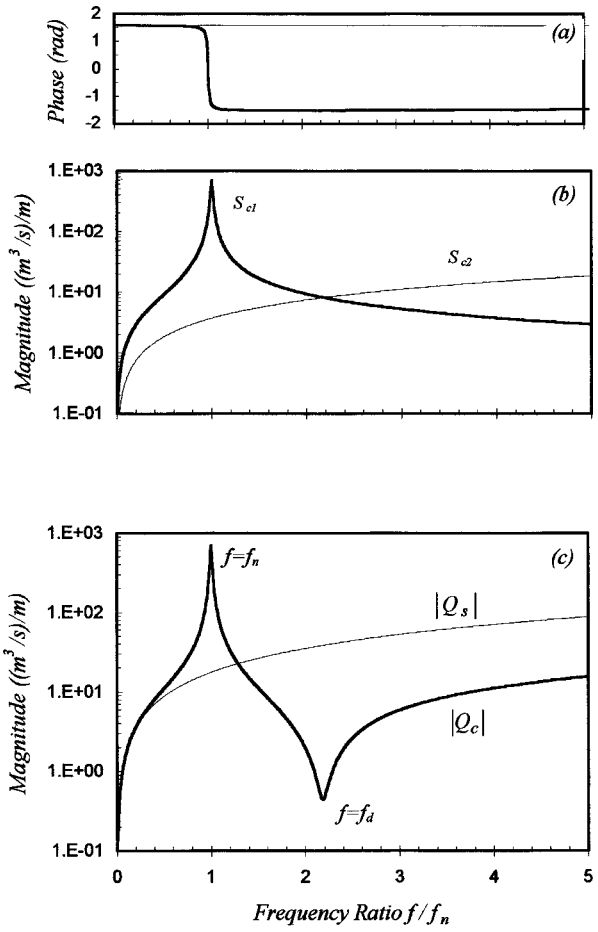

FIG. 3. Phase (a) and magnitude (b) of the source strength of surfaces S_{c1} and S_{c2}, and magnitude (c) of source strength of weak radiating cell $|Q_c|$ and original structure $|Q_s|$.

$$V(r) = \begin{cases} V_p = \dfrac{c_m + k/i\omega}{i\omega m_p + c_m + k/i\omega}, & 0 \leqslant r \leqslant d \\ V_h(r) = \dfrac{V_p + V_s}{2} + \cos\left(\dfrac{\pi r}{b-c}\right) \cdot \dfrac{V_p - V_s}{2}, & d < r < b \\ V_s, \quad b \leqslant r \leqslant a, \end{cases} \tag{3}$$

which implies that the velocity profile of the shim is assumed to simulate a cosine function which varies V_p at $r=d$ to V_s at $r=b$, where r is the radius from the center of the cell.

At low frequency where the acoustic wavelength λ is much larger than the source dimension (i.e., $\lambda \gg a$), the acoustic power can be computed from the source strength as[18]

$$W = \frac{\alpha}{2}\pi\rho c\left(\frac{|Q|}{\lambda}\right)^2, \quad \lambda \gg a, \tag{4}$$

where $\alpha=1$ for a free-field source and 2 for a baffled source, ρ is the fluid density, c is the speed of sound, and λ is the acoustic wavelength.

For the sake of describing the general acoustic behavior of the cell, the magnitude and phase of the source strength of the two surfaces forming the cell are plotted in Figs. 3(a) and 3(b). Moreover, the magnitudes of the source strength of both the cell and piston structure are shown in Fig. 3(c). These responses are plotted as a function of frequency normalized by the natural frequency of the plate–shim–cavity system, $f_n = 1/2\pi\sqrt{k/m_p}$. The sound power level reduction achieved by the cell as compared to the original piston is plotted in Fig. 4, again as a function of the normalized frequency. From Figs. 3(a) and 3(b), the general response of the cell can be described for the following frequency regions: below, around, and above the resonance of the plate–shim–cavity system. It can be seen in Fig. 3(a) that, below the natural frequency of the system, the motion of the two surfaces is in phase and the sound radiated by the two surfaces adds to obtain the net radiation of the cell. At frequencies well below resonance, $f/f_n \leqslant 0.4$, the velocities of the two surfaces are nearly the same, and thus the cell radiates the same acoustic power as the original structure, and thus no power reduction is observed as seen in Fig. 4. When the frequency is around resonance, the plate response greatly exceeds that of the piston due to dynamic amplification, and the relative phase goes through a 180° variation. The plate motion completely dominates the system response, resulting in an overall increase in the sound radiation from the structure. Above resonance, the motion of the two surfaces is out-of-phase and the radiation from the surfaces subtracts producing sound power reduction (see Fig. 4). Selecting proper areas will minimize the source strength of the resulting cell over a wide frequency range leading to the consequent sound reduction. From Figs. 3 and 4, it is clear that there is a frequency where the volume velocity Q_c is a minimum and thus the sound reduction a maximum. Note that the volume velocity does not vanish at this frequency because the damping of the system does not result in a perfect out-of-phase motion of the two cells' surfaces, i.e., the weak radiating cell behaves as a nearly perfect dipole. This frequency is referred as the cell's dipole frequency, f_d. To achieve optimal reduction in practice, the resonance of the system should then be placed below the frequency range of desired reduction and the dipole frequency where maximum sound reduction is desired. The control of tonal noise from transformers is a typical example where the cell should be designed so that the dipole frequency is tuned to the fre-

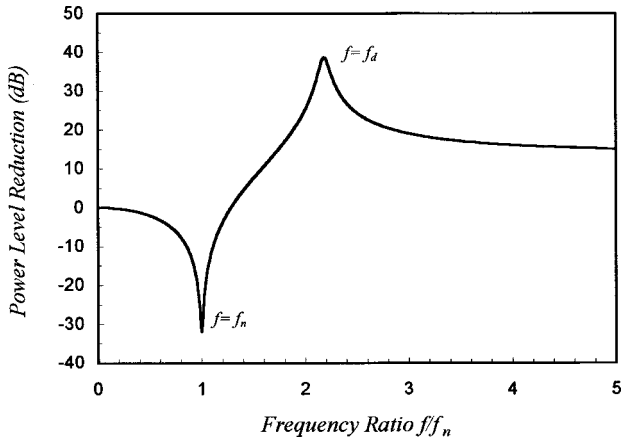

FIG. 4. Sound power level reduction achieved by the cell.

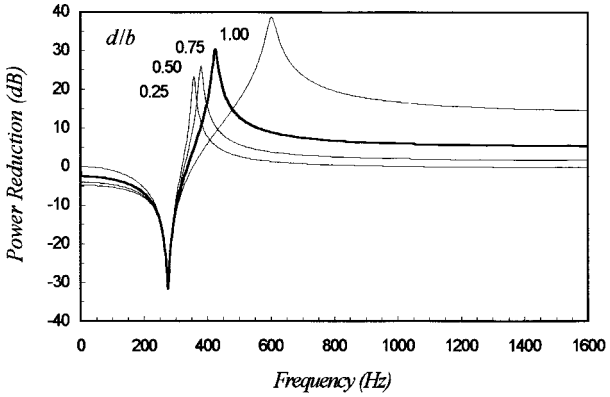

FIG. 5. Parametric study on d/b ratio.

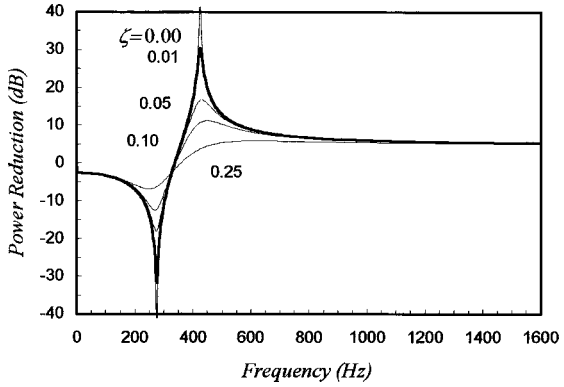

FIG. 7. Parametric study on damping ratio, ζ.

quency of the transformer noise tine, e.g., first harmonic of the line frequency (120 Hz). In Fig. 4, the increase in the sound power level is visualized at the resonance frequency, but more importantly, notice the region of maximum reduction around the dipole frequency where the source strength is minimized, i.e., a nearly perfect dipole is created with 38 dB of power reduction.

II. PARAMETRIC STUDY

The simplified model developed and properties used in the previous section served the purpose of introducing the concept of the weak radiating cell as well as to gain some insight into the behavior of the cell. In this section, parameters from realistic engineering materials will be used to study the system response and performance to assess the practicality of the concept. In addition, the influence on the cell performance to parameter variations will also be investigated. Here, the goal of the weak radiating cell is to reduce the sound radiation at frequencies below 1600 Hz, and thus the cell is designed to this end.

Referring to Fig. 2, the rigid element is assumed here to be built from epoxy foam, commercially known as structural foam used in the automotive industry.[20] The advantage of this material is its high modulus of elasticity ($E=642\times10^6$ Pa) and low density ($\rho=0.48$ g/cm^3) which is useful to minimize the overall weight of the cell which is a critical goal in some applications such as in aircraft interior noise. The dimensions of the rigid element are piston radius $a=57$ mm, cavity radius $b=51$ mm, and cavity height $L=51$ mm.

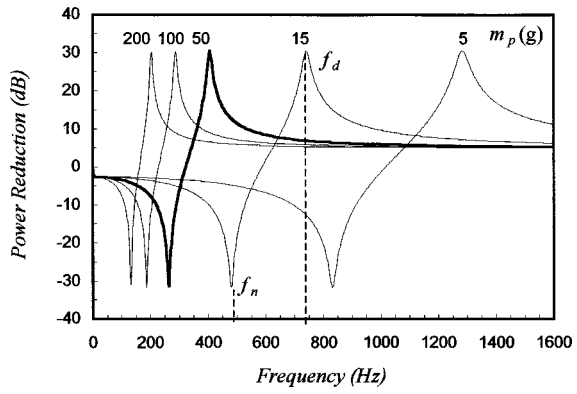

FIG. 6. Parametric study on system resonance, f_n.

The fundamental axial resonance of the rigid element was computed to be 3623 Hz, which implies that this element behaves as rigid below 1600 Hz.[21] The circular center plate forms the second surface. This plate should have the necessary mass for the desired dynamics of the cell and sufficient bending stiffness to essentially behave as a rigid plate in the frequency region of interest. Although a number of materials can be used, this plate is assumed here to be made of Plexiglas (modulus of elasticity $E=2758$ Mpa, Poisson's ratio $\sigma=0.4$, and density $\rho=1300$ kg/m^3) with a thickness of $l_p=6.4$ mm and a radius of $d=38$ mm. With these parameters, the fundamental bending plate resonance is 8811 Hz, which is again outside the frequency range of interest.[21] The flexible shim that attaches the center plate to the rigid element should be designed to be flexible in the vertical direction while providing some degree of stiffness in the plane normal to the intended motion. Here it is assumed that the shim is constructed of brass (modulus of elasticity $E=104$ GPa, density $\rho=8500$ kg/m^3, and loss factor $\eta=0.01$) with a uniform thickness of $l_s=0.2$ mm and radius a.

The stiffness of the system has two components. Assuming clamped boundary conditions, the stiffness of the annular shim can be computed from the work by Leissa.[22] In addition, the stiffness due to the fluid in the cavity is computed from the internal acoustic pressure. Assuming the fluid in the cavity is inviscid and the acoustic process is adiabatic, the stiffness due to the fluid in the cavity is given as[18]

$$k_f=\frac{c^2\rho S_{c1}^2}{V_0}, \tag{5}$$

where $\rho=1.21$ kg/m^3 is the fluid density assumed to be air, and $c=343$ m/s is the speed of sound, and V_0 is the initial volume of the cavity.

Using the above materials and dimensions, the overall mass of the cell is 108 g. The sound power level reduction of this baseline cell is plotted in Figs. 5–7 as a thick line. From these figures, the resonance frequency of the cell is $f_n=276$ Hz while the dipole frequency is $f_d=426$ Hz. Above the resonance of the cell, reduction is achieved starting at 338 Hz and then throughout the frequency band.

The first parameter investigated is the area ratio of the two radiating surfaces. This can be achieved by changing the ratio of the inner, d, to outer, b, diameter of the shim. It is assumed that the mass of the center plate does not change

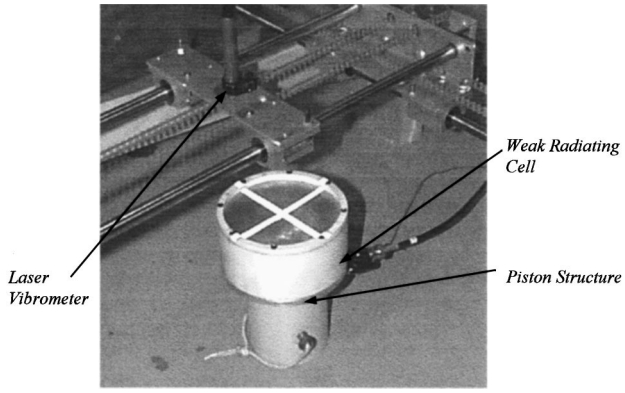

FIG. 8. Single weak radiating cell on a piston structure.

while the thickness of the shim is adjusted to keep the same natural frequency of the system. Figure 5 reveals that both the dipole frequency and the maximum reduction are sensitive to the area ratio which increases with the ratio d/b.

The next parameter to be investigated is the system resonance frequency. This can be altered by changing either the thickness or density of the plate to affect the mass and/or by changing the shim thickness to modify the stiffness. In this study, the shim thickness was held constant while the mass was changed. The resulting sound power reductions are shown in Fig. 6. As expected, the dipole frequency of maximum reduction occurs at lower frequencies as the mass is increased. However, the maximum level of power reduction is insensitive to the mass. Another interesting factor is the ratio of the dipole to the natural frequencies which decreases with the natural frequency of the system. Since it is important to minimize the overall weight of the cell for some applications, the mass should be minimized. This implies a minimization of the stiffness to yield a predetermined resonance frequency. The lowest stiffness is bounded by the size of the air cavity assuming a negligible contribution from the shim. For further reduction in the weight, the height of the cavity can be decreased. However, this increases the cavity stiffness. Note that as the size of the cell is proportionally reduced, the stiffness due to the fluid decreases in the same proportion as the cell size.

One approach to alleviate the increase in the radiated power at frequencies near the resonance is by introducing damping. Thus the effect of the shim-damping ratio on the system response is examined and shown in Fig. 7. As expected, increasing the energy dissipation leads to a reduction of the response at resonance. However, it also decreases the maximum sound reduction because it affects the relative phase between the motion of the two surfaces, i.e., the two surfaces are less out-of-phase as the damping increases. Consequently, there is a sound reduction trade off to introducing damping into the system.

III. EXPERIMENTAL VALIDATION

To verify the theoretical concept of a weak radiating cell, a cell was experimentally tested. The cell used for experimental verification possessed the dimensions and physical properties of the baseline cell analyzed in the numerical section, which is pictures in Fig. 8. The center mass was

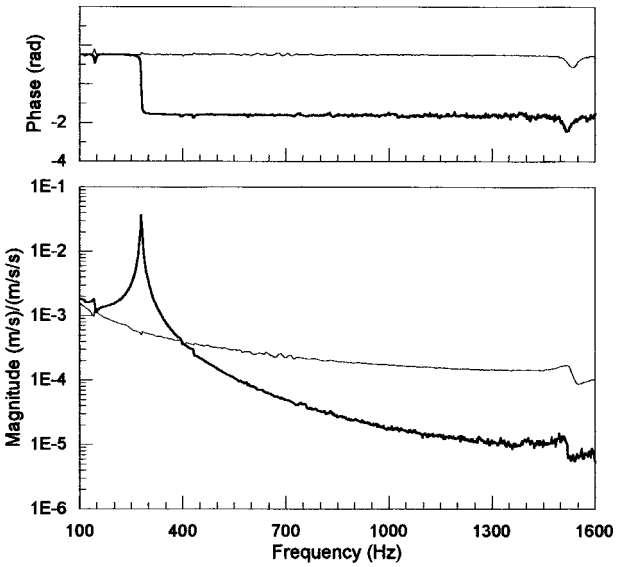

FIG. 9. Velocity response of inner (—) and outer (—) surfaces of weak radiating cell.

epoxied to the brass shim which was clamped to the rigid element using a thin ring of PVC and machine screws. The cell was then screwed to a rigid circular aluminum plate to ensure a tightly sealed cavity. The aluminum plate was mounted to a shaker and driven with white noise from 0 to 1600 Hz. An accelerometer was positioned on the bottom side of the piston. The acceleration of the piston structure was used to normalize all the experimental data. The untreated piston structure, i.e., aluminum plate, is again used as a basis for the performance of the weak radiating cell. Both laser vibrometer scan and acoustic pressure measurements were taken to assess to dynamics and acoustic performance of the cell.

First, a laser vibrometer mounted to an automated traverse was utilized to scan the surface of the untreated piston and cell, which facilitated modal and source strength analysis (see Fig. 8). The velocity response, normalized by the piston acceleration, of both the inner plate and of the outer annular ring are presented in Fig. 9. The fundamental resonance of the cell occurs at 282 Hz where the phase goes through a 180° variation. The mode shape is visualized in Fig. 10, which was obtained from a velocity scan across the surface of the cell. In this figure, the dashed lines indicate the location of the shim, i.e., $r=\mp b$ and $r=\mp d$. The second mode of the cell is a rocking motion that is not excited by the

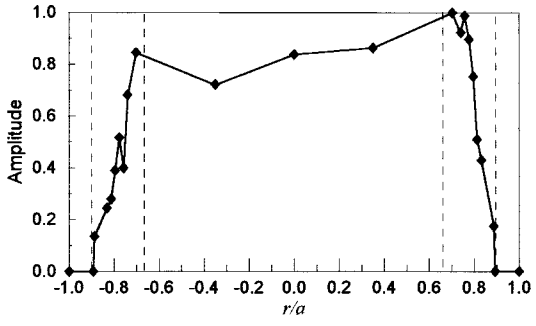

FIG. 10. Velocity profile across cell surface at 282 Hz.

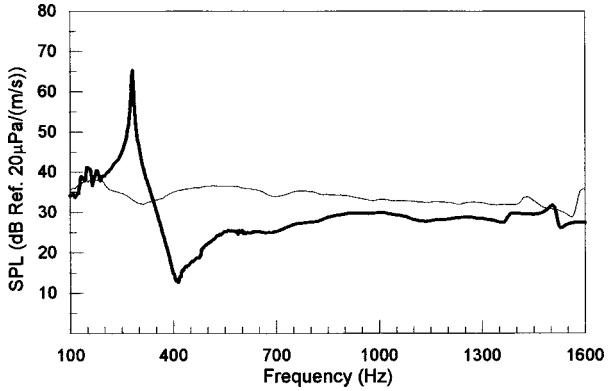

FIG. 11. Experimentally measured sound pressure levels due to piston (—) and cell (—).

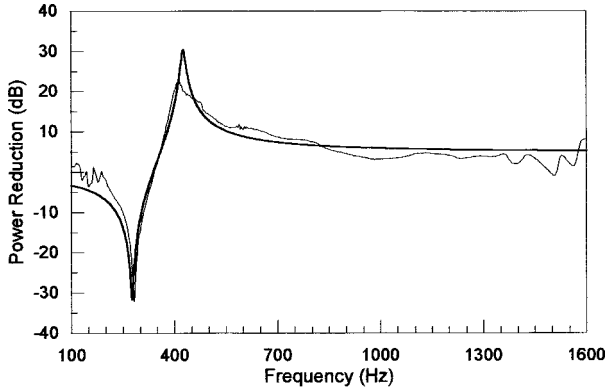

FIG. 12. Experimental (—) and analytical (—) sound power level reduction.

uniform motion of the piston. It is important to remark that the presence of the rocking mode does not affect the system since it is itself a dipole source. The velocity response of the outer annular ring in Fig. 9 also shows that this element behaves as a rigid element in the frequency range 0–1600 Hz.

The second set of tests performed was pressure measurements. Both the original piston and the weak radiating cell were placed on a baffle such that both the cell and piston surfaces were flush to the baffle during their respective test cases. These experiments were performed in an anechoic chamber with a cutoff frequency of 250 Hz. The sound radiation was then monitored with a microphone positioned 75 cm above the center of the systems. The sound pressure levels for each case are given in Fig. 11, which shows that the dipole effect of the cell produces a significant decrease in the pressure level above the resonance of the cell at the dipole frequency which occurs at 414 Hz.

Since in the 0–1600 Hz frequency range of concern the acoustic wavelength is larger than the cell's dimension, the piston and cell are assumed to radiate as baffled simple sources. The acoustic power can then be computed using the pressure data as follows:[18]

$$W=\frac{2\alpha\pi R^2P^2}{\rho c}, \quad \lambda \gg a, \tag{6}$$

where R is the distance to the microphone from the source and P is the pressure amplitude. The sound power level reduction computed from the pressure data is plotted in Fig. 12. There is an increase in the radiated power around the resonance of the cell. However, significant reduction levels are achieved throughout the frequency range above resonance, i.e., $f \geqslant 342$ Hz, with a maximum reduction of 22.9 dB at the dipole frequency $f_d = 414$ Hz, i.e., the region of maximum reduction is where a nearly perfect dipole acoustic source is created. For comparison purposes, the analytically predicted sound power reduction is also plotted in Fig. 12, which shows very good agreement with the experimental results. A summary between experimental and analytical results is tabulated in Table I. The experimental values in this table were obtained from the experimental pressure data. Included in the table are the system resonance frequency, dipole frequency, and the sound power level reduction at the dipole frequency and in the frequency ranges 100–1600 Hz and 400–1600 Hz. The 400–1600 Hz bandwidth is an important frequency range since both the theoretical model and experimental verification produces power reduction throughout this range. The resonance frequencies and overall power level reductions match very closely. The only discrepancy between the analytical and experimental values is in the reduction at the dipole frequency.

IV. CONCLUSIONS

The concept of a weak radiating cell as a low-frequency passive control device for radiating structures has been introduced. In general, the concept converts the motion of a structure, assumed to radiate as a monopole, into an acoustic dipole source by creating two surfaces whose response is out-of-phase and of nearly equal magnitude. Conceptually, applying an array of weak radiating cells to small partitions on a larger structure will create an array of distributed dipoles, thus minimizing the radiated sound from the structure. An analytical model was developed to predict the response and performance of a weak radiating cell applied to a simple piston structure. The reduction in sound power level between the piston and the piston with a cell applied was used to evaluate its performance. An overall power reduction of 6.7 dB between 400 and 1600 Hz was predicted with a maximum reduction of over 30 dB at the dipole frequency. A parametric study on the area ratio, system resonance frequency, and shim-damping ratio revealed important information for the optimum design of the cell.

Experiments to validate the concept of a weak radiating cell on a simple piston structure were performed. Pressure data were taken on a baffled weak radiating cell in an anechoic chamber while a laser vibrometer scan of the cell

TABLE I. Comparison of experimental and analytical results.

Variable	Experimental	Analytical
Resonance frequency, f_n	282 Hz	276 Hz
Dipole frequency, f_d	414 Hz	426 Hz
Sound power reduction at f_d	22.9 dB	30.3 dB
Sound power reduction L_{wt} (100–1600 Hz)	−8.1 dB	−9.5 dB
Sound power reduction L_{wt} (400–1600 Hz)	6.2 dB	6.7 dB

surface allowed for modal and source strength analysis. An overall sound power level reduction of 6.2 dB was achieved between 400 and 1600 Hz with a maximum reduction of over 22 dB at the dipole frequency. These results closely match theoretical predictions and validate the potential of the weak radiating cell concept.

[1] B. S. Murray and J. F. Wilby, ''Helicopter Cabin Noise—Methods of Source and Path Identification and Characterization,'' Proceedings of an International Specialist Symposium held at NASA Langley Research Center, Hampton, VA, May 22–24, 1978, NASA Conference Publication 2052 (1978).

[2] J. F. Wilby, ''Aircraft interior noise,'' J. Sound Vib. **190**, 545–564 (1996).

[3] K. Brungardt, J. Vierengel, and K. Wiessman, ''Active Structural Acoustic Control of Noise from Power Transformers,'' Noise-Con '97, Pennsylvania State University, June 15–17, 1997, pp. 173–182.

[4] R. A. Prydz, L. S. Wirt, H. L. Kuntz, and L. D. Pope, ''Transmission loss of a multilayer panel with internal tuned Helmholtz resonators,'' J. Acoust. Soc. Am. **87**, 1597–1602 (1990).

[5] J. Lee and G. W. Swenson, Jr., ''Compact Sound Absorbers for Low Frequencies,'' Noise Control Eng. J. **38**, 109–117 (1992).

[6] R. L. St. Pierre, Jr. and G. H. Koopman, ''A Design Method for Minimizing the Sound Power Radiated from Plates by Adding Optimally Sized, Discrete Masses,'' Transactions of the ASME Special 50th Anniversary Design Issue, Vol. 117, pp. 243–251, June 1995.

[7] M. R. Jolly and J. Q. Sun, ''Passive tuned vibration absorbers for sound radiation reduction from vibrating panels,'' J. Sound Vib. **191**, 577–583 (1996).

[8] P. A. Nelson and S. J. Elliott, *Active Control of Sound* (Academic, San Diego, 1992).

[9] J. Aldrin, D. C. Conrad, and W. Soedel, ''Investigation of passive and adaptive dynamic absorbers applied to an automatic washer suspension design,'' Proc. SPIE **2720**, 50–61 (1996).

[10] M. A. Franchek, M. W. Ryan, and R. J. Bernard, ''Adaptive passive vibration control,'' J. Sound Vib. **189**, 565–585 (1995).

[11] S. A. Gentry, C. Guigou, and C. R. Fuller, ''Smart foam for applications in passive–active noise radiation control,'' J. Acoust. Soc. Am. **101**, 1771–1778 (1997).

[12] B. D. Johnson, ''Broadband control of plate radiation using a piezoelectric, double-amplifier active-skin,'' Master's Thesis, Virginia Polytechnic Institute and State University, 1997.

[13] R. L. St. Pierre, Jr., W. Chen, and G. H. Koopman, ''Design of Adaptive Panels with High Transmission Loss Characteristics,'' American Society of Mechanical Engineering, New York. Presented at the 1995 ASME International Mechanical Engineering Congress and Exposition, San Francisco, CA, November 12–17, 1995.

[14] K. Naghshineh and V. B. Mason, ''Reduction of sound radiated from vibrating sources via active control of local volume velocity,'' Appl. Acoust. **47**, 27–46 (1996).

[15] T. W. Leishman and J. Tichy, ''A fundamental investigation of the active control of sound transmission through segmented partition elements,'' Proceedings from Noise-Con 97 held at the Pennsylvania State University, Vol. 2, pp. 137–148, June 15–17, 1997.

[16] M. E. Johnson and S. J. Elliott, ''Active control of sound radiation using volume velocity cancellation,'' J. Acoust. Soc. Am. **98**, 2174–2186 (1995).

[17] S. J. Sharp, G. H. Koopman, and W. Chen, ''Transmission loss characteristics of an active trim panel,'' Proceedings from Noise-Con 97 held at The Pennsylvania State University, pp. 149–160, June 15–17, 1997.

[18] L. E. Kinsler, A. R. Frey, A. B. Coppens, and J. V. Sanders, *Fundamentals of Acoustics*, 3rd ed. (Wiley, Canada, 1982).

[19] W. T. Thomson, *Theory of Vibration with Applications*, 4th ed. (Prentice–Hall, New Jersey, 1993).

[20] Novacore Structural Foam Brochure, Novamax Technologies, 13650 E. 10 Mile Road, Warren, MI.

[21] B. W. Ross, ''Attenuation of structurally radiated noise with an array of weak radiating cells,'' Master's Thesis, Virginia Polytechnic Institute and State University (1997).

[22] A. Liessa, *Vibration of Plates* (Acoustical Society of America, New York, 1993), pp. 32–33.

Sound absorption of stretched ceilings with an impervious synthetic membrane

Ivan Bosmans,[a] Walter Lauriks, Geert Lombaert, Joris Mermans, and Gerrit Vermeir
Laboratorium voor Akoestiek en Thermische Fysica, Katholieke Universiteit Leuven, Celestijnenlaan 200D, B-3001 Heverlee, Belgium

(Received 10 November 1998; revised 8 March 1999; accepted 7 April 1999)

The sound absorption of stretched ceilings consisting of an impervious PVC membrane is investigated. A theoretical model is used to predict the random incidence sound absorption, and results are compared with the results of an experimental setup in a reverberation chamber. The sound absorption coefficient is estimated using a general model for the acoustic transmission and absorption of a multi-layered structure. Measurements have been performed for several cavity depths, and for two different sound absorbing materials in the cavity. Both theory and experiment showed that the combination of the impervious foil and the cavity behaves as a resonant system. The sound absorption varies strongly with frequency and is highly dependent on the characteristics and the position of the sound absorbing material in the cavity. © *1999 Acoustical Society of America.* [S0001-4966(99)03307-X]

PACS numbers: 43.55.Ev, 43.55.Dt [JDQ]

INTRODUCTION

Stretched membrane ceilings consist of a special PVC foil which is mounted *in situ* by clamping it to a plastic frame along its perimeter. The foil is heated before mounting, and the membrane acquires its final tension after cooling. This type of ceiling is used as an alternative to common finishing techniques of ceilings. Apart from a special esthetical effect, stretched ceilings offer the possibility to hide technical appliances in the cavity and to realize an appropriate sound absorption when using perforated membranes. This paper will deal exclusively with the impervious type of membrane. It will be shown that, even with absorbing material in the cavity, the presence of the impervious foil can considerably reduce the absorption of the ceiling.

Early publications regarding membrane type absorbers dealt with the impedance of absorbing materials sealed with impervious screens.[1–3] Since the theoretical investigations were based on an approximate formulation for the sound propagation in porous media, considerable improvement in the modelization has been obtained with the use of Biot theory.[4–6] Based on this theory, the influence of an impervious screen on the impedance of an elastic porous layer has been treated by Lauriks *et al.*[7] in the context of an analytical formulation, and by Kang and Bolton[8] in the context of a finite element approach. In both studies, the large air cavity between the porous layer and the membrane, which is typical of stretched ceilings, was not included.

Recently, the acoustic characteristics of single and double leaf membranes have been investigated extensively by Sakagami *et al.*[9–13] Based on their initial work on infinite plate absorbers,[9] Sakagami *et al.*[10] derived a closed form expression for the absorption coefficient of an impervious cavity-backed membrane. In his model, absorption was taken into account by assigning an absorptivity to the surface of the membrane as well as to the back wall. This theoretical paper presented a parametric analysis which illustrated the ability of the model to optimize the design of membrane type absorbers. Takahashi *et al.*[11] studied the acoustic behavior of permeable membranes in multi-layered systems, using an approximate theory for sound propagation in porous media. His model was verified experimentally by measuring the absorption of a series of cavity-backed permeable membranes, each characterized by a different flow resistance. For the cases with cavity absorption, the authors suggested that low-frequency discrepancies between measurement and calculations were caused by disregarding the effect of skeleton vibration in the absorbing material.

In this paper, the absorption of impervious membrane systems is modeled by combining the advanced Biot theory with a general formulation of sound propagation in multi-layered media.[14] More specifically, the traditional transfer matrix approach will be extended to include the presence of an impervious membrane between two adjacent layers. The aim of this study is to assess the influence of cavity depth and cavity absorption on the acoustic performance of stretched ceilings.

I. THEORY

In the theory for multi-layered media,[14] sound propagation across a layer is described by means of transfer matrices. These matrices relate the stresses and displacements on one side of the layer to the corresponding quantities on the other side. The dimensions of these matrices depend on the number of parameters required to characterize the layer response. Sound propagation across a fluid, elastic solid, and elastic porous layer[15] is described using 2×2, 4×4, and 6×6 transfer matrices, respectively. The boundary conditions between two different layers are formulated based on so-called interfacial matrices, as reported in Ref. 14. The angle dependent sound absorption coefficient is quantified based on the im-

[a]Currently employed at National Research Council Canada, Institute for Research in Construction, Montreal Road, Ottawa, Ontario K1A 0R6, Canada.

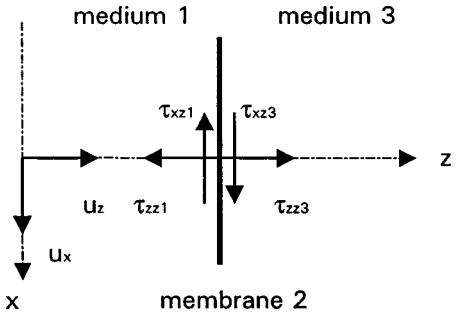

FIG. 1. Stresses and displacements at the membrane.

pedance of the multi-layered system. Finally, the random incidence absorption coefficient is obtained as:

$$\alpha_r = 2\int_0^{\theta_{\lim}} \alpha(\theta)\sin\theta\cos\theta\, d\theta, \tag{1}$$

where $\theta_{\lim}$ represents the limiting angle above which it is assumed no sound is incident on the membrane.

Since the transfer matrix approach is sufficiently documented in literature, only the modifications to the existing theory will be presented in the following paragraphs. First, the equations of motion of a thin elastic membrane will be discussed. Next, these equations will be incorporated in the transfer matrix approach by deriving new interfacial matrices for two different situations: air/membrane/air and air/membrane/porous layer. While the first case applies directly to the stretched ceilings, the second case serves as an illustration for how to deal with more complicated situations. For instance, the surface roughness of the membrane could be modeled using a very thin porous layer. However, the calculation examples and the experimental verification presented in Sec. II will deal only with the air/membrane/air configuration.

A. Equations of motion

The equations of motion of a thin elastic membrane, which is driven by a plane airborne wave incident at an angle θ with the normal to the membrane, are given by:

$$-\omega^2\left(m'' - \frac{T\sin^2\theta}{c^2}\right)u_{z2} = \tau_{zz3} - \tau_{zz1}, \tag{2}$$

$$-\omega^2\left(m'' - \frac{S\sin^2\theta}{c^2}\right)u_{x2} = \tau_{xz3} - \tau_{xz1}, \tag{3}$$

where ω is the angular frequency, c the sound speed in air, and m'' the surface density of the membrane. The parameters T and S are the membrane's tensile stress and Young's modulus, respectively, both multiplied by the thickness h of the membrane. The conventions for the displacements in the x- and z-direction, u_x and u_z, as well as the normal and shear stresses acting on the membrane, τ_{zz} and τ_{xz}, are shown in Fig. 1. The index 2 refers to the membrane, and subscripts 1 and 3 correspond to the media on both sides of the membrane. Equation (2) describes the out-of-plane response of the membrane, whereas the in-plane motion is governed by Eq. (3). The latter formula is relevant only when the membrane is in contact with a solid elastic or poro-elastic layer. In the case of an air layer, the shear stress τ_{xz} is equal to zero and the normal stress is calculated as $\tau_{zz} = -p$, where p denotes the sound pressure.

B. Interfacial matrix for two air layers separated by a membrane

The response of an air layer at the interface with the membrane is determined by the sound pressure p and the displacement normal to the membrane u_z. In the context of a transfer matrix approach, the unknown parameters of both layers can be expressed in matrix notation:

$$V_1 = [p_1 \quad u_{z1}]^T, \tag{4}$$

$$V_3 = [p_3 \quad u_{z3}]^T. \tag{5}$$

Further, the equations of motion, Eqs. (2) and (3), can be rewritten as:

$$-\omega^2\rho_1 u_{z2} = p_1 - p_3, \tag{6}$$

$$-\omega^2\rho_2 u_{x2} = 0, \tag{7}$$

where, as in the following equations, ρ_1 and ρ_2 are given as:

$$\rho_1 = m'' - \frac{T\sin^2\theta}{c^2}, \tag{8}$$

$$\rho_2 = m'' - \frac{S\sin^2\theta}{c^2}. \tag{9}$$

Finally, the continuity of the displacements of both layers and the membrane can be expressed as:

$$u_{z1} = u_{z2} = u_{z3}. \tag{10}$$

Equations (6), (7), and (10) have six unknown parameters, two unknowns of which represent the membrane displacements (u_{z2} and u_{x2}). While Eq. (7) implies that u_{x2} equals zero, u_{z2} can be eliminated by substitution of Eq. (10) into Eq. (6), leading to the following expressions:

$$\omega^2\rho_1 u_{z1} + p_1 - p_3 = 0, \tag{11}$$

$$u_{z1} - u_{z3} = 0. \tag{12}$$

Or in matrix form:

$$\left[\begin{array}{cc|cc} 1 & \rho_1\omega^2 & -1 & 0 \\ 0 & 1 & 0 & -1 \end{array}\right]\begin{bmatrix} p_1 \\ u_{z1} \\ p_3 \\ u_{z3} \end{bmatrix} = [I_{AMA}|J_{AMA}]\begin{bmatrix} V_1 \\ V_3 \end{bmatrix} = \begin{bmatrix} 0 \\ 0 \end{bmatrix}. \tag{13}$$

The resulting 2×4 interfacial matrix, which is composed of the submatrices $[I_{AMA}]$ and $[J_{AMA}]$, describes the boundary conditions for the air layers on both sides of the membrane. $[I_{AMA}]$ and $[J_{AMA}]$ contain the coefficients of the air layer in front (medium 1) and at the back (medium 3) of the membrane, respectively.

C. Interfacial matrix for an air layer and a porous layer separated by a membrane

According to the Biot theory of sound propagation through porous media,[15] the displacements and stresses at the edge of a porous layer are decomposed into contributions

from the air in the pores and from the elastic frame material. Hence, the boundary conditions between the porous layer and the membrane are written in terms of the displacement u_z^f and the normal stress τ_{zz}^f due the air, and the displacements and the stresses $(u_x^s, u_z^s, \tau_{xz}^s\ \tau_{zz}^s)$ due to the frame material. In matrix notation, the unknown quantities of the air layer in front of the membrane and the porous layer at the back are given by:

$$V_1=[p_1 \quad u_{z1}]^T, \tag{14}$$

$$V_3=[u_{x3}^s \quad u_{z3}^s \quad u_{z3}^f \quad \tau_{zz3}^s \quad \tau_{xz3}^s \quad \tau_{zz3}^f]^T. \tag{15}$$

The equations of motion, Eqs. (2) and (3), are now written as:

$$-\omega^2\rho_1 u_{z2}=p_1+\tau_{zz3}^s+\tau_{zz3}^f, \tag{16}$$

$$-\omega^2\rho_2 u_{x2}=\tau_{zx3}^s. \tag{17}$$

Finally, the continuity conditions for the displacements are formulated as:

$$u_{z2}=u_{z3}^s=u_{z3}^f=u_{z1}, \tag{18}$$

$$u_{x2}=u_{x3}^s. \tag{19}$$

By eliminating the displacements of the membrane, the boundary conditions Eqs. (16)–(19) are reduced to four equations, which can be expressed in matrix notation:

$$\left[\begin{array}{cc|ccccccc} 0 & 0 & \rho_2\omega^2 & 0 & 0 & 0 & 1 & 0 \\ 1 & 0 & 0 & \rho_1\omega^2 & 0 & 1 & 0 & 1 \\ 0 & 0 & 0 & 1 & -1 & 0 & 0 & 0 \\ 0 & 1 & 0 & 0 & -1 & 0 & 0 & 0 \end{array}\right] \left[\begin{array}{c} p_1 \\ u_{z1} \\ u_{x3}^s \\ u_{z3}^s \\ u_{z3}^f \\ \tau_{zz3}^s \\ \tau_{xz3}^s \\ \tau_{zz3}^f \end{array}\right] = \left[\begin{array}{c} 0 \\ 0 \\ 0 \\ 0 \end{array}\right], \tag{20}$$

or:

$$[I_{AMP}|J_{AMP}]\begin{bmatrix} V_1 \\ V_3 \end{bmatrix}=0. \tag{21}$$

The boundary conditions for the air layer and porous layer coupled by an elastic membrane are formulated using the 4×8 interfacial matrix in Eq. (20). In Eq. (21), $[I_{AMP}]$ contains the coefficients associated with the air layer, while $[J_{AMP}]$ contains the coefficients for the porous layer.

II. APPLICATION TO STRETCHED MEMBRANE CEILINGS

The configuration of the stretched ceiling, as it was built upside-down on the floor of the reverberation chamber, is shown in Fig. 2. The membrane consists of a 150-μm-thick PVC foil, stretched on a 3.17×3.17 m^2 plastic frame using the thermal procedure described in the Introduction. The plastic frame was fixed on a wooden enclosure. The surface density of the foil was equal to 0.17 kg/m^2. The stiffness S was taken equal to $80\,000 + j\ 8000$ N/m and the tension in the membrane was estimated as 4×10^6 N/m^2 (which is equivalent to a traction force of 600 N/m). The latter represents a practical estimate based on the change of the original membrane dimensions, while neglecting the reduction of the actual tension due to relaxation. However, the term proportional to T in Eq. (2) is always considerably smaller than m'' (actually, T should be of the order of 10^8, before this term could obtain the same order of magnitude as m''). So for all practical purposes, T can be chosen equal to zero. In the experimental setup, the depth of the cavity could be increased up to 55 cm and a porous layer could be placed in the cavity. The material parameters of the porous layers have been determined with methods described in Refs. 16–18 and are listed in Table I.

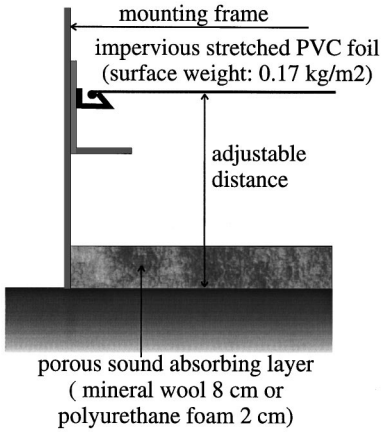

FIG. 2. Experimental setup on the floor of the reverberation chamber.

The stretched membrane ceiling was modelled as a series of two air layers (separated by a membrane), a porous layer and a thick elastic solid layer. The latter layer was introduced to approximate an infinitely rigid wall. Further, the surface of the membrane was assumed to be perfectly smooth and no effect of surface roughness was taken into account as opposed to Ref. 10.

In the following paragraphs, a series of numerical simulations will be presented to illustrate the effect various parameters on the sound absorption of the stretched ceiling. A comparison between measurement and calculation will be discussed in the final paragraphs. All calculations were carried out using the characteristics of the membrane in the experimental setup. Material 1 in Table I corresponds to the absorbing material used in the parametric analysis, whereas materials 2 and 3 represent the mineral wool and a plastic foam placed in the cavity during the experimental verification.

A. Numerical simulations and parametric study

The absorption coefficient at normal incidence of a structure with a 13-cm air cavity and a 2-cm layer of material 1 in the plenum is shown in Fig. 3. In addition, the absorption coefficient of the foam layer alone is plotted in the same Fig. 3 for comparison. A number of resonances can be observed. The first one (near 300 Hz) is the mass-spring resonance, the mass being the mass of the membrane and part of the mass of the air in the cavity (indeed, since the membrane is very light, the mass of the oscillating air cannot be neglected), and the spring being determined by the stiffness of the air between the membrane and the back wall. Above the

TABLE I. Material properties of the absorbing materials.

Parameter	Material 1 Simulation data	Material 2 Mineral wool	Material 3 Plastic foam
Density ρ (kg/m^3)	24	60	24
Young's modulus E (N/m^2)	$3\times10^4+j3\times10^3$	$14\times10^3+j14\times10^2$	$8\times10^5+j8\times10^4$
Shear modulus G (N/m^2)	$15\times10^3+j15\times10^2$	$7\times10^3+j7\times10^2$	$4\times10^5+j4\times10^4$
Flow resistivity σ (Ns/m^4)	35 000	33 500	3800
Tortuosity α_∞	1.5	1.01	1.1
Porosity H	0.98	0.98	0.99
Characteristic viscous length Λ (m)	80×10^{-6}	200×10^{-6}	170×10^{-6}
Characteristic thermal length Λ' (m)	250×10^{-6}	400×10^{-6}	200×10^{-6}

decoupling frequency of the foam given by $\omega=\rho/\sigma$ (σ being the flow resistivity), no vibrations in the frame of the porous material are excited[15] and the resonance frequency can easily be estimated with an approximate equation:

$$f_{\text{res}}=\frac{1}{2\pi}\sqrt{\frac{k}{m}}. \tag{22}$$

The mass m is given by:

$$m=m''+\tfrac{1}{3}\rho_0 d_{\text{total}}. \tag{23}$$

Here, ρ_0 is the density of air and d_{total} is the total cavity depth. The correction term for the density of air is equal to 0.06 kg/m^2 and is clearly not negligible compared to m''.

The spring constant k can be approximated by:

$$\frac{1}{k}=\frac{1}{k_0}+\frac{1}{k_{\text{por}}}, \tag{24}$$

where k_0 is the spring constant of the air in the cavity (equal to $\rho_0 c^2/d_{\text{air}}$) and k_{por} the spring constant of the air in the porous layer. The compressibility of the air in the porous material lies between the isothermal compressibility 1.4 $\times10^5$ N/m^2 and the adiabatic compressibility 10^5 N/m^2. Using these two extreme values, the mass-spring resonance, estimated with Eq. (22), has as value between 312 Hz and 321 Hz, which agrees well with the results of the complete model.

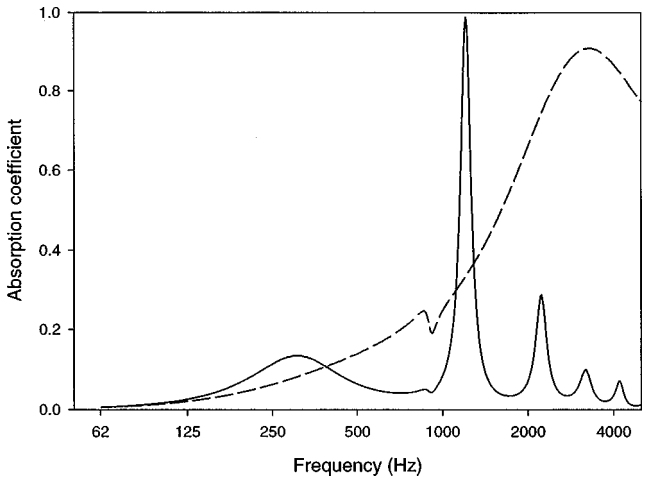

FIG. 3. Normal incidence absorption coefficient: stretched membrane ceiling (———) ($d_{\text{air}}=0.13$ m, $d_{\text{layer}}=2$ cm), 2-cm porous layer (- - -).

The other resonances in Fig. 3 are thickness resonances: without porous material in the cavity, these resonances would be located at frequencies given by:

$$f=\frac{nc}{2d}. \tag{25}$$

The actual frequencies at which the resonances occur tend to shift to lower frequencies when the porous layer is present due to the fact that the sound speed in the porous layer is lower than in free air.[15]

At low frequencies, below the mass-spring resonance, the membrane does not significantly alter the sound field and the absorption coefficient of the suspended ceiling is equal to the absorption coefficient of the porous layer. At high frequencies, the inertia of the membrane tends to dominate and more sound energy is reflected.

The small dip in the absorption curve that can be observed near 900 Hz in Fig. 3 is a result of a thickness resonance in the frame of the porous layer and its position is almost completely determined by the frames density and elastic modulus and the thickness of the layer.

Figure 4 shows the influence of the cavity depth d_{air} on the absorption coefficient, all other parameters being kept constant. As expected, all resonances shift toward lower frequencies if the cavity depth increases and their position can be estimated with Eqs. (22) and (25).

Figure 5 shows the influence of the thickness of the absorbing layer, the *total* cavity depth $d_{\text{air}}+d_{\text{layer}}$ being kept constant and equal to 15 cm. The absorption at the mass-spring resonance increases substantially with the layer thickness, while the effect on the position of the different resonances is only marginal due to the slightly lower sound speed in the porous layer. The dip due to the thickness reso-

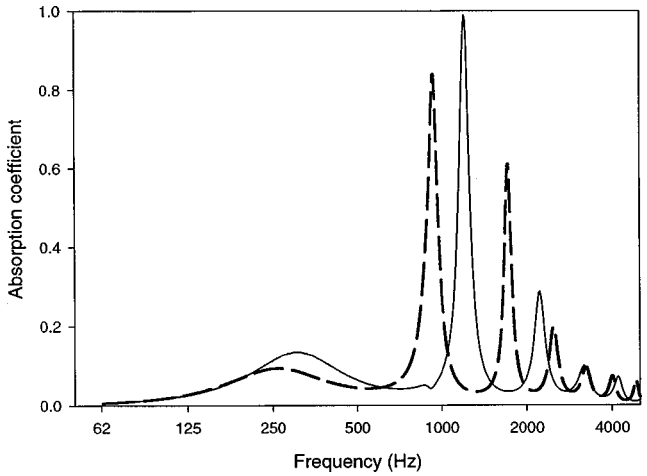

FIG. 4. Normal incidence absorption coefficient for two values of the cavity depth d_{air}: 13 cm (———), 18 cm (- - -). Remaining data as in Fig. 3.

nance in the porous layer shifts toward lower frequencies as the thickness of the layer increases.

Figure 6 shows the influence of the position of the absorbing layer in the plenum. The total cavity depth was kept equal to 15 cm, but in the first example the 2-cm-thick porous layer was placed in contact with the back wall, whereas in the second example, the porous layer was placed in the center of the cavity. Although the position of the mass-spring resonance did not change (since the total spring constant of the cavity remains unchanged), the absorption coefficient increases considerably. This is a result of the higher relative velocity of the air particles in the porous layer in the second case. The location and amplitudes of the standing waves changes and cannot be estimated with Eq. (25).

Although not completely clear in Fig. 6 due to the limited frequency resolution, the absorption coefficient is *exactly* equal to one at one specific frequency. This can be explained as follows. The membrane mainly changes the inertia of the system and it influences almost exclusively the imaginary part of the impedance. Consequently, the impedance Z in front of the membrane can be expressed in terms of

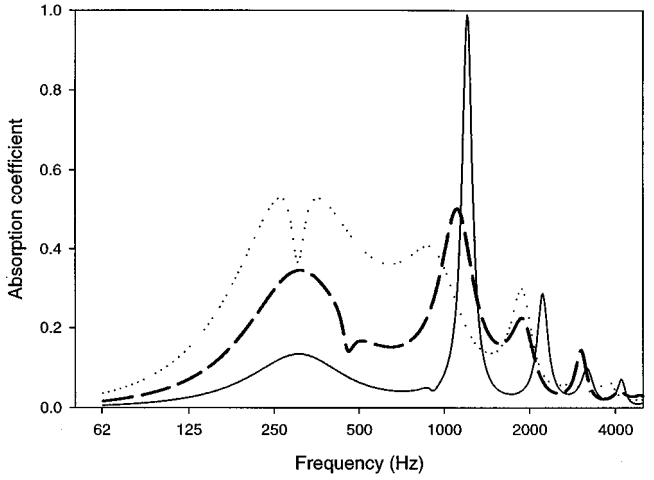

FIG. 5. Normal incidence absorption coefficient for three different values of the porous layer thickness d_{layer}: 2 cm (———), 4 cm (- - -), 6 cm (· · · ·). Total cavity depth kept constant and equal to 15 cm.

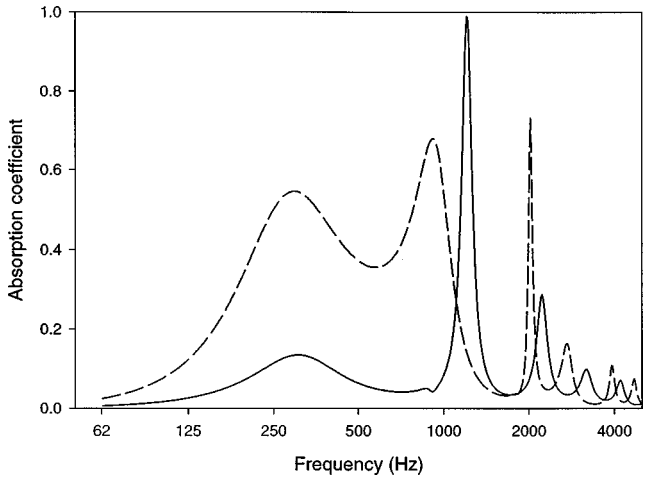

FIG. 6. Influence of the position of the absorbing layer on the normal incidence absorption coefficient: porous layer against back wall (———), porous layer in center of cavity (- - -). Total cavity depth equal to 15 cm, d_{layer}=2 cm.

the impedance Z_2 directly behind the membrane (in the cavity) as:

$$Z = Z_2 + j\omega m''. \tag{26}$$

The impedance Z_2 was calculated using the transfer matrix approach and Fig. 7(a) demonstrates that the imaginary part of Z_2 changes sign when the real part has a maximum. These maxima can be very high since there is not much absorption and for each peak in the real part, there are two intersections with the line $Z=\rho_0 c$: one where the imaginary part of the impedance is positive and one where the imaginary part of the impedance in negative. This means that it is always possible to cancel the imaginary part at one of these points by choosing an appropriate surface density of the membrane [see Fig. 7(b)]:

$$m'' = \frac{-\operatorname{Im}(Z_2)}{\omega}. \tag{27}$$

This makes the impedance Z in front of the membrane *exactly* equal to $\rho_0 c$ and the absorption coefficient exactly equal to one. Consequently, the incident energy enters the cavity unattenuated and is completely absorbed by the interaction between the standing wave and the porous layer [see Fig. 7(c)]. This occurs even if the porous layer is very thin, but at the expense of the absorber's bandwidth. This effect also explains the difference in height of the absorption peaks due to the standing waves in the cavity: If the surface density of the membrane is ''matched'' at one resonance frequency, the contribution to the imaginary part at other frequencies will not fulfil Eq. (27). By choosing the correct cavity depth and surface density of the membrane, the normal incidence absorption coefficient can be made equal to one at any desired frequency, even with a very small amount of sound absorption in the cavity.

B. Experimental results

The experimental setup described in the beginning of Sec. II was constructed on the floor of a reverberation cham-

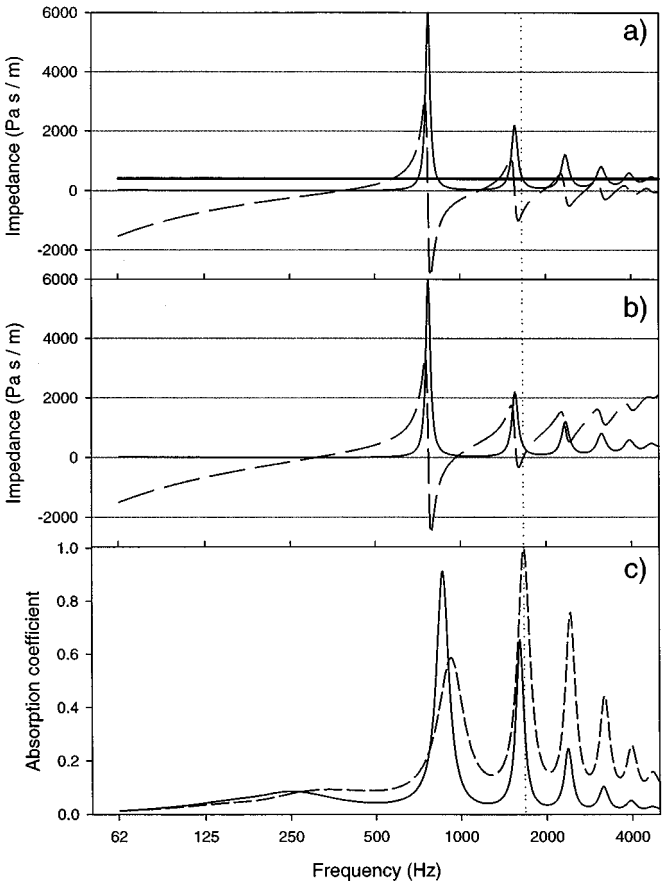

FIG. 7. Matching the membrane's density, $d_{\text{air}}=20$ cm and $d_{\text{layer}}=1$ cm. (a) Real (———) and imaginary (- - -) part of the impedance Z_2 at the back of the membrane. The horizontal line indicates the characteristic impedance of air: $\rho_0 c$. (b) Real (———) and imaginary (- - -) part of the impedance Z at the front of the membrane. The surface density of the membrane has been chosen to cancel the imaginary part at the vertical dotted line. (c) Normal incidence absorption coefficient of the stretched ceiling surface density equal to 0.17 kg/m^2 (———), matched surface density $m''=0.068$ kg/m^2 (- - -).

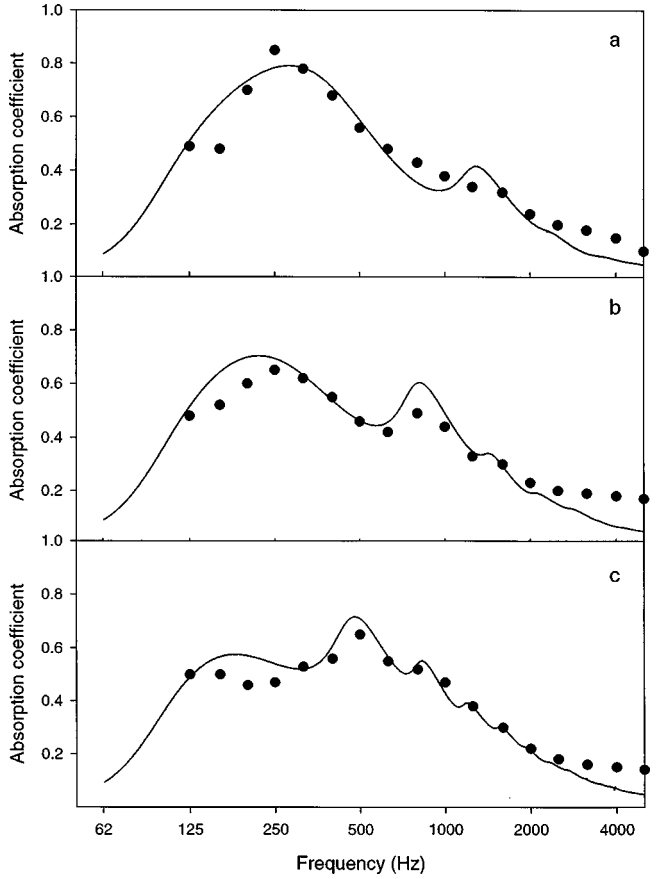

FIG. 8. Experimental data (dots) and predictions (line) for a stretched membrane ceiling with 8-cm mineral wool in the cavity, for three values of the total cavity depth: (a) 22 cm, (b) 32 cm, and (c) 52 cm.

ber, and the experiments were carried out according to ISO 354. Because the absorption of the wooden enclosure might affect the final results, a first measurement was performed with only the wooden frame in the reverberation room. The measured absorption coefficient of the frame was then used to correct the results obtained for the full setup, including the membrane and the cavity absorption.

The simulations were performed based on the theory presented in Sec. I, where the random incidence absorption coefficient is calculated using Eq. (1). Unfortunately, it is unclear as to what extent grazing sound waves were obstructed from reaching the membrane due to the presence of the wooden enclosure. The limiting angle θ_{lim} in Eq. (1) was estimated by fitting the calculations to the measurements of the first setup, leading to a value of 70°. The same integration limit was used for all other predictions, regardless of the cavity depth. Measurement and calculation are compared in Figs. 8 and 9. In accordance with ISO 354, the experimental data are presented in third octave bands. The theoretical results are plotted in narrow bands in order to identify of the various resonances.

Figure 8 shows the results for the first series of measurements. Three different cases were considered, corresponding to a total cavity depth of 22, 32, and 52 cm, respectively. The absorbing material was a 8-cm-thick mineral wool (material 2 in Table I). In spite of the abovementioned limitations and the anisotropic characteristics of the mineral wool, the agreement between model and experiment is quite satisfactory.

Figure 9 shows similar results with a 2-cm plastic foam (material 3 in Table I) in the plenum. Although the sound propagation in the foam can be modeled more accurately than the sound propagation in the mineral wool, the model systematically underestimates the measured results. This is probably due to the fact that the absorption of the foam is much lower than the absorption of the mineral wool. In this case, any additional absorption mechanism may have a significant influence on the measurements. Additional absorption could be caused by leakage through small air-gaps between the wooden enclosure and the floor of the laboratory, as observed by Takahashi *et al.*[11] in the context of a similar experiment.

III. CONCLUSIONS

The absorption coefficient of a stretched membrane ceiling with an impervious PVC foil and an elastic porous sound absorbing material in the plenum has been studied theoretically and experimentally. For this purpose, the classical transfer matrix approach was modified to model an impervious membrane between two layers. The sound absorbing

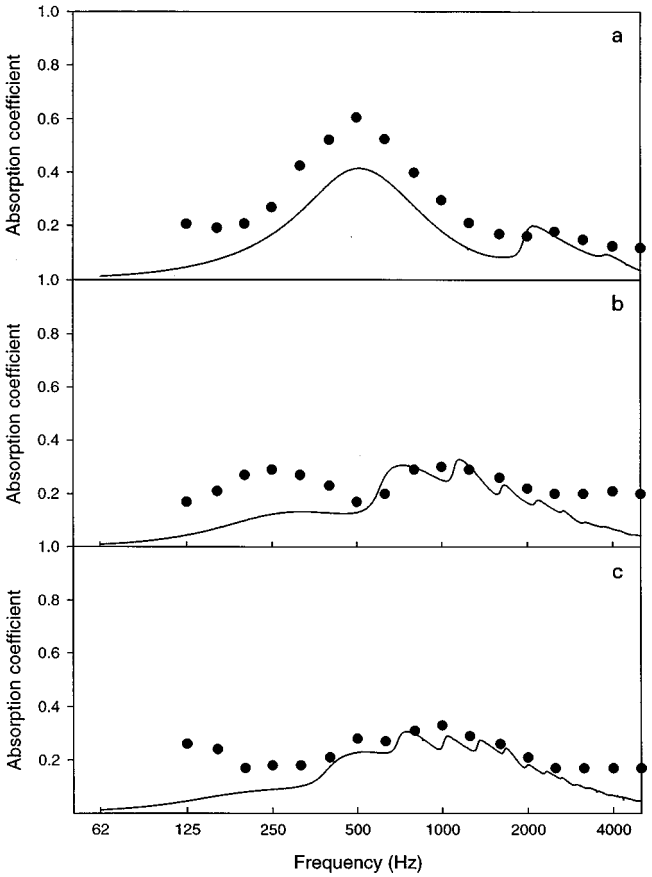

FIG. 9. Experimental data (dots) and predictions (line) for a suspended ceiling with 2-cm plastic foam in the cavity, for three values of the total cavity depth: (a) 9 cm, (b) 32 cm, and (c) 52 cm.

characteristics of membrane ceilings were illustrated by a series of numerical simulations and the resonant behavior of the system was explained based on simple theoretical considerations. The experimental verification showed good agreement between measured and calculated data for a sufficiently high cavity absorption, but a systematic overestimation was observed when only a limited amount of absorption was present in the cavity. However, the good agreement between experimental and theoretical trends suggests that the model represents a valuable tool for predicting the sound absorbing performance of stretched membrane ceilings.

ACKNOWLEDGMENTS

The authors wish to dedicate this paper to the memory of their colleague, Filip Nuytten, whose scientific efforts were of major benefit to the presented theory. The practical support of BARRISOL Belgium Cy is gratefully acknowledged.

[1] C. W. Kosten, ''Absorption of sound by coated porous wall-covering layers,'' J. Acoust. Soc. Am. **18**, 457–471 (1946).
[2] M. Schwartz and W. L. Buehner, ''Effects of light coatings on impedance and absorption of open-celled foams,'' J. Acoust. Soc. Am. **35**, 1507–1510 (1963).
[3] J. E. Masiak, ''Effect of surface films on acoustical foam performance,'' Sound Vib., 24–29 (July 1974).
[4] J. F. Allard, C. Depollier, and W. Lauriks, ''Measurement and prediction of surface impedance at oblique incidence of a plastic foam at high flow resistance,'' J. Sound Vib. **132**, 51–60 (1989).
[5] J. F. Allard, C. Depollier, P. Rebillard, W. Lauriks, and A. Cops, ''Inhomogeneous Biot waves in layered media,'' J. Appl. Phys. **66**, 2278–2284 (1989).
[6] W. Lauriks, J. F. Allard, C. Depollier, and A. Cops, ''Inhomogeneous plane waves in layered materials including fluid, solid and porous layers,'' Wave Motion **13**, 329–336 (1991).
[7] W. Lauriks, A. Cops, J. F. Allard, C. Depollier, and P. Rebillard, ''Modelization at oblique incidence of layered porous materials with impervious screens,'' J. Acoust. Soc. Am. **87**, 1200–1206 (1990).
[8] Y. J. Kang and J. S. Bolton, ''Finite element modeling of isotropic elastic porous materials coupled with acoustical finite elements,'' J. Acoust. Soc. Am. **98**, 635–643 (1995).
[9] K. Sakagami, D. Takahashi, H. Gen, and M. Morimoto, ''Acoustic properties of an infinite elastic plate with a back cavity,'' Acustica **78**, 288–295 (1993).
[10] K. Sakagami, M. Kiyama, M. Morimoto, and D. Takahashi, ''Sound absorption of a cavity-backed membrane: A step toward design method for membrane-type absorbers,'' Appl. Acoust. **49**, 237–247 (1996).
[11] D. Takahashi, K. Sakagami, and M. Morimoto, ''Acoustic properties of permeable membranes,'' J. Acoust. Soc. Am. **99**, 3003–3008 (1996).
[12] K. Sakagami, M. Kiyama, T. Uyama, and M. Morimoto, ''Absorption characteristics of a double-leaf membrane with an absorptive layer in its cavity,'' in *Proceedings 16th International Congress on Acoustics and 135th Meeting of the Acoustical Society of America*, pp. 2735–2736 (1998).
[13] K. Sakagami, M. Kiyama, T. Uyama, and M. Morimoto, ''Sound Transmission through Permeable Double-leaf Membranes,'' in *Proceedings 16th International Congress on Acoustics and 135th Meeting of the Acoustical Society of America*, pp. 1381–1382 (1998).
[14] B. Brouard, D. Lafarge, and J. F. Allard, ''A general method of modeling sound propagation in layered media,'' J. Sound Vib. **183**, 129–142 (1995).
[15] J. F. Allard, *Propagation of Sound in Porous Media* (Elsevier Applied Science, London, 1993).
[16] Ph. Leclaire, L. Kelders, W. Lauriks, C. Glorieux, and J. Thoen, ''Determination of the viscous characteristic length in air filled porous materials by ultrasonic attenuation measurements,'' J. Acoust. Soc. Am. **99**, 1944–1948 (1996).
[17] Ph. Leclaire, L. Kelders, W. Lauriks, M. Melon, N. Brown, and B. Castagnede, ''Determination of the viscous and thermal characteristic lengths of plastic foams by ultrasonic measurements in helium and air,'' J. Appl. Phys. **80**, 2009–2012 (1996).
[18] Ph. Leclaire, L. Kelders, W. Lauriks, J. F. Allard, and C. Glorieux, ''Ultrasonic wave propagation in reticulated foams saturated by different gases—High frequency limit of the classical models,'' Appl. Phys. Lett. **69**, 2641–2643 (1996).

Performance of some linear time-varying systems in control of acoustic feedback

Johan L. Nielsen[a)]
Department of Telecommunications, Norwegian University of Science and Technology, N-7034 Trondheim, Norway

U. Peter Svensson
Department of Applied Acoustics, Chalmers University of Technology, SE-41296 Gothenburg, Sweden

(Received 20 May 1997; revised 8 March 1999; accepted 8 April 1999)

Some linear time-varying (LTV) components used to control feedback in sound systems were tested experimentally in real-time simulators and rooms with and without external reverberation. Gain before instability (GBI) was measured in single channels employing frequency shifting (FS), phase modulation (PM), and delay modulation (DM) implemented on a digital signal processor. FS performed according to the established theory. For PM GBI increased almost monotonically with modulation index β, except for cases with large loop gain irregularities which displayed a reduced GBI for values of β that corresponded to low carrier suppression. Also, GBI was practically independent of the modulation frequency f_m already from 0.5 Hz even when this was much lower than the correlation distance of the loop gain transfer function. Rooms with different reverberation times gave different initial (time-invariant) GBI values but these differences decreased by the use of modulation. The GBI increase was larger for cases with external reverberation than for cases without due to increased loop gain irregularity, and the GBI results depended on f_m. Since the possible GBI increase is determined by the initial GBI, LTV system performance should be measured in terms of GBI and not GBI increase alone. Robustness increased by equalizing the loop gain before employing LTV components. DM gave little protection for low frequencies but was efficient at high frequencies. [S0001-4966(99)03407-4]

PACS numbers: 43.55.Jz [JDQ]

LIST OF ABBREVIATIONS AND SYMBOLS

DM	delay modulation
DSP	digital signal processor
FM	frequency modulation
FS	frequency shifting
LPTV	linear periodically time-varying
LTI	linear time-invariant
LTV	linear time-varying
PM	phase modulation
RE	reverberation enhancement
RTF	room transfer function
TF	transfer function
β	modulation index, in radians
Δf	maximum frequency deviation, in Hz
$\Delta f_{\max}$	average frequency distance between local maxima of the RTF magnitude, in Hz
$\Delta\tau$	maximum delay deviation, in s
$\theta(t)$	phase modulation function
B	observation bandwidth, in Hz
CS	carrier suppression, in dB
f_0	set of frequencies for which the open loop gain $S(f)$ is real-valued
f_{corr}	correlation distance, in Hz
f_m	modulation frequency, in Hz
$f_{\text{Schroeder}}$	Schroeder frequency, in Hz
$g(t,\tau)$	time-varying impulse response
$G(t,f)$	mixed time-frequency transfer function
$G_0(f)$	carrier transfer function
$G_k(f)$	for $k\neq 0$, the sideband transfer functions
GBI	gain before instability, in dB
$H(f)$	feedback transfer function
$J_k(\beta)$	Bessel functions of the first kind and order k
$m_d(t)$	normalized delay modulation function
$m_f(t)$	normalized frequency modulation function
$m_p(t)$	normalized phase modulation function
MLG	mean loop power gain, in dB
P2M	peak-to-mean ratio for the squared RTF magnitude, in dB
RT	reverberation time, in s
$S(f)$	open loop transfer function, or loop gain
T	period time for modulation functions, in s
V	room volume, in m^3

INTRODUCTION

Feedback occurs in electroacoustic systems with interconnected microphones and loudspeakers, and may lead to sound coloration and ultimately instability tendencies. Time-varying components can be used in such systems to control feedback. Many of the basic time-varying techniques were patented early,[1] but none of them have gained widespread use as general tools for feedback control. The main reasons

[a)]Now with Silence International, Gaustadalléen 21, 0349 Oslo, Norway.

for this are the high cost for related equipment, the careful calibration needed when they are installed, and their potential for unnatural, modulated sound. For the class of electroacoustic systems often referred to as reverberation enhancement (RE) systems, however, feedback is a significant problem and, despite the drawbacks, the use of time-varying components can be made worthwhile. The cost for RE systems is usually quite high to begin with, so that the inclusion of time-varying components makes a relatively small difference for the overall cost. Furthermore, such systems are often installed permanently, minimizing the need for frequent expert calibrations. Time-varying components are, therefore, used in most commercial RE systems and apparently work well.[2–5]

In 1981 Ahnert and Reichardt[6] reviewed earlier studies of time-varying techniques. These studies were often limited by either the use of analog equipment or, in the case of studies on subjective effects, the control of parameter adjustments. Digital technology has since provided improved quality and flexibility in system designs and testing. In recent years few reports have been published on the use of time-varying techniques for feedback control, and no extensive system-independent investigations have been presented, motivating a renewed study of time-varying systems.

The principal time-varying components which have been investigated for controlling feedback are frequency shifting (FS), phase (PM), and frequency modulation (FM), and delay modulation (DM). The basic mechanism of these is to smooth the irregularities of the loop gain transfer function (TF). FS was suggested by Schroeder[7] who demonstrated that the stability of a system with FS and a diffuse-field feedback TF can be analyzed using a statistical model.[8] A gain improvement of about 12 dB could theoretically be achieved in a typical room by employing FS, as he confirmed through measurements. His model also showed that this result should theoretically depend very little on the reverberation time, RT. Measurement results reported by Tapio confirmed Schroeder's model.[9] Tapio also made measurements in environments with large direct sound components and concluded that this reduced the effect of FS due to the lower irregularity of the loop gain TF. Investigations by Tilse and Peško presented results showing gain increases up to 18 dB using FS, and contradicted Schroeder's theory by reporting improvements which increased with RT.[10,11]

Mishin analyzed sinusoidal PM using an energy model, and pointed out that the optimal PM corresponds to zeros of the Bessel function of zero order, $J_0(\beta)$, for example, for the value 2.4 rad of the modulation index β.[12] However, he considered only feedback via a direct sound path. Nishinomiya experimentally tested sinusoidal FM,[13] which is equivalent to sinusoidal PM. He found an optimal value of β between 2 and 3 rad, and a gain improvement of up to 7 dB that increased with RT and decreased with increased loop gain irregularity. He also observed an optimal value for the modulation frequency, and found that it depended on RT. Guelke and Broadhurst reported an additional gain of 4 dB in their RE system using PM with $\beta=2.4$ rad and a modulation frequency of 1 Hz.[14] Tilse and Peško observed gain improvements up to 10 dB using PM, with results which depended on RT. They tested nonsinusoidal modulation functions, such as noise and triangular functions, without finding significant differences in performance from the sinusoidal case. They also carried out experiments in an anechoic room where they found a 1–2 dB improvement.[10,11]

DM is often used in commercial RE systems because of its easy implementation. However, very few results for DM performance have been reported. In a single experimental setting Mishin observed a 7–8 dB improvement using a high modulation frequency.[12]

Although the theory of FS is well established,[8] previous research has not supplied a clear picture of the efficiency of PM or DM, neither in terms of a solid theory nor in terms of experimental results. The goal of the present study is to investigate the objective performance of FS, PM, and DM through experiments using modern techniques. FS is a special form of PM, and DM is simply PM with a modulation index which increases linearly with frequency. Furthermore, PM is a technique which offers frequency independent feedback control, and consequently by focusing on PM, this study aims at providing general insight into the application of time-varying components for feedback control in rooms. Both separate modulators, and modulators cascaded with a reverberation unit as a simple model of more intricate schemes, are studied here by implementing FS, PM, and DM on a digital signal processor (DSP). Only periodical modulation functions are tested, although DSP implementations permit arbitrary, nonperiodical modulation functions.

Section I briefly reviews theory of feedback in electroacoustic systems as it applies to linear time-invariant systems. Its relation to time-varying components/modulators is introduced, and hypotheses about the stability of feedback loops employing time-varying components are proposed. Section II presents the experimental method used for measuring stability and describes the cases studied, which include both real-time simulators, that is, purely electronic setups and electroacoustic setups in real rooms. Section III presents results from the measurements and discusses their implications for the proposed hypotheses. Applications to practical systems, and possible limitations of the work presented here are discussed in Sec. IV. Conclusions are summarized in Sec. V.

I. FEEDBACK IN ELECTROACOUSTIC SYSTEMS

The problem of feedback causing coloration and instability in electroacoustic systems in rooms is well known for systems with linear time-invariant (LTI) filters.[15,16] A single electroacoustic channel is a standard positive feedback loop and therefore the open loop TF is the quantity which determines the stability of the feedback loop. The open loop TF is often called the loop gain, and will be denoted as $S(f)$ here. Because the feedback is via a room transfer function (RTF) which is irregular, the loop gain will also be irregular. When the magnitude of the loop gain is close to unity at some frequency, the decay time at that frequency will be prolonged resulting in coloration in the form of ringing, which in turn determines the practical gain limit. Eventually, instability will occur at frequencies where the value of $S(f)$ is real and larger than 1. In practical systems the useable gain is often very low which makes it relevant to use techniques-

which decrease the feedback problem. The gain of an electroacoustic system will be described here using the mean loop power gain, MLG, of the system, defined as

$$\mathrm{MLG} = \overline{|S(f)|^2}, \tag{1}$$

where the averaging is done over the frequency range of interest. A measure of the irregularity of $S(f)$ is the peak-to-mean ratio, P2M, defined as

$$\mathrm{P2M} = 10 \log \frac{\max(|S(f)|^2)}{\mathrm{MLG}} [\mathrm{dB}], \tag{2}$$

and with an expected value, $\langle \mathrm{P2M} \rangle$, for diffuse fields, as derived by Schroeder,[7] being

$$\langle \mathrm{P2M} \rangle = 10 \log[\log(B \ \ \mathrm{RT})] + 3.6 \ [\mathrm{dB}], \tag{3}$$

where B is the observation bandwidth in Hz and RT the reverberation time in s. The double logarithm in Eq. (3) leads $\langle \mathrm{P2M} \rangle$ to vary quite little with the value of $B \cdot \mathrm{RT}$, so that in a typical room with RT in the range of 1–2 s and a bandwidth B in the range of 4–5 kHz (which is used in this investigation), $\langle \mathrm{P2M} \rangle$ is 9.2–9.6 dB. A closely related quantity is the highest mean loop power gain in a feedback loop that is possible while keeping the system stable, the so-called gain before instability, GBI. Throughout this study GBI will be used as a quantification of the electroacoustic system's performance. It is defined here as

$$\mathrm{GBI} = 10 \log(\mathrm{MLG}) \ [\mathrm{dB}], \quad \text{at the point of instability.} \tag{4}$$

If the loop gain $S(f)$ is known, GBI can be predicted by the relation

$$\mathrm{GBI} = -10 \log \frac{\max(|S(f_0)|^2)}{\mathrm{MLG}} [\mathrm{dB}], \tag{5}$$

where f_0 is the set of frequencies for which $S(f)$ is real-valued. Schroeder also derived an expected value for GBI, assuming a diffuse-field RTF,[8]

$$\langle \mathrm{GBI} \rangle = -10 \log[\log(B \cdot \mathrm{RT}/22)] - 3.8 \ [\mathrm{dB}]. \tag{6}$$

The expressions for $\langle \mathrm{P2M} \rangle$ and $\langle \mathrm{GBI} \rangle$ are, apart from the sign, similar but not identical, since for the same ranges of RT and B as above for $\langle \mathrm{P2M} \rangle$, the value of $\langle \mathrm{GBI} \rangle$ is in the range of -8.0 dB to -7.3 dB. The reason for the discrepancy between the values of $\langle \mathrm{P2M} \rangle$ and $\langle \mathrm{GBI} \rangle$ is that a loop gain function $S(f)$ can have a magnitude which is larger than 1 and still be stable, as long as this does not happen at a frequency where $S(f)$ is real-valued. All calculations of expected values for the statistical parameters introduced above apply to a diffuse-field, which is a valid model of the sound field above the Schroeder frequency[17]

$$f_{\mathrm{Schroeder}} = 2000 \sqrt{\frac{\mathrm{RT}}{V}}, \tag{7}$$

where V is the room volume in m^3. Below this frequency, larger values of P2M, and consequently lower values of GBI may well be encountered. These established quantities for predicting the stability of electroacoustic systems cannot be used directly for systems with time-varying components. However; GBI can still be used to quantify the gain at the point of instability, as will be discussed in Sec. I C.

A. Linear time-varying components

Claasen and Mecklenbräuker offer a modern review of linear time-varying (LTV) components.[18] They characterize a causal linear system by its impulse response, $g(t,\tau)$, which gives the response at time, t, to an impulse applied τ time units earlier. This corresponds to a mixed time-frequency TF, $G(t,f)$, which is the Fourier Transform of $g(t,\tau)$ with respect to τ, and with t as a constant. This TF can in turn be Fourier transformed with respect to t, with f as a parameter, which results in $\hat{G}(\phi,f)$. Here, f is the input signal's frequency and ϕ is a frequency which is introduced to describe the time-dependence of the LTV system. If this time-dependence is periodical, with a time period, T, a Discrete Fourier Transform (DFT) may be used to transform $G(t,\tau)$ into a set of discrete TFs, $\hat{G}(k\Delta\phi,f)$, where the frequency ϕ takes on only the discrete values $k\Delta\phi$. The frequency step $\Delta\phi$ equals $1/T$. Finally, this set of discrete TFs can be more compactly denoted as a set, $G_k(f)$, of TFs. Having established these quantities, Claasen and Mecklenbräuker presented the input–output relationship for the class of linear periodically time-varying (LPTV) systems as

$$Y(f) = \sum_{k=-\infty}^{\infty} G_k(f - k f_m) X(f - k f_m), \tag{8}$$

which shows that the output spectrum, $Y(f)$, is a sum of weighted and shifted versions of the input spectrum $X(f)$. Consequently, each component of the input signal, or carrier, $X(f)$, generates an infinite number of new discrete components in $Y(f)$, all at new frequency values, and separated by multiples of the modulation frequency $f_m = \Delta\phi = 1/T$. $G_0(f)$ will be referred to as the carrier TF and $G_k(f)$, for $k \neq 0$, the sideband TFs. Equation (8) describes a linear system from the point of view of the input signal, or carrier, $X(f)$. A basic difference between modulators used in feedback control and in communication systems is that in feedback control the carrier, rather than the modulating signal, is the information signal.

The establishment of the TFs $G_k(f)$ can be illustrated by phase modulation, PM, the type of modulation which is central to this study. For PM, the instantaneous phase of the input signal is changed according to the phase modulation function,

$$\theta(t) = \beta m_p(t), \tag{9}$$

where $m_p(t)$ is the normalized (i.e., with a maximum amplitude of 1) phase modulation function and the modulation index β gives the maximum phase deviation in radians. For a sinusoidal input signal, $x(t) = e^{j2\pi f t}$, to the phase modulator, the output signal $y(t)$ can be written

$$y(t) = e^{j2\pi f t} e^{j\beta m_p(t)}. \tag{10}$$

This is a time-domain multiplication which corresponds to a frequency-domain convolution,

$$Y(f) = X(f) * \mathrm{FT}_t\{e^{j\beta m_p(t)}\}, \tag{11}$$

where FT_t indicates a Fourier Transform with respect to t. Equation (11) is equivalent to the relationship in Eq. (8) for the case of a periodical function $m_p(t)$. Then, the TFs, G_k, can readily be identified as the DFT coefficients,

$$G_k = \int_{-\infty}^{\infty} e^{j\beta m_p(t)} e^{j2\pi k f_m t}\, dt. \tag{12}$$

It can be observed that for PM, the signal frequency, f, does not enter into the right-hand side of Eq. (12), and consequently the modulation is frequency-independent. If the phase modulation function is $m_p(t) = \sin(2\pi f_m t)$, sinusoidal PM with the modulation frequency f_m results. Inserting this into Eq. (12), a Bessel integral results, and the sideband TFs are

$$G_k = J_k(\beta), \tag{13}$$

where $J_k(\beta)$ are the Bessel functions of the first kind and order k. As the modulation index, β, is increased, more and more sidebands, that is, new frequency components, are generated, further and further away from the input signal's frequency.

In the following sections, only LPTV components will be discussed. Practical implementations might use nonperiodical modulation functions, and as will be seen, in the present study of objective system performance, only small differences are found between different periodical modulation functions, and consequently, it can be hypothesized that no fundamental differences would occur between periodical and nonperiodical modulation functions.

The LPTV components discussed below are always normalized so that

$$\sum_{k=-\infty}^{\infty} |G_k|^2 = 1, \tag{14}$$

and the electronic gain is a separate component placed before or after the LPTV component. A central property of LPTV components is the carrier suppression, CS, which is

$$\mathrm{CS} = -20\log|G_0| \quad [\mathrm{dB}]. \tag{15}$$

A type of modulation closely related to PM is frequency modulation, FM, which changes the instantaneous frequency of the input signal according to the frequency variation

$$f(t) = \Delta f \cdot m_f(t), \tag{16}$$

where $m_f(t)$ is the frequency modulation function and Δf is the maximum frequency deviation in Hz. The frequency variation function relates to the phase modulation function $\theta(t)$ as

$$f(t) = \frac{1}{2\pi}\frac{\partial\theta(t)}{\partial t}. \tag{17}$$

Consequently, sinusoidal PM corresponds to sinusoidal FM with the frequency variation

$$f(t) = \beta f_m \cos(2\pi f_m t), \tag{18}$$

and the maximum frequency deviation can be identified as

$$\Delta f = \beta f_m. \tag{19}$$

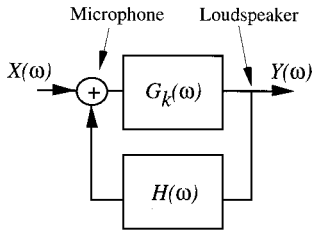

FIG. 1. A feedback loop with an LPTV filter, characterized by a set of sideband transfer functions $G_k(\omega)$, and an LTI feedback transfer function $H(\omega)$.

As a result, sinusoidal FM is identical to sinusoidal PM with the modulation index, $\beta = \Delta f / f_m$. Another type of modulation which is related to PM is delay modulation, DM, which is a delay, $d(t)$, varied around a value, τ_0, according to a normalized delay modulation function, $m_d(t)$, and a maximum delay deviation $\Delta\tau$

$$d(t) = \tau_0 + \Delta\tau m_d(t). \tag{20}$$

This corresponds to PM with a normalized phase modulation function,

$$m_p(t) = -m_d(t), \tag{21}$$

and the modulation index,

$$\beta = 2\pi f \Delta\tau; \tag{22}$$

that is, DM is the same as PM for which the modulation index, β, is proportional to the carrier frequency, f, so that, following Eq. (13), the sideband TFs can be written

$$G_k(f) = J_k(2\pi f \Delta\tau). \tag{23}$$

The last example of modulation described here is frequency shifting, FS, which is equivalent with PM using a linearly increasing phase modulation function,

$$\theta(t) = 2\pi f_m t, \tag{24}$$

where f_m is the frequency shift in Hz. Due to the wrapping property of the phase, this can be interpreted as an LPTV system. It completely suppresses the carrier signal and generates a single sideband TF; that is,

$$G_k = \begin{cases} 1, & k = 1 \\ 0, & k \neq 1 \end{cases} \text{ or } \begin{cases} 1, & k = -1 \\ 0, & k \neq -1 \end{cases}. \tag{25}$$

In order to demonstrate that FS actually is a type of PM, the frequency shift is denoted by f_m, the modulation frequency. In the current study only the basic LPTV elements FS, PM, and DM will be tested, but in some cases, they are cascaded with an LTI reverberation unit. Such a cascading does not affect the sideband TFs $G_k(f)$. More complex LTV components[19] would lead to frequency dependent sideband TFs. The number of significant sidebands does, however, increase with the modulation index, or the delay deviation, in a way similar to the basic PM and DM.

B. A linear periodically time-varying component in a feedback loop

The use of an LPTV component in an electroacoustic system in a room can be depicted schematically as in Fig. 1,

where the feedback TF is denoted $H(f)$. In the frequency-domain electroacoustic systems using LPTV components aim at smoothing the LTI part of the loop gain by sampling it at different frequencies in each round through the loop. Viewed in the time domain, the build-up of coloration tones is avoided by making signal components return with a different phase in each round-trip. Zadeh presented a criterion for the stability of LTV systems whereby a bounded input always leads to a bounded output signal.[20] A necessary and sufficient criterion is that the closed loop impulse response must be absolutely integrable for all values of t. Zadeh also generalized the Nyquist criterion to LTV systems. However, these criteria are not directly useful for a feedback loop in the form of an electroacoustic system in a room because the closed loop impulse response can generally not be derived. The complexity of the closed loop is evident from the relationship in Eq. (8) which demonstrates that a large number of new components will be generated for each round through the loop. If the feedback is via a direct-sound path, a theoretical analysis might be feasible; but when the feedback is via a diffuse-field RTF, statistical models are the only possibility. So far, no solutions have been found for such feedback loops. Despite the lack of theoretical models, the stability of a feedback loop with an LTV component can be measured. An observed overall increment, or decrement, of the output signal amplitude, respectively, reflects the stability or instability of the feedback loop. Examples of stable and unstable output signals from a feedback loop with an LPTV component are shown in Ref. 21.

1. Single-sideband components—Frequency shifting (FS)

FS has a single-sideband TF [see Eq. (25)] and a feedback loop using FS can be theoretically analyzed, as Schroeder has shown for a diffuse-field feedback RTF.[8] An input signal of frequency f_0 will be shifted to f_0+f_m, and its energy modified by $|S(f_0+f_m)|^2$ before returning to the microphone. Assuming that the successive samples of $S(f_0+if_m)$ are independent, the original signal power will, after N such round trips, be modified by

$$M_N=\prod_{i=1}^{N}|S(f_0+if_m)|^2. \tag{26}$$

Expressed in dB, and assuming N is large, this becomes

$$10\log M_N=\sum_{i=1}^{N}10\log|S(f_0+if_m)|^2 \approx N\overline{10\log|S(f)|^2}=N\cdot\overline{L}. \tag{27}$$

Stability requires that M_N converges to zero as N approaches infinity or, equivalently, that the mean of the loop power gain level is negative:

$$\overline{L}=\overline{10\log|S(f)|^2}<0 \ \text{dB}. \tag{28}$$

In Eq. (1), the quantity MLG was introduced to describe the loop gain. Schroeder showed that for a diffuse-field RTF, the relation between the MLG and the mean level is[8]

$$\overline{L}=\overline{10\log|S(f)|^2}=10\log\overline{|S(f)|^2}-2.5 \ \text{dB}, \tag{29}$$

which has the consequence, see Eq. (28), that the maximum possible MLG, or the GBI, is

$$\text{GBI}=10\log\text{MLG}_{\max}=L_{\max}+2.5 \ \text{dB}=2.5 \ \text{dB}. \tag{30}$$

Since, theoretically, FS completely smooths $10\log|S(f)|^2$, it is the most efficient feedback controlling LTV component.

The increase in GBI is the difference between the GBI with FS and the initial GBI (i.e., without FS). A typical initial GBI for feedback through a room is around -10 dB (with a larger bandwidth than the 4–5 kHz studied here) and increases in GBI of up to 12 dB have been measured using FS.[8] A larger loop gain irregularity leads to a lower initial GBI and, consequently, possibilities for even larger increases in GBI using FS.

Schroeder's experiments demonstrated an optimal value of the frequency shift, f_m, around 4/RT Hz.[8] The explanation for this observed optimal value of f_m is found in the frequency correlation function of an RTF. The quantity called the correlation distance, f_{corr}, is defined as the frequency for which the magnitude of the frequency correlation function is 0.5. For diffuse-field RTFs the expected value of f_{corr} has been derived[22] as

$$\langle f_{\text{corr}}\rangle=\frac{4.4}{\text{RT}}[\text{Hz}]. \tag{31}$$

The optimal value for the frequency shift, 4/RT Hz, as observed by Schroeder, is close to this expected value for f_{corr}. The frequency correlation function falls off rapidly at f_{corr}, but only slowly at higher values. Increasing f_m above this value should, therefore, not provide further improvements in the feedback control. For cases where $S(f)$ includes two cascaded diffuse-field TFs, no theoretical values for f_{corr} are available. Since a measurement of f_{corr} would be calculation intensive, the more easily measured quantity, $\Delta f_{\max}$, which is the average frequency distance between the local maxima of $|S(f)|$, can be used as an indicator of the value of f_{corr}. This is possible since the expected diffuse-field value of $\Delta f_{\max}$ is 4/RT,[17] which is close to the value in Eq. (31).

If f_m is smaller than f_{corr}, the correlation between successive samples of $S(f)$ will be high. If at the same time the loop gain is high, momentary level build-ups will occur. Consequently, although the system is perfectly stable from a theoretical point of view, it will still show periods of seemingly unstable behavior and might saturate the electronic components. These momentary level build-ups have been demonstrated both analytically[23] and with computer simulations.[24] Therefore, when testing stability, the results may indicate electronic component saturation rather than the true GBI. An increase in RT does not significantly influence the loop gain irregularity, P2M, as is seen in Eq. (3), but it does affect f_{corr}, as is shown in Eq. (31). As a result, only if f_m has a low value, should varying RT cause momentary level build-ups and degrade the FS performance.

2. Multiple-sideband components

When an LPTV system has multiple-sideband TFs, such as for PM, the summing of contributions from successive round-trips through the feedback loop becomes more com-

plicated than for FS, and no closed loop solutions for these cases have been found. Still, some qualitative discussion can be presented.

A distinct difference between FS with its single sideband and LPTV components with multiple sidebands, such as PM, is that some components generated during successive rounds of the feedback loop will always be shifted back to the carrier frequency, regardless of the sideband spacing. Therefore, it can be hypothesized that the number of sidebands with relatively high amplitudes is decisive for a multiple-sideband system since the larger the number of sidebands, the larger the proportion of sideband energy which will be transported away from the carrier signal frequency. This implies that the GBI value basically should increase with the modulation index, β, up to a theoretical maximum which could be expected to be the same as for FS, 2.5 dB. However, if the carrier suppression, CS, has a low value, it, rather than the number of sidebands, might be the limiting factor for the GBI value. The value of CS is an upper bound for the possible GBI increases; if, for example, a modulator suppresses the carrier by 2 dB, the GBI with the modulator could never be more than 2 dB higher than without the modulator. Furthermore, since there will be sideband components which will be shifted back to the carrier frequency, the possible GBI increase will be even lower than the CS value. A complicating factor, however, is that for sinusoidal PM, positive and negative sidebands of odd numbers will have opposite signs. Consequently, the first sidebands will always generate components of opposite signs, and if these two sideband components are correlated, a partial cancellation will occur when they are shifted back to the carrier. The first two sideband components are correlated if the modulation frequency, f_m, is below $f_{\text{corr}}/2$, and interestingly, this could suggest that the performance of PM with low modulation frequencies could be less limited by the value of CS than PM with high modulation frequencies.

For sinusoidal PM a modulation index, β, which is larger than 2 rad guarantees that the value of CS, which is $-20\log J_0(\beta)$ according to Eqs. (15) and (13), is larger than 8 dB. The first two values of β for which CS is infinitely high are 2.4 rad and 5.5 rad, of which 2.4 rad has been suggested to be an optimal value for PM in previous studies, as reviewed in the Introduction. The discussion above suggests that there is no optimal value of β, except if the CS is low for certain values of β, and as a result cause a performance degradation for the modulator. The first minimum of CS, 7.9 dB, occurs at $\beta=3.8$ rad and the behavior of GBI around this value will be determined by whether CS, or simply the value of β, is the limiting factor.

It was argued in Sec. I B 1 that, for FS, the frequency shift must be larger than f_{corr} to avoid temporary level build-ups, but for LPTV components with many sidebands, the modulation frequency can probably be significantly lower without causing such build-ups since the many sidebands are spread over a wider frequency range.

Using reverberation units in electroacoustic systems will cause increased irregularities in $|S(f)|$ because of the convolution of the two reverberation processes[25] and, as a result, a lower initial GBI. In such cases feedback control by LTV components that smooth the irregularities may give large GBI increases. The value of f_{corr} for $S(f)$ can also be expected to be lower with reverberation units than without, which might increase the effectivity of low modulation frequencies.

Increased loop gain irregularity can also be expected in multi-channel RE systems with dependent channels. GBIs of -12 dB have been reported for multi-channel RE systems using time-varying reverberation units,[4] an improvement of 6 dB or more over conventional systems. Quantitative predictions of LTV system performance seem difficult to make without a more developed model of the feedback process than discussed above. It can be observed, however, that both the sideband TFs for PM and the statistics of a diffuse-field RTF are frequency independent [see Eqs. (3), (6), (13), and (31)]. As a result, PM offers constant performance across frequencies. On the other hand, DM has a modulation index which increases linearly with frequency, as is shown in Eqs. (22) and (23). Consequently, the degree of modulation may be excessive at high frequencies and insufficient at low frequencies.

C. Research issues to be addressed

In the previous paragraphs, issues have been raised related to the stability of feedback loops with LPTV components using the GBI value as a measure of performance.

One hypothesis is that the performance of such a feedback loop is determined by the number of strong sidebands for the LPTV component, which means that GBI is expected to increase as the modulation index, β, is increased.

A second hypothesis is that the increase in GBI can never be higher than a few decibels below the CS value. These first two hypotheses both predict an increasing GBI with increased β. In addition, for sinusoidal PM the GBI might show local minima around $\beta=3.8$ rad, at least for cases with low values of initial GBI. Such local minima might be more pronounced when f_m is greater than f_{corr}, and not so obvious if f_m is less than f_{corr}.

It was further hypothesized that a low modulation frequency might be more efficient in a feedback loop with a low f_{corr} such as when cascaded reverberation units are used, than in feedback loops with a high f_{corr}.

Finally, it is hypothesized that GBI is not highly dependent on f_m as long as the LPTV component has many strong sidebands. For LPTV components with few sidebands, the performance might improve with increased modulation frequency up to f_{corr} of the loop gain.

All GBI results are expected to vary significantly between individual examples of $S(f)$, but the hypothesized relationships discussed above should apply to GBI results averaged over many examples of $S(f)$, or channels.

The aim of the experiments in this study is to address these issues and test the suggested hypotheses using PM as the primary example of an LPTV component.

II. IMPLEMENTATION AND EXPERIMENTS

FS, PM, and DM were tested in a feedback loop, as is illustrated in Fig. 2. The various experimental configurations

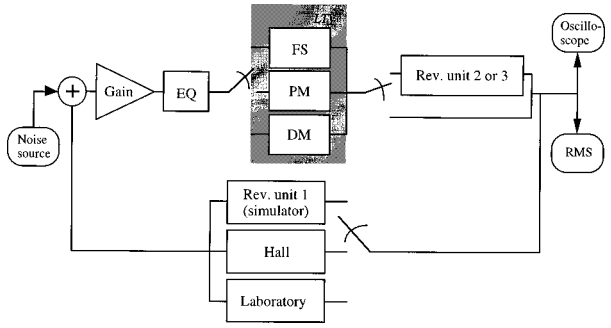

FIG. 2. Schematic view of the feedback loop used in the experiments indicating the tested configurations. All filter components, represented by rectangular boxes, outside the gray area are LTI filters. The equalizer, EQ, was left out for some of the configurations which used PM. Furthermore, some DM configurations also used a high-pass filter at 500 Hz cascaded with the EQ. The output signal from the feedback loop was monitored using an oscilloscope and an rms meter.

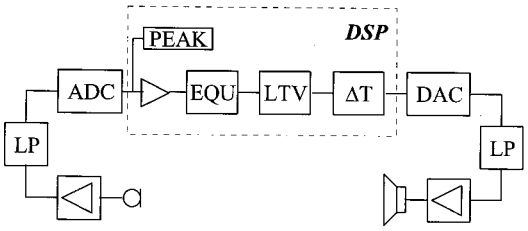

FIG. 3. The electronic components of the electroacoustic channel used in the experiments.

are detailed in Table I. The feedback TF was either a Yamaha SPX990 reverberation unit with an RT of 1.5 s (Rev. unit 1), one of four different channels in a standard 240-m^3 rectangular laboratory with an RT of 1.0 s, or one of four different channels in a small 5000-m^3 concert hall with an RT of 1.6 s. The RT of the lab could be increased to 9 s by removing absorption material. All microphones were positioned in the diffuse-field relative to the loudspeakers and the direct sound was further reduced by aiming the small two-way loudspeakers away from the omnidirectional microphones.

The electronic parts of the electroacoustic channel are shown schematically in Fig. 3. It consists of anti-aliasing and reconstruction filters, AD converter (ADC) and DA converter (DAC), a peak value meter, a gain control, an equalizer, a modulator, and a delay. All components between the ADC and the DAC in Fig. 3 were implemented on a Motorola DSP56001 digital signal processor using a sampling frequency of 16 kHz. For the cases in real rooms, transducers and amplifers were included in the electroacoustic channel, whereas for the purely electronic cases the microphone corresponded to an electronic summation.

The digital equalizer was implemented by cascading second-order filters.[26] The channels were individually equalized and $|S(f)|^2$, smoothed with a moving 1/3-octave window, was equalized to obtain a maximum output in all frequency bands. A DM was implemented by varying the length of a shift register. This was done by changing the placement of the output taps and reducing the time quantization effects by interpolation. With this method any specified modulation function could be used. PM and its special case of FS were implemented by generalizing the Hartley SSB modulator.[27] This method has been used previously in analog FS[28] and PM.[29] Detailed descriptions of the DSP implementations can be found in Ref. 30.

As is shown in Table I, for some of the purely electronic cases, the modulator was cascaded with a Yamaha SPX1000 reverberation unit (Rev. unit 2) having an RT of 1.5 s to mimic a sound system with external reverberation. For some cases in the laboratory, the modulator was cascaded with a Klark DN 780 reverberation unit (Rev. unit 3) with an RT of 1.9 s.

The experiments were performed as follows. The open loop gain $S(f)$ for the various systems under test (with the modulators operating at zero modulation) was measured with

TABLE I. The different configurations tested in the feedback loop, illustrated schematically in Fig. 2. The tested ranges of modulation frequencies f_m and modulation indices β are given. All cases except PM+Noeq(Lab9) used equalization in addition to the indicated LTI components. The modulation functions for PM and DM were all sinusoidal, but for the case PM(Hall) nonsinusoidal functions were tested as well, as is described in Sec. II.

Case	Modulator	No. of channels studied	Forward branch		Feedback TF		f_m [Hz]	β [rad]	Δt [ms]	Band width B [kHz]
			LTI components	RT [s]	Type	RT [s]				
FS	FS	1			Rev. unit 1	1.5	0.5–5	⋯	⋯	4
FS+Rev	FS	1	Rev. unit 2	1.5	Rev. unit 1	1.5	0.5–5	⋯	⋯	4
PM(Sim)	PM	1			Rev. unit 1	1.5	0.5–5	1.0–5.5	⋯	4
PM+Rev(Sim)	PM	1	Rev. unit 2	1.5	Rev. unit 1	1.5	0.5–5	1.0–5.5	⋯	4
PM(Hall)	PM	4			Hall	1.6	0.5–2	1.5–5.5	⋯	4.5
PM(Lab1)	PM	1			Lab.	1.0	0.5–4	1.7–3.2	⋯	2
PM(Lab9)	PM	4			Lab.	9.0	0.5–4	1.5–5.5	⋯	5
PM+Noeq(Lab9)	PM	4	No Eq. was used.		Lab.	9.0	0.5–4	1.5–5.5	⋯	5
PM+Rev(Lab1)	PM	4	Rev. unit 3	1.9	Lab.	1.0	0.5–4	1.5–5.5	⋯	5
DM	DM	4			Lab.	1.0	1	⋯	0.15–1	5
DM+HP	DM	4	HP (500 Hz)		Lab.	1.0	1	⋯	0.15–1	5
DM+Rev	DM	4	Rev. unit 3	1.9	Lab.	1.0	1	⋯	0.15–1	5
DM+Rev+HP	DM	4	Rev. unit 3 +HP (500 Hz)	1.9	Lab.	1.0	1	⋯	0.15–1	5

TABLE II. Initial GBI and some other loop gain parameters for the tested cases, as measured with zero modulation. Values within parentheses are theoretical values, as given by Eqs. (3), (6), and (31).

Case	No. of channels studied	RT [s]	Initial GBI [dB]	⟨GBI⟩	P2M [dB]	⟨P2M⟩	$\Delta f_{\max}$ [Hz]	$\langle f_{\text{corr}} \rangle$ [Hz]	$f_{\text{Schroeder}}$ [Hz]
FS/PM(Sim)	1	1.5	−9.4	(−7.7)	9.7	(9.4)	3.3	(2.9)	⋯
FS/PM+Rev(Sim)	1	1.5/1.5	−14.0	⋯	14.2	⋯	2.9	⋯	⋯
PM(Hall)	4	1.6	−8.0	(−7.8)	9.5	(9.5)	3.4	(2.8)	(35)
PM(Lab1)	1	1.0	−7.5	(−7.5)	⋯	(9.3)	⋯	(4.4)	(130)
DM(Lab1)	4	1.0	−8.7	(−7.5)	9.5	(9.3)	3.4	(4.4)	(130)
PM+Rev(Lab1)	4	1.0/1.9	−12.3	⋯	14.2	⋯	2.9	⋯	(130)
DM+Rev(Lab1)	4	1.0/1.9	−12.9	⋯	14.2	⋯	2.9	⋯	(130)
PM(Lab9)	4	9	−10.7	(−9.0)	11.2	(10.3)	1.1	(0.5)	(390)
PM+Noeq(Lab9)	4	9	−17.2	(−9.0)	18.7	(10.3)	1.1	(0.5)	(390)

an MLS impulse response measurement system. From the measured loop gain the MLG, P2M, and initial GBI were calculated using Eqs. (2) and (5), and $\Delta f_{\max}$ was estimated by counting the local maxima of $|S(f)|$. Then the loop was closed and the GBI measured for the various systems, operating both at zero modulation and at different modulation settings. The system under test was excited, as shown in Fig. 2, by a noise generator either added into the loop electronically, for the purely electronic cases, or by using a separate loudspeaker for the cases in real rooms. After the excitation was turned on, the electronic gain in the loop was adjusted digitally in steps while the output level of the time-variant system was monitored. The lowest MLG which caused a systematic level increase after the initial build-up was interpreted as the GBI. The result could be determined with an accuracy of about 0.1 dB.

It might be suspected that the performance of a time-varying system would be sensitive to when the system was excited. In the experiments the excitation signal, the excitation times and the initial conditions of the system turned out to have no influence on the GBI values as has also been previously observed in computer simulations.[21] Measurements repeated with longer time intervals usually gave GBI values within 0.1 dB.

A selection of modulation frequencies, f_m, and modulation indices, β, were tested in the experiments, as is shown in Table I. Most of the results were obtained with sinusoidal modulation functions, but for PM(Hall) three multi-tone functions were also investigated: (1) a triangular function (denoted below as Tri), which has lower maximum frequency deviation than an equivalent sinusoidal; (2) a ''soft-triangular'' function (denoted below as TriSoft) synthesized by two frequency components which also gives lower maximum frequency deviation but smoother phase transitions; and (3) several pseudo-random multi-tone functions (denoted below as PMR) made up of eight partial tones.

III. RESULTS FROM THE EXPERIMENTS

Table II shows the measured values of RT, initial (time-invariant) GBI, loop gain irregularity P2M, and $\Delta f_{\max}$ for the different experimental configurations. The results for the hall and for the laboratory are mean values averaged over four channels. Also presented in Table II are the theoretical diffuse-field results ⟨GBI⟩, ⟨P2M⟩, $f_{\text{Schroeder}}$, and $\langle f_{\text{corr}} \rangle$, as given by Eqs. (3), (6), (12), and (31), for the cases without cascaded reverberation units. All cases, except one, displayed values of P2M and GBI close to the theoretical diffuse-field values. The one exception was the case in the laboratory with long RT and no equalization of $|S(f)|^2$, which showed a much higher value of P2M, and a corresponding lower initial GBI, than the theoretical values. This deviation was caused partly by insufficient modal overlap below 390 Hz (see $f_{\text{Schroeder}}$ in Table II) and partly by excessive absorption above 1 kHz.

As expected, the value of P2M was larger with a cascaded reverberator than without. Furthermore, $\Delta f_{\max}$ was reduced by the cascading of the reverberator and, as discussed in Sec. I B 1, the correlation distance, f_{corr}, is correspondingly expected to be reduced.

A. Frequency shifting (FS)

The GBI results for FS in the simulator, and FS cascaded with a reverberator in the simulator, are shown in Fig. 4. GBI increased rapidly as a function of frequency shift f_m, and for the lowest shifts, very large momentary level increases occurred and saturated the equipment. In theory, GBI may, therefore, be higher than presented.

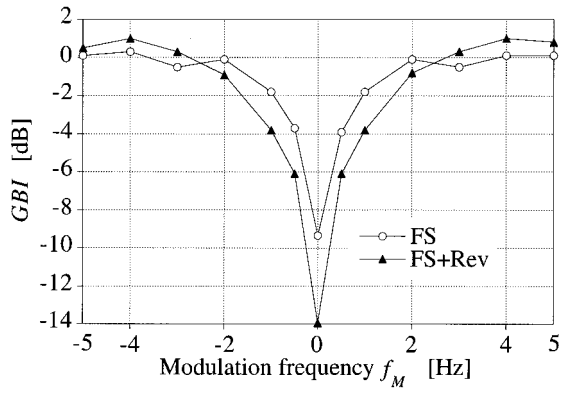

FIG. 4. GBI results for FS presented as function of the frequency shift, or modulation frequency f_m, as measured in the purely electronic feedback loop. FS refers to FS alone and FS+Rev refers to FS cascaded with a reverberation unit.

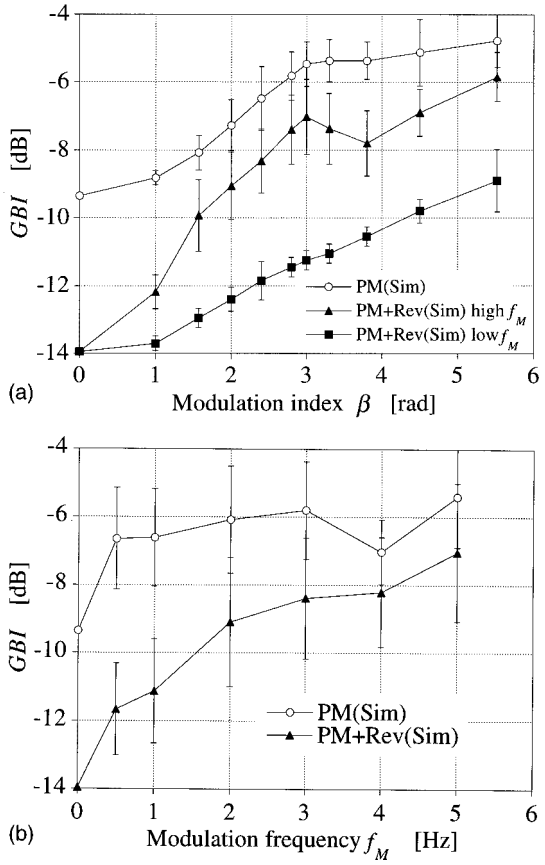

FIG. 5. GBI results for sinusoidal PM as measured in the purely electronic feedback loop. (a) GBI as a function of modulation index β. GBI results are mean values over six different settings of f_m for the case PM(Sim). For PM+Rev(Sim) GBI results are mean values over four different settings of f_m (high f_m) and over two settings of f_m (low f_m), respectively; (b) GBI as a function of modulation frequency f_m. GBI results are mean values over ten settings of β. Error bars indicate standard deviations.

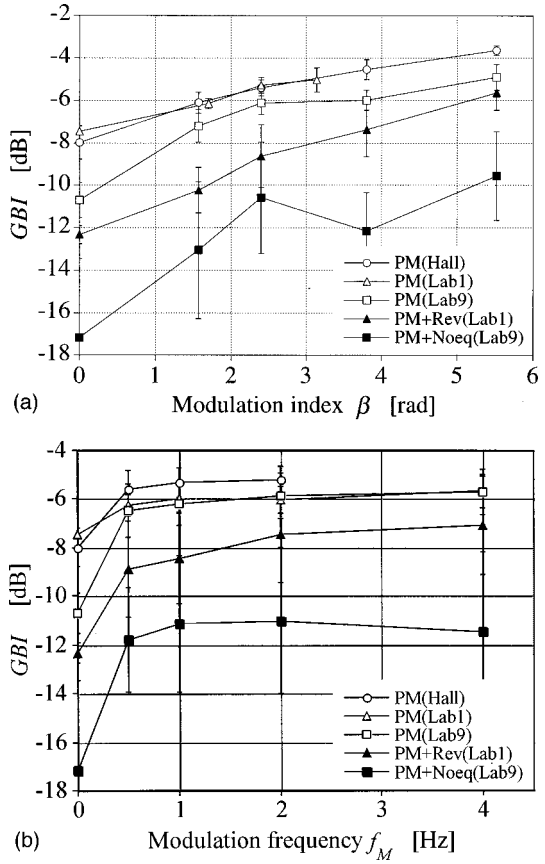

FIG. 6. GBI results for sinusoidal PM as measured in real rooms. (a) GBI as a function of modulation index β. GBI results are mean values over four different channels and over four different settings of f_m, except for PM(Lab1) where a single channel was tested. (b) GBI as a function of modulation frequency f_m. GBI results are mean values over four different channels and over four settings of β, except for PM(Lab1) (see above). Error bars indicate standard deviations.

For the FS without a cascaded reverberator, the maximum GBI was reached at an f_m of approximately 2 Hz, which is below the theoretical correlation distance, f_{corr}, of 2.9 Hz (see Table II). Adjusting f_m above 2 Hz did not systematically influence GBI. No notable difference between positive and negative values of f_m were observed, which agrees with Schroeder's theory and measurements.[8] Here, stable situations were observed with MLGs as high as 1.0 dB, confirming that GBI values close to the theoretical maximum, 2.5 dB, can be attained. This may well have been observed by others, but all previous results have been expressed as GBI increase without giving reference values of MLG.

The maximum GBI was approximately the same for the case of FS with, and without, a cascaded reverberation unit. The total GBI increase was, however, higher with the reverberation unit because of its lower initial GBI, which in turn, was the result of the larger loop gain irregularity P2M. Also, the maximum GBI was reached at a higher f_m with the reverberation unit (approximately 4 Hz) than without (approximately 2 Hz). This contradicts the hypothesis that the performance for a low value of f_m would be better in feedback loops with low f_{corr} (i.e., with the reverberation unit) than with high f_{corr} (i.e., without the reverberation unit). This observation will be discussed further in Sec. III B 2.

B. Phase modulation (PM)

In Fig. 5(a) and (b) GBI results for sinusoidal PM in the simulator, with and without a cascaded reverberation unit, are shown as a function of modulation index, β, and modulation frequency, f_m, respectively. The GBI results presented in Fig. 5(a) are mean values averaged over f_m, either over all six settings (0.5–5 Hz), for the case PM (Sim), over two settings (0.5–1 Hz) for the case PM+Rev(Sim) with low f_m, or over four settings (2–5 Hz), for the case PM+Rev(Sim) with high f_m. In Fig. 5(b), the GBI results are averaged over ten settings of β (1–5.5 rad). The error bars indicate standard deviations. Figure 6(a) and (b) presents the GBI results for sinusoidal PM in the real rooms as a function of β and f_m, respectively. GBI results in Fig. 6(a) are mean values averaged over four independent channels and four settings of f_m (0.5–4 Hz), except for the hall where 4 Hz was not used, and for PM(Lab1) which refers to a pilot experiment where only a single channel was tested. In Fig. 6(b) the GBI results are mean values averaged over four settings of β (1.5–5.5 rad).

TABLE III. The trend in GBI for cases with PM around β=3.8 rad, where CS has a local minimum of 7.9 dB. The cases are sorted in descending order by the clarity of the observed minima around β=3.8 rad.

Case	No. of channels studied	Initial GBI [dB]	GBI at β =3.8 rad [dB]	GBI increase at 3.8 rad [dB]	Trend in GBI around β=3.8 rad
PM+Noeq(Lab)	4	−17.2	−12.2	+5.0	Clear minimum
PM+Rev(Sim), high f_m	1	−14.0	−7.8	+6.2	Clear minimum
PM(Lab9)	4	−10.7	−6.0	+4.7	Flat (2.4 rad–3.8 rad)
PM(Sim)	1	−9.4	−5.4	+4.9	Flat (3.2 rad–3.8 rad)
PM+Rev(Sim), low f_m	1	−14.0	−10.6	+3.4	Increasing
PM(Hall)	4	−8.0	−4.6	+3.4	Increasing
PM+Rev(Lab1)	4	−12.3	−7.4	+4.9	Increasing. Flat for f_m=4 Hz
Range of values		9.2	7.6	2.8	

1. Influence of modulation index β, carrier suppression CS and initial GBI

For most cases using PM, both in the simulator as is shown in Fig. 5(a) and in the real rooms as is shown in Fig. 6(a), the GBI was increasing monotonically with β, however, for some cases, GBI either flattened out or had a minimum around β=3.8 rad. As discussed in Sec. I B 2, the carrier suppression CS for sinusoidal PM has a local minimum around β=3.8 rad. Consequently, the performance around this value of β reflects whether or not CS is a limiting factor for the modulator's performance. A minimum in GBI occurred for the cases PM+Rev(Sim) with high f_m [see Fig. 5(a)] and PM+Noeq(Lab9) [see Fig. 6(a)]. As is seen in Table II, these two cases also had the two lowest values of initial GBI, −17.2 dB and −14.0 dB, respectively. Consequently, both the hypothesis that GBI should increase with β, and that the carrier suppression CS should be limiting only for low values of initial GBI, are supported.

Nevertheless, the relationship between CS and the GBI results deserve further consideration. Table III summarizes the observations around β=3.8 rad, with the cases sorted by the clarity of the observed minimum in GBI around β=3.8 rad. The cases with the highest GBI increases at 3.8 rad are those with the most pronounced minima tendencies around 3.8 rad. This indicates that they are the most affected by the CS value. Furthermore, the two cases with the lowest GBI increases show no such minima. The only exception to this pattern is the case PM+Rev(Lab1) which had a high GBI increase but still showed no minimum around 3.8 rad, just a flat region for the individual setting of f_m=4 Hz. This offers some support for the hypothesis that, around β=3.8 rad, a low f_m might offer better performance than a high f_m. However, being based on a single case, no solid conclusion should be drawn.

Nevertheless, as is shown in Table III, the increase in GBI at β=3.8 rad fall within 2.8 dB across all cases. This is a smaller range than at other values of β and, as such, suggests that another mechanism is dominating at β=3.8 rad than at other values of β. This mechanism could be the carrier suppression, as was described above. The data in Table III suggest that the maximum GBI increase at 3.8 rad is 5–6 dB, which is 2–3 dB below the CS value (7.9 dB). For some cases, with high initial GBI, this is no limitation, but for cases with low initial GBI, a GBI increase of 5–6 dB is a limitation.

The optimal performance found by Nishinomiya[13] for values of β in the range of 2–3 rad is likely explainable by low initial GBI values. Furthermore, the increase in GBI observed here was higher for the cases with low initial GBI; that is, the worse the initial conditions were, the larger the improvement using PM became, as Nishinomiya's results also indicated. This illustrates that focusing only on the increase in GBI can be misleading as a measure of performance; the large improvements are not caused by the modulator *per se*, but by the poor initial conditions.

The results generally show that if the initial GBI is as low as −14 dB to −17 dB, GBI will have a minimum around β=3.8 rad. On the other hand, an initial GBI as high as −8 dB causes no such minimum. For the range of initial GBI between −12 dB and −9 dB, GBI may have a small minimum, or flatten out, for some channels and for some values of f_m. Consequently, only when the initial GBI is very low can an optimal value of β be found.

2. Influence of modulation frequency f_m and correlation distance f_{corr}

As can be seen in Figs. 5(b) and 6(b), for all cases without cascaded reverberation, GBI depended very little on the modulation frequency, f_m, above 0.5 Hz, even when this was clearly lower than the correlation distance f_{corr} (theoretically 0.5 Hz, 2.8 Hz, 2.9 Hz, and 4.4 Hz; see Table II). FS, with its single sideband, did not perform well for values of f_m which were lower than f_{corr}. The momentary level increases observed for FS did not occur for PM to the same degree. Together, these results support the hypothesis that the performance of modulators with many strong sidebands depends very little on f_m, and that f_m does not need to be higher than f_{corr}.

However, for some cases GBI depended on f_m. For the PM case in the simulator, a minimum in GBI at 4 Hz was observed for all values of β, as is evident in Fig. 5(b). This may have been caused by local maxima of $|S(f)|$ being close together for this specific sample of $S(f)$, so certain loop gain TFs might be sensitive to the value of f_m. The large standard deviations in Fig. 5(b), which might lead to suspicions about the significance of the minimum at 4 Hz, are caused by the dependency of the GBI on β. The minimum happened for every individual value of β, and should therefore be considered a real effect.

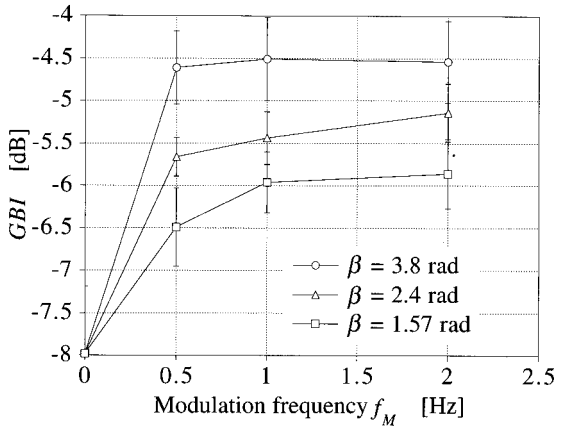

FIG. 7. GBI results for sinusoidal PM as measured in the hall, shown as a function of modulation frequency f_m for three individual settings of β. The GBI results are mean values over four different channels. Error bars indicate standard deviations.

GBI also depended on f_m when looking at individual values of β. In Fig. 7 the GBI in the hall is shown as a function of f_m for three settings of β, for each of which the mean values have been averaged over the four channels. For the two lowest settings, 1.57 and 2.4 rad, GBI increased with f_m. Furthermore, in the laboratory with long RT [i.e., case PM(Lab9)], GBI depended on f_m, for the lowest settings of β, in a manner similar to the GBI results shown in Fig. 7. Nishinomiya found optimal values for f_m in his PM experiments.[13] However, he used quite a low modulation index, 2.0 rad, in his experiments, which gives relatively few sidebands. These findings all support the hypothesis that, for low modulation indices (up to ca. 2–2.4 rad) which lead to few sidebands, GBI might increase with f_m, however, not up to the correlation distance f_{corr}.

For the two cases with cascaded reverberation, GBI depended on f_m, as is quite pronounced in Fig. 5(b) and slightly less so in Fig. 6(b). For the FS with cascaded reverberation, GBI also depended on f_m (see Fig. 4). These findings contradict the hypothesis that a low f_m is more efficient for cases with low f_{corr} (as with cascaded reverberation units) than for cases with high f_{corr} (as without reverberation units). It also contradicts the hypothesis that GBI does not depend on f_m when there are many sidebands (which occurs for high values of β) since the dependency on f_m was present for all modulation indices, as is evident for the PM+Rev cases in Figs. 5(b) and 6(b).

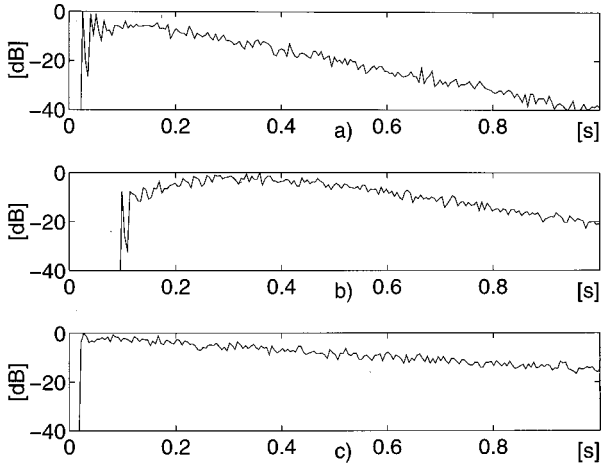

FIG. 8. Locally integrated open loop impulse responses for the cases: (a) Simulator; (b) Simulator with cascaded reverberation unit; (c) laboratory with long RT, one channel.

Figure 8(a)–(c) illustrates the initial parts of the squared and smoothed loop gain impulse responses for: (a) a single reverberation process with an RT of 1.5 s; (b) a cascade of two independent reverberation processes, both with RTs of 1.5 s; and (c) a single reverberation process with an RT of 9 s. The figure illustrates the two primary changes of the open loop impulse response when a reverberation unit is cascaded: an increased direct sound delay and a more gradual build-up process. This suggests that an explanation for the findings for the cases with cascaded reverberation units could possibly be found by studying the build-up processes of the loop gain functions. Further studies are needed to find out if these, or other properties of cascaded reverberation processes might explain the findings here.

3. Influence of reverberation time RT

The experimental configurations without cascaded reverberation units, but with loop gain equalization, were three different rooms and the electronic simulator. These had RT values 1.0 s [PM(Lab1)], 1.5 s [PM(SIM)], 1.6 s [PM(Hall)], and 9 s [PM(Lab9)]. The results for these four cases in Figs. 5(a) and 6(a) show GBI values all within 1.5 dB for any $\beta>2$ rad, with the case with the longest RT displaying the lowest GBI values. Since the initial GBI values differ as much as 3.2 dB, the performance without modulators varied more than with modulators. This suggests that the initial conditions of the feedback loop depend on the room's RT, but that differences in GBI using modulators are primarily a consequence of the initial conditions.

This supports Schroeder's theory for FS which predicts that there is no effect of RT on the GBI value. However, Nishinomiya,[13] Tilse,[10] and Peško[11] have all concluded that a longer RT would give a larger GBI increase. Their observations may have been correct, but the explanations were possibly misguiding since the reason for the dependency on RT likely was not the increase of RT *per se*, but rather the lower initial GBIs. In typical rooms with RTs from 0.5 to 1.5 s, no clear RT dependence was demonstrated in the earlier studies; only rooms with higher RTs showed larger GBI increases and these rooms were similar to the laboratory used here without employing loop gain equalization. These earlier results with GBI increases of 7–10 dB are consistent with the results in Fig. 6(a) for the case without equalization [PM +Noeq(Lab9)]. This large GBI increase was caused by a low initial GBI, which in turn was a consequence of that the Schroeder frequency was so high that the diffuse-field conditions not were fulfilled in the whole frequency range measured. In conclusion, the results here show that the initial GBI can depend much on RT, and accordingly, the increase in GBI can depend on RT. This dependence should, however, not be interpreted as a difference in the modulator's performance, only as a difference in initial conditions.

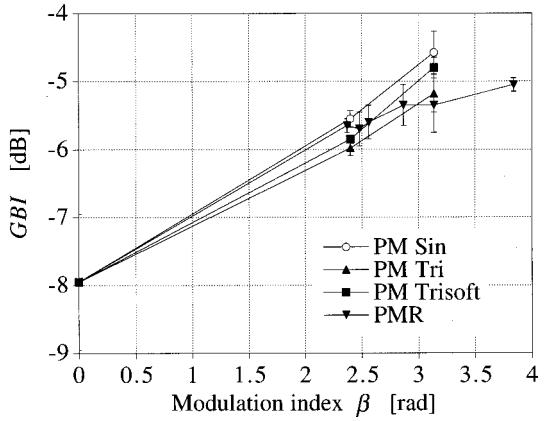

FIG. 9. GBI as function of modulation index β for PM with different modulation functions as measured in the hall. The GBI results are mean values, averaged over two channels, and over the values 0.5 and 1 Hz for f_m, except for the multitone function which used six different functions with a modulation period of 2 s.

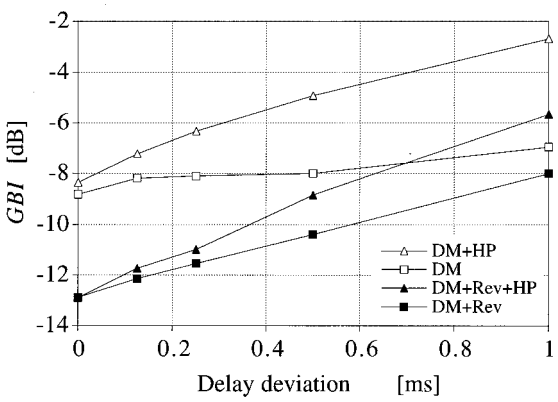

FIG. 10. GBI results for sinusoidal DM as measured in the laboratory. GBI is shown as a function of delay deviation with a modulation frequency of 1 Hz. The GBI results are mean values over four different channels. Standard deviations for the mean GBI values are given in Table IV.

4. Maximum GBI and robustness

The theoretical GBI limit of 2.5 dB for FS is expected to apply to multiple-sideband systems as well, even if the maximum GBI observed here never exceeded −4 dB. A GBI as high as −1 dB has been reported with PM in a simulator feedback loop with a lower bandwidth.[21] Increasing β above 4.5–5.5 rad might give larger GBI values since an increasing trend is observed for the highest settings of β in Figs. 5(a) and 6(a). However, because of the very unnatural sound for the highest values of β, the results reported here should be seen as providing practical limits. Increasing f_m above 4 or 5 Hz is not expected to offer any further improvement in GBI since the results in Figs. 5(b) and 6(b) show very little dependence on f_m above 0.5 Hz.

The use of PM always resulted in higher GBI than without PM. PM is therefore evidenced to be a robust method for increasing GBI. Still, for some individual channels, certain values of f_m might give poor performance.

An important step toward achieving robust functioning is to optimize the time-invariant part of the system, such as by equalization. This will reduce the loop gain irregularity and potentially result in a GBI which increases monotonically with increased modulation index. As is indicated by the low standard deviations across different channels and across modulation frequencies for cases without cascaded reverberation units and with loop gain equalization in Figs. 5(a) and 6(a), the resulting GBI value should be possible to predict within approximately 2–3 dB. In Figs. 5(a) and 6(a), the larger variance for the cases with a cascaded reverberator compared to the cases without a cascaded reverberator is primarily caused by the dependence on f_m.

Even if irregular loop gain functions gave large GBI increases, cases with lower GBI increases reached higher absolute GBIs. This also supports the need for equalization of the time-invariant system before employing LTV components. However, finding automated methods for this is a separate, and substantial, task. The loop gain irregularities might partly be caused by frequency response variations of the transducers. These frequency response variations should be as small as possible in order to minimize the need for equalization.

5. Nonsinusoidal modulation functions

Nonsinusoidal PM functions were tested in the hall. The GBI results shown in Fig. 9 demonstrate small differences between the various modulation functions. The range of modulation indices used in the experiments was, however, quite small, and a single modulation frequency was tested. Although the various nonsinusoidal functions exhibit different phase and frequency deviations, and consequently also different sideband distributions, the main character of the sideband pattern is the same for the nonsinusoidal and the sinusoidal modulation functions. Tilse and Peško studied PM using noise as a modulation function, but reported results which were comparable to the sinusoidal functions.[10,11] Based on these observations, the value of the modulation index seems to be the most influential factor for the performance of PM, regardless of the type of modulation function.

C. Delay modulation (DM)

The GBI results using DM in the laboratory with an RT of 1.0 s are presented in Fig. 10. All GBI results are mean values averaged over four different channels for $f_m = 1$ Hz, and standard deviations are given in Table IV. In the configurations using DM, instability consistently occurred at low signal frequencies, which contrasted with the results using PM. Consequently, DM results in poor performance at low signal frequencies. The spread in GBI between channels was large, as is illustrated by the large variance across channels

TABLE IV. The standard deviations for the mean values of GBI for sinusoidal DM, presented in Fig. 10.

	Standard deviation [dB]				
	Delay dev.				
Case	0 ms	0.15 ms	0.25 ms	0.5 ms	1 ms
DM+HP	0.44	0.54	1.41	1.52	0.56
DM	0.99	1.55	1.67	1.67	1.67
DM+Rev+HP	1.31	1.88	1.36	0.75	1.17
DM+Rev	0.56	1.57	1.57	0.95	0.99

in Table IV. Filtering the channels with a high-pass filter at 500 Hz improved the performance substantially since DM gives very low phase modulation indices in the low frequency range. The same positive effect of high-pass filtering has been observed in computer simulations of DM in a feedback loop.[21]

When cascading a reverberation unit, case DM+Rev, the increase in GBI was somewhat higher than without the reverberation unit. This is due, in part, to an observed tendency of the initial instability frequencies to be higher with the cascaded reverberation unit than without it, and in part to the increased loop gain irregularity. However, the GBI for any given value of the delay deviation was still lower with the reverberation unit than without it.

The results for PM in the present study demonstrate that GBI for a known value of β can be predicted within 2–3 dB. That being the case, the performance of DM should be predictable from the value of β as a function of signal frequency, and this confirms that, as stated in the Introduction, PM is the type of modulation which gives most insight into the feedback issue.

IV. DISCUSSIONS

This study has focused on investigating PM since this offers valuable insight into feedback control, in general, using time-varying components. Practical systems rarely use PM, and instead use DM because of its easy implementation. It has, however, been argued here that the stability of an electroacoustic system using DM can be predicted by calculating the corresponding modulation index as a function of signal frequency, and uses the PM results for the stability prediction. Furthermore, systems might in practice use modulators or other time-varying components in much more intricate structures than those examined here. In such cases, highly frequency dependent properties might be displayed, but corresponding modulation indices can still be calculated. The PM results here provide a guide for the prediction of GBI even for such complex systems.

In most cases tested, the loop gains were equalized, giving P2M values which were close to the theoretical values for diffuse fields. It might be argued that electroacoustic systems will, in practice, always encounter feedback situations with very irregular loop gains as long as automated, adaptive equalization procedures are not employed. Furthermore, it might also be argued that modulation could be such an efficient tool for feedback control that the needs for loop gain equalization would be reduced. The experiments reported here have shown the benefits of equalization even when modulation is used. In addition, the findings also explain that contradictory results in previous studies likely result from the large P2M values in those studies.

In this investigation, only periodical modulation functions have been studied, whereas in practical applications nonperiodical modulation functions might be preferred from the point of view of sound quality. However, only small differences in GBI were found between sinusoidal and other periodical modulation functions, so nonperiodical modulation functions would not likely offer better performance in terms of GBI. Modern RE systems are invariably multichannel systems and often use cascaded reverberation units. This results in low initial GBIs, which might be the reason for their successful use of time-varying components. The possibly modulated sound may also be masked to a high degree since the contribution from RE systems is always lower in level than for sound reinforcement systems, and these systems aim at enhancing the already irregular and diffuse reverberation component of the sound field.

Despite its shortcomings at low frequencies, DM of some kind is often used in RE systems because of its easy implementation. DM also seems to be subjectively efficient since the audibility for frequency deviation decreases with increasing signal frequency.[31] If low frequency feedback control could be handled by other means, for instance, by adaptive equalization or time-domain cancellation,[32] DM could provide robust and inaudible feedback control at medium-to-high frequencies. The degradation in sound quality might also be minimized by using a low f_m and the results presented here indicated efficient functioning already from 0.5 Hz. Values of f_m around 4–5 Hz tend to be the most audible ones, at least for modulators without feedback loops[31] which is unfortunate for FS which tends to need frequency shifts in that frequency range when used in smaller halls.

In spite of their wide use in RE systems, time-varying components are not currently general tools for feedback control in sound reinforcement systems due to their negative effects on the sound quality. The risk that colored sound will emerge and result in ringing tones when a system is close to instability seems to be preferred over the risk for modulated sound which can occur using time-varying components. Studies of gain before instability, as reported here, provide valuable insights into the use of time-varying components for feedback control. However, system performance should ultimately be measured in terms of sound quality at levels used in practice. A preliminary study of subjective effects related to this investigation is reported in Ref. 33. The time-varying components which provide the highest GBI are not necessarily subjectively superior to those with lower GBI. Therefore, the basic methods investigated here may not be suited for use in practical systems, and some commercial systems claim the use of more refined techniques which minimize negative subjective effects. However, the stability of any linear, time-varying system used for feedback control, however complex it may be, should be possible to explain using the concepts introduced and applied in this paper.

V. CONCLUSIONS

Linear time-varying (LTV or LPTV) components can be used to control feedback loops which have irregular open loop gain magnitude, such as electroacoustic systems in rooms. LTV systems avoid a build-up of coloration tones in the frequency domain by smoothing the loop gain, and in the time domain by varying the phase of the loop gain. The theoretical foundation of LTV components is well established but their use in feedback loops is insufficiently covered and theoretical stability analyses have been done only for frequency shifting (FS).

Experiments were carried out by measuring gain before instability (GBI) with FS, phase modulation (PM) and delay modulation (DM) combined in single-channel feedback loops with three different systems: a reverberation unit simulating a real room, a rectangular laboratory, and a small concert hall. In the simulator, the modulators were also tested with cascaded electronic reverberation.

Measurements in this investigation confirm the existing theory for FS. GBIs as high as 1 dB were observed, which is close to the theoretical maximum of 2.5 dB. Although FS is the most efficient LTV component, frequency shifts lower than the correlation distance f_{corr} of the loop gain gave large momentary level increases.

For multiple-sideband components, such as PM, the maximum possible GBI should also be 2.5 dB. Such high values were never attained in this study, but GBI increased monotonically with the modulation index, β, for most cases. However, cases with large loop gain irregularities, with an initial GBI (without modulation) on the order of -14 dB or lower, had a reduced GBI value around $\beta=3.8$ rad, where the carrier suppression (CS) is low. Consequently, optimal values of β are found only for cases with such irregular loop gains. The maximum GBI results attained were approximately -4 dB, and higher values of GBI might be achieved using higher values of β than were tested here.

For all PM cases without cascaded reverberation, GBI depended very little on the modulation frequency, f_m, above 0.5 Hz even in the cases where the value f_m was far below f_{corr}. Compared with FS, modulators with many sidebands seem to make it possible to choose a much lower value of f_m. However, for modulators with low values of β (lower than 2–2.5 rad) and, correspondingly, with few sidebands, the GBI values did depend on f_m.

For all PM cases the GBI increases were larger with cascaded reverberators than without due to the larger irregularity of the loop gains and the lower initial GBI. However, only for FS did the absolute GBI reach the same level with a cascaded reverberator as without. The cases with cascaded reverberators demonstrated a dependency on f_m which could not be explained satisfactorily. Further studies are needed to explain these findings.

No principal effect of RT was found for PM, which supports Schroeder's theory for FS. Previous investigations found greater increases in GBI for cases with longer RT but these findings were re-explained as being caused by increased loop gain irregularities due to insufficient diffuse-field conditions in the rooms tested. This suggests that the initial conditions of a feedback loop depend on the room's RT, but that differences in GBI using modulators are primarily a consequence of the initial conditions. Consequently, LTV, or LPTV, system performance should be measured in terms of GBI rather than GBI increase.

Using nonsinusoidal, periodic phase modulation functions gave similar GBI results as the sinusoidal functions.

DM is PM with a frequency dependent β. By calculating the corresponding β for DM at all signal frequencies, all results from the PM can also be used for DM. DM, as used here, gives little protection against instability for low signal frequencies but can be very efficient at controlling instability at high frequencies. This was confirmed by the results for the cases which used high-pass filtered loop gain functions at 500 Hz.

Equalization of a time-invariant system before employing LTV components improved robustness as was demonstrated by decreased differences in GBI across channels.

The results and conclusions in this study, focusing on the GBI value for PM, provide insight into the mechanisms of feedback control with LTV components. However, the LTV components providing highest GBI are not necessarily subjectively superior, making it an important topic for further studies. System performance should ultimately be measured in terms of sound quality at levels used in practical installations. In addition, systems which are more complex need to be studied. The findings in this study should provide a foundation for such future work.

ACKNOWLEDGMENTS

The authors wish to express their thanks to Professor Mendel Kleiner for support and discussions, and the School of Music and Musicology in Gothenburg who kindly gave access to their concert hall. This project received support from the Swedish Natural Science Research Council, the Johnson Foundation, the Nordic Academy for Advanced Study, and the Norwegian Research Council.

[1] W. Bürck, ''Massnahmen und Verfahren zur Verhütung der akustischen Rückkopplung,'' Frequenz **4**, 161–166 (1950).
[2] A. J. Berkhout, ''A holographic approach to acoustic control,'' J. Audio Eng. Soc. **36**, 977–995 (1988).
[3] W. R. Bray, ''Method and apparatus for increasing perceived reverberant field diffusion,'' U.S. Patent 4,727,581 (1988).
[4] D. Griesinger, ''Improving room acoustics through time-variant synthetic reverberation,'' presented at the 90th Convention of the Audio Engineering Society, J. Audio Eng. Soc. (Abstracts) **39**, 380 (1991), preprint 3014.
[5] W. C. J. M. Prinssen and M. Holden, ''System for improved acoustic performance,'' Proc. Inst. Acoust. **14**, 93–101 (1992).
[6] W. Ahnert and W. Reichardt, *Grundlagen der Beschallungstechnik* (S. Hirzel Verlag, Stuttgart, 1981).
[7] M. R. Schroeder, ''Improvement of acoustic feedback stability in public address systems,'' Proc. of the 3rd International Congress on Acoustics, pp. 771–775, Stuttgart (1959).
[8] M. R. Schroeder, ''Improvement of acoustic-feedback stability by frequency shifting,'' J. Acoust. Soc. Am. **36**, 1718–1724 (1964).
[9] E. Tapio, ''Frekvensforflytning i lydforsterkningsanlegg,'' Master's thesis, Dept. of Telecommunications, Norwegian Institute of Technology (1965), in Norwegian.
[10] U. Tilse, ''Messung der akustischen Rückkopplung mit Phasenmodulation,'' Diplomarbeit, Technische Universität Berlin (1975).
[11] F. Peško, ''Verringerrung der akustischen Rückkopplung durch Phasenmodulation,'' Proc. of the 9th International Congress on Acoustics, p. 764, Madrid (1977).
[12] L. N. Mishin, ''A method for increasing the stability of sound amplification systems,'' Sov. Phys. Acoust. **4**, 64–71 (1958).
[13] G. Nishinomiya, ''Improvement of acoustic feedback stability of public address system by warbling,'' Proc of the 6th International Congress on Acoustics, E-93-96, Tokyo (1968).
[14] R. W. Guclke and A. D. Broadhurst, ''Reverberation time control by direct feedback,'' Acustica **24**, 33–41 (1971).
[15] R. V. Waterhouse, ''Theory of howlback in reverberant rooms,'' J. Acoust. Soc. Am. **37**, 921–923 (1965).
[16] H. S. Antman, ''Extension to the theory of howlback in reverberant rooms,'' J. Acoust. Soc. Am. **39**, 399 (1966).
[17] M. R. Schroeder and K. H. Kuttruff, ''On frequency response curves in rooms,'' J. Acoust. Soc. Am. **34**, 76–80 (1962).
[18] T. A. C. M. Claasen and W. F. G. Mecklenbräuker, ''On stationary linear time-varying systems,'' IEEE Trans. Circuits Syst. **29**, 169–184 (1982).

[19] J. Dattorro, ''Effect design. Part I: Reverberator and other filters,'' J. Aud. Eng. Soc. **45**, 660–684 (1997).
[20] L. A. Zadeh, ''On stability of linear varying-parameter systems,'' J. Appl. Phys. **22**, 402–405 (1951).
[21] P. U. Svensson, ''Computer simulations of periodically time-varying filters for acoustic feedback control,'' J. Audio Eng. Soc. **43**, 667–677 (1995).
[22] M. R. Schroeder, ''Frequency-correlation functions of frequency responses in rooms,'' J. Acoust. Soc. Am. **34**, 1819–1823 (1962).
[23] F. Heiny, ''Auswirkung einer Frequenzversetzung in einem rückgekoppelten System,'' Frequenz **32**, 276–280 (1978).
[24] P. Svensson, M. Kleiner and B.-I. Dalenbäck, ''A study of periodically time-variant electroacoustic reverberation enhancement and public address systems,'' presented at the 93rd Convention of the Audio Engineering Society, J. Audio Eng. Soc. (Abstracts) **40**, 1062 (1992), preprint 3378.
[25] H. Kuttruff, ''Über die Frequenzkurven Elektroakustisch Gekoppelter Räume und ihre Bedeutung für die Künstliche Nachhallverlängerung,'' Acustica **15**, 1–5 (1965).
[26] J. L. Nielsen and B. Winsvold, ''Implementation of digital filters for reverberation enhancement systems,'' Proc. of the Nordic Acoustical Meeting, pp. 143–148, Århus (1994).
[27] S. Haykin, *Communication Systems*, 2nd ed. (Wiley, New York, 1983).
[28] M. D. Burkhard, ''A simplified frequency shifter for improving acoustic feedback stability,'' J. Audio Eng. Soc. **11**, 234–237 (1963).
[29] F. Peško, ''Beschreibung zeitvariabler Systeme zur Ermittlung der Stabilitätsgrenze bei akustischer Rückkopplung,'' Technischer Bericht nr. 152, Heinrich Hertz Institut for Schwingungsforschung, Berlin (1972).
[30] J. L. Nielsen, ''Control of stability and coloration in electroacoustic systems in rooms,'' Dr.ing. Thesis, Dept. of Telecommunications, Norwegian University of Science and Technology, Trondheim (1996).
[31] E. Zwicker and R. Feldtkeller, *Das Ohr als Nachrichtempfänger*, 2nd ed. (S. Hirzel Verlag, Stuttgart, Germany, 1967), pp. 66–68.
[32] A. Goertz, ''Einsatz von Digitalfiltern zur Unterdrückung von Rückkopplungen in Beschallungsanlagen,'' Proc. of DAGA, 247–250 (1993).
[33] P. Svensson, ''On Reverberation Enhancement in Auditoria,'' Ph.D. thesis, Dept. of Applied Acoustics, Chalmers University of Technology, Gothenburg (1994).

Time-delay estimation techniques applied to the acoustic detection of jet aircraft transits

Brian G. Ferguson
Maritime Operations Division, Defence Science and Technology Organisation, PO Box 44, Pyrmont NSW 2009, Australia

(Received 28 June 1996; revised 21 January 1999; accepted 22 January 1999)

Time-delay estimation techniques are used to observe the transits of jet aircraft. Noisy time-delay estimates are rejected by using a coincidence (or Boolean) detector. Cross correlating the beamformed outputs of two arrays of receivers leads to a significant improvement in detection performance when compared with the results of cross correlating the outputs of two single receivers. During the passage of a jet aircraft overhead, the differential time of arrival of the acoustic wave fronts at the receivers varies rapidly with time, and so the integration time for each time-delay estimate is required to be short. Also, the differential (Doppler) time scale compression between the received signals is required to be zero prior to cross correlation, otherwise the time-delay estimates will be in error. A digital time series interpolation technique, which is implemented using the discrete Fourier transform, enables the receiver waveform having the larger Doppler compression to be expanded (or time dilated) so that it has the same time base as the waveform from the other receiver. When the time scale factors of both receiver waveforms match, the cross-correlation function attains its global maximum value at a time displacement corresponding to the correct time delay. [S0001-4966(99)03105-7]

PACS numbers: 43.60.Gk, 43.28.Tc [JCB]

INTRODUCTION

Passive acoustic systems detect, classify, and localize a sound source by receiving the acoustic emissions radiated by the source and then processing the digital time series output data from one or more acoustic sensors. When the source is a turboprop aircraft, for instance, Ferguson and Quinn[1] showed that the aircraft's speed and range at the closest point of approach (localization parameters), together with the source (or rest) frequency of the propeller blade rate (a classification parameter), can be estimated by observing the change with time of the Doppler-shifted propeller blade rate. The technique involved narrow-band processing of the acoustic data from a single microphone located close to the ground. The narrow-band technique can be applied to other acoustic sources having tones in their source spectra such as helicopters and ground vehicles. However, the narrow-band technique cannot be applied to jet aircraft, as they radiate broadband acoustic energy free of tones requiring the use of other acoustic techniques to detect their transits. Time-delay estimation techniques are used to measure the time difference for an acoustic wave front to arrive at two spatially separated receivers. For the case of a broadband acoustic source and a nondispersive propagation medium, an estimate of the time delay can be obtained by cross correlating the receiver outputs and then measuring the time displacement of the maximum value of the cross-correlation function. This method is adopted here to observe the transits of jet aircraft. A similar approach was adopted by Dommermuth and Schiller[2] to localize aircraft.

Time-delay estimation theory has been applied previously to the localization and tracking of underwater acoustic sources using hydrophonic sensors.[3] The relevance of its application to the observation of jet aircraft transits using real microphone data is evaluated in this paper. Two original contributions presented here are the introduction of coincidence (or Boolean) detection to reject noisy time-delay estimates and the use of the discrete Fourier transform for differential Doppler compensation in the wideband cross-correlation processing of the sensor data. The differential Doppler effect arises when the source speed is comparable to the speed of sound propagation in the medium and the receivers are widely separated.

I. TIME-DELAY ESTIMATION

A. Background

Consider an acoustic signal that emanates from a point source and propagates through an acoustic medium, before being received at two spatially separated sensors—see Fig. 1. Assuming an isospeed propagation medium, the difference in the time of arrival of the signal at the two sensors is equal to the difference in the path lengths between the source and the sensors, divided by the constant speed of sound propagation in the medium. Thus, the signal and a delayed version of the signal, both of which are corrupted by noise, are received by the pair of sensors. An estimate of the time delay for an acoustic wave front to travel between the two sensor locations is provided by the time argument corresponding to the maximum value of the cross-correlation function (obtained by cross correlating the pair of sensor outputs).

Each receiver waveform has a signal component that originates from a common source and an additive noise component. The mathematical representation of this model is given by[4]

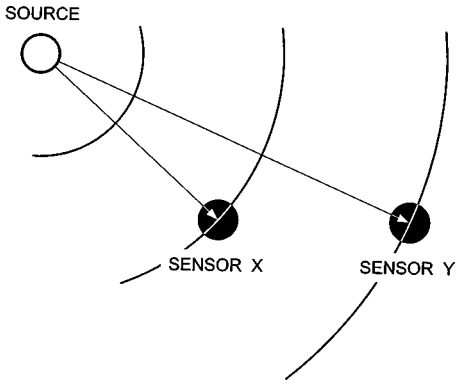

FIG. 1. Wave fronts propagating through an acoustic medium are received at spatially separated sensors.

$$x(t)=s(t)+n_x(t)$$
$$y(t)=s(t-\tau_d)+n_y(t), \quad 0\leqslant t\leqslant T, \tag{1}$$

where $x(t)$ and $y(t)$ denote the two received waveforms, $s(t)$ is the source-signal component at the receiver nearer to the source, $s(t-\tau_d)$ is the source-signal component at the other receiver which has been delayed by τ_d due to (nondispersive) propagation of the signal wave front between the two spatially separated receivers. The signal component is contaminated by additive noise at each receiver location. The noise waveforms at the respective receivers, denoted by $n_x(t)$ and $n_y(t)$, are assumed to be zero mean, stationary, Gaussian random processes which are mutually uncorrelated as well as being uncorrelated with the signal. The observation time, T, is assumed to be much larger than the value of the time delay parameter, τ_d. The model assumes that the time delay is constant, which requires the source to remain stationary relative to the sensors during the observation time interval. Finally, the relative attenuation in the signal strength due to the difference in path lengths between the source and receivers is assumed to be unity.

Techniques for estimating the differential time of arrival of an acoustic wave front at a pair of spatially separated sensors have been reviewed by Carter.[3,5] The simplest method for estimating the time delay is to compute the cross-correlation function, $R_{xy}(\tau)$, between the signal and its delayed version; the argument for which the cross-correlation function attains its maximum value corresponds to the time delay estimate, $\hat{\tau}_d$—see Fig. 2.

For the simple case where the contaminating noise terms are statistically independent, the cross-correlation function, $R_{xy}(\tau)$, for the received signals, $x(t)$ and $y(t)$, is given by

$$R_{xy}(\tau)=E[x(t)y(t+\tau)]=R_{ss}(\tau-\tau_d), \tag{2}$$

where $E[.]$ is the expectation operator and $R_{ss}(\tau)$ is the autocorrelation function of the signal, $s(t)$, transposed to have its peak value at $\tau=\tau_d$. Clearly, the peak value of the cross-correlation function occurs at the time delay $\tau_d=(\Delta d)/c$, where Δd is the path difference and c is the (assumed constant) speed of sound propagation in the medium.

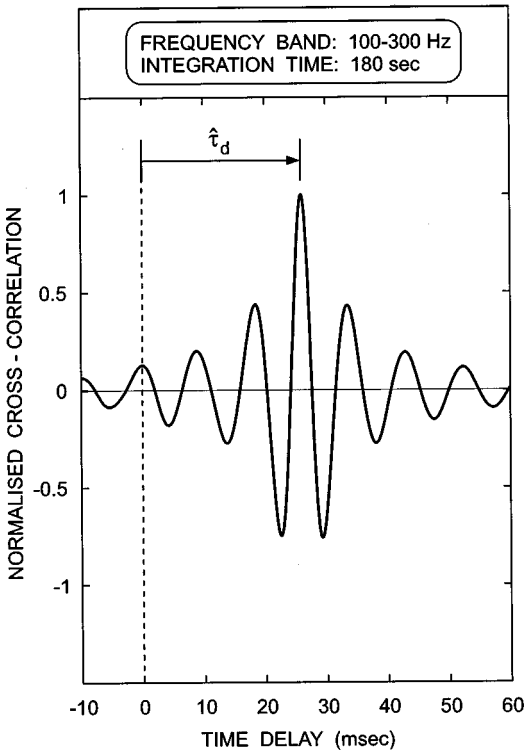

FIG. 2. The time-delay estimate corresponds to the time displacement of the peak in the cross-correlation function (or cross correlogram) obtained by cross correlating the outputs of two spatially separated receivers. In the present case, the outputs of two microphones, 29.5 ft apart, are cross correlated in the frequency band 100–300 Hz for 180 s during the static testing of a jet aircraft engine.

Alternatively, the cross-correlation function can be computed from the cross-spectral density function, $G_{xy}(f)$, of the received signals by using the Fourier transform relationship

$$R_{xy}(\tau)=\int G_{xy}(f)\exp(j2\pi f\tau)df, \tag{3}$$

where, for the model

$$G_{xy}(f)=G_{ss}(f)\exp(-j2\pi f\tau_d). \tag{4}$$

Hence, the time delay τ_d appears in the cross spectrum as a phase function which is given by

$$\phi_{xy}(f)=2\pi f\tau_d. \tag{5}$$

It can be seen that with either the time-domain or the frequency-domain approach, $R_{xy}(\tau)$ attains its maximum value when the argument $\tau=\tau_d$.

Since multiplication in one domain is a convolution in the transformed domain, it follows that

$$R_{xy}(\tau)=R_{ss}(\tau)\odot\delta(\tau-\tau_d), \tag{6}$$

where $\odot$ denotes convolution and δ denotes the delta function. This equation implies that the delta function is broadened by the Fourier transform of the signal spectrum. In the hypothetical case of white noise for which the autospectral density function is uniform over all frequencies by definition, the Fourier transform of the signal spectrum is a delta function, and no broadening occurs. For bandlimited white noise, the Fourier transform of the signal spectrum is a cosine func-

tion modulated by a sinc function, so that the broadening increases as the bandwidth decreases, that is,

$$R_{ss}=P_s\frac{\sin \pi B\tau}{\pi B\tau}\cos 2\pi f_0\tau, \tag{7}$$

where P_s is the signal power, B is the bandwidth, and f_0 is the center frequency. As the signal bandwidth becomes an increasingly smaller fraction of the center frequency, the peaks in the cross-correlation function tend to have the same amplitude, and so identification of the peak associated with the correct time delay becomes increasingly prone to ambiguity. In the limiting case of a vanishingly small bandwidth, the cross-correlation function is purely oscillatory, with a period equal to the reciprocal of the center frequency.

B. Variance of time-delay estimates

The Cramer–Rao lower bound is commonly used to set a bound on the error variance of the time-delay estimate. Maximum-likelihood time-delay estimator performance is asymptotically efficient in that it approaches the Cramer–Rao lower bound performance for sufficiently long integration times. During the transit of a jet aircraft, however, the time delay estimates vary with time, which necessitates a short integration time during which the time delay is assumed to be constant or else, only slowly varying. Maximum-likelihood time-delay estimation for short observation time intervals has been considered by Champagne *et al.*[6]

The variance of the time-delay errors about the true time delay is greater than, or equal to, the Cramer–Rao lower bound of the variance of the time-delay estimates, σ^2_{CR}, which is given by[4]

$$\sigma^2_{\mathrm{CR}}=\left\{2T\int_0^\infty (2\pi f)^2\frac{|\gamma(f)|^2}{1-|\gamma(f)|^2}df\right\}^{-1}, \tag{8}$$

where γ is the coherence function, whose magnitude squared is given by

$$|\gamma(f)|^2=\frac{G^2_{ss}(f)}{[G_{ss}(f)+G_{nn}(f)]^2}, \tag{9}$$

where $G_{ss}(f)$ is the signal autospectrum and $G_{nn}(f)$ is the noise autospectrum.

By assuming that the signal and noise are uncorrelated and are stationary random processes, it can then be shown that the Cramer–Rao lower bound for the variance of the time-delay estimate about the true value is given by[7]

$$\sigma^2_{\mathrm{CR}}\approx\frac{3}{4\pi^2T}\cdot\frac{1}{\mathrm{SNR}}\cdot\frac{1}{f_2^3-f_1^3}\quad \text{for SNR}\gg 1, \tag{10}$$

where T is the observation time and the signal and noise autospectra are assumed to have constant values (S_0 and N_0 W/Hz, respectively) over the frequency band extending from f_1 to f_2 Hz. In this case, the signal power $S=S_0(f_2-f_1)$ and the noise power $N=N_0(f_2-f_1)$, and so the signal-to-noise ratio, SNR, is equal to S_0/N_0. Thus, increasing the observation time, the frequency bandwidth, or the signal-to-noise ratio reduces the variance of the time-delay estimates. For the present application, the bandwidth is limited at high frequencies (>400 Hz) by the absorption of acoustic energy as the sound waves propagate through the atmosphere, and at low frequencies (<50 Hz) by the ambient noise (predominantly induced by wind flowing over the microphone).

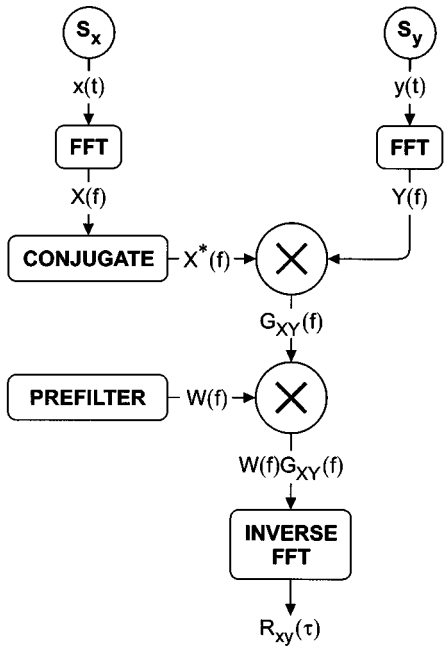

FIG. 3. Frequency-domain implementation of a generalized cross correlator.

C. Generalized broadband cross correlation

In practice, the cross-correlation function is estimated from data acquired during a finite observation time, T. Prior to computing the cross-correlation function, a generalized cross correlator prefilters the received signals to improve the accuracy of the time delay estimate, $\hat{\tau}_d$.

The generalized cross-correlation function, $R^{(G)}_{xy}(\tau_d)$, is given by[4]

$$R^{(G)}_{xy}(\tau)=\int_{-\infty}^{\infty}W(f)G_{xy}(f)\exp(j2\pi f\tau)df, \tag{11}$$

where $W(f)=H_x(f)H^*_y(f)$; $H_x(f)$ and $H_y(f)$ are the prefilter transfer functions, which must have identical phase characteristics, or equivalently, $W(f)$ is a real-valued function. Figure 3 is a block diagram showing the frequency-domain implementation of the generalized cross correlator.

Examples of various generalized cross-correlation weighting functions are:

$W_a(f)=1$, for the standard cross-correlation processor,
$W_b(f)=[G_{xx}(f)G_{yy}(f)]^{-1/2}$, for the smoothed coherence transform processor,
$W_c(f)=|G_{xy}(f)|^{-1}$, for the phase transform processor, and
$W_d(f)=|\gamma_{12}(f)|^2/|G_{xy}(f)|[1-|\gamma_{12}(f)|^2]$, for the maximum likelihood processor.

The signal-to-noise ratio, and hence the estimate of the time delay, can be improved by replacing each of the single sensors with an array of sensors, then cross correlating the beamformed outputs—see Fig. 4. With beamforming, or spatial filtering, the individual outputs of each of the array's

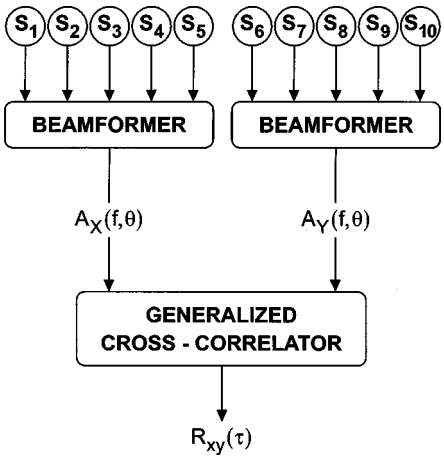

FIG. 4. Cross correlation of the beamformed outputs of two receiving arrays.

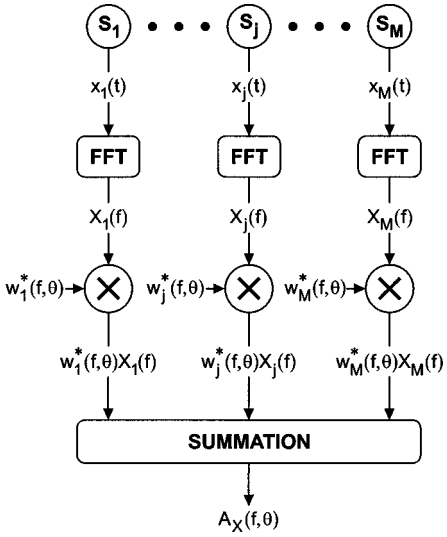

FIG. 5. Frequency-domain implementation of a spatial filter (or beamformer).

sensors are weighted before being summed. Figure 5 is a block diagram showing the frequency-domain implementation of a beamformer.

The output amplitude of the beamformer is given by[8]

$$A(f,\theta)=\mathbf{w}^H(f,\theta)\mathbf{X}(f), \tag{12}$$

where $\mathbf{w}(f,\theta)$ is the weighting vector for a frequency f and a beamsteer direction θ, the superscript H denotes transposition and complex conjugation, while $\mathbf{X}(f)$ is a column vector which has the complex narrow-band outputs of the receivers as its elements.

For a conventional frequency-domain beamformer, which is equivalent to an unshaded delay-and-sum beamformer in the time domain, the weight vector is given by

$$\mathbf{w}(f,\theta)=\mathbf{v}(f,\theta)/N, \tag{13}$$

where $\mathbf{v}(f,\theta)$ is the vector of phase delays required to bring the signal components of all the receiver outputs into phase prior to summation, and N is the number of receivers in the array. For a line array of equispaced receivers, the nth element of $\mathbf{v}(f,\theta)$ is given by

$$v_n(f,\theta)=\exp\left[-j2\pi(n-1)\frac{d}{\lambda}\cos\theta\right], \tag{14}$$

where d is the distance between sensors in the array, and $\lambda(=f/c)$ is the wavelength of the plane-wave arrivals.

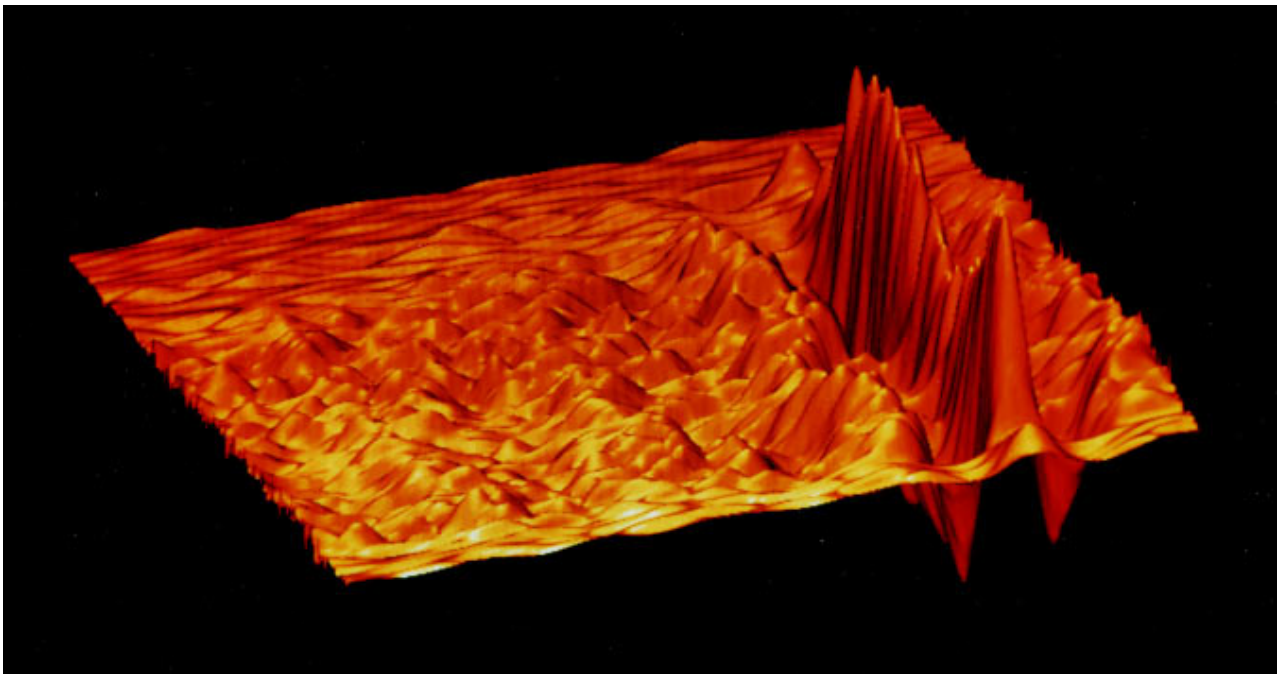

FIG. 6. Waterfall display showing the cross correlograms as a function of time over a period of 4 min. Each cross correlogram was computed after 14 integrations of the cross-spectral density function, corresponding to an observation period of 1 s. The x-axis represents the lag variable of the cross correlogram and the y-axis represents time.

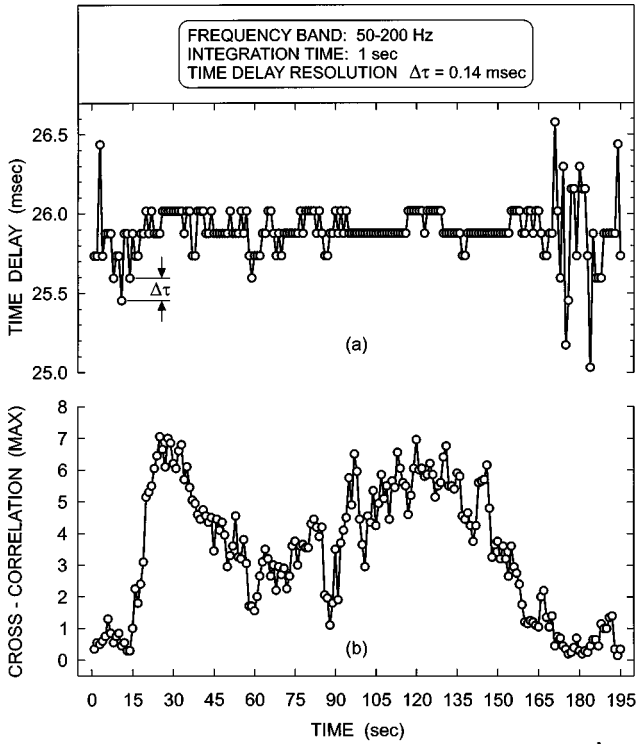

FIG. 7. Variation with time of (a) the time-delay estimates, and (b) the peak magnitude of the cross-correlation function. The acoustic source was a stationary jet engine undergoing a static operating test on the ground.

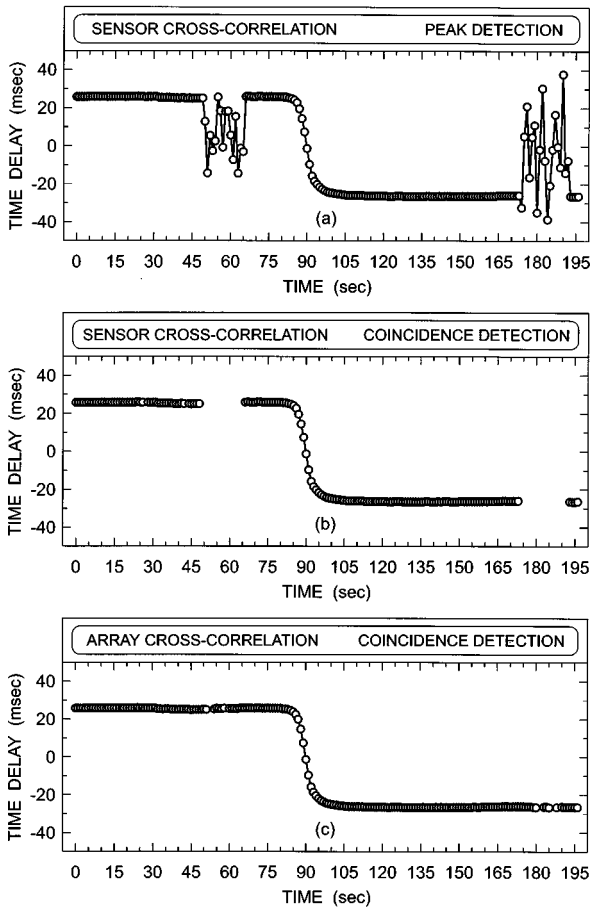

FIG. 8. Variation with time of the time-delay estimate obtained from the time displacement of the peak in the cross-correlation function for the outputs of (a) a pair of receivers over a single frequency band, (b) a pair of receivers over three overlapping frequency bands, then applying coincidence detection to the time displacements, and (c) a pair of receiver arrays over three overlapping bands, then applying coincidence detection to the time displacements. The acoustic source was a transiting jet aircraft traveling with a speed of 300 kn at an altitude of 1750 ft.

II. APPLICATION

A. Stationary jet

The outputs of two microphones are each sampled at a rate of about 7.1 kHz and then cross correlated [$W_a(f)$ equal to unity] with a cross correlogram being computed each second (that is, after 14 integrations of the cross-spectral density function) for a period of 4 min. The processing bandwidth is 50–200 Hz and the separation distance of the microphones is 29.5 ft. The source is a stationary jet engine undergoing a static test on the ground. Figure 6 is a surface plot of the cross correlograms as a function of time showing when the engine is operating (during which time the output of the cross correlator has a pronounced maximum at the time delay corresponding to the differential time of arrival of the signal wave fronts at the two microphones), and when the engine is powered down (during which time the output of the cross correlator is small due to the absence of the signal). The direction of the acoustic source is near forward endfire.

Figure 7 shows the variation of the time-delay estimates as a function of time, together with the magnitude of the peak in the cross-correlation function (displayed in Fig. 6) when the jet was operating. Small peak values in the cross-correlation function (at times 0–15 and 170–195 s) are associated with time-delay estimates having large variance, and conversely, large peak values in the cross correlograms (due to a high signal-to-noise ratio) correspond to time-delay estimates having small variance, which is consistent with Eq. (9). The time increment, $\Delta\tau$, of the time-delay estimates is equal to the reciprocal of the sampling rate, that is, $\Delta\tau = 0.14$ ms.

B. Transiting jet

For a moving source, the time-delay estimates vary with time, and so for a fast source like a jet aircraft, the observation interval, T, is (necessarily) required to be short. For example, Fig. 8(a) shows the time-delay estimates as a function of time during the transit of a jet aircraft flying with a speed of 300 kn at an altitude of 1750 ft. In this case, the microphone outputs are cross correlated over the frequency band 100–300 Hz, with the time delay associated with the peak in the cross correlogram being plotted each second. The microphones are 29.5 ft apart and aligned in the east–west direction. During the period 0–85 s, the aircraft approached from the east (corresponding to a maximum positive delay) and passed directly overhead (85–95 s). During the period 95–195 s, the aircraft departed to the west (corresponding to a maximum negative delay). A time delay of zero corresponds to the aircraft being equidistant from both sensors. The variability of the time-delay estimates is high when the noise is dominant, unlike the small variability of time-delay estimates associated with the aircraft track.

To remove the noisy time-delay estimates obtained by

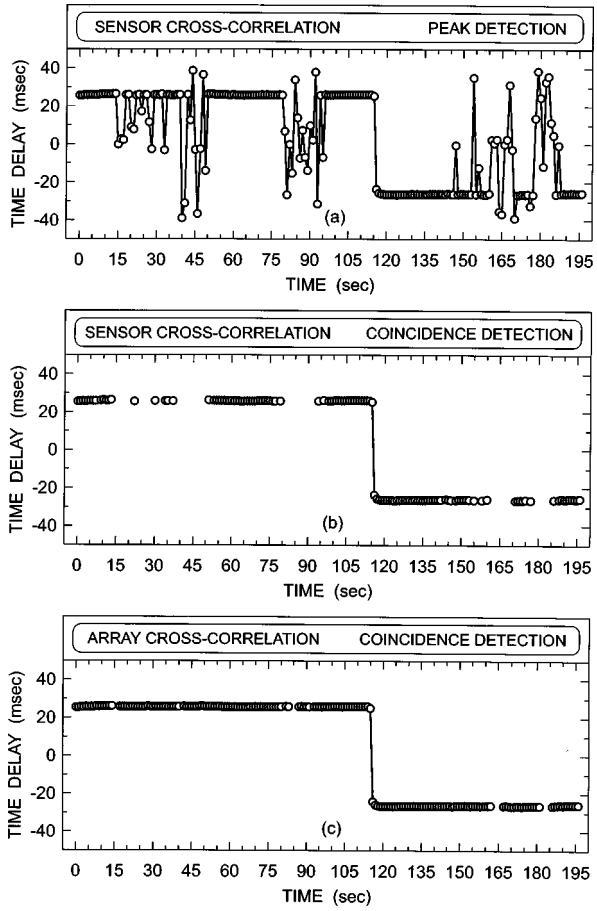

FIG. 9. Similar to Fig. 8 but the altitude of the aircraft was 300 ft.

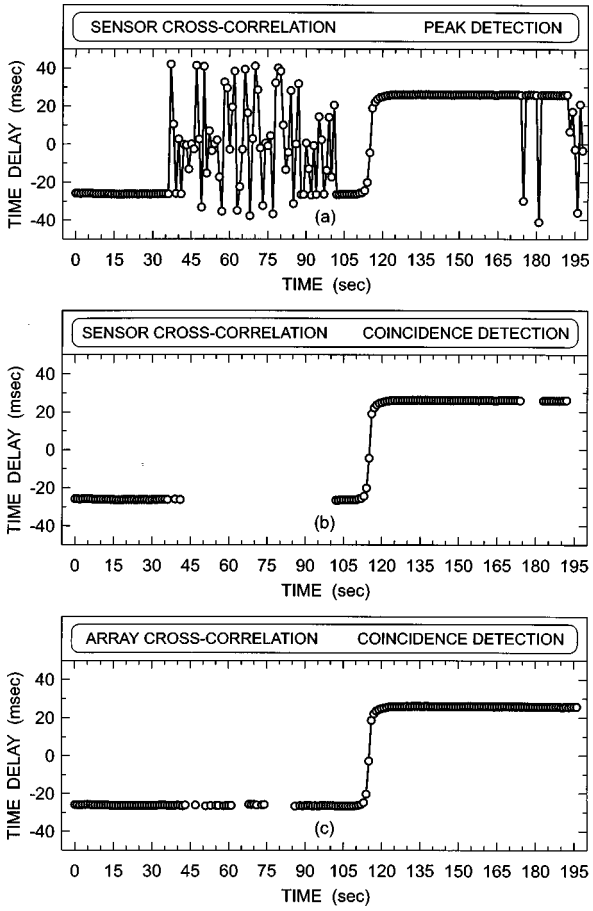

FIG. 10. Similar to Fig. 8 but the altitude of the aircraft was inbound from the opposite direction at an altitude of 1000 ft.

cross correlating the microphone outputs in the frequency band 100–300 Hz, additional cross correlograms are computed each second for two adjacent frequency bands: 50–200 and 200–400 Hz. A coincidence (or Boolean) detector is then applied to the time-delay estimates in all three frequency bands which results in the noisy time-delay estimates being eliminated. If the signal (from the jet) is present, then the time lags corresponding to the peak values of the cross correlograms for the three bands have the same value (within the time-of-arrival gate width of $\pm 3\Delta\tau$). When the signal is absent, the noisy time-delay estimates have different values in each of the bands, and hence, are rejected by the coincidence detector. Figure 8(b) shows that the effect of the coincidence-detection process is to eliminate the noisy time-delay estimates.

The adverse effect of noise on the time-delay estimation process can be reduced by replacing each single receiver with an array of receivers and then beamforming to improve the signal-to-noise ratio. When the beamformed outputs from two horizontal line arrays, each with five microphones, are cross correlated, there is a significant improvement in the detection performance—see Fig. 8(c). The beamforming process requires a value for the speed of sound propagation in air which is assumed to be 1115 ft/s (340 m/s).

Similar results are obtained by processing the acoustic data from other aircraft transits. For example, Figs. 9 and 10 show the jet transits when the aircraft speed is 300 kn and the altitude is 300 and 1000 ft, respectively.

Figure 11 represents a summary of the results for 24 aircraft transits in a histogram format. The number of noisy time-delay estimates obtained by cross correlating a pair of sensors is significantly reduced by using coincidence detection. However, coincidence detection also reduces the number of detections of the signal (from the aircraft) when the time-delay estimates in each of the three overlapping frequency bands do not match (within the time-of-arrival gate width), but this reduction in detection performance is overcome by cross correlating the beamformed outputs from a pair of arrays, rather than the outputs from a pair of single sensors. When array cross correlation is coupled with coincidence detection, the number of noisy time-delay estimates is negligible when compared with the number corresponding to the signal.

III. DIFFERENTIAL DOPPLER COMPENSATION PRIOR TO CROSS CORRELATION

The model represented by Eq. (1) assumes no relative motion between the source and the receivers, that is, $s(t)$ denotes the signal observed at the sensor nearer the source in the absence of both noise and motion relative to the source. If, for instance, the source is in motion whilst the sensors are stationary, then the observed waveforms at the two sensor locations can be modeled by[9]

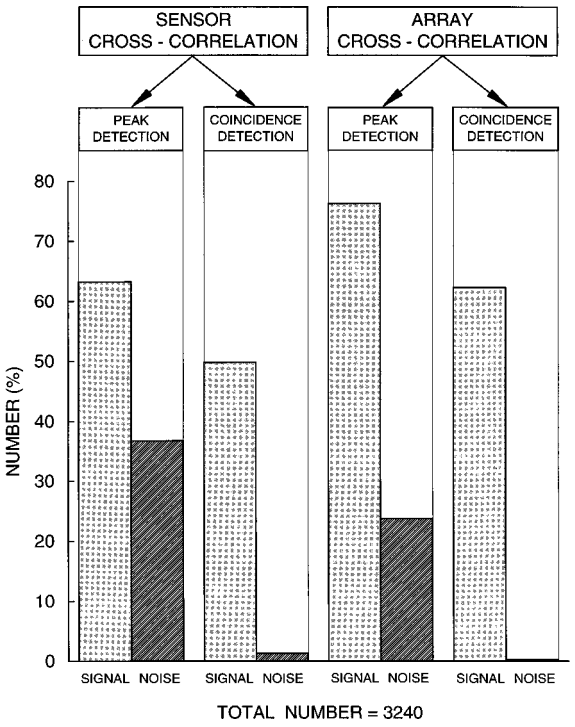

FIG. 11. Histograms showing the relative number of time-delay estimates associated with the acoustic source (signal detections) and with noise as a result of cross correlating either a pair of sensor outputs (left-hand side), or the beamformed outputs from a pair of arrays of sensors (right-hand side). The effect of noise on the time-delay estimation process is substantially reduced by coincidence detection.

$$x(t)=s(\beta_x t)+n_x(t)$$
$$y(t)=s[\beta_y(t-\tau_d)]+n_y(t), \tag{15}$$

where β_x and β_y are the respective receiver time scales that are introduced to account for the differential Doppler effect. In the present case, the relative motion between the source and the sensors results in the radial velocity component of the source at any given time being different for each receiver as the aircraft transits overhead.

Alternatively, the received waveforms can be modeled by

$$x(t)=\tilde{s}(t)+n_x(t)$$
$$y(t)=\tilde{s}[\beta(t-\tau_d)]+n_y(t), \tag{16}$$

where $\beta=\beta_y/\beta_x$.

When the relative motion between the source and the receivers leads to the value of β no longer being unity (that is, the difference in the radial velocity of the source observed at each receiver, $\beta_y-\beta_x$, is finite), then $x(t)$ and $y(t)$ tend to be uncorrelated, resulting in an erroneous estimate of the time delay, unless the time scale of one receiver's output waveform is adjusted so that β is restored to unity.

For example, Fig. 12(a) shows the cross correlogram for the outputs, denoted by $x(t)$ and $y(t)$, of two microphones separated by 29.5 ft when a stationary source (a jet engine) is present at a relative bearing of 135 deg, which corresponds to a time delay of -18.7 ms. Figure 12(b) shows the cross-correlation function for a relative time compression factor $\beta=2$. The artificial time compression resulted from the removal of every second sample from the time series data from one of the sensors prior to cross correlation. The time scaling (compression) results in the two sensor waveforms $x(t)$ and $y(\beta t)$, where $\beta=2$, being uncorrelated and hence, the estimate of the time delay is erroneous. Figure 12(c) shows the restored cross correlogram after time-scale dilation (or differential Doppler compensation) of the artificially compressed time series data. The time-scale expansion (by α) of the compressed waveform ($y(\beta t)$) is denoted by $y(\beta t/\alpha)$ and involves interpolation of the decimated time-series data using a discrete Fourier transform technique. With this method, the discrete Fourier transform of the compressed digital waveform is appended with a number of zeros, n_z, and the inverse Fourier transform computed to obtain an expanded (interpolated) waveform. This interpolated waveform is then cross correlated with the unmodified waveform from the other receiver, that is, $R_{xy}(\tau)=E\{x(t)y[\beta(t+\tau)/\alpha]\}$. The interpolation process is repeated for a range of different values of n_z. The cross-correlation function attains its global maximum value when the interpolated (or time-scaled) waveform matches the waveform of the other receiver; that is, when the time-scale dilation factor (α) is equal to the relative time-compression factor (β), that is, $\alpha=\beta=2$.

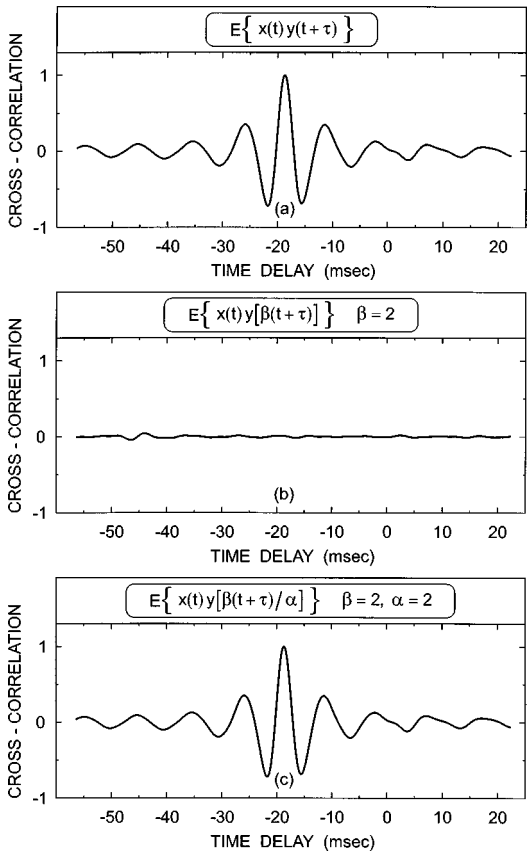

FIG. 12. Cross correlograms (a) for a stationary jet engine, (b) after one of the received waveforms is compressed by a factor of 2 and, (c) after the compressed waveform has been expanded using the interpolation technique.

Figure 13 is a color-intensity plot showing the variation of the cross-correlation function as the time-scale dilation factor, α, is increased from 1 (no time scaling of the wave-

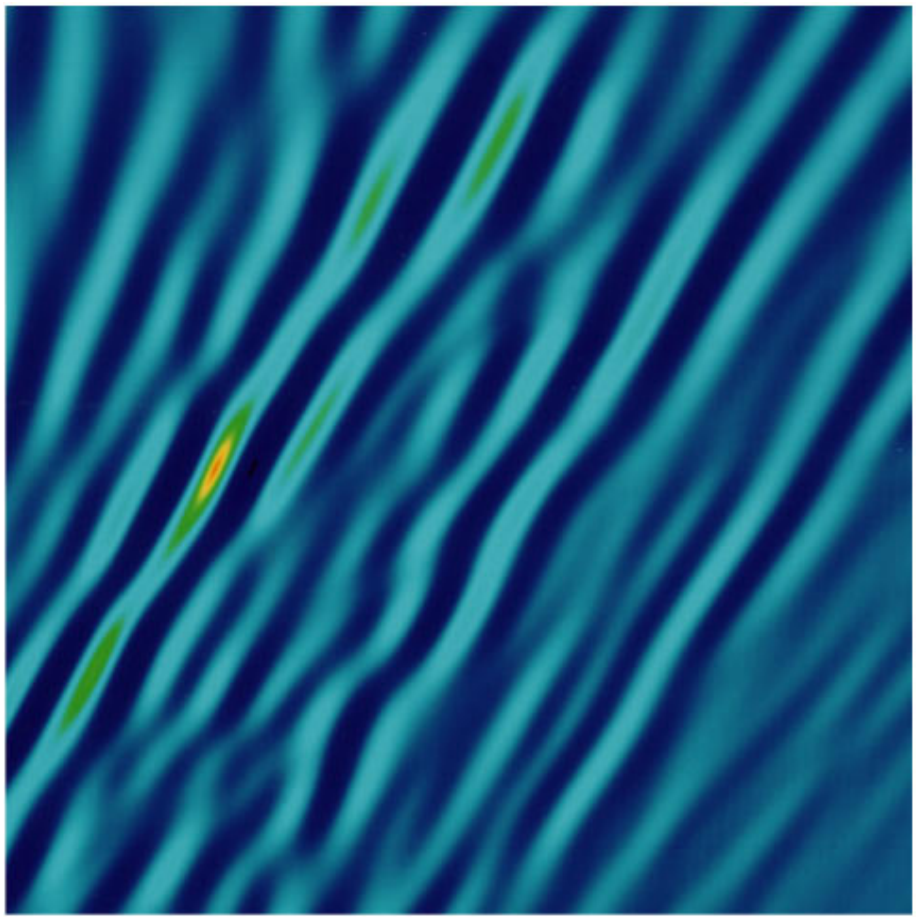

FIG. 13. Color contour plot of a wideband cross-ambiguity surface showing the variation of the cross-correlator output as a function of the time lag (abscissas) and the time-scale dilation factor (ordinates).

form) to 3. The global maximum of the cross-correlation function is reached when the the time bases of the two received waveforms match. The global maximum (which corresponds to the red area of the image) coincides with a dilation factor $\alpha=2$, which means that the interpolation process compensates exactly for the decimation process that compressed the original waveform ($y(t)$) of the relevant receiver by a factor $\beta=2$.

Similarly, Fig. 14(a) shows that the magnitude of the cross-correlation function attains its global maximum when the original compressed time series is expanded by a factor of 2; in other words, the original signal has a relative compression factor, β, equal to 2. (Expanding the compressed waveform by a factor of 2 is equivalent to time scaling the waveform by one half.) The estimate of the differential time delay, $\hat{\tau}_d$, is equal to the lag corresponding to the global maximum of the cross-correlation function—see Fig. 14(b). The interpolation technique is applicable in the present case because the signal-to-noise ratio is high; that is, the signal component corresponding to acoustic emissions from the aircraft dominates the noise component of the receiver output at each location.

Note that both the output of a passive wideband cross correlator with differential Doppler compensation (required for the present application) and the wideband cross-

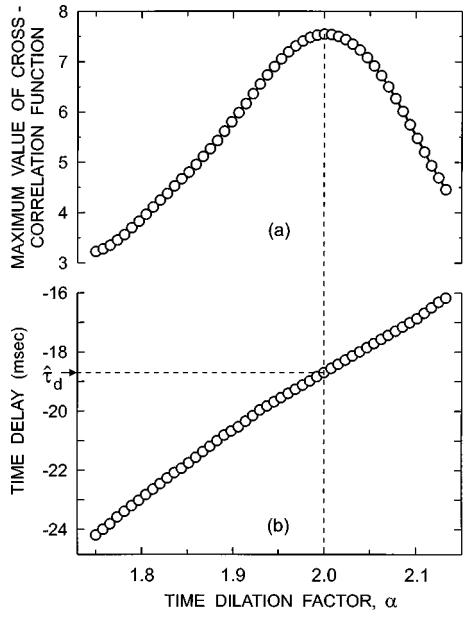

FIG. 14. (a) The peak magnitude of the cross-correlation function attains its maximum value when the time base of the compressed waveform is expanded by a factor of 2. The time bases of the received waveforms are then matched. (b) The correct time delay corresponds to the time lag corresponding to the peak in the cross-correlation function when the time bases of received waveforms match.

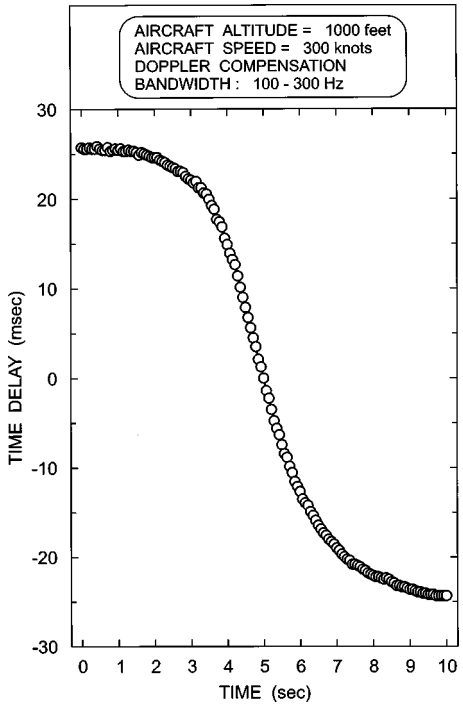

FIG. 15. Variation with time of the time-delay estimates for a jet transiting overhead with a speed of 300 kn at an altitude of 1000 ft.

ambiguity function can be expressed as a wavelet transform–see the Appendix.

Next, the wideband cross-correlation method with differential Doppler compensation is applied to real-sensor data recorded during a jet aircraft transit. To track the rapid temporal variation of the time-delay estimates during the overhead portion of the aircraft transit, the observation interval is shortened to 0.072 s from the 1-s time interval used earlier. As the jet flies overhead, the different time scales of the two received waveforms lead to inaccurate time-delay estimates. This is overcome by preprocessing the waveform having the higher time-compression factor (that is, the waveform of the receiver further from the approaching aircraft) using the interpolation method described above. The (differential Doppler-compensated) time-delay estimates are plotted as a function of time in Fig. 15 for a jet transiting overhead with a speed of 300 kn at an altitude of 1000 ft.

IV. CONCLUSION

Jet aircraft transits can be detected passively by cross correlating the outputs of two spatially separated microphones. Observation of an aircraft transit is improved by processing the acoustic data separately for three overlapping frequency bands and then applying coincidence detection, which requires the signal to have the same time delay for each of the three frequency bands; otherwise, the time-delay estimate is rejected as noisy. The detection performance of a cross correlator is improved by replacing a pair of single sensors with a pair of sensor arrays and then cross correlating the beamformed outputs.

During the overhead transit of a jet aircraft, the integration time is required to be short because the time-delay estimates vary rapidly with time. If the receiver waveforms have different time-compression factors, then the time-delay estimate will be in error unless the receiver waveform having the higher compression has its time scale dilated so that the time bases of the receiver waveforms match. The time scale can be expanded using the interpolation technique described in the paper, providing the observed signal-to-noise ratio is high, as is the case when a jet aircraft flies overhead at low altitude.

ACKNOWLEDGMENTS

The author gratefully acknowledges the contributions made to this paper by his colleague Lionel Criswick and the discussions with Brigadier Bryan Stevens on the operational implications of this work. This work was supported by the Cooperative Research Center for Robust and Adaptive Systems which is funded by the Australian Government under the Cooperative Research Centres Program.

APPENDIX: WAVELET TRANSFORM

The wavelet transform, $\mathcal{W}_y x(\alpha,\tau)$, is an operation that transforms a function, $x(t)$, by integrating it with modified versions of some kernel function, $y(t)$. The kernel function is referred to as the mother wavelet,[10] or the normalized analyzing wavelet,[11] and the modifications are translations and dilations (or inversely, compressions) of the mother wavelet.

The wideband cross-ambiguity function of $x(t)$ and $y(t)$ is given by[10]

$$\mathcal{F}_{xy}(\beta,\tau)=\sqrt{|\beta|}\int_{-\infty}^{\infty}x(t)y^*[\beta(t+\tau)]dt. \tag{A1}$$

The wideband cross-ambiguity function can be written as a wavelet transform by changing the time-scale variable in the definition of the wavelet transform

$$\begin{aligned}\mathcal{F}_{xy}\left(\frac{1}{\alpha},\tau\right)&=\frac{1}{\sqrt{|\alpha|}}\int_{-\infty}^{\infty}x(t)y^*\left(\frac{t+\tau}{\alpha}\right)dt\\&=\mathcal{W}_y x(\alpha,\tau)=\mathcal{W}_y x\left(\frac{1}{\beta},\tau\right)\\&=\mathcal{F}_{xy}(\beta,\tau).\end{aligned} \tag{A2}$$

Similarly, the output of the wideband correlation receiver is given by[10]

$$\begin{aligned}\mathcal{C}_{xy}\left(\frac{1}{\beta},\tau\right)&=\sqrt{|\beta|}\int_{-\infty}^{\infty}x(t)y^*[\beta(t+\tau)]dt\\&=\mathcal{W}_y x\left(\frac{1}{\beta},\tau\right)=\mathcal{W}_y x(\alpha,\tau),\end{aligned} \tag{A3}$$

where $x(t)$ and $y(t)$ are the input waveforms to the correlation processor.

If $y(t)$ is time scaled prior to cross correlation, as is the case in Fig. 12(c), then

$$y_\alpha(t)=\frac{1}{\sqrt{|\alpha|}}y\left(\frac{t}{\alpha}\right). \tag{A4}$$

Thus, the wavelet transform, $\mathcal{W}_y x(\alpha,\tau)$, is equal to the cross-correlation function between $x(t)$ and $y_\alpha(t)$. If the correlation operator is denoted by $\otimes$, then

$$x(t)\otimes y_\alpha^*(t)=\int_{-\infty}^{\infty}x(t)y_\alpha^*(t+\tau)dt$$

$$=\frac{1}{\sqrt{|\alpha|}}\int_{-\infty}^{\infty}x(t)y^*\left(\frac{t+\tau}{\alpha}\right)dt=\mathcal{W}_y x(\alpha,\tau). \tag{A5}$$

Hence, Fig. 12(a) represents the output of the process $x(t)\otimes y(t)$, Fig. 12(b) represents the output of $x(t)\otimes y(\beta t)$ for $\beta=2$, and Fig. 12(c) represents the output of the wideband correlation receiver $x(t)\otimes y_\alpha(\beta t)$ for $\alpha=2$.

Similarly, Fig. 13 can be viewed as either:

(1) the output of the wideband correlation receiver, $\mathcal{C}_{xy}(\alpha,\tau)$, where $1\leqslant\alpha\leqslant 3$, or
(2) the wideband cross-ambiguity function, $\mathcal{F}_{xy}(1/\alpha,\tau)$, or
(3) the wavelet transform $\mathcal{W}_y x(\alpha,\tau)$.

[1] B. G. Ferguson and B. G. Quinn, ''Application of the short-time Fourier transform and the Wigner–Ville distribution to the acoustic localization of aircraft,'' J. Acoust. Soc. Am. **96**, 821–827 (1994).
[2] F. Dommermuth and J. Schiller, ''Estimating the trajectory of an accelerationless aircraft by means of a stationary acoustic sensor,'' J. Acoust. Soc. Am. **76**, 1114–1122 (1984).
[3] G. C. Carter, ''Time-delay estimation for passive sonar processing,'' IEEE Trans. Acoust., Speech, Signal Process. **ASSP-29**, 463–470 (1981).
[4] C. H. Knapp and G. C. Carter, ''The generalized correlation method for estimation of time delay,'' IEEE Trans. Acoust., Speech, Signal Process. **ASSP-24**, 320–327 (1976).
[5] G. C. Carter, *Coherence and Time Delay Estimation* (IEEE, New York, 1993).
[6] B. Champagne, M. Eizenman, and S. Pasupathy, ''Exact maximum likelihood time delay estimation for short observation intervals,'' IEEE Trans. Signal Process. **39**, 1245–1257 (1991).
[7] A. H. Quazi, ''An overview on the time delay estimate in active and passive systems for target localization,'' IEEE Trans. Acoust., Speech, Signal Process. **ASSP-29**, 527–533 (1981).
[8] B. G. Ferguson, ''Improved time-delay estimates of underwater acoustic signals using beamforming and prefiltering techniques,'' IEEE J. Ocean. Eng. **14**, 238–244 (1989).
[9] C. H. Knapp and G. C. Carter, ''Estimation of time delay in the presence of source or receiver motion,'' J. Acoust. Soc. Am. **61**, 1545–1549 (1977).
[10] L. G. Weiss, ''Wavelets and wideband correlation processing,'' IEEE Signal Process. Mag. 13–32 (1994).
[11] D. L. Jones and R. G. Baraniuk, ''Efficient approximation of continuous wavelet transforms,'' Electron. Lett. **27**, 748–750 (1991).

Wideband reflectance tympanometry in normal adults

Robert H. Margolis[a] and George L. Saly
University of Minnesota, Department of Otolaryngology, Otitis Media Research Center, Minneapolis, Minnesota 55455

Douglas H. Keefe
Boys Town National Research Hospital, Omaha, Nebraska 68131

(Received 3 August 1998; accepted for publication 18 February 1999)

Acoustic impedance/reflectance measurements were made at various ear-canal pressures in 20 subjects with a clinical acoustic immittance instrument and an experimental impedance/reflectance system. Measurements were made over a frequency range of 226–2000 Hz with the clinical system and 125–11 310 Hz with the experimental system. For frequencies ⩽2.0 kHz, tympanograms obtained with the two systems are similar, with patterns that progress through the same orderly sequence with increasing frequency. Eardrum impedance measurements were also similar. There are small gender differences in middle-ear impedance. Reflectance patterns (reflectance versus frequency) at ambient ear-canal air pressure are characterized by high reflectance at low frequencies, two distict minima at 1.2 and 3.5 kHz, increasing reflectance to 8.0 kHz, and decreasing reflectance above that frequency. Ear-canal pressure increases reflectance at low frequencies, decreases reflectance in the region of the minimum, and increases reflectance slightly at high frequencies. Reflectance tympanograms (reflectance versus ear-canal pressure) progress through a sequence of three patterns. At low frequencies, reflectance tympanograms are ''V'' shaped, indicating that pressure increases reflectance. At frequencies near the minimum reflectance, the pattern inverts, indicating that pressure decreases reflectance. At high frequencies, the patterns are flat, indicating that ear-canal pressure has little effect. Results presented for one patient suggest that reflectance tympanometry may be useful for detecting middle-ear pathology. © *1999 Acoustical Society of America.* [S0001-4966(99)04706-2]

PACS numbers: 43.64.Ha [BLM]

INTRODUCTION

Acoustic impedance measurements made in the ear canals of human and animal subjects have been used to study normal middle-ear mechanics and to detect mechanical disturbances that result from middle-ear disease. The complex impedance concept originated by Heaviside for long electrical transmission lines (Heaviside, 1886) was first applied to acoustical systems by Webster (1919). West (1928) probably made the first acoustic impedance measurements from human ears, for use in the design of telephone receivers. Békésy (1932) measured the acoustic impedance of human ears at various static ear-canal air pressures to prove that the effects of air pressure on hearing were due to middle-ear transmission losses rather than changes in cochlear sensitivity. Although the term would not be used for 30 years, Békésy's experiment was the first use of tympanometry, the measurement of acoustic immittance in the ear canal as a function of ear-canal air pressure.[1]

The historical underpinnings of the clinical use of tympanometry originate with the informal observations of Wollaston (1820) and Wheatstone (1827) on the effects of pressurizing the ear canal on auditory sensitivity, and early otologists who recognized the importance of middle-ear pressure in the pathogenesis of otitis media (e.g., Toynbee, 1865; Politzer, 1869). These observations led to methods for assessing middle-ear function based on changes in loudness resulting from changes in ear canal air pressure, i.e., psychophysical tympanograms (Pohlman and Kranz, 1923; Van Dishoeck, 1937).

Metz reported the first significant clinical study of acoustic impedance characteristics of patients with middle-ear disease (Metz, 1946). Using a mechano-acoustic bridge (Fig. 1), Metz measured the aural acoustic impedance of patients and human temporal bones with a wide variety of middle-ear pathologies, including otitis media, otosclerosis, ossicular fixation, and Meniere's disease. He used the same instrument to indirectly record the acoustic stapedius reflex. Although he demonstrated that middle-ear disease produces measurable changes in the acoustic impedance in the ear canal, it would not be until the method of Békésy was applied to clinical studies that the technique would be clinically useful. Terkildsen and colleagues (Terkildsen and Thomsen, 1959; Terkildsen and Nielsen, 1960), working in the same hospital as Metz (Rigshospitalet, Copenhagen, Denmark), developed the first electroacoustic device to record acoustic impedance at various ear-canal air pressures. The device led to the development of the clinical acoustic immittance instruments that are in wide use today. Tympanometry has become a routine procedure in audiologic and otologic assessment. Following Terkildsen's lead, most clinical instruments measure acoustic immittance at a single low probe frequency, 226 Hz.

Early tympanometry instruments provided semi-quantitative measurements expressed in ''arbitrary compliance units.'' This led to qualitative methods for interpreting

[a]Electronic mail: margo001@tc.umn.edu

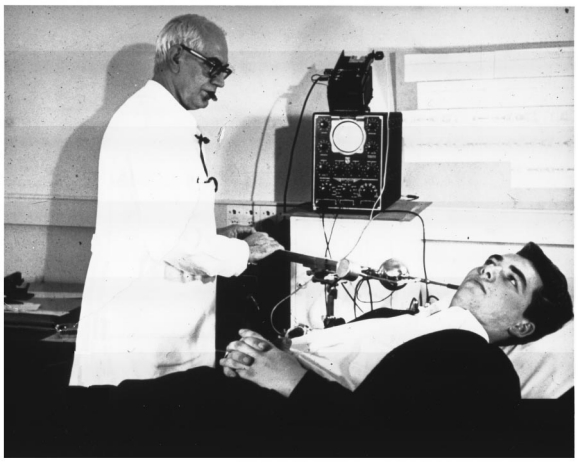

FIG. 1. Otto Metz with the Metz bridge, c. 1952.

tympanometric patterns, the most popular being that of Liden (1969), later modified by Jerger (1970). These methods classify tympanograms according to features such as the height and width of the peak. Currently produced instruments provide quantitative data for which norms have been established (Margolis and Shanks, 1991; Margolis and Hunter, 1999). Tympanometric features that have been found to be clinically useful are the compensated static admittance, tympanometric width, tympanometric peak pressure, and equivalent ear-canal volume (see Margolis and Shanks, 1991; Margolis and Hunter, 1999, for reviews).

Some investigators have found that multifrequency measurements of acoustic immittance detect some middle-ear pathologies that are not detected by single-frequency measurements. The first to study multifrequency tympanometry (MFT) in patients was Colletti (1976). He recorded single-component (impedance-magnitude) tympanograms in patients with a wide variety of middle-ear conditions. In normal subjects, tympanometric patterns progressed through a sequence of three patterns as frequency increased. The patterns changed systematically with various middle-ear pathologies.

The most important contribution to understanding the effects of measurement frequency and middle-ear pathology on tympanometric patterns is the model developed by Vanhuyse and colleagues at the University of Antwerp (Vanhuyse *et al.*, 1975). Beginning with assumptions of the effects of ear-canal air pressure on acoustic impedance, the model predicts four tympanometric patterns that depend on the relative values of resistance and reactance. As frequency increases the patterns progress through an orderly sequence that is quite consistent among subjects (Margolis *et al.*, 1985; Van Camp *et al.*, 1986; Margolis and Goycoolea, 1993). See the Appendix for a more detailed description of the Vanhuyse model.

Using the Vanhuyse model as a framework for interpreting tympanometric patterns, MFT has been found to be superior to single frequency tympanometry for detecting middle-ear pathologies. Several cases have been reported of patients with confirmed middle-ear pathology, normal 226-Hz tympanograms, and abnormal MFT (Hunter and Margolis, 1992; Margolis and Hunter, 1999). In a study of conventional and multifrequency tympanometry in chinchillas with experimentally produced middle-ear pathologies, Margolis *et al.* (1998) found higher sensitivity and specificity for MFT for significant pathology, defined as tympanic membrane mass or adhesions involving the tympanic membrane and/or ossicles.

Commercial MFT instruments measure the complex admittance of the ear by measuring the magnitude and phase of a probe tone delivered to the ear canal by a hermetically sealed probe. The instruments are calibrated by assuming the ear canal is a pure compliant element that is in parallel with the impedance of the middle ear. The magnitude and phase are measured in cylindrical cavities that are intended to represent compliance-dominated impedances spanning the magnitudes expected in human ears. Deviations from these reference phase values are used to infer the admittance phase angle of the ear. This method is considered to be valid for frequencies at which the adult human ear canal can be regarded as a lumped compliant element, i.e., $\leqslant$2.0 kHz. Above that frequency, the ear canal is more accurately modelled as a transmission line and the relationship between the acoustic impedance measured in the ear canal and the middle-ear impedance becomes more complex.

Wideband impedance measurements have been reported by several investigators using systems that are based on different calibration principles than those used by commercial instruments (Stinson *et al.* 1982; Hudde, 1983; Keefe *et al.*, 1992; Lynch *et al.*, 1994; Voss and Allen, 1994). A number of investigators have pointed out that expressing these wideband measurements in terms of energy reflectance has several advantages (Shaw and Stinson, 1981; Keefe *et al.*, 1993; Voss and Allen, 1994). One advantage is the near independence of energy reflectance on ear-canal characteristics, providing a potentially useful method for assessment of middle-ear function. The energy reflectance, the ratio of reflected to incident energy, in normal adult ears is high at low frequencies, reaches a minimum at about 3.5 kHz, and increases at higher frequencies (Keefe *et al.*, 1993; Voss and Allen, 1994). Compared to adult ears, infant ears show a lower reflectance at low frequencies with similar values at higher frequencies. Infant ears also show substantial differences in MFT patterns compared to older children and adults (Holte *et al.*, 1991). Although the source of the age-related differences in reflectance and tympanometric patterns has not been determined, there are three leading candidates: the incomplete development of the infant ear-canal wall (Keefe *et al.*, 1993); unresolved mesenchyme and other material in the newborn middle-ear (Paparella *et al.*, 1980; Eavey, 1993), and the greater thickness of the newborn tympanic membrane (Ruah *et al.*, 1991).

Energy reflectance is an attractive concept for clinical assessment because it represents the proportion of energy absorbed by the middle ear, and thus might be more closely related to hearing sensitivity than measures of input immittance. In addition, it is significantly less sensitive than impedance or admittance to probe position and standing waves in the ear canal. Middle-ear pathologies that are of clinical importance, such as otitis media, otosclerosis, and ossicular

abnormalities, are expected to change the transmission of energy into the middle-ear system. Early indications are that middle-ear pathology changes the wideband reflectance of the ear suggesting that the technique may be clinically useful (Keefe *et al.*, 1995; Margolis and Keefe, 1997; Piskorski *et al.*, 1999).

Most reports of wideband reflectance have made measurements at a single (ambient) ear-canal air pressure. Whereas variation of ear-canal air pressure was necessary for acoustic impedance measurements to become clinically useful, it is unknown whether ambient reflectance measurements will be sensitive to middle-ear pathology and whether varying the ear-canal air pressure (reflectance tympanometry) will increase the usefulness of the technique. Keefe and Levi (1996) recorded multifrequency admittance tympanograms from human infants and adults with a commercial acoustic immittance system, and converted the results to reflectance—the first reflectance tympanograms.

This investigation was designed to reveal the characteristics of wideband reflectance tympanograms in normal adult ears. For comparable measurement frequencies (226–2000 Hz), multifrequency tympanograms obtained with a clinical instrument were compared with those obtained with the wideband reflectance measurement system. In addition, the first high-frequency admittance tympanograms (2.0–11.3 kHz) are described.

I. METHODS

A. Subjects

Subjects were 20 adults (10 male, 10 female) aged 20–53 yr (mean=34 yr). Each subject passed a four-frequency (0.5, 1.0, 2.0, 4.0 kHz) hearing screen at 15 dB HL and had normal-appearing ear canals and tympanic membranes examined by otomicroscopy. Ears with abnormal tympanic membrane findings including tympanosclerosis or retraction pockets were excluded. One ear of each subject was tested. The right or left ear was randomly selected unless one ear did not meet inclusion criteria. Data from one patient with chronic ear disease are also presented.

B. Measurements

1. Multifrequency tympanometry

Multifrequency tympanograms were recorded with a commercial clinical acoustic-immittance system (Virtual 310),[2] referred to as the clinical system in this report. Tympanograms were recorded at 226 Hz and at $\frac{1}{6}$-oct frequencies from 0.5 to 2.0 kHz. The 226-Hz tympanogram was recorded in the sweep pressure mode. That is, the frequency was held constant and the ear-canal air pressure was swept from +400 to −500 daPa in 14-daPa steps with an average rate of pressure change of −250 daPa/s. The 0.5–2.0 kHz tympanograms were recorded in the sweep frequency mode. That is, the ear canal was pressurized to 400 daPa and the frequency was swept from 2.0 to 0.5 kHz. Then the ear-canal pressure was decreased by 14 daPa and the process repeated until the entire pressure range was sampled. Magnitude and phase measurements were exported to spreadsheet software for analysis.

2. Wideband reflectance

Energy reflectance was measured by a system similar to the one described by Allen (1985) and later modified by Keefe (Keefe *et al.*, 1992, 1993). The impedance/reflectance system (ZR system) consists of a measurement probe, a data acquisition card and a personal computer. The probe consisted of a small loudspeaker and microphone within an assembly over which one of a set of standard rubber tips could be mounted for insertion into a calibration tube or an ear. The data acquisition card (CAC DSP32C) generated an electrical stimulus signal driving the loudspeaker and digitized the output signal received from the microphone preamplifier. The electrical stimulus signal was a 40-ms, digitally synthesized ''chirp'' with a bandwidth spanning the frequency range 0.25–11.3 kHz. The acoustic stimulus in the calibration tube or ear canal was the chirp as modified by the transfer functions of the transducers, each of which acts as an independent acoustic load on the source transducer. The system was calibrated daily in a set of six rigidly terminated tubes with a diameter of 8.0 mm and varying in length from 47.5 to 95.4 cm. The calibration routine calculates the Thevenin source impedance and Thevenin source pressure associated with the transducers and associated signal conditioners. The source impedance and source pressure are calculated by modeling the acoustic wave propagation inside each cylindrical tube using a viscothermal transmission model based upon the measured pressure spectrum for each tube. The length of each tube was optimized based upon a starting value of its nominal geometric length (Allen, 1985). After calibration, data were acquired using the same chirp stimulus and chirp level used for calibration. Data were acquired at a sample rate of 24 kHz with a spectral resolution of approximately 12 Hz. These spectra were subsequently averaged in 1/6-octave bins. The measured pressure spectrum in the ear canal was converted into a measured impedance (or admittance) at the probe tip, and energy reflectance was calculated using standard transformations of the acoustic impedance (Keefe *et al.*, 1992). The ear-canal area is needed for this transformation, and was estimated from the size of the tip that successfully sealed the ear canal. Twelve chirps were delivered into the ear canal at a rate of 12.5 chirps per second, and the acoustic pressure response to the final eight chirps was averaged. Including processing time, a wideband analysis was completed in approximately one second.

To vary the ear-canal air pressure, a microsyringe and digital manometer were coupled to the ear-canal probe assembly through a flexible tube. Air pressure was varied manually over the range +300 to −300 daPa with the microsyringe. Measurements were made at 21 air pressures: 84 to −84 daPa in 14-daPa steps, ±100, ±150, ±200, and ±300 daPa. This maximum air pressure corresponds to a change of approximately 3% of atmospheric pressure. The fact that this change is small allows a single calibration for all ear-canal air pressures. We confirmed in preliminary measurements that the calibration was unaffected by static pressure changes.

Sound pressure and phase measurements were transformed into measures of energy reflectance or into complex acoustic admittance (conductance and susceptance). Admit-

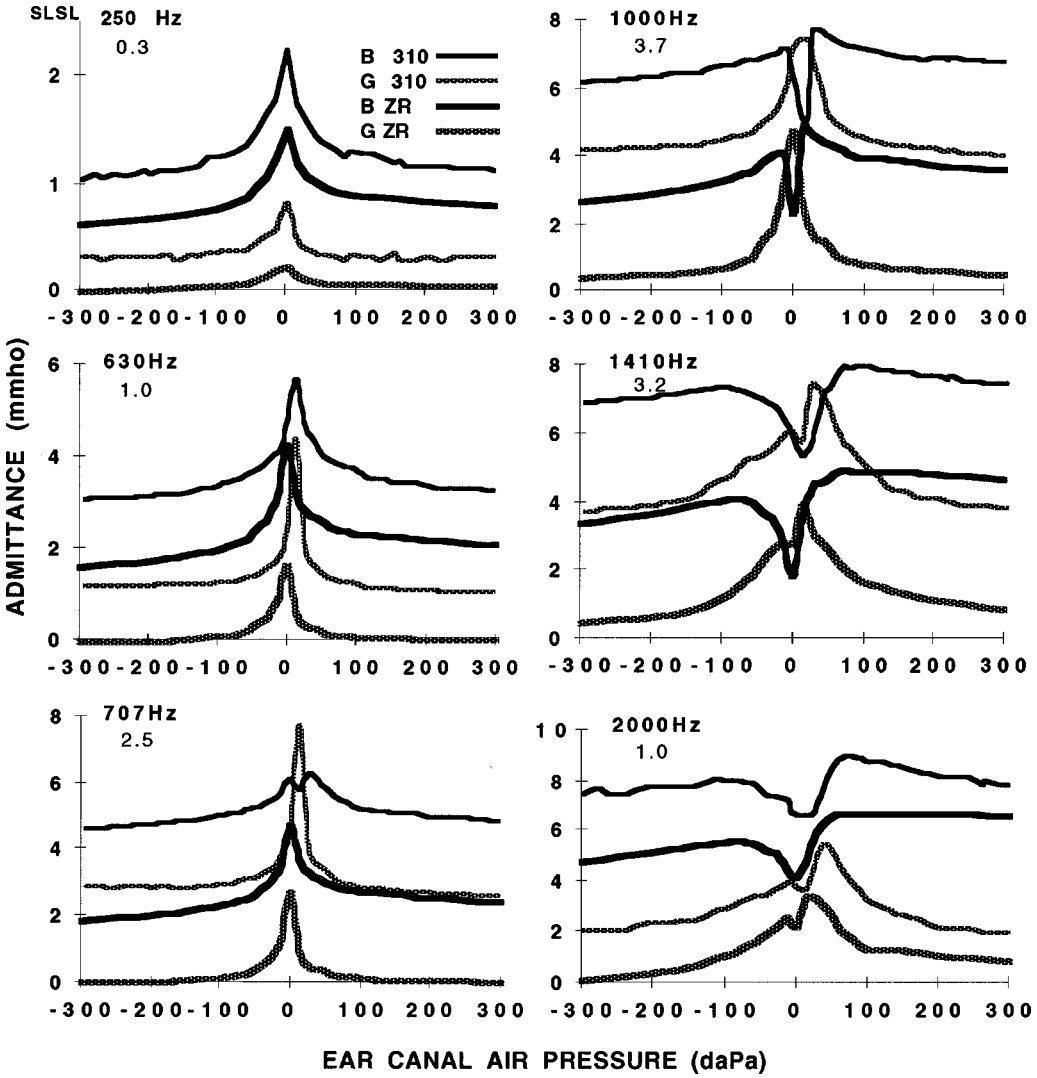

FIG. 2. Multifrequency tympanograms from a normal adult subject recorded with a clinical acoustic immittance system (310) and the wideband reflectance system (ZR). Tympanograms obtained with the 310 system are displaced upward by the amount (in mmho) shown in the upper left corner of each panel. At low frequencies (250–630 Hz), $1B1G$ patterns were obtained with both measurement systems. At 707 Hz, the pattern obtained with the clinical system changed to a $3B1G$ and the resonant frequency obtained with the clinical system was slightly lower than that obtained with the ZR system (794 vs 891 Hz). At higher frequencies (1410–2000 Hz), $3B3G$ patterns were obtained with both systems.

tance tympanograms in the 226–2000 Hz frequency range were compared to those obtained with the clinical instrument. In addition, wideband (226–11 310 Hz) admittance tympanograms were calculated from measurements made with the reflectance system.

3. Middle-ear impedance

Middle-ear impedance was estimated from the measurements obtained from both measurement systems. In order to estimate the input impedance of the middle ear, it is necessary to compensate for the effect of the volume of air enclosed in the ear canal. At low frequencies ($\leqslant$2.0 kHz) this can be accomplished by assuming that the ear canal is a pure compliant element that is in parallel with the middle ear. [See Margolis and Hunter (1999) for a discussion of this assumption.] This assumption permits a simple calculation for conversion of the measured impedance to the impedance at the tympanic membrane, i.e., the middle-ear input impedance. That is,

$$Y_{tm} = Y - Y_{ec}, \tag{1}$$

where Y_{tm} is is the complex admittance at the tympanic membrane, Y is the measured admittance, and Y_{ec} is the admittance of the volume of air enclosed by the ear canal. Y_{ec} is estimated from the admittance at high negative ear-canal pressure assuming that when the ear canal is pressurized Y_{tm} approaches zero and $Y_{ec} \approx Y$. This method will be referred to as the lumped constant method.

At frequencies $\geqslant$2.0 kHz, the assumption that the ear canal is a simple parallel compliant element is not valid and a more complex representation of the ear-canal admittance is necessary. Using a transmission line representation of the middle ear, the measured impedance can be converted to the middle-ear impedance if the length and diameter of the ear canal are known (Lynch *et al.*, 1994). In this study, the diameter was estimated from the size of the tip that was used to seal the probe assembly in the ear canal. The length was calculated using this diameter and the volume estimated from the admittance measured with an ear-canal air pressure

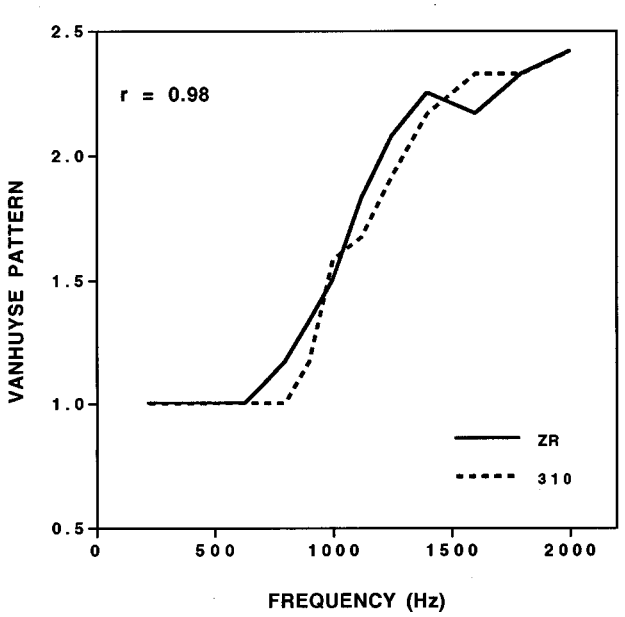

FIG. 3. ''Average'' Vanhuyse patterns for tympanograms recorded with the two measurement systems. Vanhuyse patterns were assigned a value of 1–4 for $1B1G$, $3B1G$, $3B3G$, and $5B3G$ patterns, respectively. These values were averaged for the 20 normal subjects for each measurement system.

of −300 daPa. A lossy transmission line approximation was also investigated that takes into account the viscothermal losses at the ear-canal walls, based upon a model assuming that these losses are equal to those in a short section of cylindrical tube having the same length and diameter as the ear canal. It was sufficient to use the well-known, large-diameter approximation of Kirchoff for this viscothermal-loss model.

Middle-ear impedance was estimated by three methods for compensating for ear-canal effects: the lumped constant method, and the transmission line representation of the ear canal with and without viscothermal losses.

4. Measurement error

Discussion of measurement errors and examples of measurement accuracy for ZR system measurements of cylindrical tubes with known impedances are presented by Keefe *et al.* (1992). An acoustical estimation of the cylindrical tube area is one measure of accuracy across frequency. Using a set of six cylindrical tubes that differed from those used in the calibration tube set, the error in estimating the area varied from 3% to 6%. The accuracy of the clinical system is unknown, although the choice of calibration test cavities is one source of measurement error. This is because the method assumes the test cavity impedance is that of a pure compliance, whereas the shape of the cavity may produce a resonance that causes departures in the impedance from that of a pure compliance.

II. RESULTS

A. Admittance tympanograms

Figure 2 shows two-component admittance tympanograms for one subject obtained with the two measurement systems. In general the two instruments produced similar tympanometric patterns which were consistent with the Vanhuyse model. At low frequencies (250–630 Hz), $1B1G$ patterns were obtained with both measurement systems. At 707 Hz, the pattern obtained with the clinical system changed to a $3B1G$. Tympanograms obtained with the ZR system changed to a $3B1G$ at a higher frequency (891 Hz, not shown in Fig. 2). The transition from $3B1G$ to $3B3G$ also occurred at a higher frequency for the ZR system compared to the clinical system (1410 vs 1120 Hz). These results suggest that the patterns obtained with both measurement systems follow the sequence predicted by the Vanhuyse model with the transitions between patterns occurring at systematically lower frequencies for the clinical system.

The sequence of patterns resulting from the two measurement systems, averaged across subjects, is illustrated in Fig. 3. Each tympanogram was assigned a value of 1, 2, 3, or 4 corresponding to the four patterns ($1B1G=1$, $3B1G=2$, etc.). These values were averaged for the 20 subjects at each frequency. In general, the tympanograms follow the same sequence with transitions between patterns occurring at similar frequencies. Above 0.63 kHz, the clinical system tends to produce a higher average score, indicating that the transitions between patterns tend to occur at lower frequencies compared to those produced by the wideband reflectance system. Nevertheless, with respect to tympanometric patterns, the two systems appear to produce very similar results. The correlation between the average patterns for the two measurement systems was 0.98.

The resonant frequency at the input to the middle ear can be determined from the susceptance tympanogram. The resonant frequency occurs when the minimum in the notch in susceptance is equal to the tail value (i.e., the compensated susceptance=0). In Fig. 2, for example, the 1-kHz tympanograms indicate that the test frequency is above the resonant frequency because the notch dips below the tail value. Using this method, the two instruments produced nearly identical estimates of resonant frequency (1121 and 1161 Hz for the reflectance and clinical systems, respectively). A *t*-test indicated that the difference is not significant. The resonant frequency estimates from the two systems are highly correlated ($r=0.82$), again indicating good agreement. There is good agreement between the resonant frequency estimates from this study and that from our previous study of normal adult subjects using the clinical instrument (1135 Hz, Margolis and Goycoolea, 1993).

High-frequency tympanograms (susceptance and conductance at the probe tip) for two subjects are shown in Fig. 4. In contrast to the orderly sequence of patterns that occurs below 2.0 kHz, the patterns do not appear to be systematic above 2.0 kHz. In contrast to the orderly behavior of reflectance tympanograms (discussed below), no consistent sequence of patterns was observed in high-frequency tympanometric patterns.

B. Middle-ear impedance

Middle-ear impedance was estimated from measurements obtained from the two measurement systems by the three methods for compensating for ear-canal volume described above. The results for the lumped constant and the

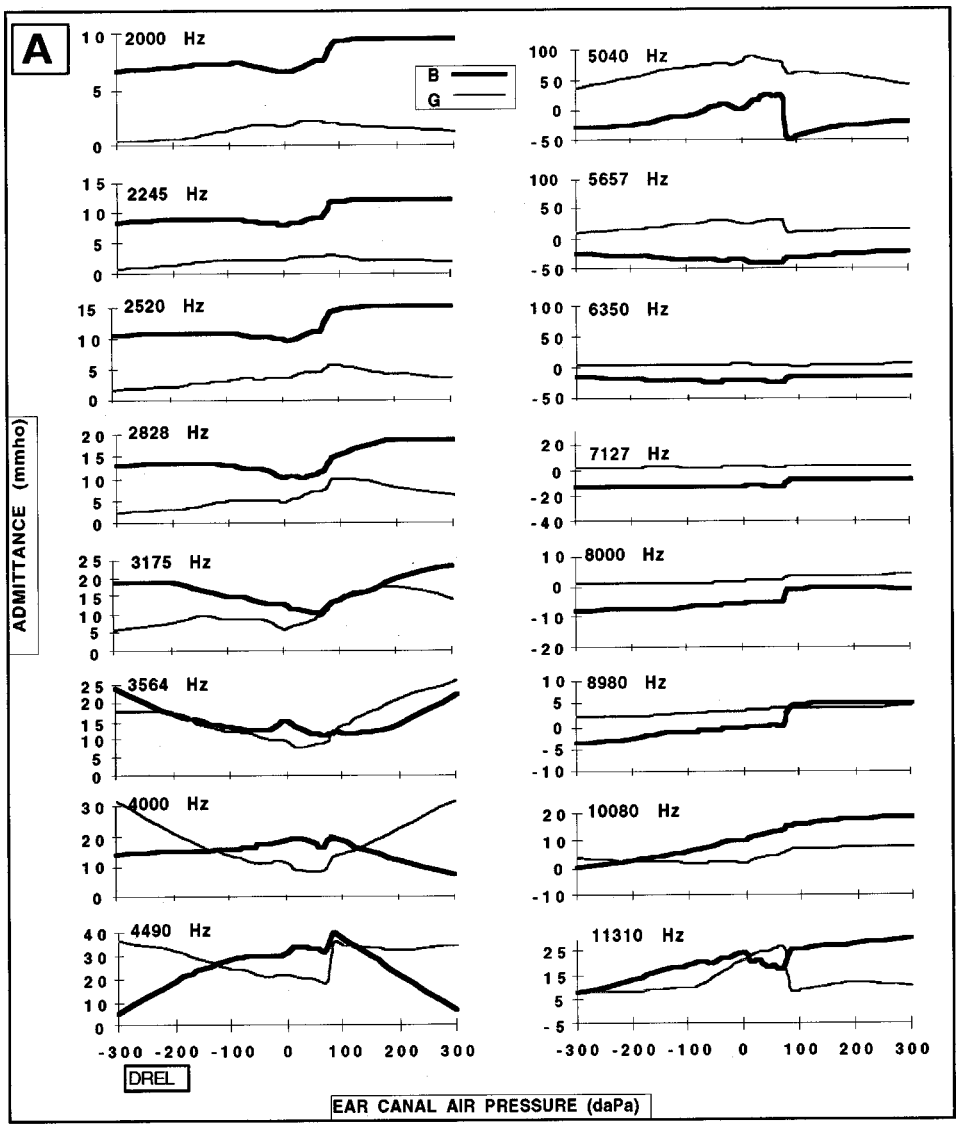

FIG. 4. High-frequency tympanograms for two normal adult ears. B=susceptance. G=conductance.

transmission line (without viscothermal losses) methods are shown in Fig. 5(a), averaged for all subjects. Also shown are measurements reported by Rabinowitz for a smaller group of normal adult subjects (Rabinowitz, 1981).

Middle-ear impedance estimated from the Virtual 310 data using the lumped constant method (circles) shows a conspicuous irregularity in both the resistance and reactance values in the region of 0.8 kHz. Resistance and reactance measured with the wideband reflectance system and compensated by the same method (squares) do not show this irregularity.

Middle-ear impedance estimates resulting from the transmission line method obtained with the wideband reflectance system ($\times$'s) are very similar to the lumped constant estimates below 1.0 kHz, suggesting that the simpler lumped constant method is valid in that frequency range. Between 1.0 and 2.0 kHz, both resistance and reactance are higher using the lumped constant method. This indicates that the assumptions underlying the lumped constant method are beginning to break down as frequency approaches 2.0 kHz.

Middle-ear impedance estimates resulting from the transmission line method, with and without viscothermal losses, are nearly identical [Fig. 5(b)], although there are small, systematic differences at low frequencies. When viscothermal losses are accounted for, the resulting resistance is larger and reactance is smaller (less negative). We conclude from Fig. 5(b) that it is unnecessary to account for viscothermal losses.

Separate analyses of variance were used to test for gender differences in compensated resistance and reactance from both instruments. The effect of gender on resistance and reactance estimates obtained from the clinical instrument did not reach statistical significance. Figure 5(c) shows average resistance and reactance measured with the wideband reflectance system for male and female subjects. The differences were statistically significant ($p<0.001$ for reactance and $p=0.02$ for resistance). For males, the resistance was higher at frequencies <1.0 kHz, and lower in the 2.0–4.0-kHz range. Relative to females, reactance for males was shifted toward positive values for frequencies <1.5 kHz. At low frequencies the male ear is less stiffness dominated with a greater resistive component. The absence of a significant gender effect in the measurements from the clinical system may be due to the higher variance in the measurements ob-

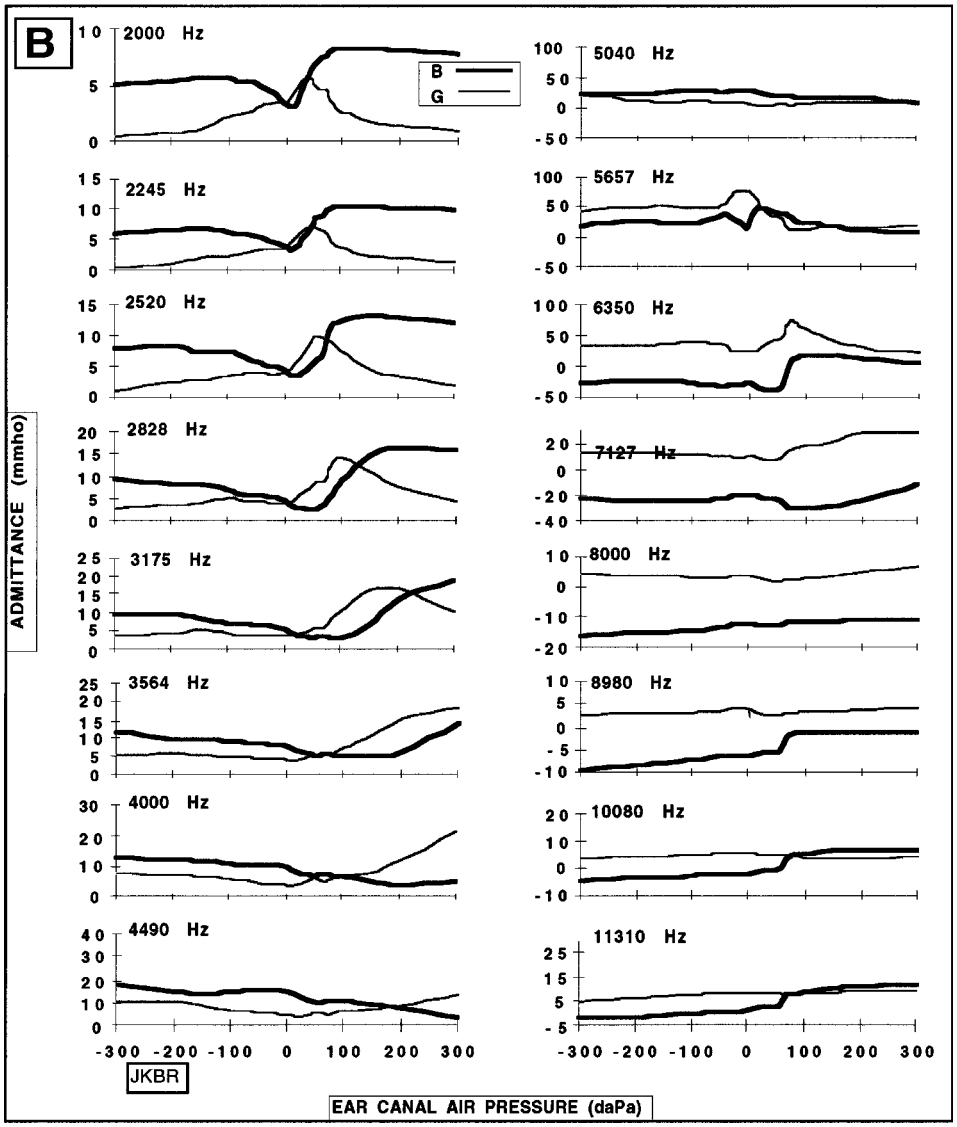

FIG. 4. (*Continued.*)

tained with that system. On the average, the variance associated with reactance measurements from the clinical system was fourfold greater than the variance of measurements from the wideband reflectance system. This reduced variance may be due to the $\frac{1}{6}$-oct averaging used in calculating the impedance with the wideband reflectance system.

The gender difference indicated in Fig. 5(c) does not appear to be related to ear-canal effects. A *t*-test was performed to analyze the effect of gender on ear canal area, estimated by the diameter of the tip used to seal the ear canal. Although the average diameter was slightly larger for male ears than female ears (11.9 vs 11.1 mm), the difference did not reach statistical significant ($p=0.17$). This suggests that there is a small but significant effect of gender on middle-ear impedance.

C. Reflectance

Figure 6 shows reflectance patterns for a representative subject (panel a) and the average of all subjects for all ear-canal pressures (panel b). Also shown is the average reflectance at three pressures to better illustrate the effect of pressurizing the ear (panel c). As others have described for the ambient ear-canal air pressure condition (Shaw and Stinson, 1981; Keefe *et al.*, 1993; Voss and Allen, 1994), reflectance is high at low frequencies, dips to minima at about 1.2 and 3.5 kHz above which reflectance increases to about 8.0 kHz, and decreases again at higher frequencies. With positive or negative ear-canal air pressure, reflectance is increased at frequencies below the 3.5-kHz minimum, decreased at frequencies just above 3.5 kHz resulting in an upward shift in the minimum, and only slightly affected by pressure at high frequencies.

The average reflectance shown in Fig. 6(b) is influenced by nonambient middle-ear pressures that exist in individual subjects. The pressure at which peak admittance occurs for a low-frequency probe tone (tympanometric peak pressure, TPP) is widely used as an estimate of the middle-ear pressure (Terkildsen and Thomsen, 1959). In Fig. 7 average reflectance is calculated for two pressure conditions—ambient pressure and TPP. The inset shows the distribution of TPPs for the 20 normal subjects. Compared to the tympanometric peak pressure condition, average reflectance at ambient ear canal pressure is higher at low frequencies, lower just above the resonant frequency, and unchanged at high frequencies.

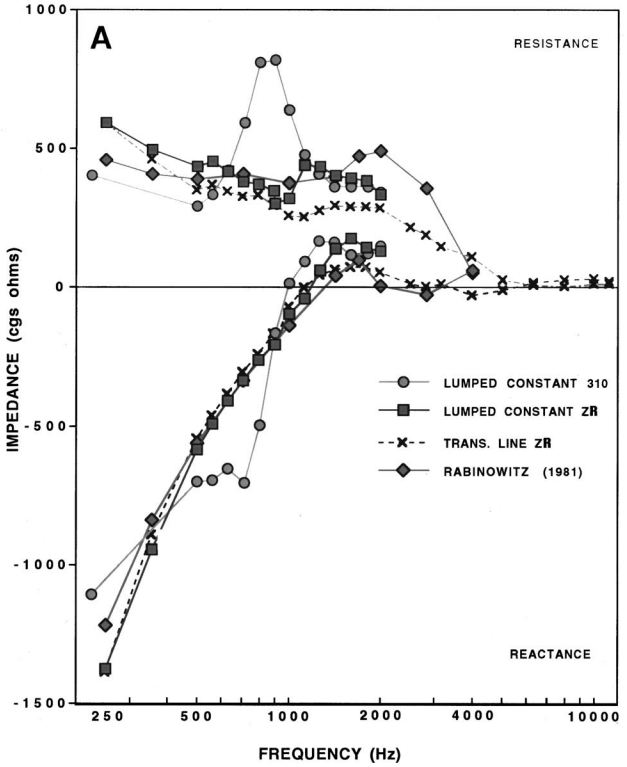

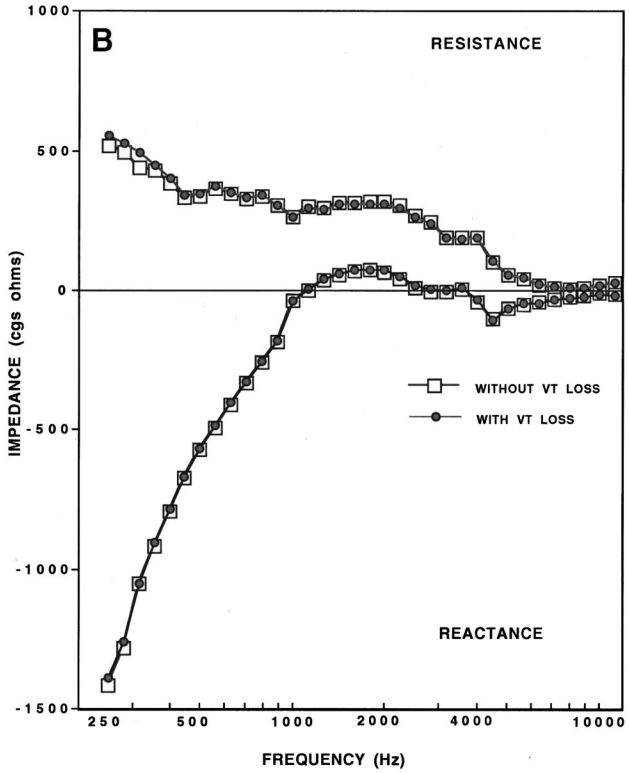

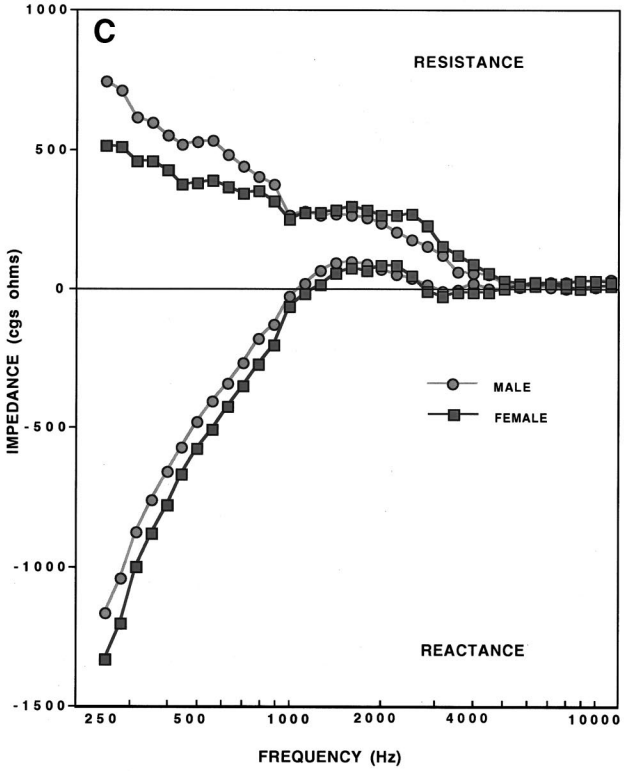

FIG. 5. (a) Middle-ear impedance determined from acoustic measurements made with the two measurement system and two methods for compensating for the volume of air in the ear canal. See text for a description of the compensation methods. Also shown are data from Rabinowitz (1981). (b) Middle-ear impedance determined from measurements made with the wideband reflectance system using two transmission line approximations of the ear canal, one with and one without an estimate of viscothermal losses. (c) Middle-ear impedance estimated from measurements made with the wideband reflectance system for male and female subjects.

This is the expected effect of the stiffening of the middle-ear system that results from pressurizing the middle ear. Although the difference is small for the normal subjects in this study, it is likely that the effect will be large for children who exhibit a greater range of middle-ear pressures, and in individual adults who may have negative pressure without significant middle-ear disease. In order to separate the effects of middle-ear pressure from those of other disease characteristics such as middle-ear effusion, it may be necessary to compensate for middle-ear pressure when comparing wideband impedance and reflectance responses in normal and impaired ears.

D. Reflectance tympanograms

Figure 8 shows wideband reflectance tympanograms for a representative subject (panel a) and the average for all subjects (panel b). These figures are simply rotations of Fig. 6(a)

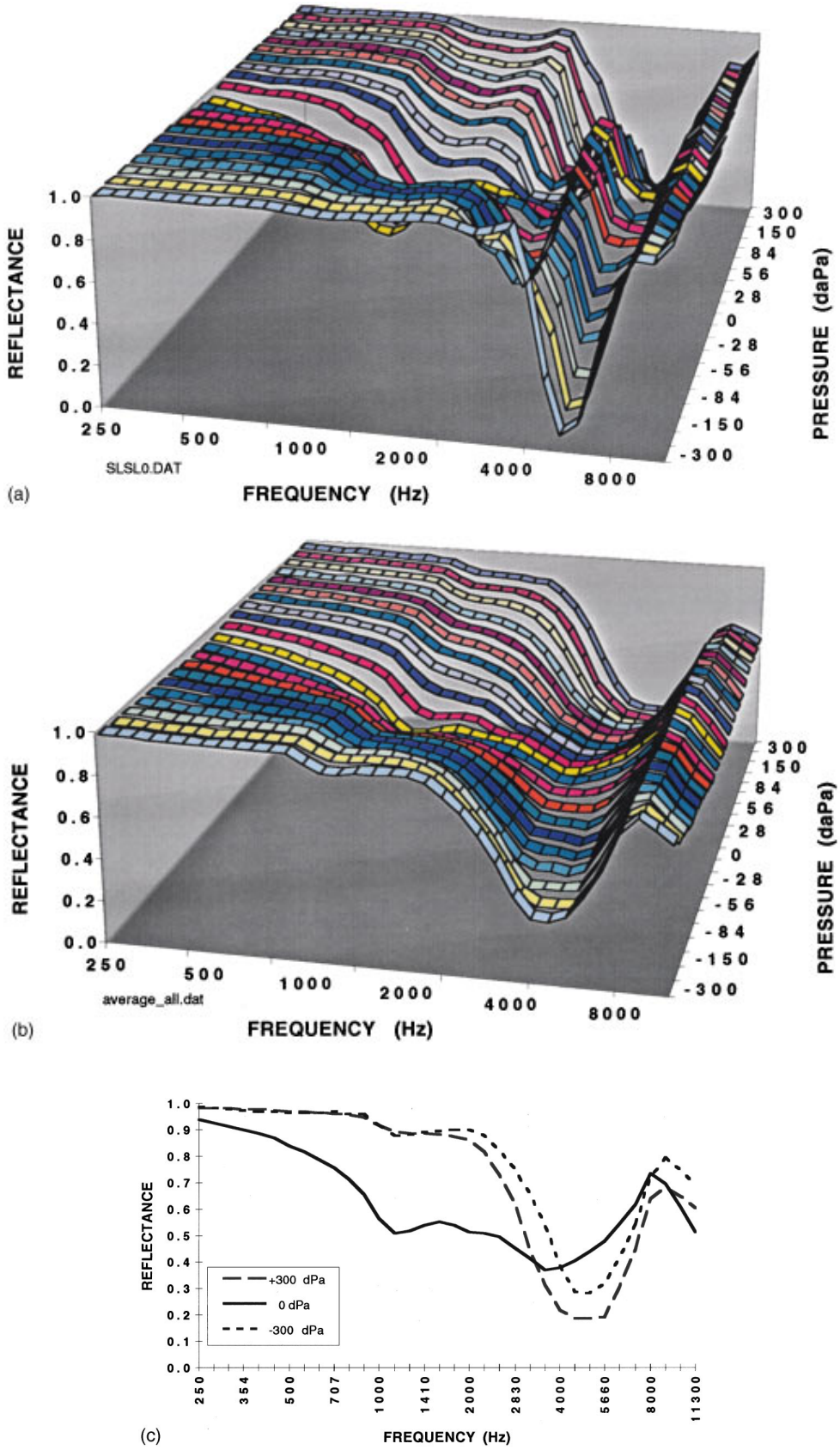

FIG. 6. (a) Reflectance as a function of frequency at various ear-canal air pressures for one normal subject. (b) Average reflectance for 20 normal subjects. (c) Average reflectance as a function of frequency for three ear-canal air pressures.

and (b) to illustrate more clearly the effects of ear-canal pressure on reflectance. As probe frequency increases, reflectance tympanograms progress through a sequence of patterns. At low frequencies, the tympanograms are ''V'' shaped. The pattern inverts at about 3.5 kHz and flattens at high frequencies. In some cases there is a transition region between the ''V'' pattern and the inverted ''V'' pattern in which the reflectance takes on a ''W'' pattern. These patterns are related to the effects of air pressure in the three frequency ranges which can be seen in Fig. 6(c). At low frequencies

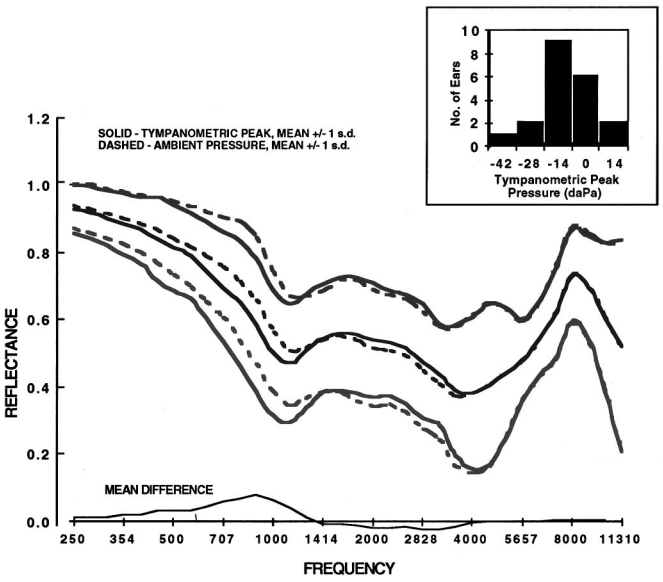

FIG. 7. Average reflectance as a function of frequency (mean±1 s.d.) for two ear-canal air pressure conditions. For each condition, the middle line represents the mean and the upper and lower lines represent the mean ±1 s.d. The solid lines are averages for the ambient ear-canal air pressure condition. The dashed lines are averages for ear-canal pressures corresponding to maximum admittance at 226 Hz (tympanometric peak pressure). The distribution of tympanometric peak pressures are shown in the inset.

pressurizing the ear canal increases the reflectance; in the 3.5–8.0-kHz range ear-canal air pressure decreases the reflectance; and above 8.0 kHz pressurizing the ear has little effect on reflectance.

The orderly behavior of high-frequency reflectance tympanograms (Fig. 8) stands in marked contrast to the disorderly behavior of two-component admittance tympanograms (Fig. 4). This is unexpected, since both sets of data are derived from the same magnitude and phase measurements. Perhaps the phase dependence of the admittance tympanograms, in a region in which phase angles are near zero (Fig. 5), produces ''jitter'' in the admittance calculations that cause the irregular patterns. Because reflectance is phase independent, the same effect does not operate on reflectance tympanograms.

III. DISCUSSION

A. Comparison of measurement systems

In general, the two instruments produced similar measurements over the 226–2000-Hz range. Tympanometric patterns were very similar (Fig. 3), the mean resonant frequency was nearly identical, and the resonant frequency estimates from the two systems were highly correlated. Middle-ear impedance measurements obtained from the two systems differed in the region of 0.8 kHz [Fig. 5(a)]. This may be due to an error in the calibration of the clinical instrument resulting from the design of the calibration cavities which have a narrow isthmus between the probe and the cavity itself, introducing a Helmholtz resonance. The calibration tubes used for the wideband reflectance system are designed so that the tip of the probe is flush with the end of the tube with no discontinuity. The impedance measurements in the 8.0-kHz region obtained from the reflectance system are more consistent with previous data [e.g., Rabinowitz, 1981; see Fig. 5(a)] and middle-ear models (e.g., Zwislocki, 1962).

Voss and Allen (1994) present a slightly different form of the middle-ear impedance magnitude, in which the measured impedance at the probe tip is compensated using a cylindrical-tube model of the ear canal. The area used in the cylindrical tube model was 0.43 cm^2 for all subjects and the length value was chosen so that a constraint on the phase was satisfied. The average impedance magnitude at 1 kHz is close to 300 cgs ohms, in agreement with our results.

B. Middle-ear impedance–ear-canal compensation methods

The middle-ear impedance was calculated using three methods to compensate for the acoustic influence of the ear canal. The lumped-constant method assumes that the ear canal is a pure compliance. The other two methods used a transmission-line model of the ear canal, which is assumed to be adequately represented as a short cylindrical tube. The model parameters in each case were the ear-canal length and area. In one variant of the transmission line model the acoustic transmission in the ear canal is assumed to be loss-free. In the other viscothermal losses at the ear-canal walls are included. As is well known from theoretical investigations, the loss-free transmission line model is identical to the lumped-constant method at sufficiently low frequencies, and the influence of viscothermal losses is negligible at sufficiently high frequencies. Small, systematic differences in the middle-ear impedance calculated from the lumped-constant and loss-free transmission line methods were observed above 1.0 kHz using the response measured by the experimental wideband system [Fig. 5(a)]. While it is often stated that the lumped-constant method is accurate up to 2.0 kHz, our results suggest that the upper limit for accuracy was only 1.0 kHz in normal adult ears. Small, but systematic, differences in the middle-ear impedance were observed between the two transmission-line models at frequencies below 0.4 kHz. This is consistent with acoustic theory, in that viscothermal effects are most important at lower frequencies (or smaller-diameter ear canals). Larger differences would be anticipated for smaller-diameter ear canals, such as in infants, but such ear canals are shorter in length, which reduces the difference. It is concluded that the need to include viscothermal losses in a transmission-line model of the human ear canal is probably not necessary, except, perhaps, for unusual cases such as collapsed ear canals in neonates or in the presence of ear-canal abnormalities.

The compensation methods employed here do not account for the effect of the soft ear canal walls. Rather, they assume that the ear canal is a rigidly enclosed space. Because we were not able to measure the impedance close to the eardrum, the magnitude of the error is unknown. One way to explore this effect would be to measure ear canal impedance in a case where the middle ear impedance is infinitely high. It is clear that ear-canal air pressure does not achieve this condition because hearing sensitivity is only slightly affected. Measurement of ear canal impedance in subjects with fluid-filled middle ears may provide a means to assess ear-

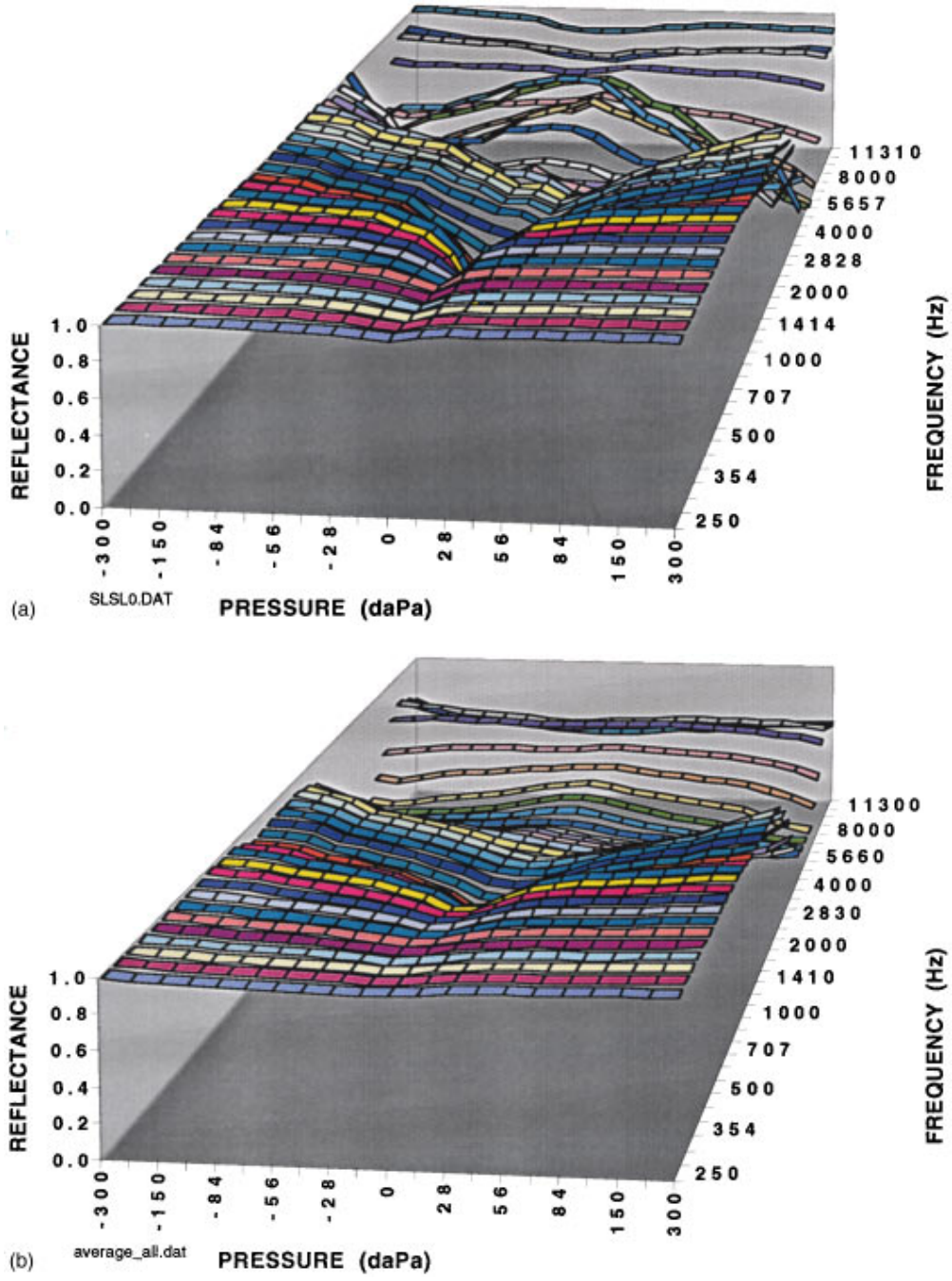

FIG. 8. (a) Reflectance tympanograms for one normal subject. (b) Reflectance tympanograms averaged for 20 normal subjects.

canal impedance characteristics. This can be accomplished by filling the middle ear of animal subjects with a viscous material and by testing patients who have middle ears that are completely filled with fluid.

The small gender differences shown in Fig. 5(c) are probably due to middle-ear rather than ear-canal effects. Although there was a small, significant gender difference in tip size used to seal the probe in the ear canal (11.9 vs 11.1 mm for females and males, respectively), this difference should be removed by the ear-canal compensation process. It is not likely that the impedance differences are related to gender-specific errors in ear canal compensation.

C. Multifrequency tympanometry

Multifrequency tympanometry has been shown to be sensitive to some middle-ear pathologies that are not detected by the conventional single-frequency test (Margolis and Shanks, 1991; Hunter and Margolis, 1992; Hunter *et al.*, 1993a, b; Margolis *et al.*, 1993; Margolis and Hunter, 1999; Margolis *et al.*, 1998). The results of this study indicate that tympanometric patterns from normal ears over the 226–2000-Hz range are in good agreement using two measurement systems that are calibrated using very different (but equally valid) methods. Tympanometric patterns conformed closely to the Vanhuyse model. Of a total of 280 tympano-

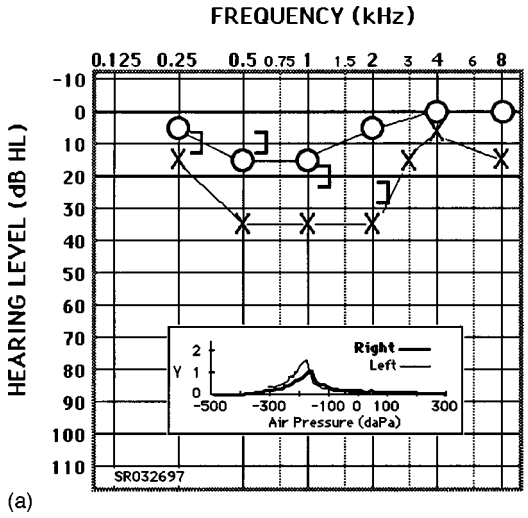

(a)

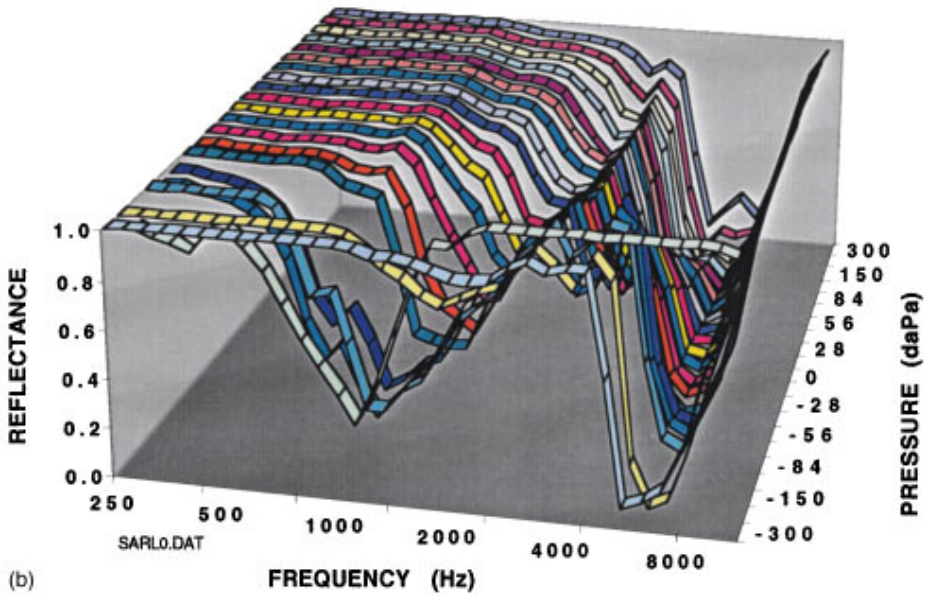

(b)

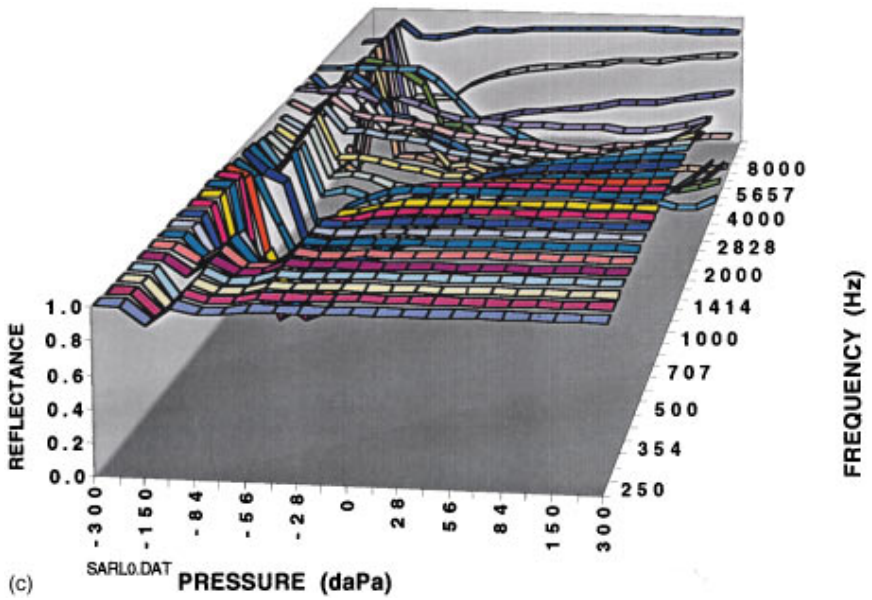

(c)

FIG. 9. (a) Audiogram and 226-Hz admittance tympanograms (insert) for a patient with chronic otitis media. Audiogram symbols: ○=right ear air conduction threshold; ×=left ear air conduction threshold;]=left ear masked bone conduction threshold. (b) Reflectance patterns for the same patient. (c) Reflectance tympanograms for the same patient.

grams obtained with each instrument (20 subjects at 14 frequencies), 97% of those obtained with the clinical system and 96% of those obtained with the reflectance system were Vanhuyse patterns. Interestingly, the ''irregular'' patterns obtained with the clinical system all occurred at high frequencies ($\geqslant$1.25 kHz) while the irregular patterns obtained with the reflectance system occurred in low frequencies ($\leqslant$1.0 kHz), suggesting different reasons for the departures from the model for the two systems.

While tympanograms obtained at frequencies $\leqslant$2.0 kHz are well behaved, in terms of an orderly adherence to the Vanhuyse model, tympanograms for higher frequencies do not appear to be very systematic. This is in contrast to the orderly behavior of reflectance patterns at those frequencies [Figs. 6(b) and 8(b)]. The chaotic behavior of tympanograms and the orderly behavior of reflectance is curious in view of the fact that they are derivations of the same source data. The complex behavior of high-frequency admittance tympanograms evident in Fig. 4 may be influenced by standing-wave effects related to the position of the probe assembly in the ear canal, which are better controlled for in the reflectance tympanogram. This complex behavior may limit the usefulness of high-frequency admittance tympanograms for identifying middle-ear pathology.

D. Reflectance tympanometry

The effect of air pressure on reflectance patterns (Fig. 6) is somewhat surprising. The stiffening effect of pressurizing the ear canal is well known. At low frequencies, ear-canal air pressure increases the stiffness causing the familiar tympanometric pattern with a single central peak. At high frequencies, the effect is more complex because of interactions between the stiffness of the tympanic membrane, which is most directly influenced by air pressure, and the mass components of the middle-ear impedance. Pressurizing the ear can cause a mass-dominated impedance to become a stiffness dominated impedance, producing the patterns that are predicted by the Vanhuyse model (see the Appendix). It is not surprising that at low frequencies, ear-canal pressure increases the reflectance in the ear canal, probably due to stiffening the eardrum. The decrease in reflectance above 3.5 kHz may be related to the predicted decrease in middle-ear impedance in that frequency range that results from stiffening the middle-ear system (Johansen, 1948). The pressure-induced decrease in reflectance in the 3.5–8.0-kHz range indicates that there is more efficient coupling of the ear canal to the middle ear in that frequency range. Whether that coupling extends to the cochlea is not known. Changes in sensitivity or loudness could be measured to determine if the decrease in reflectance is related to more sound delivery to the cochlea.

Reflectance measurements for various ear-canal pressures can be displayed in the frequency domain (Fig. 6) or in the pressure domain (Fig. 8). Experience with patients with ear disease is needed to determine which representation is more useful for detection of middle-ear disease. The reflectance tympanograms (Fig. 8) show a promising systematic sequence of patterns. The orderly transition from the V pattern to the inverted-V pattern to the flat pattern as frequency increases may provide a framework for comparing normal and abnormal ears.

Studies of abnormal ears are under way. Figure 9 shows audiometric and reflectance results for a 10-year-old boy with recurrent otitis media. His audiogram (panel a) shows a 35-dB, predominantly conductive hearing loss in the left ear. The 226-Hz admittance tympanograms were characterized by negative tympanometric peak pressure (between -150 and -250 daPa) with normal static compensated admittance and normal tympanometric width bilaterally [Fig. 9(a) insert]. Tympanograms with these characteristics are usually associated with negative middle-ear pressure without middle-ear pathology or hearing loss. Otomicroscopy of the left ear revealed tympanic membrane retraction, fibrosis, and atrophy, without evidence of middle-ear effusion. As a result of the middle-ear pressure, the reflectance pattern at ambient pressure in Fig. 9(b) is similar to the reflectance pattern of a normal ear when it is pressurized [compare to Fig. 6(a) and (b) at high positive or negative pressure]. When the ear canal is pressurized to compensate for the middle-ear pressure (near -250 daPa), abnormal patterns are obtained, indicating pathologic middle-ear changes in addition to middle-ear pressure.

When displayed in the pressure domain [Fig. 9(c)], the patterns do not follow the orderly sequence of the normal ear and appear distinctively abnormal [compare to Fig. 8(a) and (b)]. The reflectance tympanograms appear to detect a significant pathology that is responsible for the hearing loss. In this case, conventional single-frequency tympanometry failed to reveal the abnormality.

IV. CONCLUSIONS

The results of this investigation of impedance and reflectance measurements in normal adult subjects suggest the following conclusions.

(1) The experimental reflectance measurement system and the clinical system produce similar results for frequencies $\leqslant$2.0 kHz when compared on the basis of tympanometric patterns and resonant frequency estimate. The middle-ear impedance estimates differ in the 0.8-kHz region, probably due to a calibration error in the clinical system.
(2) Multifrequency tympanograms obtained with the two systems for frequencies $\leqslant$2.0 kHz consistently follow the progression of patterns predicted by the Vanhuyse model.
(3) Multifrequency admittance tympanograms for frequencies $>$2.0 kHz do not appear to follow an orderly sequence of patterns and may not be useful for detecting middle-ear pathology. On the other hand, multifrequency reflectance tympanograms progress through an orderly sequence of patterns as frequency is increased from 0.25 to 11.3 Hz. This orderly behavior might provide a useful framework for detecting pathological changes in the wideband reflectance of the middle ear.
(4) A small, statistically significant gender effect occurred in middle-ear impedance measurements made with the experimental system. The gender effect was not significant

in measurements made with the clinical system, probably due to the higher variability associated with measurements made with that instrument. The effect of gender on ear-canal diameter was not significant, indicating that the gender effect results from true differences in middle ear impedance.

(5) Pressurizing the ear canal increases the energy reflectance in the ear canal for frequencies $\leqslant$3.5 kHz, decreases reflectance in the 3.5–8.0-kHz range, and has little effect at higher frequencies. Average reflectance at ambient ear-canal pressure is systematically influenced by small, nonambient middle-ear pressures that occur in normal subjects.

(6) A case is presented in which middle-ear pathology coexists with negative middle-ear pressures. In this case the reflectance at ambient pressure resembled the reflectance of a pressurized normal ear. When the middle-ear pressure was compensated by pressurizing the ear canal, an abnormal reflectance pattern was revealed. When significant middle-ear pressures occur, it may be necessary to compensate for middle-ear pressure (by varying the ear-canal pressure) to detect middle-ear pathology, but this possibility remains to be examined systematically.

ACKNOWLEDGMENTS

This work was supported by Grant No. P50-DC03093 from the National Institutes of Health. We are grateful to Grason-Stadler, Inc., for their assistance in the design and construction of the probe used for the impedance/reflectance system, and to Dr. Paul Osterhammel for providing Fig. 1.

APPENDIX: THE VANHUYSE MODEL

The Vanhuyse model is based on assumptions of the shapes of resistance and reactance tympanograms. Because admittance, conductance, and susceptance tympanograms are simply mathematical transformations of impedance components (resistance and reactance), impedance can be manipulated and the effects on admittance, conductance, and susceptance can be observed. The reason that this approach is informative is that simple changes in impedance quantities produce complex changes in admittance quantities.

The Vanhuyse model is represented graphically in Fig. A1. Based on acoustic impedance measurements that had been made in the cat (Moller, 1965), the resistance tympanogram was assumed to be a monotonically decreasing function of air pressure, with a higher resistance for negative pressure than for positive pressure and reactance is a single-peaked function that is symmetric around ambient ear canal pressure (upper left panel of Fig. A1). The reactance values are negative because at low frequencies the ear is stiffness controlled. The absolute values of reactance are greater than resistance at all pressures. (Compare the reactance X tympanogram with the dashed line in Fig. A1.)

As the reactance tympanogram shifts from negative to positive values, four tympanometric patterns occur. These were named by Vanhuyse *et al.* according to the number of positive and negative peaks (extrema) in the susceptance and conductance patterns.

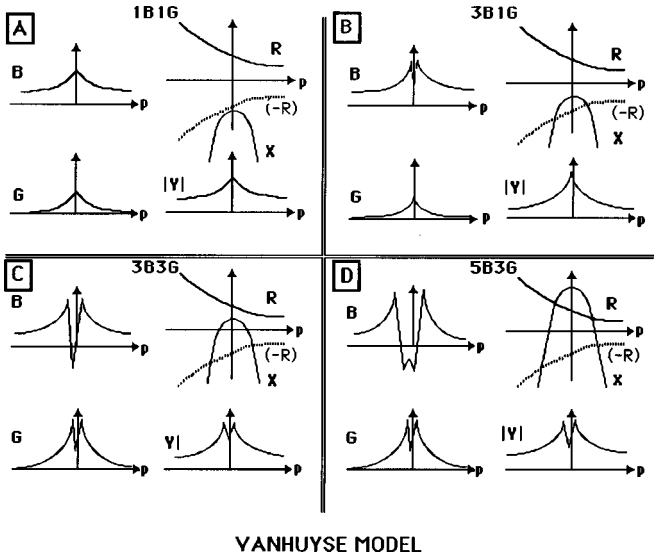

FIG. A1. Graphic representation of the Vanhuyse Model (Vanhuyse *et al.*, 1975). The model determines the shapes of susceptance (B) and conductance (G) tympanograms from assumptions of the shapes and locations of reactance (X) and resistance (R) tympanograms. The upper right corner of each panel shows the reactance and resistance tympanograms. The resistance tympanogram is also shown as negative values ($-R$) to compare its magnitude with the reactance tympanogram. The corresponding susceptance (B), conductance (G), and admittance (Y) tympanograms are also shown in each panel. (a) The $1B1G$ pattern occurs when reactance is negative (stiffness controlled) and its absolute value is greater than resistance at all pressures. (b) The $3B1G$ pattern occurs when the reactance is negative and its absolute value is less than resistance at low pressures but greater than resistance at high pressures. (c) The $3B3G$ pattern occurs when reactance is positive (mass controlled) and less than resistance at low pressures and negative at high pressures. (d) The $5B3G$ pattern occurs when reactance is positive and greater than resistance at low pressures and negative at high pressures.

1*B*1*G*. [Fig. A1, Panel A] In the $1B1G$ pattern both susceptance B and conductance G are single peaked. The admittance Y tympanogram is also single peaked. This pattern occurs when acoustic reactance is negative at all ear canal pressures and greater in absolute value than resistance. That is, $X<0$ and $|X|>R$.

3*B*1*G*. [Fig. A1, Panel B] In the $3B1G$ tympanogram, conductance G is single peaked and there is a central notch in susceptance B, resulting in three extrema. This occurs when the reactance tympanogram is shifted toward zero so that at low pressures the absolute value of reactance is less than resistance ($X<0$ and $|X|<R$) and at high pressures the absolute value of reactance is greater than resistance ($X<0$ and $|X|>R$). The model predicts that the admittance Y tympanogram is single peaked. In some cases, however, admittance can be notched in the $3B1G$ pattern (Margolis *et al.*, 1985).

3*B*3*G*. [Fig. A1, Panel C] In the $3B3G$ pattern conductance G and susceptance B are both notched. This occurs when reactance at low pressure becomes positive but remains less than resistance ($0<X<R$). That is, the ear becomes mass controlled. When the ear is pressurized, the system is stiffened and reactance is negative. The susceptance B notch dips below the tail values resulting in a negative compensated susceptance indicating a mass controlled ear. The admittance Y tympanogram is also notched.

5*B*3*G*. [Fig. A1, Panel D] In the $5B3G$ pattern, the con-

ductance G tympanogram is notched and the susceptance B tympanogram has five extrema. This occurs when the reactance X tympanogram shifts further into positive values so that at low pressures reactance is positive and greater than reactance ($X>R$). Pressurizing the ear has a stiffening effect and at high pressures the reactance is negative (stiffness controlled).

The resonant frequency at the input to the middle ear is the frequency at which the total reactance is 0. At that frequency, the stiffness reactance and mass reactance are equal but of opposite sign. According to the Vanhuyse model, the resonant frequency of the middle ear is the transition frequency from $3B1G$ to $3B3G$. Another way to identify the resonant frequency is to locate the frequency at which the compensated susceptance is zero. A number of methods for estimating resonant frequencies have been compared (Margolis and Goycoolea, 1993; Hanks and Rose, 1993). The method that appears to be optimal is the frequency at which the minimum susceptance (in the notch) is equal to the positive tail value.

The model provides an understanding of the greater complexity of tympanometric patterns as frequency increases. We know that the reactance of the ear shifts from large negative values toward zero with increasing frequency. The effect of probe frequency on tympanometric shapes can be predicted by shifting the reactance tympanogram accordingly. Shifting the reactance tympanogram from large negative values to positive values results in a sequence beginning with $1B1G$ and progressing through $5B3G$. This is the sequence that occurs in a typical normal adult ear (Margolis and Goycoolea, 1993; Margolis *et al.*, 1985).

The effects of some pathologies can also be predicted. A stiffening of the middle ear is expected to shift the reactance tympanogram toward larger negative values while an ossicular discontinuity would have the opposite effect. This approach has been found to account for the effects of frequency and many pathologies on tympanometric shapes.

[1]Throughout this article, the term ear-canal air pressure is used to refer to static or slowly changing pressure changes in the ear canal, in contrast to the acoustic pressure waves used to measure impedance/reflectance.
[2]Virtual Corporation, Portland, OR, is no longer in business.

Allen, J. B. (**1985**). ''Measurement of Eardrum Acoustic Impedance,'' in *Peripheral Auditory Mechanisms*, edited by J. Allen, J. Hall, A. Hubbard, S. Neely, and A. Tubis (Springer-Verlag, New York).

Békésy, G. v. (**1932**). ''Zur theorie des horens bei der schallaufnahme durch knochenleitung,'' Ann. Phys. **13**, 111–136.

Colletti, V. (**1976**). ''Tympanometry from 200 to 2000 Hz probe tone,'' Audiology **15**, 106–119.

Eavey, R. D. (**1993**). ''Abnormalities of the neonatal ear: Otoscopic observations, histologic observations, and a model for contamination of the middle ear by cellular contents of amniotic fluid,'' Laryngoscope **103** (Suppl. 58), 1–31.

Hanks, W. D., and Rose, K. J. (**1993**). ''Middle ear resonance and acoustic immittance measures in children,'' J. Speech Hear. Res. **36**, 218–221.

Heaviside, O. (**1886**). ''Electromagnetic induction and its propagation. Section XXIX. Oscillatory impressed force at one end of a line. Its effect. Application to long distance telephony and telegraphy,'' The Electrician (July 23), p. 149.

Holte, L. A., Margolis, R. H., and Cavanaugh, R. M. (**1991**). ''Developmental changes in multifrequency tympanograms,'' Audiology **30**, 1–24.

Hudde, H. (**1983**). ''Measurement of the eardrum impedance of human ears,'' J. Acoust. Soc. Am. **73**, 242–247.

Hunter, L. L., and Margolis, R. H. (**1992**). ''Multifrequency tympanometry: Current clinical application.'' Am. J. Audiol. **1**, 33–43.

Hunter, L. L., Margolis, R. H., Rykken, J. R., and Giebink, G. S. (**1993a**). ''Multifrequency tympanometry in children followed long-term after treatment for chronic otitis media,'' Midwinter Research Meeting of the Association for Research in Otolaryngology, St. Petersburg Beach, FL.

Hunter, L. L., Margolis, R. H., Rykken, J. R., and Grebink, G. S. (**1993b**). ''Multifrequency tympanometry in normal children and children recovering from otitis media-a preliminary report,'' in *Recent Advances in Otitis Media, Proceedings of the Fifth International Symposium*, edited by D. J. Lim, C. D. Bluestone, J. O. Klein, J. D. Nelson, P. L. Ogra (Decker Periodicals, Philadelphia).

Jerger, J. (**1970**). ''Clinical experience with impedance audiometry,'' Arch. Otolaryngol. **92**, 311–324.

Johansen, H. (**1948**). ''Relation of audiograms to the impedance formula,'' Acta Oto-Laryngol. Suppl. **74**, 65–75.

Keefe, D. H., and Levi, E. (**1996**). ''Maturation of the middle and external ears: acoustic power-based responses and reflectance tympanometry,'' Ear Hear. **17**, 361–373.

Keefe, D. H., Ling, R., and Bulen, J. C. (**1992**). ''Method to measure acoustic impedance and reflectance coefficient,'' J. Acoust. Soc. Am. **91**, 470–485.

Keefe, D. H., Bulen, J. C., Arehart, K. H., and Burns, E. M. (**1993**). ''Ear-canal impedance and reflection coefficient in human infants and adults,'' J. Acoust. Soc. Am. **94**, 2617–2638.

Keefe, D. H., Bulen, J., Harrison, W., Dunnell, J., and Norton, S. J. (**1995**). ''Impedance and reflectance in the middle ears of children,'' Midwinter Research Meeting of the Association for Research in Otolaryngology, St. Petersburg Beach, FL.

Liden, G. (**1969**). ''The scope and application of current audiometric tests,'' J. Laryngol. Otol. **83**, 507–520.

Lynch, T. J., Peake, W. T., and Rosowski, J. J. (**1994**). ''Measurements of the acoustic input impedance of cat ears, 10 Hz to 20 kHz,'' J. Acoust. Soc. Am. **96**, 2184–2209.

Margolis, R. H., and Goycoolea, H. G. (**1993**). ''Multifrequency tympanometry in normal adults,'' Ear Hear. **14**, 408–413.

Margolis, R. H., and Hunter L. L. (**1999**). ''Tympanometry—Basic Principles and Clinical Applications,'' in *Contemporary Perspectives on Hearing Assessment*, edited by W. F. Rintelmann and F. Musiek (Allyn and Bacon, Boston).

Margolis, R. H., Hunter, L. L., and Saupe, J. R., and Grebink, G. S. (**1993**). ''Tympanometric evaluation of middle ear function in children with otitis media,'' Ann. Otol. Rhinol. Laryngol. **103** (Suppl. 163), 34–38.

Margolis, R. H., and Keefe, D. H. (**1997**). ''Reflectance tympanometry,'' Midwinter Research Meeting of the Association for Research in Otolaryngology, St. Petersburg Beach, FL.

Margolis, R. H., and Shanks, J. E. (**1991**). ''Tympanometry: Basic principles and clinical applications,'' in *Hearing Assessment*, edited by W. F. Rintelmann (Pro-Ed, Austin, TX).

Margolis, R. H., Schachern, P. A., and Fulton, S. (**1998**). ''Multifrequency tympanometry and histopathology in chinchillas with experimentally-produced middle-ear pathologies,'' Acta Oto-Laryngol. **118**, 216–225.

Margolis, R. H., Van Camp, K. J., Wilson, R. H., and Creten, W. L. (**1985**). ''Multifrequency tympanometry in normal ears,'' Audiology **24**, 44–53.

Metz, O. (**1946**). ''The acoustical impedance measured on normal and pathological ears,'' Acta Oto-Laryngol. Suppl. **63**, 3–254.

Moller, A. R. (**1965**). ''Network model of the middle ear,'' J. Acoust. Soc. Am. **33**, 168–176.

Paparella, M. M., Shea, D., Meyerhoff, W. L., and Goycoolea, M. V. (**1980**). ''Silent otitis media,'' Laryngoscope **90**, 1089–1098.

Piskorski, P., Keefe, D. H., Simmons, J. L., and Gorga, M. P. (**1999**). ''Prediction of conductive hearing loss based on acoustic ear-canal response using a multivariate clinical decision theory,'' submitted to J. Acoust. Soc. Am.

Pohlman, A. G., and Kranz, F. W. (**1923**). ''The effect of pressure changes in the external auditory canal on acuity of hearing,'' Ann. Otol. Rhinol. Laryngol. **32**, 545–553.

Politzer, A. (**1869**). *The Membrana Tympani* (Wood, New York).

Rabinowitz, W. R. (**1981**). ''Measurement of the acoustic input immittance of the human ear,'' J. Acoust. Soc. Am. **70**, 1025–1035.

Ruah, C., Schachern, P., Zelterman, D., Paparella, M., and Yoon, T. (**1991**). ''Age-related morphologic changes in the human tympanic membrane. A

light and electron microscopic study,'' Arch. Otolaryngol. Head Neck Surg. **117**, 627–634.
Shanks, J. E., and Lilly, D. J. (**1981**). ''An evaluation of tympanometric estimates of ear canal volume,'' J. Speech Hear. Res. **24**, 557–566.
Shaw, E. A. G., and Stinson, M. R. (**1981**). ''Network concepts and energy flow in the human middle ear,'' J. Acoust. Soc. Am. Suppl. 1, **69**, S43.
Stinson, M. R., Shaw, E. A. G., and Lawton, W. B. (**1982**). ''Estimation of acoustical energy reflectance at the eardrum from measurements of pressure distribution in the human ear canal,'' J. Acoust. Soc. Am. **72**, 766–773.
Terkildsen, K., and Nielsen, S. Scott (**1960**). ''An electroacoustic impedance measuring bridge for clinical use,'' Arch. Otolaryngol. **72**, 339–346.
Terkildsen, K., and Thomsen, K. A. (**1959**). ''The influence of pressure variations on the impedance of the human ear drum,'' J. Laryngol. Otol. **73**, 409–418.
Toynbee, J. (**1865**). *Diseases of the Ear* (Blanchard & Lea, Philadelphia).
Van Camp, K. J., Margolis, R. H., Wilson, R. H., Creten, W. L., and Shanks, J. E. (**1986**). ''Principles of tympanometry,'' ASHA Monographs **24**, 1–88.
Van Dishoeck, H. A. (**1937**). ''Das pneumophon: ein apparat zur druckbestimmung immit telohr,'' Archiv fur Ohren-, Nasen-, und Kehlkopf-Heilkunds **144**, 53.
Vanhuyse, V. J., Creten, W. L., and Van Camp, K. J. (**1975**). ''On the W-notching of tympanograms,'' Scand. Audiol. **4**, 45–50.
Voss, S. E., and Allen, J. B. (**1994**). ''Measurement of acoustic impedance and reflectance in the human ear canal,'' J. Acoust. Soc. Am. **95**, 372–384.
Webster, A. G. (**1919**). ''Acoustical impedance, and the theory of horns and of the phonograph,'' Proc. Natl. Acad. Sci. USA **5**, 275–282.
West, W. (**1928**). ''Measurements of the acoustical impedances of human ears,'' Post Office Elect. Eng. J. **21**, 293.
Wheatstone, C. (**1827**). ''Experiments on audition,'' Quarterly J. Sci. Lit. Art. **24**, 67–72.
Wollaston, W. H. (**1820**). ''On sounds inaudible in certain ears,'' Philos. Trans. R. Soc. London **110**, 306–314.
Zwislocki, J. (**1962**). ''Analysis of the middle-ear function. I. Input impedance,'' J. Acoust. Soc. Am. **34**, 1514–1523.

Localization by interaural time difference (ITD): Effects of interaural frequency mismatch

Ben H. Bonham
Department of Otolaryngology and W. M. Keck Center for Integrative Neuroscience, Box 0732, University of California, San Francisco, California 94143-0732

Edwin R. Lewis
Department of Electrical Engineering and Computer Science, University of California, Berkeley, California 94720

(Received 20 April 1998; revised 8 March 1999; accepted 19 March 1999)

A commonly accepted physiological model for lateralization of low-frequency sounds by interaural time delay (ITD) stipulates that binaural comparison neurons receive input from frequency-matched channels from each ear. Here, the effects of hypothetical interaural frequency mismatches on this model are reported. For this study, the cat's auditory system peripheral to the binaural comparison neurons was represented by a neurophysiologically derived model, and binaural comparison neurons were represented by cross-correlators. The results of the study indicate that, for binaural comparison neurons receiving input from one cochlear channel from each ear, interaural CF mismatches may serve to either augment or diminish the effective difference in ipsilateral and contralateral axonal time delays from the periphery to the binaural comparison neuron. The magnitude of this increase or decrease in the effective time delay difference can be up to 400 μs for CF mismatches of 0.2 octaves or less for binaural neurons with CFs between 250 Hz and 2.5 kHz. For binaural comparison neurons with nominal CFs near 500 Hz, the 25-μs effective time delay difference caused by a 0.012-octave CF mismatch is equal to the ITD previously shown to be behaviorally sufficient for the cat to lateralize a low-frequency sound source. © *1999 Acoustical Society of America.* [S0001-4966(99)05206-6]

PACS numbers: 43.64.Bt, 43.64.Qh, 43.66.Pn, 43.66.Qp [RDF]

INTRODUCTION

The familiar axonal propagation delay (APD) model (Jeffress, 1948) for localizing a sound source by interaural time difference (ITD) stipulates exact frequency matching between inputs from the two ears to each binaural coincidence neuron. If we interpret exact to mean originating from exactly symmetric, single hair cells, this exact match corresponds for the cat to an alignment precision of one part in 3000 (55 000 type I afferents, 20 afferents/inner hair cell). In the mammalian auditory system, binaural neurons first occur at the level of the superior olivary complex (SOC); thus the high degree of precision in the synaptic innervation to the binaural neurons must exist even after intermediate synaptic relays in the cochlear nuclei. Does a physiological or developmental mechanism exist that is capable of identifying such exact matches and ensuring that input to a given binaural neuron arises from hair cells at precisely symmetrical locations?

In this paper, we explore the effects of possible interaural frequency mismatches (nonsymmetric innervation) on the function of low-frequency binaural comparison neurons. In particular, we examine the degree of mismatch that can occur before the APD localization model breaks down, in effect determining the limits imposed on the peripheral innervation of a single-CF channel in the APD model. To do this, we have represented the auditory periphery up to the level of the binaural comparison neurons with a linear model based on the work of Carney and Yin (1988), and we have represented the binaural comparison neurons themselves as cross-correlators. We examine the response properties of model binaural comparison neurons that receive input arising from exactly one cochlear channel (i.e., hair cell) from each ear with slight (0.2 octave or less) characteristic frequency (CF) mismatches between the two ears. Specifically, we examine the responses of the model binaural neurons to narrow-band sounds (continuous tones) and to broadband sounds (sound pressure impulses). For both the narrow-band and broadband stimuli, we investigate the relationship of response magnitude to ITD. For the narrow-band stimuli, we also investigate the relationship of best interaural phase difference (IPD) to stimulus frequency, thereby deriving the characteristic phase (CP) and delay (CD) of each model binaural comparison neuron.

Several previous investigators have proposed that input to binaurally responsive neurons might originate from different places along the basilar membrane, but only one published work (Shamma *et al.*, 1989) has addressed the quantitative effect of such a CF mismatch upon binaural cell response properties. For example, while recording from a population of neurons near the SOC, Guinan *et al.* (1972) found about half of the neurons had ''approximately equal'' best frequencies for stimulation of the two ears; consequently, about half would have had two best frequencies that were unequal. A small proportion of the neurons they recorded from were localized to the medial superior olive—a structure often implicated in processing of ITDs. Other investigators have proposed that certain aspects of physiologi-

cal data might be explained by CF mismatches. Yin and Kuwada (1983) suggested that the nonzero CP they observed of some binaural neurons in the IC could be a result of afferents originating in populations of spiral ganglion cells with different best frequencies (a CP precisely equal to zero is an obligatory characteristic of the APD model). While the IC is not generally considered to be the most peripheral stage of binaural interaction, binaural responses of IC neurons are likely to reflect interactions at more peripheral stages. Yin and Kuwada (1984) also noted that phase changes for small population differences are substantial. To date, however, no one has examined closely the physiological differences in tuning from the two ears to binaural comparison neurons and the relationship of those differences to best-ITD. Perhaps this is because, as we see here, the CF differences required to create substantial delay differences are small.

It has been suggested that the differential delays caused by binaural CF differences could be suitably used to create a system for ITD processing that required no tuned axonal delays. This idea was originally proposed by Schroeder (1977), and later implemented in a model for interaural difference processing by Shamma and colleagues (1989). The implementation described by Shamma, which used no differential axonal delays, was intended to be illustrative rather than explanatory; the authors noted that both cochlear and axonal delays would almost certainly be incorporated in the determination of best-ITD in any binaural neuron. Nevertheless, the cochlear-delay-only model was harshly criticized on the basis that CF differences required to create significant best-ITDs would be larger than CF differences observed physiologically. As we shall show, however, even small CF differences are sufficient to compensate for substantial ITDs. Shamma's particular implementation of binaural neuron afferents was based on a biophysical model of the gerbil cochlea. Here we present results from a model in which activity of afferents to binaural comparison neurons is based on physiologically measured eighth nerve responses in the cat. Thus in addition to identifying the quantitative relationship of small interaural CF mismatches to the responses of model binaural neurons, it also should be possible to compare the results presented here with physiological data available from binaural neurons in the cat brainstem.

Our results in summary are: For binaural comparison neurons receiving input from one cochlear (CF) channel from each ear, (1) interaural CF mismatches may serve to either augment or diminish the effective difference in ipsilateral and contralateral axonal time delays from the periphery to the binaural comparison neuron, (2) the magnitude of this increase or decrease in the effective time delay difference can be up to 400 μs for CF mismatches of 0.2 octaves or less for binaural neurons with CFs between 250 Hz and 2.5 kHz, (3) a 0.012-octave CF mismatch near 500 Hz will change the effective time delay difference by 25 μs—the ITD behaviorally shown to be sufficient for lateralization of a low-frequency sound source, and (4) a distinguishing effect of interaural frequency mismatch is to create nonlinearity in the nominally linear best-IPD versus frequency curve.

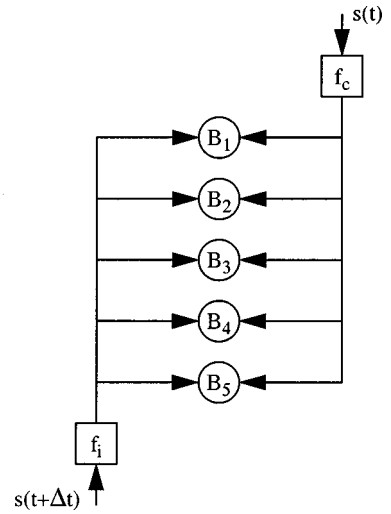

FIG. 1. Model used for analysis. Each model binaural comparison neuron (B_n) receives signals from ipsilateral and contralateral ears corresponding to sound ($s(t)$) processed through delayed gammatone filters (f_i and f_c) from ipsilateral and contralateral ears. In the absence of CF mismatches, the ladderlike afferent innervation causes binaural neurons 1–5 to be selective for different interaural time delays (Δt).

I. METHODS

To answer questions about the effect of interaural frequency mismatches on ITD localization, we constructed simple models of the auditory periphery (one each for ipsilateral and contralateral ears) and of a binaural comparison neuron. The model binaural neuron was innervated by a single channel from the ipsilateral ear and a single channel from the contralateral ear. The CFs from these two innervating channels were either identical or nearly identical; in the case where the two CFs were the same, the resulting innervation to the binaural neuron was consistent with the description of an APD model binaural neuron. Input to the model binaural neuron corresponded to sounds (narrow- or broadband) processed through the two periphery models. The response of the model binaural neuron was computed as the cross-correlation of the two inputs (see Fig. 1).

A. Auditory periphery model

The linear models of the auditory periphery were based on the time-delayed gammatone impulse responses functions described by Carney and Yin (1988; or see the Appendix), along with additional time delays corresponding to axonal propagation delays from the periphery to the binaural neurons.

The set of gammatone impulse responses were presented by Carney and Yin as a simple descriptive model (mathematical description) of the impulse responses computed by reverse-correlation (REVCOR) analysis of low-CF eighth nerve axons in the cat. Each impulse response relates sound pressure at the external ear canal to change in instantaneous spike rate in the eighth nerve axon (measured with respect to a background spike rate not correlated to the sound), and includes a CF-dependent time delay (representing the appropriate observed cochlear propagation time). The filters in our cochlear representations were graded with respect to CF;

and, through the Carney–Yin functions, they were also graded appropriately with respect to cochlear time delay (for the cat cochlea). The filter functions were normalized to yield unit energy in response to a unit impulse.

Every signal transmission path from the cochlea to the binaural comparison neurons in the SOC passes first through a synaptic relay in the cochlear nucleus. This synaptic relay is the secure synapse of the eighth nerve axons onto spherical bushy cells via the large endbulbs of Held (Rhode and Greenberg, 1992). We elected not to explicitly implement this relay synapse in our model; it would have been equivalent to adding an identical constant (synaptic) delay to every CF channel and would have had no effect on our computations.

The final element of our peripheral model corresponded to the axonal propagation delays from the cochleas to the binaural comparison neurons. For localization by ITD, it is the difference in axonal propagation delays from the ipsilateral and contralateral ears to the binaural comparison neuron that is critical, rather than the absolute time delays. To determine the range of these differences, we estimated the range of physiologically realizable differences that would be relevant for a cat. Based on an ear spacing of 10 cm, we estimated the maximum ITD, corresponding to a laterally located sound source, to be approximately 300 μs. This is the largest axonal propagation delay difference required by the APD model.

B. Binaural neuron model

In Jeffress' initial description of the APD model, the binaural neurons were described as spike coincidence detectors. Rather than modeling spike activity as point processes, we chose to base our computations on functions describing the time course of the instantaneous spike rate (or probability density). Over the course of our studies, we modeled the binaural neurons with the following candidate binaural comparison functions: cross-correlation of the filtered ipsilateral and contralateral sound pressure waveforms, cross-correlation of the rectified filtered sound pressure waveforms, peak coincidence of peaks of the filtered sound pressure waveforms, and maximum peak height of the sum of the ipsilateral and contralateral filtered sound pressure waveforms. Because cross-correlation is the binaural comparison function most commonly used in models of ITD computation (Colburn and Durlach, 1978), and because responses of neurons in the SOC and of IPD-sensitive neurons in the IC are accurately described by coincidence detection or cross-correlation (Goldberg and Brown, 1969; Yin *et al.*, 1987; Yin and Chan, 1990), we present the results we obtained with that function in this paper.

The binaural comparison function, cross-correlation, that we used here was:

$$p_{\text{bin}} = \int_{-\infty}^{\infty} p_i(t) p_c(t)\, dt, \tag{1}$$

where p_{bin} is taken to be the instantaneous spike rate of the model binaural neuron, and $p_i(t)$ and $p_c(t)$ are the instantaneous spike rates of its ipsilateral and contralateral afferent inputs, respectively. The instantaneous spike rate on each afferent input is taken to be a delayed function of the sound pressure waveform at the source filtered by the appropriate model cochlear filter; e.g.,

$$p_i(t+\Delta t_p) = f_{i,CF}(t) * s_i(t-\Delta t_A). \tag{2}$$

Here $p_i(t)$ is the instantaneous spike rate determined by convolving the appropriate cochlear filter function, $f_{i,CF}(t)$, with the modeled acoustic input, $s_i(t)$. Δt_A and Δt_P correspond to acoustic propagation delay from the sound source to the ear and axonal propagation delay from the ear to the binaural comparison neuron. For each model binaural neuron, the best-ITD for a particular class of signals (e.g., continuous tones, impulses) was taken to be the one that yielded the maximum value of p_{bin} for that class. Although the figures presented in this paper were based on the use of Eq. (1), the qualitative conclusions that we draw from them were not altered by the use of the other binaural comparison functions.

C. Analysis of model neurons

To examine the effects of CF mismatch, we initially constructed an array of model binaural neurons, each of which received input from identical CF channels from peripheral models corresponding to the ipsilateral and contralateral ears. Members of the array were distinguished by the difference in axon propagation delay of input from the two ears. Over the entire array, these differences spanned the range from 0 to 300 μs. This initially constructed array corresponded to an iso-CF population of binaural neurons described by the APD model, and formed a standard to which we could compare our later results.

For each model iso-CF binaural neuron in this array, the best-ITD was taken to be the ITD that maximized the left-hand term in Eq. (1). The best-ITD was computed both for broadband stimuli (sound pressure impulses) and for narrowband stimuli (continuous tones).

A model iso-CF neuron's response to sinusoidal sound as a function of ITD is given by the cross-correlation of the sinusoidal responses of the two peripheral filters; we computed each neuron's response for several frequencies in the passband of the peripheral filters (where the passband is defined as frequencies for which the response is within 40 dB of the maximum response).

The composite curve is another characterization commonly made for binaural neurons. It is the sum of response versus ITD for sinusoids of several frequencies. Because our peripheral models are linear and we use cross-correlation—also a linear function—the composite curve for the entire frequency continuum for the binaural neuron is exactly equal to the curve of response to broadband noise versus ITD (Yin *et al.*, 1986). In practice, a dense sampling of frequencies within the passband would be sufficient to construct an excellent approximation of the composite curve. Further, because all elements of the model are linear, the response of a binaural neuron to broadband noise as a function of ITD is identical to its response to a sound pressure impulse as a function of ITD (i.e., given by the cross-correlation of the impulse response functions of the two peripheral filters).

A further characterization of binaural neurons is derived from the graph of best interaural phase difference (IPD) versus stimulus frequency. When these data are fit with a straight line, the slope of this line is the characteristic delay (CD) of the binaural neuron and the *y*-intercept is the characteristic phase (CP) (Yin and Kuwada, 1983). While the physiological relevance of the CP and CD is not clear, these parameters do have value as descriptors; we computed values of CP and CD for the model binaural neurons. For our model, computation of best-IPD versus frequency is accomplished by taking the difference in the phase responses of the two peripheral channels.

After computing all these response parameters for the initially constructed iso-CF array, we modified the array by modest systematic perturbations of the cochlear origin (i.e., the CF) of the innervating contralateral input. In addition to modifying the frequency tuning of the contralateral input to the binaural neurons, this also modified the effective propagation delay to the binaural neurons from the contralateral ear by changing the CF-dependent cochlear delay and damping.

For each perturbation in the contralateral CF, we again computed the CP and CD for the model binaural neurons, as well as the best-ITDs for broadband and narrow-band stimuli. These binaural comparison neurons now had different CFs from the two ears, and so responses to binaurally presented tones were typically largest for tones at frequencies somewhere between the two CFs.

II. RESULTS

To provide a baseline for comparison, we first present the results of our analysis for an iso-CF binaural comparison neuron that has a 100 μs longer delay from the contralateral ear than from the ipsilateral ear, and receives input from peripheral channels with identical CFs of 800 Hz from both ears. This scheme describes a binaural neuron of the APD model that is tuned to a part of the contralateral auditory hemifield. The frequency response curve, corresponding to both ipsilateral and contralateral peripheral channels, is shown in Fig. 2. Figure 2(a) shows the impulse responses from the two ears (ipsi—solid line; contra—dashed line); the additional 100-μs contralateral axonal propagation delay (Δt_P) is clearly visible in the comparison of the contralateral and ipsilateral impulse responses. The additional delay is also apparent in comparison of the phase responses of the ipsilateral and contralateral channels shown in Fig. 2(c).

The response of the iso-CF model binaural neuron is characterized in Fig. 3. Responses to sinusoidal stimuli of several frequencies are shown in Fig. 3(a). Figure 3(b) shows the normalized responses to the same frequencies. For every stimulus frequency, the peak response occurs at 100 μs—an ITD determined by the difference in the axonal propagation delays from the peripheral filters. The composite curve shown in Fig. 3(c), formed from summing the sinusoidal response curves [Fig. 3(a)] for all frequencies, is identical to the wide-band response versus ITD curve, and also peaks at 100 μs.

In Fig. 3(d) we show the plot of best interaural phase difference (IPD) versus stimulus frequency for this iso-CF

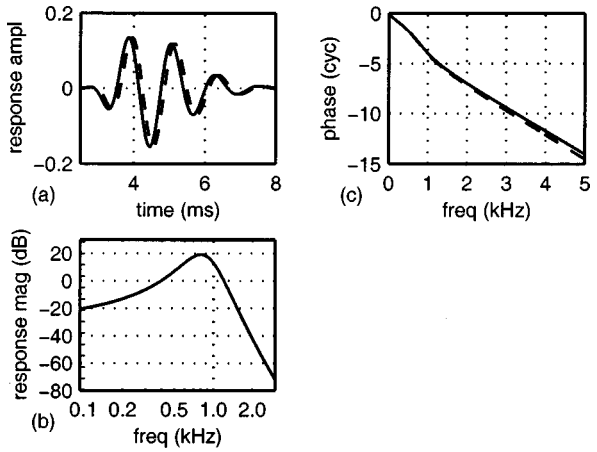

FIG. 2. Peripheral filter properties for the model binaural neuron with 100-μs contralateral delay and no CF mismatch: (a) Impulse responses, (b) frequency tuning curves, (c) phase tuning curves. Solid lines are for ipsilateral channel; dashed lines are for contralateral channel. Ipsilateral and contralateral frequency tuning curves are identical.

binaural neuron. We compute the CP and CD of this neuron by using a least-squared-error (LSE) method to find the best linear fit of phase as a function of frequency for the frequencies 200, 400, 600, 800, 1000, 1200, and 1400 Hz. These frequencies were chosen because the neuron's response to them is within 40 dB of its response to a best-frequency stimulus. For this model neuron, the only difference between the two peripheral channels is a time delay, and so the best-IPD versus frequency plot is exactly linear. While in this case the LSE fit is unnecessary, we include it here for comparison with other model neurons. The characteristic phase (*y*-intercept) of the neuron is 0, and the characteristic delay (slope) is 100 μs—the difference in propagation times from the ipsilateral and contralateral peripheral channels.

As can be seen from analysis of the model iso-CF neuron we described, the incorporation of an additional time delay has no effect on frequency tuning of the peripheral channel, but does affect the phase response by adding to it a

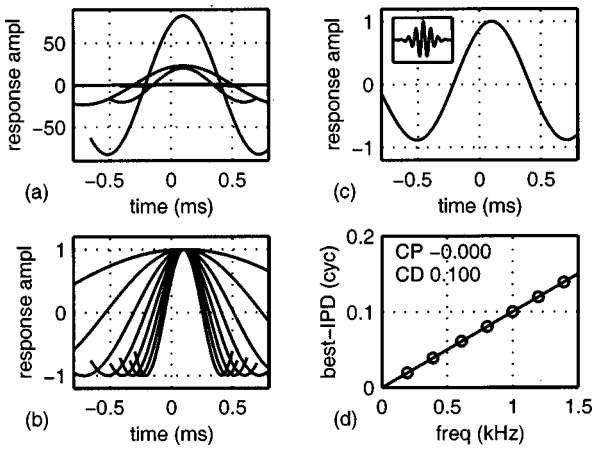

FIG. 3. Response properties of model binaural neuron with 100-μs contralateral delay and no CF mismatch: (a) Response to narrow-band stimuli (pure tones) as a function of ITD, (b) normalized curves from (a), (c) response to wide-band stimuli (sound pressure impulses) as a function of ITD—equal to the composite curve—peaks at 100 μs; inset shows response for ITDs from −5 to 5 ms, (d) best-IPD as a function of stimulus frequency.

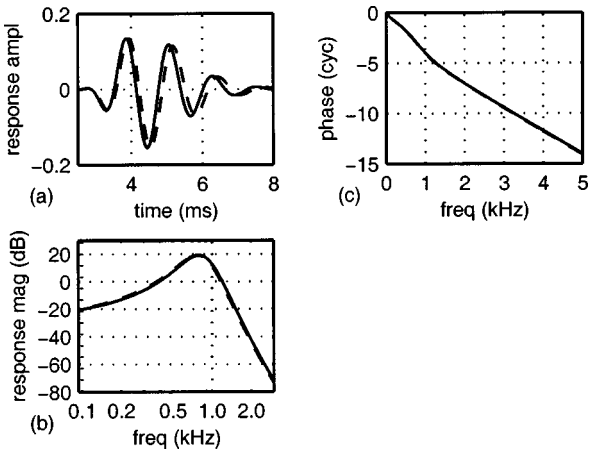

FIG. 4. Peripheral filter properties for the model binaural neuron with no time delay and 0.05-octave CF mismatch: Impulse responses (a), frequency tuning curves (b), and phase tuning curves (c). Solid lines are for ipsilateral channel; dashed lines are for contralateral channel.

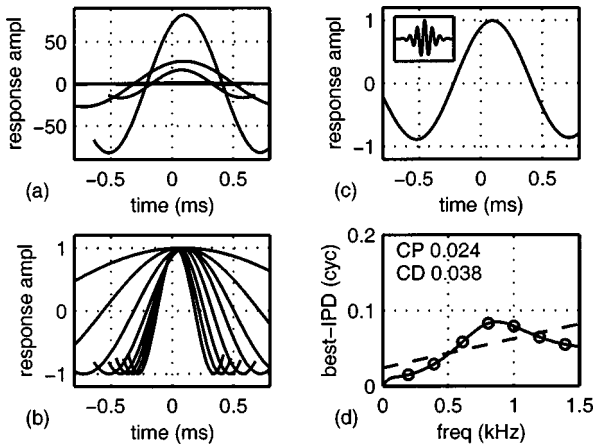

FIG. 5. Response properties of the model binaural neuron with no time delay and 0.05-octave CF mismatch (contralateral CF lower): (a) Response to narrow-band stimuli (pure tones) as a function of ITD. (b) Normalized curves from (a). (c) Response to wide-band stimuli (sound pressure impulses) as a function of ITD (equal to the composite curve) peaks at 95 μs; inset shows response from −5 to 5 ms. (d) Best-IPD as a function of stimulus frequency.

linear component whose slope corresponds to the added delay time. The added strict time delay has analogous effects on the response properties of the binaural neuron, simply shifting the best ITD by the added delay time, and adding a linear component to the best-IPD versus frequency plot.

To clearly distinguish the effects of time delay from CF mismatches, we next describe the results of our analysis for an iso-delay binaural neuron with identical propagation time delays from the two ears, but different CFs. The binaural neuron we use for this receives input from the 800-Hz ipsilateral channel, and input from the 721-Hz contralateral channel (corresponding to an 0.05-octave mismatch in CF).

Figure 4 shows the frequency tuning curves for the ipsilateral and contralateral peripheral channels of the iso-delay neuron, along with their corresponding impulse response functions and phase tuning curves. In comparing the peaks of the impulse response functions, there appears to be an effective difference in time delay from the ipsilateral and contralateral peripheral channels; this apparent delay is the manifestation of differences in the ''strict'' cochlear propagation delay (T_d) and cochlear damping time constant (T_a) in the two peripheral models (see the Appendix).

The response of this iso-delay binaural neuron is characterized in Fig. 5. Responses to sinusoidal stimuli as a function of ITD are shown in Fig. 5(a). In contrast to responses of the iso-CF neuron, these responses peak at different ITDs. Figure 5(c) shows the composite curve for the iso-delay binaural neuron; the composite curve has a maximum for an ITD of 95 μs. The wide-band response curve again exactly matches the composite curve. Thus this neuron is tuned to a part of the contralateral hemifield.

Finally, the curve of best-IPD versus stimulus frequency for the iso-delay neuron is shown in Fig. 5(d). In this case, the difference in the phase responses is not exactly linear, but exhibits a bump near the CF of the binaural neuron. For a gammatone filter, the phase response changes most rapidly near the CF of the filter; the bump in the curve of best-IPD versus stimulus frequency reflects the fact that the phase is rapidly changing at a lower frequency for the filter with the lower CF (i.e., the contralateral filter). This bump near the CF is characteristic of the model binaural neurons that have CF mismatches. From the LSE fit to the phase sample frequencies, the CP of this neuron is 0.024 cycles, and the CD is 38 μs. Curves of best-IPD versus frequency are shown in Fig. 6 for iso-delay model binaural neurons with ipsilateral CF of 800 Hz and contralateral CF mismatches of up to 0.2 octaves.

The effect of CF mismatch on a model neuron that has a specific nonzero propagation time-delay difference is described in Figs. 7 and 8. In this case, the binaural neuron receives contralateral input with axonal propagation delay 200 μs longer than the ipsilateral input. In the absence of any CF mismatch, this neuron would therefore have a best-ITD of 200 μs. Like the earlier two model neurons, for this neuron the ipsilateral input arises from the 800-Hz channel. The contralateral input to this model binaural neuron is from the 888-Hz channel—a −0.05-octave mismatch.

In Figs. 7 and 8 it can be seen that the responses to

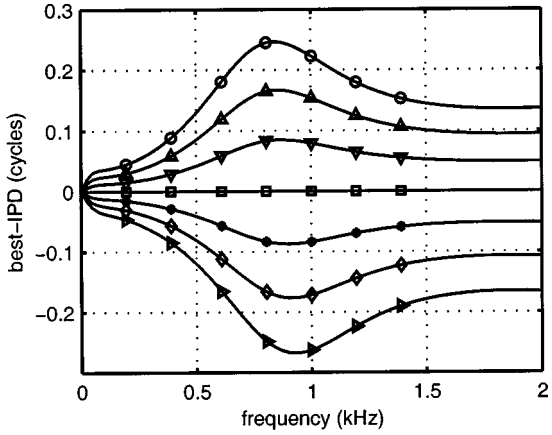

FIG. 6. Plots of best-IPD versus stimulus frequency for several binaural neurons with CF mismatches. Each model neuron had ipsilateral CF of 800 Hz. Contralateral CFs were 721, 746, 773, 800, 828, 857, and 888 Hz, corresponding to CF differences of −0.15, −0.10, −0.05, 0.0, 0.05, 0.10, and 0.15 octaves (bottom to top).

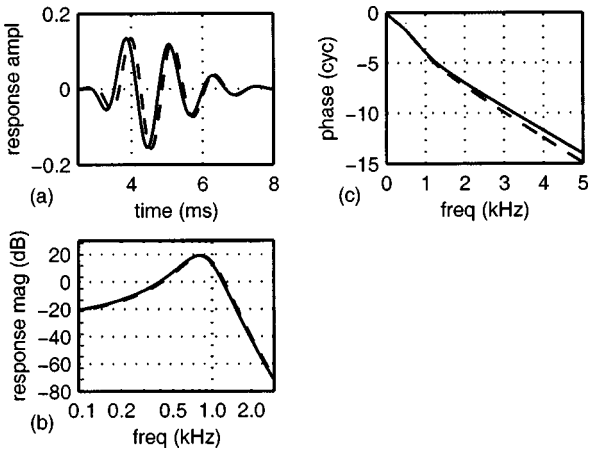

FIG. 7. Peripheral filter properties for the model binaural neuron with 200-μs time delay and -0.05-octave CF mismatch: Impulse responses (a), frequency tuning curves (b), and phase tuning curves (c). Solid lines are for ipsilateral channel; dashed lines are for contralateral channel.

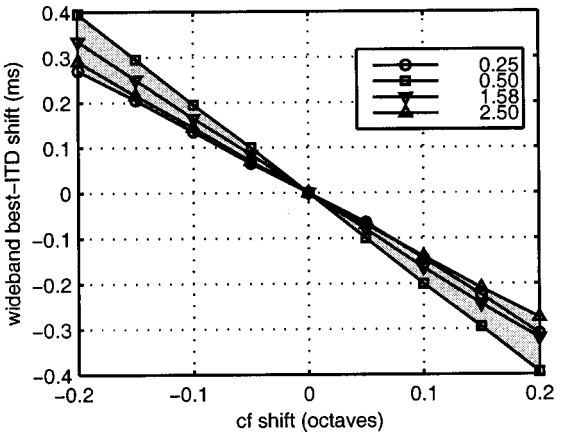

FIG. 9. Change in best-ITD due to CF mismatches up to 0.2 octaves in model neurons. Shaded area shows empirically determined upper and lower bounds for model binaural neurons with nominal CFs between 0.25 and 2.50 octaves. Also shown are curves for four specific binaural neurons with nominal CFs equal to 0.25, 0.50, 1.58, and 2.50 kHz.

sinusoids peak at different times. The composite curve for this neuron, again the same as its wide-band response versus ITD curve, peaks at 105 μs. The plot of best-IPD versus frequency once again displays the bump near the CFs characteristic of CF mismatch. For this model neuron there is also a linear component in the plot of best-IPD versus frequency that is due to the difference in axonal propagation times. From the best-IPD versus frequency plot, the LSE fit shows the CP of this neuron to be -0.022 cycles and the CD to be 157 μs.

As can be seen from the two non-iso-CF examples, an important effect of CF mismatch for these model binaural neurons is a change in the effective time delay for arrival of signals from the two ears, in effect modifying the best-ITD and hence spatial tuning of the neuron. For wide-band sounds, the range of shift in best-ITD due to CF mismatches is shown in Fig. 9 for model binaural neurons with nominal CFs between 0.25 and 2.5 kHz. It can be seen from the figure that the change in best-ITD is between 100 and 200 μs for a CF mismatch of 0.1 octaves, and increases for larger mismatches.

From Fig. 9, we can deduce what must comprise a ''single-CF channel'' for the APD model for localization by ITD. The specific question we ask is how accurate must interaural frequency matching be in order for a cat to localize sounds based only on ITD? Wakeford and Robinson (1974) showed that cats are able to lateralize 0.5- and 1.0-kHz tone bursts with ITDs of approximately 25 μs (lateralization performance is substantially poorer for 2.0-kHz tones). From our computations (cf. Fig. 9), for a binaural comparison neuron with a nominal CF near 500 Hz, 25 μs corresponds to an interaural frequency mismatch of approximately 0.012 octaves. So, we conclude that in the context of the APD model, a single-CF channel near 500 Hz should be interpreted as signals arising within a frequency band with a width of 0.012 octaves. If we assume that the inner hair cells are equally distributed per octave, this frequency band corresponds to a range of four hair cells.

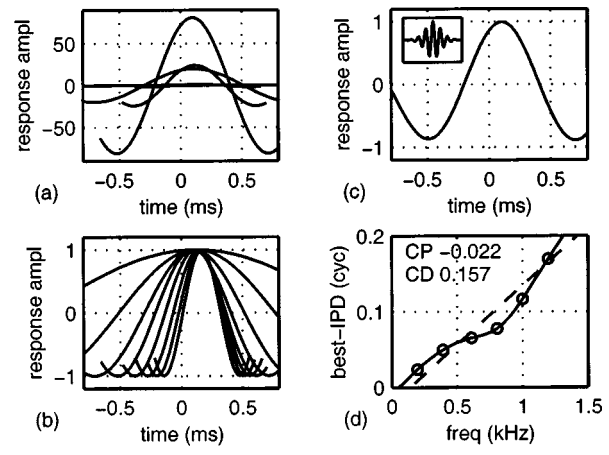

FIG. 8. Response properties of the model binaural neuron with 200-μs time delay and -0.05-octave CF mismatch (contralateral CF higher): (a) Response to narrow-band stimuli (pure tones) as a function of ITD. (b) Normalized curves from (a). (c) Response to wide-band stimuli (sound pressure impulses) as a function of ITD (equal to the composite curve) peaks at 105 μs; inset shows response from -5 to 5 ms. (d) Best-IPD as a function of stimulus frequency.

III. DISCUSSION

A. Overview

The set of Carney–Yin delayed gammatone impulse responses (Carney and Yin, 1988) provides a family of functions—one function for each CF below approximately 3 kHz—that describe the filter properties of cat cochlear channels over that frequency range. We know that the descriptions are imperfect and incomplete. They do not include the nonlinearities that we know exist in cochlear dynamics: not the memory nonlinearity of adaptation (Lewis and Henry, 1995), nor the static nonlinearities such as synchrony suppression and stochastic resonance effects imposed by the spike threshold (Javel, 1981; Greenwood, 1986; Lewis and Henry, 1995), nor the nonlinearity of two-tone suppression (Nomoto *et al.*, 1964; Sachs and Kiang, 1968), nor the dependence that we know exists between REVCOR-derived impulse responses and the ambient sound amplitude (Carney and Yin, 1988; Lewis and Henry, 1994). Nevertheless, we

know that even without incorporating any of these nonlinear properties, single-level REVCOR-derived impulse responses, upon which Carney and Yin's functions are based, can provide fairly faithful predictions of the input–output properties of cochlear channels; e.g., they can predict fairly accurately the temporal pattern of instantaneous spike rate in response to an acoustic stimulus waveform of arbitrary complexity (de Boer and de Jongh, 1978; Carney and Yin, 1988; Wolodkin *et al.*, 1996).

In the studies reported in this paper, we have explicitly excluded from our peripheral model two other cochlear channel nonlinearities—a soft-onset threshold nonlinearity (or half-wave rectification) of the filtered sound pressure waveform, and spontaneous background activity—however, we have not ignored them. The effect of including the background activity in our computations would simply have been to shift the response amplitude curves upward; and we observed from our studies that the effect of including half-wave rectification was primarily the elimination of below-zero response amplitudes. Because our computations concerned primarily time-to-peak values, inclusion of these nonlinearities does not alter our conclusions.

For the results we have presented here, we have used cross-correlation as the comparison mechanism of the model binaural neurons. We have chosen to use this comparison mechanism for several reasons. First, for sinusoidal stimuli, the computed best-ITDs (or best-IPDs) using either summation or peak coincidence of ipsilateral and contralateral inputs as the binaural comparison function are mathematically identical to those using cross-correlation as the comparison function. Second, while a similar mathematical equivalence does not hold for impulse and noise stimuli, the qualitative observations we made from our studies using summation and peak coincidence as the binaural comparison function are the same as those we present using cross-correlation. Third, comparison of binaural responses of cat medial superior olive neurons with monaural responses indicates that those neurons are accurately described as coincidence detectors (Yin and Chan, 1990). Fourth, while it is unlikely that strict cross-correlation *per se* is carried out by the biological analogues of our mathematical constructs, physiological evidence indicates that the response of real binaural IC neurons to noise and tone stimuli can be accurately described by a cross-correlation function (Yin *et al.*, 1987). While the IC itself is unlikely to be the locus of interaural time difference interaction—most IPD-sensitive neurons in the IC do not phase lock to monaural stimuli (Yin and Kuwada, 1984)—it is the predominant target of central projections from the MSO (Adams, 1979). Consequently, it is likely that the responses of IPD-sensitive neurons in the IC reflect interactions that occur at the more peripheral level of the MSO.

In the studies reported in this paper, we elected to use the delayed gammatone impulse response functions as descriptive models of the cochlear channels. Our descriptive model of binaural interaction in a brainstem neuron (our binaural comparison function) was cross-correlation. We synthesized models of binaural ITD computation by combining these descriptive models (delayed gammatone impulse responses for two CFs, plus cross-correlation). Having done so, we examined the properties that emerged from these synthetic models. The conclusions that we draw are based on those properties and therefore, ultimately, on our synthesis and the descriptive models that we incorporated into it. In today's reductionist environment in biology, one might be tempted to employ synthetic models of the cochlea (e.g., based on hair cell and basilar membrane micromechanics, the dynamics of the hair cell/cochlear axon synapse, and the dynamics of the cochlear axon spike trigger) and synthetic models of the binaural brainstem neuron. The modeling traditions of engineering lead us to believe that such an approach is far less than optimal. For the elements of our synthetic models we much prefer descriptive models, with well-defined properties and easily assessable fidelity, to synthetic models whose emergent properties and fidelity are uncertain at best.

B. Single-CF afferent channels

As originally proposed, the APD model specifies that each binaural comparison neuron receives input from only one channel from each ear, and that those channels have identical CFs. Monaural response properties (e.g., response threshold, Q10, etc.) of neurons throughout the SOC are similar to those in the auditory nerve (Goldberg, 1975), and so it is conceivable that binaural neurons are in fact innervated by a single channel from each ear. Innervation by a single channel is not a critical element of the model, as long as exact functional symmetry between the two ears is maintained. However, if we assume that there is innervation from only a single channel, the work we have presented here in part addresses the definition of ''identical CF'' or ''exact functional symmetry'' in this context of ITD localization: We find that the CFs of the innervating channels should lie within approximately 0.012 octaves of one another, depending upon the CF.

In a study of binaural neurons in the cat MSO, Yin and Chan (1990) observed that 72% (13/18) of observed interaural CF differences were within 0.2 octaves, and 77% were within 50 Hz. Conversely, 28% would have had CF differences larger than 0.2 octaves, and 22% would have had interaural CF differences larger than 50 Hz; at least some neurons in the cat MSO are not properly described as receiving input from the same CF channel from each ear. In fact, the mismatched CPDs resulting from the interaural CF differences observed by Yin and Chan would provide substantial errors in a localization system which relied upon exact interaural CF matches. To date, there have been no physiological data published that describe the relationship of best-ITD to interaural CF difference.

Anatomical and physiological studies of the nucleus laminaris (NL) in the chicken (Young and Rubel, 1983) and barn owl (Carr and Konishi, 1990), and the MSO in the cat (Smith *et al.*, 1993) have shown that these structures are possible substrates for neural implementation of the APD model. In particular, physiological and anatomical data in these studies suggest the existence of ladderlike afferent innervation of binaural neurons (Fig. 1) in the nucleus laminaris or medial superior olive, and a trend for binaural neurons with successively larger best-ITDs to lie successively further

along the neural substrate. Unfortunately those studies do not report on the magnitude of interaural CF differences in the neurons studied. Consequently those studies do not address the question we have chosen for the focus of this manuscript—the possibility that interaural CF mismatches contribute significantly to ITD selectivity.

C. Best-ITD of model binaural neurons

The curves of response versus ITD for the model neurons we have described resemble similar curves for neurons in the IC (Yin and Kuwada, 1983) and MSO (Yin and Chan, 1990). The curves of response versus ITD for sinusoidal stimuli [Figs. 3(a), (b), 5(a), (b), and 8(a), (b)] are periodic with respect to ITD, and for the model neurons described in the figures, the normalized response curves approximately intersect near the response peaks—typical of the ''peak-type'' neurons observed by Yin colleagues in the MSO and IC. Curves of response versus ITD for model neurons with larger CF mismatches (not shown) do not intersect at a point; this type of response is similar to other neurons observed by Yin and Chan in the IC. The composite curve, constructed by adding the response versus ITD curves for several sinusoidal stimuli, was shown by Yin and colleagues to be a good first order predictor of the wide-band noise response versus ITD curve in both the IC and MSO. The response curves for wide-band stimuli (i.e., the composite curves) for the three model neurons we have described [Figs. 3(c), 5(c), and 8(c)] resemble the composite curves and response curves for wide-band noise as a function of ITD from neurons in the IC and MSO.

In the APD model, if the animal is presented with simultaneous identical stimuli to the two ears, every binaural comparison neuron receives input from the left ear that differs from the input it receives from the right ear only by its absolute time of arrival. If the response amplitude of each binaural neuron is determined either by coincidence or by cross-correlation of the inputs from the two ears, the difference in the times of arrival is the best-ITD of the neuron; and that best-ITD will be independent of the stimulus waveform. Thus for every binaural comparison neuron, the best-ITD for wide-band stimuli will be exactly the same as its best-ITD for any narrow-band stimulus.

In our implementation of the APD model, small CF mismatches resulted in best-ITDs for narrow-band stimuli that were dependent upon the stimulus frequency. These variations in best-ITD were small for small CF mismatches, and became larger as CF mismatch was increased. Because best-ITD for narrow-band stimuli were a function of stimulus frequency, the best-ITD for wide-band stimuli was necessarily different from most of these.

In most models of sound source localization by ITD, axonal propagation delay differences from the left and right ears determines the best-ITD of a binaural comparison neuron. We have presented specific analyses of three model binaural comparison neurons in this paper. Innervation from the ipsilateral ear to all three neurons is identical; each receives input in the 800-Hz CF channel. The cochlear origin of innervation from the contralateral ear to all three neurons is nearly identical; each receives input from within 0.05 octaves of the 800-Hz CF channel. The best-ITD of all three of these binaural comparison neurons is approximately 100 μs. However, as we have modeled them, the axonal propagation delay differences from left and right ears for these model neurons varies from 0 to 200 μs; the best-ITD for these binaural comparison neurons is not determined solely by the axonal propagation time difference!

D. Can cochlear propagation delay alone be used for ITD localization?

A theory of ITD localization in which cochlear propagation delay (CPD), rather than axonal propagation delay, is used to compensate for ITD has been proposed by Schroeder (1977). Criticism of this CPD theory has historically been based on the unproven assumption that if CPD *alone* were used to compensate for ITD, interaural CF differences larger than those found in physiological data would be needed in order to compensate for the largest physiologically relevant ITDs. Shamma and colleagues (1989) incorporated the CPD theory in a model for binaural processing in which CPD alone was used to compensate for ITD. The peripheral filters of that model were implemented through a biophysical model of the gerbil cochlea. At that time, no information was available regarding ITD selectivity of cells in the gerbil superior olivary complex, and so that model was unable to address directly the criticism that CF differences required for localization were in excess of those observed physiologically. [Spitzer and Semple (1995) have recently published data describing responses of gerbil MSO neurons.] Nevertheless, Shamma and colleagues did provide an estimate of the maximum CF difference required for the cat which is in accord with our computations.

The REVCOR-derived peripheral filters in the model we have used here were designed with the constraint that both frequency and phase responses be similar to those of cat eighth nerve fibers, and so we are able to address the question of whether CF mismatches required by the CPD model fall within the range of observed CF differences in the cat. According to our computations, an interaural CF mismatch of 0.2 octaves or less—corresponding to 72% of the neurons examined by Yin and Chan (1990)—is sufficient to create ITD-shifts of 270 μs or more for CFs from 0.25 to 2.5 kHz. Based on Fig. 17 of the paper by Yin and Chan, approximately half of the binaural MSO neurons they studied had CFs lower than 500 Hz and approximately half had CFs between 500 and 1000 Hz. From our computations, an interaural CF mismatch of 50 Hz—corresponding to 77% of the neurons examined by Yin and Chan—is sufficient to create ITD-shifts of up to 300 μs for cells with CFs between 250 and 500 Hz, and ITD-shifts of 130 μs or more for cells with CFs between 500 and 1000 Hz; thus CF mismatches smaller than 50 Hz could create appropriate ITD-shifts in a large proportion of binaural neurons with CFs less than 1000 Hz. Neurons which have interaural CF differences greater than 50 Hz or 0.2 octaves (23% and 28% of the neurons studied by Yin and Chan) would potentially have even larger ITD-shifts caused by mismatched CPDs. We conclude from these data that the CPD theory is consistent with the interaural CF differences which have been reported. However, both axonal

propagation delay differences and CF mismatches must be considered in determining the source of ITD sensitivity of a binaural neuron.

E. Characteristic phase and delay of the model neurons

The best-ITD of binaural neurons with CF mismatches is dependent both upon differential axonal propagation delays from the two ears and CF mismatch. For binaural neurons with no CF mismatch, the best-IPD versus frequency plot is exactly a straight line passing through the origin ($CP=0$) and having a slope (CD) precisely equal to the best-ITD, which is in turn equal to the differential axonal delay. In the absence of any differential axonal delay, the dependence of phase response to frequency response allows computation of a definitive relationship of best-IPD to stimulus frequency; in the cat, this relationship is described through the gammatone filter equations. For a binaural neuron with large CF mismatch, this computation results in a graph that cannot be fit well by a straight line (cf. Fig. 6). Other filter equations appropriate for modeling peripheral responses of other species would result in definite, but different, relationships of best-IPD to stimulus frequency.

Linearity in the relationship of best-IPD to frequency is dependent upon both species and brainstem nucleus. Yin and Kuwada (1983) developed a system for classifying best-IPD versus frequency curves as linear or nonlinear. Their system compared the mean square differences of data points from the best fit line to the expected mean square differences obtained from random Monte Carlo simulations. Using this method to classify binaural neurons in the IC, they found that binaural neurons could have either linear or nonlinear plots of best-IPD versus frequency. Using the same system to classify MSO neurons in the cat, Yin and Chan (1990) reported that plots of best-IPD versus frequency were approximately linear. More sensitive tests of nonlinearity show that neurons in the rabbit IC (Kuwada *et al.*, 1987—chi-squared test) and SOC (Batra *et al.*, 1997—one-sample runs test) may have either linear or nonlinear best-IPD versus frequency plots.

We applied Yin and Kuwada's linearity test to the best-IPD versus frequency curves shown in Fig. 6, using the sample frequencies indicated by points in the figure. For model binaural neurons with ipsilateral CF of 800 Hz and contralateral CF mismatches of 0, ± 0.5, and ± 0.10 octaves, the plots of best-IPD versus frequency were classified as linear; plots from the binaural neurons with CF mismatches of $+/-0.15$ octaves were classified as nonlinear. Similar plots from neurons with CF mismatches of ± 0.125 octaves are also classified as linear by this test; this CF mismatch corresponds to an ITD shift of more than ± 200 μs. Consequently, even a binaural neuron that has a nearly linear best-IPD versus frequency curve may have a significant ITD shift caused by CF mismatch. We also applied a more sensitive runs test (Davis, 1986) of linearity similar to that described in Batra *et al.* (1997) using the points shown in Fig. 6 and six additional points spaced midway between them. To perform the runs test, we recorded the sequence of signs of deviations of samples from the best fit line, and then checked to see whether the number of runs in this sequence was greater or less than statistically expected. All the best-IPD versus frequency curves corresponding to nonzero CF mismatches contained exactly three runs and so were classified as nonlinear at the $\alpha=0.05$ level of significance. We observe that this in part reflects the noise-free nature of the computations; application of the runs test is inappropriate in this situation. Were we to include sufficient measurement noise in our model samples, the statistical test would not reject the hypothesis that these curves are linear.

Although we conclude that precise matching of ipsilateral and contralateral CFs is not necessary for binaural processing based on the APD model, we nonetheless conclude that the allowable range of mismatch is extremely narrow. Is it reasonable to expect the developmental processes for binaural neural circuitry to lead to CF matching as precise as 0.012 octaves? In a companion paper, we explore the possibility that the required precision of interaural CF matching might be reduced by appropriate intraaural CF mismatch.

ACKNOWLEDGMENTS

A preliminary version of this work was presented in 1994 at the International Hearing Symposium in Irsee, Germany. This work was funded by the Office of Naval Research (FD-N00014-91-J-1333), the National Institute for Deafness and Communication Disorders (DC00112), and the Institute for Scientific Computing Research at Lawrence Livermore National Laboratories (89-07 and 90-05).

APPENDIX: COCHLEAR FILTER MODEL

Our model cochleas were based on linear properties of low-CF eighth nerve afferents reported by Carney and Yin (1988). In the model, the response of the eighth nerve afferent with CF of f to an impulse of sound pressure is given by the set of equations:

$$T_a = 1.3\left(\frac{f}{0.456}+0.8\right)^{-2.585} + 0.4\left(\frac{f}{0.456}+0.8\right)^{-0.3447}, \quad \text{(A1)}$$

$$T_d = 8.13\left(\frac{f}{0.456}+0.8\right)^{-0.7966} - \frac{1.25}{f}, \quad \text{(A2)}$$

$$h_f(t) = \begin{cases} (t-T_d)^5 e^{-(t-T_d)/T_a}\sin(2\pi f(t-T_d)), & t \geqslant T_d \\ 0, & t < T_d \end{cases} \quad \text{(A3)}$$

(frequency is in kHz, time in ms).

Adams, J. C. (**1979**). ''Ascending projections to the inferior colliculus,'' J. Comp. Neurol. **183**, 519–538.

Batra, R., Kuwada, S., and Fitzpatrick, D. C. (**1997**). ''Sensitivity to interaural temporal disparities of low- and high-frequency neurons in the superior olivary complex. I. Heterogeneity of responses,'' J. Neurophysiol. **78**, 1222–1236.

Davis, J. C. (**1986**). *Statistics and Data Analysis in Geology* (Wiley, New York).

deBoer, E., and deJongh, H. R. (**1978**). ''On cochlear encoding: Potentialities and limitations of the reverse-correlation technique,'' J. Acoust. Soc. Am. **63**, 115–135.

Carney, L. H., and Yin, T. C. T. (**1988**). ''Temporal coding of resonances by low-frequency auditory nerve fibers: Single fiber responses and a population model,'' J. Neurophysiol. **60**, 1653–1677.

Carr, C. E., and Konishi, M. (**1990**). ''A circuit for detection of interaural time differences in the brain stem of the barn owl,'' J. Neurosci. **10**, 3227–3246.

Colburn, H. S., and Durlach, N. I. (**1978**). ''Models of binaural interaction,'' in *Handbook of Perception, Vol. IV*, edited by E. C. Carterette and M. P. Friedman (Academic, New York).

Goldberg, J. M. (**1975**). ''Physiological studies of auditory nuclei of the pons,'' in *Handbook of Sensory Physiology, Volume V/2: Auditory System*, edited by W. D. Keidel and W. D. Neff (Springer-Verlag, New York).

Goldberg, J. M., and Brown, P. B. (**1969**). ''Response of binaural neurons in the dog superior olivary complex to dichotic tonal stimuli: Some physiological mechanisms of sound localization,'' J. Neurophysiol. **32**, 613–636.

Greenwood, D. D. (**1986**). ''What is synchrony suppression?'' J. Acoust. Soc. Am. **79**, 1857–1872.

Guinan, Jr., J. J., Guinan, S. S., and Norris, B. E. (**1972**). ''Single auditory units in the superior olivary complex I: Responses to sounds and classifications based on physiological properties,'' Int. J. Neurosci. **4**, 101–120.

Javel, E. (**1981**). ''Suppression of auditory nerve responses I: temporal analysis, intensity effects and suppression contours,'' J. Acoust. Soc. Am. **69**, 1735–1745.

Jeffress, L. A. (**1948**). ''A place theory of sound localization,'' J. Comp. Physiol. Psychol. **41**, 35–39.

Kuwada, S., Stanford, T. R., and Batra, R. (**1987**). ''Interaural phase-sensitive units in the inferior colliculus of the unanesthetized rabbit: Effects of changing frequency,'' J. Neurophysiol. **57**, 1338–1360.

Lewis, E. R., and Henry, K. R. (**1994**). ''Dynamic changes in tuning in the gerbil cochlea,'' Hearing Res. **79**, 183–189.

Lewis, E. R., and Henry, K. R. (**1995**). ''Nonlinear effects of noise on phase-locked cochlear-nerve responses to sinusoidal stimuli,'' Hearing Res. **92**, 1–16.

Nomoto, M., Suga, N., and Katsuki, Y. (**1964**). ''Discharge pattern and inhibition of primary auditory nerve fibers in the monkey,'' J. Neurophysiol. **27**, 768–787.

Rhode, W. S., and Greenberg, S. (**1992**). ''Physiology of the cochlear nuclei,'' in *The Mammalian Auditory Pathway: Neurophysiology*, edited by A. N. Popper and R. R. Fay (Springer-Verlag, New York), pp. 94–152.

Sachs, M. B., and Kiang, N. Y.-S. (**1968**). ''Two-tone inhibition in auditory-nerve fibers,'' J. Acoust. Soc. Am. **43**, 1120–1128.

Schroeder, M. R. (**1977**). ''New viewpoints in binaural interaction,'' in *Psychophysics and Physiology of Hearing*, edited by E. F. Evans and J. P. Wilson (Academic, New York), pp. 455–476.

Shamma, S. A., Shen, N., and Gopalaswamy, P. (**1989**). ''Stereausis: Binaural processing without neural delays,'' J. Acoust. Soc. Am. **86**, 989–1006.

Smith, P. H., Joris, P. X., and Yin, T. C. (**1993**). ''Projections of physiologically characterized spherical bushy cell axons from the cochlear nucleus of the cat: Evidence for delay lines to the medial superior olive,'' J. Comp. Neurol. **331**, 245–260.

Spitzer, M. W., and Semple, M. N. (**1995**). ''Neurons sensitive to interaural phase disparity in gerbil superior olive: Diverse monaural and temporal response properties,'' J. Neurophysiol. **73**, 1668–1690.

Wakeford, O. S., and Robinson, D. E. (**1974**). ''Lateralization of tonal stimuli by the cat,'' J. Acoust. Soc. Am. **55**, 649–652.

Wolodkin G., Yamada, W. M., Lewis, E. R., and Henry, K. R. (**1996**). ''Spike rate models for auditory fibers,'' in *Diversity in Auditory Mechanics*, edited by E. R. Lewis, G. R. Long, R. F. Lyon, P. M. Narins, C. R. Steele, and E. Hecht-Poinar (World Scientific, Singapore), pp. 104–110.

Yin, T. C. T., and Chan, J. C. K. (**1990**). ''Interaural time sensitivity in medial superior olive of cat,'' J. Neurophysiol. **64**, 465–488.

Yin, T. C. T., Chan, J. C. K., and Irvine, D. R. F. (**1986**). ''Effects of interaural time delays of noise stimuli on low-frequency cells in the cat's inferior colliculus. I. Responses to wide band noise,'' J. Neurophysiol. **55**, 280–300.

Yin, T. C. T., and Kuwada, S. (**1983**). ''Binaural interaction in low-frequency neurons in inferior colliculus of the cat. III. Effects of changing frequency,'' J. Neurophysiol. **50**, 1020–1043.

Yin, T. C. T., and Kuwada, S. (**1984**). ''Neuronal mechanisms of binaural interaction,'' in *Dynamic Aspects of Neocortical Function*, edited by G. M. Edelman, W. E. Gall, and W. M. Cowan (Wiley, New York), pp. 263–313.

Yin, T. C. T., Chan, J. C. K., and Carney, L. H. (**1987**). ''Effects of interaural time delays of noise stimuli on low-frequency cells in the cat's inferior colliculus. III. Evidence for cross-correlation,'' J. Neurophysiol. **58**, 562–582.

Young, S. R., and Rubel, E. W. (**1983**). ''Frequency-specific projections of individual neurons in chick brainstem auditory nuclei,'' J. Neurosci. **3**, 1373–1378.

Human auditory cortex electrophysiological correlates of the precedence effect: Binaural echo lateralization suppression

Einat Liebenthal[a] and Hillel Pratt[b]
Evoked Potentials Laboratory, Behavioral Biology, Technion-Israel Institute of Technology, Haifa 32000, Israel

(Received 21 September 1998; revised 4 February 1999; accepted 19 March 1999)

Echoes lagging shortly after a sound and originating from a different location blend with the sound source perceptually. The location of the fused ''source+echoes'' is dominated by the source, suggesting suppression of echo localization. This effect is diminished monaurally, implying involvement of binaural processing. The neural substrates underlying the echo localization suppression are still unclear. The electrophysiological indications of primary auditory cortex involvement in binaural suppression of echo lateralization are presented. Position judgment and auditory-evoked potentials (AEPs) were recorded to single- and pairs of binaural and monaural clicks. The pairs simulated a source and its echo. The binaural source+echo position judgment was dominated by the source at small echo lags. With lag increase, it shifted toward the echo. The AEPs were studied for binaural processes specific to a ''real'' echo, as opposed to an identical single sound (a ''virtual'' echo). A reduction in binaural peak amplitude and area and an increase in binaural peak latency were detected specifically in the real echo-evoked middle-latency component Pa. The binaural echo Pa suppression depended upon echo lag, although less strongly than the psychoacoustic position judgment. Pa is associated with primary auditory cortex activity, thus suggesting primary cortical involvement in echo-lateralization suppression. © *1999 Acoustical Society of America.* [S0001-4966(99)05506-X]

PACS numbers: 43.64.Qh, 43.64.Ri, 43.66.Pn, 43.66.Qp [RDF]

INTRODUCTION

An echo lagging shortly after a sound source and arising from another location is not heard separately, but perceptually blends with the preceding source. The perceived location of the fused source and echo is dominated by the preceding source location. Both these phenomena of *source-echo fusion* and *echo localization suppression* are known as the precedence effect (PE) (Wallach *et al.*, 1949). Other properties of the echo, besides its location, are not perceptually suppressed in the fused sound. The echoes contribute to the fused-sound loudness, frequency content, spatiality, and richness (Scharf, 1974; Blauert, 1997). Moreover, the echoes are not completely suppressed even in the process of sound localization (Zurek, 1980; Hartmann, 1983; Rackerd and Hartmann, 1985; Lindemann, 1986; Saberi and Perrott, 1990; Shinn-Cunningham *et al.*, 1993; Litovsky and Macmillan, 1994). The extent of echo-localization suppression is primarily dependent upon echo lag. With lag increase, the perceived fused-sound location is increasingly biased toward the echo. The echo-localization suppression effect persists beyond the temporal range of source and echo fusion (Zurek, 1980; Lindemann, 1986).

The neural auditory substrates underlying the PE are unclear. The PE may be experienced with monaural hearing, but several lines of evidence indicate that it is degraded in the monaural compared to the binaural condition. Koenig (1950) reported that sound in a room is perceived as more reverberant when one ear is plugged than when heard binaurally. Hochster and Kelly (1981) reported that children with monaural deafness were confused with paired-sound localization, even when capable of correctly localizing single sounds (presumably using monaural cues). The PE is also valid when the source and echo arise from the median plane and interaural disparities are minimal (Blauert, 1971; Rakerd and Hartmann, 1992, 1994; Litovsky *et al.*, 1997). However, the echo-localization suppression is less effective in the median plane than with interaural disparities (Rakerd and Hartmann, 1992). The threshold temporal separation for detecting an echo (upper limit of source and echo fusion) is lower according to Zurek (1979) or higher (Rakerd and Hartmann, 1994) in the median plane. Thus, although the PE may have a monaural component, binaural auditory centers are undoubtedly necessary to fully appreciate both the source and echo fusion and the echo-localization suppression phenomena.

Accordingly, monaural forward masking is unlikely to account for the echo suppression. This is because monaural backward masking is also operating in the PE time range and the amplitude of both forward- and backward-masking effects depends similarly on the source and echo temporal separation (Ronken, 1970). Under binaural conditions, however, the localization of the source is stable and independent of echo lag, whereas that of the echo is strongly lag dependent (Zurek, 1980, 1987).

In this study, we focus specifically on the *binaural* processes involved in the echo-localization suppression. Furthermore, we limit our study to the coronal plane, avoiding

[a]Present address, and address for correspondence: Neuroscience Dept., Rose F. Kennedy Center, Albert Einstein College of Medicine, 1300 Morris Park Avenue, Bronx, NY 10461.
[b]Electronic mail: HILLEL@TX.TECHNION.AC.IL

depth cues and concentrating on lateralization. We look for evoked-potential correlates of echo-lateralization suppression in humans, in order to suggest binaural auditory structures involved in the suppression. The acoustic stimulation was presented through headphones so that monaural localization cues were not available. We thus used the monaural response as a control condition where no echo-lateralization suppression could occur.

Many lines of evidence suggest that the PE is mediated at a high level of the auditory system. These include animal and human studies demonstrating the necessity of temporal-lobe or auditory-cortex integrity (Cranford *et al.*, 1971; Hochster and Kelly, 1981; Cornelisse and Kelly, 1987) or maturity (Clifton *et al.*, 1981, 1984; Ashmead *et al.*, 1986; Muir *et al.*, 1989) for obtaining the PE. Other psychophysical experiments showing the influence of ongoing auditory information on echo detectability and localization reveal the dynamic aspect and complexity of the PE and have led investigators to suggest the involvement of high cognitive processing in the effect (Clifton, 1987; Blauert and Col, 1989; Saberi and Perrot, 1990; Freyman *et al.*, 1991; Clifton *et al.*, 1994; Blauert, 1997).

Evoked potentials (EPs) reflect synchronous brain activity and are thus well suited for detecting time-locked processes such as sound localization in general and echo suppression in particular. They allow simultaneous recording of activity from multiple levels of the auditory system. Because of their noninvasive nature, EPs can be used to relate electrophysiological and psychophysical data from human subjects. We recorded brainstem and thalamocortical (middle-latency) AEPs to single and pairs of binaural and monaural clicks, and isolated the binaural activity evoked by the lagging sound. Since the generators of these AEP components are known (Picton *et al.*, 1974; Legatt *et al.*, 1988; Vaughan *et al.*, 1988; Hall, 1992), the level of the echo-specific electrophysiological correlate should indicate the binaural auditory structures involved in echo-lateralization suppression. Further validation of the electrophysiological correlate was obtained by comparing its dependence on echo lag with the comparable psychophysical functions.

I. METHODS

A. General considerations

The choice of acoustic stimulation in this study was a compromise between the electrophysiological and the psychoacoustical requirements. As a first approach, relatively large echo lags of 8–12 ms were used in order to prevent overlap of the source and the echo brainstem potentials (brainstem potentials last approximately 8 ms). After determining with these echo lags that the effect was limited to the middle-latency potentials (which overlap anyway at these lags, since they last approximately 35 ms), we introduced, in a second experiment, shorter as well as longer echo lags (3, 4, and 20 ms) to better delineate the effect. In order to relate the measurements from both experiments and obtain a common reference value, the results were normalized to the size of the ''virtual'' echo (a condition recorded in both experiments). The pooled data of both experiments (named hereafter exp 1 and exp 2) are presented in the Results section.

B. Subjects

Thirty-one subjects 19 to 29 years old participated in the position judgment experiments (19 in the initial study and 12 in the second experiment). Twenty-one of these subjects participated in the EP recording (9 in the initial study and 12 in the final experiment). All subjects had normal audiometric thresholds (less than or equal to 25 dB nHL in either ear at 1–8 kHz, with less than 10-dB difference between ears). The study was approved by the institutional Helsinki committee, and all subjects were informed of the procedures before giving their consent to participate. Each subject participated in a psychophysical position judgment experiment followed by EP recording.

C. Acoustic stimulation

Acoustic stimulation consisted of trains of broadband 65-dB hearing level clicks[1] generated by transducing a square (100-μs duration) electric pulse through TDH49 headphones. Clicks were presented in five configurations (Fig. 1); (a) Binaural source: A binaural diotic click (empty bar) simulating a midline-positioned sound source. (b) Binaural source+echo pair: A pair of binaural clicks simulating a source and its echo. The source is as described in (a). In the echo (filled bar), the left-ear click was delayed relative to the right-ear click, resulting in various right lateral positions of the echo, depending on the interaural time difference (IATD). IATDs were 0–900 μs, in 150-μs steps, in the position judgment experiment, and 0–600 μs, in 300-μs steps, in the EP recording. The echo lagged 3, 4, 8, 10, 12, or 20 ms after the source in the position judgment experiment, and 4, 8, 10, 12, or 20 ms after the source in the EPs recording experiment. We called the echo in this stimulus a *''real'' echo*. (c) Binaural virtual echo: A binaural dichotic click physically identical to the real echo but presented alone, and not preceded by a source. (d) Monaural source. (e) Monaural source+echo pair, with the same echo lags as in (b). (f) Monaural virtual echo: A monaural echo delivered alone.

For configurations (e) and (f), the same stimulus was used and the EPs were synchronized in the analysis to appear at the source or echo latency. The monaural stimuli [(d), (e), and (f)] were presented only in the electrophysiological experiment, in order to isolate the binaural specific activity (see Sec. F). All monaural stimuli were presented to the right ear only. Stimuli in each configuration were presented in continuous trains, at a rate of 2.5/s.

D. Psychophysical position judgment

Subjects were asked to describe the lateral position of the binaural sources, binaural source+echo pairs, and binaural virtual echoes by assigning them a number from 1–9 according to the analog visual scale in Fig. 2 (Furst *et al.*, 1995). Single sounds with six IATDs (the source and five virtual echoes) and source+echo pairs with three echo lags (8, 10, and 12 ms in exp 1 and 3, 4, and 20 ms in exp 2) and with six echo IATDs, were presented. This resulted in 24

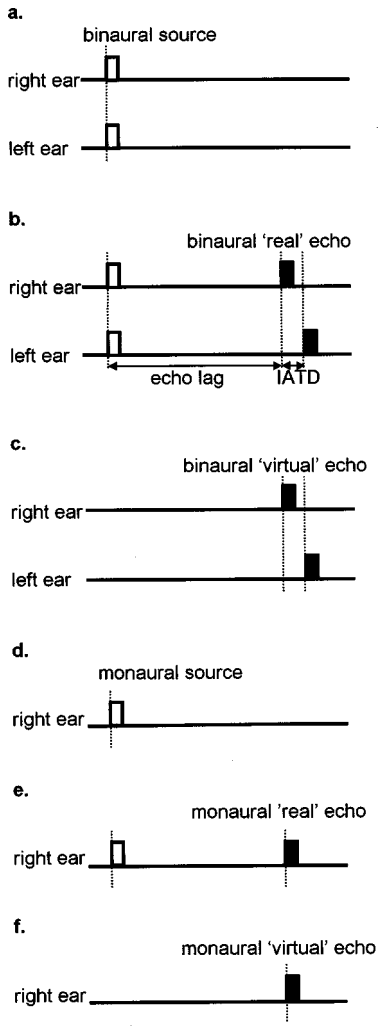

FIG. 1. Acoustic stimulation comprised of a binaural source (a), a binaural source+echo pair (b), a binaural echo presented alone (c), a monaural source (d), a monaural source+echo pair (e), and a monaural echo presented alone (f). The echo was accordingly defined as a binaural real echo (b), a binaural virtual echo (c), a monaural real echo (e), and a monaural virtual echo (f). These configurations allowed derivation of binaural- and echo-specific responses. See the text for further details.

different sound stimuli in each experiment, which were repeated five times each. The stimuli were presented in random order, in the course of two separate sessions lasting typically 20 min each. The subjects had no prior knowledge that some

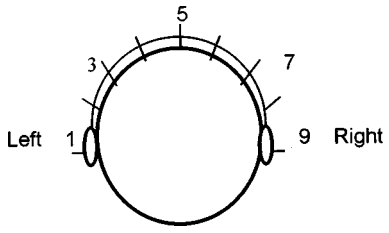

FIG. 2. Lateralization scale for the psychophysical experiment, extending along the left ear–vertex–right ear arch. Subjects were instructed to use the numeral 1 to describe complete lateralization of the auditory event to the left ear, 9 to describe complete lateralization of the auditory event to the right ear, and 5 to describe a midline-situated auditory event. The intermediate numerals were used to describe intermediate lateral positions (due to the presentation through headphones, the auditory event was always localized inside the head).

of the stimuli contained a *pair* of binaural clicks. If they reported hearing two sounds, they were asked to ignore this and concentrate on the lateral location of the entire auditory event inside their heads. Since the echo-localization suppression effect persists beyond the range of source+echo fusion, the source and echo can be lateralized together, even though they are already perceptually separated temporally (Lindemann, 1986). The subjects reported their lateral position judgment by typing a number from 1 to 9 on a computer keyboard. The response was saved to a file and automatically initiated the next sound stimulus. Response time was not restricted. The subject's five responses to each stimulus were averaged.

Analysis of the results consisted of subtracting the integer 5 (midline position) from each averaged response, in order to evaluate the lateral displacement evoked by the sound stimulus. The responses adjusted by this procedure were then normalized by representing them as a proportion of the similarly adjusted response to a matching (having the same IATD) virtual echo. Virtual-echo displacement from midline was thus 100%, describing the average right-lateral displacement usually evoked by each IATD in a single sound. The source's lateral displacement was typically around 0%, corresponding to midline position in the experiments. The source+echo pairs displacement from midline was usually within the 0%–100% range. Note that negative values of the lateral displacement judgment indicated lateralization to the left.

E. Evoked potential recording

Brainstem and middle-latency (up to 50 ms) AEPs to source, to source+echo pairs, and to virtual echoes, in binaural and monaural conditions, were recorded between vertex and spinous process of the 7th cervical vertebra (the vertex position in each subject, was measured as the midway point between the ears on the scalp midline). The potentials were differentially amplified $\times 200\,000$ between 10 and 3000 Hz. 4000 responses were digitally averaged using 1000 samples with a dwell time of 80 μs per sample, for a total analysis time of 80 ms.

A recording session typically lasted 4 h with two intermissions, and the subjects participated in 3–4 sessions taking place on different days. The subjects were instructed to remain awake throughout the session, to avoid possible effects of arousal level on middle-latency AEP. The average of two records obtained in separate sessions was used in the analysis for each stimulus condition.

The brainstem and middle-latency potentials were digitally filtered off-line, each according to the most prominent lobes in their power spectrum (for brainstem potentials: 78–1562 Hz, and for middle-latency potentials: 16–227 Hz).

F. Derivation of real echo-evoked potentials

In the responses to source+echo pairs, when the source-evoked potentials last longer than the echo lag, they overlap with the echo-evoked potentials. This occurs for the brainstem potentials in the short echo-lag condition (4 ms) and for the middle-latency potentials at all echo lags. Separation of

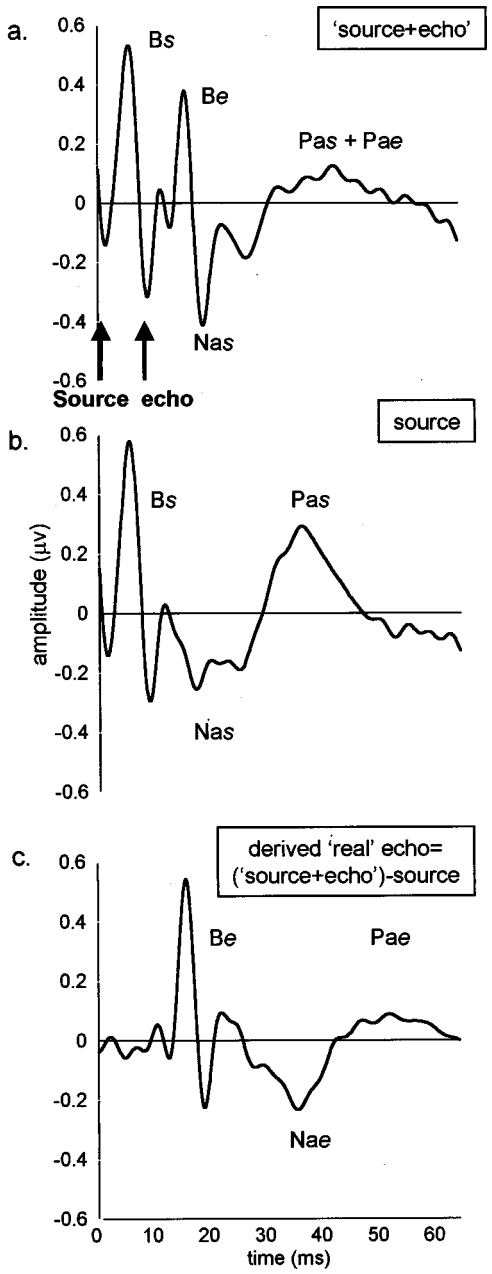

FIG. 3. Derivation of real echo-evoked potentials from the paired source+echo evoked potentials. (a) Potentials evoked in response to a source+echo pair with 10-ms echo lag. The source potentials are marked with an ''*s*'' and the echo potentials are marked with an ''*e*.'' The first two large positive peaks are the source and echo brainstem potentials (B*s* and B*e*, respectively). The thalamocortical components of interest are the negative peak Na (N*ae* overlaps P*as* and is thus not seen in this trace) followed by the positive peak Pa (P*as* and P*ae* are only partially separated). The potentials evoked by the source alone (b) are substracted from the paired source+echo evoked potentials, in order to derive the real echo-evoked potentials (c). In the derived real echo potentials, notice the baseline (in the 10 ms preceding the echo stimulation) which is close to zero. Also notice the brainstem potentials which are similar in size in response to the echo and to the source, while the thalamocortical positive peak (Pa) is strongly diminished in response to the echo relative to the source response.

the responses to the real echoes was achieved by subtracting the response to the source from the response to the source+echo pair (as shown in Fig. 3). The only assumption behind this calculation is that the source EP is not affected by whether it is followed by an echo. The waveforms resulting from this subtraction were called *derived real-echo evoked potentials*. The quantitative analysis of the real echo AEPs was performed on the derived real-echo potentials.

G. Peak amplitude, peak latency, and area measurements

Peak amplitude and peak latency of the brainstem components V and VI[2] and of the middle-latency components Na and Pa, as well as the area of Pa, were measured on the computer display using a cursor. Latencies were measured relative to stimulus onset. In the echo-evoked responses, the latencies were corrected by subtracting the echo lag. Amplitudes of the brainstem potentials were measured from the peak to the following trough. Amplitude and area of the middle-latency potentials were measured relative to baseline. Baseline for the middle-latency potentials was calculated as the average of 20 points after the source stimulus artifact (1.6 to 3.2 ms after stimulus onset). This is because, when filtered according to the middle-latency power spectrum, no substantial activity could be detected in this latency range. In addition, no exclusively binaural activity has been reported for the brainstem waves I–III, that is, up to 4.5 ms after stimulus onset (Dobie and Norton, 1980; Wrege and Starr, 1981).

The sources of the brainstem potentials are extensively reviewed by Legatt *et al.* (1988) and Hall (1992). Wave V is generated by activity in the area of the inferior colliculi; that is, by afferent lateral leminiscus fibers and possibly inferior colliculus neurons. Wave VI is attributed to activity in the medial geniculate body, with possible contributions from the inferior colliculus. The Na sources are more controversial and localized to the primary auditory cortex (Celesia, 1976; Lee *et al.*, 1984; Scherg and Von Cramon, 1986; Liegois-Chauvel *et al.*, 1994) and/or to a subcortical generator (Deiber *et al.*, 1988; Hashimoto *et al.*, 1995). Pa primarily reflects activity from bilateral generators in the primary auditory cortex (Celesia, 1976; Kaga *et al.*, 1980; Kraus *et al.*, 1982; Özdamar *et al.*, 1982; Lee *et al.*, 1984; Scherg and Von Cramon, 1986; Kileny *et al.*, 1986; Liegois-Chauvel *et al.*, 1994), summated with later activity from the secondary auditory cortex (Celesia, 1976; Scherg and Von Cramon, 1986) or from a subcortical structure (Buchwald, 1981; Kraus *et al.*, 1982; Jacobson and Newman, 1990).

The brainstem wave III, arising from activity in the caudal pons, in or near the cochlear nucleus and trapezoid body, and the slow negativity following wave V and attributed to postsynaptic potentials within the inferior colliculus (Legatt, 1988; Hall, 1992), were not systematically measured since preliminary experiments did not indicate echo-specific effect at this level. The brainstem waves IV and VII and the other middle-latency components N_0 and P_0, were not measured since they are obtained inconsistently. N_0 and P_0 may also be contaminated by myogenic activity (Picton *et al.*, 1974).

H. Determination of echo-specific electrophysiological correlates

In this study, we focused specifically on *binaural* processes related to the *echo-lateralization suppression*. We thus wished to exclude monaural processes such as forward

masking that also attenuate the echo-evoked response but cannot account for the binaural suppression. A deviation of the binaural AEP from the algebraic sum of left and right monaural AEPs is thought to reflect binaurally specific processes. Measuring this deviation is the accepted method, with EPs, to study binaural phenomena such as sound localization (Furst *et al.*, 1985; Jones and Van Der Poel, 1989; McPherson and Starr, 1993).[3]

For each AEP component, we *divided* the numerical values of binaural peak amplitude and binaural area by the corresponding measures of the algebraic sum of monaural potentials.[4] The resulting *binaural/monaural peak amplitude* and *binaural/monaural area* were then *normalized* as a fraction of the corresponding measure in the virtual echo having the same IATD. The normalized binaural/monaural peak amplitude and normalized binaural/monaural area were abbreviated to n(b/m) *peak amplitude* and n(b/m) *area*, respectively [or b/m instead of n(b/m) when unnormalized]. The normalization resulted in 100% n(b/m) peak amplitude and n(b/m) area of components in virtual echo responses, and served as a reference for evaluating the n(b/m) amplitude and n(b/m) area of the same components in the source and in the real echo responses.

The *peak latencies* (*after echo lag subtraction*) of components in the real echo AEP, were compared to the peak latencies of the components in the source and virtual echo responses, separately in the binaural and the monaural conditions. In addition, binaural relative to monaural-peak-latency disparities were calculated, by *subtracting* the monaural-peak latency from the corresponding binaural measure. The resulting *binaural–monaural peak latency shifts* ((b—m) *peak latency shifts*) were used for multiple regression analysis. The n(b/m) peak amplitude, the n(b/m) area, and the binaural-peak latency of each AEP component in the source and in the real echo responses were then tested for statistically significant differences from the respective measures in the matching virtual echo responses. AEP components that were found to be significantly different in one or more of these measures, specifically in the real echo condition as opposed to the virtual echo and the source conditions, were taken to be possible electrophysiological correlates of echo-lateralization suppression processes. Since the critical parameter influencing psychophysical echo suppression is echo lag, further validation of the electrophysiological correlates relied on testing their dependence on echo lag.

I. Statistical analysis

The dependence on echo lag and echo IATD, of the average lateral displacement judgment and of the electrophysiological measures of each AEP component, were tested with analysis of variance procedures (ANOVA). The source and virtual echo conditions were considered additional levels of the echo-lag factor. Analysis was performed separately for exp 1 and exp 2. Newman–Keuls comparisons were used to evaluate the sources of variance. Probabilities smaller than 0.05 were considered significant. Multiple regression analysis was performed to assess the correlation between psychophysical and electrophysiological measures of suppression. For multiple regression, the measures were not normalized in order to avoid distortions in the evaluation of the correlation. The psychophysical statistical analysis and the psychophysical–physiological correlations did not include IATD of 0 μs because in this situation, the source and the echo are delivered from the same midline position, and thus the psychophysical echo-lateralization suppression cannot be assessed by a lateralization task.

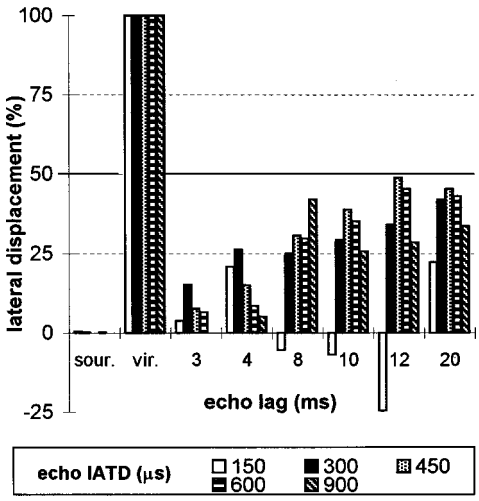

FIG. 4. The average lateral displacement of sources (labeled ''sour.,'' barely exceeding 0%), virtual echoes (labeled ''vir.'') and source+echo pairs with various echo lags and echo IATDs, all normalized to the lateral displacement of the matching virtual echo.

II. RESULTS

A. Psychophysical measurement of echo-lateralization suppression

The average lateral position judgment of all subjects is shown in Fig. 4 for the source, the virtual echoes, and the source+echo pairs, all normalized to the position judgment of a matching virtual echo (having the same IATD). The source lateral displacement is practically 0 (and thus almost unnoticeable in the graph). The virtual echoes in each IATD were defined by the normalization procedure as having 100% displacement from midline. The source+echo pair lateral displacement judgments ranged between −25% to 48% of the virtual echo lateralization and increased gradually with the echo lag [exp 1: $F(4)=37.9$, $p<0.000\,01$; exp 2: $F(2)=214$, $p<0.000\,01$; ANOVA]. It was significantly smaller for source+echo pairs with 3–4-ms echo lag (averaging 7%–15% of the virtual echo lateralization), compared to 20-ms echo lag (averaging 37% of the virtual echo lateralization; ANOVA *post hoc* test).

At 3-ms echo lag, the lateral displacement was not significantly different from that of the source. At 4-ms echo lag, the paired-sound lateral displacement did not differ from that of the source at the larger echo IATDs (600–900 μs). For echo lags of 8 ms or more, the lateral displacement parted completely from that of the source, except for 150-μs echo IATD (ANOVA, *post hoc* analysis).

At the other end of this continuum, at 12–20-ms echo lag, the source+echo pair lateral displacement approached 50% and was not significantly different from this value across most echo IATDs (300–600 μs). At the extreme echo

IATDs (150 and 900 μs), the source+echo pair lateral displacement was still significantly smaller than 50%, even at 20-ms echo lag. The 50% level describes, for each echo IATD, the midpoint between the perceived position of the virtual echo and the perceived position of the source. If the source and echo contributed equally to the source+echo pair position judgment, the paired sound would be lateralized to this middle position. A position judgment smaller than 50% shows that the perceived position of the actual paired sound was closer to the position of the source than to the position of the virtual echo.

The paired-sound perceived lateralization was thus determined only by the source at 3-ms echo lag and at 4-ms echo lag with large echo IATDs. It was determined principally by the source midline location and to a lesser extent by the lateral echo at 4–12-ms echo lag, with most of the echo IATDs. Finally, it was determined approximately equally by the source and echo lateral positions beginning with 12, 20-ms or larger echo lags, depending on the echo IATD. These results are consistent with a process of echo-lateralization suppression that is complete at the smaller echo lags and gradually weakens with the increase in echo lags, until it almost vanishes at echo lags of 12 ms and longer.

The source+echo pair lateral displacement judgment showed a biphasic dependence on echo IATD, which was significant only with exp 2 (exp 1: $F(4)=2$, $p<0.1$; exp 2: $F(4)=4$, $p<0.008$; ANOVA). It increased from 150 to 300 μs (with echoes lagging 3–4 ms) or to 450 μs (with echoes lagging 8–20 ms) echo IATD and then decreased with further increase in echo IATD. At 150-μs echo IATD, the source+echo pairs were sometimes lateralized to the left (negative values in Fig. 4) of the midline source.

B. Evoked potentials correlates of echo lateralization suppression

1. Description of the source+echo potentials

Initial evaluation of the source+echo evoked activity was done by superimposing the source+echo AEPs and the source AEPs. This allowed an appreciation of the pattern of overlap of source and echo potentials, at each echo lag. In addition, it emphasized the echo potentials' distinctive characteristics. The binaural source+echo potentials (thick line) evoked by a source and an echo lagging 4, 10, or 20 ms, are shown in Fig. 5(a) (from top to bottom, respectively), superimposed on the response to the source alone (thin line). The source AEPs are labeled with an ''*s*'' and the echo AEPs with an ''*e*.'' It can readily be seen that the shape of the echo potentials depends on the pattern of overlap with the previously evoked source potentials, which differs according to echo lag. For example, the brainstem echo EP (Be) overlapped the earliest source thalamocortical negative peak N_0s (not marked) at 4-ms echo lag, it overlaps Nas at 10-ms echo lag and it overlaps the rising slope of Pas at 20-ms echo lag. Similarly, Pa*e* overlaps with Pas' peak at 4-ms echo lag, it overlaps with Pas' descending slope at 10-ms echo lag, and it overlaps with later peaks (Nb and possibly *P*1, not marked) at 20-ms echo lag. This underscores the necessity to derive the echo EPs from the source+echo EPs, in order to compare the echo EPs across echo lags.

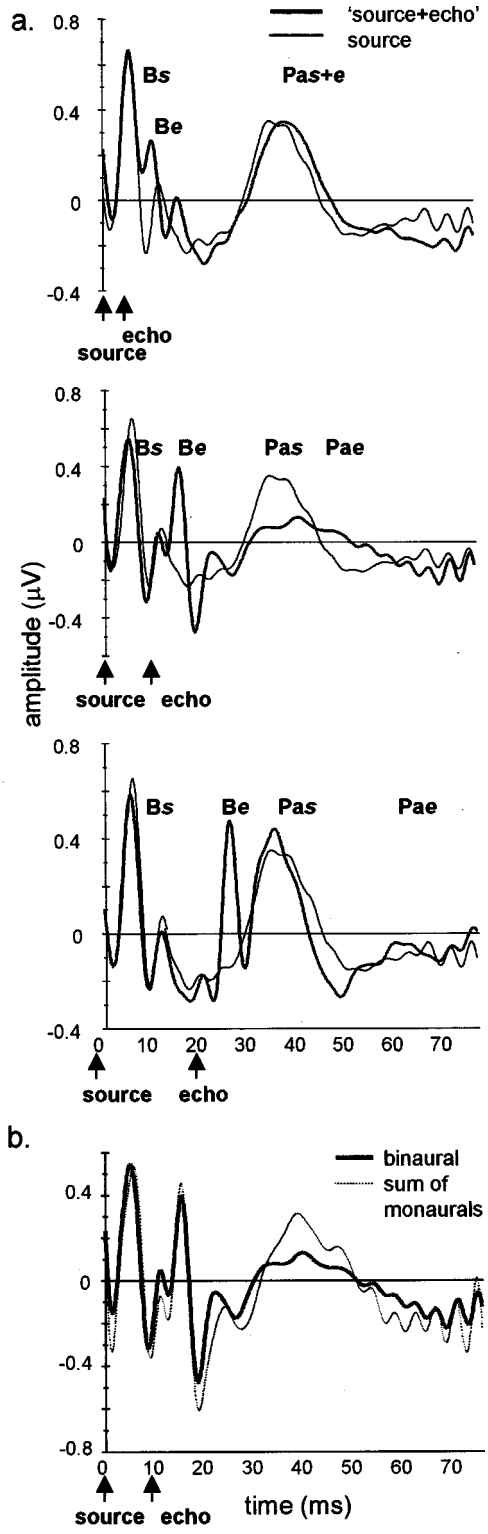

FIG. 5. (a) The source EPs (thin line) superimposed on the source+echo EPs (thick line). (b) The sum of monaural (thin stippled line) and the binaural (thick line) source+echo potentials. The source+echo responses represent the unseparated source and echo potentials. The echo lags are 4, 10, and 20 ms (upper, middle, and lower trace, respectively) in (a) and 10 ms in (b). Responses are averaged across subjects. Components are marked as in Fig. 3.

The second concern when evaluating the echo EPs is

that they are attenuated by monaural refractory processes that occur regularly with high stimulus presentation rates, but are nonspecific to binaural echo suppression. The binaural echo EPs thus have to be contrasted with the sum of monaural echo EPs, in order to particularly assess the binaural component of echo suppression. Figure 5(b) shows the binaural source+echo EPs (thick full line) superimposed on the sum of monaural source+echo EPs (thin dotted line), both with the same 10-ms echo lag (and thus a similar pattern of source and echo wave superposition). The main effect that emerges from this comparison is the reduction in binaural relative to monaural amplitude, at the latency of component Pa. As detailed above, however, quantitative assessment of components' contributions to the amplitude reduction cannot be achieved from this presentation, because of source and echo component overlap. In order to quantitatively assess the effects that are specific to the binaural real echo, it was thus necessary to (a) derive the real echo EPs from the source+echo superimposed EPs, and (b) contrast the binaural echo EPs with the sum of monaural echo EPs in each echo configuration.

2. Description of the derived real echo AEPs

The sum of monaural (thin line) and the binaural (thick line) potentials evoked by a virtual echo (a) and by real echoes lagging 4, 10, or 20 ms [(b), upper, middle, and lower trace, respectively], averaged across all subjects, are shown in Fig. 6. The real echo potentials were derived from the source+echo potentials as explained in Sec. I F. The monaural–binaural disparity in the brainstem potentials was relatively small and similar in magnitude for the virtual and for the real echoes. In contrast, there was a relatively large reduction in the Pa binaural amplitude and an increase in the Pa binaural latency, which were specific to the real echoes and were present at all echo lags. The monaural–binaural disparity in wave Pa is emphasized in the figure by dotted lines. The Pa binaural-amplitude reduction was largest for the short echo lag (4 ms) and decreased with increasing echo lags, especially during the rising portion of wave Pa. The latency increase became less prominent with the increase in echo lags and was almost undetected at 20-ms echo lag.

3. Quantitative analysis of specifically binaural echo effects

The binaural–monaural amplitude, area, and latency disparities in each stimulus condition were measured and referred to the size of the virtual echo, as explained in Sec. I H. The values of n(b/m) peak amplitude and of n(b/m) area of component Pa are shown in Fig. 7(a) and (b). The virtual echo (filled black columns) was defined by the normalization procedure as having 100% n(b/m) peak amplitude and n(b/m) area, and thus served as reference. The n(b/m) Pa peak amplitude and n(b/m) Pa area was significantly affected by the echo lag [n(b/m) Pa peak amplitude, exp 1: $F(4)=5.71$, $p<0.001$; exp 2: $F(3)=3.9$, $p<0.02$; ANOVA; n(b/m) Pa area, exp 1: $F(4)=19.1$, $p<0.000\,01$; exp 2: $F(3)=4.1$, $p<0.01$; ANOVA]. The source n(b/m) Pa peak amplitude and n(b/m) Pa area (filled white columns) did not differ significantly from the virtual echo's respective measures. In contrast, the real echo Pa n(b/m) peak amplitude and n(b/m) area (patterned columns) were significantly reduced compared to the virtual echo respective measures. The largest reduction was observed with an echo lag of 4 ms,

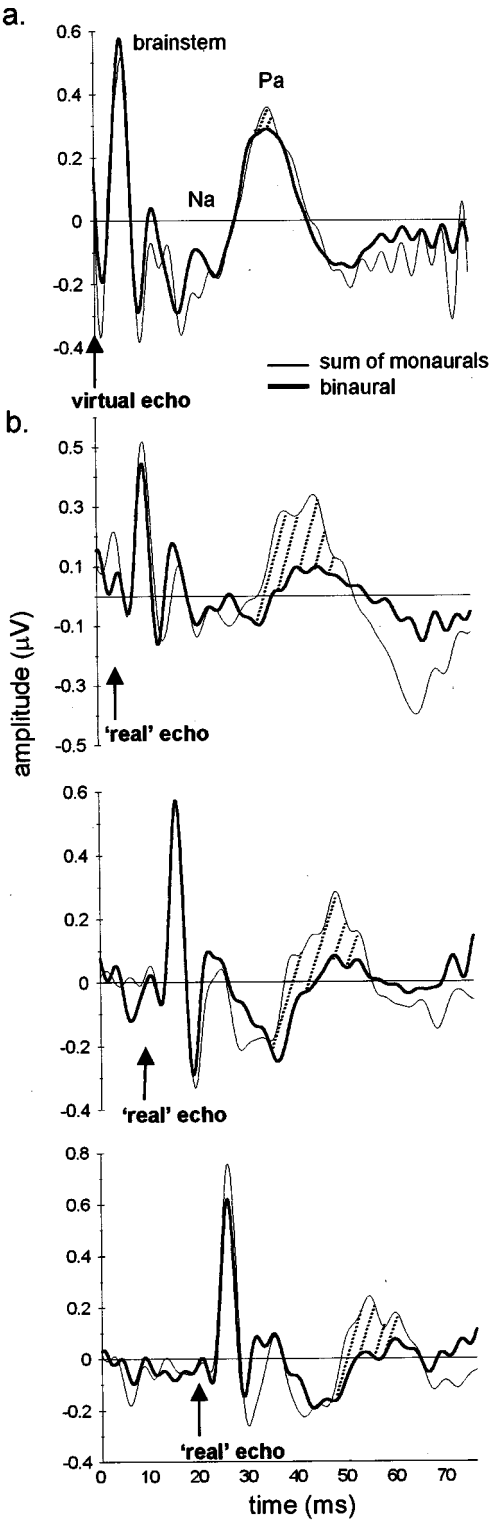

FIG. 6. The sum of monaural (thin line) and the binaural (thick line) potentials evoked by a virtual echo (a) and by real echoes (b) lagging 4, 10, and 20 ms (upper, middle, and lower trace, respectively). The real echo-evoked potentials were derived from the source+echo evoked potentials. The binaural echo IATD was 300 μs. Responses are averaged across subjects. Notice that the monaural–binaural disparity (highlighted by hatching for Pa) is small and similar in size for the virtual and the real echo brainstem responses, whereas it is very large specifically in the real echo Pa response.

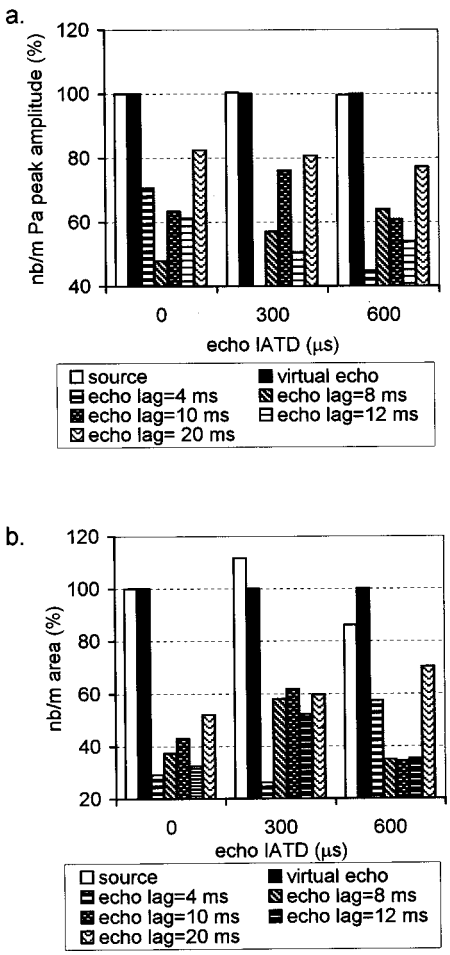

FIG. 7. The n(b/m) peak amplitude (a) and n(b/m) area (b) of component Pa in the responses to the source (filled white columns) and the virtual (filled black columns) and real (patterned columns) echoes, at various echo lags and IATDs.

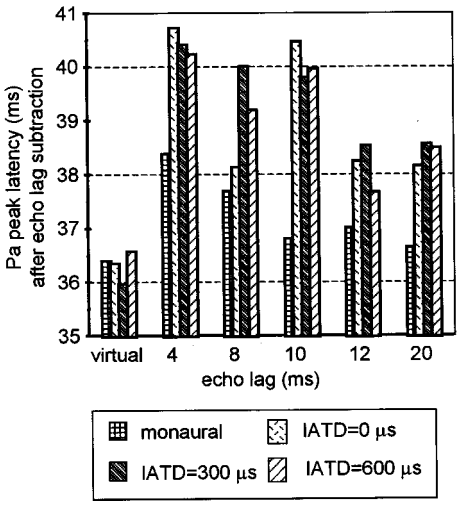

FIG. 8. Pa peak latency in the binaural and in the sum of monaural responses evoked by virtual and real echoes at various echo lags and IATDs, after echo lag subtraction.

where the average real echo n(b/m) peak amplitude was reduced to only 51% of the virtual echo n(b/m) peak amplitude, and the n(b/m) Pa area reached only 38% of the virtual echo n(b/m) area. This reduction in n(b/m) Pa peak amplitude and n(b/m) Pa area progressively declined with longer echo lags. At 20-ms echo lag, the real echo Pa n(b/m) peak amplitude reached 80% of the virtual echo counterpart and did not differ from it significantly. The reduction in area progressively declined with longer echo lags (61% for 20-ms echo lag), but remained significant even with a 20-ms lag (ANOVA, *post hoc* tests).

The binaural—but not the monaural—peak latency of Pa (after correction of echo-evoked responses by subtraction of echo lag) was significantly affected by echo lag [binaural Pa peak latency, exp 1: $df=4$, $F(4)=4$, $p<0.02$; exp 2: $F(3)=3.4$, $p<0.05$; ANOVA; Fig. 8]. The binaural peak latency was larger for real echoes compared to virtual echoes. The largest increase, averaging 4.4 ms, was noted with echoes lagging 4 ms. The increase in binaural peak latency progressively declined with longer echo lags until it became statistically nonsignificant for echoes lagging by 12- and 20-ms (2- and 2.3-ms peak latency increase, respectively; ANOVA, *post hoc* tests).

No significant effect of echo IATD was detected on the n(b/m) Pa peak amplitude or on the Pa binaural latency. The n(b/m) Pa area showed a significant increase at 300-μs echo IATD compared to 0 and 600 μs, in exp 1 only [n(b/m) Pa area, exp 1: $F(2)=5.8$, $p<0.01$, ANOVA].

No consistent specifically binaural effects were noticed on any of the real echo-evoked early components preceding Pa. No effects of echo lag on the n(b/m) peak amplitude of the brainstem potentials V and VI and the middle-latency component Na were indicated. Both the binaural and the monaural peak latencies of waves V and VI were significantly affected by echo lag [binaural peak latency, wave V, exp 1: $F(4)=37$, $p<0.000\,01$; exp 2: $F(3)=25$, $p<0.000\,01$. Wave VI, exp 1: $F(4)=5.1$, $p<0.007$; exp 2: $F(3)=32$, $p<0.000\,01$. Monaural peak latency, wave V, exp 1: $F(4)=34$, $p<0.000\,01$; exp 2: $F(3)=45$, $p<0.000\,01$. Wave VI, exp 1: $F(4)=39$, $p<0.000\,01$; exp 2: $F(3)=9$, $p<0.02$; ANOVA]. For wave Na, only the binaural–but not the monaural—peak latency was significantly affected by echo lag [exp 1: $F(4)=3.6$, $p<0.02$; exp 2: $F(3)=6$, $p<0.007$; ANOVA]. However, with these early components, the binaural peak latency was significantly increased relative to the monaural peak latency, only with some of the intermediate echo lags (8 ms for wave V, and 10 and 12 ms for wave Na) and not with the shorter echo lags, where the echo-lateralization suppression was more prominent (ANOVA, *post hoc* test). This binaural peak latency increase thus does not seem to correlate with the echo-lateralization suppression.

In summary, we found a large and significant reduction in the n(b/m) Pa peak amplitude and the n(b/m) area and an increase in the binaural Pa peak latency in response to real, compared to virtual echoes. The degree of electrophysiological suppression was dependent on echo lag. Such consistent effects were not observed for the brainstem AEPs, nor for the Na component of the middle-latency potentials.

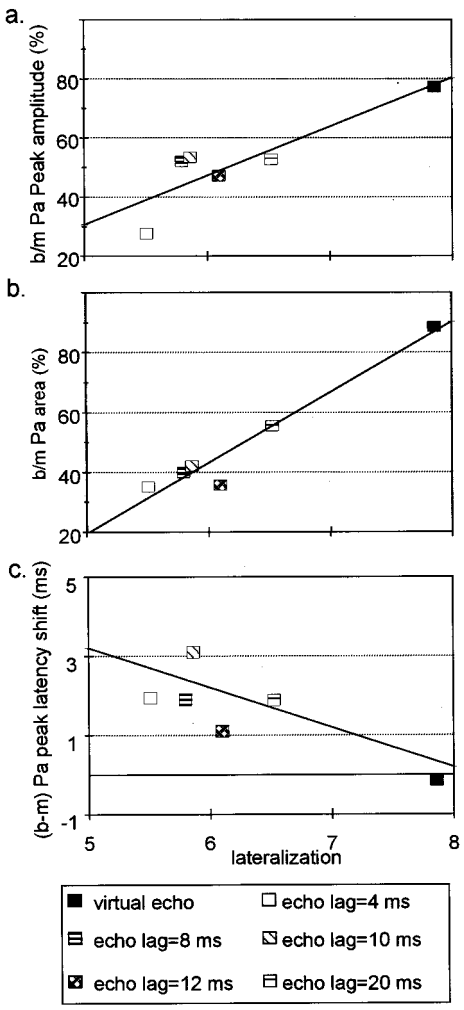

FIG. 9. Linear regression between the psychophysical lateral position judgment and the b/m echo Pa peak amplitude (a), b/m echo Pa area (b), and binaural echo Pa peak latency (c) at all echo lags and averaged across subjects and IATDs. (a) Slope: 16.5, intercept: -51.8, $R=0.88$, $P<0.02$ (T-test). (b) Slope: 23.6, intercept: -98.5, $R=0.97$, $P<0.01$ (T-test). (c) Slope: -1, intercept: 8.2, $R=-0.77$, $P<0.07$ (T-test).

C. Lateralization-echo Pa suppression correlation

The linear regression between the lateral position judgment of the virtual echo and source+echo (unnormalized) and the b/m echo Pa peak amplitude, b/m echo Pa area, and binaural echo Pa peak latency, was calculated in order to examine the relationship between the psychophysical and Pa measures of echo-lateralization suppression. All the measures were averaged across subjects and across IATDs of 300 and 600 μs (there were no significant differences between IATDs, and the average emphasized the dependence of the measures on echo lag). The correlation coefficient between the lateralization and the b/m peak amplitude of the echo Pa was 0.88 [$p<0.02$, T-test; Fig. 9(a)]. The correlation coefficient between the lateralization and the echo Pa b/m area was even higher at 0.97 [$p<0.01$, T-test; Fig. 9(b)]. The echo Pa (b-m) peak-latency shift was inversely related to the lateralization, but the correlation was only marginally significant [$R=-0.77$, $p<0.07$, T-test; Fig. 9(c)]. When the virtual echo data were excluded from the analysis, the correlation coefficients obtained between the lateralization and all three echo Pa measures were diminished and nonsignificant. However, the correlation coefficients for the echo Pa b/m peak amplitude and echo Pa b/m area were still relatively high and close to significance ($R=0.6$, $p<0.2$; $R=0.8$, $p<0.1$, respectively). In contrast, with the echo Pa (b-m) peak-latency shift, the correlation became very low and nonsignificant ($R=-0.22$, $p<0.7$, T-test). The high correlation coefficients obtained for all three echo Pa measures thus primarily reflect the decrease in these measures for real relative to virtual echoes. For the echo Pa b/m peak amplitude and b/m area, the correlation remained relatively high and close to significance when the virtual echo data were excluded. This indicates that both measures (especially the area) did increase progressively with echo lag, although not entirely regularly. The echo Pa (b-m) peak latency shift seems to be less clearly correlated with the suppression.

III. DISCUSSION

A. Summary of results

The lateral position judgment of binaural click pairs simulating a midline source followed by a right-sided echo was dominated by the source position at small echo lags. With the increase in echo lag, the source+echo pair position was increasingly biased toward the echo.

A significant and specific reduction in the n(b/m) peak amplitude and in the n(b/m) area and an increase in the binaural peak latency, were detected in the real echo-evoked Pa. The binaural echo Pa suppression was affected by echo lag and correlated with the psychophysical echo-lateralization suppression.

B. Psychophysical results

The dependence of the lateralization judgment of source+echo pairs, on the echo lag, and on the echo IATD were studied. The source+echo lateralization judgment could be separated into three levels, according to the echo lag, each showing a different degree of echo position influence. With the small echo lags (3 ms with all and 4 ms with some of the echo IATDs), the source+echo lateral position judgment was dominated by the source midline position. With echo lags of 4–12 ms, the paired-sound perceived position was already distinguishable from that of the source, and was increasingly biased toward the lateral echo. With echo lags of 12–20 ms, with most IATDs, the distance of the perceived source+echo position from the source and echo when perceived as distinct sounds was similar. These results are consistent with the echo-localization suppression PE, whereby at small echo lags echo position does not influence the paired-sound position. With the increase in echo lag, the echo-localization suppression gradually decreases, until it reaches a point when both the source and echo positions contribute equally to localization of the source+echo.

The temporal range and the progressive quality of the source+echo lateralization dependence on echo lag, as reported above, are in accordance with previous studies using diotic followed by dichotic binaural impulse pairs to study this effect (Ebata *et al.*, 1968; Lindemann, 1986). Differ-

ences in stimulus properties (duration, frequency, content) and in the nature of the task (in both earlier studies, subjects were asked to report the lateral position of the echo and not of the entire auditory event as in the present study) should, however, be considered when comparing measurements of the echo-lateralization suppression across studies.

The echo lag for reaching the 50% midway position in the present study, roughly corresponds to the $t_{i,50}$ threshold (the threshold for the echo to reach 50% of its maximal lateral displacement) described in Lindemann's study for narrow-band impulses (Lindemann, 1986). The $t_{i,50}$ ranged from 24 to 9 ms for echoes with 500-μs IATDs, depending on their central frequency. The echo lag for reaching 50% lateralization in this study equaled 12–20 ms or longer, depending on the echo IATD. This is well within the range of Lindemann's findings. The echo threshold (defined as the echo lag with which the lateral position of the echo can just be discriminated from that of the source) in Lindemann's study ranged from 9 to 3 ms depending on the impulses' center frequency. For impulses with a $t_{i,50}$ of 20 and 12 ms, the echo threshold equaled 6 and 4 ms, respectively. Although we did not psychophysically test for the echo threshold in the present study, statistical analysis of our results shows that the source+echo position differed from the source position with echoes lagging at least 4 or 8 ms, depending on the echo IATD. This threshold range, suggested by our results for discriminating the paired-sound location from the source location, is within the echo threshold range in Lindemann's study and is similar to the 4–6-ms echo threshold value corresponding to the 12–20-ms $t_{i,50}$. Ebata *et al.* (1968) found echo-threshold values of 9–10 ms for broadband impulses in the range of IATDs that we used. The larger echo-threshold values suggested by their study may be due to the longer duration of the impulses they used. Shorter click duration is known to decrease the threshold for detecting the echo as a separate sound (Babkoff and Sutton, 1966), and thus may also decrease the threshold for separate echo lateralization. The source+echo lateral displacement tended to increase with echo IATD up to values of 300–450 μs and decrease with further increase in IATD, although the dependence on echo IATD was significant only with some of the echo lags. This suggests that the echo-lateralization suppression became more effective with the large compared to the intermediate echo IATDs. This result is compatible with the effect previously studied by Shinn-Cunningham *et al.* (1993), whereby the echo-lateralization suppression increases with the difference between the source and echo IATDs. However, the dependence of the echo-lateralization suppression on echo IATD, in our results and as described by Shinn-Cunningham *et al.* (1993), is complex and shows considerable variability. Thus, it was not used in this study for validation of electrophysiological correlates of echo-lateralization suppression.

In summary, the temporal range and progressive dependence of echo-lateralization suppression on echo lag, which is the principal parameter affecting the PE, seem compatible with earlier reports on this effect with impulses (Ebata *et al.*, 1968; Lindemann, 1986). The electrophysiological correlate of echo-lateralization suppression is expected to display the largest degree of suppression at 4-ms echo lag (3 ms was not tested electrophysiologically), a decreasing degree of suppression with echo lags of 8 ms and longer, up to approximately no suppression with echo lags of 12 or 20 ms.

C. Electrophysiological results

The brainstem and middle-latency AEPs were studied for processes that are specific to a real echo in the binaural condition. A significant and echo-specific reduction in the normalized binaural-to-monaural ratios of peak amplitude and area and an increase in the binaural-to-monaural shift in peak latency of component Pa were detected. This suppression and response delay were confined to Pa, and specific to an echo in the binaural situation where the echo position was psychophysically suppressed. No consistent specifically binaural effects were noticed on any of the real echo-evoked early components preceding Pa. Thus, the specifically binaural activity evoked by the real versus the virtual echo differed only at the level of the thalamo–cortical component Pa.

The real echo-Pa suppression, as reflected by the (b/m) peak amplitude and area, was dependent on echo lag in that it was largest, on average, at 4-ms echo lag and declined with the larger echo lags. But the extent of the real echo-evoked Pa suppression was only weakly correlated with the echo lag, as indicated by the lower and non- (or only marginally) significant correlation coefficients, when the virtual echo data were removed. The low significance of the correlation between the b-m Pa peak-latency shift and the psychophysical echo suppression is probably due to the fact that the latency shift was small (1–3 ms) relative to the duration of the Pa component (approximately 22 ms), and therefore more difficult to measure with precision. For instance, at 4-ms echo lag, the binaural–monaural increase in the echo-Pa peak latency was only roughly 10% of the Pa duration. In contrast, the (b/m) echo-Pa amplitude decreased by 72% and the (b/m) Pa area decreased by 65%.

The binaural real echo Pa peak latency was not significantly affected with echo lags of 12 and 20 ms, whereas the n(b/m) Pa peak amplitude was not significantly affected with 20 ms echo lag and the n(b/m) area was significantly diminished even at 20-ms echo lag. This suggests that the upper limit for the binaural real echo Pa suppression is between an echo lag of 12 and over 20 ms. This is consistent with the psychophysical upper limit of 12–20 ms for echo-lateralization suppression (specified as the echo lag for reaching 50% lateralization), indicated in this study.

The specificity of the electrophysiological suppression to the Pa component in response to real echoes and the similar upper limit and dependence on echo lag of the psychophysical and Pa suppression suggest that the Pa suppression may indeed be a correlate of the psychophysical echo-lateralization suppression. The relatively high upper temporal limit of the echo Pa suppression suggests that the Pa suppression is a correlate of the echo-localization suppression component of the PE, rather than the source+echo fusion component which breaks down at shorter echo lags. However, we can not restrict the echo Pa suppression to the localization aspect of the PE. It could also be correlated with other echo features that were not tested in this study and may

be suppressed beyond the range of source+echo fusion. For example, it is not clear whether the echo suppression is restricted to directionality cues or involves other echo features, such as its loudness (Blauert, 1997; Freyman *et al.*, 1991).

Dependence on echo IATD was noted only with the n(b/m) Pa area. The n(b/m) Pa area's dependence on echo IATD resembled that of the lateral displacement judgment, in that both measures were augmented with intermediate echo IATDs. However, the relatively small number of echo IATD levels that were used in the electrophysiological study and the complexity of the IATD effect limit further consideration of this effect on the electrophysiological correlate.

Real echo Pa suppression also occurred with an echo IATD of 0 μs. This simulates the case where both the source and the echo arise from a medial position, but their locations within the medial plane may differ. This result supports the idea that the echo position is suppressed in this case as well, even though there are no interaural disparities in the echo. Previous studies have indeed indicated that the PE is obtained with medial front and rear sources (Blauert, 1971; Rakerd and Hartmann, 1992, 1994; Litovsky *et al.*, 1997). The present result suggests that there is *binaural* echo suppression in the medial plane, even when (in the free field) monaural cues must be used for localizing the echo.

Pa primarily reflects activity from bilateral generators in the primary auditory cortex. Evidence includes near-field intracranial recordings in humans (Celesia, 1976; Lee *et al.*, 1984; Liegois-Chauvel *et al.*, 1994) and animals (Arrezo *et al.*, 1975; Kaga *et al.*, 1980) localizing auditory-evoked activity at the latency of Pa (or the putative animal Pa-analogue), to the supratemporal plane in and near the primary auditory projection area. The effect of temporal-lobe lesions on Pa is controversial in that there are reports of a decrease or abolition (Kaga *et al.*, 1980; Kraus *et al.*, 1982; Özdamar *et al.*, 1982; Kileny *et al.*, 1987; Scherg and Von Cramon, 1986) concurrent with reports of no effect on this component (Parving *et al.*, 1980; Woods *et al.*, 1987). This may be due to the fact that Pa is not generated exclusively in the primary auditory cortex. Dipolar modeling studies favor the view that the scalp-recorded Pa principally reflects early tangential activity in both supratemporal auditory cortices, summated with later activity from a generator clearly distinct in orientation and latency (Scherg and Von Cramon, 1986; Deiber *et al.*, 1988; Jacobson and Newman, 1990; Polyakov and Pratt, 1994). The identity of the later generator is, however, unresolved. A deep midline generator system (Buchwald, 1981; Kraus *et al.*, 1988; Jacobson and Newman, 1990) or generators in auditory cortical association areas (Celesia, 1976; Scherg and Von Cramon, 1986) have been suggested.

In a concurrent equivalent dipole analysis, we analyzed the generators of the suppression measured at Pa's latency (Liebenthal and Pratt, 1997), using the same methodology as in Polyakov and Pratt (1994). Two major conclusions arising from the analysis support primary auditory cortex involvement in the echo suppression: First, the orientation of each of the two equivalent dipoles representing the neural activity at Pa's latency was similar in the binaural echo-evoked response, the monaural echo-evoked response, and the source-evoked response. This suggests that the reduction in the binaural echo Pa size reflects an intrinsic reduction in the activity of the Pa generators and not the activity of temporally overlapping, different generators. Second, only the earlier of the two Pa equivalent dipoles showed an echo lag-dependent suppression, with a pattern similar to the one reported here with the scalp-recorded Pa. The later Pa equivalent dipole showed no suppression at all. The earlier Pa activity arises from the primary auditory cortex (Arrezo *et al.*, 1975; Celesia, 1976; Kaga *et al.*, 1980; Scherg and Von Cramon, 1986; Deiber *et al.*, 1988; Jacobson and Newman, 1990; Liegeois-Chauvel *et al.*, 1994; Polyakov and Pratt, 1994), thus suggesting primary auditory cortex involvement in binaural echo-lateralization suppression.

This indication of primary auditory cortex involvement in binaural echo-lateralization suppression is in line with previous psychophysical studies demonstrating the dependence of the echo-localization suppression on the integrity of the temporal lobe, in humans (Hochster and Kelly, 1981; Cornelisse and Kelly, 1987), or more specifically the auditory cortex, in cats (Cranford *et al.*, 1971; Whitfield *et al.*, 1978). The necessity of maturity of the auditory cortex for echo-localization suppression has been shown in dogs (Ashmead *et al.*, 1986) and humans (Clifton *et al.*, 1981, 1984; Muir *et al.*, 1989). Cortical involvement in echo suppression is further suggested by the complexity of the effect. The echo suppression seems to result from evaluation and decision-making processes, considering the ongoing sensory input, the context in which the sounds are presented, and the listeners' experience and expectations (Morrongiello *et al.*, 1984; Clifton, 1987; Clifton and Freyman, 1989; Blauert and Col, 1989; Saberi and Perrot, 1990; Freyman *et al.*, 1991; Clifton *et al.*, 1994; Blauert, 1997). However, these implications of cortical involvement in the PE have been based solely on psychophysical measurements of the effect. The present study provides *physiological* indication for primary auditory cortex involvement in binaural echo-localization suppression in humans.

Animal single-unit correlates of echo suppression have been previously reported at binaural brainstem levels of the auditory, pathway, in the superior olive (Fitzpatrick *et al.*, 1995) and the inferior colliculus (Yin, 1994; Fitzpatrick *et al.*, 1995; Keller and Takahashi, 1996; Litovsky *et al.*, 1997; Litovsky, 1998; Litovsky and Yin, 1998a, b). The single-unit studies of the inferior colliculus echo response can be compared with our results for the brainstem waves V and VI. In the animal studies of the inferior colliculus, the main finding was that most IATD-sensitive neurons showed suppression in response to a shortly lagging stimulus in a pair of transient stimuli. The echo lag at which the lagging response was suppressed to half of its response in the absence of the source could be correlated with psychophysical measurements of the echo suppression obtained in humans. The average extents of suppression of the inferior colliculus responses to monaural and to binaural echoes were found to be of similar amplitude (Yin, 1994; Fitzpatrick *et al.*, 1995; Litovsky and Yin, 1998b). In the present study, the peak latency of the brainstem potentials V and VI was found to depend on echo lag, under both binaural and monaural con-

ditions. Consistent with the previous studies, however, there was no specifically binaural echo suppression with the brainstem waves V and VI.

The cortical electrophysiological correlate of the PE observed in the present study may now allow further insight into the cortical mechanisms involved in the binaural echo suppression in humans. Additional manipulation of source and echo features will be required to further establish the PE correlate obtained in this study and determine the extent of PE-related phenomena that may involve cortical processing. Of special interest are the dynamic properties of the effect, such as the buildup and breakdown of echo suppression (Clifton, 1987; Clifton and Freyman, 1989; Freyman *et al.*, 1991; Clifton *et al.*, 1994), that are thought to be mediated cortically.

The present study also suggests a behavioral correlate for the middle-latency component Pa. Kraus *et al.* (1982) were unable to find a correlation between Pa and language processing. The Pa correlate of binaural echo-lateralization suppression suggested here raises the possibility that Pa reflects neural processes related to auditory-scene analysis.

The echo suppression is only a particular aspect of the processing performed on the acoustic waves reaching the ears, in order to segregate them into auditory events and organize them into a sensible auditory scene (auditory-scene analysis is discussed extensively in Handel, 1986, and Bregman, 1990). Pa could reflect processes related to the enhancement of important auditory information and the suppression of other information considered redundant or irrelevant.

ACKNOWLEDGMENTS

The authors wish to thank Dr. Herbert Vaughan for his valuable comments and suggestions on earlier versions of this manuscript. The contributions of Dr. Judy Gravel, Dr. Elyse Sussman, and two anonymous reviewers are also acknowledged. This study was supported by the Julius & Dorothea Harband Fellowship, the Technion VPR Fund, and the Israel Science Foundation.

[1]An apparent limitation to the use of click stimuli is that the click-evoked brainstem response mainly reflects activation originating in the high-frequency regions of the cochlea (Don and Eggermont, 1978), whereas IATD sensitivity for lateralization is most important in low-frequency sounds. This is probably not a major concern in the present study, because it is the earlier brainstem components (I and III) that represent high-frequency activity. The later brainstem wave V, which was measured in the present study, appears to reflect activation from more apical regions that are sensitive to low-frequencies (Don and Eggermont, 1978). Also, with the TDH-49 earphones and moderate intensity level used in this study, even the early brainstem response represents activation of cochlear regions sensitive to roughly 1–4 kHz (Hall, 1992). It thus includes some of the range of IATD sensitivity for lateralization (up to roughly 1.6 kHz).

[2]In the traces of Figs. 4–6, filtered according to the middle-latency power spectrum, the higher frequency brainstem components are cut off and fused into one peak. We thus generally called this peak ''brainstem'' potential. But, the evaluation of the distinct brainstem components was performed on traces filtered according to their power spectrum (not shown here).

[3]The binaural–monaural disparity, as described in the above studies, is routinely measured by *subtracting* the binaural potentials from the sum of monaural potentials. The resulting binaural–monaural subtraction waveform reflects both amplitude and latency disparities between the monaural and binaural peaks and disrupts the ability to (a) correlate each of the measures separately with the psychophysical phenomenon, and (b) relate the difference waveform peaks to the binaural and monaural peaks and thus to the physiological generators. This problem is emphasized in the middle-latency echo responses recorded in this study, because there are relatively large binaural–monaural latency disparities. In order to by-pass the latency disparities, in the present study we measured the ratios of binaural and monaural peak amplitudes and areas.

[4]We actually recorded only the right monaural potentials to save subjects experimental time and preserve their cooperation. The sum of monaural potentials was obtained by multiplying the right monaural potentials by two. Consistent asymmetry between left and right EPs is not expected for the normal-hearing group of subjects and midline electrode configuration used in this study. In any case, even if there were an asymmetry, it would be similar for the real and virtual echo EPs and would thus not bias the measurement of the real relative to virtual echo suppression.

Arrezo, J., Pickoff, A., and Vaughan, Jr., H. G. (**1975**). ''The sources and intracerebral distribution of auditory evoked potentials in the alert Rhesus monkey,'' Brain Res. **90**, 57–73.

Ashmead, D., Clifton, R., and Reese, E. (**1986**). ''Development of auditory localization in dogs: Single source and precedence-effect sounds,'' Dev. Psychobiol. **19**, 91–104.

Babkoff, H., and Sutton, S. (**1966**). ''End point of lateralization for dichotic clicks,'' J. Acoust. Soc. Am. **39**, 87–102.

Blauert, J. (**1971**). ''Localization and the law of the first wavefront in the median plane,'' J. Acoust. Soc. Am. **50**, 466–470.

Blauert, J. (**1997**). *Spatial Hearing* (MIT Press, Cambridge, MA).

Blauert, J., and Col, J. P. (**1989**). ''Etude de quelques aspects temporels de l' audition spatiale,'' Note-Laboratoire de Mecanique et d' Acoustique, No. 118, Centre Nationale de la Recherche Scientifique.

Bregman, A. S. (**1990**). *Auditory scene analysis: The Perceptual Organization of Sound* (MIT Press, Cambridge, MA).

Buchwald, J. S., Hinman, C., Norman, R. J., Huang, C.-M., and Brown, K. A. (**1981**). ''Middle and long-latency evoked responses recorded from the vertex of normal and chronically lesioned cats,'' Brain Res. **205**, 91–109.

Celesia, G. G. (**1976**). ''Organization of auditory cortical areas in man,'' Brain **99**, 403–414.

Clifton, R. K., Morrongiello, B. A., Kulig, J. W., and Dowd, J. M. (**1981**). ''Newborns' orientation toward sound: possible implications for cortical development,'' Child Dev. **52**, 833–838.

Clifton, R. K., Morrongiello, B. A., and Dowd, J. M. (**1984**). ''A developmental look at an auditory illusion: The precedence effect,'' Dev. Psychobiol. **17**, 519–536.

Clifton, R. K. (**1987**). ''Breakdown of echo suppression in the precedence effect,'' J. Acoust. Soc. Am. **82**, 1834–1835.

Clifton, R. K., Freyman, R. L., Litovsky, R. Y., and McCall, D. (**1994**). ''Listeners' expectations about echoes can raise or lower echo threshold,'' J. Acoust. Soc. Am. **95**, 1525–1533.

Clifton, R. K., and Freyman, R. L. (**1989**). ''Effect of click rate and delay on the breakdown of the precedence effect,'' Percept. Psychophys. **46**, 139–145.

Cornelisse, L. E., and Kelly, J. B. (**1986**). ''The effect of cerebrovascular accident on the ability to localize sounds under the conditions of the precedence effect,'' Neuropsychol. **25**, 449–452.

Cranford, J., Ravizza, R., Diamond, I., and Whitfield, I. (**1971**). ''Unilateral ablation of the auditory cortex in the cat impairs complex sound localization,'' Science **172**, 286–288.

Deiber, M. P., Ibanez, V., Fisher, C., Perrin, F., and Mauguiere, F. (**1988**). ''Sequential mapping favours the hypothesis of distinct generators for Na and Pa middle latency auditory evoked potentials,'' Electroencephalogr. Clin. Neurophysiol. **71**, 187–197.

Dobie, R. A., and Norton, S. J. (**1980**). ''Binaural interaction in human auditory evoked potentials,'' Electroencephalogr. Clin. Neurophysiol. **49**, 303–313.

Don, M., and Eggermont, J. J. (**1978**). ''Analysis of the click-evoked brainstem potentials in man using high-pass noise masking,'' J. Acoust. Soc. Am. **63**, 1084–1092.

Ebata, M., Sone, T., and Nimura, T. (**1968**). ''On the perception of direction of echo,'' J. Acoust. Soc. Am. **44**, 542–547.

Fitzpatrick, D. C., Kuwada, S., Batra, R., and Trahiotis, C. (**1995**). ''Neural responses to simple simulated echoes in the auditory brainstem of unanesthetized rabbit,'' J. Neurophysiol. **74**, 2469–2486.

Freyman, R. L., Clifton, R. K., and Litovsky, R. Y. (**1991**). ''Dynamic processes in the precedence effect,'' J. Acoust. Soc. Am. **90**, 874–884.

Furst, M., Levine, R. A., and McGaffigan, P. M. (**1985**). ''Click lateralization is related to the β component of the dichotic brainstem auditory evoked potentials of human subjects,'' J. Acoust. Soc. Am. **78**, 1644–1651.

Furst, M., Levine, R. A., Korczyn, A. D., Fullerton, B. C., Tadmor, R., and Algom, D. (**1995**). ''Brainstem lesions and click lateralization in patients with multiple sclerosis,'' Hearing Res. **82**, 109–124.

Hall III, J. W. (**1992**). *Handbook of Auditory Evoked Responses* (Allyn and Bacon, Boston), pp. 50–55.

Handel, S. (**1986**). *Listening: An Introduction to the Perception of Auditory Events* (MIT Press, Cambridge, MA).

Hartmann, W. M. (**1983**). ''Localization of sound in rooms,'' J. Acoust. Soc. Am. **74**, 1380–1391.

Hashimoto, I., Mashiko, T., Yoshikawa, K., Mizuta, T., Imada, T., and Hayashi, M. (**1995**). ''Neuromagnetic measurements of human primary auditory response,'' Electroencephalogr. Clin. Neurophysiol. **96**, 348–356.

Hochster, E. M., and Kelly, J. B. (**1981**). ''The precedence effect and sound localization by children with temporal lobe epilepsy,'' Neuropsychol. **19**, 49–55.

Jacobson, G. P., and Newman, C. W. (**1990**). ''The decomposition of the middle latency auditory evoked potential (MLAEP) Pa component into superficial and deep source contributions,'' Brain Topogr. **2**, 229–236.

Jones, S. J., and Van Der Poel, J. C. (**1989**). ''Binaural interaction in the brainstem auditory evoked potentials: evidence for a delay line coincidence detection mechanism,'' Electroencephalogr. Clin. Neurophysiol. **77**, 214–224.

Kaga, K., Hink, R. F., Shinoda, Y., and Suzuki, J. (**1980**). ''Evidence for a primary cortical origin of a middle latency auditory evoked potential in cats,'' Electroencephalogr. Clin. Neurophysiol. **50**, 254–266.

Keller, C. H., and Takahashi, T. T. (**1996**). ''Responses to simulated echoes by neurons in the barn owl's auditory space map,'' J. Comp. Physiol. A **178**, 499–512.

Kileny, P., Paccioretti, D., and Wilson, A. F. (**1987**). ''Effects of cortical lesions on middle-latency auditory evoked responses (MLR),'' Electroencephalogr. Clin. Neurophysiol. **66**, 108–120.

Koenig, W. (**1950**). ''Subjective effects in binaural hearing,'' J. Acoust. Soc. Am. **22**, 61–62.

Kraus, N., Özdamar, O., Hier, D., and Stein, L. (**1982**). ''Auditory middle latency responses (MLRs) in patients with cortical lesions,'' Electroencephalogr. Clin. Neurophysiol. **54**, 275–287.

Lee, Y. S., Lueders, H., Dinner, D. S., Lesser, R. P., Hahn, J., and Klem, G. (**1984**). ''Recording of auditory evoked potentials in man using chronic subdural electrodes,'' Brain **107**, 115–131.

Legatt, D. A., Arezzo, J. C., and Vaughan, Jr., H. G. (**1988**). ''The anatomic and physiologic bases of brain stem auditory evoked potentials,'' Neurol. Clin. **6**, 681–704.

Liebenthal, E., and Pratt, H. (**1997**). ''Evidence for primary auditory cortex involvement in the echo suppression precedence effect: a 3 CLT study,'' J. Basic Clin. Physiol. Pharmacol. **8(3)**, 185–201.

Liegois-Chauvel, C., Musolino, A., Badier, J. M., Marquis, P., and Chauvel, P. (**1994**). ''Evoked potentials recorded from the auditory cortex in man: evaluation and topography of the middle latency components,'' Electroencephalogr. Clin. Neurophysiol. **92**, 204–214.

Lindemann, W. (**1986**). ''Extension of a binaural cross-correlation model by contralateral inhibition. II. The law of the first wave front,'' J. Acoust. Soc. Am. **80**, 1623–1630.

Litovsky, R. Y., Rakerd, B., Yin, T. C., and Hartmann, W. M. (**1997**). ''Psychophysical and physiological evidence for a precedence effect in the median sagittal plane,'' J. Neurophysiol. **77**, 2223–2226.

Litovsky, R. Y. (**1998**). ''Physiological studies of the precedence effect in the inferior colliculus of the kitten,'' J. Acoust. Soc. Am. **103**, 3139–3152.

Litovsky, R. Y., and Yin, T. C. (**1998a**). ''Physiological studies of the precedence effect in the inferior colliculus of the cat. I. Correlates of psychophysics,'' J. Neurophysiol. **80**, 1285–1301.

Litovsky, R. Y., and Yin, T. C. (**1998b**). ''Physiological studies of the precedence effect in the inferior colliculus of the cat. I. Neural mechanisms,'' J. Neurophysiol. **80**, 1302–1316.

Litovsky, R. Y., and Macmillan, N. A. (**1994**). ''Sound localization precision under conditions of the precedence effect: Effects of azimuth and standard stimuli,'' J. Acoust. Soc. Am. **96**, 752–758.

McPherson, D. L., and Starr, A. (**1995**). ''Auditory time-intensity cues in the binaural interaction component of the auditory evoked potentials,'' Hearing Res. **89**, 162–171.

Morrongiello, B. A., Kulig, J., and Clifton, R. K. (**1984**). ''Developmental changes in auditory temporal perception,'' Child Dev. **55**, 461–477.

Muir, D. W., Clifton, R. K., and Clarkson, M. G. (**1989**). ''The development of a human auditory localization response: a U-shaped function,'' Can. J. Psychol. **43**, 199–216.

Özdamar, Ö., Kraus, N., and Curry, F. (**1982**). ''Auditory brain stem and middle latency responses in a patient with cortical deafness,'' Electroencephalogr. Clin. Neurophysiol. **53**, 224–230.

Parving, A., Salomon, G., Elberling, C., Larsen, B., and Lassen, N. A. (**1980**). ''Middle components of the auditory evoked response in bilateral temporal lobe lesions,'' Scand. Audiol. **9**, 161–167.

Picton, T. W., Hillyard, S. A., Krausz, H. I., and Galambos, R. (**1974**). ''Human auditory evoked potentials. I. Evaluation of components,'' Electroencephalogr. Clin. Neurophysiol. **39**, 179–190.

Polyakov, A., and Pratt, H. (**1994**). ''Three-channel Lissajous' trajectory of human middle latency auditory evoked potentials,'' Ear Hear. **15**, 390–399.

Rakerd, B., and Hartmann, W. M. (**1985**). ''Localization of sound in rooms. II. The effects of a single reflecting surface,'' J. Acoust. Soc. Am. **78**, 524–533.

Rakerd, B., and Hartmann, W. M. (**1992**). ''Precedence effect with and without interaural differences-sound localization in three planes,'' Abstract, J. Acoust. Soc. Am. **92**, 2296.

Rakerd, B., and Hartmann, W. M. (**1994**). ''More on the precedence effect in three planes,'' Abstract, ASA 127th Meeting.

Ronken, D. A. (**1970**). ''Monaural detection of a phase difference between clicks,'' J. Acoust. Soc. Am. **47**, 1091–1099.

Saberi, K., and Perrott, R. (**1990**). ''Lateralization thresholds obtained under conditions in which the precedence effect is assumed to operate,'' J. Acoust. Soc. Am. **87**, 1732–1737.

Scharf, B. (**1974**). ''Loudness summation between tones from two loudspeakers,'' J. Acoust. Soc. Am. **56**, 589–593.

Scherg, M., and Von Cramon, D. (**1986**). ''Evoked dipole source potentials of the human auditory cortex,'' Electroencephalogr. Clin. Neurophysiol. **65**, 344–360.

Shinn-Cunningham, B. G., Zurek, P. M., and Durlach, N. I. (**1993**). ''Adjustment and discrimination measurements of the precedence effect,'' J. Acoust. Soc. Am. **93**, 2923–2932.

Vaughan, Jr., H. G., and Arezzo, J. C. (**1988**). ''The neural basis of event-related potentials,'' in *Human Event-Related Potentials EEG Handbook*, edited by T. W. Picton (Elsevier Science, New York), pp. 76–80.

Wallach, H., Newman, E. B., and Rosenzweig, M. R. (**1949**). ''The precedence effect in sound localization,'' Am. J. Psychol. **52**, 315–336.

Whitfield, I. C., Diamond, I. T., Chiveralls, K., and Williamson, T. G. (**1978**). ''Some further observations on the effects of unilateral cortical ablation on sound localization in the cat,'' Exp. Brain Res. **31**, 221–234.

Woods, D. L., Clayworth, C. C., Knight, R. T., Simpson, G. V., and Naeser, M. A. (**1987**). ''Generator of middle- and long latency auditory evoked potentials: implications from studies of patients with bitemporal lesions,'' Electroencephalogr. Clin. Neurophysiol. **68**, 132–148.

Wrege, K. S., and Starr, A. (**1981**). ''Binaural interaction in human auditory brainstem evoked potentials,'' Arch. Neurol. **38**, 572–580.

Yin, T. C. T. (**1994**). ''Physiological correlates of the precedence effect and summing localization in the inferior colliculus of the cat,'' J. Neurosci. **14**, 5170–5186.

Zurek, P. M. (**1979**). ''Measurements of binaural echo suppression,'' J. Acoust. Soc. Am. **66**, 1750–1757.

Zurek, P. M. (**1980**). ''The precedence effect and its possible role in the avoidance of interaural ambiguities,'' J. Acoust. Soc. Am. **67**, 952–964.

Zurek, P. M. (**1987**). ''The precedence effect,'' in *Directional Hearing*, edited by W. A. Yost and G. Gourevitch (Springer, Berlin), pp. 85–105.

Near-field responses from the round window, inferior colliculus, and auditory cortex of the unanesthetized chinchilla: Manipulations of noiseburst level and rate

R. F. Burkard[a)]
Center for Hearing and Deafness, Department of Communication Disorders and Sciences, and Department of Otolaryngology, University at Buffalo, Buffalo, New York 14214

C. A. Secor
Center for Hearing and Deafness, University at Buffalo, Buffalo, New York 14214, Cleveland V.A. Hospital, Cleveland, Ohio 44195, and Cleveland Clinic, Cleveland, Ohio 44195

R. J. Salvi
Center for Hearing and Deafness, Department of Communication Disorders and Sciences, and Department of Otolaryngology, University at Buffalo, Buffalo, New York 14214

(Received 10 September 1998; revised 15 February 1999; accepted 25 March 1999)

Few studies have compared the response properties of near-field potentials from multiple levels of the auditory nervous system of unanesthetized animals. The purpose of this study was to investigate the effects of brief-duration noisebursts on neural responses recorded from electrodes chronically implanted at the round window, inferior colliculus and auditory cortex of chinchillas. Responses were obtained from seven unanesthetized chinchillas to a noiseburst-level and noiseburst-rate series. For the noiseburst-rate series, a 70 dB pSPL noiseburst was varied in rate from 10 to 100 Hz using conventional averaging procedures, and from 100 to 500 Hz using pseudorandom pulse trains called maximum length sequences (MLSs). Response thresholds were similar for the compound action potential (CAP), inferior colliculus potential (ICP) and auditory cortex potential (ACP). With decreasing noiseburst level, there were decreases in the amplitudes and increases in the latencies of the CAP, ICP and ACP. The shapes of the mean normalized amplitude input/output (I/O) functions were similar for the ICP and ACP, while the normalized I/O functions for the first positive peak (P_1) and first negative peak (N_1) of the CAP differed from each other and from the ICP and ACP. The slopes of the latency/intensity functions were shallowest for the CAP, intermediate for the ICP, and steepest for the ACP. With increasing rate, the latency shift was least for the CAP, intermediate for the ICP and greatest for the ACP. The amplitude of P_1 of the CAP varied little with rate. All other potentials showed a pronounced decrease in amplitude at high stimulation rates. Excluding CAP P_1, proportional amplitude decrease with rate was greatest for the ACP, intermediate for N_1 of the CAP and least for the ICP. Responses were present in most animals at all recording sites, even for the highest rate (500 Hz) used in this study. For all potentials, the MLS procedure allowed the collection of a response at rates well above those where sequential responses would have overlapped using conventional averaging procedures.
[S0001-4966(99)01907-4]

PACS numbers: 43.64.Ri, 43.64.Qh, 43.64.Pg [RDF]

INTRODUCTION

Auditory brainstem responses (ABRs) and other surface-recorded auditory evoked potentials (AEPs) have been used to investigate the effects of various stimulus manipulations on response latencies and amplitudes, in both humans and other mammals (Picton *et al.*, 1974; Burkard and Hecox, 1983, 1987; Burkard and Voigt, 1989, 1990; Burkard *et al.*, 1996a, b). While surface potentials offer the advantage of being noninvasive, and hence are appropriate for human use, it is not possible to unambiguously identify the response generators using these responses. Surface-recorded AEPs that likely arise from cortical generators have latencies extending out beyond 100 ms (Picton *et al.*, 1974; Moller, 1994). With stimulus presentation rates above several Hz, responses obtained using a conventional averaging procedure overlap, making the study of temporal response properties of the auditory cortex problematic. This temporal overlap of surface-recorded AEPs can be overcome by the use of maximum length sequence (MLS) trains combined with a cross-correlation procedure (Eysholdt and Schreiner, 1982; Picton *et al.*, 1992). However, this procedure does not preclude the temporal overlap of responses emanating from multiple neural generators.

To quantify the response from a specific region of the auditory nervous system, it is necessary to record invasively using microelectrodes to isolate the response from single units, or by using gross electrodes placed in the brain region of interest. The former technique samples the response of a few neurons per animal, and is most easily accomplished in an acute experiment involving surgery and anesthesia. How-

[a)]Send all correspondence to: Robert Burkard, Center for Hearing & Deafness, University at Buffalo, 215 Parker Hall, Buffalo, NY 14214. Electronic mail: RFB@acsu.buffalo.edu

ever, comparison with the surface-recorded responses is problematic due to different response metrics between evoked potentials and single-unit responses. Specifically, response magnitude of single-units are typically reported in spikes per second, while response magnitude of auditory evoked responses is typically in peak or peak-to-peak amplitude in voltage units. Implantation of near-field electrodes followed by a recovery period allows the study of animals chronically without anesthesia (Salvi *et al.*, 1990; Burkard *et al.*, 1997a). In this way, the sampling and anesthesia problems associated with single-unit recordings are avoided. The generator of the potential is known, avoiding one problem of surface-recorded potentials, while allowing the study of latency and amplitude changes across stimulus conditions and electrode site.

Few studies have investigated near-field responses from multiple levels of the auditory nervous system in the unanesthetized preparation. Recording from multiple levels of the auditory system in the same animal is desirable, as responses to an ototoxic agent may differ with the level of the auditory nervous system. For example, in response to noise-exposure, the amplitude of the compound action potential (CAP) is invariably decreased, while the amplitude of the inferior colliculus potential (ICP) may actually be enhanced following noise exposure (Salvi *et al.*, 1990). Gerken *et al.* (1986) investigated near-field responses from the cochlear nucleus and inferior colliculus (IC) in cats before and after a noise exposure that produced a permanent threshold shift. In some animals, the ICP showed substantial response enhancement post-noise exposure, while no animals showed such response enhancement following noise exposure when recording from the cochlear-nucleus. Amplitude enhancement has also been reported in the guinea pig auditory cortex potential (ACP) following noise exposure (Popelar *et al.*, 1987; Syka *et al.*, 1994). Interestingly, this ACP amplitude enhancement post-noise exposure is only observed in the unanesthetized guinea pig. When recordings were made in guinea pigs under urethane anesthesia, the ACP amplitude was reduced post-noise exposure. Thus the ACP response in the anesthetized animal paralleled the amplitude reduction seen in the CAP and ICP (Popelar *et al.*, 1987). These studies demonstrate that response amplitudes from different levels of the auditory system can respond in a qualitatively different fashion in response to acoustic trauma. Furthermore, anesthesia can influence the nature of these amplitude changes subsequent to acoustic trauma, most notably at the level of the auditory cortex.

The present investigation represents a normative study aimed at quantifying the CAP, ICP and ACP in normal, unanesthetized chinchillas. We investigated responses to noiseburst level, in order to study response threshold and to quantify latency/intensity functions and amplitude/intensity functions from auditory nerve (AN) to cortex. Rate studies include both conventional rate manipulations, and the use of maximum length sequences (MLSs). This latter technique uses pseudorandom pulse trains and a cross-correlation procedure (Eysholdt and Schreiner, 1982; Burkard *et al.*, 1990), and allows the collection of evoked responses at much higher stimulation rates than is feasible using conventional averaging procedures. The MLS technique has mainly been used with surface-recording techniques where there is considerable temporal overlap in the responses from different neural generators. The MLS technique has not yet been used to study near-field responses at multiple levels of the auditory nervous system. Thus, the present investigation provides new information concerning the effects of very high stimulation rates on the near-field responses of the AN, IC and auditory cortex (AC) in the unanesthetized chinchilla.

I. METHODS

A. Subjects

Seven adult chinchillas served as experimental animals. Chinchillas were anesthetized with ketamine (60 mg/kg) and acepromazine (0.6 mg/kg). A gold-ball electrode was implanted at the right round window to record the CAP. Tungsten wire electrodes were implanted in the left IC to record the ICP, and in the left AC to record the ACP. IC and AC electrodes were implanted by positioning the electrodes using stereotaxic coordinates. Electrodes were advanced while presenting acoustic stimulation through a hollow earbar. The presence of a large near-field response indicated that the electrode was in or near the appropriate auditory structure. The exact location of each electrode was not verified anatomically. A tungsten electrode, implanted in the anterior cranium at midline, served as the common lead for all recordings. All animals had their right ear acoustically stimulated, and hence the CAP was recorded ipsilaterally, and the ICP and ACP were recorded contralaterally.

B. Instrumentation

Noisebursts were produced by routing white noise (Koep Precision Standards) through an electronic switch (Tucker-Davis model SW1), through a custom-built attenuator/current amplifier to an Etymotic ER2 insert earphone. Noisebursts were shaped with a Hanning window, with 0.25 ms rise and fall times. Total noiseburst duration (from 10% of peak amplitude at onset to 10% of peak amplitude at offset) was approximately 0.7 ms. The earphone was coupled to the chinchilla's ear with an Etymotic insert earphone foam plug. The flexible probe tube of an Etymotic ER-7C probe microphone was threaded through the foam plug and extended several mm beyond the foam tip into the chinchilla's ear canal. Real ear peak sound pressure level (pSPL) was determined by routing the output of the ER-7C through a low-pass filter set to 20 kHz, displaying the output on an oscilloscope and converting to dB pSPL by use of the microphone sensitivity.

Electrical activity was recorded between the active electrode (round window, IC or AC) and the common electrode. This activity was amplified ($10\,000\times$) and filtered (100–3000 Hz; Stanford Research System model SR560 bioamplifier) and digitized at 20 kHz by an Ariel DSP-16 board housed in a personal computer. For conventional evoked po-

tentials, the recorded time epoch corresponded to the interstimulus interval, but response waveforms were displayed for 12.5 ms for the CAP and the ICP, and 25 ms for the ACP.

C. Procedures

Data collection occurred several weeks following electrode implantation. Unanesthetized chinchillas were placed in a restraining device (Snyder and Salvi, 1994) inside a sound-attenuating chamber. Chinchillas rested quietly in the restraining device, with some animals moving or vocalizing intermittently. Animals appeared awake during the recording procedures; however, the level of arousal was not directly assessed. For the level series, noisebursts were presented at a 25 Hz rate, and click level varied from 20 to 80 dB pSPL in 10 dB steps. Each response was the summed response to 250 stimulus presentations. Threshold was determined with 5 dB resolution. The rate series consisted of conventional responses and MLS responses. For both procedures, noiseburst envelope was identical (0.25 ms Hanning rise/fall time noiseburst). Thus, MLS and conventional noiseburst trains only differed in the temporal patterns of noiseburst presentation. For conventional responses, 70 dB pSPL noisebursts were presented at rates of 10, 25, 50, 75 and 100 Hz. Each response was the summed response to 250 stimulus presentations. For MLS responses, stimuli were presented in trains of 64 noisebursts, and responses to 10 trains were averaged prior to cross-correlation with the appropriate recovery sequence (see Burkard *et al.*, 1990 for details of this procedure). Unlike the conventional noiseburst trains that used a constant time between noisebursts for a given stimulation rate, the MLS procedure as performed herein uses a pseudorandom interval in which the time between noisebursts ranged from some specified minimum time between noiseburst onset (called the minimum pulse interval), to pulse intervals that are up to 7 times the minimum pulse interval in the sequence. The average interval is roughly twice the minimum pulse interval. Noisebursts were presented with minimum intervals of 5, 3, 2 and 1 ms, which correspond to average stimulation rates of approximately 100, 167, 250 and 500 Hz. Two responses were obtained for each stimulus condition.

II. RESULTS

A. Noiseburst level

Figure 1 shows responses to the click level series from one chinchilla. Figure 1(a), (b) and (c) shows the CAP, ICP and ACP, respectively. The initial positive peak (P_1), and the initial negative peak (N_1) will be the CAP dependant variables, with their time from click onset representing the latency measure, and their amplitude measured relative to the pre-response baseline. For both the ICP [Fig. 1(b)] and ACP [Fig. 1(c)], response latency will be to the initial positive peak, and the amplitude measure will be from the initial positive peak to the following trough. In the summary figures that follow, mean latency or amplitude data points are only shown if at least four of the seven animals showed a response for a given stimulus condition. The vertical lines in each summary figure represent one standard deviation. Latencies are corrected for the 0.9 ms acoustic delay of the ER2 earphones.

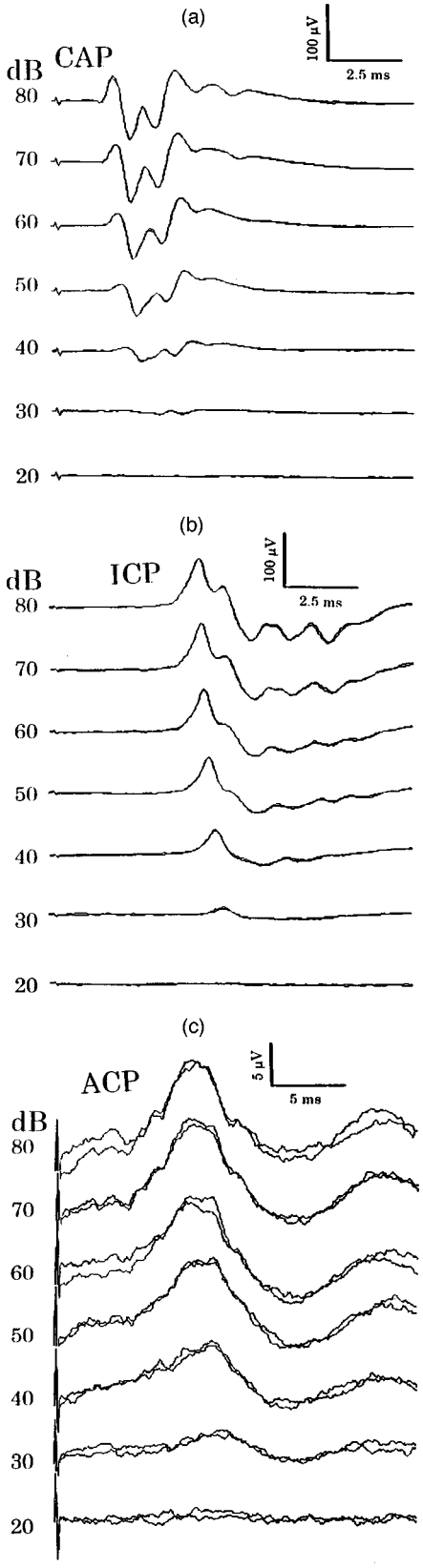

FIG. 1. Responses from one chinchilla for all noiseburst levels are shown. For each condition, two responses are superimposed. The CAP, ICP and ACP are shown in (a), (b) and (c), respectively. In each figure, positive voltage at the near-field electrode is plotted upward.

TABLE I. Noiseburst response thresholds in dB pSPL.

Chinchilla	CAP	ICP	ACP
5160	5	15	15
5165	10	10	20
5281	20	20	25
5282	20	15	25
5283	30	20	15
5284	20	20	30
5286	25	20	25
MEAN	18.6	17.1	22.1

Table I shows the lowest noiseburst level at which a response was observed in each animal, for each electrode site. A comparison of the mean thresholds shows that the lowest threshold is for the ICP (17.1 dB pSPL). The mean CAP threshold was only 1.5 dB higher (18.6 dB pSPL) and the ACP threshold was 5 dB higher (22.1 dB pSPL) than ICP threshold. Across electrode sites, mean threshold to noiseburst stimuli only varied by 5 dB. Within animal, thresholds across electrode site varied from as little as 5 dB (chinchilla #s 5281, 5286) to as much as 15 dB (chinchilla # 5283). Overall, threshold varied little across electrode site. Threshold across electrode site was statistically evaluated with a one-way repeated-measure ANOVA. This analysis failed to reach significance at the $p=0.05$ level.

Figure 2 plots mean response latencies across noiseburst level. As expected, response latency is greater for responses from more rostral electrodes. With increasing noiseburst level, there is a mean decrease in response latencies. The latency difference between CAP P_1 and N_1 appears to be a constant value of roughly 0.75 ms, regardless of noiseburst level. The ACP latency shows the greatest latency decrease with increasing noiseburst level. This is better shown in Fig. 3, which plots the change in peak latency (relative to the latency to the 80 dB pSPL noiseburst). The latency shift is similar for all responses for decreases in level from 80 dB pSPL to 60 dB pSPL. Reductions in noiseburst level below 60 dB pSPL produced a divergence of these functions. The greatest latency shift occurred for the ACP, the ICP showed less latency shift, and CAP N_1 and P_1 showed the least latency shift. Although small in magnitude, the mean latency

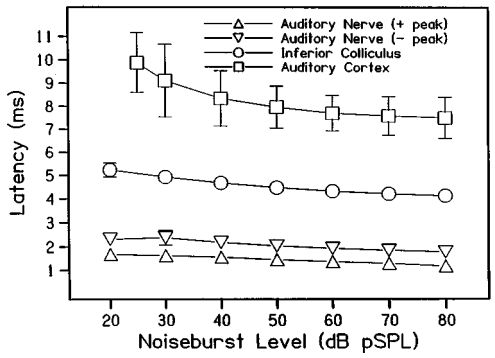

FIG. 2. Mean response latencies are plotted across noiseburst level. The parameter is response measure. The vertical lines represent one standard deviation. Each mean value represents up to 7 (and a minimum of 4) observations.

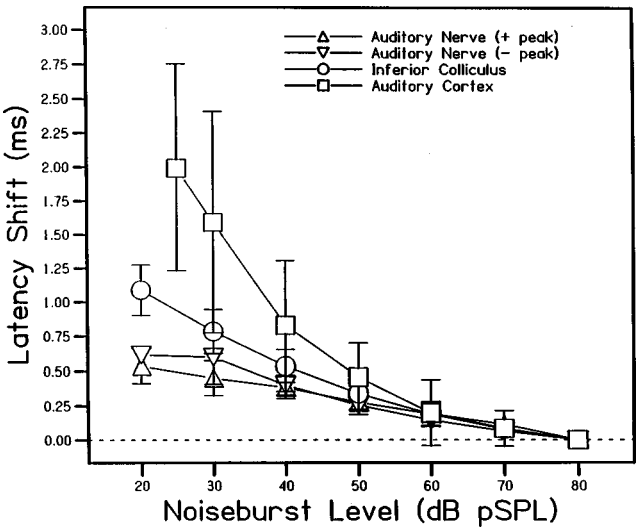

FIG. 3. Mean response latency shifts (*re*: latency at 80 dB pSPL noiseburst condition) are plotted across noiseburst level. The parameter is response measure. The vertical lines represent one standard deviation. Each mean value represents up to 7 (and a minimum of 4) observations.

shift across noiseburst level is smaller for CAP P_1 than N_1.

Response amplitudes across noiseburst level are shown in Fig. 4(a), (b), and (c) for the CAP, ICP and ACP, respectively. All responses show an increase in amplitude with increasing noiseburst level. For the CAP [Fig. 4(a)], mean P_1 amplitude increases monotonically with increasing noiseburst level, while N_1 shows a rollover in amplitude above 60 dB pSPL. The ICP [Fig. 4(b)] and ACP [Fig. 4(c)] grow in amplitude at low levels, but saturate above 60 dB pSPL. Figure 5 shows the normalized amplitude ratio data (relative to the amplitude at 80 dB pSPL) across noiseburst level for the CAP, ICP and ACP. This normalization was performed to allow comparison of response amplitude changes with level across electrode site. CAP P_1 amplitude shows a reasonably linear growth from 30 to 80 dB pSPL, in contrast to the rollover shown in the CAP N_1 function. The shapes of the normalized (amplitude ratio) growth functions for the ICP and ACP are remarkably similar, despite the large (an order of magnitude) differences in mean amplitudes [see Fig. 4(b) and (c)]. Both the ICP and ACP show amplitude saturation for noiseburst levels above 60–70 dB pSPL.

B. Noiseburst rate

Figure 6 shows responses from one chinchilla for all noiseburst rates used in this study. Figure 6(a), (b), and (c) shows responses from the CAP, ICP and ACP, respectively. In each figure, conventional responses are shown in the left panel, and MLS responses are shown in the right panel. The CAP responses to 100 Hz rates for the conventional and MLS techniques are similar in morphology [see Fig. 6(a)]. This is also true for the ICP [Fig. 6(b)]. This comparison is not possible for the ACP, as the ACP response is not completed within 10 ms, and thus we cannot compare the response morphology for conventional and MLS procedures at similar rates. It was possible to measure the positive ACP peak latency in only three of seven animals at 100 Hz, but not the peak-to-trough amplitude, because the negative

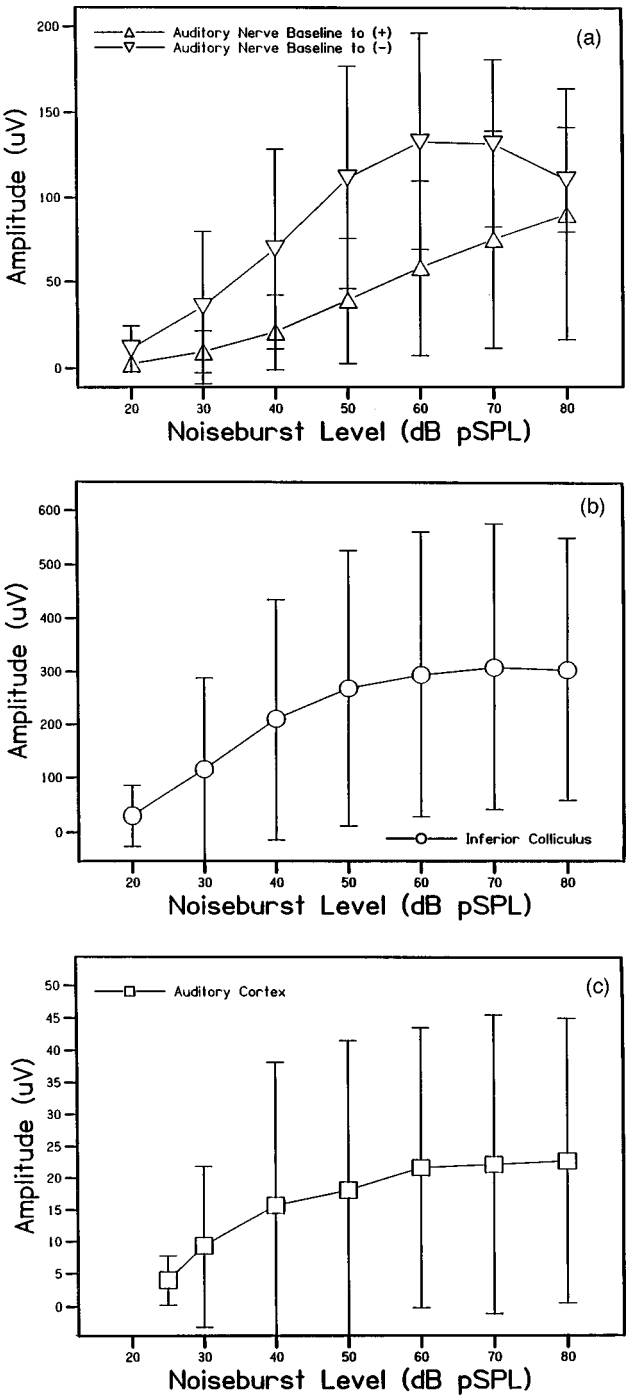

FIG. 4. Mean response amplitudes are plotted across noiseburst level. (a), (b) and (c) show CAP, ICP and ACP data, respectively. The vertical lines represent one standard deviation. Each mean value represents up to 7 (and a minimum of 4) observations.

trough was not present. Thus, there will be no ACP latency or amplitude data shown for the 100 Hz, conventional averaging condition. CAP, ICP and ACP responses were observed in the majority of chinchillas for the MLS procedure at the 500 Hz rate.

Figure 7 plots mean response latency across noiseburst rate. Open symbols show conventional responses, while filled symbols show MLS responses. Note that the latencies of both CAP responses are nearly identical for the conventional and MLS responses at 100 Hz. For the ICP, the latencies are slightly greater for MLS than conventional averaging at 100 Hz. Response latencies generally increase with increasing rate. Figure 8 plots the change in response latency (relative to the latency at the 10 Hz rate) across noiseburst rate. There is only a small CAP P_1 latency shift with rate (<0.1 ms). CAP N_1 showed a somewhat larger mean latency shift with rate than that seen for CAP P_1. The ICP showed a greater latency shift than CAP N_1, and the ACP

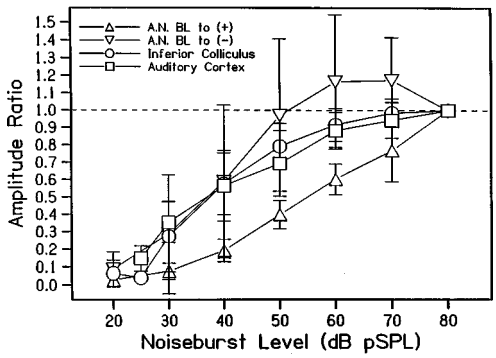

FIG. 5. Mean relative response amplitudes (*re*: amplitude at 80 dB pSPL noiseburst condition) are plotted across noiseburst level. The parameter is response measure. The vertical lines represent one standard deviation. Each mean value represents up to 7 (and a minimum of 4) observations.

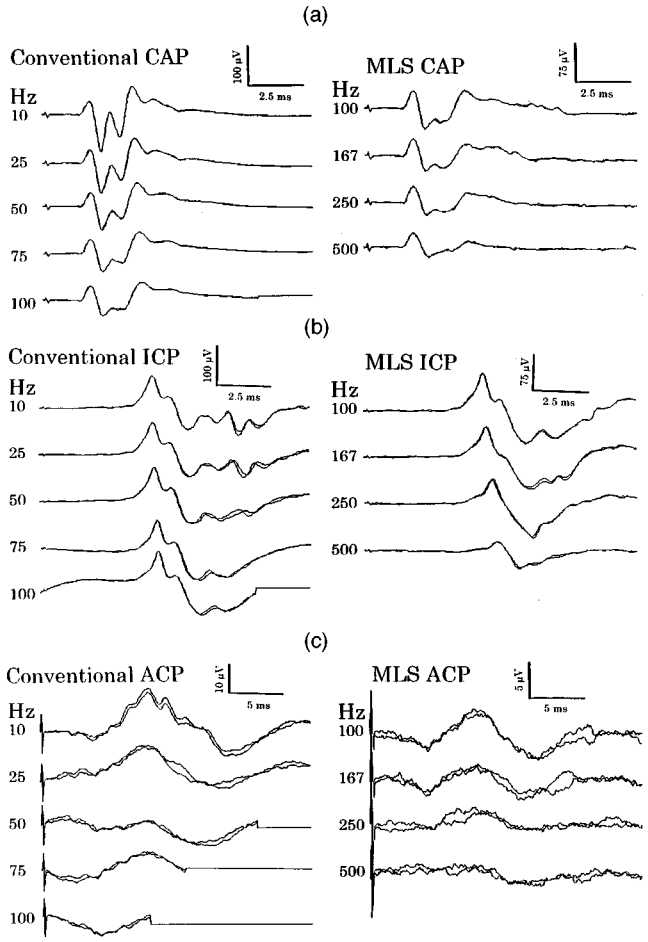

FIG. 6. Responses from one chinchilla for all noiseburst rates are shown. For each condition, two responses are superimposed. The left panel shows conventional responses, while the right panel shows MLS responses. The CAP, ICP and ACP are shown in (a), (b) and (c), respectively. In each figure, positive voltage at the near-field electrode is plotted upward.

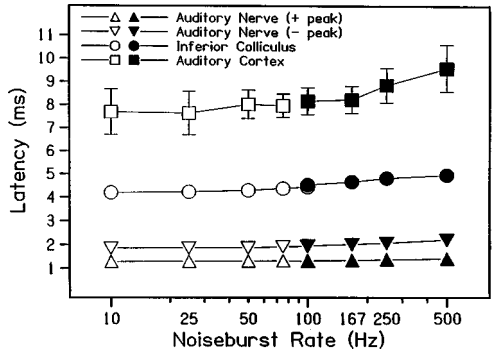

FIG. 7. Mean response latencies are plotted across noiseburst rate. The parameter is response measure. The open symbols show conventional responses, while the filled symbols show MLS responses. The vertical lines represent one standard deviation. Each mean value represents up to 7 (and a minimum of 4) observations.

showed the largest latency shift with increasing rate. Thus, the more rostral the component, the greater the rate-induced latency shift.

Figure 9 plots response amplitudes across noiseburst rate. Figure 9(a), (b) and (c) shows CAP, ICP and ACP data, respectively. For the CAP, P_1 shows little change in amplitude across rate, while N_1 drops substantially in amplitude with increasing rate [Fig. 9(a)]. ICP amplitude appears independent of noiseburst rate for conventional averaging rates from 10 to 100 Hz, but systematically decreases in amplitude as the rate increases from 100 to 500 Hz for the MLS trains [Fig. 9(b)]. The discontinuity in response amplitude at 100 Hz, for the conventional versus MLS procedures, may reflect a strong dependence of ICP amplitude on the minimum time between noisebursts (10 ms for the conventional 100 Hz rate; 5 ms for the MLS at the 100 Hz rate), rather than the average time between noisebursts (10 ms for both conventional and MLS procedures). ACP amplitude decreases with rate, even for the rate increase from 10 to 25 Hz [Fig. 9(c)]. The plateau in the ACP amplitude/rate function at 50 to 75 Hz was, in part, due to the attrition of a low amplitude ACP response from one animal for the 75 Hz condition. The absence of a plotted ACP datum point at 100 Hz for the conventional rate series is due to overlap of sequential cortical responses at this

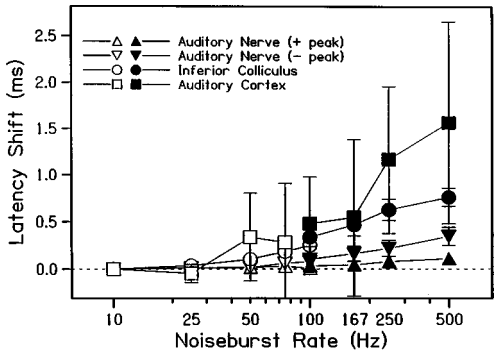

FIG. 8. Mean response latency shifts (*re*: latency at 10 Hz noiseburst condition) are plotted across noiseburst level. The parameter is response measure. The open symbols show conventional responses, while the filled symbols show MLS responses. The vertical lines represent one standard deviation. Each mean value represents up to 7 (and a minimum of 4) observations.

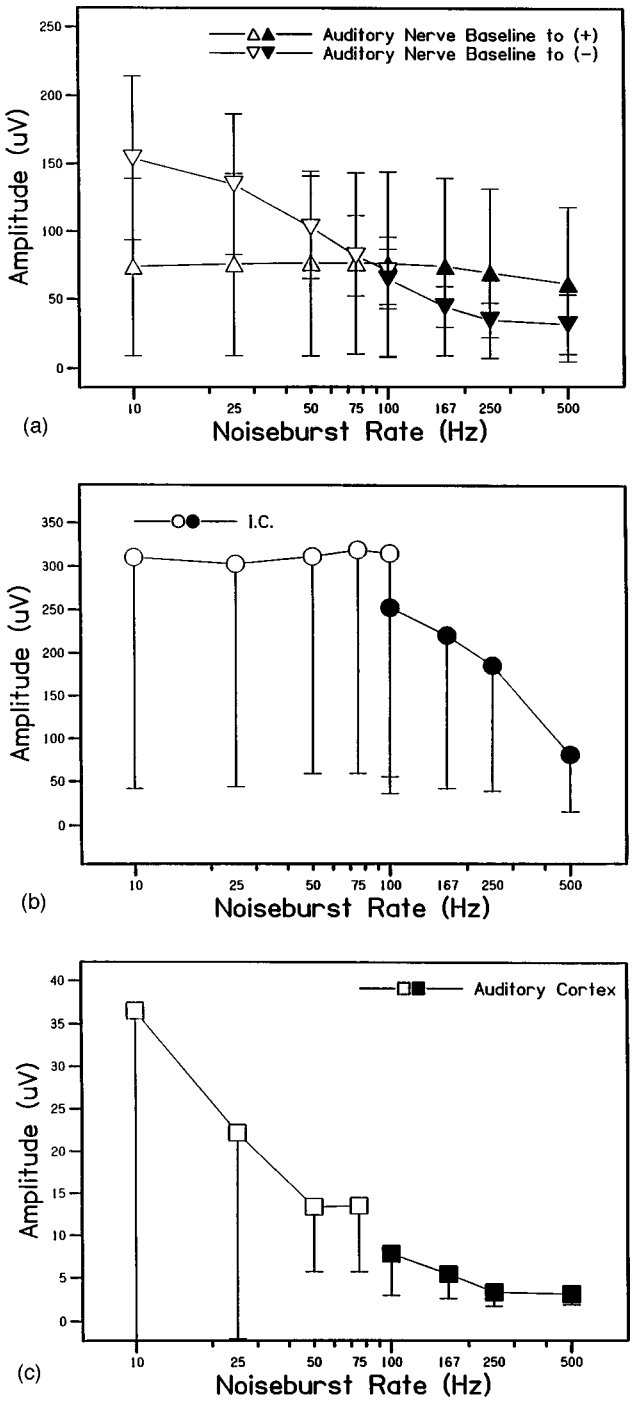

FIG. 9. Mean response amplitudes are plotted across noiseburst rate. The open symbols show conventional responses, while the filled symbols show MLS responses. (a), (b) and (c) show CAP, ICP and ACP data, respectively. The vertical lines represent one standard deviation. Each mean value represents up to 7 (and a minimum of 4) observations.

rapid rate, a problem that is eliminated by the use of the MLS procedure. The relative amplitude change across rate and response measure is better appreciated in Fig. 10, which plots the proportional response amplitude (relative to the amplitude at the 10 Hz rate) across rate. Several points are noteworthy. CAP P_1 amplitude is least affected by increasing rate, followed by the ICP. CAP N_1 and ACP both show a monotonic decrease in amplitude with increasing rate. The normalized ACP amplitude shows a larger decrease than that

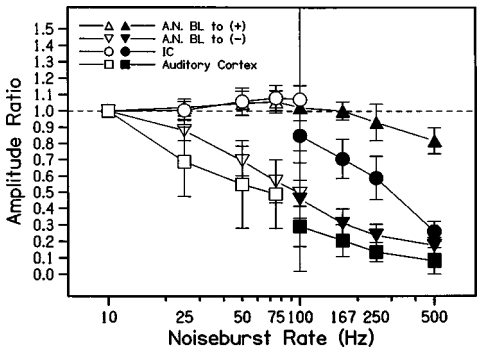

FIG. 10. Mean relative response amplitudes (*re*: amplitude at 10 Hz noiseburst condition) are plotted across noiseburst rate. The parameter is response measure. The open symbols show conventional responses, while the filled symbols show MLS responses. The vertical lines represent one standard deviation. Each mean value represents up to 7 (and a minimum of 4) observations.

of N_1 at all noiseburst rates. Note also that at the 100 Hz rate, the mean MLS response amplitude ratio is less than the conventional response amplitude ratio, for both CAP N_1 and the ICP.

III. DISCUSSION

A. Thresholds

There was little difference in response threshold across electrode site. As there is, to our knowledge, no published data comparing response threshold across electrode site in awake chinchillas, it is not possible to compare our findings with those in the literature. In guinea pig, however, Popelar *et al.* (1994) showed that CAP, ICP and ACP thresholds were very similar to toneburst stimuli. They used one group of animals that were lightly sedated with ketamine/xylazine, and a second group of unanesthetized animals. Noting no differences in responses, Popelar *et al.* (1994) collapsed across groups when showing their threshold data. For auditory evoked potentials (AEPs) in humans, attention, arousal and anesthesia have minimal effects on the CAP or ABR responses, with more substantial influences on the middle latency and long-latency AEPs (Picton and Hillyard, 1974; Kileny and McIntyre, 1985; Hall, 1992). It may be that the similarities in thresholds for the CAP, ICP and ACP are, in part, the result of using unanesthetized chinchillas in the present study, and mildly sedated or unanesthetized guinea pigs in the study of Popelar *et al.* (1994).

B. Noiseburst level

The latencies of the CAP, ICP and ACP decreased with increasing noiseburst level, and response amplitudes increased. This was also reported by Phillips and Burkard (1999) to noisebursts for the chinchilla ICP. ICP latency decrease and amplitude increase has been reported for increasing click level in the unanesthetized chinchilla (Burkard *et al.*, 1997a). For the auditory brainstem response (ABR), there is a decrease in peak latencies and an increase in peak amplitudes with increasing noiseburst level for both humans (Barth and Burkard, 1993) and gerbils (Burkard, 1991).

Latency shifts with increasing noiseburst level varied with electrode site, with the least change for the CAP, intermediate change for the ICP and greatest change for the ACP. Human ABR waves I and V show similar changes in latency with increasing click level (Starr and Achor, 1975; Stockard *et al.*, 1979; Cox, 1985). The various waves of the chinchilla ABR, presumably reflecting activity from the AN through rostral brainstem, show parallel shifts in peak latency with changes in click level (Burkard *et al.*, 1997b; Durand *et al.*, 1997). Thus, the latency shift of the near-field potentials from the AN and IC did not parallel the ABR latency shifts from either humans or chinchillas. In a study comparing the ICP and ABR to click stimuli in unanesthetized chinchillas, Burkard *et al.* (1997b) found a greater shift in ICP latency with changes in click level than were observed for the various ABR peaks. These data suggest that latency shifts recorded from electrodes placed in the near field of a response generator may differ from those recorded in the far field. Alternatively, the primary generators contributing to the ABR peaks reported by Burkard *et al.* (1997b) may emanate from auditory structures caudal to the IC.

C. Noiseburst rate

In the present study, we found an increase in latency and a decrease in amplitude with increasing rate for the various response measures. Similar changes have been reported for the chinchilla ICP with changes in click rate (Burkard *et al.*, 1997a). The later in time (and hence more rostral) the response, the greater the latency shift with increasing rate. For the ABR in humans (Burkard and Hecox, 1987; Eysholdt and Schreiner, 1982), gerbils (Burkard, 1994; Burkard and Voigt, 1989, 1990), cats (Burkard *et al.*, 1996a) and chinchillas (Burkard *et al.*, 1997b; Durand *et al.*, 1997), there is a greater peak latency shift with increasing click rate for the later ABR peaks. In the present study, the ABR results are extended by showing that supra-brainstem structures, in this case the auditory cortex, also show the same trend.

There was great variation in the sensitivity of response amplitude to noiseburst rate of the various response components. CAP P_1 varied little in amplitude across noiseburst rate, decreasing only about 20% when rate was varied from 10 to 500 Hz (see Fig. 10). The ICP changed little in amplitude when noiseburst rate was increased from 10 to 100 Hz, but decreased substantially in amplitude for rate increases from 100 to 500 Hz. Both the CAP N_1 and the ACP showed substantial decreases in amplitude with increasing rate. While the CAP N_1 changed minimally in amplitude for rate changes from 10 to 25 Hz, the ACP dropped in amplitude with increasing rate, even for rate increases from 10 to 25 Hz. A plot of relative amplitude change with increasing rate (Fig. 10) reveals that at all rates, the ACP proportional amplitude is less than the CAP N_1 proportional amplitude. Thus, it appears that the cortical response amplitude is more greatly affected by increasing rate than is the CAP N_1 amplitude. Interestingly, the ICP amplitude is very resistant to stimulus rate. Burkard *et al.* (1997a) reported a small ICP amplitude enhancement (*re*: the amplitude at 10 Hz) for click rates ranging from 25 to 100 Hz, with a decrease in amplitude for click rates ranging from 100 to 1000 Hz using the

MLS procedure. Our findings are almost identical herein. How the ICP resists amplitude decreases with rate, in the presence of a declining CAP N_1 amplitude, is a curiosity. One possible explanation of this phenomenon may be related to the degree of neural synchrony that is required to produce a coherent response at various locations in the auditory nervous system. Davis (1976) discusses the effect of differences in discharge latencies of the single neurons contributing to an ensemble response, such as the CAP. Specifically, random latency differences within units (latency jitter) or systematic differences in response latency (due to, e.g., traveling-wave delays) will lead to reduced peak amplitudes of the ensemble response, and a broadening of the waveform. Davis further states: ''Problems of synchronization are much more serious for the very fast action potentials of axons in EcochG than for the slow dendritic potentials of the vertex potentials'' (Davis, 1976; p. 48). Moller (1994) reported that the near-field response from the human IC consists of a small positive peak followed by a broad, large negative wave, not unlike the ICP in the chinchilla. Moller (1994) suggests that the initial positive deflection probably represents lateral lemniscus activity, while the broad negative wave is probably dendritic activity from the IC. Perhaps the difference in susceptibility to rate-induced amplitude decrements of N_1 of the CAP and ICP is because the former response is primarily the result of action potentials, while the latter is largely the result of graded dendritic potentials.

Only a few studies have investigated cortical responses to stimuli at presentation rates above 100 Hz. This is because if one is using conventional averaging, when interstimulus intervals are less that the duration of the response, sequential responses overlap making response interpretation problematic. As seen in Fig. 6(c), for conventional averaging, one cannot observe the ACP response at the 100 Hz rate because the response is delayed beyond the time at which the next noiseburst is presented. In contrast, the 100 Hz MLS response is easily visualized due to the response recovery procedure utilized. Thus, the MLS procedure makes it feasible to evaluate rate effects over a greater range than is possible using conventional averaging. In a study looking at middle latency and long latency AEPs in human subjects, Picton *et al.* (1992) reported clearly recognizable middle latency AEPs for interstimulus intervals (ISIs) down to 10 ms, while long latency AEPs could only be observed for ISIs of several hundred ms. In the present study, we observed the CAP, ICP and ACP in most animals at an MPI of 1 ms, corresponding to an average stimulation rate of 500 Hz.

The presence of CAP responses at very high stimulation rates has been reported previously. For example, Peake *et al.* (1962) showed that CAPs were present to 1 ms noisebursts for the highest rates tested (up to 800 Hz), with responses present above 1000 Hz for 0.1 ms noisebursts. Kiang *et al.* (1965) reported that time-locked activity from single eighth-nerve fibers occurred at click rates up to 1000 Hz. Although auditory nerve single-unit responses have not been investigated to MLS trains, Burkard and Palmer (1996) investigated responses from chopper units in the ventral cochlear nucleus of the urethane-anesthetized guinea pig to conventional and MLS click trains. Synchronized activity to conventional and MLS click trains was observed in a subset of chopper units for click trains with average rates of 500 Hz or above. We are unaware of studies that have systematically investigated responses of IC neurons to clicks varying over a wide range of repetition rates. However, some single- and multi-unit recordings from the IC of barbiturate-anesthetized cats show activity synchronized to the envelope of amplitude-modulated (AM) tones at modulation frequencies at and above 500 Hz (Langner and Schreiner, 1988). Indeed, the peak synchronization of several IC units studied by Langner and Schreiner (1988) occurred at frequencies above 500 Hz.

Ribaupierre *et al.* (1972) investigated responses from single units in the unanesthetized cat auditory cortex to trains of clicks. The highest rate at which each unit time-locked to the click train was reported. In most units, the highest time-locking click rate occurred at between 50 and 100 Hz, but a subset of units showed time-locked responses at rates at and above 200 Hz, with one unit time-locking its response to click rates up to 1000 Hz. Schreiner and Raggio (1996) investigated responses from the primary auditory cortex of barbiturate-anesthetized cat to electrical pulses and acoustical click stimuli. For each unit, the highest click rate that elicited a synchronized response was determined. Across units, the mean of this highest acoustic click rate was roughly 10 Hz, with a standard deviation of 6.42 Hz. Similarly, Eggermont (1994) studied responses from single units from the auditory cortex of the barbiturate-anesthetized cat. He found that AM noisebursts and click trains produced band-pass modulation rate transfer functions, with peaks in the 8–10 Hz range, while amplitude or frequency modulated tones produces low-pass modulation rate transfer functions, with best modulation frequencies near 4 Hz. The values of these highest driven rates reported by Eggermont (1994) and Schreiner and Raggio (1996) are substantially below those reported by Ribaupierre *et al.* (1972). These studies differed in the use of anesthesia, with Ribaupierre *et al.* (1972) using a muscle relaxant, and Eggermont (1994) and Schreiner and Raggio (1996) using barbiturate anesthesia. Goldstein *et al.* (1959) investigated near-field responses from the auditory cortex of the cat to click stimuli. They found that the maximum click rate at which cortical responses cortical were observed decreased from approximately 200 Hz click rates in the unanesthetized cat to approximately 100 Hz in the anesthetized (Dial or Nembutal) preparation. In a recent study, Steinschneider *et al.* (1998) recorded multiunit activity and current source density patterns from primary auditory cortex of awake monkeys to click trains. They reported an upper limit of ensemble phase locking of roughly 400 Hz, values close to our 500 Hz responses observed in the present investigation in the unanesthetized chinchilla. Although the present study does not directly address the great variability in the upper limits of time-locked activity from the auditory cortex, it is yet another study showing time-locked activity in an unanesthetized preparation at rates well above 100 Hz.

D. The CAP P_1 wave

The CAP P_1 wave changes little in amplitude with increasing rate [see Figs. 9(a) and 10]. In this regard, it be-

haves like the summating potential (Eggermont, 1976). However, the summating potential is generated by the hair cells, and is thus pre-neural (Dallos, 1973). If pre-neural, CAP P_1 latency should not vary with noiseburst level or rate (Davis, 1976). This is clearly not the case. As shown in Figs. 2 and 3, there is an increase in CAP P_1 latency with decreasing noiseburst level. Although small in magnitude, there is also an increase in CAP P_1 latency with increasing rate (see Figs. 7 and 8). Our data indicate that this potential behaves like the summating potential in terms of its resistance to amplitude changes with rate, but it acts like a neural generator in terms of its latency shift across noiseburst level and rate.

ACKNOWLEDGMENTS

We would like to thank John Durrant for his comments regarding the summating potential. This work was supported by NIH-NIDCD DC03600 and The Center for Hearing and Deafness.

Barth, C., and Burkard, R. (**1993**). ''The effects of noiseburst risetime and level on the human BAER,'' Audiology **32**, 225–233.

Burkard, R. (**1991**). ''The effects of noiseburst risetime and level on the gerbil brainstem auditory evoked response,'' Audiology **30**, 47–58.

Burkard, R. (**1994**). ''Gerbil brainstem auditory evoked responses (BAERs) to maximum length sequences,'' J. Acoust. Soc. Am. **95**, 2126–2135.

Burkard, R., and Hecox, K. (**1983**). ''The effect of broadband noise on the human brainstem auditory evoked response. I. Rate and intensity effects,'' J. Acoust. Soc. Am. **74**, 1204–1213.

Burkard, R., and Hecox, K. (**1987**). ''The effect of broadband noise on the human brainstem auditory evoked response. III. Anatomic locus,'' J. Acoust. Soc. Am. **81**, 1050–1063.

Burkard, R., and Palmer, A. (**1996**). ''Responses of chopper units in the ventral cochlear nucleus of the anesthetized guinea pig to clicks-in-noise and click trains,'' Hearing Res. **110**, 234–250.

Burkard, R., McGee, J., and Walsh, E. (**1996a**). ''The effects of stimulus rate on the feline BAER during development. I. Peak latencies,'' J. Acoust. Soc. Am. **100**, 978–990.

Burkard, R., McGee, J., and Walsh, E. (**1996b**). ''The effects of stimulus rate on the feline BAER during development. II. Peak amplitudes,'' J. Acoust. Soc. Am. **100**, 991–1002.

Burkard R., Secor, C., and McFadden, S. (**1997b**). ''A comparison of the near-field response from the inferior colliculus and the auditory brainstem response in the chinchilla,'' presented at the 1997 midwinter meeting of the Association for Research in Otolaryngology, St. Petersburg Beach, FL.

Burkard, R., Shi, Y., and Hecox, K. (**1990**). ''A comparison of maximum length and Legendre sequences to derive BAERs at rapid rates of stimulation,'' J. Acoust. Soc. Am. **87**, 1656–1664.

Burkard, R., Trautwein, P., and Salvi, R. (**1997a**). ''The effects of click level, click rate, and level of background masking noise on the inferior colliculus potential (ICP) in the normal and carboplatin-treated chinchilla,'' J. Acoust. Soc. Am. **102**, 3620–3627.

Burkard, R., and Voigt, H. (**1989**). ''Stimulus dependencies of the gerbil brainstem auditory evoked response (BAER). I. Effects of click level, rate and polarity,'' J. Acoust. Soc. Am. **85**, 2514–2525.

Burkard, R., and Voigt, H. (**1990**). ''Stimulus dependencies of the gerbil brainstem auditory evoked response. III. Additivity of click level and rate with noise level,'' J. Acoust. Soc. Am. **88**, 2222–2234.

Cox, L. C. (**1985**). ''Infant assessment: Development and age-related considerations,'' in *The Auditory Brainstem Response*, edited by J. Jacobson (College-Hill, San Diego), pp. 297–316.

Dallos, P. (**1973**). *The Auditory Periphery. Biophysics and Physiology* (Academic, New York).

Davis, H. (**1976**). ''Principles of electric response audiometry,'' Ann. Otol. Rhinol. Laryngol. **85**, 1–96.

Durand, B., Secor, C., Trautwein, P., and Burkard, R. (**1997**). ''Normative studies of the chinchilla ABR: Effects of click level and rate,'' presented at the 1997 midwinter meeting of the Association for Research in Otolaryngology, St. Petersburg Beach, FL.

Eggermont, J. (**1976**). ''Summating potentials in electrocochleography: Relation to hearing disorders,'' in *Electrocochleography*, edited by R. Ruben, C. Elberling, and G. Salomon (University Park Press, Baltimore), pp. 67–87.

Eysholdt, V., and Schreiner, C. (**1982**). ''Maximum length sequences. A fast method for measuring brainstem-evoked responses,'' Audiology **21**, 242–250.

Gerken, G., Simhadri-Sumithra, R., and Bhat, K. (**1986**). ''Increase in central auditory responsiveness during continuous tone stimulation or following hearing loss,'' in *Basic and Applied Aspects of Noise-Induced Hearing Loss*, edited by R. Salvi, D. Henderson, R. Hamernik, and V. Colletti (Plenum, New York), pp. 195–209.

Goldstein, M., Kiang, N., and Brown, R. (**1959**). ''Responses of the auditory cortex to repetitive acoustic stimuli,'' J. Acoust. Soc. Am. **31**, 356–354.

Hall, J. (**1992**). *Handbook of Auditory Evoked Responses* (Allyn and Bacon, Boston).

Kiang, N. (**1965**). *Discharge Patterns of Single Fibers in the Cat's Auditory Nerve*, Research Monograph No. 35 (MIT Press, Cambridge).

Kileny, P., and McIntyre, J. (**1985**). ''The ABR in intraoperative monitoring,'' in *The Auditory Brainstem Response*, edited by J. Jacobson (College-Hill, San Diego), pp. 237–251.

Langner, G., and Schreiner, C. (**1988**). ''Periodicity coding in the inferior colliculus of the cat. I. Neuronal mechanisms,'' J. Neurophysiol. **60**, 1799–1822.

Moller, A. (**1994**). ''Neural generators of auditory evoked potentials,'' in *The Auditory Brainstem Response*, edited by J. Jacobson (College-Hill, San Diego), pp. 23–46.

Peake, W., Kiang, N., and Goldstein, M. (**1962**). ''Rate functions for auditory nerve responses to bursts of noise: Effect of changes in stimulus parameters,'' J. Acoust. Soc. Am. **34**, 571–575.

Phillips, D., and Burkard, R. (**1999**). ''Timing of auditory response initiation in the inferior colliculus of the awake chinchilla,'' J. Acoust. Soc. Am. **105**, 2731–2737.

Picton, T., Champagne, S., and Kellett, A. (**1992**). ''Human auditory evoked potentials recorded using maximum length sequences,'' Electroencephalogr. Clin. Neurophysiol. **84**, 90–100.

Picton, T., and Hillyard, S. (**1974**). ''Human auditory evoked potentials. II: Effects of attention,'' Electroencephalogr. Clin. Neurophysiol. **36**, 191–199.

Picton, T., Hillyard, S., Krausz, H., and Galambos, R. (**1974**). ''Human auditory evoked potentials. I: Evaluation of components,'' Electroencephalogr. Clin. Neurophysiol. **36**, 179–190.

Popelar, J., Syka, J., and Berndt, H. (**1987**). ''Effect of noise on auditory evoked responses in awake guinea pigs,'' Hearing Res. **26**, 239–247.

Popelar, J., Erre, J., Aran, J., and Cazals, Y. (**1994**). ''Plastic changes in ipsi-contralateral differences of auditory cortex and inferior colliculus evoked potentials after injury to one ear in the adult guinea pig,'' Hearing Res. **72**, 125–134.

Ribaupierre, F., Goldstein, M., and Yeni-Komshian, G. (**1972**). ''Cortical coding of repetitive acoustic pulses,'' Brain Res. **48**, 205–225.

Salvi, R., Saunders, S., Gratton, M., Arehole, S., and Powers, N. (**1990**). ''Enhanced evoked responses amplitudes in the inferior colliculus of the chinchilla following acoustic trauma,'' Hearing Res. **50**, 245–258.

Schreiner, C., and Raggio, M. (**1996**). ''Neuronal responses in cat primary auditory cortex to electrical cochlear stimulation. II. Repetition rate coding,'' J. Neurophysiol. **75**, 1283–1300.

Snyder, D., and Salvi, R. (**1994**). ''A novel chinchilla restraint device,'' Lab Animal **23**, 42–44.

Starr, A., and Achor, J. (**1975**). ''Auditory brain stem responses in neurological disease,'' Arch. Neurol. **32**, 781–788.

Steinschneider, M., Reser, D., Fishman, Y., Schroeder, C., and Arezzo, J. (**1998**). ''Click train encoding in primary auditory cortex of the awake monkey: Evidence for two mechanisms subserving pitch perception,'' J. Acoust. Soc. Am. **104**, 2935–2955.

Stockard, J., Stockard, J., Westmoreland, B., and Corfits, J. (**1979**). ''Brainstem auditory evoked responses: normal variation as a function of stimulus and subject characteristics,'' Arch. Neurol. **36**, 823–831.

Syka, J., Rybalko, N., and Popelar, J. (**1994**). ''Enhancement of the auditory cortex evoked responses in awake guinea pigs after noise exposure,'' Hearing Res. **78**, 158–168.

Detection of time- and bandlimited increments and decrements in a random-level noise

Michael G. Heinz
Speech and Hearing Sciences Program, Division of Health Sciences and Technology, Massachusetts Institute of Technology, Cambridge, Massachusetts 02139 and Hearing Research Center,[a] Biomedical Engineering Department, Boston University, Boston, Massachusetts 02215

C. Formby
Division of Otolaryngology-HNS, Department of Surgery, University of Maryland School of Medicine, 16 South Eutaw Street-Suite 500, Baltimore, Maryland 21201

(Received 28 August 1998; revised 11 January 1999; accepted 12 April 1999)

The purpose of this study was to compare detection of increments and decrements occurring over limited regions of time and frequency within a 500-ms broadband (0–6000 Hz) noise. Three listeners tracked detection thresholds adaptively in a two-interval, two-alternative forced-choice task. Thresholds were measured for both increments and decrements in level [$\Delta L = 10\log_{10}(1 + \Delta N_0/N_0)$ dB, where N_0 is the spectral power density of the noise] as a function of signal duration ($T = 30-500$ ms) for a range of signal bandwidths ($W = 62-6000$ Hz) that were logarithmically centered around 2500 Hz. Listeners were forced to rely on temporal- and spectral-profile cues for detection due to randomization of overall presentation level from interval to interval, which rendered overall energy an inconsistent cue. Increments were detectable for all combinations of W and T, whereas decrements were not consistently detectable for $W < 500$ Hz. Narrow-band decrements were not detectable due to spread of excitation from the spectral edges of the noise into the decrements. Increment and decrement thresholds were similar for $W \geqslant 1000$ Hz. Temporal- and spectral-integration effects were observed for both increments and decrements. The exceptions were for random-level conditions in which the signal matched the bandwidth or duration of the standard. A multicue decision process is described qualitatively to explain how the combination of temporal- and spectral-profile cues can produce temporal- and spectral-integration effects in the absence of overall-energy cues. © *1999 Acoustical Society of America.* [S0001-4966(99)06107-X]

PACS numbers: 43.66.Ba, 43.66.Dc, 43.66.Fe, 43.66.Mk [RVS]

INTRODUCTION

Speech signals contain a continually changing combination of spectral and temporal cues that form the basis for a listener's perception. While many important temporal and spectral cues have been identified, a thorough understanding of how these cues are detected and combined by the listener is lacking. The goal of this research is to understand how temporal- and spectral-profile cues are individually detected, and how these cues are combined by listeners to perform detection. Temporal- and spectral-profile cues arise when there is a change in level across time or frequency, respectively. Green and his colleagues (e.g., Green *et al.*, 1983; Green, 1988) have extensively studied the ability of listeners to perform intensity discrimination by making simultaneous comparisons of level in different frequency regions of a stimulus, i.e., (spectral) profile analysis. The majority of these studies has used a nonharmonic tone complex, in which the signal increases the level of one of the tones above that of the reference tones, thus producing a change in the spectral profile. Gilkey (1987) has shown that listeners can use within-interval comparisons across time as well as within-interval comparisons across frequency (spectral-profile analysis) to enhance the detection of a brief tonal signal in a noise masker.

Formby *et al.* (1994) measured masked-detection thresholds for a range of noise-burst signals with bandwidths and durations approximating those found in speech. Detection thresholds were measured both in a fixed- and random-level uncorrelated broadband noise masker as a function of signal bandwidth and duration. The results were described in terms of three cues that listeners used for detection of the time- and bandlimited signals: (1) a traditional energy cue arising from the difference in energy between the signal-plus-standard interval and the standard-alone interval; (2) a spectral-profile cue arising from the relative level difference between the signal frequency region and the spectral fringe of the standard within the signal-plus-standard interval; and (3) a relative timing cue introduced by the gating of a brief signal on and off within the longer standard. In this paper, we will refer to these three cues as *overall-energy*, *spectral-profile*, and *temporal-profile cues*, respectively.

The experimental design used by Formby *et al.* (1994) allowed for the systematic study of each of the three cues in a masked-detection task. They were able to isolate and study the spectral-profile cue in random-level conditions when the duration of the signal and masker were matched. These con-

[a]Address and author to whom correspondence should be addressed. Electronic mail: mgheinz@mit.edu

ditions are similar to the majority of the (spectral) profile analysis experiments described by Green (1988) and subsequently by other investigators (e.g., Kidd *et al.*, 1989; Ellermeier, 1996). Likewise, the temporal-profile cue was the only cue available in random-level conditions when the signal and masker were matched spectrally. Many experiments have examined intensity discrimination of noise under similar conditions (i.e., with a temporal-profile cue and no spectral-profile cue); however, the majority of these studies has used a continuous masker without overall-level randomization (e.g., Green, 1960; Campbell, 1963; Raab *et al.*, 1963; Schacknow and Raab, 1976; Penner, 1978). Formby *et al.* (1994) established the temporal-profile cue to be an independent and salient cue that was as prominent as either the spectral-profile cue or the overall-energy cue in the detection process. The overall-energy cue was the lone cue for fixed-level conditions when the signal and masker were matched both temporally and spectrally. This condition can be considered an intensity-discrimination task performed with a gated broadband noise signal and pedestal, similar to experiments reported by Raab and Goldberg (1975), Schacknow and Raab (1976), Houtsma *et al.* (1980), and Buus (1990).

In this paper, we extend the experimental design used by Formby *et al.* (1994) to the measurement of detection thresholds for a range of time- and bandlimited increment and decrement signals in a broadband noise. The noise signals were correlated with a time- and bandlimited portion of the gated broadband noise. This method of stimulus generation had the primary advantage over uncorrelated signal and masker conditions that the increment signals were directly comparable to corresponding decrement signals. The experiments in the current study are reminiscent of experiment I reported by Moore *et al.* (1989), who measured and compared the detectability of spectral peaks and notches in a broadband noise as a function of peak- or notch-bandwidth. However, the peaks and notches in their stimuli were always matched in duration to the gated standard, and thus did not contain any temporal-profile cues, which were investigated in this study.

I. METHOD

A. Subjects

Three subjects, author CF (age 43), SF (age 27), and JZ (age 23) participated as listeners. Each had audiometrically normal hearing sensitivity. Subjects CF and SF had previous experience as listeners in laboratory studies, whereas JZ had not previously participated in any perceptual studies. Each subject received about 2 h of practice on a representative sample of the stimulus conditions prior to the start of formal data collection.

B. Procedure

The psychoacoustic experiments were implemented using an existing paradigm from the Tucker-Davis Technology (TDT) XPERIMENTER software package that was modified to incorporate our method of generating the increment and decrement stimuli. The subject's task on each two-interval, two-alternative forced-choice (2I, 2AFC) trial was to respond by computer keyboard to the observation interval that he or she believed contained the signal stimulus. The alternative observation interval contained the standard stimulus. The signal stimulus was presented with equal *a priori* probability in the two observation intervals of a given trial. Each 500-ms observation interval was visually displayed on the computer monitor. Visual feedback of the correct interval was provided after the subject entered a response for each trial.

The increment or decrement in level ($\Delta L = 10\log_{10}(1 + \Delta N_0/N_0)$ dB, where N_0 is the spectral power density of the noise), was tracked adaptively across a block of 50 trials to obtain a 70.7%-correct detection threshold (Levitt, 1971). The adaptive algorithm decreased the value of ΔL after two consecutive correct responses, and increased the value of ΔL after one incorrect response. The value of ΔL was decreased or increased by a factor of 1.7783 until three response reversals occurred. Thereafter, ΔL was increased or decreased by a factor of 1.2589. Adjustment of ΔL (in dB) by a constant factor can be expected to correspond to equal-ratio steps of d', because it is reasonable to assume that d' is proportional to ΔL (e.g., Durlach *et al.*, 1986; Green, 1988). Equal-ratio steps of d' are consistent with adjustment of signal level in equal-dB steps for a tone-in-noise detection task in which d' is proportional to signal intensity. Each threshold estimate from a 50-trial block corresponded to the geometric mean of ΔL at the last even number of small-step reversals (typically, 12–16 reversals per 50-trial block).

Each listener provided at least three threshold estimates for each of the stimulus conditions measured. In some cases (mostly decrement conditions), additional thresholds were measured until three consistent estimates of ΔL (within 5 dB of one another) were obtained, in which case the three closest measurements were used. Geometric means of ΔL in dB and associated standard errors (calculated on the logarithms of the ΔLs) were calculated for each listener from the three consistent threshold estimates. On average, the three threshold estimates from each listener had standard errors that were within 18% of the geometric mean. Extra measurements were primarily collected only when ΔL was large due to the constant relative standard error and the 5-dB criterion that was used.

C. Stimuli

An idealized spectrogram representation of the signal and standard intervals is shown in Fig. 1 for an increment condition. The standard stimulus consisted of a broadband noise with bandwidth $W_{ST}=6000$ Hz and total duration $T_{ST}=500$ ms (including rise/fall times). The noise was gated on and off with 16.9-ms raised-cosine rise/fall times. The signal stimulus contained a time- and bandlimited region that was incremented within the broadband noise. The incremented region had a bandwidth W that was logarithmically centered around 2500 Hz for $W \leqslant 4000$ Hz. The conditions with $W=6000$ Hz, i.e., $W=W_{ST}$, corresponded to incrementing all frequency components within the broadband noise. The incremented region was always centered temporally within the 500-ms noise and had a total duration T. Linear rise/fall times of 10 ms were applied to the onset and offset of the incremented region. The spectrum level within

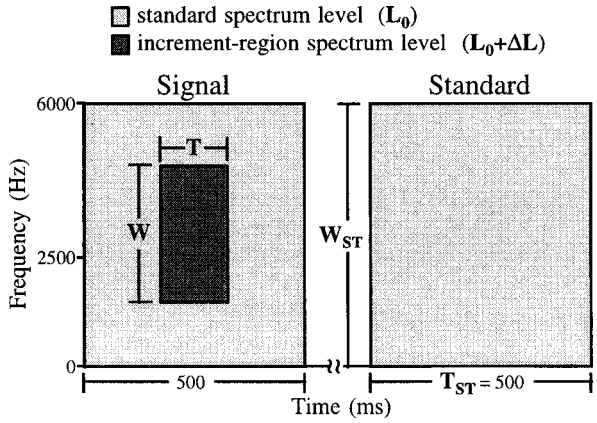

FIG. 1. Idealized spectrogram representation for an increment-detection trial. The signal stimulus is shown in the first interval and the standard stimulus is shown in the second interval. The legend denotes the spectrum levels for the standard (L_0) and the incremented region ($L_0+\Delta L$). Increment bandwidth (W) and duration (T) are shown in interval one. The bandwidth (W_{ST}) and duration (T_{ST}) of the standard are shown in interval two. Decrement conditions were identical, except the spectrum level of the time- and bandlimited signal region was $L_0-\Delta L$.

the incremented region was $L_0+\Delta L$ (or $L_0-\Delta L$ for decrement conditions), where L_0 is the spectrum level of the standard noise in dB SPL.

Both increment and decrement thresholds were measured as a function of signal duration ($T=30$, 40, 60, 80, 160, 320, and 500 ms) for a wide range of signal bandwidths ($W=62$, 125, 250, 500, 1000, 2000, 4000, and 6000 Hz). The presentation levels of the signal interval and the standard interval were varied randomly, uniformly, and independently over a 20-dB range ($L_0=20-40$ dB SPL) from interval to interval of each trial. The purpose of randomizing the levels was to prevent or discourage the listeners from relying on the across-interval overall-energy cue (see Green, 1988). Formby *et al.* (1994) reported for their uncorrelated noise-in-noise stimuli that masked-detection thresholds were unaffected by randomizing overall level for all conditions, except those in which the signal bandwidth matched the masker bandwidth and the signal duration approached the masker duration. We therefore also measured fixed-level ($L_0=40$ dB SPL) detection thresholds for increments with $W=4000$ and 6000 Hz and decrements with $W=6000$ Hz.

D. Stimulus generation and apparatus

All stimuli described in this report were produced with TDT hardware. Each stimulus was generated digitally by programming an array processor (TDT, model AP2). For an increment (as shown in Fig. 1) or decrement stimulus, two separate temporal waveforms were initially generated, one to produce the temporal-fringe regions (i.e., pre- and postsignal regions with flat spectrum) and one to produce the signal region. Both waveforms were generated by specifying the magnitude and phase spectrum of the associated regions, and then implementing an inverse fast Fourier transform (IFFT) procedure with a frequency binwidth of 9.765 Hz (40-kHz sampling rate and 4096-point FFT). The temporal-fringe spectrum was generated by specifying flat magnitude and random phase within the 6000-Hz passband. Magnitude and phase were set to zero outside the passband. The magnitude spectrum of the signal-region waveform was identical to that of the temporal-fringe waveform, except that components within the frequency region of the signal (bandwidth W) were specified at a level ΔL dB above (for increments) or below (for decrements) the fringe level. The two waveforms used to generate the temporal fringe and the signal region had identical, randomly chosen phase spectra. This strategy was necessary to avoid phase discontinuities when the two waveforms were combined later in the procedure. The IFFT procedure produced two 102.4-ms waveforms that were repeated in time to produce a 500-ms duration for both the temporal-fringe and signal-region waveforms. Each waveform was windowed appropriately to produce the desired linear 10-ms rise/fall transitions for the signal region. The two waveforms were added to produce the stimulus for the signal interval shown in Fig. 1. The discrete-time stimulus was windowed on and off with 16.9-ms raised-cosine rise/fall transitions. This procedure generated a noise stimulus in which each spectral component had constant phase across the three temporal regions of the signal stimulus. The standard stimulus was produced in an identical manner with ΔL set to 0 dB, and with a different random-phase spectrum. The resulting bandlimited stimuli had spectral parameters (e.g., center frequency and bandwidth) that were within 4.883 Hz of the nominal values. Stimuli were played out through a digital-to-analog converter (DAC) (TDT, model DA1) with 16-bit precision and a sampling period of 25 μs. The DAC output was low-pass filtered (TDT, model FT5) below 7500 Hz to prevent aliasing, then attenuated (TDT, model PA4), and delivered monaurally through an earphone (Telephonics, model TDH-39) to the listener who was seated in a double-walled sound-attenuating room. The overall-level randomization was accomplished by varying the analog attenuation randomly prior to delivery of the stimulus to the headphones.

II. RESULTS AND DISCUSSION

A. Detection as a function of duration

Group geometric means and standard deviations were calculated from the mean estimates of ΔL in dB for each of the three listeners. The group means and across-listener standard deviations (bars) for both increments and decrements are plotted on a logarithmic scale[1] in Fig. 2 as a function of increment or decrement duration. Increment thresholds are represented by filled symbols, and decrement thresholds by open symbols. Each panel represents a different bandwidth condition. Random-level conditions for $W=62$ to 6000 Hz are shown in the top eight panels. Fixed-level conditions for $W=4000$ and 6000 Hz are shown in the bottom two panels.

1. Increments

The detection trends for increment conditions were similar across the three listeners, and the group mean results are representative of the individual data. Increments were detectable for all combinations of bandwidth and duration. The largest group threshold value was about 13 dB for the combination of the smallest increment parameters (i.e., $W=62$ Hz and $T=30$ ms). Increment-detection thresholds for

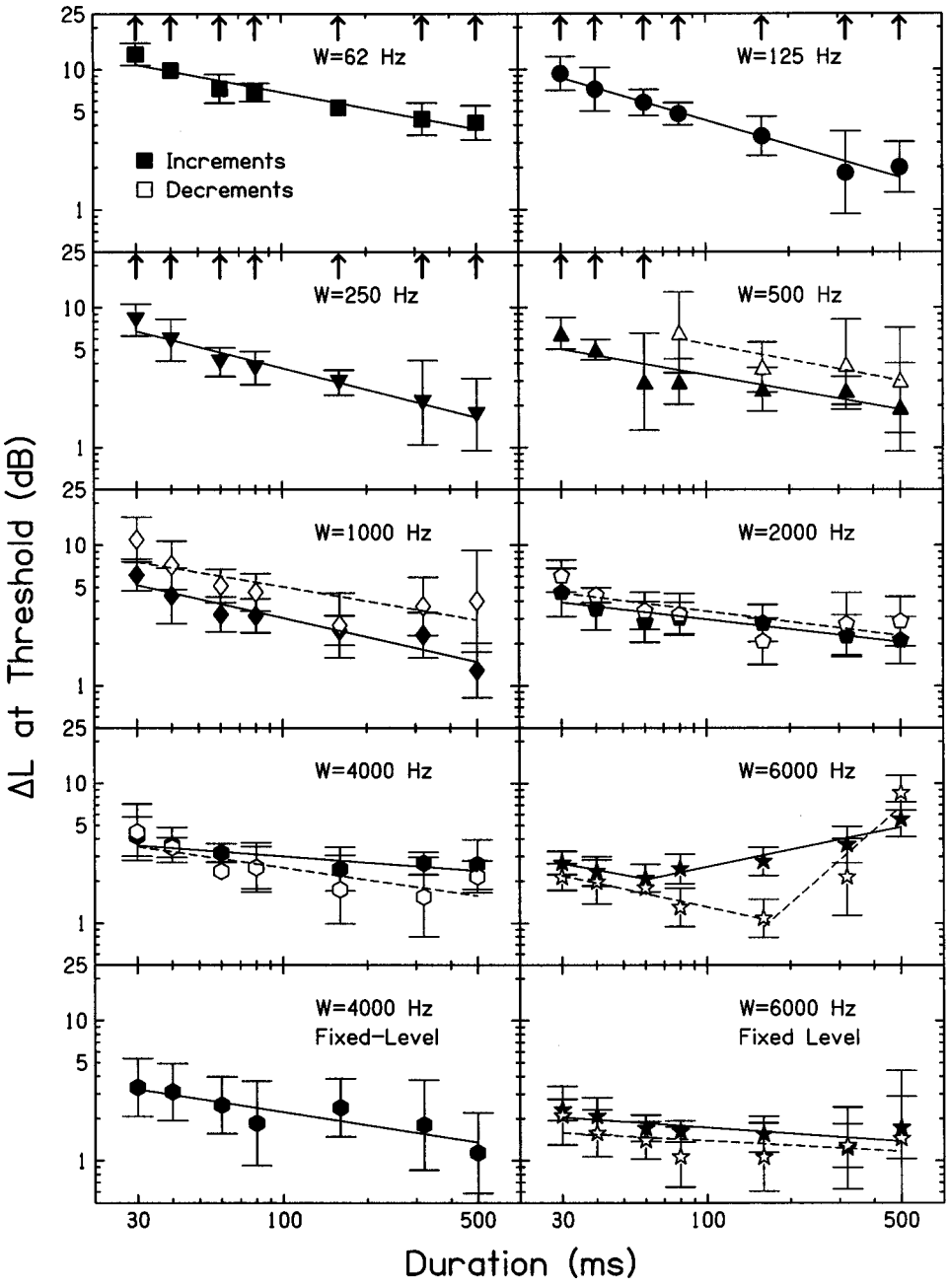

FIG. 2. Increment- (filled symbols) and decrement- (open symbols) detection thresholds are shown as a function of increment or decrement duration. Geometric means of ΔL in dB are plotted on a logarithmic scale with associated standard deviation bars. Each panel corresponds to a different bandwidth. The top eight panels represent random-level conditions, and the bottom two panels show the data for fixed-level conditions for broad bandwidths. Upward arrows indicate decrements that were not consistently detectable by all three listeners. Solid and dashed lines represent least-square fits to the increment- and decrement-detection thresholds, respectively.

$W \leqslant 4000$ Hz declined systematically as a function of increasing duration. The increment-detection thresholds therefore demonstrated a temporal-integration effect. The relation between ΔL and duration on a log–log scale can be described well as a straight line, as has been reported previously for level discrimination of tones as a function of duration (Florentine, 1986). The solid lines in Fig. 2 represent least-square fits to the increment-detection thresholds for $T = 30$ to 500 ms (two-line fits were used for the random-level $W = 6000$ Hz condition as discussed below). Table I summarizes the temporal-integration effect in terms of the slopes (with associated standard errors) and correlation coefficients of the fitted lines. The temporal-integration slopes systematically became shallower (from -0.58 to -0.15)[2] as bandwidth was increased from 125 to 4000 Hz, with the exception of $W = 1000$ Hz. The slope for $W = 62$ Hz was -0.38, and did not fit with the general trend in the present study; however, this slope is consistent with slopes reported by Florentine (1986) that ranged from -0.2 to -0.35 for level discrimination of tones. Temporal-integration slopes resulting from a signal-energy analysis (i.e., $10 \log_{10}(\Delta N_0 / N_0)$ as a function of $10 \log_{10}(T)$) decreased from -0.93 (0.09) for $W = 125$ Hz to -0.21 (0.08) for $W = 4000$ Hz, where the standard errors of the slopes are in parentheses. The general finding of shallower slopes for larger bandwidths is consistent with the results of Formby *et al.* (1994), who reported that temporal-integration time constants decreased with increasing bandwidth for time- and bandlimited noise signals in an uncorrelated noise masker. Scholl (1962) and van den Brink and Houtgast (1990b) found similar results for noise and deterministic signals, respectively. They found that efficient temporal integration was only possible for narrow-band signals, and inefficient temporal integration resulted for broadband stimuli.

TABLE I. Temporal-integration slopes and correlation coefficients r for the fitted lines shown in Fig. 2 for both increment and decrement detection. The values in parentheses are standard errors of the slopes. All bandwidth (W) conditions correspond to random-level presentation, except for the two fixed-level conditions indicated by FL. Decrement bandwidths for which detection thresholds could not be measured are indicated by CNM. Decrement-detection thresholds were not measured (NM) for the $W = 4000$ Hz, fixed-level condition.

	Increments		Decrements	
W (Hz)	Slope	r	Slope	r
62	−0.38 (0.05)	0.96	CNM	CNM
125	−0.58 (0.04)	0.99	CNM	CNM
250	−0.51 (0.05)	0.96	CNM	CNM
500	−0.35 (0.08)	0.88	−0.37 (0.13)	0.91
1000	−0.45 (0.06)	0.95	−0.34 (0.12)	0.83
2000	−0.23 (0.04)	0.91	−0.25 (0.10)	0.81
4000	−0.15 (0.06)	0.80	−0.29 (0.09)	0.86
4000 (FL)	−0.31 (0.07)	0.90	NM	NM
6000	−0.36 (0.06)	0.99	−0.43 (0.06)	0.97
	0.41 (0.07)	0.96	1.74 (0.57)	0.97
6000 (FL)	−0.14 (0.06)	0.76	−0.11 (0.09)	0.54

The chief exception to the general trend described above was the random-level condition for the largest increment bandwidth, $W = 6000$ Hz. Increment detection measured for this condition (shown in Fig. 2 by the filled stars in the second panel from the bottom on the right) did not improve monotonically with signal duration. Performance became systematically worse as duration increased for values of $T \geqslant 60$ ms (i.e., performance demonstrated a ''bowl-like'' effect). Two lines were fit to the detection thresholds for this condition, where the break point at $T = 60$ ms was chosen by visual inspection.[3] The conditions with $T \geqslant 60$ ms represent increments in a broadband noise for which detection became more difficult as the duration of the increment was increased. Conversely, the corresponding fixed-level condition for $W = 6000$ Hz (shown by the filled stars in the bottom-right panel of Fig. 2) yielded the temporal-integration effect expected for a broadband noise (Green, 1960; Campbell, 1963; Raab *et al.*, 1963; Penner, 1978). The temporal-integration slope for the fixed-level $W = 6000$ Hz condition was −0.14.

The discrepancy measured between the random- and fixed-level conditions for $W = 6000$ Hz can be understood in terms of the cues available for detection. The spectral-profile cue was unavailable for both conditions because the signal and standard bandwidths were matched. The temporal-profile cue was the only cue available for the random-level $W = 6000$ Hz condition, and thus it appears that the temporal-profile cue was diminished systematically as duration was increased above 60 ms. The overall-energy cue was available in the fixed-level condition. Apparently, the listeners were able to use the overall-energy cue in the fixed-level condition to improve detection as duration was increased, despite the reduction in the temporal-profile cue as duration was increased. Similarly, the increment-detection thresholds measured for $W = 4000$ Hz in the fixed-level condition yielded a steeper slope (−0.31) than did the corresponding thresholds measured for $W = 4000$ Hz in the random-level condition (slope = −0.15). The amount of temporal integration observed for the fixed-level condition with signal bandwidth matched to the standard bandwidth was consistent with previous studies of temporal-integration for broadband noise (Green, 1960; Campbell, 1963; Raab *et al.*, 1963; Penner, 1978) up to $T = 320$ ms. For example, the equivalent uncorrelated signal-to-noise ratio for our data was −1.5 dB for $T = 30$ ms, −4.7 dB for $T = 320$ ms, and −3.0 dB for $T = 500$ ms. Corresponding data from Campbell (1963) yielded roughly −4.5 dB for $T = 30$ ms, −8 dB for $T = 320$ ms, and −9 dB for $T = 500$ ms. The lack of temporal integration above $T = 320$ ms in the present study is likely due to the use of a gated masker. The temporal-profile cue for our gated stimulus conditions was not present for $T = 500$ ms, whereas the temporal-profile cue for a continuous masker remains present for all durations.

Both the temporal- and spectral-profile cues were absent for the signal condition that matched the increment bandwidth and duration to those of the standard (i.e., $W = 6000$ Hz and $T = 500$ ms). The fixed-level ΔL for this condition was 1.7 dB, while the random-level ΔL was 5.5 dB (more than a factor of 3 higher). The performance in the random-level condition is consistent with a general theoretical prediction for this task that an increment should be detectable by an ideal processor based on an across-interval energy comparison when the increment in energy exceeds 23.46% of the overall range of random-level variation (see Green, 1988, pp. 19–21). This limit for an ideal processor, which corresponds to a ΔL of 4.7 dB for our 20 dB of random level variation, is only slightly lower than the performance demonstrated by our listeners (geometric mean of $\Delta L = 5.5$ dB). Thus, we may conclude that without either the temporal- or spectral-profile cues available to the listener, performance for this random-level condition was likely based upon an across-interval, overall-energy comparison.[4]

2. Decrements

Decrement detection was measured for the same set of bandwidth and duration values used to evaluate increment detection. The only exception was that decrement detection was not measured in the fixed-level condition for $W = 4000$ Hz. In general, decrement detection was a more difficult listening task than increment detection. This conclusion is drawn from the fact that there were more conditions for which listeners had to contribute additional threshold estimates to obtain three consistent estimates. For a number of decrement-detection conditions, consistent threshold estimates were never obtained because decrements were not detectable for these conditions. Consistent individual decrement thresholds above $\Delta L = 25$ dB were never obtained. Thus, decrement conditions we report as undetectable by our listeners (indicated by an upward arrow in Fig. 2) represent conditions for which thresholds, if they existed, were greater than $\Delta L = 25$ dB. The open symbols in Fig. 2 represent the group mean thresholds measured for those conditions in which consistent threshold estimates were obtained from at least two of our three listeners. In general, the decrement-detection thresholds shown for the group in Fig. 2 are representative of individual performance. Only in a few cases, mentioned below, were there differences in performance across listeners.

The pattern of decrement-detection thresholds for $W \leqslant 500$ Hz is in marked contrast to the companion increment-detection thresholds in Fig. 2 for the corresponding ranges of bandwidth and duration. These decrement bandwidths were not consistently detectable for the listeners. Listener SF showed the greatest sensitivity to decrements across all conditions of bandwidth and duration. She was unable to detect decrements for any duration paired with $W \leqslant 125$ Hz. For $W = 250$ Hz, she was able to detect decrements for $T \geqslant 60$ ms. Her thresholds for $W = 250$ Hz systematically decreased from 15.2 to 2.6 dB (a factor of almost 6) as decrement duration was increased from $T = 60$ to 500 ms. Decrements for $W = 500$ Hz were detectable by SF for all decrement durations. Her thresholds decreased from 5.11 to 1.64 dB (a factor of about 3) as duration was increased from $T = 60$ to 500 ms. Her thresholds for $T = 30$ and 40 ms were 20.79 and 8.89 dB, respectively. In contrast to listener SF, listeners JZ and CF were unable to detect any decrements for $W \leqslant 250$ Hz. For $W = 500$ Hz, listener JZ was able to detect decrements for all $T \geqslant 80$ ms, whereas listener CF was able to detect decrements for all $T \geqslant 80$ ms except $T = 500$ ms. Thus, the group decrement-detection threshold for $W = 500$ Hz and $T = 500$ ms is the mean result only for listeners SF and JZ. This is the lone group-mean decrement-detection threshold shown in Fig. 2 that does not include a threshold estimate from each listener. The fact that listener CF was unable to detect any decrement level for the condition pairing $W = 500$ Hz and $T = 500$ ms was unexpected because he was able to detect decrements of shorter duration for $W = 500$ Hz. A spectral-profile cue should have been available to him for the $T = 500$ ms condition, even though the temporal-profile cue was removed. This result may indicate that CF was relying strongly on the temporal-profile cue for $W = 500$ Hz.

Our results for narrow-band decrements are similar to the trends reported by Moore *et al.* (1989) for the detection of bandlimited peaks and notches in a broadband masker. They found that narrow-band notches were much more difficult to detect than corresponding narrow-band peaks for peaks and notches matched in duration to the masker. Only two of their three listeners were able to detect a 125-Hz notch centered at 1 kHz, while none of their three listeners could detect a 1000-Hz notch centered at 8 kHz. These notch widths both correspond to 12.5% of the corresponding center frequency. This percentage corresponds to a notch width of 312.5 Hz for our stimuli, and thus is in the range of bandwidths for which our listeners began to show sensitivity to decrements.

For large bandwidth conditions ($W \geqslant 1000$ Hz), decrements were consistently detectable by all three listeners. The only trend in the group-mean thresholds for $W \geqslant 1000$ Hz that was not representative of individual performance was the increase in the decrement thresholds for $T \geqslant 160$ ms and $W = 1000$ Hz. This increase was only observed for listener CF. Thresholds for SF and JZ continued to decrease slightly for $T \geqslant 160$ ms. This finding suggests that listener CF may have been relying more strongly on the temporal-profile cue for this signal bandwidth. This idea is consistent with the finding that, in the absence of a temporal-profile cue, listener CF was unable to detect a 500-Hz decrement for $T = 500$ ms.

In general, all three listeners demonstrated a temporal-integration effect for the decrement conditions that were consistently detectable (i.e., $80 \leqslant T \leqslant 320$ ms for $W = 500$ Hz and all T for $W \geqslant 1000$ Hz). The dashed lines in Fig. 2 represent least-square fits to the decrement-detection thresholds. The slopes and correlation coefficients are summarized in Table I. The temporal-integration slopes for random-level decrement detection decreased slightly from -0.37 to -0.29 as bandwidth was increased from $W = 500$ to 4000 Hz. For most decrement bandwidth conditions there was a slight increase in decrement threshold for the largest values of duration. This change in performance is coincident with the loss of the temporal-profile cue. The general trend of reduced temporal integration as bandwidth increased was similar to the effect described earlier for increment detection. Again, the chief exception to the temporal-integration effect was the random-level condition for $W = 6000$ Hz, for which decrement-detection thresholds were nonmonotonic as duration increased. Decrement detection became worse as duration increased above $T = 160$ ms, as indicated by the two-line fit shown in Fig. 2. The random- and fixed-level functions for decrement detection measured with $W = 6000$ Hz diverged for $T \geqslant 320$ ms. By contrast, the corresponding random- and fixed-level increment thresholds for $W = 6000$ Hz began to diverge for $T \geqslant 60$ ms. This pattern of detection suggests that the broadband temporal-profile cue may have been more difficult for the listeners to resolve for increments than for decrements.

The amount of temporal integration was similar for increments and decrements across the range of bandwidths over which decrements were detectable (see slopes in Table I). However, decrement-detection thresholds tended to be slightly higher than corresponding increment-detection thresholds for small bandwidths, and to become slightly lower than corresponding increment thresholds as bandwidth was increased. Irwin and Purdy (1982) found broadband noise increment and decrement detection measured in terms of ΔL to be roughly equal. Forrest and Green (1987) found decrement thresholds to be slightly lower than corresponding increment thresholds for $T \geqslant 10$ ms. *A priori*, one might have expected that increments and decrements would have been detected equally well because they represent an equal change in level within the signal region. However, the effects of peripheral filtering and neural adaptation likely complicate a simple interpretation of the results. We believe that much of the discrepancy between increment and decrement detection as a function of signal bandwidth can be explained by the peripheral filtering of the auditory system. A basic property of multicomponent signals is that decreasing the level of k out of n components, where n is the total number of components within a peripheral filter, results in a maximum decrease in the overall ΔL of $10\log_{10}(n) - 10\log_{10}(n-k)$. Conversely, the overall ΔL that results from increasing the level of k components is unbounded. This property of multicomponent signals results in an asymmetry between the excitation patterns produced by increment and decrement stimuli (Moore *et al.*, 1989; Ellermeier, 1996). Spread of ex-

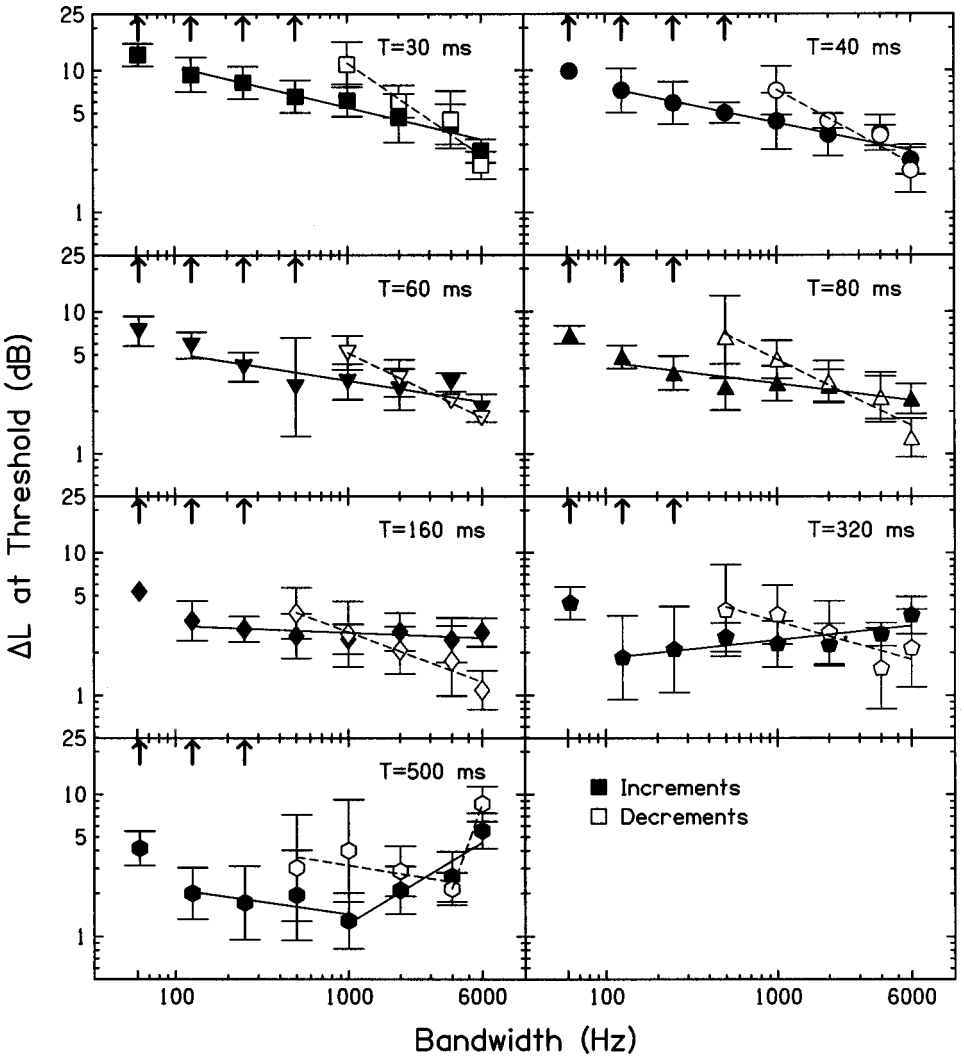

FIG. 3. Increment- (filled symbols) and decrement- (open symbols) detection thresholds are shown as a function of increment or decrement bandwidth for random-level conditions. Geometric means of ΔL in dB are plotted on a logarithmic scale with associated standard deviation bars. Each panel corresponds to a different duration. Upward arrows indicate decrements that were not consistently detectable by all three listeners. Solid and dashed lines represent least-square fits to the increment- and decrement-detection thresholds, respectively.

citation for both increments and decrements originates at the spectral edges of the signal region, but the excitation spreads away from the signal region for increments and into the signal region for decrements. Thus, the signal frequency region in the decrement condition is masked by the flanking standard noise. It follows that there should be a large critical-band effect for decrement detection, but a relatively small critical-band effect for increments (consistent with our data and that of Moore *et al.*, 1989). We will examine this hypothesis later in terms of the differences between predicted excitation patterns for increments and decrements.

B. Detection as a function of bandwidth

The group detection thresholds for increments and decrements are replotted in Fig. 3 as a function of signal bandwidth. Increment- (filled symbols) and decrement- (open symbols) detection thresholds for the random-level conditions are shown in different panels for each of the seven values of duration ranging from $T=30$ to 500 ms. These data are the same geometric means and standard deviation bars shown in Fig. 2, but are replotted to compare the improvement in increment and decrement detection as a function of signal bandwidth. This representation of the results provides an opportunity to assess spectral integration. The notion of spectral integration is that as signal bandwidth is increased, detection should improve systematically as more information becomes available to the listener. Many studies have provided evidence that detection is enhanced by the presence of signal energy in multiple auditory channels (e.g., Green, 1958, 1960; Green *et al.*, 1959; Scholl, 1962; Spiegel, 1979; Buus *et al.*, 1986; van den Brink and Houtgast, 1990a,b). Green (1958) and Buus *et al.* (1986) have discussed several mathematical models to explain spectral integration. Both studies concluded that listeners appear to combine information linearly from multiple auditory channels; however, Buus *et al.* (1986) suggested that the combination might not be optimal. Another consideration in the present study is that the external variability due to the noise stimuli is reduced as the bandwidth is increased, which could also lead to improved performance.

1. Increments

The increment-detection thresholds shown in Fig. 3 decreased as bandwidth was increased for $W \leqslant 4000$ Hz and $T < 160$ ms. This improvement in performance with increasing bandwidth reflects a spectral-integration effect for increment detection. The increment thresholds are described well by the solid lines that represent least-square fits for bandwidths

TABLE II. Spectral-integration slopes and correlation coefficients r for the fitted lines shown in Fig. 3 for both increment and decrement detection. The values in parentheses are standard errors of the slopes.

	Increments		Decrements	
T (ms)	Slope	r	Slope	r
30	−0.29 (0.03)	0.98	−0.83 (0.15)	0.99
40	−0.25 (0.03)	0.98	−0.66 (0.11)	0.99
60	−0.19 (0.05)	0.88	−0.58 (0.02)	1.00
80	−0.15 (0.03)	0.92	−0.60 (0.09)	0.99
160	−0.05 (0.03)	0.67	−0.45 (0.06)	0.99
320	0.13 (0.04)	0.82	−0.34 (0.10)	0.92
500	−0.17 (0.10)	0.75	−0.20 (0.15)	0.60
	0.73 (0.17)	0.93	3.40 (0.00)	1.00[a]

[a]Line was fit to only two points.

ranging from $W=125$ to 6000 Hz (two-line fits were used for $T=500$ ms).[5] Table II summarizes the slopes and correlation coefficients for the fitted spectral-integration lines. The amount of spectral integration decreased systematically as duration was increased. Specifically, spectral-integration slopes for increment detection decreased from −0.29 to −0.05 as duration was increased from $T=30$ to 160 ms. The finding that spectral integration decreased as duration increased is consistent with previous reports that efficient spectral integration is only possible for brief stimuli (e.g., Scholl, 1962; van den Brink and Houtgast, 1990a,b). The chief exception to the spectral-integration trend was observed for the longest-duration random-level conditions $T=320$ and 500 ms. For $T=500$ ms, both the temporal-profile and overall-energy cues were unavailable to the listener. The nonmonotonic increment-detection thresholds for $T=500$ ms indicate that the spectral-profile cue was systematically diminished as bandwidth was increased above $W=1000$ Hz. The increment-detection thresholds for $T=500$ ms show the same bowl-like shape that was observed for the random-level, $W=6000$ Hz increment-detection condition in Fig. 2 (i.e., where the spectral-profile and overall-energy cues were absent and the temporal-profile cue was varied). The lack of spectral integration from $W=125$ to 1000 Hz for long-duration increments is consistent with the detection of band-limited peaks reported by Moore *et al.* (1989).

2. Decrements

Group decrement thresholds are represented in Fig. 3 by the open symbols, with least-square fits shown by the dashed lines. Recall that narrow-band decrements were not consistently detectable, and that the narrowest bandwidth for decrement detection varied with duration. For $T\leqslant 60$ ms, decrements were not detectable for $W\leqslant 500$ Hz, while for $T\geqslant 80$ ms decrements were not detectable for $W\leqslant 250$ Hz. In general, thresholds decreased as bandwidth was increased beyond the narrowest decrement bandwidth affording detection. Thus, listeners demonstrated a spectral-integration effect for decrements with $T\leqslant 320$ ms. The amount of spectral integration for decrements decreased systematically as duration was increased. Specifically, the spectral-integration slopes decreased from −0.83 to −0.34 as duration was increased from $T=30$ to 320 ms. The spectral-integration slopes for decrements were, in general, steeper than for corresponding increments of equal duration. The main exception to the spectral-integration effect was the $T=500$ ms condition, for which decrement-detection thresholds were nonmonotonic and increased dramatically for $W>4000$ Hz. The dramatic threshold elevation corresponds to the loss of the spectral-profile cue and the absence of the temporal-profile and overall-energy cues.

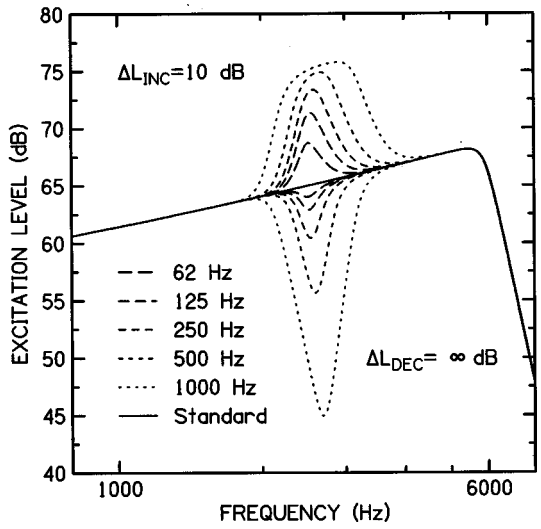

FIG. 4. Excitation-pattern analysis of the increment and decrement conditions used in this study. Excitation level as a function of frequency was calculated from the excitation-pattern model of Glasberg and Moore (1990). Increment conditions shown represent $\Delta L=10$ dB. Decrement conditions shown represent a complete decrement, i.e., $\Delta L=\infty$dB. The asymmetry between the effective change in excitation level for increments and decrements is evident for comparable bandwidths.

C. Asymmetry between increments and decrements

In this section, we examine further the hypothesis that the discrepancy between increment and decrement detection for narrow bandwidths is due to spread of excitation associated with peripheral filtering (Moore *et al.*, 1989; Ellermeier, 1996). The supposition is that the spread of excitation for increments is away from the spectral edges of the increment, and thus serves to create a broader effective increment. In contrast, the spread of excitation for decrements extends from the spectral edges of the noise standard into the decrement. This spread serves to create a narrower effective decrement.

In order to quantify this hypothesis, we have examined the predicted excitation patterns for each of our increment and decrement conditions using the excitation-pattern model of Glasberg and Moore (1990). We have used this model to provide an estimate of the excitation level as a function of frequency for steady-state noises with spectra corresponding to our increment and decrement stimuli. A similar analysis was shown by Ellermeier (1996) for his profile stimuli consisting of a nonharmonic tone complex with variable numbers of components spread across a fixed frequency range. Predicted excitation patterns for our narrow bandwidth increment and decrement conditions are shown in Fig. 4. The excitation pattern for the fixed-level ($L_0=40$ dB SPL) noise standard is shown by the solid line. The family of excitation patterns that lies above the noise standard represents incre-

ment conditions with $\Delta L = 10$ dB. The excitation patterns below the standard represent decrement conditions with $\Delta L = \infty$ dB (i.e., a complete decrement with no energy within the signal bandwidth). A complete decrement was chosen because we were seeking to determine the effective decrement in excitation level for conditions that were not detectable for any decrement level. The family of excitation patterns for increment and decrement conditions is shown for bandwidths ranging from $W = 62$ to 1000 Hz, with the bandwidths identified in the legend. This range of bandwidths includes conditions for which decrements were undetectable ($W < 500$ Hz) and conditions for which decrements were roughly as detectable as corresponding increments ($W \geqslant 1000$ Hz).

The asymmetry between the excitation patterns for increments and decrements can be seen in Fig. 4. The change in excitation level at the center of the decrements for $W = 62$, 125, 250, and 500 Hz were 0.99, 2.13, 4.63, and 9.50 dB, respectively. Conversely, the change in excitation level for the corresponding $\Delta L = 10$ dB increments were 3.73, 6.33, 8.28, and 9.70 dB, respectively. Clearly, for narrow-bandwidth decrements, the effective decrement in excitation level was restricted due to peripheral filtering more than for the corresponding increments. This set of simulations helps to explain why our listeners were only able to detect decrements consistently with $W \geqslant 500$ Hz.

The actual changes in excitation level predicted by the model correspond to steady-state signals, and therefore are most analogous to our long-duration ($T \geqslant 160$ ms) conditions. A simple single-channel interpretation of intensity discrimination suggests that performance at threshold corresponds roughly to a 1-dB change in excitation level near the center frequency of the signal (e.g., Zwicker, 1956). This finding indicates that the long-duration $W = 62$ Hz decrements would have been just detectable. We do not wish to pursue a specific quantitative analysis here, due to the numerous assumptions involved with the excitation-pattern model and the corresponding interpretation. It is apparent, however, that the excitation-pattern model does predict the basic trend in our data, namely that narrow-band decrements are more difficult to detect than narrow-band increments. This finding can be explained by the asymmetry between the spread of excitation for increments and decrements.

D. Comparison of increment detection measured with correlated and uncorrelated signals

Both the current study and the study by Formby *et al.* (1994) measured the detection of time- and bandlimited increments in a broadband noise stimulus; however, the method of generating the increments was slightly different in the two studies. Formby *et al.* (1994) generated an increment by adding a noise burst signal (with bandwidth W, duration T, and spectral density S_0) to an uncorrelated noise masker (with bandwidth W_{ST}, duration T_{ST}, and spectral density N_0). Because the signal and masker were uncorrelated, the noise spectral density within the increment was $S_0 + N_0$. In the current study, the time- and bandlimited increment was generated by setting the spectrum level within the increment to be ΔL dB higher than the spectrum level of the noise standard. This procedure is equivalent to correlated addition of an attenuated version of the portion of the noise standard corresponding to the signal region. Thus, the spectrum level within the increment was $L_0 + \Delta L$ in dB SPL. To compare increment-detection performance from the current study to that in Formby *et al.* (1994), the results must be expressed in the same metric (see Grantham and Yost, 1982; Green, 1988). Individual threshold estimates for each listener from the current study, measured as ΔL in dB, were converted to equivalent masked-detection units with the following equation,

$$10 \log_{10}(S_0/N_0) = 10 \log_{10}(10^{(\Delta L/10)} - 1), \quad (1)$$

where S_0 represents the spectral density of an equivalent uncorrelated signal that would have produced a spectrum level of $L_0 + \Delta L$ in dB SPL within the increment region.

The increment-detection thresholds from Formby *et al.* (1994) and the current study are compared in Fig. 5. Group-mean increment-detection thresholds, in terms of $10 \log_{10}(S_0/N_0)$ in dB, are plotted with across-listener standard deviations (bars) as a function of total signal duration for bandwidth ranging from $W = 62$ to 6000 Hz. The detection thresholds from Formby *et al.* (1994) are shown by the open symbols and represent fixed-level conditions for all bandwidth values. Detection thresholds from the current study are shown by filled symbols and represent random-level conditions for $W = 62$ to 2000 Hz and fixed-level conditions for $W = 4000$ and 6000 Hz. Performance from the two studies is essentially identical for all bandwidth and duration values. The good correspondence between the two studies was reassuring and demonstrates that, as far as the listener is concerned, there is no difference between adding an uncorrelated noise or a correlated noise to a pedestal as long as they both result in the same increase in level. Raab *et al.* (1963) showed the same result for broadband 500-ms noise signals added to a continuous noise masker across a wide range of masker levels.

In addition to the differences in stimulus generation, the conditions from the two studies also differed in the available cues for detection. An overall-energy cue was available in the Formby *et al.* (1994) study, but was absent in the current study for $W \leqslant 2000$ Hz. Temporal- and spectral-profile cues were available in both studies. Both sets of increment detection thresholds shown in Fig. 5 demonstrate the same temporal- and spectral-integration trends. The similar performance in the two studies suggests that temporal- and spectral-profile cues are the important cues used by listeners for the detection of time- and bandlimited increments.

III. GENERAL DISCUSSION

A. Increments and decrements

The purpose of this study was to compare the detection of time- and bandlimited increments and decrements in a broadband noise. The biggest difference between increment and decrement detection was found for the effect of signal bandwidth. Increments were detectable for all bandwidths measured (i.e., bandwidth ranging from $W = 62$ to 6000 Hz).

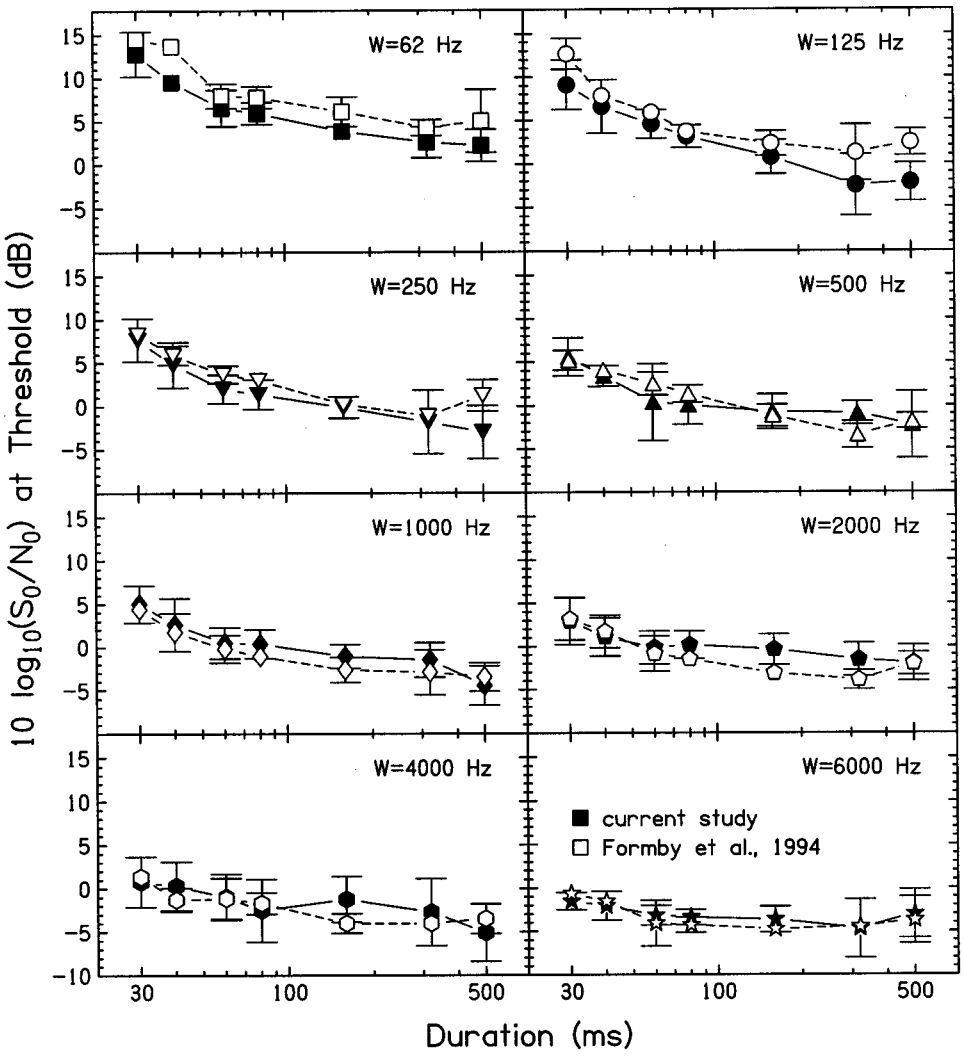

FIG. 5. Comparison of increment-detection performance measured with a correlated noise signal (current study, filled symbols) and measured with an uncorrelated noise signal (Formby *et al.*, 1994, open symbols). Increment performance is represented in terms of $10\log_{10}(S_0/N_0)$ in dB, where N_0 is the spectral density of the noise standard and S_0 represents the increment in spectral density. Values of $10\log_{10}(S_0/N_0)$ in dB were calculated for the current study from ΔL in dB using Eq. (1) (see the text). Group-mean increment-detection thresholds are plotted as a function of increment duration, with standard deviation bars. Each panel represents a different bandwidth. All conditions from Formby *et al.* (1994) represent fixed-level conditions. Thresholds from the current study for $W \leqslant 2000$ Hz represent random-level conditions, while thresholds for $W \geqslant 4000$ Hz represent fixed-level conditions.

Conversely, decrements were not consistently detectable for $W < 500$ Hz, but were detectable for all durations for $W \geqslant 1000$ Hz. The asymmetry between the excitation patterns for increments and decrements shown in Fig. 4 suggests that much of this effect can be explained by spread of excitation due to peripheral filtering. For narrow-band decrements, the spread of excitation from the spectral edges of the noise standard into the signal-frequency region masks the decrement.

The smallest bandwidth for which all three listeners were consistently able to detect long-duration ($T \geqslant 80$ ms) decrements was $W = 500$ Hz. This finding agrees roughly with typical estimates of critical bandwidths at 2500 Hz, which was the center frequency of the decrements. Representative estimates of the critical bandwidth at 2500 Hz are in the range of 295 Hz (Glasberg and Moore, 1990) to 380 Hz (Zwicker and Fastl, 1990). These estimates are intermediate in frequency between the decrement bandwidth $W = 250$ Hz, for which listener SF first showed an ability to detect a decrement, and $W = 500$ Hz, for which listeners CF and JZ demonstrated initial sensitivity to decrements. Moore *et al.* (1989) have also reported conditions for which notch widths of 12.5% of the center frequency were only detectable by two of their three listeners for a center frequency of 1 kHz, and were not detectable by any of their listeners for a center frequency of 8 kHz. In both cases, notch widths of 25% of the center frequency were detectable by all three listeners. This range of intersubject variation is consistent with normal variability reported in the literature for auditory-filter bandwidth and critical-bandwidth estimates (Patterson and Moore, 1986). Bandwidth estimates up to and exceeding 20% of the signal frequency (which we would infer from the results of CF and JZ) have been reported for some tasks and measurement conditions (Zwicker and Fastl, 1990; Leek and Summers, 1993).

The peripheral filtering interpretation of the decrement-detection data suggests that the asymmetry between increment and decrement detection should diminish as the bandwidth becomes much larger than the critical band. As bandwidth increases, the masking effect decreases because spread of excitation fills only a portion of the decremented frequency region. This prediction is consistent with our finding that decrement-detection thresholds became more similar to increment-detection thresholds as bandwidth was increased from $W = 500$ to 2000 Hz. Moore *et al.* (1989) also found that peak- and notch-detection thresholds became more similar as bandwidth was increased. It is not clear why decrement-detection thresholds in the present study continued to improve and became lower than increment-detection

thresholds as bandwidth was increased above $W = 2000$ Hz.

Temporal- and spectral-integration effects were observed for increments and decrements for $W \geqslant 1000$ Hz. The amount of temporal integration decreased as bandwidth was increased. Similarly, the amount of spectral integration decreased as duration was increased. These findings are consistent with reports by Scholl (1962) and van den Brink and Houtgast (1990a,b) who found that efficient temporal integration was only possible for narrow-band signals, and likewise efficient spectral integration was only possible for brief-duration signals. A larger temporal-integration effect for narrow-band stimuli than for broadband stimuli is also consistent with Irwin and Kemp (1976) and Irwin and Purdy (1982), who found a threefold reduction in estimated temporal-integration time constants between the detection of sinusoidal signals and broadband noise signals.

The primary exceptions to the general temporal- and spectral-integration trends were for the random-level conditions in which either duration was varied when signal and masker were matched spectrally, or bandwidth was varied when the signal and masker were of equal duration. In these conditions, we found that increment- and decrement-detection thresholds demonstrated a bowl-like effect, where thresholds became larger as the duration or bandwidth was increased above some moderate value. We believe that these findings can be explained by considering the availability of temporal- and spectral-profile cues as well as overall-energy cues in these conditions.

B. Multicue interpretation of results

In this study, the majority of the detection results was dependent on temporal- and spectral-profile cues. The overall-energy cue was purposely rendered an inconsistent cue by randomizing overall presentation level across the observation intervals of each trial. Thus, it is important to consider how temporal- and spectral-profile cues could be combined to account for the increment- and decrement-detection results.

The temporal-integration effect has traditionally been thought of as arising from a process that integrates signal energy over time. It is therefore of interest to consider how the temporal-integration effect in our data could be produced in a detection task based solely on temporal- and spectral-profile cues. The temporal-integration effect reflects an increase in the available information for detection as signal duration increases. Information from the temporal-profile cue was present for all $T < 500$ ms, but appears from the random-level $W = 6000$ Hz condition to have been systematically reduced as duration was increased above a moderate value. Thus, the temporal-integration effect does not appear to be the result of information from the temporal-profile cue. The spectral-profile cue was available at all points in time within the signal region for $W < 6000$ Hz. Thus, the information available from the spectral-profile cue increased systematically as duration was increased. Consequently, a scheme in which information from the spectral-profile cue was combined across time could produce a temporal-integration effect independent of random-level variation for $W < 6000$ Hz. This explanation is consistent with the absence of a temporal-integration effect for $W = 6000$ Hz when the stimuli were presented in the random-level paradigm and the spectral-profile cue was absent. The temporal-integration effect was present for the same condition with fixed-level presentation because the overall-energy cue was available.

The spectral-integration effect observed in our data can be explained in a way similar to the temporal-integration effect. This spectral-integration effect reflects an increase in available information for detection as bandwidth was increased. The temporal-profile cue was available for all frequencies within the signal region for $T < 500$ ms. Accordingly, a scheme in which information from the temporal-profile cue was combined across all frequency channels may account for the spectral-integration effect, and this effect should be independent of the randomization of overall presentation level.

The two schemes described above did not specify how the information from the profile cues might be calculated or combined. There are at least three ways that we can envision a general profile cue (temporal or spectral) being evaluated by a listener. Green (1988) described a method for (spectral) profile analysis based on a theory proposed by Durlach *et al.* (1986). This method is based on within-interval comparisons of the relative levels within and outside the signal (increment or decrement). The level of the signal is estimated from the region (either spectral or temporal) within the increment or decrement, and this level is compared to an estimate of level from the fringe region outside the signal. As the signal increases in duration or bandwidth, the fringe region is concomitantly reduced. Thus, as the amount of information in the signal increases, the amount of information in the fringe decreases. This prediction is consistent with the bowl-like trends observed for the broadband conditions in Fig. 2 and the long-duration conditions in Fig. 3 (i.e., conditions in which the temporal- and spectral-profile cues were isolated, respectively). For these conditions, performance did not improve monotonically with increasing duration or bandwidth. The best performance was obtained for moderate values of signal duration or bandwidth, where the durations or bandwidths of the signal and fringe regions were roughly equal. The benefit from further increases in duration or bandwidth was counteracted by a reduction in the information within the fringe region.

Another method for evaluating a profile cue could be based on the detection of edges. Shamma (1985, 1989) has evaluated the detection of spectral edges based on a hypothesized lateral inhibition network for spectral shape analysis. Reports of lateral suppression may be relevant to this method (e.g., Houtgast, 1972). In the time domain, temporal overshoot and undershoot effects may serve as the counterpart to lateral suppression to accentuate temporal edges at onset and offset of increment and decrement signals (Formby *et al.*, 1997, 1998). Adaptation in auditory-nerve fibers (Smith and Zwislocki, 1975) and activity from onset and offset cells at higher levels of the auditory pathway (Rhode *et al.*, 1983; Rouiller and Ryugo, 1984; Walton *et al.*, 1997) may provide mechanisms for temporal edge detection. This mechanism could be similar to the ''change detector'' proposed by Mac-

millan (1971, 1973) and recently discussed by Oxenham (1997) and Moore and Peters (1997). It is unlikely that edge detection was used in isolation, if at all, by our listeners because edge cues do not provide a straightforward way of accounting for the bowl-like effects observed in Figs. 2 and 3.

A third hypothesis for profile-cue evaluation is that detection performance is based on the relative dissimilarity (in time, frequency, or both) of the signal and standard. Formby *et al.* (1994) discussed the possibility of a temporal-profile cue arising whenever a gated signal is presented asynchronously within a longer-duration gated masker. In the current study, the listeners could have compared relative temporal and spectral differences between the increment or decrement signals with respect to the standard. This judgment may have been performed either by comparing relative differences within each interval of each trial or by comparing the profiles successively across the signal-plus-standard and the standard-alone intervals of each trial. The prediction from this scheme, that performance will improve as the signal and standard become more dissimilar, is inconsistent with the initial improvement in performance demonstrated in the bowl-like trends observed in Figs. 2 and 3.

Our detection data across all bandwidth, all duration, and random- and fixed-level conditions suggest that the listener may evaluate the temporal-profile, spectral-profile, and overall-energy cues separately and somehow combine the information from each cue. It is unclear, however, from the qualitative description above how the listener combines these three cues quantitatively. To address this issue for our increment and decrement stimuli, a multichannel computational model was implemented with a phenomenological auditory-nerve model (Carney, 1993) and a multicue decision process (Heinz and Carney, 1997). The spectral-profile cue was quantified by calculating at each point in time the peak-to-peak difference in simulated neural activity (smoothed with a 20-ms time constant) across all frequency channels. The result was a metric that quantified the spectral-profile cue as a function of time. The temporal-profile cue was quantified as a function of frequency in an analogous manner (i.e., by calculating at each frequency the difference between the maximum and minimum over time of the smoothed neural activity). The total contribution of each cue was evaluated by integrating the spectral-profile metric across time and the temporal-profile metric across frequency. An equally weighted linear combination of the contributions of both profile cues (and an overall-energy cue for fixed-level conditions) was used as the basis for the decision in a simulated two-interval, two-alternative forced-choice task. Preliminary modeling results indicate that this multicue decision process produces the main qualitative trends shown in Figs. 2 and 3 for the increment- and decrement-detection thresholds, including temporal- and spectral-integration effects in the presence of overall-level randomization, and the critical-band effect for decrements.

This multicue decision scheme can be thought of in part as a ''multiple-looks'' model of the type that has been described by Viemeister and Wakefield (1991) for the time domain. However, our model can be viewed as a more general multiple-looks model, in which multiple looks (or information samples) are calculated both in time and frequency. Furthermore, our modeling suggests that the looks should include information other than short-term energy (i.e., that profile cues should form at least some of the looks, both in time and frequency). In our model, temporal looks were calculated by evaluating the presence of the spectral-profile cue at short-duration intervals, while spectral looks were calculated by evaluating the temporal-profile cue within narrow frequency regions.

Our decision process is consistent with Viemeister and Wakefield's (1991) multiple-looks model inasmuch as there is no long-duration integration of energy; however, the uniform weighting of information in the present model is likely to differ from the optimal weighting postulated by Viemeister and Wakefield. In the present model, there is long-duration integration of information similar to the information-integration model described by Green and Swets (1966). Conversely, it is possible to hypothesize a scheme in which long-duration integration of energy within each frequency channel precedes an across-channel comparison. A decision process similar to that described by Dau *et al.* (1996, 1997) could also potentially account for the temporal- and spectral-integration effects observed in the present study. Dau *et al.* (1997) reported that a multichannel template-based decision process accounted for the spectral- and temporal-integration effects for amplitude-modulation detection. In their model, information was combined linearly across all activated frequency channels and with a multiple-looks strategy across time.

C. Implications of the presence of temporal- and spectral-profile cues in previous studies

Finally, our results suggest the need to consider the potential roles of temporal- and spectral-profile cues in some of the past detection and discrimination studies. Forrest and Green (1987) and Plack and Moore (1991) have attempted to control for the absolute-energy cue by randomizing overall level in the measurement of detection thresholds for broadband increment and decrement stimuli. The spectral-profile cue was absent in both of these studies because the broadband pedestal and the increment or decrement signals were matched spectrally. Thus, a temporal-profile cue appears to have been the main cue available in these experiments. In most other increment- and decrement-detection studies (including most studies using silent gap signals), the overall-energy cue has not been controlled, and thus both overall-energy and temporal-profile cues were available to the listeners. Eddins and his colleagues (Eddins *et al.*, 1992; Eddins and Green, 1995) analyzed a large set of temporal gap-detection results and concluded that energy was the salient cue in their studies. Moore and Peters (1997) have suggested that the smaller temporal-integration effect in their increment- and decrement-detection data for tones in a low-pass filtered noise supports a change-detector hypothesis. Our data suggest that Moore and Peters' (1997) results may be based on a combination of temporal- and spectral-profile cues as well as an overall-energy cue. If their results were based on a change detector acting on the temporal-profile

cue, then their results should be unaffected by overall-level randomization. Another example where temporal-profile cues may be important is the typically reported result that intensity discrimination for tones or noise is generally better for continuous pedestals than for gated pedestals (e.g., Schacknow and Raab, 1976; Viemeister and Bacon, 1988; Bacon and Viemeister, 1994). The relative contributions from the temporal-profile cue and the overall-energy cue remain to be resolved in some of these reports. Kidd *et al.* (1989) have pointed out the need to consider the ability of a listener to detect a spectral-profile cue in previous studies in which the signal produced a change in the spectral profile. The results of the present study further suggest the need to consider listeners' ability to make use of spectral- and temporal-profile cues in previous studies in which there was either a spectral- or temporal-profile cue available.

IV. SUMMARY

The current study was designed to compare directly the detection of time- and band-limited increments and decrements in a random-level noise. Increment- and decrement-detection thresholds were measured as a function of signal bandwidth W and duration T, using a noise standard with $W_{ST}=6000$ Hz and $T_{ST}=500$ ms. We have reached the following conclusions:

(1) The greatest difference in the detection of increments and decrements was observed as a function of bandwidth. Decrements were not consistently detectable for $W<500$ Hz, while increments were detectable for all bandwidths between $W=62$ and 6000 Hz.
(2) Asymmetry in the spread of excitation for increments and decrements due to peripheral filtering accounts for narrow-band decrements (roughly less than a critical bandwidth) being undetectable, as demonstrated by excitation patterns for equal-bandwidth increments and decrements.
(3) Increment and decrement thresholds were similar for broadband conditions. Both increment and decrement thresholds revealed temporal- and spectral-integration effects, independent of random-level variation in most conditions. Temporal integration decreased as signal bandwidth was increased, and spectral integration decreased as signal duration was increased. Decrement thresholds showed roughly the same amount of temporal integration as comparable increment thresholds, but the spectral-integration effect was greater for decrement detection than for increment detection.
(4) Exceptions to the general temporal- and spectral-integration trends were observed when the signal had either the same duration or bandwidth as the noise standard. For $W=W_{ST}$, thresholds increased as T approached T_{ST}. Likewise for $T=T_{ST}$, thresholds increased as W approached W_{ST}.
(5) The temporal- and spectral-integration effects observed in the absence of overall-energy cues are consistent with a multicue decision process that combines information from temporal- and spectral-profile cues. The integration of the spectral-profile cue across time accounts for the temporal-integration effect, while integration of the temporal-profile cue across frequency accounts for the spectral-integration effect.
(6) The ability of listeners to detect temporal- and spectral-profile cues must be considered in any study that uses fixed-level stimuli and that offers listeners profile cues in either time or frequency.

ACKNOWLEDGMENTS

The authors are grateful to Søren Buus, Christine Mason, Laurel Carney, and an anonymous reviewer for many helpful comments and suggestions. Peggy Nelson and Virginia Richards provided constructive criticism on an earlier version of this manuscript. We would like to acknowledge Jake Zeiders and Sarah Ferguson for serving as listeners, and Sarah for her help in data collection. We thank Amy Shutt for editorial assistance in preparing this manuscript. This work was supported in part by NIH awards (R01 DC00951) and (T32 DC00038) and a subcontract from the Office of Naval Research.

[1]Plotting ΔL in dB on a logarithmic scale is consistent with the adaptive tracking paradigm we used (i.e., each increase or decrease in ΔL in the tracking procedure represents an equal distance on the logarithmic scale). A logarithmic scale thus provided variation in our estimates that was essentially independent of the geometric mean. Buus and Florentine (1991) provide a compelling argument and example to illustrate that plotting ΔL in dB on a logarithmic scale allows a proper interpretation of the data because d' is proportional to ΔL in dB for a wide range of stimulus conditions, including broadband noise.

[2]The absolute values of the temporal-integration slopes were influenced by the definition of signal duration. For example, slopes for W ranging from 62 to 4000 Hz were on average reduced by 0.09 when plateau duration was used instead of total duration. The general trends as a function of bandwidth were not influenced by the definition of signal duration.

[3]Two-line fits may be appropriate for other conditions as well; however, for simplicity we have only used two-line fits for conditions in which a temporal-profile cue was the only available cue.

[4]It should be noted that this conclusion does not necessarily apply to other random-level conditions for which $T<T_{ST}$ or $W<W_{ST}$ and threshold is greater than $\Delta L=4.7$ dB. The ideal limit based on overall energy is higher than $\Delta L=4.7$ dB for conditions in which $T<T_{ST}$ or $W<W_{ST}$, e.g., for $W=62$ Hz and $T=30$ ms, the ideal limit is $\Delta L=34.5$ dB.

[5]The $W=62$ Hz thresholds were not included in the fits because performance for $W=62$ Hz does not follow the general trends of the broader bandwidth conditions, as discussed previously.

Bacon, S. P., and Viemeister, N. F. (**1994**). ''Intensity discrimination and increment detection at 16 kHz,'' J. Acoust. Soc. Am. **95**, 2616–2621.
van den Brink, W. A. C., and Houtgast, T. (**1990a**). ''Efficient across-frequency integration in short-signal detection,'' J. Acoust. Soc. Am. **87**, 284–291.
van den Brink, W. A. C., and Houtgast, T. (**1990b**). ''Spectro-temporal integration in signal detection,'' J. Acoust. Soc. Am. **88**, 1703–1711.
Buus, S. (**1990**). ''Level discrimination of frozen and random noise,'' J. Acoust. Soc. Am. **87**, 2643–2654.
Buus, S., Schorer, E., Florentine, M., and Zwicker, E. (**1986**). ''Decision rules in detection of simple and complex tones,'' J. Acoust. Soc. Am. **80**, 1646–1657.
Buus, S., and Florentine, M. (**1991**). ''Psychometric functions for level discrimination,'' J. Acoust. Soc. Am. **90**, 1371–1380.
Campbell, R. A. (**1963**). ''Detection of a noise signal of varying duration,'' J. Acoust. Soc. Am. **35**, 1732–1737.

Carney, L. H. (**1993**). ''A model for the responses of low-frequency auditory-nerve fibers in cat,'' J. Acoust. Soc. Am. **93**, 401–417.
Dau, T., Püschel, D., and Kohlrausch, A. (**1996**). ''A quantitative model of the effective signal processing in the auditory system. I. Model structure,'' J. Acoust. Soc. Am. **99**, 3615–3622.
Dau, T., Kollmeier, B., and Kohlrausch, A. (**1997**). ''Modeling auditory processing of amplitude modulation. II. Spectral and temporal integration,'' J. Acoust. Soc. Am. **102**, 2906–2919.
Durlach, N. I., Braida, L. D., and Ito, Y. (**1986**). ''Towards a model for discrimination of broadband signals,'' J. Acoust. Soc. Am. **80**, 63–72.
Eddins, D. A., Hall, J. W., and Grose, J. H. (**1992**). ''The detection of temporal gaps as a function of frequency region and absolute noise bandwidth,'' J. Acoust. Soc. Am. **91**, 1069–1077.
Eddins, D. A., and Green, D. M. (**1995**). ''Temporal integration and temporal resolution,'' in *Hearing*, edited by B. C. J. Moore (Academic, San Diego), pp. 207–242.
Ellermeier, W. (**1996**). ''Detectability of increments and decrements in spectral profiles,'' J. Acoust. Soc. Am. **99**, 3119–3125.
Florentine, M. (**1986**). ''Level discrimination of tones as a function of duration,'' J. Acoust. Soc. Am. **79**, 792–798.
Formby, C., Heinz, M. G., Luna, C. E., and Shaheen, M. K. (**1994**). ''Masked detection thresholds and temporal integration for noise band signals,'' J. Acoust. Soc. Am. **96**, 102–114.
Formby, C., Ferguson, S. H., and Heinz, M. G. (**1997**). ''Auditory temporal microstructure: Evidence of under- and over-shoot at onset and offset of a narrowband noise masker measured in an off-frequency masked detection task,'' J. Acoust. Soc. Am. **102**, 3161(A).
Formby, C., Heinz, M. G., Ferguson, S. H., and Sherlock, L. P. (**1998**). ''Temporal over- and under-shoot effects accentuate temporal edges at onset and offset of a narrowband masker,'' Abstracts of the 21st Midwinter Meeting of the Association for Research in Otolaryngology, p. 172.
Forrest, T. G., and Green, D. M. (**1987**). ''Detection of partially filled gaps in noise and the temporal modulation transfer function,'' J. Acoust. Soc. Am. **82**, 1933–1943.
Gilkey, R. H. (**1987**). ''Spectral and temporal comparisons in auditory masking,'' in *Auditory Processing of Complex Sounds*, edited by W. A. Yost and C. S. Watson (Erlbaum, Hillsdale, NJ), pp. 26–36.
Glasberg, B. R., and Moore, B. C. J. (**1990**). ''Derivation of auditory filter shapes from notched-noise data,'' Hearing Res. **47**, 103–138.
Grantham, D. W., and Yost, W. A. (**1982**). ''Measures of intensity discrimination,'' J. Acoust. Soc. Am. **72**, 406–410.
Green, D. M. (**1958**). ''Detection of multiple component signals in noise,'' J. Acoust. Soc. Am. **30**, 904–911.
Green, D. M. (**1960**). ''Auditory detection of a noise signal,'' J. Acoust. Soc. Am. **32**, 121–131.
Green, D. M. (**1988**). *Profile Analysis: Auditory Intensity Discrimination* (Oxford University Press, New York).
Green, D. M., McKey, M. J., and Licklider, J. C. R. (**1959**). ''Detection of a pulsed sinusoid in noise as a function of frequency,'' J. Acoust. Soc. Am. **31**, 1446–1452.
Green, D. M., and Swets, J. A. (**1966**). *Signal Detection Theory and Psychophysics* [Wiley, New York, reprinted (1988) by Peninsula, Los Altos, CA].
Green, D. M., Kidd, Jr., G., and Picardi, M. C. (**1983**). ''Successive versus simultaneous comparison in auditory intensity discrimination,'' J. Acoust. Soc. Am. **73**, 639–643.
Heinz, M. G., and Carney, L. H. (**1997**). ''A psychophysiological multi-cue model for the detection of time- and band-limited increments and decrements in noise,'' Abstracts of the 20th Midwinter Meeting of the Association for Research in Otolaryngology, p. 229.
Houtgast, T. (**1972**). ''Psychophysical evidence for lateral inhibition in hearing,'' J. Acoust. Soc. Am. **51**, 1885–1894.
Houtsma, A. J. M., Durlach, N. I., and Braida, L. D. (**1980**). ''Intensity perception XI. Experimental results on the relation of intensity resolution to loudness matching,'' J. Acoust. Soc. Am. **68**, 807–813.
Irwin, R. J., and Kemp, S. (**1976**). ''Temporal summation and decay in hearing,'' J. Acoust. Soc. Am. **59**, 920–925.
Irwin, R. J., and Purdy, S. C. (**1982**). ''The minimum detectable duration of auditory signals for normal and hearing-impaired listeners,'' J. Acoust. Soc. Am. **71**, 967–974.
Kidd, Jr., G., Mason, C. R., Brantley, M. A., and Owen, G. A. (**1989**). ''Roving-level tone-in-noise detection,'' J. Acoust. Soc. Am. **86**, 1310–1317.
Leek, M. R., and Summers, V. (**1993**). ''Auditory filter shapes of normal-hearing and hearing-impaired listeners in continuous broadband noise,'' J. Acoust. Soc. Am. **94**, 3127–3137.
Levitt, H. (**1971**). ''Transformed up–down methods in psychoacoustics,'' J. Acoust. Soc. Am. **49**, 467–477.
Macmillan, N. A. (**1971**). ''Detection and recognition of increments and decrements in auditory intensity,'' Percept. Psychophys. **10**, 233–238.
Macmillan, N. A. (**1973**). ''Detection and recognition of intensity changes in tone and noise: The detection-recognition disparity,'' Percept. Psychophys. **13**, 65–75.
Moore, B. C. J., Oldfield, S. R., and Dooley, G. J. (**1989**). ''Detection and discrimination of spectral peaks and notches at 1 and 8 kHz,'' J. Acoust. Soc. Am. **85**, 820–836.
Moore, B. C. J., and Peters, R. W. (**1997**). ''Detection of increments and decrements in sinusoids as a function of frequency, increment, and decrement duration and pedestal duration,'' J. Acoust. Soc. Am. **102**, 2954–2965.
Oxenham, A. J. (**1997**). ''Increment and decrement detection in sinusoids as a measure of temporal resolution,'' J. Acoust. Soc. Am. **102**, 1779–1790.
Patterson, R. D., and Moore, B. C. J. (**1986**). ''Auditory filters and excitation patterns as representations of frequency resolution,'' in *Frequency Selectivity in Hearing*, edited by B. C. J. Moore (Academic, London), pp. 123–177.
Penner, M. J. (**1978**). ''A power law transformation resulting in a class of short-term integrators that produce time-intensity trades for noise bursts,'' J. Acoust. Soc. Am. **63**, 195–201.
Plack, C. J., and Moore, B. C. J. (**1991**). ''Decrement detection in normal and impaired ears,'' J. Acoust. Soc. Am. **90**, 3069–3076.
Raab, D. H., Osman, E., and Rich, E. (**1963**). ''Effects of waveform correlation and signal duration on detection of noise bursts in continuous noise,'' J. Acoust. Soc. Am. **35**, 1942–1946.
Raab, D. H., and Goldberg, I. A. (**1975**). ''Auditory intensity discrimination with bursts of reproducible noise,'' J. Acoust. Soc. Am. **57**, 437–447.
Rhode, W. S., Oertel, D., and Smith, P. H. (**1983**). ''Physiological response properties of cells labeled intracellularly with horseradish peroxidase in cat ventral cochlear nucleus,'' J. Comp. Neurol. **213**, 448–463.
Rouiller, E. M., and Ryugo, D. K. (**1984**). ''Intracellular marking of physiologically characterized cells in the ventral cochlear nucleus of the cat,'' J. Comp. Neurol. **225**, 167–186.
Schacknow, P. N., and Raab, D. H. (**1976**). ''Noise-intensity discrimination: Effects of bandwidth conditions and mode of masker presentation,'' J. Acoust. Soc. Am. **60**, 893–905.
Scholl, H. (**1962**). ''Über die bildung der Hörschwellen und Mithörschwellen von impulsen,'' Acustica **12**, 91–101.
Shamma, S. A. (**1985**). ''Speech processing in the auditory system II: Lateral inhibition and the central processing of speech evoked activity in the auditory nerve,'' J. Acoust. Soc. Am. **78**, 1622–1632.
Shamma, S. A. (**1989**). ''Spatial and temporal processing in central auditory networks,'' in *Methods in Neuronal Modeling*, edited by C. Koch and I. Segev (MIT Press, Cambridge).
Smith, R. L., and Zwislocki, J. J. (**1975**). ''Short-term adaptation and incremental responses of single auditory-nerve fibers,'' Biol. Cybern. **17**, 169–182.
Spiegel, M. F. (**1979**). ''The range of spectral integration,'' J. Acoust. Soc. Am. **66**, 1356–1363.
Viemeister, N. F., and Bacon, S. P. (**1988**). ''Intensity discrimination, increment detection, and magnitude estimation for 1-kHz tones,'' J. Acoust. Soc. Am. **84**, 172–178.
Viemeister, N. F., and Wakefield, G. H. (**1991**). ''Temporal integration and multiple looks,'' J. Acoust. Soc. Am. **90**, 858–865.
Walton, J. P., Frisina, R. D., Ison, J. R., and O'Neill, W. E. (**1997**). ''Neural correlates of behavioral gap detection in the inferior colliculus of the young CBA mouse,'' J. Comp. Physiol. **181**, 161–176.
Zwicker, E. (**1956**). ''Die elementaren Grundlagen zur Bestimmung der Informationskapazität des Gehörs,'' Acustica **6**, 365–381.
Zwicker, E., and Fastl, H. (**1990**). *Psychoacoustics* (Springer, New York).

Vowel-specific effects in concurrent vowel identification[a)]

Alain de Cheveigné[b)]
Laboratoire de Linguistique Formelle, CNRS/Université Paris 7, 2 place Jussieu, case 7003, 75251, Paris, France and ATR Human Information Processing Research Laboratories, 2-2 Hikaridai, Seika-cho, Soraku-gun, Kyoto 619-02, Japan

(Received 5 May 1998; accepted for publication 15 March 1999)

An experiment investigated the effects of amplitude ratio (−35 to 35 dB in 10-dB steps) and fundamental frequency difference (0%, 3%, 6%, and 12%) on the identification of pairs of concurrent synthetic vowels. Vowels as weak as −25 dB relative to their competitor were easier to identify in the presence of a fundamental frequency difference (ΔF_0). Vowels as weak as −35 dB were not. Identification was generally the same at $\Delta F_0 = 3\%$, 6%, and 12% for all amplitude ratios: unfavorable amplitude ratios could not be compensated by larger ΔF_0's. Data for each vowel pair and each amplitude ratio, at $\Delta F_0 = 0\%$, were compared to the spectral envelope of the stimulus at the same ratio, in order to determine which spectral cues determined identification. This information was then used to interpret the pattern of improvement with ΔF_0 for each vowel pair, to better understand mechanisms of F_0-guided segregation. Identification of a vowel was possible in the presence of strong cues belonging to its competitor, as long as cues to its own formants $F1$ and $F2$ were prominent. ΔF_0 enhanced the prominence of a target vowel's cues, even when the spectrum of the target was up to 10 dB below that of its competitor at all frequencies. The results are incompatible with models of segregation based on harmonic enhancement, beats, or channel selection. [S0001-4966(99)01307-7]

PACS numbers: 43.66.Ba, 43.71.An, 43.71.Es [WS]

INTRODUCTION

Our everyday environment contains multiple acoustic sources, some of which we must attend to, others which we must ignore. Their amplitudes are rarely the same. With luck, the target might have a greater amplitude than its competitors, and be easy to hear. Or, at least such might be the case during some *time interval* that the auditory system can attend to, or within some *spectral region* that it can isolate by simple filtering. However, it often occurs that a target is weaker than the interference most of the time, and in most frequency regions, in which case the auditory system must employ a more sophisticated process to segregate one from the other.

Experiments that investigate the usefulness of harmonicity or ΔF_0 cues are usually performed with pairs of vowels of approximately equal amplitude (see de Cheveigné *et al.*, 1995, 1997b for reviews). Exceptions are an experiment by McKeown (1992), who introduced systematic intervowel amplitude differences in addition to the ΔF_0 parameter, similar experiments by Meyer and Berthommier (1995), and a series of experiments that used an adaptive paradigm to determine identification thresholds (Demany and Semal, 1990; Assmann and Summerfield, 1990; Summerfield, 1992; Summerfield and Culling, 1992; Culling, Summerfield, and Marshall, 1994; Culling and Summerfield, 1995). Thresholds with that paradigm ranged typically between −5 and −25 dB, depending upon the condition, demonstrating that relatively accurate identification (70%) of weak targets is possible, especially when segregation cues are present.

In a recent study (de Cheveigné *et al.*, 1997a), we performed a constant-stimuli experiment similar to that of McKeown, with ΔF_0's of 0% and 6% and target/competitor amplitude ratios of −20 to 20 dB in 10-dB steps. The effects of ΔF_0 turned out to be particularly strong for weak targets. The experiment to be reported here is an extension of that experiment to a wider range of amplitude ratios (−35 to 35 dB, in 10-dB steps), and a larger set of ΔF_0's (0%, 3%, 6%, 12%). In the previous experiment, vowels were synthesized in ''Klatt phase,'' which simulates the pattern of starting phases of natural vowels (Klatt, 1980). Corresponding partials had different starting phases, resulting in a complex pattern of vector summation at $\Delta F_0 = 0\%$. In the current experiment, corresponding partials of both vowels are given identical starting phases, with the result that the spectral envelopes of double-vowel stimuli are easier to predict. Beyond a general curiosity about performance over this larger parameter space, the experiment was motivated by several specific questions. (a) Is there a minimum target/competitor ratio below which a ΔF_0 is ineffective? (b) Is there a tradeoff between amplitude ratio and ΔF_0? In other words, might a large ΔF_0 be effective at target levels so low that a small ΔF_0 is ineffective? (c) What spectral features determine vowel identification in this situation? When the relative amplitude is varied, the spectrum of the stimulus varies between that of one vowel and that of the other. Features that allow identification of the first vowel (whatever they may be: formants, center of gravity, etc.) fade away, while those that allow identification of the other are strengthened. By correlating these changes with response rates, it is possible to know which cues are necessary for vowel identification. The pattern of errors itself may be instructive. The set of detailed responses for individual vowel pairs is thus a good test bed

[a)]Part of this work was described in an ATR technical report (de Cheveigné, 1997a).
[b)]Electronic mail: cheveign@ircam.fr

TABLE I. Formant frequencies (Hirahara and Kato, 1992) and bandwidths (BW).

	/a/	/e/	/i/	/o/	/u/	BW
$F1$	750	469	281	468	312	90
$F2$	1187	2031	2281	781	1219	110
$F3$	2595	2687	3187	2656	2469	170
$F4$	3781	3375	3781	3281	3406	250
$F5$	4200	4200	4200	4200	4200	300

for models of vowel perception, in the footsteps of Assmann and Summerfield (1989).

This paper is based on one experiment, the results of which are described in three parts. First, responses are averaged over vowel pairs and analyzed as a function of ΔF_0 and target/competitor amplitude ratio. Next, response rates for individual vowel pairs at $\Delta F_0 = 0\%$ are compared to their spectral envelopes, to determine what spectral features are important for perception of vowels in competition. Finally, the *increase with* ΔF_0 of the percentage of correct vowel responses is analyzed for each vowel pair. The aim is to make sense of ΔF_0 effects based on what the previous analysis told us about cues to identification. Such detailed analysis should provide insight as to the nature of F_0-guided segregation.

I. METHODS

Methods were similar to those of de Cheveigné *et al.* (1997a, b). Stimuli were based on synthetic tokens of Japanese vowels /a/, /e/, /i/, /o/, /u/, with frequencies and bandwidths listed in Table I [Single vowels are denoted between slashes (/a/), and so are vowel pairs (/ae/) when the target/competitor relationship is unimportant. When necessary to distinguish a target and a competitor, the vowels are separated by a slash (a/e) (target/competitor).] Vowels were synthesized at a sampling rate of 20 kHz. Their duration was 270 ms, including 20-ms raised-cosine onsets and offsets (250-ms ''effective duration'' between-6-dB points). Fundamental frequencies (F_0's) ranged from 124 to 140 Hz. The starting phase of each harmonic was given a ''random'' value that was the same for all vowels in all conditions. Such a random phase pattern produces vowel waveforms that are less peaky than sine, cosine, or Klatt phase (produced by the formulas of Klatt, 1980). All vowel tokens were scaled to the same standard rms amplitude after synthesis.

Vowels were paired, one vowel was scaled with respect to the other by a factor chosen between -35 and 35 dB in 10-dB steps, the two were added, and their sum was scaled to the standard rms amplitude. Double-vowel stimuli are thus weighted sums of their constituents. At $\Delta F_0 = 0$, the starting phase of each harmonic is the same in both vowels, and therefore its amplitude in the sum can be calculated without considering complex phase-dependent vector summation. The double-vowel spectral envelope is therefore the weighted sum of the individual vowel spectra, with the same weighting factors as the vowels themselves. This is illustrated for the vowel pair /oe/ in Fig. 1(a). Thick lines represent spectra of individual vowels, and each of the eight thin lines represents the spectrum of a weighted sum. Some are

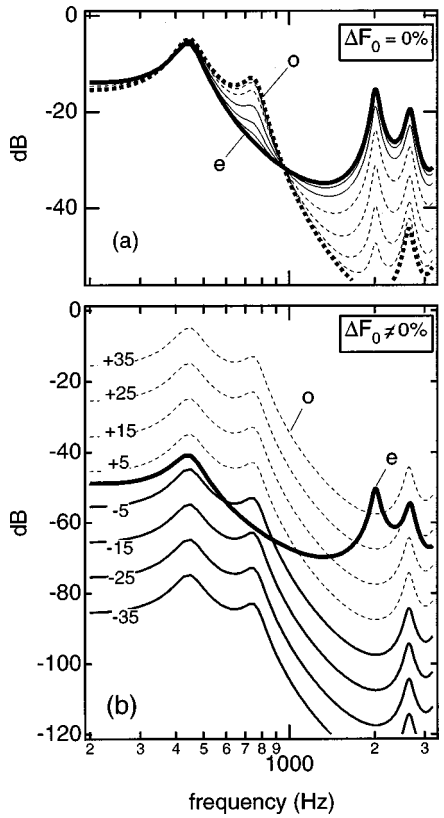

FIG. 1. (a) Spectral envelopes of single vowels /o/ and /e/ (thick lines) and weighted sums with amplitude ratios ranging from -35 to 35 dB in 10-dB steps (thin lines). Dotted lines correspond to stimuli dominated by /o/, full lines to stimuli dominated by /u/. In some places the thin lines are indistinct because they merged with the thick lines. Single vowels were not used as stimuli. The plot includes the first three formants ($F1$, $F2$, and $F3$), but excludes $F4$ and $F5$. (b) Spectral envelopes determining the amplitudes of partials of an /oe/ double vowel when $\Delta F_0 \neq 0\%$. Partials belonging to the harmonic series of /e/ are determined by the thick line, and those belonging to /o/ by the thin lines for each value of the o/e amplitude ratio. Dotted lines correspond to stimuli dominated by /o/, full lines to stimuli dominated by /e/. The origin of the ordinate scale is arbitrary: what counts is the relative levels between envelopes.

indistinct in places because they merged with one or the other thick lines. As the amplitude ratio varies from -35 to 35 dB, the spectral envelope of the pair gradually metamorphoses from that of one vowel to that of the other. Another example is the vowel pair /ou/ in Fig. 2(a). Single vowels (represented as thick lines) were not used as stimuli.

At $\Delta F_0 \neq 0$, the spectrum of the vowel pair is made up of two interleaved harmonic series, each a scaled version of the spectrum of a constituent vowel. This is illustrated for vowel pair /oe/ in Fig. 1(b). The thick line determines the amplitude of partials of /e/, and the thin lines determine that of partials of /o/ for each of the values of the o/e amplitude ratio. Dotted lines are for positive values of the o/e ratio, and full lines for negative values. The origin of the ordinate in this plot is arbitrary: of interest is the relative amplitude of one vowel versus the other. Notice for example that when the o/e amplitude ratio is -35, -25, or -15 dB, the spectrum is dominated everywhere by /e/. For other values, it is dominated by the first vowel in some places, and by the second in others. It is never dominated by /o/ everywhere. Another example is the vowel pair /ou/ in Fig. 2(b). These two vowel

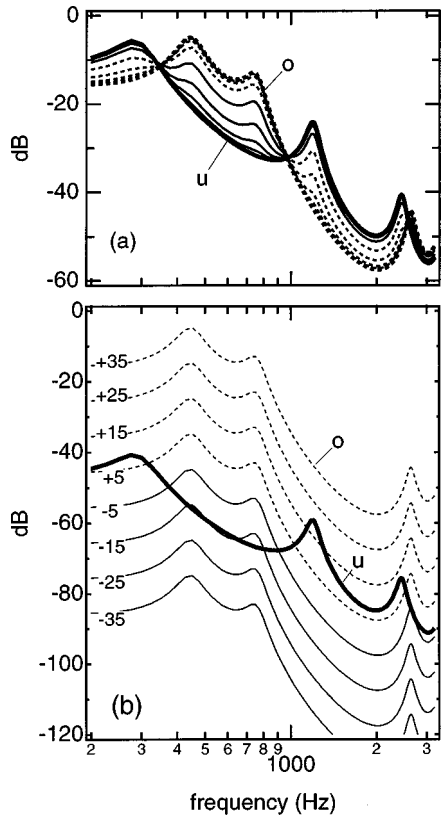

FIG. 2. Same as Fig. 1, for /ou/.

pairs are used to discuss pair-wise results in Sec. II. The other eight vowel pairs are described in the Appendix.

Fundamental frequencies were chosen by pairs arithmetically centered on 132 Hz, to obtain ΔF_0's of approximately 12% (124, 140 Hz), 6% (128, 136 Hz), 3% (130, 134 Hz), and 0% (132 Hz). F_0's were placed symmetrically about 132 Hz to avoid any influence of the mean F_0, and all conditions were repeated with both F_0 orders (low/high and high/low).

Vowels within a pair were always different. There were a total of (vowel pair=/ae/, /ai/, /ao/, /au/, /ei/, /eo/, /eu/, /io/, /iu/, /ou/)×(amplitude ratio=−35, −25, −15, −5, 5, 15, 25, 35 dB) ×(2F_0 orders)×(ΔF_0=0%, 3%, 6%, 12%)=640 double-vowel stimuli within a stimulus set. Ideally, the stimulus set should have contained a proportion of single vowels to make it consistent with the description made to the subjects (see below). However, the 25- and 35-dB amplitude ratio conditions are very similar to single vowels, and *stricto sensu* single vowels were omitted to reduce the stimulus set size.

Subjects were 15 Japanese students (seven male and eight female, aged 18 to 22 years) recruited for a series of ten experiments on concurrent vowel identification and paid for their services. The experiment described in this paper was the third of that series. The subjects were told that a stimulus could be either a single vowel, or two simultaneous vowels that were not the same, and they were instructed to report freely one or two vowels according to what they heard. There was no feedback. Stimuli were presented diotically via earphones, at a level of 63 to 70 dBA SPL (depending on the pair).

The response for each double-vowel stimulus was scored twice: each vowel in turn was nominated the ''target'' and the other the ''competitor,'' and then the roles were reversed. A target was deemed identified if its name was among the one or two vowels reported by the subject. The proportion of vowels correctly identified (constituent-correct, or target-correct identification rate) was calculated for each condition. The average number of vowels reported per stimulus was also recorded. For pair-wise analysis, response rates were recorded for all five vowels: the two constituent vowels and the three not present in the stimulus but sometimes reported nevertheless.

II. RESULTS

A. Results averaged over pairs

Identification rates were submitted to a repeated-measures analysis of variance (ANOVA) with factors amplitude ratio and ΔF_0. Probabilities reflect, where necessary, a correction factor applied to the degrees of freedom to compensate for the correlation of repeated measures (Geisser and Greenhouse, 1958). Amplitude ratio was highly significant [$F(7,98)=420.12$, $p<0.0001$, $GG=0.34$], as was ΔF_0 [$F(3,42)=96.32$, $p<0.0001$, $GG=0.45$]. Their interaction was also highly significant [$F(21,294)=27.60$, $p<0.0001$, $GG=0.20$] (a trivial consequence of the fact that the scores had a limited range). Identification rates are plotted in Fig. 3(a), together with rates measured in a previous experiment with different subjects (de Cheveigné *et al.*, 1997a). Results were similar between experiments, except that weak targets at $\Delta F_0=0\%$ were better identified in the present experiment. Identification rates increased as a function of target/competitor amplitude ratio. ΔF_0 had no measurable effect at −35, 15, 25, and 35 dB, but at all other amplitude ratios identification increased with ΔF_0. The greatest increase was between 0% and 3%. The step from 3% to 6% was significant at −15 dB [$F(1,294)=19.81$, $p=0.007$, $GG=0.20$], but not at other ratios. The difference between 6% and 12% was not significant at any ratio.

With respect to the first two questions raised in the Introduction, it can be said: (a) ΔF_0 effects exist down to a target/competitor ratio of −25 dB, but at −35 dB they are too small to be measurable. (b) At all amplitude ratios, large ΔF_0's (6% or 12%) are no more effective than small ΔF_0's (3%). The plateau beyond 3% or 6% in the improvement of identification with ΔF_0, previously observed for equal amplitude vowels, persists at target/competitor ratios down to −25 dB. There is no tradeoff between ΔF_0 and amplitude ratio.

The average number of vowels reported per stimulus was also submitted to a repeated-measures ANOVA with factors amplitude ratio and ΔF_0. Amplitude ratio was highly significant [$F(3,42)=83.32$, $p<0.0001$, $GG=0.40$], as was ΔF_0 [$F(3,42)=42.57$, $p<0.001$, $GG=0.42$] and their interaction [$F(9,126)=16.11$, $p<0.0001$, $GG=0.31$]. The number of vowels reported is plotted in Fig. 3(b), together with data from the previous study (de Cheveigné *et al.*, 1997a). The number of vowels reported was greater at 3% than 0% at all amplitude ratios except 35 dB. The increment between

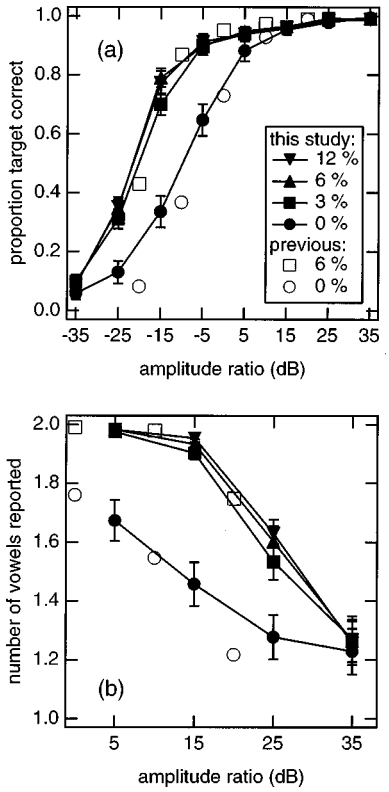

FIG. 3. (a) Target identification rate as a function of target/competitor amplitude ratio, for ΔF_0's of 0%, 3%, 6%, and 12%. Error bars represent ±one standard error of the mean. Open symbols are from a previous study (de Cheveigné, 1997a). (b) Average number of vowels reported per stimulus as a function of the amplitude ratio between vowels.

3% and (6%, 12%) was not significant, except at 25 dB [$F(1,126)=8.47$, $p=0.027$, $GG=0.31$]. The increment between 6% and 12% was not significant at any ratio.

B. Pair-wise results

Originally, the experiment was designed to exploit data averaged over vowel pairs (as in most studies of this type). However the detailed vowel-pair-specific responses can be used to find what features underlie the perception of steady-state vowels (at least when they compete with other vowels). Response rates at each amplitude ratio can be compared to the shape of the spectrum at the same ratio, and responses for each vowel can be related to the presence and strength of particular spectral features. This proposal has at least three weaknesses: (a) The amount of information is considerable and expensive to describe. (b) Pair-specific data are less reliable than average data (30 responses per data point vs 600), and reliability itself is difficult to evaluate. (c) The spectral envelope, with respect to which the data are analyzed, may not be representative of spectral features available to the auditory system. These weaknesses are counterbalanced by the insight that vowel-pair-specific patterns provide concerning vowel identification.

To keep the description within reasonable limits, two pairs (/oe/ and /ou/) are selected for detailed presentation. The latter (/ou/) is typical of the majority of vowel pairs as far as ΔF_0 effects are concerned, whereas the former combines two exceptional patterns: o/e (/o/ target and /e/ background) showed the largest increase in correctly identified target vowel as a function of ΔF_0, whereas e/o showed the smallest. The pair /ou/ illustrated a previous modeling study (de Cheveigné, 1997b), and both pairs were described in detail in a previous experimental study (de Cheveigné *et al.*, 1997a). Other pairs are described in the Appendix.

Patterns of excitation along the basilar membrane (Moore and Glasberg, 1983) are an attractive alternative to spectral envelopes. They show *less* detail than spectral envelopes at high frequencies because of limited spectral resolution and/or masking, and *more* detail at low frequencies where individual harmonics are resolved by the ear. Spectral envelopes were nevertheless, preferred for the following reasons. (a) Formant positions, that are known to correlate well with vowel quality, are evident in spectral envelopes. (b) Excitation patterns display an F_0-dependent structure at low frequencies that makes their plots less legible. Vowel identification is known to be relatively insensitive to F_0, suggesting that this sort of detail is not helpful in the present discussion. (c) Excitation patterns embody one particular form of auditory processing, but there may be others that they do not reflect as well (for example, vowel quality might be derived from time-domain cues, as suggested by Meddis and Hewitt, 1992). A description closer to acoustics implies less commitment in this respect.

1. ANOVAs for the 35-dB subset

Prior to the description of pair-wise results, a series of ANOVAs was performed on a subset of conditions to derive a rough estimate of the variability of responses. Analysis of variance of the full data set was impractical because of its size and complexity, and possibly unjustified because of the severe inhomogeneity of variances (many data points were at ceiling or floor). In vowel pairs with a 35-dB amplitude ratio, the weaker vowel affects perception in a negligible way: responses do not vary according to its identity, and rates are hardly affected by ΔF_0 [Fig. 3(a)]. It is reasonable to assume that these stimuli are essentially identical to the stronger vowel by itself. Each vowel appeared as the 35-dB-stronger vowel four times in the stimulus set, and one can take advantage of this repetition to get an estimate of the variability of responses in these conditions.

Five independent ANOVAs were performed, one for each response category (vowel). For each, the dependent variable was the proportion of trials for which (a) that vowel was reported, and (b) the stronger vowel was some other vowel. The nature of the stronger vowel was the independent factor (four levels), while the weaker vowel served as a random factor (four levels). Results are given in Table II. The lower two lines of the table show that, with the exception of /i/, the number of times a spurious vowel was reported depended significantly ($p=0.05$) on the nature of the stronger vowel. The pattern of means is discussed later. The important thing to note for now is that the *standard deviation* of responses ranged between 3% and 5.5%. These values hold for the 35-dB ratio, but they will nevertheless be considered representative of variability of responses rates of weak target vowels and spurious vowels at other ratios. Based on this estimate, one can be sure that the effects described in this

TABLE II. Response rates for each of the five vowels, at a 35-dB amplitude ratio and $\Delta F_0 = 0\%$. The stronger vowel was reported on all trials: rates shown are for each of the four other vowels that could eventually be reported together with it. They are given as a function of the nature of the stronger vowel. The significance of that factor is tested by a set of ANOVAs, one per column, using the ''weaker vowel'' factor as a random factor (lower two lines). Standard deviations are calculated from the part of variance that is not accounted for by the ''stronger vowel'' factor.

Response vowel	/a/	/e/	/i/	/o/	/u/
stronger=/a/	···	7.1%	3.6%	0.9%	6.3%
stronger=/e/	8.0%	···	8.9%	1.8%	18.8%
stronger=/i/	4.5%	1.8%	···	0.0%	18.8%
stronger=/o/	0.0%	0.1%	2.7%	···	14.3%
stronger=/u/	13.4%	0.1%	3.6%	8.9%	···
standard deviation	3.62%	3.02%	3.52%	3.04%	5.48%
$F(3,3)$	9.83	3.95	2.6	7.19	4.61
p	0.0015	0.036	0.1	0.005	0.023

paper (always greater than 10%, and often consistent across several similar conditions) are reliable.

2. Pair-wise results at $\Delta F_0 = 0\%$

Results are presented in this section for two vowel pairs, /oe/ and /ou/. The other eight are described in the Appendix. Responses to the two constituent vowels and to the three vowels not present in the stimulus (spurious responses) are considered for each pair. For the vowel pair /oe/, response rates for each of the five vowels are plotted in Fig. 4(a). Thick lines represent the proportion of responses for which the constituent vowels were correctly identified. Thin lines represent response rates for the three other vowels.

Let us first consider responses for the first constituent, /o/. Identification was poor up to an o/e amplitude ratio of −15 dB, and good at 5 dB and above. By comparing responses for each value of the abscissa in Fig. 4(a) with the corresponding envelope in Fig. 1(a), changes in the spectrum can be related to changes in identification. $F1$ is the same for both vowels, and the shape and absolute amplitude of that part of the spectrum hardly change across conditions. Changes in identification can therefore be attributed to other features, presumably in the $F2$ region of /o/.

The spectral envelope for an o/e ratio of 5 dB (for which identification was good) is the lowest dotted line near formant $F2$ of /o/ in Fig. 1(a). There is quite a clear peak at $F2$ of /o/, and below 1 kHz the spectrum hardly differs from that of /o/. However, at 2 kHz there is a clear peak at $F2$ of /e/ that is not usually found in the spectrum of /o/. The presence of this spurious cue did not prevent /o/ from being identified (the cue did not lack perceptual prominence, judging from the high identification rates for /e/ at the same ratio). This illustrates a first principle: identification of a vowel is not prevented by the mere presence of cues belonging to another vowel.

Both vowels of the /oe/ pair were simultaneously identified over a range of relative amplitudes (5 and 15 dB), despite the fact that both vowels had the same $F1$. This illustrates a second principle: a formant peak may be shared between vowels. The rule of exclusive allocation (Bregman, 1990) does not apply. Bregman noted many other exceptions to this rule.

The spectral envelope for an o/e ratio of −5 dB (for which identification fell to 50%) is the uppermost full line near $F2$ of /o/. The envelope for −15 dB (for which identification fell to 20%) is the next-to-uppermost. The drop in identification rate was presumably caused by the fading away of the spectral peak at $F2$ of /o/. This illustrates a third principle: identification of a vowel requires the presence of cues to both its formants $F1$ and $F2$. The spectrum near $F2$ of /e/ hardly changed between these conditions: the drop in identification of /o/ had nothing to do with competition from cues to /e/.

Let us now consider responses for the second constituent vowel, /e/. Identification was relatively poor at o/e ratios of 25 and 35 dB, and relatively good at 15 dB and below. Referring to Fig. 1, an o/e ratio of 15 dB corresponds to the next-to-uppermost dotted line near $F2$ of /e/. Ratios of 25 and 35 dB correspond to the lowest dotted lines. The spectrum hardly differs between conditions in the common $F1$ region, or near formant $F2$ of the competing vowel /o/.

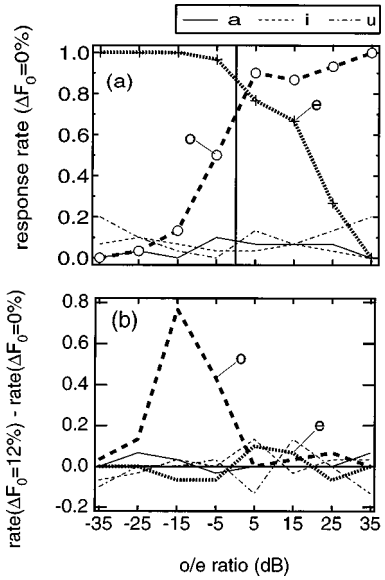

FIG. 4. (a) Response rates for vowel pair /oe/ as a function of the o/e amplitude ratio, for the constituent vowels /o/ and /e/ (thick lines) and the three vowels not in the stimulus (/a/, /i/, /u/). (b) Difference in response rates between $\Delta F_0 = 12\%$ and $\Delta F_0 = 0\%$.

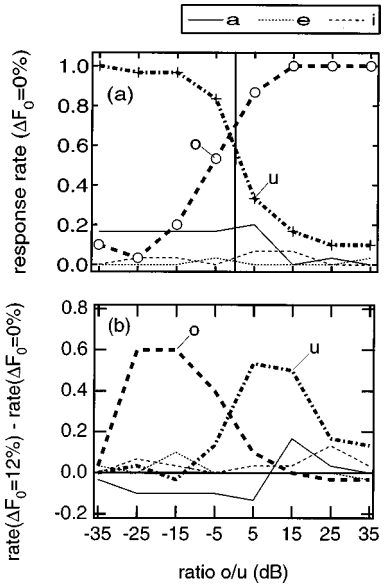

FIG. 5. Same as Fig. 4, for vowel pair /ou/.

Rather, identification seems to have varied with the spectral changes in the region of $F2$ of /o/. It is not certain what caused the loss of perceptual prominence of the $F2$ cue: upward masking from the lower part of the spectrum, masking by ambient noise, or some other cause.

Similar comparisons can be made for the pair /ou/, between responses [Fig. 5(a)] and spectral envelopes [Fig. 2(a)]. This pair is somewhat atypical in that the range over which both vowels are identified is rather restricted. There is a tradeoff between responses as if, contrary to other vowel pairs, simultaneous perception of both vowels were difficult.

It is interesting to note the large proportion of spurious /a/ responses for o/u amplitudes ranging from -35 to 5 dB. Referring to Fig. 2(a), it appears that the $F2$ formants of /o/ and /u/ were being interpreted as formants $F1$ and $F2$ of /a/ (see Fig. A1 for a picture of /a/, or Table I for its formant frequencies). This interpretation coexisted with /o/ responses (at low u/o ratios) and /u/ responses (at higher u/o ratios), implying that the same formant was being perceptually shared between /a/ and one of the constituent vowels (another counterexample for the rule of exclusive allocation). According to which vowel was reported in addition to /a/, this interpretation left the $F1$ of the other vowel ''orphaned;'' that is, not interpreted as belonging to a vowel. It is conceivable that this is what limited the number of times this otherwise plausible interpretation was made.

A final detail to notice is the high proportion of /u/ responses at high o/u ratios. This would be ascribed to chance if it weren't that /u/ responses were common for all pairs dominated by /o/ (Table II). Such /u/ responses were also common for pairs dominated by /e/ or /i/. The effect is easier to explain for /i/ (/u/ and /i/ have similar $F1$'s) than for /o/ or /e/: nothing in their spectrum seems to support perception of /u/.

As detailed in the Appendix, the three ''principles'' hold for most other vowel pairs. Identification is not disrupted by the mere presence of spurious cues, the same formant cue can be shared by both vowels, and identification of a vowel requires that cues for both its $F1$ and $F2$ be prominent. However, it is not clear what determines the prominence of a formant cue. Referring back to o/e when the amplitude ratio was reduced from 5 to -15 dB, the peak at $F2$ of /o/ underwent at least three changes: its absolute amplitude was reduced, its amplitude relative to neighboring peaks was reduced, and its local prominence (''sharpness,'' and height relative to the neighboring spectrum) was reduced (Fig. 1). The first factor is unlikely to be decisive (see the Appendix), but it is harder to decide between the other two factors.

3. Pair-wise patterns of ΔF_0 effects

The previous description of vowel identification at $\Delta F_0 = 0\%$ constitutes a good backdrop against which to analyze vowel-specific patterns of ΔF_0 effects. Results are again presented in detail for vowel pairs /oe/ and /ou/. For the vowel pair /oe/, the *difference* in response rates between $\Delta F_0 = 12\%$ and $\Delta F_0 = 0\%$ is plotted in Fig. 4(b). The difference is plotted as a function of the o/e amplitude ratio for both component vowels (/o/ and /e/, thick lines) as well as for the other three vowels (/a/, /i/, /u/, thin lines). A positive value implies that the response rate for that vowel increased when a ΔF_0 was introduced. These plots may be compared to the ''baseline'' rates measured at $\Delta F_0 = 0\%$ for the same pair [Fig. 4(a)].

Let us consider first the vowel /o/. At an o/e amplitude ratio of -15 dB, the proportion of stimuli for which /o/ was reported increased by almost 0.8, the largest effect of all vowel pairs. As /o/ has the same $F1$ frequency as its competitor, it was argued previously that identification was limited by the (lack of) prominence of cues to its $F2$. The spectral envelope of the vowel pair at $\Delta F_0 = 0\%$ is shown in Fig. 1(a). At an o/e ratio of -15 dB, the envelope shows a modest shoulder at $F2$ of /o/ (second-to-topmost full line). Apparently the ΔF_0 increased the prominence of this cue, allowing /o/ to be identified on almost all trials. ΔF_0 was also effective at -5 dB, but the effect is smaller because of a ceiling effect. It was also ineffective at -25 dB, presumably because the cue was too weak to be saved by the ΔF_0.

Figure 1(b) shows the spectral envelopes that determine the relative amplitudes of partials belonging to the two harmonic series that make up the double vowel at $\Delta F_0 \neq 0\%$. At an o/e amplitude ratio of -15 dB, the spectral envelope of /o/ at $F2$ is slightly below that of its competitor (-1.7 dB), and at -5 dB it peaks 8.3 dB above its competitor's envelope. The ΔF_0 was effective in both situations, but not at -25 dB when $F2$ of /o/ peaked at -11.7 dB below the envelope of its competitor. This gives a first hint of the conditions under which a ΔF_0 may be effective. A more complete discussion follows later.

Let us now consider the vowel /e/. The e/o target/competitor pair was exceptional in showing *no* increase of response rate with ΔF_0 [thick dotted line in Fig. 4(b)]. The lack of improvement for /e/ may be explained in at least two ways. First, the $F2$ of /e/ is prominent whatever the amplitude ratio (Fig. A1), and has little to gain from ΔF_0. Indeed, the /e/ response rate at $\Delta F_0 = 0\%$ was relatively high at all amplitude ratios. Second, its frequency is relatively high

(2031 Hz). Hypothetical within-channel segregation mechanisms (de Cheveigné, 1997b) might be less effective at higher frequencies.

For the vowel pair /ou/, the difference in response rates between $\Delta F_0 = 12\%$ and $\Delta F_0 = 0\%$ is plotted in Fig. 5. Let us consider first the vowel /o/. The ΔF_0 effect was negligible at -35 dB. It was strong at o/u ratios of -25 and -15 dB, and weaker for higher ratios because of ceiling effects. The spectral envelope of the vowel pair at $\Delta F_0 = 0\%$ is shown in Fig. 2(a). $F1$ and $F2$ of /o/ show up as shoulders that are modest at -15 dB (second-to-topmost full line), and even more modest at -25 dB. Apparently the ΔF_0 increased their prominence, allowing /o/ to be identified on 60% of all trials at -25 dB, and 80% at -15 dB.

Figure 2(b) shows the spectral envelopes that determine the harmonic series of the constituent vowels at $\Delta F_0 \neq 0\%$. At an o/u amplitude ratio of -15 dB the $F1$ and $F2$ of /o/ dominate the interformant valley of the envelope of /u/ by 1 and 3.7 dB, respectively. At -25 dB, they peaked at 9 and 6.3 dB, respectively, *below* that envelope, but ΔF_0 was nevertheless effective. It was, however, ineffective at -35 dB, where $F1$ and $F2$ of /o/ peaked, respectively, at 19 and 16.3 dB below their competitor's envelope.

Let us consider next the vowel /u/. The ΔF_0 effect was strong at o/u ratios of 5 and 15 dB, and weaker at lower o/u ratios because of the ceiling effect. For higher ratios (weaker /u/), the effect was also small. The spectral envelope of the vowel pair at $\Delta F_0 = 0\%$ is shown in Fig. 2(a). $F1$ and $F2$ of /u/ show up as small peaks at an o/u ratio of 5 dB, and as modest shoulders at 15 dB (topmost and second-to-topmost dotted lines near these formants). These cues are even more modest at 25 and 35 dB. Evidently the ΔF_0 increased their perceptual prominence. Referring to Fig. 2(b), at an o/u amplitude ratio of 5 dB, the $F1$ and $F2$ of /u/ dominate the envelope of /o/ by 3.4 and 14.7 dB, respectively. At 15 dB, $F1$ peaked at 6.6 dB below the envelope of /o/, and $F2$ at 4.7 dB above it.

It is interesting to note that ΔF_0 reduced the number of spurious /a/ responses at o/u ratios of -25 to 5 dB. This might be explained in two ways. According to one, when formants $F2$ of /o/ and /u/ are excited with different F_0's, they are harder to group together as formants $F1$ and $F2$ of /a/. According to the other, ΔF_0 increased the prominence of the $F1$ of /u/ that would be orphaned at -25, -15, and -5 dB, or that of $F1$ of /o/ that would be orphaned at 5 dB. The latter explanation is favored later on in the paper. At an o/u ratio of 15 dB, the proportion of /a/ responses *increased* with ΔF_0. This is probably a consequence of the increased prominence of $F2$ of /u/, interpreted as $F2$ of /a/.

Patterns of ΔF_0 effects for other pairs are detailed in the Appendix.

III. DISCUSSION

Results averaged over pairs were similar to those found in a previous experiment (de Cheveigné, 1997a). ΔF_0 increased both the average number of vowels reported and the proportion of vowels correctly identified, particularly for the weaker vowel of each pair. New is the observation that ΔF_0 effects were measurable down to -25 dB (-20 dB in the previous study), but not -35 dB. New also is the observation that response rates were roughly the same at ΔF_0's of 3%, 6%, and 12%, whatever the amplitude ratio. There was no tradeoff between ΔF_0 and amplitude ratio: a less favorable ratio could not be compensated by a larger ΔF_0. The ΔF_0 effect was greatest at -15 dB, both on average and for most vowel pairs, which justifies the choice of this ratio to reduce ceiling effects in this kind of experiment.

With some exceptions, pair-wise patterns of ΔF_0 effects were similar across vowel pairs. Identification usually improved over a range of target/competitor ratios (for example, -25 to -5 dB for o/u), which argues for the usefulness of this cue in everyday life. The pair-wise results may be interpreted with respect to various hypotheses and theories of sound organization and segregation.

The asymmetry of effects of ΔF_0 on both vowels of /oe/ is one striking exception to the auditory scene analysis rule, according to which effects of primitive segregation should be symmetric (Bregman, 1990). A similar exception was found in the identification of pairs of harmonic and inharmonic vowels (de Cheveigné *et al.*, 1995). Another principle, that of ''exclusive allocation,'' was also violated in the case of vowels that shared a formant but were nevertheless both well identified. Bregman (1990) noted many other exceptions to this rule.

Computer models have been proposed to ''segregate'' sound objects based on a two-dimensional time-frequency map. A first dimension (tonotopic) is an index into a filter bank representing cochlear filtering, and the second dimension is time. Spectro-temporal regions are assigned to different sources based on periodicity information (often estimated from the autocorrelation function). In response to a mixture of periodic sounds, the map may show regions that are dominated by one period or another. The map is partitioned on the basis of this information and the parts attributed to the various sounds (Weintraub, 1985; Cooke, 1991; Brown, 1992; Meddis and Hewitt, 1992; Ellis, 1996). Many conditions were found where the spectrum was *entirely* dominated by one vowel, and a partition was therefore not possible. Such models fail in those conditions and cannot explain the strong ΔF_0 effects that were observed.

Beats between partials of both vowels have been proposed to explain the effects of small ΔF_0's (Assmann and Summerfield, 1994; Culling and Darwin, 1994). In previous studies, we found evidence that weakens this hypothesis (de Cheveigné *et al.*, 1995, 1997a, b). The present study adds the observation that, for many vowel pairs, ΔF_0 effects are not greatest at amplitude ratios where beats have maximal amplitude near target formants. Effects are instead large at ratios for which the strongest beats should occur in regions unrelated to formant peaks.

In a previous study, it was speculated that a ''multiplicity'' cue might encourage subjects to report two vowels, and thus indirectly increase correct response rates in difficult conditions (such as low target/competitor ratio) for which cues to the *identity* of the weaker vowel are hard to obtain (de Cheveigné *et al.*, 1997a,b). The lack of any example of a uniform increase in response rate of all four vowels (distinct from the stronger one) argues against this hypothesis.

Across-spectrum grouping by F_0 is an attractive hypothesis. Formants belonging to the same vowel might be grouped by common F_0, and thus segregated from those of a competitor with a different F_0. The data do not support this hypothesis. Consider for example a target vowel that shares a formant with a stronger competing vowel. The F_0 of the common formant is that of the stronger vowel, and it therefore differs from the F_0 of the weak vowel's other formant when $\Delta F_0 \neq 0\%$. This should prevent correct grouping and produce a drop in identification, whereas an improvement was observed instead. Another example was found in the Appendix: for a/i, the ΔF_0 increased the number of incorrect /u/ responses more than that of correct /i/ responses, whereas grouping by F_0 should instead have favored /i/ and excluded /u/. Culling and Darwin (1993) also found evidence against this hypothesis: a vowel pair in which F_0's were swapped between first and second formants (the $F1$ of one vowel was excited with the same F_0 as the $F2$ of the other) benefited from a ΔF_0, despite the fact that different F_0's excited the $F1$ and $F2$ of each vowel.

Harmonic *enhancement* designates the general hypothesis according to which the F_0 of a target is exploited to segregate it from interference. Across-formant grouping is a variant of this hypothesis, but there are others. Previous work argued against this hypothesis, in particular because of the difficulty of estimating the target F_0 for weak targets (de Cheveigné *et al.*, 1997a). This argument is reinforced here: there is no way the auditory system could *directly* estimate the F_0 of a target vowel that is at least 10 dB beneath its competitor at all frequencies.

On the other hand, the results are consistent with the hypothesis that the *competitor's* F_0 is used to suppress it (harmonic cancellation). That F_0 is easy to estimate when the competitor is strong. One plausible model of harmonic cancellation is the channel selection model of Meddis and Hewitt (1992). However, it requires that at least *some* channels be dominated by the weaker vowel, and thus it cannot explain the entire data set. Another cancellation model is based on the time-domain ''cancellation filter'' of de Cheveigné (1993, 1997b). That model can operate at any amplitude ratio in principle, although in practice its implementation would face limits due to noise and imperfect linearity of transduction and neural processing. Within each channel, a neural cancellation filter suppresses the components of the competitor (based on its period), and the remainder of this operation constitutes evidence of the weaker vowel. The filter's dynamic range needs to be sufficient for this remainder to be distinguishable from noise. The limited amplitude range over which ΔF_0 was effective might reflect the limited dynamic range of such a mechanism.

Vowel identification was not impaired by the mere presence of cues to another vowel. A nonzero ΔF_0 rendered cues to both vowels more prominent, but there was no evidence that the increased prominence of cues to one vowel was detrimental to the other. There was no evidence of a cognitive competition between cues to each vowel. For pattern-matching, an extra formant peak poses a problem for a template-matching model using a Euclidean distance. Spectral differences are squared before summation, and locally large differences due to an extra formant have a disproportionate weight that may mask similarity over the rest of the spectrum. Pattern matching is likely to be unreliable.

The problem might be alleviated by replacing the square by a compressive nonlinearity, so as to emphasize small distributed differences over large localized ones. Another solution might be to synthesize *hybrid* templates (similar to the spectral envelopes in Fig. A1), and perform matching to them. A related scheme was proposed by Kopec and Bush (1989) for recognition of mixed speech. A third solution would be to somehow mark the spurious channels as unreliable, and exclude them from the distance calculation. A fourth would be to include only *positive* template-minus-token differences in the distance calculation. They alone constitute strong evidence of a mismatch: negative differences might be simply due to the dominance of part of the spectrum by the competitor. The last two schemes are among the ''missing data'' techniques proposed for speech recognition by Cooke, Morris, and Green (1996, 1997).

Our discussion of cues to vowel identification has limitations that were pointed out earlier. The spectral envelope differs from the representation available to the auditory system. Only formants $F1$ and $F2$ were considered, and higher formants were ignored. The description in terms of formants itself may be questioned (Rosner and Pickering, 1994). No account was taken of the fact that subjects usually had to choose the weaker vowel from a limited set of candidates (four), and that choosing one was equivalent to excluding the three others. Prominence of cues was evaluated qualitatively based on visual criteria, quantitatively based on amplitude differences between target and competitor at formant peaks of the target, and indirectly based on response rates. The relevance of those criteria to vowel perception is, however, unsure. The next step should be to construct quantitative models and test them on the response data. That is beyond the scope of the present paper, but raw data of this and other similar experiments are freely available to the interested reader.

IV. CONCLUSIONS

(1) ΔF_0 improved the identification of vowels as weak as -25 dB relative to their competitor, but at -35 dB the effects were no longer measurable.

(2) Improvement for weak targets was generally no greater at $\Delta F_0 = 6\%$ or 12 % than at $\Delta F_0 = 3\%$, whatever the target/competitor ratio. There was no tradeoff between factors: an unfavorable amplitude ratio could not be compensated by a larger ΔF_0.

(3) Identification of a vowel was generally not affected by the presence and prominence of cues belonging to the competing vowel. It depended only on the prominence of the target vowel's cues.

(4) Patterns of identification could generally be understood by assuming that the cues to identification of a vowel were its $F1$ and $F2$. However, the generality or uniqueness of this interpretation were not tested. In general, identification of a vowel required that both its formants be individually prominent, or else shared with the competitor, or at least potentially masked by the competitor.

(5) Sharing of a formant between vowels was not detrimental to the identification of either vowel. The principle of ''exclusive allocation'' did not apply.
(6) ΔF_0 improved target identification for certain vowel pairs over a wide range of amplitude ratios (at least 20 dB). This confirms the ecological value of F_0-guided segregation. On average, and for most vowel pairs, ΔF_0 effects were largest at -15 dB.
(7) ΔF_0 effects were observed when the target's spectral envelope was up to 10 dB below that of the competitor. Below that level, ΔF_0 effects were rare and small.
(8) Results were consistent with the hypothesis that segregation is based on a mechanism of harmonic cancellation. The limited dynamic range of ΔF_0 effects may be interpreted as reflecting the limited accuracy of that mechanism.

ACKNOWLEDGMENTS

The experiment was carried out at ATR Human Information Processing Research Laboratories, under a research agreement between ATR, the Center National de la Recherche Scientifique, and Paris 7 University. The author thanks ATR for its kind hospitality, and the CNRS for leave of absence. Hideki Kawahara participated in the preparation, and Rieko Kubo supervised the experiments. John Culling kindly provided the software for stimulus synthesis, and Willy Serniclaes kindly offered advice on statistical analysis. Thanks to two anonymous reviewers and the editor for very helpful advice on a previous version of this manuscript.

APPENDIX: DETAILS OF PAIR-WISE RESULTS

A. Spectral envelopes at $\Delta F_0 = 0\%$

Spectral envelopes of all pairs (other than /oe/ and /ou/) at $\Delta F_0 = 0\%$ are plotted in Fig. A1. Envelopes for /oe/ and /ou/ were plotted in Figs. 1 and 2. In each graph, isolated vowels (which were not presented as stimuli) are represented by thick lines, and mixtures (which were presented as stimuli) by the eight thin lines. Some of these are indistinct in places because they merged with one or the other thick lines.

B. Pair-wise results at $\Delta F_0 = 0\%$

Each vowel (target) is considered in competition with each of the other vowels (competitor). Response rates for all 20 target/competitor pairs at $\Delta F_0 = 0\%$ are plotted in Fig. A2 as a function of the target/competitor amplitude ratio. Each row of graphs corresponds to the same target vowel, and each column to the same competitor vowel. The diagonal is empty because vowels were not paired with themselves. Graphs that fall symmetrically relative to the diagonal correspond to both orderings of the same stimulus pair (for example, a/e and e/a both correspond to /ae/), with oppositely oriented abscissas. They share two abscissa values: 5 dB on one corresponds to -5 dB on the other.

Open circles are response rates for the target vowel (generally weaker), and crosses are rates for the competitor (generally stronger). Smooth lines represent a fit to these data by the following function:

$$R(x) = 1/(1 + e^{-(a/2)(x-b)}), \tag{A1}$$

where R is the response rate, x is the amplitude ratio in dB, b is the $R = 0.5$ intercept in dB, and a is the slope at intercept in dB^{-1}. For each vowel pair, the function was fit to eight response-rate data points (-35 to 35 dB) using the nonlinear fit procedure of the JMP statistics package (SAS Institute). Jagged lines near the abscissa are response rates for the three vowels not present in the stimulus. Whatever its role, each vowel (/a/, /e/, etc.) is coded in a distinctive line style (full, dotted, etc.) that is the same for all graphs.

Parameters of the fit for each target/competitor pair are given in Table AI. The smallest intercept (b) was -24 dB, for a/i (Fig. A2), and the greatest was -2 dB, for u/a. The smallest slope at intercept (a) was 0.21 for o/i and the greatest was 0.51 for a/o. Some general trends are evident in the table. Intercepts for /a/ were relatively low, indicating that it was robust with respect to interference. Intercepts for /u/ were relatively high, suggesting that it was vulnerable. The vowel /a/ was a relatively effective masker, while /o/ was a relatively weak masker (except when /u/ was the target).

1. Principles of vowel identification at $\Delta F_0 = 0\%$

In these data there are many examples of the ''first principle,'' according to which identification of a vowel is not prevented by cues belonging to a competing vowel. The target is usually well identified at ratios for which cues to the competing vowel are conspicuous in the spectral envelope (Fig. A1). When the target/competitor ratio is increased, these cues change while target identification does not. Conversely, when the ratio is decreased, they change very little while target identification changes greatly. One can wonder whether these cues, that are *visually* prominent (and also numerically on a log scale), are also *perceptually* prominent. An answer can be found in the fact that, in most panels of Fig. A2, the fit curves intersect at a high value. This indicates that over a certain range of amplitude ratios, cues to both vowels are perceptually effective. One might object that disruptive effects of cues to a competing vowel exist, but are masked by ceiling effects. This objection cannot be waived completely. One can, however, note that subjects were under no pressure to report two vowels, and that when they did so must indicate the presence of convincing cues.

The second principle is that both vowels can share a common formant, and nevertheless both be identified simultaneously. The principle of exclusive allocation described by Bregman (1990) does not hold. Four pairs out of ten share a formant: /ao/, /au/, /oe/, and /iu/ (Fig. A1).

The third principle is that identification of a vowel requires that both $F1$ and $F2$ be prominent. The necessity of the presence of cues to *both* formants is easiest to see in vowel pairs that share a formant. The spectral region of the common formant generally changes little across conditions, and identification appears to vary with the prominence of the other formant. Target/competitor pairs for which this is true

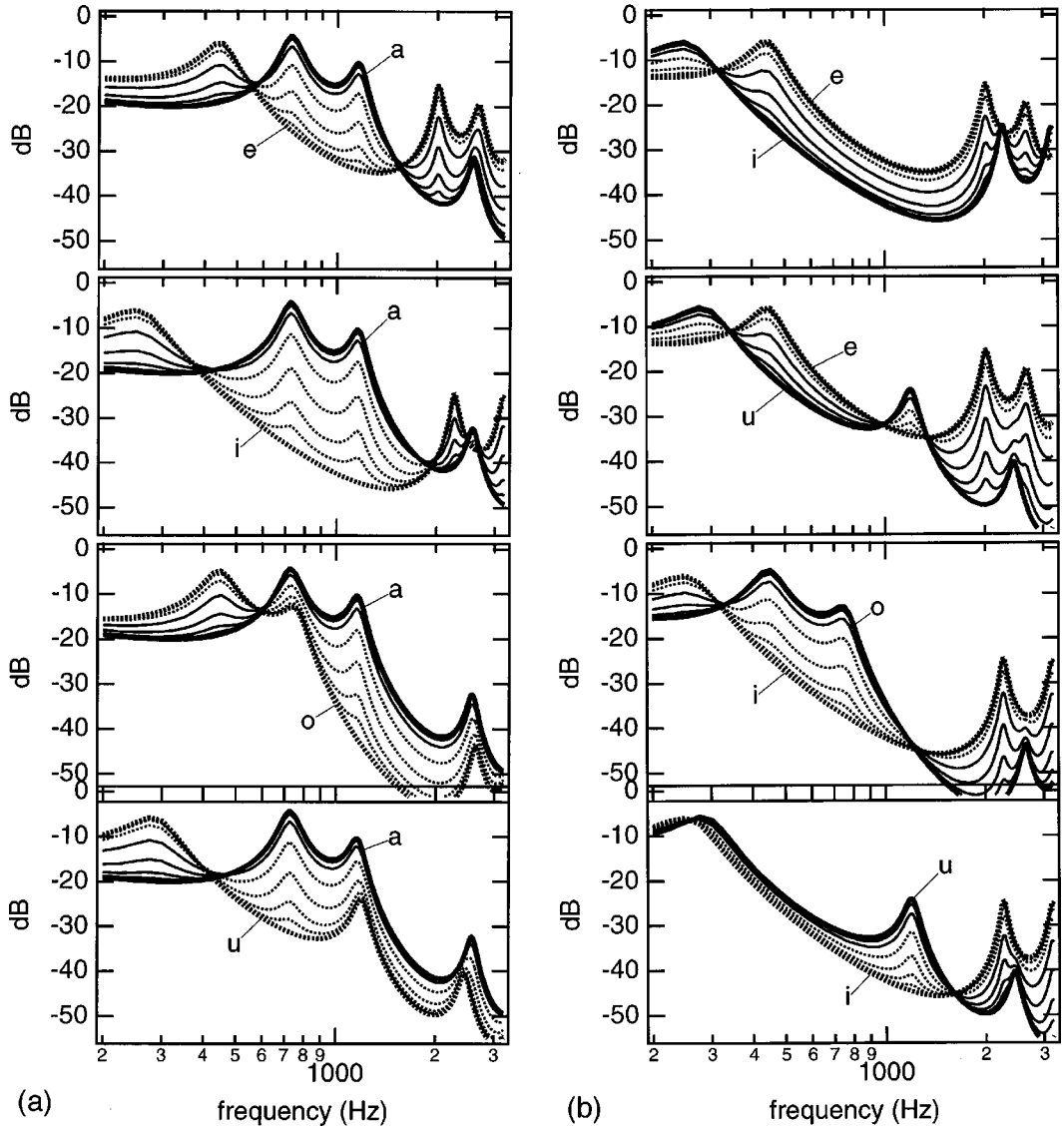

FIG. A1. Spectral envelopes of single vowels (thick lines) and weighted sums of pairs of vowels (thin lines), with amplitude ratios ranging from −35 to 35 dB in 10-dB steps. The plots include the first three formants ($F1$, $F2$, and $F3$), but exclude $F4$ and $F5$. Each graph corresponds to a different vowel pair. Together with Figs. 1(a) and 2(a), all ten vowel pairs are covered.

are a/o, o/a, a/u, u/a, o/e, e/o, i/u, and u/i. For a given vowel, the ''critical formant'' can be either $F1$ or $F2$. For example, in a/u identification varied with the prominence of $F1$ of /a/, whereas in a/o it varied with that of its $F2$.

Response rates decrease when cues to $F1$ and/or $F2$ become less prominent. However, prominence is not easy to define objectively. As noted in Sec. II B 2, at least three factors might underlie the prominence of formant peaks: their *absolute* amplitude, their amplitude *relative* to the competitor's formants, and their *local prominence* (amplitude relative to the neighboring spectral envelope, and ''sharpness''). Absolute amplitude is probably not a determining factor, as presentation levels were reasonably high, and thresholds for a given target vowel varied among competitors (Table AI). Support for local prominence comes from the fact that the lowest intercepts in Table AI are for a/i (−24 dB), a/u (−23 dB), and e/o (−18 dB), for which the deep interformant valleys of the competing vowels seem to favor the local prominence of target formants [Figs. A1 and 1(a)]. Evidence against it comes from e/o: the ''local prominence'' of the peak at $F2$ of /e/ hardly changed over the range over which identification of /e/ varied [Fig. 1(a)].

It is worth examining the spectral shapes for which formant cues were perceptually *ineffective*. Setting an arbitrary threshold at 10% and scanning through Fig. A2, one notes a certain number of data points that fall below this threshold. The corresponding spectral envelopes show cues to the target formants that are very modest indeed. The spectral envelope of the stimulus often differs by no more than a few dB from that of the competitor alone. An example is the −35-dB value of the a/e ratio (lowest dotted line near formants of /a/ in the appropriate plot of Fig. A1). Slightly more conspicuous ''noneffective'' cues are the shoulder at $F2$ of /a/ at −25 dB for a/o (second-to-lowest dotted line in Fig. A1), or the peak at $F2$ of /e/ at −25 dB for e/o (second-to-lowest dotted line in Fig. 1). Perceptually ineffective cues are objectively

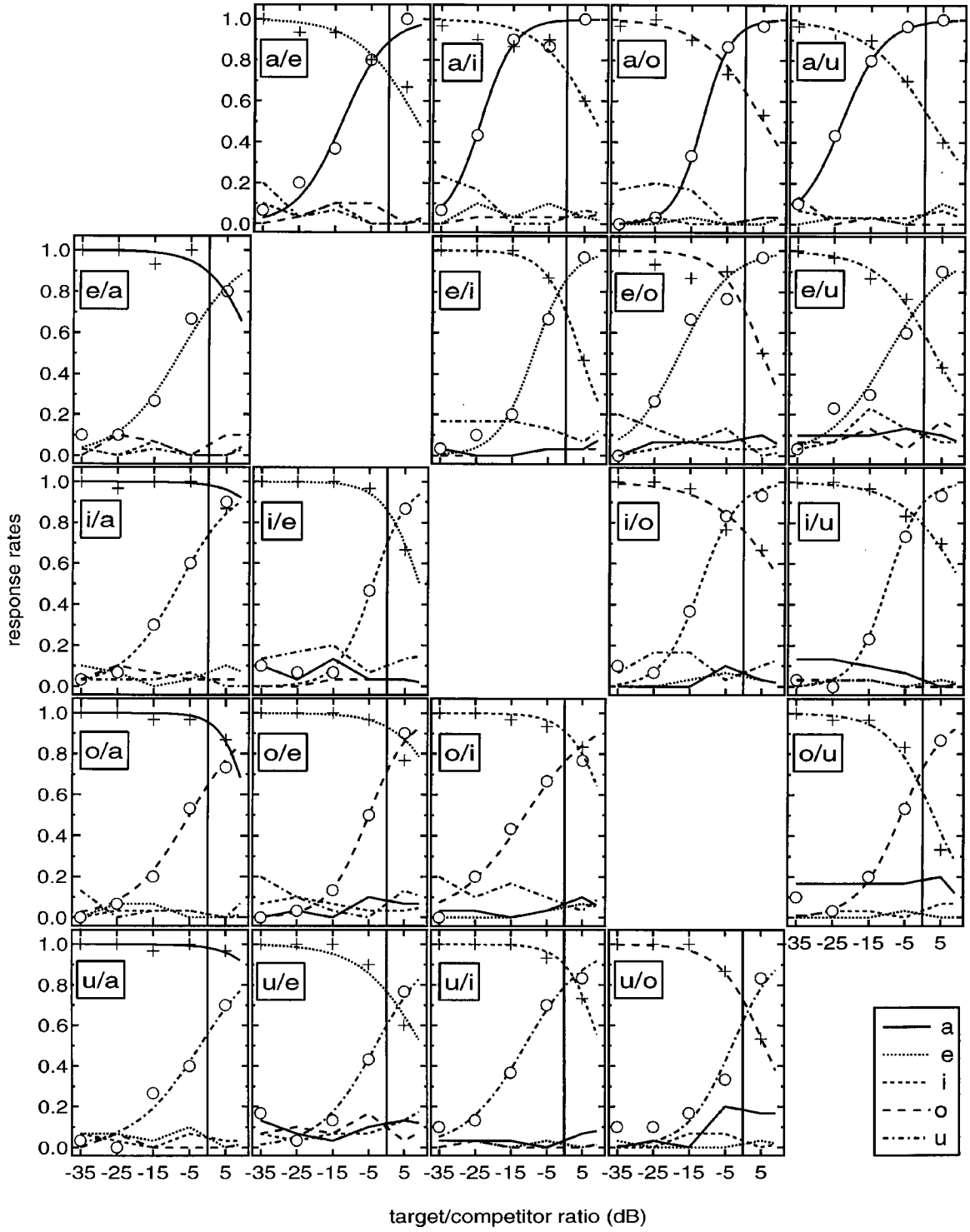

FIG. A2. Pair-wise responses at $\Delta F_0 = 0\%$. Each graph represents the response rates for all five vowels as a functions of the amplitude ratio. Graphs are given for each of the 20 target/competitor vowel pairs. Graphs on a row share the same target (generally weaker); graphs in a column share the same competitor (generally stronger). Open circles are data points for the target; crosses are data points for the competitor. Smooth lines are a function fit to these data (see the text). The jagged lines near the abscissa are response rates for the three vowels other than target and competitor (''spurious'' vowel responses).

very weak. By contrast, only slightly less modest spectral cues suffice to affect identification on a measurable number of trials.

2. Spurious responses

One might have imagined that the presence of a very weak vowel would have a rather indistinct effect, causing subjects to report at random a second vowel in addition to the stronger vowel. While there is a sort of ''noise floor'' evident in the spurious vowel responses in Fig. A2, it is not random: responses were usually dominated by one vowel, sometimes two, rarely three or four (the only example of four responses greater than 10% is the −15-dB point of e/u in Fig. A2). The dominant response (other than the strong vowel) was usually the weaker stimulus vowel, but at low amplitude ratios it was sometimes superseded by another

TABLE AI. First column: names of target/competitor vowel pairs. Second and third column: ratio between spectral envelopes of target and competitor at $F1$ and $F2$ of target (when both vowels have the same rms amplitude). Fourth and fifth column: intercept (abscissa at 50%) and slope at intercept of the fit to the target identification psychometric function. Last two columns: ratio between target and competitor spectral envelopes at $F1$ and $F2$ of target at criterion (see the text). Values are given only for target/competitor pairs for which the ΔF_0 effect size reached the criterion value (0.3), and only for formants that controlled target identification (shared formants were excluded).

	Ratio (dB)		Psychometric function		Ratio at criterion (dB)	
Pair	at $F1$	at $F2$	intercept (dB)	slope (dB^{-1})	at $F1$	at $F2$
a/e	21.3	23.8	−13	0.32	6.3	8.8
a/i	32.4	34.1	−24	0.44	7.4	9.1
a/o	8.9	32.2	−12	0.51	···	17.2
a/u	27.3	14.3	−23	0.35	···	···
e/a	13.3	26.3	−8	0.24	−1.7	11.3
e/i	18.6	23.5	−9	0.40	−6.4	···
e/o	−0.9	42	−18	0.29	···	···
e/u	15.0	34.6	−10	0.24	−10	9.6
i/a	13.6	16.1	−8	0.26	···	···
i/e	7.5	1.0	−4	0.42	−7.5	···
i/o	8.8	31.4	−12	0.39	−6.2	16.4
i/u	0.5	22.1	−10	0.44	···	7.1
o/a	14.2	−7.7	−5	0.24	−10.8	···
o/e	0.9	13.3	−5	0.36	···	−1.7
o/i	19.6	24.2	−11	0.21	4.6	9.2
o/u	16.0	18.7	−6	0.33	−9	−6.3
u/a	14.1	−11.7	−2	0.22	−0.9	···
u/e	7.3	10.3	−3	0.26	−7.7	−4.7
u/i	2.9	20.7	−11	0.24	···	5.7
o/u	8.4	19.7	−3	0.32	−6.6	4.7

vowel not present in the stimulus. Response rates for individual spurious vowels were as large as 20%.

The vowel /a/ was often reported for stimuli dominated by /u/ (last column in Fig. A2). The two vowels share similar $F2$'s, but it is hard to explain why /a/ was reported in the absence of evidence of its $F1$, except in the case of /ou/ where the $F2$ of /o/ can be interpreted as the $F1$ of /a/ (Sec. II B 2). The vowel /e/ was only rarely reported as a spurious response. The vowel /i/ was often reported for the pair e/u at −15 and −5 dB. Apparently the $F1$ of /u/ and $F2$ of /e/ were interpreted as belonging to /i/ (Fig. A1), an interpretation that leaves orphaned the $F1$ of /e/. The vowel /o/ was reported at certain levels for pairs e/u and e/a. This is easy to explain in the case of e/a: $F1$'s of /e/ and /a/ can be interpreted as $F1$ and $F2$ of /o/, and it is perhaps surprising that this interpretation was not made more often. Finally, the vowel /u/ was often reported for stimuli strongly dominated by /i/, /e/, or /o/ (Table II). The vowel /u/ has a similar $F1$ to /i/, but it shares no formants with /e/ or /o/. On the other hand, it has an $F2$ similar to that of /a/, but /u/ responses were less common with that vowel than with the other three. It is hard to account for the large number of /u/ responses for stimuli that lack either its $F1$ (a/o) or its $F2$ (/ei/, /io/), or both (/eo/). The vowel /u/ may possibly serve as a sort of ''default'' response. It is perhaps worth noting that the vowel /u/ is often devocalized in Japanese.

To summarize, spurious vowel responses were generally not random. They sometimes occurred despite the lack of specific cues to the vowel reported (typically /u/). More often, they were the result of cues present in the stimulus being reassembled in an incorrect but plausible way. In view of this fact, it is perhaps surprising that they did not occur more often.

C. Pair-wise patterns of ΔF_0 effects

1. ΔF_0 effects for constituent vowels

Differences in response rates between $\Delta F_0 = 12\%$ and $\Delta F_0 = 0\%$ are plotted in Fig. A3 for eight of the ten vowel pairs. The other two (/oe/ and /ou/) were plotted in Figs. 4(b) and 5(b). For most target/competitor pairs, ΔF_0 was effective over a range of amplitude ratios. For some (a/e, e/a, o/a, u/a, i/e, e/u, u/e, o/i, u/i, o/u, u/o) the range was at least 20 dB, for others it was more limited (a/o, i/o). The *upper* end of the range is the result of a ceiling effect: identification that is good at $\Delta F_0 = 0\%$ cannot be improved by a ΔF_0. The *lower* limit reflects the breakdown of segregation mechanisms when the target was too weak. This limit is worth examining in detail, as it may give cues to the nature of the segregation mechanisms. Let us quantify the ''lower limit'' as the lowest amplitude ratio for which the increase with ΔF_0 exceeded a criterion value (0.3). This criterion is purely arbitrary and unrelated to any judgment of significance. The criterion was not met for three target/competitor pairs out of 20 (i/a, a/u, and e/o). For the others it was met at either −25 dB (a/i, o/a, e/i, e/u, o/u) or at −15 dB (remaining pairs).

The amplitude ratios between spectral envelopes of target and competitor at formants $F1$ and $F2$ of the target, at

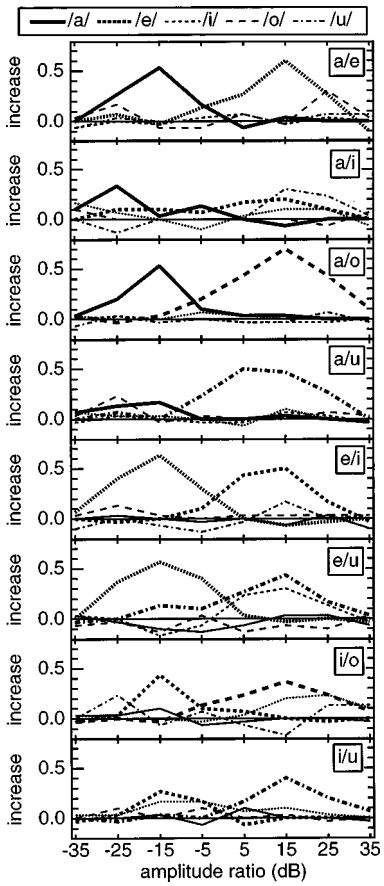

FIG. A3. Increase in response rates between $\Delta F_0 = 0\%$ and 12% as a function of intervowel amplitude ratio, for eight vowel pairs [the other two are plotted in Figs. 4(b) and 5(b)]. Thick lines: responses for vowels present in the stimulus. Thin lines: spurious vowel responses.

criterion, are given in the last two columns of Table AI. Excluded from this table are data for the three pairs that missed the criterion, and for formants that were shared between target and competitor and were therefore prominent in all conditions. For some pairs, the ratios at both target formants (or at the single formant that controlled identification) were positive (a/e, a/i, a/o, i/u, o/i, u/i). For others they were negative (e/i, i/e, o/a, o/e, o/u, u/a, u/e). For a few pairs, one ratio was negative, the other positive. The range of values was quite wide: -10.8 to 17.3 dB.

This pattern can be confronted with three possible models of concurrent vowel segregation: channel selection (Meddis and Hewitt, 1992), beats (Assmann and Summerfield, 1994; Culling and Darwin, 1994), and harmonic cancellation (de Cheveigné, 1997b). Channel selection requires that the target vowel dominate at least some parts of the spectrum: it cannot explain ΔF_0 effects for a target everywhere weaker than its competitor. It thus cannot account for the full data set.

Beats should be most effective when they are strong at formants of the target, that is, when the amplitude ratio at those formants is close to 0 dB. The -10.8-dB amplitude ratio at criterion for o/a is consistent with that hypothesis: the resulting modulation depth of about 30% is possibly effective, and it decreases with a further reduction in o/a ratio, consistent with the decrease in ΔF_0 effect size. The hypothesis fares less well for pairs that have a *positive* ratio at criterion. Starting from the ratio at criterion, a reduction should *increase* the size of ΔF_0 effects, contrary to what is observed. Conversely, an increase in ratio should diminish the amplitude of beats at formant peaks, thus diminishing ΔF_0 effect size, again contrary to what is observed. When a formant peak emerges above its competitor's spectrum, the locus of maximum beats splits and shifts along each flank of the formant peak. This might lead to confusion if beats were used to signal formant positions. ΔF_0 effects were nevertheless strong in such conditions. The beat hypothesis is thus hard to reconcile with these data.

The ideal, linear version of the harmonic cancellation model can exploit the presence of a mistuned target, however weak (de Cheveigné, 1997b). In practice, the dynamic range of the mechanism would be limited by noise and the imperfect linearity of a neural cancellation filter. The smallest ratio of envelopes at criterion (-10.8) might be interpreted as reflecting the limit of the dynamic range of such neural processing. However, in that case it is hard to explain why corresponding figures are not similar for other vowels.

Three vowel pairs gave ΔF_0 effects too small to meet the 0.3 criterion (i/a, a/u, and e/o). The case of e/o was discussed in Sec. II B 3. For a/u, identification of /a/ depended on the prominence of its $F1$, that emerged relatively well between formants of /u/ at all levels (Fig. A1), leading to good identification at $\Delta F_0 = 0\%$ and thus small ΔF_0 effects. For i/a the small effect size is partly due to a tendency to group the $F1$ of /i/ and the $F2$ of /a/ together and interpret them as /u/. This occurred despite the fact that these two formants were excited by different F_0's, an argument against the hypothesis of across-frequency grouping of formants by F_0.

A few data points show a *decrease* in identification rate with ΔF_0, but the effects were small and probably due to experimental noise. It seems safe to say that ΔF_0 was either beneficial or indifferent to identification according to the condition, but never detrimental.

2. ΔF_0 effects for spurious vowel responses

In many cases, a ΔF_0 increased the response rates for spurious vowels as well as (or instead of) correct vowels. In a few cases they were *reduced* instead. This section reviews the conditions in which a ΔF_0 affected spurious responses for each vowel pair.

For /ou/, the decrease in /a/ responses with ΔF_0 for o/u ratios of -25 to 5 dB (and its increase at 15 dB) were noted in Sec. II B 3. For /ae/ (Fig. A3), the number of /o/ responses increased at an a/e ratio of 25 dB. A possible explanation is that ΔF_0 increased the prominence of the $F1$ of /e/ that was interpreted as belonging to /o/. The amplitude of the $F1$ peak of /e/ relative to /a/ in that condition was -11.7 dB. For /ai/, at a/i ratios of 15 and 25 dB, the number of incorrect /u/ responses increased more than that of correct /i/ responses. Apparently, ΔF_0 enhanced the prominence of $F1$ of /i/, required for both interpretations. It is not clear why the incorrect interpretation was preferred. If anything, formant grouping by F_0 should have favored the correct interpretation

(another argument against this hypothesis). The ratio of envelopes at $F1$ of /i/ in these conditions was -1.4 and -11.4 dB, respectively.

For /eu/ at e/u ratios of 5, 15, and 25 dB, the number of incorrect /i/ responses increased almost as much as that of correct /u/ responses. Apparently, ΔF_0 enhanced the prominence of the $F1$ of /u/ required for both interpretations. The ratio of envelopes at $F1$ of /u/ in these conditions was 2.7, -7.7, and -17.7 dB, respectively. At some e/u ratios, response rates for spurious vowels decreased, possibly a simple effect of the increased prominence of cues to the ''correct'' vowels.

For /io/ at i/o ratios of 15 and 25 dB, the number of incorrect /e/ responses increased together with correct /i/ responses. Apparently, ΔF_0 enhanced the prominence of the $F1$ of /o/ required for both interpretations. For /iu/ at i/u ratios of -15 and -5 dB, the number of incorrect /e/ responses increased slightly together with correct /i/ responses. ΔF_0 enhanced the prominence of the $F2$ of /i/ required by both interpretations, but the increase in /e/ responses is hard to explain in the absence of any cue to $F1$ of /e/.

Overall, neither the increases in incorrect vowel response rates, nor their baseline rates themselves, were very large. A *uniform* increase over all four vowels (other than the stronger) was never observed. Such an increase was to be expected if a hypothetical ''multiplicity cue'' signaled the presence of an extra vowel without providing information about its identity. Rate increases with ΔF_0 usually concerned one vowel (correct or incorrect), sometimes two, and in rare cases three. In other cases, a decrease was observed instead of an increase. The hypothesis of a multiplicity cue is therefore improbable.

Assmann, P. F., and Summerfield, Q. (**1989**). ''Modeling the perception of concurrent vowels: Vowels with the same fundamental frequency,'' J. Acoust. Soc. Am. **85**, 327–338.

Assmann, P. F., and Summerfield, Q. (**1990**). ''Modeling the perception of concurrent vowels: Vowels with different fundamental frequencies,'' J. Acoust. Soc. Am. **88**, 680–697.

Assmann, P. F., and Summerfield, Q. (**1994**). ''The contribution of waveform interactions to the perception of concurrent vowels,'' J. Acoust. Soc. Am. **95**, 471–484.

Bregman, A. S. (**1990**). *Auditory Scene Analysis* (MIT, Cambridge, MA).

Brown, G. J. (**1992**). ''Computational auditory scene analysis: a representational approach,'' Sheffield, Department of Computer Science, unpublished doctoral dissertation.

Cooke, M., Morris, A., and Green, P. (**1996**). ''Recognizing occluded speech,'' Proceedings of the ESCA Workshop on the Auditory Basis of Speech Perception, Keele, edited by W. Ainsworth and S. Greenberg, pp. 297–300.

Cooke, M., Morris, A., and Green, P. (**1997**). ''Missing data techniques for robust speech recognition,'' Proceedings ICASSP, pp. 863–866.

Cooke, M. P. (**1991**). ''Modelling auditory processing and organization,'' Sheffield, Department of Computer Science, unpublished doctoral dissertation.

Culling, J. F. (**1996**). ''Signal processing software for teaching and research in psycholinguistics under UNIX and X-windows,'' Behav. Res. Methods Instrum. Comput. **28**, 376–382.

Culling, J. F., and Darwin, C. J. (**1993**). ''Perceptual separation of simultaneous vowels: Within and across-formant grouping by $F0$,'' J. Acoust. Soc. Am. **93**, 3454–3467.

Culling, J. F., and Darwin, C. J. (**1994**). ''Perceptual and computational separation of simultaneous vowels: Cues arising from low frequency beating,'' J. Acoust. Soc. Am. **95**, 1559–1569.

Culling, J. F., and Summerfield, Q. (**1995**). ''Perceptual segregation of concurrent speech sounds: absence of across-frequency grouping by common interaural delay,'' J. Acoust. Soc. Am. **98**, 785–797.

Culling, J. F., Summerfield, Q., and Marshall, D. H. (**1994**). ''Effects of simulated reverberation on the use of binaural cues and fundamental frequency differences for separating concurrent vowels,'' Speech Commun. **14**, 71–95.

de Cheveigné, A. (**1993**). ''Separation of concurrent harmonic sounds: Fundamental frequency estimation and a time-domain cancellation model of auditory processing,'' J. Acoust. Soc. Am. **93**, 3271–3290.

de Cheveigné, A. (**1997a**). ''Ten experiments in concurrent vowel segregation,'' ATR Human Information Processing Research Labs technical report, TR-H-217.

de Cheveigné, A. (**1997b**). ''Concurrent vowel segregation III: A neural model of harmonic interference cancellation,'' J. Acoust. Soc. Am. **101**, 2857–2865.

de Cheveigné, A., Kawahara, H., Tsuzaki, M., and Aikawa, K. (**1997a**). ''Concurrent vowel identification I: Effects of relative level and $F0$ difference,'' J. Acoust. Soc. Am. **101**, 2839–2847.

de Cheveigné, A., McAdams, S., Laroche, J., and Rosenberg, M. (**1995**). ''Identification of concurrent harmonic and inharmonic vowels: A set of the theory of harmonic cancellation and enhancement,'' J. Acoust. Soc. Am. **97**, 3736–3748.

de Cheveigné, A., McAdams, S., and Marin, C. (**1997b**). ''Concurrent vowel identification II: Effects of phase, harmonicity and task,'' J. Acoust. Soc. Am. **101**, 2848–2856 (in preparation).

Demany, L., and Semal, C. (**1990**). ''The effect of vibrato on the recognition of masked vowels,'' Percept. Psychophys. **48**, 436–444.

Elllis D. (**1996**). Prediction-driven computational auditory scene analysis,'' MIT unpublished doctoral dissertation.

Geisser, S., and Greenhouse, S. W. (**1958**). ''An extension of Box's results on the use of the F distribution in multivariate analysis,'' Ann. Math. Stat. **29**, 885–889.

Hirahara, T., and Kato, H. (**1992**). ''The effect of $F0$ on vowel identification,'' in *Speech Perception, Production and Linguistic Structure*, edited by Y. Tohkura, E. Vatikiotis-Bateson, and Y. Sagisaka (Ohmsha, Tokyo), pp. 89–1120.

Klatt, D. H. (**1980**). ''Software for a cascade/parallel formant synthesizer,'' J. Acoust. Soc. Am. **67**, 838–844.

Kopec, G. E., and Bush, M. A. (**1989**). ''An LPC-based spectral similarity measure for speech recognition in the presence of co-channel speech interference,'' Proceedings IEEE ICASSP, pp. 270–273.

McKeown, J. D. (**1992**). ''Perception of concurrent vowels: The effect of varying their relative level,'' Speech Commun. **11**, 1–13.

Meddis, R., and Hewitt, M. J. (**1992**). ''Modeling the identification of concurrent vowels with different fundamental frequencies,'' J. Acoust. Soc. Am. **91**, 233–245.

Meyer, G., and Berthommier, F. (**1995**). ''Vowel segregation with amplitude modulation maps: a re-evaluation of place and place-time models,'' Proceedings ESCA Workshop on the Auditory Basis of Speech Perception, Keele, edited by W. Ainsworth and S. Greenberg, pp. 212–215.

Moore, B. C. J., and Glasberg, B. R. (**1983**). ''Suggested formulae for calculating auditory-filter bandwidths and excitation patterns,'' J. Acoust. Soc. Am. **74**, 750–753.

Rosner, B. S., and Pickering, J. B. (**1994**). *Vowel Perception and Production* (Oxford University Press, Oxford).

Summerfield, Q. (**1992**). ''Roles of harmonicity and coherent frequency modulation in auditory grouping,'' in *The Auditory Processing of Speech: From Sounds to Words*, edited by M. E. H. Schouten (Mouton de Gruyter, Berlin), pp. 157–166.

Summerfield, Q., and Culling, J. F. (**1992**). ''Auditory segregation of competing voices: absence of effects of FM or AM coherence,'' Philos. Trans. R. Soc. London, Ser. B **336**, 357–366.

Weintraub, M. (**1985**). ''A theory and computational model of auditory monaural sound separation,'' University of Stanford, unpublished doctoral dissertation.

Growth of simultaneous masking for $f_m < f_s$: Effects of overall frequency and level

Sid P. Bacon,[a] Larissa N. Boden, Jungmee Lee, and Jennifer L. Repovsch
Psychoacoustics Laboratory, Department of Speech and Hearing Science, P.O. Box 871908, Arizona State University, Tempe, Arizona 85287-1908

(Received 1 February 1999; accepted for publication 15 April 1999)

Growth-of-masking (GOM) functions were obtained in three groups of normal-hearing subjects using a simultaneous-masking paradigm. In all cases, the signal frequency (f_s) was higher than the masker frequency (f_m), either by a certain ratio (1.44) or by a certain distance [3 equivalent rectangular bandwidths (ERBs)]. The purpose was to evaluate the effect of overall frequency on the slope of the steep portion of the GOM function, and to evaluate the change in slope that can occur at high levels. Signal frequency ranged from 400 to 5000 Hz, and masker level ranged from 40 to 95 dB SPL. On average, the slope of the steep portion of the GOM function was about 1.4 for signal frequencies from 400 to 750 Hz, and 2.0 for signal frequencies from 1944 to 5000 Hz. This is consistent with the possibility that the cochlea may behave more linearly at the apical (low-frequency) region than at the basal (high-frequency) region. In addition, for signal frequencies at and above 750 Hz, the slope of the masking function changed from a value much greater than 1.0 to a value of 1.0 at high levels. The change in slope was better correlated with signal sensation level (i.e., amount of masking) than with either signal or masker SPL; the lack of a change at the lower signal frequencies may reflect the smaller amounts of masking there. The change to a linear growth of masking may represent a change in the response to the signal from compressive to linear at high levels. [S0001-4966(99)04707-4]

PACS numbers: 43.66.Dc, 43.66.Ba [RVS]

INTRODUCTION

In tone-on-tone masking, the slope of the growth-of-masking (GOM) function depends upon the frequency relation between the masker and signal. The function is relatively steep when the masker frequency (f_m) is well below the signal frequency (f_s), that is when $f_m/f_s \ll 1.0$, but the slope of the function decreases systematically as f_m/f_s increases to values >1.0 (Wegel and Lane, 1924; Egan and Hake, 1950; Schöne, 1977; Bacon and Viemeister, 1985). The present paper focuses on simultaneous masking and the situation where $f_m \ll f_s$, in which case the slope of the GOM function is typically much greater than 1.0. Indeed, the slope can be as large as about 2.0–2.5 (Zwicker, 1976, 1979; Schöne, 1977; van der Heijden and Kohlrausch, 1995; Gregan *et al.*, 1998). This nonlinear growth of masking is reflected as ''upward spread of masking'' in masking patterns (Wegel and Lane, 1924; Egan and Hake, 1950).

Although the mechanisms underlying simultaneous masking are not especially well understood, it may be possible to understand at least qualitatively the steep GOM function by appealing to the growth of response at the basilar membrane (Oxenham and Moore, 1995; Nelson and Schroder, 1996, 1997; Gregan *et al.*, 1998; also see Oxenham and Plack, 1997, for a similar discussion regarding the growth of forward masking). In particular, if we assume that signal detection depends upon a certain signal-to-masker ratio in terms of excitation at the location along the basilar membrane corresponding to the signal frequency place, then the slope of the GOM function should depend upon how both the signal and the masker excitation grow with level. Based on basilar membrane input–output (I–O) functions, it is well established that, *at the signal frequency place*, the response to the signal will be compressive over a large range of levels, whereas the response to the masker will be linear (e.g., Robles *et al.*, 1986; Nuttall and Dolan, 1996; Ruggero *et al.*, 1997). Thus, to maintain a constant signal-to-masker ratio in terms of excitation, for every 10-dB increase in masker level (and hence masker excitation), the signal must be increased by more than 10 dB.

Essentially this same argument was made recently by Pang and Guinan (1997) in interpreting the GOM functions that they obtained from cat auditory-nerve fibers. Their masker was a 300-Hz-wide band of noise centered at 500 Hz, and their simultaneously presented signal was a 6000- or 8000-Hz tone. On average, the masking function for fibers with a characteristic frequency (CF) near f_s had a slope of about 2.0, consistent with psychophysical data obtained in simultaneous masking.

If we assume that the steep slope of the GOM function for $f_m \ll f_s$ reflects the fact that the response to the signal is compressed, then it should be possible to use GOM functions to gain insight into this compressive nonlinearity. The present paper is concerned with two aspects of GOM functions: (1) the possible influence of overall frequency on the slope of the function, and (2) the change in slope that can occur at high levels.

Very few studies have examined whether the slope of the GOM function is invariant with overall frequency, at least over a wide frequency range. The results from Schöne

[a]Electronic mail: spb@asu.edu

(1977) suggest that the slope does not change appreciably as f_s varies from 700 to 4800 Hz (f_s always 4 Barks above f_m). However, Moore and Glasberg (1987) obtained slopes that were greater for relatively high signal frequencies, from 1000 to 9495 Hz, than they were for a lower one of 450 Hz ($f_s = 1.8 f_m$ in all cases). The difference between the two studies may be that in order to see an effect of overall frequency, it may be necessary to include signal frequencies lower than about 700 Hz. One motivation for examining the slope over a wide range of frequencies is that such information may provide (indirect) evidence regarding how compression varies along the cochlea. If the steep slope of the GOM function reflects compression of the response to the signal, then the slope of the function should be proportional to the amount of compression. There is some physiological (Cooper and Yates, 1994; Cooper and Rhode, 1995) and psychophysical (Rosen and Stock, 1992; Lee and Bacon, 1998; Hicks and Bacon, 1999) evidence that suggests that the low-frequency (apical) region may process sounds more linearly than the high-frequency (basal) region. Thus, we might expect more gradual slopes at low than at high signal frequencies. To evaluate the effects of overall frequency on the slope of the GOM function, the present study used signal frequencies ranging from 400 to 5000 Hz.

In a recent paper, Gregan *et al.* (1998) showed that the slope of the GOM function ($f_s/f_m = 1.44$) changes from a value of about 2.0 to a value near 1.0 at high signal levels. This effect had been observed previously (Zwicker, 1976, 1979; Schöne, 1977), and can even be seen in some of the functions in the classical papers of Wegel and Lane (1924) and Egan and Hake (1950). Nevertheless, this change in slope has received little attention, perhaps because the preponderance of GOM functions in the literature do not change slope at high levels (e.g., Wegel and Lane, 1924; Egan and Hake, 1950; Bacon and Viemeister, 1985; Moore and Glasberg, 1987; Stelmachowicz *et al.*, 1987; Murnane and Turner, 1991; Nelson and Swain, 1996; Nelson and Schroder, 1997). Gregan *et al.* (1998) suggested that the functions may not have changed slope in those studies simply because the signal did not reach high enough levels. The cause of the change in slope at high levels is unclear. However, inasmuch as the steep slope that exists throughout most of the GOM function can be accounted for by the response to the signal being compressed, it might be argued that the change to a linear slope reflects a change in the signal's response growth from compressive to linear at high levels. Because the change in slope at high levels has not been observed consistently, one purpose of the present study was to determine its generality by measuring GOM functions in a relatively large group of subjects for a variety of different signal frequencies and signal durations.

In summary, the intent of the present study was twofold. First, to measure GOM functions in simultaneous masking ($f_m \ll f_s$) to determine whether the slope of the (steep portion of the) GOM function varies with overall frequency. Second, to examine the generality of the change to a linear slope that can occur at high signal levels.

I. METHOD

A. Subjects

Three crews of subjects participated. They were tested sequentially, with conditions for each new crew chosen to more or less replicate and extend those of the previously tested crew(s). Crew 1 consisted of four subjects (two females and two males, with ages ranging from 23 to 27 years), crew 2 consisted of three subjects (two females and one male, with ages ranging from 23 to 32 years), and crew 3 consisted of three subjects (all female, with ages ranging from 21 to 24 years). One subject (the second author) was common to crews 2 and 3, and thus a total of nine different subjects participated. All had thresholds of 15 dB HL or less (ANSI, 1989) for octave test frequencies from 250 to 8000 Hz. Subjects who were not associated with the laboratory were paid an hourly wage for their participation.

B. Apparatus and stimuli

The general aspects of the stimuli that were similar for the three crews are described here, whereas aspects that were specific to a given crew are described below. The sinusoidal signals and maskers were digitally generated and produced at a 20-kHz sampling rate. They were presented through separate channels of a digital-to-analog converter (TDT DA1); each channel was low-pass filtered at 8 kHz (Kemo VBF 25.01; 135 dB/oct). The starting phase of each was 0°, and they were gated with 5-ms $\cos^2$ rise/fall times. The level of the masker was fixed throughout a block of trials, whereas the level of the signal was varied adaptively via a programmable attenuator (Wilsonics PATT). In order to mask potential cues due to the detection of the cubic difference tone (CDT), a low-pass noise was presented continuously. The noise (GenRad 1381) was low-pass filtered (Kemo VBF 25.01; 135 dB/oct) at a cutoff frequency equal to $2f_m - f_s$. The spectrum level of the noise was 20 (crews 1 and 3) or 30 (crew 2) dB SPL. The masker, signal, and low-pass noise were added together before being presented monaurally (right ear) through a TDH-49P headphone mounted in an MX/51 cushion.

1. Crew 1

Three different f_s—f_m pairs were used; f_s was 518, 1944, or 4320 Hz and f_m was 360, 1350, or 3000 Hz, respectively. Thus, f_s was equal to $1.44 f_m$ for all pairs. The masker duration was 100 ms, and the signal duration was 10, 20, or 40 ms (all durations include the 5-ms rise/fall times). The signal was temporally centered within the masker. The masker ranged in level from 40 to 95 dB SPL.

2. Crew 2

Three different $f_s - f_m$ pairs were used; f_s was 750, 2000, or 5000 Hz and f_m was 480, 1386, or 3566 Hz, respectively. Thus, f_s was 3 equivalent rectangular bandwidths (ERBs; Glasberg and Moore, 1990) above f_m for all pairs. (The 3-ERB separation for the mid-frequency pair corresponds to the same frequency ratio of 1.44 that was used for crew 1.) The masker duration was 300 ms, and the signal

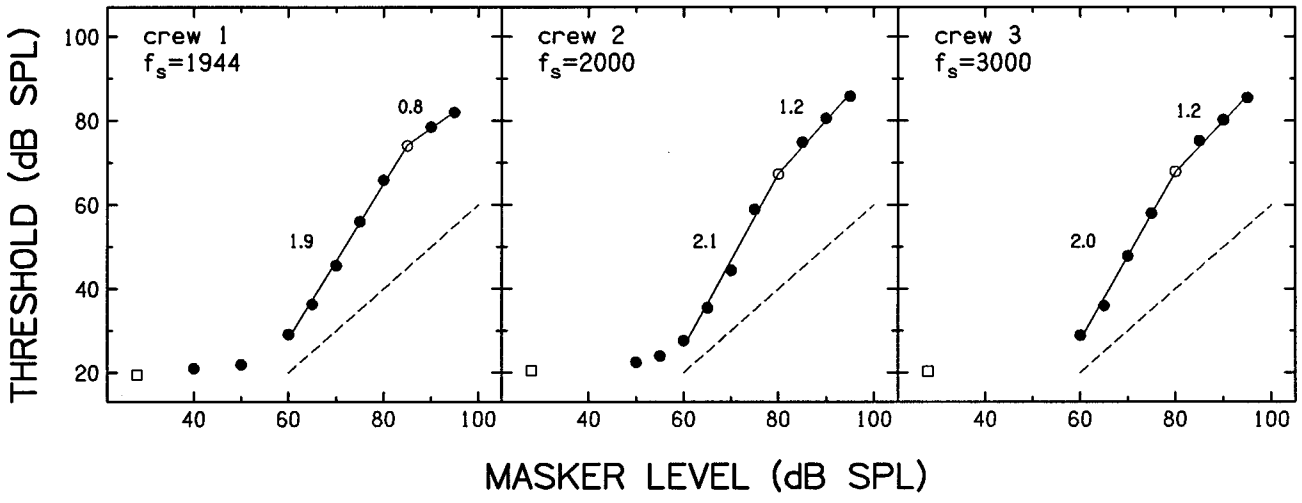

FIG. 1. Representative growth-of-masking (GOM) functions for a signal frequency of about 2000 or 3000 Hz. Signal duration was 20 ms. Each panel shows the results averaged across a given listening crew. Quiet thresholds are shown by unfilled squares, and masked thresholds are shown by circles. The lines connecting the masked thresholds represent the best two-line fit to the data, excluding those points representing less than 5–10 dB of masking. The value adjacent to each straight-line segment is the slope of that segment. Points represented by an unfilled circle were included in both straight-line fits. The dashed line represents linear growth of masking (slope of 1.0).

duration was 20 or 200 ms (all durations include the 5-ms rise/fall times). The signal was temporally centered within the masker. The masker ranged in level from 50 to 95 dB SPL. To reduce the possibility that the signal might be detected in the nontest ear, noise (GenRad 1381) was presented continuously to that ear. It was filtered only by the TDH-49P headphone. The spectrum level of the noise was 10 dB SPL.[1]

3. Crew 3

Three different $f_s - f_m$ pairs were used; f_s was 400, 626, or 3000 Hz and f_m was 226, 388, or 2110 Hz, respectively. Thus, f_s was 3 ERBs above f_m for all pairs. The masker duration was 300 ms, and the signal duration was 20 or 200 ms (all durations include the 5-ms rise/fall times). The signal was temporally centered within the masker. The masker ranged in level from 60 to 95 dB SPL. As for crew 2, broadband noise was presented to the contralateral ear at a spectrum level of 10 dB SPL.

C. Procedure

Testing was completed in a double-walled, sound-treated booth. An adaptive, two-interval, forced-choice paradigm was used. The masker was presented in both intervals; the signal was presented in one of the two intervals (chosen at random), and the subjects' task was to choose the interval that contained the signal. A three-down, one-up decision rule that tracked 79.4% correct (Levitt, 1971) was employed. Each run consisted of 50 or 60 trials. A 5-dB step size was used for the first two reversals, after which a 2-dB step size was used. The first two reversals (three, if the total number of reversals was odd) were discarded, and the threshold estimate for a given run consisted of the average of the signal levels at the remaining reversal points. Runs were discarded on the rare occasions when the standard deviation of the threshold estimate was greater than 5 dB or when the number of reversals used for the threshold estimate was less than six. Three threshold estimates were averaged to produce a threshold for a given condition. If the standard deviation of this average was greater than 3 dB, an additional estimate was obtained and included in the average. This continued until the standard deviation was less than 3 dB, or a total of six estimates was obtained and averaged. Most (95%) of the thresholds obtained here had a standard deviation less than 3 dB.

II. RESULTS

A. Representative GOM functions

Although the durations and frequencies of the signal (and masker) differed across the listening crews, all three were tested with a duration of 20 ms and a frequency of about 2000 or 3000 Hz. These GOM functions are shown in Fig. 1. Because the results were similar within a listening crew, only the group average is shown. Within a panel, the average quiet threshold for the signal is shown to the far left as an unfilled square. The masked thresholds are shown by circles. The lines connecting the masked thresholds represent the best two-line fit to the data (points representing less than about 5–10 dB of masking were excluded from the fits); these lines were chosen to minimize the least-squared deviations. The r^2 values were 0.99 for all three crews. The value adjacent to each straight-line segment is the slope of that segment. The data point represented by the unfilled circle was included in both straight-line fits. Finally, the dashed line represents a linear function (slope of 1.0).

As can be seen, despite some differences in stimuli, the results are similar for the three crews. As expected, the initial segment of these masking functions had a slope much greater than 1.0. For all three crews, the slope of the masking function changed from a value of about 2.0 to a value of about 1.0 at high masker and signal levels. These results thus extend and confirm earlier findings of a change in slope at high levels (Zwicker, 1976, 1979; Schöne, 1977; Gregan *et al.*, 1998). That noise in the contralateral ear (crews 2 and 3) did

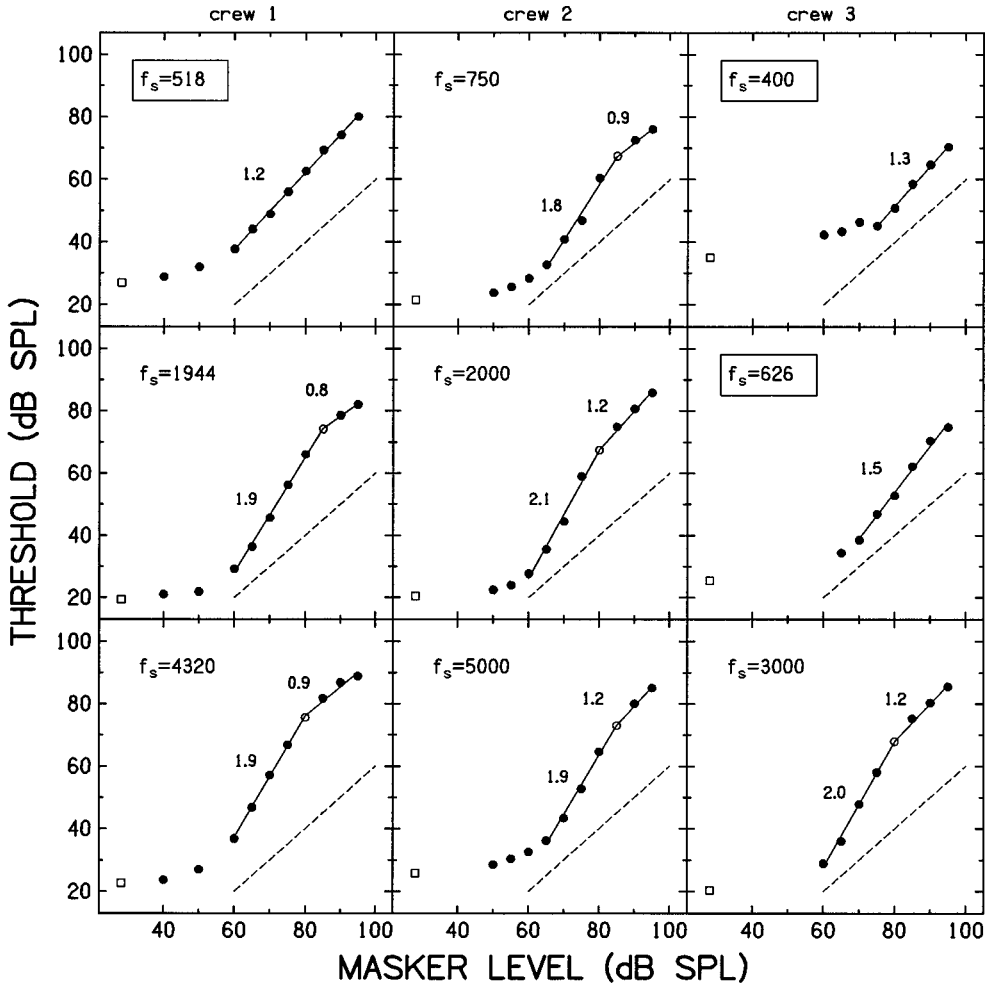

FIG. 2. GOM functions for all signal frequencies and a signal duration of 20 ms. The results are averaged across subjects in crew 1 (left column), crew 2 (middle column), and crew 3 (right column). Signal frequency increases from the top row to the bottom row. The functions were fitted with a single straight line (three lowest frequencies; frequency key enclosed within a box) or two straight lines as in Fig. 1. The dashed line in each panel represents linear growth of masking (slope of 1.0).

not eliminate this change in slope indicates that the change cannot be accounted for by detection of the signal in the nontest ear. We discuss this change in slope at high levels in more detail in Sec. II C.

B. Effect of overall frequency

The GOM functions for all signal frequencies are shown in Fig. 2. As for Fig. 1, the results are shown only for a signal duration of 20 ms (the only duration common to all three crews); note that the three panels of Fig. 1 are shown again here. The group average results for the different crews are shown in separate columns; within a column, f_s increases from top to bottom. The results within a panel are organized as they were in Fig. 1, with the exception that, for the three lowest signal frequencies (400, 518, and 626 Hz), the functions were fitted with only one straight line (r^2 values were all 0.99); these three panels are highlighted by boxing the frequency key within the panel. For all other frequencies, the results are similar to those in Fig. 1. The slope of the masking function changed from a value of about 2.0 to 1.0 at high levels; the r^2 values for these two-line fits were all 0.99. Thus, the slope of the GOM function does not appear to vary appreciably with frequency for signal frequencies from 750 to 5000 Hz. This is similar to the results of Schöne (1977). The functions are clearly different for the three lowest frequencies. They are described extremely well by a single straight line with a slope ranging from 1.2 to 1.5. Thus, the slopes are shallower at these frequencies than they are at the higher frequencies, and there is no obvious change in slope at high levels (although there is a hint that the slope of the function for $f_s = 626$ Hz may be starting to decrease at the highest level, functions were fitted with two lines only if at least three points would be included in that second line). As discussed below, this may be related to the fact that there was generally less masking at these lower frequencies. It could also be related to the fact that the slopes are closer to 1.0 to begin with, making a change to a linear slope—if one existed—less obvious.

To examine the effect of overall frequency on the slope of the GOM function a bit further, Fig. 3 shows a scatter plot depicting slope as a function of f_s (this is either the initial slope of a two-line fit or the slope of a one-line fit). The left panel shows the results for the data of individual subjects, whereas the right panel shows the results for the data aver-

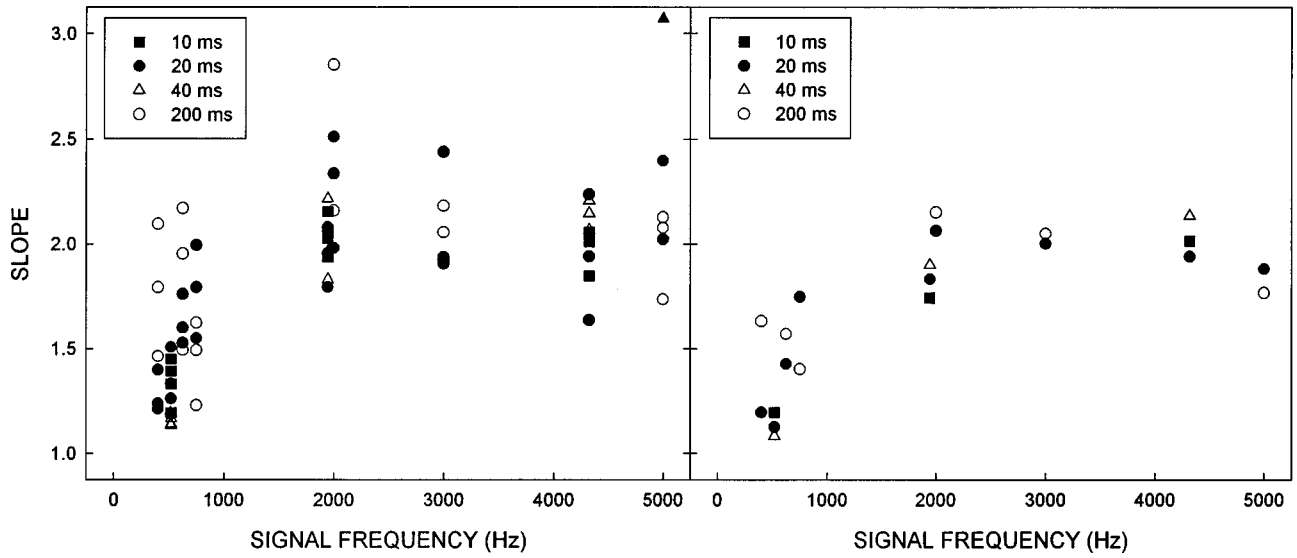

FIG. 3. Scatter plot showing the slope as a function of signal frequency (this is either the initial slope of a two-line fit or the slope of a one-line fit). The left panel shows the results for the individual GOM functions, whereas the right panel shows the results for the GOM functions averaged across subjects within a given listening crew. The different signal durations are represented by unique symbols. The filled triangle in the left panel at 5000 Hz marks a point whose value (3.9) is off the scale, and which should be interpreted cautiously (see the text for more detail).

aged across subjects within a crew (such as in Figs. 1 and 2). The different signal durations are represented by unique symbols; in general, there was no systematic effect of signal duration. [The filled triangle in the left panel at 5000 Hz marks a point whose value (3.9) is off the scale. This value should be interpreted cautiously, as the initial slope for this function alone was based on only two points, because the subject experienced little masking until the masker was at 80 dB SPL. Moreover, as a consequence, the data from this subject slightly reduced the slope of the function averaged across subjects, from 2.1 to 1.9 for the 20-ms signal and from 1.85 to 1.80 for the 200-ms signal.] Despite the considerable scatter, the slope tends to be shallower for the lowest signal frequencies. In terms of the fits to the data averaged across subjects (right panel), there is little overlap in the slope values between the four lowest (400, 518, 626, and 750 Hz) and the five highest signal frequencies (1944, 2000, 3000, 4320, and 5000 Hz). For the lowest frequencies, the slope value for the group average data lies between 1.2 and 1.8, with a mean of 1.4; for the highest frequencies, the slope ranges from 1.8 to 2.2, with a mean of 2.0.

C. Change in slope at high levels

As shown in Fig. 2, there is a clear change in slope at high levels for signal frequencies of 750 Hz and above. The change in slope at high levels thus appears to be a consistent and rather general effect for cases where $f_m \ll f_s$. It may represent a fundamental aspect of auditory processing. In order to understand the nature of this secondary slope at high levels, it is important to characterize various aspects of it, such as its value, the point at which it begins, and whether it is influenced more by signal or masker level. For all masking functions (individual and group average) that were fitted with two straight lines, the average slope of the second line was 0.97, indicating essentially linear growth of masking at high levels.

In order to describe the level at which the slope changed to linear, the breakpoints in the two-line fits (represented, for example, by the open circles in Fig. 2) were tabulated. On average, the breakpoint occurred at a signal SPL of 70 dB, corresponding to a signal sensation level (SL) of 51 dB (i.e., 51 dB of masking). The level of the masker at the breakpoint was 82 dB SPL.

To determine whether the change in slope is influenced more by signal or masker level, the ''local'' slope between any two adjacent points on each function was determined along the entire masking function. Scatter plots were then created, plotting this slope versus either signal SL, signal SPL, or masker SPL (in all cases, the level was determined by averaging the level of the two points that were used to create the local slope). Some examples are shown in Fig. 4, where the local slope is plotted as a function of signal SL (the solid line is described later). These are the same three signal frequencies that were shown in Fig. 1, but in this case each panel represents ''fits'' to the individual masking functions. In addition, each signal duration tested is represented. For all three crews, the local slope increases and then decreases with increasing signal level.[2] The slope reaches a maximum value of about 3.0 for a signal SL close to 35 dB, and declines to a value of 1.0 at a signal SL around 60 dB (a value slightly greater than the average value of the breakpoint determined from the two-line fits). At signal levels above 60 dB SL, the local slope value remains between 0.5 and 1.0, except for crew 1, where a few values approach 0.0 (this was also seen for $f_s = 4320$ Hz for this crew). This may reflect detection of the signal in the nontest ear at the highest signal levels (recall that crew 1 alone was not tested with a noise in the contralateral ear).

The scatter plots for all nine signal frequencies were fitted with a second-order linear regression line chosen to minimize the squared deviations; the fits for the scatter plots in Fig. 4 are shown as a solid line. The r^2 values were used

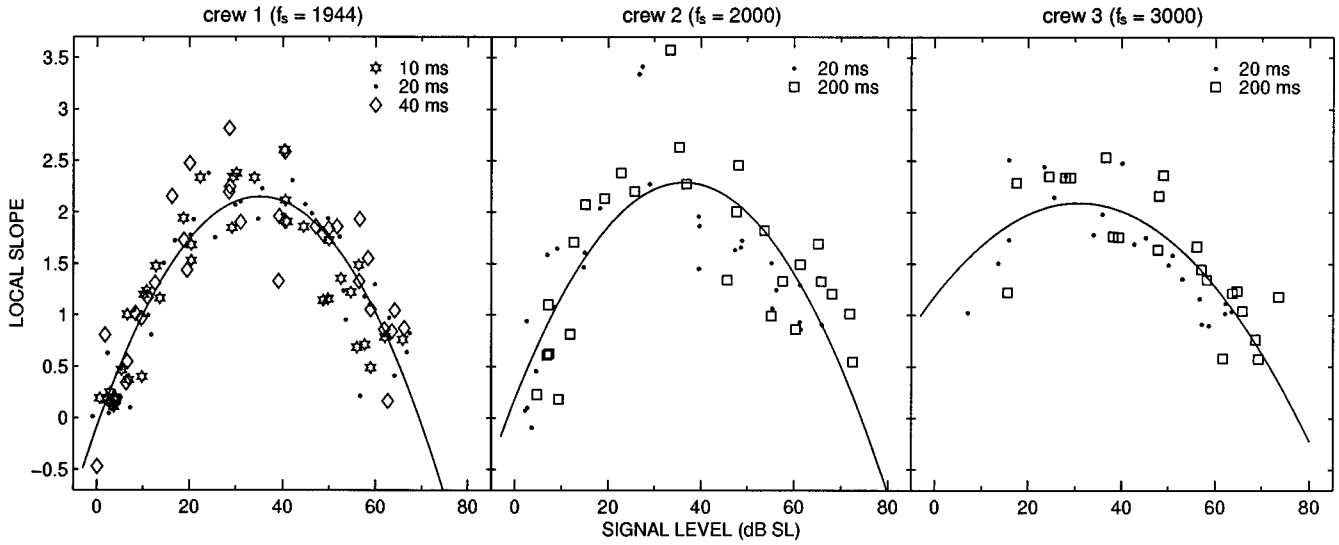

FIG. 4. Scatter plot showing the local slope as a function of signal level (dB SL) for the three listening crews. See the text for details. The solid line represents the best-fitting second-order linear regression.

to determine whether the local slope values were more highly correlated with signal SPL, signal SL, or masker SPL. When averaged across all nine signal frequencies, the r^2 values were 0.41, 0.53, and 0.46, respectively. When averaged across the six highest signal frequencies (i.e., excluding the frequencies for which the masking functions generally were well described by a single straight line), the r^2 values were 0.52, 0.59, and 0.53, respectively. Thus, although all three level metrics are obviously highly correlated with one another, the shape of the masking function seems to be somewhat more dependent upon signal SL. This, coupled with the fact that the breakpoint occurs at about 50 dB SL, may help explain why the masking functions for the three lowest signal frequencies generally do not change slope at high levels (see Fig. 2): the amount of masking produced at those frequencies is generally less than 50 dB.

III. DISCUSSION

A. Effect of overall frequency

1. Comparisons with previous studies

The results from the present study indicate that the slope of the initially steep portion of the GOM function ($f_m \ll f_s$) depends upon overall frequency. The slope is consistently less than 2.0 (often less than 1.5) for signal frequencies from 400 to 750 Hz, and consistently about 2.0 or greater for signal frequencies from near 2000 to 5000 Hz. This slope at higher frequencies is consistent with the slope of between 2.0 and 2.5 obtained by others (e.g., Zwicker, 1976, 1979; Schöne, 1977; Moore and Glasberg, 1987; van der Heijden and Kohlrausch, 1995; Gregan *et al.*, 1998). Very few tone-on-tone masking studies, however, have included (masker and) signal frequencies below 750 Hz, and even fewer have also included higher frequencies for comparison. Wegel and Lane (1924) provided masking functions for masker frequencies from 200 to 3500 Hz (and for several signal frequencies for each f_m). Although it is difficult to obtain accurate estimates of slope from most of their functions, given the relatively limited range of masking (particularly for $f_m \ll f_s$), it appears that the slope is shallower (and indeed close to 1.0) for signal frequencies below about 700 Hz. Schöne (1977) included masker and signal frequencies from below to well above 750 Hz, but he generally combined results across frequency (for a given $f_m - f_s$ frequency separation in Barks), thus precluding an evaluation of the effect of overall frequency. One of his figures (Fig. 1) allows a comparison across a restricted range of those frequencies, and, as noted in the Introduction, the slope did not change appreciably as f_s increased from 700 to 4800 Hz. Zwicker and Jaroszewski (1982) obtained masking patterns for masker frequencies from 250 to 6030 Hz, but unfortunately the masker level was generally not high enough (it was $\leqslant$60 dB) to evaluate the slope of the masking function for $f_m \ll f_s$. Finally, Moore and Glasberg (1987) obtained GOM functions ($f_s/f_m = 1.8$) for signal frequencies of 450, 1800, 5400, and 9495 Hz. The average slope across their three subjects who were tested at all four signal frequencies was 1.86, 2.34, 2.56, and 2.62, respectively. [Although the average slope at 450 Hz is generally greater than that observed here for signal frequencies of 626 Hz and below, it was skewed by the especially large slope value (2.53) of one subject.] The results of Moore and Glasberg are thus generally consistent with the present results.

The above comparisons were with studies that employed simultaneous masking. It is also worth comparing our findings with those obtained using nonsimultaneous masking. There are several such studies that have found steeper slopes at higher frequencies. For example, using a forward-masking paradigm, Kidd and Feth (1981) obtained steeper slopes at signal frequencies of 1500 and 3000 Hz than at 375 or 750 Hz ($f_s = 1.5\, f_m$ in all cases). Hicks and Bacon (1999) recently reported a similar finding ($f_s = 1.44\, f_m$ in all cases). And finally, using a pulsation-threshold paradigm, Verschuure (1981) found that his ''masking patterns'' increased linearly with level for a ''masker'' frequency of 500 Hz, but nonlinearly (greater upward spread of masking) for a fre-

quency of 1000 or 2000 Hz. Taken together, evidence from both simultaneous and nonsimultaneous masking suggest that growth of masking ($f_m \ll f_s$) is more linear at low frequencies than at high.

2. Implication for changes in nonlinearity along the cochlea

As discussed in the Introduction, it may be possible to understand the steep slope of the GOM function in terms of the response properties of the basilar membrane. To summarize, basilar membrane I–O functions suggest that the response to the masker *at the signal frequency place* will be linear, whereas the response to the signal at that place will be compressed (e.g., Ruggero *et al.*, 1997). Consequently, the signal must be increased more than the masker in level in order to maintain a constant signal-to-masker ratio in terms of excitation. The slope of the masking function should thus be proportional to the degree of compression; the greater the compression, the steeper the slope. Although these simultaneous-masking functions may not provide an accurate estimate of the amount of compression *per se* (see the discussion below), they should nevertheless allow comparisons of the relative amounts of compression in different frequency regions. The results presented here and in Moore and Glasberg (1987) for simultaneous masking and in Kidd and Feth (1981), Verschuure (1981), and Hicks and Bacon (1999) for nonsimultaneous masking, suggest that there is less compression at low frequencies than at high, where ''low frequencies'' corresponds to frequencies below about 700 Hz, and ''high frequencies'' may correspond to any frequency above 700 Hz. In the present study, none of the GOM functions had a slope (at least of the initial segment) of 1.0, suggesting at least a certain degree of compression at all frequencies tested. The GOM results are thus broadly consistent with a growing set of psychophysical and physiological results suggesting that the apical region of the cochlea behaves more linearly than does the more basal region (for a review, see Lee and Bacon, 1998, and Hicks and Bacon, 1999).

Although the steep slope of the masking function may reflect compression of the signal's response, there is reason to believe that the slope of the functions obtained here underestimates the degree of compression at the basilar membrane. Direct measurements of basilar membrane motion for a tone equal to the CF of the recording site have revealed I–O functions with highly compressive slopes of about 0.2, while I–O functions for a tone well below CF have a slope of 1.0 (e.g., Sellick *et al.*, 1982; Yates *et al.*, 1990; Ruggero, 1992; Ruggero *et al.*, 1997). Inasmuch as the GOM function reflects these response growths, the signal would have to be increased by 5 dB for every 1-dB increase in masker level. That is, the I–O functions predict a GOM function with a slope of 5.0, which is much greater than the slopes observed here and elsewhere. Although there are many obvious experimental differences between recordings of basilar membrane motion and psychophysical masking, one possible explanation for the difference between the predicted and obtained slopes lies in the difference in stimulus presentation. In particular, the physiological measures of response growth were obtained for single tones presented in isolation, whereas the GOM functions were obtained for two tones presented simultaneously. This raises the possibility that, in the psychophysical experiments, the masker may have suppressed the signal to some degree. Indeed, it has been suggested that simultaneous masking may be largely due to suppression, particularly for conditions where $f_m \ll f_s$ (e.g., Javel *et al.*, 1983; Delgutte, 1990). As noted by Oxenham and Plack (1997), this suppression could reduce the slope of the GOM function, given that the growth of response at the basilar membrane to a tone at CF becomes more linear in the presence of a lower frequency suppressor (Ruggero *et al.*, 1992). There are two reasons to believe that the simultaneous presentation of the masker and signal may be largely responsible for the more gradual slope than predicted, and that the masking observed here may be influenced considerably by suppression. First, the slope of 2.0 observed in the psychophysical masking experiments is the same as that observed in a simultaneous-masking experiment at the level of the auditory nerve (Pang and Guinan, 1997). Further, Pang and Guinan (1997) argued that most of the masking they observed was due to suppression, and noted that their growth of masking was similar in rate to the growth of suppression observed previously by others (e.g., Abbas and Sachs, 1976; Costalupes *et al.*, 1987). The similarity between the psychophysical and physiological results suggests that other experimental differences between behavioral and physiological measurements (e.g., the opportunity to listen off-frequency or to combine information across an array of nerve fibers in the behavioral paradigm) may not be especially important to the slope of the masking function. The second reason to believe that the simultaneous presentation of the masker and signal has a large influence on the slope of the GOM function is that Oxenham and Plack (1997) measured GOM functions in forward masking with slopes close to 6.0, more similar to that predicted based on basilar membrane I–O functions. (It is worth mentioning, however, that there are no other published reports of such steep slopes in forward masking.)

3. Implication for calculating excitation patterns

Masking patterns are often useful estimates of the spread of excitation within the auditory system. Excitation patterns can be calculated for essentially any arbitrary input (e.g., Glasberg and Moore, 1990). These patterns are used, for example, as a front end for data compression schemes (Johnston, 1988); components of a sound that will be masked need not be encoded for perceptual purposes. The shape of the excitation pattern is usually assumed to be independent of overall frequency (for a given masker level) when plotted on a Bark scale. The GOM functions obtained here suggest that the way in which the masking pattern changes shape with level is not invariant with overall frequency. Thus, it may not be appropriate to shift a fixed pattern up and down the Bark (or ERB) scale; an excitation pattern derived from a masking pattern at a relatively high frequency may overestimate the amount of excitation (at least on the high-frequency side) at low frequencies. Without obtaining complete masking patterns over a wide range of levels and frequencies, it is unclear to what extent the excitation patterns will vary with

overall frequency. It may thus be reasonable to extend the present results to at least a few other $f_m - f_s$ relationships, to characterize more completely the entire masking pattern.

B. Change in slope at high levels

The change in slope at high levels that had been observed previously by a few others (especially Schöne, 1977; Zwicker, 1979; Gregan *et al.*, 1998) was observed consistently here, at least for signal frequencies at and above 750 Hz. For those frequencies, the slope of the masking function changed from a value near 2.0 to a value of 1.0 at high levels. It is of interest to speculate on the nature of this change in slope.

1. Detection of the CDT

One possibility is that the change in slope could reflect the detection of a CDT at high levels. The presence of a CDT might change the slope to a value <1.0, given that it would represent a masking situation where $f_m > f_s$ (where f_s is now the CDT). However, detection of a CDT seems unlikely in the present study, given the presence of the low-pass noise for all subjects. Furthermore, the slope changes to a value of 1.0, not something noticeably <1.0.

2. Cross hearing

Another possible explanation for the change in slope at high levels is that it reflects the detection of the signal in the nontest ear. As discussed by Wegel and Lane (1924), the presence of a slope near 0.0 in some of their data can be accounted for this way. A slope near 1.0 could also be obtained if both the masker and signal were present in the nontest ear at levels where—in the test ear—masking was first beginning to take place [note that the slope of the GOM function can be near 1.0 over the first 5 to 10 dB of masking in the test ear (see Fig. 3)]. This explanation, however, seems unlikely, in that noise in the contralateral ear was presented to the subjects in crews 2 and 3.

3. Middle-ear muscle reflex

The middle-ear muscles are known to contract in response to intense acoustic stimulation, and thus would likely contract at the higher masker levels used in the present study (on average, the breakpoint in the two-line fits occurred at a masker SPL of 82 dB, whereas the local slope began to decrease at a masker SPL of 73 dB). Because contraction of the middle-ear muscles results in an attenuation of relatively low frequencies, the reflex could attenuate the lower frequency masker more than the higher frequency signal, thereby causing the signal to be easier to detect (Borg and Zakrisson, 1974). This masking release could reduce the slope of the masking function at high levels. However, this explanation would not be able to account for the change in slope for the highest masker–signal pairs (1350–1944, 1386–2000, 2110–3000, 3000–4320, and 3566–5000 Hz), because the middle-ear muscle reflex provides little or no attenuation of frequencies above about 1300 Hz (Rabinowitz, 1977, as cited in Wilson and Margolis, 1991). Thus, although the middle-ear muscle reflex could have influenced the masking at high levels for the lower frequency pairs, it cannot account for the general finding of a change in slope at high levels.

4. Off-frequency listening

Another possible explanation for the linear slope at high levels is related to off-frequency listening. In particular, if the subjects were to detect the signal at a place considerably basal to the signal frequency place, then the growth of response to the signal at that place would be linear [for the same reason that the response to the masker at the (more basal) signal frequency place is linear]. In other words, the masking function would likely be linear if subjects were to make decisions based on signal (and masker) excitation on the basal or high-frequency side of the excitation pattern, because the growth of response there would be linear in response to both the masker and signal. Consistent with this are auditory-nerve data from Pang and Guinan (1997), where the slope of the masking function was found to be close to 1.0 when the signal frequency was about half an octave below the fiber's CF (masker located well below the signal frequency). To examine the influence of off-frequency listening, subjects in crew 2 were retested in the presence of a high-pass noise. Signal frequency was 2000 Hz (f_m was 1386 Hz), and signal duration was 200 ms. The cutoff frequency of the noise was 2500 Hz ($1.25\,f_s$), which is likely to mask the frequency regions where the response to the signal would be linear (e.g., Ruggero *et al.*, 1997). The spectrum level of the noise was 30 dB. Two high masker levels (85 and 95 dB SPL) were used to ensure that the signal level would be in a region where the masking function was linear. Thresholds did not change in the presence of the high-pass noise. Two additional subjects (one from crew 3, and one new subject associated with the laboratory) were recruited and tested in the presence of an even more intense noise. In this case, f_s was 4320 Hz and f_m was 3000 Hz. The noise was bandpass with cutoff frequencies of either 1.17 and $1.32\,f_s$ or 1.27 and $1.41\,f_s$. The spectrum level of the noise was 50, 60, or 70 dB. The masker level was 95 dB SPL. Masked thresholds were unaffected by the bandpass noise. Thus, although it is difficult to rule out off-frequency listening completely, these pilot results strongly suggest that off-frequency listening cannot explain the change in slope at high levels.

5. Changes in response growth at high levels

The last two possible explanations considered here refer to changes in the response growth of the signal at the signal frequency place. The first of these was suggested by Gregan *et al.* (1998), namely that the change in slope at high levels might reflect subtle cochlear damage. This explanation was based on a recent finding that, following small amounts of cochlear damage (yielding threshold shifts of about 5–10 dB), the basilar membrane I–O function changes from compressive to more nearly linear at high SPLs for a tone at CF (Ruggero *et al.*, 1997). Thus, if the normal-hearing subjects tested here and elsewhere (Schöne, 1977; Zwicker, 1979; Gregan *et al.*, 1998) had small amounts of cochlear damage, then the slope of the GOM functions might be expected to

change to linear at high signal levels. Although plausible, this explanation seems unlikely. If the change in slope were due to a pathological state of the cochlea, then one might not expect that state to be similar across all subjects and across a relatively large portion of the cochlea. Yet, the local slope started to decrease at about 35 dB SL for all subjects and for all signal frequencies from 750 Hz and above. This consistency seems more appropriately attributed to a *normal* aspect of auditory processing, although, admittedly, the homogeneity of our subjects in terms of age and hearing sensitivity tempers this argument against auditory pathology.

Finally, the last explanation discussed here was originally offered by Zwicker (1979), in a paper in which he suggested that the change in slope at high levels reflects a saturation of the active, nonlinear processing provided by the outer hair cells. In support of this, it is known that the gain provided by the outer hair cells decreases with increasing stimulus level (e.g., Ruggero *et al.*, 1997), and hence that the influence of the outer hair cells on the motion of the basilar membrane decreases with increasing level. Because the outer hair cells are responsible for the compressive response of the basilar membrane (e.g., Ruggero *et al.*, 1996), it might be reasonable to assume that the amount of compression will decrease as the influence of the outer hair cells decreases. This would thus predict—inasmuch as the slope of the GOM function is influenced by the degree of compression—a masking function whose slope decreases with increasing signal level. A possible problem with this explanation, however, is that Ruggero *et al.* (1997) found basilar membrane I–O functions that were compressive up to stimulus levels of 100 dB SPL, yet the GOM functions change slope at signal levels much lower than that.

IV. SUMMARY

The purpose of the present study was to measure GOM functions in simultaneous masking ($f_m \ll f_s$) over a wide frequency range to determine whether the steep portion of the function varies with overall frequency, and to examine the generality of the previously reported change to a linear slope at high levels. The results indicate that, on average, the slope of the steep portion of the GOM function is shallower (average slope value of 1.4) for signal frequencies at and below 750 Hz than it is for frequencies higher than that (average slope value of 2.0). This suggests that the response of the cochlea may be more compressive at high than at low frequencies. The slope of the GOM function in simultaneous masking, however, may underestimate the degree of compression as a result of the signal being suppressed at least somewhat by the masker. For signal frequencies of 750 Hz and higher, the slope of the masking function changes from a value of about 2.0 to a value of 1.0 at signal levels corresponding to a value of 50 dB SL. The cause of this change in slope is unclear, although it may represent a change in response to the signal from compressive to linear at high levels.

ACKNOWLEDGMENTS

This research was supported by NIDCD Grant No. DC01376. The results from crew 2 are from an undergraduate Honor's thesis submitted by the second author to the Honor's College at Arizona State University. We thank Dr. Li Liu for assistance with data analysis, and Dr. Michelle Hicks, Dr. David Nelson (a formal reviewer), and one anonymous reviewer for their comments on a previous version of this manuscript.

[1]Preliminary testing of one subject showed a near 0-slope region at high signal (and masker) levels, suggesting that this subject was detecting the signal in the nontest ear (Wegel and Lane, 1924). Broadband noise was presented to the nontest ear to eliminate this effect. Signal frequency was 750 or 2000 Hz (f_m was 480 or 1386, respectively), and the masker level was 85, 90, or 95 dB SPL. The masked threshold in the test ear increased when the noise was introduced into the nontest ear at a spectrum level of 0 dB, and increased further when the level of the noise was increased to 10 dB. The threshold did not increase further when the noise was increased to 20 dB. Thus, a spectrum level of 10 dB was deemed sufficient to mask the nontest ear.

[2]The finding that the local slope increases and then decreases with level suggests that the GOM functions generally would be more appropriately fitted with a sigmoidal function than with two straight lines, as was done here (e.g., Figs. 1 and 2). We opted, however, for the straight-line fits (with typical r^2 values of 0.99) to better compare the slopes obtained here with those reported in the literature obtained using single straight lines.

Abbas, P. J., and Sachs, M. B. (**1976**). ''Two-tone suppression in auditory-nerve fibers: Extension of a stimulus–response relationship,'' J. Acoust. Soc. Am. **59**, 112–122.

ANSI (**1989**). ANSI S3.6-1989, *Specifications for Audiometers* (American National Standards Institute, New York).

Bacon, S. P., and Viemeister, N. F. (**1985**). ''Simultaneous masking by gated and continuous sinusoidal maskers,'' J. Acoust. Soc. Am. **78**, 1220–1230.

Borg, E., and Zakrisson, J.-E. (**1974**). ''Stapedius reflex and monaural masking,'' Acta Oto-Laryngol. **78**, 155–161.

Cooper, N. P., and Rhode, W. S. (**1995**). ''Nonlinear mechanics at the apex of the guinea-pig cochlea,'' Hearing Res. **82**, 225–243.

Cooper, N. P., and Yates, G. K. (**1994**). ''Nonlinear input–output functions derived from the responses of guinea-pig cochlear nerve fibers: Variations with characteristic frequency,'' Hearing Res. **78**, 221–234.

Costalupes, J. A., Rich, N. C., and Ruggero, M. A. (**1987**). ''Effects of excitatory and non-excitatory suppressor tones on two-tone rate suppression in auditory nerve fibers,'' Hearing Res. **26**, 155–164.

Delgutte, B. (**1990**). ''Physiological mechanisms of psychophysical masking: Observations from auditory-nerve fibers,'' J. Acoust. Soc. Am. **87**, 791–809.

Egan, J. P., and Hake, H. W. (**1950**). ''On the masking pattern of a simple auditory stimulus,'' J. Acoust. Soc. Am. **22**, 622–630.

Glasberg, B. R., and Moore, B. C. J. (**1990**). ''Derivation of auditory filter shapes from notched-noise data,'' Hearing Res. **47**, 103–138.

Gregan, M. J., Bacon, S. P., and Lee, J. (**1998**). ''Masking by sinusoidally amplitude-modulated tonal maskers,'' J. Acoust. Soc. Am. **103**, 1012–1021.

Heijden, M. van der, and Kohlrausch, A. (**1995**). ''The role of envelope fluctuations in spectral masking,'' J. Acoust. Soc. Am. **97**, 1800–1807.

Hicks, M. L., and Bacon, S. P. (**1999**). ''Psychophysical measures of auditory nonlinearities as a function of frequency in individuals with normal hearing,'' J. Acoust. Soc. Am. **105**, 326–338.

Javel, E., McGee, J., Walsh, E. J., Farley, G. R., and Gorga, M. P. (**1983**). ''Suppression of auditory nerve responses II. Suppression threshold and growth, iso-suppression contours,'' J. Acoust. Soc. Am. **74**, 801–813.

Johnston, J. D. (**1988**). ''Transform coding of audio signals using perceptual noise criteria,'' IEEE J. Sel. Areas Commun. **6**, 314–323.

Kidd, G., and Feth, L. L. (**1981**). ''Patterns of residual masking,'' Hearing Res. **5**, 49–67.

Lee, J., and Bacon, S. P. (**1998**). ''Psychophysical suppression as a function of signal frequency: Noise and tonal maskers,'' J. Acoust. Soc. Am. **104**, 1013–1022.

Levitt, H. (**1971**). ''Transformed up–down methods in psychoacoustics,'' J. Acoust. Soc. Am. **49**, 467–477.
Moore, B. C. J., and Glasberg, B. R. (**1987**). ''Factors affecting thresholds for sinusoidal signals in narrow-band maskers with fluctuating envelopes,'' J. Acoust. Soc. Am. **82**, 69–79.
Murnane, O., and Turner, C. W. (**1991**). ''Growth of masking in sensorineural hearing loss,'' Audiology **30**, 275–285.
Nelson, D. A., and Schroder, A. C. (**1996**). ''Release from upward spread of masking in regions of high-frequency hearing loss,'' J. Acoust. Soc. Am. **100**, 2266–2277.
Nelson, D. A., and Schroder, A. C. (**1997**). ''Linearized response growth inferred from growth-of-masking slopes in ears with cochlear hearing loss,'' J. Acoust. Soc. Am. **101**, 2186–2201.
Nelson, D. A., and Swain, A. C. (**1996**). ''Temporal resolution within the upper accessory excitation of a masker,'' Acustica **82**, 328–334.
Nuttal, A. L., and Dolan, D. F. (**1996**). ''Steady-state sinusoidal velocity responses of the basilar membrane in guinea pig,'' J. Acoust. Soc. Am. **99**, 1556–1565.
Oxenham, A. J., and Moore, B. C. J. (**1995**). ''Additivity of masking in normally hearing and hearing-impaired subjects,'' J. Acoust. Soc. Am. **98**, 1921–1934.
Oxenham, A. J., and Plack, C. J. (**1997**). ''A behavioral measure of basilar-membrane nonlinearity in listeners with normal and impaired hearing,'' J. Acoust. Soc. Am. **101**, 3666–3675.
Pang, X. D., and Guinan, Jr., J. J. (**1997**). ''Growth rate of simultaneous masking in cat auditory-nerve fibers: Relationship to the growth of basilar-membrane motion and the origin of two-tone suppression,'' J. Acoust. Soc. Am. **102**, 3564–3575.
Rabinowitz, W. M. (**1977**). ''Acoustic-reflex effects on the input admittance and transfer characteristics of the human middle-ear,'' unpublished doctoral dissertation, Massachusetts Institute of Technology, Cambridge, MA.
Robles, L., Ruggero, M. A., and Rich, N. C. (**1986**). ''Basilar membrane mechanics at the base of the chinchilla cochlea I. Input–output functions, tuning curves, and response phases,'' J. Acoust. Soc. Am. **80**, 1364–1374.
Rosen, S., and Stock, D. (**1992**). ''Auditory filter bandwidths as a function of level at low-frequencies (125 Hz–1 kHz),'' J. Acoust. Soc. Am. **92**, 773–781.
Ruggero, M. A. (**1992**). ''Responses to sound of the basilar membrane of the mammalian cochlea,'' Curr. Opin. Neurobiol. **2**, 449–456.
Ruggero, M. A., Robles, L., and Rich, N. C. (**1992**). ''Two-tone suppression in the basilar membrane of the cochlea: Mechanical basis of auditory nerve rate suppression,'' J. Neurophysiol. **68**, 1087–1099.
Ruggero, M. A., Rich, N. C., Robles, L., and Recio, A. (**1996**). ''The effects of acoustic trauma, other cochlear injury, and death on basilar membrane responses to sound,'' in *Scientific Basis of Noise-Induced Hearing Loss*, edited by A. Axelsson, H. Borchgrevink, R. P. Hamernik, P.-A. Hellstrom, D. Henderson, and R. Salvi (Thieme Medical, New York), pp. 23–35.
Ruggero, M. A., Rich, N. C., Recio, A., Narayan, S. S., and Robles, L. (**1997**). ''Basilar-membrane responses to tones at the base of the chinchilla cochlea,'' J. Acoust. Soc. Am. **101**, 2151–2163.
Schöne, P. (**1977**). ''Nichtlinearintäten im mithörschwellen-tonheitsmuster von sinustönen,'' Acustica **37**, 37–44.
Sellick, P. M., Patuzzi, R., and Johnstone, B. M. (**1982**). ''Measurement of basilar membrane motion in the guinea pig using the Mössbauer technique,'' J. Acoust. Soc. Am. **72**, 131–141.
Stelmachowicz, P. G., Lewis, D. E., Larson, L. L., and Jesteadt, W. (**1987**). ''Growth of masking as a measure of response growth in hearing-impaired listeners,'' J. Acoust. Soc. Am. **81**, 1881–1887.
Verschuure, J. (**1981**). ''Pulsation patterns and nonlinearity of auditory tuning. I. Psychophysical results,'' Acustica **49**, 288–295.
Wegel, R. L., and Lane, C. E. (**1924**). ''Auditory masking of one pure tone by another and its possible relation to the dynamics of the inner ear,'' Phys. Rev. **23**, 266–285.
Wilson, R. H., and Margolis, R. H. (**1991**). ''Acoustic-reflex measurements,'' in *Hearing Assessment*, edited by W. F. Rintelmann (pro-ed, 2nd ed.).
Yates, G. K., Winter, I. M., and Robertson, D. (**1990**). ''Basilar membrane nonlinearity determines auditory nerve rate-intensity functions and cochlear dynamic range,'' Hearing Res. **45**, 203–220.
Zwicker, E. (**1976**). ''Influence of a complex masker's time structure on masking,'' Acustica **34**, 138–146.
Zwicker, E. (**1979**). ''A model describing nonlinearities in hearing by active processes with saturation at 40 dB,'' Biol. Cybern. **35**, 243–250.
Zwicker, E., and Jaroszewski, A. (**1982**). ''Inverse frequency dependence of simultaneous tone-on-tone masking patterns at low levels,'' J. Acoust. Soc. Am. **71**, 1508–1512.

Discrimination of frequency steps linked by glides of various durations

Aleksander Sek[a] and Brian C. J. Moore
Department of Experimental Psychology, University of Cambridge, Downing Street, Cambridge CB2 3EB, England

(Received 19 October 1998; revised 9 February 1999; accepted 25 March 1999)

Thresholds were measured for detecting steps in frequency linked by glides of various durations. The goals were to assess the relative importance of place and temporal information for this task, and to determine whether there is a mechanism for detecting dynamic frequency changes *per se*, as opposed to comparing the initial and final frequencies of the stimuli. Subjects discriminated a 500-ms sinusoid of constant frequency from a sinusoid with three parts: an initial part with constant frequency, a downward frequency glide, and a final part with constant frequency. The overall duration was 500 ms, and the glide duration was varied from 5 to 500 ms. In one special case, the portion of the stimuli when a glide might occur was replaced by a brief silent interval. The center frequency was fixed at 0.5, 1, 2, 4, or 6 kHz (condition 1), or varied randomly from one stimulus to the next over a 4-ERB range around the nominal center frequency (condition 2). The randomization impaired performance, but thresholds remained lower than the best that could be achieved by monitoring either the initial or final frequency of the stimuli. Condition 3 was like condition 2, but for each stimulus a glide in level was added at the time when a frequency glide might occur, so the initial and final levels differed; the glides in level varied randomly in extent and direction from one stimulus to the next over the range ± 20 dB. This impaired performance, but thresholds remained lower than the best that could be achieved by monitoring changes in excitation level on only one side of the excitation pattern. Excitation-pattern models of frequency discrimination predict that thresholds should not vary across center frequency when expressed as the change in ERB number, ΔE. For all conditions, ΔE values increased at 6 kHz, suggesting a role for temporal information at lower frequencies. The increase was smallest for the longest glide duration, consistent with a greater relative role of place information when there was no steady state portion. Performance was better when a brief glide was present than when no glide was present, but worsened with increasing glide duration. The results were fitted well by a model based on the assumption that information from the steady parts of the stimuli (perhaps extracted mainly using temporal information) was combined with information from the glides (perhaps extracted mainly using place information). [S0001-4966(99)01807-X]

PACS numbers: 43.66.Fe, 43.66.Hg, 43.66.Ba [RVS]

INTRODUCTION

Traditionally, there have been two classes of theory to explain the ability to detect and discriminate frequency changes in sinusoids. One class assumes that frequency discrimination is based on changes in the place distribution of activity in the auditory system. For example, Zwicker (1956, 1970) proposed a model for the detection of frequency modulation (FM) based on the concept of the excitation pattern. He suggested that FM could be detected if it resulted in a change in the amount of excitation greater than 1 dB at any point on the excitation pattern. The alternative class of theory assumes that frequency discrimination is based on information contained in the temporal patterns of firing in the auditory nerve (phase locking) (Siebert, 1970; Goldstein and Srulovicz, 1977).

Models based on excitation patterns generally make the prediction that the threshold for detection of a frequency change at a given center frequency should be a constant proportion of the critical bandwidth or the equivalent rectangular bandwidth (ERB) of the auditory filter at the center frequency, regardless of the center frequency. Put another way, if the threshold is expressed as the change in ERB number, the threshold should be independent of center frequency (the ERB scale is obtained by using the ERB as the unit of frequency. For example, the value of the ERB for a center frequency of 1 kHz is about 130 Hz, so an increase in frequency from 935 to 1065 Hz represents a step of one ERB. The ERB number is analogous to number of Barks. See Glasberg and Moore, 1990). Data on the frequency discrimination of pulsed tones generally do not conform well to this prediction (Moore, 1974; Moore and Glasberg, 1986, 1989; Sek and Moore, 1995). However, the prediction holds reasonably well for the detection of FM (Zwicker, 1956; Zwicker and Fastl, 1990), especially when the modulation is at a rate of 10 Hz or higher (Sek and Moore, 1995; Moore and Sek, 1996).

These and other findings have led to the proposal that pulsed-tones frequency discrimination is largely based on

[a]Present address: Institute of Acoustics, Adam Mickiewicz University, Matejki 48/49, 60-769 Poznan, Poland.

temporal information for frequencies up to 4–5 kHz (Moore, 1973a,b, 1974; Goldstein and Srulovicz, 1977; Sek and Moore, 1995; Moore, 1997; Micheyl *et al.*, 1998), while the detection of frequency modulation for rates above about 10 Hz is largely based on excitation-pattern cues (Zwicker, 1956; Zwicker and Fastl, 1990; Moore and Sek, 1994, 1995; Sek and Moore, 1995).

There is no clear consensus as to the mechanisms underlying the detection and discrimination of frequency glides. Dooley and Moore (1988) measured thresholds for the detection of frequency glides in 500-ms tones over a wide range of center frequencies (0.5–0.8 kHz). They compared the thresholds with the predictions of Zwicker's (1956) model and concluded that ''the discrepancies are not large enough to provide strong evidence against the model.'' Madden and Fire (1996) measured thresholds for detecting frequency glides and for discriminating frequency glides of different extents (referred to as transition spans), using 50-ms tone glides. The thresholds were roughly a constant proportion of the ERB of the auditory filter over a range of center frequencies from 0.5 to 6 kHz. They took this as support for an excitation-pattern model. In a second study (Madden and Fire, 1997), they used both a 50-ms duration and a 400-ms duration. They concluded that the results for both durations were consistent with a mechanism that monitors the changes in excitation level at the most steeply sloping part of the excitation pattern evoked by the stimuli (the low-frequency side).

Moore and Sek (1998) replicated and extended the results of Madden and Fire (1996, 1997). They included conditions where large glides in level were superimposed on the stimuli. The glides in level varied randomly in direction (increasing versus decreasing level) and in extent from one stimulus to the next. This was expected to markedly disrupt the usefulness of cues based on monitoring changes in excitation level on one side of the excitation pattern. For some conditions, performance was too good to be explained in terms of the discrimination of changes in excitation level on one side of the excitation pattern. Thresholds, expressed in ERBs, did not vary greatly with center frequency (0.5, 2, or 6 kHz), suggesting that discrimination did not depend strongly on information derived from phase locking. However, there was a trend for performance to be worse at 6 kHz than at 0.5 or 2 kHz, which is consistent with a small role for phase locking information at the two lower frequencies. Moore and Sek concluded that excitation-pattern cues probably played a dominant role in the discrimination of frequency glides, but that subjects used information from both sides of the pattern, rather than monitoring just one side.

In the present experiment, we used stimuli that can be regarded as forming a continuum between two extremes. At one extreme, the task was to detect a difference in frequency between two steady tone bursts. We assumed that this task would be based largely on the use of temporal information, for frequencies up to 4 kHz. At the other extreme, the task was to detect a frequency glide in stimuli with no steady-state portion. We assumed that this task would be based largely on the use of place (excitation-pattern) information. Intermediate stimuli contained both steady portions and frequency glides. We wished to determine whether and how information from the steady-state portion and the glide could be combined. As in our earlier experiment (Moore and Sek, 1998), we included conditions where the center frequency of the stimuli was randomized, to reduce the ability to make use of information from either the start or end frequencies of the stimuli. We also included a condition where the glide in frequency was accompanied by a glide in level that varied randomly in extent and direction from one stimulus to the next over the range ± 20 dB. This was intended to disrupt cues based on changes on one side of the excitation pattern. There have been previous studies of the detection and discrimination of frequency glides bounded by plateaus with steady frequency (Nabelek and Hirsh, 1969; Tsumara *et al.*, 1973; Arlinger *et al.*, 1977). However, those studies did not include conditions where the center frequency was roved or where glides in level were superimposed on the frequency glides.

We also included a set of conditions in which the shortest frequency glide was replaced by a brief silent interval. We were interested in whether performance would be affected by the presence of the brief glide. Some researchers have suggested that glides are detected by sampling the frequencies at the start and end of the stimuli, and basing judgments on the difference between the two samples (Pollack, 1968). This is sometimes called ''endpoint sampling'' or ''snapshot'' theory. If this is the case, performance should be essentially unaffected by whether or not a glide is present between two plateaus in frequency. On the other hand, there may be a mechanism specifically sensitive to dynamic changes in frequency (Nabelek and Hirsh, 1969; Tsumara *et al.*, 1973; Dooley and Moore, 1988). If so, and if information from endpoint sampling can be combined effectively with information about dynamic changes in frequency, then performance should be improved by the presence of a brief frequency glide between two plateaus in frequency. The present experiment was designed to decide between these two possibilities.

I. THE EXPERIMENT

A. Procedure and stimuli

An adaptive two-alternative forced-choice (2AFC) task tracking the 70.7% correct point on the psychometric function was used. The mean level of the stimuli was 70 dB SPL. The silent interval between the two stimuli in each trial was 500 ms. All stimuli had 5-ms raised-cosine rise/fall ramps during which the frequency was constant. In what follows, durations are specified excluding these 5-ms ramps.

In one set of conditions, subjects discriminated a 500-ms sinusoid of constant frequency from a sinusoid with three parts: an initial part with constant frequency f_{start} and duration d_{steady}; a downward frequency glide between f_{start} and f_{end}, with duration d_{glide}; and a final part with frequency f_{end} and duration d_{steady}. The glides were linear on an ERB scale (see below for details). The overall duration of the three portions was 500 ms, and the value of d_{glide} was 5, 10, 20, 50, 100, 200, or 500 ms. Thus the value of d_{steady} varied from 247.5 to 0 ms. In condition 1, the center frequency was fixed

at 0.5, 1, 2, 4, or 6 kHz. In condition 2, the center frequency varied randomly from one stimulus to the next over a 4-ERB range (±2 ERBs) around the nominal center frequency. This was done to reduce the ability to use information from either the start or end frequencies of the stimuli. The scale relating ERB number to frequency was based on the equation given by Glasberg and Moore (1990):

$$\text{ERB number} = 21.4 \log_{10}(4.37F + 1),$$

where F is frequency in kHz. Following arguments given by Moore and Sek (1998), it can be shown that the smallest possible threshold that could be achieved by monitoring only the start or endpoint frequencies of the stimuli is 1.88 ERBs.[1]

Condition 3 was like condition 2, except that a glide in level occurred at each time when a glide in frequency might occur. The glide in level was linear in dB/s and it varied randomly in extent and direction from one stimulus to the next over the range ±20 dB. Thus the levels of the initial and final parts of the stimuli, where the frequency was steady, also varied randomly from one stimulus to the next. The glide in level was present in both intervals of the 2AFC task. This was intended to disrupt cues based on changes in excitation level on one side of the excitation pattern. Following arguments given by Moore and Sek (1998), it can be shown that the smallest possible threshold that could be achieved by monitoring only one side of the excitation pattern evoked by the stimuli is about 0.82 ERBs. Note that the glide in level was synchronized with the glide in frequency; the level was constant during the initial and final portions of the stimuli where the frequency was constant.

In another set of conditions, the task was to discriminate a pair of 250-ms tone bursts with the same frequency, and with a 5-ms silent interval between them, from two bursts with different frequencies, the second burst having a lower frequency than the first. As for the other stimuli, all bursts had 5-ms rise/fall times. This task is similar to a traditional frequency discrimination task using pulsed tones, except that it does not require the subject to identify the direction of the frequency change. Sek and Moore (1995) also used such a task, and referred to the resulting thresholds as ''difference limens for a change in frequency.'' This set of conditions was similar to the conditions for the shortest glide duration, except that the glide was replaced by a brief silent interval. For convenience we refer to this set of conditions as having a glide duration of 0 ms. The conditions were analogous to those for the frequency glides. In condition 3, the level was constant within each tone burst, but varied randomly from one burst to the next over the range ±20 dB.

One complication in condition 3 is that, sometimes, the level of the first half of the stimulus would have been markedly higher than that of the second half, in which case forward masking might have made the initial part of the second half inaudible. Indeed, the brief interval between the two bursts might not have been audible on some trials. Our stimuli had 5-ms rise/fall times, so the ''effective'' interval between the two halves of each stimulus was about 10 ms. Plomp's (1964) data suggest that a 10-ms silent interval between two burst of sound (with near-instantaneous rise/fall times) would just be detectable when the level of the first exceeds that of the second by 20 dB. For our stimuli, the level of the first half of a given stimulus would have exceeded that of the second half by 20 dB or more on only about 12% of trials. Thus we can conclude that the influence of forward masking would have been small.

Subjects were required to indicate the interval in which the stimulus frequency changed. Lights were used to mark the observation intervals and to provide feedback. Subjects were allowed as long as they wanted to make a response. The next trial began 1 s after a response had been made. Subjects were tested individually in a double-walled sound-attenuating chamber. We denote the difference in frequency between f_{start} and f_{end} by ΔF (in ERBs). At the start of a run, the value of ΔF was chosen on the basis of pilot trials to be large enough to make the task reasonably easy. The value of ΔF was changed by a factor of 1.5 until four reversals occurred. Thereafter it was changed by a factor of 1.25 and eight further reversals were obtained. The threshold for a run was estimated as the geometric mean value of ΔF at the last eight reversals. Four runs were obtained for each condition. Subsequently, runs were rejected in cases where the standard deviation of the logarithm of the values of ΔF at the last eight reversals was greater than 0.25; we have found that such runs are often associated with ''outliers.'' This happened in 11 cases out of 1440 (8 durations×5 frequencies×3 conditions×3 subjects×4 repetitions). Therefore, thresholds reported are usually based on four runs, but occasionally on only three. Subjects were tested first in condition 1, then in condition 2, and then in condition 3, although they were given practice on each condition. Testing was blocked by frequency, but the order of testing the frequencies was randomized for each subject.

Stimuli were generated using a Tucker-Davis array processor (TDT-AP2) in a host PC and a 16-bit digital to analog converter (TDT-DD1) operating at a 50-kHz sampling rate. They were attenuated (TDT-PA4) and sent through an output amplifier (TDT-HB6) to a Sennheiser HD414 earphone. This earphone is designed to mimic the diffuse-field response of the ear. The response at the eardrum is not flat, but it does vary smoothly with frequency. The mean level at each center frequency is specified as the level at the eardrum, based on probe microphone measurements (Rastronics Portarem 2000 system, mean results for eight persons, not the subjects of the present experiment). It is possible that, in the conditions with no glides in level in the electrical signal, the frequency glides resulted in glides in level in the acoustic signal that provided usable detection cues. However, the superimposed larger glides in level in condition 3 would have prevented such cues from being useful.

B. Subjects

Three subjects were tested. One was author AS. The other two subjects were paid for their service. All subjects had absolute thresholds less than 20 dB HL at all audiometric frequencies and had no history of hearing disorders. All had previous experience in psychoacoustic tasks. They were given practice in all conditions until their performance ap-

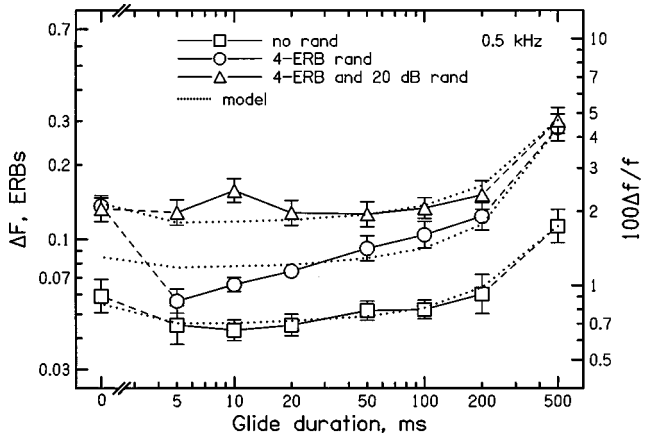

FIG. 1. Thresholds for a center frequency of 0.5 kHz, expressed in ERBs and plotted as a function of glide duration, with condition as parameter. Thresholds are plotted on a logarithmic scale. Corresponding values of $100\Delta f/f$ (i.e., the relative change in frequency in percent) are shown on the right-hand ordinate. Error bars indicate ± one standard error across subjects. Dotted lines show predictions of a model that is described in the text.

peared to be stable; this took between 10 and 15 h. The thresholds gathered during the practice sessions were discarded.

II. RESULTS

The standard deviation of the threshold estimates (across the three or four runs for a given condition and subject) was roughly a constant proportion of the mean threshold value. Hence, in what follows, geometric means are used throughout, and analyses of variance (ANOVAs) are based on the logarithms of the threshold values. Also, thresholds will be plotted on logarithmic scales. The pattern of results was similar across subjects, so only data averaged across subjects (geometric means) will be presented.

Figures 1–5 show thresholds, expressed in ERBs, plotted as a function of glide duration, d_{glide}. Corresponding values of $100\Delta f/f$ (i.e., the relative change in frequency in percent) are shown on the right-hand ordinate of each figure. Each curve shows results for one condition. Each figure shows results for one center frequency. The general pattern of the results was similar for all center frequencies. Performance was worse for condition 2 than for condition 1. In other words, randomizing the center frequency of the stimuli did impair performance. This could indicate that subjects monitored the start or end frequencies of the stimuli in condition 1, rather than comparing the start and end frequencies or detecting the glide *per se*. However, it may also be the case that the randomization of the center frequency made it more difficult for subjects to build up an internal representation of the stimuli to be discriminated, or that it had a distracting effect. For all glide durations and all center frequencies, thresholds in condition 2 were lower than the smallest possible threshold that could be achieved by monitoring only the start or endpoint frequencies of the stimuli (1.88 ERBs).

The introduction of the random changes in level (condition 3) further impaired performance. The effect was slightly greater at 6 kHz than at the lower center frequencies. Averaged across glide duration, the mean ratio of thresholds for condition 3 and condition 2 was 1.5, 1.5, 1.4, 1.6, and 1.9 for center frequencies of 0.5, 1, 2, 4, and 6 kHz. The slightly greater effect at 6 kHz is consistent with a greater role of excitation-pattern cues at that center frequency. However, even at 6 kHz, the thresholds in condition 3 were lower than the smallest possible threshold that could be achieved by monitoring only one side of the excitation pattern evoked by the stimuli (about 0.82 ERBs). Therefore, to the extent that excitation-pattern cues were being used, subjects must have compared excitation-pattern changes on the two sides of the

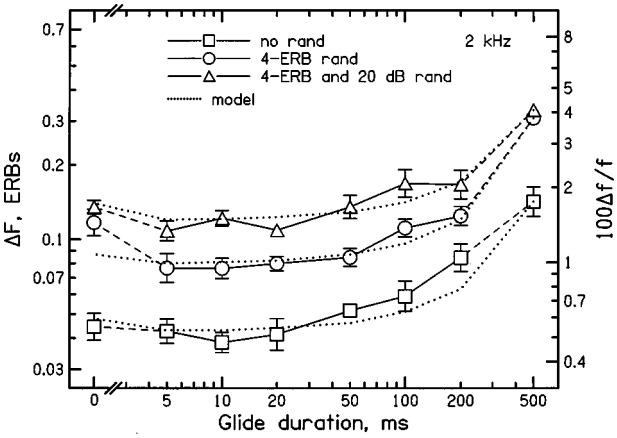

FIG. 3. As Fig. 1, but for a center frequency of 2 kHz.

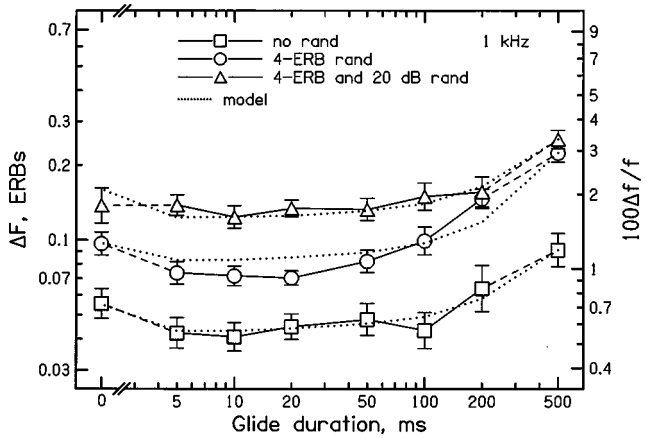

FIG. 2. As Fig. 1, but for a center frequency of 1 kHz.

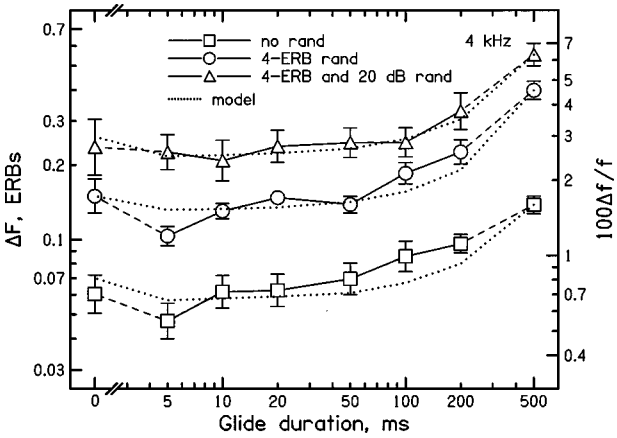

FIG. 4. As Fig. 1, but for a center frequency of 4 kHz.

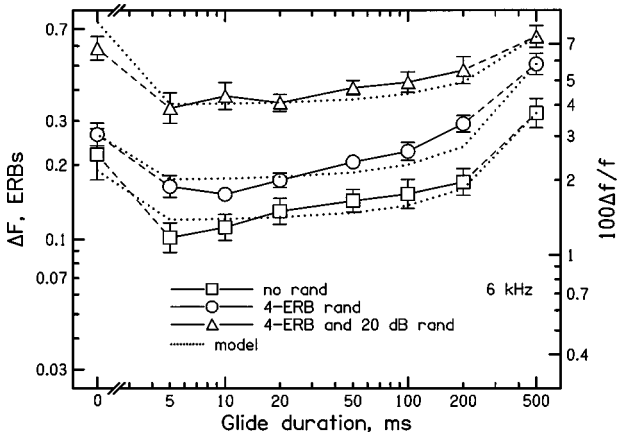

FIG. 5. As Fig. 1, but for a center frequency of 6 kHz.

pattern (Demany and Semal, 1986) or monitored the position of the peak of the excitation patten.

For the 0-ms glide duration, the randomization of level had relatively little effect on thresholds for center frequencies up to 2 kHz; the ratio of thresholds for condition 3 and condition 2 was 1.4 or less. The ratio increased to 1.6 at 4 kHz and 2.2 at 6 kHz. The small effect at low frequencies and greater effect at high frequencies is consistent with previous findings on the effects of level randomization on pulsed-tones frequency discrimination (Henning, 1966; Emmerich *et al.*, 1989; Moore and Glasberg, 1989). These results are consistent with the idea that the frequency discrimination of pulsed tones is mainly based on temporal information at low frequencies, and on place information at high frequencies. Again, however, the thresholds at 6 kHz in condition 3 were lower than the smallest possible threshold that could be achieved by monitoring only one side of the excitation pattern (about 0.82 ERBs).

For the conditions where frequency glides were present (glide durations from 5 to 500 ms), performance tended to worsen with increasing glide duration. The increase was especially marked between the glide durations of 200 and 500 ms. The stimuli with glide duration equal to 500 ms were the only ones for which there was no portion with constant frequency at the start and end of the stimuli (d_{steady} was equal to 0). This suggests that performance for the other glide durations depends partly upon subjects comparing the start and endpoint frequencies of the stimuli; stable frequencies at the start and end would help in determining those frequencies.

Interestingly, performance tended to be better for $d_{\text{glide}} = 5$ ms than for $d_{\text{glide}} = 0$ ms. This trend was reasonably clear for conditions 1 and 2, but was less clear for condition 3, except at 6 kHz. Thus the presence of a brief frequency glide led to improved performance, even when the start and endpoint frequencies were stable for a relatively long duration. We will return to this point later. Comparing the two extreme conditions, with no frequency glide ($d_{\text{glide}} = 0$ ms) and no portion with steady frequency ($d_{\text{glide}} = 500$ ms), it is noteworthy that for all frequencies up to 4 kHz, performance was better for the former than for the latter. Thus subjects were better at detecting a frequency difference between two 250-ms tone bursts than they were at detecting a difference in endpoint frequencies of a 500-ms frequency glide. However, at 6 kHz, the difference between the two extremes was less.

To assess the statistical significance of these effects, a within-subjects analysis of variance (ANOVA) was conducted on the logarithms of the threshold values, with factors glide duration, center frequency, and condition (1, 2, or 3). All of the main effects were highly significant: for glide duration, $F(7,14) = 75.18$, $p < 0.001$; for center frequency, $F(4,8) = 40.15$, $p < 0.001$; for condition, $F(2,4) = 102.7$, $p < 0.001$. The interaction of glide duration and center frequency was significant, $F(28,56) = 1.75$, $p = 0.038$, as was the interaction of duration and condition, $F(14,28) = 7.41$, $p < 0.001$.

The GENSTAT package used gave estimates of the standard errors of the differences between the mean thresholds for the different conditions. These standard errors were used to assess the significance of the differences between means using *t*-tests and the degrees of freedom associated with the residual term in the analysis of variance (Lane *et al.*, 1987, p. 110); this procedure is sometimes called the least-significant-difference test (Snedecor and Cochran, 1967). Averaged across conditions and frequencies, the mean threshold for the 0-ms glide was significantly higher than the mean threshold for the 5-ms glide; $t(14) = 8.32$, $p < 0.001$. The same was true for each condition separately: for condition 1, $t(28) = 6.7$, $p < 0.001$; for condition 2, $t(28) = 10.1$, $p < 0.001$; for condition 3, $t(28) = 3.56$, $p < 0.002$. The same was also true for each frequency separately; for 0.5 kHz, $t(56) = 5.4$, $p < 0.001$; for 1 kHz, $t(56) = 2.45$, $p < 0.02$; for 2 kHz, $t(56) = 3.12$, $p < 0.01$; for 4 kHz, $t(56) = 3.02$, $p < 0.01$; for 6 kHz, $t(56) = 8.2$, $p < 0.001$.

Averaged across conditions and frequencies, the mean threshold for the 500-ms glide was significantly higher than the mean threshold for any other glide duration; $t(14) => 16$, $p < 0.001$. The same was true for each condition separately: for condition 1, $t(28) > 10$, $p < 0.001$; for condition 2, $t(28) > 13$, $p < 0.001$; for condition 3, $t(28) > 11$, $p < 0.001$. The same was also true for each frequency separately; for 0.5 kHz, $t(56) > 9$, $p < 0.001$; for 1 kHz, $t(56) > 5.7$, $p < 0.001$; for 2 kHz, $t(56) > 9.6$, $p < 0.001$; for 4 kHz, $t(56) > 6.5$, $p < 0.001$; for 6 kHz, $t(56) > 6.8$, $p < 0.001$.

The changes in performance with center frequency are more easily seen by plotting thresholds as a function of center frequency, with glide duration as parameter. This is done separately for each condition in Figs. 6–8. To avoid clutter in the figures, data are plotted only for glide durations of 0, 5, 50, and 500 ms.

For condition 1 (no randomization, Fig. 6), thresholds for all glide durations hardly varied with frequency up to 4 kHz, and then increased at 6 kHz. The increase was more marked for the 0-ms condition than for the other conditions. For condition 2 (center frequency randomized over a 4-ERB range, Fig. 7), thresholds tended to increase more progressively as the frequency was increased from 1 to 6 kHz. For condition 3 (center frequency randomized and random changes in level superimposed on frequency changes, Fig. 8), the thresholds were roughly constant for frequencies up to 2 kHz, and increased above that, especially for the 0-ms glide duration. The results for condition 3 for the 500-ms

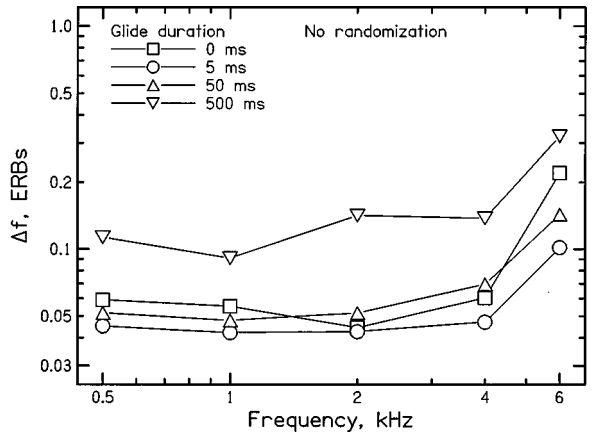

FIG. 6. Thresholds for condition 1 (no randomization), expressed in ERBs and plotted as a function of center frequency with glide duration as parameter.

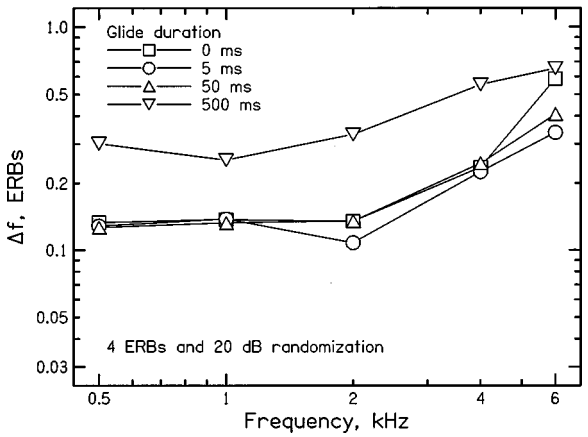

FIG. 8. As Fig. 6, but for condition 3 (center frequency randomized over a 4-ERB range and random glides in level added at times when the frequency glides might occur).

glide duration can be compared with the results of Moore and Sek (1998) for a 400-ms duration (their 0-ERB transition span with center frequency randomized over a 4-ERB range and with ±20 dB random glides in level). The mean thresholds in the previous study were slightly higher than those of the present study, but the pattern of the results across frequency was similar; thresholds were slightly higher at 6 kHz than at 0.5 or 2 kHz. The effect of frequency was slightly greater in the present study than in the study of Moore and Sek (1998). The increase in thresholds for all conditions for the 6-kHz center frequency suggests some role for a temporal mechanism at lower frequencies regardless of glide duration.

III. DISCUSSION

The results for condition 1 (fixed center frequency) and condition 2 (center frequency roved over a 4-ERB range) showed that performance was better than would be expected if subjects made optimal use only of the start or endpoint frequencies of the stimuli. The results for condition 3 (in which random glides in level were superimposed on the frequency glides) showed that performance was better than would be expected if subjects made optimal use of changes in excitation level on one side of the excitation pattern. It can be concluded that subjects were discriminating the changes in frequency *per se*, but they were not doing this by monitoring changes in excitation level on just one side of the excitation pattern.

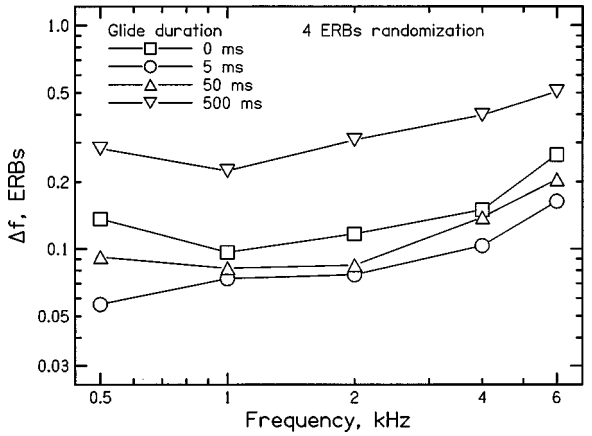

FIG. 7. As Fig. 6, but for condition 2 (center frequency randomized over a 4-ERB range).

It has been proposed that there are two mechanisms for the detection of frequency glides bounded by transitions (Tsumara *et al.*, 1973). As described in the Introduction, several researchers have also proposed that there is a mechanism specifically concerned with the detection of glides (Sergeant and Harris, 1962; Gardner and Wilson, 1979). Our results lend clear support to the idea that there is a glide detection mechanism that is distinct from a sampling mechanism. The strongest evidence is the small but consistent (and statistically significant) decrease in threshold that we found between the 0-ms and the 5-ms glide durations. Recall that, for the former, the glide was actually replaced by a brief silent interval. If the only mechanism involved were based on sampling of the endpoint frequencies, then performance should have been essentially the same for these two conditions. The fact that the performance improved when the brief glide was added indicates that the glide itself provided information additional to that provided by the endpoint frequencies. The decrease was found for all three of our conditions, indicating that both endpoint sampling and glide detection played a role even when the center frequency was randomized (which would prevent a strategy based on monitoring only the start or the endpoint frequency) and when random glides in level were present (which would have prevented a strategy based on monitoring only one side of the excitation pattern).

To explain the pattern of results in more detail, consider the following. For the 0-ms glide duration, only endpoint sampling was available. For the 500-ms glide duration, glide detection was probably the main source of information. For the other glide durations, both forms of information may have been used. The accuracy of endpoint sampling would have decreased as d_{glide} was increased (and d_{steady} was decreased). On the other hand, thresholds for detecting frequency glides (without plateaus of steady frequency at the start and end) appear to be almost independent of duration (Sergeant and Harris, 1962; Pollack, 1968; Dooley and Moore, 1988; Madden and Fire, 1997; Moore and Sek, 1998), although these studies only examined glide detection

for durations down to 50 ms. Thus one would expect the best performance for the shortest glide duration; in this case the accurate information derived from sampling the stable initial and final frequencies could be combined with the duration-independent information about the glide. This was exactly the pattern of results observed.

To quantify this explanation, we use a simple model based on the concepts of signal detection theory (Green and Swets, 1974). We assume that for $d_{\text{glide}}=0$ ms (when there was no frequency glide), the only information available was from endpoint sampling. We denote the threshold (corresponding to a d' value of 0.76) obtained for this condition by Δf_{end}. We assume that, for other values of d_{glide}, the value of d' that would be obtained from endpoint sampling alone is given by:

$$d'_{\text{end}}=(0.76\times\Delta f\times\text{SF})/\Delta f_{\text{end}}, \tag{1}$$

where Δf is the threshold for that value of d_{glide} and SF is a scaling factor related to the value of d_{steady}; SF has a value of 1 for $d_{\text{steady}}=250$ ms, and decreases as d_{steady} decreases. For simplicity, we assumed that the relationship of SF to $d_{\text{steady}}$was the same at all frequencies, and for values of d_{steady} in the range 150–250 ms, was given by

$$\text{SF}=d_{\text{steady}}/250. \tag{2}$$

We assumed that for $d_{\text{glide}}=500$ ms (when $d_{\text{steady}}=0$ ms), the only information available was from glide detection. We denote the d' value that would result from glide detection alone as d'_{glide}. For $d_{\text{glide}}=500$ ms, $d'_{\text{glide}}=0.76$. For intermediate values of d_{glide}, the value of d'_{glide} is assumed to be given by:

$$d'_{\text{glide}}=(0.76\times\Delta f)/\Delta f_{\text{glide}}, \tag{3}$$

where Δf_{glide} is the threshold for a glide duration of 500 ms and, as before, Δf is the threshold for that value of d_{glide}.

We initially consider two models for the way in which information from the two sources might be combined. The first model assumes that information from endpoint sampling and glide detection is determined by independent mechanisms (for example by temporal and place mechanisms, respectively), each limited by its own internal noise, and that information from the two sources is combined optimally. We refer to this as the ''independent noise'' model. In this case, the resulting d' value is given by:

$$d'=\sqrt{\{(d'_{\text{end}})^2+(d'_{\text{glide}})^2\}}. \tag{4}$$

This value of d' should always be equal to the target value of 0.76. Substituting from Eqs. (1) and (3), and rearranging terms, we get:

$$\Delta f=1/\sqrt{\{(\text{SF}/\Delta f_{\text{end}})^2+(1/\Delta f_{\text{glide}})^2\}}. \tag{5}$$

Thus the value of the threshold, Δf, for any glide duration from 5 to 200 ms can be predicted from the values of Δf_{end} and Δf_{glide} (i.e., the thresholds for glide durations of 0 and 500 ms, respectively), together with the value of the scaling factor, SF, for that glide duration, as defined by Eq. (2).

The second model assumes that information from endpoint sampling and glide detection is determined by a common mechanism, or that the ability to use the two sources of information is limited by a common internal noise which occurs after information from the two sources has been combined. We refer to this as the ''common noise'' model. In this case, the d' value resulting from combining the two sources of information is simply the sum of d'_{end} and d'_{glide}, and the value of Δf is predicted to be:

$$\Delta f=1/\{(\text{SF}/\Delta f_{\text{end}})+(1/\Delta f_{\text{glide}})\}. \tag{6}$$

A generalization of these models, assuming that the noise associated with the two sources of information is partly independent and partly common, is

$$d'=\{(d'_{\text{end}})^{\alpha}+(d'_{\text{glide}})^{\alpha}\}^{1/\alpha}, \tag{7}$$

where α is a constant between 1 and 2. The value of Δf is then predicted to be

$$\Delta f=1/\{(\text{SF}/\Delta f_{\text{end}})^{\alpha}+(1/\Delta f_{\text{glide}})^{\alpha}\}^{1/\alpha}. \tag{8}$$

The predictions of the generalized model were compared to the data. In principle, the values of Δf_{end} and Δf_{glide} are determined by the thresholds for the conditions with $d_{\text{glide}}=0$ ms and 500 ms, respectively. Hence the threshold values for intermediate glide durations can be predicted from these thresholds. However, small errors in the obtained value of Δf_{end} could have a substantial effect on the overall goodness of fit; the obtained value of Δf_{glide} was not so critical, as Δf_{glide} was usually markedly larger than Δf_{end} and therefore Δf_{glide} had a smaller influence on the predicted threshold, as can be seen from Eq. (8). Therefore, when fitting the data, the value of Δf_{glide} was taken as the experimentally determined value of threshold for $d_{\text{glide}}=500$ ms, but the value of Δf_{end} was adjusted for each condition and frequency to give the best overall fit to the data; the adjustments from the experimentally obtained values were generally less than the standard error (SE) across subjects. The only exceptions were for condition 2 at 0.5 kHz, condition 2 at 2 kHz, and condition 3 at 6 kHz. There was only one case (condition 2 at 0.5 kHz) where the adjustment was greater than 2 SE.

TABLE I. Goodness of fit of the generalized model to the data for three values of α, 1, 1.5, and 2. The table shows the root-mean-square deviation between the logarithms of the predicted thresholds and the logarithms of the obtained thresholds.

	Frequency, kHz				
α	0.5	1.0	2.0	4.0	6.0
1	0.101	0.096	0.101	0.114	0.051
1.5	0.068	0.043	0.051	0.055	0.088
2	0.076	0.060	0.056	0.056	0.126

The overall goodness of fit was estimated by calculating the root-mean-squared deviation between the logarithms of the predicted thresholds and the logarithms of the obtained thresholds. This was done for several values of α. The outcome, for $\alpha=1$, 1.5, and 2 is shown in Table I. The results for center frequencies from 0.5 to 4 kHz were well fitted with a value of α of 1.5. The fitted values obtained using this value are shown as the dotted lines in Figs. 1–4. The only clear deviation of the data from the fitted values was for condition 2 at a frequency of 0.5 kHz, where the data dif-

fered markedly from the predicted values for glide durations of 0 and 5 ms. However, the data for these two cases look somewhat ''out of line'' with the data for the other two conditions. When a value of $\alpha=2$ was used to fit the data, the difference in threshold between the 0- and 5-ms glide durations, was systematically underestimated. When a value of $\alpha=1$ was used to fit the data, that same difference was systematically overestimated. We can conclude that the results for frequencies up to 4 kHz are consistent with a model in which information from endpoint sampling and from glide detection is extracted by partly independent mechanisms, but performance is partly limited by an internal noise that is common to both mechanisms, or occurs after the information from the two mechanisms has been combined.

At 6 kHz, the decrease in threshold between the 0-ms and 5-ms glide durations was somewhat greater than at the lower frequencies. The data for this frequency were fitted best with $\alpha=1$. When α was set to 1.5 or 2, the difference in threshold between the 0- and 5-ms glide durations was systematically underestimated. Thus the results at 6 kHz are consistent with a model in which information from endpoint sampling and from glide detection is determined by a common mechanism and/or by an internal noise that occurs after the information from the two mechanisms has been combined.

IV. CONCLUSIONS

This experiment examined thresholds for the detection of frequency steps either when the steps were connected by frequency glides of various durations, or when the glide was replaced by a brief silent interval (referred to as 0-ms glide duration). The following conclusions can be drawn from the results:

(1) For all glide durations and all center frequencies, thresholds were higher when the center frequency was randomized over a 4-ERB range than when it was held constant within a block of trials. When the center frequency was randomized, performance was always better than the best that could be achieved by monitoring only the initial or final frequency of the stimuli. Therefore, in this condition, subjects either compared the start and end frequencies, or detected the frequency glide *per se*, or both.

(2) Performance was impaired even more (compared to randomization of center frequency alone) when random glides in level were superimposed on the glides in frequency, or, for the 0-ms glide duration, when the level of every tone burst was randomized. However, performance with the random level changes was always better than the best that could be achieved by monitoring changes in excitation level on one side of the excitation pattern.

(3) For all glide durations and all conditions, performance worsened at the highest center frequency tested (6 kHz), suggesting the involvement of a temporal mechanism at lower frequencies. The worsening tended to be greater when no glide was present, consistent with a greater role for a temporal mechanism at low frequencies when the stimuli were steady rather than gliding tones.

(4) Performance was better for a glide duration of 5 ms than for a glide duration of 0 ms. This is not consistent with the hypothesis that performance depends only on sampling the endpoint frequencies of the stimuli. Rather, it suggests that information about the glide *per se* was combined with information based on endpoint sampling.

(5) The overall pattern of results could be explained reasonably well by a model in which it was assumed that information from sampling the endpoint frequencies (which depends on the duration of the frequency plateaus on either side of the glide) was combined with information from the glide (which was assumed to be independent of glide duration). For frequencies from 0.5 to 4 kHz, the best fit was obtained using a model in which the two sources of information were partially independent, perhaps being derived by different mechanisms—a temporal mechanism for endpoint sampling and a place mechanism for glide detection. For a frequency of 6 kHz, the best fit was obtained using a model in which the two sources of information were based on a common mechanism, or, equivalently, that performance was limited by a noise occurring after the two sources of information had been combined.

ACKNOWLEDGMENTS

This work was supported by the Wellcome Trust and by the MRC. We thank Brian Glasberg for assistance with the analysis of the results and Tom Baer, Hedwig Gockel, Walt Jesteadt, John Madden, and an anonymous reviewer for helpful comments on an earlier version of this paper.

[1]The argument given by Moore and Sek (1998) was as follows: If the frequency change in the signal interval is ΔF, then, if there is no randomization of center frequency, the start and endpoint frequencies in the signal and standard intervals each differ by $0.5\Delta F$. Following arguments given by Green (1998, pages 19–20), if the center frequency of each stimulus is randomly varied over a range R, then the change in start or endpoint frequency required to give 70.7% correct, assuming perfect resolution of frequency, is $0.235R$. Therefore, given the 4-ERB randomization range used, the smallest possible threshold (expressed as ΔF) that could be achieved by monitoring the start or endpoint frequency is $0.47\times4=1.88$ ERBs.

Arlinger, S. D., Jerlvall, L. B., Ahren, L. B., and Holmgren, E. C. (**1977**). ''Thresholds for linear frequency ramps of a continuous pure tone,'' Acta Oto-Laryngol. **83**, 317–327.

Demany, L., and Semal, C. (**1986**). ''On the detection of amplitude modulation and frequency modulation at low modulation frequencies,'' Acustica **61**, 243–255.

Dooley, G. J., and Moore, B. C. J. (**1988**). ''Detection of linear frequency glides as a function of frequency and duration,'' J. Acoust. Soc. Am. **84**, 2045–2057.

Emmerich, D. S., Ellermeier, W., and Butensky, B. (**1989**). ''A reexamination of the frequency discrimination of random-amplitude tones, and a test of Henning's modified energy-detector model,'' J. Acoust. Soc. Am. **85**, 1653–1659.

Gardner, R. B., and Wilson, J. P. (**1979**). ''Evidence for direction-specific channels in the processing of frequency modulation,'' J. Acoust. Soc. Am. **66**, 704–709.

Glasberg, B R., and Moore, B. C. J. (**1990**). ''Derivation of auditory filter shapes from notched-noise data,'' Hearing Res. **47**, 103–138.

Goldstein, J. L., and Srulovicz, P. (**1977**). ''Auditory-nerve spike intervals as an adequate basis for aural frequency measurements,'' in *Psychophysics and Phyiology of Hearing*, edited by E. F. Evans and J. P. Wilson (Academic, London).

Green, D. M. (**1988**). *Profile Analysis* (Oxford University Press, Oxford).

Green, D. M., and Swets, J. A. (**1974**). *Signal Deteection Theory and Psychophysics* (Krieger, New York).

Henning, G. B. (**1996**). ''Frequency discrimination of random amplitude tones,'' J. Acoust. Soc. Am. **39**, 336–339.

Lane, P., Galwey, N., and Alvey, N. (**1987**). *Genstat 5. An Introduction* (Clarendon, Oxford).
Madden, J. P., and Fire, K. M. (**1996**). ''Detection and discrimination of gliding tones as a function of frequency transition and center frequency,'' J. Acoust. Soc. Am. **100**, 3754–3760.
Madden, J. P., and Fire, K. M. (**1997**). ''Detection and discrimination of frequency glides as a function of direction, duration, frequency span and center frequency,'' J. Acoust. Soc. Am. **102**, 2920–2924.
Micheyl, C., Moore, B. C. J., and Carlyon, R. P. (**1998**). ''The role of excitation-pattern cues and temporal cues in the frequency and modulation-rate discrimination of amplitude-modulated tones,'' J. Acoust. Soc. Am. **104**, 1039–1050.
Moore, B. C. J. (**1973a**). ''Frequency difference limens for narrow bands of noise,'' J. Acoust. Soc. Am. **54**, 888–896.
Moore, B. C. J. (**1973b**). ''Frequency difference limens for short-duration tones,'' J. Acoust. Soc. Am. **54**, 610–619.
Moore, B. C. J. (**1974**). ''Relation between the critical bandwidth and the frequency-difference limen,'' J. Acoust. Soc. Am. **55**, 359.
Moore, B. C. J. (**1997**). *An Introduction to the Psychology of Hearing*, 4th ed. (Academic, San Diego).
Moore, B. C. J., and Glasberg, B. R. (**1986**). ''The role of frequency selectivity in the perception of loudness, pitch and time,'' in *Frequency Selectivity in Hearing*, edited by B. C. J. Moore (Academic, London).
Moore, B. C. J., and Glasberg, B. R. (**1989**). ''Mechanisms underlying the frequency discrimination of pulsed tones and the detection of frequency modulation,'' J. Acoust. Soc. Am. **86**, 1722–1732.
Moore, B. C. J., and Sek, A. (**1994**). ''Effects of carrier frequency and background noise on the detection of mixed modulation,'' J. Acoust. Soc. Am. **96**, 741–751.
Moore, B. C. J., and Sek, A. (**1995**). ''Effects of carrier frequency, modulation rate and modulation waveform on the detection of modulation and the discrimination of modulation type (AM vs FM),'' J. Acoust. Soc. Am. **97**, 2468–2478.
Moore, B. C. J., and Sek, A. (**1996**). ''Detection of frequency modulation at low modulation rates: Evidence for a mechanism based on phase locking,'' J. Acoust. Soc. Am. **100**, 2320–2331.
Moore, B. C. J., and Sek, A. (**1998**). ''Discrimination of frequency glides with superimposed random glides in level,'' J. Acoust. Soc. Am. **104**, 411–421.
Nabelek, I. V., and Hirsch, I. J. (**1969**). ''On the discrimination of frequency transitions,'' J. Acoust. Soc. Am. **45**, 1510–1519.
Plomp, R. (**1964**). ''The rate of decay of auditory sensation,'' J. Acoust. Soc. Am. **36**, 277–282.
Pollack, I. (**1968**). ''Detection of rate of change of auditory frequency,'' J. Exp. Psychol. **77**, 535–541.
Sek, A., and Moore, B. C. J. (**1995**). ''Frequency discrimination as a function of frequency, measured in several ways,'' J. Acoust. Soc. Am. **97**, 2479–2486.
Sergeant, R. L., and Harris, J. D. (**1962**). ''Sensitivity to unidirectional frequency modulation,'' J. Acoust. Soc. Am. **34**, 1625–28.
Siebert, W. M. (**1970**). ''Frequency discrimination in the auditory system: place or periodicity mechanisms,'' Proc. IEEE **58**, 723–730.
Snedecor, G. W., and Cochran, W. G. (**1967**). *Statistical Methods* (Iowa University Press, Ames, IA).
Tsumara, T., Sone, T., and Nimura, T. (**1973**). ''Auditory detection of frequency transition,'' J. Acoust. Soc. Am. **53**, 17–25.
Zwicker, E. (**1956**). ''Die elementaren Grundlagen zur Bestimmung der Informationskapazität des Gehörs,'' Acustica **6**, 356–381.
Zwicker, E. (**1970**). ''Masking and psychological excitation as consequences of the ear's frequency analysis,'' in *Frequency Analysis and Periodicity Detection in Hearing*, edited by R. Plomp and G. F. Smoorenburg (Sijthoff, Leiden).
Zwicker, E., and Fastl, H. (**1990**). *Psychoacoustics—Facts and Models* (Springer-Verlag, Berlin).

Tonal portrait of a pipe organ

Howard F. Pollard
6 Wren Place, Cronulla, NSW 2230, Australia

(Received 23 November 1998; accepted for publication 24 March 1999)

Measurement techniques are described that enable the steady state tone color (timbre) of a musical instrument to be quantified. The system is applied to sounds from the pipe organ in the Great Hall of Sydney University. A one-third octave normalized loudness spectrum that is independent of pitch is derived for each set of notes from selected ranks of pipes. From the normalized spectrum, sharpness and tristimulus coordinates are computed, the latter being independent of both pitch and loudness. Measurements made on different ranks of pipes or made at different times are compared with the aid of spectrum dissimilarity and tristimulus diagrams. © *1999 Acoustical Society of America.* [S0001-4966(99)01207-2]

PACS numbers: 43.66.Jh, 43.75.Np, 43.66.Cb [WJS]

INTRODUCTION

The object of this investigation is to measure a number of acoustical features that are associated with the timbre of a particular musical instrument. A pipe organ has been chosen for analysis since it possesses a wide variety of timbres and it is easy to sustain steady sounds during measurement. An organ is designed to be an integral part of the architecture and acoustical environment of a building. Organ sounds are therefore intended to be a composite of the properties of the pipes and the building.

The ranks of pipes available on the different keyboards include many different combinations of pitch, timbre, and loudness. Since a large number of pipes are involved, a limit needs to be placed on the number of ranks of pipes to be included as typical and the number of notes tested in each rank. An analysis of every note in every rank might be valuable to an organ builder but such a complete study is not necessary for the present purpose. A complete tonal study would include analyses of starting transients as well as steady tones. Only steady sounds are considered in this study.

It is important to relate the measurements to the hearing characteristics of the human system. The acoustical properties of the inner ear are well established but less is known of the manner in which the human brain assesses tone quality. A skilled listener can make a tonal assessment in a very short time. When listening to a sequence of notes on an instrument or voice, most musicians can quickly identify the class of tone, whether the tone is of good or indifferent quality, and whether a performance is good or otherwise. The brain's wide tolerance ranges for musical sounds of a given class make any assessment based on physical analysis difficult. Memory plays an important role in establishing an acoustical template for a given class of sound.

An acoustical portrait of a solo instrument, such as a violin, flute, or trumpet, requires that a series of representative notes be analyzed in both the time and frequency domains to produce the required transient and steady characteristics. Filter analysis of the steady state for each note leads to values of loudness and measures of timbre such as sharpness[1] (see Sec. I B 2) and tristimulus coordinates[2] (see Sec. I B 3). Some form of normalized spectrum[3–5] (see Sec. I B 1) for the set of notes is useful for characterizing the overall steady tone of the instrument.

For an organ the above procedure needs to be carried out for the main representative ranks of pipes and combinations. The minimum requirement includes measurements on a Principal 8′, Flute 8′, Reed 8′, and Principal chorus on each manual. In addition, a test chord on each Principal chorus and on full organ is useful for overall loudness comparison with other organs.[6] Although measurements are quoted only for a pipe organ, the methods employed can be applied to any musical instrument.

The use of the term *timbre* (French for quality of sound) can be misleading since it is often used to include starting transient characteristics and fluctuations as well as steady state properties. Terms such as *tone color*, *tone quality*, *chroma*, etc. have been suggested for the steady state properties of sounds not associated with pitch or loudness, leaving timbre as an umbrella term to describe the overall ''quality'' of a sound.

A. Measurement of plenum sounds

An extensive examination of organ sounds has been carried out by Lottermoser and Meyer[7–9] at PTB, Germany. Measurements of single note spectra and sound pressure levels as well as octave band analyses of plenum sounds (Principal choruses) on both old and modern organs have been thoroughly documented.

Plenum sounds were measured using a microphone located 15 m from the pipes. In order to minimize the effects of standing waves, a cluster of three successive notes was played at a time, the resulting sound pressure being divided by $\sqrt{3}$. Four such clusters were recorded in each octave (CC#D, D#EF, F#GG#, AA#B, thus including all available notes) over the pitch range C_2 to C_6. Octave band spectra of each cluster were measured, producing a set of 16 spectra. This number was found sufficient to reveal major tonal trends within each instrument and between different instruments.

 0001-4966/99/106(1)/360/11/$15.00

The differences in plenum sounds between German romantic and baroque type organs were particularly marked. The spectra of romantic organs have a single maximum at low harmonic numbers, whereas baroque organ spectra have two maxima; the lower maximum corresponding to the lower harmonics of the 16′ and 8′ ranks while the upper maximum corresponds to the mixture stops. The location of the upper maximum determines the type of tonal effect produced in analogy with the coloration produced in speech sounds by the vowel formants. This type of analysis has been used with considerable success during the reconstruction of famous baroque organs.

B. Experiments of Plomp and de Laat

Plomp and de Laat[5] applied data reduction methods to octave band spectra obtained by Lottermoser and Meyer[7,9] for 14 different organs leading to a presentation in terms of a spectrum space diagram. The original data consisted of the spectra of four three-note clusters per octave, each spectrum being analyzed into octave bands. Plomp and de Laat averaged the sets of spectra for the three octaves starting with C_2, C_3, and C_4, thus reducing the data to three average spectra, each analyzed into five octave bands. Finally, the three spectra were averaged, resulting in a single mean octave band spectrum for each plenum sound. The mean spectra of the 14 organs so produced were treated as points in a five-dimensional Euclidean space which were then subjected to principal-components analysis.[10] It was found that 98% of the total variance was carried by only three dimensions (83% being carried by the first two dimensions). Dimensions I is largely determined by the overall level of the sound. Dimension II is highly correlated with the slope of the spectrum; a large coordinate corresponding with many higher partials. Dimension III compares the center octave with the lowest and highest ones. Famous German baroque organs with their rich harmonic spectra were found to have large values of Dimension II; three romantic organs had lower values.

In an experiment conducted by Plomp,[11] subjective timbre judgments were made on the steady state parts of a number of organ tones. Multi-dimensional analysis was used to process the subjective timbre comparisons. A two-dimensional plot was used to display the results; the vertical scale correlated with the extent of the spectrum of the sound; the horizontal dimension was not identified. Close agreement was reported between subjective estimates when compared with physical measurements. There was a clear differentiation on the graph between the main classes of organ tone: flutes, diapasons, and reeds.

C. Long-time-average-spectrum (LTAS) method

A useful technique has been developed by Jansson and Sundberg[4,12–14] for obtaining an average spectrum of a series of played musical notes. The sound to be analyzed consists of a whole tone scale, covering the frequency range of interest, with a duration of at least 20 s. The average spectrum so formed depends on the fundamental frequencies present, the spectrum envelopes, and the intensity levels. The recorded sound is analyzed by a filter bank of 23 bands which approximates to the ear's critical bands. The filter outputs are rectified, smoothed, converted into logarithmic units, sampled, and quantized in steps of 1 dB, then stored in a computer.[13]

In an examination of organ stops[12] at Nysatra church before and after restoration, a whole tone scale over the range C_2 to C_6 was played slowly for each stop and recorded at 10 microphone positions approximately 2.0 m apart, 1.75 m above floor level. In comparing two related sounds, dissimilarity analysis was applied to separate the total dissimilarity into a level dissimilarity and a shape dissimilarity,[11] thus normalizing loudness differences.

An LTAS is sensitive to the acoustical properties of the played instrument, how the music is performed, and to certain factors in the written music (for instance, the range of notes is important but not their distribution). The LTAS method has proven useful in monitoring tonal changes occurring with musical instruments, such as changes made to individual stops during restoration of an organ[12] and in quality comparisons of violins.[14]

D. Feature analysis

1. Plenum sounds

One-third octave band spectra of plenum combinations on four Sydney organs have been measured and converted into loudness spectra[6] using Stevens Mark VII method.[15] A 10-note test chord (similar to the final chord in many organ pieces) was used consisting of notes C_2 and C_3 played on the pedals (manuals coupled but no pedal stops); notes G_3, C_4, E_4, G_4 played with the left hand; and notes C_5, E_5, G_5, C_6 played with the right hand. Measurements were made in a number of typical listening positions. This type of measurement is useful in comparing loudness values and for delineating the overall tonal spectrum.

2. Individual notes

One-third octave spectra of all C and G notes on selected stops of four Sydney organs were measured,[16] the spectra and their associated loudness values providing a useful spectral picture of the tones available. Such data, however, need to be processed further according to hearing characteristics and supplemented with starting transient data.

3. Tonal feature analysis

Pollard[17,18] has described a system for processing the spectra of musical sounds and the extraction of features relevant to the perception of the sounds, including the analysis of transient sounds. One-third octave spectral data are converted into loudness units and a number of quantities computed including sharpness[1] and tristimulus coordinates.[2] For a set of notes played on a particular instrument, a normalized spectrum[3] may be constructed which categorizes the steady state sound. Dissimilarity spectra[3] may be formed between successive notes of a series or between two normalized spectra.

I. EXPERIMENTAL METHOD

A. Choice of measurement position

The choice of a ''typical'' measurement position poses a complicated problem. Since a pipe organ is a distributed source with the pipes arranged laterally in ranks, the sound from individual pipes will travel to a microphone along quite different paths. The tone of each pipe may vary at different times, depending on periodic adjustments by the organ tuner, as well as the temperature and humidity in the auditorium. Additional factors that affect the recorded sound are the number of people present and the arrangement of seating and furnishings which are all potentially variable.

An audience is usually seated in the far field of the radiated organ sound where it is greatly influenced by the room acoustics. Far field sound is very sensitive to spatial fluctuations so that it is customary to average measurements made at a number of different locations or to use a rotating microphone.

Characteristics such as the starting transients of the organ pipes are heard more distinctly in the near field of the instrument, a region not favored by most listeners as the sound can be harsher and lacking in reverberation. For measurement purposes a useful choice is the boundary between the near and far fields.

B. Steady sounds

Recordings of organ sounds were made at a distance of 9 m from the three-manual Beckerath organ in the Great Hall, University of Sydney. This distance is close to the boundary between direct and reverberant sound. Each sound was analyzed by a one-third octave band analyzer that averaged 40 sample spectra in a time interval of 4 s. The digitized output of the analyzer was stored in a computer for conversion into loudness units and extraction of tonal features.

An organ builder would no doubt elect to analyze most pipes in an organ or at least every note in selected ranks of pipes. Since a large organ will have more than 50 ranks, each consisting of at least 61 pipes, such a task would be monumental. In order to categorize the sound from a particular rank, a smaller number of notes is found to be sufficient. Individual C and G notes from C_2 to C_6 were recorded for a number of representative stops including a Principal 8′; Flute 8′, and Reed 8′ for each manual. Also recorded were the plenum combinations (e.g., Principal 8′ to Mixture) on each manual. This choice includes some of the basic sounds of an organ; a more comprehensive study would include many of the combination sounds used by organists.

1. Normalized spectrum

A characteristic average loudness spectrum for a chosen rank of pipes may be found by forming a normalized spectrum. The loudness spectrum of C_4 (middle C) is used as a reference point. This choice is made for computational convenience and is not critical. The spectrum components of each of the other notes are frequency shifted to coincide with those for C_4 and then the loudness values are averaged. A normalized spectrum is an average spectrum that is independent of pitch. Since many ranks of organ pipes show progressive variations in tone color from bass to treble, the standard deviation for the average loudness values can be high. Larger than normal deviations were often found for the lowest notes tested (C_2 and G_2). The set of notes C_3 to C_6 was found to be sufficiently representative of a rank of pipes.

In comparing two normalized spectra a difference graph is useful. Such a comparison may be rendered independent of loudness differences by using the dissimilarity analysis described by Jansson.[13] The *total dissimilarity* between two spectra, defined by Plomp,[19] measures the distance between two points (the interpoint distance) in a multi-dimensional space in which the number of dimensions is equal to the number of filter bands used in the analysis. By shifting one set of loudness values (in sones) progressively up or down by small steps, a minimum interpoint distance may be found. This condition corresponds to the two spectra being equalized in overall loudness. The total dissimilarity then consists of a *level dissimilarity* (the loudness shift) and a *spectrum shape dissimilarity*. The latter is independent of both pitch and loudness.

2. Sharpness

In a comprehensive study of the timbre of steady sounds involving multi-dimensional analysis, Bismarck[1] concluded that sharpness was the factor carrying most of the variance. He defined sharpness as the loudness centroid on a frequency scale in which critical bandwidths have equal lengths. If one-third octave filters are used as an approximation to critical bands, sharpness (SH) may be defined as

$$\mathrm{SH}=\sum_{i=1}^{n} N_i m_i \Big/ \sum_{i=1}^{n} N_i , \tag{1}$$

where N_i is the band loudness in sones, m_i is the band number, and n is the number of the highest band included. For loudness computations, the band groupings recommended by ISO[20] are used: Band 1 combines all one-third octave bands up to a center frequency (CF) of 80 Hz; Band 2 combines one-third octave bands 100, 125, and 160 Hz; Band 3 combines bands 200 and 250 Hz; then follow all bands from 315 Hz onward.

According to Plomp[19] ''timbre depends upon the absolute frequency position of the spectral envelope rather than upon its position relative to the fundamental frequency.'' Sharpness is a determining factor in the estimation of timbre. Does this conclusion mean that the sharpness of a pure tone should increase with pitch? Bismarck[1] and Fletcher[21] both maintain that increasing the pitch of a pure tone increases its loudness and its timbre. This will be true if the intensity of

TABLE I. Loudness and sharpness for a pure tone with intensity level 50 dB.

Frequency (Hz):	250	500	1000	2000	4000
Loudness (sones):	1.4	2.2	2.2	2.9	4.0
Sharpness:	3.0	6.0	9.0	12.0	15.0

the pure tone is maintained. Table I shows the loudness[15] and sharpness for a pure tone with an intensity level of 50 dB. Both the loudness and sharpness increase with increasing frequency.

[When standard ISO band numbers are used for m_i in Eq. (1), the sharpness found may be termed *absolute sharpness*. For some purposes it is useful to define sharpness relative to the fundamental of the sound rather than to ISO band 1. *Relative sharpness*, SH(rel), may be calculated from Eq. (1) with the band containing the fundamental tone assigned as band 1. A low value of SH(rel) indicates a sound with strong fundamental tone, a high value indicates a relatively ''brighter'' sound with many high harmonics.]

3. Tristimulus coordinates

There are a number of individual factors contributing to a subjective judgment of timbre.[1,17] When experimental data are reduced using multi-dimensional analysis three dimensions appear to be sufficient to categorize timbre.[2,9] The analytical procedure introduced by Pollard and Jansson[2] accepts this simplification and reduces spectrum measurements to three normalized coordinates. Three groups are formed as follows:

Group 1: the loudness of the band containing the fundamental tone

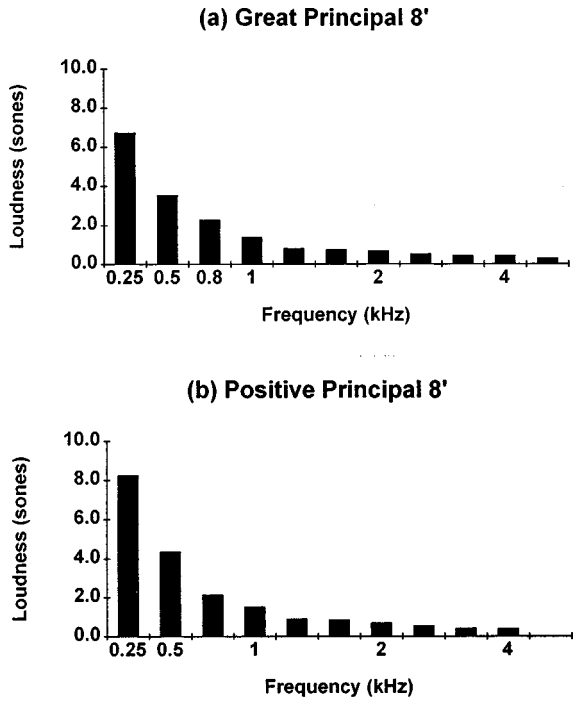

FIG. 1. Normalized loudness spectra for (a) Great Principal 8′, (b) Positive Principal 8′ of the organ in the Great Hall, University of Sydney.

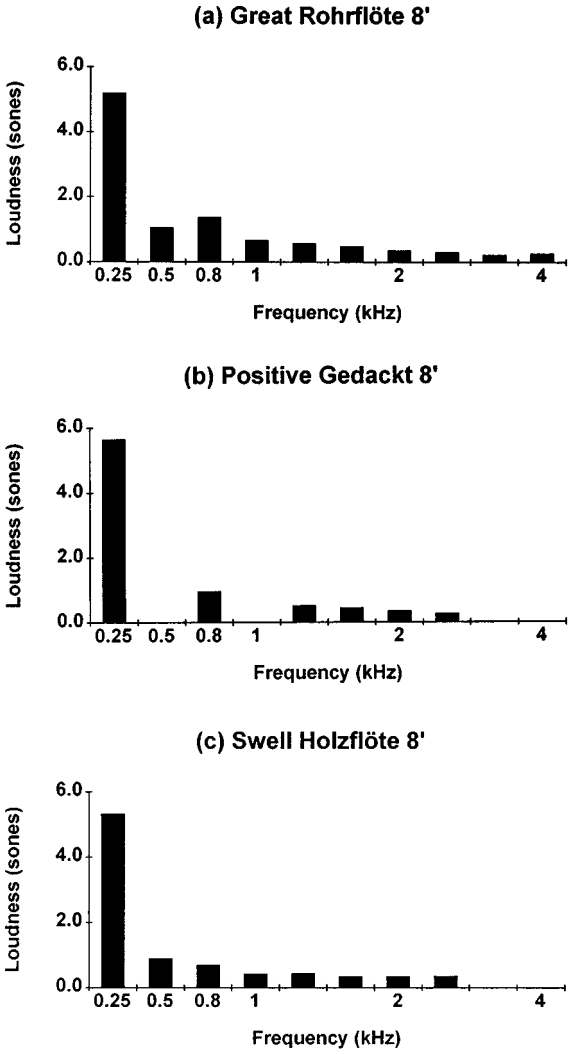

FIG. 2. Normalized loudness spectra for (a) Great Rohrflöte 8′, (b) Positive Gedackt 8′, (c) Swell Holzflöte 8′.

Group 2: the equivalent loudness of the bands containing partial tones 2, 3, and 4

Group 3: the equivalent loudness of the bands containing partial tones 5 and greater.

This grouping acknowledges the importance of the fundamental of a musical sound in relation to its role in determining the pitch of the sound and its effect on timbre relative to the mid-frequency and high-frequency partial tones. The sum of the three loudness groups may be written as

$$N = N(1) + N(2,4) + N(5,n), \tag{2}$$

where $N(1)$ is the loudness of the fundamental, $N(2,4)$ is the equivalent loudness of partials 2 to 4, $N(5,n)$ is the equivalent loudness of partials 5 to n. Each term on the right-hand side of Eq. (2) is called a tristimulus value from which a set of normalized tristimulus coordinates x, y, z may be derived:

$$x = N(5,n)/N, \quad y = N(2,4)/N, \quad z = N(1)/N. \tag{3}$$

The tristimulus coordinates represent only timbre. The advantages of using normalized coordinates (for which x

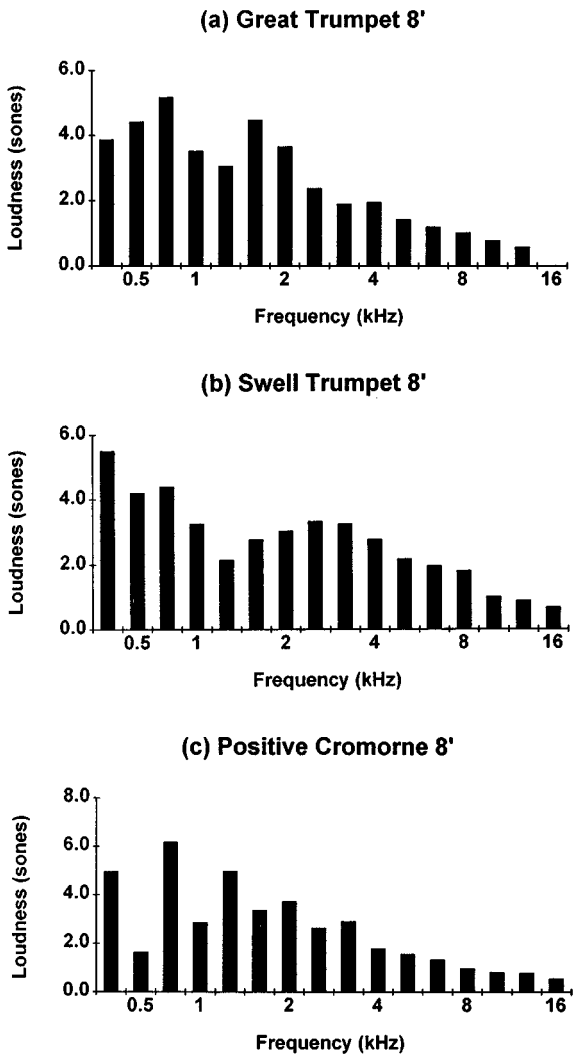

FIG. 3. Normalized loudness spectra for (a) Great Trumpet 8′, (b) Swell Trumpet 8′, (c) Positive Cromorne 8′.

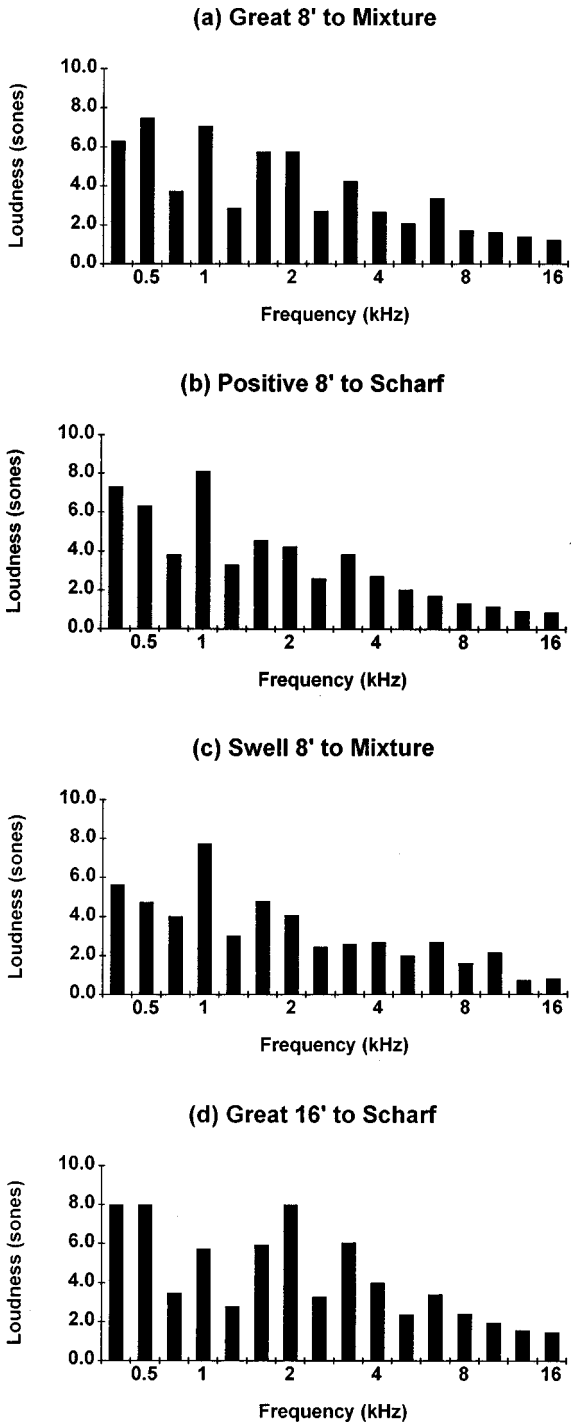

FIG. 4. Normalized loudness spectra for (a) Great 8′ to Mixture IV, (b) Positive 8′ to Scharf IV-VI, (c) Swell 8′ to Mixture V-VII, (d) Great 16′ to Scharf IV.

$+y+z=1$) and taking the fundamental as reference are: (1) this representation is independent of both loudness and pitch and (2) two-dimensional graphs may be drawn for any pair of coordinates. For instance, a graph of x vs z is useful for showing the balance between high-frequency partials and the fundamental; a graph of x vs y emphasizes the balance between high-frequency and mid-frequency partials.

II. EXPERIMENTAL RESULTS FOR THE GREAT HALL ORGAN, UNIVERSITY OF SYDNEY

A. Normalized loudness spectrum analysis

The organ in the Great Hall of the University of Sydney was built by Rudolf von Beckerath of Hamburg, assisted by Ronald Sharp of Sydney, and installed in 1972. There are four divisions comprising Great (13 stops), Positive (13 stops), Swell (15 stops), and Pedal (12 stops). Altogether there are 53 speaking stops, 78 ranks, and 3947 pipes. The playing action is mechanical, the stop controls are electromagnetic.

Figures 1–4 show normalized loudness spectra for the 8′ principals, flutes, reeds, and main flue choruses, respectively. Although the two principal stops of Fig. 1 are quite similar, the first two harmonics of the Positive Principal 8′ are stronger than those of the Great Principal 8′ resulting in a noticeably ''fuller'' sound. The three flutes shown in Fig. 2 have quite different sounds, especially the Positive Gedackt 8′ which is a closed pipe producing only odd harmonics. The Great Rohrflöte 8′, a metal gedackt with an internal chimney, has prominent third and fifth harmonics from C_3 to C_4; the second and fourth harmonics then become relatively

TABLE II. Sharpness, loudness, and loudness level for normalized spectra, Great Hall organ, University of Sydney.

	Codes	Sharpness	Loudness (sones)	Loudness Level (phons)
Principals				
Great Principal 8′	GP8	6.8	9.4	72.4
Positive Principal 8′	PP8	6.3	11.0	74.6
Flutes				
Great Rohrflöte 8′	GR8	6.2	6.5	67.1
Positive Gedackt 8′	PG8	5.2	6.3	66.6
Swell Holzflöte 8′	SH8	5.4	6.2	66.4
Reeds				
Great Trumpet 8′	GT8	10.4	14.0	78.1
Swell Trumpet 8′	ST8	11.0	15.1	79.2
Positive Cromorne 8′	PC8	10.7	14.9	78.9
Plena				
Great 8′ to Mixture	G8M	11.0	20.0	83.2
Positive 8′ to Scharf	P8S	9.4	19.0	82.5
Swell 8′ to Mixture	S8M	10.9	18.1	81.8
Great 16′ to Scharf	G16S	11.2	22.2	84.7

more prominent especially in the octave C_5 to C_6. The normalized spectrum, an average from C_3 to C_6, shows a moderately strong third harmonic which is the most characteristic tone of this particular rank. In Table II are values of sharpness, loudness (sones), and loudness level (phons) for the sounds shown in Figs. 1–4.

Sharpness and loudness (or loudness level) are two important properties of a normalized loudness spectrum. It is useful to show these two quantities on the same figure, following Plomp and de Laat,[5] as an indicator of the tonal effect of the steady state sound. Figure 5(a) shows the regions occupied by the organ sounds listed in Table II. Principal and flute sounds have lower sharpness and loudness values than reeds and plena. (Either loudness in sones or loudness level in phons may be used for the *x*-axis. Loudness level is sometimes preferred as the scale is similar to a standard decibel scale. It should however be noted that values of loudness level are higher than corresponding A-weighted decibels for organ sounds[22] by up to 15 dB.) Figure 5(b) is an expanded graph of sharpness against loudness for the principal and flute stops of the Great Hall organ. The changes in sharpness with increasing harmonic development are clearly visible, as are the relative values of loudness for the different sounds. Figure 5(c) is an expanded graph of sharpness versus loudness for the reed stops and plenum sounds.

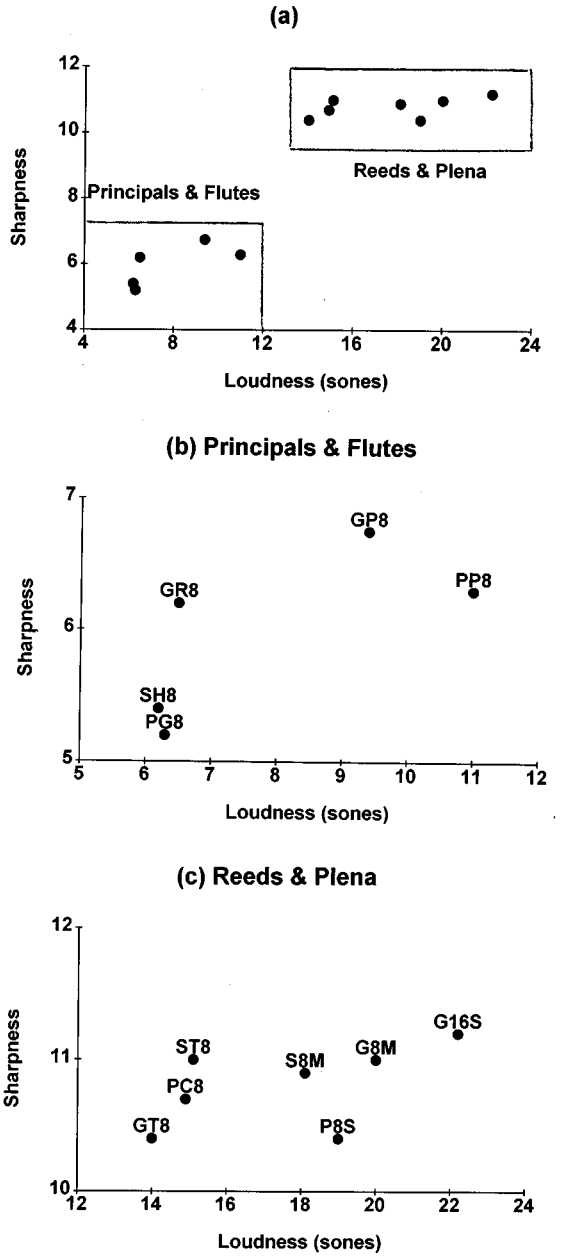

FIG. 5. (a) Sharpness plotted against loudness (sones) showing the regions occupied by the different organ tones listed in Table II. The principal and flute sounds occupy a region of lower sharpness and loudness than the reeds and plena. (b) Expanded sharpness—loudness graph for the principal and flute stops listed in Table II. The codes for the organ sounds are included in Table II. (c) Expanded sharpness—loudness graph for the reed stops and plena sounds listed in Table II.

B. Tristimulus analysis

In Table III are shown values of the tristimulus coordinates x, y, z for the Great Hall organ sounds. Figure 6(a) is an x-z tristimulus diagram for the sounds of Table III. Reeds and plena sounds occupy a region typical of ''bright'' sounds (high x), while the region occupied by flute and principal sounds is one with high fundamental content (z) relative to high frequencies. Expanded diagrams of these two regions are shown in Fig. 6(b) and (c).

Also shown in Table III are values of the ratio x/z that provides information related to sharpness but with a different interpretation. x/z measures the proportion of high-frequency partial tones compared with the fundamental tone, whereas sharpness is the balance point between high and low frequencies. x/z can be used to quantify ''brightness,'' a rather vague term used frequently by musicians and psychoacousticians. Absolute sharpness is a valuable parameter but it includes pitch information. The ratio x/z is independent of pitch and relates only to timbre. [x/z is more closely related to relative sharpness which is also independent of pitch since

TABLE III. Tristimulus coordinates for normalized spectra corresponding to data given in Table II.

	Code	x	y	z	x/z
Principals					
Great Principal 8′	GP8	0.132	0.351	0.517	0.26
Positive Principal 8′	PP8	0.114	0.347	0.539	0.21
Flutes					
Great Rohrflöte 8′	GR8	0.125	0.235	0.640	0.20
Positive Gedackt 8′	PG8	0.106	0.136	0.758	0.14
Swell Holzflöte 8′	SH8	0.098	0.169	0.733	0.13
Reeds					
Great Trumpet 8′	GT8	0.455	0.355	0.190	2.39
Swell Trumpet 8′	ST8	0.449	0.296	0.255	1.76
Positive Cromorne 8′	PC8	0.457	0.324	0.219	2.09
Plena					
Great 8′ to Mixture	G8M	0.448	0.339	0.213	2.10
Positive 8′ to Scharf	P8S	0.384	0.363	0.253	1.52
Swell 8′ to Mixture	S8M	0.422	0.367	0.211	2.00
Great 16′ to Scharf	G16S	0.473	0.295	0.232	2.04

it is tied to the fundamental of the sound. In Table III, relative sharpness values may be found by subtracting 2 from each of the (absolute) sharpness values.]

In Fig. 7 are shown graphs of x/z against loudness for (a) the Great stops, (b) the Positive stops, and (c) the Swell stops using data from Table III. Flute and principal sounds have values of x/z less than 0.5 and low to moderate loudness, while for the reeds and plena sounds x/z values are above 1.5 and loudness is higher. Figure 7 confirms the intended role of plenum combinations, i.e., that they should sound bright and loud.

III. APPLICATIONS TO TONAL PROBLEMS

The system of measurements described above are useful for examining a number of problems concerning the tonal properties of a musical instrument on which a sequence of notes can be played. Such measurements describe the tone colors available and can be used to study tonal variations and changes.[18,23] In the case of an organ, the overall tone color of the main sounds available on each manual can be documented together with any systematic variations from bass to treble or changes introduced by periodic maintenance.

A particular set of measurements on an instrument represents an acoustical ''snapshot'' of the state of the instrument at that time. For an organ, the location chosen for the measurements is important. At another time and in a different location in the auditorium the snapshot will be different. Tonal adjustments made during regular maintenance, changes in the seating arrangements in the auditorium, the variable effect of different audiences, etc., all make changes to the measurements.

A. Comparisons between different stops

Tonal differences between similar sounds on different manuals may be displayed by finding the dissimilarity between their normalized spectra. Figure 8 shows spectrum dissimilarity diagrams for (a) the Positive Principal 8′ compared with the Great Principal 8′, (b) the Positive 8′ to Scharf compared with the Great 8′ to Mixture, (c) the Swell Trumpet 8′ compared with the Great Trumpet 8′. The measured values of loudness, sharpness, and x/z are included in the figure caption.

In Fig. 8(a), the main tonal differences occur in the first two bands confirming the observation made in Sec. II A that the Positive Principal 8′ has a ''fuller'' sound than the Great

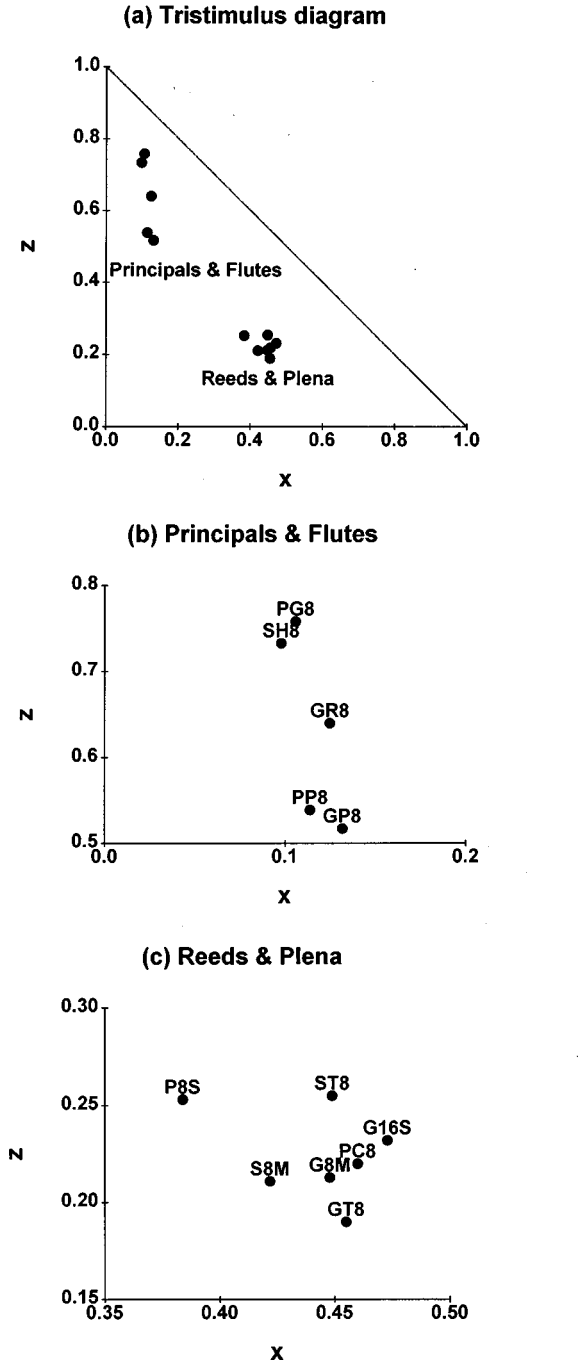

FIG. 6. (a) Tristimulus diagram, using data from Table III, in which coordinate z is plotted against x. The z axis shows the proportion of fundamental tone present, the x axis the proportion of high-frequency partial tones. (b) Expanded section of a tristimulus diagram for the principal and flute stops of the Great Hall organ. The codes for the organ sounds are included in Table III. (c) Expanded section of a tristimulus diagram for the reed stops and plena of the Great Hall organ.

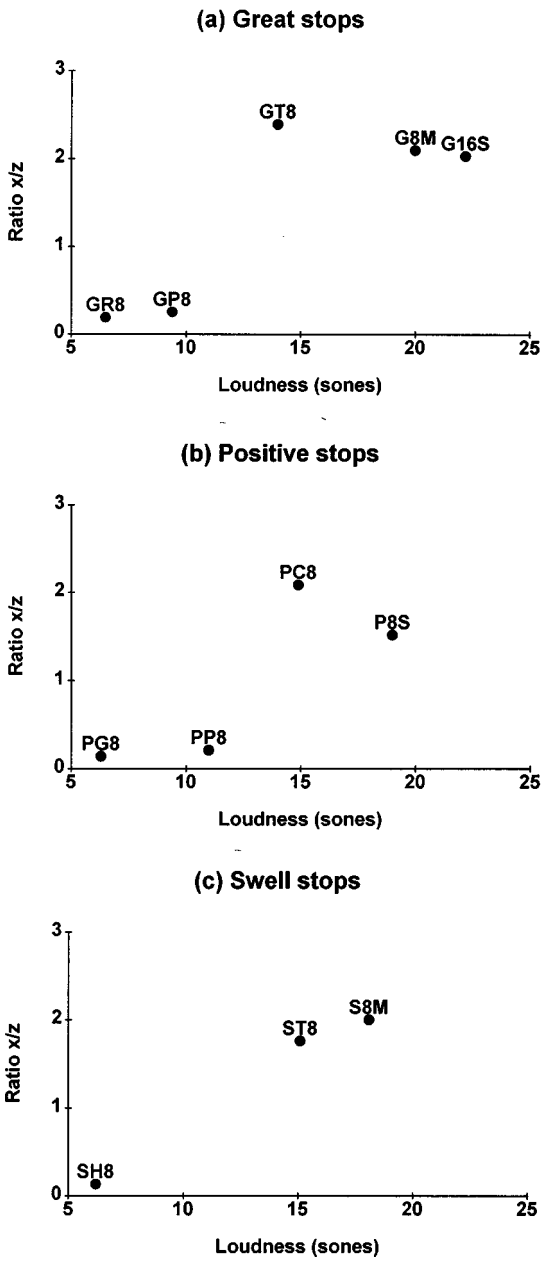

FIG. 7. Graphs of the tristimulus coordinate ratio x/z as a function of loudness for (a) the Great stops, (b) the Positive stops, (c) the Swell stops listed in Table III.

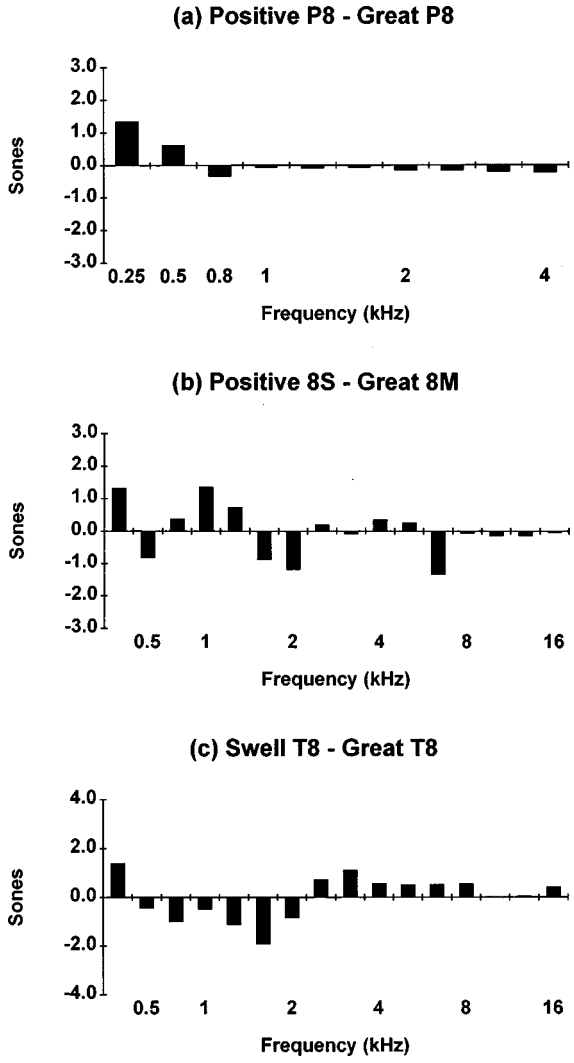

FIG. 8. (a) Spectrum dissimilarity between the normalized spectra for Positive Principal 8′ and Great Principal 8′. The fundamental and second partial tone of Positive Principal 8′ are louder than the corresponding tones of Great Principal 8′. An increment of 0.2 sone was added to each partial tone of the Great Principal 8′ to minimize the overall loudness difference. Following are measured values of loudness, sharpness, and x/z for each sound:

	Loudness (sones)	Sharpness	x/z
Positive Principal 8′	11.0	6.30	0.21
Great Principal 8′	9.4	6.75	0.26

(b) Spectrum dissimilarity between main choruses on Great and Positive. Measured values:

	Loudness (sones)	Sharpness	x/z
Positive 8′ to Scharf	19.0	10.4	1.5
Great 8′ to Mixture	20.0	11.0	2.1

(c) Spectrum dissimilarity between Swell Trumpet 8′ and Great Trumpet 8′.
Measured values:

	Loudness (sones)	Sharpness	x/z
Swell Trumpet 8′	15.0	11.0	1.8
Great Trumpet 8′	14.0	10.4	2.4

Principal 8′. Figure 8(c) shows that the Positive 8′ to Scharf is louder in bands 250, 1000, and 1250 Hz, while the Great 8′ to Mixture is louder in bands 500, 1600, 2000, and 6300 Hz. Both sharpness and x/z values indicate that the Great combination has an overall brighter sound. The tonal differences between these two sounds were shown in a different way in Fig. 6(c) with the Positive 8′ to Scharf having greater z and lower x than the Great 8′ to Mixture.

Figure 8(c) shows that the Swell Trumpet 8′ has louder fundamental and high-frequency partial tones, while the Great Trumpet 8′ has louder mid-frequency partial tones. The differences were shown in a different way in Fig. 6(c), the Swell Trumpet 8′ having a greater z coordinate with both sounds having similar x coordinates.

B. Tonal variations from bass to treble

For a number of reasons connected with the design and construction of pipes, there is always a variation in tone color from bass to treble along a rank of pipes. An important part of an organ builder's art is the scaling of a rank of pipes[24] to maintain uniform loudness and tone color throughout the rank. This is not always possible so that individual pipes will have tonal differences. Fortunately, from a listening viewpoint, the ear/brain is very tolerant of such variations.

An x-z graph of selected notes is useful in documenting such changes. Figure 9(a) shows the two regions occupied by the C and G notes of the Great Principal 8′ and Great Trumpet 8′. Lines join the sequence of points from C_3 to C_6. Figure 9(b) and (c) shows expanded views of these two regions. The changes in the Great Principal 8′ do not follow a regular pattern; the variations, however, lie within a particular region of the diagram. Similar measurements made at different times or on different Principal ranks show somewhat similar patterns within the same region.

There is a more systematic variation in the Great Trumpet 8′ pipes. The latter have a bright sound in the bass (high x) with a progressive shift to lower x values in the treble. This trend is shown clearly in Fig. 9(d), a plot of x and z as functions of the Great Trumpet 8′ notes. Changes in y were much smaller than changes in x and z. Similar trends are observed in other reed stops measured.

Loudness values from note to note also show variations. Figure 10 shows loudness values for the Great Principal 8′ and Great Trumpet 8′. While the loudness of the Great Principal 8′ is reasonably uniform, except for note C_5, the loudness of the Great Trumpet 8′ falls off in the treble. There has always been difficulty in maintaining the loudness of reed pipes in the treble region.

Many of the recorded changes appear to reflect the subjective nature of the organ tuner's adjustments and the consequences of changes from time to time in external factors such as the temperature and humidity. The tone of each individual flue pipe depends on many variables. From the data available there appears to be an inverse relationship between the ratio x/z and the loudness. It may be that, if a change occurs in the value of x/z for a given pipe, a compensating change in loudness is made by the tuner. This aspect of flue pipes needs further investigation.

C. Tonal differences due to adjustments during maintenance

Significant changes can occur following regular maintenance or periodic tonal adjustments. Both the loudness and tone color of the pipes in a rank may experience changes. For instance, Fig. 11 shows the spectrum dissimilarity between normalized spectra for (a) the Great Principal 8′, GP8, (b) the Great Trumpet 8′, GT8, and (c) the Great 8′ to Mixture, G8M, before and after a tonal overhaul of the organ during which the two reed stops were revoiced. For GP8 there are small alterations in the first two bands following a rebalanc-

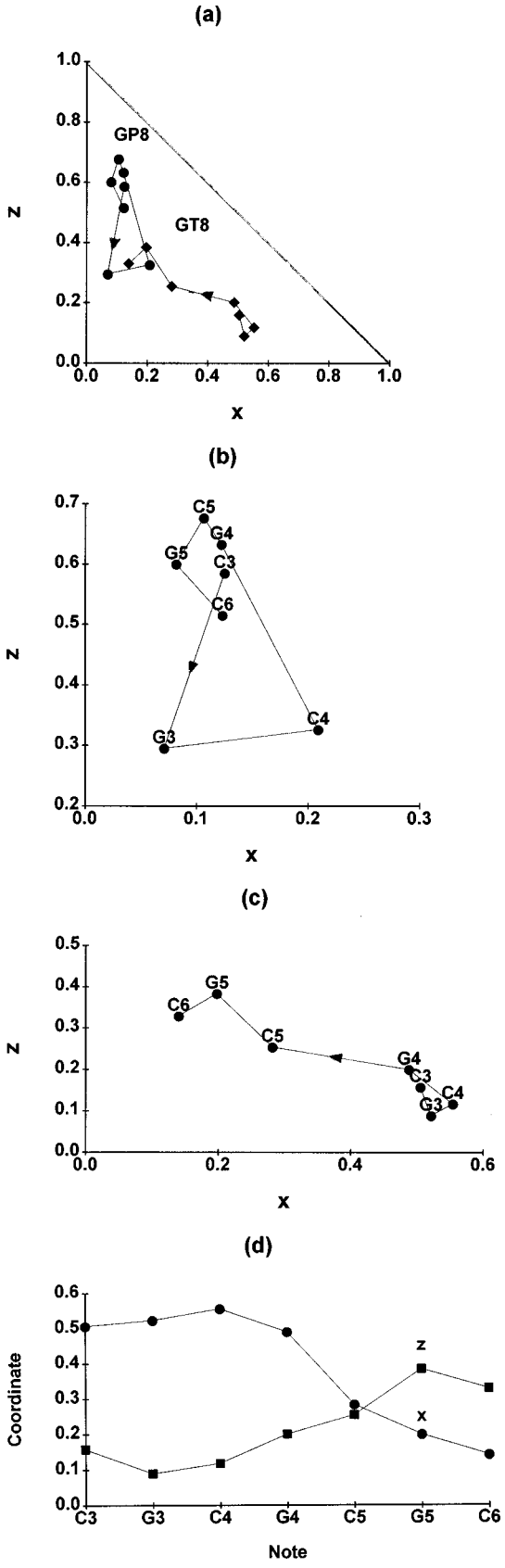

FIG. 9. (a) Tristimulus diagram (x-z) showing the regions occupied by the C and G notes of the Great Principal 8′ (solid circles) and Great Trumpet 8′ (solid diamonds). Lines join the sequence of points from C_3 to C_6. (b) Expanded x-z diagram for the Great Principal 8′ notes. (c) Expanded x-z diagram for the Great Trumpet 8′ notes. (d) Tristimulus coordinates x and z as functions of notes tested for the Great Trumpet 8′.

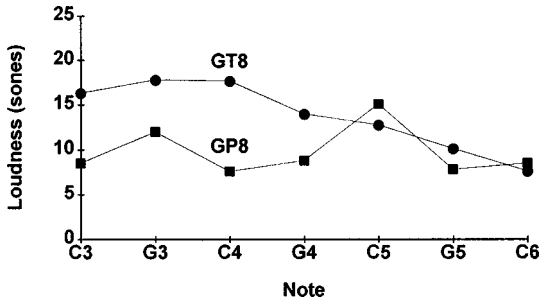

FIG. 10. Loudness as a function of notes tested for the Great Principal 8′ and Great Trumpet 8′.

ing of this rank; for GT8 significant changes in the 500- to 2000-Hz bands; for G8M significant changes in the 500, 1600, 4000, and 6300 bands.

Table IV shows the changes in sharpness, loudness, and tristimulus coordinates for GP8, GT8, G8M, and ST8 (the Swell Trumpet 8′). In Fig. 12, x/z is shown as a function of loudness for GT8, G8M, and ST8. GP8 is not included as there is only a small increase in x/z (brightness) and a small decrease in loudness. For GT8 there is a decrease in brightness and an increase in loudness; for G8M a significant increase in brightness with little change in loudness; for ST8 a significant increase in brightness and a small increase in loudness.

TABLE IV. Changes in sharpness, loudness, and tristimulus coordinates following overhaul of Great Hall organ, University of Sydney.

	Code	x	y	z	x/z
Great Principal 8′	GP8	0.013	0.064	−0.077	0.07
Great Trumpet 8′	GT8	0.033	−0.053	0.020	−0.07
Great 8′ to Mixture	G8M	0.049	−0.036	−0.013	0.38
Swell Trumpet 8′	ST8	0.029	0.025	−0.054	0.61

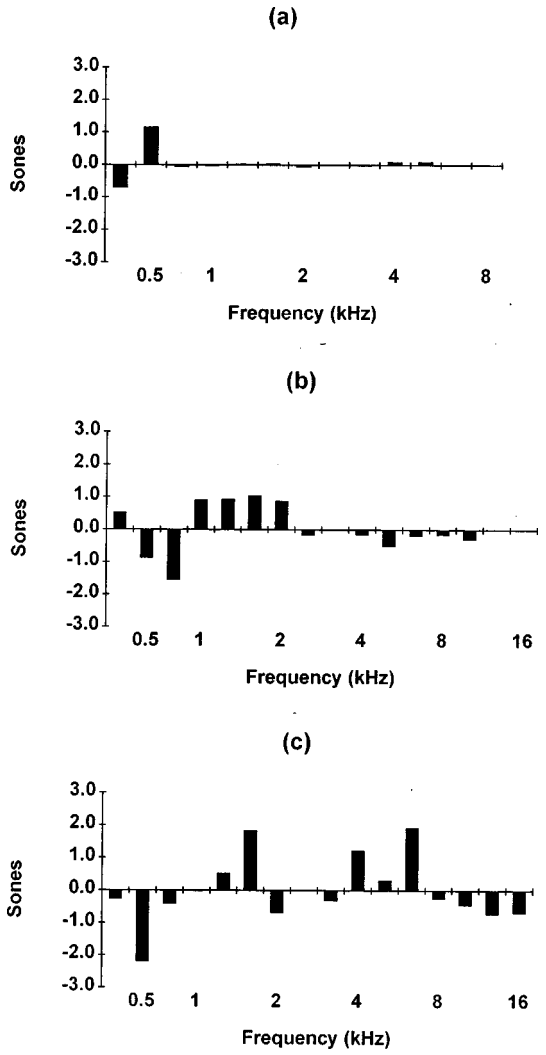

FIG. 11. Spectrum dissimilarity between the normalized spectra measured before and after a tonal overhaul of the Great Hall organ, (a) Great Principal 8′, (b) Great Trumpet 8′, (c) Great 8′ to Mixture. The graphs show the loudness values after overhaul minus corresponding values before. For the Great Principal 8′ there were small changes in the first two bands, for the Great Trumpet 8′ significant changes in the 500- to 2000-Hz bands, for the Great 8′ to Mixture significant changes in the 500-, 1600-, 4000-, and 6300-Hz bands. Changes in loudness are negligible except for the Great Trumpet 8′ which increased by 1.2 sone.

IV. SUMMARY

When the term timbre is applied to organ sounds it often includes a number of factors[17] such as starting transients and spectral fluctuations as well as the steady state. For the steady state component of timbre the term tone color has been adopted.

To specify the tone color of organ sounds a good starting point is to examine some form of average loudness spectrum. A spectrum normalized for pitch has been used in this study for which an average loudness and sharpness may be computed as well as further quantities related to timbre such as tristimulus coordinates. The latter coordinates are normalized for both pitch and loudness and lead to convenient two-dimensional graphical presentations.

These two techniques may be applied to a number of tonal problems involving comparisons between similar stops, the study of tonal variations, and an investigation of tonal changes resulting from an overhaul of the organ. The methods are applicable to comparisons between different instruments provided suitable reference normalized spectra are adopted.

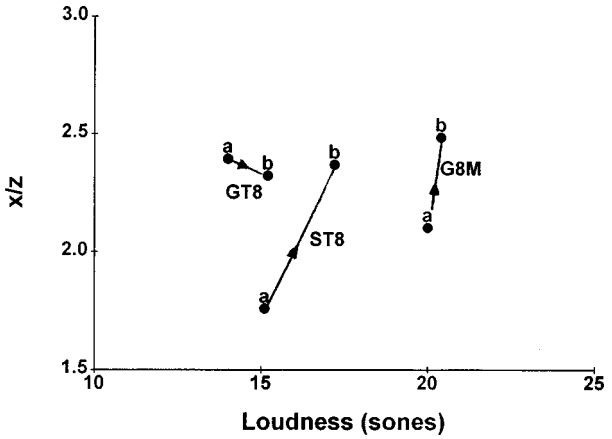

FIG. 12. Tristimulus coordinate ratio x/z as a function of loudness for the Great Trumpet 8′ (GT8), Great 8′ to Mixture (G8M), and the Swell Trumpet 8′ (ST8). Points marked ‘a’ represent values before overhaul, those marked ‘b’ represent values after. The arrows show the direction of change.

ACKNOWLEDGMENTS

Gratitude is expressed to the University of New South Wales and the Australian Institute of Nuclear Science and Engineering for access to equipment and facilities.

[1] G. von Bismarck, ''Sharpness as an attribute of the timbre of steady sounds,'' Acustica **30**, 159–172 (1974).
[2] H. F. Pollard and E. V. Jansson, ''A tristimulus method for the specification of musical timbre,'' Acustica **51**, 162–171 (1982).
[3] H. F. Pollard, ''Timbre measurement,'' Acoust Aust **18**, 65–69 (1990).
[4] E. V. Jansson and J. Sundberg, ''Long-time-average-spectra applied to analysis of music. Part I: Method and general applications,'' Acustica **34**, 15–19 (1975).
[5] R. Plomp and J. A. P. de Laat, ''Comparisons of organs in a spectrum space,'' Acustica **55**, 193–194 (1984).
[6] H. F. Pollard, ''Loudness of pipe organ sounds I. Plenum combinations,'' Acustica **41**, 65–74 (1978).
[7] W. Lottermoser and J. Meyer, *Orgelakustik in Einzeldarstellungen* (Verlag das Musikinstrument, Frankfurt, 1966).
[8] W. Lottermoser and J. Meyer, ''Acoustical design of modern German organs,'' J. Acoust. Soc. Am. **29**, 682–689 (1957).
[9] W. Lottermoser, ''Vergleichende untersuchungen an orgeln,'' Acustica **3**, 129 (1953).
[10] H. H. Harman, *Modern Factor Analysis* (University of Chicago Press, London, 1967).
[11] R. Plomp, ''Fysikaliska motsvarigheter till klanfarg hos stationara ljud, in var horsel och musiken,'' Royal Swedish Academy of Music, Stockholm (1979).
[12] J. Sundberg and E. V. Jansson, ''LTAS applied to analysis of music Part II: An analysis of organ stops,'' Acustica **34**, 269–274 (1976).
[13] E. V. Jansson, ''LTAS applied to analysis of music Part III,'' Acustica **34**, 275–280 (1976).
[14] A. Gabrielsson and E. V. Jansson, ''LTAS and rated qualities of twenty-two violins,'' Acustica **42**, 47–55 (1979).
[15] S. S. Stevens, ''Perceived level of noise by Mark VII and decibels (E),'' J. Acoust. Soc. Am. **51**, 575 (1972).
[16] H. F. Pollard, ''Loudness of pipe organ sounds II. Single notes,'' Acustica **41**, 75–85 (1978).
[17] H. F. Pollard, ''Feature analysis of musical sounds,'' Acustica **65**, 232–244 (1988).
[18] H. F. Pollard, ''Feature analysis and musical timbre,'' J. Catgut Acoust. Soc. **1 (Ser II)**, 16–24 (1988).
[19] R. Plomp, *Aspects of Tone Sensation* (Academic, London, 1976).
[20] ISO Recommendation R132–1966(E), ''Method for calculating loudness level.''
[21] H. Fletcher, ''Loudness, pitch and timbre of musical tones and their relations to the intensity, the frequency and the overtone structure,'' J. Acoust. Soc. Am. **6**, 59–69 (1934).
[22] H. F. Pollard, ''Loudness measures for some synthetic sounds,'' Acustica **44**, 157–159 (1980).
[23] H. F. Pollard, ''Timbre and loudness of flute tones,'' Acoust Aust **24**, 45–6 (1996).
[24] N. H. Fletcher, ''Scaling rules for organ flue pipe ranks,'' Acustica **37**, 131–138 (1977).

Gap detection thresholds as a function of tonal duration for younger and older listeners

Bruce A. Schneider[a)]
Department of Psychology, University of Toronto at Mississauga, 3359 Mississauga Road, Mississauga, Ontario L5L 1C6, Canada

Stanley J. Hamstra
Department of Surgery, University of Toronto, 510 Banting Institute, 100 College Street, Toronto, Ontario M5G 1L5, Canada

(Received 9 December 1998; revised 3 March 1999; accepted 25 March 1999)

Twenty normal hearing younger and twenty older adults in the early stages of presbycusis, but with relatively normal hearing at 2 kHz, were asked to discriminate between the presence versus absence of a gap between two equal-duration tonal markers. The duration of each marker was constant within a block of trials but varied between 0.83 and 500 ms across blocks. Notched-noise, centered at 2 kHz, was used to mask on- and off-transients. Gap detection thresholds of older adults were markedly higher than those of younger adults for marker durations of less than 250 ms but converged on those of younger adults at 500 ms. For both age groups, gap detection thresholds were independent of audiometric thresholds. These results indicate that older adults have more difficulty detecting a gap than younger adults when short marker durations (i.e., durations characteristic of speech sounds) are employed. It is shown that these results cannot be explained by linear models of temporal processing but are consistent with differential adaptation effects in younger and older adults. [S0001-4966(99)01107-8]

PACS numbers: 43.66.Mk, 43.66.Sr [JWH]

INTRODUCTION

Older adults, including those with audiometric thresholds in the normal range, often complain that they have trouble hearing in a variety of situations. For example, it is not uncommon for older adults to inform their audiologist that they can hear sounds fairly well, and can understand speech in a quiet environment, but find it difficult to understand conversations in noisy environments, especially when there are multiple talkers (see Pichora-Fuller, 1997, for a review). While several investigators (e.g., Humes, 1996; van Rooij and Plomp, 1990, 1992) have argued that these difficulties are primarily a consequence of hearing loss, others (e.g., Bergman, 1980; Duquesnoy, 1983; Plomp, 1986; Schneider, 1997) have suggested that auditory processes, other than the ability to hear pure tones in quiet, might be involved. Recent evidence (e.g., Lutman, 1991; Stuart and Phillips, 1996; Schneider, 1997) suggests that one of the factors that may be contributing to the speech understanding difficulties of older adults is a loss of temporal resolution.

A common way of investigating temporal resolution is by means of gap detection. In gap-detection experiments, listeners are asked to detect the presence of a short interruption in an otherwise continuous sound. A number of studies have shown that gap-detection thresholds are elevated in those individuals with sensorineural hearing losses (Irwin *et al.*, 1981; Fitzgibbons and Wightman, 1982; Tyler *et al.*, 1982; Florentine and Buus, 1984; Buus and Florentine, 1985; Fitzgibbons and Gordon-Salant, 1987; Glasberg *et al.*, 1987; Irwin and McAuley, 1987; Long and Cullen, 1988; Moore and Glasberg, 1988; Moore *et al.*, 1989). Because many of the impaired listeners in these studies were older adults, there can be little doubt that older adults with substantial hearing losses are likely to have poorer temporal resolution than younger adults. However, the evidence for age-related changes in temporal resolution in the absence of any clinically significant degree of hearing loss is equivocal. For example, Moore *et al.* (1992) determined the minimal gap that could be detected in a tonal signal for young normals, an elderly group with good hearing, and an elderly group with hearing loss. Because the majority of the older adults in the good hearing group had gap-detection thresholds that were within the range of those of younger adults, Moore *et al.* (1992) concluded that temporal resolution (as measured by gap detection) did not necessarily decrease with age. Schneider *et al.* (1994) and Snell (1997), however, found significant age effects in gap detection studies of younger and older adults with good hearing. Snell's (1997) older adults, who were matched to a group of younger listeners with respect to their audiometric thresholds, had gap-detection thresholds that were 27%–37% larger than those of the younger listeners for gaps in a short noise burst. The older adults in Schneider *et al.* (1994), who were required to discriminate the presentation of two very short tone pips, separated by a period of time, from a continuous tone of equivalent total duration and energy, had gap-detection thresholds that were approximately twice as large as those of younger listeners.

The Moore *et al.* (1992) study suggests that, in the absence of significant sensorineural hearing loss, there is very little age-related loss in temporal acuity, while the Schneider *et al.* (1994) and Snell (1997) studies came to the opposite

[a)]Electronic mail: bschneid@credit.erin.utoronto.ca

conclusion. However, there are procedural differences between the studies that may have affected their outcome. Moore *et al.* (1992) asked subjects to detect gaps in 400-ms tones. Moreover, gaps were produced by gating the signal using a cosine-squared fall/rise time of 1 ms, and the resultant spectral splatter was masked by a white noise low passed at 3 kHz (spectrum level 40 dB lower than that of the signal). Schneider *et al.* (1994) asked subjects to detect a gap between two 2-kHz tone pips, where each tone pip was obtained by multiplying a 2-kHz carrier by a Gaussian envelope with a standard deviation of $\frac{1}{2}$ ms. They argued that with short tone pips of this nature, a noise masker was not necessary because of the spectral similarity between the two tone pips separated by a gap and the continuous short tone of equivalent duration and energy. Snell (1997) asked listeners to detect a cosine-squared dip in the amplitude of short noise bursts. Thus the experiments differed in four ways: (1) the use of tones versus noise; (2) the duration of the leading and lagging stimuli which bounded the gap; (3) the manner in which the stimulus was switched off and on during the gap; and (4) the presence of noise to mask off-frequency listening. The present study investigates which, if any, of these factors might be responsible for the difference in results when tonal stimuli are used.

What sort of factors might produce an age effect for the detection of a gap between two Gaussian tone pips but not necessarily for a gap between two longer duration tones? Consider, for the moment, how age-related changes in auditory function might affect the performance of an observer who monitors the energy output from an auditory filter centered on the frequency of the carrier tone (e.g., Penner, 1975, 1977; Moore *et al.*, 1989). A listener of this sort is usually modeled by passing the squared output of a linear filter through a temporal window which integrates the squared output to obtain the total energy passing through that window at that moment of time. Now consider what happens to the output of this sliding temporal window when the input to the filter is a long duration tone containing a short gap. When the temporal window is processing a continuous tone with a gap, the total energy passing through it will be large and unchanging until it encounters the gap. When, however, the window encounters the gap, the energy passing through this window will be reduced. When the window passes beyond the gap, the energy output will return to its pre-gap level. The extent of the dip will depend primarily on four factors: (1) the size of the gap; (2) the abruptness with which the tone is turned off during the gap; (3) the bandwidth of the filter; and (4) the size of the temporal window. Clearly as gap duration increases, the extent of the dip in energy output will increase. Just as clearly, decreasing the slope of the stimulus' off ramp will decrease the rate of decline in energy as the window enters the gap, and for short duration gaps, the dip in energy during the gap will be smaller than it would be for a steeper off ramp. Also, because of ringing in the auditory filter, the narrower the bandwidth of the auditory filter, the smaller the extent of the dip at a fixed gap duration. Finally, the larger the temporal window size the more gradual the drop in energy with tone offset, and the more shallow the dip.

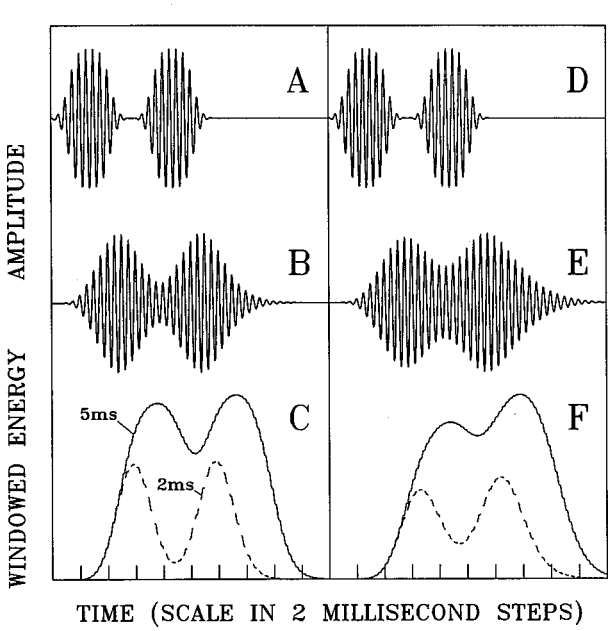

FIG. 1. (A) Time waveform for a 2-ms gap between two short 2-kHz tones. (B) The output of a gamma tone filter (filter 1, impulse response envelope $= k \cdot t^{2.475} e^{-1477.75t}$) centered at 2 kHz to input waveform (A). (C) Integral of the squared waveform in (B) over a 5-ms time period (solid line) and a 2-ms time period (dashed line). (D) Same time waveform as in (A). (E) The output of a gamma tone filter (filter 2, impulse response envelope$= k \cdot t^{2.475} e^{-1000t}$) centered at 2 kHz to input waveform (D). (F) Integral of the squared waveform in (E) over a 5-ms time period (solid line) and a 2-ms time period (dashed line).

The consequences of age-related changes in either the frequency bandwidth of the auditory filter or the width of the temporal window are illustrated in Fig. 1 for two 2.5-ms tone pips separated by a gap of 2 ms. Figure 1(A) shows the input (a gap between two tone pips) to a 2-kHz filter (filter 1). The output from that filter [shown in Fig. 1(B)] is then squared and passed through one of two rectangularly shaped temporal windows. The first temporal window integrates energy over a 5-ms period [Fig. 1(C), solid line]; the second temporal window integrates energy over a 2-ms period [Fig. 1(C), dashed line]. Note that the smaller the temporal window, the more rapid is the response to the gap between the two tone pips, and for relatively short gaps, the more pronounced the dip in energy.

Figure 1(D) shows the input to a second 2-kHz filter (filter 2), whose bandwidth is narrower than that of filter 1. Note that even though the input to both filters is identical, the response of filter 2 to the gap is slower and less profound than that of filter 1 [Fig. 1(E)]. Consequently, the extent of the dip in energy is less extensive [see Fig. 1(F)]. Therefore, if age narrows the auditory filter, then gap detection thresholds should increase with age. Similarly, if temporal window size increases with age, then gap detection thresholds should increase with age.

Gap-detection thresholds could also be higher in older adults than in younger adults if older adults require a larger dip in energy output to reach threshold. If, as is reasonable to assume, there is some sort of internal noise in the sliding temporal window and the amount of internal noise is greater in older than in younger adults, this would lead to a reduc-

tion in intensity resolution. Alternatively, older adults may be less efficient at processing signals in noise so that they would require a greater increment in signal intensity to notice a difference. Recent results (He *et al.*, 1998) have shown that intensity resolution does, indeed, decrease with age. Thus a loss of intensity resolution could produce a larger gap-detection threshold.

Given these potential candidates for an age effect in gap detection, we can now ask how such age effects might be affected by: (1) different decay rates in the physical stimulus; and (2) different durations of the leading and lagging markers defining the gap. Suppose, for example, that the extent of ringing in the auditory filter was greater in older than in younger adults (an unlikely event given the results of Patterson *et al.*, 1982). When the tone is turned off and on rather abruptly (as in Fig. 1), the extent of the dip will be greater for younger [e.g., Fig. 1(B) and (C)] than for older adults [e.g., Fig. 1(E) and (F)]. However, if the tone were to be turned off and on very slowly, the effects of neural ringing on the output of the temporal window would be negligible, and the extent of the dip should be the same for younger and older adults. Similarly, suppose that older adults had larger temporal windows than younger adults. When the tone is turned off and on rather abruptly, the extent of the dip in energy should be greater for younger adults [see, for example, the difference in the extent of the dip for 2- and 5-ms windows in Fig. 1(C) and (F)]. However, both the 2- and 5-ms temporal windows will be able to follow relatively slow changes in tone amplitude equally well. Therefore, if the age effect is due to either age-related changes in auditory filter width or to age-related changes in temporal window size, the difference in gap-detection thresholds between younger and older adults should decrease as the off and on ramping of the tone is slowed. Schneider *et al.* (1998) varied the fall and rise time of tone pips by varying the standard deviation of their envelopes (larger standard deviations produce slower fall/rise times). As expected, gap-detection thresholds increased with increases in standard deviation, however, they increased at the same rate for younger and older listeners. Thus the Schneider *et al.* (1998) study suggests that neither age-related differences in frequency selectivity or in temporal window size can explain the age effects found for short duration tonal markers.

If younger and older adults do not differ with respect to either auditory filter width or temporal window size, what other factors could be responsible for age-related differences in gap-detection thresholds? One possibility, mentioned above, is that older adults simply require a more profound dip in energy output from the temporal window in order to detect a gap. However, if older adults are less sensitive than younger adults to a dip in energy, then their gap-detection thresholds should be higher at all marker durations. To see why this should be true consider the response of an auditory filter [such as the one shown in Fig. 1(B)] to a gap in a continuous tone. In a linear system the response of a filter to a gap is virtually independent of the duration of the tone preceding the gap as long as its duration exceeds the filter's ringing time. With respect to the filter used to generate Fig. 1(B), the filter's response during the gap is virtually independent of marker duration provided that the leading tone is longer than 15 ms. Thus if younger and older adults differ only with respect to their sensitivity to dips in energy, age-related differences in gap detection should be found at all marker durations, and the size of this age effect should be constant for marker durations that are longer than the filter's ringing time.

To see how marker duration affects gap detection, we systematically varied marker duration from very short to very long while keeping the rise and decay time of the tonal markers constant. We also used a notched-noise at all marker durations to insure that detection was not based on off-frequency listening. According to a linear temporal window model, for both younger and older adults, gap-detection thresholds and the extent of any age difference in these thresholds should not be affected by marker duration for durations longer than 15 ms. Therefore, an interaction between age and marker duration (a large age effect at short but not long marker durations) would be incompatible with a linear model and would suggest that the auditory system's response to the termination and reinstatement of a stimulus changes with marker duration at different rates for younger and older adults. For example, if the time course and/or extent of adaptation differed between younger and older adults, then an increase in marker duration could differentially affect the gap-detection performance of these two age groups, resulting in an interaction between age and marker duration.

I. METHOD

A. Subjects

Twenty young adults (mean age: 21.9 years; s.d.: 1.7) and 20 older adults (mean age: 72.4 years; s.d.: 5.2) participated. The older adults were volunteers recruited from a pool of seniors from the local community. The younger adults were students at University of Toronto at Mississauga. All had pure tone thresholds of less than or equal to 40 dB HL (ANSI S3.6, 1969) in the ear tested for frequencies between 200 and 2000 Hz (older subjects: mean at 2 kHz=16.8 dB HL s.d.=10.5 dB; younger subjects: mean at 2 kHz=6.8 dB HL; s.d.=10.9 dB). Hearing levels for all of the younger adults, and all but two of the older adults at 2 kHz were $\leqslant$ 30 dB HL. Hearing levels for the older adults at 3, 4, 6, and 8 kHz averaged 26.7, 33.7, 39.7, and 43.5 dB HL, respectively. Thus the older adults could be characterized as being in the early stages of presbycusis, but having relatively normal hearing at 2 kHz. Hearing levels for the younger participants were $\leqslant$ 30 dB HL at all frequencies tested. Subjects were paid a nominal amount for their participation. None of the subjects reported any history of auditory disorder.

B. Apparatus and stimuli

Stimuli were generated digitally with a sampling rate of 20 kHz and converted to analog form using a 16-bit Tucker Davis Systems (TDS) digital-to-analog converter. To construct the amplitude envelope for leading and lagging markers, a series of temporally spaced Gaussian envelopes were summed. Each Gaussian envelope had a standard deviation of $\frac{1}{2}$ ms, and the Gaussian envelopes were spaced $\frac{1}{2}$ ms apart.

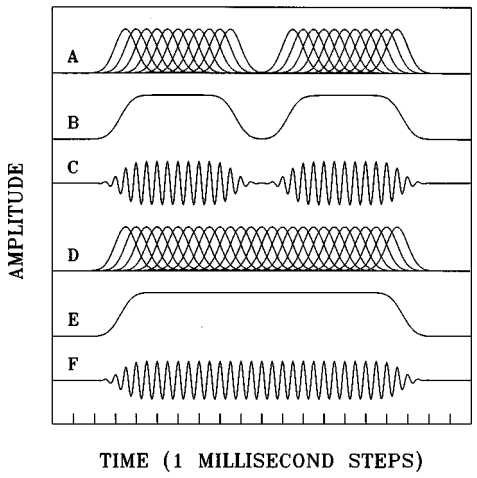

FIG. 2. The 22 Gaussian functions (s.d.$=\frac{1}{2}$ ms) in panel (A) are added together to define the envelope in panel (B). This envelope is multiplied by a 2-kHz tone to produce the two tone pips shown in panel (C). The 27 tone pips in panel (D), when added together form the envelope in panel (E), which when multiplied by the 2-kHz carrier, produces the single short tone.

Figure 2(a) shows two sets of 11 Gaussian envelopes whose standard deviations are $\frac{1}{2}$ ms, spaced $\frac{1}{2}$ ms apart. Figure 2(b) shows the sum of these two sets of 11 Gaussian envelopes. (The summed envelopes have been normalized so that their peak amplitudes are 1.0.) Note that the summed envelopes have ogival rise and decay times and flat tops. It can also be shown that the amplitude of the envelope at the location of the peaks of the first and last of the Gaussians in the series are 3 dB down from the flat portion of each summed envelope.

The time between the peaks of the first and last Gaussian envelopes in a marker defines marker duration. In this example, marker duration is equal to 5 ms. The duration of the gap, Δt, is defined as the time between the end of the leading marker (the location of the peak of the last Gaussian), and the beginning of the lagging marker (location of the peak of the first Gaussian). In Fig. 2, the duration of the gap is 2 ms. Note that for short gap durations such as these, the amplitude envelopes do not decay to zero during the gap. Therefore, for short gap durations, the tone is reduced in amplitude but not turned entirely off.

Figure 2(d) shows the series of 27 Gaussian envelopes used to construct the envelope of the comparison tone [Fig. 2(e)]. Note that when these Gaussian envelopes are summed, the result is an envelope with the same rise and decay times as the rise and decay times used for the leading and lagging markers, but without a gap. A 2-kHz tone, which was aligned in cosine phase with the peaks of the Gaussians, was multiplied by the normalized summed amplitudes shown in Fig. 2(b) and (e) to obtain the gap and continuous tones shown in Fig. 2(c) and (f). Before multiplication, however, both envelopes were normalized so that after multiplication, the total energy in each stimulus was equal to the total amount of energy in the stimulus defined by multiplying two widely separated Gaussian envelopes (technically, between two Gaussian envelopes, standard deviation$=\frac{1}{2}$ ms, spaced infinitely far apart) by a 90 dB SPL, 2-kHz tone. Thus all stimuli in this experiment (both gap and no-gap stimuli at all marker durations) were identical in terms of total energy.

Signals were embedded in a notched-noise to mask spectral splatter. For short duration markers, the notched-noise masker was not necessary because of the spectral similarity of the gap and no-gap stimuli (see Schneider *et al.*, 1994). However, the amount of spectral splatter for no-gap stimuli decreases as marker duration increases, so that listeners could discriminate between the two stimuli on the basis of spectral cues, namely, the presence versus absence of energy at frequencies outside the 2-kHz region. Without the masker, listeners could hear a click at the longer marker durations whenever a gap was introduced, but could not hear a click when the masker was present. The masker, which was used at all marker durations, was a notched-noise, produced by passing the output of an analog white-noise generator (General Radio 1381), through a Grason–Stadler filter, in band-reject mode, to produce a notch between 970 and 4000 Hz. The rate of falloff at each edge of the notch was 35 dB/octave. The spectrum level of the noise outside the notch was 50 dB SPL/Hz up to 5 kHz, whereupon it declined at a rate of 12 dB/octave.[1] The continuous analog notched-noise was added to the signal channel and presented to the stimulated (left) ear over a TDH-49 earphone.

The duration of leading and lagging markers ranged from 2.5 to 500 ms. Markers defined by single tone pips were also included to duplicate the conditions in Schneider *et al.* (1994). The duration of these markers were also defined as the time difference between the points on the Gaussian envelope that were 3 dB down from peak amplitude. Thus the duration of the single tone pip markers was defined as 0.83 ms.

C. Procedure

Gap-detection thresholds were determined as follows. At each marker duration, stimuli were presented in a 2IFC paradigm, and a staircase procedure was used to determine the 79.7% point on the psychometric function (Levitt, 1971). At the beginning of a run, the gap size was set to 36 ms. Each trial, which was initiated by pressing a button, consisted of two 500-ms intervals separated by a 100-ms silent period, except for the 500-ms marker duration where duration of each interval was 1200 ms. The gap stimulus was randomly assigned to one of the two intervals. The other interval contained the no-gap stimulus of equal total duration and energy. Each stimulus began 100 ms into the interval. Subjects indicated which interval they thought contained the gap stimulus by pressing one of two buttons that corresponded to the two intervals. Lights on the response box marked the beginning of the trial and each interval and also provided immediate feedback to the subjects as to whether or not each response had been correct. The size of the gap was adjusted on a trial-by-trial basis according to a 3 down, 1 up rule. Each run was terminated after 12 reversals. Gap-detection threshold for that run was defined as the average of the last eight reversals. Marker duration was changed after each run in an irregular order which was the same for each subject. Subjects cycled through marker durations a total of four times so that there were four runs at each marker duration.

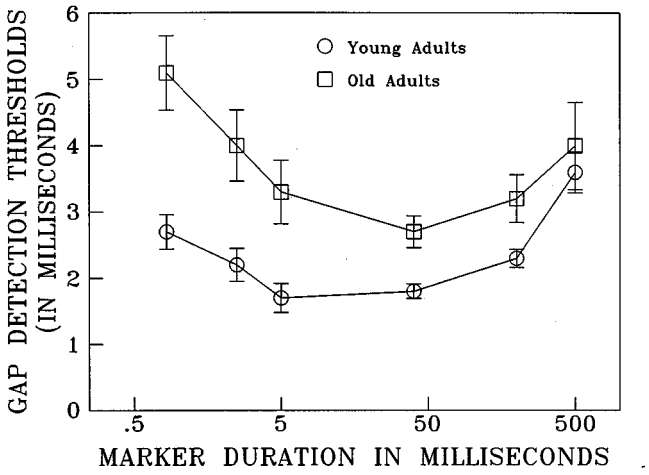

FIG. 3. Gap-detection thresholds as a function of marker duration for younger and older adults.

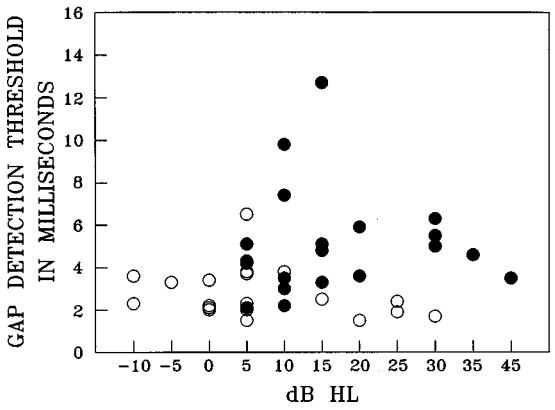

FIG. 4. Gap-detection thresholds for younger (open circles) and older adults (filled circles) as a function of hearing level at 2 kHz. Marker duration=0.83 ms.

Because the older subjects were sometimes highly variable on the first run at a marker duration, the first run at each marker duration was considered an orientation run for all subjects and hence, was not included in subsequent analyses. Total testing time for each subject was approximately 90 min, not including time allowed for breaks. Typically, two sessions were required per subject. Four of the younger adults were unavailable for their sessions involving 500-ms markers only. The data from these four young adults were not included in the repeated measures analysis of variance, but were included in all other calculations.

II. RESULTS

Figure 3 shows average gap-detection thresholds as a function of marker duration for younger and older listeners. The gap-detection thresholds of older listeners are significantly higher than those of the younger listeners at the shortest duration tested. The extent of this age difference (2.4 ms) at the shortest marker duration is nearly equivalent to that observed by Schneider *et al.* (2.7 ms), who used comparable markers but a different psychophysical method (constant stimulus versus staircase). However, the size of this difference decreases with increasing marker duration until it vanishes when marker duration equals 500 ms. A 2 (age) by 6 (marker duration) repeated measures analysis of variance (ANOVA) confirms this visual impression: there was a significant main effect due to age, $F(1,34)=7.275$, $p=0.011$; a significant main effect due to marker duration, $F(5,170)=12.433$, $p<0.001$; and a significant age×marker duration interaction, $F(5,170)=4.012$, $p<0.002$. *T*-tests indicated significant age differences at marker durations of 0.83 ms, $t(38)=3.804$, $p=0.001$; 2.5 ms, $t(38)=2.949$, $p=0.007$; 5 ms, $t(38)=3.019$, $p=0.006$; 40 ms, $t[38]=3.426$, $p=0.002$; and 200 ms, $t(38)=2.329$, $p=0.029$ ms.

Figure 4 plots individual gap-detection thresholds as a function of each individual's hearing level at 2 kHz for both younger and older adults for the 0.83-ms marker duration. This figure shows the gap-detection threshold to be independent of hearing level for listeners whose hearing is relatively normal at 2 kHz. The Pearson product-moment correlations between gap-detection threshold and hearing level were −0.28 and +0.03 for younger and older adults, respectively. Correlations were equally small at other marker durations, ranging from −0.28 to 0.36 for young adults, and from −0.04 to 0.32 for older adults. The average correlation coefficient[2] between gap-detection threshold and hearing level was −0.04 for younger adults and 0.14 for older adults. Thus temporal acuity at 2 kHz, as indexed by gap detection, appears to be independent of hearing level at 2 kHz, for listeners whose hearing at 2 kHz is in the normal range.

There was also a good degree of intrasubject consistency across marker duration. Pearson product-moment correlation coefficients were computed for gap-detection thresholds at one marker duration versus those at another marker duration for all pairs of marker durations. These correlation coefficients averaged 0.66 for young adults and 0.70 for older adults. Thus subjects who had high gap-detection thresholds at one duration tended to have high thresholds at other durations.

III. DISCUSSION

Gap-detection thresholds are much lower for younger adults than for older adults at short marker durations with this age difference decreasing and eventually disappearing for 500-ms marker durations. These results also confirm previous reports that gap-detection thresholds are independent of audiometric thresholds, suggesting that age-related changes in temporal acuity may occur independently from age-related changes in audiometric acuity for listeners whose hearing is in the normal range at the test frequency.

For younger listeners there is very little variation in gap-detection thresholds for marker durations between 2.5 and 250 ms, a result that is consistent with the results from Phillips *et al.* (1997), who varied the duration of a leading noise marker from 5 to 300 ms (the trailing noise marker was 300 ms in duration, see their Fig. 3, within-band conditions). Penner (1975, 1977), however, found that detection thresholds for gaps in a gated noise burst increased over the first 20 ms of marker duration. The reasons for this discrepancy are

uncertain (see Phillips *et al.*, 1997, for a description of procedural differences).

In the Introduction we showed that for marker durations longer than the ringing time of the auditory filter, simple temporal window models predict that gap-detection performance should be independent of marker duration, and that the size of the age effect, if any, should also be independent of marker duration. Figure 3, however, shows that gap-detection thresholds change with marker duration and that thresholds for younger and older adults converge at longer marker durations.

A. Adaptation

Because the amount of adaptation and the degree of recovery from it is known to vary with tone duration, it is possible that the effects observed in Fig. 3 are a consequence of neural adaptation. To understand how age differences in adaptation and recovery from adaptation might produce a pattern of results like that in Fig. 3, consider the sequence of neural events that are likely to be observed in primary auditory afferents when there is a gap between two short duration tones. When the leading marker is first turned on there is a transient response which quickly decays (within 25 ms in the Mongolian gerbil, Westerman and Smith, 1984) to an asymptotic, steady-state level. When the leading marker is turned off, the relative firing rate will drop rapidly to zero and remain there until the lagging marker begins. At that point there will be a brief transient response whose magnitude will depend upon the duration of the gap. The form and shape of this second transient response is similar to but lower in magnitude than the transient response that occurs at the beginning of the leading marker. As the duration of the gap is increased, the break in the pattern of firing is prolonged and the size of the transient response upon reintroduction of the tone is increased. This second transient response quickly decays, however, to the steady-state level. (For examples of firing patterns that have these characteristics, see Harris and Dallos, 1979, Figs. 3 and 13.)

Figure 5 (solid lines) illustrates the pattern of neural firing we might find for gaps between two 40-ms markers. The large transient response to the leading marker quickly decays to its steady-state value. When the leading marker ends, firing rate drops rapidly. When the second marker begins, there is a secondary transient response that also decays quickly to the asymptote. Note that the size of this transient response increases with gap duration so that at very long durations recovery from adaptation is virtually complete. Also shown in Fig. 5 (dotted lines) is the pattern of results that would be expected of an individual whose adaptation function was the same as that illustrated by the solid lines, but whose recovery from adaptation was not as extensive. Note that the magnitude of the second transient is much smaller for this individual. Thus if younger adults have adaptation and recovery functions like those illustrated by the solid lines, whereas older adults have recovery functions like those illustrated by the dotted lines, younger adults would have lower gap-detection thresholds than older adults. [The model that was used to generate the patterns shown in Fig. 5 is a modification of the model presented by Trehub *et al.* (1995) and is described in the Appendix.]

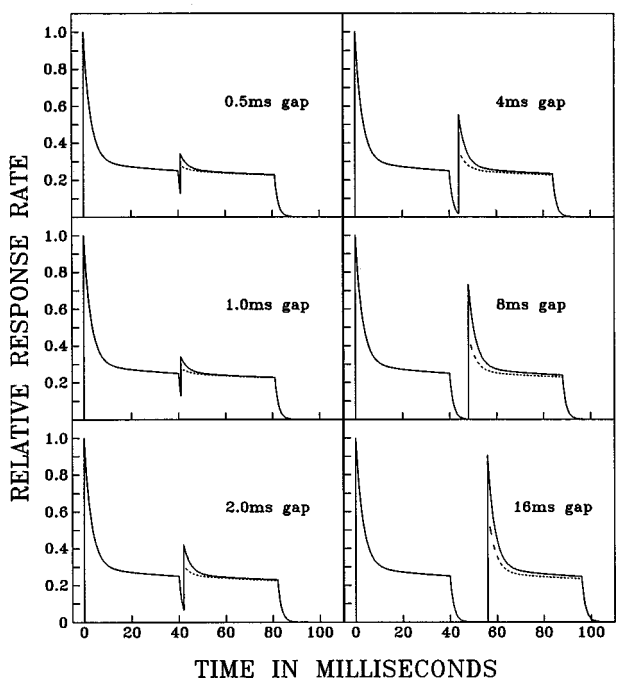

FIG. 5. Relative response rate as a function of time for hypothetical neural units exposed to two 40-ms tones separated by gaps of varying duration. The response parameters of these hypothetical units are assumed to differ between younger (solid lines) and older (dashed lines) adults (see text for details). The first tone is assumed to start at 0 ms.

Harris and Dallos (1979) showed that the degree of recovery from adaptation was also a function of the duration of the adapting tone (see their Fig. 13) such that, for a fixed gap duration, the size of the transient response to the onset of the lagging marker decreases with marker duration. Figure 6 (top panels) illustrates what would happen to neural firing rate for a gap of 2 ms (solid lines), as a function of marker duration (MD). Note that for very short marker durations, recovery from adaptation is virtually complete for a gap of this size. Note, however, that the size of the second transient decreases with increases in marker duration. This effect is indicated more clearly in the middle panels where response rate is plotted on the same time scale (the gap is assumed to begin at 0 ms in all plots). Also plotted (see dotted lines) is the neural response to the continuous tone (the no-gap stimulus) whose total duration is equal to that of the gap stimulus.

A comparison of the neural response patterns for the gap and no-gap stimuli (see Fig. 6, top and middle panels) would seem to suggest that gap detection should get worse as marker duration is increased because the size of the second transient declines with marker duration. However, if we pass these neural patterns through a temporal window, we can no longer be certain that gap-detection thresholds should increase uniformly with marker duration. In the bottom panel of Fig. 6, the neural responses for both gap and no-gap stimuli have been passed through a rectangular temporal window whose width is 9.5 ms (the value suggested by the work of Moore *et al.*, 1989). Here we assume that the responses are simply summed over a 9.5-ms period. Note that for short duration stimuli the effect of passing the stimuli

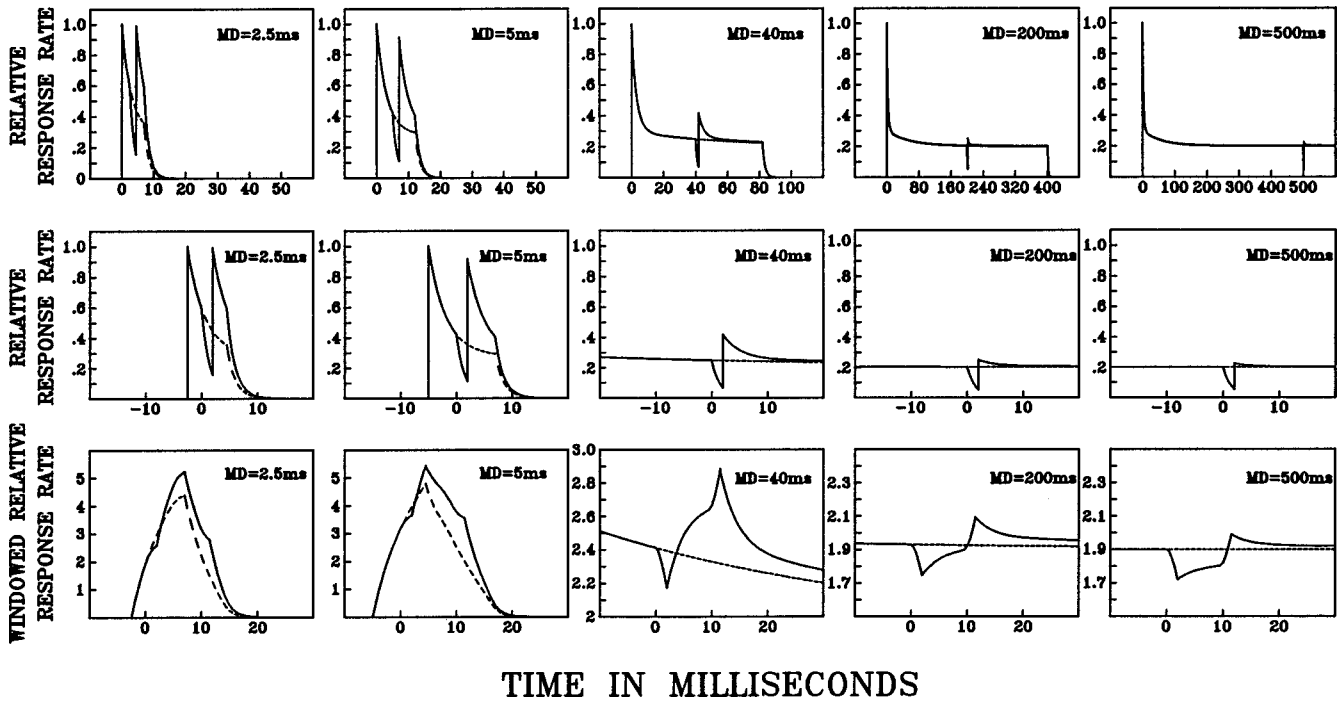

FIG. 6. Top panels. Solid lines. Relative response rate as a function of time for hypothetical neural units of younger adults exposed to two tones separated by a 2-ms gap. The dashed line shows the relative response rate to the no-gap stimulus of equivalent duration and energy. The parameter, MD, is the marker duration of each tone. Middle panels. Relative response rates for the time period from 20 ms before the start of the gap (0 ms in this plot) until 20 ms after the start of the gap. Bottom panels. The sum of the neural responses rates over a 9.5-ms window for the period beginning 10 ms before the start of the gap (0 ms in this plot) and ending 30 ms after the start of the gap.

through a temporal window is to produce two unimodal patterns, with the summed response pattern being larger for the gap stimulus. Thus for short gaps and short marker durations, it is possible that the two patterns (gap and no-gap) are discriminated on the basis of total neural counts passing through the temporal window. For longer durations, however, the output from the temporal window does show a drop during the gap followed by a peak, with the size of the difference between the peak and trough declining with increasing marker duration. Hence, for longer duration markers, gap-detection thresholds should increase with marker duration.

If Fig. 6 is taken as a representation of the neural events corresponding to the presentation of gap and no-gap stimuli to a young adult, Fig. 7 could represent an adult whose adaptation function and temporal window duration was equivalent to that illustrated in Fig. 6, but whose recovery from adaptation was not as complete as that of a younger adult. A comparison of Figs. 6 and 7 indicates that the difference in temporal window output for gap and no-gap stimuli at short marker durations is much more pronounced for younger adults (Fig. 6) than for older adults (Fig. 7). For intermediate marker durations (see, for example, MD=40 ms) the difference in temporal window output patterns for gap and no-gap stimuli is also quite a bit more pronounced in younger adults. However, as marker duration increases, the advantage enjoyed by younger adults decreases. Hence this model would predict that gap-detection thresholds for younger and older adults should converge at longer marker durations.

It should be noted that the parameters of the model for younger adults were selected so as to provide a good fit to auditory firing patterns in nonhuman mammals (see the Appendix for details). Thus there is no guarantee that the model accurately reflects the time course for adaptation and for recovery from adaptation in humans. Nevertheless, it does predict that for longer durations, performance in a gap-detection task should worsen in young listeners. That is exactly what Fig. 3 indicates.

An examination of Fig. 6 also shows that if neural output from the primary auditory afferents is integrated over a temporal period, as is assumed in the model, it is possible that the basis for gap discrimination is not the same for short marker durations as it is for longer marker durations, a fact also noted by Penner (1975). An examination of the response patterns for 2.5-and 5-ms markers indicates that gap and no-gap stimuli could be discriminated either on the basis of total neural count, or possibly by the total duration of neural activity (see Fig. 6). Recall that He *et al.* (1998) found that intensity increment thresholds for older adults were substantially higher than those for younger adults. Similarly, there is some evidence that temporal discrimination is poorer in older adults (Abel *et al.*, 1990; Fitzgibbons and Gordon-Salant, 1994). Thus, if gap discrimination is based on total neural counts over a particular time period, and/or on the total duration of neural activity, then older adults would be particularly disadvantaged *vis a vis* younger adults at shorter marker durations.

In the present study we have suggested that long marker durations in younger adults adversely affect gap detection by adapting the transient response to presentation of the trailing marker. Recently, Moore and Peters (1997) reported that decrement-detection thresholds were much worse for a continuous pedestal than for a gated pedestal for decrements of

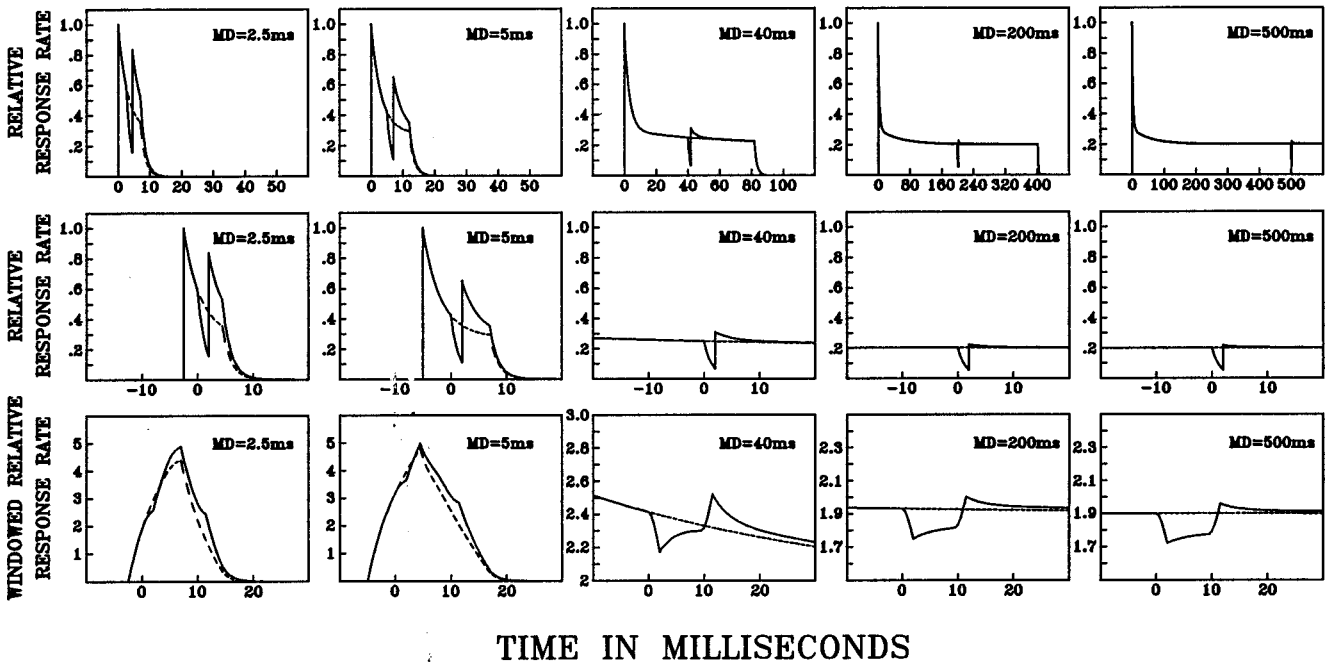

FIG. 7. Top panels. Solid lines. Relative response rate as a function of time for hypothetical neural units of older adults exposed to two tones separated by a 2-ms gap. The dashed line shows the relative response rate to the no-gap stimulus of equivalent duration and energy. The parameter, MD, is the marker duration of each tone. Middle panels. Relative response rates for the time period from 20 ms before the start of the gap (0 ms in this plot) until 20 ms after the start of the gap. Bottom panels. The sum of the neural responses rates over a 9.5-ms window for the period beginning 10 ms before the start of the gap (0 ms in this plot) and ending 30 ms after the start of the gap.

10- and 20-ms duration. They suggested that this decrease in performance could be related to long term neural adaptation. In terms of the model proposed here, the neural adaptation caused by a continuous pedestal would suppress the transient response that should follow at the end of the decrement. If, however, the pedestal was also gated, there would be time for recovery from adaptation between pedestal presentations. Hence, there should be a larger transient response following the end of the decrement in a gated pedestal, resulting in lower detection thresholds for the decrement when the pedestal was gated. Thus the results of the Moore and Peters (1997) study are also consistent with the model of neural adaptation presented here.

B. Attention

The ability to detect a gap between two long duration markers may be affected by the listeners' ability to focus their attention at the precise point of time at which the gap occurs. If older adults are less able than younger adults to predict exactly when, during the stimulus, the gap should occur, they might be disadvantaged relative to younger adults. Studies of temporal discrimination of relatively short tones (Abel *et al.*, 1990; Fitzgibbons and Gordon-Salant, 1994) indicate that older adults have higher duration increment thresholds than younger adults. Thus they would not be as good as younger adults at predicting when the gap should occur. However, we could not find any studies in the literature in which duration discrimination was determined for younger and older adults for stimuli as long as 500 ms. If we assume that the ability to discriminate changes at these longer durations does not differ between younger and older adults, then we would expect their gap-detection thresholds to converge at longer durations.

IV. CONCLUSIONS

The present study indicates that older adults have poorer temporal resolution (as measured by gap detection) than younger adults for short duration stimuli, but not for longer duration stimuli. We have shown that this result cannot be explained by a linear temporal window model but is consistent with a temporal window model that includes the effects of adaptation. According to the adaptation version of the temporal window model, temporal acuity at short durations is reduced in older adults because recovery from adaptation is not as rapid as it is in younger adults. Thus older adults have more difficulty detecting a gap than younger adults when short marker durations, but not long marker durations are employed. Since the durations at which older adults show a deficit are those characteristic of speech sounds, this deficit might have an adverse effect on the older adult's ability to perceive speech.

ACKNOWLEDGMENTS

This research was supported by a grant from the Natural Sciences and Engineering Research Council of Canada. We thank Jane Carey and Grace Azevedo for their assistance in data collection, and Kim Yue for programming assistance.

APPENDIX

As in Trehub *et al.* (1995), the time course of neural adaptation was assumed to be governed by a double exponential function of the type suggested by Westerman and Smith (1984). Specifically, if $r(t)$ represents the rate of neural firing as a function of time, the normalized rate function is obtained by dividing firing rate by the maximum observed firing rate, $\mathrm{Max}[r(t)]$. Thus

$$\frac{r(t)}{\mathrm{Max}[r(t)]} = \frac{a_1 e^{-t/\lambda_1} + a_2 e^{-t/\lambda_2} + r_s}{a_1 + a_2 + r_s}, \quad t \leqslant t_m, \qquad \text{(A1)}$$

where a_1, λ_1 are constants regulating the short-term decay functions, a_2, λ_2 are the constants governing the initial rapid decay, r_s is the asymptotic firing rate, t is time in ms, and t_m is the duration of the masker in ms. For adults, the asymptotic firing rate was assumed to be 20, the short-term constants were set to $a_1 = 10$ and $\lambda_1 = 57$ ms, and the rapid decay constants were set to $a_2 = 70$, $\lambda_2 = 3$ ms. The values of the times constants λ_1, λ_2 of the two exponential decay functions were the mean values found to fit the adaptation functions of Mongolian gerbils (Westerman and Smith, 1984).

During the gap period, Δt, it is assumed that normalized firing rate rapidly decays in an exponential fashion to a value of 0. During this period

$$\frac{r(t)}{\mathrm{Max}[r(t)]} = e^{-(t-t_m)/\lambda_3}\left[\frac{a_1 e^{-t_m/\lambda_1} + a_2 e^{-t_m/\lambda_2} + r_s}{a_1 + a_2 + r_s}\right], \quad t_m < t \leqslant t_m + \Delta t, \qquad \text{(A2)}$$

where $\lambda_3 = 1.5$ ms. The value of 1.5 ms for this time constant was chosen to produce a decay time that would reflect neural ringing in the auditory filter.

Neural activity at the time at which the tone is reintroduced is considered to be a weighted sum of two processes.[3] The first consists of the adaptation level that would have been present had there been no gap. The second is the amount of recovery from adaptation produced by the interruption of the tone. The amount of recovery from adaptation is assumed to be an exponential function of the duration of the gap. Once the stimulus is turned back on, it is assumed that the rate of decay of the recovery component is identical to the rate of decay in the firing rate when the tone is first turned on. Finally, the time constant for the recovery component is itself assumed to be an exponential function of the duration of the first marker. Thus

$$\frac{r(t)}{\mathrm{Max}[r(t)]} = \frac{\left[\begin{array}{l} e^{-\Delta t/a_3(1-e^{-t_m/\lambda_4})}(a_1 e^{-t/\lambda_1} + a_2 e^{-t/\lambda_2}) + r_s \\ +(1-e^{-\Delta t/a_3(1-e^{-t_m/\lambda_4})})(a_1 e^{-(t-t_m-\Delta t)/\lambda_1} + a_2 e^{-(t-t_m-\Delta t)/\lambda_2}) \end{array}\right]}{a_1 + a_2 + r_s}, \quad t_m + \Delta t < t, \qquad \text{(A3)}$$

for the duration of the lagging tone. For younger adults, the values of $a_3 = 100$, $\lambda_4 = 500$ ms were chosen so as to generate response patterns such as those shown in the post-stimulus time histograms shown in Figs. 3 and 13 from Harris and Dallos (1979).

Older adults were assumed to recover more slowly from adaptation. To model this, we assumed a time constant, $\lambda_4 = 150$ ms, for older adults. Thus younger and older adults were assumed to differ only with respect to the time constant for recovery from adaptation.

[1]The spectral splatter for any stimulus composed of a sum of in-phase Gaussian-enveloped tone pips, spaced at integer multiples of the carrier tone's period, is bounded by the spectral energy density function for a single tone pip. For a Gaussian-enveloped ($\sigma = \frac{1}{2}$ ms), 2-kHz tone pip, spectral energy at 3.5 kHz is 96.4 dB down from the energy at 2 kHz. Therefore, an upper limit of 5 kHz on the notched-noise is sufficient to mask any high-frequency spectral splatter.

[2]Correlation coefficients were averaged by first transforming them to *z*-scores using Fisher's transformation (see Hays, 1973), averaging the transformed scores, and then using the reverse transformation to obtain the average correlation coefficient.

[3]In Trehub *et al.* (1995), recovery from adaptation was also considered to be the sum of the same two processes. However, the first process, the adaptation level that would have been present had there been no interruption in the stimulus, was given a weighting of 1. For very short marker durations, a weight of 1 can result in transients produced by the onset of the lagging marker that exceed those produced by the leading marker. To correct for this problem, the weighting was changed in this paper.

Abel, S. M., Krever, E. M., and Alberti, P. W. (**1990**). ''Auditory detection, discrimination and speech processing in aging, noise-sensitive and hearing-impaired listeners,'' Scand. Audiol. **19**, 43–54.

Bergman, M. (**1980**) *Aging and the Perception of Speech* (University Park Press, Baltimore).

Buus, S., and Florentine, M. (**1985**). ''Gap detection in normal and impaired listeners: The effect of level and frequency,'' in *Time Resolution in Auditory Systems*, edited by A. Michelson (Springer-Verlag, London), pp. 159–179.

Duquesnoy, A. J. (**1983**). ''The intelligibility of sentences in quiet and in noise in aged listeners,'' J. Acoust. Soc. Am. **74**, 1136–1144.

Fitzgibbons, P. J., and Gordon-Salant, S. (**1987**). ''Temporal gap resolution in listeners with high-frequency sensorineural hearing loss,'' J. Acoust. Soc. Am. **81**, 133–137.

Fitzgibbons, P. J., and Gordon-Salant, S. (**1994**). ''Age effects on measures of auditory duration discrimination,'' J. Speech Hear. Res. **37**, 662–670.

Fitzgibbons, P. J., and Wightman, F. L. (**1982**). ''Gap detection in normal and hearing-impaired listeners,'' J. Acoust. Soc. Am. **72**, 761–765.

Florentine, M., and Buus, S. (**1984**). ''Temporal gap detection in sensorineural and simulated hearing impairments,'' J. Speech Hear. Res. **27**, 449–455.

Glasberg, B. R., Moore, B. C. J., and Bacon, S. P. (**1987**). ''Gap detection and masking in hearing-impaired and normal-hearing subjects,'' J. Acoust. Soc. Am. **81**, 1546–1556.

Harris, D. M., and Dallos, P. (**1979**). ''Forward masking of auditory nerve fiber responses,'' J. Neurophysiol. **42**, 1083–1107.

Hays, W. L. (**1973**). *Statistics for the Social Sciences*, 2nd ed. (Holt, Rinehart, & Winston, New York).

He, N-J., Dubno, J. R., and Mills, J. H. (**1998**). ''Frequency and intensity discrimination measured in a maximum-likelihood procedure from young and aged normal-hearing subjects,'' J. Acoust. Soc. Am. **103**, 553–565.

Humes, L. E. (**1996**). ''Speech understanding in the elderly,'' J. Am. Acad. Audiol. **7**, 161–167.

Irwin, R. J., Hinchcliff, L., and Kemp, S. (**1981**). ''Temporal acuity in normal and hearing-impaired listeners,'' Audiology **20**, 234–243.
Irwin, R. J., and McAuley, S. F. (**1987**). ''Relations among temporal acuity, hearing loss, and the perception of speech distorted by noise and reverberation,'' J. Acoust. Soc. Am. **81**, 1557–1565.
Levitt, H. (**1971**). ''Transformed up–down methods in psychoacoustics,'' J. Acoust. Soc. Am. **49**, 467–477.
Long, G. R., and Cullen, J. K. (**1988**). ''Measures of signal processing in persons with sensorineural hearing loss below 6 kHz,'' J. Speech Hear. Res. **31**, 659–669.
Lutman, M. E. (**1991**). ''Degradations in frequency and temporal resolution with age and their impact on speech identification,'' Acta Oto-Laryngol. Suppl. **476**, 120–126.
Moore, B. C. J., and Glasberg, B. R. (**1988**). ''Gap detection with sinusoids and noise in normal, impaired, and electrically stimulated ears,'' J. Acoust. Soc. Am. **83**, 1093–1101.
Moore, B. C. J., Glasberg, B. R., Donaldson, E., McPherson, T., and Plack, C. J. (**1989**). ''Detection of temporal gaps in sinusoids by normally hearing and hearing-impaired subjects,'' J. Acoust. Soc. Am. **85**, 1266–1275.
Moore, B. C. J., and Peters, R. W. (**1997**). ''Detection of increments and decrements in sinusoids as a function of frequency, increment, and decrement duration and pedestal duration,'' J. Acoust. Soc. Am. **102**, 2954–2965.
Moore, B. C. J., Peters, R. W., and Glasberg, B. R. (**1992**). ''Detection of temporal gaps in sinusoids by elderly subjects with and without hearing loss,'' J. Acoust. Soc. Am. **92**, 1923–1932.
Patterson, R. D., Nimmo-Smith, I., Weber, D. L., and Milroy, R. (**1982**). ''The deterioration of hearing with age: Frequency selectivity, the critical ratio, the audiogram, and speech threshold,'' J. Acoust. Soc. Am. **72**, 1788–1803.
Penner, M. J. (**1975**). ''Persistence and integration: Two consequences of a sliding integrator,'' Percept. Psychophys. **18**, 114–120.
Penner, M. J. (**1977**). ''Detection of temporal gaps in noise as a measure of the decay of auditory sensation,'' J. Acoust. Soc. Am. **61**, 552–557.
Phillips, D. P., Taylor, T. L., Hall, S. E., Carr, M. M., and Mossop, J. E. (**1997**). ''Detection of silent intervals between noises activating different perceptual channels: Some properties of ''central'' auditory gap detection,'' J. Acoust. Soc. Am. **101**, 3694–3705.
Pichora-Fuller, M. K. (**1997**). ''Language comprehension in older listeners,'' J. Speech Lang. Pathol. Audiol. **21**, 125–142.
Plomp, R. (**1986**). ''A signal-to-noise ratio model for the speech reception threshold of the hearing impaired,'' J. Speech Hear. Res. **29**, 146–154.
Schneider, B. A. (**1997**). ''Psychoacousitics and aging: Implications for everyday listening,'' J. Speech Lang. Pathol. Audiol. **21**, 111–124.
Schneider, B. A., Pichora-Fuller, M. K., Kowalchuk, D., and Lamb, M. (**1994**). ''Gap detection and the precedence effect in young and old adults,'' J. Acoust. Soc. Am. **95**, 980–991.
Schneider, B. A., Speranza, F., and Pichora-Fuller, M. K. (**1998**). ''Age-related changes in temporal resolution: Envelope and intensity effects,'' Can. J. Exp. Psych. **52**, 184–191.
Snell, K. B. (**1997**). ''Age-related changes in temporal gap detection,'' J. Acoust. Soc. Am. **101**, 2214–2220.
Stuart, A., and Phillips, D. P. (**1996**). ''Word recognition in continuous and interrupted broadband noise by young normal-hearing, older normal hearing, and presbyacusic listeners,'' Ear Hear. **17**, 478–489.
Trehub, S. E., Schneider, B. A., and Henderson, J. L. (**1995**). ''Gap detection in infants, children, and adults,'' J. Acoust. Soc. Am. **98**, 2532–2541.
Tyler, R. S., Summerfield, Q., Wood, E. J., and Fernandes, M. A. (**1982**). ''Psychoacoustic and phonetic temporal processing in normal and hearing-impaired listeners,'' J. Acoust. Soc. Am. **72**, 740–752.
van Rooij, J. C. G. M., and Plomp, R. (**1990**). ''Auditive and cognitive factors in speech perception by elderly listeners. II. Multivariate analyses.'' J. Acoust. Soc. Am. **88**, 2611–2644.
van Rooij, J. C. G. M., and Plomp, R. (**1992**). ''Auditive and cognitive factors in speech perception by elderly listeners. III: Additional data and final discussion,'' J. Acoust. Soc. Am. **91**, 1028–1033.
Westerman, L. A., and Smith, R. L. (**1984**). ''Rapid and short-term adaptation in auditory nerve responses,'' Hearing Res. **15**, 249–260.

Compensation strategies for the perturbation of French [u] using a lip tube. II. Perceptual analysis

Christophe Savariaux[a] and Pascal Perrier
Institut de la Communication Parlée, UPRESA CNRS 5009, INPG and Université Stendhal, Grenoble, France

Jean-Pierre Orliaguet
Laboratoire de Psychologie Expérimentale, UPRESA CNRS 617, Université Pierre Mendès-France, Grenoble, France

Jean-Luc Schwartz
Institut de la Communication Parlée, UPRESA CNRS 5009, INPG and Université Stendhal, Grenoble, France

(Received 10 March 1998; revised 20 November 1998; accepted 29 March 1999)

A perceptual analysis of the French vowel [u] produced by 10 speakers under normal and perturbed conditions (Savariaux *et al.*, 1995) is presented which aims at characterizing in the perceptual domain the task of a speaker for this vowel, and, then, at understanding the strategies developed by the speakers to deal with the lip perturbation. Identification and rating tests showed that the French [u] is perceptually fairly well described in the $[F1,(F2-F0)]$ plane, and that the parameter $(((F2-F0)+F1)/2)$ (all frequencies in bark) provides a good overall correlate of the ''grave'' feature classically used to describe the vowel [u] in all languages. This permitted reanalysis of the behavior of the speakers during the perturbation experiment. Three of them succeed in producing a good [u] in spite of the lip tube, thanks to a combination of limited changes on $F1$ and $(F2-F0)$, but without producing the strong backward movement of the tongue, which would be necessary to keep the $[F1,F2]$ pattern close to the one measured in normal speech. The only speaker who strongly moved his tongue back and maintained $F1$ and $F2$ at low values did not produce a perceptually well-rated [u], but additional tests demonstrate that this gesture allowed him to preserve the most important phonetic features of the French [u], which is primarily a back and rounded vowel. It is concluded that speech production is clearly guided by perceptual requirements, and that the speakers have a good representation of them, even if they are not all able to meet them in perturbed conditions. [S0001-4966(99)01407-1]

PACS numbers: 43.70.Bk, 43.71.Es [WS]

INTRODUCTION

The nature of the phonetic representations of speech in the speaker–listener interaction is crucial for the understanding of speech perception and production processes. As concerns speech perception, the debate is focused on the *invariance* problem: do physical invariants exist that are linked to the invariant phonological input, and, in case they do, where are they hidden in the physical signals? A debate was recently published in the *Journal of the Acoustical Society of America*, which analyzed the role of articulation constraints in the speech perception process (McGowan and Faber, 1996). It confirms that the arguments are essentially about three major hypotheses: (1) invariance is in the acoustical signal, and can be found in ''features determined from the sound through patterns of acoustic properties'' (Stevens, 1996; in relation with his quantal theory of speech perception, Stevens, 1989); (2) invariance is to be found at the articulatory level, and, according to the direct realist theory (Fowler, 1996) or the motor theory of speech perception (Liberman and Mattingly, 1985), ''speech gestures'' are the central objects of speech perception; and (3) there is no invariance, but a given amount of information is provided by acoustical signals ''playing the role of supplementing the multimodal information already in place in the listener's speech processing system'' (Lindblom, 1996; in relation with his theory of adaptive dispersion, Lindblom, 1987).

As concerns speech production, the question is about the representations of speech from the speaker's point of view. It is obviously strongly related to the nature of the perceptual end product, since the speaker must control his vocal apparatus in such a way that listeners correctly perceive the message. However, the question is complicated by the fact that, whatever the physical (acoustical or articulatory) characterization of the task, speakers have degrees of freedom in excess to produce it: various muscle recruitments can underlie the same position of an articulator (Maeda and Honda, 1994; Honda, 1996); various articulator positions, and then various vocal tract shapes, can generate similar acoustical signals (Schroeder, 1967; Mermelstein, 1967; Atal *et al.*, 1978; Maeda, 1990; Boë *et al.*, 1992); various acoustical patterns can be observed for the same phoneme (see Perkell and Klatt, 1986, for a review). Thus, considering speech produc-

[a]Author to whom correspondence should be addressed, at: Institut de la Communication Parlée, 46 avenue Félix Viallet, F-38031 Grenoble Cédex 1, France. Electronic mail: savario@icp.inpg.fr

tion within an ''action–perception'' framework, once the perceptual objective associated with the phonetic input is determined, the challenge is to understand how it is specified in the speaker's mind at the motor and articulatory levels.

This question can be investigated by exploring the plasticity and variability of the vocal-tract geometry for a constant phonemic input. For this aim, a classical paradigm consists of producing variability in a controlled way through perturbation experiments (see, e.g., Abbs and Gracco, 1984; Lindblom *et al.*, 1979). This paper presents the second part of a labial perturbation study of vowel production, which was focused on the vowel [u] (Savariaux *et al.*, 1995). The perturbation experiment was designed in order to (1) know more about the space (articulatory or acoustical) where the speech production task is specified, and (2) observe the strategies adopted by the speakers to reach the intended vowel. The analysis was made both on articulatory and acoustic data and suggested that the goal of speech production is primarily auditory, even if the achievement of this goal by the speaker can be influenced, and possibly prevented, by the use of learned standard articulatory strategies. Since our perturbation paradigm induces speakers to adopt unusual articulatory strategies and then produce unusual acoustical patterns, an additional study is presented here that was carried out to take into consideration perceptual aspects in an attempt to better understand how the production of the vowel [u] is specified. From identification and category-rating experiments, it was thus possible to propose a perceptual description of the speech production task based on a combination of spectral parameters (formants and fundamental frequencies). The compensatory strategies of the speakers were then reanalyzed in relation to both the perceptual and articulatory data.

I. CONTEXT OF THE STUDY

A. A recollection of the initial labial perturbation study

In the labial perturbation study (Savariaux *et al.*, 1995), a 25-mm-diameter tube[1] was inserted between the lips of the speaker; 11 native speakers of French were asked to produce the isolated vowel [u] under this condition. On the basis of acoustical simulations, we demonstrated that compensating for the acoustical changes in the $[F1,F2]$ space induced by the labial perturbation is theoretically possible, by retracting the tongue body towards the pharynx. The experiment was designed to check whether the subjects were actually able to achieve the compensation predicted by the model. In the case of compensation, the question was whether it was immediate or whether the speakers improved the quality of their [u] productions with training.

The acoustical signals together with x-ray pictures were gathered at three successive stages in a single session: (1) without lip tube (N condition); (2) immediately after the tube was inserted between the lips and without any preparation time (PF condition); (3) at the end of a 19-trials adaptation session where the speakers were asked to reproduce the strategy that was, according to their own perceptual sensation, the most efficient one to compensate for the perturbation (PL condition).

Compensatory strategies were first exclusively assessed in the acoustical space by studying the relative differences existing between the $(F1,F2)$ formant patterns produced under the perturbed (PF and PL) conditions and those measured for the normal (N) condition. Compensation was considered to be achieved if and only if the relative formant differences were less than 10%. Further information about the analysis procedure, as well as detailed results, are available in the original paper. The main conclusions of this study can be summarized as follows:

(1) In the PF condition, none of the speakers produced a complete compensation, but seven of them significantly moved their tongue backwards, though not enough. That is, they kept the vocal-tract constriction within the same velopalatal region as in the normal condition, but provided a slight correction movement in the right direction to compensate. However, a complete compensation in the $[F1,F2]$ space would have required moving the constriction location further back into the velopharyngeal region. It was suggested that speakers were using an internal representation of the derivatives of the articulatory-to-acoustical relationships while planning their articulatory movements, before the production of any acoustical speech signal. Thus, most speakers were making the correct gesture; however, they did not immediately get the appropriate amplitude of the correction.

(2) At the end of the adaptation session (PL condition), and for the majority of the speakers, the $(F1,F2)$ pattern was either similar to, or better than the $(F1,F2)$ pattern measured immediately after the insertion of the tube (PF condition). The improvement of the [u] production in the $[F1,F2]$ space during the adaptation session was systematically associated with a backward movement of the tongue. This suggests that listening to the acoustical signal during the adaptation session was helpful to get an improvement of the $(F1,F2)$ patterns under the perturbed condition. However, the improvement is not immediate, and the ability to transform the acoustical information into articulatory changes seems to be highly speaker dependent. This variability can originate from differences in the auditory sensitivity from one speaker to the other or from interspeaker differences that may exist in the description of the articulatory-to-acoustical relationships stored in the internal representation.

(3) For all the speakers but one (speaker OD), the constriction location remained in the velopalatal region even after training. This suggests that an intrinsic prototypical articulatory pattern could have been learned by the speakers during the speech acquisition. From this perspective, the French [u] would be prototypically a velopalatal vowel. This articulatory prototype is likely to influence the choice of the initial articulation, and could then constrain and limit the range of articulatory changes that the speaker would try during the adaptation session.

In conclusion, this study supports the view of a control of speech production guided by both auditory requirements in the distal space, and articulatory prototypes providing anchor points of the auditory task in the proximal articulatory

space. Therefore, the perturbation leads to a contradiction between the auditory and the learned articulatory goals. The speakers attempt to eliminate this contradiction through the use of local articulatory-to-acoustical knowledge, at the expense of a large intersubject variability.

However, the assessment of the phonetic goal—the production of vowel [u]—was limited to the observation of $F1$ and $F2$ changes. Hence, one may have missed some other more elaborate perceptual aspects that could have influenced the way the subjects tried to compensate for the perturbation. Indeed, experimental data have shown that, in some cases, vowels could be correctly perceived in spite of a noncanonical formant pattern (see, for instance, the notion of ''perceptive mirage'' as introduced by Fowler, 1990). It is thus legitimate to suspect that a number of secondary, or more complex, parameters could also intervene in the perceptual description of vowel [u] (see Sec. I B for a theoretical overview). Therefore, a perceptual assessment of the vowels produced under perturbed vs normal conditions appeared to be necessary to check whether or not the perceptual goal—i.e., a sound that is perceived as a French [u]—had been realized by each speaker. This is the basic rationale of the present paper.

In addition, the perceptual study of perturbed vowel production has another strong interest. Indeed, the perturbation paradigm leads to the production of a set of speech stimuli that have three important features. They are *controlled*, because they correspond to a constant and well-identified phonetic goal; they are *ecological*, because they are natural stimuli, produced by human speakers; they are *atypical*, because they are uttered in a perturbation paradigm that drives the system towards its limits. Hence, this set of acoustical stimuli provides a relevant experimental corpus to know more about the acceptable perceptual space for the French vowel [u].

B. Questions about the perceptual template for [u]

The nature of the determinants of a vowel category is an old and partially unsolved problem, and research developments in the last 30 years have been essentially focused on four major issues. First, the role of formants seems to be basic (see, e.g., Carlson *et al.*, 1979; Lublinskaya *et al.*, 1980; Klatt, 1982), though the entire spectral pattern might also play a role (Bladon, 1982; Beddor and Hawkins, 1990) which has to be better understood. Second, the role of time-varying features is not yet clarified and stays a hot topic in recent debates (see, e.g., Strange, 1989; Bohn and Strange, 1995; Nearey, 1989, 1995). Third, the old suggestion by Potter and Steinberg (1950) that the relative pattern of stimulation along the basilar membrane could determine the percept led to the proposal of various tonotopical distances involving both formant and fundamental frequencies in order to deal with intersex and interspeaker normalization (e.g., Traunmüller, 1981; Syrdal and Gopal, 1986). At last, the works about $F'2$ (Carlson *et al.*, 1970; Bladon and Fant, 1978) and the center of gravity effect (Chistovich *et al.*, 1979; Schwartz and Escudier, 1989) have initiated several studies about the existence of integrated perceptual formants in case of formant proximity. Concerning more specifically the vowel [u], which is a high back-rounded vowel, it is necessary to maintain, in French, two basic features. These features are *height* (to distinguish it from the mid-high back-rounded vowel [o]) and *backness* (to distinguish it from the high front-rounded vowel [y]). To determine the perceptual correlates of each of these features, a number of proposals have been made in the literature.

First, a low $F1$ value is classically considered as the major correlate of the ''high'' feature. A number of researchers have introduced the fundamental frequency $F0$ as a normalizing parameter to deal with interspeaker variability. Traunmüller (1981) suggested that the tonotopic distance $(F1-F0)$ in bark could be the best correlate of vowel openness. However, it seems that the role of $F0$ could have been overemphasized in this formula, especially for low $F1$ values (Traunmüller, 1981; Di Benedetto, 1987). Data published by Hoemeke and Diehl (1994) for front vowels and Fahey *et al.* (1996) for back vowels lead to a complex pattern in which neither $F1$ nor $(F1-F0)$ can systematically be said to be the best correlate of the openness feature. Traunmüller (1991) even noticed that there seems to exist a large intersubject variability in the perceptual use of $F0$ for height estimation. Also relevant for [u] is the ''center of gravity effect'' introduced by Chistovich *et al.* (1979). Indeed, their data suggest that in the region of the vowel space where $F1$ and $F2$ are close together, an integrated value such as $(F1+F2)/2$ (all frequencies in bark) could be the best correlate of the vowel quality, and specifically of the contrast between the high vowel [u] and the mid-high vowel [o]. However, other data on the perceptual parameters characterizing back vowels suggest that, though an integrated value between $F1$ and $F2$ is perceptually relevant, the center of gravity seems to rely more on $F1$ than on $F2$, at least for [u] and [o] (Delattre *et al.*, 1952; Beddor and Hawkins, 1990).

Second, a low $F2$ value is classically considered to be the major correlate of the back-rounded series. To deal with interspeaker variability, $F0$ can be once more introduced as a normalizing factor. In this vein, Fant *et al.* (1974) and Mantakas (1989) provided data supporting the role of $(F2-F0)$ or $(F'2-F0)$ as a correlate of the rounding contrast in high front vowels. Hirahara and Kato (1992) support the same kind of hypothesis: the use of the tonotopic distance $(F2-F0)$ to separate in Japanese high front vs high back vowels. Other tonotopic distances between adjacent peaks (i.e., $F0$,$F1$,$F2$,$F3$) were also considered. Traunmüller (1985) suggested that $(F2-F1)$ in bark could be an important determinant of vowel quality, the more so when $(F2-F1)$ is small, which is the case for back-rounded vowels. The tonotopic distance $(F3-F2)$ in bark is proposed by Syrdal and Gopal (1986) to be a good correlate of the front–back contrast in American English. However, it is generally admitted that $F3$ does not have enough intensity to influence the quality of back vowels. This statement is indirectly confirmed by old data published by Delattre *et al.* (1952) on the perception of two-formants synthetic stimuli including various modifications of the level of either $F1$ or $F2$. Their data show that for all front vowels, a decrease of the $F2$ intensity below a given threshold leads to the perception of a back-rounded vowel. Hence, it seems clear that a basic perceptual

correlate of the ''front'' feature is the presence of a minimum amount of energy in the high-frequency region of the speech spectrum; that is, above 1.5 kHz. As concerns backrounded vowels, the ($F1$,$F2$,$F3$) typical pattern depicts a strong ($F1$,$F2$) prominence in the low-frequency region, while the intensity of $F3$ (and also of higher formants) is quite weak.

Finally, it is important to notice that the previous discussion is centered on the definition of *boundaries* for vowel categories, while a large amount of literature has been recently concerned with the issue of prototypes vs boundaries. In this framework, it has been suggested that a vowel category is associated with a nonhomogeneous domain in the vowel space. Thus, there seems to exist for each category a ''prototype'' that would be an anchor point around which stimuli, at the same time, receive the best ''quality scores'' in the identification process (Grieser and Kuhl, 1989), are identified quicker (Sussman, 1993), produce more effect in adaptation paradigms (Samuel, 1982; Miller *et al.*, 1983; Perkell *et al.*, 1993), and are stronger competitors in dichotic listening experiments (Miller, 1977). A recent series of discrimination experiments led Kuhl (1991, 1995) to introduce the concept of a ''magnet effect'' accounting for the better generalization ability around prototypes.

C. Experimental setup

The previous sections lead us to define our strategy in the following way. Considering that we have a set of controlled, ecological, and atypical stimuli providing a corpus around the French vowel [u], the corpus was examined with respect to two major questions:

(1) What is the perceptual requirement for a [u] in French?
(2) How is this requirement used by the speakers to compensate for the labial perturbation?

Given these aims, two kinds of perceptual tests were designed. First, experiment 1 focused on vowel *identification*, to assess how normal and perturbed stimuli were categorized. Second, experiment 2 focused on vowel *quality rating*, to know more about speakers' strategies in perturbed speaking conditions, as well as about the role of categories vs prototypes in the elaboration of the strategies. *A posteriori* considerations on the obtained results led us to set up a third series of experiments focused on the comparison, for selected speakers, of the identifications of the PF and PL stimuli, in order to know more about the strategy of the speakers during the adaptation session.

In this study, perceptual performance was related to the acoustical parameters that were proposed as potential correlates of vowel quality for the vowel [u]. We considered five representations in the acoustical domain: the [$F1$,$F2$] space, that indirectly provides an insight of the ($F2-F1$) and ($F1+F2$)/2 parameters; the [($F1-F0$),($F2-F0$)] and [$F1$,($F2-F0$)] spaces to assess the normalizing role of the fundamental frequency $F0$ (see Sec. I B); and finally, the [$F2$,($I1-I2$)] and [$F3$,($I1-I3$)] spaces where $I1$, $I2$, and $I3$ are, respectively, the intensities in dBs of $F1$, $F2$, and $F3$, to assess the perceptual influence of the spectrum decay and, especially, of the emergence of a high-frequency peak (all frequencies in bark).

II. EXPERIMENT 1: IDENTIFICATION TEST

A. Method

1. Subjects

In the first experiment, 17 adult listeners (14 males and 3 females), native speakers of French, served as subjects. They ranged from 19 to 46 years of age, with a mean of 26 years old. The majority of them was students at our lab, the Institut de la Communication Parlée, and all were free from speech and/or language disorders. Some of them had a basic education in phonetics. In addition, the listeners performed a control test in order to check their auditory performance and to ensure that they understood the procedure. The control test consisted of identifying seven French vowels [i, a, o, ɔ, œ, y, u] recorded, under normal conditions, by a native speaker of French, who was not a subject in the lip tube experiment. Each listener was a volunteer for the perception test and none of them had served as a subject in the lip tube experiment, nor knew the goal of the experiment.

2. Corpus

The corpus consisted of two utterances of seven vowels, namely the utterances of [u] under the N and the PL condition, plus six additional vowels included in the corpus to satisfy two requirements:

(1) To give, for each speaker, information about the maximal vowel space in the [$F1$,$F2$] plane; hence, vowels [i] and [a] were selected.
(2) To describe with enough accuracy the region located around the vowel [u] in the [$F1$,$F2$] plane; hence, vowels [o, ɔ, œ, y] were chosen.

The corpus was produced by ten of the 11 speakers[2] of the lip tube experiment. As concerns vowel [u], the sounds recorded in the x-ray room under the N (normal) and the PL (perturbed) condition were selected. The six additional vowels were recorded specifically for the perceptual tests, in a sound-treated room, around 18 months after the first experimental session, under two conditions: one normal, and one immediately after the insertion of the 25-mm-diameter tube between the speaker's lips (condition similar to the PF condition for vowel [u]). It should be noted that recording conditions (stimulus loudness and background noise) were similar for [u] and for the additional vowels, and seem indistinguishable according to the subjects. All stimuli (14 stimuli per speaker, 10 speakers) were truncated to 400 ms. The sound level was set at a comfortable level (around 55 dB SPL).

3. Procedure

The test was conducted with the EUROPEC software developed at the Institut de la Communication Parlée (Zeiliger and Sérignat, 1991). The subjects were seated in a sound-treated room. The stimuli were presented binaurally through a high-quality headphone. The experimental procedure was as follows: the subject listened to a stimulus while watching

the computer monitor, on which the list of possible responses was displayed; he/she then selected and validated his/her choice with the mouse, without any possibility of hearing the stimulus again. The next stimulus was then automatically sent to the headphone 2 s afterwards. The list of possible choices consisted of the seven vowels of the corpus, written in graphemes, and illustrated by an example of a French word such as: ''au'' (/o/) like in the word ''beau,'' ''i'' (/i/) like in ''lit,'' ''ou'' (/u/) like in ''pou,'' ''e'' (/œ/) like in ''peur,'' ''o'' (/ɔ/) like in ''port,'' ''u'' (/y/) like in ''rue,'' and ''a'' (/a/) like in ''pas.'' The phonetic characters were not displayed, because most of the listeners were not used to this kind of notation. All listeners completed the test of 140 stimuli, blocked by speaker: for each speaker, the 14 stimuli were randomly put into a sound file, and the order of presentation of the ten files associated to the ten speakers was randomly determined. Each subject listened only once to the whole set of stimuli. Notice that the identification task was not easy for mid-open vowels, which do not appear generally in isolation in French: this is typically the case for /ɔ/, which exists only in closed syllables. This could have somehow biased the corresponding identification scores, as will be seen later.

4. Acoustical parameters

The acoustical signals were processed by a 16-coefficients-LPC analysis (window length: 20 ms; window overlap: 10 ms). Frequency and intensity of the first three formants were extracted along the whole signal duration (400 ms), and the mean values were calculated. Fundamental frequency was measured through a zero-crossing algorithm, and the mean value was calculated across the whole signal duration. Frequencies were then converted into a perceptual bark scale according to the Hertz-to-bark transformation (Schroeder *et al.*, 1979)

$$F_{\text{bark}} = 7 \cdot \text{asinh}(F_{\text{Hz}}/650).$$

B. Results

1. Identification of vowels produced under normal conditions

A preliminary study consisted of the assessment of the experimental procedure, as well as of the capability of each listener to identify vowels. In this aim, it was checked whether the vowels produced in normal conditions were correctly classified.

The majority of vowels (5 among 7) was well identified (16 or 17 correct identifications). Two vowels were not well identified, namely the tokens [o] (score ranging from 11 through 17; most confusions with [ɔ]) and [ɔ] (score ranging from 4 through 15, most confusions with [a]). This must be related to the special status of /ɔ/ in French (see our remark in Sec. II A 3) and to the difficulty to differentiate in isolation [ɔ] from [a]. Altogether, these results show that all listeners were able to perfectly identify [u], and to discriminate it from neighbor categories.

TABLE I. Number of correct identifications of the vowel [u] produced under normal (N) and perturbed (PL) conditions by each of the ten speakers. In case of wrong identifications, the incorrect answers provided are written in parentheses, together with the number of listeners who made this choice.

Speakers	N condition	PL condition
BC	17	16 ([o]:1)
CH	17	17
GA	17	17
JY	17	0 ([œ]:17)
LJ	16 ([o]:1)	1 ([o]:13; [ɔ]:3)
LR	17	17
ML	17	1 ([œ]:16)
MP	17	17
OD	17	17
YP	17	17

2. Identification of the stimuli under normal versus perturbed conditions

The identification scores obtained for the vowel [u], pronounced by each of the ten speakers under the N and the PL condition, are given in Table I. The most remarkable result was observed in the PL condition: for seven speakers (BC, CH, GA, LR, MP, OD, and YP) the vowel [u] was perfectly well identified by all listeners, with 16 or 17 correct identifications. It should be recalled that the acoustical analysis carried out in Savariaux *et al.* (1995) led to the conclusion that only one speaker was able to completely compensate for the perturbation, based on a 10 % deviation criterion for $F1$ and $F2$ values.

The discrepancy between the conclusions brought up by the identification test and the acoustical analysis demonstrates that our 10 % deviation criterion on $F1$ and $F2$ was not able to accurately predict perceptual category constancy. Consequently, as a first attempt to characterize the perceptual objective of the speaking task, it was interesting to search for the outlines of the perceptual category of the isolated vowel [u], within an acoustical representation including $F0$, formant frequencies, and formant amplitudes.

3. Relation between identification scores and spectral parameters

No simple linear relation could be found between the frequencies of formants $F1$ and $F2$ or their deviations from the normal values, and the identifications provided by the listeners. However, as emphasized by Fig. 1(A), in which all stimuli are plotted in the $[F1,F2]$ plane, a separation can be found in the acoustical space between well-identified and badly identified vowels [u]. To take the normalizing parameter $F0$ into consideration (see Sec. I B), additional representations were made of the distributions of the stimuli in the $[(F1-F0),(F2-F0)]$ and $[F1,(F2-F0)]$ planes [see, respectively, Fig. 1(B) and (C)]. While the distinction between ''good'' and ''bad'' exemplars is quite the same in the $[F1,F2]$ and $[F1,(F2-F0)]$ planes, it seems poorer in the $[(F1-F0),(F2-F0)]$ plane. Hence, in relation to the debate about the normalizing role of $F0$ onto $F1$ (see Sec. I B),

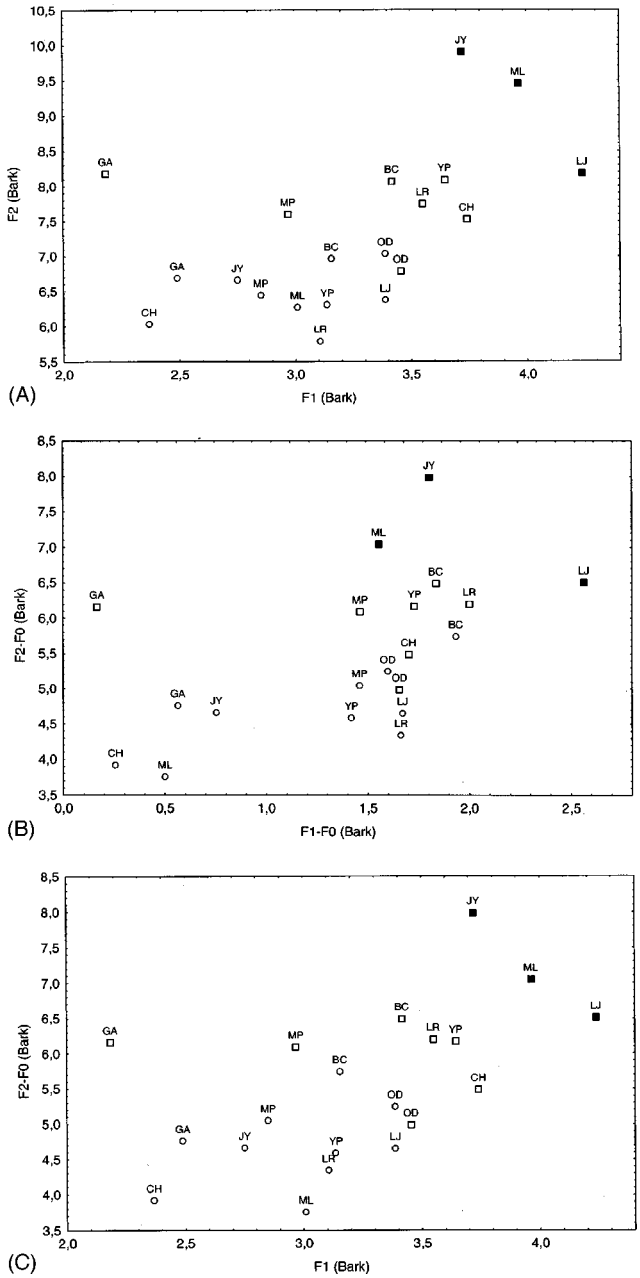

FIG. 1. (A) Distribution of all stimuli in the $[F1,F2]$ plane. Circles correspond to stimuli produced under normal (N) condition and squares to those produced under perturbed (PL) condition. The badly identified stimuli are displayed by filled boxes. (B) Same display for the distribution of all stimuli in the $[F1-F0,F2-F0]$ plane. (C) Same display for the distribution of all stimuli in the $[F1,F2-F0]$ plane.

the present data rather support Traunmüller's observation (1981) that for low $F1$-values, the tonotopic distance $(F1-F0)$ is not a good correlate of the perceptual categorization. Together, this figure shows that for high values of $F1$ and $(F2-F0)$ (above 4 bark for $F1$; above 7 bark for $F2-F0$), the vowel was not perceived as a [u] anymore. This suggests the existence of threshold values for $F1$ and for $F2$ or $(F2-F0)$. Beyond these thresholds, the perception changes from [u] to [o], when $F1$ increases (speaker LJ), and from [u] to [œ], when $F2$ increases (speakers JY and ML). Hence, these thresholds seem to provide a basic specification of category boundaries for the vowel [u] in French.

C. Discussion

The results of experiment 1 showed that under the PL condition, seven among the ten speakers (OD, MP, BC, GA, CH, LR, and YP) were able to keep their [u] within the appropriate category. This observation suggests that the perturbation induced by the lip tube could have been much less disturbing than was originally presumed from the acoustical theory. On the other hand, as we discussed in Sec. I B, the perceptual space is not homogeneous within a given category, some realizations of a phoneme being possibly ''better'' than others. In this perspective, it is logical to study whether speakers are inclined, and able, to organize their articulation in order to produce a sound close to the best representative of the category. Such a hypothesis is coherent with the concept proposed by Lindblom (1996), that speakers are able to control the amount of information necessary for the listeners. In the same vein, Perkell *et al.* (1993, 1998) also observed experimental evidences of motor-equivalence strategies that are supporting the idea of a speech-production control that takes into account the heterogeneity of the perceptual space in a given phonetic category.

Hence, the purpose of experiment 2 was to study the prototypicality of the perturbed stimuli by determining how listeners rated vowel quality within the category [u].

III. EXPERIMENT 2: RATING TASK

A. Method

1. Subjects

In this experiment, 18 adult listeners, 14 males and 4 females, served as subjects. Among them, 16 had participated in the first perceptual test. They had no evidence of any auditory or perceptual trouble. They ranged from 19 to 46 years of age, with a mean of 26.8 years. As in the first experiment, the subjects were volunteers, and did not know the underlying objectives of the study.

2. Stimuli

The vowel [u] produced by the ten speakers during the lip tube experiment under the N and the PL condition served as stimuli. Thus, a total of 20 stimuli of 400-ms duration were presented to the listeners. The two stimuli from the same speaker were presented in sequence, the [u] produced under the N condition being systematically followed by the [u] produced under the PL condition. This order of presentation was chosen in order to make the listener implicitly compare the perturbed realization with the natural preceding one, then giving the natural utterances the status of reference. Thus, the corpus consisted of ten sets of two stimuli. The sets were randomly stored in sound files, and five files were created in order to have five rating estimations per stimuli for each listener. The listeners did not know about the way the stimuli were stored and presented.

3. Procedure

The rating test was conducted 1 month after the identification test. The listeners were instructed that they would hear various pronunciations of the vowel [u], and that they

TABLE II. Mean values and standard deviations (in parentheses) of the ratings provided by 18 listeners for the vowel [u] produced under normal (N) and perturbed (PL) conditions by each of the ten speakers; F test for the ''condition'' factor: * for $p<0.05$; ** for $p<0.01$.

Speakers	N condition	PL condition
BC	5.1	2.8
	(1.4)	(0.6)
		**
CH	5.7	5.8
	(0.7)	(0.7)
GA	6.1	5.8
	(0.8)	(0.8)
JY	6.2	1.2
	(0.8)	(0.4)
		**
LJ	5	1.7
	(1.4)	(0.6)
		**
LR	5.2	3.7
	(1.0)	(0.8)
		**
ML	6	1.2
	(0.7)	(0.4)
		**
MP	5.6	5.2
	(0.9)	(0.6)
		*
OD	6.7	3.7
	(0.4)	(1.2)
		**
YP	5.2	3.8
	(1.4)	(1.1)
		**

would have to evaluate the quality of the sound within this category. A 1-to-7 rating scale was presented to the listeners, with the following explanations: the rating ''1'' should correspond to ''a bad vowel [u], that is not representative of the perceptual category of the natural vowel,'' while the rating ''7'' should be given to a sound that is perceptually ''a very good vowel [u], i.e., a canonical representative of the natural vowel.'' No specific instructions were provided about the intermediate levels 2 to 6. The order of presentation of the five sound files was randomly determined for each listener. The analysis of the signals was based on the same spectral parameters as in Sec. II A 4.

B. Results

1. Perceptual scores

The average ratings of the 90 occurrences (18 listeners, five ratings per listener) of the vowel [u] produced under the N and the PL condition are presented in Table II for each speaker separately. These average values were computed as follows: first, mean values and variances of the five ratings were calculated for each stimulus and each listener; second, for each stimulus, averages of the means and variances were computed and are provided in Table II.

A two way analysis of variance (ANOVA) [condition (2)$\times$speaker (10)] with repeated measures of both factors revealed a main effect of the ''speaker'' factor [$F(9,153)=41.9$; $p<0.01$]. Therefore, the large variability of the mean values observed, even in the N condition, among speakers is statistically significant. However, it appears that the global average ratings of the vowels recorded under the N condition were always higher than or equal to 5, whomever the speaker. Hence, a perceptually good [u] is taken to correspond to a global average rating of 5 or higher.

The ANOVA also revealed a noticeable effect of the ''condition'' factor [$F(1,17)=266.7$; $p<0.01$] as well as an interaction between the condition and speaker factors [$F(9,153)=55.3$; $p<0.01$]. In addition, it was observed that, except for speaker CH, the mean value in the N condition was systematically larger than in the PL condition, but that the extent of the difference was speaker dependent. A simple effect analysis shows that these differences were significant for eight of the ten speakers. However, for one of these eight speakers (MP), the average ratings were larger than 5 for both conditions. Hence, his vowel [u] produced under perturbed condition was still a perceptually good vowel. Altogether, for speakers CH, GA, and MP, the vowel [u] produced under the perturbed condition after the adaptation session was rated a good instance of [u].

These results suggest that three speakers among ten were able to completely compensate for the lip perturbation. Very surprisingly, speaker OD, who produced very similar [$F1$,($F2-F0$)] patterns in both conditions, did not belong to this set of three speakers, while his vowel [u] produced under normal conditions obtained a very good rating (6.7). This will be discussed later.

2. Acoustical correlates of perceptual ratings

A study of the correlation between spectral parameters and ratings was then performed. The spectral parameters under consideration were the following: (1) the raw parameters $F0$, $F1$, and $F2$ (in bark); (2) the distances ($F1-F0$), ($F2-F0$) to account for the normalizing effect of $F0$ (in bark); (3) the average value ((($F2-F0$)+$F1$)/2) to account for a center of gravity effect (in bark). First, all occurrences of the vowel [u] produced under the N and the PL conditions were taken into consideration. As could be expected from the literature about the perception of vowel [u] (see Sec. I B), $F2(r=0.77)$, ($F2-F0$)($r=0.78$), $F1(r=0.71)$ and ($F1-F0$)($r=0.59$) were all correlated significantly with the rating values. More specifically, the high correlation observed for the parameter ((($F2-F0$)+$F1$)/2)($r=0.83$) supports Chistovich *et al.*'s (1979) hypothesis of the center of gravity effect in the perception of the vowel [u]. Only the parameter $F0$ was not significantly correlated with the rating values.

In a second stage, the stimuli produced under the N and the PL conditions were analyzed separately. Within the class of the stimuli produced under the N condition, no significant correlation was observed, as could be expected from the very little variations of the spectral parameters observed across speakers for that condition. On the opposite, within the class associated with the PL condition all parameters except $F0$ were significantly correlated with the rating values. These observations are coherent with the hypothesis of the *nonhomogeneity* of the acoustical vowel space (see Sec. I B), and of the existence of a ''*prototypical*'' region where small spectral changes do not affect the good quality of the vowel.

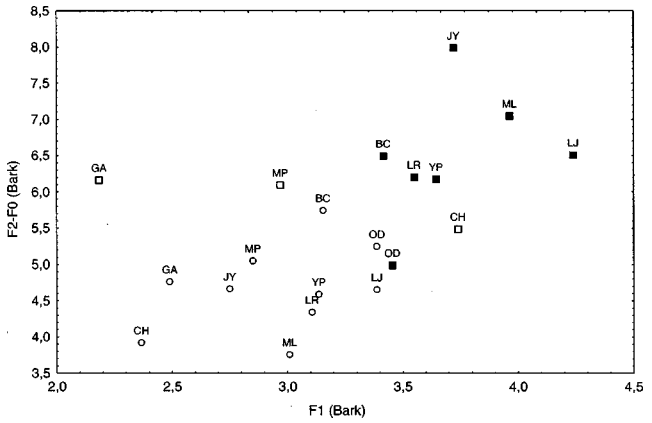

FIG. 2. Distribution of all stimuli in the $[F1,F2-F0]$ plane. Circles correspond to stimuli produced under normal (N) condition and squares to those produced under perturbed (PL) condition. The stimuli which are rated at a mean value smaller than 5 (not a good [u]) are displayed by filled boxes.

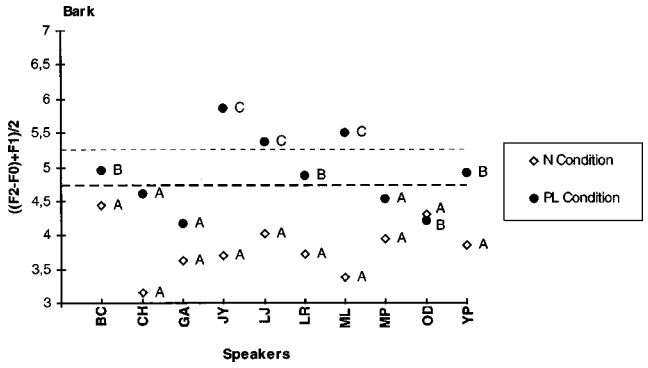

FIG. 3. Distribution of stimuli, produced by each speaker, under normal (N) and perturbed (PL) conditions along the $((F2-F0)+F1)/2$ axis. *A* = good [u]; *B* = poor [u]; *C* = not a [u].

Outside this region, spectral changes should modify the quality, and even its identification, when changes are going beyond the thresholds that were found in Sec. II B 3 to delimit the perceptual category of the vowel [u]. Hence, for the set of stimuli produced under the PL condition, significant correlations were observed for $F1(r=0.68)$, $(F1-F0)(r=0.57)$, $F2(r=0.67)$ and $(F2-F0)(r=0.69)$.

In Fig. 2, the repartition of the stimuli is displayed, as in Fig. 1(C), in the $[F1,(F2-F0)]$ plane in relation with their average rating. In this figure, it can be observed that:

(1) For all stimuli that obtained an average rating greater than 5, $(F2-F0)$ is essentially smaller than 6 bark, except when $F1$ is very low (less than 3 bark) as suggested by speakers MP and GA. An exception is provided by the stimulus produced by speaker OD under the PL condition, which is included in this region of the plane, in spite of its low, average rating (3.7). An analysis of this specific case is proposed below (Sec. IV B).
(2) If $(F2-F0)$ is higher than 7 bark or if $F1$ is higher than 4 bark, the average rating is smaller than 2. This is in line with the results of experiment 1, where it was shown that the vowels located in this region of the $[F1,(F2-F0)]$ plane were not identified as a vowel [u].
(3) If $F2$ is between 6 and 7 bark, and if $F1$ is between 3 and 4 bark, the stimuli are perceived as a vowel [u], but their quality is far from prototypical, since they were rated at a level located between 3 and 5.

Thus, it seems that to achieve a perceptually good [u], the speakers should try to keep the middle point between $F1$ and $(F2-F0)$, below a certain value. This is summarized in Fig. 3, where the frequency $(((F2-F0)+F1)/2)$ is plotted speaker by speaker, in the N and the PL conditions. In this figure, each stimulus is labeled according to the following code: (1) *A* corresponds to the sounds that were rated as a good [u] (score$\geqslant$5); (2) *B* corresponds to the sounds that were clearly identified as a vowel [u] but were not rated as good ($3\leqslant$score<5); (3) *C* corresponds to the sounds that were not clearly identified as [u] (in experiment 1) and obtained rating scores $\leqslant 2$ (in experiment 2).

It can be noted that, except for speaker OD in the PL condition, all the stimuli associated with the *A* label are below the stimuli with a *B* label, and that all the stimuli with a *C* label are on the top of Fig. 3. The shift from category *A* to category *B* happens somewhere around 4.75 bark, and the shift from category *B* to category *C* around 5.25 bark. This explains the very significant correlation between $(((F2-F0)+F1)/2)$ and the rating value, and confirms that this center of gravity of $F1$ and $(F2-F0)$ is helpful in linking acoustical parameters and perceptual effects for French [u].

Notice that, while $F2$ and $(F2-F0)$ produced more-or-less equal performances in the contrast of [u] and non-[u] in experiment 1, $F2$ appears here less efficient than $(F2-F0)$ in experiment 2. Indeed, the positions of ''bad-[u]'' stimuli produced by speakers BC, LR, and YP in the PL condition are better separated from other ''good-[u]'' stimuli in Fig. 1(C) than in Fig. 1(A).

It is now possible to understand what kinds of strategy could have underlain the articulatory changes provided by the ten speakers, including speaker OD, during the lip tube experiment.

C. Analysis of the compensatory strategies observed during the perturbation experiment

1. Compensation by a combined effect of F0, F1, and F2

Experiment 2 demonstrates that, from a perceptual point of view, speakers CH, MP, and GA were able to compensate for the perturbation. However, articulatory data showed that they did not provide the expected strong reorganization of their vocal-tract geometry, and acoustical measurements confirmed that they did not completely compensate for the large increase of $F2$ induced by the perturbation. From the above analysis of the acoustical correlates of the perceptual ratings, it can be concluded that these speakers were successful, in spite of the lip tube, because they could make the best use of the latitude offered by the variety of $(F0,F1,F2)$ combinations that are associated with the desired perceptual effect. The observation of the articulatory configurations measured for these speakers under the perturbed condition reveals two main tendencies for the compensatory strategies.

Speaker CH moved the tongue back slightly, but not enough to bring $F2$ back to its normal value (7.53 vs 6.03

bark); the constriction remained located in the velopalatal part of the vocal tract. However, a larger movement amplitude was not necessary, because this speaker had a relatively high $F0$ (higher than 2 bark, even in the normal condition), making a slight back movement of the tongue sufficient to keep the $(F2-F0)$ parameter smaller than the 6 bark threshold, and to maintain the $(((F2-F0)+F1)/2)$ parameter at a low value. Note (Fig. 3) that in the normal condition, this speaker had the lowest value of the $(((F2-F0)+F1)/2)$ parameter, way below the border area around 4.75 bark. Hence, the increase of $F2$ induced by the lip tube probably had less influence on the perception of his vowel [u] than for other speakers. Consequently, a large tongue gesture was not necessary to ensure a compensation. This observation suggests that, depending upon speaker-specific properties of the vocal source, the impediment induced by the lip perturbation could have been very different among speakers.

The strategy adopted by speaker GA seems to have been quite different. Similarly to speaker CH, backward tongue movement under the PL condition was not large enough to significantly reduce the increase of $F2$ (8.1 vs 6.69 bark). However, contrary to speaker CH, the initial $F0$ value was not very high. Hence, in spite of a small $F0$ increase, the $(F2-F0)$ parameter was still higher than the 6 bark threshold. Therefore, the good rating of the vowel [u] that he pronounced under the PL condition can only be explained by the low value of $F1$ (2.18 bark). Indeed, $F1$ noticeably decreased from the normal production (2.49 bark) to the perturbed one, and it should be noted that the corresponding value of $F1$ was the lowest one observed among all speakers. This is a consequence of the movement of the tongue, since this movement caused a backward lengthening of the vocal tract constriction, that became essentially twice as long in the PL condition as in the N condition, while keeping a similar cross-sectional area. The low $F1$ value ensured that the $(((F2-F0)+F1)/2)$ parameter remained low enough, and the perceptual objective was reached.

Speaker MP presents some similarities to speaker GA. His backward tongue-movement amplitude was too small, and the resulting $F2$ value was still much too high (7.6 bark in the PL condition vs 6.44 bark in the N condition). In spite of a small increase of $F0$, the $F2-F0$ value was still higher than the 6 bark threshold. Due to the tongue movement, the vocal-tract constriction became much larger. However, contrary to the case of speaker GA, this enlargement did not induce a decrease of $F1$. This can be explained by the observation that, for speaker MP, the cross-sectional area of the constriction slightly increased as the tongue moved backward. Nevertheless, the low initial $F1$ value in the N condition led to an $F1$ value in the PL condition lower than 3 bark. This low $F1$ value, superimposed to the limited increase of $(F2-F0)$, might explain why speaker MP achieved the desired perceptual effect in spite of the lip perturbation.

The other speakers, except speaker OD, did not fully compensate, either in the acoustical domain or from a perceptual point of view. However, it is interesting to notice the large $F0$ increase observed for speaker BC (almost 0.4 bark), and, to a certain extent, for speakers YP (0.2 bark) and LR (0.11 bark). For these three subjects, the vowel was identified as a [u]. This suggests that an $F0$ increase may have helped to enhance the quality of the vowel [u] in the presence of the lip tube perturbation. It should be noted that the trend to increase $F0$ in the perturbed condition was not general: in fact, $F0$ decreased from N to PL for four speakers, and the average value for the whole set of speakers increased only slightly, from 1.78 bark in the N condition to 1.84 bark in the PL condition.

The case of speaker OD appears very specific. Indeed, the compensation was obvious in the articulatory domain, with a large backward tongue movement, and it had clear consequences in the acoustical domain: the stimuli recorded under the N and the PL conditions were almost superimposed in the $[F1,(F2-F0)]$ plane (Fig. 3). However, experiment 2 demonstrates that the stimulus recorded under the N condition clearly belonged to the prototypical region of vowel [u], while the one recorded under the PL condition was perceptually quite unsatisfactory. Hence, the interpretation of speaker OD's compensatory strategy requires us to consider spectral parameters other than $F1$ and $(F2-F0)$.

2. How to interpret the backward movement of the tongue produced by speaker OD

In a complementary study, $F3$ frequency, together with the intensities $I1$, $I2$, and $I3$ of formants $F1$, $F2$, and $F3$ respectively, was analyzed. In order to take into account the possible variation of the global energy of the signal from one condition to the next, the formant intensities were normalized in relation to $F1$ intensity. The differences $(I1-I2)$ and $(I1-I3)$ were then considered.

Figures 4(A) and (B) plot the stimuli of all speakers in the $[(F2-F0),(I1-I2)]$, and $[F3,(I1-I3)]$ planes, respectively. Both the intensity parameters and the $F3$ frequency offer a means of distinguishing between OD's stimuli under the N and the PL condition. The clearest distinction between these stimuli can be observed along the $(I1-I2)$ axis: under the perturbed condition, the relative intensity of $F2$ was smaller. This phenomenon was observed in general within the whole set of speakers, but it was especially clear for speaker OD, since his perturbed production of vowel [u] had the highest $(I1-I2)$ value. The $(I1-I3)$ parameter also distinguishes between OD's normal and perturbed stimuli. However, such a distinction does not correspond to a general trend among all speakers. Hence, the perceptual effect of this parameter is not clear. Globally, there is some trend in Fig. 4(B) that well-rated stimuli correspond somewhat with low $F3$ and $I3$ values. However, this trend is weak: the well-rated stimuli produced by speakers CH and MP under the PL condition had high $F3$ frequencies, similar to the one measured for OD, with higher relative amplitude.

To assess, for speaker OD, the third formant role in the perception of vowel [u], a simple perceptual test was performed. The spectra of his stimuli recorded under the N and the PL condition were low-pass filtered to the range [0–1500 Hz] with a Chebyshev filter. Thus, the potential role of $F3$ in the perception was discarded. For the test, the corpus consisted of four stimuli (two nonfiltered and two filtered); 14 among the 18 listeners, who had participated in the previous

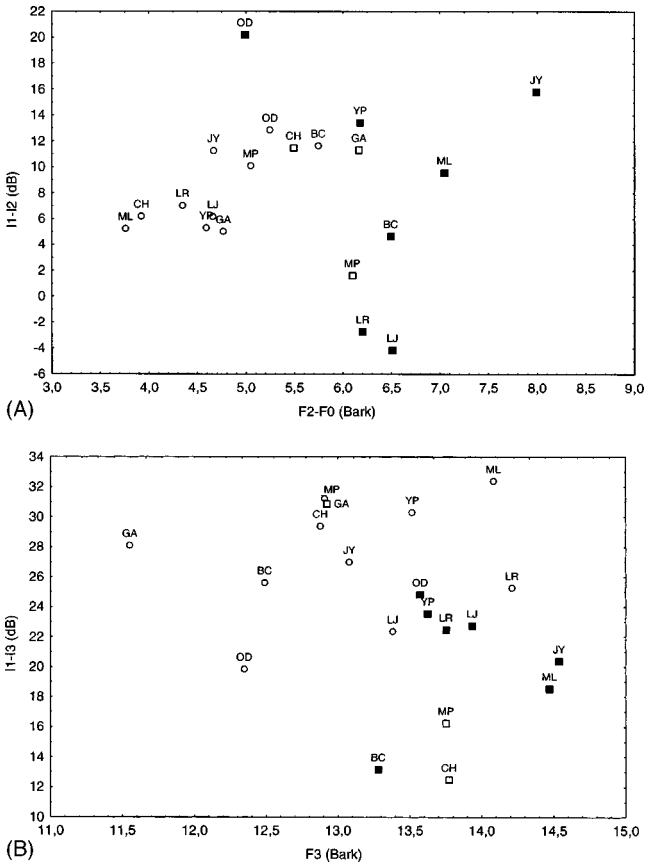

FIG. 4. (A) Distribution of all stimuli in the $[F2-F0,I1-I2]$ plane. Same display as Fig. 2. (B) Distribution of all stimuli in the $[F3,I1-I3]$ plane. Same display as Fig. 2.

rating test, served as subjects. The rating scale consisted of four levels: ''This is not the vowel [u],'' ''This is the vowel [u] with poor quality,'' ''This is the vowel [u] with good quality,'' and ''This is the vowel [u] with very good quality.'' It appeared *a posteriori* that the distinction between the last two categories was not completely clear to the listeners. Hence, we merged them in the analysis.

The results showed that the perturbed stimulus obtained a better rating when it was filtered. Without filtering, 48.6% of the listeners perceived the stimulus as a [u] with ''good'' or ''very good quality,'' while 17.1% of them did not identify the vowel [u]. After filtering, the rating of good or very good quality increased to 64.3%, while only 4.3% of the listeners did not identify the vowel [u]. For the stimuli recorded under the N condition, the impact of the filtering is quite negligible. Without filtering, 100% of the listeners perceived the stimulus as a [u] with good or very good quality; after filtering, this rate decreased slightly to 98.6%, 1.4% of the listeners (i.e., two listeners among the 14) providing the evaluation ''poor quality.'' The results tend to attest to the role played by $F3$ in the perception of the vowel [u] produced by speaker OD under the PL condition, and confirm that considering $F0$, $F1$, and $F2$ is not completely sufficient to assess compensation in the perceptual domain.

Altogether, these data raise a last question. Indeed, it appears that speaker OD did not fully compensate for the perturbation in the perceptual domain, though he used exactly the strategy predicted from the acoustical theory to offer the compensation in the $[F_1,F_2]$ plane. Hence the question is: what improvement was induced by this articulatory strategy? This is the purpose of the next experiment, in which a comparison of the identification of the PF and the PL stimuli was carried out for speaker OD and for two other speakers representative of the main compensatory behaviors.

IV. EXPERIMENT 3: COMPARING THE IDENTIFICATIONS OF THE PF AND THE PL STIMULI

In this last experiment, the stimuli in the PL condition were compared with the stimuli produced immediately after the insertion of the tube, without any preparation time (PF condition). Since we have suggested that the ultimate task space of speech production is the perceptual domain, this comparison offers a way to understand what perceptual criteria could have guided the speakers during the adaptation session. For this aim, a classification test was performed in order to know more about the phonetic quality of these stimuli. The analysis of stimuli was limited to three speakers who are considered to be prototypical for the general trends observed in the articulatory and perceptual domains as regards the compensatory strategies: articulatory movements from PF to PL, that were large enough to induce significant spectral changes likely to influence the perceptual rating of the perturbed [u] (speakers OD and GA; OD chosen as prototype); small articulatory movement from PF to PL, with good perceptual ratings of the perturbed [u] in the PL condition (speakers CH and MP; CH chosen as prototype); no or small articulatory movement from PF to PL, with unsatisfactory perceptual ratings of the perturbed [u] in the PL condition (speakers JY, BC, LJ, LR, ML, and YP; JY chosen as prototype).

A. Corpus and procedure

Fourteen listeners among the previous 18 served as subjects. In addition to speaker OD's stimuli, the stimuli recorded under the N, PF, and PL conditions for speakers JY and CH were selected. The corpus consisted then of a total of 9 stimuli (3 speakers×3 conditions). The same procedure as in experiment 1 was used: listening to a stimulus, selection and validation of the response, and then listening to the next stimulus. The response was selected from the same list of seven items as in experiment 1: ''au'' (/o/) like in the word ''beau,'' ''i'' (/i/) like in ''lit,'' ''ou'' (/u/) like in ''pou,'' ''e'' (/œ/) like in ''peur,'' ''o'' (/ɔ/) like in ''port,'' ''u'' (/y/) like in ''rue,'' and ''a'' (/a/) like in ''pas.'' The stimuli were presented only once, but no time constraint was given for the response. Two seconds after the mouse validation, another stimulus was presented. There were five occurrences of each stimulus; hence, a total of 70 responses for each stimulus was analyzed. This test was performed 3 months after the identification test of experiment 1.

B. Results

The results are presented in Table III.

For speakers CH and JY, the identification of the stimulus produced under the PL condition was similar to the one observed in experiment 1: 100% and 5% of the occurrences

TABLE III. Number of correct identifications of the vowel [u] produced under N, PF, and PL conditions by speakers OD, JY, and CH. Same presentation as in Table I.

Speakers	N condition	PF condition	PL condition
OD	68 ([o]:2)	31 ([œ]:31; [o]:4; [i]:3; [a]:1)	28 ([o]:31; [ɔ]:6; [œ]:3; [y]:2)
JY	70	4 ([œ]:66)	4 ([œ]:65; [o]:1)
CH	70	70	70

were correctly classified, respectively. As concerns speaker CH, the stimulus under the PF condition was perfectly well-classified. Remember that, from the analysis of the whole set of speakers, it was proposed that in case of a strong lip perturbation, the compensation could not be reached immediately after the insertion of the tube (PF condition) and would require a training period. Therefore, our interpretation is that, for this speaker, the impact of the lip tube was less strong as expected; hence, the perfect identification of the PF stimuli. As concerns speaker JY, no relevant difference was observed between the identifications of the PF and the PL stimuli. This result confirms that this speaker did not find any appropriate strategy to compensate.

For speaker OD, the results were not as clear. Whereas the identification score in the N condition was similar to the one in the first test, strong differences were observed in the PL condition between experiment 1 and this experiment. Thus, the absence, in the current test, of auditory references within the speakers' maximal vowel space seems, in a first analysis, to have had more impact on the perceptual evaluation of speaker OD's stimuli, than for the other speakers. This is not surprising, because the acoustical signal recorded for OD under the PL condition was already shown to be perceptually neither very good (and then easily identifiable) nor very bad (and easily discarded as a [u]).

These results bring interesting insights into the objectives that could have underlain the compensatory strategy observed for speaker OD. For the PF condition, the identifications were equally distributed between a [u], a back-rounded vowel, and an [œ], a central vowel. For the PL condition, the identifications were essentially either [u] or [o], two back-rounded vowels. This observation suggests that the strong articulatory changes observed for speaker OD from the PF to the PL condition (a large backward movement of the tongue) induced a shift in the phonetic classification of the sound. From clearly ambiguous (either a back rounded or a central one) in the PF condition, the sound became clearly a back and rounded vowel in the PL condition. Thus, although speaker OD's stimulus in the PL condition was not perceived as a good [u], it is possible to suggest the strategy chosen by speaker OD during the adaptation session: try to maintain the produced stimulus inside the back category typical of a [u], even if the ''height'' feature is not completely preserved.

V. GENERAL DISCUSSION

We defined two main stages for the present study. First, we intended to take advantage of the acoustical stimuli produced in the perturbation experiment presented by Savariaux *et al.* (1995) to explore the perceptual space around the French oral vowel [u], with the hope that these atypical stimuli would help to provide information about the perception of such back-rounded vowels. The second stage consisted of exploiting this characterization of the perceptual goal associated to [u] in French, in order to better understand the speaker's task for this vowel and to better interpret the speakers' strategies in the lip tube experiment. We shall discuss these two points in this order.

A. [u] in the listener's mind: confirmations and refinements on a ''grave'' vowel

This set of experiments enabled us to propose a progressive focus on the perceptual template for vowel [u] in French, in the following way. First, experiment 1 confirmed that the perceptual goal for [u] is basically associated with the control of two parameters that have to be low enough: one mainly linked with $F1$, ensures the ''high'' feature (to contrast with [o]), and the other, mainly linked with $F2$, ensures the velopalatal feature (to contrast with [œ] in our experiment). Second, the correlation analyses in experiments 1 and 2 suggest that $F0$ does not seem to contribute significantly to the perception of the high feature; hence, $F1$ is more appropriate than $(F1-F0)$ as a correlate of the high feature. This is essentially in line with the data discussed in Sec. I B. Third, $F0$ seems, on the contrary, to contribute to the normalization of $F2$; hence, $(F2-F0)$ in bark provides the basic correlate of the back feature for [u] [see Fig. 1(C)]. Fourth, it appears that the parameter $(((F2-F0)+F1)/2)$ (all frequencies in bark) might summarize the effects of $F1$ and $(F2-F0)$ and provide a good overall correlate of the grave feature classically used to describe the vowel [u] in all languages (Jackobson *et al.*, 1963). It is of particular interest to notice that this parameter might be associated with the center of gravity introduced by Chistovich and colleagues in 1979, normalized to a certain extent by $F0$. Indeed, $(((F2-F0)+F1)/2)$ might be seen as $((F1+F2)/2-F0/2)$, with the first term $(F1+F2)/2$ being the true center of gravity, and $F0/2$ the normalizing term. It is also remarkable that this parameter happens to set both the category boundary (around 5.25 bark; see Fig. 3) and the prototypicality index for [u] with a boundary between good and poor representatives around 4.75 bark (see Fig. 3). At last, a too-high intensity of $F3$ seems to play an additional, though marginal, role degrading the [u] quality: this is demonstrated by the data on low-pass filtered stimuli recorded for speaker OD under the PL condition (see Sec. III C 2).

B. [u] in the speaker's mind: addenda to the lip tube experiment

This perceptual characterization of the vowel [u] in French leads us to reconsider the conclusions elaborated during the previous analysis of the lip tube experiment on the sole basis of acoustical parameters (Savariaux *et al.*, 1995). First, producing with the lip tube an $(F1,F2)$ pattern similar to the one measured during a normal articulation is not necessary to achieve a compensation in the perceptual domain. Since the perceptual objective combines at least $F0$, $F1$, and

$F2$, the speakers have some freedom in adjusting the control of their vocal source and vocal tract to compensate. This ends up with the fact that three speakers, and not one, as proposed in Savariaux *et al.* (1995), did actually achieve the compensation in perceptual terms. For this aim, none of them produced the expected strong backwards movement of the tongue: all of them combined, to different extents, some reduced changes of the three basic spectral parameters influencing the perception of the vowel [u].

Second, and this is a consequence of our first point, we must acknowledge that the impact of the lip tube was not the same for all speakers. Slight differences between two speakers, in fundamental frequency or in tongue arching (which helped to lengthen the constriction without moving it), could make the compensation task more or less difficult.

Third, a strong backward movement of the tongue is not a perfect compensation strategy, since it induces, simultaneously with the desired correction of the $(F1,F2)$ pattern, changes in formant intensities and in the spectral shape beyond 1500 Hz that may have a negative impact on the perception. However, this articulatory strategy is appropriate to maintain the vowel [u] within the ''back and rounded'' phonetic category, and to prevent it from becoming a central vowel. This explains speaker OD's strategy.

The fact that, in spite of a bad perceptual effect, the majority of the speakers kept the canonical velopalatal configuration of a French vowel [u] in the lip tube conditions, confirms the hypothesis proposed in Savariaux *et al.* (1995) that, at a certain level of the speech production control, the task is encoded in articulatory terms. However, the perceptual analysis of the stimuli persuades us to soften the suggestion that this canonical configuration could have constrained and limited the range of articulatory changes that a speaker was likely to provide in the presence of the lip tube. The absence of any relevant articulatory modification observed for some of the speakers can now be explained differently. These speakers were perhaps not able to produce the appropriate combined changes in $F0$, $F1$, and $F2$, and because the strong backward movement of the tongue is not a perfect strategy, they could have decided to adopt the canonical configuration that is usually associated with the vowel [u].

The main conclusion of Savariaux *et al.* (1995) is therefore strengthened by the perceptual study. The speech production *objective* is intrinsically a *perceptual* one, and the speakers seem to have a clear representation of it. They also have a good representation of the relations between the articulatory and the perceptual levels, since those who were strongly perturbed by the lip tube and provided a noticeable compensation from the PF to the PL condition did rapidly converge towards the appropriate changes. A projection of the perceptual objective into the articulatory level seems to exist, and it can be hypothesized that it helps in the ongoing control of normal speech production. However, the articulatory description of the task does not replace the perceptual objective, and, in perturbed speech production, its impact on the articulation seems, at most, secondary.

ACKNOWLEDGMENTS

The authors are grateful to the speakers who served as subjects in the lip tube experiment, and to the 19 listeners who participated in the perceptual tests. Special thanks are due to Professor Lebeau, to Professor Crouzet, and to Mrs. Martin from Grenoble University Hospital, who collected the x-ray data. This work was supported by the Esprit Basic Research Project No. 6975, Speech Maps.

[1]An error was made when giving the size of the lip tube in page 2430 of Savariaux *et al.*'s (1995) paper. Indeed, the diameter was said to be equal to 20 mm. Its true dimension is 25 mm, as attested by Figs. 4, 6, and 8 of the same article.

[2]Speaker JM (see Savariaux *et al.*, 1995) was removed from the current analyses. Indeed, preliminary tests of the quality of his natural production of [u] showed that his vowel was correctly classified, but was not perceived as a good [u].

Abbs, J. H., and Gracco, V. L. (**1984**). ''Control of complex motor gestures: Orofacial muscle responses to load perturbations of lip during speech,'' J. Neurophysiol. **51**, 705–723.

Atal, B. S., Chang, J. J., Mathews, M. V., and Tukey, J. W. (**1978**). ''Inversion of articulatory-to-acoustic information in the vocal tract by a computer-sorting technique,'' J. Acoust. Soc. Am. **63**, 1535–1555.

Beddor, P. S., and Hawkins, S. (**1990**). ''The influence of spectral prominence on perceived vowel quality,'' J. Acoust. Soc. Am. **87**, 2684–2704.

Bladon, R. A. W. (**1982**). ''Arguments against formants in the auditory representation of speech,'' in *The Representation of Speech in the Peripheral Auditory System*, edited by R. Carlson and B. Granström (Elsevier Biomedical, Amsterdam), pp. 95–102.

Bladon, R. A. W., and Fant, G. (**1978**). ''A two-formant model and the cardinal vowels,'' STL-QPSR **1**, pp. 1–8.

Boë, L-J., Perrier, P., and Bailly, G. (**1992**). ''The geometric variables of the vocal tract controlled for vowel production: Proposals for constraining acoustic-to-articulatory inversion,'' J. Phonetics **20**, 27–38.

Bohn, O. S., and Strange, W. (**1995**). ''Discrimination of coarticulated German vowels in the silent-center paradigm: 'Target' spectral information non needed,'' in *Proceedings of the XIIIth International Congress of Phonetic Sciences* (KTH, Stockholm, Sweden), Vol. 2, pp. 270–273.

Carlson, R., Granström, B., and Fant, G. (**1970**). ''Some studies concerning perception of isolated vowels,'' STL-QPSR **2–3**, pp. 19–35.

Carlson, R., Granström, B., and Klatt, D. (**1979**). ''Vowel perception: The relative salience of selected acoustic manipulations,'' STL-QPSR **34**, pp. 19–35.

Chistovitch, L. A., Sheikin, R. L., and Lublinskaya, V. V. (**1979**). '' 'Centers of gravity' and the spectral peaks as the determinants of vowel quality,'' in *Frontiers of Speech Communication Research*, edited by B. Lindblom and S. Öhman (Academic, London), pp. 143–157.

Delattre, P., Liberman, A. M., Cooper, F. S., and Gertsman, J. (**1952**). ''An experimental study of the acoustic determinants of vowel color; observations on one- and two-formant vowels synthesized from spectrographic patterns,'' Word **8**, 195–210.

Di Benedetto, M. G. (**1987**). ''On vowel height: Acoustic and perceptual representation by the fundamental and the first formant,'' in *Proceedings of the XIth International Congress of Phonetic Sciences* (Academy of Sciences, Tallin, Estonia), Vol. 5, pp. 198–201.

Fahey, R. P., Diehl, R. L., and Traunmüller, H. (**1996**). ''Perception of back vowels: Effects of varying $F1-F0$ bark distance,'' J. Acoust. Soc. Am. **99**, 2350–2357.

Fant, G., Carlson, R., and Granström, B. (**1974**). ''The [e]–[ø] ambiguity,'' in *Proceedings of Speech Communication Seminar*, Stockholm, pp. 117–121.

Fowler, C. A. (**1990**). ''Calling a mirage a mirage: Direct perception of speech produced without a tongue,'' J. Phonetics **18**, 529–541.

Fowler, C. A. (**1996**). ''Listeners do hear sounds, not tongues,'' J. Acoust. Soc. Am. **99**, 1730–1741.

Grieser, D., and Kuhl, P. K. (**1989**). ''Categorization of speech by infants: Support for speech-sound prototypes,'' Dev. Psychol. **25**, 577–588.

Hirahara, T., and Kato, H. (**1992**). ''The effect of $F0$ on vowel identification,'' in *Speech Perception, Perception and Linguistic Structure*, edited

by Y. Tohkura, E. Vatikiotis-Bateson, and Y. Sagisaka (Ohmsha, Tokyo and IOS, Amsterdam), pp. 89–112.
Hoemeke, K. A., and Diehl, R. L. (**1994**). ''Perception of vowel height: The role of $F1-F0$ distance,'' J. Acoust. Soc. Am. **96**, 661–674.
Honda, K. (**1996**). ''Organization of tongue articulation for vowels,'' J. Phonetics **24**, 39–52.
Jakobson, R., Fant, G., and Halle, M. (**1963**). *Preliminaries to Speech Analysis* (MIT Press, Cambridge, MA).
Klatt, D. H. (**1982**). ''Prediction of perceived phonetic distance from critical-band spectra: A first step,'' in Proceedings of the IEEE ICASSP, pp. 1278–1281.
Kuhl, P. K. (**1991**). ''Human adults and human infants show a 'perceptual magnet effect' for the prototypes of speech categories, monkeys do not,'' Percept. Psychophys. **50**, 93–107.
Kuhl, P. K. (**1995**). ''Mechanisms of developmental change in speech and language,'' in *Proceedings of the XIIIth International Congress of Phonetic Sciences* (KTH, Stockholm, Sweden), Vol. 2, pp. 132–139.
Liberman, A. M., and Mattingly, I. G. (**1985**). ''The motor theory of speech perception revised,'' Cognition **21**, 1–36.
Lindblom, B. (**1987**). ''Adaptive variability and absolute constancy in speech signals: Two themes in the quest for phonetic invariance,'' in *Proceedings of the XIth International Congress of Phonetic Sciences* (Academy of Sciences, Tallin, Estonia), Vol. 3, pp. 9–18.
Lindblom, B. (**1996**). ''Role of articulation in speech perception: Clues from production,'' J. Acoust. Soc. Am. **99**, 1683–1692.
Lindblom, B., Lubker, J., and Gay, T. (**1979**). ''Formant frequencies of some fixed-mandible vowels and a model of speech motor programming by predictive simulation,'' J. Phonetics **7**, 147–161.
Lublinskaya, V. V., Escudier, P., and Carré, R. (**1980**). ''Study of the formant detection thresholds,'' J. Acoust. Soc. Am. **67**, 102.
Maeda, S. (**1990**). ''Compensatory articulation during speech: Evidence from the analysis and synthesis of vocal tract shapes using an articulatory model,'' in *Speech Production and Speech Modelling*, edited by W. J. Hardcastle and A. Marchal (Kluwer Academic, Dordrecht), pp. 131–149.
Maeda, S., and Honda, K. (**1994**). ''From EMG to formant patterns of vowels: The implication of vowel systems spaces,'' Phonetica **51**, 17–29.
Mantakas, M. (**1989**). ''Application du second formant effectif F'2 à l'étude de l'opposition d'arrondissement des voyelles antérieures du français.'' Thèse de Docteur de l'INPG, Systèmes Electroniques.
McGowan, R. S., and Faber, A. (**1996**). ''Introduction to papers on speech recognition and perception from an articulatory point of view,'' J. Acoust. Soc. Am. **99**, 1680–1682.
Mermelstein, P. (**1967**). ''Determination of the vocal-tract shape from measured formant frequencies,'' J. Acoust. Soc. Am. **41**, 1283–1294.
Miller, J. L. (**1977**). ''Properties of feature detectors for VOT: The voiceless channel of analysis,'' J. Acoust. Soc. Am. **62**, 641–648.
Miller, J. L., Connie, C. M., Schermer, T. M., and Kluender, K. R. (**1983**). ''A possible auditory basis for internal structure of phonetic categories,'' J. Acoust. Soc. Am. **73**, 2124–2133.
Nearey, T. M. (**1989**). ''Static, dynamic and relational properties in vowel perception,'' J. Acoust. Soc. Am. **85**, 2088–2113.
Nearey, T. M. (**1995**). ''Evidence for the perceptual relevance of vowel-inherent spectral change for front vowels in Canadian English,'' in *Proceedings of the XIIIth International Congress of Phonetic Sciences* (KTH, Stockholm, Sweden), Vol. 2, pp. 678–681.
Perkell, J. S., and Klatt, D. H., editors (**1986**). *Invariance and Variability in Speech Processes* (Erlbaum, Hillsdale, NJ).
Perkell, J. S., Matthies, M., Svirsky, M., and Jordan, M. (**1993**). ''Trading relations between tongue-body raising and lip rounding in production of the vowel /u/: A pilot 'Motor Equivalence' study,'' J. Acoust. Soc. Am. **93**, 2948–2961.
Perkell, J. S., Matthies, M. L., and Zandipour, M. (**1998**). ''Motor equivalence in the production of /ʃ/,'' J. Acoust. Soc. Am. **103**, 3085(A).
Potter, R. K., and Steinberg, J. C. (**1950**). ''Toward the specification of speech,'' J. Acoust. Soc. Am. **22**, 807–820.
Samuel, A. G. (**1982**). ''Phonetic prototypes,'' Percept. Psychophys. **31**, 307–314.
Savariaux, C., Perrier, P., and Orliaguet, J. P. (**1995**). ''Compensation strategies for the perturbation of the rounded vowel [u] using a lip-tube: A study of the control space in speech production,'' J. Acoust. Soc. Am. **98**, 2428–2442.
Schroeder, M. R. (**1967**). ''Determination of the geometry of the human vocal tract by acoustic measurements,'' J. Acoust. Soc. Am. **41**, 1002–1010.
Schroeder, M. R., Atal, B. S., and Hall, J. L. (**1979**). ''Objective measure of certain speech signal degradations based on masking properties of human auditory perception,'' in *Frontiers of Speech Communication Research*, edited by B. Lindblom and S. E. G. Ohman (Academic, London), pp. 217–229.
Schwartz, J.-L., and Escudier, P. (**1989**). ''A strong evidence for existence of a large-scale integrated spectral representation in vowel perception,'' Speech Commun. **8**, 235–259.
Stevens, K. N. (**1989**). ''On the quantal nature of speech,'' J. Phonetics **17**, 3–45.
Stevens, K. N. (**1996**). ''Critique: Articulatory-acoustic relations and their role in speech perception,'' J. Acoust. Soc. Am. **99**, 1693–1694.
Strange, W. (**1989**). ''Dynamic aspects of coarticulated vowels spoken in sentence context,'' J. Acoust. Soc. Am. **85**, 2135–2153.
Sussman, J. E. (**1993**). ''A preliminary test of prototype theory for a [ba]-[da] continuum,'' J. Acoust. Soc. Am. **93**, 2392.
Syrdal, A. K., and Gopal, H. S. (**1986**). ''A perceptual model of vowel recognition based on the auditory representation of American English vowels,'' J. Acoust. Soc. Am. **79**, 1086–1100.
Traunmüller, H. (**1981**). ''Perceptual dimension of openness in vowels,'' J. Acoust. Soc. Am. **69**, 1465–1475.
Traunmüller, H. (**1985**). ''The role of the fundamental and the higher formants in the perception of speaker size, vocal effort, and vowel openness,'' Paper presented at the Franco–Swedish Seminar on Speech, SFA, Grenoble, France (April 1985).
Traunmüller H. (**1991**). ''The context sensitivity of the perceptual interaction between $F0$ and $F1$,'' in *Proceedings of the XIIth International Congress of Phonetic Sciences* (Université de Provence, Aix-en-Provence, France), Vol. 5, pp. 62–65.
Zeiliger, J., and Sérignat, J.-F. (**1991**). ''EUROPEC software v4.1, User's guide,'' Esprit BR Project No. 2589, SAM-ICP-045.

A comparison of intergestural patterns in deaf and hearing adult speakers: Implications from an acoustic analysis of disyllables

Areti Okalidou[a)]
Ph.D. Program in Speech and Hearing Sciences, Graduate School, City University of New York, 33 West 42nd Street, New York, New York 10036

Katherine S. Harris[b)]
Ph.D. Program in Speech and Hearing Sciences, Graduate School, City University of New York, 33 West 42nd Street, New York, New York 10036 and Haskins Laboratories, 270 Crown Street, New Haven, Connecticut 06511-6695

(Received 18 July 1997; revised 5 February 1999; accepted 8 February 1999)

Coarticulation studies in speech of deaf individuals have so far focused on intrasyllabic patterning of various consonant–vowel sequences. In this study, both inter- and intrasyllabic patterning were examined in disyllables /ə#CVC/ and the effects of phonetic context, speaking rate, and segment type were explored. Systematic observation of $F2$ and durational measurements in disyllables minimally contrasting in vocalic ([i], [u,] [ɑ]) and in consonant ([b], [d]) context, respectively, was made at selected locations in the disyllable, in order to relate inferences about articulatory adjustments with their temporal coordinates. Results indicated that intervocalic coarticulation across hearing and deaf speakers varied as a function of the phonetic composition of disyllables (b_b or d_d). The deaf speakers showed reduced intervocalic coarticulation for bilabial but not for alveolar disyllables compared to the hearing speakers. Furthermore, they showed less marked consonant influences on the schwa and stressed vowel of disyllables compared to the hearing controls. Rate effects were minimal and did not alter the coarticulatory patterns observed across hearing status. The above findings modify the conclusions drawn from previous studies and suggest that the speech of deaf and hearing speakers is guided by different gestural organization. © *1999 Acoustical Society of America.* [S0001-4966(99)01607-0]

PACS numbers: 43.70.Dn, 43.66.Sr [WS]

INTRODUCTION

A few acoustic studies (Monsen, 1976; Rothman, 1976; Waldstein and Baum, 1991; Baum and Waldstein, 1991) have investigated the issue of coarticulation, i.e., the phonetic variations of a segment due to its assimilation with neighboring segments, in the productions of deaf speakers, and concluded that deaf speakers coarticulate less than normals. Monsen (1976) and Rothman (1976) based their conclusions on the observation that the second formant transitions were flatter in the speech of deaf than hearing speakers. Using CV(C) words, Monsen (1976) measured the second formant frequency at voice onset and at 20-ms intervals during the first 120 ms of the vowel. Deaf adolescent speakers exhibited a reduced $F2$ frequency change over the 120-ms interval, showing a smaller $F2$ difference between vowel onset and the vowel 120 ms later than hearing adolescents. Rothman (1976) studied coarticulation in the utterance ''Take a CVC aside,'' using CVC nonsense words. He measured $F2$ and $F3$ frequency ranges at the onset, midpoint, and offset of vocalic segments of the utterance. He showed that deaf speakers (a) had smaller $F2$ and $F3$ frequency ranges than their hearing counterparts at the onsets or offsets of vocalic segments averaged across the utterances with variable CVC contexts, (b) had smaller $F2$ transition ranges from schwa onset to schwa offset, as averaged across /ə-lVt/ contexts, and (c) had a smaller spread of $F2$ frequency values across the transition onsets of utterances with variable CVC context.

Each of these studies had several methodological limitations. In Monsen's study, subject selection was less than optimal because (a) a heterogeneous hearing-impaired sample was used, with hearing loss ranging from severe to profound (PTA range in the better ear: 65.6–103.9 dB HL), and (b) deaf subjects were adolescents, ages 13–15, and therefore, detection of formants in their speech was difficult because of widely spaced harmonics (a result of high $F0$) and other phonatory problems related to voice changes during puberty. In addition, the $F2$ values were measured over an absolute interval (120 ms) regardless of the speaker's segment durations and regardless of syllable type (open or closed syllable). In Rothman's study, data were averaged across subjects in a single group, across contexts, and sometimes, across measurement points. Also, data were examined selectively in that perceptually incorrect tokens were eliminated from the deaf sample to reduce intertoken variability.

Apart from the methodological limitations outlined above, there is a major drawback to the interpretations of

[a)]Currently at: Department of Logotherapy, Technological Educational Institute of Patras, 263 34 Koukouli, Patra, Greece. Electronic mail: okalidou@compulink.gr
[b)]Electronic mail: loumau@erols.com

Monsen and Rothman. Their results may also be interpreted in the opposite direction, i.e., that deaf speakers coarticulate more than hearing, because flat, and sometimes shorter, formant transitions in CV sequences can also occur when most of the anticipatory lingual movement of the vowel gesture takes place during the consonant closure preceding the vowel (Nittrouer *et al.*, 1989). Overall, an interpretation of articulatory patterning based on examination of such a small portion of the acoustic signal, the CV syllable, may result in misleading conclusions.

Two recent studies (Waldstein and Baum, 1991; Baum and Waldstein, 1991) examined anticipatory and carryover coarticulation in the speech of deaf (PTA range=90–105 dB HL or greater) and hearing children using the methodology of Nittrouer *et al.* (1989). In the study by Waldstein and Baum (1991), both lip-rounding and lingual effects of the vowel on the preceding consonant of CV words were studied, respectively, by measurements of centroids—at early and late locations within the consonant of CV words—and by $F2$ measurements—at 20 ms before vowel onset. Deaf children, overall, showed smaller centroid and $F2$ ratios of Ci/Cu pairs than hearing children; an exception was noted for $F2$ ratios of [ti]/[tu]. In the study by Baum and Waldstein (1991), the lip-rounding and lingual effects of the preceding vowel on the final consonant of VC syllables were studied, respectively, by centroid measurements—at consonant onset and at 50 ms later—and by $F2$ measurements—at consonant onset for /iʃ-uʃ/ pairs only. At consonant onset, deaf children showed smaller centroid ratios, iC/uC, and smaller $F2$ ratios, /iʃ/uʃ/, than hearing children. In both studies it was concluded that deaf children produce more reduced anticipatory and carryover coarticulation of vowel context than hearing children.

With respect to lingual coarticulation, it appears that the results of these two studies did not allow for ''centralization'' and ''reduced coarticulation'' to be distinguished. By direct comparisons, they attempted to measure the magnitude of coarticulation of deaf against that of hearing speakers without taking into account their differences in the articulatory working space. In their data, as well as in other studies (Monsen, 1976; Rubin, 1984; Shukla, 1989; Subtelny *et al.*, 1992), the average $F2$ values of /i/ and /u/ were closer in the speech of deaf speakers than in their hearing counterparts, suggesting smaller differences in front cavity size for the former group. Thus the smaller $F2$ ratios (Ci/Cu or iC/uC) for deaf than hearing children during the consonant are at least partly attributable to the smaller separation of /i/-/u/ at vowel midpoint. Moreover, a reduced lingual coarticulation was not evidenced in the alveolar context (ti/tu), suggesting that the coarticulatory patterns of deaf speakers may vary depending on context. Examination of lingual coarticulation was made over a single measurement rather than over an interval. Finally, they employed deaf subjects with hearing losses at the lower end of the profound category (PTA in the better ear=90+ dB HL) which yields the greatest variability in speech performance (Boothroyd, 1985).

In conclusion, the studies on coarticulation of deaf speakers so far have yielded ambiguous and incomplete results. They examined a narrow portion of the acoustic signal to draw inferences for a broad, dynamic phenomenon, i.e., intersegmental coordination in running speech. Coarticulation studies of adults with normal hearing (Alfonso and Baer, 1982; Recasens, 1985) have shown that the coarticulatory effects of a stressed vowel can extend across a consonantal boundary into a preceding vowel. Examination over a more extended utterance string is needed to obtain information about the coarticulatory patterns of deaf speakers and compare them with their hearing counterparts. Recasens (1989) has indicated furthermore that vowel-to-vowel influences are mediated by phonetic context constraints from the intervocalic consonant, hence, the study of coarticulation over different phonetic contexts should provide important information on articulatory organization and the nature of articulatory constraints in the speech of deaf speakers.

Another important variable that has been overlooked in previous studies on coarticulation of deaf speakers is the effect of speaking rate on coarticulation. Although a great degree of variation exists in the way that hearing speakers enact their articulatory maneuvers as a function of increased rate (Tuller *et al.*, 1982), several studies have reported that increases in speaking rate may result in increased coarticulation/coproduction (Bell-Berti and Krakow, 1991; Byrd and Tan, 1996; Gay, 1978, 1981; Munhall and Löfqvist, 1992; Zsiga, 1994). Hence, at a faster rate there were increases in intra-articulatory overlap of neighboring segments for velic gestures (Bell-Berti and Krakow, 1991) and laryngeal gestures (Munhall and Löfqvist, 1992). Also, increased gestural overlap in consonant sequences (Byrd and Tan, 1996; Zsiga, 1994) occurred as a function of increased rate, although speaker-specific and context-specific variations were observed. In earlier studies, Gay (1978, 1981) found acoustic and physiological evidence of increased gestural overlap in CV sequences (/pV/) at fast rates, that is, more similar values between the onset and the target frequency of the vowel, and an earlier onset of genioglossus muscle activity relative to the orbicularis oris muscle in /əpipə/ sequences (Gay, 1981).

It has been well documented that deaf speakers speak at a slower rate than their hearing counterparts (Osberger and Levitt, 1979; Osberger and McGarr, 1982), thus their segment durations are longer. In view of the effects of speaking rate on coarticulation/coproduction outlined above, it might be hypothesized that the reduced coarticulation of the deaf speakers is a byproduct of their slow speaking rates. The purpose of the present study, then, was to examine both inter- and intrasyllabic patterning of consonant–vowel sequences across hearing status, employing systematic analysis of the effects of phonetic context (b_b, d_d), segment type (vowels, consonants) and speaking rate, over an extended utterance, the disyllable /ə#CVC/. The utterances of hearing speakers at normal rate were compared with the utterances of deaf speakers at normal and at fast speaking rates, respectively.

A segmental approach was initially used in this study where $F2$ effects were examined in relation to traditional acoustic entities such as ''consonants'' and ''vowels'' in a disyllabic utterance. However, according to the developmental account of coproduction (Studdert-Kennedy, 1987, 1989),

TABLE I. Audiometric pure-tone results in dB HL at each frequency for deaf speakers. Note. NR indicates no response, i.e., ''NR110'' indicates no response at 110 dB HL. DNT indicates ear was not tested.

Audiometric frequencies	D1 right ear (in dB HL)	D1 left ear (in dB HL)	D2 right ear (in dB HL)	D2 left ear (in dB HL)	D3 right ear (in dB HL)	D3 left ear (in dB HL)
125 Hz	NR85	85	100	75	70	65
250 Hz	NR100	90	100	90	75	75
500 Hz	105	95	115	90	90	95
1000 Hz	125	110	DNT	105	115	110
2000 Hz	NR125	125	NR125	NR125	115	120
4000 Hz	NR120	NR120	NR120	NR120	125	130
8000 Hz	NR110	NR110	NR110	NR110	NR110	NR110

the segment is a recurrent pattern of gesture(s) that gradually emerges from children's syllabic babbling and early word productions. Implicit in this account, as well as in the general theory of articulatory phonology (Browman and Goldstein, 1986, 1989), is the notion that a given gestural constellation may reflect either segmental or syllabic organization; the minimal units of speech in different populations may vary depending on the span of their gestural organization (Nittrouer, 1985; Nittrouer *et al.*, 1989). For example, a set of the supralaryngeal gestures listed below may take place for the production of /s/, i.e., jaw raising, tongue tip fronting, tongue tip raising, and velum raising. Yet, another set of supralaryngeal gestures, that is, jaw raising, velum raising, tongue tip lowering and fronting, and tongue dorsum raising and backing, may take place for the production of /su/. The minimal speech unit is segmental, when the tightly coupled gestures belonging to /s/ are temporally differentiated from the tongue dorsum raising and backing for /u/; it can also be syllabic, when, for example, tongue dorsum raising for target [u] and tongue tip lowering for target [s] are produced as part of a single tongue gesture (possibly, at the expense of segmental accuracy, as suggested by studies of Nittrouer and her colleagues on children's speech). The present study employs a gestural framework to infer articulatory patterns from acoustic $F2$ patterns in the deaf speakers' productions.

A final point should be made. Previous studies tended to examine average data across deaf subjects, failing to address that this population exhibits a great amount of intersubject variability in speech production patterns. In the present study, intersubject differences were more apparent by studying the coarticulatory effects for each subject separately, as in single case studies. Discernible patterns across subjects within a group were then evidence for generalizing conclusions to speakers with similar background and profiles.

I. METHOD

A. Subjects

Three hearing adults (H1=male, 26 years old, H2 =male, 41 years old, H3=male, 29 years old) and three deaf adults (D1=male, 39 years old, D2=female, 54 years old, D3=male, 61 years old) participated in the study. The subjects were naïve to the purposes of the experiment. All were monolingual speakers of English. The hearing speakers spoke dialects typical of the Northeastern United States, did not have a history of speech and language problems, and had passed an audiological screening test at 500 Hz, 1000 Hz, and 4000 Hz.

Because the speech of deaf speakers is highly variable, partly due to background factors, including onset, type and degree of hearing loss, and educational training, care was taken to recruit individuals who had similar profiles with respect to these variables. Another primary criterion for subject selection was to pick deaf speakers whose residual hearing was either absent or minimal: A pure tone average (PTA) threshold of 106 dB HL was used as the lower cutoff point, beyond which residual hearing is not useful for the purposes of speech acquisition or speech reception (Boothroyd, 1984). A drawback of the subject selection was that the deaf speakers were not matched in age to their hearing counterparts.

The deaf speakers had no other documented handicaps. They were orally trained in oral/aural schools for the deaf, so that their educational and speech training history was known and their audiological history could be reliably traced from school records. Information on the deaf subjects' auditory experiences and communication modes is given below: Subject D1 was first fitted binaurally between the ages of 2.5 or 3 years, and has used amplification regularly and continuously. Subject D2, while she had used auditory training devices during her oral education years, was first fitted with a hearing aid at the age of 35 years and used it thereafter during working hours. Subject D3 was first fitted with a hearing aid at the age of 12 years, discontinued its use during a long period of his life (22–41 years) and restarted wearing it 20 years ago, on a regular basis, until the time of the recording. All three deaf subjects were proficient users of the English language and used oral speech on a day-to-day basis. Subject D1 used oral speech as the only means of communication. Subject D2 used the English language (oral speech) as a first language but also alternatively used manual communication when addressing deaf people at work and some family members at home. Subject D3 used oral speech as his primary mode of communication at work and at home, although he reported limited use of manual communication with some family members.

The deaf speakers had a similar type, onset, and degree of hearing loss i.e., a stable, bilateral, sensorineural, profound hearing loss with prelingual onset, possibly since birth. The results of a complete audiological evaluation, conducted within 24 months of this study, are provided in Tables I and II. Their cause of hearing loss was either unknown or

TABLE II. Audiological profiles, speech intelligibility, amplification, and frequency of oral speech by deaf speakers. See Boothroyd (1984, 1985) for details on intelligibility testing.

Subj.	Better ear PTA in dB HL	Better ear speech detection thresholds in dB HL	Better ear most comfortable listening level (MCL) in dB HL	Speech discrimination scores % of words recognized	% words correctly understood by listeners	Use of amplification	Frequency of use of oral speech
D1	107	80	100	13% (AB word lists)	46%	binaural aids	daily, always
D2	107	90	105	<10% (NU-6 lists)	23%	monoaural aid	daily, quite often
D3	110	90	105	10% (NU-6 lists)	16%	monaural aid	daily, most often

reported as genetic and two of them, D1 and D3, were mainstreamed during their later school years. Their intelligibility scores based on Boothroyd's (1984, 1985) isophonemic word lists were obtained from a different study (McGarr *et al.*, 1993) and are also shown in Table II, along with other relevant information. It is observed that the deaf speakers vary in their speech abilities from each other. However, in order to avoid biasing the results toward normal coarticulation patterns, the tokens in the deaf sample used for analysis were not screened nor selected based on their perceptual accuracy (see Sec. I C).

B. Materials

CVC nonsense syllables were embedded in a carrier phrase ''a __ again.'' Alveolar (d_d) and bilabial (b_b) consonant environments were used to assess intergestural overlap in two distinct cases, where consonant and vowel were articulated by the same articulatory system, i.e., the tongue, or by two different articulatory systems, i.e., the lips and the tongue, respectively. The embedded vowels were the point vowels /i/, /u/, /ɑ/. These vowels form maximally contrasting pairs in the $F2$ dimension, /i-a/ and /i-u/, thus they maximize the vowel effects on the schwa. Ten tokens of each utterance type were produced at normal and fast speaking rates. A total of 120 utterances (2 Consonants×3 Vowels×10 Repetitions ×2 Rates) were collected per speaker, yielding a total of 720 utterances.

Speakers were recorded using a Panasonic digital SV-255 tape recorder and a Shure SM-10 headband unidirectional microphone. A Radio Shack mini-microphone was attached with adhesive tape under the subject's nostrils to sample the nasal acoustic output. A digital metronome with both audible ticks and light flashes was used to induce faster speaking rates. Deaf participants relied on the light flashes. Metronome rate was set at 25% faster than the speaker's normal conversational rate. This percentage approximately matches the durational shortening obtained when speakers are asked to change from self-selected ''normal'' to ''fast'' speaking rates (Gay, 1981; Tuller *et al.*, 1982; Smith *et al.*, 1983).

C. Procedures

Recordings were made in sound-attenuated rooms. The utterance tokens were elicited in randomized order. The rate conditions were presented in alternating order across trial blocks, i.e., normal, fast, normal, fast. Initially, subjects read a set of instructions and were familiarized with the orthographic code for CVC nonsense words. Then, prior to the recording, they read some CVC utterances at random, at their normal, conversational rate, to ensure readiness, and to allow for an assessment of their normal rate by metronome. After the recording of the first trial block, the experimenter set the metronome at 25% faster than the speaker's normal rate. Subjects were asked to pace themselves to the metronome during a training period while practicing different utterances from the corpus of material. Once their pace was established (i.e., the stressed CVC word occurred at the same moment as the light flash), the metronome was switched off and recording of the second trial block began. The same procedure was repeated for the recording of the next two trial blocks. Subjects took a 5-min break in between trial blocks.

Tokens were generally not excluded from analysis based on their perceptual accuracy, except in two circumstances: (a) subjects corrected themselves, or (b) the experimenter did not observe visual evidence of consonantal closure in initial position, final position, or both. To avoid intrusive noise, subjects were cautioned to speak only after the page was flipped. During the recordings, the subject's speaking rate was checked periodically against its preset metronomic reading by the experimenter.

D. Data analysis

Utterances were played back from a Sony DAT Walkman TCD-D7 tape recorder and digitized at 12 500 samples per s using ''WAVEXAM,'' a speech editing and analysis program. Durational measurements were made using the WAVEXAM program. Frequency measurements were made on the Computerized Speech Lab (CSL) by Kay Elemetrics.

1. Measurement of durations

Five durational measurements were made in each utterance, the schwa, the ''closure,'' the CVC syllable, the stressed vowel, and the phrase. Figure 1 presents an example of waveform segmentation. The following segmentation rules were applied.

a. Schwa. The left and right cursors were placed at the onset and offset of complex periodic activity, respectively. The schwa offset was defined as the point at which complex periodic activity changed abruptly into a low-amplitude phonatory interval. In some samples, especially those of H3, the early part of the schwa contained several ms of aperiodic activity. In such cases, the spectrographic record was reviewed in order to determine the continuity of the formants

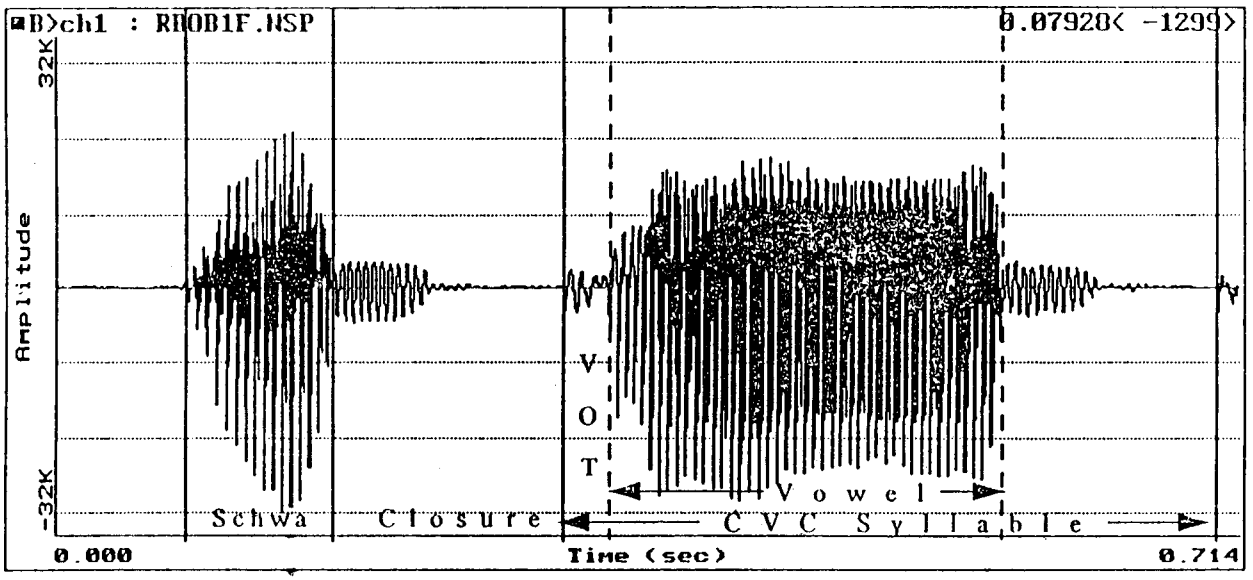

FIG. 1. The utterance /əbɑb/ by hearing speaker H2.

in the aperiodic portion of the schwa with the rest of the schwa. If there was continuity the schwa onset was set at the beginning of the aperiodic portion.

b. Closure. The closure boundaries were determined by placing the cursors between the schwa offset and the burst of the first consonant of the CVC syllable. It was initially assumed that this interval, apart from the consonant closure, may also contain a word boundary interval. Often a low-amplitude phonatory interval was included at the early part of the closure interval. It was inferred that, for a brief time, speakers continued phonating after their vocal tract was closed. In less than 3% of the cases, in which the burst could not be readily identified, the onset of periodic activity of the stressed vowel was used as the right-hand boundary.

c. Stressed syllable (CVC). This interval was defined by placing the cursors at the consonant release of the first and second consonants. The closure before the burst of the first consonant was not included because it was confounded with the word boundary interval. In 6% of the cases, mostly at the fast rate of hearing subjects, the consonant release of the second consonant was weak. In these cases, a judgment of the stressed syllable interval was made by referring to the waveform display and listening to the acoustic signal. The cursor was placed at a location indicating a change of amplitude in the waveform display.

d. Stressed vowel (V). The left and right cursors were placed at the onset and offset of complex periodic activity, respectively.

e. Phrase. This portion began at the onset of phonation in the schwa and ended at the offset of phonation of the alveolar nasal in ''again.''

2. Measurement of second formant frequency

Measurements were made at five locations throughout the disyllable /ə#CVC/: Schwa Onset (ə1), Schwa Midpoint (ə2), Schwa Offset (ə3), Transition Onset (Ton), and Stressed Vowel Midpoint (Vm). The Transition Onset was the point of onset of the second formant. In over 99% of cases, the vowel durational midpoint and $F2$ extreme value coincided. The extreme formant value was recorded in all cases, including those where the durational midpoint was slightly before vowel midpoint. Relative rather than absolute measurements were adopted because the amount of intersegmental overlap at fixed temporal points varies with the speaker's segmental durations.

To aid the reader in the analysis of gestural relations among CV sequences in the disyllabic utterance, we will alternatively refer to schwa offset as consonant constriction, to transition onset as consonant release, and to the interval between them as consonant closure. These acoustic locations will also serve as points of vocalic offset and onset, respectively.

A qualitative analysis for detection of oral formants was made for a given utterance type uttered by a single speaker. Printouts of wide-band spectrographic displays of all tokens of a given utterance type and speaking rate were obtained and inspected. Inspection of spectrographic displays obtained from the microphone placed under the subject's nostrils was used to rule out the presence of nasal formants in the examined region.

Second formant measurements were made by Fourier analysis, using a combination of wide-band spectrographic and discrete Fourier transform (DFT) analysis to resolve spectral ambiguities. The spectrographic analysis was conducted using a 4.0 ms (i.e., 50 samples/s) Hamming window with high frequency pre-emphasis. The DFT analysis was conducted using a 5.12 ms (i.e., 64 samples/s) or a 10.24 ms (i.e., 128 samples/s) Hamming window, depending on spectral resolution. Cursor placement was allowed to shift + or −2 glottal cycles in order to obtain accurate measurement.

Forty $F2$ measurements, equally balanced across the different measurement points of a disyllable, were measured from the CSL files by another observer, using the same measurement protocol. Six disyllables were randomly taken from

TABLE III. Means, standard deviations (in ms), and ratio of durations at normal rate for hearing speaker and at normal and fast rates for deaf speakers. The numbers in parenthesis correspond to the fast rate condition for deaf speakers. *Note*. CVC=consonant–vowel–consonant syllable. H=Hearing speaker. D=Deaf speaker.

		Schwa	Closure	Vowel	CVC	Phrase
H1	M	60	87	172	236	825
	s.d.	15	9	28	25	41
H2	M	52	112	226	303	1022
	s.d.	13	15	42	36	76
H3	M	47	85	161	223	783
	s.d.	15	8	22	21	29
D1	M	132 (72)	74 (63)	244 (123)	336 (180)	1167 (741)
	s.d.	27 (19)	13 (12)	5 (21)	47 (19)	100 (53)
	Ratio	0.54	0.85	0.51	0.53	0.63
D2	M	270 (121)	228 (154)	448 (292)	792 (486)	2277 (1488)
	s.d.	73 (88)	43 (28)	51 (52)	71 (78)	166 (106)
	Ratio	0.45	0.67	0.65	0.61	0.65
D3	M	133 (101)	104 (94)	216 (180)	366 (310)	1208 (1031)
	s.d.	18 (15)	12 (12)	29 (26)	35 (43)	88 (48)
	Ratio	0.76	0.90	0.83	0.85	0.85

the speech of deaf speakers and two disyllables were randomly taken from the speech of hearing speakers. The overall interobserver reliability was $r = +0.94$.

II. RESULTS

A. Durations

The durations of hearing speakers at normal rate were examined and compared with the durations of deaf speakers at normal and and fast speaking rates, respectively. Based on previous findings, showing that the speech of deaf speakers is slower than hearing speakers (Osberger and Levitt, 1979; Osberger and McGarr, 1982), the prediction was that the productions of deaf speakers at their fast rate would resemble the productions of hearing speakers at their normal rate with respect to phrase and segment durations.

All three deaf speakers produced significantly different durations (at all measured intervals of the utterance) at normal as opposed to fast rates, as indicated by the univariate results of 2×2×3 (Rate×Consonant Context×Vowel Context) Manovas, performed for each speaker (Okalidou, 1996). Exception was noted for speaker D3, where pairwise comparisons, using the Bonferroni correction ($a = 0.0167$), indicated that closure duration in disyllables containing the vowel [u] did not vary significantly as a function of rate [$F(1,107) = 3.568$; $p = 0.0616$ ns]. The statistical treatment and results are described in greater detail in the appendices to Okalidou's thesis (Okalidou, 1996).

Table III presents the means and standard deviations of the durations of schwa, closure, stressed vowel, CVC syllable, and phrase, at normal rate for hearing speakers and at normal and fast rates for deaf speakers, together with their ratio of durations at fast over normal rate. Comparisons of the durations across hearing status at normal rate showed that the deaf speakers had longer schwa, closure, and CVC durations than hearing speakers. This finding conforms with earlier findings.

A comparison of the durations of the hearing speakers at normal rate with the durations of the deaf speakers at fast rate indicated that: (a) the CVC syllable and phrase durations for D1 at fast rate fell within the range of the hearing speakers at normal rate, while D3 was only slightly longer; (b) D2's CVC and phrase durations at fast rate were still substantially longer than the hearing speakers; and (c) the deaf speakers uniformly showed longer schwa durations than hearing speakers. For the same comparison, the durations of segments were normalized for subject differences in disyllable duration, by dividing the mean durations of the schwa, closure, and CVC by the total duration of the disyllable /ə#CVC/, as averaged across consonant and vowel contexts. The derived values yielded the proportion of the total disyllable (/ə#CVC/) duration taken by the schwa, closure, and CVC and were plotted in Fig. 2, as percentages of the mean disyllable duration, across vowel, and consonant contexts, for each speaker. As seen in Fig. 2, the relative CVC durations of deaf speakers at fast rate were similar to the ones of hearing speakers at normal rate. Moreover, deaf speakers showed longer relative schwa durations and shorter relative closure durations than the hearing speakers. Based on the shorter relative closure durations for the deaf compared to

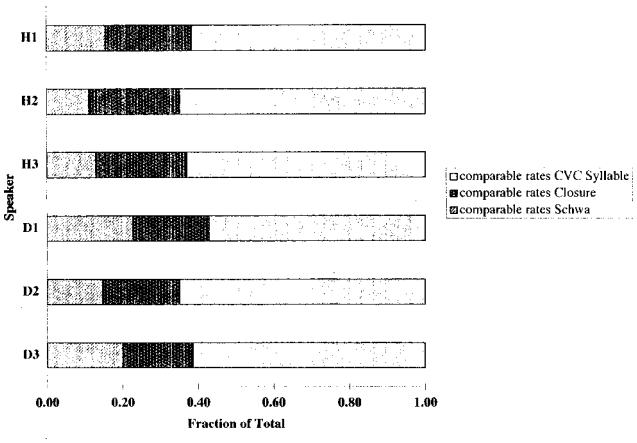

FIG. 2. Mean schwa, closure, and stressed syllable (CVC) durations as a percentage of the mean total duration of the disyllable /ə#CVC/. Data for hearing and deaf speakers at normal and similar rates, i.e., normal rate for hearing speakers and fast rate for deaf speakers.

TABLE IV. Average durations (in ms) of disyllables for hearing speakers at normal rate and for deaf speakers at normal and fast rates. The means in parenthesis correspond to the fast rate condition for deaf speakers. The ratio of fast over normal rate for each disyllable type is given for deaf speakers. *Note*. The ratio of durations at fast over normal rates indicates the durational change at fast rate. H=hearing speaker; D=deaf speaker; N=normal speaking rate; F=fast speaking rate; /ə/=schwa; V=vowel. Columns labeled ''əbVb'' and ''ədVd'' contain mean durations of disyllables pooled over vowel context [i], [u], [ɑ].

		əbib	əbub	əbɑb	əbVb	ədid	ədud	ədɑd	ədVd
H1	M	292	274	310	292	292	284	322	299
H2	M	347	341	357	348	351	349	390	363
H3	M	273	262	278	271	259	259	291	269
D1	M	458 (253)	456 (245)	460 (233)	458 (244)	479 (260)	475 (255)	481 (264)	478 (260)
	Ratio	0.55	0.54	0.51	0.53	0.54	0.54	0.55	0.54
D2	M	1036 (569)	1068 (612)	1010 (550)	1038 (577)	1105 (626)	1083 (618)	1070 (603)	1086 (638)
	Ratio	0.55	0.57	0.54	0.56	0.57	0.57	0.56	0.59
D3	M	539 (409)	519 (447)	469 (393)	509 (416)	504 (418)	488 (420)	478 (383)	490 (407)
	Ratio	0.76	0.86	0.84	0.82	0.83	0.86	0.80	0.83

the hearing speakers, it is safe to conclude that the deaf speakers did not exhibit abnormal pausing at the word boundary compared to their hearing counterparts.

The durations of disyllables as a function of consonant context, i.e., /əbVb/ vs /ədVd/, were examined. Table IV lists the average durations of each of the six disyllable types as well as the /əbVb/ and /ədVd/ duration means for each speaker, at the specified rates. An inspection of Table IV indicates that there appeared to be no systematic differences between alveolar and bilabial disyllable durations for any speaker at the specified rates. Table V lists the average schwa durations in alveolar and bilabial disyllables for each speaker at the specified rates. Again, no systematic pattern of shorter schwa durations in one context than another was discerned, for either the deaf or the hearing speakers. It is concluded that the hearing and deaf speakers in this study did not exhibit context-specific durational changes.

B. Intervocalic effects

The effect of the stressed vowel on the schwa was assessed as a function of (a) phonetic context, comparing bilabial disyllables (/əbVb/) with alveolar disyllables (/ədVd/) uttered by hearing and deaf speakers and (b) speaker group, comparing disyllables uttered by hearing speakers at normal rate with ones uttered by deaf speakers at fast rate. Those rates presumably would yield similar segment and syllable durations. The vowel effect on the schwa was calculated by comparing disyllabic minimal pairs contrasting in vowels, e.g., /əbib/ vs /əbub/. The $F2$ difference at schwa onset, schwa midpoint, and at schwa offset between disyllable pairs served to estimate the magnitude of vowel effects on the schwa.

1. Intervocalic effects at normal rate for both speaker groups

Pairs with maximally contrasting vowels in the $F2$ dimension, [i]-[u] and [i]-[ɑ], were studied to infer lingual front/back effects on the schwa. Four pairs of disyllable contrasts were examined, two for each consonantal frame, i.e., /əbib/ vs /əbub/, /əbib/ vs /əbɑb/, /ədid/ vs /ədud/, and /ədid/ vs /ədɑd/.

The $F2$ means among contrasting /əbVb/ pairs are plotted in the top and middle panels of Fig. 3, respectively, for deaf and hearing speakers. The greater the $F2$ difference at a given point the greater the coarticulation at that point. The hearing speakers showed greater [i]-[u] and [i]-[ɑ] differences during the schwa than deaf speakers, as indicated by the first three measurement points

A 2×3 multivariate factorial analysis (MANOVA) for each speaker was performed. Each 2×3 MANOVA examined the $F2$ means at five measurement points as a function of consonant (b_b and d_d) and vowel context ([i], [u], [ɑ]). Univariate analyses for all six Manovas yielded significant main effects of consonant and vowel contexts as well as

TABLE V. Average schwa durations (in ms) for hearing speakers at normal rate and for deaf speakers at normal and fast rates. The means in parenthesis correspond to the fast rate condition for deaf speakers. The schwa ratio at fast over normal rate for each disyllable type is given for deaf speakers. *Note*. The ratio of schwa durations at fast over normal rates indicates the durational change at fast rate. H=hearing speaker; D=deaf speaker; N=normal speaking rate; F=fast speaking rate; /ə/=schwa; V=vowel. Columns ''əbVb'' and ''ədVd'' contain mean schwa durations pooled over vowel context [i], [u], [ɑ].

Ss		əbib	əbub	əbɑb	əbVb	ədid	ədud	ədɑd	ədVd
H1	M	64	58	50	57	60	69	57	62
H2	M	55	56	49	53	46	56	53	51
H3	M	49	41	37	42	55	53	49	52
D1	M	138 (72)	118 (70)	122 (60)	126 (68)	148 (77)	137 (79)	129 (71)	138 (76)
	Ratio	0.52	0.60	0.50	0.54	0.52	0.58	0.55	0.55
D2	M	260 (98)	256 (95)	248 (101)	255 (98)	334 (224)	280 (109)	288 (116)	(301) 150
	Ratio	0.38	0.37	0.41	0.38	0.67	0.39	0.40	0.50
D3	M	137 (89)	129 (103)	134 (118)	134 (103)	136 (95)	136 (105)	126 (99)	133 (99)
	Ratio	0.65	0.79	0.88	0.77	0.69	0.77	0.79	0.75

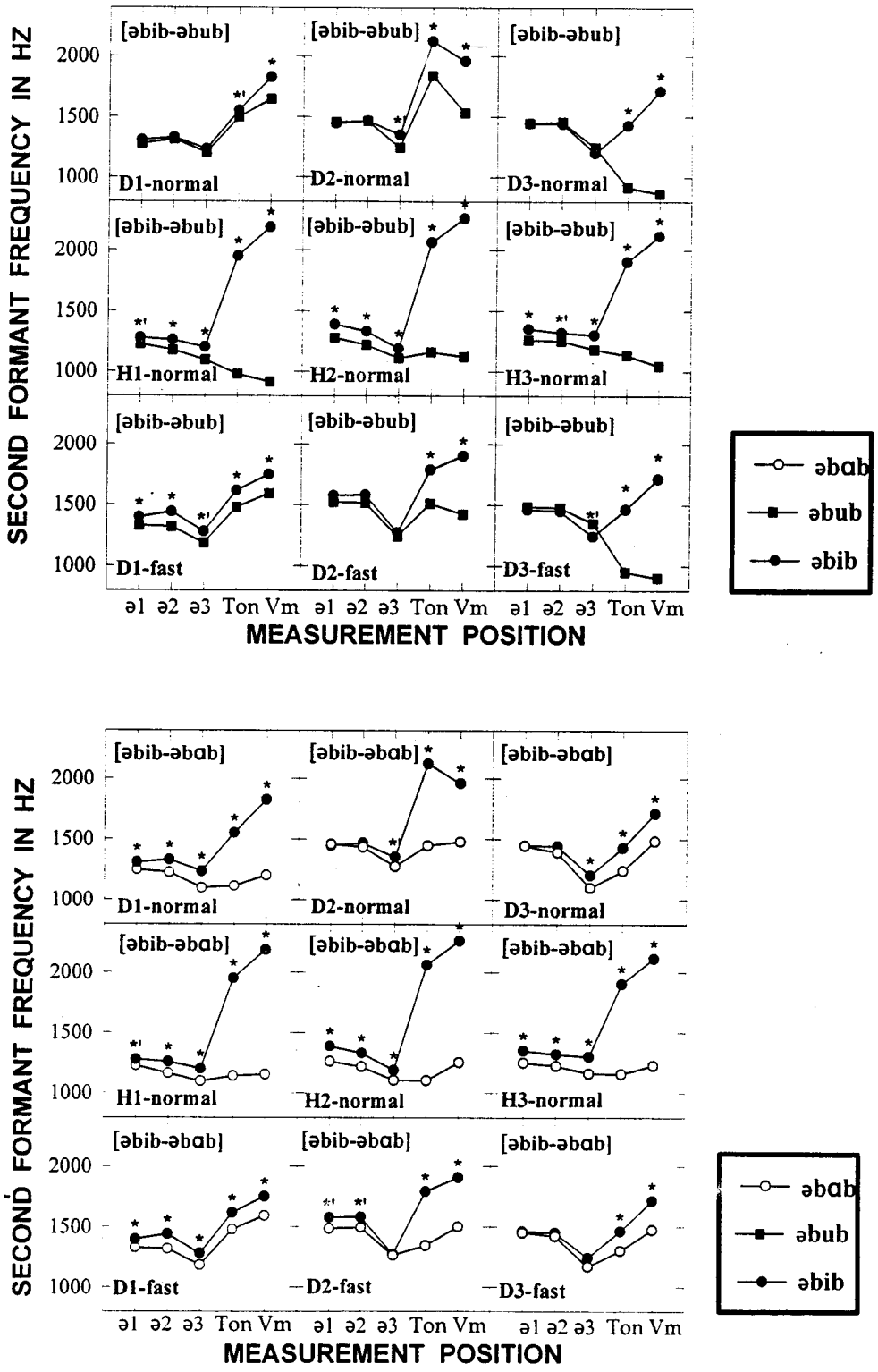

FIG. 3. $F2$ means at five measurement points (ə1=schwa onset; ə2=schwa midpoint; ə3=schwa offset; Ton =transition onset; Vm=vowel midpoint) of bilabial disyllables contrasting in vowel context. Data are shown for hearing and deaf speakers at normal and similar rates. The asterisks show significance at $p=0.005$ level; the symbols (*′) show significance at $p=0.0599$ level.

significant consonant context×vowel context interactions for at least some of the $F2$ values of the disyllable unit. Since both the main effects and the interactions were statistically significant, emphasis was placed on the pairwise comparisons between disyllables where effects were looked at separately for each consonant–vowel combination.

Pairwise comparisons among the $F2$ means of /əbV$_1$b-/əbV$_2$b/ pairs were calculated, using the Bonferroni correction ($a=0.0056$).[1] The measurement points at which the $F2$ means of a given disyllable pair were significantly different are noted with the symbol ‘‘*’’ in Fig. 3. In bilabial disyllables, the $F2$ means at schwa onset, midpoint, and offset for all three hearing speakers were significantly different; however, only D1 exhibited significantly different $F2$ means, as early as schwa onset, in /əbib/ vs /əbɑb/ disyllables.

The $F2$ means for contrasting /ədVd/ pairs are plotted in the top and middle panels of Fig. 4, respectively, for deaf

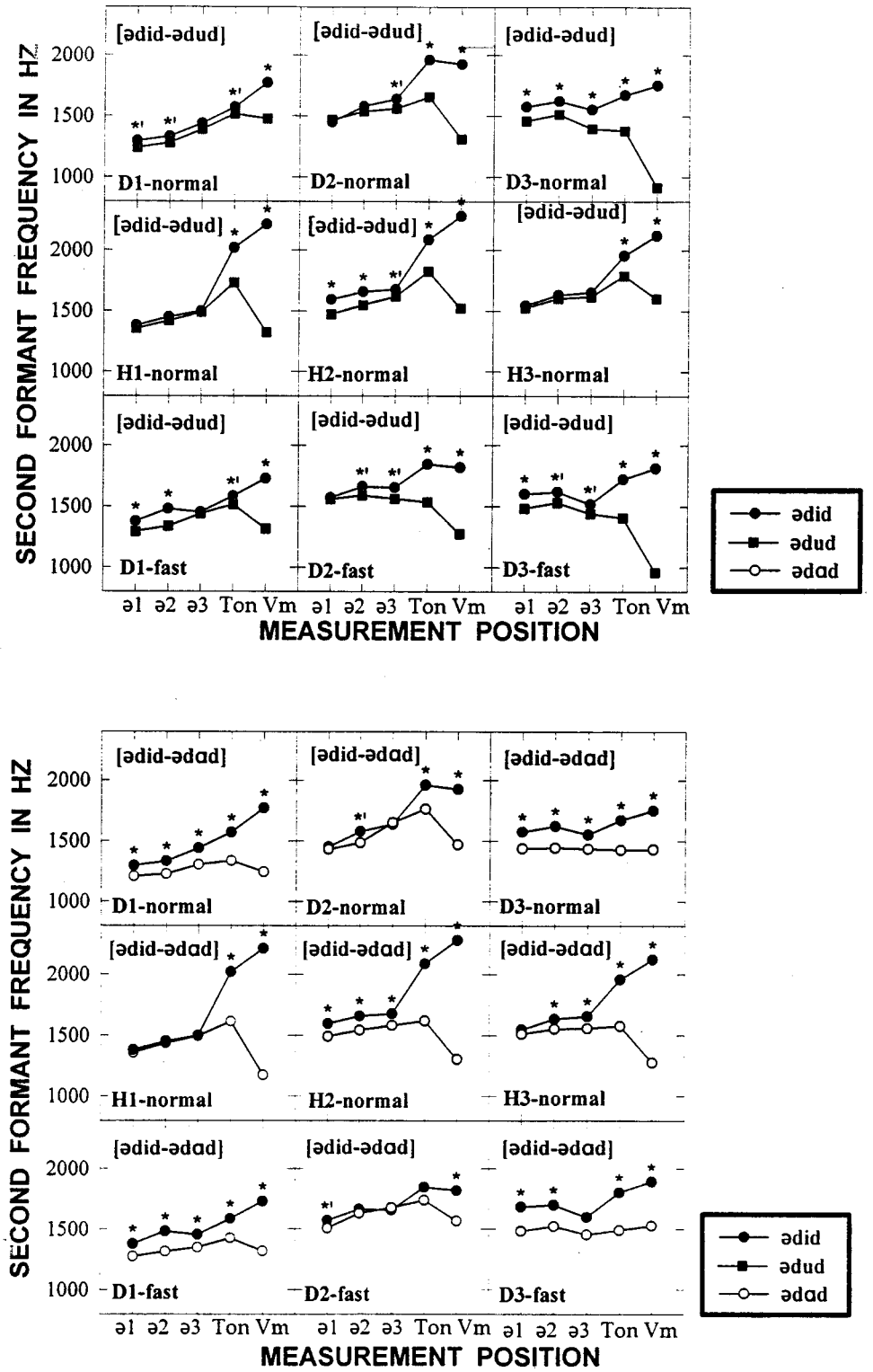

FIG. 4. $F2$ means at five measurement points (ə1=schwa onset; ə2=schwa midpoint; ə3=schwa offset; Ton =transition onset; Vm=vowel midpoint) of alveolar disyllables contrasting in vowel context. Data are shown for hearing and deaf speakers at normal and similar rates. The asterisks show significance at $p=0.005$ level; the symbols (*′) show significance at $p=0.0599$ level.

and hearing speakers. Pairwise comparisons between the $F2$ means of /ədV$_1$d-ədV$_2$d/ pairs were calculated, using the Bonferroni correction ($a=0.0056$) for determination of the significance level. The deaf speakers tended to show greater /i-u/ and /i-ɑ/ differences during the schwa than hearing speakers, as revealed by the stars in Fig. 4 which indicate statistical significance. For two deaf speakers (D1 and D3), the $F2$ means between /ədVd/ pairs were significantly different as early as the schwa onset; one hearing speaker, H2, showed the same effect. Similarly, for the third deaf speaker (D2), the comparison between the $F2$ means already approached significance at schwa offset in /ədid-ədud/, while H1 and H3 did not show the effect until the consonant release (Ton).

Overall, the vowel effects on the preceding schwa were greater for the hearing than the deaf speakers in /əbVb/ disyllables and tended to be greater for the deaf than the hearing speakers in /ədVd/ disyllables, although one hearing

speaker matched the prevailing pattern of the deaf speakers. The tendency for greater vowel-to-vowel influences in alveolar disyllables for the deaf than the hearing speakers, although present, is not readily generalizable because of the small sample size used. However, it is safe to conclude that the deaf speakers did not exhibit reduced intervocalic coarticulation in alveolar disyllables. Finally, there were no systematic durational differences within groups that could account for the coarticulatory differences observed across contexts, that is, the durations of disyllables did not vary as a function of bilabial versus alveolar context.

2. Intervocalic effects at similar rates across speaker groups

The question addressed was whether coarticulation patterns across hearing status become more alike as differences in segment durations diminish. The disyllables uttered at normal rate by hearing speakers were compared with the disyllables uttered at fast rate by deaf speakers.

The overall pattern was similar to the one noted at normal rate, i.e., the hearing speakers showed greater vowel effects on the schwa than deaf speakers, although small increases of schwa–vowel effects were noted for two deaf speakers. The middle and bottom panels of Fig. 3 show the $F2$ means, at five measurement points, for /əbVb/ pairs (i.e., for /əbib-əbub/ and /əbib-əbɑb/ contrasts), at similar rates.

For all hearing speakers, the $F2$ means among /əbVb/ pairs were significantly different as early as the schwa onset. D1's fast productions resembled the hearing pattern even more than his normal productions, i.e., the $F2$ means of both /əbib-əbub/ and /əbib-əbɑb/ pairs were significantly different as early as the schwa onset. D2's /əbib-əbɑb/ pair also resembled the hearing pattern, i.e., the comparison between $F2$ means approached significance as early as the schwa onset. The greater $F2$ differences during the schwa, in these two deaf speakers, are primarily due to greater [i] than [ɑ] effects on the schwa, as indicated by the greater raising of $F2$ values before [i] than before [ɑ] in the fast (bottom panel of Fig. 3) as compared with the normal (top panel of Fig. 3) utterances.

For alveolar disyllables, the effects at similar rates are in the same direction and slightly stronger than the ones noted at normal rates, i.e., the deaf speakers tended to show greater vowel effects on the schwa than the hearing speakers. The middle and bottom panels of Fig. 4 show the $F2$ means, at five measurement points, for /ədVd/ pairs (i.e., for /ədid-ədud/ and /ədid-ədɑd/ contrasts) at similar rates. Deaf speaker D2 (/ədid-ədud/ and /ədid-ədɑd/), and to a smaller extent, deaf speaker D1 (/ədid-ədud/) exhibited increased $F2$ differences in the schwa as a function of increased speaking rate. The increased $F2$ differences were mostly due to increased [i] effects on the schwa. For the deaf speakers, in five out of six cases, the $F2$ means were significantly different as early as the schwa onset; only one hearing speaker, H2, showed the same effect. D2 showed significant vowel differences as early as the schwa onset in /ədid-ədɑd/, but the effects were not significant at schwa midpoint and at schwa offset. This is a case in which the demands of the upcoming consonant and vowel on the articulators are antagonistic because of the front constriction for /d/ versus a back constriction for /ɑ/. In conclusion, the overall trends noted at normal rate were also noted at similar rates, i.e., hearing speakers showed greater vowel effects on the schwa than deaf speakers in /əbVb/ contexts and deaf speakers tended to show greater vowel effects on the schwa than hearing speakers in /ədVd/ contexts. As seen above for any given rate, duration differences of disyllables as a function of bilabial versus alveolar context could not account for the coarticulatory differences observed.

We also observed that there was an overlap in the coarticulatory patterns of deaf and hearing speakers, in that, the ''deviant'' pattern in /ədVd/ was also exhibited by one hearing speaker and the ''normal'' pattern in /əbVb/ was also exhibited by one deaf speaker. This indicates that interspeaker differences in coarticulation may span across the notion of a ''normalcy'' boundary and that perceptually incorrect utterances may be a composite of several ''deviant'' productions or coproduction patterns within one speaker.

C. Consonant to vowel effects

The effects of consonant on the schwa and the stressed vowel were assessed at normal and at similar rates, in disyllabic minimal pairs contrasting in consonants (/əbib-ədid/, /əbub-ədud/, and /əbɑb-ədɑd/). The greater the $F2$ difference between the minimal pairs at a given measurement point, the greater the consonant–vowel overlap within at least one of the disyllables of the pair. The effects of the consonant on the schwa were examined at schwa onset and schwa midpoint; the effects of consonant on the stressed vowel were examined at vowel midpoint; finally, the spectral effects of consonant closure were examined at consonant constriction and release.

1. Effects across speaker groups at normal rates

There was more evidence of consonantal influence on the schwa in the productions of the hearing speakers than in the productions of the deaf speakers. Also, the hearing speakers showed marked consonant effects on the [u] center as opposed to the deaf speakers whose consonant effects at vowel midpoint were reduced or idiosyncratic. The $F2$ means of contrasting /əbVb/-/ədVd/ pairs are plotted in Fig. 5.

Statistically significant patterns (using the Bonferroni correction, $a=0.0056$) were obtained from pairwise comparisons of 2×3 multivariate analyses (MANOVAS), one for each speaker, where the $F2$ means at five measurement points were examined as a function of consonant (b_b, d_d) and vowel context ([i], [u], [ɑ]). The measurement points at which the $F2$ means of the disyllable pair were significantly different are noted with stars in Fig. 5. Note, again, that the pairwise comparisons between the $F2$ means of disyllable pairs were performed because all six 2×3 Manovas yielded significant consonant context×vowel type interactions.

With respect to the consonant effects on the schwa, all three hearing speakers exhibited significantly different $F2$ means between /əbVb/-/ədVd/ contrasts as early as the schwa onset as opposed to only one deaf speaker, D3, who showed similar effects in one context, /əbib/-/ədid/. It is con-

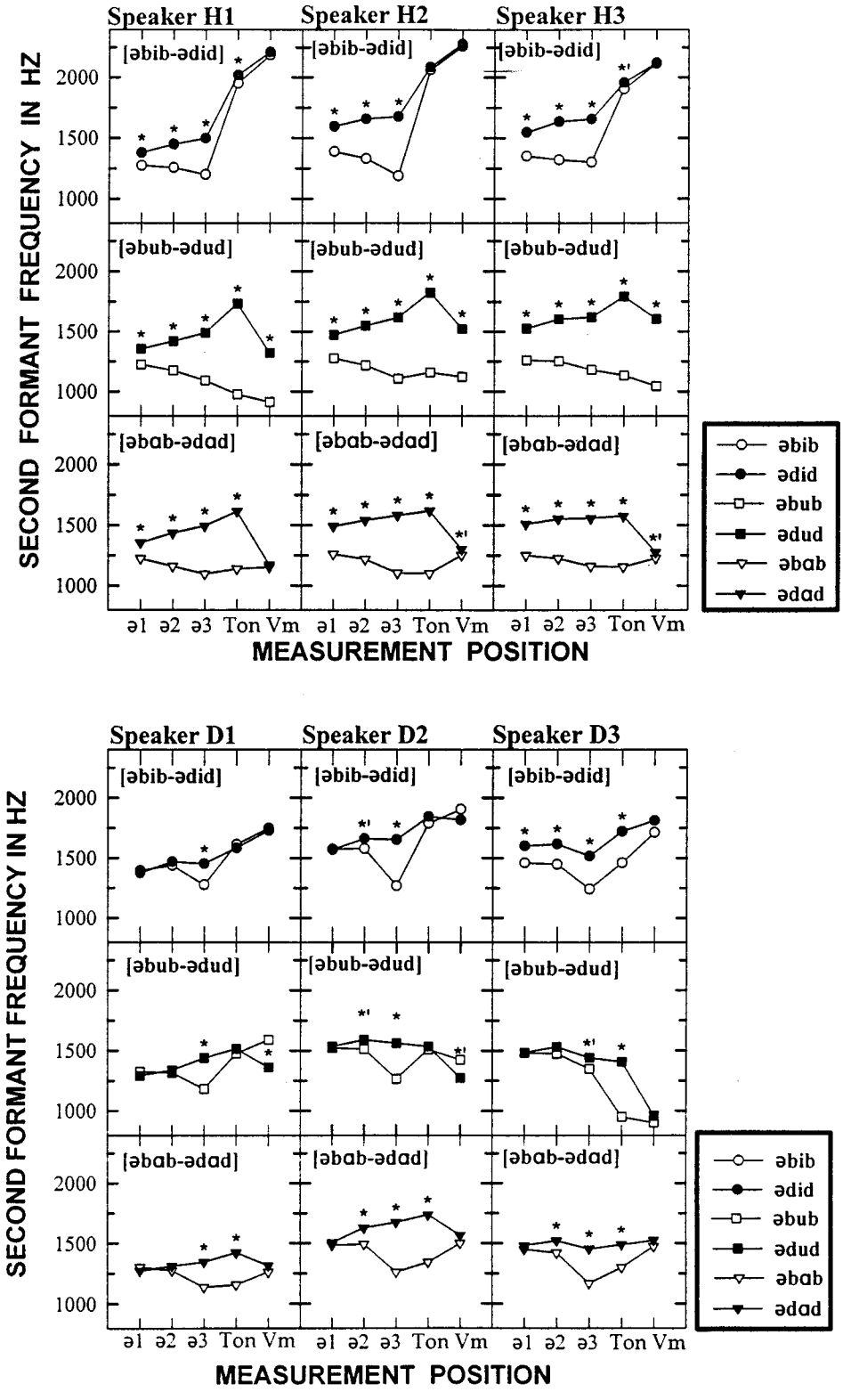

FIG. 5. $F2$ means at five measurement points (ə1=schwa onset; ə2=schwa midpoint; ə3=schwa offset, Ton =transition onset, Vm=vowel midpoint) of disyllables contrasting in consonant context. Data are shown for hearing and deaf speakers at normal and similar rates. The asterisks show significance at $p=0.005$ level; the symbols (*′) show significance at $p=0.0599$ level.

cluded that hearing speakers begin movement toward consonant constriction earlier than the deaf speakers.

With respect to the consonant effects on the stressed vowel midpoint, all hearing speakers displayed significantly different $F2$ means for /bub/-/dud/ pairs: The $F2$ values for /dud/ were higher than for /bub/. This pattern suggests interaction of the tongue dorsum ([u] constriction) with the tongue blade (/d/ contact) so that the [u] constriction is shifted anteriorly. In contrast, deaf speakers showed less systematic consonant effects on the stressed vowel midpoint. D1 and D2 had higher $F2$ at [u] centers in bilabial than alveolar contexts, while D3 showed a tendency for higher $F2$ at [u] centers in alveolar than bilabial contexts.

With respect to the effects of consonant context we note that at consonant release, hearing speakers uniformly showed significantly different $F2$ means among disyllable pairs containing back vowels (/əbub-ədud/, /əbɑb/-/ədɑd/). Deaf speakers also showed significantly different $F2$ means at

consonant release that were consistent for the /əbɑb/-/ədɑd/ pair only. Thus the hearing speakers contrasted bilabial and alveolar consonant releases before back vowels, while the deaf speakers showed consistent effects of consonant release only before the low vowel [ɑ] for which tongue and jaw were both lowered; before high vowel [u], which calls for tongue/jaw raising immediately after the lowering of jaw/tongue for consonant release, consonant effects were less consistent in the deaf speakers.

From all of the above, it is concluded that the productions of the deaf speakers, when compared to those of the hearing speakers at normal rate, generally entailed a deviant pattern of consonant–vowel coproduction, which was characterized by a lack of differentiation of tongue from jaw movements or of tongue dorsum from tongue blade movements.

2. Effects across speaker groups at comparable rates

The disyllables uttered at normal rate by hearing speakers were compared with the disyllables uttered at fast rate by deaf speakers. The consonant effects on the schwa and the stressed vowel across hearing status were very similar to the ones noted at normal rates. The $F2$ means of contrasting /əbVb/-/ədVd/ pairs for each speaker are plotted in Fig. 6. The stars in Fig. 6 show the significant patterns from pairwise comparisons (using the Bonferroni correction) of a $2\times2\times3$ multivariate factorial analysis (MANOVA), computed for each speaker, where the $F2$ means between contrasting disyllables were examined as a function of rate, consonant context, and vowel context. It can be readily seen that all hearing speakers exhibited significantly different $F2$ means as early as schwa onset whereas only D3 in /əbib/-/ədid/ resembled the hearing pattern. Some changes were noted for D2, where the aberrant consonant effects at consonant release and at vowel midpoint for /əbib/-/ədid/ and /əbub/-/ədud/ decreased with increases in rate. It was concluded that hearing speakers have more pronounced and consistent effects of consonant context on the vocalic segments of disyllables /əCVC/ than deaf speakers, at both normal and at similar rates.

3. Some observations across rates

Deaf speakers overall showed smaller $F2$ differences at the vowel midpoints across contexts than hearing speakers (Figs. 3, 4, 5, 6), indicating that they have aberrant vocalic centers. This finding conforms with previous studies (Rubin, 1985; Shukla, 1989; Subtelny *et al.*, 1992) which demonstrated that deaf speakers have a somewhat neutralized vowel space.

A striking aspect of Figs. 5 and 6 is that the $F2$ patterns of deaf speakers showed discontinuities in their progression from the schwa to the stressed syllable, such as reversals in contextual order (e.g., for deaf speaker D1, $F2$ in /əbub/ is lower than /ədud/ at consonant constriction and higher than /ədud/ at vowel midpoint). Such discontinuities were not present in the $F2$ patterns of hearing speakers. This indicates that during the schwa, hearing speakers have more precise control of the direction of the tongue and jaw movements toward the consonant and following vowel.

Another important observation from Figs. 5 and 6 is that there were qualitative differences in the $F2$ trajectories between /d/ constriction and /d/ release in /ədud/ across hearing status. Hearing speakers exhibited sharp positive $F2$ slopes whereas deaf speakers did not. These acoustic differences suggest differences across hearing status in /d/ articulation for the [u] context.

III. DISCUSSION

Previous studies have employed prelingually deaf speakers with either a wide range of hearing losses or with losses at the higher end of the profound category, and design choices that maximize intersubject variability in speech performance (Boothroyd, 1985). In this experiment, a small sample of deaf adult speakers was employed to investigate patterns of coarticulation. Stringent audiological criteria were employed, which lead us to presume that speech acquisition took place with minimally useful residual hearing, and that the coarticulatory patterns of the deaf speakers in this sample did not reflect substantial auditory monitoring.

A drawback of the present sample apart from its small size was the age difference between deaf and hearing speakers. The deaf speakers were on the average older than the hearing speakers. Studies (Smith *et al.*, 1987; Yorkston and Beukelman, 1981) on healthy aging have shown that older subjects speak at a slower rate than younger subjects. With respect to the deaf subjects in this sample, however, both the younger (D1) and the older (D3) subject spoke at a slower rate relative to their hearing counterparts, indicating what has been previously reported by other studies (Osberger and Levitt, 1979; McGarr and Osberger, 1982), that deaf speakers generally speak at slower rates than hearing speakers. Nevertheless, it is possible that age could have limited the ability of the oldest subject (D3) to speed up at the fast rate.

Both hearing and deaf speakers exhibited a great amount of variability in their coarticulation patterns. For example, H1 showed no vowel-to-schwa influences in alveolar disyllables, whereas H2 showed effects as early as the schwa onset (Fig. 3). Alternatively, D1, at normal rate, showed a vowel influences during the schwa in /əbib-əbab/ whereas D2 and D3 did not. Furthermore, the speech intelligibility profiles of deaf speakers provided some indications toward the resemblance of their coarticulatory patterns to the hearing pattern. The most intelligible deaf speaker, D1, who also had an early and consistent history of amplification and used oral speech as the only mean of communication, resembled the hearing pattern more in his coarticulation patterns than the other deaf speakers, especially when speeding up.

A. Gestural patterns in deaf versus hearing adult speakers

1. Intervocalic effects

The findings of the present study modify the conclusion drawn from previous studies that deaf speakers' productions are consistently less coarticulated than normal (Monsen, 1976; Rothman, 1976; Waldstein and Baum, 1991). Previous

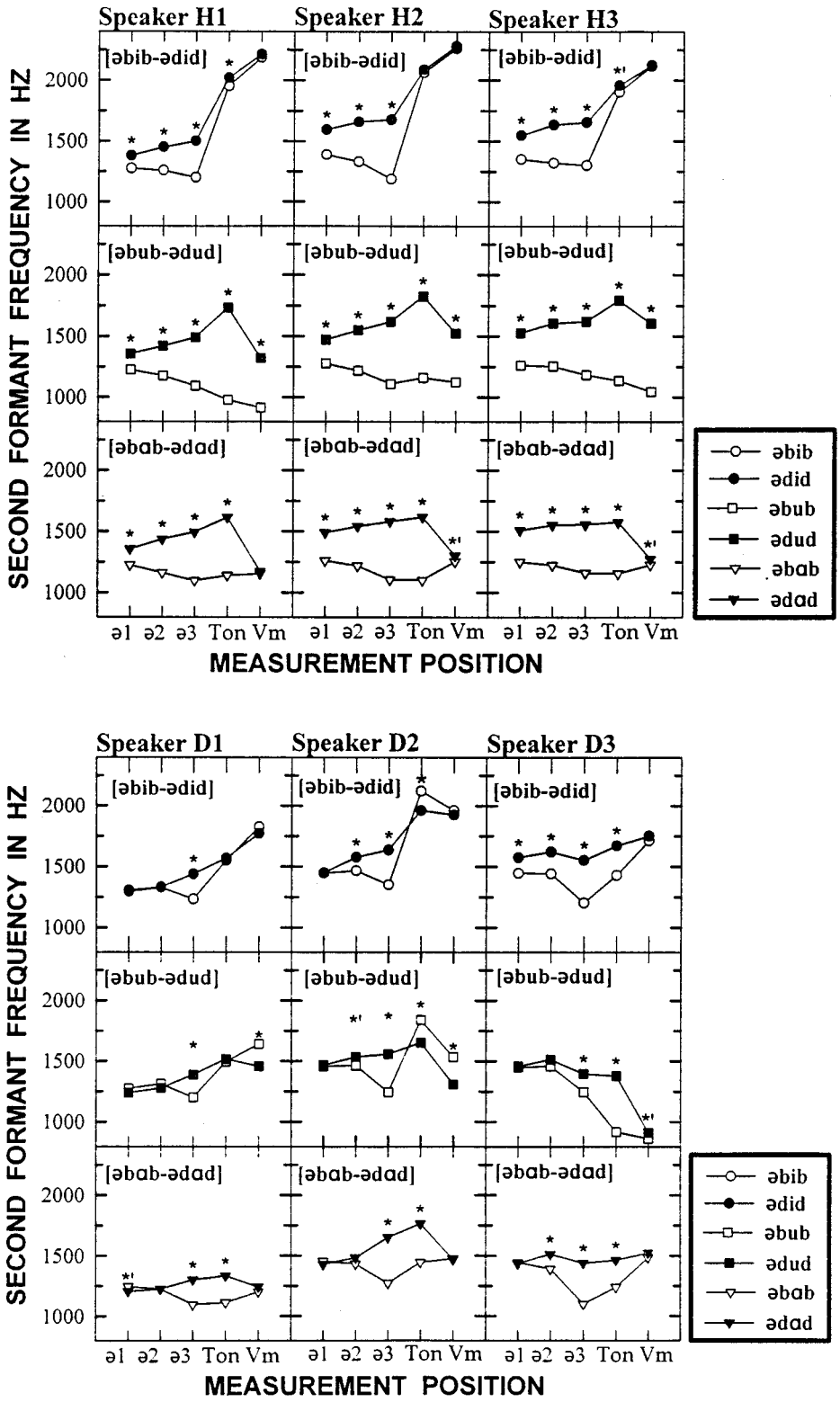

FIG. 6. *F*2 means at five measurement points (ə1=schwa onset; ə2=schwa midpoint; ə3=schwa offset; Ton =transition onset; Vm=vowel midpoint) of disyllables contrasting in consonant context. Data are shown for hearing and deaf speakers at similar rates. The asterisks show significance at $p=0.005$ level; the symbols (*′) show significance at $p=0.0599$ level.

studies, examining the formant paths contained within the CV syllable unit alone, indicated that deaf speakers show reduced anticipation of upcoming vowel constrictions at the vowel onset or immediately before it. An investigation over a larger utterance span, i.e., disyllables /ə#CVC/, in this study, revealed that deaf speakers, in fact, may show influences of the stressed vowel (/i/, /u/, /ɑ/) as early as the schwa. For certain phonetic contexts (ə#dVd), two of the three deaf speakers did not exhibit reduced intervocalic coarticulation relative to the hearing pattern but rather a tendency for greater stressed vowel effects on the schwa than the hearing speakers. The fact that deaf speaker D2 did not show similarly strong vowel effects on the schwa as the other two deaf speakers at normal rate may be related to her overall much slower rate compared to them; once her rate increased significantly, D2 showed more comparable vowel effects on

the schwa to the other deaf speakers. In conclusion, the temporal extent of intervocalic overlap differed across hearing status depending on the phonetic composition of the disyllable (bilabial versus alveolar context). The data of the present study were based on a small number of subjects, thus caution should be used in generalizing the results over the population of deaf speakers, particularly the ones that do not have closely similar audiological profiles.

2. Consonant-to-vowel effects

All hearing speakers showed greater consonant influences than deaf speakers during the schwa. Deaf speakers, on the other hand, exhibited interspeaker variability in the temporal extent of consonant influences during schwa. Overall, deaf speakers showed less marked, sometimes aberrant, consonant effects at the [u] center compared to hearing speakers. The hearing pattern in this study, i.e., the anterior shift of tongue dorsum constrictions ([u]) as a result of coarticulation with the tongue blade (/d/), is in agreement with Goodell's (1991) results showing that normal adults shift the [u] center toward the alveolar place of articulation of sibilant /s/, in /susu/ utterances. On the other hand, only one deaf speaker, D3, showed /d/ effects on the [u] center that were of small magnitude, whereas two deaf speakers, D1 and D2, seemed to place the tongue dorsum ([u] constriction) more anteriorly in bilabial than in alveolar contexts.

Thus deaf speakers showed less coarticulation during consonant-to-vowel coproduction relative to the hearing speakers. In the case of /ədud/, they tended to preserve the [u] ''target'' instead of showing /d/ effects on the [u] center, possibly because their lingual productions were less diversified into the component gestures, i.e., tongue blade and tongue dorsum. Furthermore, in the case of /əbub/, they had difficulty coordinating the actions of independent articulators, such as the lips and the tongue, for CV production. These findings are in agreement with previous studies (Rothman, 1976) which showed reduced consonant effects on vocalic centers in the speech of deaf speakers.

3. Vowel-to-consonant effects

Differences in vowel-to-consonant coarticulation across hearing status were inferred from looking at the spectral effects of consonant release (measurement point ''transition onset''). For disyllable pairs containing back vowels (/əbɑb/-/ədɑd/, /əbub/-/ədud/), deaf speakers exhibited reduced consonant effects at consonant release. Because the measurement point ''transition onset'' represents the spectral effects of both consonant release and vowel onset, one can conclude that the deaf speakers showed reduced consonant effects due to greater vowel influences at that measurement point. Other studies, however, have not reached a similar conclusion with respect to vowel-to-consonant influences in the speech of deaf speakers. Waldstein and Baum (1991) observed opposite effects in another context (/kV/), where deaf children failed to show spectral effects of /k/ fronting in /ki/ relative to /ku/ syllables. These discrepancies in the coarticulatory patterns could be attributed to a number of factors, such as differences in age, context, or learning effects. Alternatively, according to the gestural framework, these effects on segmental structure may denote larger underlying production units, that is, a single gesture rather than abnormal overlap between two temporally distinct, articulatory constrictions. In any case, one should keep in mind that the constriction locations of the vowels of deaf speakers, in this and other studies, are different from the hearing norm; thus the functional constraints of the deaf production system, and its coarticulation principles must be different.

4. Consonant and vowel production

The differences in vowel production across hearing status seen in the present study are on a par with earlier findings (Rubin, 1985; Shukla, 1989; Subtelny *et al.*, 1992) which showed that deaf speakers produce somewhat centralized vowels. However, in this study, the deaf speakers also made less adequate consonant constrictions than their hearing counterparts in /ədud/ and /ədid/. As seen in Figs. 3 and 4, the $F2$ trajectories of deaf speakers tended to be relatively flat between consonant constriction and release, while hearing speakers displayed a sharp increase over this interval. A higher $F2$ at /d/ release than at /d/ constriction in /ədud/ for hearing speakers indicates tongue fronting during /d/ closure which is not related to the following vowel—the longer relative consonant closures in hearing than deaf speakers are consistent with the presence of substantial lingual movement during closure for hearing speakers. On the other hand, the similar $F2$ values at /d/ constriction and at /d/ release in /ədud/ for deaf speakers indicate that tongue positions are more similar, perhaps reflecting a flatter contact area.

This finding, coupled with the weak consonant effects on the [u] center, suggests a pattern of consonant–vowel coproduction for deaf speakers where vowel precision and, even more so, consonant precision are compromised as a result of less differentiated gestural patterns. We assume that consonant precision is compromised more than the vowel precision because consonant effects were weak across the board whereas vowel effects were more often present. Note that a flatter tongue contact can also be inferred for /ədɑd/ compared to /ədud/ productions in hearing speakers, perhaps reflecting, in this case, incipient lowering and backing of the tongue body before /ɑ/.

5. Effects of speaking rate on coarticulation

The findings on the effects of rate on coarticulation did not validate the hypothesis that the faster productions of deaf speakers will result in greater coarticulation and will resemble the patterns of hearing speakers. The overall coarticulatory differences observed across hearing status at normal rate remained unaltered across speaking rates. Only small effects occurred in the direction of increased coarticulation as a function of increased rate, namely, intervocalic coarticulation increased for deaf speakers D1 and D2 for certain bilabial and alveolar disyllables. Furthermore, the increased rate had the effect of reducing the aberrant coarticulatory patterns in one deaf speaker D2, i.e., the effects of bilabial consonant on vocalic centers.

B. Gestural organization in deaf versus hearing speakers

The results of the present study cannot be altogether accounted for simply by differences in articulatory posturing or by differences in speaking rate between the two groups of speakers. With respect to articulatory posturing, the differences in consonant production across hearing status were not exhibited in every context, for example, in /ədɑd/, both hearing and deaf speakers exhibited little evidence of forward tongue movement (as indicated by $F2$ increase) during the alveolar closure. In addition, the differences in vowel constrictions (i.e., at the stressed vowel midpoint of disyllables) across hearing status did not determine the extent of intervocalic influences, at least for alveolar disyllables. One would expect that since deaf speakers produced more neutralized vowels compared to the hearing speakers, the small acoustic distance between their vowel centers would consequently lead to less extensive overlap between the schwa and the stressed vowel. This general pattern was not observed.

If simple durational scaling was responsible for the coarticulation differences between hearing and deaf speakers at normal rate, one would consistently observe less coarticulation in the speech of deaf than hearing speakers, because the disyllable and segment durations of the former are longer so that segments would overlap less in intersegmental patterning. However, for alveolar disyllables uttered at normal rate, deaf speakers did not exhibit reduced vowel influences during the schwa compared to hearing speakers. Moreover, at similar rates, the same overall coarticulatory patterns were observed in both groups of speakers as at normal rate. The lack of change in coarticulatory effects with changes in rate further supports the assumption that simple changes in overall duration cannot account for the differences found.

Nevertheless, a closer look into the relative durational patterns across hearing status at similar rates, i.e., at normal rate for hearing speakers and at fast rate for deaf speakers, indicated differences that may have influenced the coarticulatory patterns observed across hearing status. The relatively longer consonant closures in hearing than deaf speakers may have resulted in decreased schwa-vowel overlap in alveolar disyllables for the former group. According to Recasens (1989), alveolar consonant contacts constrain the intervocalic coarticulatory patterns of the tongue dorsum; consequently, the longer the closure duration of the alveolar contacts the less the intervocalic overlap. Moreover, for CVCs of equal duration, the relatively longer closure durations in hearing than deaf speakers denote relatively shorter stressed vowel durations for them, therefore, the vowel center in the hearing speakers would have been more influenced by the surrounding consonants. Thus it is suggested that at similar rates, the relative durational variation in the utterance portions across hearing status interacts with the constraints of segmental structure during intersegmental patterning.

From all the findings, we conclude that the acoustic differences observed across hearing status at several locations of minimally contrasting utterances may be the result of different gestural organization in deaf versus hearing speakers, which consists of both temporal and spatial differences in articulatory movement. The gestural organization comprises the articulatory strategy during coproduction of consonant–vowel sequences and the gestural segregation into functional units.

The fact that, for certain contexts (e.g., /ədVd/), deaf speakers exhibited early vowel effects during schwa with concurrent reduced consonant effects with respect to hearing listeners does not conform with the general expectation of coarticulation models, where the onset of effects of neighboring segments on a given segment (in our case, the schwa) is greater for immediately upcoming segments (the consonant) than following ones (the vowel) (Bell-Berti and Harris, 1981). These results along with the spectral findings on consonant formation provide possible insights into the gestural organization of deaf speakers. It appears that, at least for certain contexts, deaf speakers use longer and less precise tongue movements than hearing speakers during the production of syllable sequences in running speech, compromising the rapid gestures required for consonants. In other words, their tongue gestures are less sharply differentiated into the functional subsystems (e.g., tongue tip, tongue dorsum) that are marshalled for production of consonant–vowel gestural sequences. Acoustic evidence for the lack of functional lingual subsystems is also found in the reduced /d/ effects at [u] center for deaf as compared to hearing speakers. The tongue tip, undifferentiated from the action of the tongue body, does not curl up to the alveolar ridge; thus the [u] constriction location remains posterior regardless of context. A consequence of such articulatory patterning is that tongue action is not the multifold composite of gestures seen in normal speech (three distinct, although interacting, constriction locations for the schwa, /d/, and stressed vowel in /ədVd/) but, rather, a single extended gesture toward one vowel constriction location (from /ə/ to vowel), accompanied by an intervening, transient gesture of the jaw/tongue complex (elevation and lowering) for consonant constriction. Moreover, deaf speakers had difficulty controlling the actions of two independent articulators, i.e., the lips and the tongue, in that they showed reduced vowel effects on the schwa in bilabial disyllables as well as aberrant effects of bilabial consonants on vocalic centers.

The findings of the present study suggest that the gestural patterning of deaf speakers resembles that of children in certain respects. Although investigations of children's coarticulatory patterns generally present conflicting findings (Katz *et al.*, 1991; Sereno *et al.*, 1987; Sereno and Lieberman, 1987), one group of investigators (Nittrouer *et al.*, 1989; Nittrouer, 1993) reported evidence that children's gestures in CV sequences, where both consonant and vowel are articulated by the tongue, are not well segregated. Up to 7 years old, children's tongue gestures tended to be longer in duration and more extensively overlapped than those of adults. From this result, Nittrouer *et al.* (1989) and Goodell and Studdert-Kennedy (1991, 1993) inferred that independent control of successive gestures by anatomically linked articulators (e.g., tongue tip and tongue body) in CV sequences is more difficult for children than adults.

The deaf speakers' patterns, like the children's patterns,

indicate that independent control of successive consonant–vowel gestures by anatomically linked articulators (e.g., tongue tip and tongue body in /ədud/) is more difficult than for normal adults. For both groups of speakers (children and deaf speakers), it may also be true that the ability to exploit the independence of two different articulators (tongue and lips) responsible for production of successive segments (consonant and vowel) is a skill acquired with maturation of the speech mechanism. In the Goodell and Studdert-Kennedy (1991, 1993) study, children showed reduced /bV/ overlap compared to adults in ba/bi pairs, as assessed at vowel onset. In the present study, deaf speakers showed reduced or aberrant effects in bilabial disyllables. However, it should be kept in mind that despite the gross similarities with children's data, some of the deaf speakers' specific patterns—such as a more fronted lingual contact at the vocalic center of /əbub/ than /ədud/ or reduced intervocalic overlap in bilabial disyllables—were not found in the early developmental patterns.

Finally, the findings of the present study shed light on the concept of coarticulation. These results, although different from Repp's (1986) data on children, conform with Repp's statement that coarticulation is an umbrella term encompassing many different types of intersegmental patterns. Some types of coarticulation are found in developing speech, deaf speech, or both, whereas other types of coarticulation are found in normal established speech. In our account, the speech of deaf adults contrasts with normals in some ways that are similar to the contrast between adults and young children. Naturally, different maturation factors play a role in the two cases. The similarity may arise because deaf speakers have not developed the fine motor control of normal adults because motor control must be refined by auditory feedback.

ACKNOWLEDGMENTS

The research reported here was part of a thesis completed by the first author and submitted to the City University of New York in partial fulfillment of the requirements for the doctoral degree in Speech and Hearing Sciences. We thank the deaf speakers for their participation, Clarke School for the Deaf for offering their facilities; Lawrence Raphael and Arthur Boothroyd, who served as thesis advisors; Mark Weiss and Richard McGowan for suggestions regarding analysis procedures. We thank Anders Löfqvist for his helpful comments. Finally, we are particularly grateful to Michael Studdert-Kennedy for his insightful suggestions on several drafts of this manuscript.

[1]The Bonferroni correction was applied in order to consider the pairwise comparisons as posthoc. In this procedure, the 0.05 level of significance is divided by the number of pairwise comparisons made per (M)ANOVA. Following the Bonferroni correction, the overall probability of making one or more Type 1 errors for all pairwise comparison tests is at most 0.05. In this MANOVA, the level of significance, according to the Bonferroni correction, was $a + 0.05/9 = 0.0056$, where 9 is the number of pairwise comparisons. On this basis, we will adopt a slightly looser criterion of significance than customary.

Alfonso, P. J., and Baer, T. (**1982**). ''Dynamics of vowel articulation,'' Lang, Speech **25**, 151–174.

Baum, S. R., and Waldstein, R. S. (**1991**). ''Perseveratory coarticulation in the speech of profoundly hearing-impaired and normally-hearing children,'' J. Speech Hear. Res. **34**, 1286–1292.

Bell-Berti, F., and Harris, K. S. (**1981**). ''A temporal model of speech production,'' Phonetica **38**, 9–20.

Bell-Berti, F., and Krakow, R. A. (**1991**). ''Anticipatory velar lowering: a coproduction account,'' J. Acoust. Soc. Am. **90**, 112–123.

Boothroyd, A. (**1984**). ''Auditory perception of speech contrasts by subjects with sensorineural hearing loss,'' J. Speech Hear. Res. **27**, 134–144.

Boothroyd, A. (**1985**). ''Evaluation of speech production in the hearing impaired. Some benefits of forced choice testing,'' J. Speech Hear. Res. **28**, 185–196.

Browman, C. P., and Goldstein, L. M. (**1986**). ''Toward an articulatory phonology,'' Phonology Yearbook **3**, 219–252.

Browman, C. P., and Goldstein, L. M. (**1989**). ''Articulatory gestures as phonological units,'' Phonology **6**, 151–206.

Byrd, D., and Tan, C. C. (**1996**). ''Saying consonant clusters quickly,'' J. Phonetics **24**, 263–282.

Gay, T. (**1978**). ''Effect of speaking rate on vowel formant movements,'' J. Acoust. Soc. Am. **63**, 223–230.

Gay, T. (**1981**). ''Mechanisms in the control of speech rate,'' Phonetica **38**, 148–158.

Goodell, E. W. (**1991**). ''Gestural Organization in the Speech of 22- to 32-Month Old Children,'' Ph.D. thesis, University of Connecticut.

Goodell, E. W., and Studdert-Kennedy, M. (**1991**). ''Articulatory organization in early words: From syllable to phoneme,'' Proceedings of the XIIth International Congress of Phonetic Sciences, Vol. 4 (pp. 166–169). Aix-en-Provence, France: Universite de Provence.

Goodell, E. W., and Studdert-Kennedy, M. (**1993**). ''Acoustic evidence for the development of gestural coordination in the speech of 2-year olds: A longitudinal study,'' J. Speech Hear. Res. **36**, 707–727.

Katz, W. F., Kripke, C., and Tallal, P. (**1991**). ''Anticipatory coarticulation in the speech of adults and young children: Acoustic, perceptual and video data,'' J. Speech Hear. Res. **34**, 1222–1232.

McGarr, N. S., Campbell, M. M., Boothroyd, A. and Coloprisco, D. (**1993**). ''Reducing listener effects in evaluating speech intelligibility of hearing-impaired talkers,'' Paper presented at the annual meeting of the American Speech-Language-Hearing Association, November 1993, Anaheim, California, ASHA 35 (Abstract).

Monsen, R. B. (**1976**). ''Second formant transitions of selected consonant–vowelcombinations in the speech of deaf and normal-hearing children,'' J. Speech Hear. Res. **19**, 279–289.

Munhall, K., and Löfqvist, A. (**1992**). ''Gestural aggregation in speech: Laryngeal gestures,'' J. Phonetics **20**, 111–126.

Nittrouer, S. (**1985**). ''The Role of Coarticulation in the Perception of Speech by Young Children (3–7 Years).'' Ph.D. thesis, City University of New York.

Nittrouer, S. (**1993**). ''The emergence of mature gestural patterns is not uniform: Evidence from an acoustic study,'' J. Speech Hear. Res. **36**, 959–972.

Nittrouer, S., Studdert-Kennedy, M., and McGowan, R. S. (**1989**). ''The emergence of phonetic segments: Evidence from the spectral structure of fricative-vowel syllables spoken by children and adults,'' J. Speech Hear. Res. **32**, 120–132.

Okalidou, A. (**1996**). ''Coarticulation in deaf and hearing talkers,'' Ph.D. thesis, City University of New York.

Osberger, M. J., and Levitt, H. (**1979**). ''The effect of timing errors on the intelligibility of deaf children's speech,'' J. Acoust. Soc. Am. **66**, 1316–1324.

Osberger, M. J., and McGarr, N. S. (**1982**). ''Speech production characteristics of the hearing-impaired,'' in *Speech and Language: Advances in Basic Research and Practice*, edited by N. J. Lass (Academic, New York), pp. 221–283.

Recasens, D. (**1985**). ''Coarticulatory patterns and degrees of coarticulatory resistance in Catalan CV sequences,'' Lang, Speech **28**, 97–114.

Recasens, D. (**1989**). ''Long range coarticulatory effects for tongue dorsum contact in VCVCV sequences,'' Haskins Laboratories Status Report on Speech Research, SR-99/100, pp. 19–37.

Repp, B. H. (**1986**). ''Some observations on the development of anticipatory coarticulation,'' J. Acoust. Soc. Am. **79**, 1616–1618.

Rothman, H. (**1976**). ''A spectrographic investigation of consonant–vowel transitions in the speech of deaf adults,'' J. Phonetics **4**, 129–136.

Rubin, J. (**1984**). ''Static and dynamic information in vowels produced by the hearing-impaired,'' Ph.D. thesis, City University of New York.
Sereno, J. A., Baum, S. R., Marean, G. C., and Lieberman, P. (**1987**). ''Acoustic analysis and perceptual data on anticipatory labial coarticulation in adults and children,'' J. Acoust. Soc. Am. **81**, 512–519.
Sereno, J. A., and Lieberman, P. (**1987**). ''Developmental aspects of lingual coarticulation,'' J. Phonetics **15**, 247–257.
Shukla, R. S. (**1989**). ''Phonological space in the speech of hearing impaired,'' J. Communication Disorders **22**, 317–325.
Smith, B. L., Sugarman, M. D., and Long, S. H. (**1983**). ''Temporal characteristics of the speech of normal elderly adults,'' J. Speech Hear. Res. **30**, 522–528.
Studdert-Kennedy, M. (**1987**). ''The phoneme as a perceptuomotor structure,'' in *Language Perception and Production*, edited by A. Allport, D. MacKay, W. Prinz, and E. Scheerer (Academic, London), pp. 67–84.
Studdert-Kennedy, M. (**1989**). ''The early development of phonological form,'' in *Neurobiology of Early Infant Behavior*, edited by C. von Euler, H. Forssberg, and H. Lagercrantz (MacMillan, Basingstoke, England), pp. 287–301.
Subtelny, J. D., Whitehead, R. L., and Samar, V. J. (**1992**). ''Spectral study of deviant resonance in the speech of women who are deaf,'' J. Speech Hear. Res. **35**, 574–579.
Tuller, B., Harris, K. S., and Kelso, S. J. A. (**1982**). ''Stress and rate: Differential transformations of articulation,'' J. Acoust. Soc. Am. **71**, 1534–1543.
Waldstein, R. S., and Baum, S. R. (**1991**). ''Anticipatory coarticulation in the speech of profoundly hearing-impaired and normally hearing children,'' J. Speech Hear. Res. **34**, 1276–1285.
Yorkston, K. M., and Beukelman, D. R. (**1981**). ''An analysis of connected speech samples of aphasic and normal speakers,'' J. Speech Hear. Dis. **45**, 27–36.
Zsiga, E. C. (**1994**). ''Acoustic evidence for gestural overlap in consonant sequences,'' J. Phonetics **22**, 121–140.

Effect of vocal effort on spectral properties of vowels

Jean-Sylvain Liénard[a)]
LIMSI-CNRS—BP 133, 91403 Orsay Cedex, France

Maria-Gabriella Di Benedetto
Dipartimento INFOCOM, Università degli Studi di Roma ''La Sapienza,'' via Eudossiana 18, 00184 Rome, Italy

(Received 29 July 1998; revised 8 March 1999; accepted 5 April 1999)

The effects of variations in vocal effort corresponding to common conversation situations on spectral properties of vowels were investigated. A database in which three degrees of vocal effort were suggested to the speakers by varying the distance to their interlocutor in three steps (close—0.4 m, normal—1.5 m, and far—6 m) was recorded. The speech materials consisted of isolated French vowels, uttered by ten naive speakers in a quiet furnished room. Manual measurements of fundamental frequency $F0$, frequencies, and amplitudes of the first three formants ($F1$, $F2$, $F3$, $A1$, $A2$, and $A3$), and on total amplitude were carried out. The speech materials were perceptually validated in three respects: identity of the vowel, gender of the speaker, and vocal effort. Results indicated that the speech materials were appropriate for the study. Acoustic analysis showed that $F0$ and $F1$ were highly correlated with vocal effort and varied at rates close to 5 Hz/dB for $F0$ and 3.5 Hz/dB for $F1$. Statistically $F2$ and $F3$ did not vary significantly with vocal effort. Formant amplitudes $A1$, $A2$, and $A3$ increased significantly; The amplitudes in the high-frequency range increased more than those in the lower part of the spectrum, revealing a change in spectral tilt. On the average, when the overall amplitude is increased by 10 dB, $A1$, $A2$, and $A3$ are increased by 11, 12.4, and 13 dB, respectively. Using ''auditory'' dimensions, such as the $F1-F0$ difference, and a ''spectral center of gravity'' between adjacent formants for representing vowel features did not reveal a better constancy of these parameters with respect to the variations of vocal effort and speaker. Thus a global view is evoked, in which all of the aspects of the signal should be processed simultaneously. [S0001-4966(99)02707-1]

PACS numbers: 43.70.Fq, 43.70.Gr, 43.70.Hs [AL]

INTRODUCTION

The present study investigates the interaction between linguistic and nonlinguistic information in speech, by analyzing the effects of vocal effort on the acoustic properties of vowels. The range of vocal efforts taken into account is small, so as to reflect the range of unconscious variations introduced by the speaker in everyday conversational situations. The general framework of this study is a better understanding of the causes for speech variability.

A few studies can be found in the literature that have examined this question. Schulman (1989) analyzed the case of shouted speech, in which speech variability was provoked by an extreme vocal effort. He found a substantial increase in the fundamental and the first formant frequencies ($F0$ and $F1$) as a consequence of increasing vocal effort.

The Lombard effect, i.e., the tendency for a speaker to alter the speech in the presence of noise, is also related to the problem of speech modifications due to vocal effort. Junqua (1993) showed, on the basis of acoustic analysis of Lombard speech, that the first formant (for male and female speakers) and the fundamental frequency are significantly increased in Lombard versus normal speech. Junqua also found that the second formant frequency was increased in Lombard speech, but only for female speakers.

Traunmüller (1989) examined the role of the fundamental frequency and formants in the perception of speaker size, vocal effort, and vowel openness. On the basis of perceptual experiments using synthetic stimuli, he showed that whereas the perceived phonetic quality of the vowel remained constant, the listeners perceived an increase in vocal effort when $F0$ and $F1$ in front vowels, and also $F2$ in back vowels, were moved upward. Traunmüller also found that the listeners perceived a decrease in speaker size, when all formants were moved upward.

Granström and Nord (1992) analyzed the influence of speaking style, defined as weak, normal, and strong, and thus corresponding to the view of vocal effort reported in the present paper, on long-term average spectra. Results showed that the average fundamental frequency was increased considerably in the loud version, and that the relative level of the fundamental and the slope of the spectrum also varied significantly. In particular, in the strong speaking style condition, the long-term average spectra were tilted upward.

Sluijter and Van Heuven (1996) and Sluijter *et al.* (1997) analyzed vocal effort as a function of other cues such as overall intensity, pitch and syllable duration in the production, and perception of lexical stress in Dutch. These investigators showed that the change of spectral balance induced by an increase of vocal effort was a relevant cue for stress.

The present study focuses on the effects of vocal effort on the acoustic properties of French oral vowels. Isolated

[a)]Please address all correspondence to: Jean-Sylvain Liénard, LIMSI-CNRS BP 133, 91403 ORSAY Cedex, France, Electronic mail: lienard@limsi.fr

French vowels, uttered by several speakers at different vocal efforts, were recorded and analyzed. The vocal effort of the speakers varied within an everyday life range, from weak to strong. Therefore, the range did not cover extreme efforts such as whispered or shouted speech. In addition, the recordings were not made in a laboratory, but were obtained under low-constrained recording conditions. The speech materials were perceptually validated by a test of perceived vowel identity, speaker gender, and vocal effort. An acoustic analysis was also carried out. The fundamental frequency ($F0$), formants ($F1$, $F2$, and $F3$), formant amplitudes ($A1$, $A2$, $A3$), and two measurements of overall amplitude (A and AX), were manually estimated. Section I contains the description of the database, its validation, and the acoustic measurements. The results of the investigation on the link between vocal effort and the acoustics of vowels are presented in Sec. II. Finally, Sec. III contains the discussion and the conclusions.

I. DATABASE

A. Speech materials and recording procedure

The present study was based on the analysis of a small corpus of French oral vowels, included in a database named CORENC. The CORENC database consists of 12 (9 oral and 3 nasals) isolated French vowels (9 orals [i, e, ɛ, y, ø, œ, ɑ, o, u] and 3 nasals [ɔ̃, ɑ̃, ɛ̃]) uttered by 10 native speakers (5 males and 5 females) at 3 degrees of vocal effort, and recorded in 1 session. Only the oral vowels of the database were used for the purpose of the present study. Requesting speakers to utter isolated vowels was legitimated by the fact that, in French, the above vowels pronounced in isolation may be interpreted as lexical words such as, for example, ''y'' (English translation: ''there'') for [i], ''et'' (English: ''and'') for [e], ''ai'' (English: ''have'') for [ɛ]. The above set of vowels is smaller than the entire set of French vowels. One of the excluded vowels is [ɔ], as in the word ''sol'' (English: ''ground''), which in isolation does not correspond to any lexical word, and therefore could cause difficulties in the production by native speakers, as well as in the notation by nonphonetician listeners in the perceptual tests. The nasal vowel [œ̃] was not included either, because many French speakers do not distinguish it from [ɛ̃]. Finally, although traces of the old distinction between the anterior [a] and posterior [ɑ] still remain in some word pairs such as ''patte / pâte'' (English: ''leg'' versus ''paste''), it was decided to follow the contemporary pronunciation, which adopts a median version between [a] and [ɑ] and which will be indicated by [ɑ].

The recording session was made with the speaker seated in a well-defined location of a furnished room. This natural setting was consistent with the approach adopted in the present study, i.e., keeping as close as possible to everyday life conditions. It should be noted that as a consequence there might be less control over parameters related to the speakers and measurements. The speech materials were recorded by means of a LEM DO21B omnidirectional microphone. This microphone is widely used in broadcast live recordings; its frequency response extends from 20 to 18 000 Hz. The curve stays within 1 dB from 50 to 3000 Hz and rises slightly (within 5 dB) in the vicinity of 6000 Hz. This omnidirectional microphone was chosen in order to minimize the acoustical effects of any slight movement of the speaker. The distance between the speaker's mouth and the microphone was about 30 cm in all recordings. Thus a 5-cm change of the speaker's head position with respect to the microphone, which corresponds to a somewhat large movement, produced a change of the sound level limited to 1.5 dB, which is quite small considering the setup of the experiment. During the recordings, the input level of the tape recorder was kept unchanged. This aspect of the recording protocol yields the possibility of a straight comparison between token amplitudes.

The recording was under the control of a single experimenter with no hearing impairment and aware of the purpose of the experiment. While the speaker did not change his/her position during the experiment, the experimenter could stand in three different locations in the room, always facing the speaker. The three locations corresponded to a distance between the speaker and the experimenter's mouth of about 1.5, 0.4, and 6 m (normal, close, and far conditions, respectively, denoted as N, C, and F conditions). On the average, the dynamic interval of voice intensity induced by the variation from the C to the F condition was 9 dB.

Corresponding to each location condition, the same introductory sentence was uttered by the experimenter at a level he felt to be appropriate to the distance separating him from the speaker. In turn, the speaker uttered the introductory sentence. This introductory interaction thus allowed both interlocutors to adjust their vocal effort to the situation, before proceeding with the recording of the series of vowels. The above protocol is in agreement with the notion of informational mutuality of natural speaker–listener interactions presented by Lindblom (1987). The vowels were elicited as follows. The experimenter pronounced one vowel. The speaker had been instructed to repeat it immediately. Then the experimenter pronounced the next vowel and the process was repeated until the whole series of vowels was completed.

The vowels corresponding to a given location were thus recorded in series. The experimenter always started with the N condition, and correspondingly the N vowel set was recorded for a given speaker. Then the experimenter moved on to the C condition, and the C vowel set was recorded. The experimenter ended with the F condition, to induce the F vowel set to be produced. Within each series, the vowels were presented to the speakers according to a fixed order which was the same for all speakers.

The experimenter acted as a reference target but also controlled the identify of the vowels produced by the speaker. In the case of errors, he induced a correction by repeating again the same vowel until the speaker pronounced it right. During the experiment, this kind of mistake occurred quite rarely. In addition, the experimenter also checked that the speech produced by the speaker was audible. Actually, it never occurred that the speaker was asked to speak more loudly or more softly. No additional selection was imposed on the speech material.

The analog recordings were then sampled at 10 kHz and

manually segmented into tokens, one for each vowel, leaving a 50-ms silent interval before the onset and after the offset of the vowel. The average length of a vowel file was of the order of 4000 samples corresponding to an average vowel duration of 300 ms. This duration is typical of a vowel in the final, pre-pausal position of an utterance in fluent, spontaneous French. The segmented signal data are available on request as a set of binary files (PC-coded two-byte integers, no header, one file per token).

B. Perceptual evaluation

The database was perceptually validated for the identity of the vowel, the vocal gender of the speaker (male/female), and the vocal effort (induced by the C, N, or F recording conditions). It should be noted that the perceptual validation test was carried out on the entire CORENC database, which as mentioned in the preceding section includes three nasal vowels. Five listeners participated individually in the validation phase. All listeners were native French speakers, with no hearing impairment, aged 20–35 years, and spent most of their lives in the Paris area. The speakers and listeners belonged to separate groups and were not familiar to each other. Before taking the test, the listeners were familiarized with the task by listening to 40 practicing tokens. The listeners received the following instructions; They were told to indicate the identity of the vowel, the gender, and the vocal effort by checking a box on a paper form. The listener could also decide not to give an evaluation by checking a box labeled with a question mark. The speech stimuli were randomized and presented to the listeners through professional headsets (Beyer DT48, closed headsets). There was no calibration at the level of the headset. The speech stimuli were not energy normalized. The time elapsed between two stimuli was about 15 s. The level was adjusted to be comfortable at the beginning of the practicing session and remained unchanged throughout the session. Each segment was presented once.

At the end of the validation test, each token was classified according to the following figures:

(1) Percentage of listeners who correctly identified the token as the vowel requested by the experimenter. The listeners could chose among 13 values (12 possible vowels, and 1 ''?'' option);
(2) Percentage of listeners who correctly identified the speaker's gender. The listeners could chose among 3 values (2 possible genders, and 1 ''?'' option);
(3) Percentage of listeners who correctly identified the vocal effort implicitly requested from the speaker by the experimenter. The listeners could chose among four values, presented as ''low voice,'' ''medium voice,'' ''strong voice,'' and ''?.''

The results of the evaluation, referring to the oral vowels of the database, are reported in Table I. Table I shows the error rates on vowel identity, speaker gender, and vocal effort. There were 270 tokens (27 tokens for each speaker). An answer with the ''?'' checked would always be counted as an error.

TABLE I. Perceptual validation of the CORENC database. Results obtained on only oral vowels are reported. Error rates by speaker on vowel identity, speaker gender, and vocal effort. There were 270 tokens (27 tokens per speaker). Each token was heard once by five listeners.

Speaker	Gender Female/Male	Vowel error rate %	Gender error rate %	Vocal effort error rate %
AM	F	4.4	8.9	36.3
CB	F	14.8	0.7	43.7
JB	F	11.1	40.0	36.3
MF	F	20.7	5.2	49.6
SB	F	5.9	3.7	45.2
BB	M	7.4	4.4	45.9
DB	M	3.0	0.7	45.9
JP	M	12.6	1.5	31.1
MB	M	6.7	3.0	40.0
OB	M	5.9	1.5	37.8
Average %		9.3	7.0	41.2

For vowel identity, error rates varied with the speaker and ranged from 3.0% to 20.7%, yielding an average error rate of 9.3%.

For gender, the overall error rate (7.0%) indicated that the gender was easily identified by the listeners. It should be observed that most of the errors occurred with one single female speaker (JB) (see Table I, 40.0% against the 3.3% average for the nine other speakers). This particular speaker took great care in producing the different degrees of vocal effort requested. However, her tokens in the C condition were often falsely perceived as produced by a male speaker.

The vocal effort evaluation was a difficult task, due to the modest variation in level from one condition to the other. As indicated above, this variation corresponded to about 9 dB for a given speaker. The difference in level between the weakest and the strongest tokens of the database was about 40 dB, and therefore the 9-dB range was around a value which was specific to each speaker. Under these conditions, the 41.2% error rate obtained for vocal effort evaluation was significantly better than chance (66.7% expected in the case of a random choice among three equiprobable answers, 75% if one considers the ''?'' as a fourth equiprobable possibility). This result indicated some ability of the listeners to perceive variations in speech level, but did not allow them to decide whether these variations could be attributed to the vocal effort requested, or to the usual voice level of the speaker considered.

Table II shows the results as a function of the distance condition, obtained by pooling all speakers. Chi-square tests were applied to these results in order to compare rates expected by chance with observed rates. Results indicated that the observed variation of the error rates were not statistically significant at $p<0.05$ ($\chi^2=1.2$ for vowel identity, 0.59 for gender, and 0.17 for vocal effort). Thus the perceptual study does not reveal any significant influence of the distance condition on the perception of vowel identity, speaker's gender, and vocal effort.

C. Data analysis and acoustic measurements

The following parameters were estimated: fundamental frequency ($F0$), formant frequencies ($F1$, $F2$, $F3$), for-

TABLE II. Error rates on oral vowel identity, speaker gender, and vocal effort, as a function of distance condition.

Perceived descriptors	C condition 0.4 m	N condition 1.5 m	F condition 6 m	All conditions pooled
% errors on vowel identity	12.0	8.0	7.8	9.3
% errors on speaker gender	7.6	8.0	5.3	7.0
% errors on vocal effort	40.0	40.7	42.9	41.2

mant amplitudes ($A1$, $A2$, $A3$), and two amplitude parameters. The first amplitude parameter (A) was the amplitude of the frame where formant frequencies and amplitudes were measured. The second one (AX) was the amplitude of the frame where the energy of the signal was maximum. Those two parameters A and AX were considered for representing the amplitude of the token because the frame where formant frequencies and amplitudes were measured was selected on the basis of the stability of the formants, and therefore did not systematically correspond to the frame of maximum energy. The speech materials were analyzed using the spectrographic analysis program UNICE by VECSYS (1989). Two experienced investigators manually estimated the above parameters by visual examination of narrow-band spectra. These spectra were obtained by windowing the signal with a Hamming window of 25.6 ms and then pre-emphasizing the signal with a high-pass filter (first-order filter with coefficient value of 0.95, yielding a +6 dB/octave pre-emphasis above 100 Hz). Wide-band spectra, as well as LPC spectra, were available and were used to refine the frame choice and parameter measurements. All measurements except AX were made in one frame, which was selected to correspond to the best representative of the vowel token, as visually estimated from spectral stability and formant structure. This frame was generally located about 50 ms after vowel onset. Since the sound level controls were kept constant during the recordings, all amplitudes remained comparable among each other for all vowel tokens of the database.

For the nasal vowels, the usual formant measurements may not be appropriate. In particular, the main nasal zero in the low-frequency portion of the spectrum may cause some indetermination on $F1$ and $A1$ values. Consequently, the values measured for these vowels will not be reported nor used in the present study.

D. Statistical analyses

Multi-way analyses of variance (ANOVA) were used to analyze the data of the present study. Three factors were considered: speakers (ten speakers), vowels (nine vowels), and distance condition (three distance conditions). One three-way ANOVA was carried out for each acoustic parameter ($F0$, $F1$, $F2$, $F3$, $A1$, $A2$, $A3$, A, and AX), and also for some combinations and transformations of the above parameters, such as formants in Bark, formant differences, spectral centers of gravity. Newman-Keuls *post hoc* tests were used to analyze significant effects and interactions.

II. RESULTS

A. Effects on amplitudes

The results of a three-way ANOVA test applied to the five dependent variables, $A1$, $A2$, $A3$, A, and AX, reported in Table III, indicated that:

(a) The variation of $A1$ with distance condition was highly significant [$F(2,144)=168.4$, $p<0.001$]. As expected, $A1$ also varied significantly with speakers [$F(9,144)=23.3$, $p<0.001$], indicating that each speaker has his/her own usual voice level, and with vowels [$F(8,144)=9.1$, $p<0.001$]. The only slight interaction between factors concerned speaker and distance condition [$F(18,144)=2.9$, $p<0.001$], indicating that each speaker has his/her own way of increasing $A1$ when increasing vocal effort.

(b) The variation of $A2$ with distance condition was highly significant [$F(2,144)=144.9$, $p<0.001$]. $A2$ also varied significantly with speakers [$F(9,144)=23.7$, $p<0.001$], and vowels [$F(8,144)=25.5$, $p<0.001$] (note the higher significance of $A2$ compared to $A1$). The only slight interaction between factors concerned speaker and distance condition [$F(18,144)=2.9$, $p<0.001$] (see comment above).

(c) The variation of $A3$ with distance condition was highly significant [$F(2,144)=197.4$, $p<0.001$]. $A3$ also varied significantly with speakers [$F(9,144)=23.5$, $p<0.001$], and vowels [$F(8,144)=84.9$, $p<0.001$] (note the higher significance of $A3$ compared to both $A1$ and $A2$). The only slight interaction between factors concerned speaker and distance condition [$F(18,144)=5.0$, $p<0.001$] (see comment above).

(d) The variation of AX with distance condition was highly significant [$F(2,144)=439.1$, $p<0.001$]. The parameter AX also varied significantly with speakers [$F(9,144)=38.6$, $p<0.001$], indicating that a speaker has his/her own usual voice level, but not with vowels, contrarily to what observed for $A1$, $A2$, and $A3$. The only significant interaction was between speaker and distance condition [$F(18,144)=8.1$, $p<0.001$] indicating that each speaker has his/her own way of increasing AX when increasing vocal effort.

(e) The variation of A with distance condition was highly significant [$F(2,144)=148.8$, $p<0.001$]. The parameter A varied significantly with speakers [$F(9,144)=26.4$, $p<0.001$], but not with vowels as for AX, and contrarily to what was observed for $A1$, $A2$, and $A3$. The only significant interaction was between speaker and distance condition [$F(18,144)=2.88$, $p<0.001$]

TABLE III. Results of a three-way ANOVA applied on amplitudes A and AX, and formant amplitudes $A1$, $A2$, and $A3$. Main effects and interactions of factors speaker, vowel, and distance condition are reported for each dependent variable in terms of F ratio, significance of F, and percentage of explained variance.

Dependent variable		$A1$	$A2$	$A3$	AX	A
Main effect						
Speaker	F	23.3	23.7	23.5	38.6	26.4
	Significance of F	<0.001	<0.001	<0.001	<0.001	<0.001
	% explained variance	21.7	20.2	12.3	20.5	28.0
Vowel	F	9.1	25.5	84.9	2.5	1.3
	Significance of F	<0.001	<0.001	<0.001	NS	NS
	% explained variance	7.5	19.3	39.6	0	0
Distance condition	F	168.4	144.9	197.5	439.1	148.8
	Significance of F	<0.001	<0.001	<0.001	<0.001	<0.001
	% explained variance	34.9	27.5	23.0	51.7	35.1
Two-way interactions						
Speaker*vowel	F	1.8	1.9	2.6	2.1	1.4
	Significance of F	NS	NS	NS	NS	NS
	% explained variance	0	0	0	0	0
Speaker*distance condition	F	2.9	2.9	5.0	8.1	2.9
	Significance of F	<0.001	<0.001	<0.001	<0.001	<0.001
	% explained variance	5.4	4.9	5.3	8.6	6.1
Vowel*distance condition	F	1.3	0.9	0.6	0.7	0.6
	Significance of F	NS	NS	NS	NS	NS
	% explained variance	0	0	0	0	0

indicating that each speaker has his/her own way of increasing AX when increasing vocal effort.

(f) In summary, it was noted above that $A1$, $A2$, and $A3$ varied significantly with the factor vowel, while AX and A did not. Thus no specific vowel intensity effect, as reflected either by AX or A, was observed on our data. The above test also revealed an increase in significance of the factor vowel going from $A1$ to $A3$. However, the amplitude remained constant across vowels, indicating a compensatory effect between formant amplitudes.

In addition, the only significant factor of interaction was related to speaker and distance condition, indicating that each speaker has a specific way of varying the observed parameters. Newman-Keuls *post hoc* tests revealed that all analyzed amplitude parameters increased significantly when moving from the C to the F condition, for all speakers. This observation is illustrated by Fig. 1 which shows, for each speaker, the average values of $A1$, $A2$, and $A3$, as a function of distance condition.

The ANOVA on A and AX showed that these two parameters behaved in a very similar way. The average values of A and AX, for each speaker, as a function of the distance condition, are shown in Fig. 2. As observed above, A and AX increased significantly for all speakers going from the C to the F condition. As expected, AX was higher than A and both parameters represented well the distance condition. It was decided to select AX for numerically quantifying vocal effort.

The parameters AX, $A1$, $A2$, and $A3$ were then analyzed in their interaction with the factor distance condition. Figure 3(a) shows the variation of the maximum amplitude AX (expressed in dB) in the three distance conditions (C, N, and F). The plotted values correspond to averages computed over all vowels and speakers in a given distance condition and were equal to 46.7 (close condition, standard deviation=3.6), 49.7 (normal condition, standard deviation=4.1), and 55.6 (far condition, standard deviation=3.1), indicating that the average AX value increased with vocal effort; AX increased of 3 dB going from C to N, and of 5.9 dB going from N to F.

Formant amplitude variations with distance condition were then analyzed as a function of AX. Figure 3(b) shows the variations of $A1$, $A2$, and $A3$ (all expressed in dB) as a function of AX in the three distance conditions (C, N, and F). As can be noted, $A1$, $A2$, and $A3$ had the same behavior, i.e., they all increased with vocal effort. The variation amount of

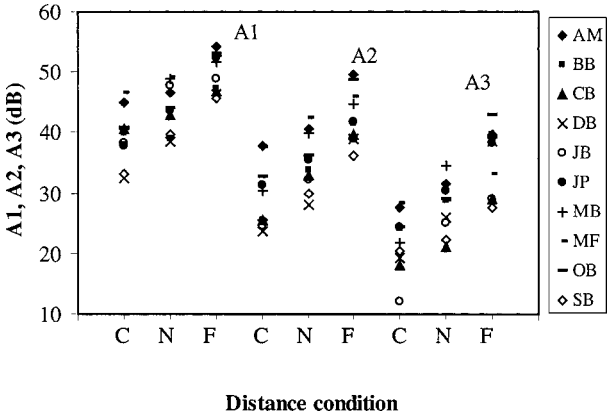

FIG. 1. Formant amplitudes $A1$, $A2$, and $A3$, expressed in dB, as a function of distance condition, for each speaker, all vowels pooled.

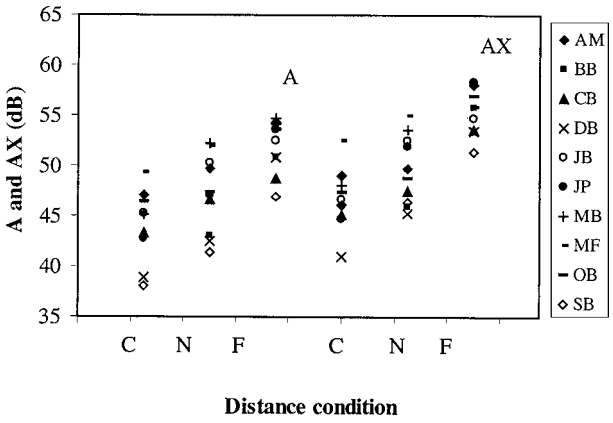

FIG. 2. Amplitude A (computed in the same frame as $A1$, $A2$, and $A3$) and maximum amplitude AX (computed in the frame of maximum energy), expressed in dB, as a function of distance condition, for each speaker, all vowels pooled.

$A1$, $A2$, and $A3$ were very similar going from C to N, while there was a difference going from N to F ($A3$ and $A2$ increased of about 2.5 dB more than $A1$). The average variation going from C to F was 11.9 dB (10.4, 12.3, and 13.2 for $A1$, $A2$, and $A3$, respectively). A linear regression analysis was applied to the data. Results showed that $A1$, $A2$, and $A3$ were highly linearly correlated to AX and in particular that:

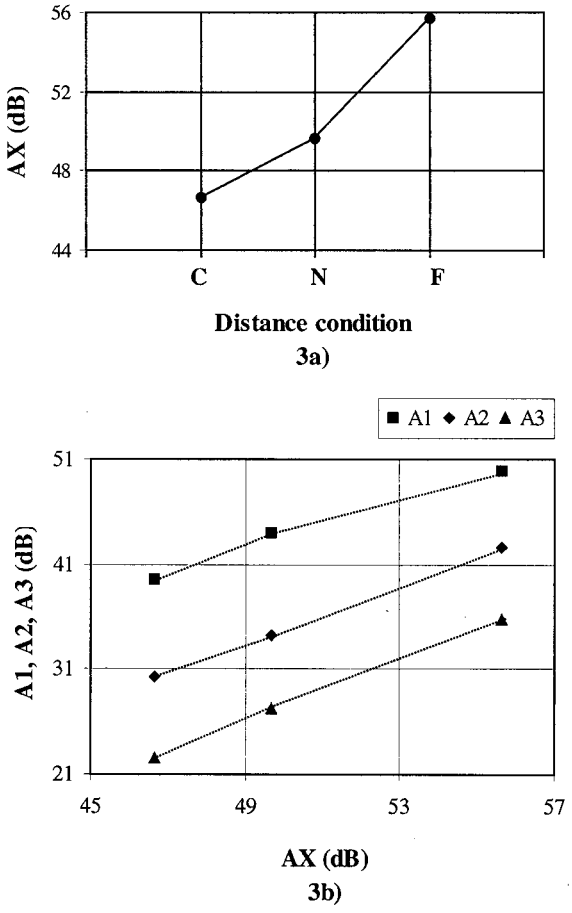

FIG. 3. Maximum amplitude AX in dB, averaged over all vowels and speakers, as a function of distance condition (a), and $A1$, $A2$, and $A3$, averaged over all vowels and speakers, as a function of AX (b).

- $A1$ varied of 1.10 dB/1 dB with AX [$r^2=0.7$, $p<0.005$];
- $A2$ varied of 1.24 dB/1 dB with AX [$r^2=0.64$, $p<0.005$];
- $A3$ varied of 1.30 dB/1 dB with AX [$r^2=0.66$, $p<0.005$].

Note in particular the high correlation between AX and $A1$, together with the similar increase in the three distance conditions, i.e., 1.1 dB/1 dB. However, as discussed above, these two parameters behaved differently as a function of vowel. That $A2$ and $A3$ increased more than $A1$ going from C to F indicated that the high part of the spectrum became more prominent with vocal effort, due to the reinforcement of the upper harmonics. This effect was assessed statistically on our data. A three-way ANOVA for studying the factors of the difference $A1-A3$ was performed. It revealed that $(A1-A3)$ varied significantly with distance condition [$F(2,144)=10.0$, $p<0.001$].

We further verified that the above effects were not due to an overall increase in sound level. To this aim, normalized $A1$, $A2$, and $A3$ values were computed. These normalized values, $A1$norm, $A2$norm, and $A3$norm, were obtained by substracting from the formant amplitudes (in dB) the amplitude of the frame A (in dB). Results of an ANOVA on the normalized formant amplitude parameters, reported in Table IV, indicated a significant effect of the factor ''distance condition,'' which rejected the hypothesis that the observed variations on unnormalized formant amplitudes were due to overall amplitude variation. The normalized formant amplitudes were not affected by any significant interaction effect. In particular, there was no significant interaction between speaker and distance condition, contrary to what was observed on the unnormalized amplitudes. Therefore, we observed no dependency of the spectral tilt on the factor speaker.

B. Effects on fundamental and formant frequencies

A three-way ANOVA was applied to the dependent variables $F0$, $F1$, $F2$, and $F3$. Factors were speakers, vowels, and distance condition. Results, reported in Table V, indicated that:

(a) $F0$ and formant frequencies varied significantly with the factor speaker, for $F0$ [$F(9,144)=494.3$, $p<0.001$], for $F1$ [$F(9,144)=17.7$, $p<0.001$], for $F2$ [$F(9,144)=74.4$, $p<0.001$], and for $F3$ [$F(9,144)=37.2$, $p<0.001$]. This effect was expected, since as well known, $F0$ and formants vary from speaker to speaker.

(b) Variations of all frequency parameters were also significant for the factor vowel, for $F0$ [$F(8,144)=26.4$, $p<0.001$], for $F1$ [$F(8,144)=738.7$, $p<0.001$], for $F2$ [$F(8,144)=2976.4$, $p<0.001$], and for $F3$ [$F(8,144)=70.9$, $p<0.001$]. This result was again expected for formant frequencies. As regards $F0$, it confirms the recognized language-independent effect of ''intrinsic $F0$.''

(c) $F0$ and $F1$ varied significantly with distance condition, for $F0$ [$F(2,144)=593.6$, $p<0.001$], and for $F1$ [$F(2,144)=31.30$, $p<0.001$], while $F2$ and $F3$ did not: the variation was not significant for $F2$

TABLE IV. Results of a three-way ANOVA applied on formant amplitudes $A1$, $A2$, and $A3$, normalized with respect of the total amplitude. Main effects and interactions of factors speaker, vowel, and distance condition are reported for each dependent variable in terms of F ratio, significance of F, and percentage of explained variance.

Dependent variable		$A1$ norm	$A2$ norm	$A3$ norm
Main effect				
Speaker	F	4.4	5.6	9.4
	Significance of F	<0.001	<0.001	<0.001
	% explained variance	7.3	7.9	12.4
Vowel	F	18.4	25.8	30.2
	Significance of F	<0.001	<0.001	<0.001
	% explained variance	27.1	32.4	35.2
Distance condition	F	18.1	19.3	17.8
	Significance of F	<0.001	<0.001	<0.001
	% explained variance	6.7	6.1	5.2
Two-way interactions				
Speaker*vowel	F	1.5	2.1	1.8
	Significance of F	NS	NS	NS
	% explained variance	0	0	0
Speaker*distance condition	F	1.5	1.8	1.6
	Significance of F	NS	NS	NS
	% explained variance	0	0	0
Vowel*distance condition	F	2.7	1.0	1.6
	Significance of F	NS	NS	NS
	% explained variance	0	0	0

$[F(2,144)=0.3,\ p>0.001]$ nor for $F3$ $[F(2,144)=1.9,\ p>0.001]$. This effect will be investigated further in this same section.

(d) There was no significant interaction between speaker and vowel for $F0$, while all formants were affected by a significant interaction between these factors [for $F1$ $[F(72,144)=2.8,\ p<0.001]$, for $F2$ $[F(72,144)=10.3,\ p<0.001]$, and for $F3$ $[F(72,144)=2.3,\ p$

TABLE V. Results of a three-way ANOVA applied on $F0$, $F1$, $F2$, and $F3$. Main effects and interactions of factors speaker, vowel, and distance condition are reported for each dependent variable in terms of F ratio, significance of F, and percentage of explained variance.

Dependent variable		$F0$	$F1$	$F2$	$F3$
Main effect					
Speaker	F	494.3	17.7	74.4	37.2
	Significance of F	<0.001	<0.001	<0.001	<0.001
	% explained variance	70.7	2.4	2.6	26.4
Vowel	F	26.4	738.7	2976.4	70.9
	Significance of F	<0.001	<0.001	<0.001	<0.001
	% explained variance	3.4	90.3	93.7	44.8
Distance condition	F	593.6	31.3	0.3	1.9
	Significance of F	<0.001	<0.001	NS	NS
	% explained variance	18.9	1	0	0
Two-way interactions					
Speaker*vowel	F	1.6	2.8	10.3	2.3
	Significance of F	NS	<0.001	<0.001	<0.001
	% explained variance	0	3.1	2.9	12.8
Speaker*distance condition	F	7.8	2.2	1.6	1.3
	Significance of F	<0.001	NS	NS	NS
	% explained variance	2.2	0	0	0
Vowel*distance condition	F	2.6	1.7	1.7	1.9
	Significance of F	NS	NS	NS	NS
	% explained variance	0	0	0	0

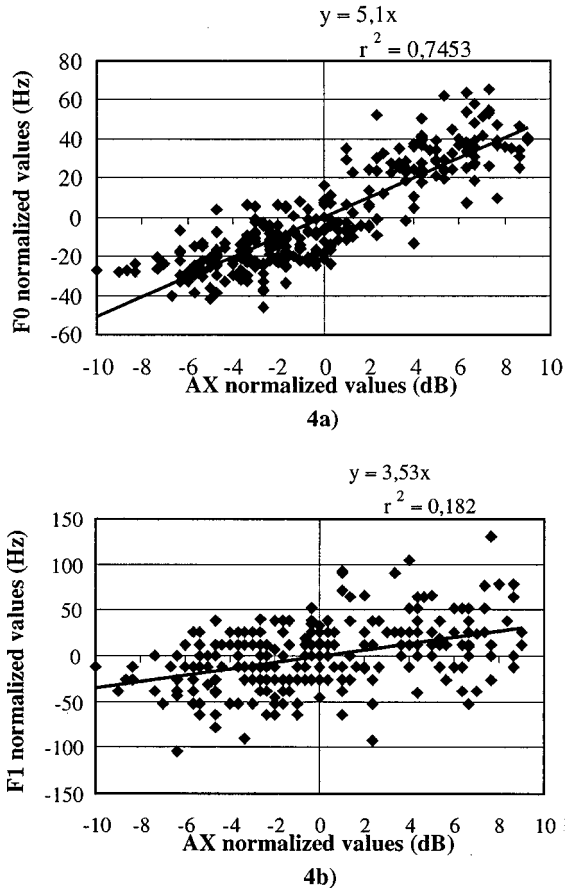

FIG. 4. $F0$ (a) and $F1$ (b) normalized values as a function of AX normalized values. Normalization was obtained by taking the difference of any value with the average of the three values observed in the three distance conditions, for any given vowel and speaker. This plot illustrates the variation of $F0$ and $F1$ with vocal effort, for all vowels and speakers. The linear regression coefficient, in Hz/dB, gives a statistical evaluation of the elementary frequency variation for a 1-dB variation of the vocal effort.

<0.001]]. This result indicated that each speaker varied the formant frequencies of each vowel in a different way, while this was not the case for $F0$. Therefore, speakers seem to have a homogenous behavior as regards $F0$ variations with vowels.

(e) The opposite effect of point (d) was observed on the speaker versus distance condition interaction. Here, formants did not vary significantly while $F0$ did [$F(18,144)=2.8$, $p<0.001$].

(f) There was no significant interaction between vowel and distance condition for any of the frequency parameters. This result indicated that the variation of $F0$ and $F1$ with distance condition [see comment (c)] was not significantly different among vowels.

The effect observed in comment (c) was further investigated. A correlation analysis on normalized $F0$ and $F1$ values versus distance condition, represented by AX, was carried out. The normalized values were obtained by averaging, for each vowel of each speaker, the $F0$, $F1$, and AX values, and by substracting from the $F0$, $F1$ and AX values the above average values. In this way, the amount of variation of $F0$ and $F1$ with distance condition, for a given vowel and speaker, could be isolated. Results of the correlation test

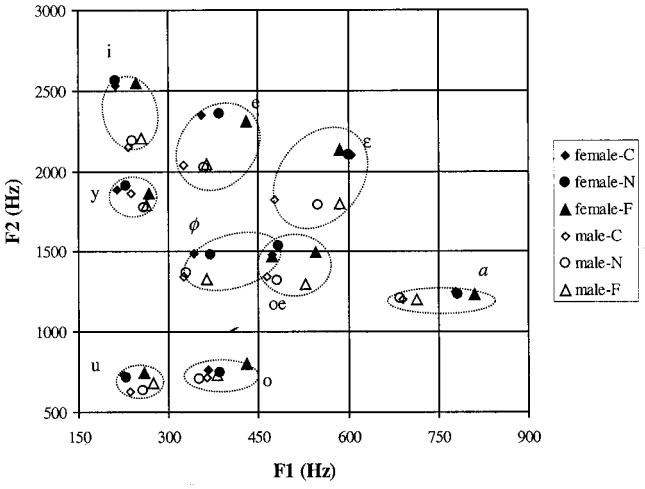

FIG. 5. Representation in the $F1$ vs $F2$ plane of the vowels of the CORENC database, in the three distance conditions (♦=Close condition, ●=Normal condition, ▲=Far condition). Female speakers are represented by filled patterns, male speakers are represented by unfilled patterns. Each dot is an average value over the speakers of the same gender category.

showed that $F0$ and $F1$ were highly correlated with AX. In particular, the Spearman rank correlation coefficient was equal to 0.85 and 0.41, for $F0$ and $F1$, respectively. A linear regression analysis was then carried out in order to verify whether the correlation of $F0$ and $F1$ with AX was close to linear. Results indicated that $F0$ and AX were highly linearly correlated (linear correlation coefficient: $r^2=0.75$) and that the rate of variation of $F0$ with AX was about 5.1 Hz/dB. This law of variation with distance condition should be intended as valid for a given vowel and speaker. Results of the linear regression analysis on $F1$ vs AX indicated that the rate of variation of $F1$ with AX was of 3.5 Hz/dB but was not close to linear (linear correlation coefficient: $r^2=0.18$). These results are reported in Fig. 4(a) and (b) for $F0$ and $F1$, respectively. The larger scattering of $F1$ values as compared to $F0$ values is responsible for the low value of r^2. This may be attributed to the difficulty of measuring $F1$ precisely, especially with high-pitched voices, even with the help of an LPC spectrum. The correlation of AX and $F1$ is better demonstrated by the Spearman rank correlation test, which is less sensitive to the scattering of the observations.

In regard to $F2$ and $F3$, comment (c) reported no significant variations with distance condition. Since on the contrary $F1$ varied with this same factor, both effects caused the vowel triangle in the $F1$ vs $F2$ coordinates to shift to higher $F1$ values when going from the C to the F condition, rather than to expand or to contract. This observation is illustrated in Fig. 5 which shows the $F1$ vs $F2$ values for each vowel, averaged over female and male speakers separately, in the three distance conditions.

C. Combined effect of vocal effort on formant amplitudes and frequencies

The observed variations of the fundamental and of formant amplitudes and frequencies described in the previous paragraph presented a different pattern for each parameter. However, the perceptual test, presented in Sec. II, indicated that vowel identity was preserved through the variation in

TABLE VI. Results of a three-way ANOVA applied on $F1-F0$, $F2-F1$, and $F3-F2$ (all frequencies in Bark). Main effects and interactions of factors speaker, vowel, and distance condition are reported for each variable in terms of F ratio, significance of F, and percentage of explained variance.

Dependent variable		$F1-F0$	$F2-F1$	$F3-F2$
Main effect				
Speaker	F	38.7	22.8	7.9
	Significance of F	<0.001	<0.001	<0.001
	% explained variance	5.2	1.1	1.0
Vowel	F	749.4	2173.4	864.6
	Significance of F	<0.001	<0.001	<0.001
	% explained variance	88.6	95.5	92.3
Distance condition	F	8.6	19.8	1.5
	Significance of F	<0.001	<0.001	NS
	% explained variance	2.13	0.79	0
Two-way interactions				
Speaker*vowel	F	2.6	4.8	4.0
	Significance of F	<0.001	<0.001	<0.001
	% explained variance	2.7	1.9	3.8
Speaker*distance condition	F	2.4	2.0	1.0
	Significance of F	NS	NS	NS
	% explained variance	0	0	0
Vowel*distance condition	F	2.1	3.3	3.1
	Significance of F	NS	<0.001	<0.001
	% explained variance	0	0.3	0.7

vocal effort. Therefore, it was decided to investigate further the relations between the observed variations, in order to explain the constancy in the perceived phonetic properties of the speech data, and in particular vowel height and vowel backness. Traditional vowel representations make use of $F1$ and $F2$ as acoustic correlates of the above phonetic features. Since $F1$ varied greatly with vocal effort, the consequence was an increase in scattering of the vowel areas in the $F1-F2$ plane, due to vocal effort.

1. Representation of vowel height

The marked variation in $F1$ values with vocal effort suggested that vowel height might be better represented by some different parameter. As shown, $F1$ and $F0$ both increased with vocal effort. Consequently, the difference between $F1$ and $F0$ might show less variation than $F1$ when vocal effort was increased.

This parameter was proposed in the literature by Traunmüller (1981) on the basis of a perceptual effect. Syrdal and Gopal (1986) used it to classify American–English vowels along vowel height dimension and reported an improvement of representation with respect to $F1$. Coherently with the perceptual view of vowel representation, and its associated auditory parameter $F1-F0$, the $F1-F0$ values were expressed in Bark.

A three-way ANOVA was applied to $F1-F0$ (both frequencies were in barks). Factors were speakers, vowels, and distance condition. Results, reported in Table VI, indicate that:

(a) $F1-F0$ varied significantly with the factor speaker $[F(9,144)=38.7,\ p<0.001]$.
(b) $F1-F0$ varied significantly with the factor vowel $[F(8,144)=749.4,\ p<0.001]$.
(c) $F1-F0$ varied significantly with distance condition $[F(2,144)=8.6,\ p<0.001]$.
(d) There was a significant interaction between speaker and vowel $[F(72,144)=2.6,\ p<0.001]$.
(e) The opposite effect of point (d) was observed on the speaker versus distance condition interaction and on the vowel versus distance condition interaction.

Therefore, the $F1-F0$ parameter behaved similarly to the $F1$ parameter. In fact, significant, and nonsignificant effects were present for both parameters according to the same rules. Although $F1-F0$ varied significantly with vocal effort, it did vary much less than $F1$ (for $F1-F0$: percentage of explained variance with distance condition=2.1, while for $F1$: 18.9). This result indicated that the $F1-F0$ parameter had, to some degree, a normalization effect on the variations due to distance condition. Regarding speaker normalization, the percentage of explained variance was higher for $F1-F0$ (equal to 5.2) than for $F1$ (equal to 2.4). Therefore, the $F1-F0$ parameter did not seem to act as a normalizer for speaker variations effects. A similar result was observed on American–English vowels (Di Benedetto, 1995). Finally, both $F1-F0$ and $F1$ varied quite significantly and similarly with the factor vowel. No significant interaction between vowel and distance condition was highlighted.

The correlation of $F1$ with $F0$ was tested; these two parameters were highly correlated (Spearman rank correlation coefficient=0.43). However, $F0$ itself varied very significantly with vowel amplitude (AX), and, as noted in the previous section, $F1$ was also highly correlated to AX with a

very similar correlation coefficient value (Spearman rank correlation coefficient=0.41). Linear regression analysis indicated that the linear correlation coefficient of $F1$ and $F0$ was 0.21, which was slightly higher but very similar to the value found for $F1$ and AX (0.18). Therefore, although a significant correlation of $F1$ with $F0$ was found, a similar correlation between $F1$ and AX was also observed. The correlation between $F1$ and $F0$ might be motivated by the variation of $F0$ with AX in different distance conditions (or vice versa).

In conclusion, the results of the present study indicate that vowel height might be represented by $F1-F0$ as well as by $F1$. However, the use of $F1-F0$ did show a significant variation with distance condition, smaller than that obtained with $F1$, and appeared to increase inter-speaker variations.

2. Representation of vowel backness

Rather than representing vowel backness by $F2$, the distance of $F2$ to $F1$ and of $F2$ to $F3$ was investigated by analyzing the variations of the $F2-F1$ and $F3-F2$ parameters. These parameters (expressed in Bark) have been proposed in the past (Syrdal, 1985; Syrdal and Gopal, 1986) to correspond to auditory dimensions of the front–back distinction. In American–English, $F3-F2$ was lower than 3.5 Bark for front vowels only.

A three-way ANOVA was applied to the $F2-F1$ and $F3-F2$ distances (all frequencies were in Bark). Factors were speaker, vowel, and distance condition. Results, reported in Table VI, indicated that:

(a) $F2-F1$ and $F3-F2$ varied significantly with the factor speaker [for $F2-F1$ [$F(9,144)=22.8$, $p<0.001$], and for $F3-F2$ [$F(9,144)=7.9$, $p<0.001$]].
(b) $F2-F1$ and $F3-F2$ varied significantly with the factor vowel [for $F2-F1$ [$F(8,144)=2173.4$, $p<0.001$], and for $F3-F2$ [$F(8,144)=864.6$, $p<0.001$]].
(c) $F2-F1$ varied significantly with distance condition [$F(2,144)=19.8$, $p<0.001$] while $F3-F2$ did not.
(d) The only significant interaction was between speaker and vowel, for both $F2-F1$ and $F3-F2$. No interaction between vowel and distance condition was highlighted.

From this analysis, it appeared that $F3-F2$ was better suited than $F2-F1$ for representing vowel backness, since it did not vary with distance condition. In addition, results also showed that:

- The $F3-F2$ difference was lower than 3.5 Bark for [i, y, e, ɛ], i.e., for front vowels of the French vowel system.
- The $F2-F1$ difference was lower than 3.5 Bark for [ɑ, o]. This result was similar to the finding that $F2-F1$ only differentiated [ɑ] and [ɔ] from the other vowels in American–English (Syrdal, 1985).

Accordingly, it was concluded that for French vowels (as for American–English vowels) vowel backness was better represented by $F3-F2$ than by $F2-F1$. Results were comparable for $F2$ and $F3-F2$. The $F3-F2$ difference slightly reduced the variation with speaker, but the variation with distance condition was slightly increased.

Since the above parameters did not take into account amplitude variations, the use of auditory dimensions was further investigated. In fact, the ''auditory dimensions'' are based conceptually on the spectral center of gravity effect, which should take into account the relative amplitudes of the formants, something which is not considered in the pure formant differences; The categorical perceptual effect named Spectral Center of Gravity was found by Chistovich and her colleagues (Chistovich *et al.*, 1979). These experimenters pointed out that if a two formant stimulus must be matched by a one formant stimulus, the matching criterion depends upon the distance between the location of the two formants. If the two formants are placed closer than 3.5 Bark approximately, the subjects match this stimulus with one formant located in a position corresponding to a weighted average of the two formants. In this case, the match is dependent upon the amplitudes of the formants. If the distance is greater than 3.5 Bark, the two formants are matched to one formant located at one of the two formants. In this case, insensitivity over a large range of amplitude variations is observed.

ANOVA tests were thus carried out on the center of gravity between $F2$ and $F3$, and the center of gravity between $F1$ and $F2$. The centers of gravity were obtained as follows:

- The center of gravity in the region of $F2$ and $F3$ was computed by taking into account the $F2$ and $F3$ frequencies and $A2$ and $A3$ amplitudes (expressed in physical units, not in dB). The frequency of the center of gravity F_{23} was equal to: $F_{23}=(A_2F_2+A_3F_3)/(A_2+A_3)$;
- The center of gravity F_{12} between $F1$ and $F2$ was computed as for $F2$ and $F3$.

Results showed that the centers of gravity behaved very similarly to the respective frequency differences $F3-F2$ and $F2-F1$. However, the interaction between the factors speaker and vowel was not significant for the center of gravity F_{12}. In addition, a significant effect between vowel and distance condition was found for both centers of gravity {for F_{12} [$F(16,144)=3.3$, $p<0.001$], and for F_{23} [$F(16,144)=3.1$, $p<0.001$]}, although this effect explained only 0.3% and 0.7% of the variance. This point was investigated further, in order to understand whether a different effect was present for those vowels for which integration should occur according to the spectral center of gravity effect. Newman–Keuls *post hoc* tests were carried out. In regard to F_{12}, results showed that the differences in the values corresponding to different distance conditions were not significant for the vowels [ɛ, œ, ɑ], while the above differences were significant for all the other vowels. In regard to F_{23}, the differences with distance condition were significant for the vowels [u, o], and nonsignificant for all the other vowels. Therefore, no systematic association of the behavior of the centers of gravity with the application of the integration effect could be highlighted from the data of the present study.

III. DISCUSSION AND CONCLUSIONS

The present study investigated the acoustic and phonetic effects of vocal effort variations in real-life conditions corresponding to usual conversation situations.

For this purpose, a database was recorded, for which three degrees of vocal effort were suggested to the speakers by varying the distance to their interlocutor in three steps: close (0.4 m), normal (1.5 m), and far (6 m). Ten naive speakers uttered the speech materials, consisting of French isolated vowels, in a quiet furnished room.

The perceptual validation test of the recorded tokens checked the correctness in terms of perceived identity of the vowel, perceived gender of the speaker, and perceived degree of vocal effort. In regard to vowel identity, gender, and vocal effort evaluation, the average error rates were 9.3%, 7.0%, and 41.2%, respectively. These scores were uniform for the three vocal effort conditions, indicating that there appeared to be no relation with distance condition.

In regard to vowel identity, the above results can be compared with those obtained by Assman *et al.* (1989), although some caution should be taken since these investigators analyzed a different language and used a different experimental protocol. In Assman *et al.*, ten vowels of Canadian English, uttered in isolation by ten speakers, were presented to the listeners in random order; an error rate between 9% and 11% was found. The above order of magnitude was very close to the results of the present listening test.

Acoustic analysis of the speech materials was carried out to determine the main acoustical parameters (fundamental frequency, amplitude, frequency, and amplitude of the first three formants). Variations of the acoustic parameters with the degree of vocal effort were investigated. Results indicated that the fundamental frequency $F0$ increased linearly with vocal effort at a rate close to 5 Hz/dB. A Spearman-rank correlation test revealed that the first formant frequency $F1$ was strongly correlated with vocal effort although the linear correlation between these two variables was not high; If a linear relation was considered the rate of variation would be of about 3.5 Hz/dB. On the contrary, the second and third formants did not vary significantly with vocal effort.

The tendency for $F1$ and $F0$ to increase with vocal effort was in agreement with the results reported by Schulman (1985) and Junqua (1993). However, the present data do not highlight any particular difference in the behavior of $F2$ for female speakers with respect to male speakers, and do not confirm the observation reported by Junqua in Lombard speech. Similarly, regarding the results presented by Traunmüller, the present data do not exhibit any systematic increase of $F2$ for back vowels.

The amplitudes of the three formants were found to increase with vocal effort in an almost parallel way; however, a detailed examination of the variation rates revealed a significant reinforcement of the high part of the spectrum (spectral tilt): For a 10-dB variation of the token maximum amplitude AX, the formant amplitudes $A1$, $A2$, and $A3$ would increase of 11, 12.4, and 13 dB, respectively. This result confirms the data presented by Granström and Nord (1992), since the spectral tilt was observed and statistically assessed on the basis of long-term spectra. It also confirms and refines the results of Sluijter and Van Heuven (1996) who observed an approximately equal increase (5–10 dB) of the three formant amplitudes of two vowels [a:] and [ɔ] in stressed (versus nonstressed) position, while the lowest part of the spectrum (below 0.5 kHz) changed less or remained constant.

The variations of the acoustical parameters were then examined for the stability of the phonetic qualities of the tokens. Using ''auditory'' dimensions such as the $F1-F0$ difference for representing the vowel height, and a ''spectral center of gravity'' between close formants, produced results similar to those obtained with the raw formant parameters. The auditory parameters, as well as the formants by themselves, were shown to correctly represent phonetic qualities such as height and backness, but did not prove to be significantly better than the formants in regard to insensitivity to the variations of vocal effort and speaker. Regarding vowel backness, the $F3-F2$ difference produced results similar to those found in other languages such as American–English vowels (Syrdal, 1986), namely it discriminated front vowels from back vowels in French. This difference did not vary significantly neither with speaker, nor with distance condition; However, the same properties were found for $F2$ alone. In regard to vowel height representation by the $F1-F0$ difference, $F1-F0$ did show less variation than $F1$ in regard to vocal effort; However, it was found that the above difference varied significantly with speaker by a larger amount than $F1$, and thus did not seem to have a speaker normalization effect. Further analysis is needed to understand whether the apparent relation between $F1$ and $F0$ is genuine, or is in fact an induced effect due to the joint variation of both parameters with vowel amplitude.

As a general comment, the present study confirms that the increase of vocal effort in vowels is usually realized by four joint acoustical phenomena: an increase of the acoustical energy of the signal (overall level), an increase of the voice pitch, an enrichment of the high part of the spectrum, and a raise of the first formant frequency. Further studies should be conducted in order to decide whether these features are to be related to production constraints (muscular adjustments of the larynx, opening of the mouth), to perception constraints (placement of more energy in the spectral zone where the ear is more sensitive), or to both of them. Actually, the abovementioned acoustical correlates of vocal effort are systematic enough to convey some information from the speaker to the listener. From this point of view they may contribute to code some linguistic information such as the lexical stress. They may also be used by the listener, jointly with other prosodic parameters, to get some nonlinguistic information on the speaker (physical size, estimated distance to the listener, mood, self-confidence, sociolinguistic origin, etc.). One could observe that these multiple acoustical consequences of a single notion (strong versus weak voice) are redundant, so that if transmission fails in a given channel it can still succeed in another one. For instance, the acoustical level of the signal at the listener's ear is not a good correlate of the vocal effort exerted by the speaker, because it depends on distance and reverberation. However, information on the vocal effort is still recoverable through the other features. Another observation is that, as vocal effort information is disseminated in several aspects of the signal, some indices which are supposed to convey vowel information (for instance $F1$) also depend on vocal effort, as

well as on other nonlinguistic information such as the speaker's gender. In order to circumvent the resulting variability, as human perception does, using new combinations of parameters such as the formant differences or the centers of gravity may not be sufficient. It may be necessary to consider that all of the aspects of the signal information have to be simultaneously decoded because all of them interact at the signal level (Liénard, 1995). In the particular case of vocal effort, interpreting a given value of $F1$ as a vowel index and a value of $F0$ as a prosodic index are undetermined problems, unless the listener can use some knowledge of the speaker's gender as well as on the vocal effort he/she is producing; This knowledge may be found in other aspects of the signal, such as the gross value of $F0$ and the spectral tilt. Thus the present study, by evidencing the numerous interactions between linguistic and nonlinguistic aspects of oral communication, pleads in favor of a global apprehension of speech and voice, too long considered separately.

ACKNOWLEDGMENTS

We would like to thank Dr. Ann Syrdal and an anonymous reviewer, as well as the editor, Dr. Anders Löfquist, for their constructive comments during the review process. This work was partly funded by an international cooperation between CNRS (Center National de la Recherche Scientifique, France) and CNR (Consiglio Nazionale delle Ricerche, Italy).

Assman, P. F., Nearey, T. M., and Hogan, J. T. (**1982**). ''Vowel identification: orthographic, perceptual and acoustic aspects,'' J. Acoust. Soc. Am. **71**, 975–989.

Chistovich, L. A., Sheikin, R. L., and Lublinskaya, V. V. (**1979**). ''Centres of gravity and spectral peaks as the determinants of vowel quality,'' in *Frontiers of Speech Communication Research*, edited by B. Lindblom and S. Öhman (Academic, London), pp. 143–157.

Di Benedetto, M. G. (**1994**). ''Acoustic and perceptual evidence of a complex relation between $F1$ and $F0$ in determining vowel height,'' J. Phonetics **22**, 205–224.

Granström, B., and Nord, L. (**1992**). ''Neglected dimensions in speech synthesis,'' Speech Commun. **11**, 459–462.

Junqua, J. C. (**1993**). ''The Lombard reflex and its role on human listeners and automatic speech recognizers,'' J. Acoust. Soc. Am. **93**, 510–524.

Liénard, J. S. (**1995**). ''From speech variability to pattern processing: A nonreductive view of speech processing,'' in *Levels in Speech Communication: Relations and Interactions*, edited by C. Sorin *et al.* (Elsevier Science B.V., Amsterdam).

Lindblom, B. (**1987**). ''Adaptive variability and absolute constancy in speech signals: two themes in the quest for phonetic invariance,'' Proceedings of the XIth International Congress of Phonetic Sciences, August 1–7, Tallin, Estonia, USSR, pp. 9–18.

Schulman, R. (**1989**). ''Articulatory dynamics of loud and normal speech,'' J. Acoust. Soc. Am. **85**, 295–312.

Sluijter, A. M. C., and Heuven, V. J. Van (**1996**). ''Spectral balance as an acoustic correlate of the linguistic stress,'' J. Acoust. Soc. Am. **100**, 2471–2485.

Sluijter, A. M. C., Heuven, V. J. Van, and Pacilly, J. J. A. (**1997**). ''Spectral balance as a cue in the perception of linguistic stress,'' J. Acoust. Soc. Am. **101**, 503–513.

Syrdal, A. K. (**1985**). ''Aspects of a model of the auditory representation of American English vowels,'' Speech Commun. **4**, 121–135.

Syrdal, A. K., and Gopal, H. S. (**1986**). ''A perceptual model of vowel recognition based on the auditory representation of American English vowels,'' J. Acoust. Soc. Am. **79**, 1086–1100.

Traunmüller, H. (**1981**). ''Perceptual dimensions of openness in vowels,'' J. Acoust. Soc. Am. **69**, 1465–1475.

Traunmüller, H. (**1989**). ''Articulatory dynamics of loud and normal speech,'' J. Acoust. Soc. Am. **85**, 295–312.

VECSYS. (**1989**). *The uNICE User Manual* (VECSYS—3 rue de la Terre de fue, 91952 courtaboeuf Cedex, France.

Analysis and perception of spectral 1/*f* characteristics of amplitude and period fluctuations in normal sustained vowels

Naofumi Aoki and Tohru Ifukube
Research Institute for Electronic Science, Hokkaido University, N12 W6 Sapporo, 060-0812 Japan

(Received 6 June 1998; revised 3 March 1999; accepted 29 march 1999)

Two kinds of fluctuations are always observed in the steady parts of normal sustained vowels. One is amplitude fluctuation, defined as the cyclic changes of maximum peak amplitudes. The other is period fluctuation, defined as the cyclic changes of pitch periods. The primary purpose of this paper is to present quantitative descriptions of amplitude and period sequences obtained from normal sustained vowels. These fluctuation sequences consisted of maximum peak amplitudes or pitch periods extracted successively from 512 consecutive pitch periods in the steady part. Results of the frequency analysis indicated that their frequency characteristics seemed to be subject to the spectral $1/f$ power law. In order to investigate the possibility that the frequency characteristics of the fluctuation sequences influence the voice quality of sustained vowels, psychoacoustic experiments were conducted. Amplitude and period sequences evaluated in the experiments were spectral $1/f^0$ (white noise), $1/f$, $1/f^2$, and $1/f^3$ sequences, respectively. The experimental results indicated that the subjective voice quality of synthesized sustained vowels could reflect the differences in the frequency characteristics of the fluctuation sequences. [S0001-4966(99)01507-6]

PACS numbers: 43.71.Bp, 43.70.Gr [WS]

INTRODUCTION

Normal sustained vowels always contain cyclic change of maximum peak amplitudes and pitch periods, even in their most steady parts where these values are considered to be quite stable (Lieberman, 1961; Hiki *et al.*, 1966; Hollien *et al.*, 1975; Horii, 1975). In this paper, they are labeled as amplitude fluctuation and period fluctuation, respectively. In addition, the sequences which consisted of maximum peak amplitudes or pitch periods extracted successively from the steady part of normal sustained vowels are labeled as amplitude sequence (AS) or period sequence (PS), respectively.

One of the major objectives of the research on these voice fluctuations is to examine their applicability for quantitative discrimination of pathological voices from normal cases. Since the characteristics of AS and PS obtained from sustained vowels produced by speakers with laryngeal pathology tend to deviate from those of normal sustained vowels, both the fluctuation sequences are considered to contain potentially significant information for diagnostic screening of pathological voices.

As is summarized in the literature (Pinto and Titze, 1990), a variety of measures has been devised for diagnostic screening. A number of the measures focus on the deviations of the successive values in AS and PS defined, respectively, as shimmer and jitter (Koike, 1973; Hollien *et al.*, 1975; Kitajima and Gould, 1976; Horii, 1979, 1980; Milenkovic, 1987; Titze *et al.*, 1987; Childers and Wu, 1990; Pinto and Titze, 1990; Scherer *et al.*, 1995; Bielamowicz *et al.*, 1996). Since the size of jitter and shimmer tends to be larger for pathological sustained vowels than for normal cases, these differences would give potentially useful information for the discrimination between pathological and normal sustained vowels (Lieberman, 1963; Hecker and Kreul, 1971; Koike, 1973; Kitajima and Gould, 1976; Kasuya *et al.*, 1983, 1986; Askenfelt and Hammarberg, 1986; Hillenbrand, 1987; Eskenazi *et al.*, 1990; Martin *et al.*, 1995).

On the other hand, several studies have pointed out that the differences in the dynamic characteristics of AS and PS could be a factor which causes the differences in voice quality between pathological and normal sustained vowels. The viewpoints of these studies are (1) temporal characteristics (Lieberman, 1961), (a) autocorrelation (Koike, 1969; von Ledan and Koike, 1970), (3) random fractal nature (Baken, 1990), (4) nonlinear dynamics (Herzel *et al.*, 1994), and (5) frequency characteristics of the fluctuation sequences (Endo and Kasuya, 1994).

The temporal characteristics of the fluctuation sequences obtained from normal sustained vowels are suggested to be not completely random processes. The current values in the fluctuation sequences are influenced by the previous values in the sequences (Lieberman, 1961). The randomness of the fluctuation sequences parametrized by the fractal dimension also suggested that they are not completely random (Baken, 1990).

In addition, the randomness of the fluctuation sequences was evaluated by visualizing their autocorrelation function (Koike, 1969; von Leden and Koike, 1970), attractor patterns in the phase space (Herzel *et al.*, 1994), and their frequency characteristics (Endo and Kasuya, 1994). These studies also indicated that the dynamic characteristics of the fluctuation sequences could be applicable for diagnostic screening, since the dynamic characteristics derived from pathological sustained vowels tended to be different from normal cases.

In order to establish the methodology of diagnostic

screening from the viewpoint of the dynamic characteristics of fluctuation sequences, further investigation is required. The relationship between the dynamic characteristics of the fluctuation sequences and the corresponding speech perception could be useful information to design measures for diagnostic screening.

Another major objective of the research on the voice fluctuations is the enhancement of synthesized sustained vowels (Childers and Hu, 1994; Klatt and Klatt, 1990; McCree and Barnwell, 1995). Synthesized sustained vowels would be perceived as buzzer-like without incorporating amplitude and period fluctuations. A number of studies have indicated that the size of the standard deviation of AS and PS significantly influences the voice quality of synthesized sustained vowels. It has been suggested that the buzzer-like voice quality can be improved, if the standard deviation of AS and PS incorporated into synthesized sustained vowels are optimized (Wendahl, 1963, 1966; Hiki *et al.*, 1966; Coleman, 1969, 1971; Rozsypal and Millar, 1979). On the other hand, it is also indicated that the large standard deviations of AS and PS are associated with rough voice quality as perceived in pathological cases. This finding could be consistent with studies which have indicated that the size of shimmer and jitter can be useful measures for the diagnostic screening of pathological voices from normal cases. The size of shimmer and jitter tends to be large as the size of the standard deviation of AS and PS becomes larger. The size of the standard deviation of AS and PS appears to be one of the important factors in enhancing the voice quality of synthesized sustained vowels.

Furthermore, it is also indicated that the dynamic characteristics of the sequences can be another significant factor to enhance the voice quality of synthesized sustained vowels. Several studies have suggested that the frequency characteristics of AS and PS would influence the voice quality (Kobayashi and Sekine, 1991; Komuro and Kasuya, 1991; Aoki and Ifukube, 1996). For the enhancement of the voice quality of synthesized sustained vowels, it seems potentially useful to investigate what features of the frequency characteristics of the fluctuation sequences contribute to the enhancement.

The primary purpose of the present study was to describe statistically the characteristics of AS and PS obtained from normal sustained vowels. Speech analysis was conducted to gain information which would be potentially useful for modeling the fluctuation sequences. The size of the standard deviation and the frequency characteristics of the fluctuation sequences were included in the speech analysis. In addition, psychoacoustic experiments investigated how the synthesized sustained vowels characterized by chosen frequency characteristics of AS and PS were perceived. The experiments aimed to examine whether or not the differences in their frequency characteristics were associated with subjective differences in the voice quality of synthesized sustained vowels.

I. SPEECH ANALYSIS

This section describes several statistical characteristics of AS and PS obtained from normal sustained vowels. The speech analysis included the investigation of the size of the standard deviation and the frequency characteristics of both fluctuation sequences. In addition, their stationarity, distribution, and the correlation between AS and PS were investigated to obtain the information for modeling the fluctuation sequences.

A. Speech samples

Ten male subjects between 22 and 26 years of age who did not suffer from any laryngeal disorders were selected in order to obtain normal sustained vowels. Each subject was requested to phonate the sustained vowel /a/ as steadily as possible in a soundproof anechoic room (Rion, audiometry room) toward an electret condenser microphone (Audiotechnica, AT822) at a distance of about 15 cm from the mouth. The sustained vowels were directly recorded onto a hard disk by way of a microphone mixer (Mackie, microseries 1202-VLZ), a low-pass filter (8th-order Bessel characteristic), and an analog-to-digital converter (Digidesign, audiomedia II). The sampling rate and quantization level were 44.1 kHz and 16 bits, respectively. The cutoff frequency of the low-pass filter was set to 5 kHz.

Speakers phonated the vowels at a pitch and loudness that was comfortable. The duration of the phonation was requested to be approximately 10 s. All records contained a steady portion of at least 512 pitch periods lasting over approximately 4 s, in which the mean pitch period was found to range from 7.6 to 9.1 ms. The calculated mean pitch period of all speech samples was 8.3 ms. The sound-pressure level (SPL) was also measured by a precision noise meter using the C weighting condition (Brüel & Kjær, type 2209), which was placed about 15 cm from the mouth. Measured SPL ranged from 80 to 86 dB for all subjects. The gain of the microphone mixer was adjusted for each subject for an optimal recording level. Twenty speech samples were taken per subject, since at least 15 speech samples were required to guarantee statistical significance in the fluctuation sequences of normal sustained vowels (Scherer *et al.*, 1995). Two hundred speech samples in total (20 utterances $\times$ 10 subjects) were obtained.

B. Extraction of AS and PS

Since updated values for each cycle of both fluctuations were required to form fluctuation sequences, each value of AS and PS was extracted from the digitized speech samples using a peak-picking method and a zero-crossing method, respectively (Hollien *et al.*, 1973; Hori, 1975, 1979, 1980; Titze *et al.*, 1987; Doherty and Shipp, 1988; Titze and Liang, 1993). The resolution of the extraction for AS was set to be better than a 0.1% accuracy level. It is reported that this accuracy level is guaranteed if the maximum peak amplitudes are represented by more than 9 bits (Titze *et al.*, 1987). This requirement was satisfied by adjusting proper recording levels in the sampling session. Maximum peak amplitudes were represented by more than 13 bits, so that this condition would be considered sufficient for satisfying the required accuracy level. In this study, a parabolic interpolation technique was also employed in order to improve the accuracy of the extraction (Titze *et al.*, 1987).

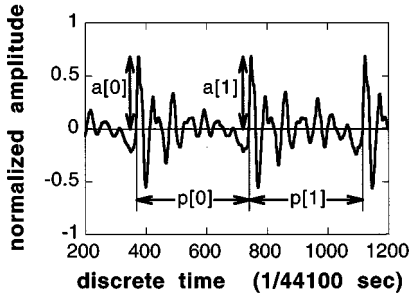

FIG. 1. Definition of amplitude sequence (AS) and period sequence (PS). Amplitudes of the speech sample are normalized to vary from −1 to 1, which corresponds to −32 768 to 32 767 (16 bits quantization level). From consecutive 512-pitch periods, the AS denoted by $a[n]$, $n=0,1,...,511$ and the PS denoted by $p[n]$, $n[0],1,...,511$ were successively extracted.

The resolution which is better than a 0.1% accuracy level requires an extremely high sampling rate for the extraction of PS (Horii, 1979; Milenkovic, 1987; Titze *et al.*, 1987; Titze and Liang, 1993). It is reported that more than 500 samples are required to represent each cycle in order to satisfy this accuracy level. According to this criterion, a sampling rate greater than 65.8 kHz is necessary if the pitch period is 7.6 ms, as it is our highest case. Although such a high sampling rate is desirable for accurate extraction of PS, it is also reported that the zero-crossing method with a linear interpolation can be a remedy to decrease the required sampling rate without sacrificing the accuracy (Titze *et al.*, 1987). In this study, the linear interpolation scheme was employed to prevent the degradation of the accuracy of the extraction caused by utilizing a 44.1-kHz sampling rate.

The extraction of fluctuation sequences was performed in the following order. First, the middle portion of each speech sample was extracted by using an editing program for acoustic signals (Digidesign, SOUND DESIGNER II) after visually and acoustically inspecting that particular unsteadiness was not detected in this portion. The extracted portion was referred to as a steady part. From the steady part, PS was then extracted successively from consecutive 512 pitch periods. AS was also extracted from the same 512 pitch periods. Figure 1 illustrates the definition of AS and PS, where the amplitudes of the speech sample were normalized to range from −1 to 1, which corresponds to −32 768 to 32 767, the quantization level of 16 bits. Figure 2 shows an example of a pair of AS and PS obtained from one of the speech samples.

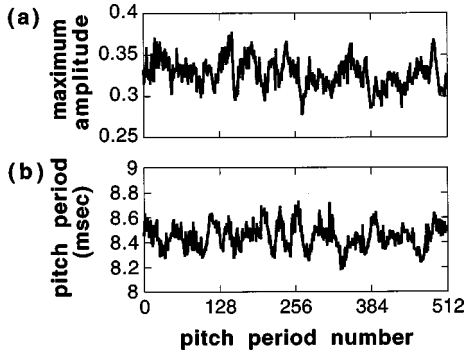

FIG. 2. Examles of (a) AS and (b) PS obtained from one of the speech samples. The AS shown in (a) is represented by using the same normalization as in Fig. 1.

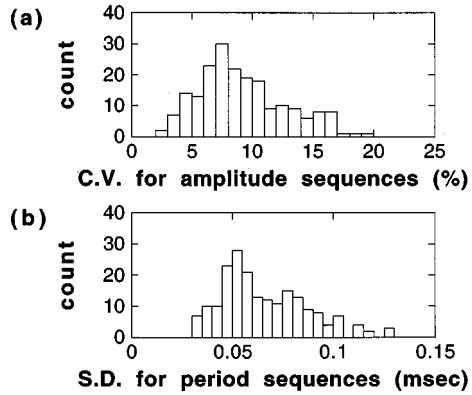

FIG. 3. Distributions of (a) the coefficient of variation (C.V.) of AS and (b) standard deviation (s.d.) of PS obtained from all speech samples.

C. Distributions of the coefficient of variation of AS and the standard deviation of PS

As mentioned earlier, the size of the standard deviation of AS and PS is considered to be a significantly important factor that influences the voice quality of sustained vowels. The standard deviations of both fluctuation sequences were statistically analyzed in order to investigate their valid size for normal sustained vowels.

Since the gain of the microphone mixer was adjusted depending on the loudness of the subject, the magnitudes of AS were represented by arbitrary units. Therefore, coefficient of variation (C.V.) was chosen as a measure for the size of AS (Pinto and Titze, 1990). C.V. is a measure which represents the standard deviation of a sequence normalized by the mean. The distribution of the C.V. of AS is shown in Fig. 3(a). It ranged from 2% to 20% and its mode was found at around 7.5%. The mode as within the normative range for the normal AS, which was reported to be 6.68%±3.03% (mean ± standard deviation %) (Scherer *et al.*, 1995).

Standard deviation (s.d.) itself was employed as a measure to compare the size of PS. As shown in Fig. 3(b), the s.d. of PS ranged from 0.03 to 0.13 ms and its mode was around 0.05 ms. In addition, the C.V. of PS was also calculated for the comparison with the normative range reported in the literature (Scherer *et al.*, 1995). The C.V. of PS ranged from 0.5% to 1.6% and its mode was found at around 0.8%. The mode was within the normative range 1.05±0.40% for the normal PS (Scherer *et al.*, 1995).

The correlation of the size of AS and PS, both of which were obtained from an identical speech sample, was also investigated for the development of the model of the fluctuation sequences. Figure 4 shows the scattergram plotted for C.V. of AS versus s.d. of PS. Although a moderate positive correlation coefficient ($r=0.64$) was obtained from the scattergram as average tendency (Bendat and Piersol, 1971), there was a variety of the combinations which obscures the meaning of the average correlation coefficient. For example, one of the cases showed that the C.V. of AS was small, while the s.d. of PS was large, and vice versa. Such deviations

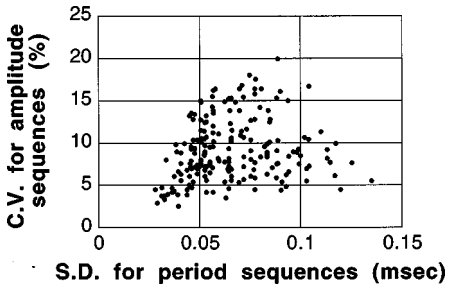

FIG. 4. The scattergram obtained from all speech samples shows the correlation of the size between AS and PS obtained from the identical speech sample. The average correlation coefficient is 0.64.

were found among individual speech samples, even from the same subject.

The size of fluctuation sequences investigated in terms of the C.V. for AS and the s.d. for PS would be useful information when we develop the model of the fluctuation sequences. Since it was difficult to make any meaningful conclusion that AS and PS were correlated or independent in their size, the size of PS for AS or AS for PS could be chosen rather arbitrarily for the preliminary model.

D. Stationarity of AS and PS

For developing the model of the fluctuation sequences, it is useful to examine whether the size of fluctuation sequences changes as the duration of the sequences changes. In order to clarify this issue, the stationarity of AS and PS was investigated. In this study, stationarity was defined as the time invariance of the mean and the variance of the sequence (Bendat and Piersol, 1971).

A runs test was employed in order to judge whether a fluctuation sequence was a stationary or nonstationary process. The test examined whether the changes of short-time mean and variance of a sequence were acceptable as those of a stationary process (Bendt and Piersol, 1971). Table I shows the results of the tests. The severity of the tests defined by the level of significance was chosen to be $\alpha=0.01$. The numbers of (A) AS and (B) PS for each subject in Table I represent the fluctuation sequences which were acceptable as stationary out of 20 sequences. Almost all of AS (92%) as well as PS (96%) were acceptable as stationary processes.

TABLE I. The results of the runs test which determined whether (A) AS and (B) PS were stationary or nonstationary processes. The level of significance was set to $\alpha=0.01$ for the test. The table represents the numbers of the fluctuation sequences acceptable as stationary processes out of the 20 sequences from each subject.

Subject	(A)	(B)
A.H.	16	19
M.Y.	18	18
I.M.	18	20
S.Y.	17	20
Y.T.	20	19
H.S.	17	20
M.I.	18	18
M.S.	20	19
S.S.	19	18
T.S.	20	20
total	183/200 (92%)	191/200 (96%)

TABLE II. The results of the *chi*-squared test which determined whether the distributions of (A) AS and (B) PS were Gaussian. The level of significance was set to $\alpha=0.01$ for the tests. The table represents the numbers of the sequences acceptable as Gaussian out of the 20 sequences from each subject.

Subject	(A)	(B)
A.H.	12	15
M.Y.	11	9
I.M.	16	12
S.Y.	15	10
Y.T.	12	16
H.S.	10	17
M.I.	11	8
M.S.	14	10
S.S.	9	7
T.S.	11	15
total	121/200 (61%)	119/200 (60%)

In conclusion, AS and PS extracted from the steady part of normal sustained vowels would be regarded as stationary processes. The size of fluctuation sequences would not change, even though their duration changed. This result shows one of the features of the fluctuation sequences to be taken into account for their model.

E. Distributions of AS and PS

The distribution of fluctuation sequences is one of the important features for developing their model. It has been reported that the distributions of AS and PS are seemingly regarded as Gaussian (Komuro and Kasuya, 1991; Aoki and Ifukube, 1996). This tendency was reexamined in this study.

Table II shows the results of the *chi*-squared test which examined whether the distribution of a sequence was classified as Gaussian (Bendat and Piersol, 1971). The numbers of (A) AS and (B) PS for each subject in Table II represent the fluctuation sequences which were acceptable as Gaussian out of 20 sequences. The level of significance was chosen to be $\alpha=0.01$ for the test.

The results indicated that the Gaussian distribution was considered to be one of the possible choices in modeling, since more than half of the distributions of AS (61%) and PS (60%) were acceptable as Gaussian. However, the results did not clearly confirm that the Gaussian distribution was always necessary for their model, since it appeared that a number of the distributions were not acceptable as Gaussian. Further investigation of their distribution in order to develop more precise models of the fluctuation sequences were left for future study.

F. Correlation between AS and PS

The correlation between AS and PS also influences the model of the fluctuation sequences. Correlation coefficients were calculated from all the pairs of AS and PS (Bendat and Piersol, 1971). Since individual tendency was not particularly different from subject to subject, pooled distribution of the correlation coefficients was obtained from all subjects.

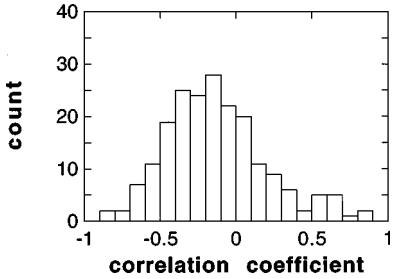

FIG. 5. Distribution of correlation coefficients between AS and PS obtained from the identical speech samples. The mean and the standard deviation of the distribution are −0.12 and 0.32, respectively.

The result is shown in Fig. 5. The mean and standard deviation of the distribution were −0.12 and 0.32, respectively. Since the correlation coefficients tended to center approximately at zero, both fluctuation sequences are likely to be modeled as processes as independent of each other.

G. Frequency characteristics of AS and PS

This study investigated the dynamic characteristics of the fluctuation sequences from the viewpoint of their frequency characteristics (Endo and Kasuya, 1994). The frequency characteristics of AS and PS were estimated using the 512-point fast Fourier transform (FFT) with Hamming window (Bendat and Piersol, 1971). As a result, it was found that the gross approximation of the frequency characteristics was subject to the spectral $1/f^{\beta}$ power law (Mandelbrot, 1977; Voss and Clarke, 1978; Keshner, 1982; Musha and Yamamoto, 1995), although the details might deviate from this approximation. This tendency was consistent among all fluctuation sequences.

Figure 6 shows examples of the frequency characteristics of AS and PS. The value of the exponent β was estimated by the least-squares line fitting (Bendat and Piersol, 1971). The value of β is equivalent to the gradient of the fitted line in the frequency characteristics represented in the log–log scale. The value of β of this example was 0.99 for AS and 0.96 for PS.

The average frequency characteristics of AS and PS are shown in Fig. 7. It was found that the mean value of β was

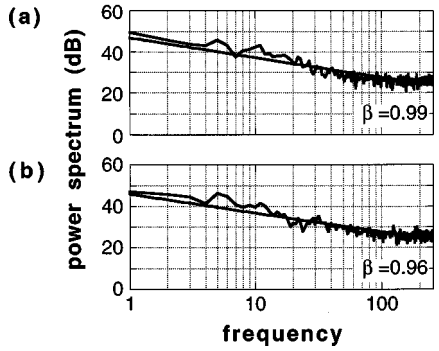

FIG. 6. Examples of the frequency characteristics of (a) AS and (b) PS obtained from a speech sample. The highest frequency is represented as 256 due to the 512-point FFT. The least-squares line fitting indicates that $\beta = 0.99$ for the AS and $\beta = 0.96$ for the PS in modeling these frequency characteristics by spectral $1/f^{\beta}$ power law.

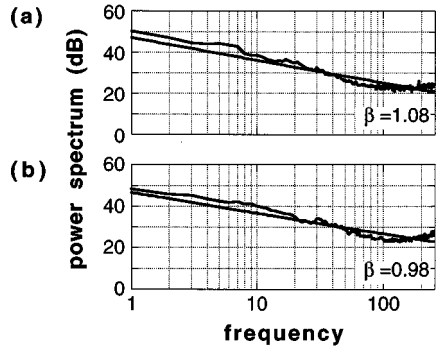

FIG. 7. Mean frequency characteristics of (a) AS and (b) PS obtained from all speech samples. As in the case of Fig. 6, the value of β is close to 1; $\beta = 1.08$ for the AS and $\beta = 0.98$ for the PS.

1.08 for AS and 0.98 for PS. The calculated standard deviation of β was 0.13 for AS and 0.17 for PS, respectively. Since the value of β tended to center approximately at 1, the results of frequency analysis would indicate that both fluctuation sequences can be modeled as spectral $1/f$ processes as a preliminary choice.

H. SUMMARY

The results of the speech analyses are summarized as follows. The size of the fluctuation sequences varied in the range of 2% to 20% in terms of C.V. for AS, for 0.03 to 0.13 ms in terms of s.d. for PS. The mode of C.V. for AS was 7.5%, and s.d. for PS was 0.05 ms. The correlation of the size between AS and PS was not particularly characterized by the average correlation coefficient. The results of the runs test indicated that both fluctuation sequences could be modeled as stationary processes. As a preliminary choice, the distribution of both fluctuation sequences can be modeled as Gaussian, since more than half of the distributions of AS and PS were considered to be Gaussian. Furthermore, AS and PS could be modeled as processes independent of each other, since AS and PS did not consistently show a strong correlation. Although the results of the frequency analysis suggested much finer models, both fluctuation sequences would be roughly modeled as spectral $1/f^{\beta}$ processes, where the β is equivalent to 1 as a gross approximation.

II. PSYCHOACOUSTIC EXPERIMENTS

As mentioned earlier, several studies have suggested that the frequency characteristics of AS and PS influence the voice quality of synthesized sustained vowels (Kobayashi and Sekine, 1991; Komuro and Kasuya, 1991; Aoki and Ifukube, 1996). In order to explore the influence of the frequency characteristics of fluctuation sequences on speech perception, a series of psychoacoustic experiments was conducted. The purpose of the experiments was to investigate how the differences in their frequency characteristics caused the subjective differences in the voice quality of synthesized sustained vowels.

A. Stimuli

Stimuli for the psychoacoustic experiments were sustained vowels /a/ produced by a partial autocorrelation

(PARCOR) synthesizer (Rabiner and Schafer, 1978; Kondoz, 1994). They were characterized by the different combinations of AS and PS.

The filter coefficients of the PARCOR synthesizer were derived from one of the speech samples whose AS and PS showed the representative characteristics of all fluctuation sequences investigated in this study. The C.V. of the AS was 7.5% and the s.d. of the PS was 0.05 ms. Both fluctuation sequences were acceptable as stationary processes. Their distributions were also acceptable as Gaussian. Since the correlation coefficient between the AS and PS was -0.06, they were considered not strongly correlated with each other. Their frequency characteristics were approximated by the spectral $1/f^{\beta}$ power law, in which β was 0.99 for the AS and 0.96 for the PS. Both frequency characteristics are, respectively, shown in Fig. 6. Furthermore, the mean pitch period calculated from the PS was 8.4 ms, which was close to the average of all speech samples. Both fluctuation sequences were employed in synthesizing stimuli.

The filter order of the PARCOR synthesizer was set to 40 for the condition of a 44.1-kHz sampling rate (Rabiner and Schafter, 1978; Kondoz, 1994). It was visually inspected that the frequency characteristics of the PARCOR filter in this condition appropriately represented four dominant formants below the cutoff frequency of the low-pass filter of 5 kHz. The coefficients of the PARCOR filter were not altered during the synthesis. This condition was based on the assumption that the characteristics of the vocal tract filter for normal sustained vowels do not substantially change during the phonation. In order to synthesize sustained vowels, impulse trains, which are conventionally used for synthesizing voiced speech, were employed as source signals of the PARCOR synthesizer (Rabiner and Schafer, 1978; Kondoz, 1994). Period fluctuations in the stimuli were implemented by the pulse-position modulation (Lathi, 1968). It employed PS as the modulating signals. In order to guarantee the accuracy of the modulation at a 44.1-kHz sampling rate, impulse trains represented in the analog form were passed through a -6-dB/oct low-pass filter and sampled at a 44.1-kHz sampling rate. This low-pass filter theoretically consisted of both -12-dB/oct glottal characteristics and $+6$-dB/oct radiation characteristics from the mouth (Rabiner and Schafer, 1978; Kondoz, 1994). After synthesizing sustained vowels by the PARCOR filter, cyclic gain adjustments defined by AS were employed to incorporate amplitude fluctuations.

Each stimulus consisted of 128 pitch periods. Since the mean pitch period was set to 8.4 ms, the duration of each stimulus was approximately 1 s. A linearly increasing or decreasing gate function whose duration was 10 ms was employed at the beginning and the end of each stimulus in order to prevent click-like sounds.

The psychoacoustic experiments investigated four different conditions in regard to AS and PS. In conditions 1 and 2, the frequency characteristics of AS were manipulated, while all of the stimuli employed the PS obtained from the speech sample. On the other hand, PS was changed from stimulus to stimulus in conditions 3 and 4, while all of the stimuli employed the AS obtained from the speech sample.

TABLE III. Fluctuation sequences characterizing the stimuli.

	Stimulus	Conditions 1 and 2	Conditions 3 and 4
	a	AS (speech sample)	PS (speech sample)
	b	no AS	no PS
	c		
$\beta 0$	*d*	AS ($1/f^0$ sequences)	PS ($1/f^0$ sequences)
	e		
	f		
$\beta 1$	*g*	AS ($1/f$ sequences)	PS ($1/f$ sequences)
	h		
	i		
$\beta 2$	*j*	AS ($1/f^2$ sequences)	PS ($1/f^2$ sequences)
	k		
	l		
$\beta 3$	*m*	AS ($1/f^3$ sequences)	PS ($1/f^3$ sequences)
	n		

Thus, conditions 1 and 2 focused on how fluctuations in AS influenced perception, while conditions 3 and 4 focused on how perception was influenced by the different frequency characteristics of PS.

Fourteen stimuli labeled from ''*a*'' to ''*n*'' were produced for each condition. Fluctuation sequences employed to characterize the stimuli are summarized in Table III. Stimulus ''*a*'' employed the AS and the PS obtained from the speech sample. Although stimulus ''*a*'' was not the speech sample itself, its voice quality was considered to reflect the characteristics of the AS and the PS of the speech sample. Since stimulus ''*a*'' was used as a reference stimulus in evaluating all stimuli including stimulus ''*a*'' itself, it was also labeled the reference stimulus. Comparisons between the reference stimulus and stimulus ''*a*'' were the control for the experiment. Stimulus ''*b*'' was produced without amplitude or period fluctuation. This stimulus was aimed to examine whether amplitude or period fluctuation was an important factor for speech perception. In addition, four stimulus groups, each of which consisted of three stimuli, were produced. The three stimuli of each stimulus group employed AS or PS whose frequency characteristics were classified in the same category, while the fluctuatiaon sequences themselves were different from each other, since randomization used for producing the fluctuation sequences was different. The four stimulus groups were labeled as $\beta 0$, $\beta 1$, $\beta 2$, and $\beta 3$ according to the frequency characteristics of the fluctuation sequences. Stimulus group $\beta 0$, which consisted of stimulus ''*c*,'' ''*d*,'' and ''*e*,'' employed spectral $1/f^0$ sequences (white noise). Stimulus group $\beta 1$, which consisted of stimulus ''*f*,'' ''*g*,'' and ''*h*,'' employed spectral $1/f$ sequences. Stimulus group $\beta 2$, which consisted of stimulus ''*i*,'' ''*j*,'' and ''*k*,'' employed spectral $1/f^2$ sequences. Stimulus group $\beta 3$, which consisted of stimulus ''*l*,'' ''*m*,'' and ''*n*,'' employed spectral $1/f^3$ sequences.

The value of the exponent β in the spectral $1/f^{\beta}$ sequences for each stimulus group was considered to be a rather preliminary choice. The integer values from 0 to 3 were employed, since there was no *a priori* knowledge about the relationship between speech perception and the values of β. This condition also aimed to examine whether or not the perceptual effects were categorized by the values of β.

The C.V. of all AS was set to 7.5% for condition 1 and 15% for condition 2, in which the C.V. of the AS obtained from the speech sample was also readjusted. Condition 2 aimed to examine whether or not the larger C.V. of AS influenced the experimental result compared with condition 1. The s.d. of PS was set to 0.05 ms for all stimuli throughout conditions 1 and 2.

On the other hand, the s.d. of PS was set to 0.05 ms for condition 3 and 0.10 ms for condition 4. Condition 4 aimed to examine whether or not the larger s.d. of PS influenced the experimental result compared with condition 3. The C.V. of AS was set to 7.5% for all stimuli throughout conditions 3 and 4.

All of AS and PS employed in the stimulus groups were fractional Brownian motions produced by the FFT method (Saupe, 1988; Voss, 1989). Gaussian white noise was first transformed to the frequency domain, then passed through the low-pass filter characterized by the spectral $1/f^{\beta}$ power law. The result was transformed back into the time domain. Although the speech analysis indicated that the distributions of AS and PS were not necessarily Gaussian, the fluctuation sequences employed in this study were simply assumed as Gaussian.

The power spectrum of a spectral $1/f^{\beta}$ sequence is represented as

$$S_v(f)=|T(f)|^2 S_w(f)\propto|T(f)|^2, \tag{1}$$

where $S_v(f)$ is the power spectrum of a spectral $1/f^{\beta}$ sequence $v(t)$, $T(f)$ is the frequency characteristics of a spectral $1/f^{\beta}$ filter, and $S_w(f)$ is the power spectrum of Gaussian white noise.

Thus, the spectral $1/f^{\beta}$ filter is required to be

$$|T(f)|=1/f^{\beta/2}. \tag{2}$$

The typical sequences produced by this method are shown in Fig. 8. These are the examples of spectral $1/f^0$ (white noise), $1/f$, $1/f^2$, and $1/f^3$ sequences, respectively. The smoothness of the sequences increase as the value of β increases. Simultaneously, the sequences prove to be nonstationary process. These are attributable to the dominance of the low-frequency components in the sequences for a larger β.

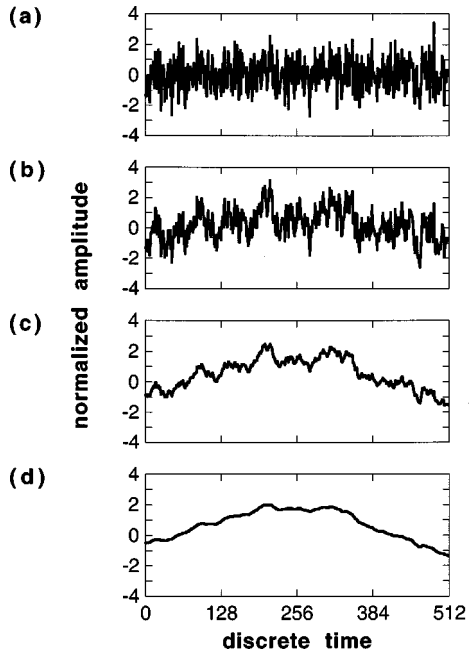

FIG. 8. Variations of $1/f^{\beta}$ sequence. The values of the exponent β are (a) zero, (b) 1, (c) 2, and (d) 3. The mean and the standard deviation are normalized to be zero and 1.

B. Subjects

Twenty subjects consisting of 12 males and eight females participated in the experiment. Their age ranged from 20 to 26 years. None of them was experienced in psychoacoustic experiments. All reported having no hearing problems.

C. Procedures

All stimuli were synthesized using a personal computer (Apple, Macintosh Quadra 800). The stimuli were passed through a digital-to-analog converter (Digidesign, audiomedia II) and then low-pass filtered (8th-order Bessel characteristic). The sampling rate and quantization level were 44.1 kHz and 16 bits, respectively. The cutoff frequency of the low-pass filter was set to be 10 kHz. The stimuli were presented through a monitor speaker (Denon, USC-101) which was attached to a premain amplifier (Sansui, AU-α 507XR). The speaker was placed 1.5 m in front of the subject in a soundproof anechoic room (Rion, audiometry room). The SPL of the stimuli was set to 65 dB upon presentation.

Each subject took part individually in the experiment of all four conditions. Each condition consisted of 14 paired-comparison trials to evaluate the similarity between the preceding stimulus *A* and the succeeding stimulus *B*. The stimulus *A* was the reference stimulus. The stimulus *B* was one of the 14 stimuli produced for each condition. The order of the presentation in regard to stimulus *B* was randomized.

The stimulus *A* and *B* were presented to the subject twice in the form of an *AB* pair. There was a 1-s silent interval between stimulus *A* and *B*, and a 2-s silent interval between the first and second *AB* pair. For the judgment, a 6-s interval was given to the subject after listening to the two *AB* pairs.

The subject was asked to judge whether or not the voice quality of stimulus *B* was perceived as the same as that of stimulus *A*. They were forced to select one of the following three choices, (1) ''same,'' (2) ''undecided,'' or (3) ''different.'' The three-point scale aimed to examine whether or not the subject could correctly distinguish the voice quality between a stimulus of artificially produced fluctuation sequences and a stimulus of the fluctuation sequences obtained from the speech sample. The five- or seven-point scale, which is conventionally used to grade the differences in the voice quality, was not employed (Kreiman *et al.*, 1993). In order to compare the experimental results, the above three choices were translated into the numerical measured called similarity, which was defined as (1) 100%, (2) 50%, and (3) 0% corresponding to the three choices (Ifukube *et al.*, 1991).

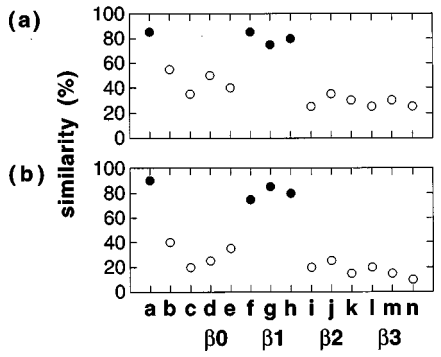

FIG. 9. The similarity of each stimulus is summarized in (a) for condition 1 and (b) for condition 2. Filled circles represent the results of χ^2 test that examined whether or not the similarity of each stimulus was acceptable as being in the same category of the control stimulus *a*. All stimuli of the stimulus group $\beta 1$ were acceptable as in the same category of the stimulus *a*. The level of significance for the test was set to $\alpha = 0.01$.

D. Results of practice trials

Prior to the experiment of four conditions, each subject took part in the practice stage consisting of 12 paired-comparison trials. Half of the 12 trials were practice runs for conditions 1 and 2. The other half of the trials were for conditions 3 and 4. Each half included a comparison between the reference stimulus and the control stimulus ''*a*'' that was the same as the reference stimulus itself. Since they were the same stimuli, responses for this comparisons were expected to be same. The errors with regard to this comparison occurred with five subjects as to AS and three subjects as to PS out of 20 subjects. This result suggested that most of the subjects could correctly detect the sameness between the same stimuli. In addition, most of the subjects judged these as the same even though they were not familiar with such kind of psychoacoustic comparison tests. The subjects were not informed of the correctness of their responses. Any criteria which might influence their judgments were not given to the subjects before or after the practice trials.

E. Results of conditions 1 and 2

The results of conditions 1 and 2 are summarized in Fig. 9(a) and (b), respectively. The similarity of each stimulus is represented by either an open or filled circle as the average of the results over all subjects.

It appeared that the control stimulus *a* and the stimulus group $\beta 1$ tended to be evaluated as more similar to the reference stimulus rather than the other stimuli throughout conditions 1 and 2. These results indicated that most of the subjects could not distinguish the voice quality of the stimulus group $\beta 1$ from that of the reference stimulus. The larger C.V. of AS examined in condition 2 did not substantially influence this tendency.

As for the other stimuli, most of the subjects reported that the voice quality of the stimulus group $\beta 0$ was rougher than that of the reference stimulus. Particular changes in the loudness were perceived in the stimulus group $\beta 2$ and $\beta 3$, while such features were not perceived in the reference stimulus. Some of the subjects also reported that the loudness changes of stimulus *b* were perceived as flat compared with the reference stimulus. These differences could be a subjective clue for the discrimination between the reference stimulus and these stimuli.

In order to evaluate the experimental results objectively, the independence between the control stimulus *a* and the other stimuli with regard to the response distributions in the three-point scale was examined by the *chi*-squared test (Bendat and Piersol, 1971). The level of significance for the test was chosen to be $\alpha = 0.01$.

The filled circles shown in Fig. 9 represent the stimuli whose response distributions were acceptable as in the same category as that of the stimulus *a*. Since all the stimuli of the stimulus group $\beta 1$ were acceptable as the same throughout conditions 1 and 2, it can be indicated that the voice quality of the stimulus group $\beta 1$ could be perceived as the same as the stimulus *a*, namely the reference stimulus.

F. Results of conditions 3 and 4

The results of conditions 3 and 4 are summarized in Fig. 10(a) and (b), respectively. It appeared that the control stimulus *a* and the stimulus group $\beta 1$ tended to be evaluated as more similar to the reference stimulus rather than the other stimuli throughout conditions 3 and 4. These results indicated that most of the subjects could not distinguish the voice quality of the stimulus group $\beta 1$ from that of the reference stimulus. The larger s.d. of PS examined in condition 4 did not substantially influence this tendency.

As for the other stimuli, most of the subjects reported that the voice quality of the stimulus group $\beta 0$ was rougher than that of the reference stimulus. Unstable changes in the pitch were perceived in the stimulus group $\beta 2$ and $\beta 3$, while such features were not perceived in the reference stimulus. Furthermore, most of the subjects reported that the stimulus *b* was perceived as buzzer-like compared with the reference stimulus. These differences could be a subjective clue for the discrimination between the reference stimulus and these stimuli.

The filled circles shown in Fig. 10 represent the stimuli whose response distributions in the three-point scale were acceptable as in the same category as that of the control stimulus *a* in terms of the *chi*-squared test (Bendat and Piersol, 1971). The level of significance for the test was chosen

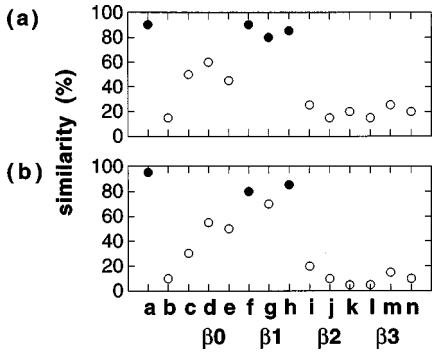

FIG. 10. The similarity of each stimulus is summarized in (a) for condition 3 and (b) for condition 4. Filled circles represent the results of χ^2 test. Most of the stimuli of the stimulus group $\beta 1$ (five cases out of six) are acceptable as in the same category of the control stimulus *a*. The level of significance for the test was set to $\alpha = 0.01$.

to be $\alpha=0.01$. Since five cases out of six were acceptable as the same throughout conditions 3 and 4, it can be indicated that the voice quality of the stimulus group $\beta 1$ could be classified as in almost the same category of the stimulus *a*, namely the reference stimulus.

G. SUMMARY

In spite of the different conditions, the stimulus group $\beta 1$ and the control stimulus *a* tended to be evaluated as similar to the reference stimulus throughout the four conditions. On the other hand, the other stimulus groups and stimulus *b* were not evaluated as being similar.

Since the similarity of stimuli *a* and *b* tended to be judged as low, it can be concluded that AS and PS play significant roles in the speech perception of sustained vowels, as mentioned in the previous literature (Wendahl, 1963, 1966; Hiki *et al.*, 1966; Coleman, 1969, 1971; Rozsypal and Millar, 1979). The results of the other stimuli suggest that the differences in the frequency characteristics of AS and PS can significantly influence speech perception. High similarity between the stimulus group $\beta 1$ and the reference stimulus was obtained. These results could be attributable to the similarity of the frequency characteristics of the fluctuation sequences between stimulus group $\beta 1$ and the reference stimulus.

Since there were no large differences in the similarity among all the stimuli of the stimulus group $\beta 1$, the randomization for producing the fluctuation sequences could have little effect on the speech perception. In addition, it seemed that the similarity of the stimulus group $\beta 1$ could not be significantly influenced by the differences in the size of the fluctuation sequences. The similarity of the stimulus group $\beta 1$ was consistently evaluated high throughout conditions 1 and 2 or conditions 3 and 4.

III. DISCUSSION

The results of the psychoacoustic experiments suggest that the frequency characteristics of fluctuation sequences could be a significant factor which influences the voice quality of sustained vowels. Compared with other stimulus groups, the stimuli which were characterized by spectral $1/f$ sequences tended to be evaluated as more similar to the reference stimuli. This result could be attributable to the fact that the frequency characteristics of the spectral $1/f$ sequences were close to those of the AS or the PS employed in the reference stimuli.

The spectral $1/f$ power law is often observed in a variety of natural phenomena, including fluctuation sequences obtained from biomedical signals, such as heart-rate fluctuation (Mandelbrot, 1977; Voss and Clarke, 1978; Keshner, 1982; Musha and Yamamoto, 1995). Although the spectral $1/f^{\beta}$ sequences are generally classified as nonstationary processes with the condition of $1<\beta$, the quasistationarity is observed in spectral $1/f$ sequences (Mandelbrot, 1977; Voss and Clarke, 1978; Keshner, 1982; Saupe, 1988; Voss, 1989; Wornell, 1996). The mean and the mean-square value of spectral $1/f^{\beta}$ sequences are subject to the following relationship with the condition of $1<\beta<3$ and $\beta=2H+1$ (Saupe, 1988; Voss, 1989; Wornell, 1996):

$$\langle v(rt)\rangle = r^{H}\langle v(t)\rangle, \qquad \langle v^{2}(rt)\rangle = r^{2H}\langle v^{2}(t)\rangle, \tag{3}$$

where $v(t)$ is a spectral $1/f^{\beta}$ sequence, r is the resolution factor of the sequence, H is the Hurst exponent, and $\langle\cdot\rangle$ is the expectation operator.

Since the mean and the variance derived from Eq. (3) are considered to change as the resolution factor r changes, $1/f^{\beta}$ fluctuations are classified as nonstationary processes with the condition of $1<\beta$. However, the mean and the variance of $1/f$ sequences, which are derived from Eq. (3) with the condition of $\beta\rightarrow 1$, namely $H\rightarrow 0$, are statistically invariance even though the resolution factor r changes. This nature of spectral $1/f$ sequences is known as self-similarity, which guarantees the quasistationarity of the sequences (Mandelbrot, 1977; Voss and Clarke, 1978; Keshner, 1982; Saupe, 1988; Voss, 1989; Wornell, 1996).

Taking these characterisics into consideration, AS and PS modeled as either spectral $1/f^{2}$ or $1/f^{3}$ sequences are classified as nonstationary processes. The typical examples of spectral $1/f^{2}$ and $1/f^{3}$ sequences shown in Fig. 8(c) and (d) exemplify their nonstationarity. Compared with spectral $1/f^{0}$ and $1/f$ sequences shown in Fig. 8(a) and (b), nonstationary changes in the short-time mean of spectral $1/f^{2}$ and $1/f^{3}$ sequences are easily detected.

The nonstationary changes in the loudness and the pitch by spectral $1/f^{2}$ or $1/f^{3}$ sequences are considered to have caused subjective differences in the voice quality from the reference stimulus which was characterized by stationary AS and PS. Taking account of the result of the speech analysis in which almost all fluctuation sequences would be acceptable as stationary processes, spectral $1/f^{2}$ and $1/f^{3}$ sequences could not be appropriate models for AS and PS of normal sustained vowels.

Compared with these nonstationary sequences, spectral $1/f$ sequences are considered to be more appropriate models for AS and PS due to their quasistationarity. The psychoacoustic experiment also subjectively supported the validity of the models. Considering the result of the speech analysis in which the fluctuation sequences were suggested to be approximated as spectral $1/f$ processes, it could be concluded that the models of spectral $1/f$ sequences are potentially useful choices for AS and PS of normal sustained vowels.

In this study, gross approximation of the frequency characteristics of fluctuation sequences was its only focus. However, the result of the frequency analysis suggested the possibility of much finer models. For example, it was found that the frequency characteristics in the high-frequency region tended to elevate greater than the spectral $1/f$ power law, as shown in Figs. 6 and 7. It will be of interest to investigate how finer models influence speech perception. In addition, it will also be of interest to examine how the perceptual differences are caused by the value of β as it gradually changes

from 1. These issues are currently being investigated by the authors for developing more detailed models of the fluctuation sequences.

Some previous studies also developed the model of PS for normal sustained vowels from the viewpoint of its frequency characteristics (Kobayashi and Sekine, 1991; Komuro and Kasuya, 1991). These models have represnted the frequency characteristics of PS by autoregression (AR) (Kobayashi and Sekine, 1991) or autoregressive moving-average (ARMA) (Komuro and Kasusya, 1991) forms of digital filter. Similarly to the results presented in this paper, these studies also indicated that the frequency characteristics of PS would be a key factor for the voice quality of sustained vowels. The gradual decreasing characteristics found in the high-frequency region were suggested to be a feature of PS which could be related to the voice quality of normal sustained vowels.

The decreasing characteristics of AS as well as PS were also pointed out by other previous studies (Kakita *et al.*, 1986; Hirama and Kakita, 1989; Titze and Liang, 1993; Endo and Kasuya, 1994). A speech analysis of normal sustained vowels showed decreases of high-frequency components of both AS and PS (Kakita *et al.*, 1986; Hirama and Kakita, 1989). These fluctuation sequences were extracted from three Japanese vowels /a/, /i/, and /u/ phonated by one adult male speaker. Such decreasing characteristics were also suggested by the speech analysis of PS obtained from normal sustained vowels /a/ (Titze and Liang, 1993). It is also reported that the decreasing characteristics of AS and PS might be one of the features of normal sustained vowels compared with pathological cases (Hirama and Kakita, 1989; Endo and Kasuya, 1994).

From these two viewpoints: (1) speech perception caused by fluctuation sequences, and (2) speech analysis of fluctuation sequences, it might be suggested that the decreasing characteristics are considered to be one of the features of the fluctuation sequences obtained from normal sustained vowels. Such decreasing characteristics could be a significant factor for the voice quality of normal sustained vowels.

IV. CONCLUSIONS

The present study statistically showed several aspects of AS and PS of normal sustained vowels. The speech analysis indicated that both fluctuation sequences would be approximated as spectral $1/f$ sequences in terms of their frequency characteristics.

In addition, the psychoacoustic experiments indicated that voice quality of sustained vowels appeared to be influenced by the frequency characteristics of the fluctuation sequences. The results of the present study are considered to provide potentially useful information for exploring the speech perception caused by fluctuation sequences and for developing their appropriate models for enhancing the voice quality of synthesized sustained vowels.

ACKNOWLEDGMENTS

We thank Dr. Strange at the University of South Florida and three anonymous reviewers for their useful comments. We also thank Dr. Katagiri and Dr. Pruitt at ATR, Japan and Dr. Takaya at the University of Saskatchewan, Canada for their useful advice in revising this paper.

Aoki, N., and Ifukube, T. (**1996**). ''Two $1/f$ fluctuations in sustained phonation and their roles on naturalness of synthetic voice,'' in *Proceedings ICECS 96* (IEEE, Rodos), pp. 311–314.

Askenfelt, A. G., and Hammarberg, B. (**1986**). ''Speech waveform perturbation analysis: A perceptual-acoustic comparison of seven measures.'' J. Speech Hear. Res. **29**, 50–64.

Baken, R. J. (**1990**). ''Irregularity of vocal period and amplitude: A first approach to the fractal analysis of voice,'' J. Voice **4**, 185–197.

Bendat, J. S., and Piersol, A. G. (**1971**). *Random data: Analysis and Measurement Procedures* (Wiley, New York).

Bielamowicz, S., Kreiman, J., Gerratt, B. R., Dauer, M. S., and Berke, G. S. (**1996**). ''Comparison of voice analysis systems for perturbation measurement,'' J. Speech Hear. Res. **39**, 126–134.

Childers, D. G., and Wu, K. (**1990**). ''Quality of speech produced by analysis-synthesis,'' Speech Commun. **9**, 97–117.

Childers, D. G., and Hu, H. T. (**1994**). ''Speech synthesis by glottal excited linear prediction,'' J. Acoust. Soc. Am. **96**, 2026–2036.

Coleman, R. F. (**1969**). ''Effect of median frequency levels upon the roughness of jittered stimuli,'' J. Speech Hear. Res. **12**, 330–336.

Coleman, R. F. (**1971**). ''Effect of waveform changes upon roughness perception,'' Folia Phoniatr. **23**, 314–322.

Doherty, E. T., and Shipp, T. (**1988**). ''Tape recorder effects on jitter and shimmer extraction,'' J. Speech Hear. Res. **31**, 485–490.

Endo, Y., and Kasuya, H. (**1994**). ''Spectral analysis of fundamental period perturbation and its modeling,'' Jpn. J. Logop. Phoniatr. **35**, 193–198 (in Japanese).

Eskenazi, L., Childers, D. G., and Hicks, D. M. (**1990**). ''Acoustic correlates of vocal quality,'' J. Speech Hear. Res. **33**, 298–306.

Hecker, M. H. L., and Kruel, E. J. (**1971**). ''Descriptions of the speech of patients with cancer of the vocal folds. Part I: Measures of fundamental frequency,'' J. Acoust. Soc. Am. **49**, 1275–1282.

Herzel, H., Berry, D., Titze, I. R., and Saleh, M. (**1994**). ''Analysis of vocal disorders with methods from nonlinear dynamics,'' J. Speech Hear. Res. **37**, 1008–1019.

Hiki, S., Sugawara, K., and Oizumi, J. (**1966**). ''On the rapid fluctuation of voice pitch,'' J. Acoust. Soc. Jpn. **22**, 290–291.

Hillenbrand, J. (**1987**). ''A methodological study of perturbation and additive noise in synthetically generated voice signals,'' J. Speech Hear. Res. **30**, 448–461.

Hirama, J., and Kakita, Y. (**1989**). ''Characteristics of a pathological rough voice based on the power spectrum of fluctuations,'' Jpn. J. Logop. Phoniatr. **30**, 225–230 (in Japanese).

Hollien, H., Michel, J., and Doherty, E. T. (**1973**). ''A method for analyzing vocal jitter in sustained phonation,'' J. Phonetics **1**, 85–91.

Horii, Y. (**1975**). ''Some statistical characteristics of voice fundamental frequency,'' J. Speech Hear. Res. **18**, 192–201.

Horii, Y. (**1979**). ''Fundamental frequency perturbation observed in sustained phonation,'' J. Speech Hear. Res. **22**, 5–19.

Horii, Y. (**1980**). ''Vocal shimmer in sustained phonation,'' J. Speech Hear. Res. **23**, 202–209.

Ifukube, T., Hashiba, M., and Matsushima, J. (**1991**). ''A role of 'waveform fluctuation' on the naturality of vowels,'' J. Acoust. Soc. Jpn. **47**, 903–910 (in Japanese).

Kakita, Y., Hirama, J., Hamatani, K., Ohtani, M., and Suzuki, M. (**1986**). ''Fluctuation of the fundamental frequency and the maximum amplitude,'' Trans. Comm. Speech Res., Acoustic. Soc. Jpn. **S85–103**, 805–812 (in Japanese).

Kasuya, H., Kobayashi, Y., and Kobayashi, T. (**1983**). ''Characteristics of pitch period and amplitude perturbations in pathologic voice,'' in *Proceedings ICASSP 83* (IEEE, Boston), pp. 1372–1375.

Kasuya, H., Ogawa, S., and Kikuchi, Y. (**1986**). ''An acoustic analysis of pathological voice and its application to the evaluation of laryngeal pathology,'' Speech Commun. **5**, 171–181.

Keshner, M. S. (**1982**). ''$1/f$ noise,'' Proc. IEEE **70**, 212–218.

Kitajima, K., and Gould, W. J. (**1976**). ''Vocal shimmer in sustained phonation of normal and pathologic voice,'' Ann. Otol. Rhinol. Laryngol. **85**, 377–381.

Klatt, D. H., and Klatt, L. C. (**1990**). ''Analysis, synthesis, and perception of

voice quality variations among female and male talkers,'' J. Acoust. Soc. Am. **87**, 820–857.
Kobayashi, T., and Sekine, H. (**1991**). ''The role of fluctuations in fundamental period for natural speech synthesis,'' J. Acoust. Soc. Jpn. **47**, 539–544 (in Japanese).
Koike, Y. (**1969**). ''Vowel amplitude modulations in patients with laryngeal diseases,'' J. Acoust. Soc. Am. **45**, 839–844.
Koike, Y. (**1973**). ''Application of some acoustic measures for the evaluation of laryngeal dysfunction,'' Stud. Phonol. **7**, 17–23.
Komuro, O., and Kasuya, H. (**1991**). ''Characteristics of fundamental period variation and its modeling,'' J. Acoust. Soc. Jpn. **47**, 928–934 (in Japanese).
Kondoz, A. M. (**1994**). *Digital Speech* (Wiley, New York).
Kreiman, J., Gerratt, B. R., Kempster, G. B., Erman, A., and Berke, G. S. (**1993**). ''Perceptual evaluation of voice quality: Review, tutorial, and a framework for future research,'' J. Speech Hear. Res. **36**, 21–40.
Lathi, B. P. (**1968**). *Communication Systems* (Wiley, New York).
Lieberman, P. (**1961**). ''Perturbations in vocal pitch,'' J. Acoust. Soc. Am. **33**, 597–603.
Lieberman, P. (**1963**). ''Some acoustic measures of the fundamental periodicity of normal and pathologic larynges,'' J. Acoust. Soc. Am. **35**, 344–353.
Mandelbrot, B. B. (**1977**). *The Fractal Geometry of Nature* (Freeman, New York).
Martin, D., Fitch, J., and Wolfe, V. (**1995**). ''Pathologic voice type and the acoustic prediction of severity,'' J. Speech Hear. Res. **38**, 765–771.
McCree, A. V., and Barnwell III, T. P. (**1995**). ''A mixed excitation LPC vocoder model for low bit rate speech coding,'' IEEE Trans. Speech Audio Process. **3**, 242–250.
Milenkovic, P. (**1987**). ''Least mean square measures of voice perturbation,'' J. Speech Hear. Res. **30**, 529–538.
Musha, T., and Yamamoto, M. (**1995**). ''1/f-like fluctuations of biological rhythm'' Noise Physical Syst., 22–31.
Pinto, N. B., and Titze, I. R. (**1990**). ''Unification of perturbation measures in speech signals,'' J. Acoust. Soc. Am. **87**, 1278–1289..
Rabiner, L. R., and Schafer, R. W. (**1978**). *Digital Processing of Speech Signals* (Prentice-Hall, Englewood Cliffs, NJ).
Rozsypal, A. J., and Miller, B. F. (**1979**). ''Perception of jitter and shimmer in synthetic vowels,'' J. Phonetics **7**, 343–355.
Saupe, D. (**1988**). ''Algorithms for random fractals,'' in *The Science of Fractal Images*, edited by H.-O. Peitgen and D. Saupe (Springer, New York), pp. 71–136.
Scherer, R. C., Vail, V. J., and Guo, C. G. (**1995**). ''Required number of tokens to determine representative voice perturbation values,'' J. Speech Hear. Res. **38**, 1260–1269.
Titze, I. R., Horii, Y., and Scherer, R. C. (**1987**). ''Some technical considerations in voice perturbation measurements,'' J. Speech Hear. Res. **30**, 252–260.
Titze, I. R., and Liang, H. (**1993**). ''Comparison of $F0$ extraction methods for high-precision voice perturbation measurements,'' J. Speech Hear. Res. **36**, 1120–1133.
von Leden, H., and Koike, Y. (**1970**). ''Detection of laryngeal disease by computer technique,'' Arch. Otolaryngol. **91**, 3–10.
Voss, R. F., and Clarke, J. (**1978**). '' '1/f noise' in music: Music from 1/f noise,'' J. Acoust. Soc. Am. **63**, 258–263.
Voss, R. F. (**1989**). ''Random fractals: Self-affinity in noise, music, mountains, and clouds,'' Physica D **38**, 362–371.
Wendahl, R. W. (**1963**). ''Laryngeal analog synthesis of harsh voice quality,'' Folia Phoniatr. **15**, 241–250.
Wendahl, R. W. (**1966**). ''Laryngeal analog synthesis of jitter and shimmer auditory parameters of harshness,'' Folia Phoniatr. **18**, 98–108.
Wornell, G. W. (**1996**). *Signal Processing with Fractals* (Prentice-Hall, Englewood Cliffs, NJ).

The role of *F*1 in the perception of voice onset time and voice offset time

Jörgen Pind
Department of Psychology, University of Iceland, Oddi, Reykjavík, IS-101 Iceland

(Received 25 August 1998; revised 2 December 1998; accepted 26 March 1999)

An important speech cue is that of voice onset time (VOT), a cue for the perception of voicing and aspiration in word-initial stops. Preaspiration, an [h]-like sound between a vowel and the following stop, can be cued by voice offset time, a cue which in most respects mirrors VOT. In Icelandic VOffT is much more sensitive to the duration of the preceding vowel than is VOT to the duration of the following vowel. This has been explained by noting that preaspiration can only follow a phonemically short vowel. Lengthening of the vowel, either by changing its duration or by moving the spectrum towards that appropriate for a long vowel, will thus demand a longer VOffT to cue preaspiration. An experiment is reported showing that this greater effect that vowel quantity has on the perception of VOffT than on the perception of VOT cannot be explained by the effect of *F*1 frequency at vowel offset. © *1999 Acoustical Society of America.* [S0001-4966(99)03707-8]

PACS numbers: 43.71.Es [JH]

INTRODUCTION

The perception of voicing and aspiration has received considerable attention in the speech perception literature over the past three decades. A significant contribution to this field is to be found in the original work of Lisker and Abramson (1964), which set forth the notion that stop consonant voicing and aspiration could be subsumed under a single speech cue of voice onset time (VOT), this being the time from oral release of the stop to voice onset. Subsequent research has dealt with many aspects of VOT as a speech cue including the effect of speech rate on VOT production and perception (e.g., Pind, 1995b; Summerfield, 1981; Volaitis and Miller, 1992). Particular acoustic properties of VOT and their role in perception have also been investigated, e.g., the role of *F*1 in the perception of VOT. Lisker (1975), Summerfield and Haggard (1977), and Kluender (1991) have shown that *F*1 frequency at voicing onset has a major effect on the location of VOT boundaries, the lower *F*1 is at onset the more VOT is needed to cue aspirated stops.

Icelandic has two categories of voiceless stops in syllable-initial position. These are traditionally described as being voiceless unaspirated [p,t,c,k] and voiceless aspirated [p^h,t^h,c^h,k^h] (there are no voiced stops in Icelandic). The difference between these two series is nicely captured with the VOT metric, the former series having short-lag VOTs, the latter series long-lag VOTs. In addition to aspiration of syllable-initial consonants, Icelandic also has medial aspiration of consonants, so-called preaspiration, which is uncommon in the world's languages (Maddieson, 1984). The acoustic consequence of preaspiration is a period of voicelessness before the closure for the stop (Thráinsson, 1978). Orthographically, this occurs before the sequences -pp-, -tt- and -kk, thus *happ*, [hahp], ''luck,'' *hatt*, [haht], ''hat, accusative,'' takk [t^hahk], ''thank you.'' Preaspiration also occurs before a stop+nasal or liquid, as for instance in *vopn* [vɔhpn̥] ''weapon.'' Preaspiration is usually of full segmental length (Pétursson, 1972).

Preaspiration occurs at the end of the vowel and before the stop closure and thus is part of the syllable rhyme (the syllable less any consonantal attack). Icelandic has distinctions of quantity in the rhyme (Benediktsson, 1963; Pind, 1986), distinguishing long and short vowels and consonants. A vowel is long if followed by one or no consonant, otherwise it is short (with the exception that before a cluster of p,t,k,s+v,j,r the vowel is usually long). This rule also applies to geminates. Before a single consonant a vowel is long but short before a geminate consonant. A three-way distinction is thus possible in stressed rhymes of Icelandic as illustrated by the following examples: *flak* [fla:k], ''fillet,'' a long vowel followed by a short stop; *flagg* [flak:], ''flag,'' a short vowel followed by a long (geminate) stop; *flakk* [flahk], ''roaming,'' a short vowel followed by preaspiration and a short stop. Preaspiration always follows a short vowel in Icelandic, never a long one. The rhyme is of roughly comparable duration in these three syllable types, V:C, VC:, and VhC (Garnes, 1976).

It is useful to define a metric of ''Voice Offset Time'' (VOffT) (Pind, 1995a). VOffT is a speech cue which is analogous to VOT forming an almost exact mirror-image of VOT. VOffT comes at the end of a vowel rather than at its beginning as does VOT. It consists of the preaspirated segment, i.e., the devoiced part of the vowel which comes before the closure of the stop. It is measured from the end of aspiration (where it turns into the silence of the closure) to the beginning of aspiration, i.e., where the voicing of the preceding vowel ceases. VOffT is thus a mirror-image of VOT except for the fact that VOT usually includes the word-initial burst of the stop. VOffT does not include the burst since this comes after the closure. Basically then in a language like Icelandic, which has no prevoiced or voiced stops, VOT consists of the initial burst followed by a period of aspiration at the beginning of a vowel, and VOffT consists of a period of aspiration at the end of the vowel.

Previous perception experiments (Pind, 1995a) have shown that preaspiration can readily be cued by Voice Offset

Time (VOffT). Provided the durational relationship of vowel and closure are appropriate, i.e., that the vowel is short, listeners find it just as easy to hear preaspiration cued by VOffT as post-aspiration cued by VOT. Both vowel and closure duration can influence the perception of VOffT as a cue for preaspiration. Increasing the duration of the vowel will call for a longer VOffT at the preaspiration boundary, increasing the closure duration will have the opposite effect (Pind, 1995a). This is as expected if quantity is having a major effect on the perception of preaspiration since both vowel and consonant duration define quantity in Icelandic. The ratio of vowel to rhyme duration is in fact the major cue for quantity in Icelandic (Pind, 1986, 1995b) although the spectrum of the vowel is also an important cue for quantity in the control vowels, e.g., [ɛ] (Pind, 1998).

Although VOT and VOffT can be synthesized with similar synthesis parameters, these speech cues show a marked difference in perception in one respect. Phoneme boundaries for VOffT are greatly influenced by the duration of the preceding vowel (Pind, 1996), whereas VOT shows only limited effect of the duration of the following vowel. In one experiment, lengthening the vowel from 132 to 232 ms moved the VOT boundaries in [pa–p^{h}a] continua from 29.7 to 35.5 ms, a shift of a little less than 6 ms. The corresponding shift for comparable VOffT continua, [ap–ahp], was close to 22 ms, from 30.7 to 52.6 ms of VOffT, using the same range of vowel durations. Clearly the shift for VOffT is considerably greater than seen for VOT, and thus it is doubtful whether these shifts could be explained in terms of rate-dependent normalization, as is commonly done for the VOT shifts (e.g., Volaitis and Miller, 1992).

Experiments reported in a recent article (Pind, 1998) point to the importance of vowel quantity in explaining this difference between VOT and VOffT. VOT is syllable initial and can be followed by either phonemically short or long vowels. Preaspiration, coming *after* the vowel, can only follow a phonemically short vowel. In experiments using synthetic speech it was shown that changing the quantity of the vowel [ɛ] in either of two ways, by increasing its duration or by changing the vowel spectrum toward that of a long vowel, had similar effects on the amount of VOffT needed to cue preaspiration. Phoneme boundaries for preaspiration moved to longer values of VOffT in both cases. This finding strongly supports the hypothesis that the asymmetric ''vowel duration effect'' as seen in the case of VOT and VOffT is in fact a ''vowel length effect'' since it does not just apply to length changes induced by changes in vowel duration.

Pind (1998) noted one possible problem with this last experiment. To change the spectrum of the vowel [ɛ] toward that of a long vowel it is necessary to lower the frequency of $F1$ since long [ɛ] in Icelandic has a lower $F1$ than does short [ɛ]. As mentioned previously, it has been clearly demonstrated that the frequency of $F1$ at voicing onset has an effect on the location of the phoneme boundaries for VOT. Is it possible that a similar effect might have been operating in the case of VOffT perception and thus causing or at least contributing to the aforementioned vowel length effect? The purpose of this paper is to investigate this possibility experimentally by systematically varying $F1$ frequency at vowel onset (in the case of VOT) and at vowel offset (in the case of VOffT). Pind (1998) mentioned arguments for discounting the possibility that $F1$ frequency would have a greater effect on the perception of VOffT than VOT, noting in particular that changing the formant frequencies never had just an effect on the perception of VOffT, it also affected the proportion of long and short vowel responses in those cases where no preaspiration was heard. For this reason it is hypothesized that $F1$ will affect the perception of VOT and VOffT in a comparable manner. If so, this would lend support to the hypothesis entertained by Pind (1998) that the major reason that VOffT is more sensitive to the duration of the adjacent vowel than VOT is phonotactic. Phonotactics have, of course, often been shown to influence speech perception (e.g., Massaro and Cohen, 1983).

I. METHOD

A. Participants

Twelve undergraduate psychology majors at the University of Iceland participated in the experiment for course credit. All reported normal hearing. Participants were native speakers of Icelandic.

B. Stimuli

This experiment used synthetic speech made with the Sensimetrics SenSyn synthesizer, a version of the Klatt cascade/parallel formant synthesizer (Klatt and Klatt, 1990). The synthesizer was run in the cascade configuration with an update interval of 4 ms.

The stimuli consisted of two sets. The first set consisted of four [ka–k^{h}a] continua differing in the onset frequency and duration of the $F1$ transition. These stimuli were modeled after stimuli used in an earlier study by Kluender (1991), but synthesized using similar parameters as the stimuli of Pind (1998). Thus the cascade branch of the synthesizer was used rather than the parallel branch as Kluender had done. The four stimulus continua were distinguished by two different $F1$ onset frequencies (150 and 450 Hz) and three different $F1$ transition durations (20, 40, and 60 ms). The last value of 60 ms is shorter than Kluender's value of 80 ms. The shorter value was used since informal listening tests revealed that an 80-ms-long transition sounded very abnormal in the VOffT stimuli.

The overall duration of the VOT stimuli was 132 ms and they were synthesized with a fixed fundamental frequency of 125 Hz. All the stimuli contained the vowel [a], the formants of the steady state being fixed at 750, 1275, and 2425 Hz, respectively, for $F1$, $F2$, and $F3$. The vowel was synthesized with a slightly breathy quality (parameter AH=40 dB).[1] Following Kluender, no initial burst was used in the [ka–k^{h}a] series. This also served to make the VOT and VOffT segments more comparable.

VOT was synthesized with a combination of aspiration and frication, the latter in the frequency region of $F2$ and $F3$, while simultaneously cutting off the amplitude of voicing and increasing the bandwidth of $F1$ from 60 to 200 Hz. The transitions for $F2$ and $F3$ were 40 ms long and con-

TABLE I. $F1$ onset frequency (in the case of VOT) or offset frequency (for VOffT) and transition durations in the four stimulus series.

	$F1$ onset/offset frequency	Transition duration
Series A	450 Hz	20 ms
Series B	150 Hz	40 ms
Series C	450 Hz	40 ms
Series D	150 Hz	60 ms

TABLE II. Average phoneme boundaries for all 12 participants in all conditions of the experiment. Phoneme boundaries are expressed in ms of VOT or VOffT.

	VOT	VOffT
Series A	31.25	27.59
Series B	33.79	31.75
Series C	31.96	29.85
Series D	37.56	31.22

sisted of a linear fall of $F2$ from 1900 to 1275 Hz, while $F3$ rose linearly from 2100 to 2425 Hz.

The four VOT continua differed in the frequency of $F1$ at onset and transition duration; see Table I. For all continua VOT was varied in 4-ms steps from the starting value of 0 ms to the maximum value of 60 ms (16 steps). This yields a total of 4 (conditions)$\times$16 (VOT values)$=$64 stimuli.

The second set of stimuli consisted of four VOffT continua, [ak–ahk]. These stimuli consisted of a vowel part, being an exact mirror-image of the stimuli for the VOT continua, followed in each case by 120 ms of silence and ending in a burst appropriate for a velar release. With a 132-ms-long vowel this amount of silence lends the syllable approximately neutral with respect to quantity.

C. Procedure

Participants took part in the experiment in two sessions. In the first session they took the VOT test, in the second session the VOffT test. Each session was structured in the following manner, described here for the VOT test. There were three practice blocks followed by five experimental blocks. The first practice block played five instances of a clear *ga* stimulus (VOT$=$0 ms, series B) followed by five instances of a clear *ka* stimulus (VOT$=$60 ms, series B). The stimuli were played at a comfortable listening level over Sennheiser HD-530-II circumaural headphones. Subjects responded to the stimuli either by clicking with a mouse pointer on the words *ga* or *ka*, displayed in large type on the computer screen, or by pressing the buttons ''g'' or ''k.'' In the first practice trial subjects received feedback on their responses. This was also the case for block two which again consisted of the same two stimuli played five times each in random order. In the third practice block all 64 stimuli were played once each in randomized order. Subjects received no feedback. These practice trials were followed by five experimental blocks each containing two exemplars of each stimulus in randomized order. Subjects thus provided a total of ten responses of each stimulus in the experimental trials.

Identical procedures were used in the experiment involving the Voice Offset Time continua. Here the response labels used were *ak*/*agg* (for syllables having no preaspiration) and *akk* (for syllables having preaspiration). Two response labels are given for no preaspiration, indicating a syllable with a short (agg) or a long (ak) vowel. Both possibilities are given so as not to prejudge whether the listener would hear the syllables as having a short or a long vowel. It is clear that both labels indicate no preaspiration.

II. RESULTS

Phoneme boundaries were calculated for the responses of individual participants by fitting a rescaled tanh function to the data (Hukin and Darwin, 1995). Average phoneme boundaries are presented in Table II. The phoneme boundaries for the VOT series range on average from 31.25 ms in series A to 37.56 ms in series D. A one-way repeated measures ANOVA with series as the main effect shows that this difference is significant $F(3,33)=10.206$, $p<0.001$. Pairwise comparisons, using the Bonferroni correction, shows series D to be significantly different from the other series ($p<0.01$). Other comparisons were not statistically significant.

For the VOffT series the phoneme boundaries range from 27.59 ms of VOffT in the A series to 31.75 ms of VOffT in the B series. These two series thus differ by 4.16 ms of VOffT which is just over half the difference seen in the VOT series, although the difference in spread is not significantly different in the VOT and VOffT series, $t(11)=0.951$, n.s.

A one-way repeated measures ANOVA of the VOffT results with stimulus series as the main effect shows that its effect is significant $F(3,33)=11.356$, $p<0.001$. Pairwise comparisons, again using the Bonferroni correction, show series A and D, A and B, and B and C to be significantly different ($p<0.01$). Other comparisons were not statistically significant.

The patterning of results seen in the present experiment is similar to that found by Kluender (1991). Thus he found the shortest phoneme boundaries for the A series, followed by the C, B, and D series, the very same ordering seen in the VOT experiment here. The results for the VOffT experiment is slightly different in that the ordering, from shortest to longest phoneme boundaries, is A<C<D<B, but B and D are not significantly different here. Overall the patterning of results is therefore comparable, the major finding of the present study being that $F1$ offset does not have a greater effect on VOffT perception than does $F1$ onset on VOT perception. A notable difference between the present results for VOT and those of Kluender is the fact that his results shows greater spread in the location of phoneme boundaries, these ranging from approximately 20 ms in the A series to around 45 ms in the D series (Kluender, 1991, Fig. 4). Most of this greater spread can be attributed to Kluender's D series which had a transition duration of 80 ms compared to the 60-ms transition duration used in the present experiment.

III. DISCUSSION

This paper elaborates on previous studies dealing with the perception of preaspiration, cued by VOffT in Icelandic (Pind, 1995a, 1996, 1998). These studies had shown a much greater influence of abutting vowel duration on VOffT than on VOT. In a previous paper it was argued that this was natural, giving the phonotactics of these speech cues in Icelandic. VOT is syllable-initial and can precede either a long or a short vowel and is minimally affected by vowel quantity (cf. Pind, 1995b). VOffT, however, belongs to the syllable rhyme and can, in Icelandic at least, only follow a phonemically short vowel. Since vowel duration changes will affect the quantity of the vowel, it is to be expected that this will also affect the perception of VOffT. Thus, increasing the duration of the vowel, keeping other aspects of the speech stimulus constant, will lead to changes in the perceived length of the vowel which will decrease the likelihood of the listener perceiving preaspiration.

The hypothesis finds support in experiments showing that the phoneme boundaries for preaspiration move to longer values of VOffT, irrespective of whether perceived vowel quantity is changed toward a long vowel by durational or spectral means (Pind, 1998). One potential problem with this finding was the fact that to change the spectrum toward that of a long vowel, in this case for the vowel [ɛ], it is necessary to lower the frequency of the first formant. It is well known that a lower $F1$ needs a longer VOT, other things being equal, to cue the perception of voicelessness or aspiration (Kluender, 1991; Summerfield and Haggard, 1977). Perhaps this could explain the fact that VOffT boundaries moved to longer values when the spectrum of a preceding [ɛ] was changed from that appropriate for a short vowel to that of a long vowel. The experiment reported here tested for this possibility. If the first formant frequency is the critical factor, capable of explaining the vowel length effect previously discussed, one would hypothesize that VOffT should show greater sensitivity in perception toward $F1$ frequency than does VOT, since it shows a greater length effect. The present experiment does not accord with this hypothesis. The effect of $F1$ frequency on the perception of VOffT is comparable to that seen for VOT. It is thus concluded that the major factor underlying the effect of vowel length on the perception of VOT and VOffT is in fact the different location of the speech cues of VOT and VOffT in the syllable.

ACKNOWLEDGMENTS

This research was supported by the Icelandic Science Foundation and by the Research Foundation of the University of Iceland. I am grateful to Thórunn H. Halldórsdóttir for help in running the experiment and to two anonymous reviewers for very constructive remarks on an earlier version of the paper.

[1]The breathy quality was introduced to make the stimuli sound more natural. In the Klatt synthesizer it is necessary to align the step size of VOffT with the pitch period, otherwise it is not possible to control the effective duration of VOffT. Using a VOffT step size of 4 ms and a fundamental frequency of 125 Hz (period=8 ms) accomplishes this. Stimuli on a fixed fundamental frequency tend to sound unnatural. They can be made to sound more natural by giving the vowel a slight breathy quality.

Benediktsson, H. (**1963**). ''The nonuniqueness of phonemic solutions: Quantity and stress in Icelandic,'' Phonetica **10**, 133–153.

Garnes, S. (**1976**). *Quantity in Icelandic: Production and Perception* (Helmut Buske Verlag, Hamburg).

Hukin, R. W., and Darwin, C. J. (**1995**). ''Comparison of the effect of onset asynchrony on auditory grouping in pitch matching and vowel identification,'' Percept. Psychophys. **57**, 191–196.

Klatt, D. H., and Klatt, L. C. (**1990**). ''Analysis, synthesis, and perception of voice quality variations among female and male talkers,'' J. Acoust. Soc. Am. **87**, 820–857.

Kluender, K. R. (**1991**). ''Effects of first formant onset properties on voicing judgments result from processes not specific to humans,'' J. Acoust. Soc. Am. **90**, 83–96.

Lisker, L. (**1975**). ''Esit VOT or a first-formant transition detector.'' J. Acoust. Soc. Am. **57**, 1547–1561.

Lisker, L., and Abramson, A. S. (**1964**). ''A cross-language study of voicing in initial stops: Acoustical measurements,'' Word **20**, 384–422.

Maddieson, I. (**1984**). *Patterns of Sound* (Cambridge University Press, Cambridge).

Massaro, D. W., and Cohen, M. M. (**1983**). ''Phonological context in speech perception,'' Percept. Psychophys. **34**, 338–348.

Pétursson, M. (**1972**). ''La préaspiration en Islandais moderne. Examen de sa réalisation phonétique chez deux sujets,'' Studia Linguistica **XXVI**, 61–80.

Pind, J. (**1986**). ''The perception of quantity in Icelandic,'' Phonetica **43**, 116–139.

Pind, J. (**1995a**). ''Constancy and normalization in the perception of Voice Offset Time as a cue for preaspiration,'' Acta Psychol. **89**, 53–81.

Pind, J. (**1995b**). ''Speaking rate, VOT and quantity: The search for higher-order invariants for two Icelandic speech cues,'' Percept. Psychophys. **57**, 291–304.

Pind, J. (**1996**). ''Rate-dependent perception of aspiration and pre-aspiration in Icelandic,'' Q. J. Exp. Psychol. **49A**, 745–764.

Pind, J. (**1998**). ''Auditory and linguistic factors in the perception of voice offset time as a cue for preaspiration,'' J. Acoust. Soc. Am. **103**, 2117–2127.

Summerfield, Q. (**1981**). ''On articulatory rate and perceptual constancy in phonetic perception,'' J. Exp. Psychol. Hum. Perc. Perf. **7**, 1074–1095.

Summerfield, Q., and Haggard, M. (**1977**). ''On the dissociation of spectral and temporal cues to the voicing distinction in initial stop consonants,'' J. Acoust. Soc. Am. **62**, 435–448.

Thráinsson, H. (**1978**). ''On the phonology of Icelandic preaspiration,'' Nord. J. Ling. **1**, 3–54.

Volaitis, L. E., and Miller, J. L. (**1992**). ''Phonetic prototypes: Influence of place of articulation and speaking rate on the internal structure of voicing categories,'' J. Acoust. Soc. Am. **92**, 723–735.

Context-independent dynamic information for the perception of coarticulated vowels

James J. Jenkins,[a] Winifred Strange,[b] and Sonja A. Trent
Department of Psychology, University of South Florida, 4200 Fowler Avenue, Tampa, Florida 33620

(Received 29 October 1998; revised 12 March 1998; accepted 6 April 1999)

Most investigators agree that the acoustic information for American English vowels includes dynamic (time-varying) parameters as well as static ''target'' information contained in a single cross section of the syllable. Using the silent-center (SC) paradigm, the present experiment examined the case in which the initial and final portions of stop consonant–vowel–stop consonant (CVC) syllables containing the same vowel but different consonants were recombined into mixed-consonant SC syllables and presented to listeners for vowel identification. Ten vowels were spoken in six different syllables, /bVb, bVd, bVt, dVb, dVd, dVt/, embedded in a carrier sentence. Initial and final transitional portions of these syllables were *cross-matched* in: (1) silent-center syllables with original syllable durations (silences) preserved (mixed-consonant SC condition) and (2) mixed-consonant SC syllables with syllable duration equated across the ten vowels (fixed duration mixed-consonant SC condition). Vowel-identification accuracy in these two mixed consonant SC conditions was compared with performance on the original SC and fixed duration SC stimuli, and in initial and final control conditions in which initial and final transitional portions were each presented alone. Vowels were identified highly accurately in both mixed-consonant SC and original syllable SC conditions (only 7%–8% overall errors). Neutralizing duration information led to small, but significant, increases in identification errors in both mixed-consonant and original fixed-duration SC conditions (14%–15% errors), but performance was still much more accurate than for initial and finals control conditions (35% and 52% errors, respectively). Acoustical analysis confirmed that direction and extent of formant change from initial to final portions of mixed-consonant stimuli differed from that of original syllables, arguing against a target+offglide explanation of the perceptual results. Results do support the hypothesis that temporal trajectories specifying ''style of movement'' provide information for the differentiation of American English tense and lax vowels, and that this information is invariant over the place of articulation and voicing of the surrounding stop consonants.
[S0001-4966(99)05107-3]

PACS numbers: 43.71.Es, 43.71.An, 43.70.Fq [JH]

INTRODUCTION

A rich literature on the perception of vowels has developed over the last two decades, much of which has been devoted to exploring the role that dynamic (time-varying) information can play in vowel identification. Because this work has been reviewed so often during the last few years, a further review will not be undertaken here. The reader can find reviews from a variety of viewpoints in Andruski and Nearey (1992), Benguerel and McFadden (1989), Broad and Clermont (1987), DiBenedetto (1989a, b), Fourakis (1991), Fox (1989), Harrington and Cassidy (1994), Hillenbrand *et al.* (1995), Jenkins *et al.* (1994), Miller (1989), Moon and Lindblom (1994), Nearey (1989), Pols and van Son (1993), Rosner and Pickering (1994), Strange (1989a, b), Strange and Bohn (1998), and Zahorian and Jagharghi, (1993). Although there is still a fair amount of disagreement about the nature of the dynamic information, just what it is that such information specifies, and how far its temporal locus extends beyond the vowel proper, there are only a few defenders (e.g., Harrington and Cassidy, 1994) of a simple ''vowel target'' theory such as that proposed 50 years ago by Joos (1948).

Research in our laboratory on dynamic information for vowels began with the realization that listeners had little problem in identifying vowels in consonant–vowel–consonant (CVC) syllables, even when the productions of many different speakers (men, women, and children) were intermixed in the presentation of stimulus materials. This was a rediscovery of what was evident in the perceptual data of Peterson and Barney (1952) and reconfirmed in our laboratory by Shankweiler *et al.* (1977). These studies demonstrated that there was sufficient information for the identification of the vowel in the single syllable itself. This in turn meant that speaker normalization either took place simultaneously with the hearing of the syllable or, alternatively, that speaker normalization was not required. When we directed attention to the syllables themselves, we found, as Tiffany (1953) had suggested earlier, that vowels were more readily identified when they were embedded in CVC syllables than when they were uttered in isolated, steady-state form (Gottfried and Strange, 1980; Strange *et al.*, 1976; Verbrugge *et al.*, 1976). These findings led us away from the speaker

[a]Electronic mail: J3cube@aol.com
[b]Currently at the Department of Speech and Hearing Sciences, Graduate Center, City University of New York.

normalization problem that had been our original concern and toward a study of the kinds of dynamic (time-varying) information that were available in the spoken syllable itself.

The fact that consonant–vowel coarticulation appeared to help rather than hinder listeners in identifying the speaker's intended vowel led us to a series of experiments that attempted to push the limits in examining the contribution to vowel perception of information in the transitions into and out of the vocalic nuclei of CVC syllables. For this purpose we developed the ''silent-center'' experimental technique, by which we examined the identification of vowels in citation-form syllables after the vowel nucleus had been attenuated to silence. Surprisingly, we found that the vowels in such altered syllables were accurately identified, even though more than half of the syllable had been silenced (Jenkins *et al.*, 1983; Strange *et al.*, 1983). The silent-center technique also contributed a new method for studying the contribution of relative duration information to vowel identification. This was done by neutralizing the usual duration differences among vowels by the use of a fixed silent interval between the initial and final transitional portions of the syllables. As expected, the neutralization of duration information degraded the accuracy of vowel identification somewhat but, even so, fixed-duration silent-center syllables were markedly superior to fixed-duration syllable centers (vocalic nuclei excised from CVC syllables). This finding emphasized the robustness and relative importance of the syllable onset and offset information in specifying American English vowels (Strange, 1989b; Strange *et al.*, 1983; see also Parker and Diehl, 1984).

Further studies moved toward more natural stimuli by applying the silent-center technique to CVC syllables where several different stop consonants were used and the syllables were produced in sentence context rather than in citation form. Again, in spite of the fact that the syllables in sentence context were quite short and showed ''target undershoot,'' and in spite of the fact that the consonantal context varied from one token to another, the transitional information in syllable onsets and offsets taken together was sufficient to support accurate vowel identification (Strange, 1987, 1989b).

To rule out the possibility that vowels in SC syllables were perceived accurately because static formant targets were recoverable by interpolation across the silent interval, Verbrugge and Rakerd (1986) created ''hybrid silent-center'' syllables by cross-pairing the initial and final portions of citation-form CVC syllables produced by two different speakers, one male and one female. Even in this strange situation, with the speaker changing during the silent interval of the syllable, vowel identification was still fairly accurate, and not significantly worse than for nonhybrid SC syllable control stimuli produced by the same speakers (hybrids = 27% errors vs SC controls = 23% errors). This research was repeated with similar results by Andruski and Nearey (1992) using the citation-form productions of four speakers. While error rates were again rather high (averaging 31% errors), there were no significant differences between identification accuracy for hybrid and nonhybrid conditions.

These hybrid studies were further extended in our laboratory using the recordings of two speakers (a male and a female) producing CVC syllables in sentences, with results showing appreciably greater overall identification accuracy (average = 13% errors), and again, no differences between hybrid and nonhybrid conditions (Jenkins *et al.*, 1994). The success of these hybrid syllable experiments argues that the information which specifies coarticulated vowels is sufficiently abstract to be speaker independent. Thus, we have come to think of the acoustic dynamics of the transitions into and out of the vowel as embodying information concerning the style of articulatory movement that produces the intended vowel (cf. Strange and Bohn, 1998). We conclude from all of the above research that time-varying relational parameters, defined over syllable onsets and offsets together, provide perceptually important information for the identification of American English vowels, whether they be produced in citation-form utterances or in sentence-length materials. This dynamic information is sufficient to support accurate vowel identification even when the consonants and/or the speakers vary unpredictably from trial to trial, necessitating accommodation to variability in target formant frequencies associated with coarticulatory target undershoot and speaker vocal-tract size and shape.

As the final study in this series, the present work evaluated the identifiability of vowels when the initial and final segments were taken from syllables containing different (stop) consonants. The question asked was whether the dynamic information is specific to the particular CVC syllable in which it was produced (context-dependent information) or whether the vowel information is specified in a sufficiently abstract manner that the same vowel is perceived even when the transitions are out of or into consonants which differ in place of articulation and/or voicing (context-independent information). To prepare such a test, mixed-consonant SC syllables were created by combining onsets and offsets of different syllables, spoken by the same speaker, in a common carrier sentence. The final segment of a particular CVC syllable was replaced by the final segment of a different syllable with the same vowel but with a different consonant (e.g., the initial portion of /bɪb/ was combined with the final portion of /dɪt/). The question was whether the identity of the vowel would still be preserved in spite of the discontinuity of formant trajectories that were presumably moving to and from different consonant loci to different formant maxima or minima.[1]

In his target+offglide theory of vowel perception, Nearey (1989; Andruski and Nearey, 1992) hypothesized that vowel identity is maintained in SC syllables because the target is specified in the initial portion, while the direction and extent of formant movement is inferred from the relative position of the formants at the beginning of the final portion. That is, vowel identity is preserved in SC syllables because ''vowel-inherent spectral change'' (VISC) is recoverable by comparison across syllable onsets and offsets. It was argued earlier (Jenkins *et al.*, 1994) that the fact that vowel identity is preserved in hybrid syllables, for which the direction and extent of formant movement is not preserved, argues against such a position. Likewise, if the direction and extent of formant change across the silent portions of mixed-consonant SC syllables differs from the original SC syllables, a

target+offglide account would predict a disruption in vowel identification. If, however, dynamic spectro-temporal information, *other than VISC*, remained invariant across different consonants, we might expect relatively accurate vowel identification in mixed consonant SC conditions. To examine whether, as expected, the direction and extent of formant change from initial to final portions of mixed-consonant SC syllables did indeed differ from the original SC syllables, a comparison of formant change in the original and mixed-consonant stimuli was performed.

I. PERCEPTION OF MIXED-CONSONANT SILENT-CENTER SYLLABLES

The present study examined perception of silent-center syllables in which initial and final portions of CVC syllables, containing the same vowel but different stop consonants, were recombined in two conditions. In the mixed-consonant SC condition, the temporal information associated with the vowel produced in the CVC syllables from which the final portion was taken was retained. That is, the syllable duration (counting the silent portion) was appropriate for the vowel and final (voiced or voiceless) consonant. In the fixed-duration mixed-consonant SC condition, all silent durations between recombined initial and final components of syllables were set to the same (average) duration across the ten different vowels, thus eliminating relative duration differences as information for vowel identity. Duration differences associated with final consonant voicing were retained. Performance on these two mixed-consonant SC conditions was compared with earlier data on (original) SC syllables, and on initial portions alone and final portions alone.

If, as has been claimed in earlier papers (Jenkins *et al.*, 1994; Jenkins and Strange, in press; Strange and Bohn, 1998), the dynamic information specified over syllable onsets and offsets together is invariant with respect to the vowel (i.e., specifies the ''style of movement'' associated with the particular vowel) and context independent, we predict that vowel identification in mixed-consonant SC syllables would be better than for initials or finals control conditions, and perhaps not significantly worse than for the original SC syllables. If, on the other hand, vowels in SC syllables are identified on the basis of context-dependent trajectory cues, then we would expect that identification of vowels in mixed-consonant SC conditions would be worse than in the original SC syllables. Because earlier research had shown that neutralizing relative duration differences led to a small, but significant, increase in vowel-identification errors, we expected that performance in the fixed-duration mixed-consonant SC condition would show a similar increase in errors. However, vowel identification should still be better than for either initials or finals control conditions.

A. Method

1. Stimulus materials

Speech materials were the same as those used in Strange (1989b), experiment 3. The speaker was a young adult male who was a native of Ohio but who had resided in Florida for 15 years at the time of recording. He spoke with no appreciable regional accent and his normal rate of speech was quite rapid. The speech script consisted of ten vowels (/i, ɪ, e, ɛ, æ, ɑ, ʌ, o, ʊ, u/) spoken in six consonantal contexts (/bVb/, /bVd/, /bVt/, /dVb/, /dVd/, /dVt/) in the fixed carrier sentence ''I say the word CVC some more.'' Several repetitions of each sentence were recorded using a ReVox A-77 tape recorder and a Panasonic low-impedance microphone. The speaker was coached somewhat on his productions of /ʊ/, which in the opinion of the second author were not sufficiently rounded. After the recording session was completed, two instances of each utterance were chosen for inclusion in the final speech corpus on the basis of acceptable voice quality and loudness, for a total of 120 sentences (10 vowels×6 consonantal contexts×2 tokens). This final corpus was filtered at 4900 Hz and converted to digitized waveform files using a DEC PDP 11/34 computer (10-kHz sampling rate, 12-bit resolution).

Durations of sentences and target syllables, the number of pitch periods in the target syllables, and the voice onset time (VOT) of the initial consonant in the target syllable were calculated from the digital waveforms. Sentence length varied from 1240 to 1600 ms, with a mean of 1390 ms. Length of the target syllable was defined as the duration from initial consonant burst to final consonant closure (the end of significant energy in the upper harmonics). Number of pitch periods in the target syllable varied from 10 to 22. VOT was measured from consonant burst to the onset of clear periodicity and varied from 3–34 ms, with a mean of 13 ms.

Three discrete portions of each target syllable were identified: (1) an initial component, which included the initial consonant release burst and aspiration plus the first three pitch periods, (2) a final component, which included the last four pitch periods prior to final consonant closure plus closure murmur, if any, and (3) a center component, which was the portion of the vocalic signal between the initial and final components. The centers ranged in duration from 27 to 147 ms and included from 3 to 15 pitch periods. The proportion of the total syllable duration defined as the center averaged 45% for the short vowels /ɪ, ɛ, ʌ, ʊ/, 61% for the long vowels /e, æ, ɑ, o/, and 54% for the intermediate vowels /i, u/. Measurement data by consonantal context are summarized in Table I.

Two modified syllable conditions were generated from the digital waveform files of the target syllables. First, for each of the sets of tokens (repetitions one and two) 60 mixed-consonant silent-center (mixed SC) syllables were generated by combining initial and final portions taken from syllables containing the same vowel but different consonants. The interval between the initial and final portions was attenuated to silence. The duration of silence was appropriate for the original vowel and final consonant (i.e., the same as in the original syllable from which the final portion was taken). Six different mixed SC syllable types were generated for each vowel: two were ''mismatched'' relative to the original syllables with respect to final consonant voicing (initial/dVd/+final/dVt/;initial/dVt/+final/dVd); two were mismatched on consonant place of articulation (initial/dVd/+final/bVb/;initial/bVb/+final/dVd/); and two were mis-

TABLE I. Duration measurements (ms) for test stimuli.

Syllable portion	Syllable context					
	/b–b/		/b–d/		/b–t/	
	Mean	Range	Mean	Range	Mean	Range
Total	171	133–228	177	123–215	144	110–178
Initial	40	33–48	39	31–48	42	37–50
VOT	13	9–19	12	3–34	14	7–20
Center	91	49–147	88	47–133	61	34–103
Final	39	37–41	40	38–46	41	35–50
	/d–b/		/d–d/		/d–t/	
Total	169	120–215	175	134–212	151	102–186
Initial	40	34–50	39	34–47	42	36–49
VOT	12	6–18	12	7–19	11	9–12
Center	89	37–134	96	56–134	67	27–99
Final	40	38–44	40	38–44	42	35–60

matched on both place and voicing (initial/bVb/+final/dVt/; initial/dVt/+final/bVb/). Thus, there were six mismatched syllables for each of two tokens of ten vowels, yielding a total of 120 syllables ($6\times10\times2$).

A fixed-duration, mixed-consonants silent-center condition (fixed D mixed SC) was generated in which initial and final portions taken from different consonantal contexts were recombined as in the condition above, but the silent intervals between initial and final portions were equated across all ten vowels within each consonantal context and each repetition. For instance, the average of the silent intervals for all ten vowels of the first repetition of original /bVb/ syllables was inserted in all fixed D mixed SC syllables containing a final portion taken from the first repetition of /bVb/ syllables. Thus, across the 120 syllable corpus, syllable durations differed appropriately as a function of final consonant identity, but were neutralized with respect to vowel identity.

Target syllables in both conditions were placed back into carrier sentences such that the initial part of the carrier sentence was the one originally associated with the initial portion of the modified syllable, and the end of the carrier sentence was the one originally associated with the final portion of the modified syllable. Thus, any coarticulatory influence of preceding and following context was retained.

Four other conditions, controls for the mixed-consonants conditions, were the same as those reported in Strange (1989b, experiment 3). A silent-center syllable (SC) condition was generated by simply attenuating the center portions of the target syllables to silence without modifying the original temporal relationship between initial and final portions and without modifying consonantal context. Fixed-duration silent-center syllables (Fixed DSC) were generated such that within each repetition, the silent interval between the initial and final components was the average duration of the ten center portions within each consonantal context. Thus, duration appropriate to the consonant was preserved, but intrinsic vowel-duration differences were removed. An initials (I) stimulus condition consisting of only the initial portions of target syllables with the center and final portions attenuated to silence and a finals (F) condition consisting only of the final portions of target syllables with the initial and center portions attenuated to silence were also generated. For the SC, fixed D SC, I, and F conditions, all modified syllables were reinserted into their original carrier sentences.[2]

Six separate listening tests, one for each syllable condition, were prepared by converting the digitized files back to analog signals and filtering and recording them on audiotape. Stimuli were randomized within each repetition with the constraint that the same vowel or same consonantal context did not occur more than two times consecutively. The interstimulus interval was 4 s; blocks of ten items were separated by 8 s. The same randomization order was used in all six tests, and each token appeared only once, for a total of 120 items per test, divided into two blocks. One block consisted of all stimuli constructed from the first repetitions, while the second block consisted of stimuli constructed from the second repetitions generated by the speaker. Thus, differences due to long-term effects on fundamental frequency and speech rate were controlled within blocks.

Familiarization stimuli consisted of 40 unmodified CVC stimuli produced by an adult female in the same carrier sentence as used in the tests and recorded in four blocks of ten stimuli each. All ten vowels occurred four times each; the six consonantal contexts occurred six to eight times each.

2. Procedures

Subjects were asked to identify each vowel in the target syllables by marking a key word on a response sheet that contained the same vowel. The response sheets contained rows of the following ten key words: *ape, if, eek, heck, as, ah, ooze, up, oh, hook*. Prior to testing, an extensive task-familiarization procedure was completed. First, the experimenter pronounced each key word, pointing out possible orthographic confusions. Next, each listener pronounced the key words and the experimenter corrected any mispronunciations and took note of the listener's dialect. Listeners then responded to five practice blocks of ten items each, with feedback. The first of these was presented live-voice by the experimenter; for the remaining four blocks, the recorded familiarization test was used. Performance on the final two practice blocks was used as the criterion for inclusion of a

TABLE II. Mean errors (in percent of opportunities) for each stimulus condition and modal error response (when error rate was greater than ten percent).

Vowels	Stimulus condition					
	Silent centers with duration		Fixed duration silent centers		Controls	
Short	Original	Mixed	Original	Mixed	Initials	Finals
Vowels						
ɪ	3	4	19/ɛ/	13/ɛ/	15/ɛ/	9
ɛ	2	10	14/æ/	25/æ/	63/æ/	30/ʌ/
ʌ	2	4	10	9	38/ɑ/	33/ɛ/
ʊ	44/ʌ/	41/ʌ/	58/ʌ/	68/ʌ/	49/ʌ/	42/ʌ/
Mid-vowels						
i	10	0	2	2	3	13/ɪ/
u	3	5	4	4	13/ʊ/	16/ʊ/
Long vowels						
e	1	1	1	2	61/ɛ/	98/ɪ/
æ	8	4	17/ɛ/	11/ɛ/	17/ɛ/	90/ɛ/
ɑ	2	3	5	2	6	86/ʌ/
o	2	7	8	13/ʌ/	88/ʌ/	99/ʊ/
Overall	7%	8%	14%	15%	35%	52%
Overall-/ʊ/	4%	4%	9%	9%	34%	53%

listener's data in the study. Listeners who made more than three errors, or more than one error on the same vowel, were excluded from the study. (Also excluded were listeners who were bilingual or who had a history of hearing problems.)

After task familiarization, participants listened without responding to the first 20 trials of the test stimuli to become familiar with the particular stimulus condition on which they were to be tested; no feedback was given. The regular testing session then began with no further feedback. In total, familiarization and testing lasted approximately 50 min. Familiarization and test recordings were presented via a Tascam reel-to-reel tape recorder and TDH-39 earphones at 75 dBA to groups of two to four listeners in a small office in which there was some ambient noise.

3. Listeners

Undergraduate students from psychology or introductory speech-science classes at the University of South Florida served as listeners and were awarded extra-credit points for their participation. All students included in the study were native speakers of American English who reported no known hearing problems. A total of 134 participants (96 female and 38 male) were tested; 96 (72%) met the acceptability requirements and passed familiarization criteria; their data were retained for analysis.

Sixteen listeners were tested in each of the six stimulus conditions in an independent-groups design. In each condition, approximately one half listened to the block containing the first repetitions followed by the second block; the remainder heard the second block followed by the first. Across all conditions, 58 subjects spoke a Florida dialect, 15 a Northeastern dialect, 13 a Midwestern or Western dialect, and 10 a Southern dialect other than Floridian. Dialect groups were distributed approximately equally across the six stimulus conditions.

B. Results

In tabulating the data, an error was defined as a response other than the vowel intended by the speaker in the original utterance, or an omission. Because subjects were encouraged to respond to all trials, there were very few omissions. Table II presents average error data for each of the six stimulus conditions, expressed as percentages of opportunities summed over listeners and consonantal contexts. Error rates on each of the ten intended vowels are given, as well as the modal error response for vowels misidentified more than 10% of the time. The vowels are arranged by their intrinsic duration: four short vowels, two mid-duration vowels, and four long vowels. Overall error rates summed over all ten vowels, and over nine vowels, excluding /ʊ/, are also presented in the final two rows. (Data from the original SC, fixed D SC, I, and F conditions are taken from Strange 1989, experiment 3.)

The differences in mean errors across stimulus conditions (summed over all vowels and consonant contexts) were highly reliable, as analyzed by a one-way analysis of variance, $F(5,90)=157.03$, $p<0.001$. *Post hoc* Tukey tests of pair-wise comparisons of stimulus conditions using a significance level of 0.05 indicated that mean errors on the original SC and mixed SC conditions were not significantly different from each other, but were reliably lower than in the fixed D SC and fixed D Mixed SC conditions in which intrinsic vowel duration information was not present. Performance in the initials condition was significantly better than in the finals condition, but performance in both of these conditions was significantly worse than in all four SC conditions.

Table III presents average error data for both mixed SC and fixed D mixed SC conditions for each consonantal context, collapsed over all ten vowels. Separate analyses of variance for repeated measures were performed on the data with

TABLE III. Mean errors (and standard deviations) expressed as percentage of opportunities in each mixed syllable condition. The first two letters indicate the syllable from which the initial portion of the test syllable was taken, and the second two letters indicate the syllable from which the final portion of the test syllable was taken.

Conditions	Mixed SC		Fixed d mixed SC	
	Mean	(s.d.)	Mean	(s.d.)
Voicing mismatch				
dd–dt	5	(4)	14	(8)
dt–dd	12	(7)	20	(9)
Both conditions	9	(5)	17	(7)
Place mismatch				
dd–bb	9	(5)	16	(7)
bb–dd	4	(5)	10	(8)
Both conditions	7	(4)	13	(6)
Place and voicing mismatch				
dt–bb	10	(5)	18	(8)
bb–dt	5	(6)	11	(9)
Both conditions	8	(5)	15	(8)

the tokens grouped by the phonetic feature of the change (voicing, place, and place and voicing). For the mixed SC condition, the feature analysis was not statistically significant ($F(2,30)=2.30$, $p>0.10$) but for the fixed D mixed SC condition the analysis reached significance ($F(2,30)=6.688$, $p<0.01$). A least significant difference test on these data showed that the tokens that involved a change in the *voicing* produced significantly more errors than the other two feature changes, but that changes in *place* were not significantly different from changes in *place and voicing* combined. The pattern of changes was the same in both experimental conditions. Changes in *voicing* of the final portion of the syllable produced the highest error rates (mean=8.75% errors per listener in mixed SC and 17.19% errors in fixed D mixed SC), changes of both *place and voicing* produced fewer errors (7.81% and 14.3%) and changes of *place* produced the fewest errors (6.72% and 12.81%). It should be noted that the variation in the means was quite small, only 2% for the mixed SC condition and less than 5% for the fixed D mixed SC condition.

Finer-grained analysis of the data suggest that grouping the data by type of phonetic feature change is inappropriate. Separate analyses of variance were conducted for mixed SC and fixed D mixed SC conditions, grouping the data by the specific syllable combinations involved (e.g., DD–DT, DT–DD, DD–BB, etc). For the mixed SC condition, the result indicated that the specific combinations were more important sources of variance than the features involved. The differences among the types of tokens were statistically significant [$F(5,75)=10.846$, $p<0.01$] and planned comparisons revealed significant differences between the conditions that involved the same feature (i.e., changing from a voiced ending to a voiceless ending produced fewer errors than changing from a voiceless ending to a voiced ending [$F(1,75)=25.006$, $p<0.01$]; changing from a voiced labial to an unvoiced alveolar produced fewer errors than vice versa [$F(1,75)=13.226$, $p<0.01$]; and changing from a voiced labial to a voiced alveolar produced fewer errors than the reverse [$F(1,75)=25.006$, $p<0.01$]. Results of the analysis for the fixed D mixed SC condition exactly paralleled the results for the mixed SC condition: means for specific syllable types were significantly different [$F(5,75)=9.010$, $p<0.01$]; changing from a voiced ending to a voiceless ending produced fewer errors than changing from a voiceless ending to a voiced ending [$F(1,75)=9.816$, $p<0.01$]; changing from a voiced labial to an unvoiced alveolar ending produced fewer errors than vice versa [$F(1,75)=13.360$, $p<0.01$]; and changing from a voiced labial to voiced alveolar ending produced fewer errors than the reverse [$F(1,75)=9.816$, $p<0.01$]. Whether these findings are merely a peculiarity of these particular stimuli or have more general significance cannot be determined from the current experiment because it was not designed to test such an hypothesis. Again, it must be noted that the differences in error rates between conditions were very small and would not have been statistically significant except for the very high correlation between the individual listeners' performance across the conditions.

Overall, then, vowels in the two mixed-consonant conditions were identified no less accurately than the vowels in their matched nonmixed counterparts. As in earlier studies, neutralization of intrinsic duration differences led to a significant increase in errors for both the original SC and mixed-consonant SC conditions, but these two conditions did not differ from each other in spite of the consonant mismatch in the latter. Overall accuracy on all of the silent-center conditions was significantly and appreciably superior to the identification accuracy achieved in the initials and finals control conditions. Thus, dynamic spectral information specified over syllable onsets and offsets together (plus duration information) was sufficient to maintain accurate vowel identification, even when the syllable onsets and offsets were interchanged such that coarticulatory effects on the vocalic nuclei may have differed from the original syllables. In order to examine the extent to which interpolated formant trajectories differed across the original and mixed silent-center conditions, acoustical analysis was undertaken.

II. FORMANT CHANGE IN ORIGINAL AND MIXED-CONSONANT SILENT-CENTER SYLLABLES

The perceptual data argue that vowels in cross-spliced silent-center syllables were perceived as accurately as were the vowels in the original silent-center syllables. Thus, disruptions of the formant trajectories and other dynamic information specifying vowel identity must have been within limits that have little effect on the identification functions for American English vowels, or, alternatively, the information for vowel identification is distributed across the onsets and offsets of syllables in such a redundant or abstract manner that the specific changes in formant trajectories do not disturb the overall identification function. If Nearey's hypothesis that dynamic information can be described exhaustively by defining formant parameters at two points in the trajectory—the target (specified by formant values at the end of the initial portion of SC syllables) and the direction and extent of formant movement in the vocalic nucleus (defined by the change from target values to values at the beginning

of the final portion of SC syllables)—then we would predict from the perceptual data that these values did not differ markedly in original and mixed SC conditions. If, however, the direction and extent of change of formants did differ across the original and the mixed-consonant SC syllables, it could be concluded that Nearey's characterization of dynamic information was not sufficiently rich to capture all of the perceptually relevant information used by listeners to identify American English vowels.

For each set of stimuli, spectral analysis was performed using ILS software (1979). A 20-pole linear predictive coding (LPC) analysis was computed over consecutive 20-ms Hamming-windowed sections updated every 10 ms to determined the center frequencies of the first three formants. Where there was ambiguity in the LPC analysis, fast Fourier transform (FFT) analysis was performed to augment the decision as to the best values to use for the formants. For the purposes of this experiment, the frequencies of the first two formants were tabulated from two locations in each test syllable: the end of the initial segment and the beginning of the final segment. These values were converted into barks for further comparisons.

Figures 1 and 2 show the difference in $F1$ and $F2$ (in barks) between the values at the end of the initial portion of each syllable and the beginning of the final portion. Figure 1 presents the formant change plots for the front vowels (tense vowels on the left, lax vowels on the right), while Fig. 2 presents the same data for the back vowels (note that the coordinate ranges are different for the two figures, reflecting relatively more formant movement for many of the back vowels). For each vowel, the original syllables (SC) are shown by open squares, while the mixed SC syllables are shown by closed diamonds.

If $F1$ and $F2$ had essentially the same values at the end of the initial portion and the beginning of the final portion (i.e., if formants were at steady state across the silenced portion), the values would cluster tightly around the zero point on each graph. To the extent that the points do not cluster at the origin, either coarticulatory variation or vowel inherent spectral change (VISC) may be inferred. VISC can be defined here as context-independent change; that is, consistent direction of movement across all tokens of the vowel. The quadrants represent four different patterns of change in direction for $F1$ and $F2$, while the distance from the origin is a measure of the extent of change. For example, in the plot for the original SC syllables containing /e/, it is apparent that there was a significant decrease in $F1$ (about 1.6 bark on average) and an increase in $F2$ (about 0.8 bark on average) across the center of the syllable. All 12 original syllables (6 contexts $\times 2$ repetitions) showed this pattern of movement, reflecting VISC for this vowel, with the extent of change varying somewhat as a function of consonantal context.

Looking first at the data for the original SC syllables, one can see that vowels differed in the amount of VISC. As expected, the tense vowels i, e, o, u were diphthongized toward the articulatory periphery ($F1$ lowered, $F2$ raised for front vowels, lowered for back vowels) with only a few tokens showing atypical direction of formant movement. In contrast, the front lax vowels /ɪ, ɛ, æ/ tended to show the opposite pattern of change from the tense front vowels: $F1$ raised and $F2$ lowered. There tended to be more exceptions to the overall direction of movement across tokens and less movement for the short lax vowels, /ɪ, ɛ/. The back lax vowels /ʌ, ʊ/ for this speaker showed no consistent patterns of change across all contexts, nor did /ɑ/. Formant change for these vowels reflected only coarticulatory variation in formant movement patterns.

Looking next at the change patterns for the mixed SC syllables, it is clear that for several of the vowels, both the direction and extent of formant change differed from the original. Tokens showed greater variability (increased scatter of the points) and in many cases differences in directions of movement across tokens. The scatter in the values was examined by comparing the variances of the points in the original SC syllables for $F1$ and $F2$ with the variances in the mixed SC syllables for those measures. In absolute terms, in only two cases ($F1$ for /ʌ/ and $F1$ for /o/), were the variances smaller for the mixed SC syllables than the SC syllables. In the other 18 cases, the variances for mixed SC syllables were larger. In seven cases, the variances for the mixed SC syllables were statistically significantly larger: $F1$ and $F2$ for /ɪ/ and /u/; $F1$ for /æ/ and $F2$ for /ɑ/ and /ʊ/. In these cases, the ratio of the two variances exceeded 3.5 ($df = 11$, $p < 0.05$). This indicates that the target+offglide information was reliably disrupted in the mixed SC syllables, but these differences did not produce additional difficulties in identification of the vowels. If one considers only the vowels for which significant changes in variance were detected on $F1$ or $F2$ or both, there is essentially no difference in identification accuracy between the SC conditions and the mixed SC condition. In absolute terms, the mixed-consonants conditions are trivially better than the SC conditions (about half of one percent).

Consider first the short vowels, /ɪ, ɛ, ʌ, ʊ/. For /ɪ/ and /ɛ/, there was relatively little change in the formant values for the original SC syllables, while in the mixed SC condition the variability increased, especially in $F1$, which was about as likely to fall as it was to rise. $F2$ variability increased for /ɪ/, and for both vowels was somewhat more likely to rise than in the original syllables. Thus, for some tokens, the direction of change for these lax vowels was more similar to their spectrally adjacent tense counterparts. As noted above, however, identification of these vowels remained highly accurate in the mixed SC condition, and errors, when they occurred, were not confusions with tense vowels. Both /ʌ/ and /ʊ/ showed remarkably more scatter in the mixed SC condition than in the original SC condition, especially with respect to $F2$, which was about equally likely to rise or fall by fairly large amounts (up to 2.5 barks). In the case of /ʌ/ the vowel was accurately identified in both conditions, and in the case of /ʊ/ the vowel was very poorly identified in both conditions. The rather large variation in formant change patterns of these syllables from the original to the mixed SC condition simply had no measurable perceptual consequences.

The mid-length vowels, /i/ and /u/, showed quite different patterns. For /i/ there was very little difference between the two experimental conditions except for a slight increase in variability on both formants, but for /u/ the variability in

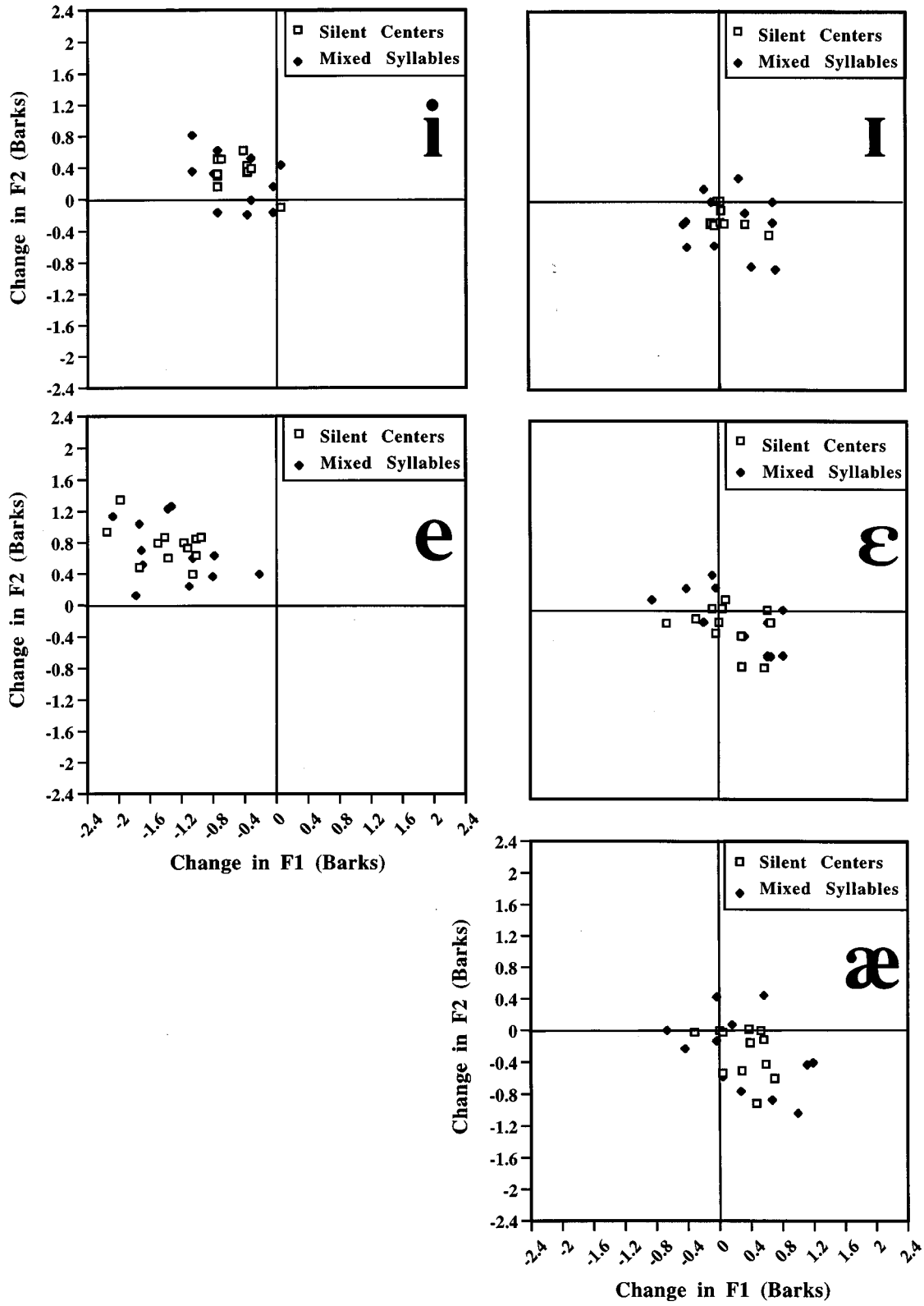

FIG. 1. The points show differences (in barks) in $F1$ and $F2$ for the front vowels between the values at the end of the initial portion of each syllable and at the beginning of the final portion. Differences for the original syllables (SC syllables) are shown by open squares, and differences for the cross-matched syllables (MC syllables) are shown by filled diamonds for each of the 12 syllables involving each vowel. Note that the scale for the back vowels is different from the scale for the front vowels for both axes.

$F2$ increased markedly, with differences ranging from increases of almost 2 barks to decreases of more than 3.5 barks. Nevertheless, identification performance remained almost perfect.

The long vowels showed no single pattern. The vowels /e/ and /æ/ revealed only slight increases in variability in the mixed SC condition over the SC condition. The vowel /e/ showed the usual drop in $F1$ and increase in $F2$ that

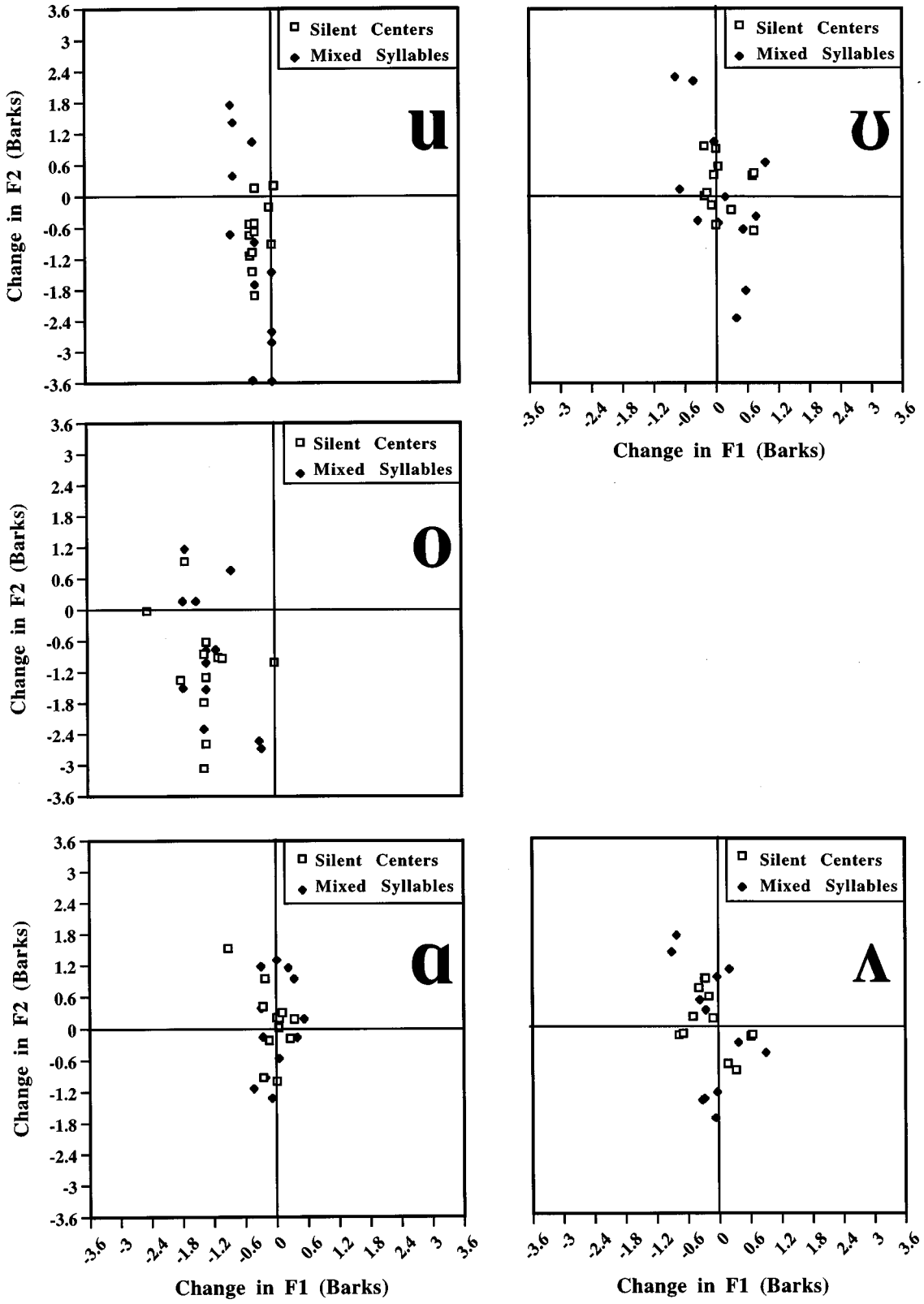

FIG. 2. The points show differences (in barks) in $F1$ and $F2$ for the back vowels between the values at the end of the initial portion of each syllable and at the beginning of the final portion. Differences for the original syllables (SC syllables) are shown by open squares, and differences for the cross-matched syllables (MC syllables) are shown by filled diamonds for each of the 12 syllables involving each vowel. Note that the scale for the back vowels is different from the scale for the front vowels for both axes.

ordinarily accompanies its dynamic movement toward /i/, while /æ/ generally showed an increase in $F1$ and decrease in $F2$. The vowel /ɑ/ displayed somewhat greater variability but in no consistent direction in either condition. On the other hand, /o/ showed a consistent drop in $F1$ in both conditions, while $F2$ changes ranged from a fall of almost 3 barks to a rise of 1.2 barks. Again, it must be remarked that none of the differences between patterns of change produced

an appreciable change in the accuracy of identification of the vowels.

III. DISCUSSION

This study was designed to examine whether the dynamic spectro-temporal information for vowel identity available in the onsets and offsets of CVC syllables, taken together, was specific to the place and voicing characteristics of the surrounding stop consonants (context dependent), or whether it was invariant over those features (context independent) and therefore could be considered intrinsic to the vowel. Results of the perceptual study indicated that onsets and offsets could be interchanged in silent-center syllables without disrupting vowel identification, even though acoustical analysis indicated that such interchanges markedly affected interpolated formant trajectories. This result, taken together with the results of the hybrid syllables studies (Andruski and Nearey, 1992; Jenkins *et al.*, 1994; Verbrugge and Rakerd, 1986), in which syllable onsets and offsets from speakers of different gender were recombined, argue against the simple hypothesis that subjects ''compute'' the target formant information for vowel identity by interpolating across the silent interval of silent-center syllables. Furthermore, the lack of correspondence between acoustic variation in the mixed-consonant conditions and perceptual performance argues against the sufficiency of a target+offglide description of the perceptually relevant dynamic information for coarticulated vowels.

A recent silent-center study of German vowels by Strange and Bohn (1998) showing results similar to those reported for American English vowels also suggests that vowel inherent spectral change (VISC) descriptions of dynamic information do not alone account for the perceptual results of the silent-center studies. Although German vowels are not diphthongized, they were identified quite well in silent-center conditions with or without relative duration information. Acoustical analysis indicated that while spectral change across initial and final portions reflected coarticulatory influences, but not vowel intrinsic differences, $F1$ temporal trajectories did differentiate spectrally similar tense and lax vowels. Jenkins *et al.* (1994) also hypothesized that $F1$ temporal trajectory patterns in American English vowels remained constant across hybrid silent-center syllables and could account for accurate identification, despite disruption of target+offglide information.

The data in the present study are compatible with an account of vowel perception in which temporal trajectories, which we have hypothesized are the result of different ''styles of movement'' for so-called tense and lax vowels, provide important information for distinguishing vowels in American English. They also suggest that this information is invariant over changes in place of articulation and voicing of the surrounding consonants, at least within the manner class of stop consonants. It is for future research to determine whether this holds true for consonants of other manner classes, for speakers of different dialects of American English, and for vowels of other languages.

Returning to the theme of the introduction, it is apparent that our series of studies makes two major claims concerning the perception of American English vowels: first, that the vowels are well specified by dynamic (time-varying) information without appreciable ''normalization'' from other sources of information, and, second, that such dynamic information is readily available over the onsets and offsets of syllables (taken together) whether produced in citation form or in sentence context. While it is convenient to represent vowels as ''points'' in an $F1-F2$ space, it is clear that such a representation fails to capture perceptually critical aspects of the signal that listeners do in fact use. The static space does not provide for duration information, trajectory movement of the formants during the entire course of the syllable, and other information about the ''style of change'' that specifies the vowel gestures.

In short, our studies (as well as the studies of many others) compel us to conclude that there is a wealth of information across the entire syllable that participates in (or can participate in) the listeners' identification of the vowel. While our research does not speak specifically to the detailed question of what the many sources of acoustic information may be, it argues that the style of change is expressed in many general or abstract acoustic characteristics. We believe that this characterization of the information is compatible with the view of vowels as gestures with dynamic parameters that give rise to a host of time-varying acoustic patterns that are unique to the production of that intended vowel (Fowler and Rosenblum, 1991; Fowler, 1996). At present, this seems to us to be the most economical and persuasive point of view.

IV. CONCLUSIONS

(1) Vowel-identification accuracy was well maintained when syllable onsets and offsets containing different stop consonants were interchanged in mixed-consonant silent-center syllables.
(2) While the neutralizing of relative duration differences increased vowel-identification errors somewhat, performance was still far superior to that achieved when only syllable onsets or syllable offsets were presented.
(3) Acoustical analyses comparing formant change across the silences of original and mixed silent-center syllables indicated the target+offglide information (vowel inherent spectral change) was often disrupted in the mixed SC stimuli.
(4) The fact that disruption of target+offglide information did not produce an increase in perceptual errors suggests that other forms of spectro-temporal information available in syllable onsets and offsets taken together were sufficient to maintain accurate perception of American English vowels.
(5) These results, in conjunction with others on the perception of coarticulated vowels from our laboratory and elsewhere, argue against both simple target theories and elaborated target theories of vowel perception (Strange, 1989a).

ACKNOWLEDGMENTS

This research was begun under NINCDS Grant No. 22568 and completed under NIDCD Grant No. 00323. Assistance was also received from the Office of Sponsored Research of the University of South Florida. The series of experiments mentioned in the introduction would not have been possible without the technical assistance of Haskins Laboratories. Assistants who contributed to the conduct of this research and its analysis were Bruce Goshe, Linda Katz, Elizabeth Lewis, and Salvatore Miranda. Goshe was also the speaker who produced the stimuli for the study. Gratitude is also expressed to the ATR Human Information Processing Research Laboratories (Kyoto, Japan) for assistance during the preparation of this manuscript.

[1]For symmetry, we wanted to study the effects of cross-splicing initial and final portions of syllables in which different vowels were embedded in the same consonant contexts (e.g., the initial portion of /bæb/ combined with the final portion of /bʌb/). Because many of the syllable offsets in isolation sound very much alike regardless of the original vowel, we were interested in knowing whether some finals could substitute for others even if they were not taken from a syllable with the appropriate vowel. Our efforts to conduct experiments with such ''mixed-vowel'' stimuli were unsuccessful. Such recombined syllables were frequently heard as multiple utterances. Listeners reported hearing parts of two syllables and impressions of multiple vowels. Without a common vowel, in most cases, the initial and final segments of syllables simply would not fuse perceptually.

[2]The mixed-consonants conditions reported here were studied at the same time as the conditions reported in Strange, 1989b. Listeners were randomly assigned to these conditions from the same pool of participants. Thus, the comparisons reported here are justified by the usual randomization of assignment of listeners. Results were mentioned in Strange, 1989b, but have not been reported in detail before now.

Andruski, J. E., and Nearey, T. M. (**1992**). ''On the sufficiency of compound target specification of isolated vowels and vowels in /bVb/ syllables,'' J. Acoust. Soc. Am. **91**, 390–410.

Benguerel, A.-P., and McFadden, T. U. (**1989**). ''The effect of coarticulation on the role of transitions in vowel perception,'' Phonetica **46**, 80–96.

Broad, D. J., and Clermont, F. (**1987**). ''A methodology for modeling vowel formant contours in CVC context,'' J. Acoust. Soc. Am. **81**, 155–165.

Di Benedetto, M. G. (**1989a**). ''Vowel representation: Some observations on temporal and spectral properties of the first formant frequency,'' J. Acoust. Soc. Am. **86**, 55–66.

Di Benedetto, M. G. (**1989b**). ''Frequency and time variations of the first formant: Properties relevant to the perception of vowel height,'' J. Acoust. Soc. Am. **86**, 67–77.

Fourakis, M. (**1991**). ''Tempo, stress, and vowel reduction in American English,'' J. Acoust. Soc. Am. **90**, 1816–1827.

Fowler, C. A. (**1996**). ''Listeners do hear sounds, not tongues,'' J. Acoust. Soc. Am. **99**, 1730–1741.

Fowler, C. A., and Rosenblum, L. D. (**1991**). ''The perception of phonetic gestures,'' *Modularity and the Motor Theory of Speech Perception*, edited by I. G. Mattingly and M. Studdert-Kennedy (Erlbaum, Hillsdale, NJ).

Fox, R. A. (**1989**). ''Dynamic information in the identification and discrimination of vowels,'' Phonetica **46**, 97–116.

Gottfried, T. L., and Strange, W. (**1980**). ''Identification of coarticulated vowels,'' J. Acoust. Soc. Am. **68**, 1626–1635.

Harrington, J., and Cassidy, S. (**1994**). ''Dynamic and target theories of vowel classification: Evidence from monophthongs and diphthongs in Australian English,'' Lang. Speech **37**, 357–373.

Hillenbrand, J., Getty, L. A., Clark, M. J., and Wheeler, K. (**1995**). ''Acoustic characteristics of American English vowels,'' J. Acoust. Soc. Am. **97**, 3099–3111.

Jenkins, J. J., and Strange, W. (**1999**). ''Perception of dynamic information for vowels in syllable onsets and offsets,'' Percept. Psychophys. (in press).

Jenkins, J. J., Strange, W., and Edman, T. R. (**1983**). ''Identification of vowels in 'vowelless' syllables,'' Percept. Psychophys. **34**, 441–450.

Jenkins, J. J., Strange, W., and Miranda, S. (**1994**). ''Vowel identification in mixed-speaker, silent-center syllables,'' J. Acoust. Soc. Am. **95**, 1030–1043.

Joos, M. A. (**1948**). ''Acoustic phonetics,'' Language **24** (Suppl.), 1–136.

Miller, J. D. (**1989**). ''Auditory-perceptual interpretation of the vowel,'' J. Acoust. Soc. Am. **85**, 2114–2134.

Moon, S. Y., and Lindblom, B. (**1994**). ''Interaction between duration, context, and speaking style in English stressed vowels,'' J. Acoust. Soc. Am. **96**, 40–55.

Nearey, T. M. (**1989**). ''Static, dynamic, and relational properties in vowel perception,'' J. Acoust. Soc. Am. **85**, 2088–2113.

Parker, E. M., and Diehl, R. L. (**1984**). ''Identifying vowels in CVC syllables: Effects of inserting silence and noise,'' Percept. Psychophys. **36**, 369–380.

Peterson, G. E., and Barney, H. L. (**1952**). ''Control methods used in the study of vowels,'' J. Acoust. Soc. Am. **24**, 175–184.

Pols, L. C. W., and van Son, R. J. J. H. (**1993**). ''Acoustics and perception of dynamic vowel segments,'' Speech Commun. **13**, 135–147.

Rosner, B. S., and Pickering, J. B. (**1994**). *Vowel Perception and Production* (Oxford University Press, New York).

Shankweiler, D. P., Strange, W., and Verbrugge, R. R. (**1977**). ''Speech and the problem of perceptual constancy,'' *Perceiving, Acting and Knowing: Toward an Ecological Psychology*, edited by R. Shaw and J. Bransford (Erlbaum, Hillsdale, NJ).

Signal Technology, Inc. (**1978**). INTERACTIVE LABORATORY SYSTEM computer software (Goleta, CA).

Strange, W. (**1987**). ''Information for vowels in formant transitions,'' J. Memory Lang. **26**, 550–557.

Strange, W. (**1989a**). ''Evolving theories of vowel perception,'' J. Acoust. Soc. Am. **85**, 2081–2087.

Strange, W. (**1989b**). ''Dynamic specification of coarticulated vowels spoken in sentence context,'' J. Acoust. Soc. Am. **85**, 2135–2153.

Strange, W., and Bohn, O.-S. (**1998**). ''Dynamic specification of coarticulated German vowels: Perceptual and acoustical studies,'' J. Acoust. Soc. Am. **104**, 488–504.

Strange, W., Jenkins, J. J., and Johnson, T. L. (**1983**). ''Dynamic specification of coarticulated vowels,'' J. Acoust. Soc. Am. **74**, 695–705.

Strange, W., Verbrugge, R. R., Shankweiler, D. P., and Edman, T. R. (**1976**). ''Consonant environment specifies vowel identity,'' J. Acoust. Soc. Am. **60**, 213–224.

Tiffany, W. R. (**1953**). ''Vowel recognition as a function of duration, frequency modulation and phonetic context,'' J. Speech. Hear. Dis. **18**, 289–301.

Verbrugge, R. R., and Rakerd, B. (**1986**). ''Evidence of talker-independent information for vowels,'' Lang. Speech **29**, 39–57.

Verbrugge, R. R., Strange, W., Shankweiler, D. P., and Edman, T. R. (**1976**). ''What information enables a listener to map a talker's vowel space?,'' J. Acoust. Soc. Am. **60**, 198–212.

Zahorian, S. A., and Jagharghi, A. J. (**1993**). ''Spectral shape versus formants as acoustic correlates for vowels,'' J. Acoust. Soc. Am. **94**, 1966–1982.

Functional neuroimaging of speech perception in six normal and two aphasic subjects

C. J. Mummery and J. Ashburner
Wellcome Department of Cognitive Neurology, Institute of Neurology, Queen Square, London WC1N 3BG, United Kingdom

S. K. Scott[a)]
Medical Research Council, Cognition and Brain Sciences Unit, 15 Chaucer Road, Cambridge CB2 2EF, United Kingdom

R. J. S. Wise
Imperial College School of Medicine, Cyclotron Unit, Hammersmith Hospital, Du Cane Road, London W12 0NN, United Kingdom

(Received 19 May 1998; revised 18 December 1998; accepted 8 February 1999)

This positron emission tomography study used a correlational design to investigate neural activity during speech perception in six normal subjects and two aphasic patients. The normal subjects listened either to speech or to signal-correlated noise equivalents; the latter were nonspeech stimuli, similar to speech in complexity but not perceived as speechlike. Regions common to the auditory processing of both types of stimuli were dissociated from those specific to spoken words. Increasing rates of presentation of both speech and nonspeech correlated with cerebral activity in bilateral transverse gyri and adjacent superior temporal cortex. Correlations specific to speech stimuli were located more anteriorly in both superior temporal sulci. The only asymmetry in normal subjects was a left lateralized response to speech in the posterior superior temporal sulcus, corresponding closely to structural asymmetry on the subjects' magnetic resonance images. Two patients, who had left temporal infarction but performed well on single word comprehension tasks, were also scanned while listening to speech. These cases showed right superior temporal activity correlating with increasing rates of hearing speech, but no significant left temporal activation. These findings together suggest that the dorsolateral temporal cortex of both hemispheres can be involved in prelexical processing of speech. [S0001-4966(99)00107-1]

PACS numbers: 43.71.Pc [WS]

INTRODUCTION

A striking characteristic of spoken language is the rate and accuracy with which it can be comprehended (Liberman *et al.*, 1967). Prior to comprehension, the acoustic properties of the input must be processed and the individual speech sounds (phonemes) categorized, the lexical percept remaining robust despite, at times, considerable variance in the signal resulting from distortions (Miller, 1951). This robustness is a consequence of a speech perception mechanism which performs extensive acoustic processing of the input, which can ''compensate'' for degraded input; for example, incomplete articulation leading to neutralized phonemes. In this paper we assume this processing represents the prelexical processing of the speech input: the auditory analysis performed before meaning is derived. We will contrast this with the processing of acoustic stimuli closely matched to comprehensible speech.

Although no single cue determines the comprehensibility of speech, optimal speech perception requires auditory processes that can respond to rapid frequency changes, as some consonants are differentiated by changes in one or more of their component frequencies (formants) occurring over less than 50 ms (Fitch *et al.*, 1997). These temporal processing skills are considered to be a property of the left cerebral hemisphere, based on dichotic listening studies and observations on split brain patients (Studdert-Kennedy and Shankweiler, 1970; Levy and Trevarthen, 1977). However, word deafness (an inability to perceive heard words in the absence of any other major aphasic disturbance) is most frequently associated with bilateral temporal lobe lesions (Buchman *et al.*, 1986), suggesting that the right hemisphere may be involved in the perception of speech.

I. GENERAL METHOD AND RATIONALE

Current neuroimaging techniques permit the investigation of the extent of right hemisphere involvement in speech processing, by facilitating the imaging of neural activity in the intact human brain. This study used a particular method, positron emission tomography (PET). A slow intravenous bolus of a positron emitting isotope of water ($H_2{}^{15}O$) is used as an index of cerebral perfusion. Increases in local net synaptic activity result in greater regional cerebral blood flow (rCBF), signaled by an increase in the local accumulation of $H_2{}^{15}O$ in the tissue. The regional concentrations of cerebral $H_2{}^{15}O$ can be detected by PET scanning. The realignment, normalization, and smoothing of a sequence of perfusion im-

[a)]Address for correspondence: Dr. S. K. Scott, Institute of Cognitive Neuroscience, Alexandra House, 17 Queen Square, London WC1N 3AR, United Kingdom. Electronic mail: sophie.scott@ucl.ac.uk

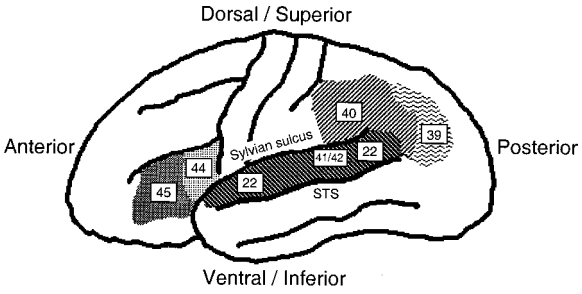

FIG. 1. Diagrammatic representation of the left hemisphere showing classical perisylvian language areas. Shaded regions represent distinct cytoarchitectonic regions as defined by Brodmann, with Brodmann numbers superimposed.

Middle superior temporal gyrus	BA 41/42	Primary auditory cortex
Anterior superior temporal gyrus	BA 22	
Posterior superior temporal gyrus	BA 22/40	Wernicke's area
Superior temporal sulcus	BA 22	sulcus separating superior and middle temporal gyri
Angular gyrus	BA 39	classically associated with reading
Supramarginal gyrus	BA 40	
Inferior frontal gyrus	BA 44/45	Broca's area

ages from each subject can resolve *peaks* of activity that are >5 mm apart (Fox *et al.*, 1985). Changes in local activity between scans, obtained with the subjects under different behavioral conditions, can be used to relate function to structure. Frequently, studies using this technique have subtracted the activation measured during one scan (a ''baseline'' task) from the activation seen during the experimental task. Thus in Zatorre *et al.* (1992), activity detected when subjects listened to tones was subtracted from activity measured when they listened to speech, revealing bilateral activation of anterior superior temporal lobe regions (see Fig. 1 for explanation of the anatomical terminology used here, and the relationship to previous functional maps of the human brain). This ''subtraction'' methodology has the merit of simplicity, but incorporates a number of assumptions; in particular, it assumes the insertion of only the cognitive process under investigation in the comparison of experimental to baseline tasks (Friston *et al.*, 1997). An alternative is the parametric design, in which the stimulus or task is varied parametrically across scans and correlated with regional neural activity (rCBF), without the need for a ''baseline'' task. In one such study, word rate was the varied parameter, and in different scans different rates of spoken words were presented to the subjects (Price *et al.*, 1992): the authors were able to identify regions in the left and right superior temporal gyri (STG) that increased in activity with increasing rates of speech. The assumption of linearity of blood flow with activity can be tested with nonlinear fits to the measured response; thus, Price and colleagues found a nonlinear response in the left posterior STG, indicating that this region was involved in a speech process that was independent of the rate of stimulus perception.

In addition to the design selected, the details of the experimental task are important in interpreting the results. Previous neuroimaging studies examining speech perception have shown varying results depending on the activation task used; for example, whether the identification of the individual speech sounds (phonemes) of a spoken word is implicit or an explicit part of a phoneme detection task. Our aim in this study was twofold. First, we wished to investigate the contribution of the dorsolateral temporal cortex (DLTC) of both cerebral hemispheres to implicit speech perception, attempting to dissociate regional activations common to the acoustic processing of speech and complex nonspeech sounds from those specific to spoken words. The nature of the nonspeech sounds has an important role; a comparison of speech with tones or noise bursts leaves the possibility that differences in activation are a result of the speech being a more complex stimulus. The stimuli should not be so speech-like, however, that they engage a speech mode of processing. The nonspeech stimuli used here was signal-correlated noise (SCN; Schroeder, 1968) which forms a stimulus with the same instantaneous amplitude as the speech signal, but with a white spectrum; it thus contains none of the spectral information such as transients and formants that lead to intelligible speech. Signal-correlated noise preserves the amplitude envelope of speech sounds, so these stimuli have preserved segmental information about manner of articulation, and the tempo, rhythm and syllabicity of the speech without comprehension being possible (Rosen, 1992); it thus forms an appropriately complex nonspeech contrast.

In the context of this normal activation, the second aim of our study was a preliminary investigation of the contribution of the right hemisphere to speech perception in recovered aphasics. This study focused on two patients, who have had infarction of the left DLTC. Both were initially aphasic, that is, unable to comprehend spoken language, and both have recovered speech comprehension, albeit to differing degrees. Single word comprehension (particularly for concrete nouns) commonly improves in aphasic patients. The aim of this part of the study was to investigate how this is mediated after extensive left hemisphere damage: the patients could either be perceiving speech using cortex at the margins of the lesion in the left DLTC, or by processing the acoustic and phonetic properties of the words in the contralateral (right) DLTC. We performed a correlational (parametric) analysis to investigate which of these hypotheses was correct.

II. SPEECH PERCEPTION IN NORMAL SUBJECTS

A. Material and methods

1. Subjects

Six right-handed, healthy male volunteers took part (aged between 26 and 58 years). Each gave informed, written consent. All had English as their first language. The study involved the administration of <5 mSv (effective dose equivalent) of radioactivity per subject and was approved by the Administration of Radioactive Substances Advisory Committee (Department of Health) and the research ethics committee at the National Hospital for Neurology and Neurosurgery.

2. Method

Brain activation was measured using positron emission tomography (PET). The dependent variable in functional imaging studies is the haemodynamic response; a local increase

in net synaptic activity is associated with an increased local metabolism, which is matched by an increase in rCBF. Water labeled with a positron-emitting isotope of oxygen ($H_2{}^{15}O$) was used as the tracer to demonstrate changes in rCBF (equivalent to changes in tissue concentration of $H_2{}^{15}O$). The resolution of the technique meant that the activity at the level of neural systems (i.e., local populations of billions of synapses) was observed. Analysis involved relating changes in local tissue activity (normalized for global changes in activity between scans) to the type of stimuli (speech versus SCN) and their rate of presentation.

Twelve estimations of rCBF were made on each subject with a Siemens/CPS ECAT Exact HR+(962) with a field of view in the *z* axis of 15 cm. Data acquisition was performed in 3-D mode, with the lead septa between detector rings removed. For each scan 8 mCi of $H_2{}^{15}O$ (half-life 2.1 min) was administered as slow intravenous bolus. After a delay of approximately 40 s, the tracer reached the cerebral circulation and the head counts peaked about 30 s later (depending on individual circulation time). The interval between successive $H_2{}^{15}O$ administrations was 8 min. The total counts per voxel during the buildup phase of radioactivity served as an estimate of rCBF. Thus local activity was integrated over 30 s (the temporal resolution of the technique), corresponding to summing the neural transients that occurred in response to each stimulus. The stimuli were started 15 s before the arrival of tracer in the brain, and continued for 15 s after the head counts peaked. Correction for the attenuation of a proportion of emitted photons by the tissues was made by performing a transmission scan with an exposed $^{68}Ge/^{68}Ga$ external source at the beginning of the study. Images were reconstructed by filtered back projection (Hanning filter, cutoff frequency 0.5 Hz), giving a transaxial resolution of 6.5 mm full width at half-maximum (FWHM). The reconstructed images contained 128×128 pixels, each $2.05\times2.05\times2.00\,mm^3$ in size. The accumulated counts over the scanning period reliably reflect blood flow in the physiological range (Fox and Mintun, 1989; Mazziotta *et al.*, 1985). Subsequently, T1-weighted magnetic resonance (MR) images, with a voxel size of $1\times1\times3\,mm^3$, were obtained with a 2.0 T Vision system (Siemens GmbH, Erlangen, Germany).

3. Design and stimulus presentation

There were twelve PET scanning conditions (six presentation rates and two experimental conditions—speech and SCN), which were randomized within and across subjects to control for time effects. During scanning, the normal subjects heard either spoken words or SCN sounds, presented binaurally, at rates of 1, 5, 15, 30, 50, and 75 per min. In the 1 per min condition subjects heard one stimulus before the scan started and they anticipated hearing further stimuli. The presented words were bisyllabic nouns, matched for frequency (6–20 000), concreteness (400–700), and imageability (300–700) on the MRC Psycholinguistic Database (Coltheart, 1981), and were prerecorded on a tape by a speaker, rate being controlled by a metronome. The signal-correlated noise (SCN) stimuli were made by digitizing a sample of these spoken nouns (varying the segmental duration and initial manner of articulation), then multiplying the signals with white noise. Each subject prior to his study subjectively matched the stimuli for loudness, by listening to a section of each stimulus type and adjusting the amplification until they were subjectively similar. The task instruction was to pay attention to the stimuli without responding.

4. Data analysis

The data were analyzed with statistical parametric mapping (SPM 96 software, Wellcome Department of Cognitive Neurology, London, UK), implemented in PRO MATLAB (Mathworks, Inc., Sherborn, MA). Prior to statistical analysis the images from each subject were realigned using the first as a reference to correct for any interscan head movements (Friston *et al.*, 1995a). A mean rCBF image was created for each subject. Each subject's MRI anatomical scan was coregistered to his mean PET image and then stereotactically transformed to a standard MRI template in the Talaraich and Tournoux space (1988). The same transformation matrix was subsequently applied to the PET images (Friston *et al.*, 1995a). When stereotactically normalized, one voxel in the transformed image represented 2 mm in the *x* and *y* dimensions and 4 mm in the *z* dimension. Images were smoothed using an isotropic Gaussian kernel (16 mm FWHM) to accommodate intersubject differences in gyral anatomy, structure-function relationships and to optimize the signal-to-noise ratio. Finally, the data were analyzed using a blocked one-way ANCOVA with global activity as a subject-specific confounding covariate, and regionally specific differences were assessed using appropriate contrasts and covariates to create SPMs of the *t* statistic (that were subsequently transformed into *Z* scores) (Friston *et al.*, 1995b). Analyses were performed to examine the main effects of task (listening to speech or SCN stimuli); the main effects of stimulus presentation rate; and, finally, the task by rate interaction, to demonstrate those areas that were disproportionately activated by either spoken words or signal correlated noise.

In the absence of *a priori* hypotheses about where regional activations may occur, it is recommended that the threshold be set at $P<0.05$, corrected for analyses of voxels across the whole volume of the brain (approximately, $P<0.000\,1$, uncorrected, *Z*-score >4.3). However, significant effects were expected to occur in the DLTC of both hemispheres, and for these defined regions the significance threshold was set at $P<0.001$, uncorrected (*Z*-score >3.1). For all other regions, significance was set at $P<0.05$, corrected. Only regions satisfying these criteria are reported.

In addition to the PET analysis, a structural analysis of the MRI data was performed, looking for regional asymmetry in gray/white matter mass within the temporal lobes. Differences in voxel signal for gray and white matter on the MR images were used to investigate anatomical asymmetries in this specified region. The MR images were realigned, stereotactically normalized, and smoothed to 12 mm. They were then flipped, left to right, and contrasted with the unflipped images. The technique used (voxel-based morphology) was implemented with statistical parametric mapping (SPM 96) as previously described (Wright *et al.*, 1995). Significance was set at $P<0.001$, uncorrected, for dorsolateral temporal

TABLE I. Regions of significant activation in the categorical contrast of speech and signal correlated noise.

Region	*xyz* coordinates[a]	*Z*-score
Left anterior STG/STS (BA 22)	−48, 2, −12	4.9
Left middle STG/STS (BA 22)	−54, −28, 4	6.6
Left posterior STG/STS (BA 22)	−54, −38, 8	5.5
Right anterior STG/STS (BA 22)	54, 2, −4	5.1
Right middle STG/STS (BA 22)	52, −14, 4	6.4
Right dorsal midbrain	12, −30, −20	4.8
	26, −30, 16	3.9

[a]Coordinates, in mm, in the stereotactic space of Talairach and Tournoux for peak voxels within a particular activated region. Abbreviations: BA =Brodmann's area, STG=superior temporal gyrus; STS=superior temporal sulcus.

cortex, with the hypothesis that the gray/white matter mass would be higher in or around the left posterior STG than the right (Wada *et al.*, 1975).

B. Results

A simple comparison of speech with SCN conditions, irrespective of rate, identified regions more active when processing speech than when processing SCN stimuli. This analysis showed activation of left and right STG extending ventrally into the superior temporal sulci (STS), with additional activation in right dorsal midbrain (Table I). The subsequent parametric analysis, which investigated the relationships between activity and rate of hearing either speech or SCN, identified regions that increased in activity with increasing rates of both types of stimuli, or with speech alone. Both linear and nonlinear fits (second-order polynomials) were investigated (Büchel *et al.*, 1996).

Regions which increased *linearly* in activity with both speech and SCN stimuli were found in the transverse temporal gyrus (TTG) and adjacent STG in both hemispheres [Fig. 2(a) and Table II]. Across rates activity was greater for speech [Fig. 2(c)]. There were no regions showing significant decreases in activity with rate, and no regions for which a nonlinear fit was significant.

Regions which increased linearly in activity with increasing rates of speech alone (i.e., that did not respond to increasing rates of SCN), were revealed as an interaction, specified in the same SPM96 design matrix that investigated the main (common) effects of stimulus rate. This interaction was significant in both STS, both anterior and ventral to the TTG. Smaller in extent compared to those regions correlating with both speech and nonspeech stimuli, there was increasing activity with increasing numbers of speech stimuli in these more anterior regions. There was one region of asymmetry—a response in the left posterior ventral STG/STS [Fig. 2(b) and (d) and Table II]. There was no region in either contrast for which nonlinear fits were significant.

In the morphometric analysis of the subjects' MR images, the only asymmetry of gray/white matter mass in the temporal lobes corresponded closely to the area of functional

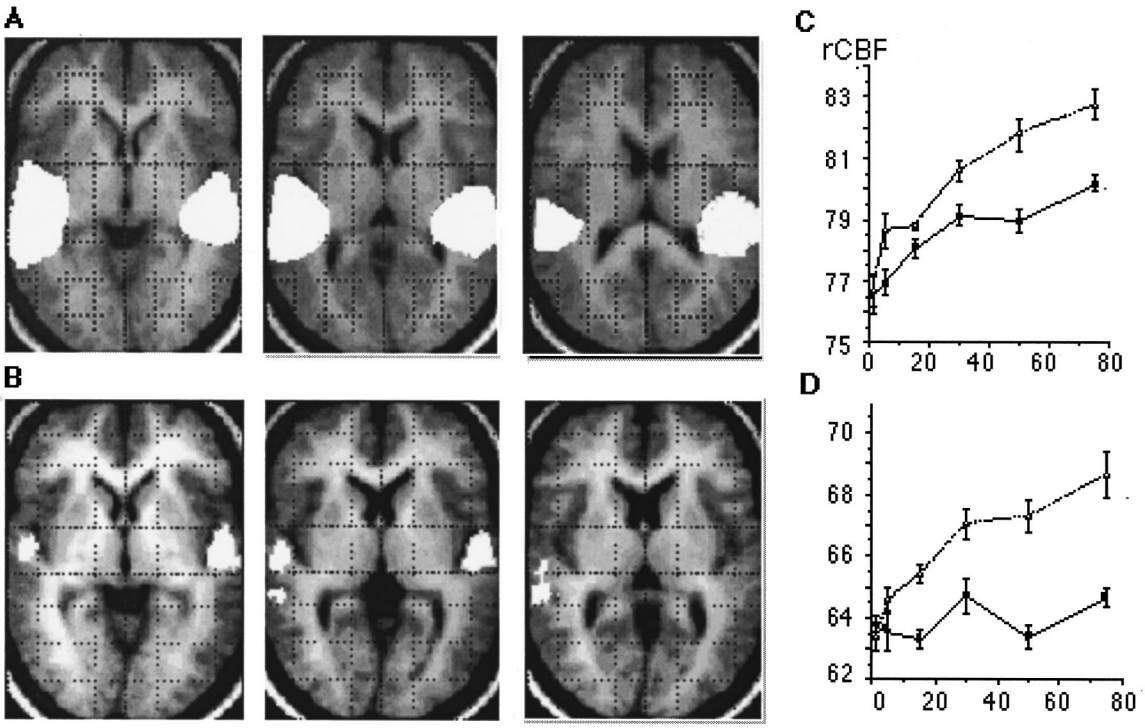

FIG. 2. (a) Regions of significantly increased regional cerebral blood flow (rCBF) correlating with rate independent of stimulus. The data is displayed on transverse slices of the subjects' average normalized MRI (magnetic resonance image); the measurements refer to the height in mm from the AC-PC line. For all data shown, $p<0.001$ (uncorrected). (b) Regions of significantly increased rCBF correlating with rate for speech stimuli only. (c) Graph displaying the regression of adjusted rCBF activity against word presentation rate for the voxel with the most significant *z*-score in the region where there was a significant linear correlation of activity with rate for both speech and nonspeech stimuli. The dotted lines represent changes with speech; the solid lines represent changes with signal-correlated noise. (d) Graph displaying the regression of adjusted rCBF activity against word presentation rate for the voxel with the most significant *z*-score in the region where there was a significant linear correlation of activity with rate for speech stimuli only. The dotted lines represent changes with speech; the solid lines represent changes with signal correlated noise.

TABLE II. Peak voxels showing the significance (*Z* score) of the correlation of activity with stimulus rate.

Regions common to speech and SCN	*xyz* coordinates[a]	*Z*-score
Right TTG/STG (BA 41/42/22)	44, −24, 4	8.3
	54, −28, 8	8.1
Left TTG/STG (BA 41/42/22)	−48, −34, 8	8.0
Regions specific to speech		
Right anterior ventral STG/STS	54, −6, 0	4.4
(BA 22)	50, −12, 4	4.3
	50, −20, 0	3.9
	52, 2, −8	3.4
Left anterior ventral STG/STS	−54, −14, 0	3.8
(BA 22)	−52, −4, 0	3.5
	−54, 4, −8	3.7
Left Posterior STG/STS (BA 22)	−56, −34, 8	3.8
	−58, −26, 8	3.3

[a]Coordinates, in mm, in the stereotactic space of Talairach and Tournoux for peak voxels within a particular activated region. Abbreviations: BA =Brodmann's area, TTG=transverse temporal gyrus; STG=superior temporal gyrus; STS=superior temporal sulcus.

asymmetry, the distance between the most significant voxels in the functional (coordinates −56, −34, 8) and anatomical (coordinates −46, −34, 14) analyses being 10 mm (Fig. 3). As can be seen, the structural analysis yields a maxima 10 mm medial to that of the functional, correlating with the observation that the functional asymmetry is within the sulcus.

III. PERCEPTION OF SPEECH BY APHASIC PATIENTS

A. Clinical description

1. Patient EJ

EJ is a 38-year-old, right-handed woman who suffered an infarct of the whole of her left DLTC 18 months prior to her PET study. Although initially aphasic, her spontaneous speech is now fluent, without phonemic or semantic paraphasic errors. Her comprehension during conversational speech is good, although she does complain of impaired comprehension for speech spoken too quickly, or if there is background noise, particularly other conversations. She has good auditory single word and sentence comprehension [52/68, chance=17/68, on blocks D to T of the TROG, a standard test of sentence comprehension (Bishop, 1982)]. However, she is impaired at the modified Token test (8/15) (De Renzi and Faglioni, 1978), which requires the manipulation of colored shapes after a series of simple commands, and she has a reduced span for verbal material (digit, letter, and word spans of 3–4), indicating a short-term memory deficit.

2. Patient SS

Patient SS, a 42-year-old, right-handed man, had a more extensive infarct 6 months before study, including most of the left DLTC. Initially globally aphasic, he still has virtually no comprehensible speech, his output consisting of speech sounds rather than words or nonwords. His comprehension of single words, although not sentences, had improved considerably by the time of the PET study. Therefore, when tested on items of the PALPA (Kay *et al.*, 1992), two weeks prior to PET scanning, he scored 79/80 (chance=40/80) on the first half of the auditory lexical decision task (which contains 40 words of high and low frequency and imageability, and 40 nonwords differing by one or more phonemes from the words, with the patient making a yes/no decision as to whether the word is real or not); and 30/40 (chance=8/40) on auditory word-to-picture matching, with 7/10 close semantic errors [the subject matches the heard word to one of five pictures—the target (e.g., carrot), a close semantic distractor from the same superordinate category (e.g., cabbage), a more distant semantic distractor (e.g., lemon), a visually related distractor (e.g., saw) or an unrelated distractor (e.g., chisel)]. This result suggests a residual problem accessing the semantic system. On auditory synonym judgement, SS correctly differentiated whether 14/15 pairs of heard words were close in meaning when the words were of high imageability (e.g., ship–boat), but only scored at chance level (8/15) when the pairs were words of low imageability (e.g.,

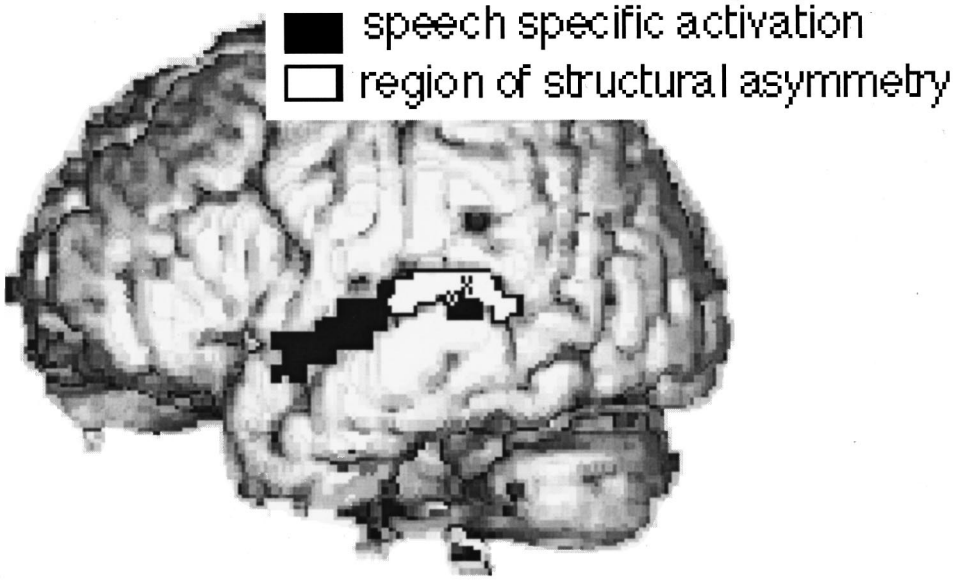

FIG. 3. Three-dimensional rendering of brain MRI showing functional and structural symmetry within the left temporal lobe. For all data shown, $p<0.001$ (uncorrected). The most significant voxels are indicated in each condition: ''x'' corresponds to the most significant voxel in the structural analysis (coordinates −46, −34, 14; $Z=4.8$); ''o'' corresponds to the most significant voxel in the posterior STS in the word-specific analysis (coordinates −56, −34, 8).

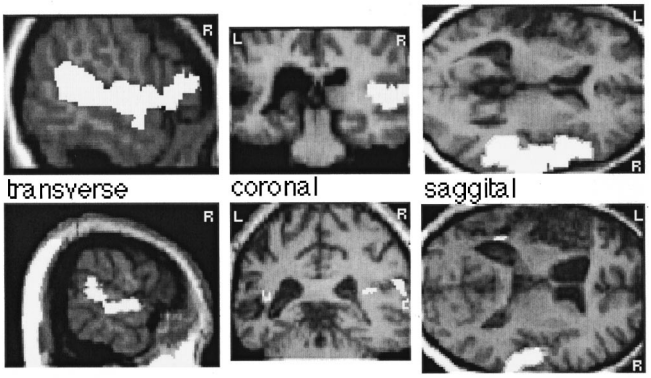

FIG. 4. Normalized MRI sections of patient EJ (a), and patient DS (b), showing left DLTC infarction, and regions where there was a significant linear correlation of adjusted activity with spoken word presentation rate ($P<0.001$, uncorrected).

idea–notion). This ''concreteness'' effect is not uncommon in aphasic patients and implies a postlexical deficit (Franklin, 1989).

B. Methods

Both subjects had 12 PET $H_2{}^{15}O$ activation scans, listening to words at rates of 0 through to 90 words per min. These were the same word stimuli used in the previous experiment. They were not presented with the SCN stimuli since it was their residual processing of speech items that was of interest, in the context of the normal study results. The instruction to both patients was to listen and pay attention to the words without making a response. The methods were identical in other respects to those used in the first experiment. Analysis investigated the correlation of regional cerebral activity with the rate of hearing words. Each patient's PET images were coregistered to their individual MRI to allow accurate localization of function.

C. Results

Analysis of regions that increased in activity with increasing speech rates revealed extensive positive correlations in the right STG/S and right TTG in both patients (Fig. 4). There were *no* left temporal correlations in EJ ($P>0.50$, uncorrected), and only a small residual region of the medial left TTG responded in SS. Since both aphasic patients had mature lesions, the assumption was that vascular reactivity around the infarct had returned: that is, peri-infarct activation would have been observed if it had been present. Peri-infarct activations around mature infarcts have been observed previously (Price *et al.*, 1998). Furthermore, in SS activation was observed in the most medial part of the left TTG, the only residue of superior temporal cortex left after his stroke, and this was directly adjacent to the infarct. Coregistering the left hemisphere regions activated by speech in the normal subjects on to the left hemispheres of the two patients shows that the temporal infarct in both patients entirely encompassed these regions.

IV. DISCUSSION

Functional imaging has already contributed a great deal to our understanding of spoken word perception. Early PET studies on listening to words or nonwords, without response from the subjects, showed bilateral STG activations (e.g., Petersen *et al.*, 1988; Wise *et al.*, 1991). Further studies compared listening to words with listening to noise/tones (Zatorre *et al.*, 1992; Demonet *et al.*, 1992) and showed bilateral activation of the anterior ST regions. The present study has, by using a parametric design for both speech and SCN, clearly distinguished auditory cortical areas specialized for processing speech from more generic areas that respond to both types of input. Comparison with activation seen in patients with left temporal infarcts reveals the functional role of this activation in recovery from aphasia. Since we have used nonspeech sounds that are similar to the speech stimuli in terms of complexity and duration, we can make a strong claim for bilateral activation of speech stimuli that is not a consequence of spoken words being acoustically unlike tones or simple white noise along these dimensions. The use of a passive listening task avoids activation associated with more strategic responses being required. The use of a parametric design enables us to delineate more accurately the nature of the neural responses.

The categorical results on normal subjects show that the receptive fields for heard words is larger than for SCN stimuli, extending anteriorly down the ventral STG of both hemispheres, more posteriorly on the left. The transverse temporal gyri and dorsal part of the STG showed strong positive correlations regardless of stimulus, whereas the ventral STG/STS bilaterally and the left posterior STS showed correlation of activity with spoken word stimuli alone. This dorsal/ventral distinction has been noted before using a similar task compared to listening to noise (Binder *et al.*, 1996). It is consistent with electrophysiological work on monkeys, which has shown that the lateral STG has a unimodal auditory function, whereas the more ventral regions or STS are multimodal (Jones and Powell, 1970; Desimone and Gross, 1979). Extrapolating to work on humans, this work supports the notion that language functions are more a property of the ventral STG/STS (Binder *et al.*, 1996).

Parametric designs have been used in previous neuroimaging language studies. The correlation between the rate of hearing words and activity in bilateral TTG and middle parts of STG was initially demonstrated by Price *et al.* (1992), close to the regions showing correlation of activity with both types of stimuli in the present experiment. They also found a nonlinear response in the left posterior STG (coordinates -58 -34 12), distinct from that seen in other superior temporal regions, which were virtually linear. However, more recent studies using fMRI have found the response to words in the posterior STG is similar to that found in primary auditory cortex (Binder *et al.*, 1994; Dhankhar *et al.*, 1997) showing a monotonic, nonlinear response which decays at rates above 100 wpm. A further PET study of the response to hearing words at different rates could not reproduce the specific response curve in the left posterior STG of Price and colleagues (Wise *et al.*, in press). A possible explanation for this discrepancy is that the baseline in the study of Price

et al. (1992) was ''rest''—the subjects were forewarned prior to the scan that they would hear no words. In this study ''baseline'' was listening to words at a very slow rate: that is, the subjects were anticipating stimuli throughout the scan. The same was true for the study by Wise *et al.* (in press). Although only the linear fits were significant for the relationship between word rate and rCBF increases, both the STG and STS show a slight decrease in slope at the higher rates; the extent and significance of this potential ''turn-over'' cannot be determined without more data points at higher word rates.

The symmetry of activation in bilateral STG/STS suggests that both hemispheres participate in the processing of spoken words. Auerbach *et al.* (1982) suggested that word deafness due to loss of prephonological auditory processing is associated with bilateral temporal lobe lesions, but that a unilateral left temporal lesion causes word deafness due to a deficit in phoneme discrimination and identification. A more recent clinical and psychophysical study of a patient does not support this, however; the patient had an initial infarction of the left dorsolateral temporal lobe and presented with Wernicke's aphasia, but subsequently developed word deafness after a right temporal infarct (Praamstra *et al.*, 1991). Loss of spoken word comprehension only occurred after the second, right hemisphere infarct. Using the SCN stimulus, we have attempted to differentiate between acoustic processing and phonetic, speech specific processing. We argue that this study, interpreted in the light of other functional neuroimaging studies, indicates that prelexical processing normally involves both hemispheres, supporting the latter viewpoint.

This study has employed a passive listening task, as we were interested in the preattentive, automatic processing of spoken language, which occurs without conscious awareness (Schneider and Shiffrin, 1977; Shiffrin and Schneider, 1977). A study using MEG (Poeppel *et al.*, 1996) has shown modulation of activation in auditory cortex when listening to identical speech stimuli, based on the nature of the task, that is, active phoneme discrimination compared to passive listening. This influence of task may account for differences in activation found in this study compared to previous studies of speech perception which have employed an explicit, active task. For example, in two PET studies of sequential phoneme detection, contrasted with a pitch judgement on pure tones also showed significant bilateral anterior STS activations (Demonet *et al.*, 1992, 1994). These were asymmetrical, being greater on the left than on the right, as found in the discrimination task of Poeppel *et al.* (1996). Another common feature of explicit phoneme detection was a left dorsolateral frontal activation (Zatorre *et al.*, 1996; Fiez *et al.*, 1995). These active, explicit tasks require both the processing of the sensory input and a more central, attention-based decision about the percept. They result in activation in frontal structures (Demonet *et al.*, 1992, 1994; Zatorre *et al.*, 1996; Fiez *et al.*, 1995), left-sided when the feature is phonetic and right-sided when it is pitch.

The nature of the task employed is relevant to understanding the performance of patients. Aphasic patients show impairment of phoneme discrimination and identification (Basso *et al.*, 1977; Blumstein *et al.*, 1977: for review, see Fitch *et al.*, 1997), suggesting a superiority of the left hemisphere in speech perception. However, performance on phonetic feature detection may not represent a measure of general speech perception *per se* (Riedel *et al.*, 1985) and it correlates poorly, if at all, with tests of word comprehension in aphasic patients (Blumstein *et al.*, 1977). Together, the functional imaging and neuropsychological evidence indicate that active, phonetic feature detection is dependent on predominantly left-lateralized processes, whereas implicit speech processing can be supported by both hemispheres, probably by making use of a number of acoustic cues. We claim that automatic prelexical processing accounts for the speech-specific, bilateral anterior STS activations seen in this study.

The results in the two patients strengthen these conclusions. Both had recovered single word comprehension, and when presented with speech, both showed activity in the right STG/STS, comparable with that seen in the normal subjects. As neither showed activity in the left DLTC (other than in a small residue of medial primary auditory cortex in SS), the implication is that prelexical processing was dependent on the right DLTC, and that it is the right hemisphere which is supporting their speech perception. As we cannot infer premorbid functional lateralization from poststroke studies, we do not know the extent of SS and EJ's right hemisphere involvement in language processing, prior to their strokes. The solution to this problem will be to study a greater number of patients with left temporal infarcts. Such a study can also address the influence of factors such as sex (Shaywitz *et al.*, 1995; Buckner *et al.*, 1995) on recovery of speech perception.

We cannot determine the functional role of the asymmetry shown in left posterior STS by the normal subjects, since this was a passive listening task. The cost of avoiding explicit, attention-based activation is an inability to define what specific feature of the spoken words has resulted in this lateralized functional response. However, the psychophysical data on the patients and the previous functional imaging findings suggest some interesting (though speculative) possibilities concerning the function of this region. The speech-specific cortex in the left posterior STS, a region of both functional and anatomical asymmetry in this study on normal subjects, is accepted as the core of Wernicke's area, despite varying opinions about its extent (Bogen and Bogen, 1976). One previous PET study on normal subjects specifically identified this region as the locus of long-term mental representations of the whole sound structure of familiar words (Howard *et al.*, 1992), and anatomical imaging in patients has shown that the degree of damage to the left posterior temporal lobe is predictive of the amount of recovery made in terms of auditory comprehension (Selnes *et al.*, 1983; Naeser *et al.*, 1987). Although this region was infarcted in both SS and EJ, who both recovered single word comprehension, it has been previously observed (Selnes *et al.*, 1983, 1984; Naeser *et al.*, 1987) that infarction of ''Wernicke's area'' did not preclude recovery of single word comprehension to within the normal range, but that recovery was less likely if the lesion is large, including extension into more ventral regions of the temporal lobe and into deep white

matter. Although SS was not normal at auditory comprehension, he was able to differentiate well between heard words and nonwords (auditory lexical decision), at least when restricted to a two-way choice. EJ, with her lesion confined largely to the left STG, recovered both single word and sentence comprehension; her verbal working memory deficit is congruent with theories that identify the posterior temporal/inferior parietal junction as the site of memory transients, holding the sound structure of a heard word in short-term memory for a few seconds.

V. CONCLUSIONS

This study has demonstrated that both hemispheres are implicated in the passive processing of heard words, when compared to the processing of complex speechlike stimuli. This is supported by the evidence of right hemisphere activations in two initially aphasic patients who show some recovery of spoken single word comprehension. The evidence from previous neurolinguistic and functional imaging studies is that there is a left temporal lobe bias in explicit phoneme identification. Although both the functional and anatomical asymmetry of the posterior DLTC probably reflects specialization processing on the left, evidence from this study interpreted in the light of others identifies a right hemisphere capacity for auditory prelexical processing.

Auerbach, S. H., Allard, T., Naeser, M., Alexander, M. P., and Albert, M. L. (**1982**). ''Pure word deafness: analysis of a case with bilateral lesions and a defect at the prephonemic level,'' Brain **105**, 271–300.

Basso, A., Casati, G., and Vignolo, L. A. (**1977**). ''Phonemic identification defect in aphasia,'' Cortex **13**, 85–95.

Binder, J. R., Frost, J. A., Hammeke, T. A., Rao, S. M., and Cox, R. W. (**1996**). ''Function of the left planum temporale in auditory and linguistic processing,'' Brain **119**, 1239–1247.

Binder, J. R., Rao, S. M., Hammeke, T. A., Yetkin, F. Z., Jesmanowicz, A., Bandettini, B. S., Wong, E. C., Estkowski, L. D., Goldstein, M. D., Haughton, V. M., and Hyde, J. S. (**1994**). ''Functional magnetic resonance imaging of human auditory cortex,'' Ann. Neurol. **35**, 662–672.

Bishop D. V. M. (**1982**). *Test for the Reception of Grammar* (Medical Research Council, London).

Blumstein, S. E., Baker, E., and Goodglass, H. (**1977**). ''Phonological factors in auditory comprehension in aphasia,'' Neuropsychologia **15**, 19–30.

Bogen, J. E., and Bogen, G. M. (**1976**). ''Wernicke's region—where is it?'' Ann. (N.Y.) Acad. Sci. **280**, 834–843.

Büchel, C., Wise, R. J. S., Mummery, C. J., Poline, J. B., and Friston, K. J. (**1996**). ''Nonlinear regression in parametric activation studies,'' Neuroimage **4**, 60–66.

Buchman, A. S., Garron, D. C., Trost-Cardamone, J. E., Wichter, M. D., and Schwartz, M. (**1986**). ''Word deafness: one hundred years later,'' J. Neurol. Neurosurg. Psychiat. **49**, 489–99.

Buckner, R. L., Raichle, M. E., and Petersen, S. E. (**1995**). ''Dissociation of human prefrontal cortical areas across different speech production tasks and gender groups,'' J. Neurophysiol. **74**, 2163–2173.

Coltheart, M. (**1981**). ''The MRC Psycholinguistic Database,'' Q. J. Exp. Psychol. **33A**, 497–505.

Demonet, J. F., Price, C., Wise, R., and Frackowiak, R. S. J. (**1994**). ''A PET study of cognitive strategies in normal subjects during language tasks. Influence of phonetic ambiguity and sequence processing on phoneme monitoring,'' Brain **117**, 671–682.

Demonet, J. F., Chollet, F., Ramsay, S., Cardebat, D., Nespoulous, J. L., Wise, R., Rascol, A., and Frackowiak, R. (**1992**). ''The anatomy of phonological and semantic processing in normal subjects,'' Brain **115**, 1753–1768.

De Renzi, E., and Faglioni, P. (**1978**). ''Normative data and screening power of a shortened version of the Token Test,'' Cortex **14**, 41–49.

Desimone, R., and Gross, C. G. (**1979**). ''Visual areas in the temporal cortex of the macaque,'' Brain Res. **178**, 363–380.

Dhankhar, A., Wexler, B. E., Fulbright, R. K., Halwes, T., Blamire, A. M., and Shulman, R. G. (**1997**). ''Functional magnetic resonance imaging assessment of the human brain auditory cortex response to increasing word presentation rates,'' J. Neurophysiol. **77**, 476–483.

Fiez, J. A., Raichle, M. E., Miezin, F., and Petersen, S. E. (**1995**). ''Processing effect of stimulus characteristics and task demands,'' J. Cog. Neurosci. **7**, 357–375.

Fitch, R. H., Miller, S., and Tallal, P. (**1997**). ''Neurobiology of speech perception,'' Annu. Rev. Neurosci. **20**, 331–353.

Fox, P. T., and Mintun, M. A. (**1989**). ''Noninvasive functional brain mapping by change-distribution analysis of averaged PET images of $H_2{}^{15}O$.'' J. Nucl. Med. **30**, 141–149.

Fox, P. T., Perlmutter, J. S., and Raichle, M. E. (**1985**). ''A stereotactic method of anatomical localization for positron emission tomography,'' J. Comput. Assist. Tomogr. **9**, 141–153.

Franklin, S. (**1989**). ''Dissociations in auditory word comprehension; evidence from nine fluent aphasic patients,'' Aphasiology **3**, 189–207.

Friston, K. J., Holmes, A. P., Worsley, K. J., Poline, J. P., Frith, C. D., and Frackowiak, R. S. J. (**1995b**). ''Statistical parametric maps in functional imaging: a general linear approach,'' Human Brain. Mapping **2**, 189–210.

Friston, K. J., and Buechel, C. (**1997**). ''Neuroimaging and the non-linear brain,'' Int. J. Psychophysiol. **25**, 72.

Friston, K. J., Ashburner, J., Frith, C. D., Poline, J-B., Heather, J. D., and Frackowiak, R. S. J. (**1995a**). ''Spatial registration and normalization of images,'' Human Brain. Mapping **2**, 165–188.

Howard, D., Patterson, K., Wise, R., Brown, W. D., Friston, K., Weiller, C., and Frackowiak, R. (**1992**). ''The cortical localization of the lexicons,'' Brain **115**, 1769–1782.

Jones, E. G., and Powell, T. P. (**1970**). ''An anatomical study of converging sensory pathways within the cerebral cortex of the monkey,'' Brain **93**, 793–820.

Kay, J., Lesser, R., and Coltheart, M. (**1992**). *Psycholinguistic Assessments of Language Processing in Aphasia* (PALPA) (Erlbaum, Hove, East Sussex).

Levy, J., and Trevarthen, C. (**1977**). ''Perceptual, semantic and phonetic aspects of elementary language processes in split-brain patients,'' Brain **100**, 105–118.

Liberman, A. M., Cooper, F. S., Shankweiler, D. P., and Studdert-Kennedy, M. (**1967**). ''Perception of the speech code,'' Psychol. Rev. **74**, 431–461.

Mazziotta, J. C., Huang, S-C., Phelps, M. E., Carson, R. E., Carson, R. E., MacDonald, N. S., and Mahoney, K. (**1985**). ''A non-invasive positron computed tomography technique using oxygen-15 labelled water for the evaluation of neurobehavioral task batteries,'' J. Cereb. Blood Flow Metab. **5**, 70–78.

Miller, G. A. (**1951**). *Language and Communication* (McGraw-Hill, New York).

Naeser, M. A., Helm-Estabrooks, N., Haas, G., Auerach, S., and Srinivasan, M. (**1987**). ''Relationship between lesion extent in 'Wernicke's area' on computed tomographic scan and predicting recovery of comprehension in Wernicke's aphasia,'' Archives of Neurology **44**, 73–82.

Petersen, S. E., Fox, P. T., Posner, M. I., Mintun, M., and Raichle, M. E. (**1988**). ''Positron emission tomographic studies of the cortical anatomy of single-word processing,'' Nature (London) **331**, 585–589.

Poeppel, D., Yellin, E., Phillips, C., Roberts, T. P., Rowley, H. A., Wexler, K., and Marantz, A. (**1996**). ''Task-induced asymmetry of the auditory evoked M100 neuromagnetic field elicited by speech sounds,'' Brain Res. Cogn. Brain Res. **4**(4), 231–242.

Praamstra, P., Hagoort, P., Maasen, B., and Crul, T. (**1991**). ''Word deafness and auditory cortical function: A case history and hypothesis,'' Brain **114**, 1197–1225.

Price, C. J., Howard, D., Patterson, K., Warburton, E. A., Friston, K. J., and Frackowiak, R. S. J. (**1998**). ''A functional neuroimaging description of two deep dyslexic patients,'' J. Cog. Neurosci. **10**, 303–315.

Price, C., Wise, R., Ramsay, S., Friston, K., Howard, D., Patterson, K., and Frackowiak, R. S. J. (**1992**). ''Regional response differences within the human auditory cortex when listening to words,'' Neurosci. Lett. **146**, 179–182.

Riedel, K., and Studdert-Kennedy, M. (**1985**). ''Extending formant transitions may not improve aphasics' perception of stop consonant place of articulation,'' Brain Language **24**, 223–232.

Rosen, S. (**1992**). ''Temporal information in speech: acoustic, auditory and linguistic aspects,'' Philos. Trans. R. Soc. London, Ser. B **336**, 367–373.

Schneider, W., and Shiffrin, R. M. (**1977**). ''Controlled and automatic hu-

man information processing: I. Detection, search and attention,'' Psychol. Rev. **84**, 1–66.
Schroeder, M. R. (**1968**). ''Reference signal for signal quality studies,'' J. Acoust. Soc. Am. **44**, 1735–1736.
Selnes, O. A., Niccum, N., Knopman, D. S., and Rubens, A. B. (**1984**). ''Recovery of single word comprehension: CT-scan correlates,'' Brain Language **21**, 72–84.
Selnes, O. A., Knopman, D. S., Niccum, N., Ruens, A. B., and Larson, D. (**1983**). ''Computed tomographic scan correlates of auditory comprehension deficits in aphasia: a prospective recovery study,'' Ann. Neurol. **13**, 558–566.
Shaywitz, B. A., Shaywitz, S. E., Pugh, K. R., Constable, R. T., Skudlarski, P., Fulbright, R. K., Bronen, R. A., Fletcher, J. M., Shankweiler, D. P., Katz, I., and Gore, J. C. (**1995**). ''Sex differences in the functional organization of the brain for language,'' Nature (London) **373**, 607–609.
Shiffrin, R. M., and Schneider, W. (**1977**). ''Controlled and automatic human information processing: II. Perceptual learning, automatic attending, and a general theory,'' Psychol. Rev. **84**, 127–190.
Studdert-Kennedy, M., and Shankweiler, D. (**1970**). ''Hemispheric specialization for speech perception,'' J. Acoust. Soc. Am. **48**, 579–594.
Talaraich, P., and Tournoux, J. (**1988**). *A Stereotactic Coplanar Atlas of the Human Brain* (Thieme, Stuttgart).
Wada, J. A., Clarke, R., and Hamm, A. (**1975**). ''Cerebral hemispheric asymmetry in humans. Cortical speech zones in 100 adults and 100 infant brains,'' Archives of Neurology **32**, 239–246.
Wise, R. J. S., Greene, J., Büchel, C., and Scott, S. K. (**1999**). ''Brain regions involved in articulation,'' Lancet **353**, 1057–1061.
Wise, R., Chollet, F., Hadar, U., Friston, K., Hoffner, E., and Frackowiak, R. (**1991**). ''Distribution of cortical neural networks involved in word comprehension and word retrieval,'' Brain **114**, 1803–1817.
Wright, I. C., McGuire, P. K., Poline, J. B., Travere, J. M., Murray, R. M., Frith, C. D., Frackowiak, R. S., and Friston, K. J. (**1995**). ''A voxel-based method for the statistical analysis of gray and white matter density applied to schizophrenia,'' Neuroimage **2**(4), 244–252.
Zatorre, R. J., Evans, A. C., Meyer, E., and Gjedde, A. (**1992**). ''Lateralization of phonetic and pitch discrimination in speech processing,'' Science **256**, 846–849.
Zatorre, R. J., Meyer, E., Gjedde, A., and Evans, A. C. (**1996**). ''PET studies of phonetic processing of speech: review, replication, and reanalysis,'' Cereb. Cortex **6**, 21–30.

Acoustic evidence for dynamic formant trajectories in Australian English vowels

Catherine I. Watson[a] and Jonathan Harrington
Speech Hearing and Language Research Center, Macquarie University, Sydney 2109, Australia

(Received 19 September 1997; revised 18 September 1998; accepted 5 March 1999)

The extent to which it is necessary to model the dynamic behavior of vowel formants to enable vowel separation has been the subject of debate in recent years. To investigate this issue, a study has been made on the vowels of 132 Australian English speakers (male and female). The degree of vowel separation from the formant values at the target was contrasted to that from modeling the formant contour with discrete cosine transform coefficients. The findings are that, although it is necessary to model the formant contour to separate out the diphthongs, the formant values at the target, plus vowel duration are sufficient to separate out the monophthongs. However, further analysis revealed that there are formant contour differences which benefit the within-class separation of the tense/lax monophthong pairs. © *1999 Acoustical Society of America.* [S0001-4966(99)05706-9]

PACS numbers: 43.72.Ar, 43.70.Fq, 43.70.Hs [JH]

INTRODUCTION

In the last 50 years, many different kinds of investigations have established the first two formant center frequencies as the main determiners of vowel quality. Research into articulatory-to-acoustic modeling (Stevens, Kasowski, and Fant, 1953; Fant, 1960), studies of acoustic phonetic cues (Peterson and Barney, 1952; Ladefoged, 1967), as well as various different kinds of speech perception experiments (Delattre *et al.*, 1952; Klein, Plomp, and Pols, 1970) have all demonstrated the strong correlation between the first two formant frequencies and decreasing phonetic height and backness, respectively, thereby establishing a quadrilateral-like shape when vowel tokens are plotted in the $-F2/-F1$ plane (Essner, 1947; Joos, 1948). The formant frequencies are usually extracted at the acoustic vowel target (Lindblom, 1963; Lehiste and Peterson, 1961) which is presumed to be the section of the vowel that is least influenced by phonetic context effects: the vowel target is therefore closest in quality to the same phonetic vowel in a citation-form production in a context that is largely uninfluenced by flanking consonants.

Although the effectiveness of the first two, or possibly first three, formant frequencies in vowel separation is indisputable, it is also recognized that temporal information provides many kinds of cues to vowel quality. Some of these are very well-known. For example, the tense and lax vowels in English are acoustically long and short in duration, respectively, resulting in minimal pairs such as ''heed''/''hid'' and, in Australian English, ''dark''/''duck,'' in which the durational cues are as important as those due to formant differences. Equally, most varieties of English include diphthongs that have an early first target compared with that of monophthongs, as well as spectral transitions which either attain or (more commonly) point towards a second target (Bladon, 1985; Fox, 1983; Gay, 1970; Gottfried, Miller, and Meyer, 1993). The time at which the target occurs (relative to the vowel onset and offset) may provide another source of temporal information: some vowels may have long or short vowel onglides or offglides resulting in a considerable temporal displacement of the vowel target from the temporal midpoint (e.g., for American English, see Lehiste and Peterson, 1961; Huang, 1986; Strange, 1989b; for Australian English, see Bernard, 1981; Cox, 1996; Harrington, Fletcher, and Beckman, in press; Harrington, Cox, and Evans, 1997).

Since vowels are distinguished not only in height and backness as cued principally by formants at the vowel target, but also by various temporal features as represented by some of the time-varying cues of the kind described above, it is perhaps not surprising that a number of acoustic studies (Harrington and Cassidy, 1994; Hillenbrand *et al.*, 1995; Huang, 1992; Nearey and Assmann, 1986; Zahorian and Jagharghi, 1993) as well as various perception experiments in which spliced sections of syllables were presented to listeners for identification (e.g., Benguerel and McFadden, 1989; Jenkins, Strange, and Miranda, 1994; Strange *et al.*, 1976; Strange, Jenkins, and Johnson, 1983; Strange, 1989a), have found that vowels are suboptimally differentiated if the acoustic information is entirely based on a static spectral slice either as formants, or some other kind of parameterization at the vowel target.

Thus, acoustic classification studies in Harrington and Cassidy (1994), Hillenbrand *et al.* (1995), Huang (1992), and Zahorian and Jagharghi (1993) have all found that vowels of different quality are more effectively separated when the acoustic parameters are based on spectral information extracted at multiple time points, rather than just at the vowel target. As discussed in Harrington and Cassidy (1994), at least part of the reason for this finding is that diphthongs in particular, which are characterized by a trajectory between two targets (Bladon, 1985; Holbrook and Fairbanks, 1962), remain largely undifferentiated from those monophthongs to which their first targets are closest in quality in a single-target space. To a certain extent, the reasoning in Harrington and Cassidy (1994) is consistent with a number of studies by

[a]Electronic mail: watson@srsuna.shlrc.mq.edu.au

Nearey (Andruski and Nearey, 1992; Nearey and Assmann, 1986) which have shown that, for Canadian English at least, many vowels which might have been assumed to be monophthongal in fact exhibit a quasidiphthongal quality. Therefore, the spectral change which is observed in some of these vowels cannot just be attributed to the influence of phonetic context, but is instead a systematic property of the vowel itself, in much the same way that the movement towards a low $F1$ and high $F2$ approaching the vowel offset is an inherent feature of the diphthong /aɪ/ in Australian English, Southern British English, and no doubt many other varieties of English (Wells, 1982).

The numerous speech-perception experiments by Strange, Jenkins, and colleagues (see, e.g., Jenkins *et al.*, 1994 and Strange, 1989b for reviews of this literature) are founded on a very different interpretation of the way in which time-varying spectral information benefits vowel discrimination. Their experiments are usually based on presenting listeners with various kinds of edited speech stimuli for identification. In some of these, the syllables contain only the initial and final transitions and exclude the relatively steady-state part of the vowel; in others, listeners are asked to identify the vowel from syllables without transitions, i.e., containing only the section around the target. Most of these studies show that listeners identify vowels from the targetless (transition-only) syllables either with a very low error rate, or as well as from the original unmodified syllables (e.g., Benguerel and McFadden, 1989; Fox, 1989; Jenkins, Strange, and Edman, 1983; Nearey, 1989; Parker and Diehl, 1984; Rakerd and Verbrugge, 1987; Verbrugge and Rakerd, 1986), and there is also recent evidence (Hillenbrand and Gayvert, 1993) to show that when vowels were synthesized from the steady-state values in Peterson and Barney (1952), they were not accurately identified by listeners. At one level—which is perhaps not in dispute—Strange, Jenkins, and colleagues (henceforth SJ) conclude that there must be considerable information contained in the vowel transitions (perhaps as much, if not more than at the target) for vowel identification to be possible despite the fact that the section of the vowel which is usually assumed to contain the most important information—i.e., the vowel target—has been discarded. At another level, which is certainly more controversial, SJ attribute listeners' identifications of vowels from targetless syllables to the theory that vowel perception is made with reference to dynamic articulatory information which is predominantly encoded in the syllable's transitions (e.g., Fowler, 1987, and Strange, 1987). This idea is, in turn, based on the earlier action theory framework of speech production as developed by Fowler and colleagues (Fowler, 1980, 1983, 1986; Fowler and Rosenblum, 1989), and on the more recent task-dynamic model of speech production (Browman and Goldstein, 1992; Saltzman and Munhall, 1989) which SJ believe to be ''on the right track'' from the point of view of our understanding of how listeners decode segments phonetically from the acoustic speech signal (Jenkins *et al.*, 1994).

There are, however, at least two major unresolved issues that arise from the body of research on vowel dynamics carried out by SJ in the last 20 years. First, although SJ relate the results of their perception experiments to the existence of articulatory-dynamic features that are coded in the acoustic signal and that are primary in listeners' identification of vowels, the exact nature of these cues remains elusive: as Jenkins *et al.* (1994) state, the acoustic phonetic attributes of a vowel may be represented by a multitude of targets, rather than two, three, or four targets—which essentially implies that it is the whole dynamic spectral trajectory, rather than any number of static targets, which cues the vowel. Second—and this is closely related to the first point—it has not been established how much of the dynamic spectral change is relevant to vowel identification and what proportion is attributable to other factors: as Jenkins *et al.* (1994) acknowledge, numerous studies over the last 50 years have shown that a good deal of spectral change is caused by context effects that might *complicate*, rather than enhance, the relationship between the acoustic signal and the vowel class.

The research methodology for the present investigation is closely based on Harrington and Cassidy (1994) and is similar to other investigations (e.g., Huang, 1986, and Zahorian and Jagharghi, 1993) which seek to determine the extent to which the dynamic aspects of the vowel's acoustic signal contribute to its identification beyond the ''static'' information which is available at the vowel target. Essentially, the aim of this research is to begin to find answers to the following question: if two classification algorithms are applied to the same body of acoustic vowel data, such that the first is based on vowel-target information alone and the second on both vowel-target and dynamic information throughout the vowel's time course, to what extent are vowels more effectively separated in the second space compared with the first? This is the approach taken in Harrington and Cassidy (1994), but in contrast to that study, the present one is based on a larger group of talkers (62 male, 70 female) and a different dynamic classification algorithm. In Harrington and Cassidy (1994), the contribution of dynamic information to vowel separation beyond that encoded at the target was estimated by comparing classification scores obtained from three time slices in the vowel with those from a single time slice at the midpoint using either a Gaussian model or a time-delay (recurrent) neural network to classify the vowels. The general conclusion from that study was that, since only diphthongs but not monophthongs were more effectively separated in the classifications from three time slices compared with one, the results were more consistent with a target theory of vowel distinction than the dynamic theory proposed by SJ. Part of the aims of the present study is to reassess this interpretation by classifying a large number of vowels using an algorithm that represents the dynamic behavior of the formants with a discrete cosine series. The advantage of this approach over that taken in Harrington and Cassidy (1994) is twofold: first, it does not require the extraction of spectral information at a number of arbitrary time points; second, the parameters from the discrete cosine series are considerably less correlated with each other than those obtained by merely sampling the formant tracks. The second aim of the paper is to try to define more precisely the nature of the dynamic information that characterizes some (or all) vowels when classifications from the dynamic algorithm show superior scores compared with single-target classifications. Finally, we consider the ad-

equacy of the discrete cosine series as an algorithm for representing dynamic changes in the vowel's spectral shape.

I. EXPERIMENT 1

There are two aims in this experiment. The first is to assess the adequacy of classifying vowels (diphthongs and monophthongs) from target information plus total vowel duration alone. This assessment is made by comparing the results of a classification from the target-only space with a dynamic space formed from the discrete cosine transformation (DCT) applied to the formant trajectories. If there is information for vowel separation beyond that which is represented at the vowel target, then the separation between the vowels should be greater in DCT space.

The second part is an investigation into whether modeling the formant contour might benefit the within-class separation of the monophthongs. Once again, we will compare the results of a classification from a target-only space to a dynamic space formed by modeling the formant trajectories with DCT coefficients. To neutralize as far as possible the obvious contribution from acoustic vowel duration differences, this parameter is excluded in the classifications.

A. Method

1. Talkers

The vowels that were analyzed were taken from the isolated word materials collected under the Australian National Database of Spoken Language (ANDOSL) (Millar, Harrington, and Vonwiller, in press; Millar *et al.*, 1994; Vonwiller *et al.*, 1995). In selecting the talkers for ANDOSL, an attempt was made to cover three age ranges (18–30, 31–45, 46+ yrs) and also to select Australian English talkers from the main accent types that form a continuum from *cultivated* to *broad*, where cultivated bears the closest resemblance to British English received pronunciation (RP) and broad is identified as the most characteristically ''Australian'' accent and shares some characteristics with London Cockney English (Cochrane, 1989; Horvath, 1985). *General* Australian is the third recognized major accent type and falls between these two categories on this continuum (Blair, 1993; Horvath, 1985). This accent variation is determined primarily by socioeconomic factors, and there is scarcely any regional accent variation in Australia. (See Cox, 1996; Bernard, 1967; and Harrington *et al.*, 1997 for acoustic phonetic analyses of Australian English vowels and Harrington and Cassidy, 1994 for a comparison with RP vowels.) The talkers were also balanced for gender. A total of 266 talkers were recorded as part of the ANDOSL project, of which 140 subjects were nonaccented native speakers of Australian English, born in Australia, and with the exception of three subjects, of Anglo/Celtic origin (Vonwiller *et al.*, 1995). Six of these talkers did not complete the recording sessions for the list of single-word utterances, leaving 134 subjects who participated in the isolated word task. Two further subjects were removed from consideration because exceptionally, they produced rhotic vowels (Australian is nonrhotic). The present study is concerned with the isolated-word productions from the remaining 132 talkers.

The differences between the three accent types, although perceptible, are minor compared with the extent of accent variation found in American English. The acoustic phonetic studies by Bernard (1970), Cox (1998), Harrington *et al.* (1997), and Watson, Harrington, and Evans (1998) of Australian English vowels all show that the differences in vowel quality are confined primarily to the duration of the onglide in the tense high vowels (most extensive for ''broad''), a raised $F2$ in broad /u/ (as in WHO'D) which may be due either to less lip-rounding and/or more tongue-fronting, and various first target differences in the rising diphthongs /aɪ aʊ eɪ/ (as in HIGH, HOW, and HAY, respectively). However, even these accent differences are generally not sufficient to substantially increase the overlap between different vowel categories. This was substantiated by a pilot study in which we carried out many of the classifications to be reported in this paper on the data from the male general talkers alone: the classification scores never showed any significantly greater overlap between the vowel categories than from the same classification applied to the male talkers' vowels pooled across the three accent categories. We repeated this study for the female talkers and got exactly the same results.

2. Materials

As described in Millar *et al.* (in press), and Vonwiller *et al.* (1995), the ANDOSL talkers read citation-form productions of 25 different words. For the present paper, we selected the words from an /hVd/ or /hV/ context. In addition, we also selected HOIST and TOUR words to include the /ɔɪ ʊə/ diphthong nuclei, neither of which occurred in the /hV/ or /hVd/ context. This gave us 19 words in total.

All of the word tokens were labeled phonetically at the Speech Hearing and Language Research Center, Macquarie University, using the procedures described below and in Croot, Fletcher, and Harrington (1992). Any words that were incorrectly produced (e.g., /hæd/ for HARD) were removed from consideration; we also rejected all TOUR words which had been produced with a monophthongal /ɔ/ nucleus (as in HOARD). The final distribution of the words used in this study, together with their (phonological) subcategorisations *tense monophthong*, *lax monophthong*, *rising diphthong*, and *falling diphthong* used in this paper, are shown in Table I.

3. Recording, digitization, labeling

The subjects were all recorded in an anechoic environment at the National Acoustics Laboratories, Sydney. The material was recorded in a single session, and, for the isolated word lists, was presented to the subjects on a computer screen one word at a time to avoid list intonation (see Millar *et al.*, in press, for further details). The speech data was digitized at 20 000 Hz with a 16-bit resolution and the first three formant center frequencies and their bandwidths were automatically tracked in ESPS/Waves (the settings were 12th-order linear predictive coding analysis, cosine window, 49-ms frame size, and 5-ms frame shift).

All automatically tracked formants were checked for accuracy, and hand corrections were made when considered necessary. Formant tracking errors were especially common

TABLE I. The list of vowels used in the study, the words from which they were extracted, and the number of vowel tokens from the female speakers and male speakers, respectively.

Tense monophthongs				Lax monophthongs			
		Number of tokens				Number of tokens	
Word	Phoneme	Female	Male	Word	Phoneme	Female	Male
HEED	i	70	62	HID	I	70	62
WHO'D	u	69	62	HOOD	ʊ	70	62
HOARD	ɔ	70	61	HOD	ɒ	69	62
HARD	a	68	62	HUD	ʌ	70	62
HEARD	ɜ	68	62	HEAD	ɛ	69	62
				HAD	æ	70	62
Rising diphthongs				Falling diphthongs			
		Number of tokens				Number of tokens	
Word	Phoneme	Female	Male	Word	Phoneme	Female	Male
HAY	eɪ	70	62	HEAR	ɪə	70	60
HOE	oʊ	70	62	HAIR	ɛə	70	61
HOIST	ɔɪ	70	62	TOUR	ʊə	63	48
HIDE	aɪ	70	62				
HOW	aʊ	70	62				

in vowels which have $F1$ and $F2$ close together (i.e., back-rounded vowels such as HOARD) but also in some high-front vowels when $F2$ and $F3$ merged. Occasionally, a formant that was very low in amplitude might not have been tracked (e.g., $F3$ in high-back vowels) and for a few very high-pitched voices, the fundamental was sometimes mistracked as $F1$. Predictably, many more errors occurred for the female data than for the male data. Approximately one-third of all the vowels required some hand correction, and this was done by redrawing the formant tracks by hand using either the Waves or EMU (Harrington and Cassidy, in press) tools, occasionally after recalculating the spectrogram with different fast Fourier transform (FFT) sizes to allow a closer examination of some of the harmonics in relation to the tracked formants.

The acoustic onset of the vowel was marked at the onset of voicing as shown by strong vertical striations in the spectrogram, and by the onset of periodicity in the waveform. The acoustic offset of the vowel in the /hVd/ context was marked at the closure of the [d] corresponding to a cessation of regular periodicity for the vowel and/or a substantial decrease in the amplitude of the waveform. The acoustic vowel target was marked as a single time point between the acoustic onset and offset according to the criteria (see, also, Harrington *et al.*, 1997). For high- and mid-front vowels, the target was marked where $F2$ reached a peak; for mid- and high-back vowels, the target was marked where $F2$ reached a trough; for open vowels, the target was marked at the $F1$ peak. When there was no evidence for a target based on formant movement (this could happen especially in central vowels), then other acoustic criteria were used such as the time at which the amplitude reached its maximum value. If there was no acoustic evidence of any kind for a target—which implies neither formant nor amplitude change between the acoustic onset and offset of the vowel—the target was marked at the vowel's temporal midpoint. In rising diphthongs, two targets were marked using the same sets of criteria as for the monophthongs; however, only the first target was used in this study. For the three falling diphthongs, only the first target could be reliably marked at the $F2$ maximum (HERE, HAIR), or the $F2$ minimum (TOUR).

Figure 1 shows the averaged trajectories for the first three formants for each vowel class from the male data. The tokens were time aligned at the vowel target (first target for diphthongs) and averaged separately in each vowel class.

4. The discrete cosine transformation

Similar to Zahorian and Jagharghi (1993), we represented the time-varying nature of the formant trajectories by modeling the trajectories with coefficients of the discrete cosine transform (DCT). The cosine basis function we used to model the trajectories was

$$C(m)\cos(\theta), \tag{1}$$

where $C(m)$ is the amplitude of the mth cosine and θ is related to the number of sample points in a trajectory. The amplitudes of the cosines, $C(m)$, are the output of a DCT. There are several ways the DCT can be expressed (Rao and Yip, 1990): the form chosen was

$$C(m)=\frac{2}{N}k_m\sum_{n=0}^{N-1}x(n)\cos\left(\frac{(2n+1)(m-1)\pi}{2N}\right)$$
$$m=1,...,N, \tag{2}$$

where $x(n)$, $n-0,...,N-1$ is the trajectory of the feature being modeled, N is the number of points in the trajectory, $C(m)$ denotes the mth DCT coefficient, and k_m is $1/\sqrt{2}$ when $m=1$, and is 1 when $m\neq 1$.

Figure 2 shows the second formant frequency trajectories for /i/ (from HEED) and /a/ (from HARD) and their decomposition into the first three cosines of the basis function [see Eq. (1)]. The first cosine is a straight line (the dc offset) at a value proportional to the mean of the original

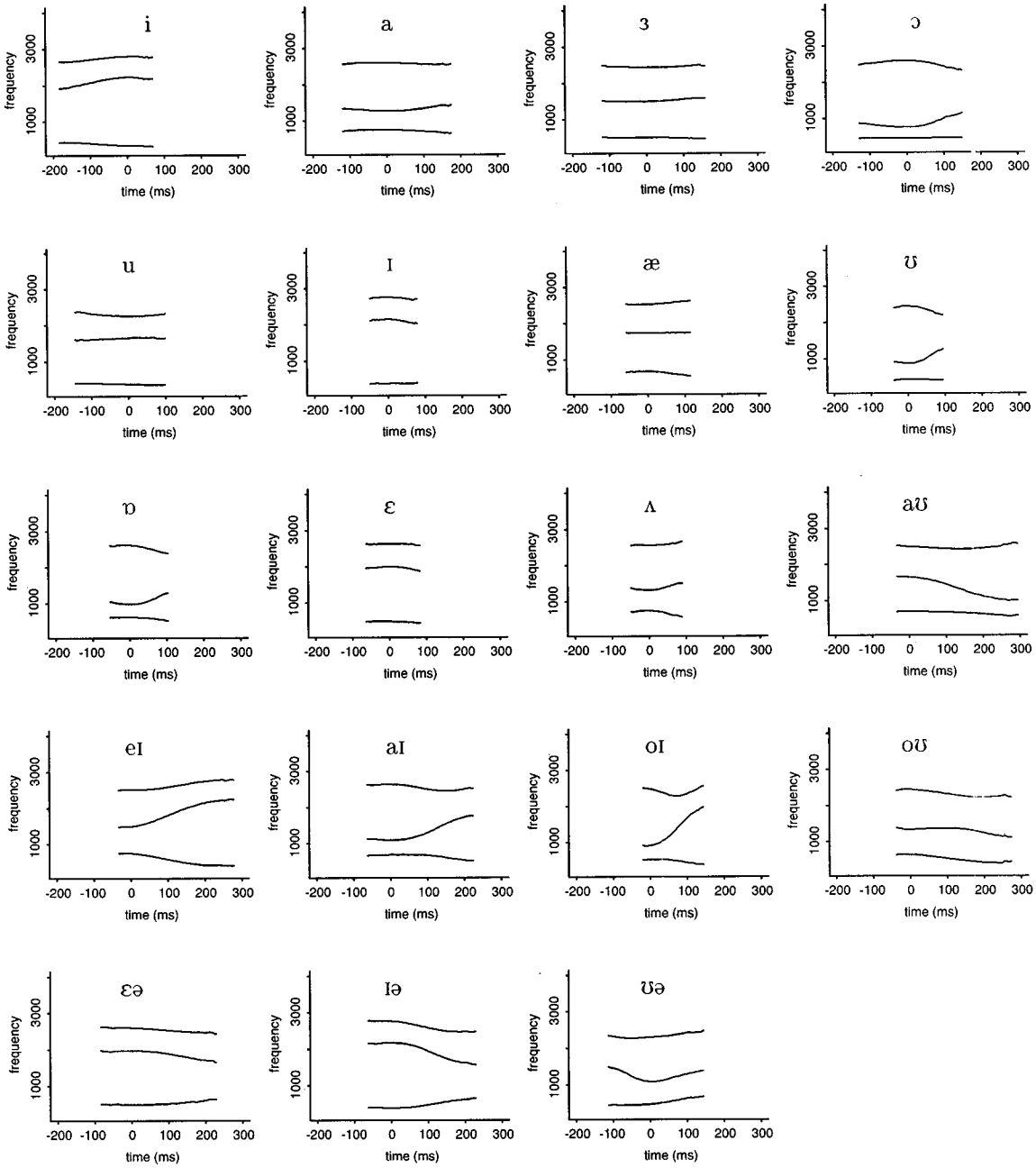

FIG. 1. The averaged formant trajectories for the first three formants for each vowel class from the male data, aligned at the target for the monophthongs and the first target for the diphthongs. The averaged formant trajectories were truncated at the left/right edges at the average durations from the vowel target to the vowel onset/offset. For each vowel, the target is positioned at 0 ms.

formant trajectory calculated between the formant onset and offset. The second basis function is a half-cycle cosine wave which models both the direction and the magnitude of tilt of the formant trajectory's tilt. The third basis function, which is a whole-cycle cosine wave, is a measure of the trajectory's curvature. Consider, for example, the $F2$ trajectory of a high-front vowel in a flanking labial context. In this case, the curvature would be extreme because the trajectory has to span the divergent low $F2$ labial loci and the high $F2$ target. By contrast, a mid-front vowel in a flanking alveolar context would have a much lower value on this parameter because the consonant loci and $F2$ target values are very similar (resulting in an almost straight-line trajectory).

We performed an initial pilot study to decide which DCT coefficients we should use to encode the formant trajectories. We considered the female and male data separately. The results of this study (Table II) give the percentage of vowels correctly identified in vowel classification experiments when the first three formant trajectories were encoded with different combinations of the first three coefficients of the DCT. From these results, we concluded that the first and second DCT coefficients played significant roles in separating the vowels, whereas the third coefficient did not. The total number of vowels correctly classified using the first two coefficients to encode the formant trajectories was significantly greater than using the first and third coefficients, the second and third coefficients, and the first coefficient only ($\alpha \ll 0.002$; the significance levels were Bonferroni-corrected

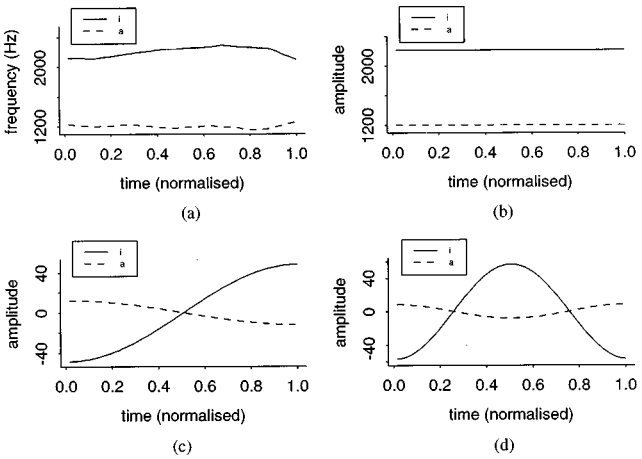

FIG. 2. The F_2 trajectory of an /i/ token and an /a/ token and their representation from the first three elements in the cosine basis function.

to reduce the probability of a type I error due to multiple testing). Further, there was no significant different in the vowel classification scores from the first two DCT coefficients and the first three DCT coefficients. We repeated the test for the monophthong vowels only and got exactly the same findings. For these reasons, we decided to represent each formant trajectory with the first two discrete cosine transformation (DCT) coefficients (a six-parameter space). This is in contrast to earlier studies (e.g., Zahorian and Jagharghi, 1993) where the first three DCT coefficients were used.

Further support for using just the first two DCT coefficients to model the Australian English formant trajectories can be seen in Fig. 1. The trajectories are not complex shapes, and the most distinguishing features are the mean values of the formants and the slope of the formant trajectories. The means cannot by themselves function to distinguish some tense from lax vowels (e.g., /a/ from /ʌ/), nor monophthongs from diphthongs that have similar formant values at the first target (e.g., /a/ from /aI/). Neither is the discriminating power of the slope (the second DCT coefficient) sufficient by itself because most monophthongs have similar slopes but different means.

5. Classification procedure

All results reported in this paper were obtained using a Gaussian classification technique. In Gaussian classification, the centroid and covariance matrix of the training set are estimated for each vowel class. Tokens from the test set are then classified based on their Bayesian distances to each of the class centroids.

A ''round-robin'' procedure was used to train and test the classifier. In this procedure, all the tokens for a single speaker were used as a test set and the remaining speakers' tokens formed the training set. This was repeated for all the speakers in turn, and the overall classification score was the summation of the individual results.

In the experiment, vowel-classification scores from two sets of parameters were compared with each other. In the first part of the experiment, the first set was formed from a four-dimensional space that included $F1-F3$ at the vowel target and acoustic vowel duration. The second set was formed from a seven-dimensional space that included the first two DCT coefficients of $F1-F3$ and acoustic vowel duration.

The results of the target and DCT analyses were compared using a *t*-test on data broken down on a per-speaker basis. On a vowel-by-vowel basis, all the significance levels were Bonferroni-corrected to reduce the probability of a type I error due to multiple testing. For the complete vowel set (19 in total), only the variables with $p<0.003$ are significantly different at an experiment-wide significance level of $p<0.05$. For the monophthong set (11 vowels in total), only the variables with $p<0.005$ are significantly different at an experiment-wide significance level of $p<0.05$. The female and male data were compared separately to avoid any confounding influences due to vowel normalization effects. In general, when a significant difference between two methods was identified for the female data, it was also identified in the male data (or vice versa); therefore, significant differences reported below are applicable to both the male and female data unless stated otherwise.

TABLE II. The percentage of vowels correctly identified in vowel-classification experiments when the first three formant trajectories were encoded with different combinations of the first three coefficients of the DCT.

	All vowels		Monophthongs	
Parameter set	Female	Male	Female	Male
$C(1)$	53.3	52.7	72.3	75.5
$C(1),C(2)$	84.0	86.2	81.8	85.5
$C(1),C(3)$	68.6	68.0	73.1	76.8
$C(2),C(3)$	65.2	65.1	59.4	57.1
$C(1),C(2),C(3)$	84.2	85.6	81.1	85.4

B. Results

Table III shows the results of classifications from formants at the vowel target (henceforth, *target analysis*) and vowel duration and those from the DCT coefficients (henceforth, DCT *analysis*) and vowel duration. The table shows that the total number of correctly classified vowels was significantly higher in the DCT analysis than in the target analysis. On a vowel-by-vowel basis, it is predominantly the diphthongs that had a significantly greater separation in the DCT analysis than in the target analysis. This suggests that rather than all vowels being dynamic, it is the diphthongs that are best described using a dynamic method of analysis.

Some support for this view is provided by the results in Table IV, in which the same two classification experiments were carried out again, but this time by training and testing only on the (so-called) monophthongs (see Table I). In this case, the results show first very high classification scores for both the target analysis and the DCT analysis, and, in clear contrast to the experiment in which training and testing was carried out on all 19 vowel types, no significant differences between the two analyses on a vowel-by-vowel basis.

When total vowel duration was excluded as a parameter in the classification, there was still no significant difference in the classification scores for many of the monophthongs in

TABLE III. The classification scores (percent correctly classified) from the target analysis (*left column*) and from the DCT analysis (*right column*) for the male and female talkers after training and testing on the first three formant frequencies and total vowel duration. All the *p* values are given and significant differences are shown by **. Note on a vowel-by-vowel basis, the Bonferroni correction was applied ($\alpha<0.003$).

Female				Male			
	Target & duration	DCT coef. & duration	*p*		Target & duration	DCT coef. & duration	*p*
æ	87.1	91.4	0.08	æ	95.2	93.5	0.6
ɛ	68.1	56.5	0.03	ɛ	91.9	85.5	0.1
ɪ	82.9	84.3	0.7	ɪ	85.5	95.2	0.01
ɒ	79.7	89.9	0.007	ɒ	80.6	98.4	0.002**
ʊ	82.9	94.3	0.01	ʊ	91.8	96.7	0.2
ʌ	95.7	90.0	0.1	ʌ	98.4	96.8	0.3
ɜ	88.2	92.6	0.3	ɜ	88.7	95.2	0.1
a	60.3	95.6	<0.003**	a	75.8	98.4	<0.003**
i	72.9	95.7	<0.003**	i	69.4	100.0	<0.003**
ɔ	97.1	98.6	0.3	ɔ	96.7	95.1	0.6
u	84.1	88.4	0.2	u	87.1	96.8	0.01
eɪ	40.0	98.6	<0.003**	eɪ	56.5	100.0	<0.003**
ɔɪ	48.6	100.0	<0.003**	ɔɪ	64.5	98.4	<0.003**
aɪ	66.7	100.0	<0.003**	aɪ	82.3	91.9	0.08
aʊ	31.4	95.7	<0.003**	aʊ	41.9	96.8	<0.003**
oʊ	70.0	94.3	<0.003**	oʊ	37.1	90.3	<0.003**
ɪə	34.3	78.6	<0.003**	ɪə	60.0	78.3	0.02
ɛə	80.0	70.0	0.05	ɛə	85.2	88.5	0.5
ʊə	90.5	95.2	0.2	ʊə	89.6	95.8	0.3
all	71.5	90.0	<0.05**	all	77.7	94.3	<0.05**

the target analysis compared with the DCT analysis. However, as Table V shows, four vowels that form two tense/lax pairs in Australian English (/i,ɪ/ and /a,ʌ/) were more effectively separated in the DCT analysis, which suggests that there may be some differences in the shapes of the formant trajectories that contribute to their separation.

C. Discussion

The object of the first part of the experiment has been to assess how effectively vowels were separated when they are classified from a ''static'' section at the vowel target (the target analysis) and from ''dynamic'' information which was represented by discrete cosine coefficients (the DCT analysis). Consistent with Harrington and Cassidy (1994), the results of the classifications suggest that only those vowels that have traditionally been labeled ''diphthongs'' benefited significantly from the additional information which is encoded in the dynamic analysis. If those vowels that are traditionally labeled ''monophthongs'' were inherently dynamic, we would expect higher classification scores in the DCT analysis than when training and testing are carried out on these vowels alone. In summary, the results given in Tables III and IV are so far entirely compatible with a target theory of vowels: the information for monophthong identification is encoded at the vowel target, while diphthong identification requires information from more than one static spectral section.

Table V, however, suggests it would be premature to conclude that the formant trajectory shapes of monophthongs contain no useful information for the separation of /i,I/ and

TABLE IV. The classification scores (percent correctly classified) from the target analysis (*left column*) and from the DCT analysis (*right column*) for the male and female talkers following training and testing on the first three formant frequencies and total vowel duration of the monophthongs only. All the *p* values are given and significant differences are shown by **. Note on a vowel-by-vowel basis, the Bonferroni correction was applied ($\alpha<0.005$).

Female				Male			
	Target & duration	DCT coef. & duration	*p*		Target & duration	DCT coef. & duration	*p*
æ	91.4	92.9	0.3	æ	96.8	93.5	0.2
ɛ	58.1	56.5	0.03	ɛ	91.9	87.1	0.2
ɪ	82.9	84.3	0.7	ɪ	85.5	95.2	0.01
ɒ	91.3	89.9	0.3	ɒ	96.8	100	0.2
ʊ	95.7	94.3	0.6	ʊ	95.1	96.7	0.6
ʌ	97.1	91.4	0.04	ʌ	98.4	98.4	1.0
ɜ	92.6	92.6	1.0	ɜ	91.9	95.2	0.3
a	97.1	98.5	0.3	a	98.4	98.4	1.0
i	92.9	97.1	0.2	i	96.4	100.0	0.2
ɔ	98.6	98.6	1.0	ɔ	98.4	98.4	1.0
u	87.0	88.4	0.7	u	90.3	96.9	0.04
all	90.4	89.5	0.3	all	94.6	96.3	0.03**

TABLE V. The classification scores (percent correctly classified) from the target analysis (*left column*) and from the DCT analysis (*right column*) for the male and female talkers following training and testing on the first three formants of the monophthongs excluding total vowel duration. All the *p* values have been given and significant differences are shown by **. Note on a vowel-by-vowel basis, the Bonferroni correction was applied (α<0.005).

Female				Male			
	Target	DCT coef.	*p*		Target	DCT coef.	*p*
æ	90.0	90.0	1.0	æ	90.3	88.7	0.6
ɛ	52.2	58.0	0.3	ɛ	88.7	80.6	0.1
ɪ	55.7	82.9	<0.005**	ɪ	59.7	90.3	<0.005**
ɒ	91.3	94.2	0.3	ɒ	91.9	90.3	0.6
ʊ	72.9	74.3	0.8	ʊ	83.6	86.9	0.4
ʌ	62.9	80.0	0.02	ʌ	66.1	64.5	0.8
ɜ	88.2	89.7	0.7	ɜ	91.9	96.8	0.2
a	45.6	67.6	<0.005**	a	40.3	77.4	<0.005**
i	68.6	92.9	<0.005**	i	66.1	93.5	<0.005**
ɔ	82.9	87.1	0.4	ɔ	85.2	88.5	0.5
u	76.8	82.6	0.5	u	85.2	90.3	0.3
all	71.8	81.8	<0.05**	all	77.2	86.7	<0.05**

/a,ʌ/. Many researchers have shown that there are clear time-varying differences in the formants of monophthong tense–lax pairs which may contribute to their separation beyond total vowel-duration differences. It is also known that Australian tense high vowels can be produced with delayed targets that may serve to distinguish them from their lax counterparts.

Figure 3, which shows averaged time-normalized formant trajectories for these vowel pairs for both male and female talkers, suggests that these tense/lax vowel pairs may differ in the time at which the target occurs relative to the vowel onset and offset. Also shown in Fig. 3 are formant trajectories for /ɔ/ and /ʊ/ because, although Table V shows no significant differences for these vowels in the two types of classification, a closer examination of the confusion matrices pointed to fewer confusions between these vowel pairs in the DCT analysis than in the target analysis. For all three vowel pairs shown in Fig. 3, the relative time at which the vowel target occurs is delayed for the long tense vowels /i,a,ɔ/ compared with the corresponding short vowels that are similar in quality. This suggests that the time of the target is different for these tense/lax pairs: consequently, the shape of the formant contours may be different even though the respective onset, target, and offset formant values for the tense/lax pairs are quite similar. Therefore, the time of the target provides some contributory information to the distinction between such vowels, which results in a more effective separation between them in the DCT analysis compared with the target analysis.

Further evidence to support this view is shown in Table

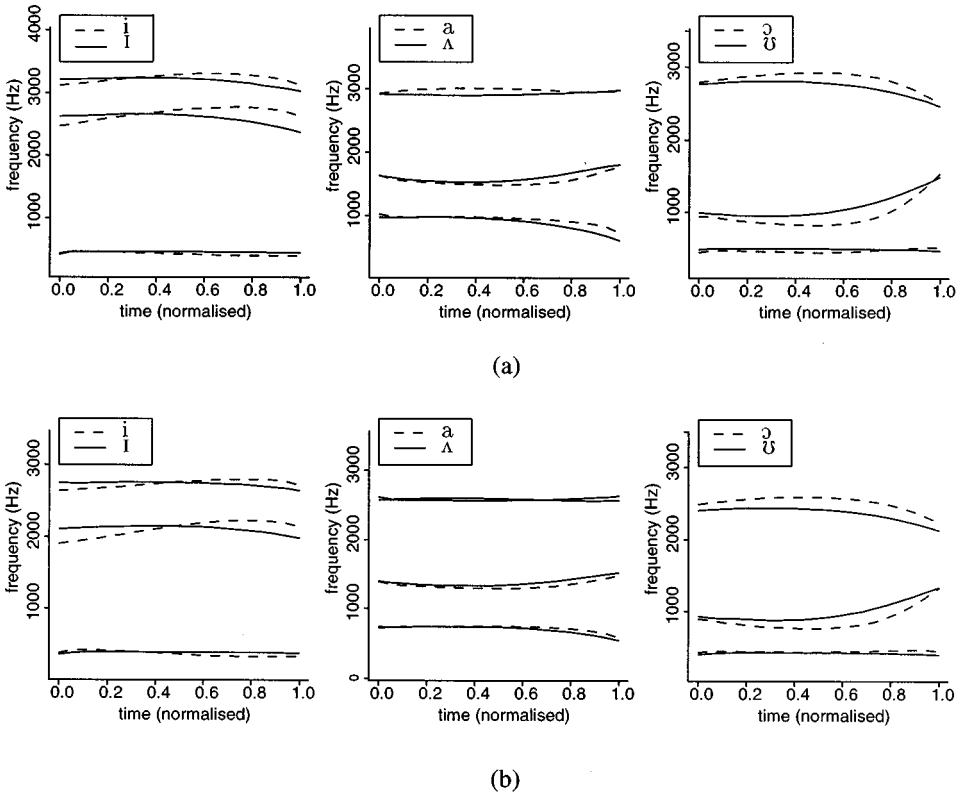

FIG. 3. Averaged time-normalized tracks of the first, second, and third formants for the tense/lax pairs /i,ɪ/, /a,ʌ/, and /ɔ,ʊ/ from (a) the female data, and (b) the male data.

TABLE VI. The mean and standard deviation for the target position (the ratio of the time between the vowel onset and the target, to the total vowel duration) for the tense/lax pairs from the female and male data.

	Female			Male	
	Mean	Standard deviation		Mean	Standard deviation
i	0.690	0.129	i	0.736	0.087
ɪ	0.357	0.107	ɪ	0.401	0.108
a	0.424	0.124	a	0.421	0.123
ʌ	0.343	0.088	ʌ	0.383	0.101
ɔ	0.484	0.087	ɔ	0.466	0.107
ʊ	0.312	0.077	ʊ	0.316	0.065

VI, which lists the mean and standard deviation of the time at which the target occurs relative to the acoustic vowel boundaries (therefore, a mean value of 0.5 would indicate the target occurs, on average, at the acoustic vowel midpoint). These data show that the lax vowels /ɪ,ʌ,ʊ/ had earlier target times (i.e., shorter onglides) than the tense vowels /i,a,ɔ/, respectively. These differences are significant for all the tense/lax pairs in the female data, and the /i,ɪ/ and /ɔ,ʊ/ tense/lax pairs in the male data ($\alpha \ll 0.003$, the significance level was Bonferroni-corrected).

II. SUMMARY

The experiments in this study of a large corpus of Australian English vowels produced by 132 male and female talkers have shown that vowels differ in the extent and nature of dynamic information which contributes to their identification. First, many vowels, which are traditionally labeled monophthongal were as adequately classified from a static section at the vowel target as from time-varying formant information that was represented by the discrete cosine transformation on the formant frequencies. Second, Australian English vowels that are traditionally labeled diphthongal were more accurately identified in the DCT space that encodes time-varying formant information than from a single static section at the target. As discussed in Harrington and Cassidy (1994), this is because these vowels are defined by at least two targets which are inadequately represented in a single-target space. Thirdly, some tense vowels traditionally labeled as monophthongs had proportionally delayed targets compared with those of their lax counterparts.

For some researchers, a dynamic theory of vowel identification and perception has been advocated which is presumed to be in opposition to a theory of classifying vowels from targets (a target classification is often assumed to be static). For example, this opposition between dynamic and static target is clearly stated by Hillenbrand *et al.* (1995), who comments that ''static spectral targets are neither necessary nor sufficient for accurate vowel recognition.'' Although we agree that time-varying information is often very important in vowel identification, we do not believe that this need imply that targets are irrelevant. As the results from our paper show, the target times of vowels can vary, and for tense/lax pairs this can be measured by different rates of spectral change. This variation in the target time is one of the ways in which vowels are dynamic. Another is that some vowels have two targets. And yet another is that there are durational differences between tense/lax vowels. These are all important sources of dynamic variation, but none of them by themselves, or together, implies that the concept of a target is not relevant to vowel identification (see, also, Harrington and Cassidy, 1994). In summary, although there is clear evidence for the presence of dynamic information that benefits vowel identification, the results of this study are entirely compatible with a target theory of vowel identification.

TABLE VII. The classification results for separating monophthongs and diphthongs using DCT analysis and vowel duration, and DCT analysis only. Significant differences are shown by ** ($\alpha < 0.01$).

	Female		
	DCT coef. & duration	DCT coef.	*p*
Monophthongs	98.3	98.3	1.0
Diphthongs	88.8	84.8	<0.01**
All	94.3	92.6	<0.01**
	Male		
	DCT coef. & duration	DCT coef.	*p*
Monophthongs	97.5	97.5	1.0
Diphthongs	87.1	83.7	<0.01**
All	93.2	91.8	<0.01**

This study has also shown that the first two coefficients of the discrete cosine transformation, which model the mean and the slope of the formant trajectory, not only effectively distinguish between the citation-form vowels produced by multiple talkers in a very similar consonantal context (mostly /hVd/ and /hV/), but also encode the dynamic information in diphthongs and in monophthong tense/lax pairs that differ in the relative timing of the vowel target. Another advantage in using a DCT analysis on the formants is that vowels can be effectively separated without the need to mark explicitly one or more vowel targets, which can be complicated when a vowel appears either not to have a steady-state section, or if the formants reach a minima or maxima at different times.

One final application for the DCT analysis is in monophthong/diphthong distinction. There was a good separation between the monophthongs and diphthongs in the DCT analysis in experiment 1 (in contrast to the target analysis). Exploiting this knowledge, we relabeled all the vowels as either monophthong or diphthong and repeated the DCT analysis as outlined in experiment 1. It can be seen from Table VII (the classification scores from DCT analysis including vowel duration) that most of the vowels were correctly identified; that is, either as monophthong or diphthong. We repeated the above analysis without including vowel duration as a parameter in order to be certain that the monophthong/diphthong distinction was primarily due to differences in the shapes of the formant contours. These results are also given in Table VII, where it can be seen that, although the total number of vowels and diphthongs correctly classified were significantly less when vowel duration was not included with the DCT analysis, all the classification rates were still very high.

Finally, it must be emphasized that, although the present corpus included all the phonemic vowels of Australian English from a large number of male and female talkers, these were all restricted to a very similar consonantal context (mostly /hVd/ and /hV/), and it is certain that other forms of dynamic vowel changes would be introduced by considering a wider range of contexts beyond those considered here. However, this need not imply that it is necessary to abandon the model that the salient information for vowel identification can be represented by one or two targets which may be variably timed relative to the vowel onset and offset. We envisage, for example, that the additional complexity introduced by variable coarticulatory influences could be modeled using a second-order differential equation that relates consonantal loci, rate of formant change, and position of the vowel target (e.g., Moon and Lindblom, 1994), together with a phase specification for timing the separate transitions towards, and away from, a vowel target, as suggested by much of the task-dynamic literature (e.g., Browman and Goldstein, 1992; Saltzman and Munhall, 1989). These issues, as well as the effectiveness of the DCT coefficients in separating vowels in multiple contexts in a similarly large acoustic speech corpus, are currently being investigated.

ACKNOWLEDGMENTS

The authors thank Steve Cassidy, Felicity Cox, Zoe Evans, William Thorpe, and in particular Sallyanne Palethorpe, James Hillenbrand, and Terry Nearey for their help and suggestions. This research was supported by an Australian Research Council large grant.

Andruski, J. E., and Nearey, T. M. (**1992**). ''On the sufficiency of compound target specification of isolated vowels in /bVb/ syllables,'' J. Acoust. Soc. Am. **91**, 390–410.

Benguerel, A.-P., and McFadden, T. U. (**1989**). ''The effect of coarticulation on the role of transitions in vowel perception,'' Phonetica **46**, 80–96.

Bernard, J. R. L. (**1967**). ''Some measurements of some sounds of Australian English.'' Unpublished doctoral dissertation, Sydney University.

Bernard, J. R. L. (**1970**). ''Towards the acoustic specification of Australian English,'' Zeitschrift fur Phonetik **2/3**, 113–128.

Bernard, J. R. L. (**1981**). ''Australian pronunciation,'' in *The Macquarie Dictionary*, edited by A. Delbridge (Macquarie Library, Sydney), pp. 18–27.

Bladon, R. A. W. (**1985**). ''Diphthongs: a case study of dynamic auditory processing,'' Speech Commun. **4**, 145–154.

Blair, D. (**1993**). ''Australian English and Australian national identity,'' in *The Languages of Australia* (Australian Academy of the Humanities, Canberra), Vol. 14, pp. 62–70.

Browman, C. P., and Goldstein, L. (**1992**). ''Articulatory phonology: an overview,'' Phonetica **49**, 155–180.

Cochrane, G. R. (**1989**). ''Origins and development of the Australian accent,'' in *Australian English: The Language of a New Society*, edited by D. Blair and P. Collins (University of Queensland Press, St. Lucia), pp. 176–186.

Cox, F. M. (**1996**). ''An acoustic study of vowel variation in Australian English.'' Unpublished doctoral dissertation, Macquarie University.

Cox, F. M. (**1998**). ''The Bernard data revisited,'' Aust. J. Ling. **18**(1), 29–55.

Croot, K., Fletcher, J., and Harrington, J. (**1992**). ''Levels of segmentation and labelling in the Australian national database of spoken language,'' in *Proceedings of the 4th International Conference on Speech Science and Technology*, edited by J. Pittam (Australian Speech Science & Technology Association, Brisbane), pp. 86–90.

Delattre, P., Liberman, A. M., Cooper, F. S., and Gerstman, F. J. (**1952**). ''An experimental study of the acoustic determinants of vowel color: observations on one- and two-formant vowels synthesised from spectrographic patterns,'' Word **8**, 195–210.

Essner, C. (**1947**). ''Recherche sur la structure des voyelles orales,'' Arch. Néerlandaises Phonétique Exp. **20**, 40–77.

Fant, G. (**1960**). *The Acoustic Theory of Speech Production* (Mouton, The Hague).

Fowler, C. A. (**1980**). ''Coarticulation and theories of extrinsic timing,'' J. Phonetics **8**, 113–133.

Fowler, C. A. (**1983**). ''Converging sources of evidence on spoken and perceived rhythms in speech: cyclic productions of vowels in monosyllabic stress feet,'' J. Exp. Psychol. **112**, 386–412.

Fowler, C. A. (**1986**). ''An event approach to the study of speech perception from a direct-realist perspective,'' J. Phonetics **14**, 3–28.

Fowler, C. A. (**1987**). ''Perceivers as realists, talkers too: commentary on papers by Strange, Diehl *et al.*, and Rakerd and Verbrugge,'' J. Mem. Lang. **26**, 574–587.

Fowler, C. A., and Rosenblum, L. D. (**1989**). ''The perception of phonetic gestures,'' Haskins Lab. Status Rep. Speech Res. **99/100**, 102–117.

Fox, R. (**1983**). ''Perceptual structure of monophthongs and diphthongs in English,'' Lang. Speech **26**, 21–49.

Fox, R. (**1989**). ''Dynamic information in the identification and discrimination of vowels,'' Phonetica **46**, 97–116.

Gay, T. (**1970**). ''A perceptual study of American English diphthongs,'' Lang. Speech **13**, 65–88.

Gottfried, M., Miller, J. D., and Meyer, D. J. (**1993**). ''Three approaches to the classification of American English diphthongs,'' J. Phonetics **21**, 205–229.

Harrington, J., and Cassidy, S. (**1994**). ''Dynamic and target theories of vowel classification: Evidence from monophthongs and diphthongs in Australian English,'' Lang. Speech **37**(4), 357–373.

Harrington, J., and Cassidy, S. (1999). *Techniques in Speech Acoustics* (Kluwer Academic, Dordrecht).

Harrington, J., Cox, F., and Evans, Z. (**1997**). ''An acoustic analysis of cultivated, general, and broad Australian English speech,'' Aust. J. Ling. **17**, 155–184.

Harrington, J., Fletcher, J., and Beckman, M. E. (in press). ''Manner and place conflicts in the articulation of accent in Australian English,'' in *Papers in Laboratory Phonology 5*, edited by M. Broe (Cambridge University Press, Cambridge).

Hillenbrand, J., and Gayvert, R. T. (**1993**). ''Vowel classification based on fundamental frequency and formant frequencies,'' J. Speech Hear. Res. **36**, 647–700.

Hillenbrand, J., Getty, L. A., Clark, M. J., and Wheeler, K. (**1995**). ''Acoustic characteristics of American English vowels,'' J. Acoust. Soc. Am. **5**, 3099–3111.

Holbrook, A., and Fairbanks, G. (**1962**). ''Diphthong formants and their movements,'' J. Speech Hear. Res. **5**, 38–58.

Horvath, B. M. (**1985**). *Variation in Australian English: The Sociolects of Sydney* (Cambridge University Press, Cambridge).

Huang, C. B. (**1986**). ''The effect of formant trajectory and spectral shape on the tense/lax distinction in American vowels,'' in *Proceedings IEEE International Conference on Acoustics, Speech and Signal Processing* (Institute of Electrical & Electronic Engineers, Tokyo), pp. 893–896.

Huang, C. B. (**1992**). ''Modelling human vowel identification using aspects of format trajectory and context,'' in *Speech Perception, Production and Linguistic Structure*, edited by Y. Tohkura, E. Vatikiotis-Bateson, and Y. Sagisaka (IOS, Amsterdam), pp. 43–61.

Jenkins, J., Strange, W., and Edman, T. (**1983**). ''Identification of vowels in 'vowelless' syllables,'' Percept. Psychophys. **34**, 441–450.

Jenkins, J. J., Strange, W., and Miranda, S. (**1994**). ''Vowel identification in mixed-speaker silent-center syllables,'' J. Acoust. Soc. Am. **95**, 1030–1043.

Joos, M. (**1948**). ''Acoustic phonetics,'' Language **24**, 1–136.

Klein, W., Plomp, R., and Pols, L. C. W. (**1970**). ''Vowel spectra, vowel spaces, and vowel identification,'' J. Acoust. Soc. Am. **48**, 999–1009.

Ladefoged, P. (**1967**). *Three Areas of Experimental Phonetics* (Oxford University Press, Oxford).

Lehiste, I., and Peterson, G. (**1961**). ''Some basic considerations in the analysis of intonation,'' J. Acoust. Soc. Am. **33**, 419–425.

Lindblom, B. (**1963**). ''Spectrographic study of vowel reduction,'' J. Acoust. Soc. Am. **35**, 1773–1781.

Millar, J., Harrington, J., and Vonwiller, J. (**1997**). ''Spoken language data

resources for Australian speech technology,'' J. Electr. Electron. Eng., Aust.
Millar, J., Vonwiller, J., Harrington, J., and Dermody, P. (**1994**). ''The Australian National Database of Spoken Language,'' in *Proceedings of the International Conference on Acoustics Speech and Signal Processing* (Institute of Electrical & Electronic Engineers, Adelaide), Vol. 2, pp. 67–100.
Moon, S.-J., and Lindblom, B. (**1994**). ''Interaction between duration, context, and speaking style in English stressed vowels,'' J. Acoust. Soc. Am. **96**, 40–55.
Nearey, T. M. (**1989**). ''Static, dynamic, and relational properties in vowel perception,'' J. Acoust. Soc. Am. **85**, 2088–2113.
Nearey, T. M., and Assmann, P. F. (**1986**). ''Modelling the role of inherent spectral change in vowel identification,'' J. Acoust. Soc. Am. **80**, 1297–1308.
Parker, E. M., and Diehl, R. L. (**1984**). ''Identifying vowels in CVC syllables: effects of inserting silence and noise,'' Percept. Psychophys. **36**, 369–380.
Peterson, G., and Barney, H. (**1952**). ''Control methods used in a study of vowels,'' J. Acoust. Soc. Am. **24**, 175–184.
Rakerd, B., and Verbrugge, R. R. (**1987**). ''Evidence that the dynamic information for vowels is talker independent in form,'' J. Mem. Lang. **26**, 558–563.
Rao, K. R., and Yip, P. (**1990**). *Discrete Cosine Transform: Algorithms, Advantages, Applications* (Academic, New York).
Saltzman, E., and Munhall, K. (**1989**). ''A dynamical approach to gestural patterning in speech production,'' Ecological Psychol. **1**, 333–382.
Stevens, K. N., Kasowski, S., and Fant, G. (**1953**). ''An electrical analog of the vocal tract,'' J. Acoust. Soc. Am. **25**, 734–742.
Strange, W. (**1987**). ''Information for vowels in formant transitions,'' J. Mem. Lang. **26**, 550–557.
Strange, W. (**1989a**). ''Dynamic specification of coarticulated vowels spoken in sentence context,'' J. Acoust. Soc. Am. **85**, 2135–2153.
Strange, W. (**1989b**). ''Evolving theories of vowel perception,'' J. Acoust. Soc. Am. **85**, 2081–2087.
Strange, W., Jenkins, J. J., and Johnson, T. L. (**1983**). ''Dynamic specification of coarticulated vowels,'' J. Acoust. Soc. Am. **74**, 695–705.
Strange, W., Verbrugge, R. R., Shankweiler, D. P., and Edman, T. R. (**1976**). ''Consonant environment specifies vowel identity,'' J. Acoust. Soc. Am. **60**, 213–224.
Verbrugge, R. R., and Rakerd, B. (**1986**). ''Evidence of talker-independent information for vowels,'' Lang. Speech **29**, 39–55.
Vonwiller, J., Rogers, I., Cleirigh, C., and Lewis, W. (**1995**). ''Speaker and material selection for the Australian National Database of Spoken Language,'' J. Quant. Ling. **3**, 177–211.
Watson, C., Harrington, J., and Evans, Z. (**1998**). ''An acoustic comparison between New Zealand and Australian English vowels,'' Aust. J. Ling. **18**(2), 185–207.
Wells, J. C. (**1982**). *Accents of English: Beyond the British Isles* (Cambridge University Press, Cambridge).
Zahorian, S., and Jagharghi, A. (**1993**). ''Spectral-shape features versus formants as acoustic correlates for vowels,'' J. Acoust. Soc. Am. **94**, 1966–1982.

A microcosm of musical expression. III. Contributions of timing and dynamics to the aesthetic impression of pianists' performances of the initial measures of Chopin's Etude in E Major

Bruno H. Repp
Haskins Laboratories, 270 Crown Street, New Haven, Connecticut 06511-6695

(Received 11 January 1999; revised 8 April 1999; accepted 15 April 1999)

Four judges repeatedly assessed the overall aesthetic quality of more than 100 recorded performances of the opening of Chopin's Etude in E major on a 10-point scale. The judgments, which exhibited reasonable reliability and modest intercorrelations, were entered into regression analyses with 16 independent variables derived from earlier objective analyses of the expressive timing and dynamics of the performances [Repp, J. Acoust. Soc. Am. **104**, 1085–1100 (1998); **105**, 1972–1988 (1999)]. Only between 9% and 18% of the variance in the judges' ratings was accounted for. By contrast, timing variables accounted for 53% of the variance in one judge's ratings of synthesized performances that varied in timing only and mimicked the timing patterns of the original performances. These results indicate, first, that the aesthetic impression of the original recordings rested primarily on aspects other than those measured (such as texture, tone, or aspects of timing and dynamics that eluded the earlier analyses) and, second, that very different patterns of timing and dynamics are aesthetically acceptable for the same music, provided that other, aesthetically more crucial performance aspects are present. © *1999 Acoustical Society of America.* [S0001-4966(99)04607-X]

PACS numbers: 43.75.St, 43.75.Mn [WJS]

But all beautiful melodies share essential and multiple properties. Not least is a psychological property which perhaps can best be described as representing a kind of spiritual alienation. For all melodies tend to remove themselves from the common ground of mundane experience, revealing their special spice and character by the usual devices of touch and rubato *. ... If they are too passively integrated into the general mesh of sound, they sacrifice the prophetic, tender, and urgent qualities which mark them as independent of the collective reality.*

(Sherman, 1997, p. 45)

INTRODUCTION

The initial measures of Chopin's Etude in E major, op. 10, No. 3 (Fig. 1)[1] contain one of the most famous and beautiful melodies in the whole piano literature, and the epigraph from Russell Sherman's collection of insightful pianistic observations seems to apply perfectly to it. Many great pianists have struggled to impart to this melody the subtle and exalted expression it demands, but few have succeeded to every listener's satisfaction.

In two preceding articles, Repp (1998, 1999) has presented a detailed analysis of the expressive timing and dynamics of 115 commercially recorded performances of this famous melody. The *timing profile* of a performance was defined as its sequence of tone inter-onset interval (IOI) durations (without the initial upbeat), and its *dynamic profile* was defined as the sequence of peak sound levels immediately following tone onsets in the amplitude envelope. The grand average timing and dynamic profiles were considered typical and representative because many individual performances had timing and/or dynamic profiles that were similar to the grand average profiles. Principal components analyses were conducted to identify different ways in which individual performances deviated from these typical expressive patterns. These analyses yielded principal components (i.e., mutually uncorrelated profile shapes, four for timing and five for dynamics) that were interpreted as expressive strategies underlying the individual differences among the performances.

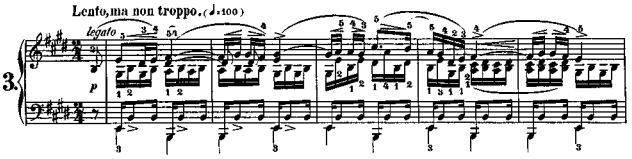

FIG. 1. The initial five measures of Chopin's Etude in E major, op. 10, No. 3 (Herrmann Scholtz edition, Leipzig: Peters, 1879). For the present purposes, the except ends on the second beat of bar 5.

While some individual performances instantiated these strategies in pure form, as it were, the majority had profiles that represented a mixture of several strategies. Indeed, the most typical individual profiles (those most similar to the grand average profile) by definition result from a weighted combination of all strategies. There was no evidence of distinct clusters or major gaps in the distributions of weights given to these strategies, which led to the conclusion that the

individual differences in expression did not arise from categorically distinct structural interpretations. Rather, it was argued that they represent different expressive shapings or characterizations of a single musical structure (cf. Shaffer, 1995). Interestingly, there were few significant relationships between expressive timing and dynamics across the many performances. These two important parameters seem to be controlled independently at the phrase level, which opens up a wealth of expressive possibilities.

In addition to its specific pattern over time, each expressive parameter has two more global properties (mean and standard deviation) that are also continuously variable. For timing, these are the basic tempo (inversely related to the average IOI duration) and the within-profile variation in IOI duration; for dynamics, they are the basic dynamic level and the within-profile dynamic variation. Although basic dynamic level could not be assessed meaningfully in the recorded performances, individual differences in the other three aspects were also discussed in the preceding articles (Repp, 1998, 1999).

These earlier analyses were objective and descriptive; nothing at all was said about the aesthetic impressions made by the various patterns of timing and dynamics. Nevertheless, these patterns clearly serve an aesthetic goal: Each pianist is trying to realize a particular conception of the music, and listeners are invited to share this conception and derive pleasure from it. It is often believed, especially among music theorists and music psychologists, that the most important function of expressive variation is to clarify and disambiguate musical structure (see, e.g., Berry, 1989; Clarke, 1985; Palmer, 1989). There may be specific contexts in which this is true, but it is hardly the case in the present musical excerpt, whose structure seems quite unambiguous. Moreover, it is not obvious what aesthetic benefits can be derived from the perception of structure as such. Music theorists and analysts may find intellectual pleasure in being able to hear structural detail or resolved ambiguities, but this is very different from the intuitive, almost visceral response of the ordinary music lover to musical expression (see Cook, 1990; Levinson, 1997). Scruton (1997) has argued convincingly that the perception of expression involves relating musical processes to real-life activities via imaginative metaphors that often remain implicit and ineffable (see also Sloboda, 1998). Musical motion, resulting from the temporal unfolding of its structure, is perceived in terms of life experience, just as a performer's life experience may provide metaphors that help give his or her performance an individual expressive shape. The listener's internal resonance to the musical motion is a kind of ''sympathetic dance'' (Scruton, 1997) that need not be, and often cannot be, described in words.

Clearly, aesthetic perception is a highly subjective and incompletely understood process, as is the creative process underlying the individual expression produced by a performer. However, aesthetic evaluation is somewhat more straightforward and more amenable to scientific study. It is the process of expressing one's relative liking for or preference among different art objects, here different performances of the same musical composition. Musical performance evaluation is usually engaged in by persons who are familiar with the work and its expressive possibilities; often they are musicians who have played the music themselves. Just as artists have a conception of the music that they are trying to realize in performance, so judges may have a conception that they expect to hear realized. In the simplest case, therefore, a judge's liking of a performance will reflect the extent to which the artist's conception (as conveyed by the performance) matches his or her own conception—that is, the extent to which he or she ''resonates'' to the performance.

However, this account is oversimplified in at least two ways. First, while the resonance metaphor may apply to any single expressive dimension, performances have multiple dimensions which may meet the judge's expectations in different degrees and which may be assigned different weights (see Levinson, 1990; Thompson *et al.*, 1998). The overall aesthetic impression, then, is a complex function of the listener's resonances to each of these dimensions. Consequently, two very different performances may be liked equally. Second, one must take into account that individuality (originality) is valued in artistic performance, at least in the standard Western classical repertoire. On purely statistical grounds, the best match to most listeners' expectations will be provided by performances that are close to the norm, because expectations are abstracted from experience with many performances and thus are close to the norm, too (Repp, 1997). Nevertheless, and paradoxically, a performance that merely delivers what is expected will often not be fully satisfactory, perhaps because this is too common an occurrence. True, one occasionally hears a performance that realizes the norm so perfectly that it may be considered definitive (by some listeners, at least). However, listeners usually expect to hear some evidence of originality, something unexpected and surprising, for which there are many possibilities, more or less convincing. What exactly makes an unexpectedly original performance convincing to one particular listener, but perhaps not to another, is a very complex question. In some cases, it could perhaps be traced back to the listener's own conception being biased in the performance's direction, but often a listener is simply ''won over'' by a great artist's very personal interpretation because it reveals as yet unimagined expressive possibilities.

Both a performer's and a listener's conception of a musical work may change over time, sometimes from one performance or hearing to the next. Some experienced artists may have multiple conceptions available at the same time, being able to choose one or the other at will, and the same may be true for some listeners, especially if they are performing artists as well. This possibility of multiple standards further complicates aesthetic judgment. Nevertheless, such judgment is rarely arbitrary. While it may be expected to be less reliable and to show larger individual differences than many other kinds of perceptual judgment, there are real differences in aesthetic quality among music performances, even at the highest level. Although it is difficult to prove through objective analysis alone that some performances are better than others, there will often be some degree of consensus among competent judges (cf. Thompson *et al.*, 1998). Given such a consensus—but even in its absence—one may then ask whether there are any objectively measurable per-

formance aspects that correlate with the judges' evaluations. Different correlations for different judges will reflect their different criteria and biases.

The aim of the present study was to determine the extent to which objectively measured aspects of expressive timing and dynamics contribute to the overall aesthetic impression of the initial phrase of Chopin's Etude in E major.[2] Repeated evaluations of most or all previously analyzed performances were obtained from four judges, on a 10-point rating scale. First, as a prerequisite to the subsequent statistical analyses, the reliability of each judge's ratings was determined across two or more sessions, and the intercorrelations among the judges' ratings were calculated. Musical aesthetic judgment, perhaps because of the aura of subjectivity that envelops it, has rarely been subjected to even this kind of basic analysis (though see Wapnick *et al.*, 1993; Thompson *et al.*, 1998), certainly not for such a large sample of expert performances. Subsequently, the judges' ratings were entered into a regression analysis, with the objective performance measurements as the independent variables, to determine how much of the systematic variance in the ratings could be accounted for. Finally, the relation of the judges' evaluations to several sociocultural characteristics of the artists was examined briefly. Although these characteristics had been found to be only weakly related to some aspects of expressive timing and dynamics, it was considered possible that they were related to other aesthetically relevant aspects of the performances and hence to the judges' ratings.

One of the judges also evaluated a set of synthesized performances that differed in timing only and mimicked the timing patterns of the original performances. The purpose of this exercise was to determine to what extent the timing variables account for aesthetic ratings when all other performance aspects are held constant. In a much smaller set of synthesized performances of the same Chopin excerpt, Repp (1997) had found that listeners preferred typical over atypical timing profiles. However, he had not obtained any ratings of the original performances from which the timing profiles had been derived. Now a direct comparison could be made, albeit for only a single listener, to examine whether there is indeed a preference shift in favor of typical timing in synthesized versus original performances.

I. METHOD

A. Judges

In view of the difficult and time-consuming nature of the task, only four judges participated. Initially, the author (BR) thought of undertaking the evaluation all by himself and therefore proceeded to collect a large amount of data for himself. To increase the generality of the findings, however, he then enlisted three additional judges (MC, NN, OS) who volunteered to participate but could not be expected to invest quite as much time and effort.

All judges were well qualified for the task and knew the Chopin Etude well. BR is an amateur pianist and music lover, 53 years old at the time, with some 35 years of experience in the informal judgment of piano performances in concert and on recordings. MC is a well-known scientist and musician, 71 years old. He has a master's degree from the Juilliard School and was a successful concert pianist in his youth. He possesses great insight into composers' individual rhythmic characteristics and into performance expression generally. NN is a pianist and musicologist, 57 years old, with special expertise on historical piano performance. OS is a 30-year-old music critic and amateur pianist who reviews live and recorded performances in several periodicals. His special interest is early music, but he is certainly familiar with Chopin's idiom. He provides a useful contrast to the three older judges, in that he is more representative of contemporary aesthetic tastes. The judges also provide a broad international spectrum: BR grew up in Austria and came to the U.S. at age 25; MC was also born in Austria but left at an early age and lived mainly in Australia and the U.S.; NN is Australian; OS is Israeli.

B. Procedure

The procedure followed by MC, NN, and OS shall be described first. These judges were mailed a tape containing 102 performances of the Chopin excerpt.[3] MC was sent a digital tape, NN and OS cassette tapes, together with instructions. The judges were asked to familiarize themselves with the range of performances by listening to at least part of the tape before starting the evaluation. The evaluative judgments were to be made on a 10-point scale, where ''1'' represented the lowest rating and ''10'' the highest, with decimal ratings a possibility. The judges were encouraged to use the whole range of the scale and to evaluate all 102 performances in a single session. The sound quality of the recordings was to be ignored as much as possible. In addition to the overall ratings, written comments on each performance were invited. An improvised answer sheet was used to record the ratings and comments. On the tape, each recorded excerpt faded out during bar 6 or 7. However, it was emphasized that only the first 5 bars were to be evaluated and that the tape should be stopped at that point for each excerpt. (Many pianists accelerate the tempo in the following bars, and the way in which this is done may have a considerable influence on the overall aesthetic impression.) A second evaluation session was conducted on another day (MC: 4 days later; NN: one week later; OS: one month later). The procedure was the same, but whereas the first session started with performance No. 1, the second session started with performance No. 52. The judges were urged not to look at their previous ratings. All three judges were completely blind to the pianists' identities, which were revealed to them only afterward.

BR had heard the performances previously when analyzing their timing and therefore could not avoid recognizing some of them. He also included 15 additional performances that he had used in an earlier study (Repp, 1997) and had not heard recently.[4] To make his evaluations as unbiased as possible, BR deleted the pianists' names from the computer files and retained only their serial numbers. He subsequently recognized only about 10% of the performances, which is not believed to have had an influence on his judgments. He evaluated the 117 performances 10 times, each time in a different random order. The first three sessions were on successive days, the fourth session three days later, the fifth session one week later, and sessions 6–10 on successive days

one week later.[5] He listened to each excerpt twice before giving a rating and added written comments during the last six sessions. Each rating session took about 2.5–3 h.

C. Synthesized performances

Following his evaluation of the original performances, BR evaluated an additional set of computer-generated performances that varied in expressive timing only. These performances were created by imposing the measured timing profiles onto a constant ''carrier.'' In the course of earlier experiments, a number of graduate student pianists had played the Chopin Etude excerpt (ending with a chord on the second beat of bar 5) on a Roland RD-250s digital piano and had been recorded via a Musical Instrument Digital Interface (MIDI). The MIDI instructions of one of the best performances were imported as text into a spreadsheet program, and the onset of the highest note in each metrical (sixteenth-note) position was located. From the onset times of these ''primary'' notes, inter-onset intervals (IOIs) were calculated. All other MIDI events (other note onsets, note offsets, pedal depressions, and pedal releases) were then linked to the nearest primary note onset by expressing their times of occurrence relative to it. Next, the measured IOIs of one of the expert performances were substituted for the IOIs of the student performance. The primary note onset times were then re-calculated by cumulatively adding the new IOIs, and the times of occurrence of all other MIDI events were obtained by adding their (positive or negative) relative times of occurrence to the new onset times of the primary notes. Thus all secondary note onsets, note offsets, and pedal events remained in their original (absolute) temporal relationships to the nearest primary note onset. The MIDI velocities (relative intensities) of all notes remained unchanged. The result was a synthesized performance with a timing pattern closely resembling that of an original performance.[6] In that way, 115 synthesized performances were created and played back under computer control on the Roland RD-250s digital piano (with ''Piano 1'' sound). Their aesthetic quality, although inferior to that of most original excerpts, was satisfactory and, moreover, their sound was free of noise or distortion. Their range of aesthetic quality seemed somewhat reduced relative to that of the original performances, since only a single expressive dimension varied.

BR evaluated the synthesized versions in five additional sessions spread over eight days, two months after his evaluation of the original excerpts. He first created a set of randomly renumbered copies of the MIDI files, so that he was totally blind to their identity. He recognized the timing of only a few highly individual performances. In each session, he listened to the excerpts in a different random order, gave each excerpt a rating on the 10-point scale (usually playing it only once, but repeating it if uncertain), and took notes.[7]

II. RESULTS

A. Use of rating categories

Figure 2 shows the frequency distribution of the four judges' ratings. There were considerable individual differences. BR used the whole range of the scale, with the most

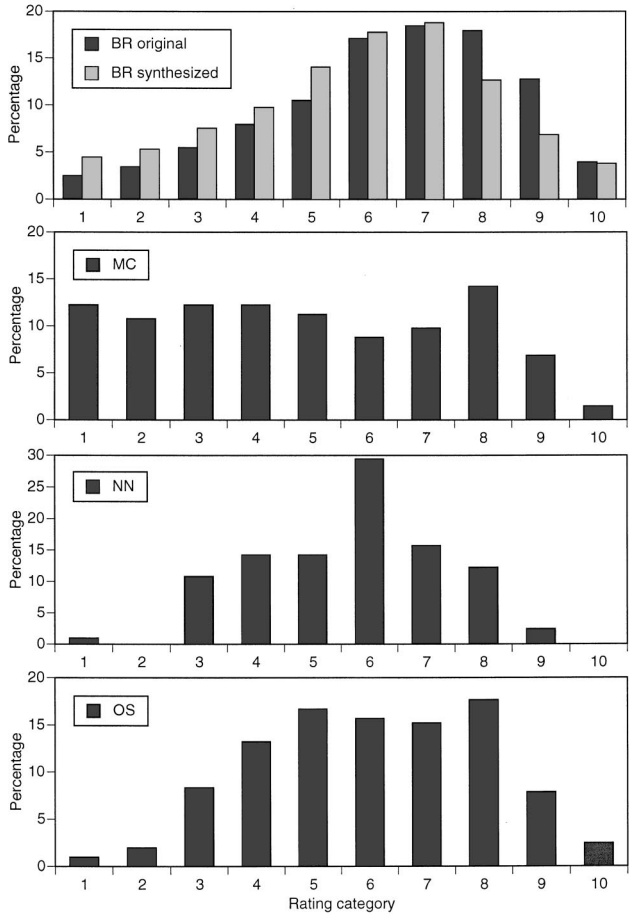

FIG. 2. Frequency histograms of the four judges' ratings.

frequent ratings being in the range of 6–8. Despite a subjective recalibration of the scale, he gave slightly lower ratings to the synthesized than to the original excerpts. (The difference would probably have been larger if original and synthesized performances had been intermixed.) MC was reluctant to use the highest categories (he never gave a straight ''10'') but frequently gave very low ratings, which resulted in an almost rectangular distribution of ratings. NN, by contrast, basically restricted himself to the middle categories (3–8) and gave many ''6'' ratings. OS also favored the middle categories, but occasionally gave very high or low ratings. MC, NN, and OS all made occasional use of decimals, whereas BR gave only integer ratings. No transformations were applied to the ratings in the following analyses.

B. Reliabilities and intercorrelations

To determine the reliability of BR's ratings of the original excerpts, the pairwise correlations among his 10 sets of ratings were computed. These 45 correlations ranged from 0.48 ($p<0.001$) to 0.77, with an arithmetic average of 0.64. Although this is not a very high reliability, it does show some consistency in what were rather difficult judgments. Of course, the average ratings were more reliable than those from single sessions. BR's average ratings of sessions 1–5 and 6–10 correlated 0.80, and the average ratings of his odd and even sessions correlated 0.92. The fact that the first correlation is lower than the second indicates some systematic

TABLE I. Intercorrelations among the four judges' average ratings of the original excerpts ($N=102$).

	MC	NN	OS
BR	0.56[a]	0.52[a]	0.30[b]
MC	-----	0.37[a]	0.21[c]
NN	-----	-----	0.29[b]

[a]$p<0.001$.
[b]$p<0.01$.
[c]$p<0.05$.

changes in preferences over time. The reliability of the ratings averaged over all 10 sessions can be estimated from either of these two ''split-half'' correlations by means of the Brown–Spearman formula $[2r/(1+r)]$; one estimate is 0.89 and the other 0.96. In other words, at least 80%(r^2) of the variance in BR's average ratings was systematic.

For each of the other three judges, only a single correlation between two sets of ratings could be computed. These correlations were 0.76 for MC, 0.50 for NN, and 0.56 for OS (whose two sessions were one month apart). For their average ratings, the Brown–Spearman formula gives reliability estimates of 0.86, 0.67, and 0.72, respectively. The systematic variance thus ranged from 45% to 74%.

The 10 pairwise correlations among BR's 5 sets of ratings of the synthesized performances ranged from 0.66 to 0.75, with an average of 0.69. The reliability of the average ratings may be estimated to be about 0.90. It is noteworthy that aesthetic quality differences resulting from timing alone could be judged at least as consistently as differences based on a larger number of performance parameters. The probable reason was that there were fewer expressive parameters to attend to and fewer possibilities for changes in their relative weights over time. Of course, practice could also have played a role.

The correlation between BR's average ratings of the original and synthesized excerpts was 0.52 ($p<0.001$). This is substantially lower than the reliability of either set of judgments and thus indicates significant changes in aesthetic preferences from one set to the other.

The intercorrelations among the four judges' average ratings of the original excerpts are shown in Table I. Although significant, they are not high and bear witness to large individual differences in aesthetic judgment. As expected, OS stands out as the one most different from the other three judges. The complete average ratings of all judges are listed in the Appendix.

C. Correlations of judges' ratings with performance characteristics

These correlations are shown in Table II. The columns represent the four judges' average ratings of the original excerpts, BR's ratings of the synthesized excerpts (BRSYN), and the difference between these ratings and BR's ratings of the original excerpts (BRDIFF). The rows represent 16 independent variables derived from the earlier performance analyses: the basic tempo estimated from the median IOI duration (TEMPO); the duration of the initial upbeat relative to the average IOI duration (UPBEAT); the within-performance coefficient of variation of the IOIs (relative modulation depth of timing, RELMOD); the performance's loading on the first unrotated principal component for timing (TUPC1) or, equivalently, its correlation with the grand average timing profile—an index of its typicality; its loadings on the four Varimax-rotated principal components for timing (the ''timing strategies,'' TPC1–TPC4); the standard deviation of the melodic peak sound levels (MELSD); the difference between the average peak sound levels of melody and accompaniment (MELACC); the loading on the first unrotated principal component for dynamics (DUPC1)—the typically index of the dynamic profile; and the loadings on the five Varimax-rotated principal components for dynamics (the ''dynamic strategies,'' DPC1–DPC5). No correlations are shown between BRSYN and the dynamic performance variables because there were no dynamic differences among the synthesized excerpts. However, it did make sense to compute correlations between BRDIFF and the dynamic variables, because these changes in ratings may reflect the effect of *removing* different aspects of expressive dynamics.

TABLE II. Linear correlations between judges' average ratings and objectively measured performance characteristics ($N=117$ for BR, $N=102$ for MC, NN, and OS). See text for explanation of abbreviations.

	BR	MC	NN	OS	BRSYN	BRDIFF
TEMPO	−0.34[a]	−0.42[a]	−0.22[c]	−0.03	−0.59[a]	−0.30[b]
UPBEAT	0.17	0.11	0.10	0.29[b]	0.24[c]	0.08
RELMOD	−0.05	−0.17	−0.12	−0.24[c]	−0.34[a]	−0.31[a]
TUPC1	0.21[c]	0.16	0.31[b]	0.19	0.48[a]	0.31[a]
TPC1	0.06	0.16	0.18	0.10	0.35[a]	0.31[a]
TPC2	0.13	0.07	0.12	0.00	−0.10	−0.23[c]
TPC3	0.05	−0.15	0.07	0.04	0.08	0.04
TPC4	−0.06	0.03	−0.18	0.04	0.02	0.07
MELSD	0.07	0.13	0.11	0.07		−0.09
MELACC	0.02	0.03	−0.03	−0.10		0.01
DUPC1	−0.05	−0.06	−0.06	0.07		0.15
DPC1	−0.04	−0.05	−0.00	0.07		0.23[c]
DPC2	0.12	−0.05	−0.01	−0.17		−0.15
DPC3	0.06	0.08	0.09	0.17		−0.02
DPC4	−0.16	0.06	−0.13	0.10		0.17
DPC5	0.02	−0.13	0.02	−0.12		−0.12

[a]$p<0.001$.
[b]$p<0.01$.
[c]$p<0.05$.

Surprisingly few of the many correlations reached significance, and none were very high. The ratings of three of the judges (BR, MC, NN) were negatively correlated with TEMPO, indicating a preference for slower over faster performances.[8] This preference was even more pronounced in BR's ratings of the synthesized excerpts. Since there was reason to expect a curvilinear (convex) relationship between tempo and preference, with the most preferred tempo somewhere in the middle, second-order polynomials were also fitted to the tempo data. This indeed improved the fit for three of the judges; only MC showed no quadratic trend at all.[9] The ''quadratic correlations'' (square roots of the variance accounted for by the quadratic function) were 0.50 for BR, 0.48 for NN, and 0.34 for OS (all $p<0.001$). The quadratic functions for these three judges were similar in shape and had their maxima in the vicinity of 30 quarter-note (or 60 eighth-note) beats per second, which is very close to the

average median tempo of the performances (Repp, 1998: Fig. 2). BRSYN and BRDIFF did not show a significant quadratic trend.

Weak positive relationships were obtained between the relative duration of the initial upbeat (UPBEAT) and the ratings of OS and BRSYN, indicating a slight preference for longer upbeats. Hints of a convex quadratic relationship, indicating a preference for intermediate upbeat durations, were found for BR ($r=0.22$, $p<0.05$) and NN ($r=0.26$, $p<0.01$).

Relative modulation depth of timing (RELMOD) was negatively correlated with the ratings of OS, BRSYN, and BRDIFF, which indicates a preference for weaker over stronger timing modulation, especially in the synthesized performances. Since here, too, a curvilinear relationship could be expected, quadratic functions were again fitted to the data. Marginally significant relationships of the expected convex form emerged for BR ($r=0.23$, $p<0.05$) and NN ($r=0.21$, $p<0.05$).

The relative typicality of the timing profiles (TUPC1) had some modest positive relationships with BR's and OS's ratings, indicating a slight preference for more typical or conventional timing. However, there was a much stronger correlation of this variable with BRSYN. This is consistent with the results of an earlier study using a smaller set of synthesized performances of the same excerpt and a group of pianist judges (Repp, 1997). Evidently, unconventional timing is more difficult to appreciate in synthesized than in original performances. There was also a positive correlation with BRDIFF.

Remarkably, there were no significant relationships between the judges' ratings of the original excerpts and any of the timing strategies or any of the dynamic variables. BRSYN and BRDIFF, however, showed a positive correlation with TPC1 loadings. Since this was the most common timing pattern and similar to TUPC1, this basically reflects the same preference for relatively typical timing patterns in synthesized performances. BRDIFF also correlated negatively with TPC2, indicating that this rather unusual timing pattern (called PC-II or Type II in Repp, 1998) was difficult to appreciate in the synthesized versions. BRDIFF also showed a small positive correlation with a dynamic variable, DPC1 (called PC-I or Type I in Repp, 1999), indicating that removal of this dynamic pattern tended to increase ratings.[10]

To determine the total amount of rating variance accounted for by the performance variables, stepwise multiple regression analyses with an inclusion criterion of $p<0.05$ were conducted on each set of ratings. Since this kind of analysis takes into account any intercorrelations among the performance variables, there was a possibility that additional significant relationships would emerge in the form of partial correlations. (Most of the intercorrelations were quite low, however, and principal component patterns are by definition orthogonal.) The results are shown in Table III.

The most noteworthy outcome is that performance variables accounted for 53% of the variance (R^2) in the BRSYN ratings, but only between 9% and 18% in the judge's ratings of the original excerpts, even though there were twice as many relevant performance variables. The estimated systematic variance in these average ratings ranged from 45% to 80%. The large amount of unexplained variance must be due to performance aspects that were not captured by the objective measurements. Even in the BRSYN ratings, a substantial portion of the systematic variance (estimated at about 80%) remains unexplained, which suggests that there are aesthetically relevant aspects of expressive timing that were not captured by the eight timing variables.

TABLE III. Results of stepwise multiple regression analyses on the ratings.

Ratings	Performance variable	(partial) r	R
BR	TEMPO	−0.36	
	DPC4	−0.20	0.39
MC	TEMPO	−0.42	0.42
NN	TUPC1	0.31	0.31
OS	UPBEAT	0.30	
	RELMOD	−0.25	0.38
BRSYN	TEMPO	−0.46	
	TUPC1	0.41	
	RELMOD	−0.21	0.73
BRDIFF	RELMOD	−0.30	
	TUPC1	0.27	
	TPC2	−0.26	
	TEMPO	−0.17	0.54

The variables that made a significant contribution to the regression equations were largely the ones that showed significant simple correlations with the ratings (Table II), with the following exceptions: For BR, TUPC1 dropped out and instead DPC4 made a significant (negative) contribution, which is a rare instance of a dynamic variable making an appearance. For NN, TEMPO dropped out. For BRSYN, UPBEAT and TPC1 dropped out, and for BRDIFF, TPC1 dropped out.

D. Correlations with sociocultural variables

The sociocultural variables were the year of recording, the artist's birth date, age at the time of recording, gender, and nationality (country of birth). Only OS's ratings showed a positive relationship with the year of recording ($r=0.38$, $p<0.001$). When a quadratic trend was included, the correlation increased to 0.45 and revealed that the increase in ratings occurred especially since about 1970. This is interesting because OS (the youngest of the judges, born in the late 1960s) grew up with these recordings. The relevant factor may have been either recorded sound quality (although OS, like the other judges, had been instructed to disregard this aspect as much as possible) or some other as yet unidentified quality associated with more recent recordings. (Although more recent recordings tend to be more typical, OS's ratings showed no significant correlation with TUPC1 or DUPC1, the typicality indices.) OS's ratings also showed a positive relationship with artists' birth dates ($r=0.23$, $p<0.05$), which of course were strongly correlated ($r=0.79$) with year of recording. There were no significant linear or curvilinear relationships of any judge's ratings with the artists' age at the time of recording, so that there is no evidence from these data that more mature artists produce better performances (of

a single phrase). Furthermore, there were no significant effects of artists' gender or nationality, although the latter analysis included only French, Polish, and Russian pianists, of whom there were sufficient numbers in the sample.

The BRSYN ratings showed small positive correlations with year of recording ($r=0.25$, $p<0.01$) and with artists' birth dates ($r=0.25$), while the BRDIFF ratings correlated with recording date only, again positively ($r=0.35$, $p<0.001$). Thus it was *not* the case that older, scratchy recordings benefitted from being partially reincarnated as synthesized performances; on the contrary, they suffered more than did more recent recordings. The presumable reason for this was that they represented more individual timing profiles that, as we have seen, were more difficult to appreciate in the context of the digital piano sound. These results also suggest that BR successfully disregarded recorded sound quality when making his evaluations of the originals.

III. GENERAL DISCUSSION

Timing and dynamics are often considered the two most important parameters of expression in piano performance. Psychological research on music performance has focused predominantly on timing and to a much lesser extent on dynamics, but the importance of dynamics has surely been recognized. A third important parameter, even less investigated but likewise appreciated, is articulation—the degree of overlap and separation of successive tones. In the present Chopin Etude excerpt, however, variation in articulation hardly played a role because *legato* was employed throughout and the damper pedal was used almost continuously. Thus timing and dynamics were the primary expressive dimensions, and it was startling to find that they accounted for only a small amount of variance in the judges' ratings.

This result was not due to low reliability of the ratings: The systematic variance in judges' average ratings (the reliability coefficient squared) ranged from about 45% to 80%, whereas the variance accounted for in the regression analyses ranged from 9% to 18%. It was also not due to significant nonlinear relationships between the ratings and the independent variables, although some small quadratic trends were noted. Thus the variance accounted for was perhaps underestimated by a few percent, but the basic result remains. Furthermore, it cannot be attributed to insensitivity or idiosyncrasy of the judges who were all experienced musicians and/or listeners. The fact that they employed somewhat different criteria in making their evaluations only increases the generality of the results.

The judges' exact criteria were not known, of course, and it would have been too cumbersome to attempt to determine them precisely, given the large number of judgments to be made. Also, appropriate methods for eliciting this information are only now beginning to be developed (see Thompson *et al.*, 1998). Even experienced judges of musical performances often do not know how they arrive at their overall assessments; this is in large part an intuitive, not a cognitive process, especially at the upper end of the scale. For example, the author (BR) feels that he rated the (to him) most excellent performances (ratings of 8 and above) on the basis of the degree to which they ''engaged his body'' and made him ''move inwardly'' with the music, which reveals little about the specific performance properties that elicited this kind of biophysical (perhaps merely metaphorical) resonance. In performances that he gave ratings of 5 or below, however, BR usually detected specific flaws that he mentioned in his comments.

One conclusion to be drawn from the results is that the different patterns of expressive timing and dynamics uncovered by the principal components analyses of the 115 performances are all aesthetically viable, as are different tempi and different degrees of expressive modulation, within broad limits. This makes sense because nearly all of the recorded pianists are distinguished concert artists who play with great expertise and conviction. Certainly there is no single optimal way of playing the Chopin phrase, even within the individual minds of the four judges: Each judge gave equally high ratings to performances of very different character. A second conclusion is that, in this particular musical excerpt, the performance aspects of primary aesthetic importance are not the ones measured in the objective performance analyses (Repp, 1998, 1999).

What then are these important but as yet unquantified aspects? Here only speculations can be offered, based in part on the judges' comments and mainly on the author's intuitions. First, there may be additional aspects of timing and dynamics that were not captured by the performance analyses. Second, there may be additional expressive dimensions.

One clue that there may be aesthetically relevant aspects of timing that were not captured by the performance analyses is offered by the finding that the timing variables accounted for only 53% of the variance of BR's ratings of the synthesized performances, whereas the systematic variance was in the vicinity of 80%. Since these performances differed in timing only, some aspect of timing must have been responsible for the unexplained 27% of the variance. One likely candidate is smoothness or continuity. Comments such as ''jerky,'' ''mannered,'' and ''distorted'' kept recurring in BR's notes, usually with reference to the same performances. This aspect is very difficult to quantify. Although Todd (1995) has proposed a principle by which the smoothness of timing might be gauged, it is difficult to apply to short melodic-rhythmic segments within a phrase. Performances considered ''jerky'' by BR generally had high degrees of relative modulation depth, so that the impression may have derived in part from exaggerated *rubato*. Performances with high relative modulation depth that were rated favorably by BR often had merely a very long initial downbeat. If the initial IOI had been omitted, perhaps the RELMOD variable would have explained more variance in BR's ratings than it did. However, this can hardly be the whole story.

BR also noted a few performances in which the basic tempo seemed to change in the course of the phrase, to their detriment. This seemed to rest mainly on a change in the speed of the accompaniment passages between melodic seg-

ments, which could be quantified more easily but probably would account for only little variance. The observation raises some interesting questions, however, about the perception of basic tempo constancy in highly modulated contexts (cf. Repp, 1994).

There are few clues to aspects of (horizontal) dynamics that may have been missed. However, occasional comments from judges concerned exaggerated or misplaced accents. In one performance, for example, a single bass note was far too loud, apparently a slip of some sort. This probably diminished the aesthetic impact of the performance, but the overall effect of such local flaws on the judges' ratings cannot have been very large.

It is possible that interactions between timing and dynamics had some aesthetic importance. Although Repp (1999) found no significant correlations between timing and dynamics in the original performances, this does not rule out the possibility that certain combinations of timing and dynamic profiles are aesthetically more appealing than others. If so, that may also explain why BR's judgments of the synthesized performances, which had a fixed and fairly typical dynamic profile, were biased in favor of more typical timing profiles (see also Repp, 1997). Research is planned to specifically investigate the aesthetic interdependence of timing and dynamics; at present, there is no direct evidence for such an interaction. Interactions may also occur very locally. For example, one of BR's most favored performances had a hesitation on the first note of the final melodic gesture that he perceived as especially poignant and moving. However, the same hesitation did not sound poignant at all in the synthesized version of this timing profile, which received a much lower rating.

Among the performance dimensions that were not properly measured and quantified, due to methodological limitations, are vertical timing and dynamics. Vertical timing refers to asynchronies among tone onsets that are nominally simultaneous in the score. Large asynchronies, usually due to the bass leading the melody, occurred in a number of performances, mostly of older vintage. While these asynchronies were occasionally annoying, they also could make a positive aesthetic contribution. Therefore, this was probably not a major factor. However, the role of smaller asynchronies that are imperceptible as such remains uncertain. They may have contributed importantly to the highlighting of the melody (see Palmer, 1996) and to the sound texture.

Vertical dynamics refers to the relative intensities of simultaneous tones, also referred to as texture. This is likely to be an important factor in the present excerpt, where the melody needs to stand out from the accompaniment (cf. the epigraph at the beginning of this article) and the accompaniment itself represents different voices with different functions. However, the dynamic contrast between melody and accompaniment was partially captured by the MELACC variable in the regression analysis, which surprisingly explained no variance at all. Since this measure was based only on the accompaniment during sustained melody tones, however, it was perhaps not representative of the texture at melody tone onsets, and certainly not of the texture within the multi-voiced accompaniment.

Another factor not considered because it is impossible to measure in acoustic recordings is pedaling. Only MC occasionally complained of ''bad pedaling.'' However, there may have been effects of pedaling on texture and sound quality that were not directly perceived as being due to pedaling. Two other factors that may have played a role are instrument quality and room acoustics. While the judges seemed to have been successful in disregarding differences in recorded sound quality (such as crackles, noise, or frequency band limitations), the quality of the piano and of the room in which it was recorded were difficult to separate from the performance itself. Needless to say, they are also almost impossible to measure in an objective way.

The author suspects that the aesthetically most important aspect of the performances was the elusive quality often referred to as ''tone'' or ''touch'' (see again the epigraph). This remains the most poorly understood aspect of pianistic skill, but quite possibly the most crucial one. It lends the melody a singing quality that listeners resonate to because it invokes processes in their own body, related to voice production and movement. It is probably a combination of several or all the factors mentioned above, especially vertical dynamics, small asynchronies, smoothness of timing, pedaling, and instrument quality. Perhaps the elusiveness of this quality rests on the fact that it involves nearly all aspects of pianistic skill, in which case it really may not have much explanatory value. Tone and touch may simply be synonymous with complete mastery of the instrument.

Beyond such mastery, the quality of the instrument itself is important. This is demonstrated by BR's ratings of the synthesized performances which confirmed Repp's (1997) observation that digital piano renditions elicit a preference for typical timing patterns. Although there are several possible explanations for this finding (discussed by Repp, 1997, and above), the most plausible one is considered to be the quality of the digital piano sound in combination with the fact that the original performance onto which the timing profiles had been grafted was not of the highest standard. These factors prevented the melody from soaring (i.e., from having the kind of aesthetic impact described metaphorically in the epigraph), and this in turn reduced the listener's tolerance for atypical and original timing patterns. True originality and individuality in performance timing, which often may reflect spontaneity of expression, seem to require a beautiful tone or touch—in other words, supreme skill *and* a fine piano.[11]

The present results then may serve as a reminder that there is still a large gap between objective performance analysis and our understanding of the aesthetic impact of a performance. It is hoped, however, that further research will slowly close this gap.

ACKNOWLEDGMENTS

This research was supported by NIH Grant No. MH-51230. Thanks are due to Manfred Clynes, Nigel Nettheim, and Omer Shomrony for lending their expertise to this project. Address correspondence to Bruno H. Repp, Haskins Laboratories, 270 Crown Street, New Haven, CT 06511-6695; e-mail: repp@haskins.yale.edu

APPENDIX: THE JUDGES' RATINGS OF THE RECORDINGS

BR's ratings represent the average of 10 sessions, those of MC, NN, and OS the average of two sessions each. Some performances were rated by BR only. The entries under BRSYN represent BR's ratings of the synthesized excerpts, averaged over five sessions.

Pianist	BR	MC	NN	OS	BRSYN	Pianist	BR	MC	NN	OS	BRSYN
Aide	6.5	5.5	6.8	7.8	7.6	Koczalski	7.2	6.3	4.8	6.5	3.6
(duplicate)	6.2	6.8	6.8	7.0	7.8	Koyama	7.0	6.0	5.8	6.3	7.2
Anda	7.2	7.9	4.3	3.3	2.8	Kyriakou	6.1	7.0	4.5	4.5	4.8
Anievas	8.0	7.0	4.0	7.0	6.4	Larrocha	5.3	1.5	3.5	5.5	4.6
Arrau—1930	9.2	8.1	6.0	6.3	6.4	Levant	6.6	6.3	4.3	5.0	4.4
Arrau—1956	6.7	6.0	8.0	7.0	7.0	Liberace	4.9	2.8	3.0	4.3	5.4
Ashkenazy—1959	6.0	6.5	5.8	5.8	5.6	Licad	5.8	6.5	4.5	7.3	6.2
Ashkenazy—1974	7.4				7.0	Lopes	8.5	4.3	7.3	5.3	9.0
Backhaus	8.2				7.0	Lortat	6.8	5.0	6.8	6.5	5.2
Badura–Skoda	5.2	3.5	5.8	4.0	5.0	Lortie	6.5				7.6
Berezovsky	8.4	4.8	6.0	8.8	6.8	Magaloff	6.3	3.8	5.3	8.3	6.0
Bingham	6.1	7.8	5.3	9.5	6.8	Magin	9.4	6.8	6.8	4.5	10.0
Binns	8.1	7.5	6.8	8.8	6.6	Malcuzinsky	7.9	4.0	4.5	7.0	6.4
Biret	6.5				4.6	Mamikonian	5.3	4.0	5.3	4.5	5.6
Brailowsky	6.9	4.0	6.8	5.5	8.2	Manz	7.0	3.0	5.3	7.5	6.4
Browning	8.2				5.8	Murdoch	4.8	4.3	5.5	5.0	5.6
Cherkassky	9.6	8.1	7.5	5.0	7.2	Niedzielski	7.9	8.5	5.5	1.5	4.6
Ciani	9.2	9.5	6.5	5.0	6.8	Novaes	6.4	3.0	4.5	6.0	5.0
Ciccolini	6.9	2.0	3.0	4.0	8.4	Paderewski	1.8	2.0	2.8	4.0	2.2
Cliburn	5.4				8.0	Pennario	3.6	1.0	3.0	4.3	3.2
Coop	6.6	2.0	6.3	9.0	7.4	Penneys	7.1	5.5	5.5	8.5	6.4
Cortot—1933	8.3				4.0	Perahia	9.0	8.0	7.5	8.3	6.0
Cortot—1942	7.1	4.0	7.3	5.5	1.4	Perlemuter	6.1				4.0
Costa	6.5	2.8	5.3	4.0	6.6	Pokorna	3.7	2.0	3.3	3.0	5.0
Crown	6.1	2.8	4.8	3.5	5.8	Pollini	7.5				3.8
Cziffra—1954	2.4	2.0	6.8	4.8	2.0	Ranki	6.6	2.3	6.0	6.5	6.8
Cziffra—1981	2.0	1.0	3.3	5.0	2.8	Renard	4.2	5.8	4.5	3.5	2.4
Darré	5.7	4.5	8.3	3.5	4.6	Richter	8.0				7.4
Donohoe	7.8	3.3	6.3	6.8	8.2	Saperton	8.2	8.8	4.0	5.0	4.2
Drzewiecki	7.0	5.3	6.3	7.5	8.0	Sasaki	6.4	4.5	6.0	7.0	5.2
Duchâble	6.1	8.3	6.0	8.5	6.8	Sauer	7.0	8.0	5.0	5.0	3.4
Egorov—1978	7.6				4.8	Schein	7.5	8.0	6.3	6.5	6.8
Egorov—1979	6.4	5.8	6.3	6.8	5.6	Shebonova	7.7	4.5	6.0	8.0	7.4
Ellegaard	7.8	6.4	7.3	6.8	4.8	Simon	7.8	2.8	5.5	8.3	6.4
Entremont	8.6				6.2	Skavronsky	6.1	4.5	6.5	8.5	6.4
Farrell	6.8	7.9	6.5	5.5	6.6	Slenczynska—1956	6.7	2.0	6.5	4.0	6.2
Fou Ts'ong	2.1	1.0	2.5	7.0	1.2	Slenczynska—1975	5.3	1.5	7.5	6.8	6.2
François	4.5	1.0	3.0	5.0	1.6	Slobodyanik	3.7	2.0	4.0	2.0	7.6
Goldenweiser	4.8	1.8	6.0	3.5	7.2	Smith	6.9	6.3	7.0	4.3	3.2
Goldsand	6.7	6.5	6.0	6.0	8.0	Sofronitzky	6.4	2.0	3.8	5.8	3.8
Goodman	6.0	3.0	4.8	7.8	6.4	Solomon	6.7	5.6	7.0	4.5	9.0
Haas, M.	5.9	2.5	5.0	8.0	4.8	Székely	4.3	4.8	6.0	8.5	6.2
Haas, W.	5.3	3.5	5.0	6.5	5.2	Timofeyeva	4.9	3.5	4.8	4.0	4.8
Haase	1.6	1.0	2.5	5.0	2.0	Uninsky	4.1	2.0	7.3	5.8	3.2
Harasiewicz	6.4				5.4	Varsi	1.2	1.0	1.0	3.0	1.2
Hesse–Bukowska	8.3	7.3	7.0	6.8	7.0	Vásáry	6.6				5.4
Hobson	7.9	3.5	7.0	5.0	7.4	Vered	7.5	8.0	7.5	5.5	8.8
Horowitz—1951	7.9				5.2	Virsaladze	7.2	6.8	6.5	6.8	9.2
Horowitz–1972	3.9	6.8	5.3	4.8	2.2	Volondat	4.6	7.5	5.0	8.3	9.0
Iturbi	6.0	4.5	4.0	7.3	6.8	Weissenberg	7.0	4.5	5.0	6.0	8.2
Janis	5.2	2.3	3.5	4.0	2.8	Wild	6.5	7.0	7.3	6.8	6.8
Johannesen	8.0	2.5	6.3	5.0	7.4	Woodward	5.4	7.5	6.3	6.3	6.8
Joyce	6.3	2.5	5.8	4.5	1.8	Woytowicz	8.6	5.5	6.0	5.3	8.8
Kahn	8.8	2.8	6.0	6.5	6.0	Yamazaki	2.7	1.5	4.3	5.3	5.0
Karolyi	7.1	4.5	4.5	7.8	6.4	Yokoyama	7.3	4.3	6.8	9.0	7.8
Katz	8.7	9.0	3.3	6.0	7.0	Zarankin	3.6	6.3	5.0	6.0	6.2
Kentner	8.2	6.1	4.8	7.3	5.0	(duplicate)	4.9	6.5	4.5	4.5	5.8
Kersenbaum	8.0	7.8	6.5	7.0	7.6	Zayas	4.9	1.0	6.0	5.0	4.0
Kilényi	6.8	7.0	6.8	8.0	7.2						

[1]The metronome indication in Fig. 1 is much too fast and must be a misprint. The music was copied from this old German edition because it is the only one that fits the first five bars into a single system.

[2]It should be emphasized that this phrase was evaluated here as an isolated excerpt, not as part of the whole composition. It is conceivable that a beautiful first phrase somehow does not fit with what follows or that a plain first phrase gains in meaning as the music continues. However, any such contextual effects are irrelevant to the present study, as long as generalization of the results to performances of the whole Etude is eschewed.

[3]This was a copy of the digital master tape the author had obtained from the International Piano Archives at the University of Maryland. Two of the performances turned out to be duplicates, but they were included in all analyses.

[4]These excerpts had been retained only as digitized sound files, some of which had a lower sampling rate and thus were not of optimal sound quality. BR felt that this did not influence his evaluations.

[5]In sessions 1–5, BR listened to digitized sound files stored in the computer, which were of slightly lower fidelity than those on the digital master tape. In sessions 6–10, he listened to a digital copy of the master tape (with randomly changed track numbers, so as to disrupt any memory for earlier judgments associated with particular serial numbers), except for the 15 additional excerpts, to which he still listened as computer files, going back and forth between tape recorder and computer, as necessary.

[6]Small differences from the timing of the originals may have arisen from two sources. First, the IOI measurements of the original excerpts (Repp, 1998) contained some human error, although it was believed to be well below the perceptual discrimination threshold. If there were any larger errors, they would have occurred in the timing of the accompaniment notes (which are more difficult to measure because of their low intensity) and would have been perceptible as a momentary irregularity, but BR heard very few such instances in the synthesized versions and believes they had little impact on his aesthetic judgments. Second, due to a peculiarity of the software used for playing the synthesized versions (MAX), the tempo of the synthesized excerpts was 2.4% faster than that of the originals. However, this affected all excerpts equally and thus should have had little effect on their relative aesthetic impressions. Another possible concern was that the synthesized excerpts ended with a prolonged chord, so that the final IOI of an imported original timing profile was not contextually appropriate (a longer IOI would be expected before a final chord). However, this, too, is unlikely to have had any effect on the overall aesthetic impression, which mainly derived from the timing of the passage as a whole.

[7]It would have been nice to construct an analogous set of synthesized performances varying in expressive dynamics only. However, this turned out to be problematic, due to the fact that only horizontal dynamics (the succession of overall peak sound levels) had been measured in the original excerpts. To construct synthesized performances from these measurements, the relative intensities of the individual notes in simultaneities (vertical dynamics) would have had to be estimated somehow, and it seemed unlikely that this could be done very accurately. Therefore, this possibility was not pursued further.

[8]The fastest performance in the sample, by Dinorah Varsi, was a true outlier in the tempo distribution (see Repp, 1998: Fig. 2) and received very low ratings from all four judges. When this performance was omitted, the correlations were slightly smaller, and that for NN fell short of significance.

[9]No separate tests were conducted to determine the significance of the improvement.

[10]In the terminology of Repp (1999), the constant dynamic profile of the synthesized performances was of Type II–III. (Its dynamic PC-II and PC-III loadings were 0.50 and 0.49, respectively, and its correlation with the average of PC-II and PC-III was 0.70.) Thus original performances with a Type I dynamic profile indeed ''lost'' this profile in their synthesized incarnations.

[11]An interesting prediction following from these considerations is that artists who play with very individual expression on a concert grand may adopt a more conventional style on a poor instrument, such as a digital piano. The quality of the instrument may affect artistic originality and spontaneity.

Berry, W. (**1989**). *Musical Structure and Performance* (Yale University Press, New Haven, CT).

Clarke, E. F. (**1985**). ''Structure and expression in rhythmic performance,'' in *Musical Structure and Cognition*, edited by P. Howell, I. Cross, and R. West (Academic, London), pp. 209–236.

Cook, N. (**1990**). *Music, Imagination, and Culture* (Clarendon, Oxford, U.K.).

Levinson, J. (**1990**). ''Evaluating musical performance,'' in *Music, Art, and Metaphysics* (Cornell University Press, Ithaca, NY), pp. 376–392.

Levinson, J. (**1997**). *Music in the Moment* (Cornell University Press, Ithaca, NY).

Palmer, C. (**1989**). ''Mapping musical thought to musical performance,'' J. Exp. Psychol. HPP **15**, 331–346.

Palmer, C. (**1996**). ''On the assignment of structure in music performance,'' Music Percept. **14**, 23–56.

Repp, B. H. (**1994**). ''On determining the basic tempo of an expressive music performance,'' Psychol. Music **22**, 157–167.

Repp, B. H. (**1997**). ''The aesthetic quality of a quantitatively average music performance: Two preliminary experiments,'' Music Percept. **14**, 419–444.

Repp, B. H. (**1998**). ''A microcosm of musical expression: I. Quantitative analysis of pianists' timing in the initial measures of Chopin's Etude in E major,'' J. Acoust. Soc. Am. **104**, 1085–1100.

Repp, B. H. (**1999**). ''A microcosm of musical expression: II. Quantitative analysis of pianists' dynamics in the initial measures of Chopin's Etude in E major,'' J. Acoust. Soc. Am. **105**, 1972–1988.

Scruton, R. (**1997**). *The Aesthetics of Music* (Oxford University Press, Oxford, U.K.).

Shaffer, L. H. (**1995**). ''Musical performance as interpretation,'' Psychol. Music **23**, 17–38.

Sherman, R. (**1997**). *Piano Pieces* (North Point Press, New York).

Sloboda, J. (**1998**). ''Does music mean anything?'' Musicae Scientiae **2**, 21–31.

Thompson, W. F., Diamond, C. T. P., and Balkwill, L.-L. (**1998**). ''The adjudication of six performances of a Chopin Etude: A study of expert knowledge,'' Psychol. Music **26**, 154–174.

Todd, N. P. McA. (**1995**). ''The kinematics of musical expression,'' J. Acoust. Soc. Am. **97**, 1940–1949.

Wapnick, J., Flowers, P., Alegant, M., and Jasinskas, L. (**1993**). ''Consistency in piano performance evaluations,'' J. Res. Music Educ. **41**, 282–292.

Cortical representation of spatiotemporal pattern of firing evoked by echolocation signals: Population encoding of target features in real time

Mathew J. Palakal[a)]
Department of Computer Science, Indiana University Purdue University Indianapolis, Indianapolis, Indiana 46202

Donald Wong
Department of Anatomy, Indiana University School of Medicine, Indianapolis, Indiana 46202

(Received 1 December 1998; accepted for publication 31 March 1999)

Target perception in echolocating bats entails the generation of an acoustic image of the target in the auditory cortex. By integrating information conveyed in the sequence of acoustic echoes, the population of cortical neurons in hypothesized to encode different target features based on its spatiotemporal pattern of neural-spike firing during the course of echolocation. A biologically plausible approach to the cortical representation of target features is employed by using electrophysiological data recorded from the auditory cortex of the FM bat, *Myotis lucifugus*. A single-neuron model of delay-sensitive neurons is first approximated by the formulation of a Gaussian function with different variables to represent the delay-tuning properties of individual cortical neurons. A cortical region consisting of delay-sensitive neurons organized topographically according to best frequency (i.e., tontopically organized) is then modeled with multiple layers of the single-neuron model. A mechanism is developed to represent and encode the responses of these neurons based on time-dependent, incoming echo signals. The time-varying responses of the population of neurons are mapped spatially on the auditory-cortical surface as a *cortical response map* (CORMAP). The model is tested using phantom targets with single and multiple glints. These simulation results provide further validation of the current auditory framework as a biomimetic mechanism for capturing time-varying, acoustic stimuli impinging in the bat's ears, and the neural representation of acoustic stimulus features by saptiotemporal-firing patterns in the cortical population. [S0001-4966(99)02407-8]

PACS numbers: 43.80.Gx, 43.80.Jz [WWLA]

LIST OF SYMBOLS

σ	delay width
β	BD of a neuron
δ	echo delay
i	frequency channel
τ	inhibition factor

INTRODUCTION

Echolocating bats use biosonar to perceive their target as an auditory image by extracting cues from the target-reflected echoes of their emitted pulses (see Popper and Fay, 1995 for recent review). A central question in target perception is how bats derive different target information from temporally spaced echoes reflected from a unitary target. For accurate target ranging, bats depend critically on the orderly time-frequency structure in the broadband FM signal (Surlykke, 1992). In discrimination of target structure, FM bats may derive temporal cues conveyed in the complex echo waveform of real targets by the different ranges that separate multiple-target surfaces (glints) Beuter, 1980; Simmons and Chen, 1989; Simmons *et al.*, 1990). Other behavioral experiments suggest that FM bats perceive real targets by the spectral notches and peaks created in the complex echo waveform by a multiglint target (Bradbury, 1970; Griffin, 1967; Habersetzer and Vogler, 1983; Mogdans and Schnitzler, 1990; Schmidt, 1988).

To gain an understanding of target perception, a number of theoretical signal-processing approaches have been used for developing bat sonar models. These approaches can generally be classified into three categories: (i) development of signal-analysis techniques to identify information-bearing parameters from the signal, and using such parameters for target identification; (ii) development of learning and classification models such as artificial neural networks for target identification; and (iii) complete biosonar models that mimic biological echolocation systems. For example, Altes (1975, 1985) developed several signal-processing algorithms for biosonar-signal classification and mapping of target shapes. Artificial neural-network models can then be used for target recognition for both airborne and underwater sonar. These neural-network models used time-domain information (Chang *et al.*, 1993), frequency-domain information (Moore *et al.*, 1991; Roiblat *et al.*, 1989) and both time- and frequency-domain information (Gorman and Sejnowski, 1988). Neural networks for three-dimensional target recognition were also developed by incorporating information about first and second harmonics in addition to time- and

[a)]Electronic mail: mpalakal@cs.iupui.edu

frequency-domain information in the network (Dror *et al.*, 1995).

Currently, there are two biomimetic models of complete sonar systems developed from signal-processing approaches. The spectrogram correlation and transformation (SCAT) model, based in large part on behavioral studies on the FM bat, *Eptesicus fuscus*, mimics an artificial bat sonar receiver (Simmons *et al.*, 1992). It has three stages: a front end that mimics the inner ear, a set of delay lines to encode echo delays, and a system that determines both the echo spectrum and time separation between echoes. These three stages broadly accomplish two important signal-processing tasks: spectrogram correlation and transformation. The output of the SCAT model is an estimate of target range and shape. The biomimetic sonar systems developed by Kuc (1997) is yet another engineering model that tries to mimic biological echolocation systems. This system essentially has a center transmitter flanked by two adjustable receivers mounted on the ends of the robot arms. The arms adaptively change their position in response to echoes for object recognition. The system accomplishes this task by incorporation both signal processing and artificial neural-network models.

Although the design of artificial sonar systems has clearly been advanced by signal-processing and modeling approaches, such systems using strictly engineering models shed little light onto how the bat's auditory system is uniquely specialized for processing its sonar signals, and how target attributes are encoded and represented in its brain. Thus, to bridge the gap between engineering and biological systems, a biologically plausible, biosonar framework was developed in which various components of the framework are directly derived from available electrophysiological data. Systems conceived in this manner could not only achieve the performance of conventional engineering models, but could also provide a valuable research tool for both validating current and guiding future behavioral and electrophysiological studies.

To date, echolocating bats have provided an excellent *animal* model for neurophysiological studies into complex-sound processing of identified stimulus features at higher centers of the auditory pathway (Popper and Fay, 1995). A major focus in understanding target perception has been to characterize the functional organization of the bat's auditory cortex (for review, see Suga, 1988; O'Neill, 1995). Specifically, single-unit recordings have probed the tuning of cortical neurons to different stimulus parameters of the biosonar signal and mapped the topographic organization of functional subregions specialized for processing particular target features. In the FM bat, *Myotis lucifugus*, cortical neurons were found to be sensitive to echo delay (Sullivan, 1982; Wong and Shannon, 1988) and the rate of change in echo-delay velocity (Tanaka and Wong, 1993); thus, it has been postulated that delay-sensitive neurons in this species code for both target distance and relative velocity. Moreover, neurons in *Myotis* cortex were also sensitive to the amplitude and frequency modulations of echoes (Condon *et al.*, 1997). Since such echo modulations mimic fluttering targets (e.g., insects), this neural sensitivity provides a basis for coding insect wingbeat, and thus target-prey selection (for review, see Schnitzler, 1987). On the basis of the sensitivity of cortical neurons to multiple stimulus features, which serve as cues for different target attributes, these neurons in *Myotis* cortex have the capacity for multidimensional target analysis.

The spatiotemporal pattern of neural-spike firing in the bat's auditory cortex has been hypothesized to provide for a neural representation or image of the target (Suga, 1990). From a computational perspective, it is conceivable that the spectrotemporal cues extracted from the sonar sounds by the cortical population are sufficient for reconstructing a unified target image. The objective of this study is to develop a computational model to depict the neural activity in the auditory cortex under stimulus conditions simulating echolocation of a *single* target. Specifically, this modeling study displays the spatiotemporal-firing pattern evoked by biosonar stimuli in a cortical population with response properties previously characterized neurophysiologically in *Myotis lucifugus*. Whereas the auditory cortex of CF-FM bats is comprised of multiple functional subregions with separate population differing in response properties, the auditory cortex of this FM bat consists primarily of a tonotopic area with delay-sensitive neurons. Furthermore, the response properties of these neurons are dynamically shaped under stimulus conditions simulating the changes in the sonar-emission pattern during echolocation. Thus, the population-firing pattern in this model could be tracked in a single region during the different stages of echolocation when target-feature encoding is accomplished using multiresolution.

I. FRAMEWORK OF THE MODEL

A. Background

The modeling framework is based on three major neurophysiological findings concerning the functional organization of the *Myotis* auditory cortex. First, delay-sensitive neurons comprised a large majority of neurons in the auditory cortex. These cortical neurons exhibit facilitative responses to artificial pulse–echo stimulus pairs presented at particular echo, and are temporally tuned to specific best delays (BDs) that evoke maximal facilitation (Sullivan, 1982; Wong and Shannon, 1988). Second, neurons in the auditory cortex are tonotopically organized according to their best frequency (BF) ranging from 20 to 100 kHz (Paschal and Wong, 1994a). Third, the delay-tuning properties of these cortical neurons are dependent on the pulse repetition rate (PRR) (Wong *et al.*, 1992) and pulse duration (PD) (Tanaka *et al.*, 1992).

The overall objective of this study involves two stages. First, the response properties of delay-sensitive cortical neurons are modeled (single-neuron model). Second, a population is created from the single-neuron model to represent the sound-evoked cortical responses, termed *cortical response map* (CORMAP), a multidimensional representation of time-frequency-delay-response. A preliminary CORMAP version showed how the responses of cortical neurons tuned to different sound frequencies varied with changes in PRR and PD inputs (Palakal *et al.*, 1995). The current CORMAP framework uses a spike-train pattern as an input arising from the

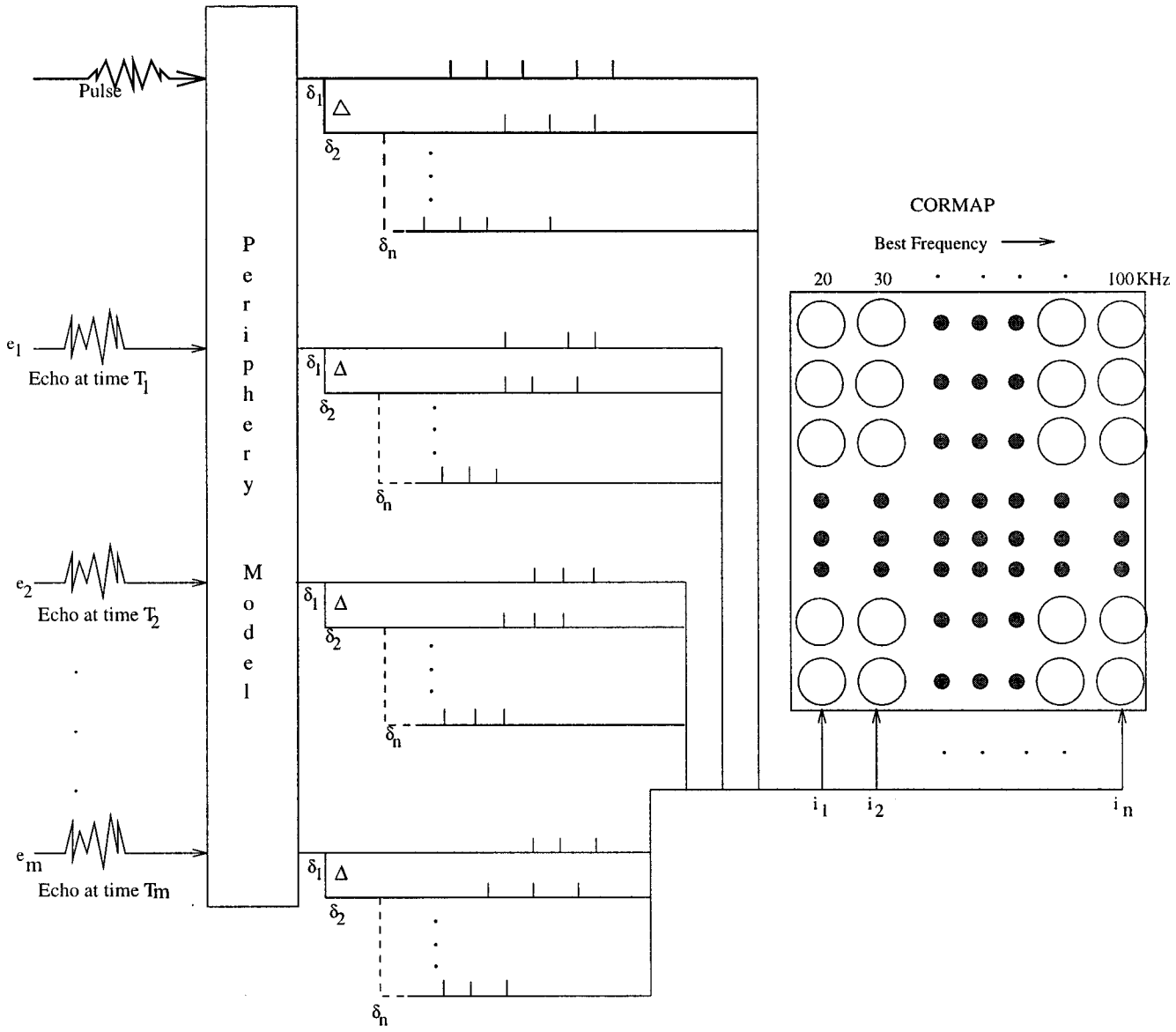

FIG. 1. The overall scheme of the auditory-system model consisting simply of the periphery and CORMAP frameworks. The acoustic inputs to the peripheral model are the outgoing (''emitted'') pulse signal and the multiple components of the echo signal returning from a complex target ($e_1, e_2, \ldots, e_m$ is the different echo-signal components reflected from an m-glint target at $T_1, \ldots, T_m$ time, respectively). The neural spike trains are generated as outputs by the peripheral model, and in turn provide the neural inputs into the CORMAP framework. The neural-spike activity evoked by each sound-signal component is represented by n individual time traces of spike firing, of which each is the firing pattern associated with a different sound-frequency channel. The fine delays ($\delta_1, \delta_2, .., \delta_n$ separated by Δ) of the different signal components are also represented in the different frequency channels. The CORMAP depicts the tonotopically organized cortical neuronal population shown here as circles. Subpopulations tuned to different best-frequency (20–100 kHz) are shown to receive only spike-firing inputs transmitted from the same frequency channel ($i_1, i_2, \ldots, i_n$).

periphery auditory system (Chittajallu and Kohrt, 1995).

The mathematical formulation of a delay-sensitive neuron is a critical first step in developing CORMAP. A single delay-sensitive neuron is modeled as a black box to receive a specific input, a spike train, and to produce the desired output, the magnitude of facilitative response. This simpler design is easier to implement than the more complex neurophysiological mechanism. The capability of the response map for the cortical population to estimate the different target characteristics would then be assessed.

The complete framework of the auditory system is comprised of the periphery model and the CORMAP (Fig. 1) In the periphery model, the inputs are the pulse and echo signals, and the output is a neural spike train evoked by the sound pair. Each echo contains n components with constant interspike-interval δ, which is equal to 1/*sampling frequency*. This spike-train pattern is the input to the CORMAP.

B. Basic assumptions about the CORMAP framework

The design of the framework is based on the following assumptions:

(i) The target distance is coded from the time interval (delay) between the outgoing pulse and incoming echo (Simmons *et al.*, 1975; Schnitzler and Henson, 1980; Schintzler, 1984).

(ii) Targets are stationary with no Doppler shift in the target-reflected echoes.

(iii) The target-reflected echo is an exact replica of the emitted pulse with simply a shift in time to introduce echo delay.
(iv) A pulse stimulus evokes an early inhibitory response followed by a later excitatory response in delay-sensitive cortical neurons (Berkowitz and Suga, 1989; Olsen and Suga, 1991).
(v) The pulse-evoked inhibition in cortical delay-sensitive neurons varies in duration among individual delay-sensitive neurons (Berkowitz and Suga, 1989; Olsen and Suga, 1991).
(vi) Cortical delay-sensitive neurons are both temporally tuned to particular BDs and topographically organized according to their best frequency (BF) in a functional region of auditory cortex (for different bat species, see O'Neill, 1995).
(vii) Every signal pair consists of a pulse followed by an echo with one or more glints.

C. The periphery model

The peripheral auditory system consists of the ear (outer, middle, and inner) and the cochlear nerve projecting to the brain. The peripheral auditory system in mammals, including bats, involves transduction of airborne vibrations (sounds) at the sensory hair-cell level and transmission of a neural-firing pattern from the population of cochlear-nerve fibers into the brain, where the acoustic signal is interpreted meaningfully.

The auditory periphery was previously modeled with the basilar membrane represented as a bank of 20 butterworth bandpass filters with constant Q-value 4 and center frequencies used by *Myotis* (Chittajallu and Kohrt, 1995; Shimozawa *et al.*, 1974). The first and last filters have center frequencies at 25 and 100 kHz, respectively, and intermediate filters spaced linearly according to the center period. The hair-cell processing was based on a hair-cell model (Meddis, 1988) that simulates data from gerbils and compares well with the other hair-cell models (Meddis, 1988; Chittajallu *et al.*, 1996).

The pulse and echo signals were generated with a sampling frequency of 250 kHz, and each signal sweeps from 100 to 20 kHz. A typical pulse–echo processing at the auditory periphery is shown in Fig. 2. The pulse signal has duration of 1.0 ms [Fig. 2(a)], and the echo signal has an echo delay of 1.2 ms [Fig. 2(b)]. The pulse–echo inputs to the peripheral model generate a spike-train pattern from different frequency channels over time [Fig. 2(c)]. The *Myotis* biosonar pulse is simulated by a linear period-modulated signal sweeping hyperbolically downward from 100 to 20 kHz with duration of 1 ms. Since the target is one or more points distributed along the range axis, a compound echo is created by several overlapping pulses delayed in time, of which the number of overlapping components determines whether the echo has a single- or multiple glints. The pulse–echo delay is the delay of the first echo glint from the pulse. In Fig. 2(d), the spikes show the echo components for frequency channels 10 and 22.

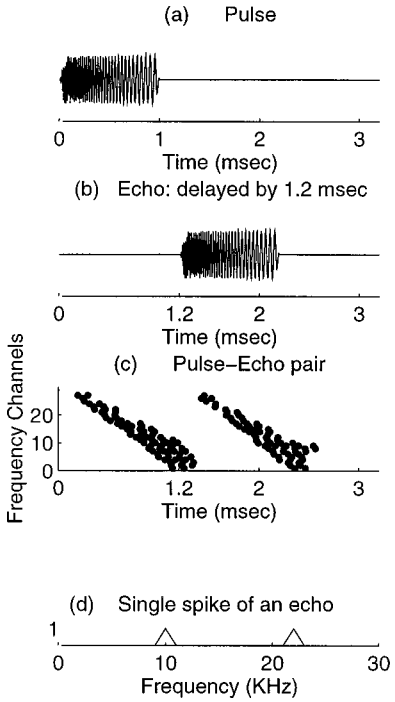

FIG. 2. Pulse–echo processing at the auditory periphery: (a) Pulse signal with duration of 1 ms sweeping downward from 100–20 kHz. (b) Echo signal is an exact copy of the pulse and delayed from the pulse by 1.2 ms. (c) Neural spike train generated by the peripheral model from pulse–echo signals. (d) A sample spike-train pattern evoked in the periphery by a single echo component at δ ms. As shown here, the spikes are transmitted only along frequency channels at 10 and ~22 kHz.

D. Model of a delay-sensitive neuron

The delay-tuning properties of a neuron can be determined from its delay-tuning curves. A neuron's delay-tuning curve is a response property defined by the probability of the neural facilitative response for different values of echo delay. Based on these delay-tuning properties, a delay-sensitive neuron can be classified as *delay-tuned* or *tracking*. Delay-

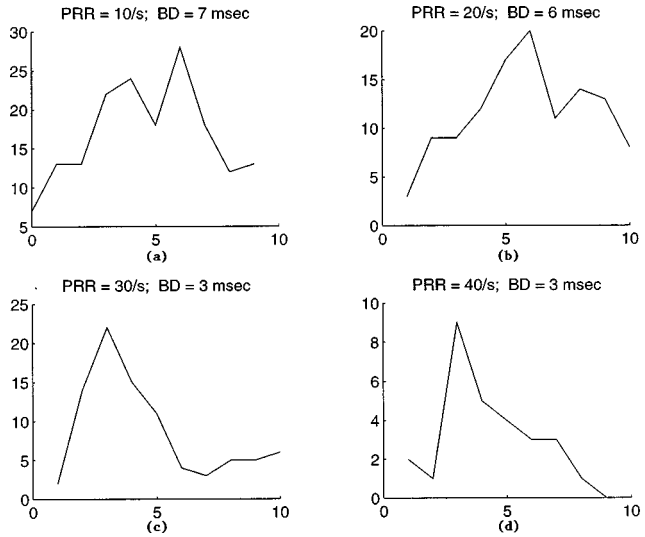

FIG. 3. Delay-tuning curves of a neuron in the tonotopic part of the *Myotis* auditory cortex as PRR was increased (PD was fixed). (Wong *et al.*, 1988): Neuron exhibits broad delay tuning at low PRR (a) and a sharper delay tuning at higher PRR (c).

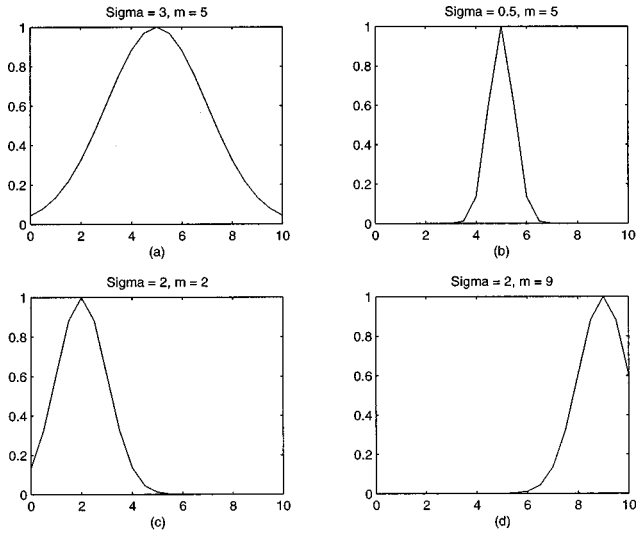

FIG. 4. First-order approximation of delay-tuning curves generated from a Gaussian function. (a) Shows an ideal Gaussian curve for $\sigma=2$, $m=5$, and the value of x ranges from 0 to 10. The influence of m and σ on the Gaussian function [(b)–(d)] is similar to the influence of PRR and PD on delay-tuning curves measured neurophysiologically (see Fig. 3).

tuned neurons have BDs that remain constant as PRR is changed, whereas the BDs of tracking neurons become shorter as PRR is increased. Figure 3(a) shows representative delay-tuning curves measured electrophysiologically (Wong *et al.*, 1992; Paschal and Wong, 1994a, b). The delay-tuning curve of a neuron exhibits its magnitude of facilitative responses at different echo delays. Another delay-tuning characteristic of a neuron is its *delay width*, the range of echo delays at which a neuron exhibits facilitative responses. A neuron can be sharply tuned [Fig. 3(c)] or broadly tuned in delay [Fig. 3(a)]. Since PRR and PD shape the delay-tuning characteristics of neurons, changes in the PRR and PD of the pulse signal would modify the delay-tuning characteristics of individual neurons.

The shape of the delay-tuning curve can be approximated by the Gaussian function of the form,

$$y(x)=e^{-(x-m)/2\sigma^2}, \tag{1}$$

for $x\geqslant 0$ and $\sigma>0$.

The ideal Gaussian curve [Fig. 4(a)] has an output function, $y(x)$, which approaches unity as x approaches m, and which diminishes as x becomes progressively larger than m. The radius of the Gaussian spherical field changes with variation in the variance, σ. The radius decreases as σ^2 decreases. By varying the term m, the peak of the curve can be shifted in time. Figure 4(c) and (d) show different curves for different values of m and σ. Thus, the Gaussian curve can change in shape and shift in time with variation in parameters m and σ.

Variations of m and σ have an effect on the Gaussian curves that is similar to variations of stimulus PRR and PD on the neurophysiologically measured delay-tuning curves. Variation in PRR influences the shape of the delay-tuning curve in a manner similar to variation of σ on the Gaussian curve. The BD of a neuron changes as PD is changed. Variation in m shifts the peak of the Gaussian curves in time (Fig. 4). Therefore, the shape of the Gaussian curve can be considered as a first approximation of a neuron's delay-tuning curve, and the Gaussian output function can be considered as a first approximation of the facilitative response magnitude. In particular, the output function of a neuron can be estimated as

$$y(\delta)=e^{-i*(\beta-\delta)^2/2*\sigma^2}, \tag{2}$$

where β is the best delay (BD) of the neuron, δ is the echo delay, i is the frequency channel (spike-train patterns of 0's and 1's arrive at each channel i as input to the neuron), and σ is the delay width.

Equation (2) shows that the output of the delay-sensitive neuron model approach unity as the term inside the parentheses approaches zero. Since σ is constant and the input, i, cannot be zero for a neuron to respond, the term $(\beta-\delta)=0$. This implies that the response magnitude of a neuron approaches unity as $\delta\rightarrow\beta$, and becomes maximal when $\delta=\beta$. This is consistent with neurophysiological results that reveal a maximal facilitative response is evoked in a neuron for echo delays at or near its BD.

The inhibitory effect of a neuron [assumption (iv)] is modeled by further modification of Eq. (2) as

$$y(\delta)=\tau*e^{-i*(\beta-\delta)^2/2*\sigma^2}, \tag{3}$$

where τ is the inhibition factor measured in time.

Figure 5 shows the input/output characteristics of the delay-sensitive neuron model. Its inputs are the pulse- and echo-evoked spike-train pattern. The neuron responds if the echo arrives at facilitative echo delays within the delay width, σ. A maximal response is evoked if the echo signal arrives at the neuron at an echo delay, δ, equal to the neuron's BD, β. The output of the neuron is calculated using Eq. (3). Based on this mathematical model for a single neuron, an entire cortical population is constructed into a framework to represent an auditory response map.

E. Pulse–echo processing using CORMAP

Inputs to the CORMAP are the neural spike-train patterns generated by the peripheral auditory system in response to the pulse and echo signals. When the spike train corresponding to the pulse arrives, all neurons tuned to the pulse frequency spectrum enter an initial inhibition state followed by excitation. Neurons tuned to different sound frequencies are inhibited at different times. Figure 6 shows the time-frequency relationship of the pulse–echo signal pair. The pulse is a linear period-modulated signal sweeping hyperbolically downward from 100 to 20 kHz with sweep duration of 1 ms. The sampling frequency is 250 kHz. The interspike interval, Δ, is

$$\frac{1}{\text{sampling frequency}}=\frac{1}{250}\ \text{ms}=0.004\ \text{ms}. \tag{4}$$

The process of obtaining spectral cues from the neural spike-train pattern is as follows:

(1) Let t be the time at which the first pulse is emitted. When the spike train corresponding to the pulse arrives at the CORMAP, the neurons enter an inhibitory state. The re-

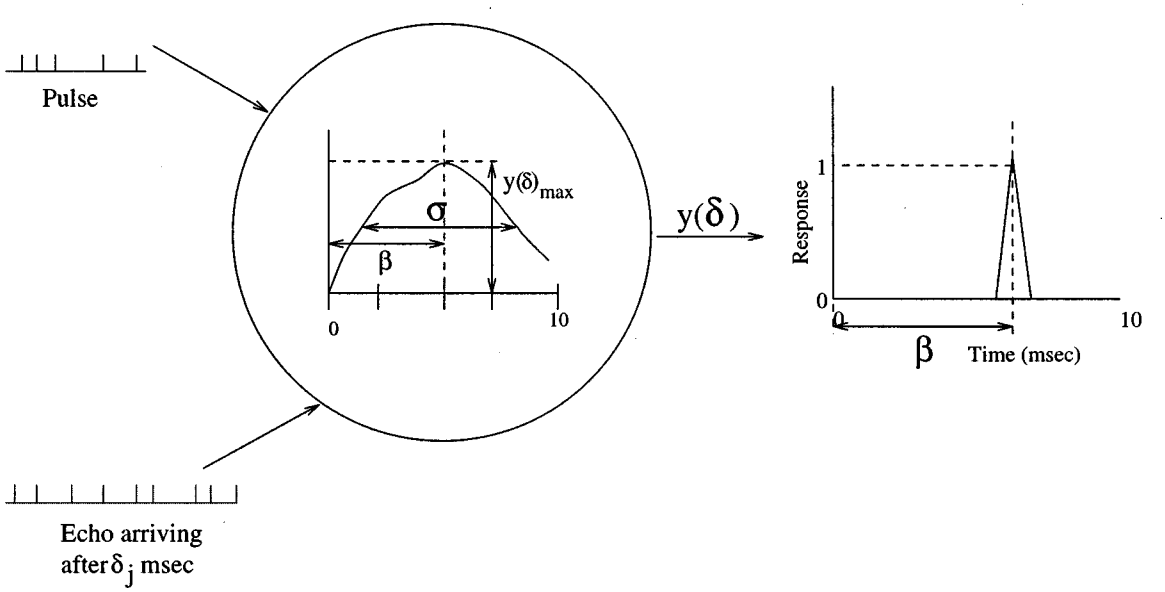

FIG. 5. Delay-sensitive-neuron model showing the input/output characteristics. The cortical neuron responds only in the window σ and a maximal response is evoked for an echo arriving at the neuron's BD, β. A submaximal response is evoked if the input spike arrives at a delay that is greater or less than β but at values within the σ window.

sponse magnitudes of the cortical population at this instance are given by

$$y(t)=\tau^{*}e^{-i_1^{*}(\beta-t_1)^2/2^{*}\sigma^2}, \tag{5}$$

where τ is the inhibition factor which allows the model to distinguish between a pulse and an echo. This term is given by

$$\tau=\begin{cases}1 & \text{if } \gamma=\sum_{i=0}^{\mathrm{PD}} i+\Delta\geqslant \mathrm{PD},\\ 0 & \text{otherwise.}\end{cases} \tag{6}$$

If $\tau=0$, then the signal is a pulse, otherwise it is an echo. In this model, the pulse duration PD is fixed at 1 ms.

(2) Once the pulse finishes arriving at the CORMAP, the echo train corresponding to echo signal will begin to arrive. Pulse–echo overlap is not considered in this version of CORMAP. Let the input at channel i_n represent the highest-frequency component of the echo, and δ_1 (ms) represents echo delay of neurons tuned to this echo-frequency component. Then, the response of those neurons tuned to this delay is calculated as

$$y(\delta_1)=\begin{cases}\tau^{*}e^{-i_n^{*}(\beta-\delta_1)^2/2^{*}\sigma^2}\\ \quad \text{if } (\beta-\sigma/2)\leqslant\delta_1\leqslant(\beta-\sigma/2),\\ 1 \quad \text{if } (\beta=\delta_1),\\ 0 \quad \text{otherwise.}\end{cases} \tag{7}$$

Equation (7) states that a facilitative response is evoked in a neuron by a pulse–echo pair, if the echo arrives at facilitative echo delays, i.e., echo delays within the delay width (σ), the facilitative response is maximal at BD (β)$=\delta_1$.

(3) Let the input at channel i_{n-1} represent the second-highest-frequency echo component and δ_2 represent its echo delay for neurons tuned to this echo-frequency component. This echo-frequency component at i_{n-1} is delayed from i_n by a time interval Δ. For all cortical neurons frequency tuned to echo component i_{n-1}, their facilitative response magnitude is maximal for $\beta=\delta_2$. Let this response be

$$y(\delta_2)=\begin{cases}\tau^{*}e^{-i_{n-1}^{*}(\beta-\delta_2)^2/2^{*}\sigma^2}\\ \quad \text{if } (\beta-\sigma/2)\leqslant\delta_2\leqslant(\beta-\sigma/2),\\ 1 \quad \text{if } (\beta=\delta_2),\\ 0 \quad \text{otherwise.}\end{cases} \tag{8}$$

(4) Thus, for the first echo that is received at time T_1, the i_n^{th} echo-frequency component has an echo delay of δ_1, and $y(\delta_1)$ is the response magnitude of a cortical neuron whose BD$=\beta_1$.

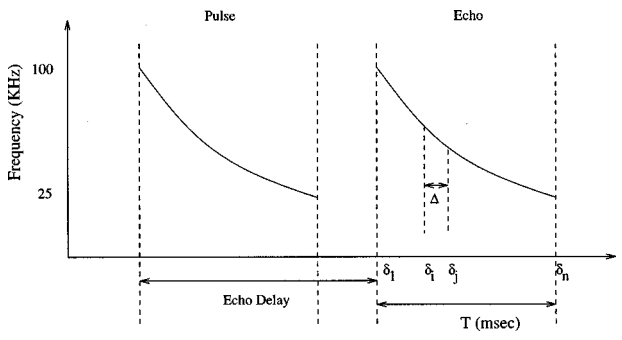

FIG. 6. Frequency sweep in time of a typical pulse–echo pair. The pulse signal sweeps hyperbolically downward from 100 to 20 kHz. The critical parameters shown are δ (represent the actual arrival times of the different echo components), Δ (interspike interval), and T (echo duration). The echo delay (time interval between pulse and echo signal onset) is a measure of target distance.

Therefore, the collective response magnitude, $y(\delta_1)$, $y(\delta_2),\ldots,y(\delta_n)$ constitutes the spatiotemporal firing of the cortical population which constitutes the neural representation of the target generated at time T_1 (Dear *et al.*, 1993). A typical target may consist of several such echo components arriving at different times. Hence, the target-image construc-

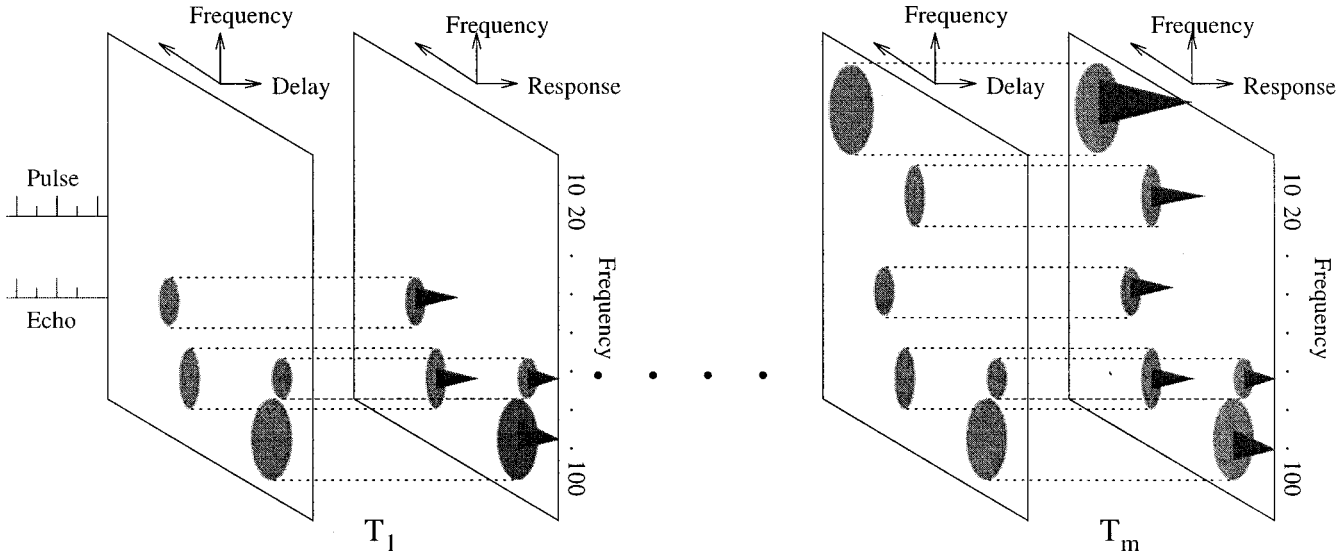

FIG. 7. Illustration of neural-image formation in CORMAP. Each window pair shows the four-dimensional representation of CORMAP in time, frequency, delay, and response magnitude. Each window pair shows neurons that respond when their best frequency and best delay matches the CORMAP inputs in frequency and echo delay. T_1 corresponds to the first echo that is received for a constant PD and PRR. The first window in a pair depicts a subpopulation of neurons (circles) in which both their BF (vertical position of circle) and BD (circle size) matches the delay and frequency of the CORMAP input at T_1. The second window shows the response magnitude of each neuron (peak height of cones on each circle). Over a period of time during the echolocation process, $T_1,\ldots,T_m$ represent the temporal snapshots of the target-reflected echoes that are neurally represented by CORMAP. At time T_m, note that a different subpopulation of neurons with different BDs is responding.

tion is a process that continues for target-reflected echoes returning at times $T_1,T_2,\ldots,T_m$. The continuous-image reconstruction represented neurally by the composite cortical responses evoked by echoes impinging on the ears at times $T_1,T_2,\ldots,T_m$ can be considered as a neural image produced by the particular target under consideration. This process is illustrated in Fig. 7.

II. SIMULATION RESULTS

The CORMAP was tested using different pulse–echo pairs of phantom targets. For every pulse, a known number of echoes is created at known echo delays to mimic the phantom targets. If an input consists of only one echo for a given pulse, then it is considered as a *one*-glint echo. Echoes from multiple points on the target surface produce *multiple*-glint echoes.

A. Single- and multiple-glint experiments

The CORMAP framework used for simulation consists of 100×30 neurons organized tonotopically and delay-tuned to particular BDs. The neurons are not organized according to the BD. There are 30 frequency channels with each channel comprised of 100 neurons (Fig. 8). The 30 frequency

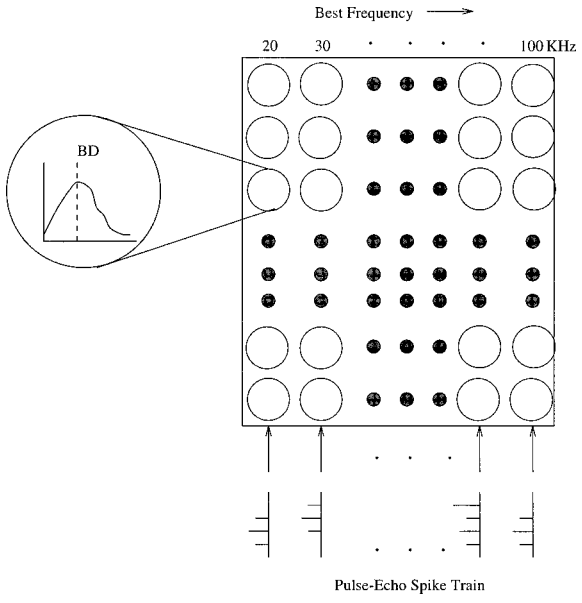

FIG. 8. The CORMAP framework used for simulation. The cortical population contains 100×30 neurons: 30 frequency channels with 100 neurons per frequency channel. Each neuron is tonotopically organized according to its BF and tuned to a particular BD for a constant PRR and PD.

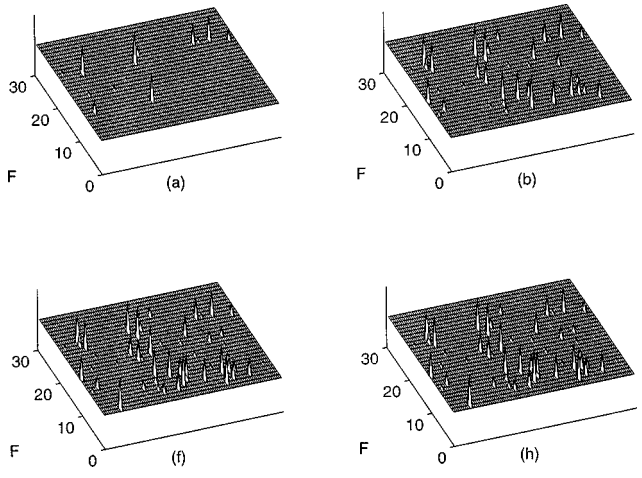

FIG. 9. Response profiles of the CORMAP model generated at different times from the one-glint experiment. Four of the nine snapshots [(a)–(h)] are shown with (h) representing the final accumulated response map. In these plots, the *y*-axis represents the frequency channels along which neurons are aligned according to their best frequency, whereas the *x*-axis has no significance, since delay-sensitive neurons in this species are not topographically organized according to their BD.

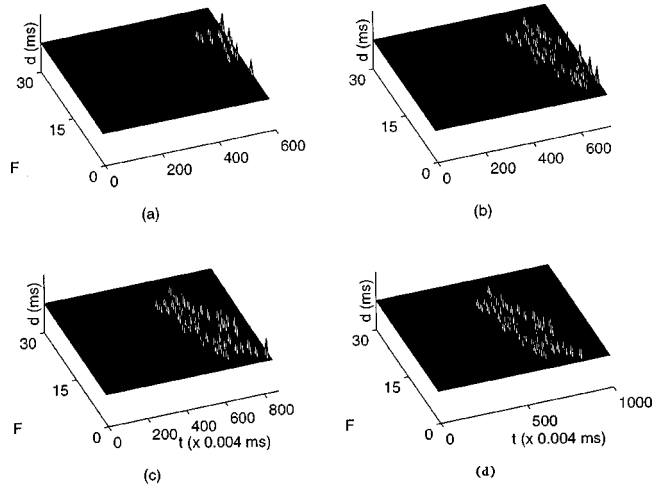

FIG. 10. The response profiles of CORMAP in Fig. 9 are replotted according to *delay* in the three-dimensional map after echo processing is completed. The *x*, *y*, and *z* coordinates correspond to time, frequency, and delay. (a) Shows the response profile of CORMAP to the first component of the echo signal, a neural display encoding target distance. The individual peak heights correspond to delay values of responding neurons.

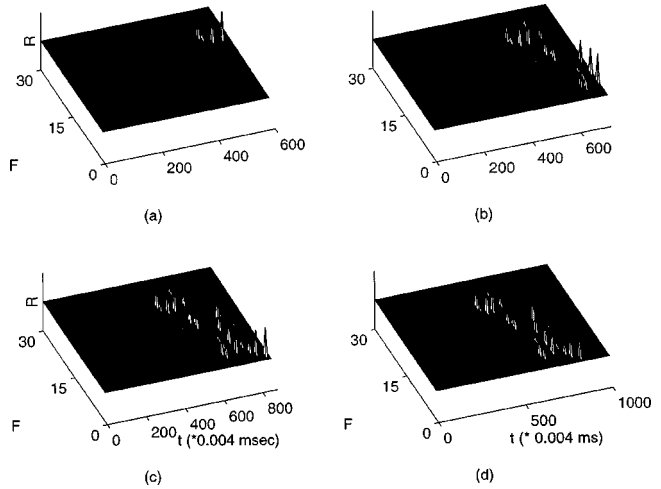

FIG. 11. The response profiles of CORMAP in Fig. 9 are replotted according to *response magnitude* in the three-dimensional map. The *x*, *y*, and *z* coordinates correspond to time, frequency, and response magnitude (R). The individual peak heights of responding neurons provide a relative measure of their maximal or submaximal response magnitudes.

channels span a frequency range of 100–20 kHz and the 100 neurons provide a range of different BDs.

Figure 9(a), (b), (f), and (h) shows the activity of neurons in the CORMAP produced by a pulse signal with a duration of 1.0 ms and an echo signal generated from a single phantom target signal and arriving with an echo delay of 1.2 ms. The pulse train generated by the periphery is first presented to the CORMAP model. When the pulse-evoked spikes arrives, neurons enter an inhibitory state at different times depending on their best frequency. The CORMAP automatically differentiates the pulse from an echo, based on the inhibition property of the neurons. The time at which a neuron is inhibited is considered its delay. Thus, if input is present in a neuron after inhibitory recovery, a maximal facilitative response is evoked in that neuron. For a neuron, $y_{p,q}$ in the grid, the output is given by Eq. (7). After pulse emission, the response $y(\delta)$ of the neurons in the layer represents different fine-delay components of the target [Fig. 9(a)]. These responses form a neural image of the target up to a specific time, δ. After Δ ms later, a different subpopulation responds to the echo by forming a new image [Fig. 9(b)]. These new responses represent the fine-delay components that take even longer to arrive. Several such ''snapshots'' were taken during the entire processing of the echo signal, four of which are shown in Fig. 9. The last snapshot, [Fig. 9(h)], shows all neurons that responded to the entire echo signal. The neurons in Fig. 9 are organized according to their BF and, hence, only the frequency axis is significant here.

Figures 10 and 11 show snapshots of CORMAP activity with the neurons manually organized along best delay and response axes for analysis purposes. The anatomic axis is no longer true in these figures. In Fig. 10, the time axis shows the actual arrival time of the echo components along with their best frequency and best delay. Therefore, this is a three-dimensional representation of the temporal process with $t \times f \times d$ where d is the delay and t is the actual arrival time of the echo components which is a function of Δ, the interspike interval (t ranges from $\delta_1, \ldots, \delta_n$). The time lag between the emitted pulse and the received echo provides an estimate of the target distance. Figure 10(a) shows a neuron in the highest frequency with a BD of 1.18 ms that responded maximally. The specified delay was 1.2 ms. The delay of 1.2 ms corresponds to the distance of 20.4 cm. The delay of 1.18 ms corresponds to a distance of 20.06 cm. The error is approximately 1.5%. Similarly, Fig. 11 shows another reorganization of the three-dimensional map with $t \times f \times r$ where r represents the actual response of the neuron.

Figures 9–11 show, as time t progresses, the response of neurons to the echo forms a continuous sequence depicting images of multiple echo-delay components. These response snapshots consisting of the neural response magnitude $y(\delta)$, the delay δ of neurons, and their best frequencies, BF, over the length of the pulse–echo cycle, T, provide multiple cues from which an approximate target signature can be estimated.

The CORMAP was also tested using signals with two- and three-glint echoes and with echo delays ranging from 1.2–2.9 ms. The target distance was estimated using the information obtained from the CORMAP snapshots. The error in distance estimation obtained this way was approximately 2%. Figure 12 compares simulation results with actual data for various experiments.

III. DISCUSSION

A. Spatiotemporal pattern of activity in auditory cortex

The aim of this study was to develop a computational model for displaying the spatiotemporal pattern of neural activity in the bat's auditory cortex under stimulus conditions mimicking echolocation. The CORMAP framework was constructed by the neural-tuning properties of individual delay-sensitive neurons and the tonotopic arrangement of these neurons in the auditory cortex of *Myotis lucifugus*, a

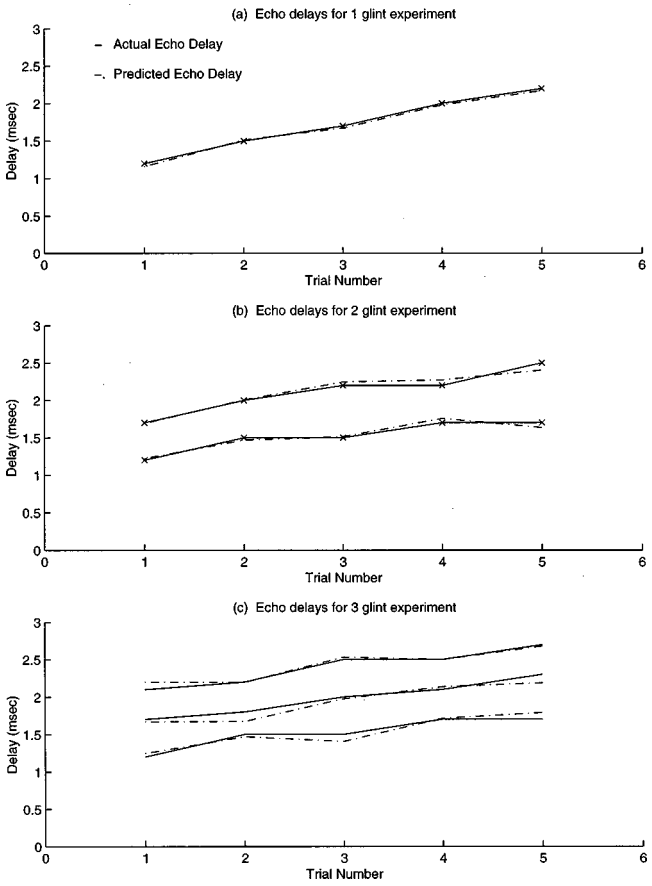

FIG. 12. Comparison of the predicted echo delay with actual echo delay specified during signal generation. The simulation was implemented using phantom targets consisting of one-, two-, and three-glint echoes for different delay values ranging between 1.0–2.5 ms. (a)–(c) Demonstrates the accuracy of CORMAP in estimating the distance of an artificial target with the different number of echo glints. The *x*-axis corresponds to different trials and the *y*-axis shows the echo delay in ms, which corresponds to target distance.

species that employs downward FM sweeps for echolocation. In contrast to current engineering or signal-processing models of bat echolocations, the CORMAP framework provides a groundwork for a biologically plausible biosonar model, which, as a first step, implements a neural map of spike firing in the bat's brain under some of the conditions naturally encountered during echolocation. In the present study, CORMAP was implemented only for a fixed PRR and PD. Since the neural-tuning properties of cortical neurons are shaped by stimulus parameters that change during echolocation, future implementation will effectively manipulate multiple stimulus parameters to generate CORMAP outputs that more accurately simulate brain activity driven dynamically by the sonar emission pattern used to meet perceptual demands during target-directed flight.

CORMAP has the capability to unravel any emergent patterns of spatiotemporal activity not evident or predictable from previous electrophysiological studies. For example, single-unit recordings have monitored spike firing from *individual* cortical loci only, while systematically changing one, rather than multiple, stimulus parameter in an inter-related fashion (e.g., PRR increases as PD and echo delay decrease). Although unit recording from multiple loci simultaneously (''multielectrode'' recording) has been recognized as a powerful approach for addressing information processing at the level of large neuronal populations (e.g., Gerstein *et al.*, 1985), the development of a multielectrode array for a relatively small bat brain remains impractical (Owens *et al.*, 1995). With the CORMAP model, a neural representation of the target could be simulated using a spatiotemporal domain to represent population spike firing. The pattern formation that emerges could potentially determine the stage at which the sequence of target echoes is sufficient for target recognition.

The CORMAP framework can also provide further insights into species-specific mechanisms underlying target perception. First, the basic neurophysiogical assumptions (IV–VI) for CORMAP reflect the findings common to delay-sensitive neurons in both FM bats such as *Myotis*, and CF-FM bats, such as the mustached and horseshoe bats (see O'Neill, 1995 for species-specific comparison). The CORMAP simulation using a fixed PRR and PD in the present study generates a spatiotemporal firing pattern in the FM–FM area of CF-FM bats that may be generally representative throughout the echolocation cycle. However, the single-neuron model in the CORMAP framework is specifically based on a key species-specific feature: the tracking properties of delay-sensitive neurons in *Myotis* cortex. The present CORMAP implementation reveals a spatiotemporal firing pattern in FM bats under a specific time in the echolocation cycle, although the formulation of this model can accommodate dynamic changes in the pulse–echo inputs (e.g., PRR and PD changes). Second, the single-neuron model is further based on delay-sensitive cortical neurons that are topographically organized along a frequency axis, and without regard to any BD map as demonstrated in the FM–FM region of CF-FM bats (O'Neill and Suga, 1982; Schuller *et al.*, 1991). Thus, the spatiotemporal firing pattern of CORMAP is a functional map based simply on a place code for sound frequency. It remains to be determined how PRR, and thus how BD is population encoded during echolocation, modulate the spatiotemporal firing pattern. For example, the cortical activity at low PRR may initially engage a discrete and relatively small cortical ensemble in target search; once a target is detected, a larger cortical ensemble is engaged to similar and progressively shorter BDs as PRR increases with later stages of echolocation. Such a spatiotemporal firing pattern is more complex and less predictable compared to the more straightforward firing pattern on a BD map, where the pattern shifts from local regions tuned to long BDs to regions tuned to progressively shorter BDs. Since the *Myotis* auditory cortex is characterized mainly by a single, relatively large tonotopic region containing delay-sensitive neurons, the ''simple spatiotemporal pattern'' hypothesis proposed by Suga (1994) is sufficient to derive multidimensional target information, and to represent a target image onto a single auditory cortical region. In contrast, the cortical mechanisms underlying target perception is likely to be more complex in CF-FM bats, where the auditory cortex of these bats is characterized by multiple, functionally identifiable regions, each containing a population of neurons with specific filter properties. The spatiotemporal pattern of population activity

would not only be distinctive to each region, but its activity would likely encode only specific target attributes. A neural representation or image of the target would thus encompass the aggregate spatiotemporal activity of multiple specialized regions.

The overall framework consists of primarily two components: a periphery model and the cortical response map model. The periphery model (see Chittajallu *et al.*, 1996 for details of the model) was used simply to generate the pulse- and echo-evoked neural spike train as the input to the CORMAP model. In the current CORMAP implementation, a pulse-train input evokes an inhibitory state in all cortical neurons; as the echo-train input begins to arrive, a small cortical population would start firing when both their BF and BD match the input sound frequency and echo delay, respectively. The cortical excitation continues in different neurons until all echoes have been inputted into CORMAP. The CORMAP output [see Fig. 9(a)–(h)] displays a pattern of cortical firing that is not random: spike firing is evoked in a neuron at a specific time and for a particular echo delay, depending on the specific sound frequency to which the neuron is tuned. The spatiotemporal-firing pattern evoked in the cortical population by a pulse–echo stimulus pair would constitute a neural representation of a target signature. A graphical display of this pattern could be constructed by a contour map of the activated cortical region during pulse–echo processing.

B. Target cue determination

The outputs of the CORMAP are the composite firing pattern of the population of delay-sensitive neurons that serves as an important cue for target recognition and classification. These outputs are: the response magnitude of the neurons, sound frequency at which the neuron is tuned, the time at which the echo arrived, and the best delay of the neuron that responded. Different types of target information can be derived from the different combinations of these outputs. For example, the echo delay provides a measure of target distance (Simmons *et al.*, 1975; Schnitzler, 1984); the response magnitude of neurons provides target-size information; and the composite responses of cortical neurons tuned to different best delays convey textural information (i.e., fine structure) about target. Thus, these three CORMAP outputs can generate a rough target signature.

The echo amplitude encodes the subtended angle of a target, and both echo amplitude and echo delay contribute to encoding target size (Suga, 1990). Since response magnitude of cortical neurons depends on echo amplitude; the response magnitude encoded by the population in CORMAP would provide a measure of subtended angle of target. Since response magnitude indirectly contributes to target-size information, the CORMAP output of response magnitude could only provide one measure of encoding target size. Furthermore, an accurate estimation of target size would not be possible in the present study, since an artificial echo of uniform amplitude was employed that is more indicative of a point target.

For the CORMAP framework to derive target attributes (e.g., distance, shape, size) of which other engineering models are capable, an additional artificial processing component (e.g., statistical or artificial neural-network models), must be included. The present CORMAP implementation did not simulate the dynamically changing PRR and PD found during target pursuit. Thus, an artificial neural network must be further developed to update the available target information by integrating successive CORMAP outputs generated by each PRR–PD combination used in processing a specific pulse–echo stimulus pair. This neural-network output can ultimately perform the target-identification task based on the observed target signatures.

The current model extracts fine echo-delay from one unitary target (see Fig. 9). However, to decipher an actual neural pattern for a particular target feature would require the model to integrate echo information over multiple echolocation cycles. This will be addressed in the future as the model undergoes further enhancement.

C. Performance of CORMAP in representing complex targets

The CORMAP framework was tested to validate two important aspects: (a) to observe the cortical response to simple and complex targets, and (b) to assess CORMAP's ability to encode target features. Three different simulations were performed. In these simulations, input consisting of only one echo for a given pulse is used as a *one*-glint; simple echo and complex target surface was simulated using *multiple*-glint echoes.

The CORMAP framework used for simulation consists of 100×30 neurons where the 30 frequency channels span a frequency range of 100–20 kHz, and the 100 neurons provide a range of different BDs between 1.0 and 10.0 ms. Therefore, the resolution of CORMAP is low, although a good indication is provided of the number of neurons that would respond for the different simulations. For the first simulation with *one* glint, a relatively small cortical population was responsive, suggesting that only a few neurons are essential to encode delay information. The delay information is the fine delays between different frequency components of the echo. As the number of glints increased from two to three, the simulations revealed a larger population that becomes responsive to encode more delay values. Both fine delays and the delays between successive echoes are encoded. However, it is important to note that this framework cannot currently achieve fine-delay acuity. The single-unit studies that document delay tuning in the millisecond range cannot implement a CORMAP resolution in the micro- or nanosecond range, as suggested in behavioral studies.

The target-distance estimation obtained from CORMAP demonstrates that the framework is capable of performing within 2% accuracy. The distance estimation is based on the delay encoded by neurons. Once the fine-delay estimate is made possible through CORMAP, target texture can also be extracted from the delays of the population of neurons that responded. In conclusion, a formulation of a biologically plausible framework is presented to represent the spatiotemporal pattern of firing of cortical neurons evoked by echolocation signals. The current framework, based on available

neurophysiological data, can provide insight into the cortical firing pattern evoked by a pulse–echo stimulus pair.

D. Future development of CORMAP

The current CORMAP framework can be modified to incorporate additional electrophysiological details. For example, the CORMAP framework could be elaborated further by modeling other response properties already determined from unit recordings of auditory-cortical neurons. Moreover, other processing interactions can be built into the framework based on our understanding of cortical–cortical interconnection or descending cortical projections on cortical processing. Feedback circuits will be incorporated to process such realistic features as moving targets (nonstationary Doppler-shifted targets). This would also enable the model to prime the next pulse in the echolocation cycle. The overall framework of the auditory pathway could include additional stages of the central auditory pathway by using electrophysiological results from the thalamus and midbrain. A more extensive framework of the auditory system provides a valuable research tool for investigating target perception in an auditory system exquisitely specialized for echolocation.

ACKNOWLEDGMENTS

The authors wish to thank Uday Murthy for implementing the CORMAP model. This research was supported in part by the National Science Foundation under Grant No. BCS-9307650.

Altes, R. A. (**1975**). ''Doppler-tolerant classification of distributed targets—A bionic sonar,'' IEEE Trans. Aerosp. Electron. Syst. **5**, 708–724.

Altes, R. A. (**1985**). ''Signal processing for target recognition in biosonar,'' Neural Networks **8**, 1275–1295.

Beuter, K. J. (**1980**). ''A new concept on echo evaluation in the auditory systems of bats,'' in *Animal Sonar Systems*, edited by R.-G. Busnel and J. F. Fish (Plenun, New York).

Berkowitz, A., and Suga, N. (**1989**). ''Neural mechanisms organization are different in two species of bats,'' Hearing Res. **41**, 255–264.

Bradbury, J. W. (**1970**). ''Target discrimination by the echolocating bat Vampyrum spectrum,'' J. Exp. Zool. **173**, 23–46.

Chang, W., Bosworth, B., and Carter, G. C. (**1993**). ''Results of using an artificial neural network to distinguish single echoes from multiple sonar echoes,'' J. Acoust. Soc. Am. **94**, 1404–1408.

Chittajallu, S. K., Khort, K. G., Palakal, M. J., and Wong, D. (**1996**). ''Computational model of bat auditory periphery,'' Math. Comput. Model. **24**, No. 1, 67–78.

Chittajallu, S. K., and Kohrt, K. G. (**1995**). ''A computational model of auditory perception,'' in Proceedings of the 32nd Annual RMBS Conference, Copper Mountain, pp. 41–46.

Condon, C. J., Galazyuk, A., White, K. R., and Feng, A. S. (**1997**). ''Neurons in the auditory cortex of the little brown bat exhibit sensitivity to complex amplitude modulation signals that mimic echoes from fluttering insects,'' Aud. Neurosci. **3**, 269–287.

Dear, P. S., Simmons, J. A., and Fritz, J. (**1993**). ''A possible neuronal basis for representation of acoustic scenes in auditory cortex of the big brown bat,'' Nature (London) **364.12**, 620–623.

Dror, I. E., Zagaeski, M., and Moss, C. F. (**1995**). ''Three-dimensional target recognition via sonar: A neural network model,'' Neural Networks **8**, 149–160.

Gerstein, G., Perkel, D., and Dayhoff, J. (**1985**). ''Cooperative firing activity of simultaneously recorded population of neurons; detection and measurement,'' J. Neurosci. **5**, 881–889.

Gorman, R. P., and Sejnowski, T. J. (**1988**). ''Analysis of hidden units in a layered network trained to classify sonar targets,'' Neural Networks **1**, 75–89.

Griffin, D. R. (**1967**). ''Discriminiative echolocation by bats,'' in *Animal Sonar Systems: Biology and Bionics*, edited by R.-G. Busnel (Plenum, New York), pp. 273–300.

Habersetzer, J., and Vogler, B. (**1983**). ''Discrimination of surface-structured targets by the echolocation bat *Myotis* during flight,'' J. Comp. Physiol. **152**, 275–282.

Kuc, R. (**1997**). ''Biomimectic sonar recognizes objects using binaural information,'' J. Acoust. Soc. Am. **102**, 698–696.

Meddis, R. (**1988**). ''Simulation of auditory-neural transduction: Further studies,'' J. Acoust. Soc. Am. **83**, 1056–1063.

Mogdans, J., and Schnitzler, H.-U. (**1990**). ''Range resolution and the possible use of spectral information in the echolocating bat, *Eptesicus fuscus*,'' J. Acoust. Soc. Am. **88**, 754–757.

Moore, P. W. B., Roiblat, H. L., Penner, R. H., and Nachtigall, P. E. (**1991**). ''Recognizing successive dolphin echoes with an integrator gateway network,'' J. Acoust. Soc. Am. **4**, 701–709.

Olson, J. F., and Suga, N. (**1991**). ''Combination-sensitive neurons in the medial geniculate body of the mustached bat: encoding of target range information,'' J. Neurophysiol. **65**, 1275–1296.

O'Neill, W. E. (**1995**). ''The bat auditory cortex,'' in *Hearing by Bats*, edited by A. N. Popper and R. R. Fay (Springer, New York), pp. 416–480.

O'Neill, W. E., and Suga, N. (**1982**). ''Encoding of target range and its representation in the auditory cortex of the mustached bat,'' J. Neurosci. **2**, 17–31.

Owens, A. L., Denison, T. J., Versnel, H., Rebbert, M., Peckerar, M., and Shamma, S. A. (**1995**). ''Multi-electrode array for measuring evoked potentials from surface of ferret primary auditory cortex,'' J. Neurosci. Methods **58**, 209–20.

Palakal, M. J., Murthy, U., Chittajallu, S. K., and Wong, D. (**1995**). ''Tonotopic representation of auditory responses using self-organizing maps,'' Math. Compu. Model. **22.2**, 7–21.

Paschal, W. G., and Wong, D. (**1994a**). ''Frequency organization of delay-sensitive neurons in the auditory cortex of the FM bat *Myotis lucifugus*,'' J. Neurophysiol. **72**, 366–379.

Paschal, W., and Wong, D. (**1994b**). ''Relationship between frequency and temporal tuning of neurons in the auditory cortex of an FM bat,'' Soc. Neurosci. Abst. **18**, 322.

Popper, A. N., and Fay, R. R. (**1995**). *Hearing by Bats* (Springer, New York).

Roitblat, H. L., Moore, P. W. B., Penner, R. H., and Au, W. W. L. (**1989**). ''Natural echolocation with an artificial neural network,'' Neural Networks **4**, 239–248.

Schmidt, S. (**1988**). ''Perception of structured phantom targets in the echolocating bat, *Megaderma Lyra*,'' J. Acoust. Soc. Am. **91**, 2203–2223.

Schnitzler, H. U. (**1984**). ''The performance of bat sonar systems,'' in *Localization and Orientation in Biology and Engineering*, edited by D. Varju and H. U. Schnitzler (Springer, Berlin), pp. 211–224.

Schnitzler, H. U., and Henson, O. W. (**1980**). ''Performance of airborne animal sonar systems: I. Microchiroptera,'' in *Animal Sonar Systems*, edited by R. G. Busnel and J. F. Fish (Plenum, New York), pp. 109–181.

Schnitzler, H. U. (**1987**). ''Echoes of fluttering insects: information for echolocating bats,'' in *Recent Advances in the Study of Bats*, edited by M. B. Fenton, P. Racey, and J. M. V. Rayner (Cambridge University Press, Cambridge), pp. 223–243.

Schuller, G., O'Neill, W. E., and Radtke-Schuller, S. (**1991**). ''Facilitation and delay sensitivity of auditory cortex neurons in CF-FM bats, *Rhinolophus rouxi* and *Pteronotus p. parnellii*,'' Eur. J. Neurosci. **3**, 1165–1181.

Shimozawa, T., Suga, N., Hendler, P., and Schuetze, S. (**1974**). ''Directional sensitivity in echolocation system in bats producing frequency-modulated signals,'' J. Exp. Biol. **60**, 53–69.

Simmons, J. A., Howell, D. J., and Suga, N. (**1975**). ''The information content of bat sonar echoes,'' Am. Sci. **63**, 204–215.

Simmons, J. A., and Chen, L. (**1989**). ''The acoustic basis for target discrimination by FM echolocating bats,'' J. Acoust. Soc. Am. **86**, 1333–1350.

Simmons, J. A., Moss, C. F., and Ferragamo, M. (**1990**). ''Convergence of temporal and spectral information into acoustic images of complex sonar targets perceived by the echolocating bat, *Eptesicus fuscus*,'' J. Comp. Physiol. A **166**, 449–470.

Simmons, J. A., Saillant, P. A., and Dear, S. P. (**1992**). ''Through a bat's ear,'' IEEE Spectr. **3**, 46–48.

Suga, N. (**1988**). ''Auditory neuroethology and speech processing: complex sound processing by combination-sensitive neurons,'' in *Auditory Func-*

tion: Neurobiological Bases of Hearing, edited by G. M. Edelman, W. E. Gall, and W. M. Cowan (Wiley, New York).
Suga, N. (**1994**). ''Multi-function theory for cortical processing of auditory information: implications of single-unit and lesion data for future research,'' J. Comp. Physiol. A **175**, 135–144.
Suga, N. (**1990**). ''Cortical computational maps for auditory imaging,'' Neural Networks **3**, 3–21.
Sullivan, W. E. (**1982**). ''Neural representation of target distance in auditory cortex of the echolocating bat *Myotis lucifugus*,'' J. Neurophysiol. **48**, 1011–1032.
Surlykke, A. (**1992**). ''Target ranging and the role of time-frequency structure of synthetic echoes in the big brown bats *Eptesicus fuscus*,'' J. Comp. Physiol. A **170**, 83–92.
Tanaka, H., and Wong, D. (**1993**). ''The influence of temporal pattern of stimulation on delay tuning of neurons in the auditory cortex of the FM bat, *Myotis lucifugus*,'' Hearing Res. **66**, 58–66.
Tanaka, H., Wong, D., and Taniguchi, I. (**1992**). ''The influence of stimulus duration on the delay tuning of cortical neurons in the FM bat, *Myotis lucifugus*,'' J. Comp. Physiol. A **171**, 29–40.
Wong, D., Maekawa, M., and Tanaka, H. (**1992**). ''The effect of pulse repetition rate on the delay sensitivity of neurons in the auditory cortex of the FM bat, *Myotis lucifugus*,'' J. Comp. Physiol. A **170**, 393–402.
Wong, D., and Shannon, S. L. (**1988**). ''Functional zones in the auditory cortex of the echolocating bat *Myotis lucifugus*,'' Brain Res. **453**, 349–352.

Vocal production mechanisms in the budgerigar (*Melopsittacus undulatus*): The presence and implications of amplitude modulation

Pamela Banta Lavenex[a)]
Program in Neuroscience, 611 Gould-Simpson, University of Arizona, Tucson, Arizona 85721

(Received 1 September 1998; revised 1 April 1999; accepted 9 April 1999)

In this paper acoustic evidence is presented for the presence of amplitude modulation in budgerigar (*Melopsittacus undulatus*) contact calls and learned English vocalizations. Previously, acoustic analyses of budgerigar vocalizations have consisted solely of visual inspection of spectrograms or power spectra (derived from Fourier transformation). Such analyses have led researchers to conclude that budgerigar vocalizations are primarily frequency-modulated, harmonic vocalizations. Although budgerigar calls have been shown to contain regions that are modulated in amplitude, the implications of this fact have been largely ignored. Amplitude modulation, the nonlinear interaction between two separate signals that results in the creation of new, heterodyne (sum and difference) frequencies, can produce a very complex Fourier spectrum that may resemble that produced by a harmonic vocalization. In this paper, the acoustic principles necessary for identifying amplitude modulation present in signals are outlined, and followed by data demonstrating that amplitude modulation is a prominent feature not only of natural budgerigar contact calls, but also of their learned English vocalizations. It is illustrated how analyzing a vocalization that contains amplitude modulation as if it were harmonic can result in misinterpretations of the acoustic and physical properties of the sound and sound source. The implications of amplitude modulation for studies of the ontogenetic, physical, and neural basis of budgerigar vocalizations are discussed, and a potential model for how the budgerigar syrinx may function to produce amplitude modulation is proposed. [S0001-4966(99)03607-3]

PACS numbers: 43.80.Ka [WWLA]

INTRODUCTION

A. Budgerigar vocal mechanisms

Natural budgerigar (parakeet) vocalizations, including contact calls and some warble song elements, have been described and investigated as frequency-modulated, harmonic signals (Heaton *et al.*, 1995; Brittan-Powell *et al.*, 1997a,b). Studies have examined the ontogeny of spectrally represented frequency modulations in calls (Brittan-Powell *et al.*, 1997a; Hall *et al.*, 1997), the effects of syringeal denervation on spectral characteristics of calls (Heaton *et al.*, 1995; Shea *et al.*, 1997), and whether production in helium alters spectral features of calls produced by syringeal denervated and normal budgerigars (Brittan-Powell *et al.*, 1997b). Acoustic features of budgerigar vocalizations have been compared to those of Gray parrots (*Psittacus erithacus*, Turney *et al.*, 1994), and humans (Silaeva, 1998). These studies, however, analyzed only the frequency spectra derived via Fourier techniques, specifically, frequency by time ''spectrograms'' or amplitude by frequency ''power spectra.''

Budgerigar contact calls, however, also display significant modulation in amplitude (Dooling and Searcy, 1981, 1985). A call may contain several frequency changes, but amplitude fluctuations are ubiquitous and easily identified in displays of both the gross temporal envelope and amplitude waveform [Fig. 1(A) and (B), respectively; amplitude by time representations of the signal]. As demonstrated here, some of this amplitude fluctuation is due to nonlinear amplitude modulation. When amplitude modulation is present in a signal, its Fourier spectrum contains additional frequency components that are produced not by the primary source(s), but rather by nonlinear interactions between two originally independent signals (Nowicki and Capranica, 1986a, b; Bradbury and Vehrencamp, 1998). To date, no study of budgerigar calls or warble song has explained the complex array of observed spectral components, investigated whether the observed spectral components are generated by a mechanism of amplitude modulation, nor examined how amplitude modulation develops ontogenetically, is produced, or is affected by perturbations of the vocal production system (e.g., neural or mechanical). Given the spectral complexity of vocalizations that can be produced by amplitude modulation, perturbations affecting that modulation may be difficult or impossible to detect in a cursory inspection of a Fourier spectrum (either spectrograms or power spectra). Indeed, cursory analyses of vaguely harmonic-like signals have led to inaccurate interpretations of the acoustic, physical, and neural mechanisms underlying avian vocalizations that contain amplitude modulation [e.g., in chickadees (Greenewalt, 1968), and in budgerigars (Heaton *et al.*, 1995 and Brauth *et al.*, 1997)].

The fact that budgerigars produce amplitude-modulated signals is itself significant. Budgerigars have a syrinx with one set of opposable membranes [like all parrots, but unlike

[a)]Present address: Pamela Banta Lavenex, Ph.D., Neurobiology, Physiology and Behavior, 196 Briggs Hall, University of California at Davis, Davis, CA 95616; Electronic mail: pabanta@ucdavis.edu

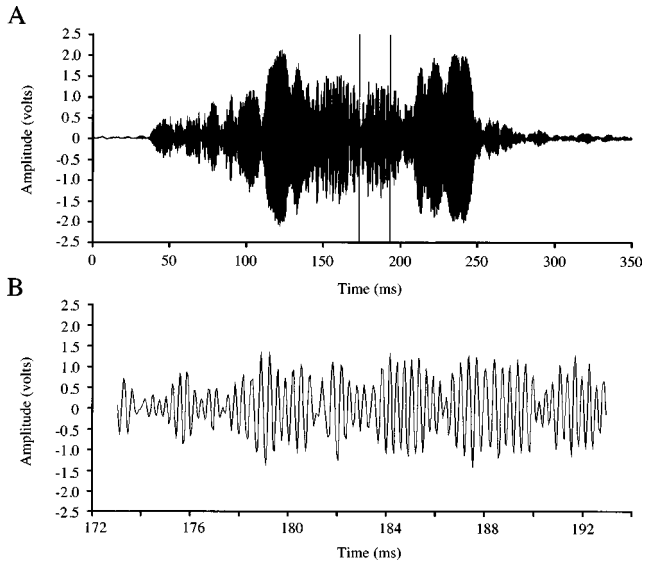

FIG. 1. A budgerigar's contact call (Forest). (A) The entire amplitude envelope. (B) Amplitude waveform of a 20-ms expanded time window from the call in (A) (173–193 ms) showing aperiodic fluctuations of the amplitude. Note the extensive modulation of amplitude that occurs throughout the call.

passerine birds that have a bipartite syrinx with two sets of membranes (Evans, 1969; Nottebohm, 1976; Gaunt and Gaunt, 1985; Suthers, 1997)], and only two pair of intrinsic syringeal muscles (Evans, 1969; Gaunt and Gaunt, 1985). Moreover, parrots are thought not to have independent control of their syringeal membranes (Nottebohm, 1976; Heaton *et al.*, 1995; Brittan-Powell *et al.*, 1997b; Brauth *et al.*, 1997). Learning how budgerigars produce two independent source signals that interact nonlinearly to produce amplitude modulation will further our understanding of syringeal mechanisms that underlie complex avian vocal productions.

In this paper, I show that budgerigars produce amplitude modulation both in their natural contact calls and when mimicking human vowel sounds. First, I redescribe key acoustic and spectral features that allow identification of a sound produced by amplitude modulation, and how nonlinear interactions generate new frequencies. I use the term ''redescribe'' intentionally, because I review material from two overlooked papers by Nowicki and Capranica (1986a, b) on the existence and implications of amplitude modulation in avian vocalizations. Moreover, because a thorough understanding of acoustic principles is necessary to evaluate the vocalizations I present, I also describe two other signal types that must be distinguished from amplitude-modulated ones in the analysis of any vocalizations: Vocalizations known as harmonic, and those produced from a linear interaction (or beating) between harmonic signals.

B. Acoustic characteristics of signals containing harmonics, amplitude modulation, and beating

The relationship between the amplitude waveform and its Fourier spectrum is critical for understanding the physical nature of any sound. The amplitude waveform is the true representation of a signal in the time domain, and is free of mathematical transformation. The wave shape of the amplitude waveform displays how frequency, amplitude, and phase of a signal vary with time. A Fourier transformation, by definition, transforms the signal into the frequency domain. A Fourier analysis decomposes each user-specified time window of an amplitude waveform into a series of pure sinusoids that, when added, produce the observed waveform. For any signal, conclusions based on independent analyses of time and frequency domains must concur. I thus describe the relationship between time and frequency domains for signals that contain harmonics, amplitude modulation, and beating.

1. Harmonics

A harmonic signal is one in which the amplitude waveform repeats itself exactly (i.e., is periodic). A pure tone or sinusoid (a signal composed of only one frequency) is the simplest form of harmonic sound, and is represented in a Fourier spectrum (i.e., either a spectrogram or a power spectrum) by a single component at the frequency the waveform repeats; this frequency is known as the fundamental frequency.

More complex, nonsinusoidal harmonic waveforms (signals composed of multiple frequencies, termed multi-frequency harmonic signals) are represented in a Fourier spectrum by an array of evenly spaced energy components (also known as a harmonic ''stack'' in a spectrogram). The fundamental frequency of the vocalization (known as the first harmonic) is usually the lowest frequency component; successive frequency components are located at exact-integer multiples of the fundamental. A multi-frequency harmonic vocalization with a waveform that repeats every 5 ms thus has a fundamental frequency of 200 Hz and component frequencies at 200, 400, 600 Hz, $n \times 200$ Hz, the fundamental may also be calculated as the highest common denominator of the component frequencies. A sound is classified as ''harmonic'' because, and only because, it repeats exactly in the time domain. Perfectly harmonic biological signals (i.e., where repetition is exact from one period to the next), however, are rare, and some fluctuation usually exists in their periodicity. This fluctuation, or ''quasi-periodicity'' (Titze, 1994), can cause higher harmonics in natural signals to be at near rather than exact-integer multiples of the fundamental frequency (e.g., if a fundamental frequency is 200 ± 2 Hz, the first several harmonics would be at close multiples of 200, but the 10th harmonic could be located at 2000 ± 20 Hz).

Figure 2(A) shows the amplitude waveform of a representative multi-frequency harmonic signal with a fundamental frequency of 183 Hz, and Fig. 3(A) is a schematic of the power spectrum (a representation of the signal after Fourier transformation) that would be generated by this signal. The waveform repeats identically every 5.5 ms, and the harmonics of the fundamental frequency are at 366, 549, and 732 Hz in the power spectrum.

2. Amplitude modulation

An amplitude-modulated vocalization is produced when one signal, the carrier signal, is modulated in amplitude by a second, the modulating signal. In general, the carrier signal has the greater frequency, and is modulated by the lower

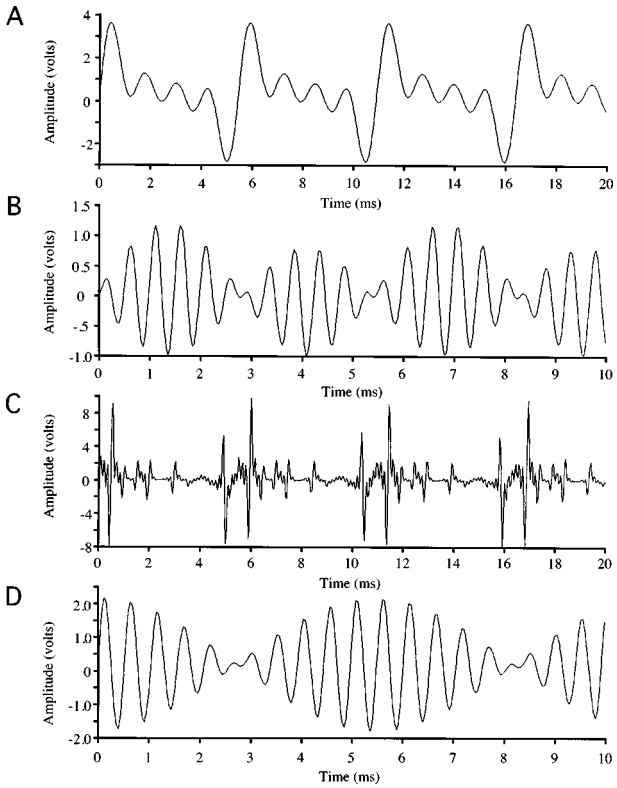

FIG. 2. Amplitude waveforms generated electronically using SIGNAL sound-analysis software (Beeman, 1996). (A) The harmonic signal generated by adding four sinusoidal signals (183, 366, 549, and 732 Hz), each with a 0.1-mV dc component (Bradbury and Vehrencamp, 1998) and an initial amplitude of 1.0 V. (B) The amplitude-modulated signal generated by multiplying two sinusoidal signals (183 and 2017 Hz), each with a 0.1-mV dc component and an initial amplitude of 1.0 V. (C) The amplitude-modulated signal generated by multiplying two multi-frequency harmonic signals (183 Hz with 4 harmonics and 2017 Hz with 3 harmonics), each with a 0.1-mV dc component and an initial amplitude of 1.0 V. (D) The beat signal generated by adding together two sinusoidal signals (1822 and 2005 Hz), each with a 0.1-mV dc component and an initial amplitude of 1.0 V.

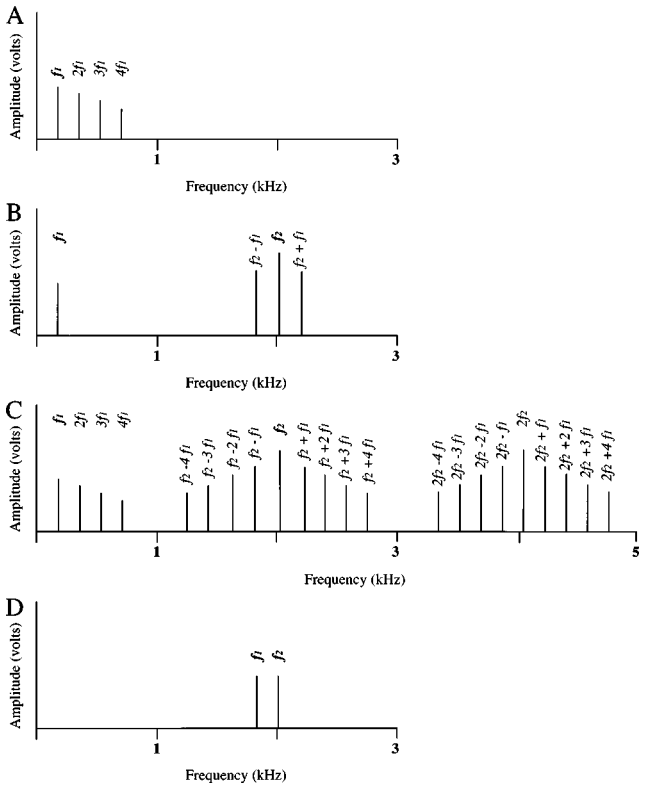

FIG. 3. Schematic Fourier power spectra for signals illustrated in Fig. 2. (A) Power spectrum of the multi-frequency harmonic signal of Fig. 2(A). The fundamental repeating unit, or fundamental frequency, is designated by the f_1 component at 183 Hz. Spacing between each component in the spectrum is also 183 Hz, and each component is found at an integral multiple of 183 Hz (e.g., 366, 549, and 732 Hz). (B) Power spectrum of the amplitude-modulated signal of Fig. 2(B). dc components in both original signals are signified by component frequencies in the spectrum that represent the fundamental frequencies of both input signals, f_1 and f_2 (183 and 2017 Hz, respectively). Sidebands occur at f_2-f_1 and f_2+f_1. (C) Power spectrum of the amplitude-modulated signal of Fig. 2(C). dc components in both original signals are signified by component frequencies in the spectrum at f_1 and f_2 (183 and 2017 Hz, respectively). The multi-frequency harmonic nature of both input signals is illustrated by the presence of numerous component frequencies at integral multiples of the modulating frequency, f_1, and multiple sidebands above and below the carrier frequency, f_2. A second harmonic of the carrier frequency is at $2f_2$ (4034 Hz), with numerous sidebands above and below it. A third harmonic of the carrier frequency would be at $3f_2$ (6051 Hz), with its full complement of sidebands, but is omitted for clarity. (D) Power spectrum of the beat signal of Fig. 1(D). This spectrum shows that the beat signal is generated from the linear interaction (addition) of two input signals: The only two components in the spectrum are those of the original input signals, f_1 and f_2 (1822 and 2005 Hz, respectively).

frequency modulating signal. Because modulation is a nonlinear process (modeled by multiplication of sinusoids represented by polynomials, see below), interactions between the carrier and modulating signals create new frequencies not present in either initial signal. When subject to Fourier transformation, the new components are represented as heterodyne sidebands (sum and difference frequencies) in the spectrum. Thus, two source signals (periodic or aperiodic) interact nonlinearly to produce a resultant output waveform that is not a harmonic series (i.e., it has no single fundamental frequency), and should not be represented by a harmonic array of components. The Fourier spectrum contains a set of component frequencies that, when summed, produce the observed waveform, but those components are not integer multiples of a fundamental frequency. Ascribing their origin to a simple harmonic process is incorrect and misleading regarding the acoustic nature of the signal and the physical nature of the source.

The process of amplitude modulation is not synonymous or analogous to the simple variation in amplitude of a signal with time that can be observed in a display of the gross temporal envelope [Fig. 1(A)]. Such modulations may or may not be due to the nonlinear process of amplitude modulation, but no conclusions can be drawn from this level of analysis. Amplitude modulation occurs uniquely when two signals interact nonlinearly and as a result produce new heterodyne sideband components and a waveform that increases and decreases in amplitude. Some linear processes (e.g., simple summation that occurs during beating), can also produce a waveform that appears modulated in amplitude (see below), but do not produce the physical phenomenon of amplitude modulation nor the new heterodyne sideband components. Thus, the presence of a modulated-amplitude waveform may indicate, but is not conclusive evidence of, an amplitude modulation process. That verification requires detailed analysis of the frequency composition of the Fourier spectrum.

Mathematically, frequencies that result from the nonlinear process of amplitude modulation can be predicted by multiplying the two original input signals. The exact spectral composition of the final output signal depends on two critical features: (1) whether the carrier and/or modulating signals are single frequency (i.e., pure tone) or multi-frequency harmonic signals; and (2) whether a direct current (dc) component exists in either signal. (Note: dc components are typically generated by a unidirectional air flow past a sound-generating organ. All voiced vocalizations, such as the vowel sounds and contact calls discussed here, thus have a dc component manifest in the spectrum as an energy component at zero Hz; Bradbury and Vehrencamp, 1998.) Consider a sound constructed from single-frequency harmonic carrier and modulating signals, each with a dc component, described by two sine waves with the formulas

$$\text{Modulating Signal} = \text{signal 1}: v_1(t) = A + B\cos 2\pi f_1 t,$$

$$\text{Carrier Signal} = \text{signal 2}: v_2(t) = C + D\cos 2\pi f_2 t,$$

where f_2 and f_1 are the carrier and modulating signals, respectively, and $f_2 \geqslant f_1$; A and C represent the dc components of each signal, and B and D the amplitudes. For simplicity, I omit the 2π symbol from subsequent equations. Multiplication of these two formulas yields

$$v_1(t) \times v_2(t) = AC + BC\cos f_1 t + AD\cos f_2 t + BD\cos f_1 t \cos f_2 t. \quad (1)$$

From simple geometric identity, two cosine terms may be represented as

$$\cos x * \cos y = 1/2\cos(x+y) + 1/2\cos(x-y), \quad (2)$$

so that the above equation is expressed as

$$v_1(t) \times v_2(t) = AC + BC\cos f_1 t + AD\cos f_2 t + 1/2\,BD\cos(f_2+f_1)t + 1/2\,BD\cos(f_2-f_1)t. \quad (3)$$

Equation (3) provides terms for the features defining an amplitude-modulated process: First, both the carrier (f_2) and the modulating (f_1) signals are present in the output signal, albeit with altered amplitudes, and are thus identifiable by their distinct component frequencies in the spectrum. Second, two sum and difference frequencies are generated that were not present in either input signal, and are found in the spectrum equidistant above and below the carrier signal, at f_2+f_1 and f_2-f_1. These frequencies, or sidebands, create a spectrum characteristic of amplitude-modulated signals with energy distributed symmetrically on either side of the carrier signal (Nowicki and Capranica, 1986a, b; Bradbury and Vehrencamp, 1998). The presence of the original input signals, f_1 and f_2, in the output signal depends upon the existence of dc components associated with each input signal. If neither input signal has a dc component (if $A=C=0$), then only the sum and difference frequencies (f_2+f_1 and f_2-f_1) are produced. If f_1 but not f_2 has a dc component, only f_2 will be in the output signal, etc. Determining amplitudes of each output component is theoretically possible from the mathematical equations; practically, the exact amplitude of each independent input signal is difficult to determine for a biological signal (unless measured just above the source[s]). I thus do not further discuss amplitude values for spectral components.

Figure 2(B) shows an amplitude waveform, and Fig. 3(B) the spectral frequencies generated by multiplying two single-frequency harmonic signals, one at 2017 Hz and one at 183 Hz, each with a dc component. Both signals are represented in the output signal waveform, and direct measure of the waveform yields components that correspond to the fundamental frequencies of the carrier and modulating signals: In Fig. 2(B), the 2017-Hz frequency is clearly identifiable, and is modulated in amplitude at a rate of 183 Hz, producing the characteristic amplitude-modulated waveform envelope. In Fig. 3(B), the 2017-Hz frequency is represented by a centrally located component surrounded on either side by components at 183-Hz intervals; note the four spectral components at the mathematically predicted frequencies: f_1, f_2, f_2-f_1, and f_2+f_1.

Consider now two multi-frequency harmonic signals, each with a dc component:

$$\text{Modulating Signal} = \text{signal 1}: v_1(t) = A + B_1\cos f_1 t + B_2\cos 2f_1 t + \cdots + B_m\cos m f_1 t,$$

$$\text{Carrier Signal} = \text{signal 2}: v_2(t) = C + D_1\cos f_2 t + D_2\cos 2f_2 t + \cdots + D_n\cos n f_2 t,$$

where $f_2 \geqslant f_1$, m and n are integers (1,2,3,...) representing the harmonics of each multifrequency signal, A and C are the dc components, and B and D the amplitudes.

Multiplication of these two signals yields

$$\begin{aligned} v_1(t) \times v_2(t) = {} & AC + B_1 C\cos f_1 t + AD_1\cos f_2 t \\ & + 1/2B_1D_1\cos(f_2+f_1)t + 1/2B_1D_1\cos(f_2 \\ & - f_1)t + CB_2\cos 2f_1 t + 1/2B_2D_1\cos(f_2 \\ & + 2f_1)t + 1/2B_2D_1\cos(f_2-2f_1)t \\ & + AD_2\cos 2f_2 t + 1/2B_1D_2\cos(2f_2+f_1)t \\ & + 1/2B_1D_2\cos(2f_2-f_1)t + \cdots. \end{aligned} \quad (4)$$

Equation (4) provides terms for three defining features of this type of amplitude modulated signal: First, because each input signal has a dc component, components that correspond to the fundamental frequencies of both the carrier (f_2) and modulating (f_1) signals are present in the output signal, and are represented by components at these frequencies in Fig. 3(C). Second, output signal components at frequencies corresponding to harmonics of each input signal occur at integer multiples of the input signals (i.e., $CB_m\cos m f_1 t$, $AD_n\cos n f_2 t$). Third, sum and difference frequencies corresponding to each cross-product, $1/2B_mD_n\cos(nf_2+mf_1)t$ and $1/2B_mD_n\cos(nf_2-mf_1)t$, produce multiple sidebands, spaced mf_1 Hz above and below each integer multiple of the carrier signal. These sideband frequencies are again products of the nonlinear multiplica-

tion process of amplitude modulation, and are not in the original input signals.

Figures 2(C) and 3(C) show the complex amplitude waveforms and spectral frequencies generated by multiplying two multifrequency harmonic signals with fundamental frequencies of 2017 Hz (with 3 harmonics) and 183 Hz (with 4 harmonics), respectively, each with a dc component [using Eq. (4)]. In Fig. 3(C), note the components that correspond to fundamental frequencies and harmonics of the original input signals (f_1 and f_2, mf_1 and nf_2, respectively), and the multiple sidebands above and below each harmonic of f_2.

When discussing amplitude-modulated signals, terms such as ''fundamental frequency'' and ''harmonic(s)'' are neither appropriate nor correct. An amplitude-modulated signal is not a harmonic signal: It has no fundamental frequency nor harmonics of that fundamental. Although the terms fundamental frequency and harmonic may be appropriate, and even helpful, for describing the separate carrier and modulating signals, they are not appropriate for describing the resultant amplitude-modulated signal. In the above explanations, I have used these terms only to describe how specific components of an amplitude-modulated spectrum arise.

3. Beating

Beating occurs when two signals sum (a linear interaction). Beating (e.g., between signals of 2005 and 1822 Hz), produces a waveform that waxes and wanes in amplitude periodically, thus resembling an amplitude-modulated signal [compare Fig. 2(B) and (D)]. The rate at which the envelope of this amplitude waveform ''beats'' (or waxes and wanes) equals the difference between the two signals (here, 183 Hz). Fourier spectra of signals produced by beating and amplitude modulation, however, are very different [compare Fig. 3(B) and (D)]. The Fourier spectrum of a beat signal contains components at, and only at, the exact frequencies of the two original signals, in contrast to the sum and difference frequencies produced by amplitude modulation. Although beating can also create what are known as difference or combination tones (i.e., perception of a 183-Hz signal), these tones are perceptual illusions produced solely by nonlinearities in auditory or neural systems of the receiver. These tones are not part of the output waveform (Roederer, 1995), and thus not represented in the Fourier spectrum.

C. The current study

Acoustic evidence for the presence of amplitude modulation in both budgerigar contact calls and English vowel productions is presented below. In the discussion that follows, implications of the presence of amplitude modulation are considered, specifically with respect to the ontogeny of budgerigar vocalizations, and the neural and mechanical bases of vocal production in budgerigars.

I. METHODS

A. Subjects

I present vocalizations from four male budgerigars. Three birds, Buddy, Forest, and Frans, were removed from a breeding aviary at fledging (4–5 weeks) and subsequently trained to produce human vocalizations. Buddy and Forest were housed alone in cages, but in auditory and visual contact with humans and other birds. Frans was housed in a soundproof isolation box, with little auditory or visual contact with other birds. Frans had at least 1 h of human interaction 5–6 days/week, and was exposed to auditory tapes (of either a human reading or soft classical and easy-listening music) for 6–8 h/day. A fourth male, M03, neither hand-raised nor trained on English vocalizations, was obtained from a commercial breeding flock and subsequently caged with 11 other budgerigars in various combinations (two–five birds at a time). All birds received food and water *ad libitum*. M03's conspecific vocalizations allowed comparisons between flock-reared and human-reared birds (i.e., Buddy, Forest, and Frans).

B. Training of English vocalizations

Buddy, Forest, and Frans were exposed to and trained to produce English words and phrases via the Model/Rival (M/R) technique (Todt, 1975; Pepperberg, 1981), or a modified version (using only one trainer; Banta and Pepperberg, 1995; Banta, 1998). Each bird was trained for ~1 h/day, 5–6 days/week, from about 6 weeks of age. Buddy, Frans, and Forest were recorded in the laboratory during training and while vocalizing freely on a perch or in their cage when they were fully adult (at least 6 months old), and when the target vocalization was produced in a clear and stable manner. Target vocalizations were single words and phrases, e.g., ''paper,'' ''cork,'' ''wood,'' ''bear,'' and ''truck.'' Birds also acquired vocalizations used during training and social interactions, e.g., ''kiss,'' ''climb,'' ''tickle,'' ''you're right,'' ''good boy,'' ''okay,'' and ''come here.'' The primary tutors for Buddy, Forest, and Frans were humans, but all three birds were at times in auditory contact with other birds (both budgerigars and Gray parrots); thus, they may have also learned some vocalizations from other birds. M03 received no formal human tutoring.

C. Audio recordings

Vocalizations were recorded on Maxell XLII audio tapes with a Sony TCM 5000 tape recorder and AKG C541 EB, Sennheiser ME 66, or Sennheiser ME 67 microphones. M03 was recorded while isolated in his cage. M03's and human (PB's) vocalizations were recorded with Fuji DR-II audio tapes on a Marantz PMD221 portable cassette recorder, and with an Audio-Technica AT835b condenser microphone.

D. Acoustic analyses

Acoustic analysis methods were as follows: Frans' and Forest's vocalizations were filtered at $<$400 Hz and at $>$10 000 Hz with a Hewlett-Packard bandpass filter (model 8056A). Buddy's vocalizations were produced at a greater amplitude, and contained less background noise than those of the other birds (he often sat closer to the microphone and preferred to vocalize when it was quiet), and thus did not require filtering. Frans' and Forest's recordings were digitized with a Kay Elemetrics 5500 DSP sona-graph (20 480

Hz sampling rate, 8-kHz frequency range). Buddy's, M03's, and PB's recordings were digitized with SIGNAL (Beeman, 1996) sound-analysis software (25 000-Hz sampling rate, 8-kHz frequency range). M03's and PB's vocalizations were first alias filtered above 10 000 Hz. Spectra and amplitude waveforms were analyzed on the Kay and with SIGNAL. For English words, 40-ms sections of vowels were isolated and analyzed; for contact calls, entire vocalizations and sections of various lengths (see Sec. II) were analyzed. Power spectra were calculated with a 1024-point transform length that resulted in 20-Hz resolution for the vocalizations of Frans and Forest, and 24.4-Hz resolution for the vocalizations of Buddy, M03, and PB (differences in frequency resolution are due to differences in sampling rate). Spectrograms were calculated with various transform lengths (see Sec. II).

II. RESULTS

A. Budgerigar contact calls exhibit amplitude modulation

Figure 4(A)–(D) show wide- and narrow-band spectrograms, a power spectrum, and an amplitude waveform, respectively, from flock-reared M03's contact call. Note the harmonic-like stack of component frequencies in the spectrograms in the region demarcated by the time cursors [Fig. 4(A),(B)]. A 1024-point power spectrum of the last 10 ms of this region [82–92 ms, where the stack occurs; Fig. 4(C)] also reveals a harmonic-like spectrum, with energy components at apparently regular intervals from 723–6973 Hz. In the spectrum, however, the maximal energy occurs at 3106, not 723, Hz. Moreover, although the first and second component frequencies at 723 and 1484 Hz are integer or near-integer multiples of 742 Hz (0.97 and 2.0, respectively), none of the other spectral components is an integer multiple of 742 Hz (e.g., 3106/742=4.186), a pattern inconsistent with a harmonic signal. Instead, energy components are evenly spaced at 742 Hz on either side of 3106 Hz, a pattern consistent with an amplitude-modulated signal having a dominant (i.e., component with greatest energy) or carrier signal of 3106 Hz. Also, an integer multiple of this dominant component (corresponding to the second harmonic of the carrier frequency) can be identified at 6211 Hz (6211/3106 =2.000), as a local energy peak with components located nearly symmetrically 723 Hz below and 762 Hz above this integer multiple component. If this vocalization were a harmonic series with a fundamental frequency of 3106 Hz, no other frequency components of significant energy would be found below the fundamental frequency or between the fundamental frequency and its second harmonic. At this point in M03's call, however, numerous components lie below this dominant component, and between the dominant component and its second harmonic, a pattern inconsistent with a harmonic signal.

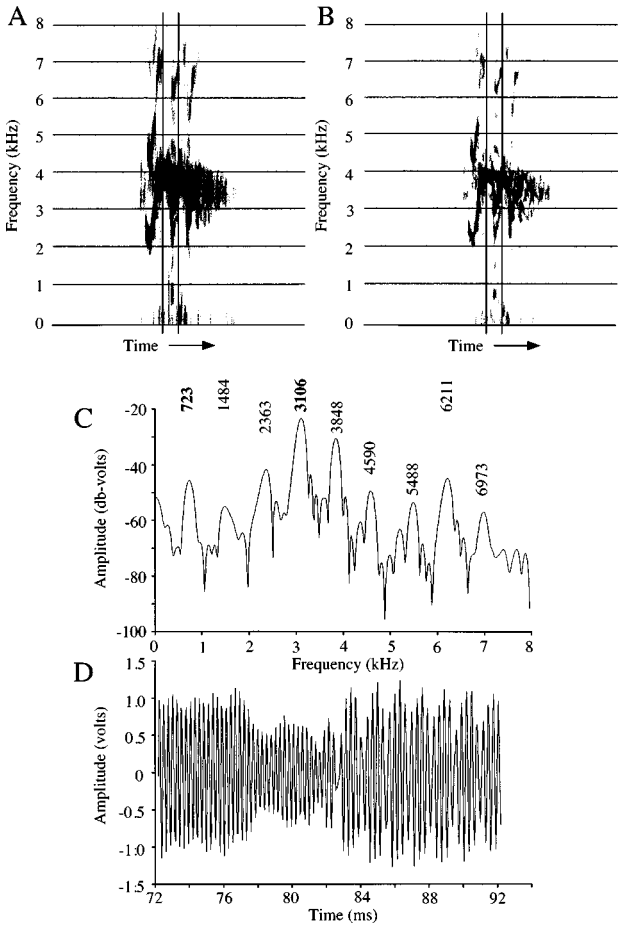

FIG. 4. M03's contact call. (A) Wideband spectrogram (500-Hz analysis filter). Time cursors demarcate the 20-ms section displayed in the amplitude waveform [(D)]. (B) Narrow-band spectrogram (150-Hz analysis filter). Time cursors demarcate the same region as in (A). (C) 1024-point power spectrum of the last 10-ms region of the waveform with periodic modulation in amplitude [(D), 82–92 ms]. The dominant component is at 3106 Hz, with components evenly spaced 742 Hz above and below. Components at 723 and 1484 Hz are at integral multiples of the modulating signal. (D) Amplitude waveform of the 20-ms period demarcated by cursors in (A) and (B), from which the 10-ms period for the power spectrum in (C) was taken. The dominant (carrier) signal measured directly from the last 10 ms of this waveform is 3349 (±94) Hz; the modulating signal is 717 (±67) Hz.

Direct inspection of the amplitude waveform [Fig. 4(D)], reveals a high-frequency signal modulated in amplitude at a much slower rate. The 20 ms of signal that precedes the stack of frequencies (only the last 10 ms shown) is characterized by a waveform of relatively constant frequency (~3850 Hz). At ~78 ms, amplitude of the oscillation decreases rapidly, but the waveform frequency remains constant. At ~83 ms, the waveform frequency drops slightly to 3349 (±94) Hz, and its amplitude begins to increase and decrease periodically, at a frequency of 717 (±67) Hz. Both the dominant frequency and rate of modulation in the waveform correspond well to the dominant frequency component (3106 Hz) and the intervals between components (742 Hz) in the spectrum, respectively, corroborating that the spectrum corresponds to an amplitude-modulated signal.

Of particular interest in this vocalization is the upper sideband at 3848 Hz [Fig. 4(C)], which is nearly identical to the dominant frequency of the portion of the signal immediately preceding this amplitude-modulated segment (at

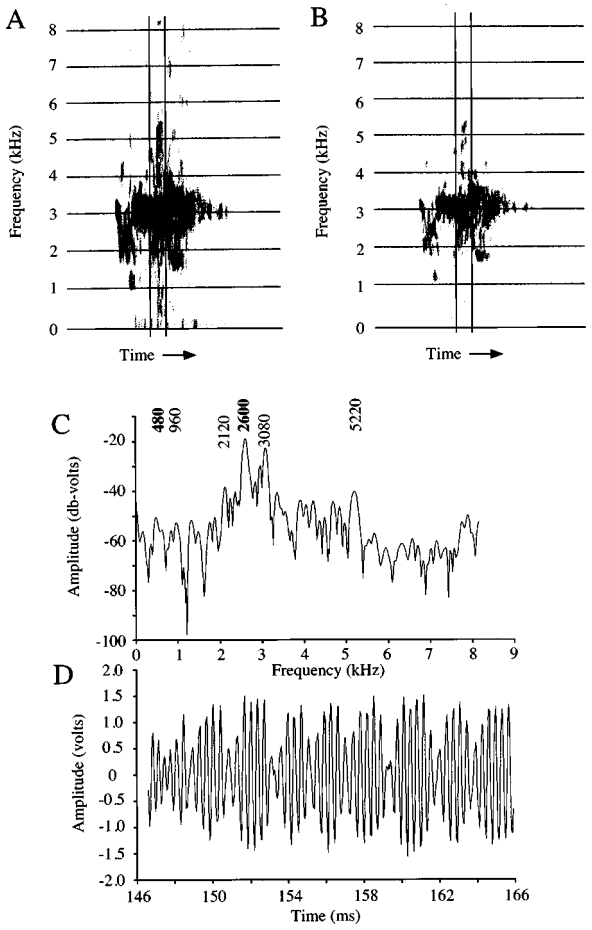

FIG. 5. Forest's contact call. (A) Wideband spectrogram (300-Hz analysis filter) of the call in Fig. 3. Time cursors demarcate the 20-ms section displayed in the amplitude waveform and analyzed in the power spectrum. (B) Narrow-band spectrogram (150-Hz analysis filter). Time cursors demarcate the same region as in (A). (C) 1024-point power spectrum of the 20-ms region demarcated by cursors in (A) and (B). Note the dominant component at 2600 Hz, and components evenly spaced 480 Hz above and below, and integral multiples of the modulating frequency at 480 and 960 Hz (D) Amplitude waveform for the 20-ms period demarcated by cursors in (A) and (B), on which the power spectrum was performed. The dominant (carrier) signal measured directly from this waveform is 2798 (±40) Hz; the modulating signal is 473 (±49) Hz.

~3850 Hz). Indeed, in the narrow-band spectrogram [Fig. 4(B)] the two segments appear almost continuous. This example demonstrates how an incorrect inference regarding the activity of the source (e.g., the frequencies produced) can arise when only the Fourier spectrum is analyzed.

Forest's contact calls (as well as those of seven of nine other budgerigars analyzed for nonlinear amplitude modulation to date) exhibit amplitude-modulation patterns similar to those of M03. Figure 1(A) shows the entire amplitude envelope of one of Forest's calls, and 1(B) an expanded section of time from that call. Note the extensive amplitude fluctuations throughout. Figure 5(A)–(D), respectively, show wide- and narrow-band spectrograms, the power spectrum, and another portion of the amplitude waveform from the call in Fig. 1. From 147–166 ms, the amplitude of the waveform [Fig. 5(D)] is modulated in a regular or periodic manner. Inspection of the wideband spectrogram at this point [Fig. 5(A), between the time cursors] reveals an apparent drop in frequency of the dominant component, accompanied by a smear of energy that extends across a large span of frequencies (from ~500–5500 Hz). Inspection of the narrow-band spectrogram [Fig. 5(B)] reveals several closely apposed component frequencies at apparently evenly spaced frequency intervals. A 1024-point power spectrum (of the 20 ms between the vertical lines) identifies the spectrum's dominant component at 2600 Hz, with components evenly distributed 480 Hz above and below this frequency, a pattern consistent with that of an amplitude-modulated signal. Components also exist at 480 and 960 Hz, but the dominant frequency, 2600 Hz, is *not* an integer multiple of 480 Hz (2600/480=5.4167); thus, this component is not simply a harmonic of a 480-Hz fundamental whose energy has been enhanced by suprasyringeal filtering. Energy at 480 and 960 Hz is consistent with components that correspond to the fundamental frequency of the modulating signal and its first integer multiple. Note the many spectral components between the carrier signal and its second harmonic (at 5220 Hz), a pattern inconsistent with that of a harmonic vocalization.

Inspection of the amplitude waveform of this section of the call [Fig. 5(D)] confirms that the spectrum is generated by an amplitude-modulated signal. Direct measure of the waveform reveals a 473 (±49)-Hz modulation superimposed upon the dominant 2798 (±40)-Hz signal. Both the dominant frequency and rate of modulation in the waveform correspond well with the dominant frequency component (2600 Hz) and the intervals between components (480 Hz) in the spectrum.

B. Human and budgerigar vowel spectra differ in their properties

When subject to Fourier analysis, most human vowels produce a quasi-harmonic spectrum consisting of a fundamental frequency and a stack of harmonic components, with each component located at an integer or near-integer multiple of the fundamental frequency (the fundamental of a human vowel is the frequency at which the vocal folds, or larynx, vibrate open and closed). Figure 6(A) and (B) show wide- and narrow-band spectrograms of a typical harmonic human vocalization, PB's ''bear'' (produced with the same intonation as used when training budgerigars). A power spectrum [Fig. 6(C)] of the /er/ sound reveals a fundamental frequency of 220 Hz, and harmonics at integer or near-integer multiples of the fundamental (i.e., 440, 659 Hz, etc.). Direct measure of the amplitude waveform [Fig. 6(D)] yields a fundamental frequency of 221 (±2) Hz (i.e., the waveform repeats every 4.5–4.6 ms).

Budgerigar vowel spectra (Figs. 7–9), in contrast, possess features of amplitude-modulated rather than harmonic signals. When represented via Fourier analysis, budgerigar vowel sounds possess a complex array of frequency components. The greatest spectral energy occurs in the middle of a group of components with significant energy distributed symmetrically on either side of this local maximum.

A 1024-point power spectrum [Fig. 7(C)] of a 40-ms section (155 to 195 ms) of Frans' /er/ in ''bear'' revealed that the maximal energy was at 1840 Hz, with component frequencies 100 Hz below and 40 Hz above the 1840-Hz

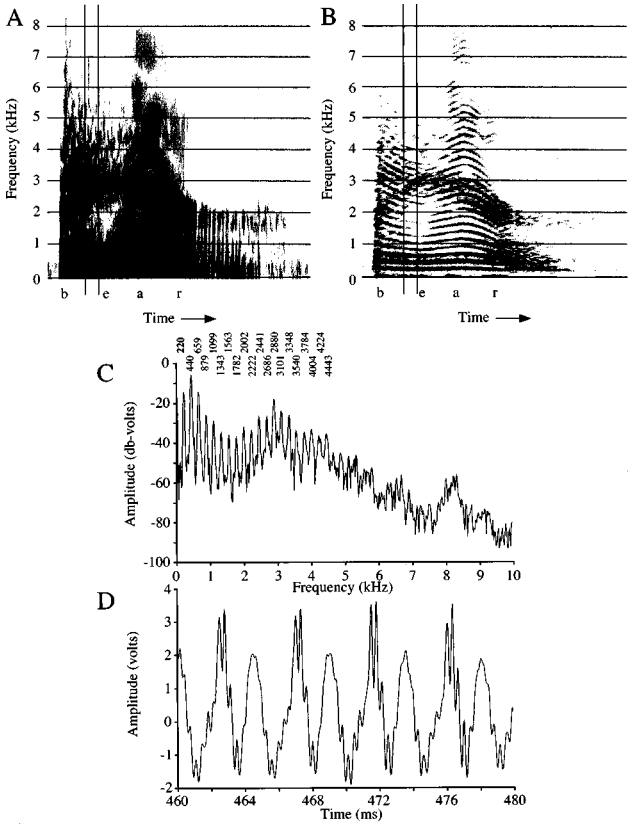

FIG. 6. A human's (PB's) production of ''bear.'' (A) Wideband spectrogram (300-Hz analysis filter). Time cursors demarcate a 40-ms section (450–490 ms). (B) Narrow-band spectrogram (45-Hz analysis filter). Time cursors demarcate the same region as in (A). (C) 1024-point power spectrum of the 40-ms section demarcated in (A) and (B). Note the integrally spaced harmonics. The fundamental frequency determined from the power spectrum is 220 Hz. In this vocalization, the component with the greatest energy is the second harmonic. (D) Amplitude waveform of a 20-ms portion of the 40-ms section demarcated by cursors in (A) and (B). The fundamental frequency determined from direct measure of the waveform is 222 (±2) Hz.

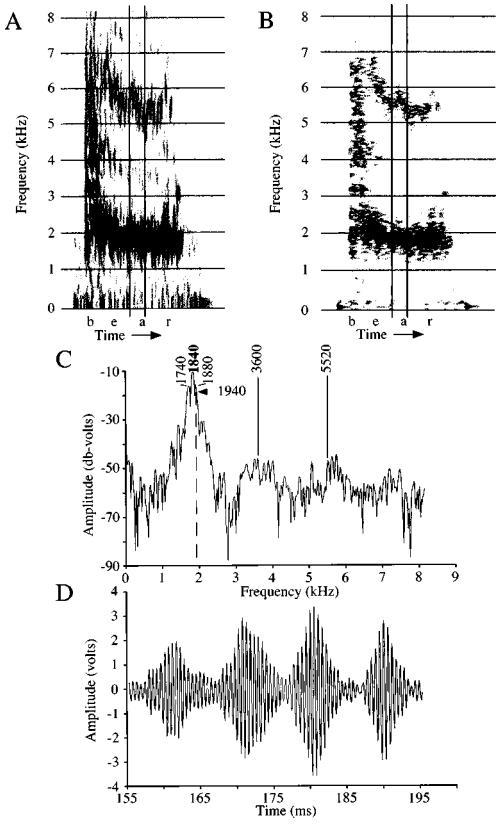

FIG. 7. Frans' production of ''bear.'' (A) Wideband spectrogram (300-Hz analysis filter). Time cursors demarcate a 40-ms section (450–490 ms). Components are located at integral multiples of the carrier frequency (3600 and 5220 Hz). (B) Narrow-band spectrogram (45-Hz analysis filter). Time cursors demarcate the same region as (A). (C) 1024-point power spectrum of the 40-ms section demarcated in (A) and (B). The dominant frequency identified in the power spectrum is 1840 Hz. Component frequencies are 100 Hz below and 40 Hz above the dominant frequency (at 1740 and 1880 Hz, respectively), but significant energy is in the spectrum at 1940 Hz (100 Hz above the carrier signal, where the dashed line and the spectrum intersect). (D) Amplitude waveform of the 40-ms section demarcated by cursors in (A) and (B). Direct measure of the amplitude waveform yielded a carrier signal of 1866 (±12) Hz, and a modulating frequency of 100 (±2) Hz.

frequency. Direct measure of frequencies in the amplitude waveform [in Fig. 7(D), from the peak of one high-frequency period to the next, or from the first peak of one slow-frequency period to the first peak of the next] yielded a dominant frequency of 1866 (±12) Hz, and a modulating frequency of 100 (±2) Hz. Returning to the spectrum, the lower 1740-Hz sideband occurs exactly where predicted (100 Hz below 1840 Hz), but the upper sideband at 1880 Hz is not 100 Hz above the carrier frequency. Note, however, the significant energy at 1940 Hz [e.g., 100 Hz above 1840 Hz; Fig. 7(C)], possibly reflecting the presence of an upper sideband at 1940 Hz that is obscured by another energy component at 1880 Hz. This possibility is discussed in greater detail below.

Thus, evidence from signal analyses suggest that Frans' /er/ vowel sound is produced by amplitude modulation. The dominant frequency identified in the waveform [Fig. 7(D)] contains the greatest energy of all components in the spectrum [Fig. 7(C)], and is surrounded on either side by energy components [Fig. 7(C)], two defining characteristics of an amplitude-modulated signal. The 1840–1866-Hz signal is the carrier; the 100-Hz signal is the modulating signal. Note the second and third integral multiples of the carrier signal near 3680 and 5520 Hz, indicating that the carrier is a multifrequency harmonic signal. The presence of the carrier signal in the spectrum indicates that the modulating signal has a dc component.

Frans' /er/ amplitude waveform envelope [Fig. 7(D)] resembles that of a classically amplitude-modulated signal. Such appearance suggests but is not definitive evidence for amplitude modulation. As described above, beating can produce a similar amplitude envelope, but a very different Fourier spectrum. For budgerigar vowel spectra, component frequencies occur symmetrically around the frequency with the greatest energy, an attribute consistent with a spectrum generated by an amplitude-modulated signal, not by beating [compare Fig. 3(B) and (C) with Fig. 3(D)].

Buddy's /er/ in ''bear'' (Fig. 8) produces a similar spectrum. A 1024-point power spectrum [Fig. 8(C)] identifies the component with maximal energy as 2656 Hz. Direct measure of the amplitude waveform yields a carrier signal of 2676 (±21) Hz and a modulating signal of 255 (±9) Hz. Frequency differences between adjacent components vary from 78–352 Hz, but numerous components are separated by 254 or 273 Hz, values close to that of the modulating signal

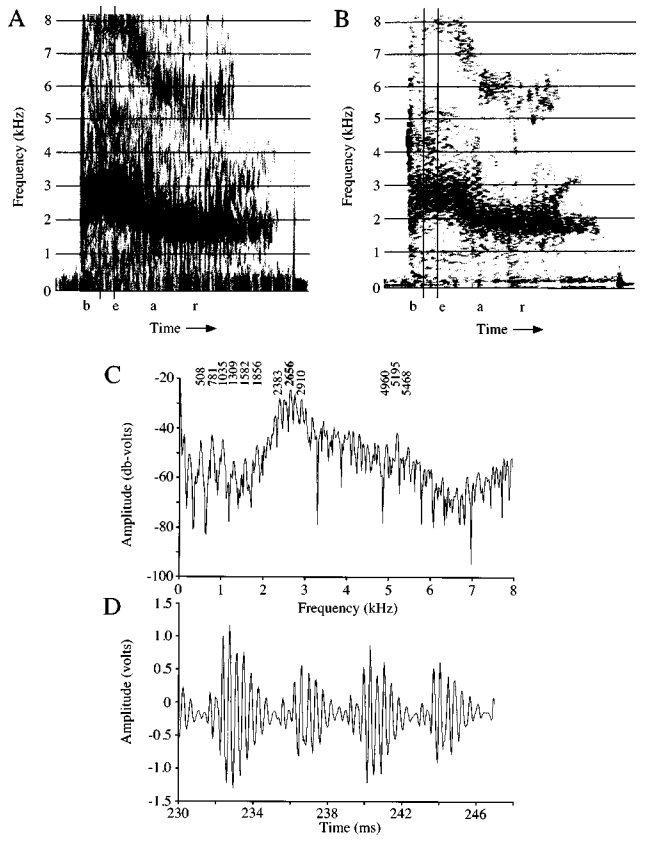

FIG. 8. Buddy's production of ''bear.'' (A) Wideband spectrogram (300-Hz analysis filter). Time cursors demarcate a 40-ms section (220–260 ms). Components are located at integral multiples of the carrier frequency (5195 and ~8000 Hz). (B) Narrow-band spectrogram (45-Hz analysis filter). Time cursors demarcate the same region as in (A). (C) 1024-point power spectrum of the 40-ms section demarcated in (A) and (B). The dominant frequency identified in the power spectrum is 2656 Hz. Component frequencies are 273 Hz below and 254 Hz above the dominant frequency (at 2383 and 2910 Hz, respectively), but other components exist between those components (at 2481 and 2754 Hz, respectively). (D) Amplitude waveform of 18 ms of the 40-ms section demarcated by cursors in (A) and (B). Direct measure of the amplitude waveform yielded a carrier frequency of 2676 (±21) Hz, and a modulating frequency of 254 (±9) Hz.

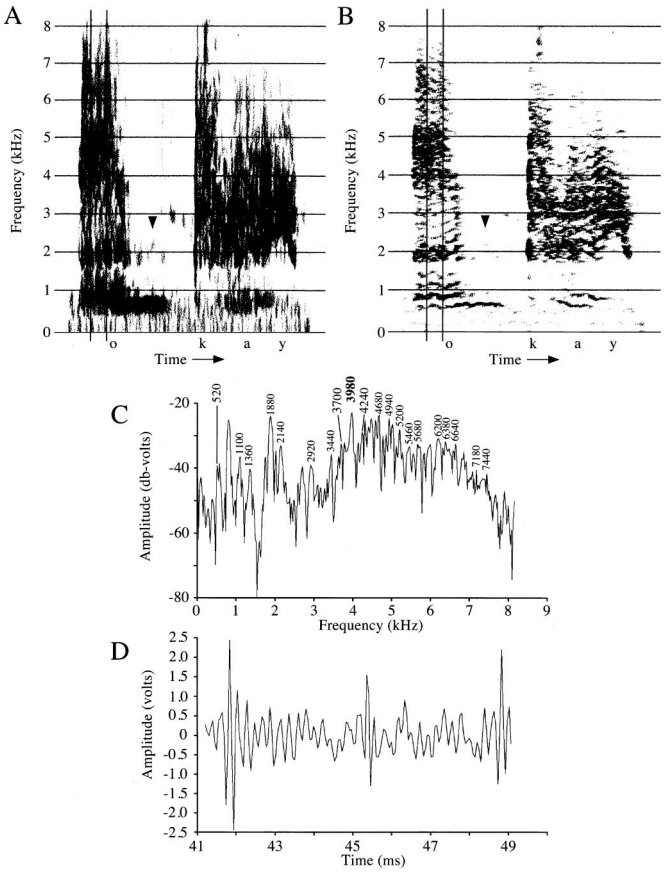

FIG. 9. Forest's production of ''okay.'' (A) Wideband spectrogram (300-Hz analysis filter). Time cursors demarcate a 40-ms section (40–80 ms) of the /o/. Note how low-frequency components extend in time beyond the region of the sound with the majority of energy (below arrowheads). (B) Narrow-band spectrogram (45-Hz analysis filter). Time cursors demarcate the same region as in (A). (C) 1024-point power spectrum of the 40-ms section demarcated in (A) and (B). The dominant frequency in the power spectrum is 3980 Hz. Numerous components are separated by either 260 or 280 Hz, including the components that are two below (at 3700 Hz) and two above (at 4240 Hz) the carrier signal. (D) Amplitude waveform of 8 ms of the 40-ms section demarcated by the cursors in (A) and (B). Direct measure of the amplitude waveform yielded a carrier signal of 4617 (±295) Hz, and a modulating signal of 279 (±21) Hz.

derived from the amplitude waveform. The component two bands below the 2656-Hz component is separated from it by 273 Hz; the component two bands above the 2656-Hz component is separated by 254 Hz. At lower frequencies (this vocalization was not filtered), a harmonic-looking series of components is separated by either 254 or 273 Hz. These components appear to be integer multiples of the fundamental frequency of the modulating signal and thus indicate a dc component in the carrier, and a multifrequency harmonic modulating signal. The second integer multiple of the carrier is visible at 5195 Hz (5195/2656=1.96), indicating its multifrequency harmonic nature. Note also the sidebands 235 Hz below and 273 Hz above the 5195-Hz component. Numerous frequency components exist between the first and second harmonics of the carrier, a pattern inconsistent with a harmonic vocalization.

Figure 9 shows Forest's ''o'' from ''okay.'' Spectral components of this sound are consistent with properties of an amplitude-modulated signal: (1) components corresponding to the fundamental of the carrier signal (3980 Hz) and integer multiples of the modulating signal are present (the fundamental of the modulating signal is 260 Hz, but its first visible component is 520 Hz because of filtering <400 Hz); (2) numerous integer multiples of the modulating signal indicate its multifrequency harmonic nature (Note: the 8000-Hz sampling range eliminates a second integer multiple of the carrier signal); and (3) numerous energy bands on both sides of the carrier signal are visible, many of which are separated by either 260 or 280 Hz.

Measurements of the amplitude waveform concur with frequencies in the spectrum. The modulating signal, at 279 (±21) Hz, corresponds to the 260–280-Hz modulating signal identified in the spectrum. The carrier signal identified in the amplitude waveform, at 4617 (±295) Hz, differs more (although only by 14%) from the 3980 Hz derived from the power spectrum than did these estimations in other birds. When the amplitude waveform is as drastically modulated in amplitude as in this bird's vocalization, however, difficulties arise during wave shape analysis in distinguishing peaks of

the carrier signal from what may be small energy peaks generated by harmonics or vocal-tract resonances of the carrier or modulating signals, or by spurious background noise.

Two other features are of particular interest in this ''o'' sound. First, note [Fig. 9(D)] the striking similarity of the shape and pattern of modulation of the amplitude waveform of this vocalization and the synthesized amplitude-modulated signal [Fig. 2(C)]. Second, note how several low-frequency components in the spectrograms [beneath arrowheads, Fig. 9(A) and (B)] extend in time beyond the portion of sound containing the broad spectrum of frequencies. A 1024-point power spectrum of this region of the vocalization (200–240 ms) reveals a dominant component at 610 Hz. Direct measure of the amplitude waveform yields a dominant frequency of 628 Hz. In this region of the vocalization, the carrier signal apparently ceases, and only what previously was the modulating signal continues to be produced. The actual fundamental frequency in this region may be 305 Hz, but preanalysis filtering $<$400 Hz may have removed the energy at the fundamental. This hypothesis is supported by the presence of four other apparently harmonic components that extend up to 2167 Hz, and that are spaced at integer or near-integer multiples of 305 Hz [i.e., Fig. 9(B), components at 915, 1267, 1909, and 2165 Hz]. This phenomenon was observed in samples of other budgerigar vocalizations, and provides further evidence for the presence of two separate and independent frequencies.

For numerous budgerigar vowel sounds (and all budgerigar vocalizations described above), I calculated the carrier- and modulating-signal periodicity directly from the amplitude waveform. Pitch-synchronous spectrum analyses verified that the carrier signal is not an integer multiple (i.e., a harmonic) of the modulating signal (i.e., carrier signal/modulating signal $\neq$ an integer). These results further support the conclusion that the carrier and modulating signals are not harmonically related.

Finally, I analyzed both budgerigar vowels and amplitude-modulated regions of contact calls for the presence of frequency modulation. Periodic frequency modulations are also capable of producing discrete sidebands (Marler, 1969). Budgerigar vocalizations clearly exhibit frequency modulations in the form of both slow and rapid transitions of the carrier signal frequency (e.g., from one frequency to another). For example, as described above, M03s contact call exhibits a rapid transition from $\sim$3850 to $\sim$3349 Hz at $\sim$83 ms in the call [Fig. 4(D)]. It is thus possible that periodic frequency modulations (e.g., periodic increases and decreases of the dominant signal) within each modulating period are responsible for the production of sideband components. My analyses showed, however, that frequency modulations of the carrier signal within single modulated periods are aperiodic modulations rather than periodic modulations (data not presented). The carrier frequencies of budgerigar vocalizations do not systematically increase, decrease, or increase and decrease in frequency within periods of the modulating envelope, but rather fluctuate around the carrier signal ''target'' frequency (the dominant frequency that the bird is attempting to produce). Furthermore, the period-to-period frequency of the carrier signal is not correlated with the peak-to-trough amplitude of the waveform (data not shown). Periodic-frequency modulation is thus not responsible for producing the discrete sideband components of budgerigar vocalization spectra.

III. DISCUSSION

A. Budgerigar vocalizations contain amplitude modulation

Evidence presented here supports the conclusion that some portions of the acoustic spectra generated by budgerigar vocalizations arise from the nonlinear process of amplitude modulation. Note, however, that not all budgerigar vocalizations exhibit the nonlinear phenomenon of amplitude modulation responsible for creating sideband frequencies (e.g., budgerigar productions of English consonants and perhaps some warble-song elements; Note: many warble song elements are clicks or buzzes which are neither harmonic nor amplitude-modulated signals). Furthermore, amplitude modulation that creates discrete sidebands is not necessarily present or obvious throughout entire vocalizations (e.g., regions within contact calls where amplitude remains relatively constant, or fluctuates aperiodically). Thus, although entire budgerigar vocalizations may not exhibit all of the key features of amplitude modulation, these features are exhibited in portions of contact calls and in learned English vowel sounds. These key features include:

(1) Vocalizations with acoustic spectra that do not conform to those produced by harmonic vocalizations. These vocalizations do not have a dominant component at what would be the predicted fundamental frequency, and calculations fail to yield either a common or a plausible fundamental frequency. Furthermore, the frequency component in the spectrum with greatest energy is not an integer or near-integer multiple of any plausible fundamental.
(2) Acoustic spectra that contain a centrally located dominant component surrounded on each side by relatively symmetrical sidebands that, collectively, represent most of the energy in the signal.
(3) Two separate periodic, or almost-periodic, signals that are identifiable in the amplitude waveform and that accurately reflect frequencies of the carrier and modulating signals identified in the spectrum. The higher-frequency carrier signal in the waveform corresponds to the dominant frequency identified in the spectrum, and the lower-frequency modulating signal in the waveform corresponds to the frequency difference between many components in the spectrum.
(4) These two separate frequencies are not integrally related (i.e., the carrier signal is not an integer multiple of the modulating signal).
(5) A localized prominent component (compared to surrounding component amplitudes) occurs at a frequency twice that of the central dominant component (i.e., an integer multiple of the fundamental frequency of the carrier signal). This component is likewise surrounded lo-

cally by a pattern of energy, consistent with sidebands in an amplitude-modulated signal.

Amplitude modulation is evident in budgerigar productions of English vowel sounds. As mentioned above, budgerigar vowel spectra contain a centrally located dominant component and numerous sideband components separated by a frequency similar to the modulating frequency (determined from the waveform). At times, however, particular sideband components can be difficult to identify definitively because they occur at positions not predicted by the modulating frequency [e.g., the 1880-Hz component in Frans' /er/ in ''bear,'' Fig. 7(C)]. Possible reasons for this inconsistency are discussed below.

For budgerigar calls, the presence of a gross temporal envelope [Fig. 1(A)] and an amplitude waveform [Fig. 1(B)] that fluctuates in amplitude is obvious [this is the case for the calls of all (more than 16) budgerigars examined to date]. However, only isolated regions of calls (e.g., approximately 10%–20% of the duration) exhibit periodic amplitude modulation [Figs. 4(D), 5(D)]. At these points, the vocalization spectrum changes drastically, and sideband components are detectable. Thus, evidence in both the time domain (in the amplitude waveform) and in the frequency domain (in the Fourier spectrum) provide consistent verification of an underlying amplitude-modulation process in the generation of these isolated portions of budgerigar contact calls. The physical and acoustical processes responsible for producing the remainder of the call are, however, not yet known. Specifically, are the frequent, obvious fluctuations in the amplitude of the waveform throughout the rest of the call also produced by nonlinear amplitude modulation, or are they spurious fluctuations in amplitude?

B. Additional acoustic mechanisms and their influence on budgerigar vocalizations

1. The complexity of nonlinear amplitude modulation

As mentioned above, budgerigar vowel spectra also deviate somewhat from what is predicted by a simple model of amplitude modulation. One reason for this deviation is that components arising as integer multiples of the fundamental frequency of the modulating signal, and those generated as sidebands (i.e., components surrounding both the carrier and integer multiples of the carrier signal) may overlap in the spectrum. A simple example illustrates this phenomenon. Consider an amplitude-modulated signal with multifrequency harmonic carrier (2000 Hz) and modulating (300 Hz) signals. Integer multiples of the 300-Hz modulating signal would be found at 300, 600, 900, 1200, 1500, 1800, 2100 Hz, etc. The carrier signal produces a component at 2000 Hz, and sidebands would surround the carrier signal at 300-Hz intervals below (at 1700, 1400, 1100, 800, 500, 200 Hz) and above (at 2300, 2600, 2900 Hz, etc.) the carrier signal. Where the modulating and sideband components overlap, however, energy would occur at 200, 300, 500, 600, 800, 900, 1100, 1200, 1400, 1500, 1700, 1800, 2000, 2100, 2300 Hz, etc. (This phenomenon also occurs where sidebands of the carrier signal and its second integer multiple overlap.) This region in the spectrum would be difficult to interpret, as it would consist of numerous closely apposed components separated by 100- and 200-Hz intervals, but not necessarily by the 300-Hz interval predicted by the modulating signal. (Note that such an array might be incorrectly interpreted to be a harmonic stack with a fundamental of 100 Hz, but with various missing harmonics.) Finally, depending on the window size of the Fourier transform, very closely apposed overlapping components may not be distinguishable, but rather may be represented as one single wideband component, further complicating the analysis. The described array of components resembles that of many budgerigar vowel spectra. By deriving specific information regarding both the carrier and modulating frequencies from the Fourier spectrum and amplitude waveform, however, the array can be identified as generated by the nonlinear process of amplitude modulation.

2. Suprasyringeal filtering

The contribution of suprasyringeal filtering to budgerigar vocalization spectra must also be considered. The present analyses cannot assess the role that the vocal tract plays to emphasize or de-emphasize frequencies created by the syrinx and other sound sources (if existent), but such filtering likely exists (Westneat *et al.*, 1993; Brittan-Powell *et al.*, 1997b). The budgerigar vocal tract likely emphasizes frequencies between 2000–4000 Hz (the dominant frequency range of contact calls; Dooling, 1986), thus emphasizing sidebands that occur near the carrier signal, but not those at other frequencies. Analyses of other budgerigar vowel productions (Banta, personal observation), suggest that budgerigars may also selectively emphasize components that occur above, while deemphasizing or filtering out those that occur below, the carrier signal.

3. Aperiodic amplitude modulation

Inspection of the amplitude waveform for the major portion of any budgerigar call (i.e., in regions that do not exhibit an amplitude-modulated spectrum with discrete sidebands) reveals a waveform that appears to be modulated in amplitude aperiodically or chaotically [Fig. 1(B)]. Interestingly, nonlinear amplitude modulation that results from the interaction between a periodic carrier signal and an aperiodic modulating signal results in a much different spectrum than those presented in Fig. 3(B) and (C). Instead of producing a spectrum with discrete sidebands of energy (i.e., line spectra), an amplitude-modulated signal with a periodic carrier signal and an aperiodic modulating signal will have a large centrally located dominant component surrounded on either side by diffuse sideband energy that may be incorrectly hypothesized as arising from aperiodic frequency fluctuations or noise. The distance that this sideband energy extends on either side of the carrier signal is determined by the instantaneous rate at which the frequency of the modulating signal is fluctuating. Because the modulating signal can fluctuate in frequency very rapidly (e.g., with each period of the carrier signal for a chaotic modulating signal), Fourier transformation results in a ''smearing'' of the sideband energy with time, thus giving the spectrum a ''broadband'' or noisy ap-

pearance. Indeed, inspection of spectrograms from both M03's and Forest's calls [Figs. 4(A) and (B) and 5(A) and (B), respectively], reveal this broadband or noisy character.

4. Beating

The simple linear summation phenomenon known as beating cannot explain all of the spectral frequencies present in portions of budgerigar calls and budgerigar vowel sounds. Although beating can produce a waveform that is modulated in amplitude, its Fourier spectrum contains only the two original input frequencies. Even if beating occurred between two multi-frequency harmonic signals, the spectrum would not contain a centrally located dominant component surrounded symmetrically by other components. Such a spectrum results only from a nonlinear process such as amplitude modulation. Thus, the modulated waveform of budgerigar vowels and calls is not produced by beating.

5. Frequency modulation

Budgerigar vocalizations and their Fourier spectra are influenced by frequency modulations, but are not the product of periodic frequency modulation, which can also produce discrete line sidebands similar to those produced by periodic amplitude modulation (Marler, 1969). My analyses showed that periodic frequency modulations do not play a role in the production of discrete sidebands in the production of budgerigar vocalization spectra (data not presented). Frequency modulation, however, may contribute to some of the spectral smearing observed around regions of contact calls where aperiodic amplitude modulation is also observed (i.e., augmenting the broadband appearance). The overall contribution of each of these mechanisms, aperiodic frequency modulation versus aperiodic amplitude modulation, to the signal spectrum is difficult to estimate when the two processes occur simultaneously, but undoubtedly, both mechanisms contribute to the complex spectra of budgerigar vocalizations. Further acoustical and physiological investigations are needed to elucidate the roles of these mechanisms in the production of budgerigar vocalizations.

6. Additional evidence for the presence of aperiodic amplitude modulation

Insufficient acoustic evidence exists to determine conclusively if all the frequent aperiodic fluctuations in amplitude observed in budgerigar calls arise via amplitude modulation, but, given its demonstrated presence in some portions of calls, and its prominence in English vowel productions, it is distinctly possible if not probable. Further evidence, however, comes from the analysis of contact calls produced by budgerigars with lesions in the vocal control nucleus NLc (central nucleus of the lateral neostriatum). NLc lesions affect the amplitude of the regions of budgerigar calls that fluctuate aperiodically, as well as regions that are clearly amplitude modulated, suggesting that amplitude throughout the entire call is regulated by a common mechanism and is under the control of a neural circuit whose primary target is the syrinx (Banta and Pepperberg, 1997; Banta, 1998). This result would not be expected if the aperiodic modulations of amplitude observed in budgerigar calls were simply spurious fluctuations as observed in all biological signals.

C. Implications of amplitude modulation for investigations of budgerigar vocalizations

Budgerigars' ability to produce amplitude modulation has significant implications for future investigations of their sound production, and necessitates re-evaluating results and interpretations of previous studies of ontogenetic, neural, syringeal, and acoustic mechanisms underlying their vocalizations. For example, fundamental frequency is an inappropriate concept when considering amplitude-modulated vocalizations. Analyzing a vocalization containing amplitude modulation as if it were harmonic may lead to serious acoustic and physical misrepresentations of the signal. Future investigations of budgerigar vocalizations must include acoustic analyses appropriate for amplitude-modulated signals (e.g., ruling out the possibility that the vocalization is harmonic; ensuring concurrence between the Fourier spectrum and the amplitude waveform), and must use appropriate terminology to refer to vocalization components. Specifically, because the present study raises serious questions as to the nature of budgerigar contact call production and suggests amplitude modulation as the underlying mechanism, use of neutral terms such as ''dominant signal'' may be preferred to terms such as fundamental frequency until the issue is resolved.

The presence of amplitude modulation in vocal signals impacts most significantly researchers' reliance on acoustic analyses performed solely with Fourier techniques. Such analyses may lead to incorrect inferences about the signal source, and the frequencies it produces. Sidebands, for example, which account for most of the components in the Fourier spectrum of a complex amplitude-modulated signal, are not source-produced frequencies, but rather result from nonlinear interactions between two other signals originally produced by the source(s). This inference is not possible solely with visual inspection of the Fourier spectrum. Only after accounting for all frequencies present in the spectrum, and reconciling the amplitude waveform and Fourier spectrum, are the acoustic properties of the source clarified.

1. Mechanical and neural substrates of budgerigar vocalizations

Analyses relying solely on visual inspection of Fourier spectra have led to misinterpretations of the physical, structural, and neural mechanisms underlying production of budgerigar vocalizations. Reports from Heaton *et al.* (1995), Brauth *et al.* (1997), and Shea *et al.* (1997) suggested that budgerigar contact calls are harmonic vocalizations, and that the fundamental frequency of these calls is significantly reduced in birds that have undergone bilateral denervation of the syrinx. Brauth *et al.* (1997) proposed a model for budgerigar syringeal function based on these findings. However, this purported decrease in fundamental frequency has not been reconciled with findings that (a) calls of syringeal denervated birds are essentially a harmonic stack of frequencies (Heaton *et al.*, 1995), and (b) the dominant frequency of these harmonic productions shifts when produced in helium, whereas the dominant frequency of calls of normal, inner-

vated birds does not (Brittan-Powell *et al.*, 1997b). This differential effect of helium would not be predicted if the source frequency was the only feature affected by denervation, but may indicate that the harmonic components of denervated budgerigar calls are produced in a fundamentally different manner than a normal bird's call. Unfortunately, the authors did not report effects of syringeal denervation on the gross temporal envelope or amplitude waveform for any calls they present. Re-evaluation of the results and interpretations from these studies in the context of amplitude modulation might greatly increase our understanding of mechanics of the budgerigar vocal apparatus.

Studies have also fallen unexpectedly short in identifying effects of lesions in the vocal control system on the production of budgerigar vocalizations. To date, few studies have documented the post-lesion fate of budgerigar calls. Hall *et al.* (1994) present data from budgerigars lesioned unilaterally and bilaterally in and around Field L and nucleus basalis (NB). No effects were found following Field L lesions, but NB lesions caused deterioration, loss of individual distinctiveness, and loss of all frequency modulation (as identified by visual inspection of Fourier spectra) of contact calls. What is not known, however, is how lesions affected the gross temporal envelope, amplitude waveform, or amplitude modulation present in these vocalizations. Lack of understanding of the acoustic nature of budgerigar vocalizations may similarly have hindered analyses of other unpublished lesion studies. In contrast, preliminary evidence from recent experiments shows that even small, unilateral lesions in the central nucleus of the lateral neostriatum (NLc) can significantly and specifically affect amplitude modulation found in both budgerigar contact calls and productions of learned English vowel sounds, although the Fourier spectra may appear relatively unaffected (Banta and Pepperberg, 1997; Banta, 1998). Consideration of the acoustic implications of amplitude modulation will facilitate future investigations to define more thoroughly and accurately effects of lesions in vocal control nuclei.

2. Vocal learning

The presence of amplitude modulation in budgerigar vocalizations has intriguing implications for studies of vocal learning. Budgerigars can continue vocal learning throughout adulthood (Brown *et al.*, 1988; Farabaugh *et al.*, 1994), and juveniles require auditory feedback to develop their calls (Dooling *et al.*, 1987). The acoustic or temporal features to which birds actually attend and learn when they begin to produce their first contact calls or modify their adult call repertoire as adults are, however, unknown. Budgerigars' ability to produce a specific pattern of amplitude modulation to mimic English vowels strongly suggests that budgerigars may also ''learn'' when and how to vary amplitude in their contact calls, as well as other conspecific vocalizations. As mentioned previously, a budgerigar call may exhibit 3–5 frequency changes throughout its duration, but 10–15, or more, amplitude changes. Whether all modulations of amplitude are due to the nonlinear process of amplitude modulation (in contrast to simple amplitude fluctuations of the gross temporal envelope, discussed above), is not yet clear but is a distinct possibility. Perhaps budgerigars learning contact calls learn not only which dominant frequency to produce, and how to vary that frequency, but also a pattern of amplitude modulation. Indeed, perhaps amplitude modulation is *the* critical acoustic feature monitored by budgerigars engaged in vocal learning. Brittan-Powell *et al.* (1997a) and Hall *et al.* (1997) investigated the ontogeny of call production in budgerigars, but not the development of amplitude modulation. Such analyses may greatly improve our understanding of mechanisms underlying vocal learning in this species.

D. Syringeal mechanisms underlying the production of amplitude modulation

Acoustic characteristics of amplitude-modulated vocalizations in songbirds were first described by Nowicki and Capranica (1986a, b). They found that the ''dee'' syllable of the black-capped chickadee (*Parus atricapillus*) call was not a simple harmonic vocalization, but rather resulted from the nonlinear interaction of two harmonic signals. The chickadee, like all songbirds, has two syringeal apertures (one on each side of the tracheobronchial junction), each with a membrane capable of producing a separate sound. Nowicki and Capranica proposed that the spectral characteristics of the ''dee'' arose because each side of the syrinx produced a different frequency. In contrast, the budgerigar, like all parrots, has a single syringeal aperture with two opposing lateral tympaniform membranes (LTMs; Nottebohm, 1976) in the tracheal portion of the tracheobronchial junction, and these membranes purportedly cannot produce sound independently (Nottebohm, 1976; Heaton *et al.*, 1995; Brauth *et al.*, 1997). Thus, how do budgerigars produce amplitude-modulated vocalizations?

A clue about budgerigar syringeal mechanisms may come from research on the monk parakeet, *Myiopsitta monachus*. This bird not only produces amplitude-modulated call-like vocalizations (''a rattling squawk''), but two intrinsic muscles of its syrinx, the syringeus and the tracheobronchialis, are temporally correlated with pulsatile elements of this vocalization (Gaunt and Gaunt, 1985). A similar mechanism may be responsible for budgerigars' production of amplitude-modulated signals. For example, the dominant or carrier frequency may be produced by a flow-induced, self-sustaining oscillation of the LTMs (achieved by Bernoulli action-like forces of air on the LTMs). The carrier frequency amplitude may then be modulated by either adducting or abducting the LTMs (i.e., moving them, respectively, into or out of the tracheal lumen, and thus into and out of the air flow). Although direct syringeal muscle activity may be responsible for producing amplitude modulations of this type in monk parakeet calls (Gaunt and Gaunt, 1985), I find amplitude-modulation rates ranging from 100–742 Hz in the budgerigar. Because these upper frequencies are far greater than the rate at which even the fastest skeletal muscle can contract, direct syringeal muscle activity is not likely responsible for producing the modulating signal in all budgerigar amplitude-modulated vocalizations.

Nonlinear oscillations of the syringeal membranes may also be responsible for producing amplitude modulation in budgerigar vocalizations. Fee *et al.* (1998) describe nonlin-

ear dynamics present in the excised syrinx of the zebra finch (*Taeniopygia guttata*). They postulate that these nonlinear mechanics are responsible for some nonlinear characteristics observed in zebra finch song, such as period doubling, mode-locking, and sudden transitions from periodic to aperiodic or chaotic signals. Tests on a biophysical model of the syrinx further support their hypotheses and suggest that, at least for mode-locking, coupling of the Bernoulli force-driven oscillation to a higher vibrational mode in the membranes may be responsible. Similar mechanisms might produce nonlinear acoustical features of budgerigar vocalizations: Smooth yet rapid transitions in amplitude, and between periodic and aperiodic or chaotic modulations, are evident in regions of calls that lack obvious spectral evidence of amplitude modulation [Fig. 1(B)]. If budgerigars indeed use such mechanisms to mimic the sounds of human speech, they must have central control over at least some aspects of the syringeal dynamics to initiate, terminate, and modulate production of this nonlinear activity. Further experiments are necessary to assess the roles of both the syrinx and the central vocal-control system in producing nonlinear acoustical features of budgerigar vocalizations.

IV. CONCLUSIONS

In summary, evidence presented here supports the conclusion that the nonlinear process of amplitude modulation significantly influences the acoustic properties of budgerigar contact calls and learned English vowel sounds. The mechanisms budgerigars use to produce amplitude modulation are, however, unknown. Future studies considering the presence of amplitude modulation should shed further light on the ontogenetic, physical, and neural bases of budgerigar vocalizations, and, in turn, these studies should further our understanding of how budgerigars produce amplitude-modulated vocalizations.

ACKNOWLEDGMENTS

I would like to thank I. M. Pepperberg, R. R. Capranica, and P. Lavenex for the enormous amounts of help, guidance, and insight they have given me throughout this study. I thank numerous undergraduate students at the University of Arizona for endless hours of assistance with training budgerigars, and S. Rubin and L. Freeman for excellent care of the breeding flock of budgerigars. I thank B. Brittan-Powell, F. Goller, and R. Suthers for helpful discussions, and C. Clark, F. Goller, P. Narins, and two anonymous reviewers for critical comments on previous drafts of this manuscript. I thank T. Glattke, S. Hopp, and P. Marler for helpful discussions and access to equipment necessary to complete this study, and D. Amaral for access to equipment. This project was supported by funds from the Whitehall Foundation (No. AS92-03 to I. M. Pepperberg), the National Science Foundation (SGER No. 9237 to I. M. Pepperberg), and the University of Arizona Program in Neuroscience and Graduate College.

Banta, P. A. (**1998**). ''Neuroethology of acquired English and conspecific vocalizations in the budgerigar (*Melopsittacus undulatus*),'' Ph.D. Dissertation, University of Arizona.

Banta, P. A., and Pepperberg, I. M. (**1995**). ''Learned English vocalizations as a model for studying budgerigar (*Melopsittacus undulatus*) warble song,'' Soc. Neurosci. Abs. **21**, 958.

Banta, P. A., and Pepperberg, I. M. (**1997**). ''Ibotenic acid lesions in budgerigar NLc affect production, but not memory, of learned English words and natural vocalizations,'' Soc. Neurosci. Abs. **23**, 797.

Beeman, K. (**1996**). SIGNAL Technology, V3.0 (Engineering Design, Belmont, MA).

Bradbury, J. W., and Vehrencamp, S. L. (**1998**). *Principles of Animal Communication* (Sinauer, Sunderland, MA).

Brauth, S. E., Heaton, J. T., Shea, S. D., Durand, S. E., and Hall, W. S. (**1997**). ''Functional anatomy of forebrain vocal control pathways in the budgerigar (*Melopsittacus undulatus*),'' Ann. (N.Y.) Acad. Sci. **807**, 368–385.

Brittan-Powell, E. F., Dooling, R. J., and Farabaugh, S. M. (**1997a**). ''Vocal development in budgerigars (*Melopsittacus undulatus*): Contact calls,'' J. Comp. Psych. **111**, 226–241.

Brittan-Powell, E. F., Dooling, R. J., Larsen, O. N., and Heaton, J. T. (**1997b**). ''Mechanisms of vocal production in budgerigars (*Melopsittacus undulatus*),'' J. Acoust. Soc. Am. **101**, 578–589.

Brown, S. D., Dooling, R. J., and O'Grady, K. (**1988**). ''Perceptual organization of acoustic stimuli by budgerigars (*Melopsittacus undulatus*): III. Contact calls,'' J. Comp. Psych. **102**, 236–247.

Dooling, R. J. (**1986**). ''Perception of vocal signals by budgerigars (*Melopsittacus undulatus*),'' Exp. Biol. **45**, 195–218.

Dooling, R. J., Gephart, B. F., Price, P. H., McHale, C., and Brauth, S. E. (**1987**). ''Effects of deafening on the contact call of the budgerigar *Melopsittacus undulatus*,'' Anim. Behav. **35**, 1264–1266.

Dooling, R. J., and Searcy, M. H. (**1981**). ''Amplitude modulation thresholds for the parakeet (*Melopsittacus undulatus*),'' J. Comp. Physiol. **143**, 383–388.

Dooling, R. J., and Searcy, M. H. (**1985**). ''Temporal integration of acoustic signals by the budgerigar (*Melopsittacus undulatus*),'' J. Acoust. Soc. Am. **77**, 1917–1920.

Evans, H. E. (**1969**). ''Anatomy of the budgerigar,'' in *Diseases of Cage and Aviary Birds*, edited by M. L. Petrak (Lea and Febiger, Philadelphia), pp. 45–112.

Farabaugh, S. M., Linzenbold, A., and Dooling, R. J. (**1994**). ''Vocal plasticity in budgerigars (*Melopsittacus undulatus*): Evidence for social factors in the learning of contact calls,'' J. Comp. Psych. **108**, 81–92.

Fee, M. S., Shraiman, B., Pesaran, B., and Mitra, P. P. (**1998**). ''The role of nonlinear dynamics of the syrinx in the vocalizations of a songbird,'' Nature (London) **395**, 67–71.

Gaunt, A. S., and Gaunt, S. L. L. (**1985**). ''Electromyographic studies of the syrinx in parrots (*Aves, Psittacidae*),'' Zoomorph. **105**, 1–11.

Greenewalt, C. H. (**1968**). *Bird Song: Acoustics and Physiology* (Smithsonian Institution, Washington, D.C.).

Hall, W. S., Brauth, S. E., and Heaton, J. T. (**1994**). ''Comparison of the effects of lesions in nucleus basalis and Field '*L*' on vocal learning and performance in the budgerigar (*Melopsittacus undulatus*),'' Brain Behav. Evol. **44**, 133–148.

Hall, W. S., Cookson, K. K., Heaton, J. T., Roberts, T., Shea, S. D., and Brauth, S. E. (**1997**). ''Audio–vocal learning in budgerigars,'' Ann. (N.Y.) Acad. Sci. **807**, 352–367.

Heaton, J. T., Farabaugh, S. M., and Brauth, S. E. (**1995**). ''Effect of syringeal denervation in the budgerigar (*Melopsittacus undulatus*): The role of the syrinx in call production,'' Neurobiol. Learn. Mem. **64**, 68–82.

Marler, P. (**1969**). ''Tonal quality of bird sounds,'' in *Bird Vocalizations*, edited by R. A. Hinde (Cambridge University Press, Cambridge), pp. 5–18.

Nottebohm, F. (**1976**). ''Phonation in the orange-winged Amazon parrot, *Amazona amazonica*,'' J. Comp. Physiol. **108**, 157–170.

Nowicki, S., and Capranica, R. R. (**1986a**). ''Bilateral syringeal coupling during phonation of a songbird,'' J. Neurosci. **6**, 3595–3610.

Nowicki, S., and Capranica, R. R. (**1986b**). ''Bilateral syringeal interaction in vocal production of an oscine bird sound,'' Science **231**, 1297–1299.

Pepperberg, I. M. (**1981**). ''Functional vocalizations by an African grey parrot (*Psittacus erithacus*),'' Z. Tierpsychol. **55**, 139–160.

Roederer, J. G. (**1995**). *The Physics and Psychophysics of Music* (Springer, New York).

Shea, S. D., Heaton, K. J., Heaton, J. T., Hall, W. S., and Brauth, S. E.

(**1997**). ''The role of contact calls in the social behavior of the budgerigar (*Melopsittacus undulatus*),'' Ann. (N.Y.) Acad. Sci. **807**, 571–573.
Silaeva, O. L. (**1998**). ''Comparative analysis of acoustic characteristics of human speech models: Prototypes and imitones of the budgerigar (*Melopsittacus undulatus*),'' Biol. Bull. **25**, 37–43.
Suthers, R. A. (**1997**). ''Peripheral control and lateralization of birdsong,'' J. Neurobiol. **33**, 632–652.
Titze, I. R. (**1994**). *Principles of Voice Production* (Prentice-Hall, Englewood Cliffs, NJ).
Todt, D. (**1975**). ''Social learning of vocal patterns and models of their application in Grey parrots,'' Z. Tierpsychol. **55**, 139–160.
Turney, S. M., Banta, P. A., and Pepperberg, I. M. (**1994**). ''Comparative acoustical analyses of learned English vocalizations of two parrot species,'' Anim. Behav. Soc. Abs. **89**.
Westneat, M. W., Long, Jr., J. H., Hoese, W., and Nowicki, S. (**1993**). ''Kinematics of birdsong: Functional correlation of cranial movements and acoustic features in sparrows,'' J. Exp. Biol. **182**, 147–171.

Acoustic detections of singing humpback whales (*Megaptera novaeangliae*) in the eastern North Pacific during their northbound migration[a)]

Thomas F. Norris[b)]
8455 Kingsland Road, San Diego, California 92123

Mark Mc Donald
2535 Sky View Lane, Laramie, Wyoming 82070

Jay Barlow
Southwest Fisheries Science Center, P.O. Box 271, La Jolla, California 92038

(Received 21 March 1998; accepted for publication 10 March 1999)

Numerous (84) acoustic detections of singing humpback whales were made during a spring (08 March–09 June 1997) research cruise to study sperm whales in the central and eastern North Pacific. Over 15 000 km of track-line was surveyed acoustically using a towed hydrophone array. Additionally, 83 sonobuoys were deployed throughout the study area. Detection rates were greatest in late March, near the Hawaiian Islands, and in early April, northeast of the islands. Only one detection was made after April. Detection rates for sonobuoys were unequal in three equally divided longitudinal regions of the study area. Two high density clusters of detections occurred approximately 1200–2000 km northeast of the Hawaiian Islands and were attributed to a large aggregation of migrating animals. The distribution of these detections corroborates findings of previous studies. It is possible that these animals were maintaining acoustic contact during migration. Two unexpected clusters of singing whales were detected approximately 900 to 1000 km west of central and southern California. The location of these detections may indicate a previously undocumented migration route between an offshore breeding area, such as the Revillagigedo Islands, Mexico, and possible feeding areas in the western North Pacific or Bering Sea. © *1999 Acoustical Society of America.* [S0001-4966(99)03706-6]

PACS numbers: 43.80.Ka [FD]

INTRODUCTION

Humpback whales (*Megaptera novaeangliae*) are undoubtedly the most studied of the large whales. In spite of this, little is known about their migratory routes, particularly in the North Pacific. In this study, numerous acoustic detections of singing humpback whales were made, revealing new information about the temporal, spatial, and behavioral characteristics of humpback whale migrations. Data were collected during a cruise conducted by the U.S. Southwest Fisheries Science Center (SWFSC) to study sperm whales (Barlow and Taylor, 1997). Fortunately, the timing and geographic area of the cruise coincided well with the northbound migration of humpback whales in the central and eastern North Pacific. This study was the first large-scale visual-acoustic survey of cetaceans in the eastern North Pacific and covered the greatest area ever surveyed using these techniques.

Humpback whales migrate annually from temperate and subpolar waters, where they feed in summer and fall, to tropical islands, coastal waters, and underwater banks, where they congregate to breed in winter through spring (Dawbin, 1966; Nishiwaki, 1966; Winn and Winn, 1978; Darling and McSweeney, 1985; Baker *et al.*, 1986). In fact, humpback whales have the longest mammalian migration ever documented (Clapham, 1996; Stone *et al.*, 1990). Long, complex songs are sung only by males during breeding season (Winn *et al.*, 1973; Winn and Winn, 1978; Lambertsen *et al.*, 1988; Medrano *et al.*, 1994). The function of singing is not well understood (Helweg *et al.*, 1992). However, most researchers agree that the primary role of song for humpback whales is similar to that for many birds, an advertisement display to attract mates and to displace or deter competitors (Winn and Winn, 1978; Tyack, 1981; Tyack and Whitehead, 1983; Frankel *et al.*, 1995). Although humpback whale songs are most often recorded in shallow water, low-latitude, breeding areas, they also have been recorded at high latitude feeding areas (Matilla *et al.*, 1987; McSweeney *et al.*, 1989), in deep water (Tyack and Whitehead, 1983; Clapham and Mattila, 1990; Frankel *et al.*, 1995), and along migration routes (Kibblewhite *et al.*, 1966; Payne and McVay, 1971; Dawbin and Gill, 1991).

The acoustic characteristics of humpback whale songs (e.g., high-intensity, repetitive signals with low-frequency energy) make them detectable at distances of 9–32 km or more using hydrophones (Winn *et al.*, 1975; Levenson and Leapley, 1978; Winn and Winn, 1978; Frankel *et al.*, 1995). In deep water (>200 m), favorable propagation characteris-

[a)]Portions of this work were reported at the 134th meeting of the Acoustical Society of America, 1–5 December 1997, San Diego, California [J. Acoust. Soc. Am. **102**, 3121 (1997)].

[b)]Present address: Science Applications International Corporation (SAIC), Martime Services, 3990 Old Town Ave., Suite 105A, San Diego, CA 92110. Electronic mail: Thomas.f.Norris@cpmx.saic.com

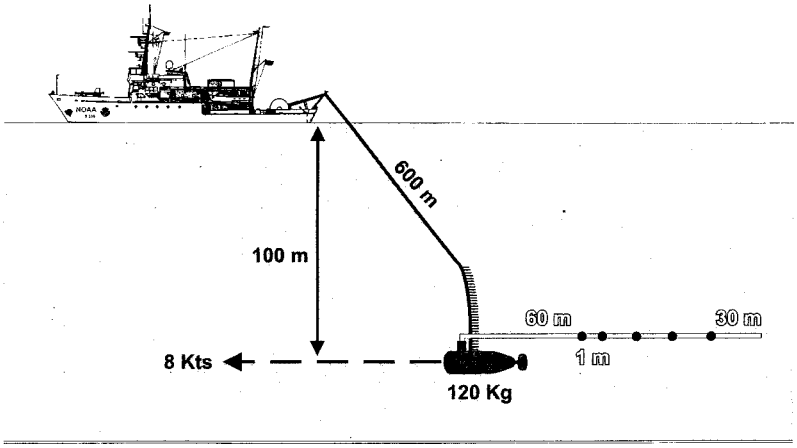

FIG. 1. Towed array acoustic system. The line with black circles (hydrophones) represents the towed array. The A/D converter and digital transmission system were encased in a pressure housing inside the towed-body. The black line (600 m) represents an oceanographic cable used to telemeter digital acoustic data to the ship.

tics and low ambient noise further increase the detection range of songs. Also, individual humpback whales often sing continuously for long periods (up to 24 h; Winn *et al.*, 1975) surfacing to breathe on average only every 14 minutes (Chu, 1988). Under these conditions, acoustic detections of singing animals are much more probable than visual detections.

Singing humpback whales have been acoustically surveyed and tracked in (or near) shallow water breeding areas using bottom-mounted hydrophone arrays, sonobuoys, and vessel deployed hydrophones (Winn *et al.*, 1975; Levenson and Leapley, 1978; Thompson and Friedl, 1982; Frankel *et al.*, 1995). Surveys of singing whales along potential humpback whale migratory routes were conducted by Clapham and Mattila (1990) in coastal and pelagic waters of the western North Atlantic, and by Dawbin and Gill (1991) along coastal waters off western Australia. In both of these studies, singing whales were detected using a single omnidirectional hydrophone deployed from a sailboat at ''recording stations.'' Although their results were limited in geographic scope (e.g., Winn *et al.*, 1975; Levenson and Leapley, 1978), or were constrained by the sampling design (e.g., nonrandom/systematic surveys; Clapham and Mattila, 1990; Dawbin and Gill, 1991), these researchers demonstrated that acoustic surveys of migrating humpbacks are effective.

More recently, Abileah *et al.* (1996) used beamformed data from the U.S. Navy's Sound Surveillance System (SOSUS) of hydrophone arrays in the North Pacific to detect singing humpback whales during their northbound migration across a large area north of Hawaii. They claimed to make over 100 detections during a 6-week period, but presented geographic locations for only six animals.

I. METHODS

Visual and acoustic surveys of cetaceans were conducted from 6 March through 10 June 1997 using NOAA's R/V MCARTHUR, a 52-m, oceanographic ship. The area and months of study were chosen to cover a large region of potential sperm whale habitat in the eastern North Pacific during their breeding season (Barlow and Taylor, 1997). Transect lines were placed systematically (given the constraints of the vessel's range) within the study area so that equal coverage occurred in four (N, S, E, W) equally divided quadrants.

Line transect sampling techniques (Buckland *et al.*, 1993) were used to visually survey all species of cetaceans encountered. NOAA/SWFSC marine mammal survey protocol (Barlow, 1995) was followed (with the exception that survey speed was reduced slightly to 7–8 kts to accommodate a towed array).

A towed hydrophone array system was incorporated into the survey to enhance detections of sperm whales. Sperm whales dive for long durations, making it difficult to detect them visually (Barlow, 1994, 1995). However, they consistently produce bioacoustic signals, and thus can be detected effectively using passive acoustics. During daylight hours, visual and acoustic surveys were conducted concurrently, but independently, to prevent acoustic and visual ''observers'' from cueing each other, and also to give both observer platforms the same opportunity to detect animals.

The towed hydrophone array system was designed primarily for detecting and determining bearings to sperm whale ''clicks.'' System frequency response was flat from approximately 10 to 16 000 Hz. Therefore, the system was capable of adequately receiving humpback whale songs which typically contain energy from 60 to 8000 Hz with dominant frequencies below 500 Hz (Levenson, 1969, 1972; Norris, 1995).

The hydrophone array (solid ''stealth'' array by ITI, Fort Worth, TX) consisted of five elements, irregularly spaced between 1 and 8 m. Two of the five hydrophones were selected electronically for digital transmission of acoustic data to the ship (Geo-Acoustics telemetry system, Ontario, Canada). Signals from these two channels were sampled at 32 kHz. The digital telemetry system and interface circuitry was housed in a 140-kg towed fish (originally designed for a towed sonar system) that was maintained at approximately 100-m depth (Fig. 1). This system was designed to be towed at near-normal marine mammal survey speeds, and at a suitable depth and distance from the ship to minimize ship noise. Gain-enhancing signal processing (e.g., beamforming) was not used.

On the ship, both channels were converted back to analog signals (effectively low-pass filtering at 16 kHz). The

signal from one channel was high-pass filtered at 1 kHz to reduce system, ship, and flow noise. Custom written spectrographic software displayed signals in real-time on a video monitor [Fig. 2(a)]. Signals from the other channel were high-pass filtered at a corner frequency of 10 Hz so that low-frequency signals produced by baleen whales could be detected.[1] Signals from both channels were input to a stereo headset for aural monitoring. Broadband signals were recorded continuously using a two-channel, DAT recorder (Sony DAT Walkman TCD-D8 or TCD-D7). Tapes which included signals of interest were saved for post-analysis and archival purposes.

Four acoustic technicians monitored signals from the towed array approximately 22 h per day. Detections of humpback whale song were noted on a computer file that stored and plotted GPS locations of the ship every 5 min (Barlow, 1997). A detection was defined as any signal heard (or seen) that exhibited characteristics unique to humpback whale song (e.g., frequency-modulated signals such as cries, moans, and whoops that are repeated in a rhythmic pattern). The following information was recorded: (1) presence/absence of humpback whale songs in a designated 20-min period each hour; (2) the estimated number of animals singing; (3) the time for any additional song detections during the remaining 40-min period; and (4) a subjective score of the signal-to-noise ratio (1–5 scale). These data were collected in order to standardize the signal monitoring and data recording effort, and to reduce the possibility of ''double counting'' the same animals (because only one detection was possible for any whale singing during each 1-h period). Song detections were included in the analysis only if at least one additional detection (from either the towed array or a sonobuoy) occurred in a 2-h period before or after the initial detection (4-h period total) or if the song detection was verified by a second bio-acoustician.

Sonobuoys (type 57A) were deployed each day (weather permitting) at a hydrophone depth setting of 122 m. Sonobuoys were used primarily to monitor for low-frequency signals produced by baleen whales, including songs of humpback whales. Occasionally, sonobuoy arrays (usually four to five sonobuoys) were deployed on groups of acoustically active sperm whales. Sonobuoy signals were transmitted to a multi-channel receiver (Greeneridge Sciences) and recorded on audio DAT [Sony DAT Walkman model TCD-D8 or TCD-D7, two channels at 48-kHz sampling rate; or a TEAC model RD135, up to eight channels at 20-kHz sampling rate; Fig. 2(b)]. Sonobuoys also were deployed when large cetaceans were encountered. Sonobuoy signals were recorded for at least 40 min or until the signal quality was considered unacceptable. Short (approximately 1 min.) signal segments were acquired in real-time every few minutes and spectrographs were produced (using Canary bioacoustical signal processing software) for visual inspection. If humpback whale songs were not detected during shipboard monitoring, DAT recordings were reviewed later by examining spectrograms made from 3-min segments of signals extracted from every 5–10 min of tape.

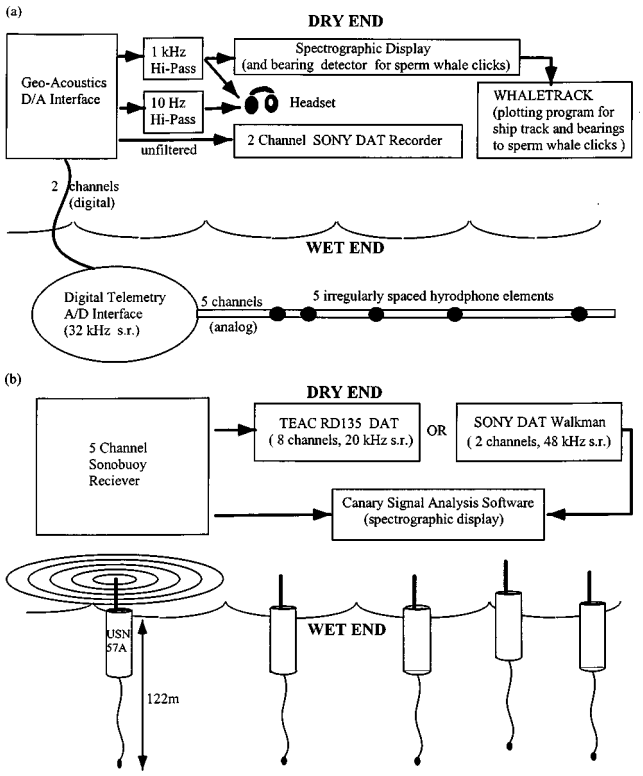

FIG. 2. (a) Towed hydrophone-array system. The digital telemetry system (housed in towed fish) was used to select signals from two hydrophones for digital transmission to the dry end. (b) Sonobuoy recording system. Up to five sonobuoys could be recorded simultaneously; however, usually only one or two were deployed at a time.

II. RESULTS

Approximately 15 400 km of track-line were acoustically surveyed with the towed array for a total of 1040 hours of effort (Fig. 3). Detection rates of humpback whale songs were greatest during leg I, 08 March–03 April (0.184 detections/hour), somewhat lower during leg II, 08 April–07 May (0.110), and lowest during leg III, 11 May–09 June (0.002). Detection rates for the towed array were unequal among the three legs ($X^2=58.64$; $df=2$; $p<0.05$). Songs were not detected after 23 May.

Humpback whale songs were detected on 30% (21 of 83) of all sonobuoys deployed over 64 days. Sonobuoy detection rates (buoys with detections/buoys deployed) were 0.423 during leg I and 0.357 during leg II. There were no detections from sonobuoys during leg III. Sonobuoy detection rates were unequal when compared among the three legs ($X^2=11.51$; $df=2$; $p<0.05$).

Overall, songs were detected on 34% (19 of 56) of days in which there was acoustic effort with the towed array, and on 28% (18 of 64) of days with at least one sonobuoy deployment. Combined, the sonobuoys and towed array resulted in detections of singing humpback whales on 36% (23 of 70) of days with acoustic effort. In comparison, only four visual sightings of humpback whales were made during 77 days (690 hours) of effort (Table I).

Detection rates of sonobuoys were unequal when compared among three equally divided longitudinal sectors of the study area ($X^2=24.13$; $df=2$; $p<0.05$; Table II). The high-

TABLE I. Summary of effort and number of humpback whale song detections per leg. Towed array detections of songs are indicated as the number of effort days and hours with at least one detection. Sonobuoy detections are indicated by the number of sonobuoys in which at least one detection of song was made. Visual detections were widely separated in space and/or time.

	Effort				Detections			
Leg no. (dates)	Days at sea	Towed array km (h)	Sonobuoys deployed	Visual km (h)	Towed array days with detection	Towed array hours with detection	Sonobuoys	Visual
Leg I	24	2581	26	3070	5	32	11	1
08 March–03 April		(174)		(207)				
Leg II	30	6865	28	3531	11	51	10	2
07 April–07 May		(463)		(238)				
Leg III	28	5998	29	3627	1	1	0	1[a]
11 May–09 June		(404)		(244)				
Total	82	15 565	83	10 228	17	84	21	4
		(1041)		(689)				

[a]Mother with calf.

est densities of detections occurred in the vicinity of the Hawaiian Islands, especially during the first NE transect of leg II (Fig. 1). Additionally, there were two distinct clusters of detections located 900–1000 km off the coast of southern and central California at approximately 30° N 130° W and 36°N 134° W, respectively (Fig. 2). These two clusters of detections were separated (due to the timing of the survey legs) by 48 days.

III. DISCUSSION

A. Temporal and spatial distribution

Greater song detection rates occurred during late March and early April compared to mid April through early June. Although these temporal trends may have been partially biased due to the high densities of singing animals encountered near the Hawaiian Islands during the end of leg I and the beginning of leg II, these results are supported by findings from other studies on relative abundances and the timing of the northbound migration of humpback whales in the Hawaiian Islands (Baker and Herman, 1981; Smultea, 1994; Mate *et al.*, 1998). Only one song detection was made after 30 April (approximately 1400 km north of the Hawaiian Islands on 23 May, leg III; Fig. 2). Late April generally denotes the end of the humpback whale winter/breeding season in the North Pacific, as most humpback whales have departed north to feeding areas (Herman *et al.*, 1980; Baker and Herman, 1981). The low detection rate for leg III may have been due to a decrease in singing behavior, a reduction in the number of animals present, or most likely, a combination of these.

Relative abundances of humpback whales at, or near, breeding areas and along migration routes have been shown to be temporally staggered with respect to age/sex classes (Nishiwaki, 1966; Dawbin, 1966, 1997; Smultea, 1994; Gabrielle, 1992; Brown *et al.*, 1995). Reproductively mature males (e.g., singers) and females depart after newly pregnant and nonreproducing females, but before females with newborn calves. As long as these age- and sex-class-related differences are accounted for, acoustic surveys can be used for examining the migratory behavior of reproductively active males, and even the timing of migration for non-singing whales.

The densities of song detections were unequally distributed with respect to three equal longitudinal sectors (Table II). As expected, the greatest densities of singers occurred near the main Hawaiian Islands (Fig. 3). Song detections were scattered broadly to the northeast and northwest of Oahu, areas where survey effort was concentrated. High densities of singing animals were detected during leg II at the northeast end of the first transect (originating in Oahu heading NE). Presumably, these animals were migrating to Alaskan feeding areas (Calambokidis *et al.*, 1997; Baker *et al.*, 1986). During late March and early April 1995, Mate *et al.* (1998) tracked the initial northbound migration of four humpback whales (a female with calf, an adult, and a possible juvenile) tagged with satellite transmitters in waters off Kauai. The adult and the smaller animal (juvenile) traveled over 1600 and 1800 km, respectively, on a heading of approximately magnetic north (10° true) before the signal was lost. At the same time, Abileah *et al.* (1996) used cross-fixing techniques with SOSUS hydrophone arrays to determine the locations of singing humpback whales in the same region. They determined four locations between approximately 30 N and 40 N which they used to ''loosely define a 'migration corridor' bounded by longitudes 150 W and 160 W.'' Although the distribution of detections from leg II of

TABLE II. Sonobuoy detections by longitudinal sectors with expected distribution if randomly distributed.

	Longitudinal sector			
	164W–150W	149W–135W	134W–120W	Total
No. of sonobuouys deployed	61	73	81	215
No. of sonobuoys with detections	16	1	4	21
No. of detections expected if random	5.96	7.13	7.91	21

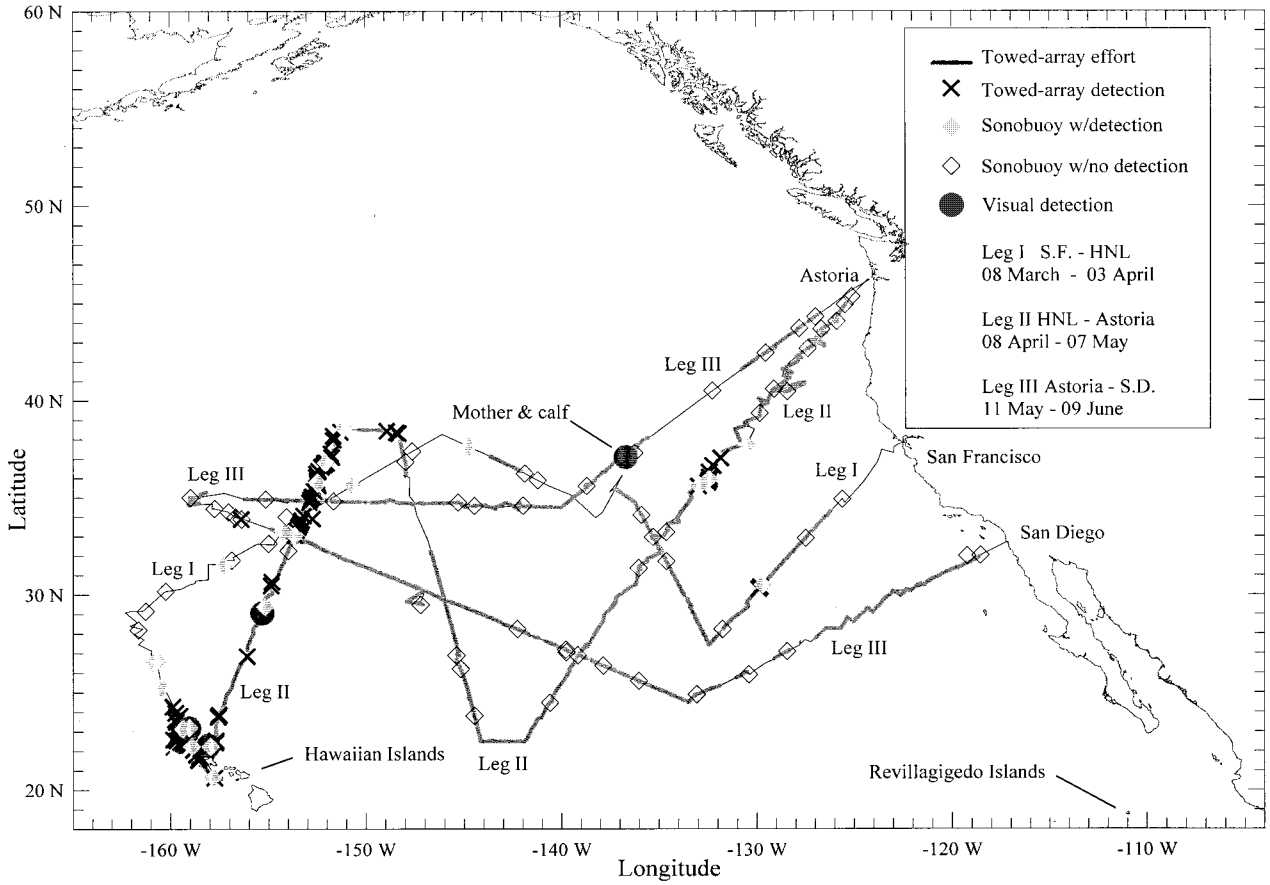

FIG. 3. Locations of acoustic and visual detections of humpback whales. Acoustic detections are not necessarily representative of individual animals (e.g., one individual may be represented by more than one ×). Towed array effort depicted by thick track lines.

our study corroborates these findings (Fig. 1), there also were numerous detections made during the end of leg I (NNE of Oahu) that were outside of boundaries of their ''migration corridor.'' However, most of these detections occurred earlier in the season and, generally, were within 200 km of the Hawaiian Islands.

The large group of acoustic detections that occurred to the northeast of Oahu (approximately 33°–38° N; Fig. 2) in mid-April can be attributed to a disperse group of singing animals migrating within general proximity (tens of miles) of each other. Assuming that these animals were traveling at similar rates and headings, this ''pulse'' of detections could have been the result of a concentration of animals that departed the Hawaiian Islands within a short period (e.g., a few days). Payne and Webb (1971) proposed that baleen whales may maintain acoustic contact over large areas (e.g., ocean basins) forming what they termed a ''range herd.'' It is possible that singing may be used by a group of humpbacks to maintain contact during migrations. Alternatively, it also is possible that these high-density regions of singing whales are an indication that courtship activity continues during migration. To examine these possibilities will require information about the behavior of both singing males and nonsinging females during migration.

Perhaps of greater interest were two clusters of detections that occurred approximately 900–1000 km off the coast of California (Fig. 3). This band of pelagic detections was not associated with islands, seamounts, or any other obvious seabed features that might indicate a previously unknown breeding area for humpback whales in North Pacific. To our knowledge, there is no other documented information about sightings or acoustic detections of humpbacks whales from this offshore region.

Humpback whales have been detected off the California coast during winter and spring from aerial surveys (Dohl *et al.*, 1983; Forney *et al.*, 1995) and from photographic identification studies (Calambokidis *et al.*, 1996). Based on aerial surveys off California, Forney and Barlow (1998) determined that winter/spring sightings of humpback whales were distributed significantly further offshore than summer/fall sightings. They suggested the possibility that offshore winter/spring animals ''are traveling through the offshore region en route to other feeding areas to the north.'' Unfortunately, in all of these studies, surveys were limited to waters within 100 nautical miles (180 km) of the coast (Forney *et al.*, 1995), or within the continental shelf break (Dohl *et al.*, 1983; Calambokidis *et al.*, 1996).

Calambokidis *et al.* (1996) collected photographic identifications of humpback whales (597 individuals) from nearshore waters (<65 km) off California, Washington, and Oregon, from April through December. These were compared to an extensive photographic catalog of whales (>700 individuals) from eastern North Pacific feeding areas (British Columbia, Canada, SE Alaska, Prince William Sound, Ko-

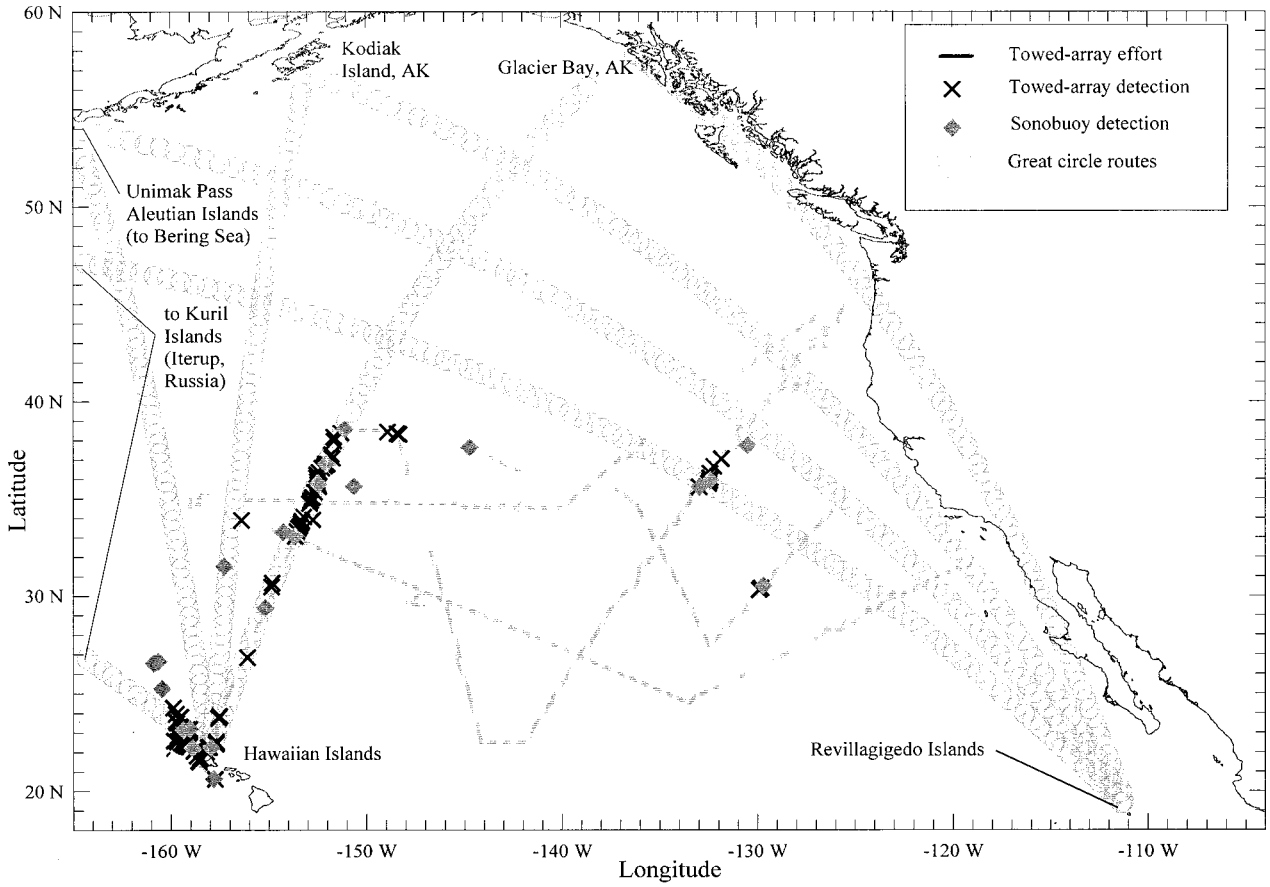

FIG. 4. Locations of all humpback whale acoustic detections with great circle routes plotted from the Hawaiian and Revillagigedo Island breeding areas to possible North Pacific feeding areas. Routes were not plotted from Hawaii to CA/OR/WA and BC (Canada) feeding areas because there is limited interchange of animals between these locations (Baker *et al.*, 1986; Calambokidis *et al.*, 1997). Great circle routes are not intended to indicate the actual paths taken by migrating whales, only possible termini.

diak Island and Shumigan Island, AK, and the Bering Sea). The paucity of matches between these two data sets led them to conclude that the waters off CA/WA/OR represented a distinct feeding area, and that animals bound for Alaskan waters (from Mexico) must ''migrate well offshore (more than 65 km), or pass earlier or later in the season than [their] sampling effort.'' Only one[2] match was found when a photographic identification catalog of humpback whales from the Revillagigedo Islands (159 individuals) was compared with those from a large (1000 individuals) catalog of whales from numerous eastern North Pacific feeding areas (Calambokidis *et al.*, 1997).

B. Implications for migratory routes

One explanation for the clusters of detections discovered offshore of California is that they represent singing animals that were migrating north from wintering/breeding areas off Mexico.[3] Furthermore, the great distance that these detections occurred from shore could indicate that these animals originated from an offshore breeding area such as the Revillagigedo Islands (Fig. 4). If these offshore detections were indeed from migrating animals that originated from the Revillagigedo Islands, whereas individuals from the Mexican mainland breeding areas are following a more coastal migration route (as appears to be the case; Calambokidis *et al.*, 1996), then there may be evidence for segregation of migration routes for humpback whales from two geographically close, but separate, breeding areas. This situation would have great implications concerning the population structure of North Pacific humpback whales. To examine these possibilities will require determining the migration routes taken by humpback whales from different breeding areas (especially those from Mexican and Japanese waters) and determining differences in migratory behaviors related to age class, sex class, and reproductive status.

Possible migratory destinations of singing humpback whales detected in this study were investigated by plotting great circle routes (i.e., the shortest possible route between two points on a globe) between Hawaiian and Revillagigedo Island breeding areas, to potential feeding areas in the North Pacific. The great circle routes (GCR) that originate from the Revillagigedo Islands and pass through the offshore cluster of detections, lead to areas in the western North Pacific or Bering Sea (e.g., the western Aleutian Islands, Kamchatka Peninsula, or Kuril Islands; Fig. 4). Obviously, plotting GCR is an oversimplified prediction of possible endpoints of migrations, and, as such, they are not meant to indicate the actual routes taken by migrating whales.

There has been limited photographic identification effort in the western North Pacific and Bering Sea. However, the

paucity of matches for whales between the Revillagigedo Islands and several well-documented feeding areas in the eastern North Pacific has led some investigators to suggest that humpback whales from the Revillagigedo Islands breeding area could be migrating to feeding areas in the western North Pacific or Bering Sea (Calambokidis *et al.*, 1997).

Although it cannot be ruled out, it is unlikely that the offshore cluster of detections were ''Hawaiian'' animals migrating to coastal feeding areas off California, Oregon, and Washington. All of these areas have been sampled thoroughly from photographic identification studies and results indicate limited interchange of animals (Perry *et al.*, 1988; Calambokidis *et al.*, 1997). There were no detections of humpback whales in the region between the offshore cluster of detections and the U.S. coast (i.e., the end of leg II and the beginning of leg III), a region that had excellent acoustic and visual coverage (Fig. 2). Therefore, it is unlikely that the offshore detections were of animals migrating from Mexican breeding areas to feeding areas in SE Alaska or the mainland U.S. coasts.

If, in fact, whales from the Revillagigedo Islands are migrating to feeding areas in the western Pacific or Bering Sea, the resulting implications are considerable. For example, humpback whales migrating between from the Hawaiian Islands and SE Alaska (and adjacent feeding areas; Baker *et al.*, 1986) and those animals migrating between the Revillagigedo Islands and western North Pacific feeding areas would cross paths in a broad region several hundred miles northeast of the Hawaiian Islands (approximately 45° N, 145° W; Fig 3). If this scenario is correct, it could explain when and where acoustic contact between singing whales is occurring, and how animals in acoustically isolated breeding regions (Mexico and Hawaii) are maintaining a similar, yet changing, version of song [Winn *et al.*, 1981; Payne and Guinee, 1983; Helweg *et al.*, 1992, 1998; Cerchio *et al.* (in press)]. The evolutionary implications of segregated but crossing migration routes for these putative stocks of whales are quite significant, however further examination of these must await substantiation of actual migration routes and an assessment the degree of reproductive isolation for animals from different breeding areas.

Recent information from photographic identification studies indicates that some humpback whales migrate between feeding and breeding areas that are on opposite (i.e., diagonally opposed) ends of their respective ocean basins (e.g., Japan to British Columbia, Canada, for North Pacific humpback whales; Darling *et al.*, 1996; and Norway to the West Indies for North Atlantic humpback whales; Stevick *et al.*, 1998). Some researchers have even speculated that humpback whales could be taking advantage of ''tail-currents'' in the North Pacific (Baker and Herman, 1981); others, however, have discounted this possibility for humpback whale migrations occurring in the northern (Mate *et al.*, 1998) and southern hemispheres (Dawbin, 1966).[4]

C. Biases, recommendations, and conclusions

In this study, systematic transects were used to survey a large study area. By coincidence, several transects were oriented parallel to the direction of migrating humpback whales. Unfortunately, in one case (e.g., the first transect of Leg II), the survey vessel was traveling in the same direction as migrating whales (Fig. 2). A more effective sampling design for humpback whales would consist of systematic transects that are arranged perpendicular (e.g., east–west) to the predominant direction of travel (e.g., south–north) for migrating whales. Another potential bias of this study was the poor towed array coverage (due to equipment malfunctions and weather constraints) of coastal regions off the western continental U.S. and NW of the Hawaiian Islands (Fig. 3). This precluded an assessment of the coastal distribution of singing/migrating humpback whales and potentially biased the trends observed near the Hawaiian islands (although sonobuoy coverage was adequate there).

To effectively use acoustic surveys to determine absolute abundances of animals, it will be necessary to determine the proportion of time animals spend singing (or producing other sounds). In humpback whales, song bout length increases throughout the breeding season (Tyack, 1981), and it is likely that bioacoustical signals produced by other mysticetes vary temporally as well. To asses this potential bias, numerous individuals must be acoustically monitored for extended periods (e.g., hours to days). This will require visually tracking or tagging animals while simultaneously monitoring their acoustic behavior. Fortunately, recent advances in tagging and tracking techniques will probably allow these data to be collected in the near future (Flagg *et al.*, 1997; Fletcher *et al.*, 1996; Frankel, 1995). Until then, acoustic surveys will be limited to describing *relative* distribution and abundances of bioacoustically active animals.

Another problem associated with acoustic survey techniques is the difficulty in reliably determining an estimate of the absolute number of animals detected based on acoustic ''contacts'' (Hiby and Hammond, 1989; Thomas *et al.*, 1986; Leaper *et al.*, 1992). In this study, the total number of hourly periods with song detections is most likely an overestimate of the actual numbers of singing animals encountered because, on average, each individual was probably detected more than once (i.e., in more than one hourly period). Conversely, the number of days with acoustic detections is a great underestimate of the actual number of animals encountered, because acoustic detections often occurred in clusters, resulting in no more than one detection counted for any group of animals (Fig. 2). Because the acoustic system in this study was not designed to localize individual whales, a statistically based estimate (e.g., using distance sampling methods) of the abundance of singing whales could not be made.

Probably the most important recommendation for future acoustic surveys is to incorporate sound source localization techniques so that the absolute number of animals encountered can be estimated more accurately. Localization with towed arrays is possible using signal arrival delays (Barlow, 1997), beamforming (Lashkari and Lowder, 1997), and hyperbolic fixing (Clark and Fristrups, 1997), or (using a more simplistic approach) with directional hydrophones (Leaper *et al.*, 1992; Winn *et al.*, 1975). Given their field-proven effectiveness, acoustic detection systems should be included as

an important component in future studies of the distribution, relative abundance, and behavior of bio-acoustically active cetaceans.

Results from this study provided new information on migratory routes of humpback whales across a large region of the eastern North Pacific. Future studies should examine migratory routes of animals from isolated breeding areas, the extent that singing occurs during migration, and differences in migratory behaviors related to differences in age, sex, and reproductive classes.

ACKNOWLEDGMENTS

We would like to acknowledge the scientific party from the SWAPS sperm whale cruise, especially the acoustic survey team of Olaf Jaeke, Duncan E. McGehee, Sarah Mesnick, Laura Morse, and Aviva Rosenberg. John Hildebrand (SIO) provided equipment and advice for the sonobuoy work. This work would not have been possible without the encouragement and financial support provided by Barbara Taylor. Laura Morse helped with initial data compilation and analysis. Sal Cerchio, Jeff Jacobsen, and Barbara Taylor reviewed drafts of the manuscript and provided useful suggestions. John Calambokidis provided information and advice about photographic identification studies. This work was supported by ONR and NOAA.

[1]Due to flow noise, ship noise, and natural ambient noise, most faint biological signals were note detectable at frequencies below 100 Hz.

[2]The Revillagigedo Island photographic sample used in this study was collected during only 1 season (compared to at least three seasons for most other areas). Recently, Jorge Urban and Jeff Jacobsen (personal comm.) have found additional matches between animals from the Revillagigedo breeding area and Alaskan feeding areas. However, the rate of matches still remains low (<5%).

[3]Most data indicates that in the Mexican Pacifc there probably are two isolated stocks of whales: a coastal mainland stock and a stock around the Revillagigedo Islands (Urban *et al.*, 1987; Alvarez *et al.*, 1988).

[4]It is interesting to note that a southeast–northwest migration route from the Revillagigedo Islands would bypass the California Current (southerly flow). If this route were to continue towards northeastern Asia, it might allow animals to take advantage of the Alaskan Stream (westerly flow) and Kamchatka Currents (southwesterly flow).

Abileah, R., Martin, D., Lewis, S. D., and Gisiner, B. (**1996**). ''Long-range acoustic detection and tracking of the Hawaii-Alaska migration,'' in MTS/IEEE Oceans 96, Ft. Lauderdale, FL, Vol. 1, pp. 373–377.

Alvarez, C., Aguayo, A., Rueda, R., and Urban, J. (**1988**). ''A note on the stock size of humpback whales along the Pacific coast of Mexico,'' Rep. Int. Whal. Commn. (special issue 12): 191–193.

Baker, C. S., and Herman, L. M. (**1981**). ''Migration and local movement of humpback whales (*Megaptera novaeangliae*) through Hawaiian waters,'' Can. J. Zool. **59**, 461–469.

Baker, C. S., Herman, L. M., Perry, A., Lawton, W. S., Straley, J. M., Wolman, A. A., Kaufman, G. D., Winn, H. E., Hall, J. D., Reinke, J. M., and Ostman, J. (**1986**). ''Migratory movement and population structure of humpback whales (*Megaptera novaeangliae*) in the central and eastern North Pacific,'' Mar. Ecol. Prog. Ser. **31**, 105–119.

Barlow, J. (**1994**). ''Recent information on the status of large whales in California,'' NOAA Tech. Mem. NMFS-SWFSC-203, Southwest Fisheries Science Center, La Jolla, CA.

Barlow, J. (**1995**). ''The abundance of cetaceans in California waters. Part I: ship surveys in summer and fall 1991,'' Fish. Bull. **93**(1), 1–14.

Barlow, J. (**1997**). ''SWAPS cruise towed acoustic system,'' unpublished report, NOAA Southwest Fisheries Science Center, La Jolla, CA.

Barlow, J., and Taylor, B. (**1997**). ''Acoustic census of sperm whales in the eastern temperate North Pacific,'' J. Acoust. Soc. Am. **102**, 3213 (abstract).

Brown, M. R., Corkeron, P. J., Hale, P. T., Schultz, K. W., and Bryden, M. M. (**1995**). ''Evidence for a sex-segregated migration in the humpback whale (*Megaptera novaeangliae*)'' Proc. R. Soc. London, Ser. B **259**, 229–234.

Buckland, S. T., Anderson, D. R., Burnham, K. P., and Laake, J. L. (**1993**). *Distance Sampling: Estimating Abundance of Biological Populations* (Chapman and Hall, London).

Calambokidis, J., Steiger, G. H., Evenson, J. R., and Flynn, K. R. (**1996**). ''Interchange of humpback whales off California and other North Pacific feeding grounds,'' Mar. Mamm. Sci. **12**(2), 215–226.

Calambokidis, J., Steiger, G. H., Straley, J. M., Quinn II, T. J., Herman, L. M., Cerchio, S., Salden, D. R., Yamaguchi, M., Sato, F., Urban, R., Jacobsen, J., von Ziegesar, O., Balcomb, K. C., Gabriele, C. M., Dahlheim, M. E., Higashi, N., Uchida, S., Ford, J. K. B., Miyamura, Y., Ladron de Guevara, P. P., Mizroch, S. A., Schlender, L., and Rasmussen, K. (**1997**). ''Abundance and population structure of humpback whales in the north Pacific basin,'' final report submitted to Southwest Fisheries Science Center, La Jolla, CA, Contract No. 50ABNF500113.

Cerchio, S., Jacobsen, J. K., and Norris, T. F. (**1999**). ''Temporal and geographic variation in songs of humpback whales (*Megaptera novaeangliae*): Synchronous change in Hawaiian and Mexican breeding assemblages,'' Behav. Ecol. Sociobiol. (in press).

Chu, K. C. (**1988**). ''Dive times and ventilation patterns of singing humpback whales (*Megaptera novaeangliae*),'' Can. J. Zool. **66**, 1322–1327.

Clapham, P. J. (**1996**). ''The social reproductive biology of Humpback Whales: an ecological perspective,'' Mamm. Rev. **26**, 27–49.

Clapham, P. J., and Matilla, D. K. (**1990**). ''Humpback whale songs as indicators of migration routes,'' Mar. Mamm. Sci. **6**(2), 155–160.

Clark, C. W., and Fristrup, K. M. (**1997**). ''Whales '95: A combined visual and acoustic survey of blue and fin whales off southern California,'' Rep. Int. Whal. Commn. **47**, 583–600.

Darling, J. D., and McSweeny, D. (**1985**). ''Observations of the migrations of North Pacific humpback whales (*Megaptera novaeangliae*),'' Can. J. Zool. **63**, 308–314.

Darling, J. D., Calambokidis, J., Balcomb, K. C., Bloedel, P., Flynn, K., Mochizuki, A., Mori, K., Sato, F., Suganuma, H., and Yamaguchi, M. (**1996**). ''Movement of a humpback whale (*Megaptera novaeangliae*) from Japan to British Columbia and return,'' Mar. Mamm. Sci. **12**(2), 281–287.

Dawbin, W. H. (**1966**). ''The seasonal migratory cycle of humpback whales,'' in *Whales, Dolphins and Porpoises*, edited by K. S. Norris (Univ. of California, Berkeley, CA), pp. 145–170.

Dawbin, W. H. (**1997**). ''Temporal segregation of humpback whales during migration in southern hemisphere waters,'' Memoirs of the Queensland Museum. **42**(1), 105–138.

Dawbin, W. H., and Gill, P. C. (**1991**). ''Humpback whale survey along the west coast of Australia: a comparison of visual and acoustic observations,'' Memoris of the Queensland Museum **30**(2), 255–257.

Dohl, T. P., Guess, R. C., Duman, M. L., and Helm, R. C. (**1983**). ''Cetaceans of central and northern California, 1980–1983: Status, abundance and distribution,'' OCS study MMS 84-0045, MMS Contract No. 14-12-0001-29090.

Flagg, M., Norris, T. F., and Croll, D. (**1997**). ''An acoustic transponder based tracking, data-telemetry, and logging system for real-time monitoring of 3-D positions and collection of other data from large marine vertebrates,'' J. Acoust. Soc. Am. **102**, 2462–3216.

Fletcher, S., LeBoeuf, B. J., Costa, D. P., and Tyack, P. L. (**1996**). ''Onboard acoustic recording from diving elephant seals,'' J. Acoust. Soc. Am. **100**, 2531–2539.

Forney, K. A., Barlow, J., and Carreta, J. V. (**1995**). ''The abundance of cetaceans in California waters. Part II: Aerial surveys in winter and spring of 1991 and 1992,'' Fish. Bull. **93**, 15–26.

Forney, K., and Barlow, J. (**1998**). ''Seasonal patterns in the abundance and distribution of California cetaceans, 1991–92,'' Mar. Mamm. Sci. **14**(3), 460–489.

Frankel, A. S., Clark, C. W., Herman, L. M., and Gabriele, C. M. (**1995**). ''Spatial Distribution, Habitat Utilization, and Social Interactions of Humpback Whales, *Megaptera novaeangliae*, off Hawai'i using Acoustic and Visual Techniques,'' Can. J. Zool. **73**(6), 1134–1146.

Gabriele, C. M. (**1992**). ''The behavior and residence characteristics of reproductive classes of humpback whales (*Megaptera novaeangliae*) in the Hawaiian Islands,'' M. S. thesis, University of Hawaii.

Helweg, D. A., Frankel, A. S., Mobley, Jr., J. R., and Herman, L. M. (**1992**). ''Humpback whale song: our current understanding,'' in *Marine Mammal*

Sensory Systems, edited by J. Thomas, R. Kastelein, and A. Supin (Plenum, New York), pp. 459–483.
Helweg, D. A., Cato, D. H., Jenkins, P. F., Garrigue, C., and McCauley, R. D. (**1998**). ''Geographic variation in South Pacific humpback whale songs,'' Behaviour **135**, 1–27.
Herman, L. M., Forrestell, P. H., and Antinoja, R. C. (**1980**). ''Study of the 1976/1977 migration of humpback whales into Hawaiian waters: composite description,'' Final Report to the U.S. Mar. Mamm. Commn. Report No. MMC-77/19, NTIS (PB80-162332, Arlington, VA.
Hiby, A. R., and Hammond, P. S. (**1989**). ''Survey techniques for estimating abundance of cetaceans,'' Behaviour Rep. Int. Whal. Commn. (special issue) **11**, 47–80.
Jacobsen, J., and Urban, Jorge (**1999**). Personal communication.
Kibblewhite, A. C., Denham, R. N., and Barnes, D. J. (**1966**). ''Unusual low frequency signals observed in New Zealand waters,'' J. Acoust. Soc. Am. **41**, 644–655.
Lambertsen, R. H., Baker, C. S., Duffield, D. A., and Chamberlin-Lea, J. (**1988**). ''Cytogenetic determination of sex among individually identified humpback whales (*Megaptera novaeangliae*),'' Can. J. Zool. **66**, 1243–1248.
Lashkari, K., and Lowder, S. (**1997**). ''Ocean Acoustic Observatory for PassiveMonitoring of the Ocean'' (abstract) Underwater Bio-Sonar and Bioacoustics Symposium, Loughborough, England, Vol. 19, Pt. 9, pp. 107–114.
Leaper, R., Chappel, O., and Gordon, J. (**1992**). ''The development of practical techniques for surveying sperm whale populations acoustically,'' Rep. Int. Whal. Commn. **42**, 549–560.
Levenson, C. (**1969**). ''Behavioral, physical, and acoustic characteristics of humpback whales (*Megaptera novaeangliae*) at Argus Island,'' Naval Oceanographic Office Informal Report No. 69–54.
Levenson, C. (**1972**). Characteristics of sounds produced by humpback whales (*Megaptera novaeangliae*), NAVOCEANO Tech. Note No. 7700-6-72 (Naval Oceanographic Office, Washington, DC).
Levenson, C., and Leapley, W. T. (**1978**). ''Distribution of humpback whales (*Megaptera novaeangliae*) in the Caribbean determined by a rapid acoustic method,'' J. Fish. Res. Board Can. **35**, 1150–1152.
Mate, B. R., Gisiner, R., and Mobley, J. (**1998**). ''Local and migratory movements of Hawaiian humpback whales tracked by satellite telemetry,'' Can. J. Zool. **76**, 863–868.
Matilla, D. K., Guinee, L. N., and Mayo, C. A. (**1987**). ''Humpback whale songs on the North Atlantic feeding grounds,'' J. Mammal. **68**, 880–883.
McSweeny, D. J., Chu, K. C., Dolphin, W. F., and Guinee, L. N. (**1989**). ''North Pacific humpback whale songs: a comparison of southeast Alaskan feeding ground songs with Hawaiian wintering ground songs,'' Mar. Mamm. Sci. **5**(2), 139–148.
Medrano, L., Salinas, M., Salas, I., Ladron de Guevara, P. L., Aguayo, A., Jacobsen, J., and Baker, C. S. (**1994**). ''Sex identification of humpback whales, *Megaptera novaeangliae*, on the wintering ground of the Mexican Pacific,'' Can. J. Zool. **72**, 1771–1774.
Nishiwaki, M. (**1966**). ''Distribution and migration of the larger cetaceans in the north Pacific as shown by Japanese whaling results,'' in *Whales, Dolphins and Porpoises*, edited by K. S. Norris (Univ. of California, Berkeley, CA), pp. 171–191.
Norris, T. F. (**1995**). ''The effects of noise on the singing behavior of humpback whales (*Megaptera novaeangliae*),'' M. S. thesis, Moss Landing Marine Laboratories, California State University.
Payne, R., and Guinee, L. (**1983**). ''Humpback whale (*Megaptera novaeangliae*) songs as an indicator of ''stocks,'' in *Communication and Behavior of Whales*, edited by R. Payne (Westview, Boulder, CO), pp. 333–358.
Payne, R. S., and McVay, S. (**1971**). ''Songs of humpback whales,'' Science **173**, 585–597.
Payne, R., and Webb, D. (**1971**). ''Orientation by means of long range acoustic signalling in baleen whales,'' Ann. (N.Y.) Acad. Sci. **188**, 110–142.
Perry, A., Baker, C. S., and Herman, L. M. (**1988**). ''Population characteristics of individually identified humpback whales (*Megaptera novaeangliae*) in the central and eastern North Pacific: a summary and critique,'' Rep. Int. Whal. Commn. (special issue) **12**, 307–317.
Smultea, M. A. (**1994**). ''Segregation by humpback whale (*Megaptera novaeangliae*) cows with a calf in coastal habitat near the island of Hawaii,'' Can. J. Zool. **72**, 805–811.
Stevick, P. T. (**1998**). ''Migration of a humpback whale (*Megaptera novaeangliae*) between Norway and the West Indies,'' Mar. Mamm. Sci. **14**(1), 162–166.
Stone, G. S., Florez-Gonzales, L., and Katona, S. K. (**1990**). ''Whale migration record,'' Nature (London) **346**, 705.
Thomas, J. A., Fisher, S. R., and Ferm, L. M. (**1986**). ''Acoustic detection of cetaceans using a towed array of hydrophones,'' Rep. Int. Whal. Commn. (special issue) **8**, 139–148.
Thompson, P. O., and Friedl, W. A. (**1982**). ''A long term study of low frequency sounds from several species of whales off Oahu, Hawaii,'' Cetology **45**, 1–19.
Tyack, P. (**1981**). ''Interactions between singing Hawaiian humpback whales and conspecifics nearby,'' Behav. Ecol. Sociobiol. **8**, 105–116.
Tyack, P., and Whitehead, H. (**1983**). ''Male competition in large groups of wintering humpback whales,'' Behaviour **83**, 132–154.
Urbán, J., and Aguayo, A. (**1987**). ''Spatial and seasonal distribution of the humpback whale, *Megaptera novaeangliae*, in the Mexican Pacific,'' Mar. Mamm. Sci. **3**(4), 333–344.
Winn, H. E., Thompson, T. J., Cummings, W. C., Hain, J., Hudnall, J., Hays, H., and Steiner, W. W. (**1981**). ''Song of the humpback whale: population comparisons,'' Behav. Ecol. Sociobiol. **8**, 41–46.
Winn, H. E., Bischoff, W. L., and Taruski, A. G. (**1973**). ''Cytological sexing of cetacea,'' Mar. Biol. **23**, 343–346.
Winn, H. E., Edel, R. K., and Taruski, A. G. (**1975**). ''Population estimates of the humpback whale (*Megaptera novaeangliae*) in the West Indies by visual and acoustic techniques,'' J. Fish. Res. Board Can. **32**(4), 449–506.
Winn, H. E., and Winn, L. K. (**1978**). ''The song of the humpback whale (*Megaptera novaeangliae*) in the West Indies,'' Mar. Biol. **47**, 97–114.

LETTERS TO THE EDITOR

This Letters section is for publishing (a) brief acoustical research or applied acoustical reports, (b) comments on articles or letters previously published in this Journal, and (c) a reply by the article author to criticism by the Letter author in (b). Extensive reports should be submitted as articles, not in a letter series. Letters are peer-reviewed on the same basis as articles, but usually require less review time before acceptance. Letters cannot exceed four printed pages (approximately 3000–4000 words) including figures, tables, references, and a required abstract of about 100 words.

Robust broadband matched-field localization: Results for a short, sparse vertical array

Brian F. Harrison[a)]
Naval Undersea Warfare Center, Submarine Sonar Department, Code 2121, Building 1320, Newport, Rhode Island 02841

Richard J. Vaccaro and Donald W. Tufts
Department of Electrical Engineering, University of Rhode Island, Kingston, Rhode Island 02881

(Received 13 April 1998; revised 29 March 1999; accepted 6 April 1999)

Matched-field localization is typically applied to signals received by long vertical arrays. A much more challenging problem is the application of these techniques to short vertical arrays. Short arrays require the use of multiple frequencies in localization processing to reduce ambiguities. In addition, any practical localization algorithm must also be robust to environmental uncertainties. In this paper, the results of applying the robust *multiple uncertainty, replica-subspace weighted projections* (MU-RSWP) localization algorithm to the broadband signal/short-array problem are presented. Simulation results for two uncertain shallow-water environments are given using a short five-element array which demonstrate the significant performance improvement in using MU-RSWP over the Bartlett processor. These results serve as an illustration of the applicability of using short arrays, in conjunction with a robust localization algorithm, for matched-field localization in realistic environmental scenarios. © *1999 Acoustical Society of America.* [S0001-4966(99)03007-6]

PACS numbers: 43.30.Wi, 43.60.Gk [SAC-B]

INTRODUCTION

Matched-field processing (MFP) exploits the complex multipath structure of acoustic signal propagation in shallow water for source localization. This processing incorporates the propagation physics which include the environmental parameters of the ocean environment. It is well-known that MFP techniques can be sensitive to uncertainties in the assumed values of the environmental parameters. Therefore, techniques which are robust to uncertainties are required for real-world applications. A survey of MFP localization techniques and issues can be found in Ref. 1.

Typically, MFP techniques are applied to signals received by a long vertical array of sensors. An array which spans the water column would provide the best localization performance with respect to ambiguous sidelobes, since it would provide an adequate sampling of the mode functions. In many applications, the use of a long vertical array is impractical and short arrays must be considered. When a short array which spans only a small portion of the water column is used for MFP, the mode functions can be severely undersampled. This can result in large ambiguities on the range–depth ambiguity surface computed at a single frequency. To help resolve these ambiguities, multiple frequencies must be used. This is accomplished by incoherently averaging ambiguity surfaces computed at widely spaced frequencies across the signal band.

In this paper, we apply the *multiple uncertainty, replica-subspace weighted projections* (MU-RSWP) localization algorithm to the broadband signal/short-array problem. A detailed description of the MU-RSWP algorithm can be found in Ref. 2. The broadband version of MU-RSWP is obtained by simply incoherently averaging MU-RSWP ambiguity surfaces computed at discrete frequencies across the signal band. MU-RSWP employs a two-step estimation process. The first step was derived as a computationally efficient approximation to the maximum *a posteriori* (MAP) processor in the presence of environmental uncertainty. Step two applies a fine-grid search procedure to those regions from step one which exceed a threshold level. We have shown previously that the performance of MU-RSWP is comparable to that of MAP while requiring only a fraction of the computations. MU-RSWP also incorporates a computationally efficient range–depth smoothing in step one for robustness to coarse-grid density.

Another proposed approach for source localization with a short array involves the adaption to this paradigm of an existing robust MFP technique developed for use with

[a)]Electronic mail: harrison_bf@ieee.org

TABLE I. Uncertainty intervals of environmental parameters for NRL environment.

Parameter	Uncertainty interval
water depth	102.5±1 m
surface sound speed	1500±2.5 m/s
bottom sound speed	1480±2.5 m/s
uppermost layer sound speed	1600±10 m/s
lowermost layer sound speed	1750±10 m/s
bottom attenuation	.35±0.1 dB/λ
bottom density	1.75±0.1

narrow-band signals received by arrays which span nearly the entire water column. A computationally intensive modification to the MV-EPC processor[3] has been proposed to address the wideband, short array problem.[4] That approach also assumes *a priori* knowledge of the power spectrum of the signal. The MU-RSWP algorithm can be applied without modification to the broadband, short-array problem in the presence of environmental uncertainty. The two-step search procedure of MU-RSWP is seen to be very effective for the solution of this problem. We present simulation results of the application of MU-RSWP in two shallow-water environments using a broadband signal with a short, sparsely populated vertical array.

I. SIMULATION RESULTS

A. Introduction

Monte Carlo simulation trials were conducted in two simulated environments with uncertainties to demonstrate the effectiveness of MU-RSWP for the broadband, short-array case. The first environment was derived from the Naval Research Laboratory (NRL) benchmark test case GENLMIS.[5] The second environment was modeled after a region in the Gulf of Mexico.[6] In both cases, a nonuniformly spaced five-element array with a 23-meter vertical aperture was considered. The source signal had a bandwidth of 500 Hz from 100–600 Hz. From the signal band, 11 frequency components spaced at 45.5 Hz were selected for processing. Increasing the number of frequency components could result in an increase in performance. However, there is certainly a point of diminishing returns in adding additional frequency components. In general, the number of frequency components selected is dependent upon the available computer resources. An input signal-to-noise ratio of 7 dB per observation was assumed for an observation interval of 200 array snapshots.

For each case, the performance of the MU-RSWP processor was compared to that of the conventional Bartlett processor over a set of 100 Monte Carlo trials. The Bartlett processor assumed the nominal values of the uncertain environmental parameters in its computations. In each trial, a unique randomly selected environmental realization was chosen from the uncertainty intervals of the environmental parameters. A correct localization was defined as an estimate within a neighborhood of ±300 m in range and ±5 m in depth of the true source location.

TABLE II. Correct localization percentages for MU-RSWP vs Bartlett.

Environment	Bartlett	MU-RSWP
NRL	41%	98%
Gulf of Mexico	34%	88%

B. NRL environment

The NRL environment is a three-layer shallow-water environment with a nominal water depth of 102.5 m. The uncertainty intervals of the environmental parameters are given in Table I. The source was located at 8900 m in range and 55 m in depth. In this case, the receiver depths in meters were: 38, 44, 52, 57, and 61. This array only spans approximately 23% of the water column.

The MU-RSWP processor used 100 random realizations of the environment for processing. For the range–depth smoothing, each region was selected to have a width of 65 m in range and 5 m in depth with five sample points across range and two sample points across depth. The total range–depth search region was 5000–10 000 m in range and 0–100 m in depth. This results in a total of 1540 subspace regions. An L_{20} norm was used in the fine-search procedure. The threshold level was set at 95% of the surface maximum.

Table II shows the correct localization percentages for the Bartlett processor and the MU-RSWP processor. The performance of the robust MU-RSWP processor is clearly superior to that of the Bartlett processor. This 98%-correct localization performance is consistent with the results obtained in Ref. 4 for the identical scenario. In the MU-RSWP fine-search step, an average of 13 regions was included, which is less than 1% of the total number of regions. This demonstrates the effectiveness of step one of MU-RSWP in narrowing the search to those regions most likely to contain the true location parameters.

C. Gulf of Mexico environment

The Gulf of Mexico environment is a three-layer shallow-water environment with a nominal water depth of 120.5 m. This environment contained six uncertain environmental parameters. The uncertain environmental parameters and their uncertainty intervals are shown in Table III. For this case, a unique randomly selected source position was chosen in each trial from within the total range–depth search region. The receiving-array sensors were located at depths in meters of: 34, 41, 48, 52, and 57.

A set of 100 random realizations of the environment was used by MU-RSWP for processing. For the range–depth

TABLE III. Uncertainty intervals of environmental parameters for Gulf of Mexico environment.

Parameter	Uncertainty interval
water depth	120.5±5 m
sediment sound speed	1650±5 m/s
rock sound speed	3000±5 m/s
sediment attenuation	0.5±0.05 dB/λ
sediment density	1.85±0.1
rock density	2.2±0.1

smoothing, each region was selected to have a width of 50 m in range and 5 m in depth with five sample points across range and two sample points across depth. The total range–depth search region was 10 000–12 000 m in range and 5–90 m in depth, resulting in 680 subspace regions. A threshold level of 95% of the surface maximum was used with an L_{20} norm for the fine-search procedure.

Table II shows the results of the trials. Again, the performance of MU-RSWP was far superior to that of the Bartlett processor. In this case, an average of 27 regions was included in the MU-RSWP fine-search procedure. This is less than 4% of the total number of regions.

II. CONCLUSION

This paper presented results of applying the MU-RSWP processor to a broadband signal received by a short, sparse vertical array. Simulation results were given for two uncertain shallow-water environments which demonstrated the superior performance of MU-RSWP over the Bartlett processor in the presence of environmental uncertainty. The results show the applicability of using short arrays with a robust algorithm for matched-field localization in realistic environmental scenarios.

[1] A. B. Baggeroer, W. A. Kuperman, and P. N. Mikhalevsky, ''An overview of matched field methods in ocean acoustics,'' IEEE J. Ocean Eng. **18**, 401–424 (1993).

[2] B. F. Harrison, R. J. Vaccaro, and D. W. Tufts, ''Robust matched-field localization in uncertain ocean environments,'' J. Acoust. Soc. Am. **103**, 3721–3724 (1998).

[3] J. L. Krolik, ''Matched-field minimum variance beamforming in a random ocean channel,'' J. Acoust. Soc. Am. **92**, 1408–1419 (1992).

[4] S. P. Czenszak and J. L. Krolik, ''Robust wideband matched-field processing with a short vertical array,'' J. Acoust. Soc. Am. **101**, 749–759 (1997).

[5] M. B. Porter and A. Tolstoy, ''The matched field processing benchmark problems,'' J. Comput. Acoust. **2**, 161–185 (1994).

[6] J. Ianniello, ''A MATLAB version of the KRAKEN normal mode code,'' Technical report TM 94-1096, Naval Undersea Warfare Center, October 1994.

Erratum: "A spectral approach to 3-D object scattering in layered media applied to scattering from submerged spheres" [J. Acoust. Soc. Am. 104, 2105–2113 (1998)]

Nicholas C. Makris
Massachusetts Institute of Technology, Cambridge, Massachusetts 02139

(Received 10 March 1999; accepted for publication 24 March 1999)

[S0001-4966(99)00807-3]

PACS numbers: 43.30.Dr, 43.30.Gv, 43.30.Bp [SAC-B]

The scattered field levels of Figs. 3 and 4 have not been properly normalized to dB *re*: 1 μPa for a source of strength 0 dB *re:* 1 μPa at 1 m. The levels given in Figs. 3(a) and 4(a) are $20\log(4\pi)$ dB too high and those in Figs. 3(b), 4(b)–(d) are $20\log(4\pi)$ dB too low. Additionally, three faint azimuthal beams appear in Fig. 3(b) within roughly 100 m range of the target and within roughly $\pm 45°$ of the *y*-axis. These minor azimuthal asymmetries are not representative of the true single-scattered field but rather are artifacts of a computational bookkeeping error.

Figure 6 below illustrates corrected estimates of the scattered field level for a source strength of 0 dB *re*: 1 μPa at 1 m, via the single-scatter [Eq. (13)] and sonar equation [Eq. (17)] approximations, in forward and backscatter azimuths for the same scenario considered in Fig. 3 of the original paper. Specifically, in backscatter, as well as other nonforward azimuths, the sonar equation yields the same overall structure and level as the single-scattered field, although discrepancies of more than 10 dB occur at some ranges. In the forward azimuth, however, both the structure and level of the sonar equation output depart from the single-scatter results, where the sonar equation typically overestimates the level by more than 10 dB. As a result, the conclusions of the original paper are unaffected by these errata. Moreover, by Babinet's principle, the field levels of Fig. 6(c) should provide a good approximation to both the *backscatter* and *forward scatter* levels of a perfectly reflecting disk, of the same effective projected area and location as the sphere, oriented broadside to the incident azimuth. A comparison of Figs. 6(c) and 6(d) then indicates that the sonar equation should significantly overestimate the *backscattered* level as well as the *forward scatter* level from such a noncompact submerged disk.

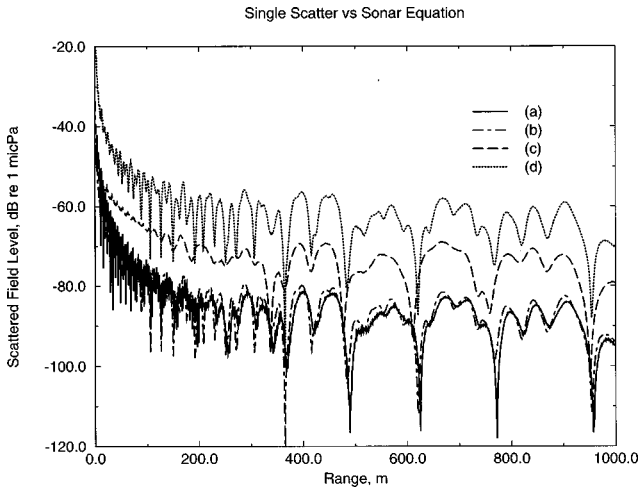

FIG. 6. Scattered field level as a function of range for same scenario as Fig. 3: 10 m radius pressure release sphere submerged in a 100 m deep Pekeris waveguide at $f=300$ Hz with source, receiver, and sphere center all at middle depth in the waveguide. (a) Single-scatter approximation along backscatter azimuth $\phi=180°$. (b) Sonar-equation approximation along backscatter azimuth $\phi=180°$. (c) Single-scatter approximation along forward scatter azimuth $\phi=0°$. (d) Sonar-equation approximation along forward scatter azimuth $\phi=0°$. Conversion to sound pressure level L_p for a source of 0 dB strength is accomplished by setting $L_p=20\log|\Phi_s(\mathbf{r})|+20\log(4\pi)$, where the scattered field $\Phi_s(\mathbf{r})$ is obtained from Eq. (13) in (a) and (c), and from Eq. (17) in (b) and (d).

 0001-4966/99/106(1)/518/1/$15.00